STEELS

Processing, Structure and Performance

Second Edition

George Krauss

STEELS

Processing, Structure, and Performance

Second Edition

George Krauss

ASM International®
Materials Park, Ohio 44073-0002
asminternational.org

First printing, February 2015

Prepared under the direction of the ASM International Technical Book Committee (2014–2015), Chadwick Korthuis, Chair.

ASM International staff who worked on this project include Scott Henry, Director, Content & Knowledge-Based Solutions; Karen Marken, Senior Managing Editor; Sue Sellers, Content Development and Business Coordinator; Madrid Tramble, Manager of Production; Kate Fornadel, Senior Production Coordinator; and Diane Whitelaw, Production Coordinator.

Library of Congress Control Number: 2014957774
ISBN-13: 978-1-62708-083-5
ISBN 10: 1-62708-083-X
SAN: 204-7586

ASM International®
Materials Park, OH 44073-0002
asminternational.org

Printed in the United States of America

Contents

Preface to the Second Edition of *Steels: Processing, Structure, and Performance*

In this twenty-first century, steel, in its many chemistries and forms and as a major material for load-carrying applications, is under intense pressure from many directions: to reduce energy and find just the right time and temperature in processing to achieve the best combination of structure and properties, to optimize alloying, to improve properties for vehicle weight reduction and safety, and to increase life in demanding applications. The last ten years have seen dynamic responses to these challenges, and production, research, development, technical conferences, and publication have not stopped. Hence, a second edition of *Steels: Processing, Structure, and Performance*. Every chapter in the first edition has been examined, and not only has recent information been added, but also important references to past discoveries and insights, not included in the first edition and in danger of being forgotten, have been added and discussed.

Structure is the unifying key to understanding steels, and the need to characterize the many elements of structure continues to expand. Where earlier, microstructure as resolved by light microscopy was emphasized, now macrostructure, crystal structure, substructure, and nanostructure and their length scales are integrated with microstructure as a function of chemistry, processing, and performance. This integration is being accelerated by analysis techniques such as electron backscatter diffraction (EBSD) and atom probe tomography (APT), only widely used since the first edition of *Steels*, as well as improvements in established light and electron microscope techniques and specimen preparation.

This second edition of *Steels* is actually the fourth volume on steels I have authored. The first volume, entitled *Principles of Heat Treatment of Steel*, American Society of Metals, 1980, was a rewritten version of *Principles of Heat Treatment* by M.A. Grossmann and E.C. Bain. As I noted in the preface of the 1980 volume, "*Principles of Heat Treatment* covered developments between 1935 and 1964, and Grossmann, Bain, and their contemporaries did their work so well that the heat treatment and metallurgy of carbon steel was almost taken for granted." Certainly, tremendous advances in understanding steels have occurred, but the statement regarding the expertise of Grossmann and Bain still rings true with respect to hardenability, a field in which austenitic grain size is no longer considered a major factor as outlined by Grossmann and Bain. Reasons for this shift are discussed in this second edition of *Steels*.

Color has been added to the second edition of *Steels*, in part to highlight microstructural features but also because new characterization techniques, such as EBSD and APT, provide so much data that color is necessary to differentiate various parameters. Almost all chapters have been updated with figures and/or discussion to illustrate structures and phenomena as well as to present new information. In addition to hardenability, the peritectic reaction and other steelmaking aspects, some new sheet steel developments, microalloying, boron effects, spherical carbide dispersions, new views of tempering, the strengthening components of tempered martensitic steels, pearlitic wire and rail steels, cracking during primary steel processing, reheat cracking in welds, hydrogen embrittlement, residual-stress development and oxidation in carburizing, and effects of rolling-contact stresses on high-carbon steel microstructures are among the topics that have been added or have received substantial modification. I hope these additions to the tutorial baseline of structures and steel products in the first edition of *Steels* will be of value to experienced ferrous metallurgists as well as new generations of individuals from many backgrounds in the materials and manufacturing communities that must produce, use, and study steel.

I sincerely thank all of my many colleagues at the Colorado School of Mines who have helped with discussions, recommendations of references, and/or by contributing figures: Scott Cowley, Corrine Packard, Brian Gorman, Gary Zito, John Chandler, Lee Rothleutner, Dean Pierce, Steven Thompson, Kip Findley, John Speer, and David Matlock. John Verhoeven, Iowa State University, and Bob Hackenberg, Los Alamos National Laboratory, helped with history; Bob Glodowski, Evraz Sratcor, Inc., with microalloying; Amy Clarke, Los Alamos National Laboratory, with APT figures; Nobuhiro Tsuji, Kyoto University, with EBSD of lath martensite; and Harry Bhadeshia, University of Cambridge, with references on rolling-contact fatigue. Karen Marken, Madrid Tramble, Kate Fornadel, and Scott Henry, ASM International, provided welcome encouragement and

professional expertise for copyediting and production of this second edition of *Steels*. My wife Ruth deserves my deep thanks for her unwavering support during this period of authorship.

George Krauss
Evergreen, Colorado
October 21, 2014

Preface to *Steels: Processing, Structure, and Performance* (2005)

This edition of *Steels* is dedicated to the men and women who make, use, study, and design with steel. It is an entry into the broad, dynamic physical metallurgy of steels, with an attempt to summarize the state-of-the-art just past the turn into the twenty-first century. Eleven new chapters expand the coverage in previous editions, and other chapters have been reorganized and brought up to date. The interrelationships between chemistry, processing, structure, and performance, i.e., the elements of physical metallurgy, are integrated for all the types of steel discussed, but as before, descriptions of the evolution, characterization, and performance of steel microstructures, with increased emphasis on deformation and fracture, are major objectives of this text. Heat treatment remains a vital aspect of the manufacture of steel products, and the coverage of thermal processing and its effect on steels is expanded in this edition. However, heat treatment has been dropped from the title of this edition to reflect a broader view of steels. Also, the chapter on cast irons, included in the 1990 edition, has been dropped in view of the sharper focus on steels.

There have been dramatic changes in steel manufacture in the 15 years since the publication of the 1990 edition. Low-carbon sheet steels have experienced the most dynamic changes: thermal processing of sheet steels on a massive continuous scale has produced new grades with only subtle changes in chemistry. Low-carbon sheet steels, together with strengthening mechanisms, developments in microalloyed forging steels, steels with bainitic and a variety of ferritic microstructures, quench and tempered steel performance, high-carbon steels for rail and ultra-high strength wire, and the causes of low toughness and embrittlement are all discussed in new chapters. I have made some brief comments on the history of steel and

noted the time frame for some important developments. A link to steelmaking and solidification is made in the chapter on the effects of primary processing on steel microstructure.

The text is meant to be informative, readable, up-to-date, and self-contained. Principles, concepts, and understanding of microstructural evolution and performance, within the framework of processing and properties, are illustrated, by plots of data, micrographs, and schematic diagrams. Some scientific and technological background is assumed, and if interested in more information or background, the reader is directed to listed references. Only a small number of references out of the massive literature on ferrous metallurgy have been selected, and a special effort has been made to include references to the most pertinent books, reviews, and technical papers on a given subject. Reference titles that often serve as mini-abstracts of paper content have been included. Each listed reference opens up further reference lists on a given topic.

The activities of the Advanced Steel Processing and Products Research Center, an industry/university cooperative research center at the Colorado School of Mines, have continued to be a vital source of research on steel, and I am grateful for the combined efforts of the industrial sponsors, students, and staff of the Center for their contributions. I thank Professors Steven Liu and John Speer, Colorado School of Mines, for their contribution of figures for this edition; Dr. Young-Kook Lee, Yonsei University, for unpublished work on high-temperature tempering; Dr. Bruce Kiefer, Morgan Construction Company, for his references on Stelmor processing; and Professor Brian Thomas, University of Illinois at Urbana-Champaign, for his references on continuous casting and inclusion-related phenomena. I value very much and am grateful for the continued insights and inspiration provided by my colleague Professor David Matlock at the Colorado School of Mines over the years. The support of my wife, Ruth, and my sons Matthew, Jonathan, Benjamin, and Thomas, with their growing families and expanding lives, is also very gratefully acknowledged.

George Krauss
Evergreen, Colorado
December, 2004

Preface to *Steels: Heat Treatment and Processing Principles* (1990)

The 1980s have been a dynamic period for manufacturing, and it is appropriate that *Principles* be expanded to describe a broader selection of ferrous alloys used in manufacturing. Not only is deeper understanding of the performance of conventionally treated steels now available, but new alloys and new processes also have been developed. For example, new alloys under active development or brought to market in the '80s include duplex stainless steels, microalloyed bar and forging steels, ultrahigh-nitrogen stainless steels, low-cobalt maraging steels, steels with low manganese and silicon that are resistant to temper embrittlement, and austempered ductile cast irons. The success of these new alloys, as well as that of improved conventional steels, is often directly coupled to advances in melting, and the 1980s have seen the widespread adoption of ladle metallurgy and other special steelmaking techniques.

The most dramatic changes in processing have come in the area of surface modification, ranging from improvements in induction heating and gas carburizing to the development of plasma, physical vapor deposition, and laser heating processes. Thermochemical modifications, coatings, solid-state transformation hardening, and rapidly solidified, thin-surface layers are all possible with the new techniques. Thus exciting possibilities exist for manufacturing surfaces with special properties and engineered materials systems incorporating ferrous alloys.

For the revised edition of *Principles of Heat Treatment of Steel* I have added chapters on new surface modification techniques, stainless steels,

tool steels, and cast irons, and have expanded four of the original chapters. Thus the revised text covers many aspects of alloying, processing, and microstructure evolution beyond those involved in conventional heat treatment of carbon steels. Also, the new surface modification techniques are often directed to producing engineered composite systems quite different from traditionally processed steels. In order to reflect the broader scope of the present edition, the title *Steels: Heat Treatment and Processing Principles* was selected. This new title moves steels to a prominent position, and recognizes the importance of processing other than heat treatment.

The principles of microstructure development, and the effects of microstructure on properties and performance, within the context of alloying, phase equilibria, and processing, remain the dominant theme of this book. About 110 new figures have been added, many of them selected to illustrate characteristic and special microstructural features of ferrous alloys. While heat treatment and thermal processing are still of prime importance, solidification, thermomechanical, mechanical, and surface deposition processing are also recognized as major factors which establish structure property relationships in a broad spectrum of ferrous alloys.

Selected literature is cited throughout the text in order to lead readers to in-depth sources of information regarding topics of special interest. Unfortunately, the references cannot recognize all who have contributed to the vast field of processing, heat treatment, and performance of steels. Handbook and manufacturing literature must be referred to for processing details and property tabulations which cannot be included here.

The Army Research Office and National Science Foundation have continued to support steel research at the Colorado School of Mines into the 1980s, and I am grateful for continuing support of the AMAX Foundation for my professorship. In 1984, the Advanced Steel Processing and Products Research Center (ASPPRC), a cooperative industry-university research center, was established at the Colorado School of Mines with a seed grant from the National Science Foundation. This Center has made possible a renewed effort to deepen understanding of steel as a vital manufacturing material. I acknowledge with gratitude the support and interest of the following organizations who were sponsors of ASPPRC at the time of the writing of this second edition: Army Materials Technology Laboratory, Bethlehem Steel Corporation, Carpenter Technology Corporation, Caterpillar Incorporated, Chaparral Steel Company, Chrysler Corporation, Dofasco, Eaton Corporation, Ford Motor Company, Inland Steel Company, Lake Ontario Steel Corporation, National Institute for Standards and Technology, LTV Steel Company, Lukens Steel Company, North Star Steel Company, Rouge Steel Company, Stelco Incorporated, The Timken Company, and United States Steel Division, USX.

With pleasure I acknowledge helpful discussions and contributions of micrographs from a broadened list of colleagues: Tohru Arai (Toyota Research Laboratories), M. Grace Burke (Westinghouse Electric Company),

J.R.T. Branco (CSM), RH. Barkalow and R.W. Kraft (Lehigh University), Tom Bell (University of Birmingham), Scott Diets (CSM), David Hoffmann (Ford Motor Company), A.S. Korhonen (Helsinki University of Technology), Tom Majewski (Caterpillar Incorporated), Jeff McClain (CSM), Bob McGrew (CSM), Tadashi Maki and Imao Tamura (Kyoto University), Eric Mittemeijer (Delft University of Technology), Hisaki Okamoto (Tottori University), Mike Rigsbee (University of Illinois), Mike Shea (General Motors Corporation), Pan Jei (CSM), Steve Thompson (CSM), George Vander Voort (Carpenter Technology Corporation), Abdul Wahid (CSM), and Shen Yun (CSM).

I thank Scott Diets for his help with the figures, and I am especially grateful for the collaboration and support of my colleague, David K. Matlock. We have shared and accomplished much together in the 1980s. My wife Ruth supported this effort in many ways, including the word processing of many revisions of the final manuscript, and I thank her deeply for her help.

George Krauss
Evergreen, Colorado
July 30, 1989

Preface to *Principles of Heat Treatment of Steel* (1980)

This book is a completely rewritten version of *Principles of Heat Treatment* by M. A. Grossmann and E. C. Bain. It is a pleasure to acknowledge the contributions of these authors. Much of their work, especially that concerning the development of hardenability concepts, is incorporated here. *Principles of Heat Treatment* covered developments between 1935 and 1964, and Grossmann, Bain, and their contemporaries did their work so well that the heat treatment and metallurgy of carbon steels was almost taken for granted. Steels, however, are wonderfully complex, and continued effort in the last twenty years has brought deeper understanding of their response to thermal and mechanical treatments. New theoretical approaches to diffusion-controlled and martensitic transformations, the characterization of fine structure by transmission electron microscopy, fractography with the scanning electron microscope, new electron beam microanalysis techniques, fracture toughness testing, continued examination of hardenability, and the relationship of microstructure and fine structure to strength, toughness, and ductility are all areas, highly developed only in the last twenty years, that I have attempted to build onto the solid foundations of steel heat treatment developed by earlier workers. My approach has been to develop the structure-property-processing relationships that underlie the many heat treatments applied to steels. The origin and characterization of microstructures are emphasized because they are so often forgotten as the source of the handbook graphs and tables of processing parameters and properties.

The give-and-take of many conferences and the contributions of many investigators to the literature have been the basis for our growing understanding of steels and their behavior. I have drawn widely from published

sources and through the cited references hope to recognize at least some university and industrial scientists and their contributions. The reference lists are by no means complete, but every paper opens up an area by listing tens or even hundreds of additional references.

Especially rewarding has been my association with other investigators. Morris Cohen initiated my interest in steel, and the enthusiasm of my colleagues and students has sustained that interest. I have learned from every thesis investigation, and examples of the work of my students are shown throughout this book.

In recent years I have benefited much from association with the treatment activities of the American Society for Metals, first through membership on the Heat Treatment Technical Division Council, and more recently as editor of the *Journal of Heat Treating.* These associations have made me aware of the scope and sophistication of new approaches to the heat treatment of steels, and I am especially grateful to Norman Kates, Dale Breen, Jon Dossett, and Joe Riopelle for their introduction to the demanding, practical world of heat treatment.

A university research effort is very much dependent on outside support. I gratefully acknowledge the Army Research Office, the National Science Foundation, the Bethlehem Steel Corporation, the AMAX Foundation, and the American Iron and Steel Institute for the support that has enabled me and my students to remain actively involved in research on the behavior of steels. I acknowledge also fruitful discussions with Professors Glenn Edwards, Tom Bell, and Norman Breyer concerning parts of the text and am grateful for micrographs supplied by Professors R.W.K. Honeycombe, Robert Hehemann, and Marvin Wayman. Mark Geib deserves special mention for his help with some of the figures. Finally, I am deeply grateful to my wife, Ruth, for her competent assistance, her unwavering support, and the typing of the manuscript—all given between a busy schedule of rehearsals and performances of the Central City Opera and the Evergreen Chorale.

George Krauss
Evergreen, Colorado
September 25, 1979

About the Author

GEORGE KRAUSS, *FASM*
ASM President (1996–97)

Dr. George Krauss is currently University Emeritus Professor at the Colorado School of Mines and a metallurgical consultant specializing in steel microstructural systems. He received the B.S. in metallurgical engineering from Lehigh University in 1955 and the M.S. and Sc.D. degrees in metallurgy from the Massachusetts Institute of Technology in 1958 and 1961, respectively, after working at the Superior Tube Company as a development engineer in 1956. In 1962–63, he was an NSF Postdoctoral Fellow at the Max Planck Institut für Eisenforschung in Düsseldorf, Germany. He served at Lehigh University as assistant professor, associate professor, and professor of metallurgy and materials science from 1963 to 1975, and in 1975, joined the faculty of the Colorado School of Mines as the AMAX foundation professor in physical metallurgy. He was the John Henry Moore Professor of Metallurgical and Materials Engineering at the time of his retirement from the Colorado School of Mines in 1997.

In 1984, Dr. Krauss was a principal in the establishment of the Advanced Steel Processing and Products Research Center, a National Science Foundation Industry-University cooperative research center at the Colorado School of Mines, and served as its first director until 1993. In addition to the three editions of the present volume, he coauthored the book *Tool Steels, Fifth Edition,* ASM International, 1998, and edited or coedited conference volumes on tempering of steel, carburizing, zinc-based coatings on steel, and microalloyed forging steels. He has published over 300 papers and lectured widely in technical conferences, universities, corporations, and ASM International chapters, including a number of keynote, invited and honorary lectures. He presented the Edward DeMille

Campbell Memorial Lecture of ASM International in 2000 and the Howe Memorial Lecture of ISS in 2003.

Dr. Krauss has served as the president of the International Federation of Heat Treatment and Surface Engineering (IFHTSE), 1989–91, and as president of ASM International, 1996–97. He is Fellow of ASM International, TMS, and IFHTSE. He has been awarded the Adolf Martens Medal of the German Society for Heat Treatment and Materials, the Charles S. Barrett Silver Medal of the Rocky Mountain Chapter of ASM, the George Brown Gold Medal of the Colorado School of Mines, and several other professional and teaching awards, including the ASM Albert Easton White Distinguished Teacher Award in 1999. He is an Honorary Member of the Iron and Steel Institute of Japan, a Distinguished Member of AIST, an Honorary Member of ASM International, and an Honorary Member of the Japan Institute of Metals.

CHAPTER 1

Introduction—Purpose of Text, Microstructure and Analysis, Steel Definitions, and Specifications

Purpose of This Book

THE PURPOSE OF THIS BOOK is to describe the physical metallurgy, i.e., the processing-structure-property relationships, of steels. *Processing* refers to the manufacturing steps used to produce a finished steel product and includes casting, hot and cold work (mechanical and thermomechanical processing), and all sorts of heat treatment (thermal processing), some of which involves changes in surface chemistry (thermochemical processing). Steelmaking is the important first step in processing and has evolved over centuries to produce today huge tonnages of high-quality steel. Thus steelmaking, its history, and its effect on the structure of solid steel are discussed briefly in subsequent chapters.

Microstructure of Steels

Size Scales

Together with steel chemistry, processing steps create the many microstructures that may form in each of the great variety of steels. The term

microstructure derives its meaning from the fact that microscopy is required to resolve characteristic features of steel internal structures that range in size from those resolvable with the unaided eye to features resolvable only by light and electron microscopy. The unaided eye can resolve 0.1 mm (0.004 in.), and more closely spaced features require microscopy of some sort. The most appropriate unit for many microstructural features of steel, for example, grain or crystal size, is the micron or micrometer (μm), 10^{-6} m, or 0.001 mm (0.00004 in.), well below features that are resolvable by eye. The light microscope has a resolution on the order of 0.5 μm and therefore is quite adequate for the characterization of many features of steel microstructures.

However, many features that affect performance are too fine to be resolved in the light microscope, for example, fine precipitates and crystal defects, and for the characterization of such features, electron microscopy must be used. In view of the fact that light microscopy was the only technique initially available, finer features now resolvable are often referred to as substructures. The electron microscope can resolve features down to the order of atomic dimensions, around one nanometer (nm), 10^{-9} m, or 0.001 μm, and therefore effectively covers the size range of structures below that resolvable in the light microscope.

Instrumentation

The above discussion relates to the size scales of the structural components that make up a given microstructure. This section briefly describes the many approaches and instruments now available to characterize not only sizes, morphology, and distribution of microstructural features but also the crystallography and the chemistry of the features. The availability of these instruments and how and what they reveal makes possible more and more complete characterization of steel structures. Examples of the structures shown by the various techniques are given throughout this book, and the techniques used to produce the images are identified in the figure captions.

Scanning Electron Microscopy. Microstructures on polished and etched steel surfaces, shown by variations in reflected light within the resolution limits of the light microscope, are well characterized (Ref 1.1, 1.2). Scanning Electron Microscopes (SEM) raster electron beams over surface features and are capable of zooming up from macroscopic features through structures on the order of size covered by light microscopy through features finer than resolvable in the light microscope. Good depth of field is provided in SEM, and therefore not only features on polished and subsequently etched surfaces but also very rough surfaces, as produced by fracture, can be evaluated (Ref 1.3).

As will be noted in the next section of this Chapter, steels are composed of many chemical elements, both beneficial and detrimental, and therefore the distribution of these elements in steel microstructures is extremely

important. In electron microscopes chemical compositions of selected microstructural features are determined by high energy electron beam interactions that cause inner shell electrons of the various atoms to be ejected with the release of X-ray energies and wavelengths characteristic of the atoms (Ref 1.4). In the scanning electron microscope the characteristic energy spectra are typically measured by solid state detectors in the process referred to as Energy Dispersive Spectroscopy (EDS). In Electron Probe Microanalyzers the spectra are resolved with better resolution by diffraction of the characteristic Xrays from single crystals in a process referred to as Wavelength Dispersive Spectroscopy (WDS) (Ref 1.3).

Auger Electron Spectroscopy. The X-ray spectra generated from the atom inner shell electrons in SEM come from volumes relatively deep in specimens, distances on the order of one micron from the specimen surfaces. However, there are electron instruments that are designed to measure spectra produced by ejection of more loosely bound outer shell electrons, electrons termed Auger electrons (Ref 1.5). These low energy electrons come from very close to specimen surfaces, on the order of a few nanometers, and therefore Auger Electron Spectroscopy (AES) is capable of showing thin concentrations of low atomic number elements exposed at fracture surfaces in specimens broken under high vacuum in Auger electron microscopes. The latter experimental technique has been very important in showing impurity atom segregation on austenitic grain boundaries, segregation phenomena that are responsible for various types of brittle grain boundary fracture in steels as discussed in Chapter 19, "Low Toughness and Embrittlement Phenomena in Steel."

Transmission Electron Microscopes. The analytical techniques discussed above all involve examination of specimen surfaces. In contrast, Transmission Electron Microscopes (TEM) make possible the evaluation of fine microstructural features within volumes of steel specimens made thin enough to permit the passage of incident high energy electron beams. Images are produced by electron diffraction from the crystal structures of the features, and diffraction patterns that identify crystal types and orientation are generated (Ref 1.6). TEM is the only analytical technique that makes possible the direct imaging of crystal defects termed dislocations. Traditionally thin foil specimens have been made by sectioning of bulk specimens and electropolishing. More recently specimens from selected small areas have been removed from bulk samples in Focused Ion Beam (FIB) instruments that use Liquid Metal Ion Sources (LMIS) of gallium to remove and thin specimens for examination in TEM (Ref 1.7).

Electron Backscatter Diffraction (EBSD). More recently, scanning electron microscopes have been developed to characterize variations in crystal orientations between microstructural features and substructures in steels. The technique used is referred to as Electron Backscatter Diffraction (EBSD) and is based on precise computer indexing of diffraction patterns produced by backscattered electrons generated by stepping the incident electron beam across specimen surfaces (Ref 1.8). Differences in

orientations of areas as close as 50 nm can be measured in new field emission SEMs. Although EBSD can be applied to thin foil analysis in the TEM, specimen preparation for the application of the technique in the SEM is not as demanding.

Atom Probe Tomography (APT). Atom Probe Tomography (APT) is a powerful technique now widely used to establish atomic level distributions of various types of atoms. Atoms are evaporated from thin needle-shaped specimens by pulsed electric fields or lasers, identified by differences in time of flight of the atoms based on their atomic weight differences, and assigned to locations in three-dimensional, high-magnification reconstructions of microstructures (Ref 1.9, 1.10)

All of the above analytical techniques and instruments have been described very briefly, primarily to indicate the type of information and how that information from each technique and instrument is obtained. Each technique and the specimen preparation for that technique are based on considerable other published theoretical and practical information, as described in detail in the listed references.

Integration of Microstructure into the Physical Metallurgy of Steel

This book begins by describing the phases or crystals of unique chemistry and structure that most commonly form in steels. These phases are arranged by processing to produce characteristic microstructures. The microstructures produced by solidification, and the solid-state transformations that produce microstructures consisting of ferrite, pearlite, bainite, and martensite, are then considered, followed by chapters that describe types of steels that are based on the production of the various types of microstructures. Properties and performance depend directly on microstructure, and therefore, microstructure-property interrelationships are incorporated into the descriptions of the various types of steel. Because steels are designed primarily for structures or load-bearing applications, attention is also paid to atomic-scale strengthening, deformation, and fracture mechanisms in the microstructural systems designed for specific applications.

Steels—Definitions

Steels are defined primarily by chemical composition, namely, that they are alloys composed of iron and other elements. For the structural and heat treatable steels of major interest in this book, carbon is an essential alloying element; thus steel may be defined as an alloy of iron and small amounts of carbon and other elements. Carbon steels are traditionally bracketed in carbon content, from negligible to about 2 wt%. Alloys without carbon are traditionally termed irons, but this boundary is challenged

by the ability of modern steelmaking to produce ultra-low carbon or interstitial-free steels, with carbon levels in the parts per million. Iron alloys containing more than 2 wt% C are called cast irons because of their dominant iron content, low melting points, and good castability. However, cast irons historically were brittle, a characteristic that differentiated them from steels with good combinations of strength and ductility. Again, the basis for this historical differentiation is challenged by modern technology: good foundry practice produces nodular and austempered ductile cast irons with good combinations of strength and toughness.

Carbon steels fall into two groups: plain carbon steels and alloy steels. Plain carbon steels, for bar and forging applications, are defined as alloys with definite ranges of carbon and a maximum of 1.65 wt% Mn, a maximum of 0.60 wt% Si, a maximum of 0.60 wt% Cu, and maxima in sulfur and phosphorus (Ref 1.11). Immediately, the latter definition shows that elements other than iron and carbon are important for the commercial characterization of steel. Alloy steels also have definite ranges of carbon and limits on manganese, silicon, copper, phosphorus, and sulfur but may also contain definite ranges or minimum quantities of aluminum, chromium, cobalt, niobium, molybdenum, nickel, titanium, tungsten, vanadium, zirconium, or any other element added to obtain a desired alloying effect (Ref 1.11). The maximum values of the ranges for the various alloying elements more accurately describe the alloy steels as low-alloy steels. Important alloy systems covered in this book in addition to carbon and alloy steels are the stainless steels and tool steels, each much more heavily alloyed than carbon or alloy steels described previously. The ranges of chemical composition for stainless and tool steels are described in later chapters.

The preceding discussion shows the great importance of defining steels by their chemistry and makes the tacit assumption that the chemistry of a steel component is uniform throughout the component. While the latter assumption may be true in the liquid state, in the solid state, alloying and residual elements are distributed non-uniformly throughout the microstructure. Solid steels consist of crystals of iron, ferrite, and/or austenite as described in Chapter 3, "Phases and Structures," and crystals of other elements incorporated into the matrix of iron crystals to produce unique microstructures. Thus, another view of steels is that they are alloys that consist of crystals of iron and other elements. Non-uniformity in microstructure may be a result of solidification or diffusion-controlled solid-state phase transformations, as described in subsequent chapters. All of the many chemical elements present in liquid steels produced by steelmaking are incorporated somewhere into the crystalline solid microstructure, sometimes by design for beneficial purposes, sometimes causing detrimental effects on performance and fracture. The beneficial effects are attributed to alloying elements (for example, the carbon, manganese, and silicon in carbon steels), and the detrimental effects in carbon steels are attributed to residual or impurity elements (for example, sulfur, phosphorus, and copper), depending on amount and distribution.

Steel Specifications

A widely used system for designating carbon and alloy steel grades has been developed by the American Iron and Steel Institute (AISI) and the Society of Automotive Engineers (SAE). Because AISI does not write specifications, currently only SAE designations are used (Ref 1.12). The SAE system consists of a four-digit AISI/SAE numbering system for the various chemical grades of carbon and alloy steels. The first two digits specify the major alloying elements, and if none are present, as for plain carbon steels, the first two digits are 10. The second two digits specify nominal carbon contents in hundredths of a percent. Table 1.1 presents the SAE system for carbon and alloy steels.

Much more information about the chemistry, processing, properties, and quality of the various grades of steel is necessary than just the nominal compositions listed in Table 1.1. For example, because exact amounts

Table 1.1 SAE-AISI designations and alloying elements in carbon and low-alloy carbon steels

Numerals and digits	Type of steel and nominal alloy content, %
Carbon steels	
10*xx*(a)	Plain carbon (Mn 1.00 max)
11*xx*	Resulfurized
12xx	Resulfurized and rephosphorized
15*xx*	Plain carbon (max Mn range: 1.00–1.65)
Manganese steels	
13*xx*	Mn 1.75
Nickel steels	
23*xx*	Ni 3.50
25*xx*	Ni 5.00
Nickel-chromium steels	
31*xx*	Ni 1.25; Cr 0.65 and 0.80
32*xx*	Ni 1.75; Cr 1.07
33*xx*	Ni 3.50; Cr 1.50 and 1.57
34*xx*	Ni 3.00; Cr 0.77
Molybdenum steels	
40*xx*	Mo 0.20 and 0.25
44*xx*	Mo 0.40 and 0.52
Chromium-molybdenum steels	
41*xx*	Cr 0.50, 0.80, and 0.95; Mo 0.12, 0.20, 0.25, and 0.30
Nickel-chromium-molybdenum steels	
43*xx*	Ni 1.82; Cr 0.50 and 0.80; Mo 0.25
43BV*xx*	Ni 1.82; Cr 0.50; Mo 0.12 and 0.25; V 0.03 min
47*xx*	Ni 1.05; Cr 0.45; Mo 0.20 and 0.35
81*xx*	Ni 0.30; Cr 0.40; Mo 0.12
86*xx*	Ni 0.55; Cr 0.50; Mo 0.20
87*xx*	Ni 0.55; Cr 0.50; Mo 0.25
88*xx*	Ni 0.55; Cr 0.50; Mo 0.35
93*xx*	Ni 3.25; Cr 1.20; Mo 0.12
94*xx*	Ni 0.45; Cr 0.40; Mo 0.12
97*xx*	Ni 0.55; Cr 0.20; Mo 0.20
98*xx*	Ni 1.00; Cr 0.80; Mo 0.25
Nickel-molybdenum steels	
46*xx*	Ni 0.85 and 1.82; Mo 0.20 and 0.25
48*xx*	Ni 3.50; Mo 0.25
Chromium steels	
50*xx*	Cr 0.27, 0.40, 0.50, and 0.65
51*xx*	Cr 0.80, 0.87, 0.92, 0.95, 1.00, and 1.05
Chromium (bearing) steels	
50xx	Cr Δ0.50 } C 1.00 min
51xx	Cr 1.02 } C 1.00 min
52xxx	Cr 1.45 } C 1.00 min
Chromium-vanadium steels	
61*xx*	Cr 0.60, 0.80, and 0.95; V 0.10 and 0.15 min
Tungsten-chromium steel	
72*xx*	W 1.75; Cr 0.75
Silicon-manganese steels	
92*xx*	Si 1.40 and 2.00; Mn 0.65, 0.82, and 0.85; Cr 0 and 0.65
High-strength low-alloy steels	
9*xx*	Various SAE grades
Boron steels	
*xx*B*xx*	B denotes boron steel
Leaded steels	
*xx*L*xx*	L denotes leaded steel

(a) The *xx* in the last two digits of these designations indicates that the carbon content (in hundredths of a percent) is to be inserted.
Source: Ref 1.13

Table 1.2 UNS Designations for ferrous metals and alloys

UNS designation	Description
Ferrous metals	
Dxxxxx	Specified mechanical properties steels
Fxxxxx	Cast irons
Gxxxxx	SAE and Former AISI carbon and alloy steels (except tool steels)
Hxxxxx	AISI H-steels
Jxxxxx	Cast steels
Kxxxxx	Miscellaneous steels and ferrous alloys
Sxxxxx	Heat and corrosion resistant (stainless) steels
Txxxxx	Tool steels
Welding filler metals	
Wxxxxx	Welding filler metals, covered and tubular electrodes classified by weld deposit composition

Source: Ref 1.14.

of elements cannot be produced commercially, acceptable ranges of carbon and other elements for a given grade must be specified. Such specifications are written not only by SAE but also by other organizations that represent various user groups of steels. Such organizations and specification systems include the American Petroleum Institute (API), the Steel Founders Society of America (SFSA), Aerospace Materials Specifications (AMS), the American National Standards Institute (ANSI), the American Society of Mechanical Engineers (ASME), the American Society for Testing and Materials (ASTM), the American Welding Society (AWS), and Military Specification (MIL) (Ref 1.12, 114). Many countries throughout the world have their own unique specification organizations and designation systems (Ref. 1.15).

There is considerable overlap, as well as differences, among the steels in the specifications written by various organizations, not only in the United States but also in Europe and Asia. As a result, the Unified Numbering System (UNS) has been developed to cross reference various numbering systems used to identify similar grades of steel. The UNS system is alphanumeric, with the prefix letter describing classes of alloys, and the digits may incorporate SAE digits and other alloy characteristics. Table 1.2 lists UNS designations for ferrous metals and alloys. Cross-references for American and international specifications for similar grades of steel are available in references 1.12 to 1.16.

REFERENCES

1.1 L. E. Samuels, *Light Microscopy of Carbon Steels*, ASM International, 1999

1.2 G. F. Vander Voort, *Metallography: Principles and Practice,* ASM International, 1984.

1.3 J. Goldstein, D. E. Newbury, D. C. Joy, and C. E. Lyman, *Scanning Electron Microscopy and X-ray Microanalysis*, *Third Edition,* Plenum Press, New York, 2007

1.4 B. D. Cullity and D. R. Stock, *Elements of X-ray Diffraction, Third Edition*, Prentice Hall, Upper Saddle River, NJ, 2001
1.5 J. C. Vickerman, *Surface Analysis-The Principle Techniques*, John Wiley & Sons, 1997
1.6 D. B. Williams and C. B. Carter, *Transmission Electron Microscopy, A Text for Materials Science, Second Edition*, Springer, 2009
1.7 L. A. Giannuzzi and F. A. Stevie, *Introduction to Focused Ion Beams: Instrumentation, Theory, Techniques and Practice*, Springer, 2005.
1.8 *Electron Backscatter Diffraction in Materials Science*, A. J. Schwartz, M. Kumar, and B. L. Adams, Editors, Kluwer Academic/Plenum Publishers, New York, 2000.
1.9 M. K. Miller, A. Cerezo, M. G. Hetherington, and G. D. W. Smith, *Atom Probe Field Ion Microscopy*, Oxford University Press, Oxford, 1996.
1.10 M. K. Miller, *Atom Probe Tomography: Analysis at the Atomic Level*, Kluwer Academic/Plenum Publishers, New York, 2000.
1.11 *Steel Bar Product Guidelines,* AIST, Warrendale, PA, 2010
1.12 *Metals and Alloys in the Unified Numbering System*, 12th Ed., SAE International, 2012
1.13 *Properties and Selection: Irons, Steels, and High-Performance Alloys,* Vol 1, *ASM Handbook,* ASM International, 1990
1.14 *Handbook of Comparative World Steel Standards,* 2nd ed., John E. Bringas, Ed., ASTM International, 2002
1.15 *Worldwide Guide to Equivalent Irons and Steels,* 5th ed., ASM International, 2006
1.16 C. W. Wegst, *Stahlschlüssel (Key to Steel)*, ASM International, 2013

CHAPTER **2**

History and Primary Steel Processing

STEEL, a workable, strong combination of iron and carbon, as noted in Chapter 1, "Introduction: Purpose of Text, Microstructure and Analysis, Steel Definitions and Specifications," started to replace bronze, the first technologically important metal, around 1200 B.C. (Ref 2.1, 2.2). Although iron was known and used for several millennia prior to that time, the production of steel required first the making of iron from its ores, followed by the addition of carbon to make steel. Finally, to demonstrate that in fact steel had been produced, quenching from a temperature high enough to produce hardness greater than attainable in iron, which is not hardenable, was required. Maddin (Ref 2.1) published a photograph of a miner's pick from northern Galilee, dated from the thirteenth to twelfth century B.C., that was shown to consist of martensite, a microstructure that is now well established as that of hardened medium- and high-carbon steels.

The early production of iron from its ores was difficult because the temperatures required for liquid iron and steel production were unattainable. Therefore, iron oxide ores were reduced with charcoal by solid-state smelting that produced iron with low-carbon content and high densities of entrapped slag inclusions. The inclusions were then fragmented, dispersed, and removed by heavy hammering or forging to produce wrought iron. In an early process in India, about 350 B.C., carbon was added to wrought iron to produce *wootz steel* by carburizing in crucibles with charcoal or rice husks (Ref 2.1, 2.2). Similar processing in crucibles to produce small batches of steel for weapons and tools continued well into the nineteenth century. In Europe, carburized wrought iron was referred to as blister steel because of the appearance of blisters or scale on the steel surfaces. Short lengths of blister steel were sometimes stacked, forged, and welded to produce the product referred to as *shear steel* (Ref 2.3).

Despite the difficulties in producing even small batches of steel for almost two millennia, early steelmakers and smiths within this period produced remarkable steel objects. In particular, Damascus and Japanese swords not only had sharp cutting edges, high hardness and strength, and good fracture resistance or toughness but also were objects of great beauty. Damascus swords, first crafted around 500 A.D., were forged from small blocks of high-carbon wootz steel (Ref 2.2, 2.4–2.7). The beautiful dark and white patterns that decorate the blades of the swords were the results of a banded microstructure. Recent scholarship has shown that the unique appearance of the swords is due to bands of fine, dispersed alloy carbides, which on etching appear white, and alternating bands of pearlite, with its fine-scale lamellar structure of alternating crystals of ferrite and cementite, which on etching appear dark. The microstructures that produce the white and dark patterns are attributed to chemical variations produced by solidification and banding in the wootz steel (Ref 2.6, 2.7). Japanese swords of great utility and beauty were produced by layer welding of high- and low-carbon steels in multiple forging steps, a process well documented in the period 900 to 1000 A.D., when sword makers began to inscribe their names on blades (Ref 2.8).

Eventually, blast furnaces that produced cast iron in large quantities for intensive industrial development in the eighteenth and early nineteenth centuries were developed (Ref 2.9–2.11). Iron ore was converted by reduction with blasts of air, charcoal, and limestone to produce cast iron in small ingots, resembling pigs, thus giving the product the name *pig iron*. The high-carbon content of cast iron lowered the melting temperatures of iron and made it readily liquid and castable. High graphite or carbide contents in solidified microstructures, together with high silicon and phosphorous contents, made cast iron too brittle to be workable. Cast irons were also brittle under tensile loads but provided excellent service under compressive loads. A beautiful example of the structural use of cast iron, where the components were designed for compressive loading, is the iron bridge built over the Severn River by Abraham Darby III, 1778 to 1780, at Coalbrookdale, England (Fig. 2.1) (Ref 2.12). Although it was soon shown to be inferior to steels, prior to the mid-nineteenth century all iron-based structures, and especially rail, were made from cast iron.

The preceding discussion shows that the bracketing of the carbon content that defined steels, from a negligible amount to about 2.0 wt% (as noted in Chapter 1, "Introduction: Purpose of Text, Microstructure and Analysis, Steel Definitions and Specifications,"), was due to processing limitations and the inability to achieve the high temperatures necessary for the direct production of liquid steel. This scenario changed dramatically in the second half of the nineteenth century when modern, high-volume liquid steelmaking replaced the earlier steel production methods. In 1856,

Fig. 2.1 The iron bridge at Coalbrookdale, England, built in 1778–1780.

Bessemer patented a process in which hot air was blown through molten pig iron to reduce carbon and silicon content; in 1858, Siemens first successfully operated an open hearth furnace in which solid or liquid pig iron and scrap were melted with combusted producer gas. In later modifications, the oxygen for the conversion of the pig iron to liquid steel was provided by iron ore. Excellent, detailed accounts of the historical development and use of the Bessemer and Siemens steelmaking processes are provided in Ref 2.10 and 2.11.

The key factor in the production of steel by the Bessemer and Siemens processes, as in all subsequent steelmaking processes, is the oxidation and removal of carbon and other elements such as the high contents of silicon, manganese, and phosphorus in pig iron (hot metal) and scrap charges to produce liquid steel of the proper composition. Carbon is removed as CO gas, and oxides of the other elements are separated into molten slag fluxed with CaO. For the oxidized liquid steel to be castable and of high quality, it must be deoxidized as a final processing step. Additions of ferromanganese, ferrosilicon, silicomanganese, and aluminum are used as deoxidants, with aluminum being the most powerful deoxidant and producing the lowest levels of residual oxygen, 2 to 4 ppm, in solid steel. The fundamentals and thermodynamics of steelmaking are described in detail by Turkdogan (Ref 2.13).

The Bessemer and Siemens processes satisfied the ever-increasing demands for steel for a century. Steel rails (much better than cast iron rails),

the beams required for buildings and bridges, and the steel for machines and vehicles were all produced by those steelmaking processes. Concomitant with the growth and improvements of these steelmaking processes in the latter half of the nineteenth century was the exciting development and application of the analytical techniques that were important to the other parts of the physical metallurgy equation: techniques that made possible the characterization of structure and properties.

The Early Metallographers—Naming of Phases and Microstructures in Steels

The application of light microscopes to the examination of polished and etched sections of irons and steels created the field of metallography that made possible the characterization of microstructure. Cyril Stanley Smith (Ref 2.14) describes the efforts that led to the remarkable discoveries of the early metallographers, including Henry Clifton Sorby (1826–1908) of England, Dimitri Tschernoff (1839–1921) of Russia, J.A. Brinnell (1849–1925) of Sweden, Adolf Martens (1850–1914) of Germany, Floris Osmond (1849–1912) of France, and Henry Marion Howe (1848–1922) and Albert Sauveur (1863–1939) of the United States. This list includes only a small number of the pioneers deeply involved in understanding steel but demonstrates the great international effort of the period. Out of their careful metallographic observations and thermal analyses came the science of the complex metallurgy of steel, which was dependent not only on room-temperature observations but also on high-temperature crystal structure changes. There were misinterpretations and arguments, as documented by Smith, but eventually the scientific framework of steel structure was established.

The need for correlations between microstructures and properties produced by variations in steel chemistry and heat treatment drove the parallel development of standardized testing techniques. A few of the early tests are used to this day, including Brinnell hardness testing, V-notch impact testing by George Augustin Albert Charpy (1865–1945), tensile testing by Tinius Olson (1845–1932) and end-quench hardenability testing by Walter E. Jominy (1893–1976)

An important result of the early metallographers was the naming of the phases and multiphase microstructures found in steels (Ref 2.14). Howe, 1888, suggested the names *ferrite*, *cementite*, and *pearlite* for the phases and structures found in slowly cooled steels, and Osmond, in 1895, suggested *martensite* in honor of Martens for the structure found in quenched and hardened steels. In 1901, Osmond suggested *austenite* in honor of William Roberts-Austen for the high-temperature crystal structure of steel. These names for the various phases and microstructures have been

accepted and are used to this day. In 1934, a unique microstructure of ferrite and cementite was named "bainite" in honor of Edgar C. Bain by his colleagues at the United States Steel Corporation. Although bainite is generically described as a microstructure consisting of ferrite and nonlamellar carbides, and martensite is defined as the result of a diffusionless shear transformation, differences in morphologies produced as a function of composition and transformation temperature required further terms: *upper* and *lower* bainite, and *lath* and *plate* martensite. These phases and microstructures are described in detail in later chapters of this book. The terms *sorbite* and *troostite* were used for fine forms of pearlite or tempered martensite but are no longer used today.

Good reviews of the early history of the physical metallurgy of steels, the naming of the phases and microstructures, and the early investigators involved in that effort, in addition to the review by Smith (Ref 2.14), have been written by Noel Kennon (Ref 2.15), John Stubbles (Ref 2.16), and Robert Hackenberg (Ref 2.17).

Current Steelmaking

New steelmaking processes introduced in the second half of the twentieth century have made the early steelmaking processes obsolete. In 1952, in the Austrian steel plants of Linz and Donawitz, oxygen–instead of the air used in Bessemer converters—was introduced by immersion of lances in charges of hot metal and scrap. This steelmaking process and further modifications of oxygen steelmaking are referred to as the *LD process* or, in the United States, as the *basic oxygen furnace (BOF) process* (Ref 2.13). The BOF process requires blast furnaces to provide hot metal, and blast furnaces in turn require plants to provide the coke necessary for blast furnace operation.

Electric arc furnace (EAF) steelmaking does not require coke or hot metal and relies solely on scrap steel charges. As a result of such increased efficiency, EAF steelmaking is now almost exclusively used to produce the blooms and billets that are hot rolled to bar for rods, wire, and forgings. The EAF is now used mainly to melt scrap, and the resulting molten steel is refined in separate ladles in processing referred to as secondary, or ladle steelmaking (Ref 2.10, 2.18). Ladle metallurgy may involve many steps, including stirring by argon gas bubbling to homogenize temperature and composition, addition of alloying elements, injection of calcium silicide or lime for desulfurization and inclusion shape control, deoxidation, and vacuum degassing to remove hydrogen that causes embrittlement in later stages of processing or application. Thus, even though the source of the EAF steel is scrap of varying composition and purity, very high-quality steel is produced by EAF melting and ladle steelmaking.

Concurrent with the development of BOF and EAF steelmaking in the latter part of the twentieth century was the use of continuous casting. Figure 2.2 schematically compares ingot casting to continuous casting and shows the great efficiencies that are accomplished by the use of the latter (Ref 2.19). Slabs for subsequent rolling to flat-rolled sheet and plate products, and blooms and billets for subsequent rolling to long products such as bar and rod, are directly produced by continuous casting without roughing or primary hot rolling. Reductions in continuously-cast section size continue to this day. In 1989, the Nucor Steel Company commissioned the first thin-slab casting mill in Crawfordsville, Ind., and at the time of this writing, continuous casting to thin strip is under intensive development. Figure 2.3 shows schematically the dramatic reductions in hot work required with continuous casting of smaller and smaller sections (Ref 2.19). Ref 2.20 presents a recent review of the development of strip casting, the newest addition to steelmaking technology. These developments and the turbulent economic times that drove the changes in steel production in the second half of the twentieth century are described by John Stubbles (Ref 2.19).

The preceding discussion briefly reviews the history of steelmaking and the changes in primary steelmaking that led to the production of modern steels. The effects of primary steelmaking on the microstructures of finished steels, namely inclusion incorporation and interdendritic segregation, are discussed in a later chapter.

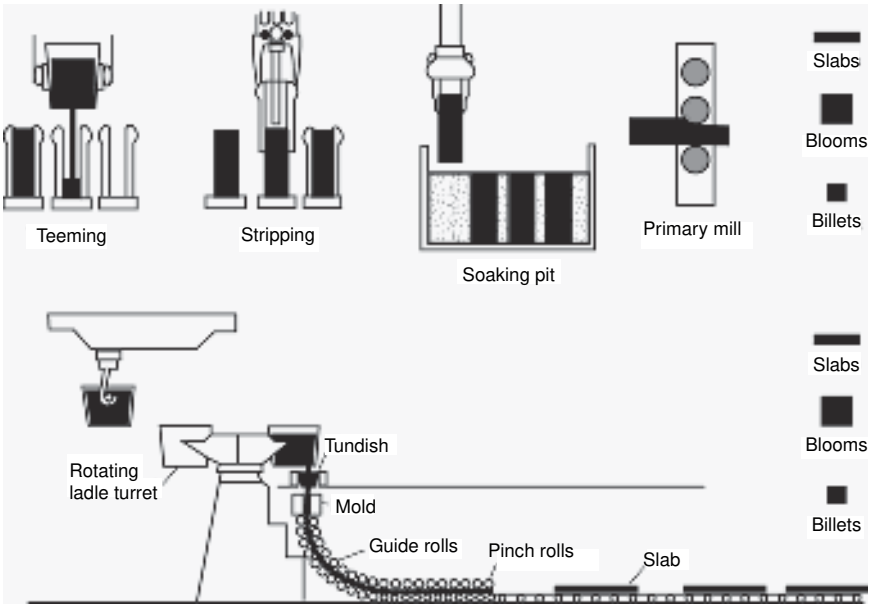

Fig. 2.2 Comparison of ingot and continuous casting of steel. Source: Ref 2.19

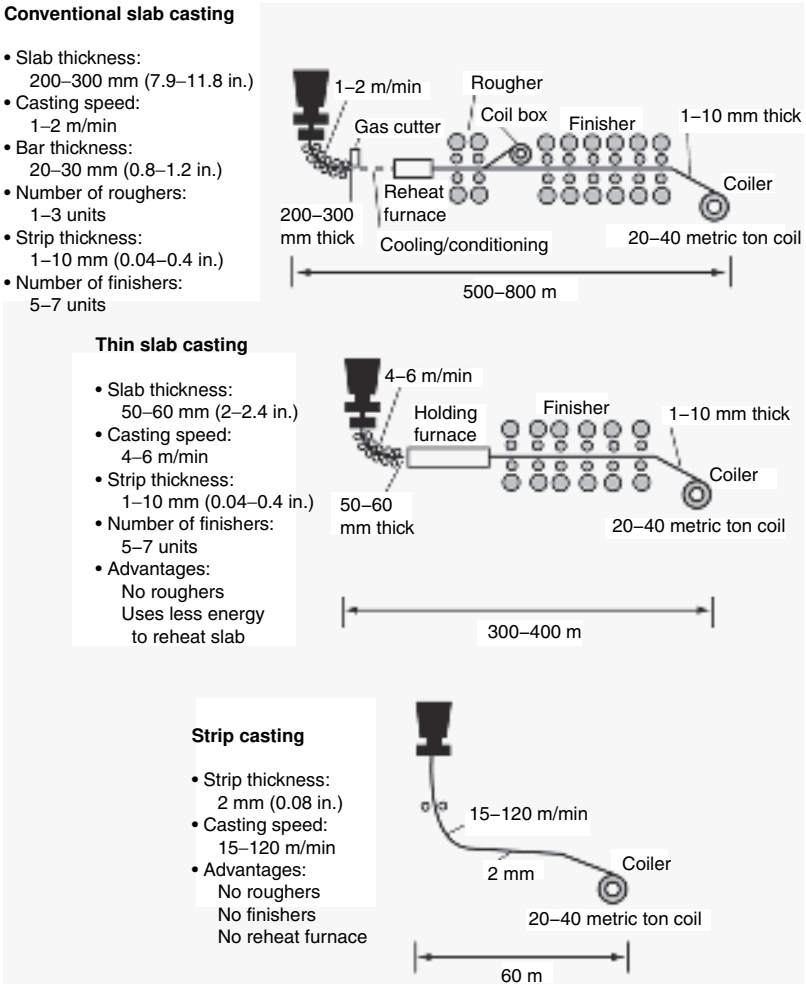

Fig. 2.3 Schematic of various continuous casting section sizes. Source: Ref 2.19

REFERENCES

2.1 R. Maddin, A History of Martensite: Some Thoughts on the Early Hardening of Iron, *Martensite: A Tribute to Morris Cohen*, G.B. Olson and W.S. Owen, Ed., ASM International, 1992, p 11–19

2.2 L.S. Figiel, *On Damascus Steel*, Atlantis Arts Press, Atlantis, FL, 1991

2.3 G. Roberts, G. Krauss, and R. Kennedy, *Tool Steels*, 5th ed., ASM International, 1998, p 1–6

2.4 O.D. Sherby and J. Wadsworth, Damascus Steels, *Scientific American*, Vol 252 (No. 2), 1985, p 112–120

2.5 J. Wadsworth and O.D. Sherby, The History of Ultrahigh Carbon Steels, *Thermomechanical Processing and Mechanical Properties of Hypereutectoid Steels and Cast Irons*, D.R. Lesuerr, C.K. Syn, and O.D. Sherby, Ed., TMS, 1996, p 1–39
2.6 J.D. Verhoeven, A.H. Pendray, and W.E. Dauksch, The Key Role of Impurities in Ancient Damascus Steel Blades, *JOM*, Vol 50, 1998, p 58–64
2.7 J.D. Verhoeven, The Mystery of Damascus Blades, *Scientific American*, 2001, p 74–79
2.8 H. Tanimura, Development of the Japanese Sword, *J. Met.*, Feb 1980, p 63–72
2.9 Evolution of Iron- and Steelmaking, *The Making, Shaping and Treating of Steel*, 10th ed., United States Steel, AISE, Pittsburgh, PA, 1985, p 1–35
2.10 *British Iron and Steel AD 1800–2000 and Beyond*, C. Bodsworth, Ed., Book 742, IOM Communications Ltd, London, 2001
2.11 K.C. Barraclough, *Steelmaking: 1850–1900*, The Institute of Metals, 1990
2.12 *The Iron Bridge and Town*, The Ironbridge Gorge Museum Trust and Jarrold Publishing, 1997
2.13 E.T. Turkdogan, *Fundamentals of Steelmaking*, Book 656, The Institute of Materials, London, 1996
2.14 C.S. Smith, *A History of Metallography*, The University of Chicago Press, Chicago, 1960
2.15 N.F. Kennon, Nomenclature of Phases and Constituents, in L.E. Samuels, *Light Microscopy of Carbon Steels*, ASM International, 1999, p 5–27
2.16 J. Stubbles, Who was Henry Howe, *Metallurgical Transactions B*, Vol 29B, 1998, p 5–16
2.17 R.E. Hackenberg, The historical development of phase transformations understanding in ferrous alloys, in *Phase transformations in steels Volume 1: Fundamentals and diffusion-controlled transformations*, E. Pereloma and D. V. Edmonds, Editors, Woodhead Publishing in Materials, 2012, p 3–55
2.18 R.J. Fruehan, *Ladle Metallurgy Principles and Practices*, ISS, Warrendale, PA, 1985
2.19 J.R. Stubbles, The New North American Steel Industry, *Iron and Steelmaker*, Dec 1995, p 19–27
2.20 S. Ge, M. Isac, and R.I.L. Guthrie, Progress of Strip Casting Technology for Steel; Historical Developments, *ISIJ International*, Vol 52, 2012, p 2109–2122

CHAPTER 3

Phases and Structures

STEEL CAN BE processed to produce a great variety of microstructures and properties. Desired results are accomplished by heating *in* temperature ranges where a phase or combination of phases is stable (thus producing changes in the microstructure or distribution of stable phases) and/or heating or cooling *between* temperature ranges in which different phases are stable (thus producing beneficial phase transformations). The iron-carbon equilibrium phase diagram is the foundation on which all heat treatment of steel is based. This diagram defines the temperature-composition regions where the various phases in steel are stable, as well as the equilibrium boundaries between phase fields. This chapter describes the iron-carbon diagram, its modification by alloying elements, and the chemistry and crystallography of the phases found in iron-carbon alloys and steels. Also briefly discussed are the crystal imperfections termed *dislocations*, important to the deformation of steels, and diffusion, the mechanism by which atoms move in solid steel to produce changes in their distribution in steel microstructures.

The Iron-Carbon Equilibrium Diagram

The iron-carbon (Fe-C) diagram is a map that can be used to chart the proper sequence of operations for thermomechanical and thermal treatments of a given steel. The iron-carbon diagram should be considered only a guide, however, because most steels contain other elements that modify the positions of the phase boundaries. The effects of alloying elements on the phase relations shown in the iron-carbon diagram are described later in this chapter. Use of the iron-carbon diagram is further limited because some heat treatments are specifically intended to produce non-equilibrium structures, whereas others barely approach equilibrium. Nevertheless, knowledge of the changes that take place in a steel as equilibrium is approached in a given phase field, or of those that result from phase transformations, provides the scientific basis for the heat treatment of steels.

Figure 3.1 shows the Fe-C equilibrium diagram for carbon contents up to 7%. As noted in Chapter 1, "Introduction: Purpose of Text, Microstructure and Analysis, Steel Definitions, and Specifications," steels are alloys of iron, carbon, and other elements that contain less than 2% carbon—most frequently, 1% or less. Therefore, the portion of the diagram below 2% carbon is of primary interest for steel heat treatment. As noted also in Chapter 1, alloys containing more than 2% carbon are classified as cast irons. Actually, two diagrams are shown in Fig. 3.1: the blue lines show the equilibrium between Fe_3C and the several phases of iron, whereas the black lines show the equilibrium between graphite and the other phases. Graphite is a more stable form of carbon than Fe_3C and, given very long periods of time, Fe_3C will decompose to graphite. Graphitization is rare in steels and requires alloying to promote graphite formation. For example, carbon and silicon contents are increased in O6 oil hardening and A10 air hardening tool steels in order to promote graphite formation for improved machinability (Ref 3.2), and boron nitrides have been found to be effective in nucleating graphite in a medium-carbon steel containing 0.53% C (Ref 3.3).

In view of the difficulty in forming graphite in steels, the Fe-Fe_3C diagram is the more pertinent for understanding the processing and heat treatment of steel. In cast irons, high carbon content and the usual high silicon additions promote graphite formation, and accordingly, cast iron technology is based much more on the Fe-graphite diagram.

The diagram in Fig. 3.1 is strictly valid only at a pressure of 1 atm. At very high pressures, the boundaries shift and new phases appear. For example, in pure iron a close-packed hexagonal crystal form of iron, epsilon iron, has been produced at high pressures (Ref 3.4). The triple point in pure iron between alpha iron, gamma iron, and epsilon iron occurs at 770K and 110 kbars (11 GPa).

Compositions of the Fe-C alloys and phases represented by the Fe-C diagram are conventionally given in weight or mass percent. The percent symbol (%), unless otherwise identified, is understood to represent weight percent, a convention that is followed in this text. Sometimes it is useful to determine compositions in atomic percent. Conversion from weight percent to atomic percent carbon in an Fe-C alloy is accomplished by the following equations:

$$\text{at.\% C} = \frac{\text{C atoms}}{\text{C atoms} + \text{Fe atoms}} \times 100 \qquad \text{(Eq. 3.1)}$$

or

$$\text{at.\% C} = \frac{\dfrac{\text{wt\% C}}{\text{at. wt C}}}{\dfrac{\text{wt\% C}}{\text{at.wt C}} + \dfrac{\text{wt\% Fe}}{\text{at.wt Fe}}} \times 100 \qquad \text{(Eq. 3.2)}$$

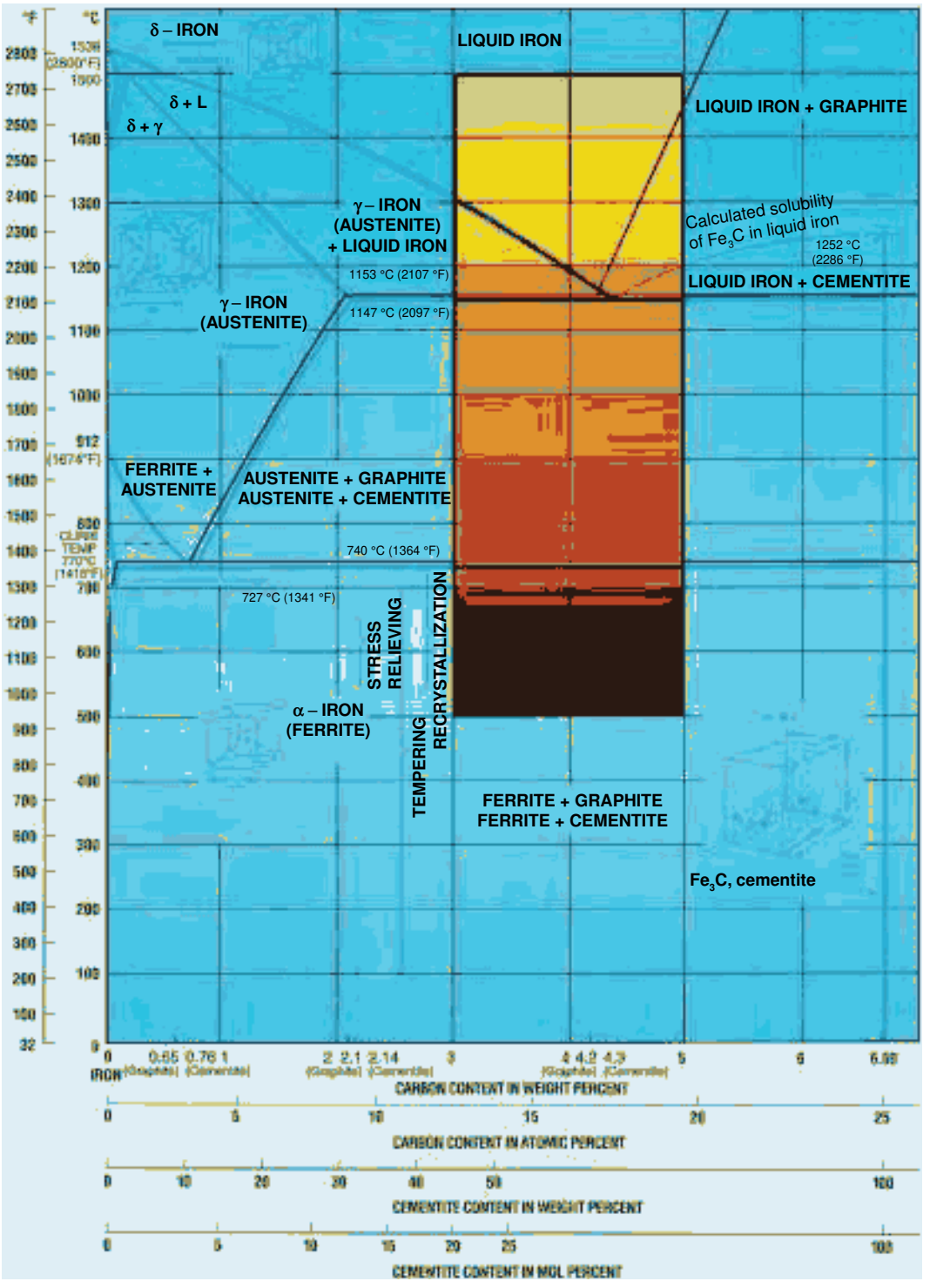

Fig. 3.1 The Fe-C equilibrium diagram up to 7% carbon. Blue lines indicate Fe-Fe_3C diagram; black lines indicate Fe-graphite diagram. The heat colors on the chart are appropriate reproductions of colors observed on a bar of steel as seen through a furnace peephole. They should be viewed under average fluorescent room lighting conditions ~500 lux. Source: Ref 3.1

Application of this calculation to an Fe-0.4C alloy shows that 0.4% C is equivalent to 1.8 at.% C, a reflection of the much lighter atomic weight of carbon (12) compared with that of iron (56). Conversion to atomic percent for steels containing elements other than iron and carbon requires an additional term in the denominator of Eq 3.1 or Eq 3.2 for each of the other elements present.

The art and science of steel processing is based on the existence of the austenite phase field in the Fe-C system. Controlled transformation of austenite to other phases on cooling is responsible for the great variety of microstructures and properties attainable by heat treatment of steels. Hot working of heavy sections into useful shapes and sizes by rolling or forging is also accomplished at temperatures where austenite is the stable phase.

Iron is an allotropic element: at atmospheric pressure, it may exist in more than one crystal form depending on the temperature. Alpha iron (ferrite) exists up to 912 °C (1675 °F); gamma iron (austenite) exists between 912 and 1394 °C (1675 and 2540 °F); and delta iron (delta ferrite) exists from 1394 °C to the melting point of pure iron, 1538 °C (2800 °F). The temperature ranges in which the various crystal forms of iron are stable make up the left vertical boundary (the pure iron end) of the Fe-C phase diagram shown in Fig. 3.1.

The three horizontal blue lines in the iron-carbon diagram represent three invariant three phase equilibria, i.e., equilibria where the compositions of the three phases and the temperature at which the three phases coexist under equilibrium conditions at constant pressure are invariant and fixed in the two-component iron-carbon system. These three-phase equilibria, assuming Fe_3C as the stable high-carbon phase, are characterized as follows:

- At 1495 °C (2725 °F): δ-ferrite + Liquid = γ-iron (austenite), a *peritectic* reaction, defined on cooling as a solid phase combining with liquid phase to form a single solid phase.
- At 1148 °C (2100 °F): Liquid = Fe_3C + γ-iron, a *eutectic* reaction, defined on cooling as a liquid phase forming two solid phases.
- At 727 °C (1335 °F): γ-iron = α ferrite + Fe_3C, a *eutectoid* reaction, defined on cooling as a solid phase forming two other solid phases.

With the addition of other alloying components to the iron-carbon system, under equilibrium conditions, the compositions of the three phases can vary and can coexist over a range of temperatures. Under non-equilibrium conditions, when the various phases do not have sufficient time to form by diffusion-controlled mechanisms, the reactions proceed over a range of temperatures. The reactions, as written, on cooling go to the right, and on heating go to the left.

Crystal Structures of Iron

The crystal structure of ferrite is characterized by the unit cell shown in Fig. 3.2. Ferrite belongs to the cubic crystal system—all three axes of the unit cell are of the same length *a* and are mutually perpendicular. The space lattice of ferrite is body-centered cubic (bcc). There are a total of two atoms per unit cell: the body-centered atom with coordinates *a*/2, *a*/2, *a*/2, and the atom at the origin of the unit cell with coordinates 0, 0, 0. The latter atom represents all the equivalent corner atoms of the unit cell, each of which is shared by eight unit cells that come together at a corner. The one-eighth atom per corner times the eight corners of the unit cell therefore accounts for one of the two atoms in a bcc unit cell.

The lattice parameter of alpha iron at room temperature is 0.286 nm (2.86 Å) (Ref 3.5). The body diagonals of the unit cell, corresponding to the <111> directions, are the directions in which the iron atoms are in contact in the bcc structure. Figure 3.2 shows that the body-centered atom has eight nearest neighbor atoms at a center-to-center distance of one-half a body diagonal, or $a\sqrt{3}/2$. Crystal structures in which the atoms are packed as closely together as possible have 12 nearest neighbor atoms, and therefore, the bcc form of iron is a more open or less dense structure than the gamma iron structure described subsequently. The difference in atomic packing between alpha and gamma is responsible for the volume expansion that occurs when the higher-density gamma iron transforms to alpha iron on cooling.

The unit cell of gamma iron or austenite is shown in Fig. 3.3. Austenite also belongs to the cubic crystal system but has a face-centered cubic (fcc) lattice. There are a total of four atoms per unit cell with coordinates 0, 0, 0; 0, *a*/2, *a*/2; *a*/2, *a*/2, 0; *a*/2, 0, *a*/2, corresponding to a corner atom and an atom in the center of each face of the unit cell. Each face atom is shared

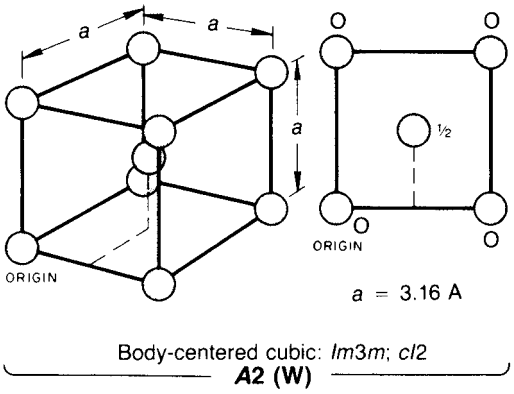

Fig. 3.2 Body-centered cubic (bcc) crystal structure. *A*2 is structure (Strukturbericht) symbol, and W is prototype metal with bcc structure. Ferrite in steel is bcc. Source: Ref 3.1

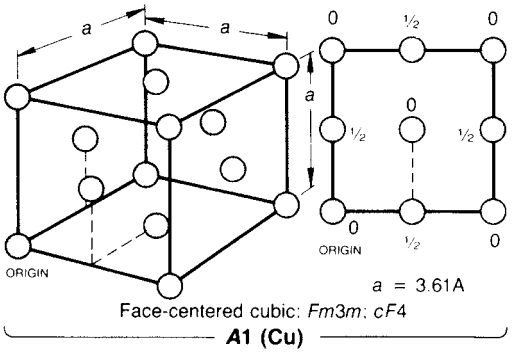

Fig. 3.3 Face-centered cubic (fcc) crystal structure. *A*1 is structure (Strukturbericht) symbol, and Cu is prototype metal with fcc structure. Austenite in steel is fcc. Source: Ref 3.1

by two adjacent unit cells; the six faces of the cubic cell thus contribute three atoms. As described previously for the bcc cell, the eight corners together contribute only one atom.

The lattice parameter of austenite, about 0.356 nm (3.56 Å), is larger than that of ferrite. However, the close-packed structure and the 4 atoms per unit cell make the density of austenite greater than that of ferrite. The face diagonals, corresponding to <110> directions, are the close-packed directions in the fcc structure and establish the center-to-center atom spacing of the 12 nearest neighbor atoms as $a\sqrt{2}/2$.

Austenite also may be characterized as a structure made up of planes of closest atomic packing stacked in a sequence that repeats every three layers. The orientation of the close-packed {111} planes relative to the unit cell may be readily identified because each (111) plane is defined by three face diagonals of the unit cell. The close-packed planes in austenite are extremely important: the dislocation motion that makes mechanical deformation of austenite possible occurs on {111} planes, and microstructural features within grains known as twins have {111} planes as boundaries. Twins are characterized by mirror symmetry of atoms across the planes separating the twins and the adjacent matrix (Ref 3.6). In austenite, twins frequently form as a result of growth accidents in the stacking of {111} planes—accidents caused by recrystallization and grain growth during heating or annealing in the temperature range where austenite is stable.

Finally, the third phase that may form in pure iron is delta ferrite, a bcc structure that is crystallographically identical to that of alpha iron. Delta ferrite forms only at temperatures close to the melting point of iron. It is generally only of academic interest in the heat treatment of carbon steels because it is replaced at lower temperatures by austenite, the usual starting structure for commercial heat treatment. However, because delta ferrite is the first phase to form during solidification of iron and steel ingots and welds, it may be associated with interdendritic segregation patterns or

concentration gradients of alloying and/or impurity elements (Ref 3.7). Hot working and homogenizing steels in the austenite range generally significantly reduce the segregation produced during solidification, and some degree of segregation may be tolerated in many applications. Residual segregation may produce the microstructural condition referred to as banding, as described in Chapter 9, "Primary Processing Effects on Steel Microstructure and Properties." Also, the volume change when delta ferrite crystals transform to austenite crystals may produce cracking during continuous casting of low-carbon steels in the carbon range 0.08 to 0.14% (Ref 3.8).

Effects of Carbon

The addition of carbon to iron produces several important changes in the phases and phase equilibria just described. Differences in the ability of ferrite and austenite to accommodate carbon result not only in important characteristics of the Fe-C diagram but also in the formation of Fe_3C. The crystal structures of the bcc ferrite and fcc austenite are modified by introducing carbon atoms into the interstices or interstitial sites between iron atoms. Austenite and ferrite in Fe-C alloys and steels are, therefore, interstitial solid solutions.

Carbon is an element that stabilizes austenite and thereby increases the range of austenite formation in steels. Figure 3.1 shows that, with the addition of carbon, the austenite field greatly expands from 912 to 1394 °C (1675 to 2540 °F)—the range in pure iron—to a wide range of temperatures and compositions. The maximum solubility of carbon in austenite reaches 2.11% at 1148 °C (2100 °F). Ferrite has a much lower ability to dissolve carbon than does austenite: the solubility decreases continuously from a maximum of only 0.02% at 727 °C (1340 °F). The limited solubility of carbon in ferrite is emphasized by the very small ferrite field shown in Fig. 3.1. An expanded portion of the low-carbon end of the Fe-C diagram showing the temperature-composition range of ferrite and the decreasing solubility of carbon in ferrite with decreasing temperature is shown in Fig. 3.4. The room temperature solubility of carbon in ferrite is almost negligible.

When the solubility limit for carbon in austenite is exceeded, a new phase—iron carbide or cementite—forms in iron-carbon alloys and steels. Cementite crystals assume many shapes, arrangements, and sizes that together with ferrite contribute to the great variety of microstructures found in steels. The various forms of cementite depend directly on thermal history or heat treatment. The crystal structures of cementite and of ferrite and austenite solid solutions are discussed in the next section, and the association and formation of those phases to produce characteristic microstructures are discussed in later chapters.

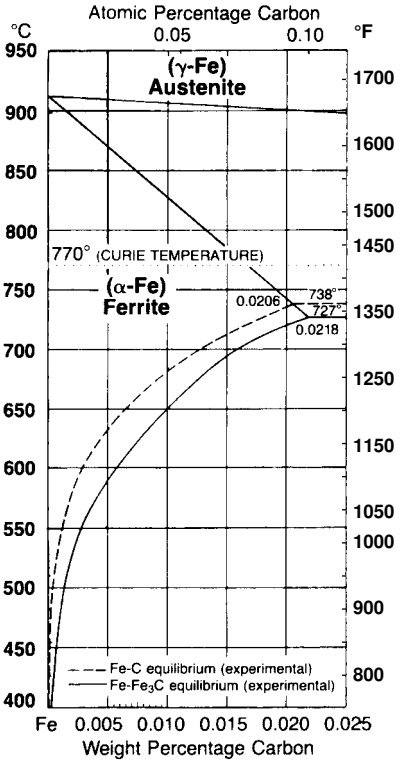

Fig. 3.4 Fe-rich side of Fe-C diagram, showing extent of ferrite phase field and decrease of carbon solubility with decreasing temperature. Source: Ref 3.1

Crystal Structures in Fe-C Alloys

The major difference between the structures of ferrite and austenite in steel and the corresponding phases in pure iron is the introduction of carbon atoms. There are two types of interstitial voids that may become sites for carbon atoms in bcc and fcc structures. Figures 3.5 and 3.6 show the octahedral and tetrahedral voids in the fcc and bcc structures, respectively. The two types of voids derive their names from the number of sides of the polyhedron formed by the iron atoms that surround a given site. A carbon atom has six nearest-neighbor iron atoms if in an octahedral site and four if in a tetrahedral site.

The sizes of the different voids vary considerably. In austenite, assuming spherical iron atoms in contact, an octahedral site could accommodate an atom 0.052 nm (0.52 Å) in radius, but a tetrahedral site could accommodate an atom only 0.028 nm (0.28 Å) in radius (Ref 3.9). Carbon atoms have radii of 0.07 nm (0.7 Å), and are therefore more readily accom-

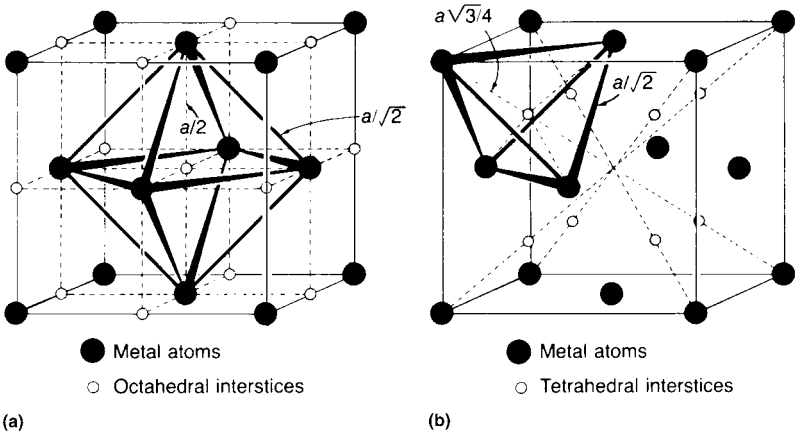

Fig. 3.5 (a) Octahedral and (b) tetrahedral interstitial voids in fcc structure. Source: Ref 3.9

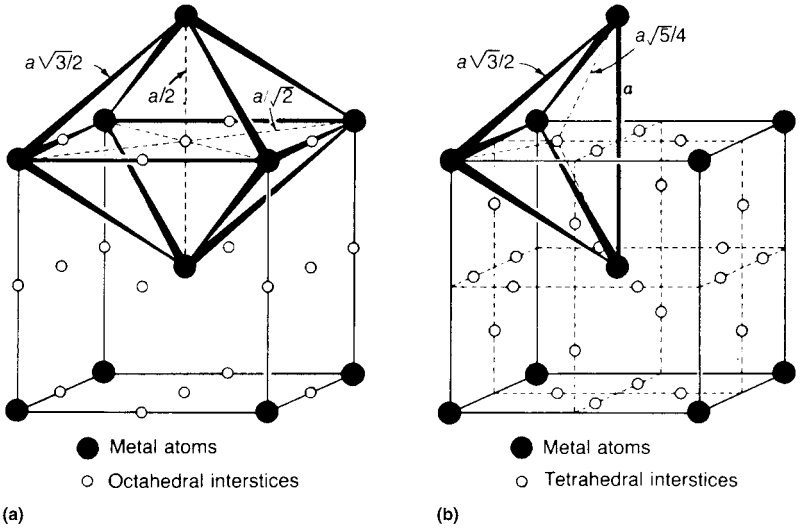

Fig. 3.6 (a) Octahedral and (b) tetrahedral interstitial voids in bcc structure. Source: Ref 3.9

modated in the octahedral voids even though some lattice expansion is required.

In ferrite the interstitial sites are much smaller, thus explaining the very limited solubility of carbon. A tetrahedral site in ferrite could accommodate an interstitial atom 0.035 nm (0.35 Å) in radius and an octahedral site, an atom only 0.019 nm (0.19 Å) in radius. The octahedral sites in ferrite, however, are not symmetrical (see Fig 3.6), and a carbon atom would severely displace only the two atoms at a distance of $a/2$, not those

at a distance of $a\sqrt{2}/2$. Carbon atoms appear to prefer the octahedral sites in ferrite (Ref 3.9) and do produce a severe distortion of the lattice in the <100> directions. In ferrite, because of the limited number of carbon atoms that can be accommodated, the lattice remains essentially cubic. If large numbers of carbon atoms present in austenite are trapped in bcc octahedral sites by rapid cooling, the cubic structure may actually become tetragonal. The latter structure typifies the martensite phase, and its formation is the object of the very important hardening heat treatments described in later chapters.

Cementite, the phase that forms when the solubility of carbon in ferrite and austenite is exceeded, is a significantly different phase from the interstitial solid solutions described previously. Cementite is a compound with a specific ratio of one carbon atom to three iron atoms and is frequently referred to as Fe_3C. Cementite contains 6.67% C and could exist alone only in an alloy at that composition, in contrast to ferrite or austenite, which may exist as single phases over a range of alloy carbon content.

Cementite is orthorhombic, with lattice parameters a = 0.452 nm (4.52 Å), b = 0.509 nm (5.09 Å), and c = 0.674 nm (6.74 Å). Its unit cell contains 12 iron atoms and 4 carbon atoms. The positions of iron and carbon atoms relative to the unit cell axes of cementite (Ref 3.9) are shown in the model of Fig 3.7 and the schematic of the unit cell in Fig. 3.8.

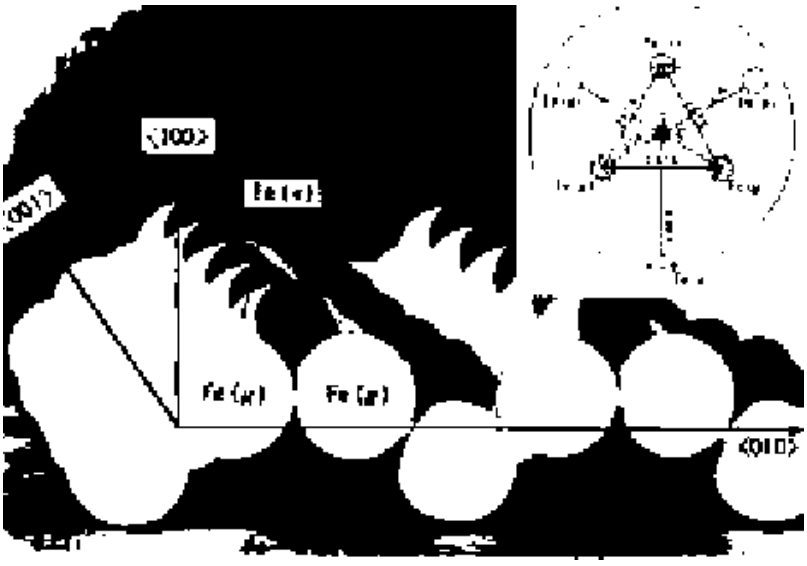

Fig. 3.7 Model of cementite structure that forms in steel. Insert is stereogram of iron nearest and next-nearest neighbor atoms around a carbon atom. Source: Ref 3.9

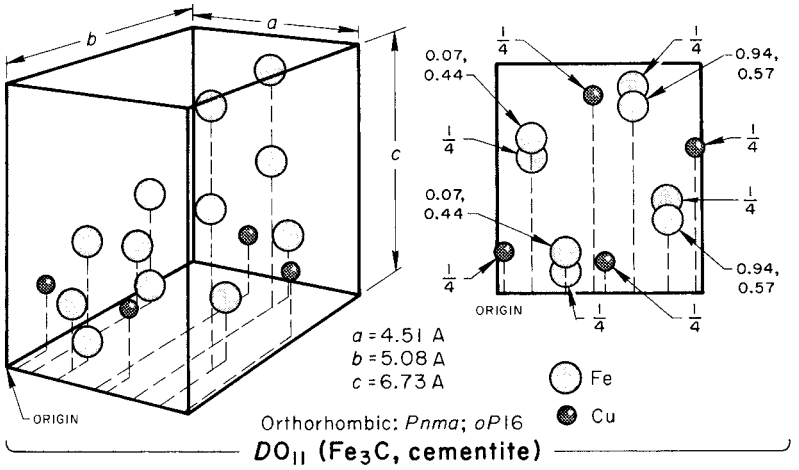

Fig. 3.8 Orthorhombic crystal structure of cementite. DO_{11} is the structure (Strukturbericht) symbol. Source: Ref 3.1

The Eutectoid Equilibrium and Effects of Alloying Elements

Up to this point, only the binary Fe-C diagram and the crystal structure of the phases that form in Fe-C alloys have been described. Steels, however, contain alloying elements and impurities that may form new phases or be incorporated into the crystal structures of austenite, ferrite, and cementite. Incorporation is usually by replacement of iron atoms if the alloy or impurity atoms are roughly the same size as iron atoms, but sometimes the atoms go into interstitial sites if they are significantly smaller than iron, as is nitrogen. In some cases, if sufficient quantities of alloying elements are present, solubility limits are exceeded and phases other than those already discussed may form. For example, small additions of chromium to Fe-C alloys at 890 °C (1635 °F) maintain the cementite structure, M_3C (M standing for a combination of chromium and iron atoms); larger additions cause the carbide M_7C_3 to form; and still larger additions produce the carbide $M_{23}C_6$ (Ref 3.10).

Some of the elements present in steels are austenite stabilizers (manganese and nickel, for instance), some are ferrite stabilizers (silicon, chromium, and niobium), and some are strong carbide formers (titanium, niobium, molybdenum, and chromium, if present in sufficient quantity).

Ferrite and austenite stabilizers expand the respective phase fields. One measure of the effect of an alloying element on the Fe-C phase diagram is whether the eutectoid temperature (indicated by the horizontal line at 727 °C, or 1340 °F, in Fig. 3.1) is raised or lowered by an alloying addition.

Austenite stabilizers lower the eutectoid temperature and thereby expand the temperature range over which austenite is stable. Figure 3.9 shows the change in eutectoid temperature with increasing amounts of several common alloying elements (Ref 3.11). Figure 3.10 shows a related effect of alloying elements on the Fe-C phase diagram: the decrease in carbon content of austenite of eutectoid composition. The type of evidence on which Fig. 3.9 and 3.10 are based is shown in Fig. 3.11 for the Fe-Cr-C system and for the Fe-Mn-C system in Fig. 3.12. The strong ferrite-stabilizing and carbide-forming characteristics of chromium account for the shrinking austenite phase field in Fig. 3.11. Manganese is an

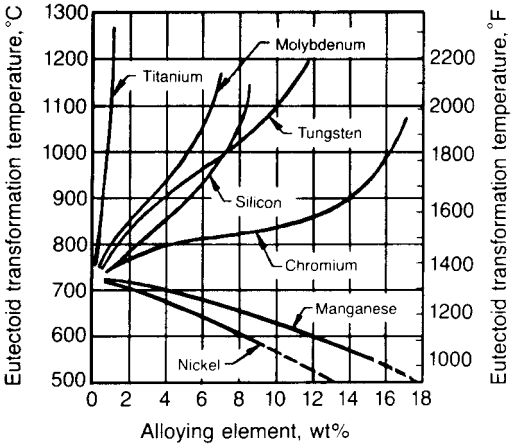

Fig. 3.9 Effect of substitutional alloying elements on eutectoid transformation temperature in steel. Source: Ref 3.11

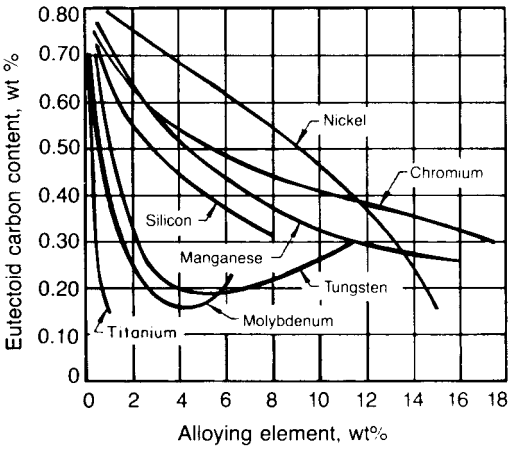

Fig. 3.10 Effect of substitutional alloying elements on the eutectoid carbon content in steel. Source: Ref 3.11

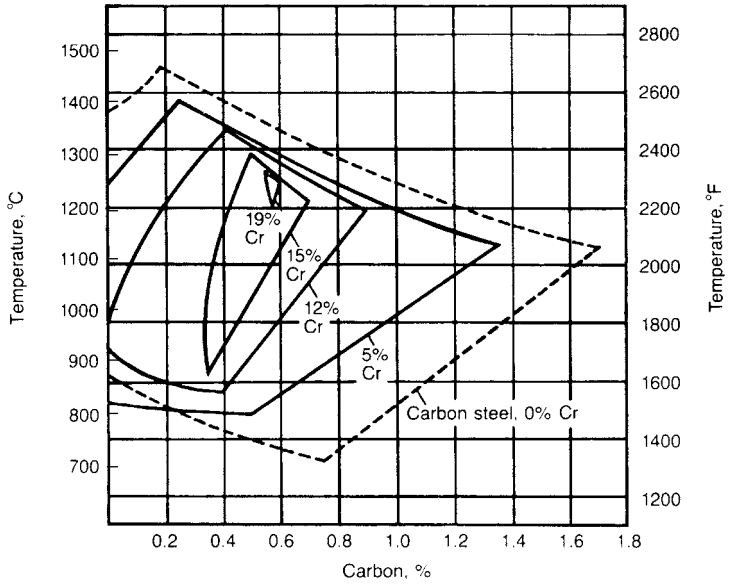

Fig. 3.11 Effect of chromium content on size of austenite phase field. Source: Ref 3.11

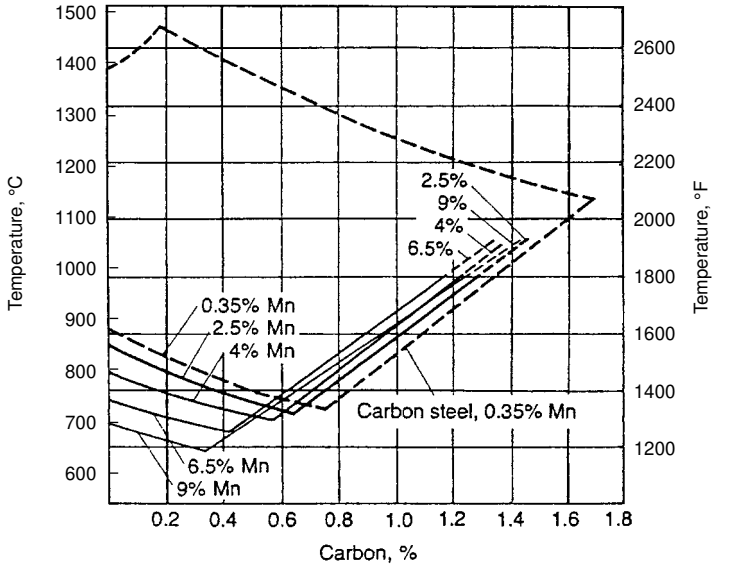

Fig. 3.12 Effect of Mn on the size of the austenite phase field. Source: Ref 3.11

austenite-stabilizing element and a moderately strong carbide-forming element, and as a result, it increases austenite stability to lower temperature in low-carbon steels and extends the austenite-cementite field in higher-carbon steels to lower-carbon contents, as shown in Fig. 3.12.

The changes in the boundaries of the various phase fields as a function of composition are captured in experimentally-determined binary and ternary phase diagrams (Ref 3.12–3.14). Thermodynamic calculations have also been used to determine ranges of phase stability in ferrous systems (Ref 3.15), and a thermochemical database and calculation system for the determination of multicomponent phase diagrams has been developed (Ref 3.16) and is commercially available (Ref 3.17).

Critical Temperatures

The boundaries between phase fields of the Fe-C diagram shown in Fig 3.1 identify temperatures for the various phase transformations that may occur in Fe-C alloys. For example, if an Fe-0.5C alloy were heated from room temperature at an extremely low rate, some of the ferrite and all of the cementite would transform to austenite at 727 °C (1340 °F), and at about 860 °C (1580 °F), the last bit of ferrite would be completely transformed to austenite.

The transformation temperatures are often referred to as *critical temperatures* and are observed by measuring changes in heat transfer or volume as specimens are heated or cooled. On heating, heat is absorbed and specimen contraction occurs as ferrite and cementite are replaced by the close-packed structure, austenite. On cooling, heat is evolved and specimen expansion occurs as austenite transforms to ferrite and cementite. The absorption or release of heat during phase transformation produces a change in slope, or *arrest*, on a continuous plot of specimen temperature versus time. The letter A is the symbol for the thermal arrests that identify critical temperatures.

There are three critical temperatures of interest in the heat treatment of steel: the A_1, which corresponds to the boundary between the ferrite-cementite field and the fields containing austenite and ferrite or austenite and cementite; the A_3, which corresponds to the boundary between the ferrite-austenite and austenite fields; and the A_{cm}, which corresponds to the boundary between the cementite-austenite and the austenite fields. These temperatures assume equilibrium conditions—that is, extended periods of time at temperature or extremely slow rates of heating or cooling. Sometimes A_1, A_3, and A_{cm} are designated as Ae_1, Ae_3, and Ae_{cm}, respectively, the letter e indicating that equilibrium conditions are assumed.

The transformations that occur at A_1, A_3, and A_{cm} are diffusion-controlled. Therefore, the critical temperatures are sensitive to composition and to heating and cooling rates. Rapid heating allows less time for diffusion and tends to increase the critical temperatures above those associated with equilibrium. Likewise, rapid cooling tends to lower the critical temperatures. The effect of heating or cooling rate is defined practically by a new set of critical temperatures designated Aĉ or Aȓ (for the arrests on heating or cooling, respectively). The terminology was developed by

the French metallurgist Osmond (Ref 3.18). Ac stands for *arrêt chauffant* and Ar for *arrêt refroidissant*. As a result of heating and cooling effects, therefore, there are two other sets of critical temperatures: Ac_1, Ac_3, and Ac_{cm}, and Ar_1, Ar_3, and Ar_{cm}. These sets of critical temperatures are shown schematically in Fig. 3.13.

Generally, the critical temperatures for a given steel are determined experimentally. However, some empirical formulas that show the effects of alloying elements on the critical temperatures have been developed by regression analysis of large amounts of experimental data. For example (Ref 3.19), the following formulas for Ac_3 and Ac_1 in degrees Celsius have been developed:

$$Ac_3 = 910 - 203\sqrt{C} - 15.2Ni + 44.7Si + 104V + 31.5\,Mo + 13.1W \qquad \text{(Eq 3.3)}$$

$$Ac_1 = 723 - 10.7Mn - 16.9Ni + 29.1Si + 16.9Cr + 290As + 6.38W \qquad \text{(Eq 3.4)}$$

These formulas present another way of describing the effect of alloying elements on both the Fe-C diagram and the transformation behavior of steels. Elements that stabilize austenite lower the Ac_3 and Ac_1 as evi-

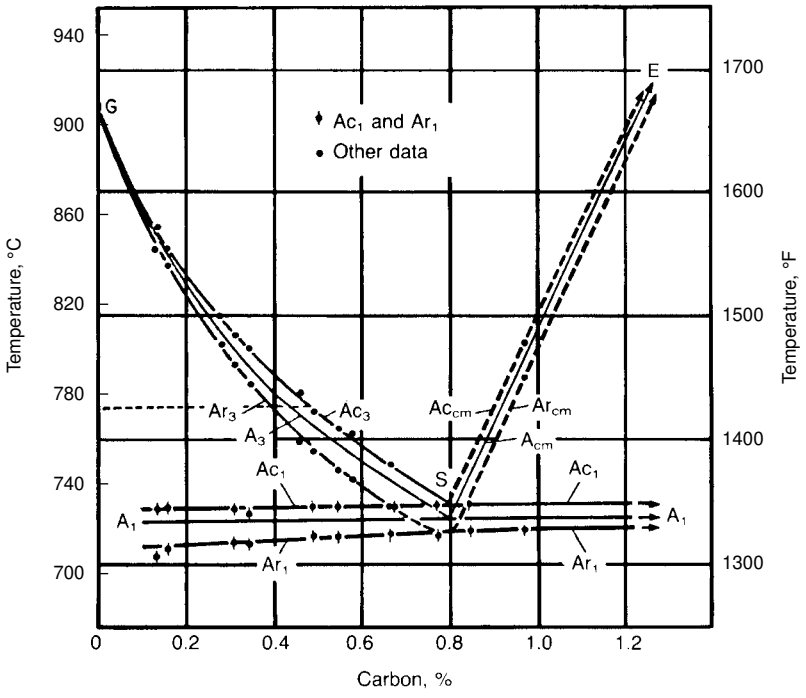

Fig. 3.13 Cooling (Ar), heating (Ac), and equilibrium (A) temperatures in Fe-C alloys. Heating and cooling at 0.125 °C/min (0.225 °F/min). Source: Ref 3.11

denced by their negative contributions to the corresponding equation, whereas elements that stabilize ferrite or carbide raise the Ac_3 and Ac_1 and make a positive contribution. The effect of alloying elements on the Ac_3 has also been determined by thermodynamic calculations (Ref 3.20).

The Peritectic Equilibrium and Reaction in Steels

The austenite phase field and the changes in microstructure that occur on cooling of the austenite provide the basis for the solid state processing and heat treatment of steels. Thus characterizing the eutectoid reaction and the effect of cooling and alloying on the reaction, as described earlier and throughout this book, is a major consideration of solid-state processing and ferrous physical metallurgy. In contrast, delta ferrite formation and the peritectic reaction, which occurs during the solidification of liquid low-carbon steel, are of vital importance for steelmaking, yet the peritectic reaction has received less attention than the eutectoid reaction. However, because of increased production of continuously cast low-carbon steels and the susceptibility to cracking of these steels, there is significant recent interest in characterizing the peritectic reaction (Ref 3.21–3.25).

Figure 3.14 shows an expanded view of the peritectic solidification region of the iron-carbon diagram (Ref 3.24). The compositions of the delta ferrite, austenite, and liquid participating in the peritectic solidification are given respectively by C_δ, C_γ, and C_{liq}. The effects of alloying elements on

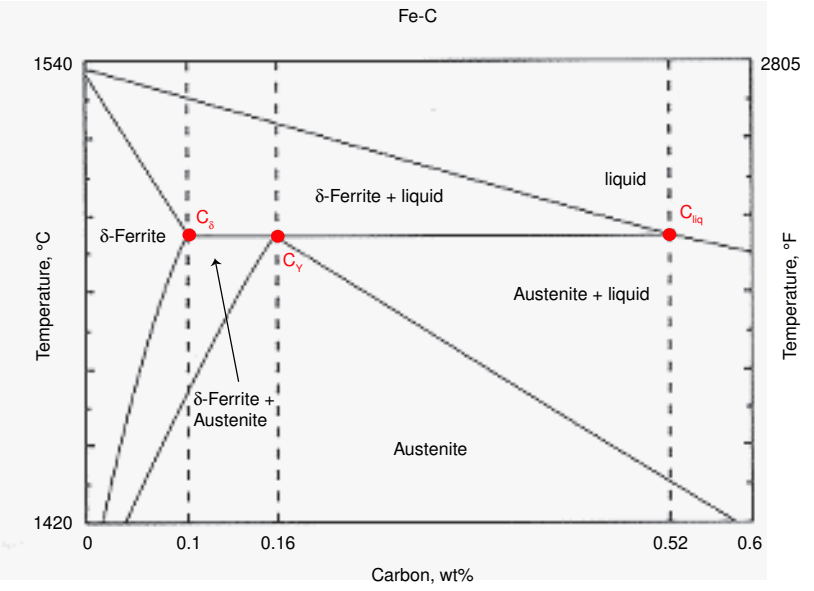

Fig. 3.14 The peritectic equilibrium in the Iron-Carbon diagram. Source: Ref 3.24

peritectic-phase compositions have been calculated (Ref 3.24, 3.25). Some elements, such as Al, V, and Mo, increase the solubility of carbon in the δ-ferrite at the peritectic, others such as Mn, Ti, and Nb decrease the solubility.

Crystal Imperfections and Slip

The preceding sections have shown that the phases that make up steel are crystalline. A very important characteristic of crystals is that they are deformable by a process termed *slip*: parts of a crystal are displaced or slip relative to other parts of the crystal along well-defined crystal planes. Figure 3.15 shows schematically how slip can cause permanent changes in the shape of a crystal. Although the results of the slip process make it appear that displacements have occurred across intact planes of atoms, the process is due to atomic scale crystal defects identified as dislocations. Dislocations are line defects that thread their way across crystals or grains in steel and migrate when applied macroscopic stresses produce critical resolved shear stresses on planes that contain the dislocations (Ref 3.26–3.29).

Figure 3.16 shows schematically the movement of an edge dislocation in a section of a crystal structure where the atoms are regularly aligned except at the dislocation. The dislocation moves in response to an applied shear stress (arrows). The atomic displacements associated with an edge dislocation are represented as the dislocation line at the bottom edge of an incomplete atom plane in a crystal, and the magnitude and direction of the resulting discontinuity is designated as the Burgers vector. As the dislocation moves across a slip plane, from (a) to (d), the top part of the crystal is displaced relative to the bottom part of the crystal. Only the atomic bonds immediately around the dislocation are broken, not those on the balance of the slip plane. When the dislocation has moved completely across the crystal, the top part is displaced relative to the bottom part by one Burgers vector of displacement, and the crystal perfection in the displaced crystal

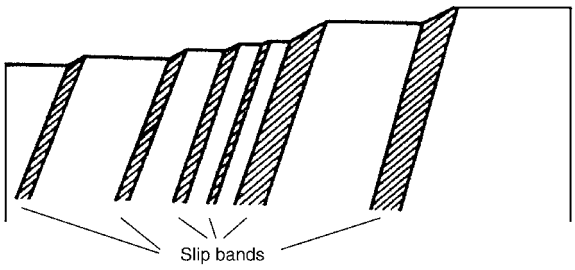

Fig. 3.15 Schematic of slip bands and associated slip steps on the surface of a single crystal. Source: Ref 3.26

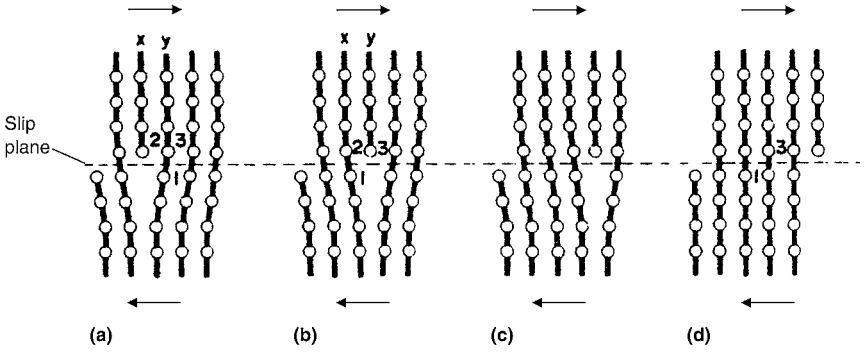

Fig. 3.16 Schematic of the progressive movement of an edge dislocation on a slip plane in a single crystal. Source: Ref 3.26

is restored. In view of the fact that the motion of one dislocation produces only a displacement on the order of atomic dimension, large-scale plastic deformation of crystalline materials requires the motion of huge numbers of dislocations. For example, in heavily deformed polycrystals, dislocation lengths per unit volume may be as high as 10^{12} cm per cubic cm.

There are two major geometries of discontinuities associated with dislocations. One is that associated with edge dislocations, as shown in Fig. 3.16. The other is that of a screw dislocation, which may be considered to be represented as the displacements associated with a spiral staircase around a dislocation line at its center. The Burgers vector of an edge dislocation is perpendicular to the dislocation line, whereas that of a screw dislocation is parallel to the dislocation line. Edge dislocations move perpendicular to resolved shear stresses, as shown in Fig. 3.16; screw dislocations move parallel to resolved shear stresses. An edge dislocation is constrained to move on a single slip plane; a screw dislocation can cross-slip from a slip plane in one orientation to a slip plane in another orientation. The latter characteristic makes possible the sustained dislocation motion and multiplication that produce the significant macroscopic changes in shape of ductile crystalline materials. While ductility is important in forming operations and fracture resistance, high strength is desirable in many applications. Increased strength is produced by designing into microstructures resistance to dislocation motion; subsequent chapters discuss the various strengthening mechanisms that operate in steels.

Slip systems in crystals are defined by combinations of slip planes and slip directions of closest atom packing. In austenite, which has an fcc crystal structure, the slip planes are the {111} planes and the slip directions are the face diagonals of the unit cell or the <110> directions. There are four orientations of {111} planes in a crystal of austenite, each with three <110> directions, making a total of 12 slip systems in austenite. The magnitude of the Burgers vector of perfect dislocations in austentite is

$a\sqrt{2}/2$ where a is the lattice parameter of the fcc unit cell. In bcc ferrite, the close-packed directions are the body diagonals of the unit cell or <111> directions, and the slip planes have been found to be {110}, {112}, and {123} planes, all of which contain <111> directions, for a total of 48 slip systems. The Burgers vector of dislocations in ferrite is $a\sqrt{3}/2$.

Dislocations can be directly resolved by high-resolution transmission electron microscopy of thin sections. The dislocation lines appear dark when oriented relative to the incident electron beam at angles that produce electron diffraction from the displaced atom planes in the strain fields of dislocations. Some examples of dislocation arrays are shown in later chapters.

The preceding discussion notes the importance of dislocations in steel but only briefly describes some of the essential features of dislocations. More information on the characteristics and other types of dislocations can be found in Ref 3.26–3.29.

Diffusion in Steel

Amazingly, atoms can move through solid steel microstructures, a process referred to as *diffusion*. It is diffusion that makes possible the remarkable changes in microstructure and properties during hot work, all types of heat treatment, and even room-temperature aging and embrittlement. Atoms move to relieve variations in concentrations due to solidification-induced segregation, across grain boundaries during recrystallization and grain growth, to dislocation strain fields to relieve lattice strains, and from and to phases during diffusion-controlled phase transformations and coarsening or dissolution of particles such as carbides. Thus diffusion is essential for the time-dependent approach to equilibrium structures with minima in free energy. Microstructural changes are described in detail in subsequent chapters for many different alloy steel systems and steel products in which control of diffusion is a critical factor in establishing desirable microstructures and properties. The theoretical, experimental, and mathematical characterization of diffusion is extensive (Ref 3.30, 3.31, 3.32), and this section is designed only to provide an introduction and to provide background to interpret Figure 3.17, a comprehensive set of data comparing the diffusivities of the various types of elements found in steels. This figure was first published by Professor William Leslie in *The Physical Metallurgy of Steels* (Ref 3.33) and adapted from unpublished work by L. S. Darken.

In steel microstructures there are gradients in the concentrations of atoms as a function of distance within grains or at phase transformation interfaces, gradients due to segregation or to redistribution of atoms during phase transformations. Typically atoms diffuse from regions of high concentration, down the concentration gradient, to regions of low concentration. Following McMahon (Ref 3.34), the rate of atom transfer during

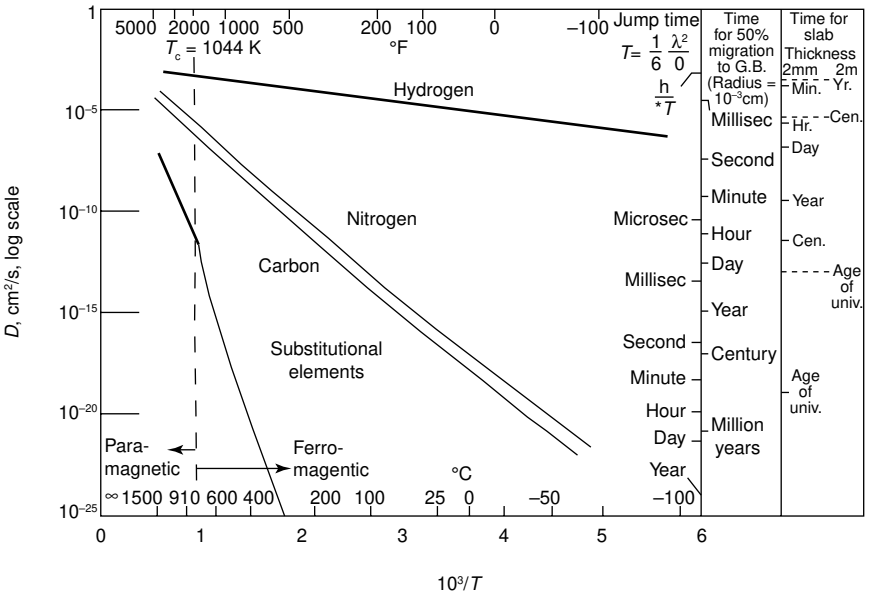

Fig. 3.17 Diffusivity of substitutional, interstitial, and hydrogen atoms in steel as a function of temperature. Source: Ref 3.33

diffusion is defined as the flux, J, mass per unit area per unit time, and is dependent on the existing concentration gradient, dc/dx, mass per unit volume per distance over which diffusion occurs. The flux and concentration gradient are related by the equation known as Fick's First Law:

$$J = D\frac{dc}{dx} \tag{Eq 3.5}$$

where D is a constant of proportionality (termed the *diffusion coefficient*) between the flux and concentration gradient. Typically D is in units of cm²/sec, as in Figure 3.17, for dimensions in cm and time in sec. D, as shown in Fig. 3.17, is strongly dependent on temperature and atom type. Further mathematical analysis of diffusion equations results in an equation:

$$x = \sqrt{Dt} \tag{Eq 3.6}$$

that provides an estimate of distances atoms might travel in a given time. It is this equation that has been used to provide the times it might take for atoms in different groups of elements to travel the distances noted in the right-hand columns of Figure 3.17. Figure 3.17 also shows the strong exponential temperature dependence of different types of atoms according to the equation:

$$D = D_0 e^{-(Q/RT)} \tag{Eq 3.7}$$

where Q is the activation energy (cal/mole), R the gas constant (2cal/mole-K), and T the temperature (in degrees Kelvin). Substitutional atoms with sizes close to that of iron, such as manganese, chromium, nickel and molybendum, diffuse strongly only at high temperatures by mechanisms associated with vacant lattice sites in the parent iron crystals or along regions of disorder as at grain boundaries. The small interstitial atoms carbon and nitrogen diffuse much more rapidly between iron atoms and even at room temperature can diffuse short distances given enough time. Finally, hydrogen, the smallest atom found in steels, can diffuse large distances in short times even at room temperature.

REFERENCES

3.1 *Metallography, Structures and Phase Diagrams,* Vol 8, 8th ed., *Metals Handbook,* American Society for Metals, 1973, p 236, 275, 276

3.2 G. Roberts, G. Krauss, and R. Kennedy, *Tool Steels,* 5th ed., ASM International, 1998

3.3 T. Iwamoto, T. Hoshino, K. Amano, and Y. Nakano, An Advanced High Strength Graphitized Steel for Machining and Cold Forging Uses, *Fundamentals and Applications of Microalloyed Forging Steels,* C.J. Van Tyne, G. Krauss, and D.K. Matlock, Ed., TMS, 1996, p 277–286

3.4 L. Kaufman and H. Bernstein, *Computer Calculation of Phase Diagrams,* Academic Press, New York, 1970

3.5 C.S. Roberts, Effect of Carbon on the Volume Fractions and Lattice Parameters of Retained Austenite and Martensite, *Trans. TMS- AIME,* Vol 197, 1953, p 203

3.6 B.D. Cullity, *Elements of X-Ray Diffraction,* Addison-Wesley, Reading, MA, 1956, p 55–60

3.7 M.C. Flemings, *Solidification Processing,* McGraw-Hill, New York, 1974

3.8 I.V. Samarasekera, Discovery—The Cornerstone of Research in Continuous Casting of Steel Billets, *The Brimacombe Memorial Symposium,* G.A. Irons and A.W. Cramb, Ed., The Metallurgical Society of CIM (MetSoc), 2000, p 399–419

3.9 C.S. Barrett and T.B. Massalski, *Structure of Metals,* 3rd ed., McGraw-Hill, New York, 1966

3.10 L.R. Woodyatt and G. Krauss, Iron-Chromium-Carbon System at 870 °C, *Metall. Trans. A,* Vol 7A, 1976, p 983–989

3.11 E.C. Bain and H.W. Paxton, *Alloying Elements in Steel,* 2nd ed., American Society for Metals, 1961

3.12 *Alloy Phase Diagrams,* Vol 3 *ASM Handbook,* ASM International, 1992

3.13 *Phase Equilibria in Iron Ternary Alloys,* G.V. Raynor and V.G. Rivlin, Ed., Book 406, The Institute of Metals, London, 1988

3.14 *Handbook of Ternary Alloy Phase Diagrams,* P. Pillars, A. Prince, and H. Okamoto, Ed., Vol 1–10 ASM International, 1995
3.15 J.S. Kirkaldy, B.A. Thomson, and E.A. Baganis, Prediction of Multicomponent Equilibrium and Transformation Diagrams for Low Alloy Steels, *Hardenability Concepts and Applications to Steel,* D.V. Doane and J.S. Kirkaldy, Ed., TMS-AIME, Warrendale, PA, 1978
3.16 B. Sundman, B. Jansson, and J.O. Andersson, The Thermo-Calc Databank System, *CALPHAD,* Vol 9 (No. 2), 1985, p 153–190
3.17 Thermo-Calc Software, Stockholm, Sweden, http://www.thermocalc.com (accessed December 2004)
3.18 F. Osmond, *Transformation du Fer,* Baudoin and Co., Paris, 1888
3.19 K.W. Andrews, Empirical Formulae for the Calculation of Some Transformation Temperatures, *JISI,* Vol 203, 1965, p 721–727
3.20 J.S. Kirkaldy and E.A. Baganis, Thermodynamic Prediction of the Ae_3 Temperature of Steels with Additions of Mn, Si, Ni, Cr, Mo and Cu, *Metall. Trans. A,* Vol 9A, 1978, p 495–501
3.21 H.W. Kerr and W. Kurz, Solidification of peritectic alloys, *International Materials Reviews*, Vol. 41, 1996, p 129-164
3.22 H. Shibata, Y. Arai, M. Suzuki, and T. Emi, Kintetics of Peritectic Reaction and Transformation in Fe-C Alloys, *Metallurgical and Materials Transactions B*, Vol. 31B, 2000, p 981–991
3.23 H. Nassar and H. Fredriksson, On Peritectic Reactions and Transformations in Low-Alloy Steels, *Metallurgical and Materials Transactions A*, Vol. 41A, 2010, p 2776–2783
3.24 R. Shepherd, I. Knopp, H-G. Brass, Improved Determination of the Effect of Alloying Elements on the Peritectic Range in Low-Alloyed Cast Steel, *Iron and Steel Technology*, October 2012, p 77–85
3.25 K.E. Blazek, O. Lanzi III, P.L. Gano, and D.L. Kellog, Calculation of the Peritectic Range for Steel Alloys, *AISTech Conference Proceedings*, 2007, Vol II, p 81–87
3.26 D. Hull and D.J. Bacon, *Introduction to Dislocations,* 3rd ed., Pergamon Press, Oxford, 1984
3.27 J. Weertman and J.R. Weertman, *Elementary Dislocation Theory,* Oxford University Press, 1992
3.28 J.P. Hirth and J. Lothe, *Theory of Dislocations,* Wiley, 1982
3.29 G.E. Dieter, *Mechanical Metallurgy,* 2nd ed., McGraw-Hill, New York, 1976
3.30 P.G. Shewmon, *Diffusion in Solids, Second Edition*, 1991
3.31 R.W. Balluffi, S.M. Allen, W.C. Carter, Kinetics of Materials, John Wiley and Sons, 2005
3.32 H. Mehrer, Diffusion in Solids, Springer, 2007
3.33 W.C. Leslie, *The Physical Metallurgy of Steels*, McGraw-Hill Book Company, 1981
3.34 C.J. McMahon, Jr., *Structural Materials*, Merion Books, Philadelphia, 2004, p 208–210.

CHAPTER 4

Pearlite, Ferrite, and Cementite

CHAPTER 3, "PHASES AND STRUCTURES," DESCRIBES the crystal structures of the phases that form in steels and the Fe-C phase diagram, which defines the temperature-composition ranges over which these phases may exist. This chapter shows how various arrangements of phases or microstructures are produced by austenite transformation to ferrite and cementite. Alloy composition and the rate at which austenite is cooled profoundly affect which microstructure forms. The emphasis in this chapter is on the microstructures produced by the diffusion-controlled transformations that occur in carbon steels during relatively slow cooling from the austenite phase field. Eutectoid and proeutectoid microstructures are described.

Eutectoid Transformation

The Fe-C diagram introduced in Chapter 3, provides the basic framework for understanding the phase transformations and microstructures of concern in this chapter. Figure 4.1 is an enlarged section of the Fe-C diagram that includes the areas most pertinent to the transformation of austenite in slowly cooled steels. Consider first the Fe-0.77C alloy, which would be completely austenitic at all temperatures down to the A_1 temperature (727 °C, or 1340 °F). If held for a very long period of time at this temperature, or cooled very slowly through A_1 (that is, under conditions approaching equilibrium), the phase diagram shows that the austenite must be replaced by a mixture of ferrite and cementite. As noted in Chapter 3, a phase transformation in which one solid phase is replaced by two different solid phases is classified as a eutectoid transformation and in the Fe-C system may be written in the form:

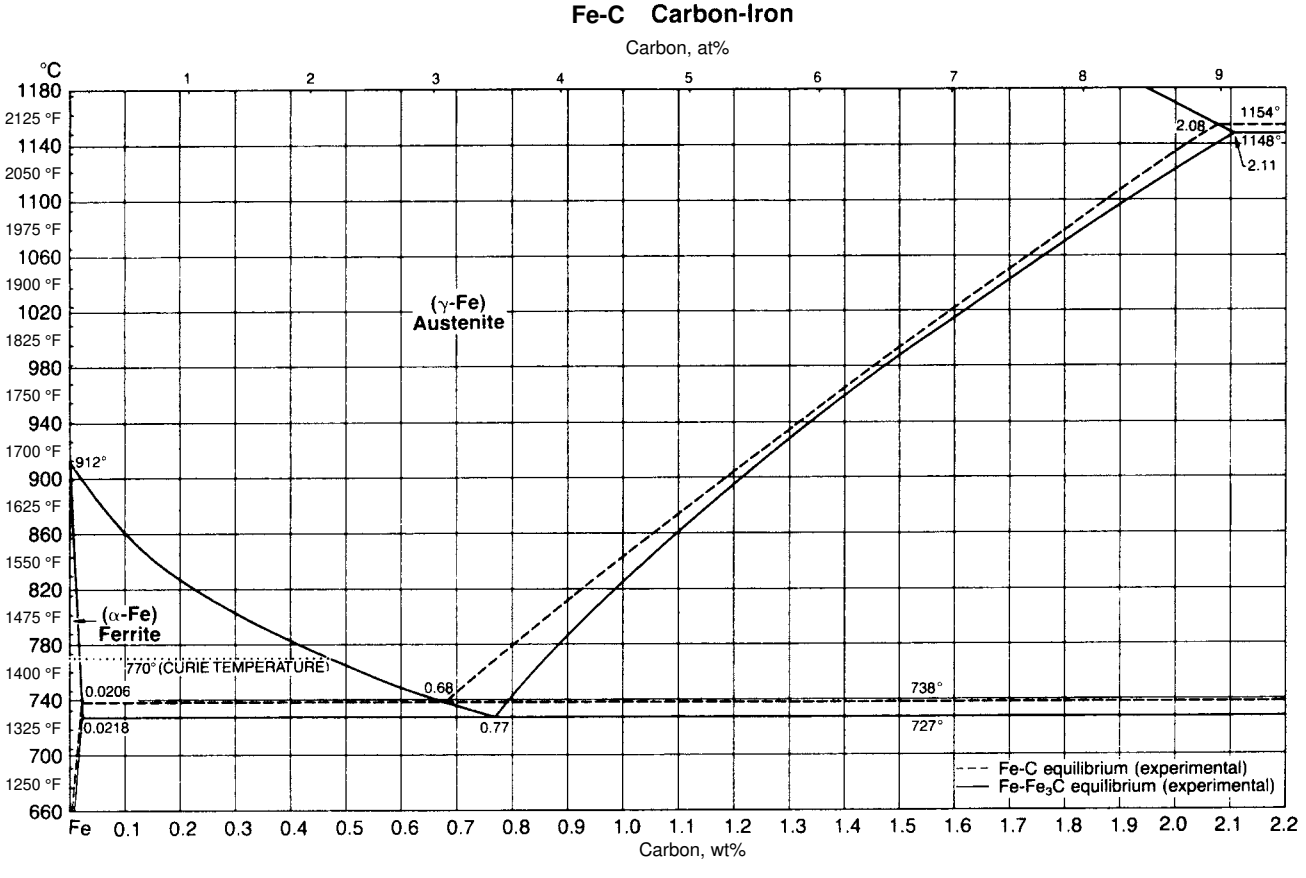

Fig. 4.1 Portion of the Fe-C diagram emphasizing regions of proeutectoid ferrite and cementite formation and the eutectoid transformation of austenite. Source: Ref 4.1

$$\gamma(0.77\%\ \mathrm{C}) \underset{\text{heating}}{\overset{\text{cooling}}{\rightleftharpoons}} \alpha(0.02\%\ \mathrm{C}) + \mathrm{Fe_3C}(6.67\%\ \mathrm{C}) \qquad \text{(Eq 4.1)}$$

This equation shows that the phases involved in the eutectoid reaction have fixed compositions and that the reaction is reversible depending on whether heat is removed or added. Ideally, the eutectoid reaction in Fe-C alloys occurs isothermally at 727 °C. Equilibrium conditions, however, are rarely obtained in actual practice, and the eutectoid reaction may in fact occur over a wide range of temperatures below A_1.

Structure of Pearlite

The eutectoid transformation in steels produces a unique microstructure termed *pearlite*. Pearlite is made up of alternate closely spaced platelets or lamellae of ferrite and cementite as shown in Fig. 4.2, a light micrograph of a furnace-cooled specimen of an Fe-0.75C alloy. Colonies of lamellae of various orientations and spacings characterize the microstructure. The spacing variations of the cementite lamellae in different areas may be due partly to differences in the angles that the lamellae make with the plane of polish, and partly to the fact that the pearlite may have formed over a range of temperatures. Assuming all the pearlite was formed at about the same temperature, and that, therefore, all the lamellae had almost identical

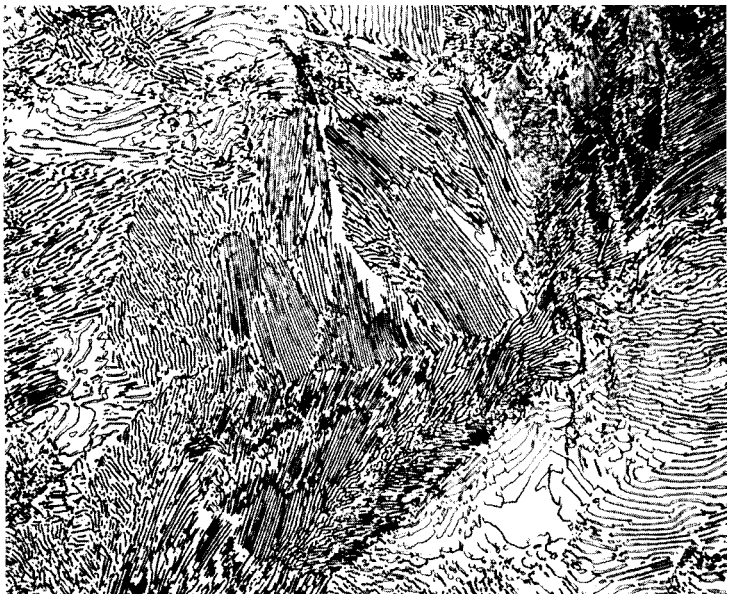

Fig. 4.2 Pearlite in a furnace-cooled Fe-0.75C alloy. Picral etch. Original magnification at 500×. Courtesy of A.R. Marder and A. Benscoter, Bethlehem Steel Corp., Bethlehem, PA

spacing, those colonies with lamellae perpendicular to the plane of polish would show the true spacing or closest spacing of the ferrite and cementite lamellae. Those lamellae at angles less than 90° would show a wider spacing. Determination of the true pearlite spacing from metallographically prepared specimens where the lamellae form a range of angles with the specimen surface requires special quantitative metallographic analyses (Ref 4.2, 4.3).

The origin of the term *pearlite* is related to the regular array of the lamellae in the colonies and the fact that etching attacks the ferrite phase more severely than the cementite. The raised and regularly spaced cementite lamellae of the colonies then act as diffraction gratings, and a pearl-like luster is produced by diffraction of light of various wavelengths from the different colonies.

The amounts of cementite and ferrite in pearlite formed at 727 °C can be determined by a calculation based on the lever rule. The lever rule can be applied to any two-phase field of a binary phase diagram to determine the amounts of the different phases present at a given temperature in a given alloy. A horizontal line, referred to as a *tie line*, represents the lever, and the alloy composition its fulcrum. The intersection of the tie line with the boundaries of the two-phase field fixes the compositions of the coexisting phases, and the amounts of the phases are proportional to the segments of the tie line between the alloy and the phase compositions. For pearlite, assume a tie line immediately below 727 °C that spans the ferrite-cementite phase field (see Fig. 4.1). Application of the lever rule calculation for the Fe-0.77C alloy, the alloy that transforms entirely to pearlite, shows that:

$$\text{wt\% } Fe_3C \text{ in pearlite} = \frac{0.77 - 0.02}{6.67 - 0.02} \times 100 = 11\% \qquad \text{(Eq 4.2)}$$

By difference, the weight percent ferrite in pearlite is 89%. Therefore, whenever austenite containing 0.77% carbon transforms to pearlite at or close to 727 °C, ferrite and cementite form in the fixed weight percentages as shown previously. The densities of ferrite and cementite, 7.87 and 7.70 g/cm^3, respectively, are so close that the volume percentages of ferrite and cementite in pearlite are essentially the same as the weight percentages. Therefore, in Fe-C alloys, the amounts of phases calculated by the lever rule with compositions by weight should correlate well with the amounts of phases revealed in light micrographs. The amounts of phases visible in micrographs are related to area percentages, which in turn are directly related to their volume percentages if the phases are uniformly distributed.

The development of a pearlite colony has been shown to initiate from either ferrite or cementite crystals (Ref 4.4, 4.5). Originally, the lamellar structure was thought to develop only by sidewise nucleation of separate

lamellae; however, branching of a single cementite crystal into parallel lamellae with spacing characteristic of a given transformation temperature has also been shown to produce the lamellar structure. According to the latter mechanism, all of the cementite in a given colony is interconnected, and a colony of pearlite may be regarded as two single crystals of ferrite and cementite. The latter structure was strikingly revealed in a serial sectioning experiment in which a pearlite colony was repeatedly photographed as successive layers were removed by polishing in 1 μm steps (Ref 4.4). All of the apparently separate cementite lamellae were shown to have a common origin. Once a pearlite colony is established by sidewise nucleation and/or branching of the ferrite and cementite, the lamellae are considered to grow by extension of their edges into the austenite, a process frequently referred to as *edgewise growth* (Ref 4.6).

Pearlite Transformation Kinetics

The preceding section described the lamellar structure of pearlite and its formation by a eutectoid reaction at or close to 727 °C (1340 °F). In actual practice, however, the formation of pearlite rarely occurs close to the A_1. Figure 4.3 shows an isothermal transformation diagram for eutectoid 1080 steel. Curves for the beginning and end of pearlite formation, obtained by cooling from the austenite phase field and holding at various temperatures below A_1, are shown. The beginning of the transformation curve is asymptotic to the A_1, thus indicating that pearlite would not form at temperatures close to A_1 unless the steel were held at temperature for extended periods of time. In commercial heat-treating practice, the slow rates of cooling that would permit pearlite formation close to the A_1 are approached only in very heavy sections or by furnace cooling. With increased undercooling below A_1, however, the time periods for the beginning and end of pearlite transformation are reduced substantially. At the nose of the transformation curve, 540 °C (1005 °F), the lowest temperature at which pearlite forms in this steel, only seconds are required for complete transformation. Below 540 °C, bainite, a non-lamellar microstructure of ferrite and cementite, is formed.

A number of factors influence the rate of pearlite formation. Perhaps most important is the fact that substantial carbon atom rearrangement must take place to accomplish the transformation of austenite (containing nominally 0.77% C) to low-carbon ferrite and high-carbon cementite according to Eq 4.1. The diffusion of carbon, as characterized by its diffusion coefficient, is temperature-dependent. One equation that has been developed (Ref 4.8) to show the temperature dependence of carbon diffusion in austenite is:

$$D_C^{\gamma} = 0.12e^{-32{,}000/RT} \qquad \text{(Eq 4.3)}$$

where D_C^{γ} is the average diffusion coefficient (cm^2/s) of carbon in austenite, R is the gas constant (1.98 cal/g-mol/K), and T is the absolute temperature (°C + 273). Equation 4.3 shows that the diffusion coefficient decreases exponentially with decreasing temperature, a powerful effect that significantly lowers the diffusion coefficient for small decreases in temperature. At first glance, the temperature dependence of diffusion appears to contradict the experimentally established fact (see Fig. 4.3) that pearlite formation is faster at lower temperatures than it is at higher temperatures. This apparent anomaly is explained by the reduction of interlamellar spacing as the temperature of pearlite transformation decreases. Thus, the distance that carbon has to diffuse to distribute itself between the ferrite and cementite decreases, and despite the fact that diffusion becomes more sluggish at lower temperatures, the growth of pearlite colonies accelerates.

The interrelationships between diffusion and the lamellar structure of pearlite help to explain how the eutectoid transformation proceeds, but not why the transformation occurs. The stability of all phases and microstruc-

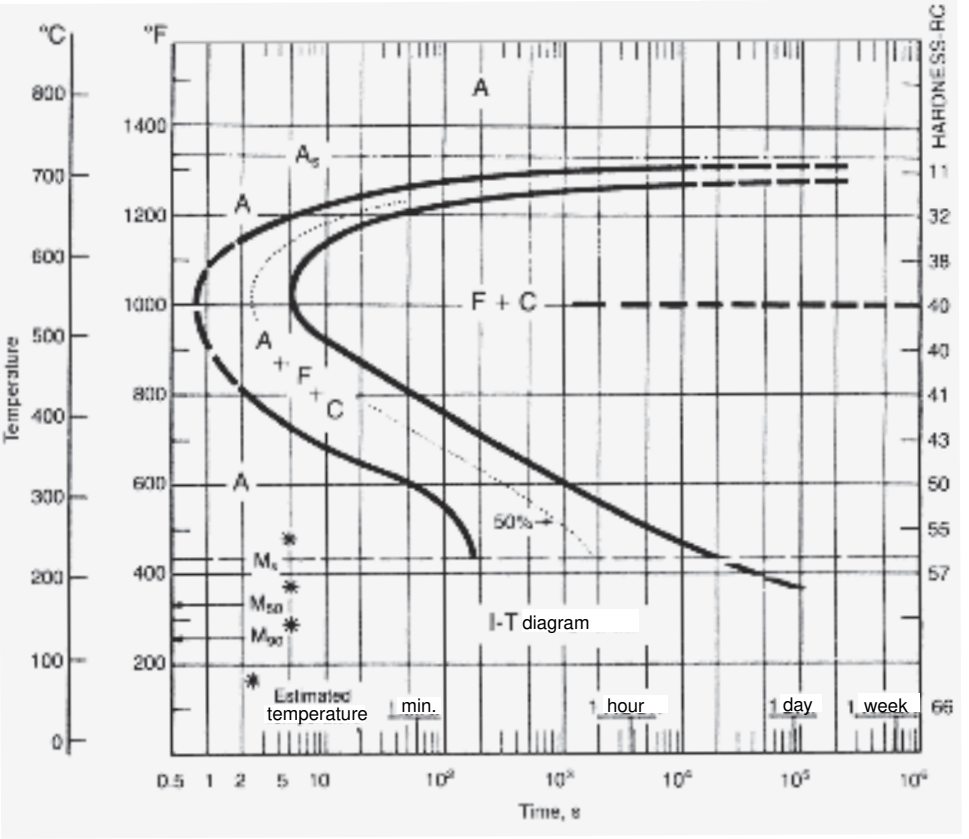

Fig. 4.3 Isothermal transformation diagram for 1080 steel containing 0.79% C and 0.76% Mn. Specimens were austenitized at 900 °C (1650 °F) and had an austenite grain size of ASTM No. 6. Source: Ref 4.7

tures in metals and alloys is based on the principle of minimum free energy. If the free energy of a given microstructure or system is not a minimum, then either a phase transformation (for example, the austenite-to-pearlite transformation under consideration here) or microstructural rearrangement without a phase change (for example, grain growth or particle coarsening) would occur in order to lower free energy to the minimum possible value.

The free energy (G) per unit volume of a phase or combination of phases is defined in terms of other thermodynamic parameters, enthalpy or heat content (H), the absolute temperature (T), and entropy (S) as follows:

$$G = H - TS \qquad \text{(Eq 4.4)}$$

Enthalpy is the total energy of a phase (or microstructure composed of several phases) per unit volume of that structure. Entropy is a measure of the degree of order associated with a given structure at a given temperature. It may be influenced by the amplitude of atom vibration, the mixing of several component types of atoms and/or vacant lattice sites in a given phase, or the degree of order associated with a given solid or liquid structure. The TS term, therefore, is a measure of the energy associated with the order of a unit volume of a given structure at a given temperature and is especially important in establishing phase stability at high temperatures. Equation 4.4 shows that the difference between the enthalpy and entropy terms defines free energy. A rigorous approach to the development of atomistic and classical thermodynamics is presented in the text by Swalin (Ref 4.9).

A helpful example of the application of the principle of minimum free energy in establishing phase stability is the melting of a solid crystal structure. With increasing temperature, H increases, but TS increases much more if the liquid, with its high degree of atomic disorder, replaces the ordered crystal structure. Therefore, above the melting point, because of its higher entropy, the liquid has the lower free energy and is the stable phase relative to the solid. Similar considerations apply to transformations between solid phases such as the transformation of austenite to ferrite and cementite.

At the Ae_1 temperature in the Fe-C system, the free energy of austenite is exactly equal to the free energy of ferrite and cementite and there is no incentive for transformation to occur, especially if interfaces or boundaries between the austenite and pearlite must be created. Interfaces accommodate structural and chemical discontinuities between phases, and therefore make positive contributions to or raise the energy of a system. However, with decreasing temperature below Ae_1, the free energy of a unit volume of a mixture of ferrite and cementite becomes much less than that of austenite. This free energy difference is frequently referred to as the driving force for transformation and increases with decreasing temperature or undercooling below the Ae_1. A larger driving force makes

possible not only the development of more colonies of pearlite but also a finer lamellar spacing within a pearlite colony, structural changes that result in increased interfacial area of two types. A higher density of pearlite colonies results in increased austenite/pearlite interfacial area, and a reduced interlamellar spacing results in increased ferrite-cementite interfacial energy within the colonies. The high driving force at low temperatures offsets the positive energy contributions due to the various interfaces produced during the austenite transformation to pearlite.

Many relationships for the change in interlamellar spacing with undercooling have been proposed (Ref 4.10), but the one most closely related to the above considerations was developed by Zener and Hillert, as presented in the following equation:

$$S = \frac{4\sigma_{\alpha/Fe_3C} T_E}{\Delta H_V \Delta T} \qquad \text{(Eq 4.5)}$$

where S is the interlamellar spacing defined by the combined width of the α and Fe_3C lamellae; σ_{α/Fe_3C} is the interfacial energy per unit area of α/Fe_3C boundary; T_E is the equilibrium temperature in degrees Kelvin (Ae_1 in the case of Fe-C alloys and steels); ΔH_V is the change in enthalpy per unit volume between austenite and the mixture of ferrite and cementite; and ΔT is the undercooling below Ae_1. Figure 4.4 shows a set of mea-

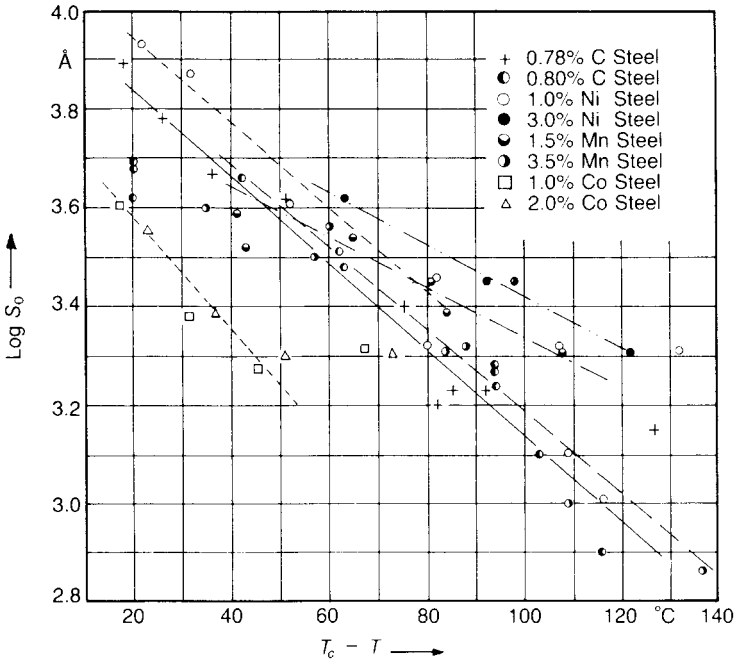

Fig. 4.4 Average true interlamellar spacings of pearlite, S_o, as a function of undercooling below Ae_1 for various steels as indicated. Source: Ref 4.2

surements illustrating the decrease in pearlite spacing with increasing undercooling for a variety of steels.

The isothermal transformation kinetics of the eutectoid transformation, i.e., the progress of pearlite formation as a function of time at a constant temperature, are based on the nucleation and growth rates of pearlite colonies. Figure 4.5 shows circular cross sections of pearlite colonies in an Fe-C alloy of eutectoid composition that has been partially transformed to pearlite. A number of colonies of pearlite have been nucleated and are in the process of growing into the austenite at the reaction temperature. In contrast to the pearlite shown in Fig. 4.2, the individual lamellae are too closely spaced to be resolved at the magnification of the micrograph, and the pearlite colonies have a dark appearance. The balance of the microstructure is white-etching martensite, formed in any untransformed austenite when it was quenched from the reaction temperature. Martensite and its formation are described in Chapter 5, "Martensite."

Johnson and Mehl (Ref 4.11), assuming that the pearlite colonies are spherical and randomly nucleated as a function of time, developed the following equation for isothermal pearlite formation:

$$f(t) = 1 - \exp[-\pi N G^3 t^4/3] \qquad \text{(Eq 4.6)}$$

where $f(t)$ is the volume fraction of pearlite formed at any time t at a given temperature, N is the nucleation rate of the colonies, and G is the rate at

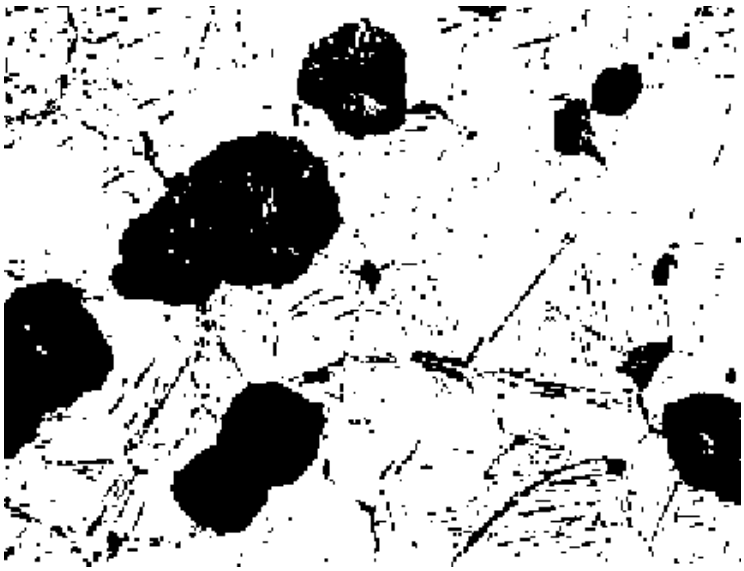

Fig. 4.5 Cross sections of spherical colonies of pearlite (dark) in eutectoid steel. Remainder of microstructure is martensite formed in austenite not transformed to pearlite at the reaction temperature. Original magnification at 250×. Courtesy of A.R. Marder and B. Bramfitt, Bethlehem Steel Corp., Bethlehem, PA

which the colonies grow into the austenite. The Johnson-Mehl equation describes mathematically the rate at which austenite is converted to a pearlitic microstructure by the nucleation and growth of pearlite colonies. At any given temperature, $f(t)$ versus time fits an S-shaped or sigmoidal curve, as shown in Fig. 4.6. The initial transformation rate is quite low and is associated with what is referred to as an *incubation period*, the time during which the first stable nuclei develop. As more and more nuclei develop and are in various stages of growth, the rate of transformation increases. Finally, the colonies impinge and the rate of transformation again slows as the microstructure gradually approaches complete transformation. The elapsed time periods needed to initiate and complete the pearlite transformation are directly related to the beginning and end of transformation curves in isothermal transformation diagrams shown schematically in Fig. 4.7. The exact beginning and end of pearlite formation at any given temperature is of course dependent on the sensitivity of the experimental techniques used to follow the transformation, but generally the accuracy is on the order of 1%. Therefore, the beginning and end of the transformation curves in Fig. 4.7 correspond to 1% and 99% transformation, respectively.

The shape of the isothermal transformation curve for eutectoid steel (Fig. 4.3) is explained by the temperature dependence of the nucleation and growth rates of the pearlite colonies. Figure 4.8 shows that both N and G in a 0.78% carbon steel increase with decreasing transformation temperature, thus, according to the Johnson-Mehl equation, accelerating the eutectoid transformation at lower temperatures. As discussed earlier, the greater driving force associated with increased undercooling produces more nuclei and smaller interlamellar spacing. The latter in turn increases

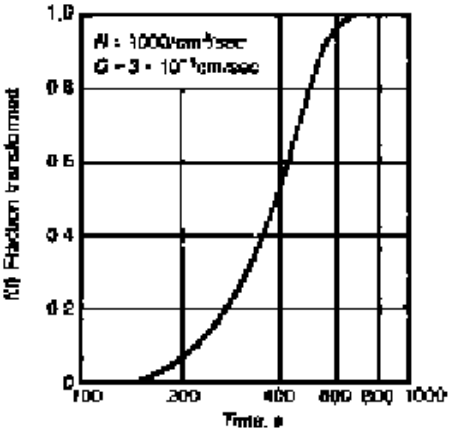

Fig. 4.6 Calculated fraction austenite transformed to pearlite as a function of time for the parameters shown. Source: Ref 4.2

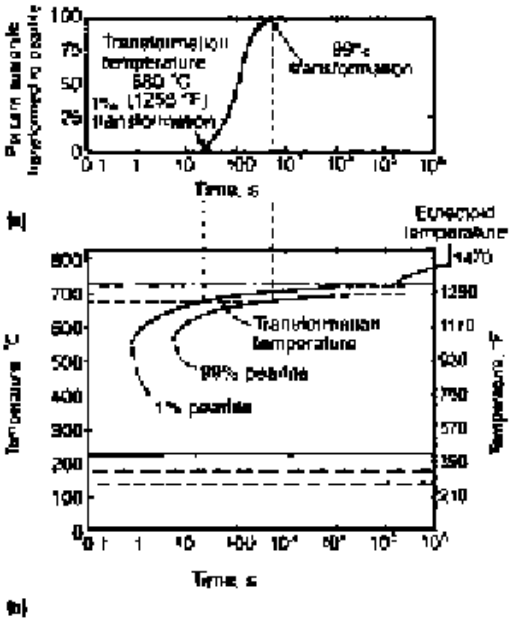

Fig. 4.7 Relationship of an isothermal reaction curve for (a) pearlite formation to (b) the time-temperature-transformation diagram. Source: Ref 4.7

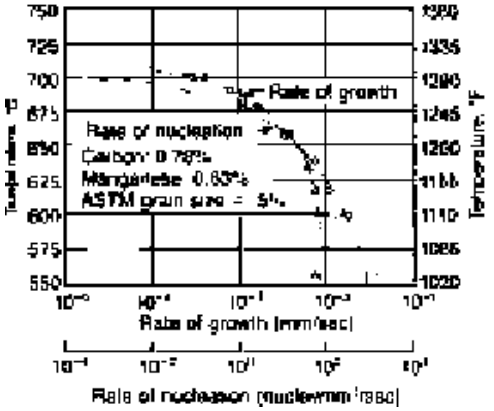

Fig. 4.8 Variation of nucleation and growth rates for pearlite formation as a function of temperature in a eutectoid steel. Source: Ref 4.12

the growth rate of the pearlite colonies by effectively reducing the distance over which carbon must diffuse at the austenite/pearlite interface.

The preceding discussion shows that the Johnson-Mehl equation offers a highly effective approach to characterizing the kinetics of pearlite transformation. The assumption that the pearlite colonies nucleate randomly in the austenite throughout the course of the transformation is not always valid, however. As shown in Fig. 4.5, the pearlite colonies invariably nu-

cleate at austenite grain boundaries. Eventually, the grain boundaries become saturated with nuclei, nucleation terminates, and the balance of the transformation is accomplished solely by growth of the grain boundary nucleated colonies into the austenite (Ref 4.13).

The mechanism of pearlite formation continues to receive theoretical and experimental attention. Perhaps the most active considerations involve the way in which carbon and other alloying elements distribute themselves between the ferrite and cementite lamellae. Earlier in this chapter it was tacitly assumed that the growth of a pearlite colony is dependent on the diffusion of carbon atoms through the austenite ahead of the pearlite interface. Such diffusion through a crystal phase is referred to as bulk, or volume, diffusion. Another possibility, however, is that the carbon diffuses along the advancing interface between the pearlite and the austenite (Ref 4.6). Such interface or grain-boundary diffusion occurs more rapidly than volume diffusion because of the more irregular or open packing of atoms at grain boundaries in comparison to the regular, close atom-packing within a grain.

Alloying Elements and Pearlite Formation

Alloying elements have a strong effect on the rate of formation and structure of pearlite. Figure 4.9 shows the distribution of alloying element

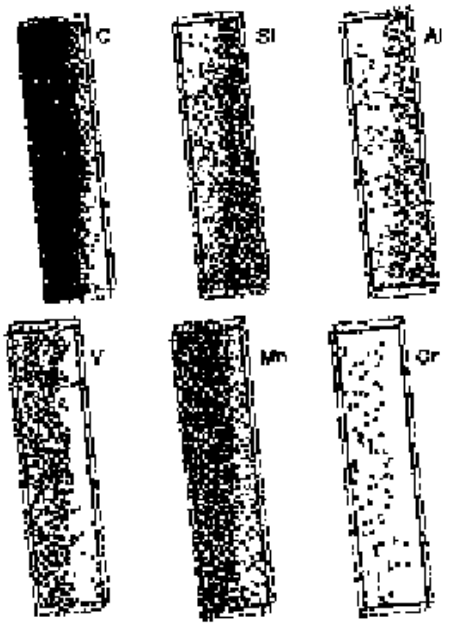

Fig. 4.9 Three dimensional atom maps in the cementite and ferrite of pearlite in a eutectoid steel transformed for 20 seconds at 500 °C (930 °F). Atom Probe Field Ion Micrograph. Source: Ref 4.14

atoms in the pearlite of a steel containing 0.85% carbon and microalloyed with vanadium (Ref 4.14). Manganese, chromium, and vanadium, carbide-forming elements, have partitioned to the cementite lamellae and silicon and aluminum have partitioned to the intervening ferrite.

The diffusional redistribution of alloying elements as austenite transforms to pearlite significantly slows the growth rate of pearlite, as shown in Fig. 4.10 and 4.11. Puls and Kirkaldy (Ref 4.10) suggest that manganese and nickel do not partition themselves between the ferrite and cementite and that, therefore, pearlite formation in Fe-C-Mn and Fe-C-Ni alloys is dependent primarily on volume diffusion of carbon in austenite. Any reduction in the rate of pearlite growth in these systems is due to the effect of manganese and nickel on the diffusion of carbon in austenite. However, chromium and molybdenum, which are strong carbide-forming elements, are considered to partition to the carbide lamellae by interface diffusion. In the Fe-C-Cr and Fe-C-Mo systems, then, pearlite growth is

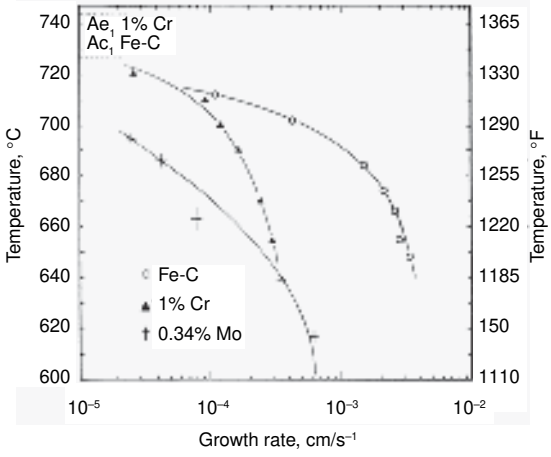

Fig. 4.10 Pearlite growth rates as a function of temperature for an Fe-0.81C alloy and eutectoid steels containing chromium and molybdenum. Source: Ref 4.10

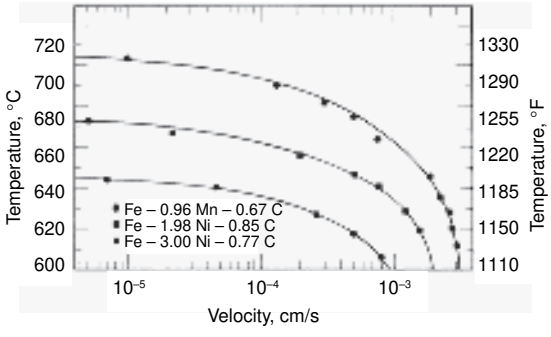

Fig. 4.11 Pearlite growth rates as a function of temperature for eutectoid steels with nickel and manganese. Source: Ref 4.10

retarded because chromium and molybdenum atoms must diffuse, a process that is much more sluggish than the diffusion of carbon because of the much larger size of the alloying element atoms compared to carbon atoms. A hot stage microscope study of the effects of alloying elements on pearlite formation in eutectoid steels ranked molybdenum, followed by Si, Ni, Co, and Mn in the order of decreasing effectiveness in suppressing the pearlite reaction (Ref 4.15).

In view of the above studies, and many more in the literature, all alloying elements slow in one way or another the diffusion-controlled growth of pearlite, an effect that is extremely valuable when martensitic microstructures, instead of those produced by diffusion, are the desired objectives of heat treatment. The practical effects of alloying elements in retarding pearlite formation in steels are the basis of the topic of hardenability discussed in Chapter 16, "Hardness and Hardenability."

Interphase Precipitation

In alloy steels containing strong nitride and carbide-forming elements such as vanadium, niobium, titanium, molybdenum, and tungsten, a special type of austenite decomposition occurs. Honeycombe and his colleagues (Ref 4.5) have shown that rows of very fine alloy carbide particles form along the interface between decomposing austenite and newly formed ferrite. In view of the fact that the carbides nucleate and grow at the interface between austenite and ferrite, the reaction is termed interphase precipitation. However, because one solid phase transforms into two other solid phases, the interphase reaction may also be classified as a eutectoid transformation, producing a special microstructure much different from lamellar pearlite.

The alloy carbides that make up the rows left behind by the moving austenite-ferrite interface are frequently on the order of 100 Å (10 nm) or less and are too fine to be resolved in the light microscope. Figure 4.12(a) is a light micrograph that shows the initiation of interphase precipitation at austenite grain boundaries in an Fe-0.75V-0.15C alloy held for 10 s at 680 °C (1255 °F). The colonies of the interphase precipitate have curved interfaces and outline the austenite grain boundaries, but no structure is visible within the colonies. The balance of the microstructure is a low-carbon martensite formed on rapid cooling after the 10 s hold at 680 °C . The rows of fine precipitates present in the colonies of interphase precipitation are shown in Fig. 4.12(b), a transmission electron micrograph taken from the Fe-0.75V-0.15C steel held for 5 min at 725 °C (1335 °F).

An interesting aspect of the mechanism of interphase precipitation is the growth of the colonies by the extension of ledges in a direction parallel to the austenite-ferrite interface. As successively nucleated ledges complete their growth, a net extension of the colonies normal to the colony interface develops. Figure 4.13 shows examples of growth ledges in an Fe-12Cr-

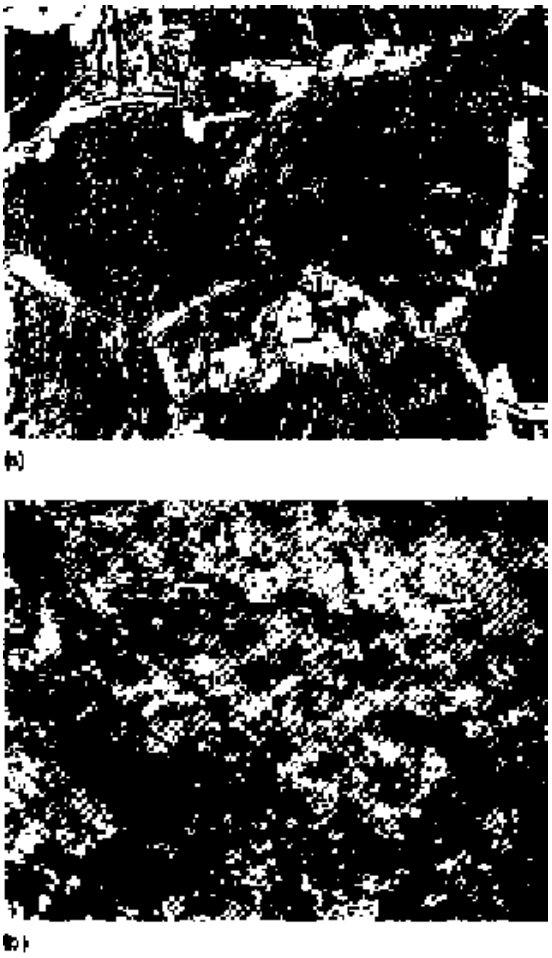

Fig. 4.12 (a) Colonies of interphase precipitation (light areas) nucleated at austenite grain boundaries of an Fe-0.75V-0.15C alloy held 10 s at 680 °C (1255 °F). Original magnification at 125×. (b) Rows of fine alloy carbides within a colony of the same steel held 5 min at 725 °C (1340 °F). Original magnification at 100,000×. Courtesy of R.W.K. Honeycombe, University of Cambridge, U.K.

0.2C steel isothermally transformed for 36 min at 650 °C (1200 °F). Arrows point to the ledges. The planar interfaces left behind by the movement of the ledges are the sites for the carbide formation, while the ledges themselves are free of particles.

Interphase precipitation is now used in steels to provide extra strengthening to ferrite/pearlite microstructures in medium-carbon steels microalloyed with vanadium and niobium (Ref 4.16). The mechanical properties of microalloyed forging steels are described in detail in Chapter 14, "Non-Martensitic Strengthening of Medium-Carbon Steels: Microalloying and Bainitic Strengthening."

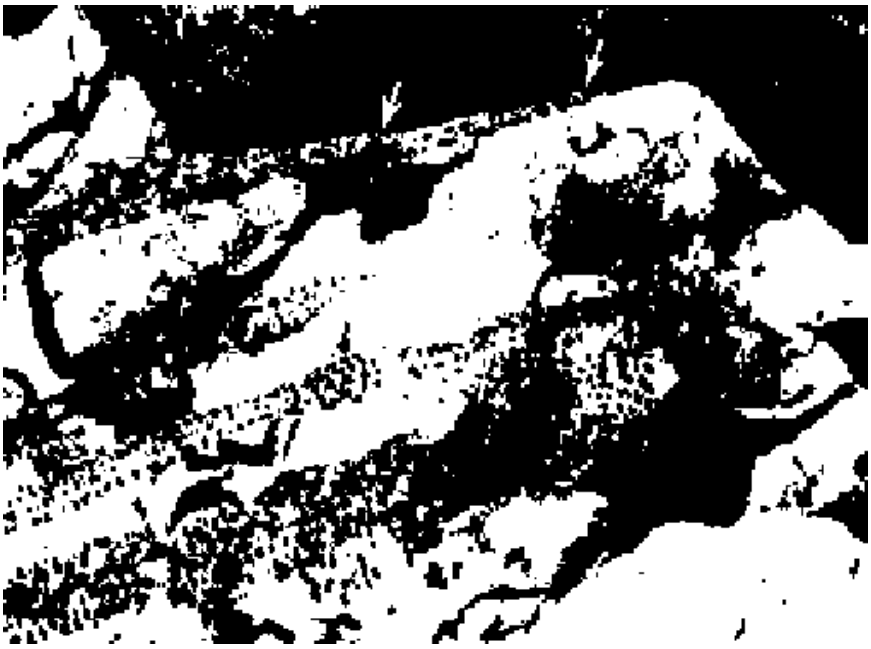

Fig. 4.13 Interphase precipitation and ledges in Fe-12Cr-0.2C steel isothermally transformed at 650 °C (1200 °F) for 36 min. Transmission electron micrograph. Original magnification about 70,000×. Courtesy of K. Campbell and R.W.K. Honeycombe, University of Cambridge, U.K.

Divorced Eutectoid Transformation—Dispersed Carbide Particles in Ferrite

A third type of eutectoid microstructure in steels, in addition to lamellar pearlite and interphase precipitation, is formed by divorced eutectoid transformation (DET). The microstructure consists of cementite particles dispersed in a matrix of ferrite, and although it has been long observed, recent work of Sherby and Verhoeven and their colleagues have only recently systematically characterized DET (Ref 4.17, 4.18). Figure 4.14 compares schematically the transformation of austenite to the lamellar ferrite/cementite microstructure of pearlite and to the dispersed cementite/ferrite microstructure produced by DET (Ref 4.18). For the latter microstructure, small dispersed carbide particles in austenite, sometimes too fine to be observable in the light microscope, are enlarged, concentrating carbon, as the high concentration of carbon in the parent austenite diffuses from the ferrite at the transformation growth front. The dispersed cementite/ferrite microstructure typically forms in high-carbon steels and at temperatures just below A_1; at greater amounts of undercooling, the transformation of austenite to the lamellar ferrite/cementite structure of pearlite is favored (Ref 4.17).

Figure 4.15 shows the effect of austenitizing temperature and carbon content on the morphology of the eutectoid microstructures formed on cooling (Ref 4.19). In steels with more than 1.0% carbon the austenite transforms to a spherical carbide/ferrite morphology on cooling from a relatively wide range of austenitizing temperatures, a result that correlates with high densities of residual spherical carbide particles in high-carbon steels that require higher austenitizing temperatures and times to dissolve completely. These residual carbide particle distributions make up the austenite/carbide structure that is the parent microstructure for the divorced eutectoid transformation. Figure 4.15 also shows that spheroidal eutectoid microstructures may also form in lower-carbon steels if austenitized in a narrow temperature range just above the A_1. The resulting spheroidized or mixed lamellar microstructures result from annealing heat treatments that produce lower hardness and higher ductility than normalizing treatments typically performed at higher austenitizing temperatures and produce more fully la-

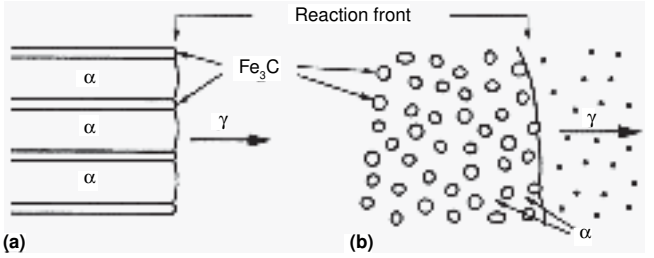

Fig. 4.14 Schematics of interface growth fronts associated with the transformation of austenite to (a) pearlite and (b) dispersed cementite particles in ferrite. Source: Ref 4.18

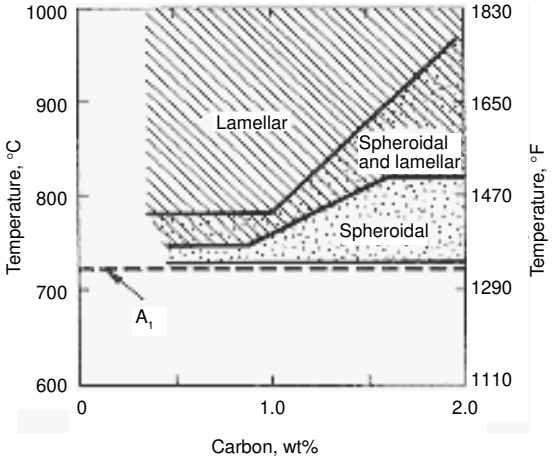

Fig. 4.15 Schematic diagram showing the effect of austenitizing temperature and steel carbon content on the morphology of the eutectoid microstructures formed on cooling after austenitizing. (Ref 4.19)

mellar pearlitic microstructures. Annealing and normalizing heat treatments are discussed in more detail in Chapter 13, "Normalizing, Annealing, and Spheroidizing Treatments; Ferrite/Pearlite and Spherical Carbides."

Proeutectoid Phases

In most steels, i.e., those not of eutectoid composition, austenite begins to transform well above the A_1 temperature. Figure 4.1 shows that ferrite forms below the A_3 temperature in steels that contain less than the eutectoid carbon content (*hypoeutectoid* steels), and cementite forms below the A_{cm} in steels containing more than the eutectoid carbon content (*hypereutectoid* steels). The ferrite and cementite that form prior to the eutectoid transformation are referred to as *proeutectoid* ferrite and cementite in order to indicate that they have formed by a mechanism other than the eutectoid transformation.

Proeutectoid ferrite and cementite are identical in crystal structure and composition to the ferrite and cementite of pearlite, but the distribution of their microstructure is quite different from their lamellar distribution in pearlite. Figure 4.16 shows a microstructure of proeutectoid ferrite and pearlite that formed in an Fe-0.4C alloy during slow cooling from the austenite phase field. The coarse network of white-etching proeutectoid ferrite is in marked contrast to the lamellar pearlite. Figure 4.1 shows that

Fig. 4.16 Proeutectoid ferrite (white network) and pearlite in an Fe-0.4C alloy air cooled from the austenite field. Nital etch. Original magnification at 500×. Courtesy of A.R. Marder and A. Benscoter, Bethlehem Steel Corp., Bethlehem, PA

proeutectoid ferrite in a slowly cooled Fe-0.4C alloy begins to form just above 780 °C (1435 °F) and continues to grow until the A_1 temperature is reached. Tie lines through the ferrite/austenite field at successively lower temperatures and the applications of the lever rule to the Fe-0.4C alloy show that the amount of proeutectoid ferrite and the carbon content of the austenite increase continuously with decreasing temperature. The low solubility of carbon in ferrite requires that the carbon content builds up in the austenite. At the A_1 temperature the carbon content of the austenite coexisting with the ferrite in the Fe-0.4C alloy, or any other hypoeutectoid steel for that matter, is 0.77%, which is just the right composition required for the eutectoid reaction, as written in Eq 4.1. Consequently, any austenite coexisting with ferrite at the A_1 temperature transforms to pearlite on cooling, producing microstructures such as those shown in Fig. 4.16. The lever rule applied to the Fe-0.4C alloy in the ferrite-austenite phase field at 727 °C (1340 °F) shows that there should be about 50% by weight proeutectoid ferrite in the microstructure according to the following calculation:

$$\text{wt\% proeutectoid ferrite} = \frac{0.77 - 0.4}{0.77 - 0.02} \times 100 \qquad \text{(Eq 4.7)}$$

Alloys or steels with less carbon than 0.4% would contain more proeutectoid ferrite; those with more carbon would contain more pearlite. Depending on the carbon content of the steel, then, it is possible to have microstructures consisting of 100% ferrite (if the carbon content is less than or equal to 0.02%) or 100% pearlite (if the carbon content is equal to 0.77%) or any combination of proeutectoid ferrite and pearlite between these extremes. Steels designated for applications that require good formability—for example, automotive panel parts—have microstructures that are predominantly ferrite, while steels selected for applications where hardness and wear resistance are most important—for example, railroad rails—have microstructures that are completely pearlitic. The properties of steels heat treated to have microstructures of ferrite and pearlite are described in Chapters 12, "Low-Carbon Steel," 13, "Normalizing, Annealing, and Spheroidizing Treatments; Ferrite/Pearlite and Spherical Carbides," and 15, "High-Carbon Steels: Fully Pearlitic Microstructures and Wire and Rail Applications."

Up to this point, only the formation of proeutectoid ferrite has been considered. Steels with carbon content greater than the eutectoid compositions form proeutectoid cementite if slowly cooled through or held in the cementite/austenite phase field (see Fig. 4.1). As the cementite (containing 6.67% C) forms, the carbon content of the austenite must decrease.

With decreasing temperature, the austenite composition follows the A_{cm} until at the eutectoid temperature the austenite contains 0.77% carbon, again just the right composition for the eutectoid reaction. The balance of the austenite then transforms to pearlite.

Figure 4.17 shows a network of proeutectoid cementite that has formed by holding an Fe-1.22C alloy at 780 °C (1435 °F) for 30 min. Some colonies of pearlite are also present, the dark circular patches, and the balance of the microstructure is martensite formed during quenching from 780 °C. The carbon content of steels rarely exceeds 1.2%; therefore, little proeutectoid cementite ever forms. Application of the lever rule in the austenite-cementite field to the 1.2% carbon alloy at 727 °C shows that only about 7% proeutectoid cementite could form. However, even though there can never be a large amount of proeutectoid cementite, the presence of a proeutectoid cementite network is considered to be very detrimental to the workability and toughness of high-carbon steels. Normalizing and spheroidizing heat treatments designed to modify or eliminate the cementite networks are discussed in Chapter 13, "Normalizing, Annealing, and Spheroidizing Treatments; Ferrite/Pearlite and Spherical Carbides."

Proeutectoid Phase Formation

Fig. 4.16 and 4.17 show, respectively, proeutectoid ferrite and cementite that have formed on austenite grain boundaries during cooling to the eutectoid transformation temperature. These proeutectoid crystal morphologies, formed by nucleation and growth along austenite grain bound-

Fig. 4.17 Proeutectoid cementite (white network) formed at austenite grain boundaries in an Fe-1.22C alloy held at 780 °C (1435 °F) for 30 min. Dark patches are pearlite colonies and the remainder of the microstructure is martensite and retained austenite. Nital etch. Original magnification at 600×. Courtesy of T. Ando, Colorado School of Mines

aries, are referred to as *grain boundary allotriomorphs* and typically form during slow cooling through either the austenite/ferrite or austenite/ cementite two-phase fields. More rapid cooling produces other morphologies of ferrite, and these morphologies, their classification, and other characteristics are discussed in detail in Chapter 7, "Ferritic Microstructures." The proeutectoid phases grow by a ledge mechanism that operates by atom transfer across steps or ledges in the interface between the parent austenite and a growing proeutectoid crystal (Ref 4.20, 4.21). Figure 4.18 shows steps at interfaces of cementite allotriomorphs formed by isothermal transformation in austenite/cementite two-phase fields of 52100 steels. Figure 4.19 shows fine growth ledges in grain boundary cementite formed

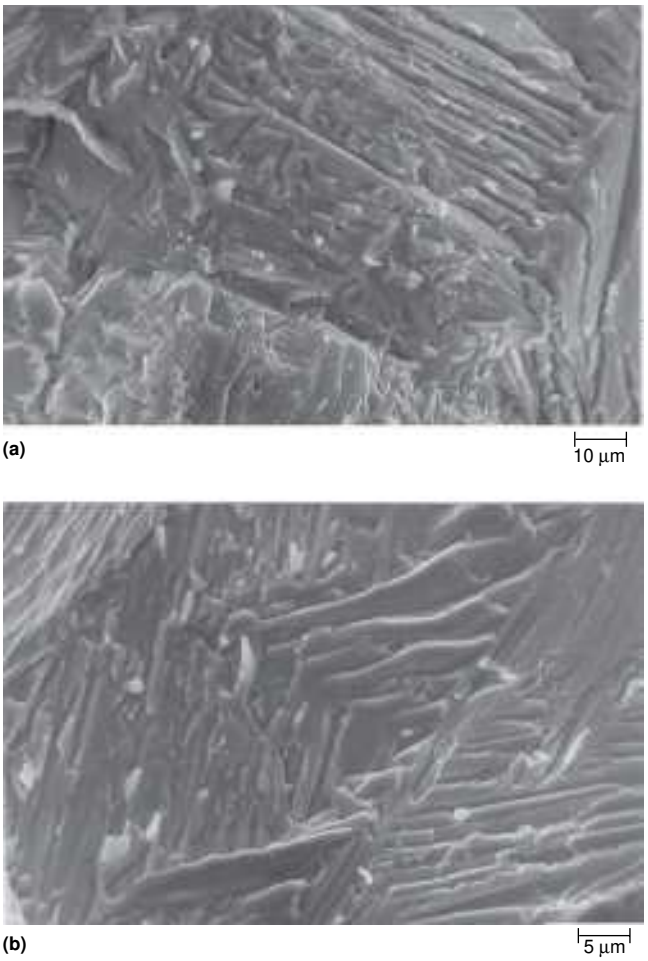

Fig. 4.18 Stepped cementite interfaces in (a) 52100 steel transformed at 785 °C (1450 °F) for 30 min and (b) 52100 steel transformed at 785 °C for 2h. SEM micrographs taken from fracture surfaces. Courtesy of T. Ando, Colorado School of Mines

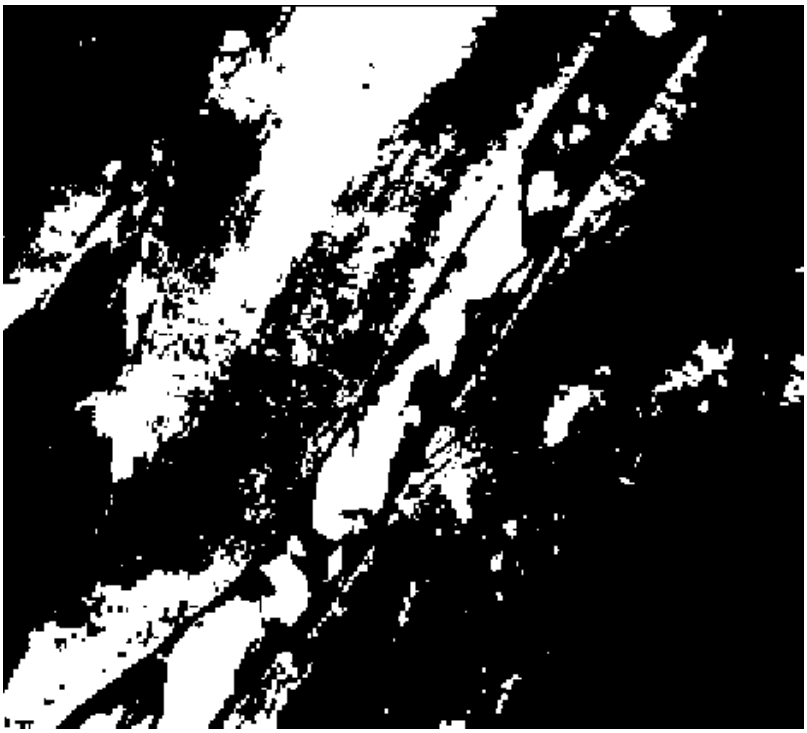

Fig. 4.19 Fine ledges. Arrows on cementite allotriomorph interface in 52100 steel transformed at 810 °C (1490 °F) for 13 min. TEM micrograph, original magnification at 40,000×. Courtesy of T. Ando, Colorado School of Mines

in 52100 steel (Ref 4.22, 4.23). A detailed review of proeutectoid cementite formation is given in Ref 4.24.

REFERENCES

4.1 *Metallography, Structures and Phase Diagrams,* Vol 8, 8th ed., *Metals Handbook,* American Society for Metals, 1973, p 276

4.2 R.F. Mehl and W.C. Hagel, The Austenite:Pearlite Reaction, *Progress in Metal Physics,* B. Chalmers and R. King, Ed., Vol 6, Pergamon Press, New York, 1956, p 74–134

4.3 D. Brown and N. Ridley, Rates of Nucleation and Growth and Interlamellar Spacing of Pearlite in a Low-Alloy Eutectoid Steel, *JISI,* Vol 204, 1966, p 811

4.4 M. Hillert, The Formation of Pearlite, *Decomposition of Austenite by Diffusional Processes,* V.F. Zackay and H.I. Aaronson, Ed., Interscience, New York, 1962, p 197–247

4.5 R.W.K. Honeycombe, Transformation from Austenite in Alloy Steels, *Metall. Trans. A,* Vol 7A, 1976, p 915–936

4.6 B.E. Sundquist, The Edgewise Growth of Pearlite, *Acta Metall.,* Vol 16, 1968, p 1413–1427
4.7 *Atlas of Isothermal Transformation and Cooling Transformation Diagrams,* American Society for Metals, 1977, p 28
4.8 C. Wells and R.F. Mehl, Rate of Diffusion of Carbon in Austenite in Plain Carbon, in Nickel and in Manganese Steels, *Trans. AIME,* Vol 140, 1940, p 279
4.9 R.A. Swalin, *Thermodynamics of Solids,* John Wiley & Sons, New York, 1962
4.10 M.P. Puls and J.S. Kirkaldy, The Pearlite Reaction, *Metall. Trans.,* Vol 3, 1972, p 2777–2796
4.11 W.A. Johnson and R.F. Mehl, Reaction Kinetics in Processes of Nucleation and Growth, *Trans. AIME,* Vol 135, 1939, p 416–458
4.12 R.F. Mehl and A. Dube´, *Phase Transformations in Solids,* John Wiley & Sons, New York, 1951, p 545
4.13 J.W. Cahn and W.C. Hagel, Theory of the Pearlite Reaction, *Decomposition of Austenite by Diffusional Processes,* V.F. Zackay and H.I. Aaronson, Ed., Interscience, New York, 1962, p 131–196
4.14 C. E. Hinchliffe and G. D. W. Smith, Strain aging of pearlitic steel wire during post-drawing heat treatments, Materials Science and Technology, Vol 17, 2001, p 148-154
4.15 B. L. Bramfitt and A. R. Marder, Effect of Cooling Rate and Alloying on the Transformation of Austenite, Metallurgical Transactions, Vol 4, 1973, p 2291
4.16 *Fundamentals and Applications of Microalloying Forging Steels,* C.J. Van Tyne, G. Krauss, and D.L. Matlock, Ed., TMS, Warrendale, PA, 1996
4.17 E.M. Taleff, C.K. Syn, D.R. Lesuer, and O.D. Sherby, Pearlite in Ultrahigh Carbon Steels: Heat Treatments and Mechanical Properties, *Metallurgical and Materials Transactions A,* Vol 27A, 1996, p 111–118
4.18 J.D. Verhoeven and E.D. Gibson, The Divorced Eutectoid Transformation in Steel, *Metallurgical and Materials Transactions A,* Vol 29A, 1998, p 1181–1189
4.19 L. E. Samuels, *Light Microscopy of Carbon Steels*, ASM International, 1999, p 177.
4. 20 G. Spanos and H.I. Aaronson, The Interfacial Structure and Habit Plane of Proeutectoid Cementite Plates, *Acta Metallurgica and Materialia,*Vol 38, 1990, p 2721–2732
4.21 G. Spanos, W.T. Reynolds, Jr., and R.A. Vandermeer, The Role of Ledges in the Proeutectoid Ferrite and Proeutectoid Cementite Reactions in Steel, *Metallurgical Transactions A,* Vol 22A, 1991, p 1367–1380
4.22 T. Ando and G. Krauss, The Isothermal Thickening of Cementite Allotriomorphs in a 1.5 Cr-1C Steel, *Acta Metallurgica,* Vol 29, 1981, p 351–363

4.23 T. Ando and G. Krauss, The Effect of Phosphorus Content on Grain Boundary Cementite Formation in 52100 Steels, *Metallurgical Transactions A,* Vol 12A, 1981, p 1283–1290

4.24 G. Spanos and M. V. Kral, The Proeutectoid Cementite Transformation in Steels, *International Materials Reviews,* Vol 54, 2009, pp 19–47

CHAPTER 5

Martensite

THIS CHAPTER DESCRIBES the diffusionless, shear-type transformation of austenite to martensite. Athermal transformation kinetics, crystallographic features, and the development of fine structure are all special characteristics of the martensitic transformation. These features are described and related to the major morphologies and microstructural arrangements of martensite, lath, and plate, which form in steel. Rapid cooling or quenching is required to form martensite, primarily to avoid the diffusion-dependent transformations described in Chapter 4, "Pearlite, Ferrite, and Cementite," but the exact cooling conditions that will result in martensite in a given steel are strongly dependent on carbon content, alloying, and austenitizing, factors that determine hardenability, a subject discussed in Chapter 16, "Hardness and Hardenability."

General Considerations

The term *martensite*, named after the pioneering German metallurgist, Adolf Martens, has long been used to designate the hard microstructure found in quenched carbon steel (Ref 5.1). More recently, however, emphasis has been placed on the nature of the transformation itself rather than on the product. Martensitic transformation also occurs in many nonferrous systems (Ref 5.2), the Cu-Al and Au-Cd systems to name just two metal systems, and in oxides such as SiO_2 (Ref 5.3) and ZrO_2 (Ref 5.4). In fact, ceramists and geologists have independently identified the characteristics of martensitic transformation in nonmetal systems and used the term *displacive* to describe transformations that would be called martensitic by metallurgists (Ref 5.3). Martensite then becomes any phase produced by a martensitic or displacive transformation, even though that phase may have significantly different composition, crystal structure, and properties than does martensite in steels.

In Fe-C alloys and steels, austenite is the parent phase that transforms to martensite on cooling. The martensitic transformation is diffusionless, and, therefore, the martensite has exactly the same composition as does its parent austenite, up to 2% carbon (see Fig. 3.1 in Chapter 3, "Phases and Structures," and Fig. 4.1 in Chapter 4, "Pearlite, Ferrite, and Cementite"), depending on the alloy composition. Because diffusion is suppressed, usually by rapid cooling, the carbon atoms do not partition themselves between cementite and ferrite (see Chapter 4, "Pearlite, Ferrite, and Cementite") but instead are trapped in the octahedral sites of a body-centered cubic (bcc) structure, thus producing a new phase, martensite. The solubility of carbon in a bcc structure is greatly exceeded when martensite forms; hence, martensite assumes a body-centered tetragonal (bct) unit cell (see Fig. 5.1) in which the *c* parameter of the unit cell is greater than the other two *a* parameters. With higher carbon concentration of the martensite, more interstitial sites are filled, and the tetragonality increases, as shown in Fig. 5.2.

Martensite is a unique phase that forms in steels. It has its own crystal structure and composition and is separated by well-defined interfaces from other phases, but it is a metastable phase present only because diffusion has been suppressed. If the martensite is heated to a temperature where the carbon atoms have mobility, the carbon atoms diffuse from the octahedral sites to form carbides. As a result, the tetragonality is relieved, and martensite is ultimately replaced by a mixture of ferrite and cementite as required by the Fe-C phase diagram. The decomposition of martensite

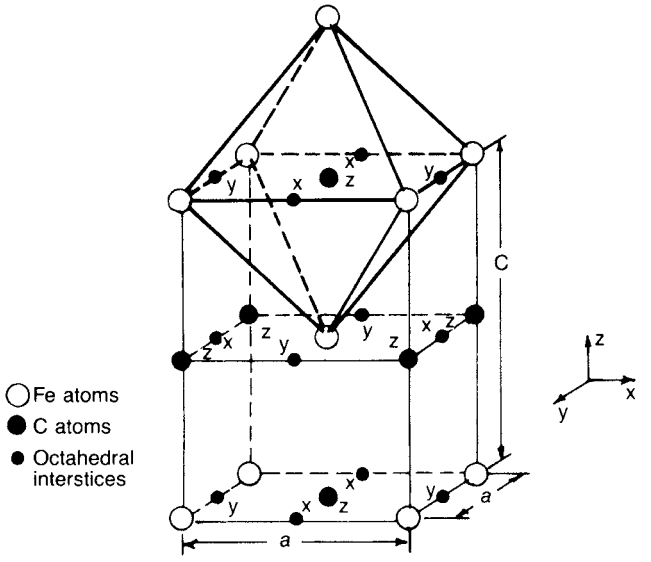

Fig. 5.1 Body-centered tetragonal crystal structure of martensite in Fe-C alloys. Carbon atoms are trapped in one set (*z*) of interstitial octahedral sites. The *x* and *y* sites are unoccupied. Source: Ref 5.5

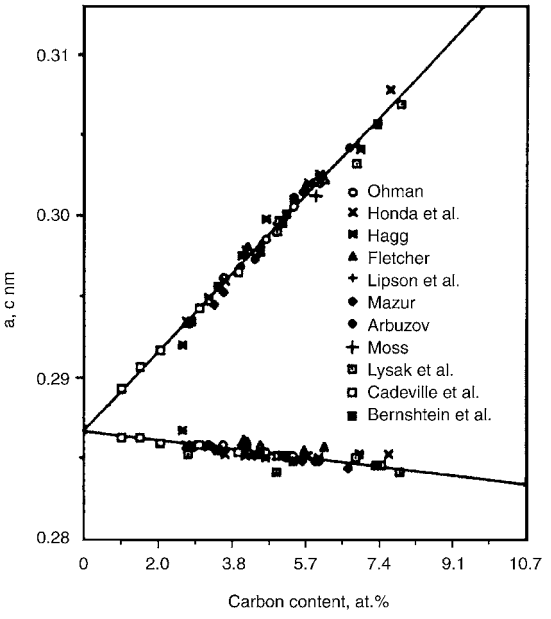

Fig. 5.2 Changes in the *c* lattice parameter (upper curve) and a lattice parameter (lower curve) of Fe-C martensite as a function of carbon content. Source: Ref 5.6

to other structures on heating is referred to as tempering and is the subject of Chapter 17, "Tempering of Steel."

Martensite forms by a shear mechanism. Many atoms move cooperatively and almost simultaneously to effect the transformation, a mechanism very much in contrast to atom-by-atom movement across interfaces during diffusion-dependent transformations. Figure 5.3 shows schematically a number of features of the shear or displacive transformation of austenite to martensite. The arrows point in the directions of shear on opposite sides of the plane on which the transformation is initiated. The martensite crystal formed is displaced partly above and partly below the surface of the austenite by the shear. Thus (as shown in Fig. 5.3), the originally horizontal surface of the parent phase is rotated or tilted into a new orientation by the shear transformation. Surface tilting is an important characteristic of shear-type or martensitic transformation. The atom-by-atom transfer across interfaces by which diffusion-controlled transformations proceed does not produce tilting but tends to produce surfaces of the product phase parallel to the surface of the parent phase.

Figure 5.3 also shows that considerable flow or plastic deformation of the parent austenite must accompany the formation of a martensite crystal. Eventually the constraints of the parent phase limit the width of a martensite crystal, and further transformation can proceed only by the nucleation of new martensite crystals. If the parent austenite could not accommodate

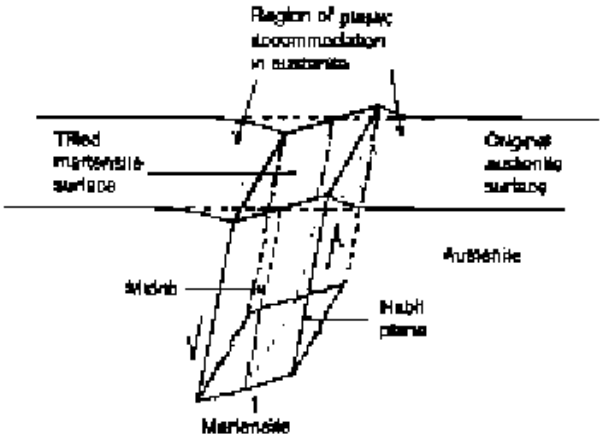

Fig. 5.3 Schematic of shear and surface tilt associated with formation of a martensite plate. Adapted from Ref 5.7. Courtesy of M.D. Geib, Colorado School of Mines

the shape change produced by the martensitic shears, separation or cracking at the martensite/parent phase interface would occur. Fortunately, austenite in steels has sufficient ductility to accommodate martensite formation. However, in many ceramic systems, the parent phase cannot accommodate the shape change, and displacive transformations must be avoided.

Martensite crystals ideally have planar interfaces with the parent austenite (see Fig. 5.3). The preferred crystal planes of the austenite on which the martensite crystals form are designated as habit planes. The habit planes vary according to alloy composition, and some examples are presented in the section on morphology in this chapter. The midrib shown in Fig. 5.3 is generally considered to be the starting plane for the formation of a plate of martensite and may in fact have a different fine structure than other parts of the plate.

An example of surface relief and its relationship to martensitic microstructure is shown in Fig. 5.4. This series of light micrographs was obtained after a prepolished Fe-0.2C alloy specimen was austenitized and quenched in a hot stage microscope with an argon gas atmosphere. Figure 5.4(a) shows the surface relief associated with the formation of hundreds of martensite crystals. The surface tilting is emphasized in some areas by the dark shadows present on surfaces tilted away from the light source. In Fig. 5.4(b), the surface relief has been almost polished away, and in Fig. 5.4(c), the surface shown in (b) has been etched. Finally, Fig. 5.4(d) shows the microstructure after the surface has been polished to remove all relief and etched once again. Comparison of Fig. 5.4(c) and (d) with Fig. 5.4(a) shows the direct correspondence of the surface relief with the martensitic units in the polished and etched microstructure. In polished and etched

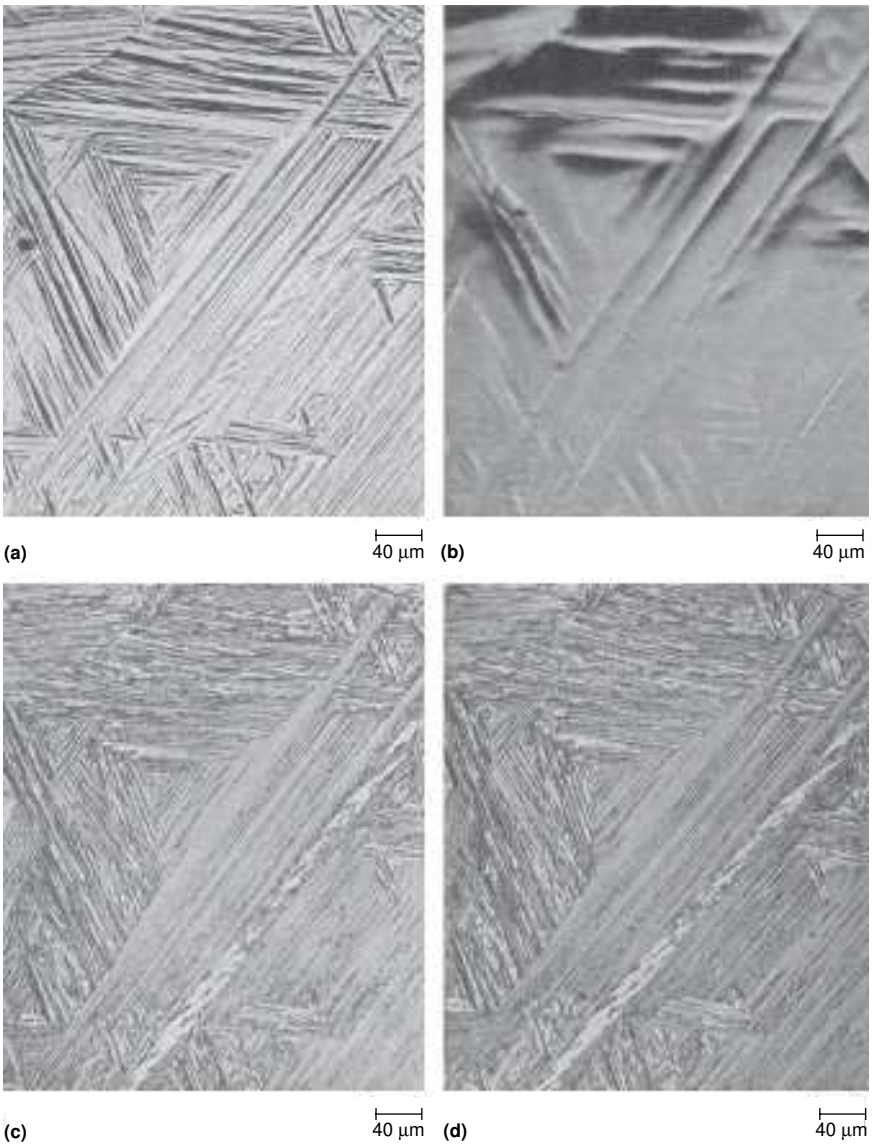

Fig. 5.4 Surface tilting and its relationship to martensitic structure in an Fe-0.2C alloy. (a) Surface tilting after quenching. (b) Partially polished surface. (c) Area in (b) after etching. (d) Same area after polishing to remove all relief and re-etching. Nital etch. Source: Ref 5.8

sections, the individual crystals of martensite appear to be long and thin and are very often characterized as acicular or needlelike. In three dimensions, however, the crystals have a lath or plate shape with flat interfaces, as shown schematically in Fig. 5.3. The needlelike shapes visible on polished and etched surfaces, therefore, are cross sections through laths or plates.

Martensitic Transformation Kinetics

The conversion of an austenitic microstructure to a martensitic microstructure in many commercial steels takes place continuously with decreasing temperature during uninterrupted cooling. This mode of transformation kinetics is referred to as *athermal* (without thermal activation) in order to differentiate it from the isothermal kinetics that characterize thermally activated diffusion-controlled transformations. Pearlite formation, for example, occurs continuously as a function of time if austenite is held at a constant temperature below A_1. Martensite formation, however, is accomplished virtually as soon as a given temperature is reached; should cooling be stopped at that temperature, no further transformation to martensite will occur. Additional transformation, usually by means of the nucleation and rapid growth of new plates of martensite, is accomplished only by cooling to lower temperatures.

Figure 5.5 shows the progress of athermal transformation in an Fe-1.86C alloy. The austenite in this high-carbon alloy is quite stable, and martensitic transformation was initiated just above room temperature. Figure 5.5(a) shows a few very large plates of martensite that formed on cooling to room temperature. The balance of the microstructure is austenite. Figures 5.5(b) and (c) show how some of the austenite retained at room temperature is transformed to new plates on successive subzero cooling to −60 °C (−75 °F) and −100 °C (−150 °F), respectively. The new plates have nucleated within the framework of the initially formed plates (see Fig. 5.5a), and the parent austenite has been subdivided into smaller and smaller units with increasing amounts of martensitic formation. Clearly, the martensitic transformation effectively ceases on reaching a given temperature, and only additional undercooling drives the transformation further.

In contrast to the Fe-1.86C alloy, most hardenable steels transform to martensite at temperatures well above room temperature. Figure 5.6 shows the transformation of austenite to martensite in an Fe-1.94Mo alloy, an alloy in which austenite transforms to martensite in the same manner as in low- and medium-carbon steels. Hot stage cinephotomicrography was required to follow the high-temperature formation of the martensite in the continuously cooled Fe-1.94Mo alloy (Ref 5.9). Figure 5.6 shows a sequence of frames taken from a film of the transformation sequence. Frame 1 shows several austenite grains that are largely untransformed, and the succeeding frames show the step-by-step formation of the martensitic microstructure. The martensite plates in Fig. 5.6 are visible only because of the surface tilting associated with transformation; it was obviously impossible to polish and etch (as in the case of the Fe-1.86C alloy) between frames during the cooling of the Fe-1.94Mo alloy. Figure 5.6 also shows that an important characteristic of the athermal transformation of the FeMo alloy, and low and medium-carbon steels that behave similarly, is

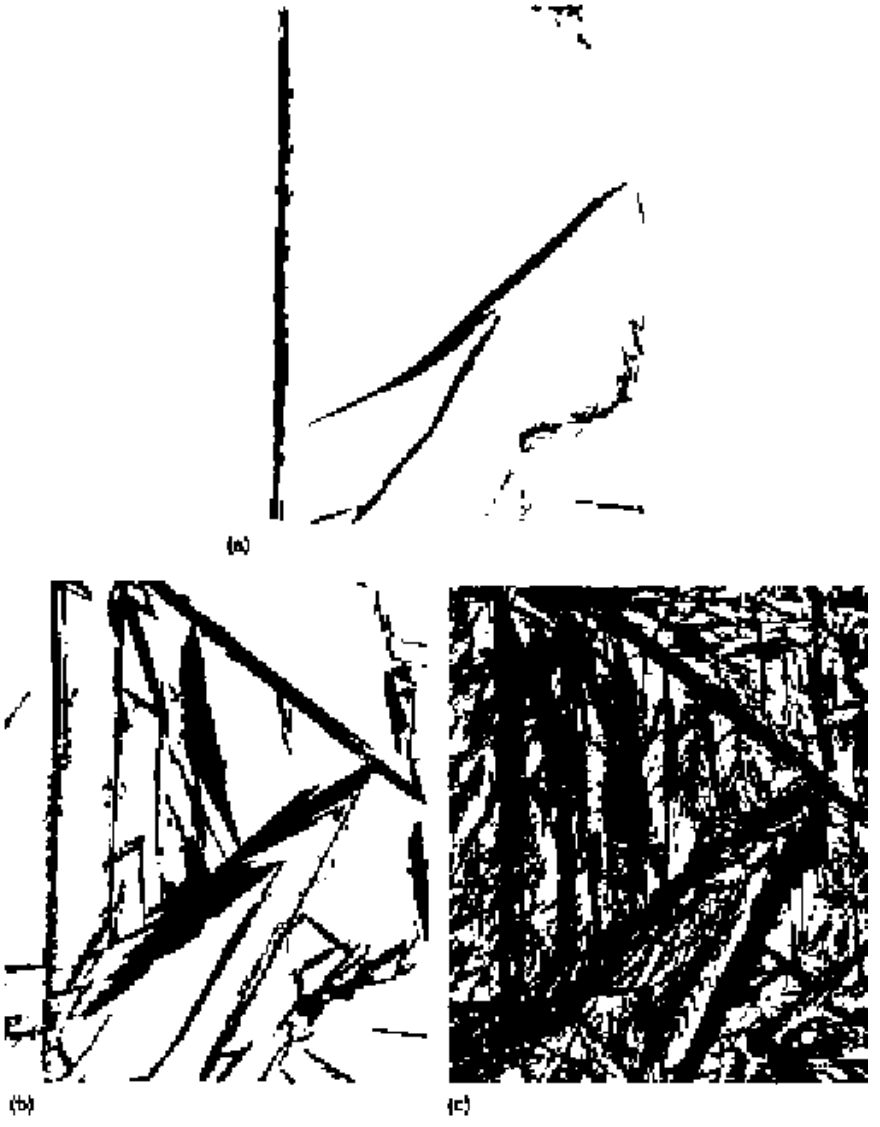

Fig. 5.5 Progress of athermal martensitic transformation in an Fe-1.8C alloy after cooling to: (a) 24 °C (75 °F); (b) –60 °C (–76 °F); and (c) –100 °C (–148 °F). Nital etch, original magnification 500×. Source: Ref 5.9

the development of parallel groups of plates or laths by nucleation and growth of new plates parallel and adjacent to existing plates.

The temperature at which martensite starts to form in a given alloy is designated as the martensite start temperature (M_s). The M_s reflects the amount of thermodynamic driving force required to initiate the shear transformation of austenite to martensite. Figure 5.7 shows that the M_s decreases significantly with increasing carbon content in Fe-C alloys and carbon steels. Carbon in solid solution increases the strength or shear re-

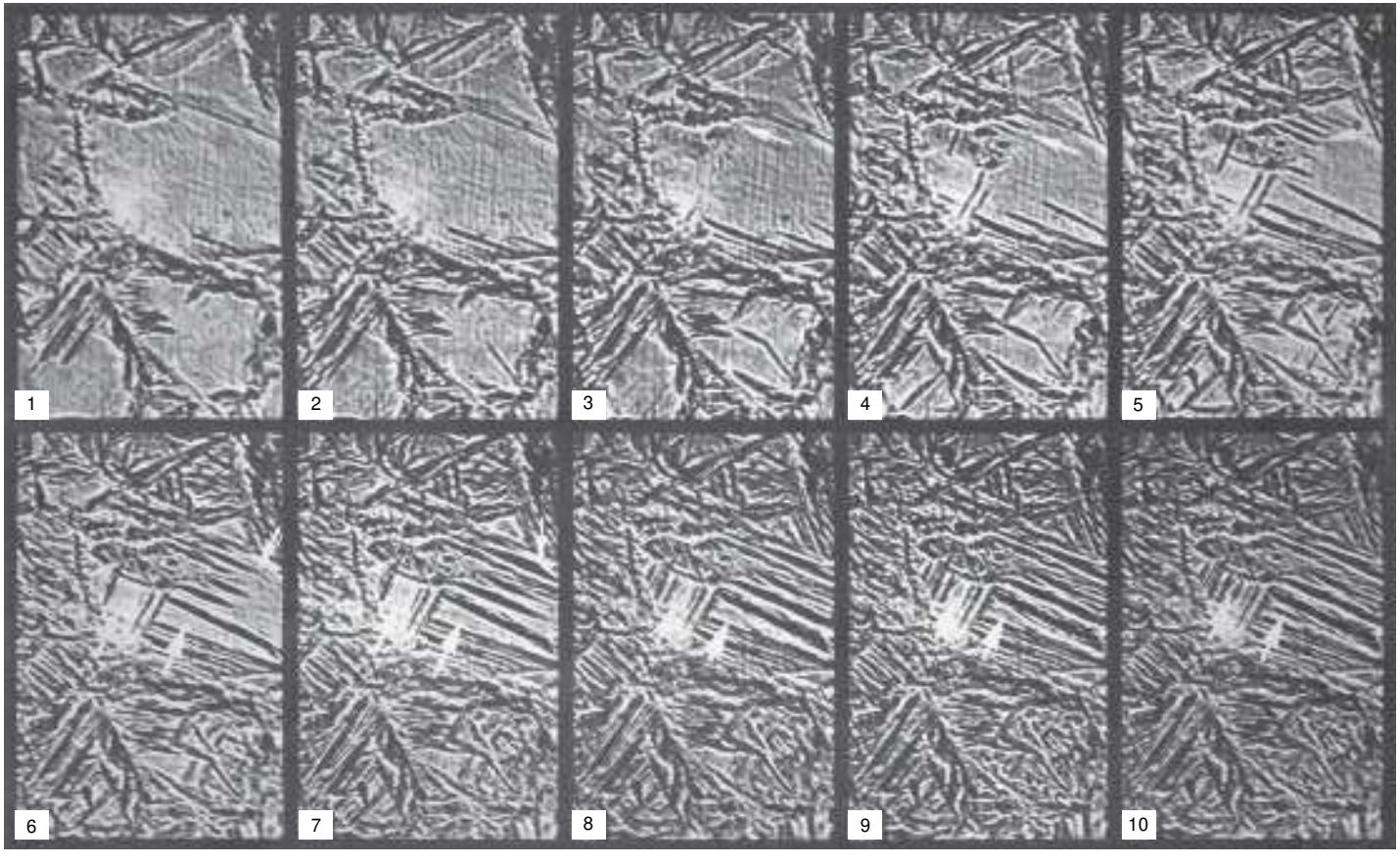

Fig. 5.6 Progress of athermal martensitic transformation in an Fe-1.94Mo alloy. Successive exposures taken of surface relief on a hot stage microscope, original magnification 105×. Source: Ref 5.9

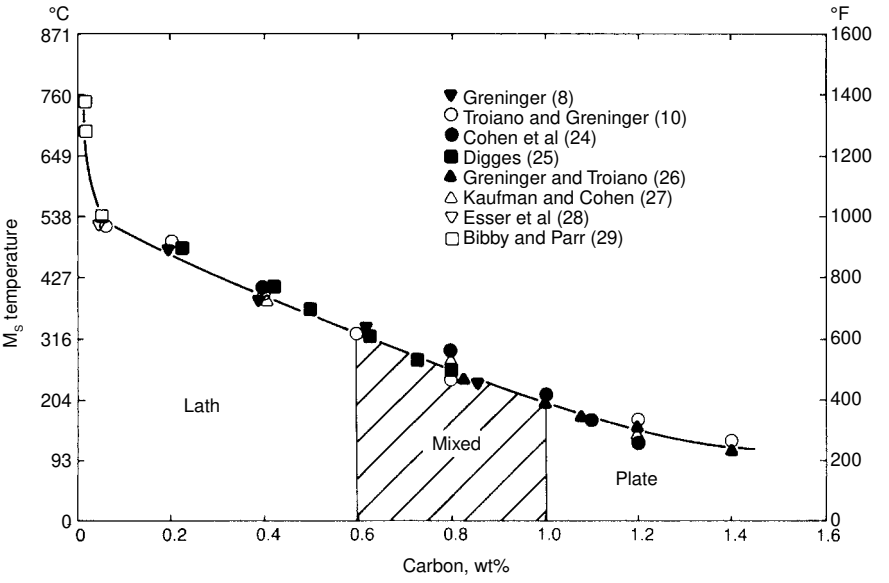

Fig. 5.7 M_S temperatures as a function of carbon content in steels. Composition ranges of lath and plate martensite in Fe-C alloys are also shown. Source: Ref 5.10; investigations indicated are identified by their numbers in this reference

sistance of the austenite and, therefore, greater undercooling or driving force is required to initiate the shear for martensite formation in higher carbon alloys. It is possible to form martensite in pure iron, but very high rates of quenching, in excess of 35,000 °C/sec (63,000 °F/sec), are required (Ref 5.11). Also, as described in detail later in this chapter, the morphology of martensite formed in low- and medium-carbon steels is lath for typical industrial quenching rates. However, plate morphologies of martensite may form in low-carbon steels when quenched at high rates (Ref 5.12–5.14).

The martensite finish temperature (M_f), or the temperature at which the martensite transformation is complete in a given alloy, is also a function of carbon content. The detection of the last small amounts of untransformed austenite is experimentally difficult (Ref 5.15); therefore, the M_f curves based on results of early investigations are only approximate. The M_f drops below room temperature even in steels with low carbon contents. Therefore, significant amounts of untransformed austenite, especially in high-carbon steels, may be present with martensite at room temperature. Figure 5.8 shows that this is actually the case. Retained austenite content, measured by X-ray diffraction techniques (Ref 5.10, 5.16) at room temperature, is as high as 30 to 40% in Fe-C alloys containing 1.2 to 1.4% C. Steels containing .3 to 0.4% C retain 2 to 4 vol% retained austenite, and even in lower carbon steels some small amount of austenite is retained between the parallel crystals of lath martensite, as shown in a

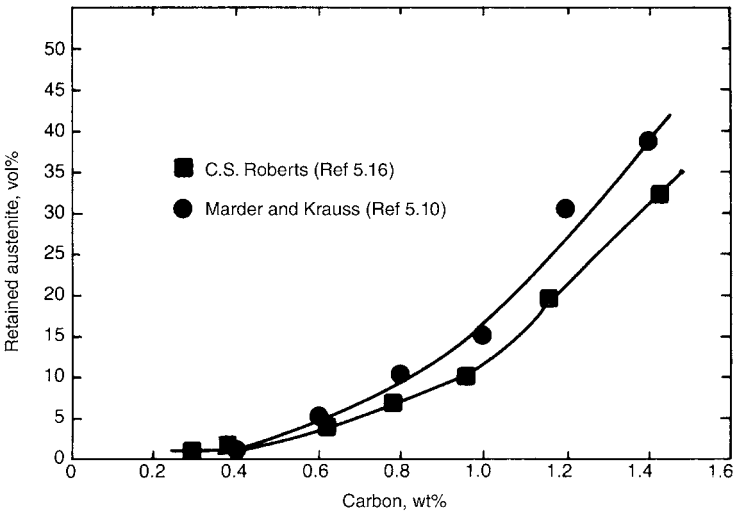

Fig. 5.8 Retained austenite as a function of carbon content in Fe-C alloys. Source: Ref 5.10

transmission electron micrograph later in this chapter. Alloying elements that stabilize austenite increase the amount of retained austenite at any given carbon level and temperature.

Alloying elements also influence the M_s temperatures of steels, and a number of equations have been developed to relate M_s to steel composition. Table 5.1 lists various equations that have been developed over the years (Ref 5.17–5.23). All alloying elements, except cobalt, lower M_s temperatures. The equations developed by Andrews (Ref 5.23) are based on measurements of M_s temperatures and compositions of a large number of steels of British, German, French, and American manufacture with maximum carbon content of 0.6%, manganese up to 4.9%, chromium up to 5%, nickel up to 5%, and molybdenum up to 5.4%. Andrews showed that 92 and 95% of measured M_s temperatures for the steels were within ±25 °C (±45 °F) of the M_s temperatures calculated from their compositions according to the ±linear and product equations, respectively. A test of Andrews' equations with M_s measurements and steel compositions published in the 1970s shows that Andrews' equations continue to give good agreement between measured and calculated M_s values with the ±25 °C limits (Ref 5.24). A later evaluation of the M_s temperature equations recommends only slight changes in the Stevens and Haynes and Andrews linear equations and incorporates the effects of cobalt and silicon (Ref 5.25). The thermodynamic driving force for martensitic transformation in terms of M_s temperatures as a function of composition has also been calculated (Ref 5.26).

Once the M_s of a steel is reached during cooling, the extent of the athermal transformation of austenite to martensite is dependent only on the

Table 5.1 List of formulas for M_s calculation from alloy composition

Investigators	Date	Ref	Equation
Payson and Savage	1944	5.17	M_s (°F) = 930 – 570C – 60Mn – 50Cr – 30Ni – 20Si – 20Mo – 20W
Carapella	1944	5.18	M_s (°F) = 925 × (1 – 0.620C)(1 – 0.092Mn)(1 – 0.033Si)(1 – 0.045Ni)(1 – 0.070Cr)(1 – 0.029Mo)(1 – 0.018W)(1 + 0.120Co)
Rowland and Lyle	1946	5.19	M_s (°F) = 930 – 600C – 60Mn – 50Cr – 30Ni – 20Si – 20Mo – 20W
Grange and Stewart	1946	5.20	M_s (°F) = 1000 – 650C – 70Mn – 70Cr – 35Ni – 50Mo
Nehrenberg	1946	5.21	M_s (°F) = 930 – 540C – 60Mn – 40Cr – 30Ni – 20Si – 20Mo
Steven and Haynes	1956	5.22	M_s (°C) = 561 – 474C – 33Mn – 17Cr – 17Ni – 21Mo
Andrews (linear)	1965	5.23	M_s (°C) = 539 – 423C – 30.4Mn – 12.1Cr – 17.7Ni – 7.5Mo
Andrews (product)	1965	5.23	M_s (°C) = 512 – 453C – 16.9Ni + 15Cr – 9.5Mo + 217$(C)^2$ – 71.5(C)(Mn) – 67.6(C) (Cr)

Source: Ref 5.17–5.23

amount of undercooling below the M_s temperature. Two equations have been developed to describe the athermal transformation kinetics of martensite formation:

$$f = 1 - 6.96 \times 10^{-15}(455 - \Delta T)^{5.32} \quad \text{(Eq 5.1)}$$

$$f = 1 - \exp - (1.10 \times 10^{-2}\Delta T) \quad \text{(Eq 5.2)}$$

where f is the volume fraction of martensite, and ΔT is the undercooling below M_s in degrees centigrade. Note that time does not appear in these equations. Equation 5.1 was developed by Harris and Cohen (Ref 5.27) for steels containing 1.1% carbon, and Eq 5.2 was developed by Koistinen and Marburger (Ref 5.28) from Fe-C alloys containing between 0.37 to 1.1% C. The data used to develop Eq 5.1 and Eq 5.2 together with measurements of Steven and Haynes (Ref 5.22) from hardenable steels containing 0.32 to 0.44% carbon are shown in Fig. 5.9. All sets of data agree closely for small amounts of undercooling, but they diverge significantly as undercooling increases. For example, at 100 °C (210 °F) below M_s, the Koistinen and Marburger data show only about 65% transformation, while the Steven and Haynes data show 90% transformation. The discrepancy is probably due to experimental difficulties in determining the amount of austenite remaining at any given temperature. Koistinen and Marburger used X-ray analysis while the other investigators used light microscopy to determine the amount of retained austenite. The detection of small amounts of retained austenite by the latter technique is difficult in high-carbon steels and virtually impossible in medium-carbon steels. Therefore, the Koistinen and Marburger equation, based on the most accurate technique for determining small amounts of retained austenite, is considered to give the best representation of martensite transformation over the entire range of undercooling.

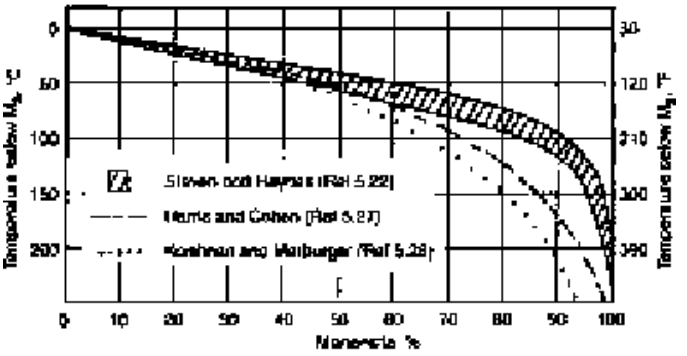

Fig. 5.9 Extent of martensite formation as a function of undercooling below M_S according to three different investigations as shown. Source: Ref 5.24

During the course of the athermal martensite formation discussed up to this point, two types of anomalies may develop: bursting and stabilization. The burst phenomenon occurs in Fe-Ni and Fe-Ni-C alloys with subzero M_s temperatures. Large numbers of martensite plates, sometimes enough to transform 70% of the austenite, form in a "burst" at a temperature designated the M_B (Ref 5.29). This transformation behavior is related to the ability of plates of martensite to nucleate other plates of martensite, a process called autocatalysis. The stimulus to nucleation is the stress, generated at the tips of plates, that helps to initiate the shear transformation process on other favorably oriented variants of the habit plane (Ref 5.30). The habit plane variants that are activated are generally not parallel to that of the initiating plate, and frequently zigzag arrays of martensite plates are observed in alloys susceptible to autocatalytic nucleation or bursting.

Stabilization, a phenomenon that reduces the ability of austenite to transform into martensite, occurs during slow cooling or interruption of cooling before complete transformation. For example, an oil-quenched steel may contain more retained austenite than the same steel water quenched, and if transformation of a steel is interrupted by holding at some temperature between M_s and M_f, no martensite transformation may occur when cooling is resumed until substantial undercooling below the hold temperature is accomplished (Ref 5.31). One explanation of stabilization assumes that carbon segregates to potential embryos, or sites of martensitic nucleation, during slow cooling or on holding of a partially transformed specimen at a constant temperature. Once segregated, the carbon atoms increase the shear resistance of the austenite, thereby effectively stabilizing the austenite.

Although athermal martensite transformation kinetics are the dominant mode of transformation in heat treatable carbon steels, isothermal transformation has been observed in Fe-Ni-Mn and Fe-Ni-Cr alloys. The isothermal transformation is time dependent and occurs at subzero temperatures; plotting this transformation frequently forms C-curves. Figure 5.10 shows

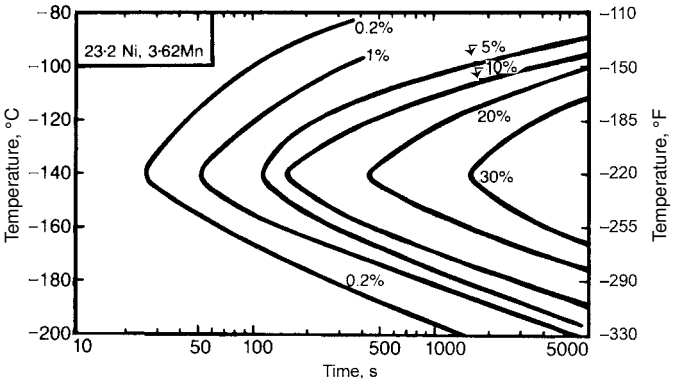

Fig. 5.10 Isothermal transformation curves for martensite formation in an Fe-23Ni-3.6Mn alloy. Curves are identified by the percentage of martensite formed. Source: Ref 5.32

a time-temperature-transformation diagram developed for isothermal martensite formation in an Fe-23Ni-3.6 Mn alloy (Ref 5.32). Mathematical modeling of isothermal transformation kinetics has made possible a separation of the effects of preexisting nucleation sites or embryos and those produced by autocatalysis (Ref 5.29, 5.33). Also, the studies of isothermal transformation have shown a relationship between embryo size and kinetic mode of transformation. Alloy systems with large embryos or lattice sites predisposed to transformation require little or no thermal activation and therefore transform to martensite athermally. Systems with smaller embryos require thermal activation to produce martensite nuclei of size sufficient to initiate transformation, a process that leads to the time-dependent isothermal kinetics. Also, it has been shown that the activation energy for isothermal martensitic nucleation in Fe-Ni-Mn alloys is inversely proportional to the chemical driving force for the transformation, i.e., the greater the driving force, the lower the activation energy (Ref 5.33, 5.34). Isothermal martensite formation has also been identified and characterized in 1.80 wt% carbon steel (Ref 5.35).

Crystallography of Martensitic Transformation

The diffusionless, shear mechanism of martensitic transformation requires good crystallographic coupling between the parent and product phases. Two important crystallographic parameters or characteristics emphasize this interrelationship between austenite and martensite in ferrous alloys. One is the orientation relationship between the crystal structure of the parent and the product martensite. The orientation relationship specifies planes and directions of the parent phase and the planes and directions in the product martensite to which they are parallel. Two well-known orientation relationships have been determined in ferrous alloy systems by

means of X-ray diffraction techniques (Ref 5.36). The Kurdjumov-Sachs orientation relationship:

$$\{111\}_A \parallel \{101\}_M$$
$$\langle 110\rangle_A \parallel \langle 111\rangle_M$$

is valid for high-carbon steels with $\{225\}_A$ habit planes. The other orientation relationship, which was determined by Greninger and Troiano and is also attributed to Nishiyama, is:

$$\{111\}_A \parallel \{011\}_M$$
$$\langle 112\rangle_A \parallel \langle 011\rangle_M$$

This relationship is observed in alloys where the martensite plates have $\{259\}_A$ habit planes.

The other crystallographic parameter that emphasizes the interrelation ship of the parent and product phases is the habit plane, already mentioned in the discussion of Fig. 5.3. In steels, the habit plane is the plane in the parent austenite on which the martensite forms and grows. When the martensitic transformation is complete, ideally the habit plane is the planar interface between any retained austenite present and the martensite crystals. In actual fact, however, the interfaces between martensite and austenite in steels might be quite irregular, and the habit plane may be truly planar only at the midrib or point of origin of a martensite crystal. The habit plane is important not only because of its association with the initiation and progress of the transformation but also because it affects the microstructural arrangements in the parent austenite grains of the many martensite plates that make up a hardened microstructure. The habit plane is a function of alloy composition, especially carbon content, and the various habit planes that characterize martensite in steels are presented in the section on morphology in this chapter.

The orientation relationship and habit plane in a given steel are parameters that relate the crystallography of austenite to martensite after transformation. Crystallography is also important in describing the martensitic transformation itself. A crystallographic theory of martensitic transformation was developed in the 1950s by Wechsler, Lieberman, and Read (Ref 5.37) and by Bowles and MacKenzie (Ref 5.38). The significance of the crystallographic theory is the understanding it provides for the origin of the internal fine structure found within any martensite crystal. The fine structure may consist of dislocations, twins, or a mixture of the two, depending on alloy composition. The presence of fine structure is a unique result of martensitic transformation but occurs to some extent in any transformation where shear and diffusion are required to form the new phase. Bainite formation is an example of the latter type of transformation.

The crystallographic theory of martensite formation is based on two important microstructural (macroscopic relative to atomic dimensions) observations: that the habit plane is unrotated and undistorted, and that the shape change that produces the surface tilting in Fig. 5.3 is homogeneous and a result of plane strain. The plane strain may be visualized as shear or displacement on planes parallel to the habit plane. Greninger and Troiano (Ref 5.39) first noted that the shape change could not be produced merely by the lattice deformation (i.e., in steels, the change in lattice from fcc austenite to bct martensite). Another deformation was necessary to satisfy the requirement of plane strain and the undistorted habit plane. This additional deformation, the lattice invariant deformation, involves deformation of the bct martensite crystal by twinning or slip but not a change of the lattice or crystal structure itself.

The major elements of the crystallographic theory for martensite formation in steels are shown schematically in Fig. 5.11 and 5.12. Figure 5.11(a) shows two adjacent fcc unit cells of austenite in which a bct unit cell has been identified. This identification of a set of atoms in the parent phase that will transform to a set of atoms in the product phase is referred to as the lattice correspondence. The atoms identified in Fig. 5.11(a) have

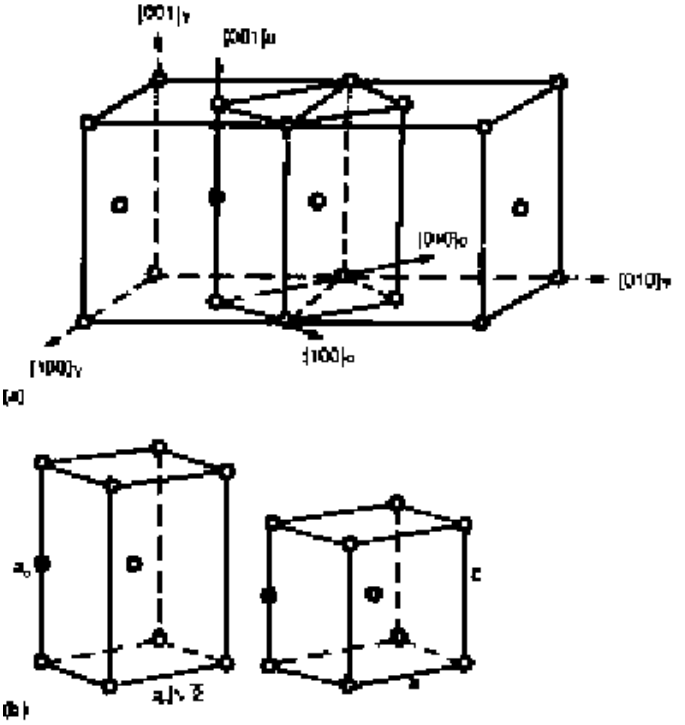

Fig. 5.11 (a) A body-centered tetragonal cell in austenite is identified by the <100>α axes. (b) The bct cell (left) before and (right) after the lattice deformation (Bain strain) from austenite to martensite. Source: Ref 5.40

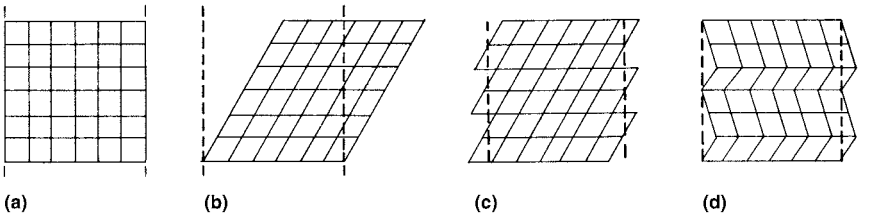

Fig. 5.12 Schematic diagrams to show (a) portion of parent crystal; (b) new lattice (martensite) produced by lattice deformation; and lattice invariant deformation by (c) slip and (d) twinning to make martensite conform to original position of parent crystal (a). Source: Ref 5.7

been isolated in the unit cell schematic on the left of Fig. 5.11(b). At this stage, the dimensions of the bct cell are still those derived from the austenitic lattice parameter. The unit cell on the right of Fig. 5.11(b) is that of martensite with lattice parameters a and c, corresponding to given carbon content (see Fig. 5.2). A lattice deformation was required to produce the martensite from austenite. In steels, the lattice correspondence shown in Fig. 5.11(a) was first identified by Bain and the lattice deformation from fcc to bct is referred to as the *Bain strain*. Figure 5.11 shows that the Bain strain produces a contraction along the c axis and an expansion along the a axes.

In general, the lattice deformation will cause rotation away from the habit plane, as shown in Fig. 5.12(a) and (b), where it is assumed that a number of cells of a parent crystal (a) are transformed to a new lattice (b). The vertical dashed lines represent the unrotated, undistorted habit plane. The constraints of the surrounding parent phase, however, cause the martensite unit to accommodate or deform by a lattice invariant deformation to the original boundaries (a) as required by the crystallographic theory. Figures 5.12(c) and (d) show, respectively, the martensite deformed by slip (dislocation movement) or twinning to satisfy on a macroscopic scale the requirement of an unrotated, undistorted habit plane. Figure 5.13 is another schematic representation of the slip (a) and twinning (b) modes of lattice invariant deformation with martensite plates. These sketches, of course, are idealized to demonstrate the concept of the lattice invariant shear. In actual crystals, when slip is the mechanism of accommodation, not only are dislocations introduced at the austenite-martensite interface, but also a high dislocation density remains in the fine structure within the plates. Examples of the latter are presented in the next section of this chapter.

The crystallographic theory of the martensitic transformation is well developed mathematically and has successfully predicted crystallographic parameters in a number of alloys. For example, if the lattice and lattice-invariant deformations are specified, the habit plane may be predicted. For development of the theory and its application, see Bilby and Christian (Ref 5.7) and Wayman (Ref 5.2). Successes and limitations of the theory are reviewed by Dunne and Wayman (Ref 5.41).

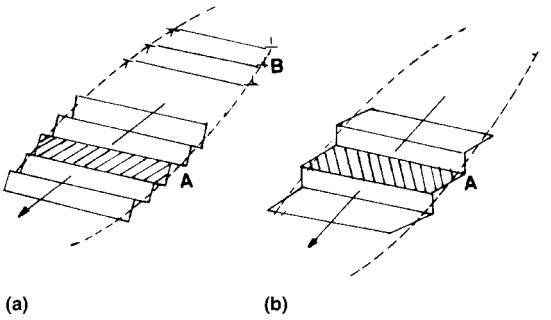

Fig. 5.13 Schematic representations of lattice invariant deformation by (a) slip and (b) twinning in martensite plates. Source: Ref 5.7

Morphology of Ferrous Martensites

Two major morphologies of martensite, lath and plate, develop in heat treatable carbon steels. Figure 5.14 shows the carbon ranges of formation and M_s temperature of the two morphologies. The boundaries of the various regions are based on characterization of high-purity Fe-C alloys and may shift in alloy steels. The designations of the two morphologies originate from the shape of the individual units of martensite. The lath designation is used to describe the stacks of board-shaped crystals of martensite that form in low- and medium-carbon steels, while the plate designation accurately describes the shape of the martensite crystals that form in high-carbon steels. The terms *lath* and *plate*, therefore, refer to the three-dimensional shapes of individual martensite crystals. In metallographic specimens, sections through the martensite laths or plates are revealed by polishing and etching. Generally, these cross-sections will appear to be needlelike or acicular, and the latter adjectives are often used to describe martensite microstructures. Other terms based on one or another feature of the different forms of martensite have been used to describe the two morphologies of martensite, but the terms lath and plate are preferred based on a poll of martensite researchers in 1971(Ref 5.9).

Until the advent of the electron microscope, the plate martensites, which could be readily resolved by light microscopy, received the most emphasis in the literature. The units of plate martensite are well within the size range resolvable in the light microscope, and frequently the retained austenite that coexists with the martensite in high-carbon alloys helps to sharply define the plates in the light microscope. On the other hand, as will be demonstrated, many of the individual units of lath martensite are below the resolution of the light microscope, and any retained austenite present is also too fine to be resolved. Although plate martensites are important in some heat treated applications, many hardenable steels have low or medium carbon content and, therefore, microstructures composed of lath mar-

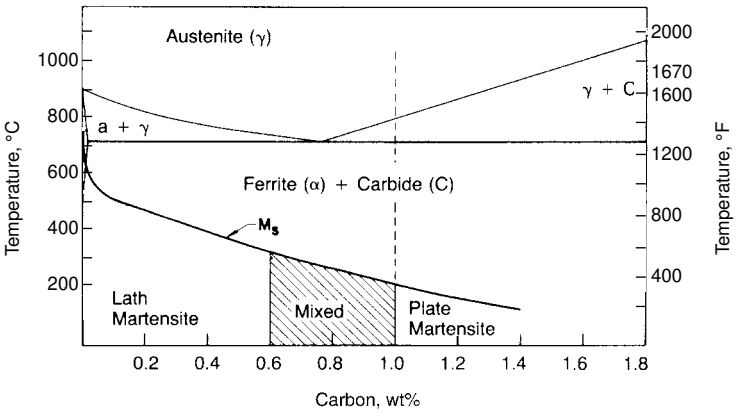

Fig. 5.14 Ranges of lath and plate martensite formation in iron-carbon alloys. Source: Ref 5.10

tensite, which by virtue of the lower carbon contents tend to resist brittle fracture. As a result, lath martensites have broad industrial significance, while microstructures with plate martensite for engineering applications are somewhat limited, but found in some tool steels and the high-carbon case structures of carburized steels as discussed in later chapters. In order to follow the historical development of the understanding of martensitic microstructures, plate martensite is described first in the following sections. The characteristics of individual units and the arrangement of the units to produce the microstructures that are put into service as a result of good heat treatment practice are described for both lath and plate martensite.

Plate Martensite

Many other ferrous systems show the same transition from lath to plate martensite (see Fig. 5.14) with increasing alloying as does the Fe-C system (Ref 5.9). Figure 5.15 shows plate martensite that was produced by cooling a single crystal of Fe-33.5Ni austenite in liquid nitrogen (−196 °C, or −320 °F). Subzero cooling was required because the high nickel content had lowered the M_s to −30 °C (−20 °F). The specimen was not polished or etched after the liquid nitrogen treatment, and therefore all features shown in Fig. 5.15 are due to the surface relief generated by the martensitic transformation. On the scale shown, the surface tilting is indeed quite homogeneous except for small dark bands visible in some of the martensite plates. These bands are deformation twins formed in response to the constraints of the austenite matrix. The deformation twins, however, are micron-sized and irregularly distributed, in contrast to the much finer and more regularly distributed fine structure that results from the lattice-invariant deformation.

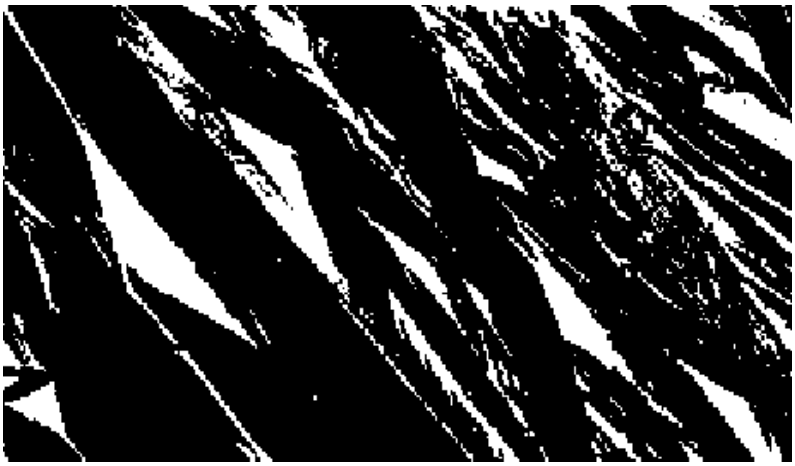

Fig. 5.15 Plate martensite formed in an austenitic single crystal of an Fe-33.5Ni alloy by cooling to –196 °C (–321 °F). Plates are visible only because of surface relief generated by martensitic transformation, light micrograph, original magnification 200×. Source: Ref 5.42

Figure 5.16 is a transmission electron micrograph of the fine structure that formed in a single plate of martensite in the Fe-33.5Ni alloy. Fine transformation twins (small dark bands), dislocations (the fine linear features), and a large deformation twin band are present. Figure 5.17 shows the dislocation fine structure at a higher magnification. Relatively straight dislocation lines in two directions are visible. By selected-area diffraction techniques (Ref 5.42), the preferred directions were shown to correspond to ⟨111⟩ directions and, therefore, the dislocations are mostly screw dislocations. This type of dislocation array is characteristic of those formed by deformation of bcc iron at low temperatures and/or high strain rates and illustrates one type of fine structure formed by the lattice invariant deformation of bcc martensite as a result of the austenitic constraints. Figure 5.18 shows another type of fine structure, very fine transformation twins, about 10 nm (100 Å) in thickness, in Fe-33.5Ni plate martensite. The twins lie on $\{112\}_m$ planes and represent another plastic deformation mode that forms in bcc crystals deformed at low temperatures and high strain rates. Also shown in Fig. 5.18 is a larger deformation twin across which the fine transformation twins have changed their orientation to a $\{112\}_m$ orientation in the twin (Ref 5.43). Examples of plate martensite in Fe-C alloys are shown in Fig. 5.5 and 5.19. Many different orientations of the martensite plates are apparent in the microstructures shown. This characteristic appearance of a plate martensitic microstructure is directly related to the habit planes of the plate martensite and the tendency of adjacent plates to assume different variants of the habit plane. Plate martensites have irrational habit planes, i.e., the planes are not defined by low

Fig. 5.16 Fine structure within martensite plates shown in Fig. 5.15. A deformation twin, fine transformation twins, and dislocations are shown. Transmission electron micrograph, original magnification 20,000×. Source: Ref 5.42

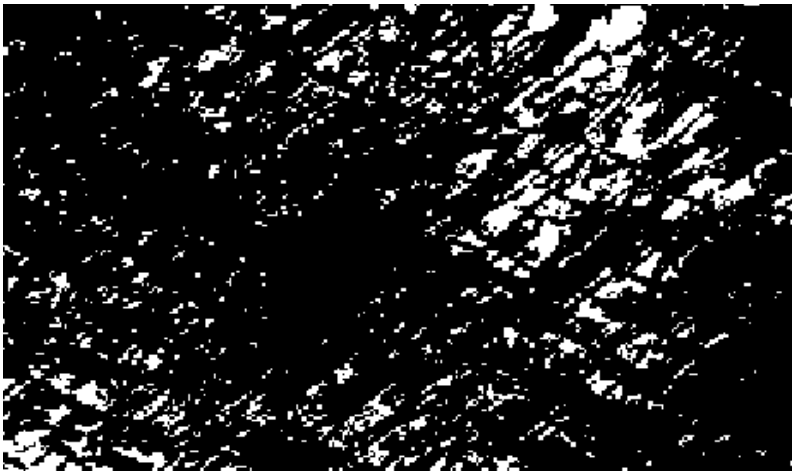

Fig. 5.17 Dislocation fine structure in martensite plates shown in Fig. 5.15. Transmission electron micrograph, original magnification 20,000×. Source: Ref 5.42

number indices such as (100) or (111). Early work by Greninger and Troiano (Ref 5.44) (see Fig. 5.20) showed that Fe-1.78C alloys had habit planes best characterized as $\{259\}_A$, and lower carbon alloys, containing 0.92% and 1.4% C, had $\{225\}_A$ habit planes. The Fe-Ni plate martensites have been the subject of extensive crystallographic studies. Figure 5.21 shows that there is considerable scatter of the habit plane in Fe-Ni alloys containing 29.0 to 35.0% nickel. The scatter may be due to compositional variations, the habit plane shifting toward $\{225\}_A$ with decreasing nickel content, or mixtures of lattice-invariant deformations such as combinations of twinning and dislocations in a given alloy (Ref 5.42).

Fig. 5.18 Fine transformation twins in plate martensite of an Fe-33.5Ni alloy. Note change in orientation of fine twins in large deformation twin. Transmission electron micrograph, original magnification 15,000×. Source: Ref 5.43

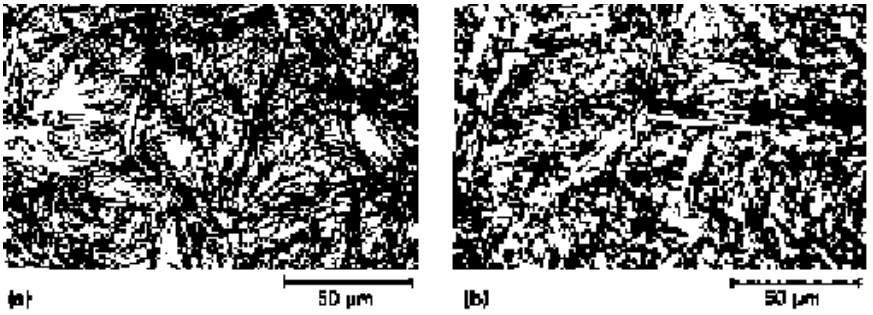

Fig. 5.19 Plate martensite and retained austenite (white patches) in (a) Fe-1.22C and (b) Fe-1.4C alloys. Light micrographs. Source: Ref 5.10

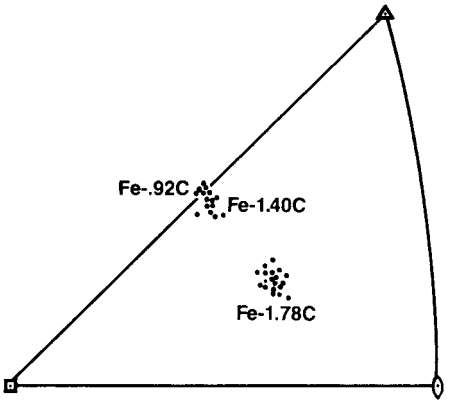

Fig. 5.20 Habit planes of Fe-C plate martensites in unit stereographic triangle. Source: Ref 5.44

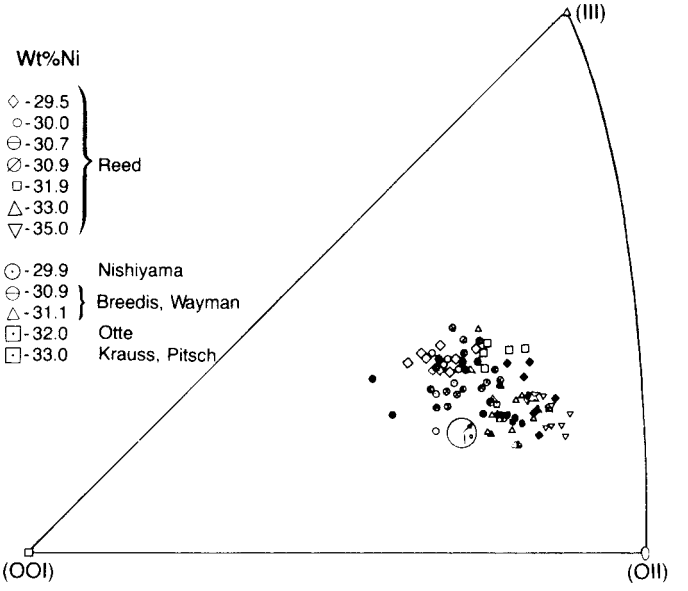

Fig. 5.21 Habit planes, clustering around $(259)_A$, of plate martensite in Fe-Ni alloys containing 29 to 35% nickel. Source: Ref 5.45

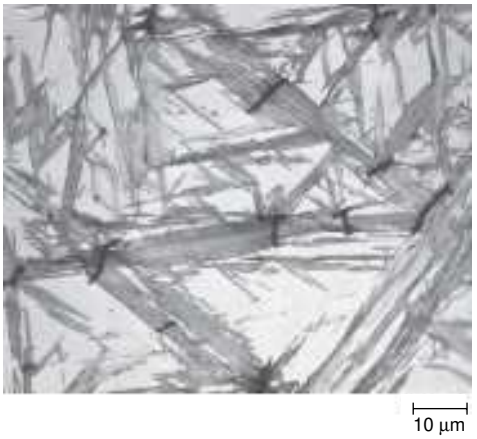

Fig. 5.22 Microcracks in plate martensite of an Fe-1.4C alloy. Source: Ref 5.47

The many orientations of martensite plates in the microstructures shown in Fig. 5.5 and 5.19 are due to the many variants of the irrational habit planes. A variant is merely a different orientation of a given {hkl} plane as defined by a different arrangement of the same hkl indices. For example, $(925)_A$, $(592)_A$, and $(952)_A$ are all variants of the $\{259\}_A$ plane. Any plane where h, k, l are all different, as is the case for $\{259\}_A$, has 24 different variants, and a plane with two indices equal, such as the $\{225\}_A$ plane, has 12 variants. Thus, the plate martensite microstructures, because of the

large number of variants possible, and the fact that adjacent plates assume different variants, appear quite haphazardly arranged, despite the fact that there is only a single habit plane for all the plates in a given alloy.

An important consequence of the nonparallel plate formation in Fe-C alloys is the development of microcracks in the martensite plates as a result of the impingement of plates of different habit plane variants (Ref 5.46). Figure 5.22 shows an example of the microcracks in the plate martensite of an Fe-C alloy. The microcracks tend to form in the largest martensite plates and therefore are not present to any great extent in steels where austenite grain size and, accordingly, martensite plate size, are fine (Ref 5.48). Also, in lower-carbon steels, the morphology shift to lath martensite eliminates the impingements and the development of microcracks (Ref 5.49). The high-carbon plate martensites are quite brittle and sensitive to microcracking. However, in Fe-Ni alloys where the martensite is much more ductile, the impingement of martensite plates is accommodated by deformation twinning rather than cracking.

Lath Martensite

Light micrographs of lath martensite in Fe-C alloys are shown in Fig. 5.23. The lath martensite units tend to be quite fine, but the characteristic acicularity of a martensitic microstructure is apparent. An important microstructural characteristic of lath martensites is the tendency of many

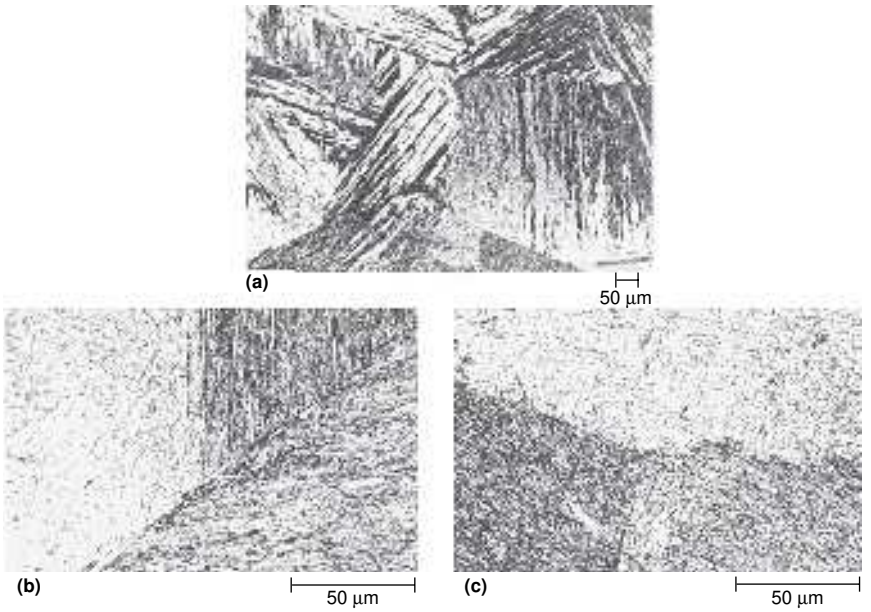

Fig. 5.23 Lath martensite microstructures in (a) Fe-0.2C, (b) Fe-0.4C, and (c) Fe-0.6C alloys. Light micrographs. Sodium bisulfite etch. Source: Ref 5.10

laths to align themselves parallel to one another in large areas of the parent austenite grain. These regions of parallel lath alignment are referred to as packets and tend to develop most prominently in lower-carbon alloys, as shown in Fig. 5.23(a). The packets can be delineated because of the different etching characteristics of the different variants or orientations of the laths in the various packets. For example, the packet structure of lath martensite is strikingly shown in Figures 5.24 (a) and (b), color light micrographs made possible by the use of polarized light and sodium bisulfite etching of martensite formed in an Fe-0.2C alloy with a coarse austenitic grain size (Ref 5.50). Each packet, composed of a high density of largely parallel martensitic crystals, is shown in a different color, and although most of the crystals are too fine to be resolved in the light microscope, the general parallel alignment or acicularity of the martensite in the packets and the differences in orientation in adjacent packets are shown.

Figure 5.25 shows the transition in martensite morphology that develops as the carbon content of the Fe-C alloys increases from 0.67 to 1.00% C. With increasing carbon content, more plates of martensite, differentiated from lath martensite by their larger size and their tendency to microcrack, are discernible in the microstructure.

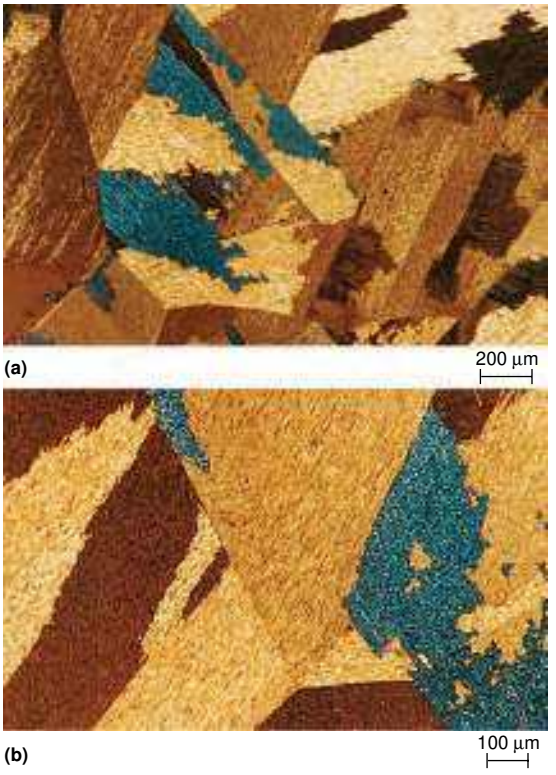

Fig. 5.24 Lath martensite packets in an Fe-0.2 wt% C alloy. Light micrograph, polarized light, sodium bisulfite etch. Courtesy of A. Marder and A. Benscoter. Source: Ref 5.50

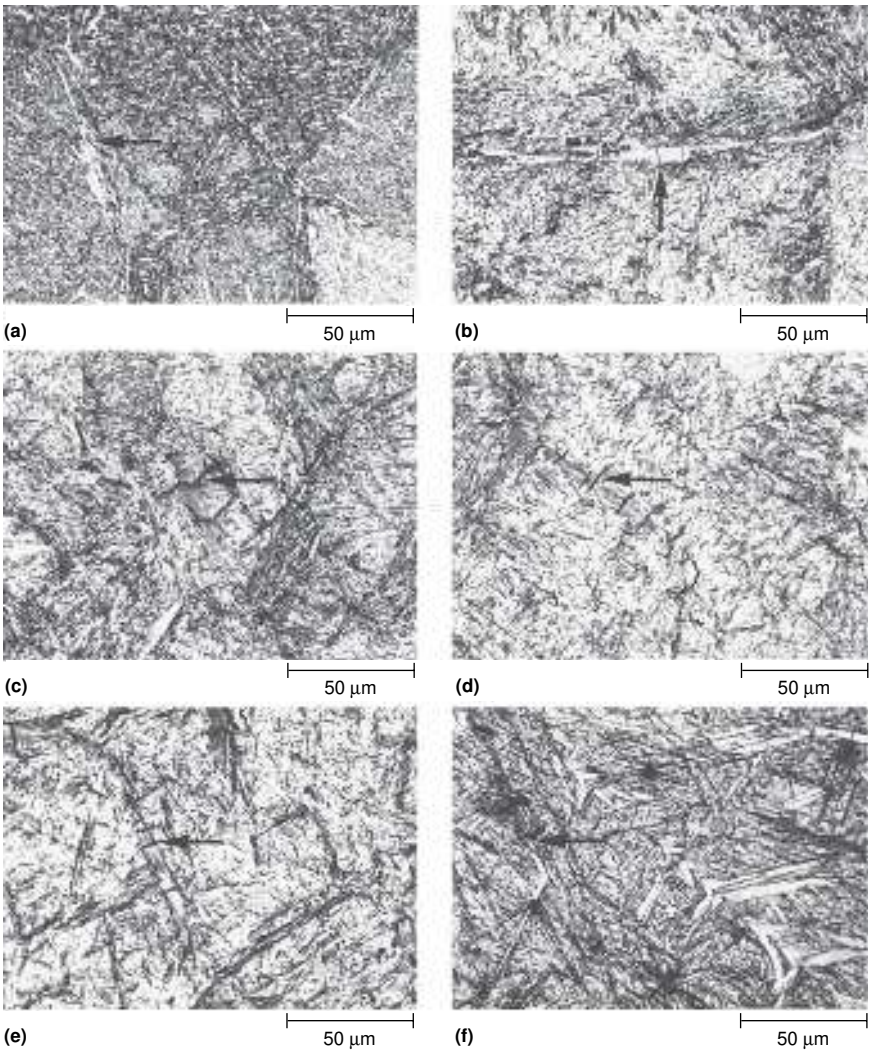

Fig. 5.25 Transition from lath to plate martensite microstructures in Fe-C alloys between 0.67 and 1.00% carbon. (a) 0.67% C. (b) 0.75%. (c) 0.82%. (d) 0.85%. (e) 0.93%. (f) 1.00%. Light micrographs. Sodium bisulfite etch. Source: Ref 5.10

A transmission electron micrograph of the lath martensite in an Fe-0.2C alloy is shown in Fig. 5.26. All of the laths, even the very thin ones, are resolved, in contrast to the light micrograph of the same structure in Fig 5.23(a) and 5.24 where many units are not clearly defined. Parts of two packets are shown. In each packet there appear to be two major orientations or variants of the martensite laths, and there are many very fine laths. Figure 5.27 shows the distribution of lath widths obtained by measurements from electron micrographs obtained from thin foils and replicas of polished and etched metallographic specimens (Ref 5.51). The important result shown in Fig. 5.27 is that most of the laths have widths smaller than 0.5 μm, the resolution limit

Fig. 5.26 Lath martensite in an Fe-0.2C alloy. Two packets, each with two habit plane variants of laths, are shown. Transmission electron micrograph. Source: Ref 5.51

of the light microscope, and therefore cannot possibly be revealed by light metallography. There are some laths with widths up to almost 2 μm, and these larger laths would, of course, be visible in the light microscope, as some are in Figures 5.23 and 5.24. It is the very fine size of most of the laths in a packet of low- or medium-carbon martensite that has over the years made the light metallographic characterization of lath martensite difficult.

The very small size of the martensitic crystals means that there is a very high crystal boundary area in lath martensitic microstructures. Measurements of lath boundary area per unit volume of martensitic microstructure on the order of 65,000 cm^2/cm^3 (cm^{-1}) have been made for the martensite of Fe-0.2C (Ref 5.51, 5.52). Some of the boundary area is associated with low-angle boundaries and some is associated with high-angle boundaries, depending on the orientation differences between the laths. On high-temperature tempering, the low-angle boundary area decreases significantly, as discussed in Chapter 17, "Tempering of Steel."

The habit plane of lath martensite, $\{557\}_A$, as measured in 1969 (Ref 5.8), is irrational, a plane close to $\{111\}_A$, as shown in Fig. 5.28. There are three $\{557\}_A$ variants clustered about each of the four $\{111\}_A$ planes, and the angle between these variants is only 16°. Laths of different habit plane

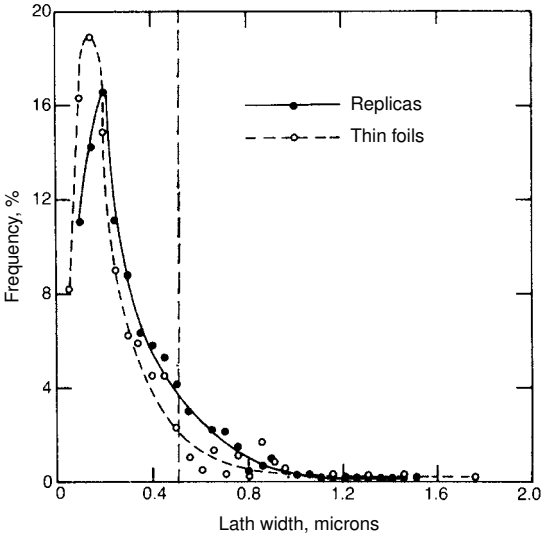

Fig. 5.27 Distribution of lath widens in Fe-0.2C martensite. Vertical line shows limit of resolution of the light microscope. Source: Ref 5.51

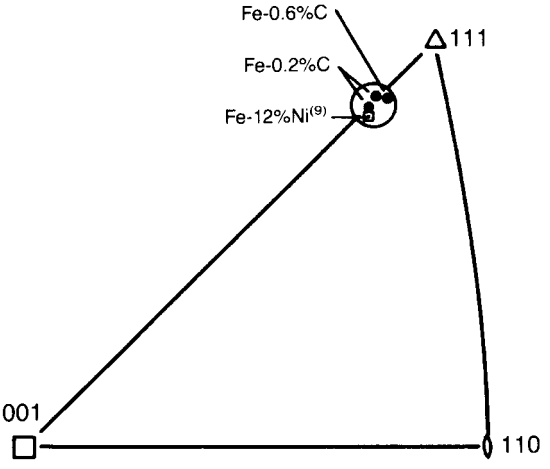

Fig. 5.28 Habit planes of lath martensite. The data points shown correspond to a (557) habit plane. Source: Ref 5.8

orientations within packets (see Fig. 5.26) frequently are observed to make angles of about 16° with each other, leading to the conclusion that the variants in a given packet all have variants close to the same $(111)_A$ plane. This coupling of variants, the small angles between variants, and the fine size of the laths give the microstructural impression that lath martensite has a $\{111\}_A$ habit with only four variants. Lath martensitic microstructures, therefore, appear much more orderly (see Fig. 5.23) than do the plate martensitic microstructures (see Fig. 5.19) with as many as 24 variants. The $[557]_A$ habit plane has also been measured in an extensive study of lath martensite in an Fe-20Ni-5Mn alloy (Ref 5.53).

Although there may be several crystallographic variants of laths in a packet of lath martensite, one variant or group of closely aligned variants may be dominant. This characteristic of a packet means that most of the laths, separated by low-angle boundaries or perhaps retained austenite, have the same crystal orientation and that a packet may be considered as a single grain or crystal, albeit a grain divided by many low-angle boundaries and containing a fine structure of many dislocations.

In low-carbon steel and iron-nickel alloys, packets or portions of packets with martensite crystals of the same habit plane and same crystallographic orientation are referred to as blocks, based on the early work of Marder and Marder (Ref 5.54). The symmetry of austenite and martensite crystals correlates with 24 variations of the Kurdjumov-Sach relationship, meaning that the martensite crystals formed in a given austenite grain may have that many different orientations or alignments of atom planes (Ref 5.55). Thus blocks are defined as regions where all of the parallel crystals have the same orientation or crystallographic alignment, and packets may consist of several blocks with slightly different orientations and habit planes. From the earlier discussion of martensite crystallinity, remember that the Kurdjumov-Sachs relationship refers to variants of the lattice relationships between austenite and martensite crystals, and that the habit planes and variants are a result of lattice-invariant deformation, also required by the plane-strain formation of martensite crystals.

Recently the application of SEM/EBSD analysis has made possible the identification of blocks of lath martensite crystals with the same or close crystallographic orientations of the crystals. Figure 5.29 shows an orientation map obtained from EBSD analysis (Ref 5.56). Each colored area rep-

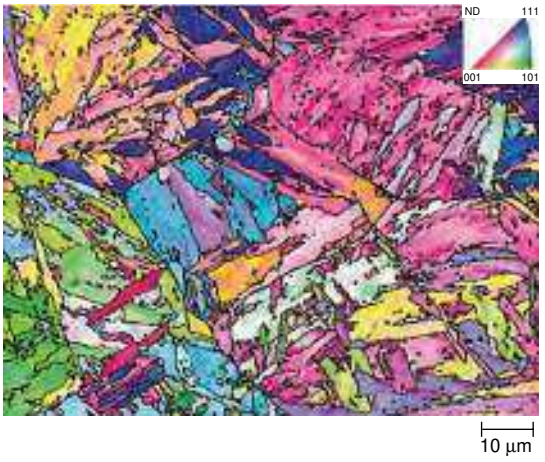

Fig. 5.29 Map of blocks, each with internal crystallographic misorientations of the martensitic crystals within the blocks of less than 10 degrees, in as-quenched low-carbon steel. Inverse pole figure map obtained from FE-SEM/EBSD analysis. Courtesy of Professor N. Tsuji, Kyoto University. Source: Ref 5.56.

resents blocks or regions where the misorientations of the martensite crystals are less than 10 degrees, according to crystallographic orientations normal to the observation plane as shown in the stereographic triangle insert. The many fine parallel crystals of martensite in a block are not shown. Further analysis showed that the crystals in each block may have been formed with two closely spaced variants of the Kurjumov-Sachs orientation relationship. The packet/block structure together with the very fine crystal size, substructure, and parallel arrangement of lath martensite within the packets has no counterpart in plate martensite and is important in establishing mechanical properties and fracture behavior of the martensite that forms in low- and medium-carbon steels.

The fine structure of lath martensite consists predominantly of a very high density of dislocations, often too high to be resolved even by electron microscopy of thin foils. However, Speich (Ref 5.57) was able to determine, indirectly by electrical resistivity measurements, a dislocation density of almost 10^{12} dislocations per square centimeter in low-carbon lath martensite.

An example of the fine structure of lath martensite in an Fe-0.2C alloy is shown in Fig. 5.30. The dislocations are tangled and arranged in incipient dislocation cells, a structure much different from the essentially straight, uniformly distributed dislocations of the Fe-Ni plate martensite shown in Fig. 5.17. The dislocation tangles are a result of a plastic deformation mode consistent with the high M_s and high-temperature range of formation of the low-carbon lath martensite (see Fig. 5.14) whereas, as already noted, the straight dislocations of the Fe-Ni martensite are consistent with low-temperature deformation of bcc iron alloys. The dislocation density of Fe-C lath martensite has been shown to increase with increasing carbon content up to 0.60% C (Ref 5.58).

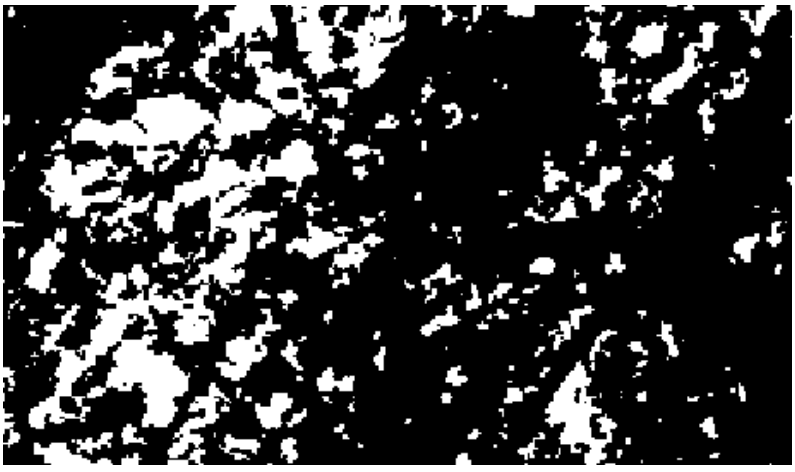

Fig. 5.30 Dislocation fine structure in lath martensite of an Fe-0.2C alloy. Transmission electron micrograph, original magnification 82,500×. Source: Ref 5.52

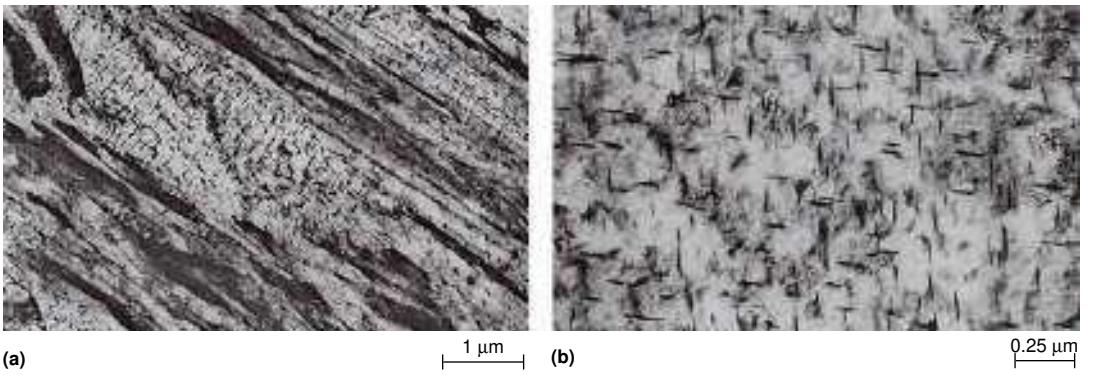

Fig. 5.31 Cementite (small linear dark features) formed in martensite during quenching of plate steels containing 0.19% carbon (Ref 5.60). Transmission electron micrographs

Another consequence of the high M_s temperatures of lath martensite formed in low-carbon steels is *autotempering* or *quench tempering*, the precipitation of cementite in martensite during quenching. Aborn (Ref 5.59) presented evidence of autotempering in an early study of structure and properties of low-carbon martensites, and Fig. 5.31 shows small plate-shaped cementite particles formed in as-quenched lath martensite crystals of plate steels containing 0.19% carbon (Ref 5.60). Large section sizes of steel that reduce cooling rates as well as high M_S temperatures promote the formation of carbides during quenching (Ref 5.61).

Although dislocations are the major fine structural component in lath martensite, fine transformation twins, a low-temperature mode of plastic accommodation, are also found to some extent in Fe-C lath martensite. The amount of fine twinning increases in accord with the decreasing M_s temperatures and lower athermal transformation ranges of lath martensite formation as carbon content increases.

The major change in morphology of martensite in Fe-C alloys and steels is the change from lath to plate morphologies, which begins in alloys containing about 0.6% C. However, there is a gradual change in morphology within the lath range, as indicated in Fig. 5.23 and more clearly shown in Fig. 5.32. In the alloys with 0.43% and 0.55% C, although the martensite units still appear to be largely parallel and quite fine, the packet structure is more difficult to define. Also, on the scale resolvable with the electron microscope, more adjoining laths assume nonparallel variants (Ref 5.62).

As noted earlier, retained austenite is part of the microstructure of steels quenched to martensite, and in low-carbon steel with lath martensite microstructures, small amounts of austenite are retained between the crystals of lath martensite. Fig. 5.33 shows an example of thin interlath retained

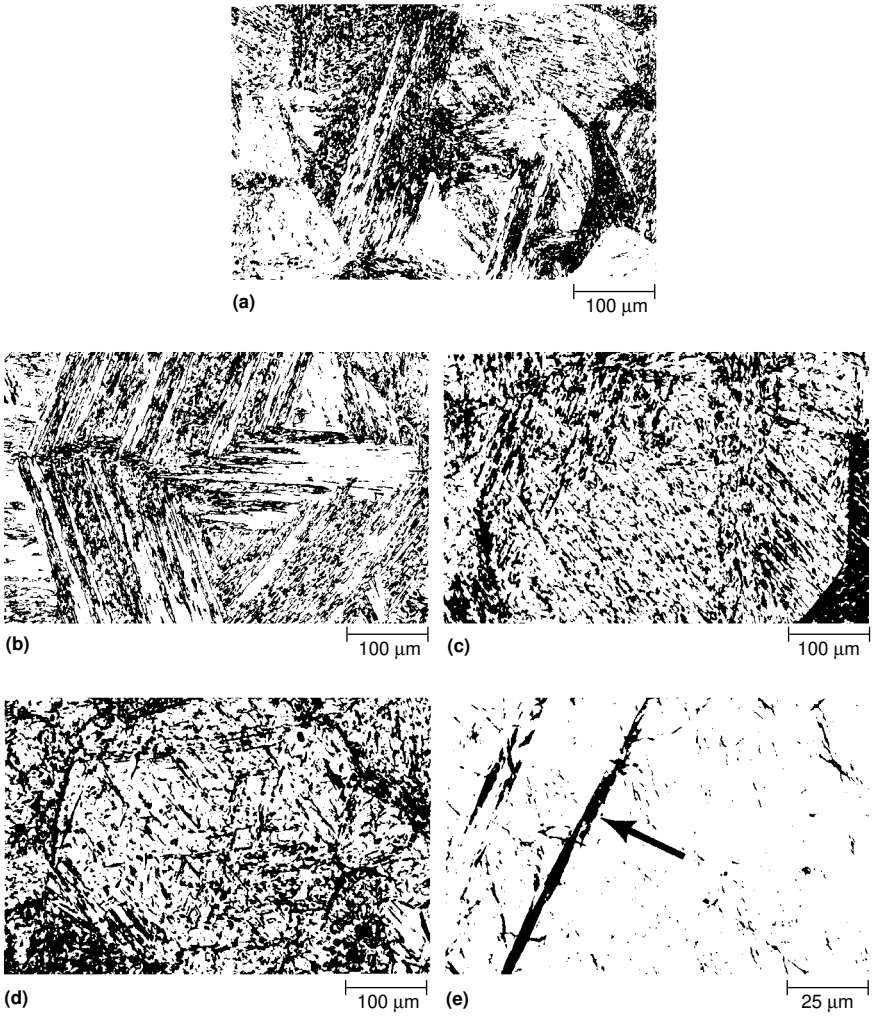

Fig. 5.32 Change in morphology of lath martensites in Fe-C alloys. (a) Fe-0.13C. (b) Fe-0.21C. (c) Fe-0.43C. (d) Fe-0.55C. (e) Fe-0.82C. Courtesy of T. Maki and I. Tamura, Kyoto University. Source: Ref 5.62

austenite in a steel containing 0.06 wt% carbon. The linear bright features were illuminated by a diffracted beam from the austensite; some martensite, the bulky bright features, was also illuminated because of a diffracted beam coinciding with the austenite beam.

REFERENCES

5.1 F. Osmond, Méthode générale pour l'analyse micrographique des aciers au carbone, *Bulletin de la societe d'Encouragement pour l'Industrie National*, Vol 10, 1895, p 480

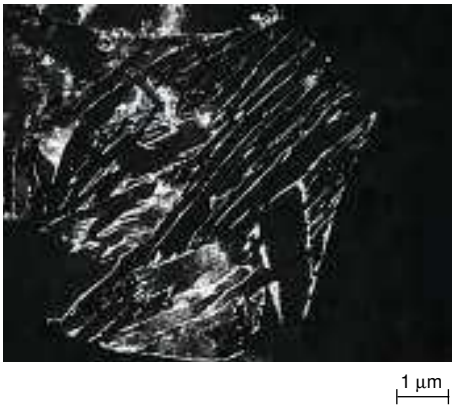

Fig. 5.33 Interlath retained austenite, the thin linear features, in a steel containing 0.06 wt% carbon. Dark-field transmisson electron micrograph. Courtesy of Professor Steven Thompson, Colorado School of Mines

5.2 C.M. Wayman, *Introduction to the Crystallography of Martensite Transformations*, Macmillan, New York, 1964

5.3 W.D. Kingery, *Introduction to Ceramics*, John Wiley & Sons, New York, 1960

5.4 G.K. Bansal and A.H. Heuer, On a Martensitic Phase Transformation in Zirconia (ZrO_2)—I. Metallographic Evidence, *Acta Metall.*, Vol 20, 1972, p 1281–1289

5.5 M. Cohen, The Strengthening of Steel, *Trans. TSM-AIME*, Vol 224, 1962, p 638–656

5.6 L. Cheng, A. Bouger, Th. H. de Keijser, and E.J. Mittemeyer, Lattice Parameters of Iron-Carbon and Iron-Nitrogen Martensites and Austenites, *Scipta Metall. et Mater.*, 1990, Vol 24, p 509–514

5.7 B.A. Bilby and J.W. Christian, The Crystallography of Martensite Transformations, *JISI*, Vol 197, 1961, p 122–131

5.8 A.R. Marder and G. Krauss, The Formation of Low-Carbon Martensite in Fe-C Alloys, *Trans. ASM*, Vol 62, 1969, p 957–964

5.9 G. Krauss and A.R. Marder, The Morphology of Martensite in Iron Alloys, *Metall. Trans.*, Vol 2, 1971, p 2343–2357

5.10 A.R. Marder and G. Krauss, The Morphology of Martensite in Iron-Carbon Alloys, *Trans. ASM*, Vol 60, 1967, p 651–660

5.11 M.J. Bibby and J. Gordon Parr, The Martensitic Transformation in Pure Iron, *JISI*, 1964, Vol 202, p 100–104

5.12 E.A. Wilson, The c to a Transformation in Low Carbon Irons, *ISIJ Int.*, 1994, Vol 34, p 615–630

5.13 D.A. Mirzayev, V.M. Schastlivtsev, and S. Ye Karzwnov, *Fiz. Metal. Metalloved.*, Vol 63 (No. 4), 1987, p 764

5.14 R.W. Fonda, G. Spanos, and R.A. Vandermeer, Observations of Plate Martensite in a Low Carbon Steel, *Scr. Metall. et Mater.*, Vol 31 (No. 6), 1994, p 683–688

5.15 G. Thomas, Retained Austenite and Tempered Martensite Embrittlement, *Metall. Trans. A*, Vol 9A, 1978, p 439–450
5.16 C.S. Roberts, Effect of Carbon on the Volume Fractions and Lattice Parameters of Retained Austenite and Martensite, *Trans. AIME*, Vol 197, 1953, p 203–204
5.17 P. Payson and C.H. Savage, Martensite Reactions in Alloy Steels, *Trans. ASM*, Vol 33, 1944, p 261–275
5.18 L.A. Carapella, Computing A^{11} or M_s (Transformation Temperature on Quenching) from Analysis, *Metal Progress*, 1944, Vol 46, p 108
5.19 E.S. Rowland and S.R. Lyle, The Application of M_s Points to Case Depth Measurement, *Trans. ASM*, 1946, Vol 37, p 27–47
5.20 R.A. Grange and H.M. Stewart, The Temperature Range of Martensite Formation, *Trans. AIME*, 1946, Vol 167, p 467–490
5.21 A.E. Nehrenberg, *Trans. AIME*, 1946, Vol 167, p 494–498
5.22 W. Steven and A.G. Haynes, The Temperature of Formation of Martensite and Bainite in Low-alloy Steel, *JISI*, Vol 183, 1956, p 349–359
5.23 K.W. Andrews, Empirical Formulae for the Calculation of Some Transformation Temperatures, *JISI*, Vol 203, 1965, p 721–727
5.24 G. Krauss, Martensitic Transformation, Structure and Properties in *Hardenable Steels, Hardenability Concepts with Applications to Steel*, AIME, Warrendale, PA, 1978, p 229–248
5.25 C.Y. Kung and J.J. Rayment, An Examination of the Validity of Existing Empirical Formulae for the Calculation of M_s Temperature, *Metall. Trans. A*, Vol 13A, 1982, p 328–331
5.26 V. Raghavan and D.P. Antia, The Driving Force for Martensitic Transformations in Low Alloy Steels, *Metall. and Mater. Trans.A*, Vol 27A, 1996, p 1127–1132
5.27 W.H. Harris and M. Cohen, Stabilization of the Austenite-Martensite Transformation, *Trans. AIME*, Vol 180, 1949, p 447–470
5.28 D.P. Koistinen and R.E. Marburger, A General Equation Prescribing the Extent of the Austenite-Martensite Transformation in Pure Iron-Carbon Alloys and Plain Carbon Steels, *Acta Metall.*, Vol 7, 1959, p 59–60
5.29 A.R. Entwisle, The Kinetics of Martensite Formation in Steel, *Metall. Trans.*, Vol 2, 1971, p 2395–2407
5.30 J.C. Bokros and E.R. Porter, The Mechanism of the Martensite Burst Transformation in Fe-Ni Single Crystals, *Acta Metall.*, Vol 11, 1963, p 1291–1301
5.31 K.R. Kinsman and J.S. Shyne, Thermal Stabilization of Austenite in Iron-Nickel-Carbon Alloys, *Acta Metall.*, Vol 15, 1967, p 1527–1543
5.32 C.H. Shih, B.L. Averbach, and M. Cohen, Some Characteristics of the Isothermal Martensitic Transformation, *Trans. AIME*, Vol 203, 1955, p 183–187

5.33 V. Raghavan and M. Cohen, Measurement and Interpretation of Isothermal Martensitic Kinetics, *Metall. Trans.*, Vol 2, 1971, p 2409–2418
5.34 S.R. Pati and M. Cohen, Nucleation of the Isothermal Martensitic Transformation, *Acta Metall.*, Vol 17, 1969, p 189–199
5.35 H. Okamoto and M. Oka, Isothermal Martensite Transformation in a 1.80 Wt Pct C Steel. *Metall. Trans. A*, Vol 16A, 1985, p 2257–2262
5.36 E.R. Petty, *Martensite, Fundamentals and Technology*, Longman, London, 1979, p 6
5.37 M.S. Wechsler, D.S. Lieberman, and T.A. Read, On the Theory of the Formation of Martensite, *Trans. AIME*, Vol 197, 1953, p 1503–1515
5.38 J.S. Bowles and J.K. MacKenzie, The Crystallography of Martensite Transformations, *Acta Metall.*, Vol 2, 1954, p 129–137, 138–147, 224–234
5.39 A.B. Greninger and A.R. Troiano, The Mechanism of Martensite Formation, *Trans. AIME*, Vol 185, 1949, p 590–598
5.40 J.W. Christian, *Martensite Fundamentals and Technology*, E.R. Petty, Ed., Longman, London, 1970, p 13
5.41 D.P. Dunne and C.M. Wayman, The Crystallography of Ferrous Martensites, *Metall. Trans.*, Vol 2, 1971, p 2327–2341
5.42 G. Krauss and W. Pitsch, The Fine Structure and Habit Planes of Martensite in an Fe-33 wt pct Ni Single Crystal, *Trans. TMS-AIME*, Vol 233, 1965, p 919–926
5.43 G. Krauss and W. Pitsch, Deformation Twins in Martensite, *Acta Metall.*, Vol 12, 1964, p 278–279
5.44 A.B. Greninger and A.R. Troiano, Crystallography of Austenite Decomposition, *Trans. AIME*, Vol 140, 1940, p 307–336
5.45 H.M. Ledbetter and R.P. Reed, On the Martensite Crystallography of Fe-Ni Alloys, *Mater. Sci. Eng.*, Vol 5, 1969–70, p 341–349
5.46 A.R. Marder and A.O. Benscoter, Microcracking in Fe-C Acicular Martensite, *Trans. ASM*, Vol 61, 1968, p 293–299
5.47 A.R. Marder, A.O. Benscoter, and G. Krauss, Microcracking Sensitivity in Fe-C Plate Martensite, *Metall. Trans.*, Vol 1, 1970, p 1545–1549
5.48 R.P. Brobst and G. Krauss, The Effect of Austenite Grain Size on Microcracking in Martensite of an Fe-1.22 C Alloy, *Metall. Trans.*, Vol 5, 1974, p 457–462
5.49 M.G. Mendiratta, J. Sasser, and G. Krauss, Effect of Dissolved Carbon on Microcracking in Martensite of an Fe-1.39 C Alloy, *Metall. Trans.*, Vol 3, 1972, p 351–353
5.50 A.R. Marder, *The Morphology and Strength of Iron-Carbon Martensite*, PhD Thesis, Lehigh University, 1968

5.51 C.A. Apple, R.N. Caron, and G. Krauss, Packet Microstructure in an Fe-0.2% C Martensite, *Metall. Trans.*, Vol 5, 1974, p 593–599
5.52 T. Swarr and G. Krauss, The Effect of Structure on the Deformation of As-Quenched and Tempered Martensite in an Fe-0.2% C Alloy, *Metall. Trans.*, Vol 7A, 1976, p 41–48
5.53 B.P.J. Sandvik and C.M. Wayman, Characteristics of Lath Martensite, *Metall. Trans. A*, Vol 14A, 1983, Part I, p 809–822; Part II, p 823–834; Part III, p 835–843
5.54 J.M. Marder and A.R. Marder, The Morphology of Iron-Nickel Massive Martensite, *Trans. ASM*, Vol 62 (No. 1), 1969, p 1–10
5.55 T. Maki, Morphology and Substructure of martensite in steels, in *Phase Transformations in Steels*, Volume 2, E. Pereloma and D. V. Edmonds, Editors,Woodhead Publishing, 2012, p 34–58
5.56 H. Kitahara, R. Ueji, N. Tsuji, and Y. Yoritoshi, Crystallographic , features of lath martensite in low-carbon steel, *Acta Mater.*, Vol 54, 2006, p 1279–1288.
5.57 G.R. Speich, Tempering of Low-Carbon Martensite, *Trans. TMS-AIME*, Vol 245, 1969, p 2552–2564
5.58 S. Morito, J. Nishikawa, and T. Maki, Dislocation Density within Lath Martensite in Fe-C and Fe-Ni Alloys, *ISIJ Int.*, Vol 43 (No. 9), 2003, p 1475–1477
5.59 R.H. Aborn, Low Carbon Martensites, *Trans. ASM*, Vol 48, 1956, p 51–85
5.60 R.P. Foley, R. K Weiss, S. W. Thompson, and G. Krauss, *Tempering Behavior of Martensitic Plate Steels Produced by Direct-Quench and Reaustenitize-and-Quench Processing*, in International Symposium on Low-Carbon Steels for the 90's, Edited by R. Asfahani and G. Tither, TMS, 1993, p 243-256
5.61 G.R. Speich, Tempering of Low-Carbon Martensite, *Trans. TMS-AIME*, Vol 245, 1969, p 2552–2564
5.62 T. Maki, K. Tsuzaki, and I. Tamura, The Morphology of Microstructure Composed of Lath Martensites in Steels, *Trans. Iron Steel Inst. Jpn.*, Vol 20, 1986, p 207–214

CHAPTER 6

Bainite

Bainite—An Intermediate Temperature Transformation Product of Austenite

AT TEMPERATURES between those at which the eutectoid transformation of austenite to pearlite and the transformation of austenite to martensite occur, a variety of unique microstructures may form in carbon steels. Davenport and Bain (Ref 6.1) showed by careful light microscopy that the microstructures formed at such intermediate temperatures were quite different from those of pearlite and martensite, and in honor of Edgar C. Bain, in 1934 his colleagues termed the unique microstructures *bainite*. Only later, in 1939 and 1942, R. F. Mehl was the first to use the term in the literature (Ref 6.2, 6.3).

Figure 6.1 is a schematic time-temperature-transformation diagram, first published by Zener (Ref 6.4) and reprinted by Bhadeshia (Ref 6.5), that

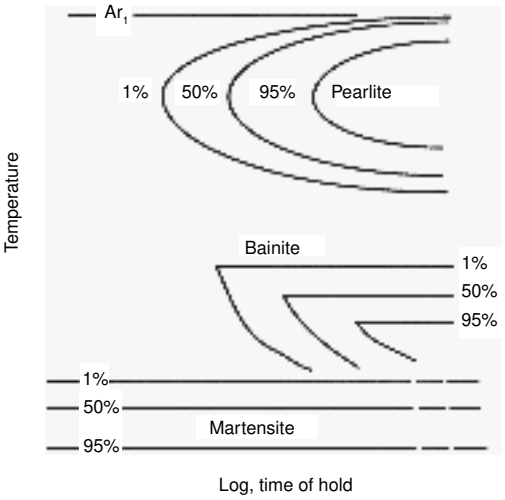

Fig. 6.1 Schematic time-temperature-transformation (TTT) diagram for a steel with well-defined pearlite and bainite formation ranges. Source: Ref 6.4, 6.5

clearly shows the intermediate temperature range, between those of pearlite and martensite, for bainite formation. Steels with carbon contents other than the eutectoid composition would of course have regions of proeutectoid phase formation at temperatures above that of pearlite formation.

The schematic diagram of Fig. 6.1 shows a well-defined time-temperature transformation range for bainite formation. Such a well-defined range of bainite transformation is characteristic of low-alloy steels, especially on continuous cooling, and several examples showing alloying effects on producing separate proeutectoid ferrite/pearlite and bainite transformation regions are presented in Chapter 10, "Isothermal and Continuous Cooling Transformation Diagrams." In plain carbon steels the transformation regions for proeutectoid ferrite/pearlite and bainite are more continuous and even overlap with decreasing temperature. In alloy steels, alloying elements may even cause the arrest of bainite transformation, causing incomplete transformation at intermediate temperatures (Ref 6.6). The extreme effects of alloying, ranging from those in plain carbon steels to those in alloyed steels, on bainitic transformation are shown schematically in the time-temperature-transformation diagrams in Fig. 6.2.

Bainite Transformation Start Temperatures

The temperature at which bainite transformation starts is referred to as the B_S temperature, and several empirical equations that show the effect of alloying elements on B_S have been determined (Ref 6.5). Steven and Hayes (Ref 6.8) established the following equation for B_S as a function of

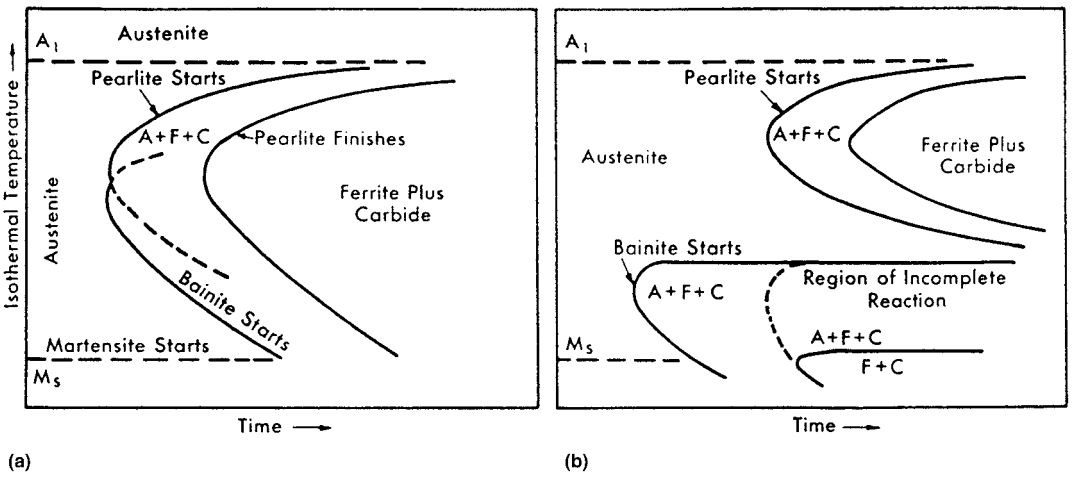

Fig. 6.2 Schematic time-temperature-transformation (TTT) diagrams for (a) plain carbon steel with overlapping pearlite and bainite transformation and (b) alloy steel with separated bainite transformation and incomplete bainite transformation. Source: Ref 6.6, 6.7

composition (in wt%) for hardenable low-alloy steels containing from 0.1 to 0.55% carbon:

$$B_S(°C) = 830 - 270(\%C) - 90(\%Mn) - 37(\%Ni) - 70(\%Cr) - 83(\%Mo) \quad \text{(Eq 6.1)}$$

For low-carbon bainitic steels, containing between 0.15 and 0.29% C, for high-temperature applications in the electric power industry, Bodnar et al. (Ref 6.9) established the following equation, with compositions of the alloying elements in wt%:

$$B_S(°C) = 844 - 597(\%C) - 63(\%Mn) - 16(\%Ni) - 78(\%Cr) \quad \text{(Eq 6.2)}$$

Bainite versus Ferritic Microstructures

Bainitic microstructures take many forms. In medium- and high-carbon steels, bainite, like pearlite, is a mixture of ferrite and cementite, and is therefore dependent on the diffusion-controlled partitioning of carbon between ferrite and cementite. However, unlike pearlite, the ferrite and cementite are present in non-lamellar arrays. As in martensite, the ferrite of bainitic microstructures may appear as acicular crystals, similar to the laths and plate-shaped crystals of martensite. Two major morphologies of ferrite-cementite bainitic microstructures have been identified, as described subsequently, and in view of the two temperature ranges at which the morphologies develop, Mehl in 1939 designated the types as *upper* (temperature) *bainite* and *lower* (temperature) *bainite* (Ref 6.2). Figure 6.3, as determined by Pickering (Ref 6.10), shows the effect of steel carbon content on transition temperatures between upper and lower bainite formation.

In low-carbon steels, at intermediate transformation temperature ranges, austenite may transform only to ferrite, resulting in two-phase microstructures of ferrite and retained austenite. The latter microstructures have morphologies quite different from the proeutectoid ferrite morphologies described in Chapter 4, "Pearlite, Ferrite, and Cementite." Although some features of the intermediate ferritic microstructures are similar to those of the classical bainites, the absence of cementite in ferritic microstructures makes possible a clear differentiation of intermediate-temperature-transformation products of austenite decomposition.

According to a microstructural definition of bainite in steels as a nonlamellar ferrite-cementite product of austenite transformation, Aaronson et al. recognize six morphologies of bainite (Ref 6.11); Fig. 6.4 shows schematically those six morphologies of cementite-ferrite microstructures considered to be bainites. Upper and lower bainites are the most

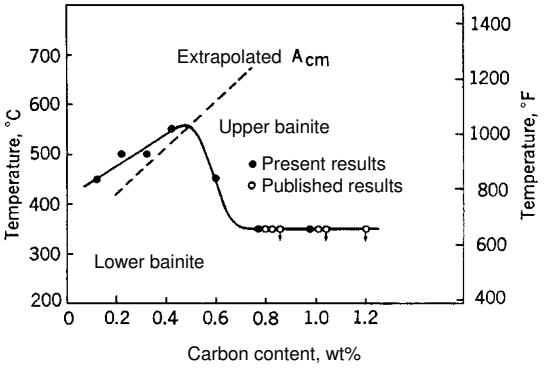

Fig. 6.3 Effect of steel carbon content on the transition temperature between upper and lower bainite. Source: Ref 6.10

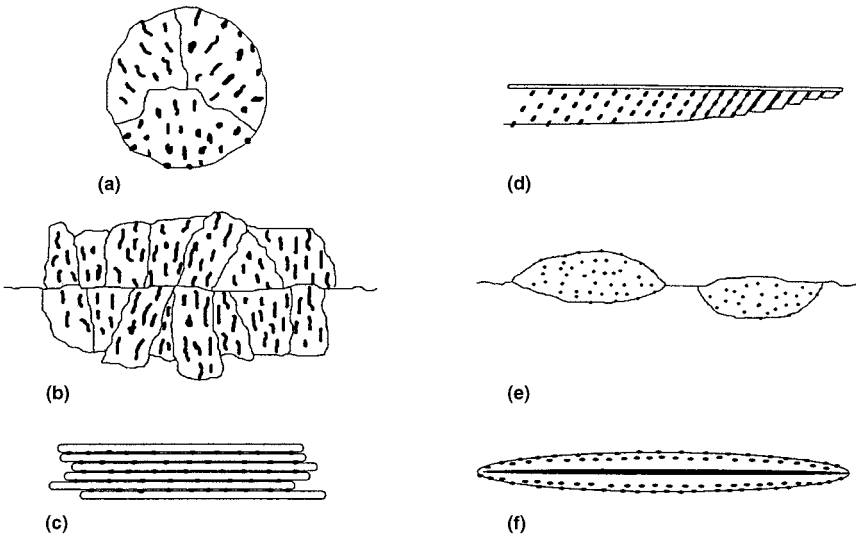

Fig. 6.4 Schematic illustrations of various ferrite (white)-cementite (black) microstructures defined as bainite according to Aaronson et al. (Ref 6.11). (a) Nodular bainite. (b) Columnar bainite. (c) Upper bainite. (d) Lower bainite. (e) Grain boundary allotromorphic bainite. (f) Inverse bainite

common forms found in medium-carbon steel and are described in more detail in later sections of this chapter. However, in the absence of cementite, intermediate-temperature-transformation products of austenite fall in the category of ferrites, as described in Chapter 7, "Ferritic Microstructures."

Upper Bainite

Upper bainite forms in the temperature range just below that at which pearlite forms, typically below 500 °C (930 °F). Figure 6.5 shows light micrographs of upper bainite formed by holding 4360 steel at 495 °C (920 °F) and 410 °C (770 °F). The bainite appears dark, and the individual ferritic crystals have an acicular shape. The bainitic transformation was not completed during the isothermal holds at the temperatures noted, and therefore the light etching areas are martensite that formed in untransformed austenite on quenching after the isothermal holds. The bainite appears dark (i.e., has low reflectivity) because of roughness produced by etching around the cementite particles of the bainitic structure. The cementite particles, however, are too fine to be resolved in the light microscope.

The feathery appearance of the clusters of ferrite crystals is clearly shown in the light micrographs and is sometimes an important identifying feature of upper bainite. Upper bainite microstructures develop by packets or sheaves of parallel ferrite crystals growing across austenite grains, producing a blocky appearance. Figure 6.6 shows the latter characteristic of upper bainite in a 4150 steel transformed at 460 °C (860 °F).

The cementite particles of upper bainite form between ferrite crystals in austenite enriched by carbon rejection from the growing ferrite crystals. Figure 6.7 is a thin foil transmission electron microscope (TEM) micrograph that shows interlath cementite in a 4360 steel transformed to bainite at 495 °C. The carbide particles, compared with those that are present in lower bainite, are relatively coarse and appear black and elongated. In some steels, especially those with high silicon content, cementite formation is retarded. As a result, the carbon-enriched austenite between the fer-

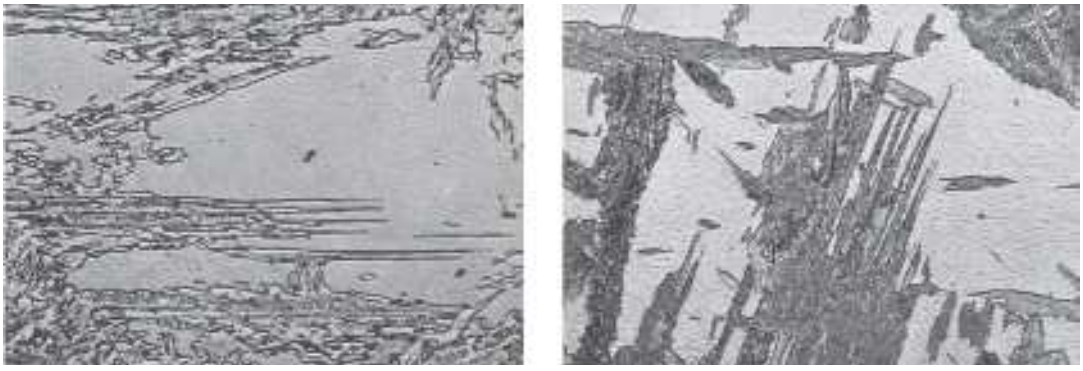

(a) (b)

Fig. 6.5 Upper bainite in 4360 steel isothermally transformed at (a) 495 °C (920 °F) and (b) 410 °C (770 °F). Light micrographs, picral etch, original magnification 750×. Source: Ref 6.12

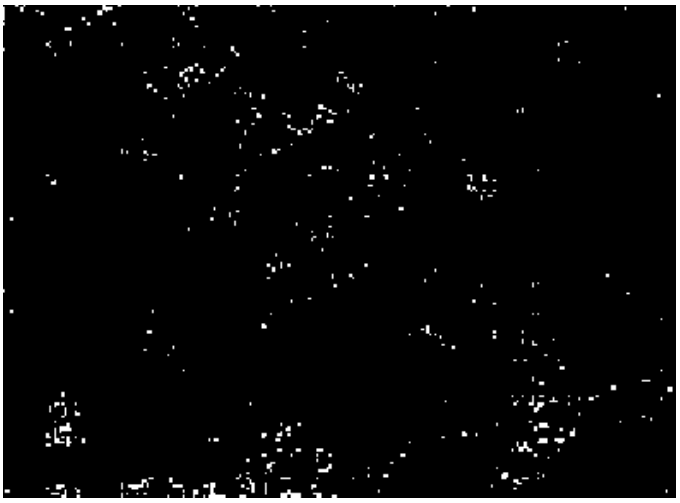

Fig. 6.6 Upper bainite (dark rectangular areas) in 4150 steel transformed at 460 °C (860 °F). Light micrograph, nital etch, original magnification 500×. Courtesy of Florence Jacobs, Colorado School of Mines

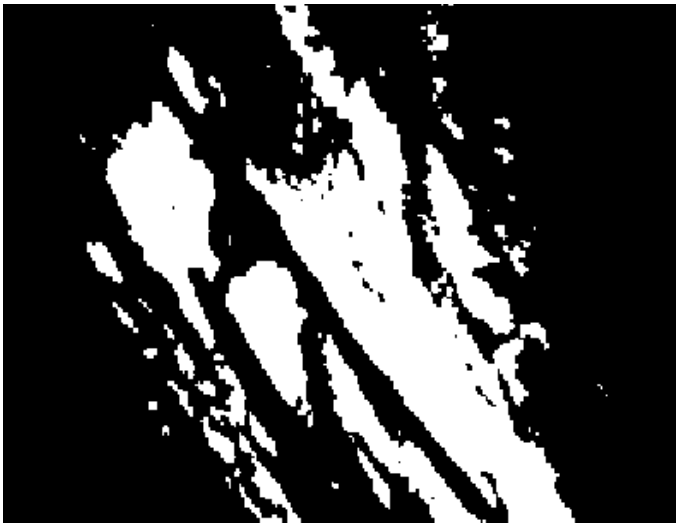

Fig. 6.7 Carbide particles (dark) formed between ferrite crystals in upper bainite in 4360 steel transformed at 495 °C (920 °F). Transmission electron micrograph, original magnification 25,000×. Source: Ref 6.12

rite laths is quite stable and is retained during transformation and at room temperature. Figure 6.8 shows retained austenite in bainite formed at 400 °C (752 °F) in a steel containing 0.6% C and 2.0% Si. The austenite in this TEM image appears gray, and an example of the austenite is marked "A."

Fig. 6.8 Retained austenite (gray, marked with A) between ferrite laths of upper bainite in 0.6% carbon steel containing 2.0% Si and transformed at 400 °C (750 °F). Transmission electron micrograph, original magnification 40,000×. Source: Ref 6.12

Lower Bainite

An example of lower bainite, obtained from a specimen of 4360 steel partially transformed at 300 °C (570 °F), is shown in Fig. 6.9. Again, the bainite etches dark and the white-etching matrix is martensite formed on cooling in the austenite not transformed to bainite at 300 °C. Lower bainite is composed of large ferrite plates that form nonparallel to one another, and analogously to plate martensite microstructures, is often characterized as acicular. The carbides in the ferrite plates of lower bainite are responsible for its dark etching appearance but are much too fine to be resolved in the light microscope.

Figure 6.10, a transmission electron micrograph, shows the very fine carbides that have formed in ferrite of lower bainite in 4360 steel transformed at 300 °C. The fine carbides typically make an angle of about 60° with respect to the long axis of the matrix ferrite crystal. In contrast to upper bainite, fine carbides form within ferrite crystals, rather than between plates, and are significantly finer than the interlath carbides of upper bainite. Recently, improvements in the resolving power of scanning electron microscopes have made possible the observation of the fine carbides in lower bainite on polished and etched sections, as shown in Fig. 6.11.

A variant of lower bainite has been identified by Okamoto and Oka in hypereutectoid steels (Ref 6.13). This form of lower bainite is termed *lower bainite with midrib* and forms isothermally at lower temperatures, 150 to 200 °C (300 to 350 °F) than the temperatures at which conventional

Fig. 6.9 Lower bainite in 4360 steel transformed at 300 °C (570 °F). Light micrograph, picral etch, original magnification 750×. Source: Ref 6.12

Fig. 6.10 Lower bainite with fine carbides within ferrite plates in 4360 steel transformed at 300 °C (570 °F). Transmission electron micrograph, original magnification 24,000×. Source: Ref 6.12

lower bainite forms, 200 to 350 °C (390 to 660 °F). Figure 6.12 shows light and TEM micrographs of lower bainite with midrib in a 1.10% carbon steel transformed at 190 °C (370 °F). The midrib is an isothermally formed thin plate of martensite which provides the interface at which the two-phase carbide-ferrite lower bainitic structure forms.

Fig. 6.11 Lower bainite, showing fine carbides in the plates of the lower bainite, on a polished and nital-etched section of a medium carbon steel. Original magnification 3,000×, Field Emission SEM micrograph

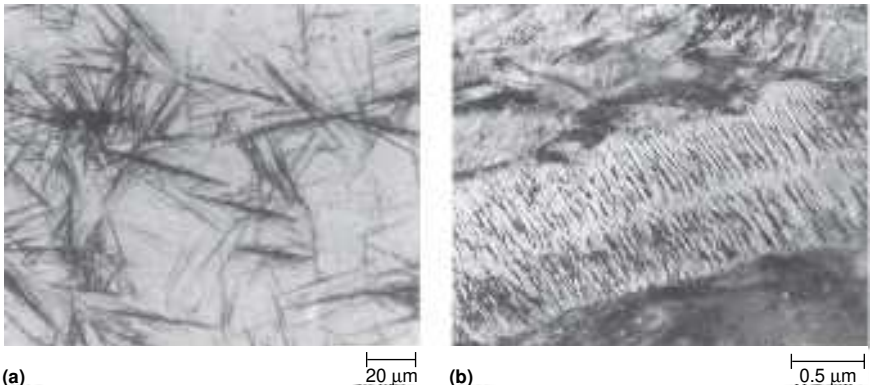

Fig. 6.12 Lower bainite with midribs in a 1.10% carbon steel transformed at 190 °C (375 °F) for 5 h. (a) Light micrograph. (b) TEM micrograph. Courtesy of H. Okamoto, Tottori University.

Bainite Formation Mechanisms

The fact that the classical bainites consist of ferrite and non-lamellar distributions of cementite attests to the need for carbon diffusion during some stage of bainite transformation. However, the relatively low temperatures at which bainites form severely restricts iron atom diffusion.

The latter feature of the transformation of austenite to bainite has led to two quite different views of ferrite nucleation in bainite (Ref 6.5, 6.11, 6.14, 6.15). One view states that the first-formed ferrite is formed by a diffusionless shear or martensitic transformation. The other view states that the first-formed ferrite nucleates and grows by a ledge-type mechanism in which short-range iron atom rearrangement can take place at ledges in the ferrite-austenite interface. The references cited provide scientific and experimental support for both sides of the argument about the nucleation and growth mechanisms of bainite, and the reader is referred to these references for more information and more extensive reference lists.

The empirical B_S equations noted earlier reflect the strong effect of alloying elements on the start of bainitic transformation. Coupled with this characteristic of steels with prominent bainite transformations is the presence of a pronounced *bay*, or region of very sluggish transformation, in time-temperature-transformation (TTT) diagrams. These regions correspond to the temperature ranges that show the marked separation of the transformation curves for pearlite and bainite in Fig. 6.1. An example of such a bay is shown in the isothermal TTT diagram for 4340 steel (Fig. 6.13). Such bays correlate with the presence of substitutional alloying elements that may partition to or from ferrite and concentrate at austenite-ferrite interfaces, creating a *solute drag*, or significant restraining force, on the formation of bainitic ferrite (Ref 6.15, 6.17). As noted relative to Fig. 6.2, the isothermal transformation of austenite to bainite may be se-

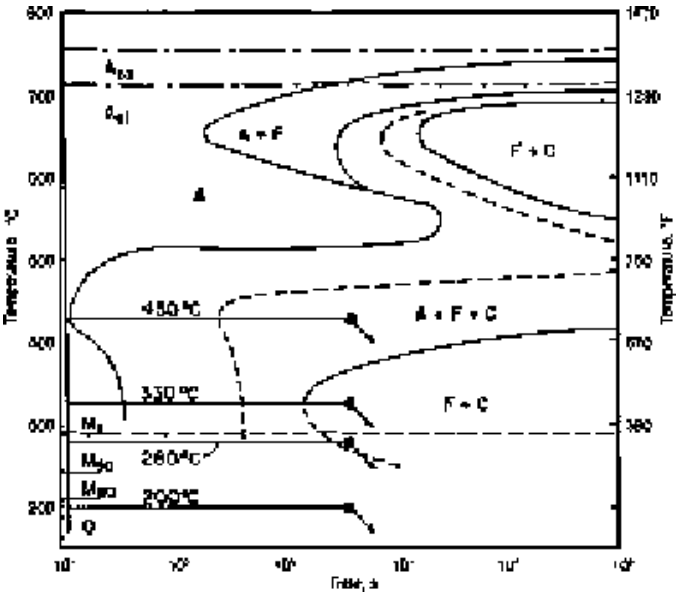

Fig. 6.13 Isothermal transformation diagram for 4340 steel and isothermal heat treatments applied to produce various microstructures for fracture evaluation. Source: Ref 6.16

verely retarded. This phenomenon is referred to as stasis and is also discussed in terms of atom partitioning and solute drag at austenite-ferrite interfaces (Ref 6.17, 6.18).

The distribution of very fine carbides in plates of lower bainite suggests that a ferrite crystal has initially formed, perhaps by a martensitic mechanism, and as a consequence of the supersaturation of the ferrite with carbon, fine carbides precipitate within the ferrite. Another explanation for the formation of lower bainite has been proposed by Spanos et al. They conclude, based on extensive transmission electron microscopy of a series of Fe-C alloys containing 2.0% Mn, that a unit of lower bainite forms by a four-step process: "(1) precipitation of a nearly carbide-free ferrite spine; (2) sympathetic nucleation of secondary plates of ferrite, usually on only one side of and at an angle of approximately 55 to 60 degrees to the initiating spine; (3) precipitation of carbides in austenite at a:c boundaries, forming gaps between adjacent secondary (ferrite) plates; and (4) an annealing process in which the gaps are filled in with further growth of ferrite and additional carbide precipitation" (Ref 6.19).

Mechanical Behavior of Ferrite-Carbide Bainites

Steels largely transformed to ferrite-carbide bainitic microstructures develop a wide range of strengths and ductilities (Ref 6.10). Ultimate tensile strengths of high-carbon lower bainitic microstructures may reach 1,400 MPa (200 ksi) and hardness may reach 55 HRC or higher. The strengths are derived from relatively fine ferrite crystal structures, high dislocation densities within the ferritic crystals, and fine dispersions of cementite. The lower the temperature of bainite formation, the finer the carbide dispersions, and the higher the hardness and strength. Lower bainite microstructures compete well with low-temperature-tempered martensites in strength and fracture resistance. Often low-alloy steels are subjected to isothermal holds to form bainite, instead of quenching to martensite, in order to reduce the stresses that produce quench cracking. The latter heat treatment is referred to as *austempering* and is discussed in more detail in Chapter 20, "Residual Stresses, Distortion, and Heat Treatment."

The type of bainite affects fracture characteristics. Hehemann et al. (Ref 6.20) showed that specimens with upper bainitic microstructures have low toughness and ductility compared with specimens with lower bainitic microstructures, and Pickering has shown that upper bainites have high ductile-to-brittle transition temperatures (Ref 6.10). These observations were confirmed in a study of 4340 steel isothermally transformed at various temperatures as shown in Fig. 6.13. Specimens quenched in oil and tempered at 200 °C (390 °F) had tempered martensite microstructures with hardness of 52 HRC, those held at 200 °C (390 °F) also transformed to tempered martensite with hardness 52 HRC, those held at 280 and 330 °C

(540 and 630 °F) transformed largely to lower bainite with hardness of 50 and 44 HRC, repectively, and those transformed at 430 °C (810 °F) transformed largely to upper bainite with hardness of 32 HRC.

Figure 6.14 shows the results of room-temperature instrumented Charpy V-notch (CVN) testing of the 4340 specimens. Instrumented impact testing measures both initiation and propagation energies. The fracture energy of the specimens with the upper bainitic microstructures was significantly lower than those with tempered martensite or lower bainite. When fracture was initiated in the upper bainite, the propagation energy dropped to zero. Fractography of the upper bainitic specimens showed, except at initiation at the notch root, that the fracture surface consisted entirely of cleavage fracture (Fig. 6.15b), a result attributed to the coarse interlath carbides and common cleavage plane of the parallel ferrite crystal in packets of upper bainite. In contrast, the fracture surfaces of the specimens transformed to tempered martensite consisted of ductile microvoid coalescence (Fig. 6.15a). Although in general, microstructures with lower strength and hardness show better ductility and fracture resistance than microstructures with higher hardness, the behavior of upper bainite, with its lower hardness compared with other microstructures in 4340 steel, contradicts this general rule. A study of the fracture behavior of 4150 steel isothermally transformed to lower and upper bainite confirms the strong susceptibility of upper bainite to cleavage fracture despite its lower hardness and strength relative to lower bainitic microstructures (Ref 6.21).

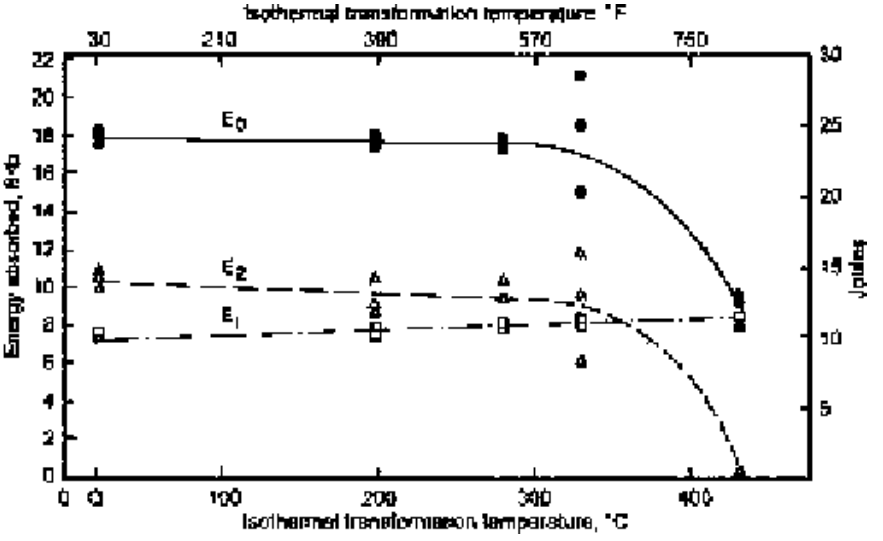

Fig. 6.14 Impact energy absorbed as a function of isothermal transformation temperature for specimens of 4340 steel. E_0 is total energy absorbed, E_1 is fracture initiation energy, and E_2 is fracture propagation energy. Source: Ref 6.16

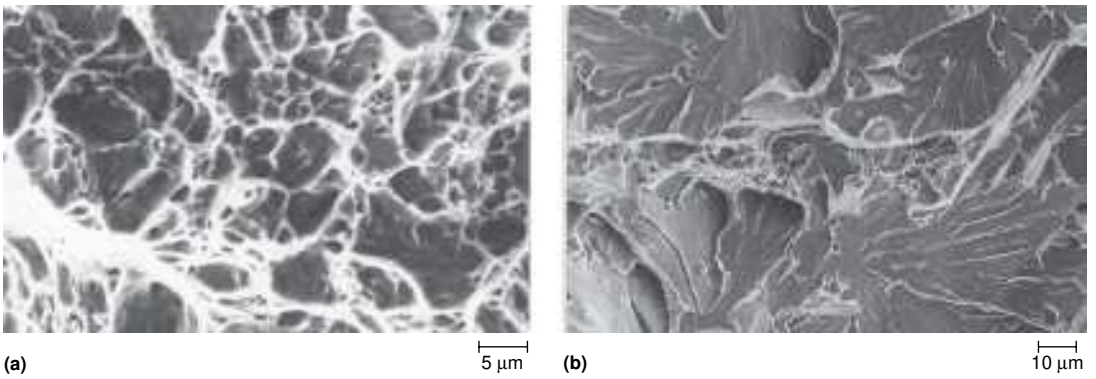

Fig. 6.15 Fracture morphologies of fracture surfaces of 4340 steel CVN specimens heat treated as: (a) oil quenched and tempered at 200 °C (390 °F) and (b) isothermally transformed at 430 °C (810 °F). Source: Ref 6.16

REFERENCES

6.1 E.S. Davenport and E.C. Bain, Transformation of Austenite at Constant Subcritical Temperatures, *Trans. AIME,* Vol 90, 1930, p 117–144; reprinted as a Metallurgical Classic, with commentary by Harold W. Paxton, in *Metall. Trans.,* Vol 1, 1970, p 3475–353; also reprinted in *Metall. Trans. A*, Vol 41A, 2010, p 1353–1390 with an Introduction by H.K.D.H. Bhadeshia, p 1351–1352

6.2 R.F. Mehl, The Physics of Hardenability - The Mechanism and the Rate of the Decomposition of Austenite, in *Hardenability of Alloy Steels,* ASM, 1939, p 1–65

6.3 G. V, Smith and R. F. Mehl, Lattice Relationships in Decomposition of Austenite to Pearlite, Bainite, and Martensite, *Transactions AIME,* Vol 150, 1942, p 211–226

6.4 C. Zener, Kinetics of the Decomposition of Austenite, *Transactions AIME,* Vol 167, 1946, p 550–595

6.5 H.K.D.H. Bhadeshia, *Bainite in Steels,* Book No. 504, The Institute of Materials, London, 1992

6.6 H.I. Aaronson, W.T. Reynolds, Jr., G.J. Shiflet, and G. Spanos, Bainite Viewed Three Different Ways, *Metall. Trans. A,* Vol 21A, 1990, p 1343–1380

6.7 R.F. Hehemann and A.R. Troiano, The Bainite Transformation, *Met. Prog.,* 1956, Vol 70 (2), p 97–104

6.8 W. Stevens and A.G. Haynes, The Temperature of Formation of Martensite and Bainite in Low-alloy Steel, *JISI,* Vol 183, 1956, p 349–359

6.9 R.L. Bodnar, T. Ohhashi, and R.I. Jaffee, Effects of Mn, Si, and Purity on the Design of 3.5NiCrMoV, 1CrMoV, and 2.25Cr-1Mo Bainitic Alloy Steels, *Metall. Trans. A,* Vol 20A, 1989, p 1445–1460

6.10 F.B. Pickering, The Structure and Properties of Bainite in Steels, in *Transformation and Hardenability in Steels,* Climax Molybdenum Company of Michigan, Ann Arbor, MI, 1977, p 109–132
6.11 W.T. Reynolds, Jr., H.I. Aaronson, and G. Spanos, A Summary of the Present Diffusionist Views on Bainite, *Mater. Trans., JIM,* Vol 32 (No. 8), 1991, p 737–746
6.12 R.F. Hehemann, Ferrous and Nonferrous Bainitic Structures, *Metallography, Structures and Phase Diagrams,* Vol 8, *Metals Handbook,* 8th ed., American Society for Metals, 1973, p 194–196
6.13 H. Okamoto and M. Oka, Lower Bainite with Midrib in Hypereutectoid Steels, *Metall. Trans. A,* Vol 17A, 1986, p 1113–1120
6.14 J.W. Christian and D.V. Edmonds, The Bainite Transformation, *Phase Transformations in Ferrous Alloys,* A.R. Marder and J.I. Goldstein, Ed., TMS, Warrendale, Pennsylvania, 1984, p 293–325
6.15 R.E. Hackenberg and G.J. Shiflet, The Influence of Alloy Element Partitioning on the Shapes of TTT Start Curves for Steels, *Austenite Formation and Decomposition,* E.B. Damm and M.J. Merwin, Ed., TMS, Warrendale, 2003, p 27–41
6.16 G. Baozhu and G. Krauss, The Effect of Low-Temperature Isothermal Heat Treatments on the Fracture of 4340 Steel, *J. Heat Treating,* Vol 4 (No. 4), 1986, p 365–372
6.17 M. Hillert and L. Höglund, The Bay Phenomenon in Steels with Reasonably Strong Carbide Formers, *Austenite Formation and Decomposition,* E.B. Damm and M.J. Merwin, Ed., TMS, Warrendale, Pennsylvania, 2003, p 3–14
6.18 W.T. Reynolds, Jr., F.Z. Li, C.K. Shui, and H.I. Aaronson, The Incomplete Transformation Phenomenon in Fe-C-Mo Alloys, *Metall. Trans. A,* Vol 21A, 1990, p 1433–1463
6.19 G. Spanos, H.S. Fang, and H.I. Aaronson, A Mechanism for the Formation of Lower Bainite, *Metall. Trans. A,* Vol 21A, 1990, p 1381–1390
6.20 R.F. Hehemann, V.J. Luhan, and A.R. Troiano, The Influence of Bainite on Mechanical Properties, *Trans. ASM,* Vol 49, 1957, p 409–426
6.21 D.R. Johnson and W.T. Becker, Toughness of Tempered Upper and Lower Bainitic Microstructures in a 4150 Steel, *J. Mater. Eng. Perform.,* Vol 2 (No. 2), 1993, p 255–263

CHAPTER 7

Ferritic Microstructures

THIS CHAPTER DESCRIBES ferritic microstructures that form during continuous cooling of carbon steels. Ferritic microstructures identified as proeutectoid ferrite have already been discussed in Chapter 4, "Pearlite, Ferrite, and Cementite," in this book. These forms of ferrite nucleate as equiaxed grains on austenite grain boundaries or as Widmanstätten side plates and grow into austenite grain interiors, rejecting carbon until there is sufficient carbon to nucleate pearlite. The latter process produces the ferrite-pearlite microstructures of low- and medium-carbon steels cooled in air after hot rolling or after normalizing heat treatments. The proeutectoid forms of ferrite, as well as the ferritic microstructures formed at lower, intermediate temperatures in the bainite range, are described in more detail in this chapter.

Depending on carbon content, alloy content, and cooling rate, several morphologies of ferrite other than equiaxed ferrite may form during continuous cooling of low-carbon steels. As noted in Chapter 6, "Bainite" in this book, some of these morphologies have similarities to bainite but without cementite formation. Also, similar to bainite, unique morphologies of ferrite form from austenite at temperatures intermediate to those at which proeutectoid ferrite/pearlite and martensite form. The nonequiaxed forms of ferrite are of great interest as an approach to produce combinations of strength and ductility better than those obtainable in very-low-carbon and low-carbon steels with equiaxed ferrite microstructures. The nonequiaxed forms of ferrite received significant attention in the conference *New Aspects of Microstructures in Modern Low Carbon High Strength Steels*, held in Tokyo in 1994 (Ref 7.1), and an entire issue of *ISIJ International* was devoted to papers from that conference (Ref 7.2). The development of low-carbon, high-strength low-alloy (HSLA) steels for U.S. Navy ship plate applications has also stimulated evaluation of unique ferritic microstructures in low-carbon steels (Ref 7.3). Also, in view of the low-carbon content of weld metal and weldable steels, the formation of

various ferritic microstructures in rapidly cooled weld metal and heat-affected zones in low-carbon steels is of great interest (Ref 7.4).

The Dubé Classification System for Proeutectoid Ferritic Microstructures

A good starting point for the classification of ferritic microstructures is the Dubé system, as amplified by Aaronson (Ref 7.5). The Dubé classification system applies to all alloy systems but relates well to the high temperature ferrite morphologies that form from austenite in steels. Figure 7.1 shows schematically various morphologies of crystals described in the Dubé system. Figure 7.1(a) represents a crystal that has nucleated on and grown along a parent-phase grain boundary. This type of crystal is termed a grain-boundary allotriomorph and, in steels, corresponds to the equiaxed ferrite that has been described in Chapter 4, "Pearlite, Ferrite, and Cementite," of this book as the proeutectoid ferrite morphology that precedes pearlite formation in hypoeutectoid steels.

Ferrite crystals in steels often have a plate or needlelike shape. This morphology is termed Widmanstätten, in honor of the French scientist Alois de Widmanstätten. In the Dubé system, such crystals are referred to as Widmanstätten side plates. Primary side plates grow directly from grain

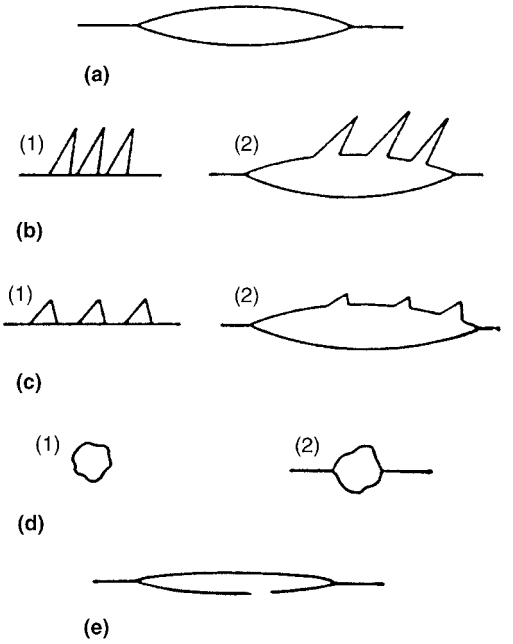

Fig. 7.1 Schematic diagrams of ferrite morphologies according to the Dubé classification system. The text describes the terms used for each morphology. Source: Ref 7.5

boundaries, as shown in Fig. 7.1(b)(1); secondary side plates grow from grain-boundary allotriomorphs as shown in Fig. 7.1(b)(2). Widmanstätten saw teeth have a more triangular appearance, as seen in Fig. 7.1(c), and also may be nucleated directly on grain boundaries or on grain-boundary allotriomorphs, as shown. Idiomorphs are equiaxed crystals that may form on grain boundaries or within grains (Fig. 7.1d). Nucleation of ferrite idiomorphs within austenite grains is rare because of the interfacial energy increase associated with the formation of completely new ferrite/austenite interfaces of ferrite crystals nucleating within austenite. In contrast, grain-boundary allotriomorphs require lower interfacial energy to nucleate because they make use of already existing high-energy, disordered austenite grain-boundary interfaces. The Dubé system also recognizes Widmanstätten plates that form intragranularly (Fig. 7.1e).

General Considerations—Cooling-Rate-Induced Changes in Ferrite

The various ferrite morphologies and other microstructural products of austenite decomposition result from increasingly restricted atom motion with decreasing temperature of transformation. Iron atom rearrangement from austenite to equiaxed ferrite crystals and long-range diffusion of carbon atoms require high temperatures. At intermediate temperatures, while interstitial carbon atoms still have good mobility, the movement of iron atoms is severely retarded, and either very short-range rearrangement at ferrite-austenite ledges or shear mechanisms are required to form non-equiaxed ferrite crystals. At very low temperatures, neither iron atoms nor carbon atoms can diffuse, and austenite transforms to martensite completely by shear, without diffusion, as described in Chapter 5, "Martensite" in this book.

Figure 7.2, as presented by Wilson (Ref 7.6), shows the changes in transformation temperature and corresponding microstructures with increasing cooling rates and decreasing temperature during continuous cooling of an Fe-0.01%C alloy. Continuous cooling arrest temperatures are clearly tied to various microstructures and independent transformation curves. When a critical cooling rate is attained for a given product of austenite decomposition, the formation of that product is suppressed, and transformation shifts to another product requiring transformation mechanisms with reduced dependence on diffusion. Ultimately, at the highest rates of cooling martensite forms, and even the lattice invariant component of martensitic transformation changes, from dislocation movement to twinning.

Temperature-induced changes in microstructure are illustrated in Fig. 7.3, a micrograph taken from a water-quenched specimen of a high-purity Fe-0.2%C alloy. The low carbon content and absence of alloying elements

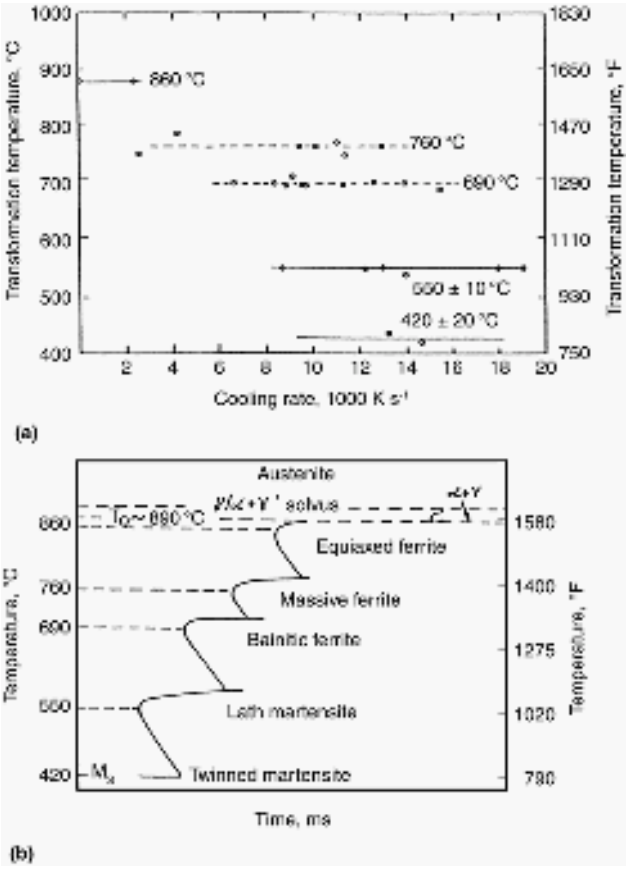

Fig. 7.2 Transformation start temperatures as a function of (a) cooling rate and (b) associated transformation curves for various austenite transformation products in an Fe-0.01%C alloy. Source: Ref 7.6

reduced hardenability, and, as a result, allotriomorphic ferrite in two orientations, marked A and B, nucleated at the start of cooling. As cooling increased, the growth of the allotriomorphs ceased and Widmanstätten side plates nucleated and grew into the austenite grains. Eventually, the tips of side plates, as shown in the upper cluster, became components of the martensite structure, supporting the action of shear in Widmanstätten ferrite formation. Not only does this example show the progression in microstructure formation at high cooling rates, but it also reflects insights into the growth of the various crystals as proposed by C.S. Smith (Ref 7.7).

Smith proposed that the crystal structure of one of the two austenite grains separated by a boundary may closely match the iron atom arrangement in a nucleated ferrite grain; that is, a definite crystallographic orientation relationship may exist between the two crystals, and the resulting interface would have a high degree of coherency. The relatively good

Fig. 7.3 Ferrite grain-boundary allotriomorphs, Widmanstätten side plates, and martensite in a quenched Fe-0.2%C alloy. Ferrite allotriomorphs A and B have orientations that favor Widmanstätten growth into different austenite grains, as described in the text. Replica electron micrograph from an extraction replica. Original magnification: 7500×. Courtesy of R.N. Caron

packing of atoms at such an interface, however, would make transfer of atoms across the interface difficult and result in a boundary with low diffusional mobility. The atom arrangement between the other austenite grain and the ferrite crystal may not match nearly as well; thus, an incoherent interface with a large degree of atomic misfit would separate the ferrite and austenite of the other austenite grain. Atoms in such an interface would easily move from face-centered cubic (fcc) packing to the body-centered cubic (bcc) structure, producing a boundary with a high degree of mobility. At high transformation temperatures and low undercooling, the incoherent boundary would migrate and produce the typical grain-boundary allotriomorph ferrite morphology. At lower temperatures, with a high degree of undercooling, the migration of the incoherent boundary by diffusion would be restricted, and the high driving force would cause the ferrite with the coherent boundary and good crystallographic coupling with the austenite to propagate, resulting in a Widmanstätten side plate.

The frequently observed growth of Widmanstätten side plates into only one grain at a boundary is explained by the Smith hypothesis and is demonstrated in Fig. 7.3. For example, allotriomorphs of orientation A have good crystallographic coupling with the austenite grain on the right, while the reverse is true of the ferrite grain marked B.

Classification Systems for Ferritic Microstructures

The similarities and differences between bainite and ferritic microstructures have been addressed in several classification systems. The basis for a system, based on isothermal decomposition of austenite, proposed by Ohmori et al. (Ref 7.8) is shown in Table 7.1. These authors recognize that ferrite formed at intermediate transformation temperatures may form without cementite and that such ferrite and the ferrite of upper bainite will have a lathlike or acicular morphology.

Bramfitt and Speer (Ref 7.9) proposed a more comprehensive system for bainite, as shown in Fig. 7.4. This system includes a category for acicular ferrite microstructures without cementite, but combined with other phases or microstructures. The other structures may be austenite, martensite, or pearlite. Frequently during the formation of acicular ferrite, austenite is retained, and on cooling to room temperature, that austenite may transform partially to martensite, producing what is now commonly referred to as the martensite-austenite (M/A) constituent of microstructures composed mostly of acicular ferrite.

Ferritic microstructures that form in low-carbon steels during continuous cooling or during isothermal holding at intermediate transformation temperatures have received considerable recent attention. Identification, characterization, and classification of the various ferritic structures are based primarily on continuous-cooling-transformation (CCT) diagrams, examples of which are shown in Fig. 7.5 and 7.6. Figure 7.5 shows the CCT diagram for an ultralow-carbon steel investigated by the ISIJ Bainite Committee (Ref 7.10). The composition of the steel is given in the figure, and the symbols identifying the various transformation products are given in Table 7.2. Figure 7.6 shows the CCT diagram for a low-carbon HSLA steel (Ref 7.11). The letters PF, WF, AF, and GF stand for polygonal ferrite, Widmanstätten ferrite, acicular ferrite, and granular ferrite, respectively. The International Institute of Welding (IIW) has also established a system for the various morphologies of ferrite (Ref 7.12). The following sections describe the various ferritic microstructures and terminologies in more detail.

Table 7.1 Morphology of bainite in isothermally transformed steels

	Criteria	
Microconstituent	**Ferrite morphology**	**Carbide distribution**
Ferrite	Lathlike	Acicular ferrite (carbide free)
Upper bainite	BI BII BIII	
Lath interface		
Lower bainite	Platelike	Within grain

Source: Ref 7.8

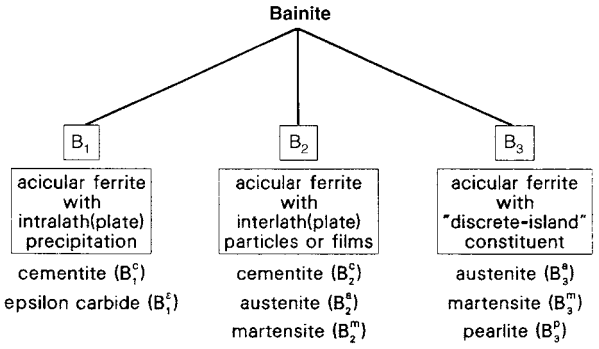

Fig. 7.4 Proposed classification system for bainitic microstructures according to Bramfitt and Speer. Source: Ref 7.9

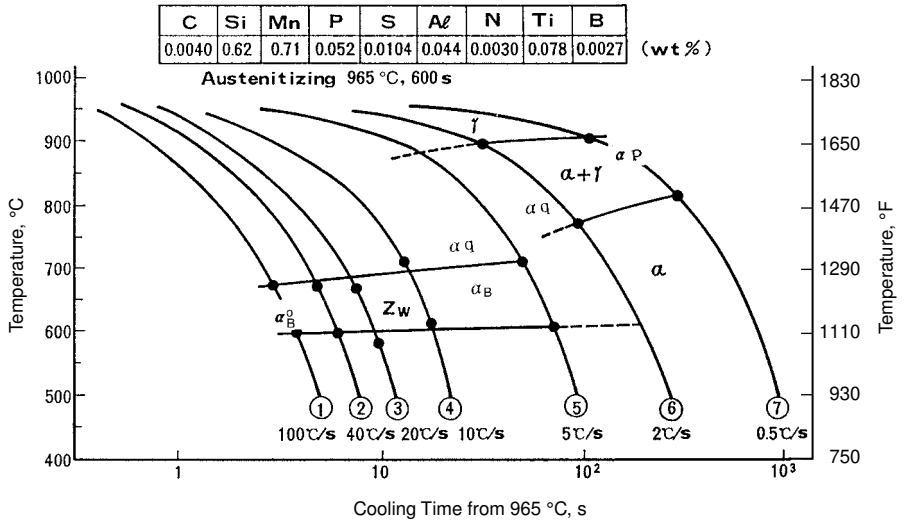

Fig. 7.5 Continuous-cooling-transformation diagram for an ultra-low-carbon steel as determined by S. Sayanaji in Ref 7.10. The symbols for the various microstructures are defined in Table 7.2.

Polygonal or Equiaxed Ferrite

This ferritic microstructure, already described as proeutectoid ferrite, forms at the highest austenite transformation temperatures and slowest cooling rates in low-carbon steels. The ferrite crystals or grains are nucleated as grain-boundary allotriomorphs and grow away from austenite grain boundaries to form equiaxed grains. In view of the latter geometry, this type of ferrite is referred to as equiaxed or polygonal ferrite (PF) and is designated α_P in the ISIJ Bainite Committee notation. The IIW system terms the equiaxed morphology as primary ferrite and distinguishes primary ferrite nucleated on austenite grain boundaries and in grain interiors

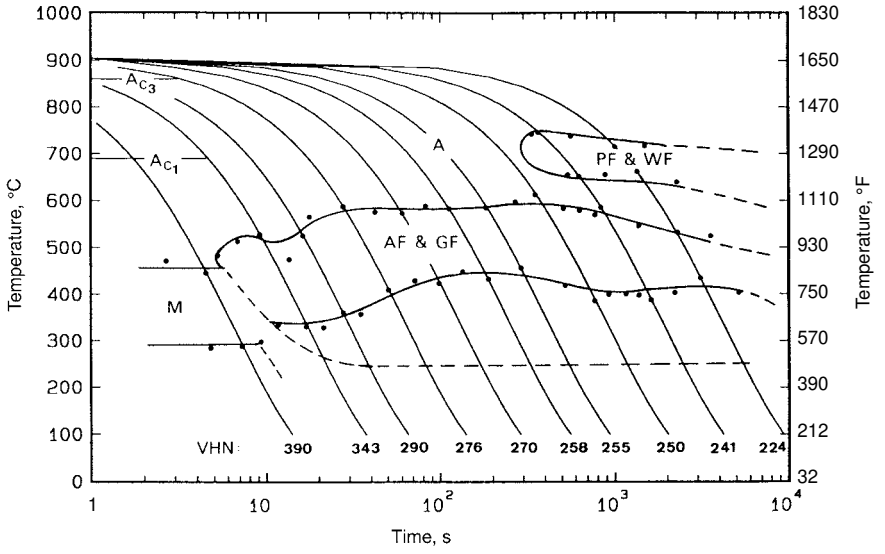

Fig. 7.6 Continuous-cooling-transformation diagram for a high-strength, low-alloy steel containing 0.06% C, 1.45% Mn, 1.25% Cu, 0.97% Ni, 0.72% Cr, and 0.42% Mo. PF, polygonal ferrite; WF, Widmanstätten ferrite; AF, acicular ferrite; GF, granular ferrite. Source: Ref 7.11

Table 7.2 Symbols and nomenclature for ferritic microstructures according to the ISIJ Bainite Committee

Symbol	Nomenclature
I_O Major matrix phases	
α_P	Polygonal ferrite
α_q	Quasi-polygonal α
α_W	Widmanstätten α
α_B	(Granular bainitic) α
α_B^O	Bainitic ferrite
α′m	Dislocated cubic martensite
II_O Minor secondary phases	
γ_r	Retained austenite
MA	Martensite-austenite constituent
α′M	Martensite
ATM	Autotempered martensite
B	BII, B2: upper bainite Bu: upper bainite B_L: lower bainite
P′	Degenerated pearlite
P	Pearlite
Θ	Cementite particle

Source: Ref 7.10

as PF(G) and PF(I), respectively. Figure 7.7 shows polygonal ferrite in a low-carbon HSLA steel isothermally transformed at 675 °C (1250 °F) for 500 s (Ref 7.13). The sections through the ferrite grains are smooth, reflect light, and therefore appear white, and the equiaxed ferrite grains are separated by continuous, linear boundaries. The dark-etching areas of the mi-

Fig. 7.7 Polygonal ferrite (light structure) formed in HSLA-80 steel isothermally transformed at 675 °C (1250 °F) for 500 s. Martensite (dark structure) has formed during cooling in austenite untransformed after the isothermal hold. Light micrograph, nital etch. Courtesy of M. Kumar. Source: Ref. 7.13

crostructure consist of martensite that formed in untransformed austenite during quenching after the 500 s hold.

Growth of polygonal ferrite is controlled by rapid substitutional atom transfer across partially coherent or disordered austenite-ferrite interfaces and long-range diffusion of carbon atoms rejected from the growing ferrite. Partitioning of substitutional alloying elements, such as manganese and nickel, may occur at interfaces of polygonal ferrite, a phenomenon that may cause significant reductions in growth rates of grain-boundary ferrite allotriomorphs (Ref 7.14, 7.15).

Widmanstätten Ferrite

Widmanstätten ferrite (WF), or α_W, has a coarse, elongated morphology, readily resolved in the light microscope. Figure 7.8 shows WF crystals formed in HSLA steel by isothermal transformation of austenite at 600 °C (1110 °F) for 100 s (Ref 7.13). The elongated WF crystals appear uniformly white, with no evidence of substructure within individual crystals. The dark areas in Fig. 7.8 are martensite formed during quenching after the isothermal hold. The dislocation density within Widmanstätten ferrite crystals is low.

Fig. 7.8 Widmanstätten ferrite (large, elongated white crystals) formed in high-strength, low-alloy steel isothermally transformed for 100 s at 600 °C (1110 °F). Dark areas are martensite formed during quenching after the isothermal hold. Light micrograph, nital etch. Courtesy of M. Kumar. Source: Ref 7.13

There is general agreement that WF forms at faster cooling rates than polygonal ferrite and in temperature ranges just below those at which equiaxed ferrite forms. Recently, the effects of substitutional alloying elements on Widmanstätten start temperatures, W_S, has been evaluated (Ref 7.15). The elongated shape and surface relief associated with Widmanstätten ferrite formation is explained by ledge mechanisms of growth (Ref 7.16, 7.17). Figure 7.9 shows a schematic model of phase growth by ledges. The ledges are identified as risers, and these interfaces between a growing ferrite crystal and the parent austenite are assumed to be partially coherent or disordered; that is, the atomic packing is assumed to be irregular and open. The latter situation gives the ledges high mobility: iron and other substitutional element atoms can readily transfer from austenite to ferrite at the ledge. The broad interfaces, identified as terraces in Fig. 7.9, in contrast to the ledges, are coherent or have good atomic matching between the two phases, making atom transfer across the terraces difficult. The ledges migrate along the long axes of Widmanstätten plates, and the migration of many ledges causes thickening of the plates in a direction normal to the direction of ledge migration.

Ledges are difficult to identify because of their small dimensions and because the austenite at the ferrite interface during plate formation trans-

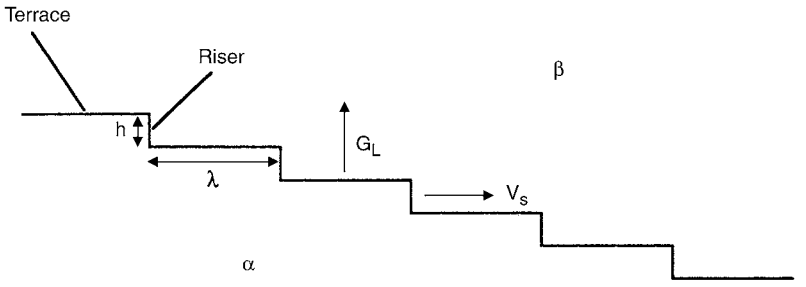

Fig. 7.9 Schematic diagram of ledge growth at interface of ferrite and parent austenite. G_L is the thickening growth rate, V_S is the lateral ledge velocity, h is the ledge height, and λ is the interledge spacing. Adapted from Ref 7.17

forms on cooling to martensite or other austenite decomposition products. However, thermionic emission electron microscopy, which permits the examination of ferrite growth at temperatures where austenite is stable, has documented the presence and motion of ledges (Ref 7.16, 7.17). In low-carbon, copper-containing steels, the precipitation of copper particles at interfaces between Widmanstätten ferrite crystals and austenite, similar to interphase eutectoid transformation described in Chapter 4, "Pearlite, Ferrite, and Cementite," has been observed (Ref 7.18). This observation provides evidence for substitutional atom diffusion during Widmanstätten plate growth. Figure 7.10 shows Widmanstätten ferrite saw teeth in copper-containing low-carbon steel. Consistent with observations of side plates, the dislocation density in the saw teeth crystals is low.

Quasi-Polygonal or Massive Ferrite

Rapid cooling of very-low-carbon steels, from temperatures where single-phase austenitic microstructures are stable to temperatures where single-phase ferritic microstructures are stable, makes possible a high-temperature transformation of austenite to ferrite without a composition change. Cooling must be rapid enough to prevent the partitioning of carbon between the austenite and ferrite when the steel passes through the two-phase ferrite-austenite phase field. Coarse ferrite grains are produced by the rapid cooling; therefore, the ferrite is referred to as massive ferrite and the transformation that produces the coarse grains is referred to as the massive transformation (Ref 7.6, 7.19). Because there is no composition change, that is, only a change in crystal structure from fcc to bcc is required, the massive transformation can be accomplished by rapid, short-range atom transfer across austenite/ferrite interfaces.

Figure 7.11 shows an example of massive ferrite formed in an ultra-low-carbon steel. Similar to polygonal ferrite, massive ferrite grains are coarse, roughly equiaxed, and their boundaries cross the boundaries of

Fig. 7.10 Widmanstätten ferrite saw teeth with low dislocation density in a copper-containing high-strength, low-alloy steel cooled at 0.1 °C/s (0.2 °F/s). Transmission electron microscopy micrograph. Source: Ref 7.11

Fig. 7.11 Quasi-polygonal ferrite formed in ultra-low-carbon steel containing 0.003% C and 3.00% Mn cooled at 50 °C/s (90 °F/s). Light micrograph. Courtesy of C.C. Tseng, Colorado School of Mines

prior-austenite grains. However, the grain boundaries of massive ferrite are irregular, and the grains often show etching evidence of a substructure. As a result, massive ferrite microstructures differ from polygonal ferrite, which has straight boundaries and no substructure. In view of the latter differences, a new term, quasi-polygonal ferrite, α_q, was assigned in the ISIJ notation to differentiate massive ferrite from polygonal ferrite. The jagged boundaries of quasi-polygonal ferrite may be caused by some interstitial or substitutional atom partitioning at migrating interfaces during transformation (Ref 7.20). Transmission electron microscopy (TEM) shows that quasi-polygonal ferrite contains high dislocation densities, dislocation subboundaries, and even M/A constituent (Ref 7.21, 7.22). The latter features of massive ferrite correlate with low yield-to-ultimate-strength ratios and high strain-hardening rates, features that produce excellent combinations of strength and ductility in continuously cooled low-carbon steels (Ref 7.1).

Bainitic or Acicular Ferrite

At high rates of cooling, austenite of low- and ultra-low-carbon steels transforms to much finer ferrite crystals than those of the ferritic morphologies described in the preceding sections. The crystals have an elongated or acicular shape and are referred to as α_B^O in the ISIJ system or as acicular ferrite, AF (Ref 7.11, 7.23–7.25). Although the austenite transforms only to ferrite, coexisting with retained austenite or M/A constituent, acicular ferrite, in groups of parallel crystals with intervening austenite, is also included in bainite classification systems. Acicular ferrite is classified by Ohmori et al (Ref 7.8) as B1 bainite, and by Bramfitt and Speer (Ref 7.9) as B_2, acicular ferrite with interlath austenite.

Figures 7.5 and 7.6 show the cooling rates at which bainitic ferrite forms relative to rates at which the other ferrite morphologies form. The range of temperatures in which acicular ferrite forms is clearly in the intermediate-temperature range. Detailed study of an HSLA-80 plate steel, containing 0.05% C, 0.50% Mn, 0.88% Ni, 0.71% Cr, and 0.20% Mo, yielded the CCT diagram shown in Fig. 7.12 (Ref 7.24). Speich and Scoonover (Ref 7.25) have produced a similar diagram for this type of steel. Acicular ferrite, and granular ferrite, as described subsequently, formed at high cooling rates in the intermediate-temperature transformation range. The classical bainitic ferrite-cementite microstructures, upper bainite, UB, and lower bainite, LB, formed only during slow cooling. Large volume fractions of polygonal ferrite first formed at low cooling rates. The rejection of carbon from the polygonal ferrite, even in the low-carbon steel, eventually concentrated carbon in untransformed austenite to levels that made the cementite component of classical bainites possible.

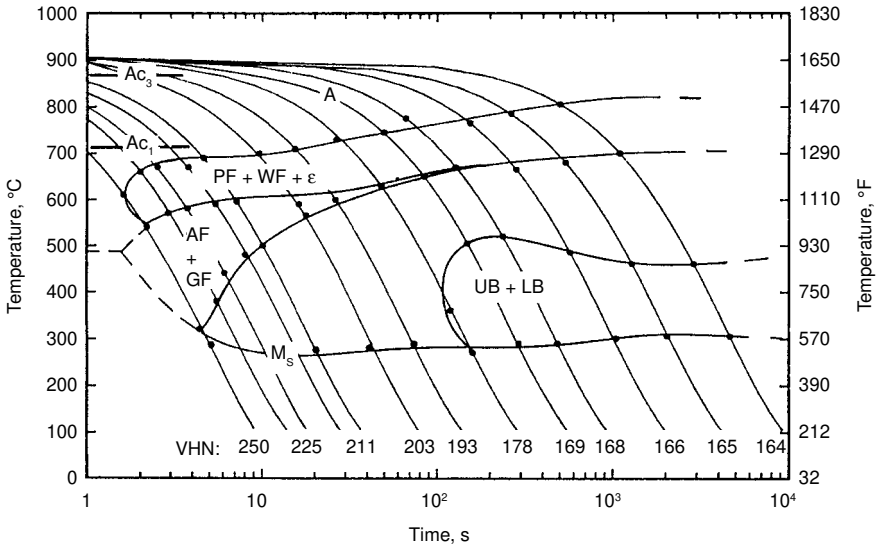

Fig. 7.12 Continuous-cooling-transformation diagram for HSLA-80 steel. Source: Ref 7.24

Figure 7.13 shows a microstructure of acicular ferrite formed at 500 °C (930 °F) in an HSLA-80 steel. The most prominent features of this light microscope image are aligned, elongated, parallel features. Transmission electron microscopy shows that the latter features are crystals of austenite or M/A constituent that have been retained between crystals of acicular ferrite. The matrix structure in Fig. 7.13 is in fact made up of many fine crystals of ferrite, but these crystals have effectively the same crystal orientation and therefore are separated only by low-angle boundaries. The latter boundaries do not etch and therefore are not visible in metallographic specimens observed in the light microscope. Another important characteristic of acicular ferrite, as determined by TEM, is a high dislocation density within the ferrite crystals.

In low-carbon steel weld metal, another distribution of acicular ferrite develops. In contrast to acicular ferrite that forms in wrought steel plate and sheet, where the ferrite crystals form parallel to one another in blocks in contact with prior-austenite grain boundaries, the acicular ferrite in welds forms in nonparallel arrays within austenite grains. The latter distribution of ferrite crystals is termed intragranular acicular ferrite (IAF) and has been shown to develop by nucleation on oxide particles within the weld metal (Ref 7.12, 7.26–7.28). Figure 7.14 shows a schematic of intragranular acicular ferrite formation, and Fig. 7.15 shows the very fine ferritic microstructure that has developed in a low-carbon steel weld. Titanium is a strong oxide former, and titanium additions to weld metal produce the oxides TiO, TiO_2, and Ti_2O_3 on which intragranular acicular ferrite nucleates.

Fig. 7.13 Acicular ferrite formed by isothermal transformation of a copper-containing HSLA-80 steel transformed for 5000 s at 500 °C (930 °F). Light micrograph, nital etch. Courtesy of M. Kumar, Colorado School of Mines

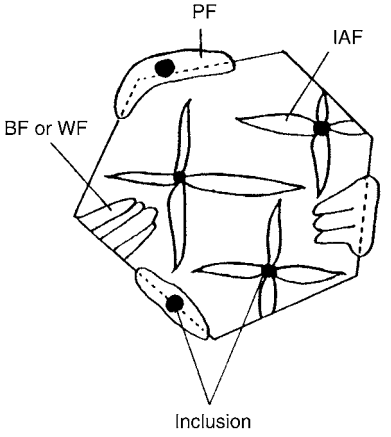

Fig. 7.14 Schematic diagram of intragranular acicular ferrite (IAF) and other ferrite morphologies in weld metal. Source: Ref 7.28

A review (Ref 7.29) of the mechanical properties of low-carbon steels with largely acicular ferrite M/A microstructures showed that yield strengths ranged from 450 to 985 MPa (65 to 145 ksi) and tensile strengths ranged from 580 to 1415 MPa (85 to 205 ksi). In view of the high dislocation density of the acicular ferrites and the retained austenite component of the microstructures, yield-to-ultimate-tensile-strength ratios were low. High strain-hardening rates produced by strain-induced transformation of

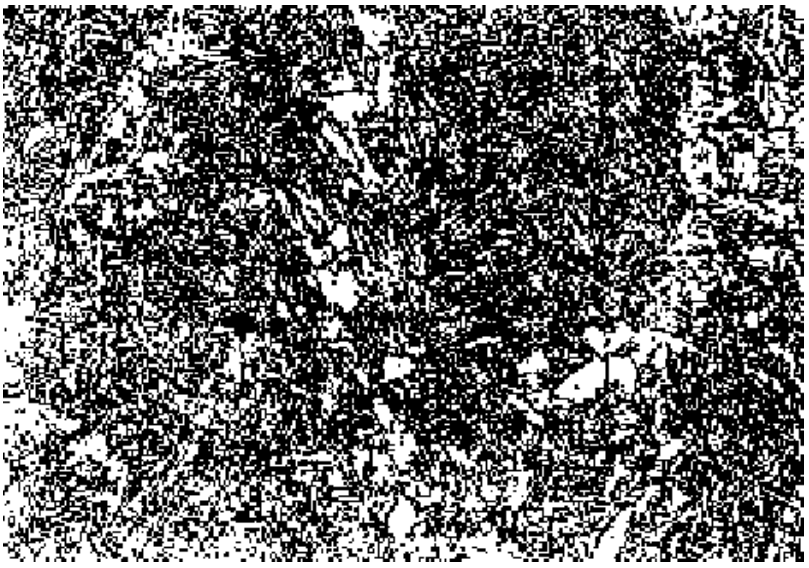

Fig. 7.15 Acicular ferrite in low-carbon weld metal. Light micrograph, nital etch. Original magnification: 500×. Courtesy of S. Liu, Colorado School of Mines

retained austenite contributed to high ultimate tensile strengths of the continuously cooled low-carbon steels. Also, the very fine intragranular acicular ferrite microstructure of low-carbon steel welds, as shown in Fig. 7.15, has been shown to produce welds of very high toughness.

Granular Ferrite or Granular Bainitic Ferrite

Granular bainitic ferrite, α_B, or granular ferrite, GF, forms at intermediate transformation temperatures in low-carbon steels (Fig. 7.5, 7.6, 7.12) and therefore has many similarities to bainitic or acicular ferrite. Earlier, this microstructure has been referred to as granular bainite by Habraken and Economopoulos (Ref 7.30), but in the absence of cementite in the microstructure, a ferrite category of terminology for this microstructure, rather than a bainite category, as described in Chapter 6, "Bainite" in this book, is preferred. Also, morphological characteristics of granular ferrite merit a category of austenite-to-ferrite transformation different from that of acicular ferrite.

Figure 7.16 shows a light micrograph of granular ferrite that has formed during continuous cooling of a modified A710 steel containing 0.33% C, 1.44% Mn, 1.20% Cu, 2.19% Ni, 0.67% Cr, and 0.46% Mo. Similar to acicular ferrite microstructures, the microstructure of granular ferrite consists of islands of retained austenite or M/A dispersed in a featureless matrix that may reveal prior-austenite grain boundaries as a result of etching. However, in contrast to acicular ferrite, the dispersed particles have a

Fig. 7.16 Granular ferrite formed by continuous cooling of a modified A710 steel (composition in text). Light micrograph, nital etch. Courtesy of B. Kloberdanz, Colorado School of Mines

granular or equiaxed morphology. The ferrite crystals of the matrix, as shown by TEM (Ref 7.10, 7.11, 7.30), are quite fine, on the order of a few micrometers in size; are equiaxed in shape; contain a high density of dislocations; and are separated by low-angle boundaries. The latter characteristic makes the boundaries hard to etch in metallographic sections and accounts for the featureless appearance of the granular ferritic matrix in light micrographs.

REFERENCES

7.1 Symposium Book, *International Symposium on New Aspects of Microstructures in Modern Low Carbon High Strength Steels,* The Iron and Steel Institute of Japan, Tokyo, 1994

7.2 Special Issue on New Aspects of Microstructure in Modern Low Carbon High Strength Steels, *ISIJ Int.,* Vol 35, 1995, p 937–1041

7.3 T.W. Montamarano, B.P. Sack, J. Gudas, M.G. Vassilaros, and H.H. Vanderveldt, High Strength Low Alloy Steels in Naval Construction, *J. Ship Prod.,* Vol 2 (No. 3), 1986, p 145–162

7.4 O. Grong and D.K. Matlock, Microstructural Development in Mild and Low Alloy Steel Weld Metals, *Int. Metall. Rev.,* Vol 31, 1986, p 27–48

7.5 H.I. Aaronson, The Proeutectoid Ferrite and the Proeutectoid Cementite Reactions, *Decomposition of Austenite by Diffusional Pro-*

cesses, V.F. Zackay and H.I. Aaronson, Ed., Interscience, New York, 1962, p 387–548

7.6 E.A. Wilson, The γ to α Transformation in Low Carbon Irons, *ISIJ Int.,* Vol 34 (No. 8), 1994, p 615–630

7.7 C.S. Smith, *Trans. ASM,* Vol 45, 1953, p 533

7.8 H. Ohtani, S. Okaguchi, Y. Fujishiro, and Y. Ohmori, Morphology and Properties of Low-Carbon Bainite, *Metall. Trans. A,* Vol 21, 1990, p 877–888

7.9 B.L. Bramfitt and J.G. Speer, A Perspective on the Morphology of Bainite, *Metall. Trans. A,* Vol 21, 1990, p 817–829

7.10 T. Araki, Chief Ed., *Atlas for Bainitic Microstructures,* Vol 1, ISIJ, Tokyo, 1992

7.11 S.W. Thompson, D.J. Colvin, and G. Krauss, Continuous Cooling Transformations and Microstructures in a Low-Carbon, High-Strength Low-Alloy Plate Steel, *Metall. Trans. A,* Vol 21, 1990, p 1493–1507

7.12 "Guide to the Light Microscope Examination of Ferritic Steel Weld Metals," Document IX-1533-88, IXJ-123-87, Revision 2, International Institute of Welding, 1988

7.13 M. Kumar, "Isothermal Decomposition of Coarse-Grained Austenite in Low-Carbon, Copper-Containing HSLA-80 Plate Steel," M.S. thesis, Colorado School of Mines, Golden, CO, 1994

7.14 H.I. Aaronson and H.A. Domian, Partition of Alloying Elements between Austenite and Proeutectoid Ferrite and Bainite, *Trans. AIME,* Vol 236, 1966, p 781–796

7.15 H.I. Aaronson, W.T. Reynolds, and G.R. Purdy, Coupled Solute Drag Effects on Ferrite Formation in Fe-C-X Systems, *Metall. Mater. Trans. A,* Vol 35, 2004, p 1187–1210

7.16 H.I. Aaronson, C. Laird, and K.R. Kinsman, Mechanisms of Diffusional Growth of Precipitate Crystals, *Phase Transformations,* American Society for Metals, 1970, p 313–396

7.17 G. Spanos, W.T. Reynolds, Jr., and R.A. Vandermeer, The Role of Ledges in the Proeutectoid Ferrite and Proeutectoid Cementite Reactions in Steel, *Metall. Trans. A,* Vol 22, 1991, p 1367–1380

7.18 S.W. Thompson and G. Krauss, Copper Precipitation during Continuous Cooling and Isothermal Aging of A710-Type Steels, *Metall. Mater. Trans. A,* Vol 27, 1996, p 1573–1588

7.19 T.B. Massalski, Massive Transformations, *Phase Transformations,* American Society for Metals, 1970, p 433–486

7.20 Symposium on the Massive Transformation, *Metall. Trans. A,* Vol 15, 1984, p 411–447

7.21 J. Cawley, C.F. Harris, and E.A. Wilson, Microstructural Studies of Low Carbon Manganese Containing Alloys, Symposium Book, *New Aspects of Microstructures in Modern Low Carbon High Strength Steels,* ISIJ, Tokyo, 1994, p 11–14

7.22 K. Shibata and K. Asakura, Transformation Behavior and Microstructures in Ultra-Low Carbon Steels, *ISIJ Int.,* Vol 35, 1995, p 982–991
7.23 Y.E. Smith, A.P. Coldren, and R.L. Cryderman, Manganese-Molybdenum-Niobium Acicular Ferrite Steels with High Strength, *Toward Improved Ductility and Toughness,* Climax Molybdenum Co., Ann Arbor, MI, 1971, p 119–142
7.24 S.W. Thompson, D.J. Colvin, and G. Krauss, Austenite Decomposition during Continuous Cooling of an HSLA-80 Plate Steel, *Metall. Mater. Trans. A,* Vol 27, 1996, p 1557–1571
7.25 G.R. Speich and T.M. Scoonover, Continuous Cooling Behaviour and Strength of HSLA 80 (A710) Steel Plates, *Processing, Microstructure and Properties of HSLA Steels,* A.J. DeArdo, Ed., TMS, Warrendale, PA, 1988, p 263–286
7.26 S. Liu and D.L. Olson, The Role of Inclusions in Controlling HSLA Steel Weld Microstructures, *Weld. J.,* Vol 65, 1986, p 139s–149s
7.27 G. Thewlis, Transformation Kinetics of Ferrous Weld Metals, *Mater. Sci. Technol.,* Vol 10, 1994, p 110–125
7.28 J.-L. Lee and Y.-T. Pan, The Formation of Intragranular Acicular Ferrite in Simulated Heat-Affected Zone, *ISIJ Int.,* Vol 35, 1995, p 1027–1033
7.29 S.W. Thompson and G. Krauss, Structure and Properties of Continuously Cooled Bainitic Ferrite-Austenite-Martensite Microstructures, *Mechanical Working and Steel Processing Proceedings,* The Iron and Steel Society, 1989, p 467–481
7.30 L.J. Habraken and M. Economopoulos, Bainitic Microstructure in Low-Carbon Alloy Steels and Their Mechanical Properties, *Transformation and Hardenability in Steels,* Climax Molybdenum Co., Ann Arbor, MI, 1967, p 69–108

CHAPTER 8

Austenite in Steel

Introduction—The Critical Importance of Austenite

THE IRON-CARBON PHASE DIAGRAM, Fig. 3.1 in Chapter 3, "Phases and Structures" in this book, shows that austenite is the crystal structure stable at high temperatures in iron and steels. As described in Chapter 3, the face-centered cubic structure of austenite has high solubility for carbon in octahedral interstitial sites of close-packed arrays of iron atoms. Multiphase ferrite-cementite microstructures, stable at room temperature, transform on heating to single-phase austenite. The high solubility of carbon in austenite causes the cementite to dissolve and the carbon concentrated in the cementite to go into solution in austenite. Without high densities of second phases such as cementite or other carbides, single-phase austenite has very high hot ductility and is readily hot worked by rolling or forging to smaller sections and complex shapes. Single-phase austenite is of course an ideal structure, and steels heated into the austenite phase field may in fact contain other phases such as inclusions, carbides (depending on alloying and time available for solution), and precipitates of microalloying elements. Nevertheless, the excellent hot ductility of austenite is a major contributor to the cost-effective manufacture of steel structures, especially when heavy, as-cast sections must be converted to smaller sections and shapes.

Austenite is the parent phase of all the microstructures described to this point: pearlite, proeutectoid phases, martensite, bainite, and various ferritic microstructures. Depending on chemical composition and cooling rate, the austenite of a given steel could transform to all of the listed microstructures. Some of the microstructures may serve in-process functions and some may serve for end applications. Thus, steel has great versatility made possible by the thermodynamic stability of austenite at high temperatures and the thermodynamic forces that drive austenite

transformation to more stable, lower-energy microstructures on cooling. The transformations to lower-energy microstructures are dependent on kinetic factors, such as processing times and temperatures that enhance or restrict diffusion-controlled mechanisms of microstructural change. Control of these factors permits the production of steels with many different microstructures and properties.

Austenite Grain Size and Measurement

Many characteristics of steel, such as hardenability and the microstructures of austenite transformation products, depend on austenitic grain size. For example, refinement of austenitic grain size in low-carbon sheet and plate steels is critical in producing fine-grained ferritic microstructures with high strength and toughness (see Chapter 11, "Deformation, Strengthening, and Fracture of Ferritic Microstructures" in this book), and the packet size of lath martensite is directly dependent on austenitic grain size (Fig. 8.1) (Ref 8.1). However, at room temperature austenite is no longer present in most transformed microstructures, and even if some is retained

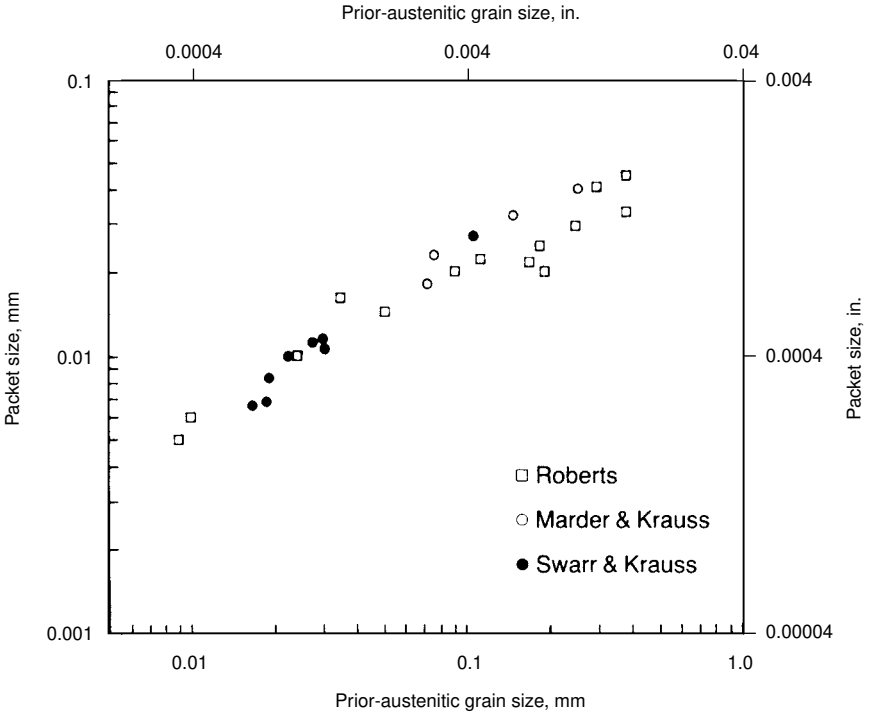

Fig. 8.1 Relationship of the packet size of lath martensite microstructures to austenite grain size. References for the various data sets are given in Ref 8.1. Roberts data are for Fe-Mn alloys and the other data are for a Fe-0.2%C alloy.

as in medium- and high-carbon martensitic microstructures, that retained austenite does not define the grain size of the parent austenite. In view of the absence of austenite itself, frequently the austenite grain size of a steel is referred to as the prior-austenite grain size.

To measure austenitic grain size, the prior-austenite grain boundaries must first be revealed. Table 8.1 shows some of the methods used to reveal austenite grain size in steels (Ref 8.2). In the category of delineation by ferrite or cementite, thin grain-boundary networks of proeutectoid ferrite or proeutectoid cementite within largely pearlitic microstructures, produced after hot rolling or normalizing, are very effective in revealing prior-austenite grain boundaries in medium- and high-carbon steels. However, in low-carbon steels where equiaxed ferrite grains grow across austenite grain boundaries and make up most of the microstructure, delineation of austenite boundaries by ferrite is not effective. Quenching from the austenite phase field to produce martensite that marks the extent of austenite grains has been effectively used to measure grain size in low-carbon steel (Ref 8.3).

Etching techniques, including those based on picric acid solutions, offer the best approach to showing prior-austenite grain boundaries in hardened steels. Nital etching tends to reveal primarily the details of martensitic microstructures. Examples of etching to reveal austenite grain boundaries are shown in Fig. 8.2 and 8.3. Figure 8.2 shows the microstructure of a quenched Fe-1.22%C alloy etched to show austenite grain boundaries (Fig. 8.2a) and plate martensite (Fig. 8.2b) (Ref 8.4). The austenite grain boundaries were revealed by etching untempered specimens in a boiling

Table 8.1 Methods to reveal austenitic grain size

Method	Comments
Picric acid solutions	Used for a wide range of steels having martensitic or bainitic structures
	Room-temperature etch
	Unpredictable, does not always work
	May give information on unrecrystallized grain shape
McQuaid-Ehn carburization	Used for a limited range of steels (mainly hypoeutectoid)
	Lengthy 8 h treatment at 925 °C (1690 °F)
	May not reflect true grain size of as-received steels
Oxidation	Used for a limited range of steels (mainly hypoeutectoid)
	Heat treatment for 1 h at 855 °C (1575 °F)
	May not reflect true grain size of as-received steels
Vacuum grooving	Used for a wide range of steels
	Heat treatment for 1 h or less at 900 °C (1652 °F)
	Full potential not known
	May not reflect true grain size of as-received steels
Delineation by ferrite or cementite	Used for a range of hypoeutectoid and hypereutectoid steels
	Heating above Ac_3, followed by controlled cooling
	Used for some as-received steels (carbon composition range limited)

Source: Ref 8.2

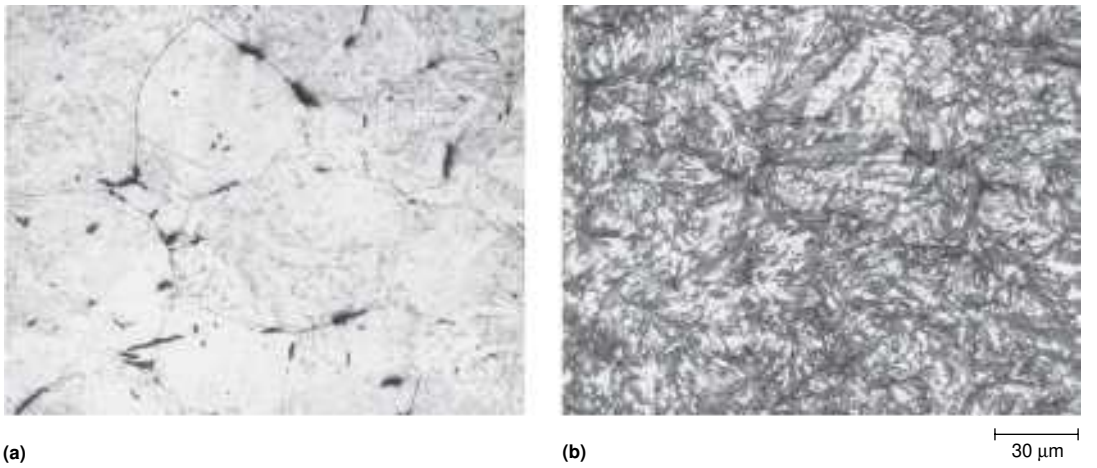

Fig. 8.2 Microstructure of an Fe-1.22%C alloy austenitized at 890 °C (1635 °F) for 2 min and water quenched. (a) Etched to show austenite grain boundaries. (b) Etched to show martensite. Etchants are given in the text. Courtesy of R. Brobst

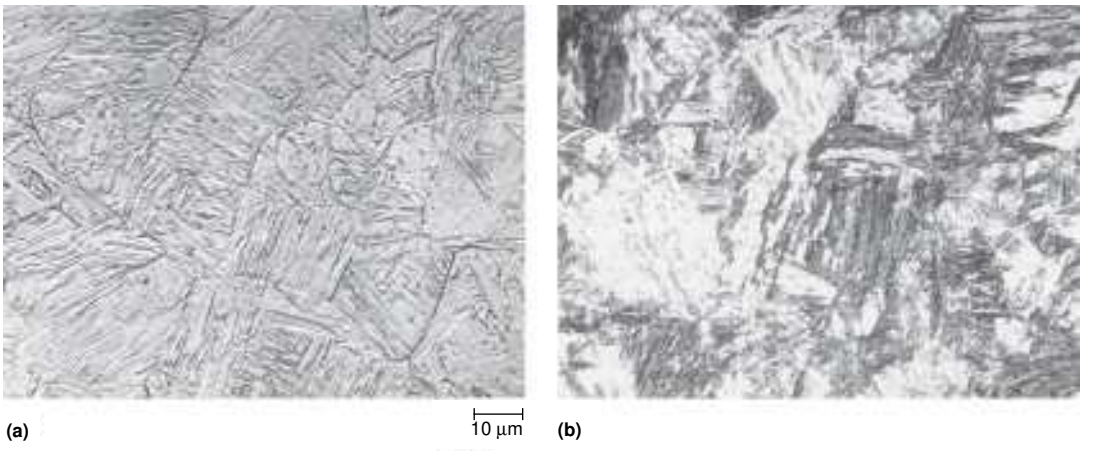

Fig. 8.3 Microstructure of an Fe-0.2%C alloy quenched to form martensite. (a) Etched to show austenite grain boundaries. (b) Etched to show microstructure of lath martensite. Etchants are given in the text. Courtesy of T. Swarr (Ref 8.1)

solution of 25 g NaOH, 2 g picric acid, and 100 mL H_2O for 15 min, followed by etching lightly in nital. Nital etching alone did not reveal the austenite grain boundaries, as shown in Fig. 8.2(b). Figure 8.3 shows a similar set of micrographs for a martensitic Fe-0.2%C alloy (Ref 8.1). In this case, the prior-austenite grain boundaries were revealed after tempering by etching in a solution of 80 mL H_2O, 28 mL oxalic acid (10%), and

4 mL H_2O_2. The lath martensite microstructure was best revealed by nital etching.

One of the most effective techniques to reveal prior-austenite grain boundaries in hardened steels is to etch with an aqueous solution saturated with picric acid and containing sodium tridecylbenzene sulfonate (Ref 8.5) with small additions of HCl (Ref 8.6). Etching with this solution attacks the prior-austenite grain boundaries. To remove intragranular microstructural features, the etched structure should be lightly repolished, leaving only the etched grain boundaries. The latter step is especially important when grain sizes are measured by electronic image analysis: intragranular features would provide signals interpreted by the system as grain boundaries. The effectiveness of the etch-polish technique in revealing prior-austenite grain boundaries in the martensitic core of a carburized steel is shown in Fig. 8.4.

Grain sizes can be measured by comparison to standards or by lineal intercept analysis (Ref 8.7–8.9). The ASTM International grain size number, n, is obtained from the expression $2^{(n-1)}$, which gives the number of grains per square inch in a microstructure examined at a magnification of 100×. Intercept methods, such as the Heyn intercept method, measure the number of grain-boundary intersections along a straight line in a properly prepared metallographic specimen, allowing for magnification and requiring intersections with at least 50 grains. Table 8.2 relates ASTM grain size numbers to intercept distances and other measures of grain size (Ref 8.7). Note that the finer the grain size, that is, the greater the number of grains per unit area or the smaller the intercept distance, the higher is the ASTM grain size number.

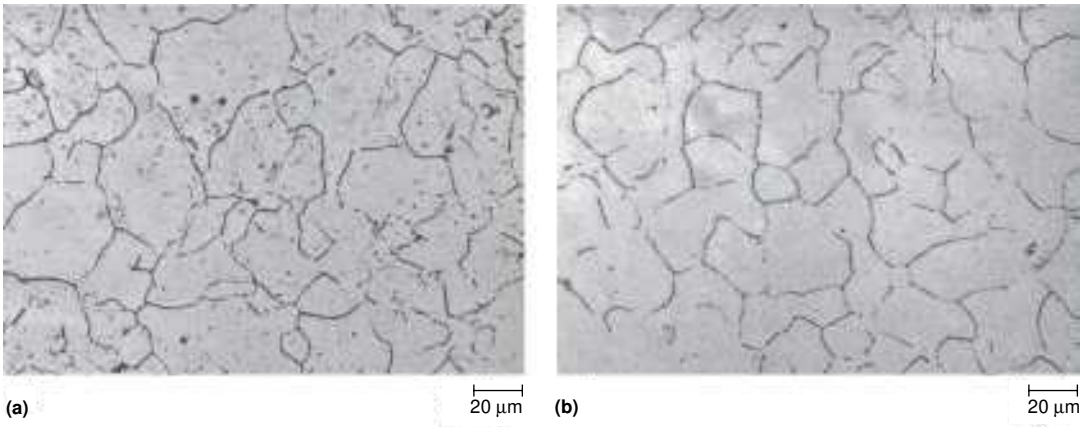

Fig. 8.4 Prior-austenite grain boundaries in the core of a carburized steel. (a) Etched and partially repolished, leaving remnants of intragranular structure. (b) Etched and repolished to remove all intragranular structure. Light micrographs; details of etching are given in the text. Source: Ref 8.5

Table 8.2 Micrograin size relationships

ASTM micrograin size No.	Calculated "diameter" of average grain		Average intercept distance(a)		Calculated area of average grain section		Average number of grains per mm³	Nominal grains per mm² at *i*×	Nominal grains per in² at 100×
	mm	in. × 10^{-3}	mm	in. × 10^{-3}	mm × 10^{-3}	in. × 10^{-3}			
00(b)	0.508	20.0	0.451	17.8	258	400	7.63	3.88	0.250
0	0.359	14.1	0.319	12.6	129	200	21.6	7.75	0.50
0.5	0.302	11.9	0.268	10.6	91.2	141	36.3	11.0	0.707
1.0	0.254	10.0	0.226	8.88	64.5	100	61.0	15.5	1.0
	0.250	9.84	0.222	8.74	62.5	96.9	64.0	16.0	1.03
1.5	0.214	8.41	0.190	7.47	45.6	70.7	103	21.9	1.41
	0.200	7.87	0.178	6.99	40.0	62.0	125	25.0	1.61
	0.180	7.09	0.160	6.29	32.4	50.2	171	30.9	1.99
2.0	0.180	7.07	0.160	6.28	32.3	50.0	172.3	31.0	2.0
2.5	0.151	5.95	0.134	5.30	22.8	35.4	290	43.8	2.83
	0.150	5.91	0.133	5.24	22.5	34.9	296	44.4	2.87
3.0	0.127	5.00	0.113	4.44	16.1	25.0	488	62.0	4.0
	0.120	4.72	0.107	4.20	14.4	22.3	578.9	69.4	4.48
3.5	0.107	4.20	0.0948	3.73	11.4	17.7	821	87.7	5.66
	0.090	3.54	0.0799	3.15	8.10	12.6	1,370	123	7.97
4.0	0.0898	3.54	0.0797	3.14	8.06	12.5	1,380	124	8.0
4.5	0.076	2.97	0.0671	2.64	5.70	8.84	2,320	175	11.3
	0.070	2.76	0.0622	2.45	4.90	7.59	2,920	204	13.2
5.0	0.064	2.50	0.0564	2.22	4.03	6.25	3,910	248	16.0
	0.060	2.36	0.0533	2.10	3.60	5.58	4,630	278	17.9
5.5	0.0534	2.10	0.0474	1.87	2.85	4.42	6,570	351	22.6
	0.050	1.97	0.0444	1.75	2.50	3.88	8,000	400	25.8
6.0	0.045	1.77	0.0399	1.57	2.02	3.13	11,000	496	32.0
	0.040	1.58	0.0355	1.40	1.60	2.48	15,600	625	40.3
6.5	0.038	1.49	0.0335	1.32	1.43	2.21	18,600	701	45.3
	0.035	1.38	0.0311	1.22	1.23	1.90	23,000	816	52.7
7.0	0.032	1.25	0.0282	1.11	1.01	1.56	31,000	992	64.0
	0.030	1.18	0.0267	1.05	0.90	1.40	37,000	1,110	71.7
7.5	0.027	1.05	0.0237	0.933	0.713	1.10	52,500	1,400	90.5
	0.025	0.984	0.0222	0.874	0.625	0.969	64,000	1,600	103
8.0	0.0224	0.884	0.0199	0.785	0.504	0.781	88,400	1,980	128
	0.0200	0.787	0.0178	0.699	0.40	0.620	125,000	2,500	161
8.5	0.0189	0.743	0.0168	0.660	0.356	0.552	149,000	2,810	181
9.0	0.0159	0.625	0.0141	0.555	0.252	0.391	250,000	3,970	256
	0.0150	0.591	0.0133	0.524	0.225	0.349	296,000	4,440	287
9.5	0.0134	0.526	0.0119	0.467	0.178	0.276	420,000	5,610	362
10.0	0.0112	0.442	0.00997	0.392	0.126	0.195	707,000	7,940	512
	0.0100	0.394	0.00888	0.350	0.10	0.155	1.00×10^6	10,000	645
10.5	0.00944	0.372	0.00838	0.330	0.089	0.138	1.19×10^6	11,200	724
	0.00900	0.354	0.00799	0.315	0.081	0.126	1.37×10^6	12,300	797
	0.00800	0.315	0.00710	0.280	0.064	0.0992	1.95×10^6	15,600	1,010
11.0	0.00794	0.313	0.00705	0.278	0.063	0.0977	2.00×10^6	15,900	1,020
	0.00700	0.276	0.00622	0.245	0.049	0.0760	2.92×10^6	20,400	1,320
11.5	0.00667	0.263	0.00593	0.233	0.045	0.0691	3.36×10^6	22,400	1,450
	0.00600	0.236	0.00533	0.210	0.036	0.0558	4.63×10^6	27,800	1,790
12.0	0.00561	0.221	0.00498	0.196	0.031	0.0488	5.66×10^6	31,700	2,050
	0.00500	0.197	0.00444	0.175	0.025	0.0388	8.00×10^6	40,000	2,580
12.5	0.00472	0.186	0.00419	0.165	0.022	0.0345	9.51×10^6	44,900	2,900
	0.00400	0.158	0.00355	0.140	0.0160	0.0248	15.62×10^6	62,500	4,030
13.0	0.00397	0.156	0.00352	0.139	0.0158	0.0244	16.0×10^6	63,500	4,100
13.5	0.00334	0.131	0.00296	0.117	0.011	0.0173	26.9×10^6	89,800	5,800
	0.00300	0.118	0.00266	0.105	0.009	0.0140	37.0×10^6	111,000	7,170
14.0	0.00281	0.111	0.00249	0.0981	0.0079	0.0122	45.2×10^6	127,000	8,200
	0.00250	0.098	0.00222	0.0874	0.00625	0.00969	64.0×10^6	160,000	10,300

(a) Value of Heyn intercept for equiaxed grains. (b) The use of 00 is recommended instead of "–1" or "minus 1" to avoid confusion. Source: Ref 8.7

Austenite Formation

Austenite formation is very much a function of starting microstructure. In pearlitic structures, austenite formation is effectively the reverse of the eutectoid reaction:

$$\alpha(0\%\ C) + Fe_3C(6.67\%\ C) = \gamma(0.77\%\ C) \qquad \text{(Eq 8.1)}$$

This equation shows that considerable diffusion of carbon is necessary for austenite formation to balance the carbon in the various phases of the reaction. Cementite is the source of carbon for the austenite, and therefore, the reaction begins at carbon-rich ferrite/cementite interfaces. In ferrite/pearlite or in spheroidized microstructures, austenite nucleates in pearlite or at cementite particles, but further growth is dependent on carbon diffusion from carbides, through the surrounding austenite, to austenite/ferrite interfaces. Figure 8.5 shows schematically various types of nucleation sites for austenite formation (Ref 8.10). Even in carbon steels with starting martensitic microstructures, austenite formation is associated with carbides and carbon diffusion because of very rapid tempering of martensite on heating to austenite formation temperatures (Ref 8.11–8.13). Nevertheless, austenite formation from martensitic or tempered martensitic microstructures is very rapid because of fine carbide distributions and short diffusion distances. Shear transformation of martensite to austenite has been documented only in iron-nickel alloys with nickel contents on the order of 30% (Ref 8.14, 8.15).

Bain and Grossman have published, based on the work of the metallographer Villela, now-classic studies of austenite formation in pearlitic and spheroidized microstructures (Ref 8.16). Figure 8.6 shows the development of austenite in the pearlitic structure of a eutectoid steel. A series of specimens were heated into the austenite field, held for the times shown, and quenched. Areas of austenite formation are visible as white patches within the lamellar pearlitic structure. The austenite, of course, transformed to martensite on quenching, but the etching differences between the newly formed martensite and the preexisting pearlite allow clear delin-

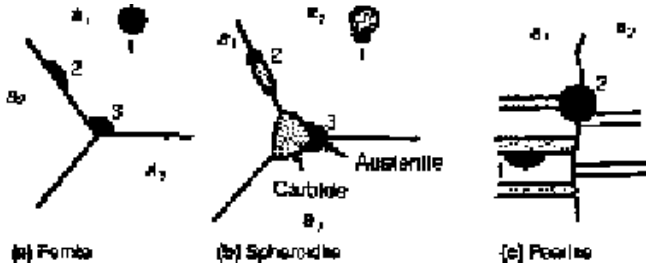

Fig. 8.5 Nucleation sites for austenite formation in microstructures of (a) ferrite, (b) spheroidite, and (c) pearlite. Source: Ref 8.10

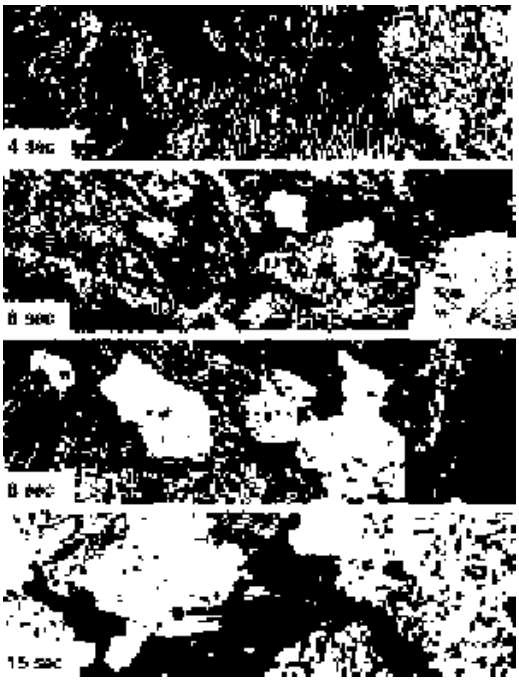

Fig. 8.6 Formation of austenite (light patches) in pearlite as a function of time. Light micrographs. Source: Ref 8.16

eation of the extent of austenite formation. In addition to the development of austenite, Fig. 8.6 shows that not all of the cementite is dissolved as the austenite grows into the pearlite. The cementite persists in the form of spheroidized particles (the small dark spots in the white areas) and dissolves only with longer holding times at temperature. Other work confirms the persistence of cementite in austenite after initial austenite formation (Ref 8.10).

When the amount of austenite formed in Fig. 8.6 is plotted as a function of time, the curve shown in Fig. 8.7 results. Austenite formation requires some incubation or time for the first nuclei to form and then proceeds at a more rapid rate as more nuclei develop and grow. At higher temperatures, the diffusion rate of carbon increases, and austenite forms more rapidly. Figure 8.8 shows the acceleration of austenite formation in a pearlitic 0.80% C steel when austenitizing temperature is raised from 730 to 751 °C (1346 to 1385 °F) (Ref 8.17).

In microstructures consisting initially of ferrite and spheroidized cementite particles, austenite forms first at the interface between the carbides and the ferrite, as noted in Eq 8.1. Figure 8.9 shows this process as a function of time. The cementite particles are soon enveloped by austenite, and later austenite formation depends on carbon diffusion through the austenite as the carbides dissolve. Figure 8.10 shows that the latter process

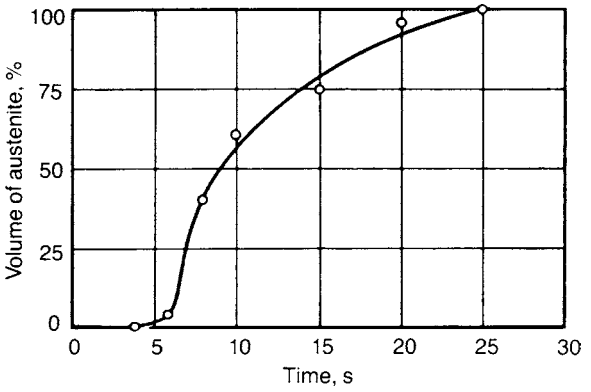

Fig. 8.7 Volume percent austenite formed from pearlite in a eutectoid steel as a function of time at a constant austenitizing temperature. Source: Ref 8.16

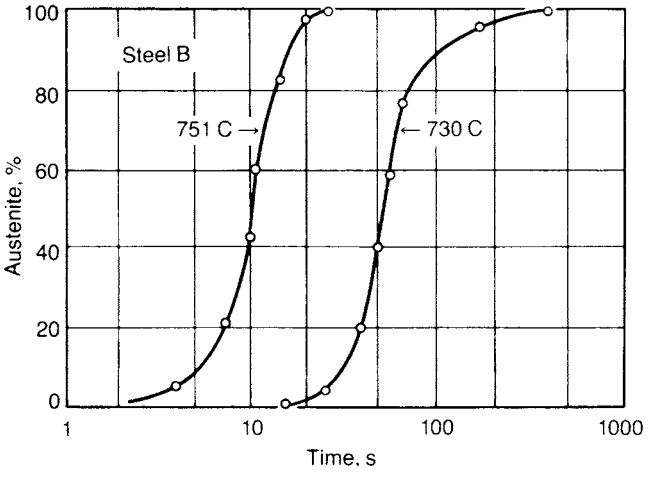

Fig. 8.8 Effect of austenitizing temperature on the rate of austenite formation from pearlite in eutectoid steel. Source: Ref 8.17

leads to a slower rate of austenite formation compared with that in a pearlitic steel (Fig. 8.7), where the closely spaced ferrite and cementite lamellae reduce the diffusion distances for austenite formation. Judd and Paxton (Ref 8.18) and Speich and Szirmae (Ref 8.10) show similar effects associated with austenite formation in microstructures of ferrite and spheroidized cementite particles. Another view of austenite formation, in a 52100 steel, is shown in Fig. 8.11. Specimens, with pearlitic microstructures, were rapidly heated in salt to the temperatures shown, held for the times shown, and quenched to martensite (Ref 8.19). The progress of austenite formation was followed by hardness measurements, and when martensite hardness reached a constant level, austenite transformation was considered to

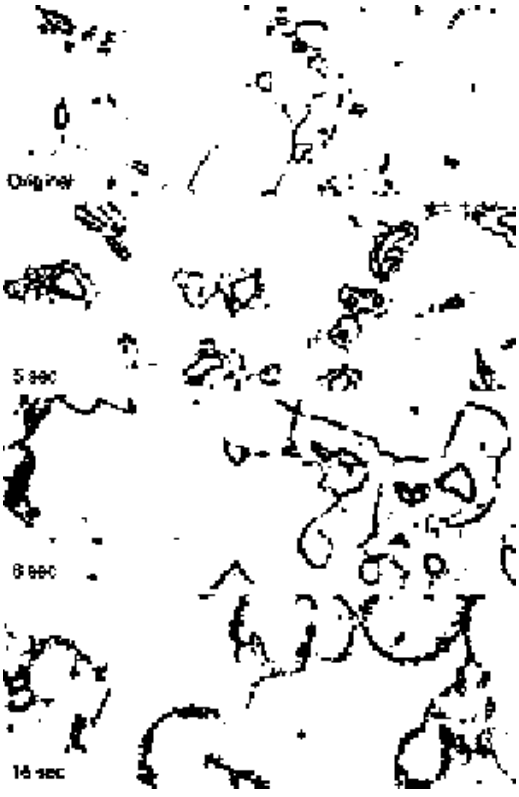

Fig. 8.9 Formation of austenite around cementite particles in spheroidized steel. Light micrographs. Source: Ref 8.16

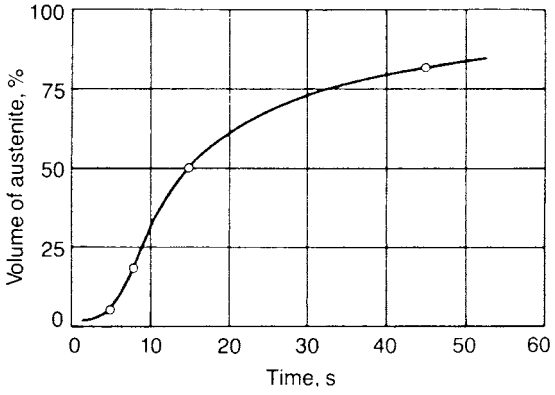

Fig. 8.10 Austenite formation from a coarse spheroidized microstructure as a function of time. Source: Ref 8.16

be complete. Austenite formation was rapid, taking less than 10 s at temperature for completion at 800 and 850 °C (1470 and 1560 °F). The slight decreases in hardness of the martensite formed after complete austenitization at the lower temperatures are a result of lower carbon content of aus-

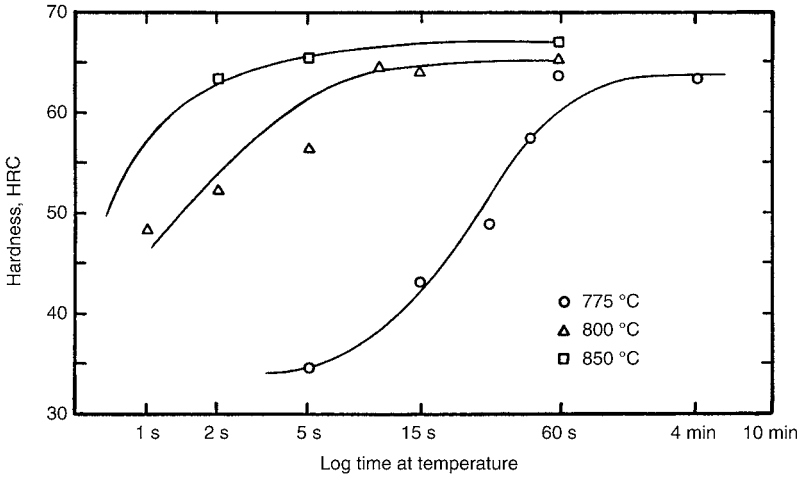

Fig. 8.11 Hardness vs. log time at three intercritical austenitizing temperatures for 52100 steel with a starting microstructure of pearlite. Courtesy of K. Hayes, Ref 8.19

tenite coexisting with higher volume fractions of carbides stable at the lower temperatures.

Time-Temperature-Austenitizing Diagrams

Impressive collections of time-temperature-austenitizing (zeit-temperature-austenitisierung) diagrams for many alloy steels have been determined by A. Rose and his colleagues at the Max-Planck-Institut für Eisenforschung (Ref 8.20, 8.21). Hollow cylindrical specimens (8 mm, or 0.31 in., diameter; 0.5 mm, or 0.02 in., wall thickness; and 9 mm, or 0.35 in., long) were induction heated at rates from 0.05 to 2400 °C/s (0.09 to 4300 °F/s). Temperatures were measured by thermocouples welded to the specimens, and dimensional changes on heating and cooling were measured by dilatometer.

Two examples of time-temperature-austenitizing (TTA) diagrams are shown here. Figure 8.12 shows a TTA diagram produced by continuous heating of a medium-carbon alloy steel: 42CrMo4, containing 0.37% C, 0.64% Mn, 1.00% Cr, and 0.21% Mo. This steel corresponds to SAE 4140. Three zones associated with austenitizing are shown. The zone between Ac_1 and Ac_3 defines the temperature range in which the ferrite/carbide microstructure coexists while austenite forms. Critical temperatures increase with increasing heating rate. Above the Ac_3, there is a zone where carbides continue to dissolve and carbon content homogenizes. For conditions above the dashed line, homogeneous, single-phase austenite of uniform composition is established.

Figure 8.13 shows the TTA diagram produced by continuous heating of the high-carbon steel 100Cr6 containing 1.00% C, 0.34% Mn, and

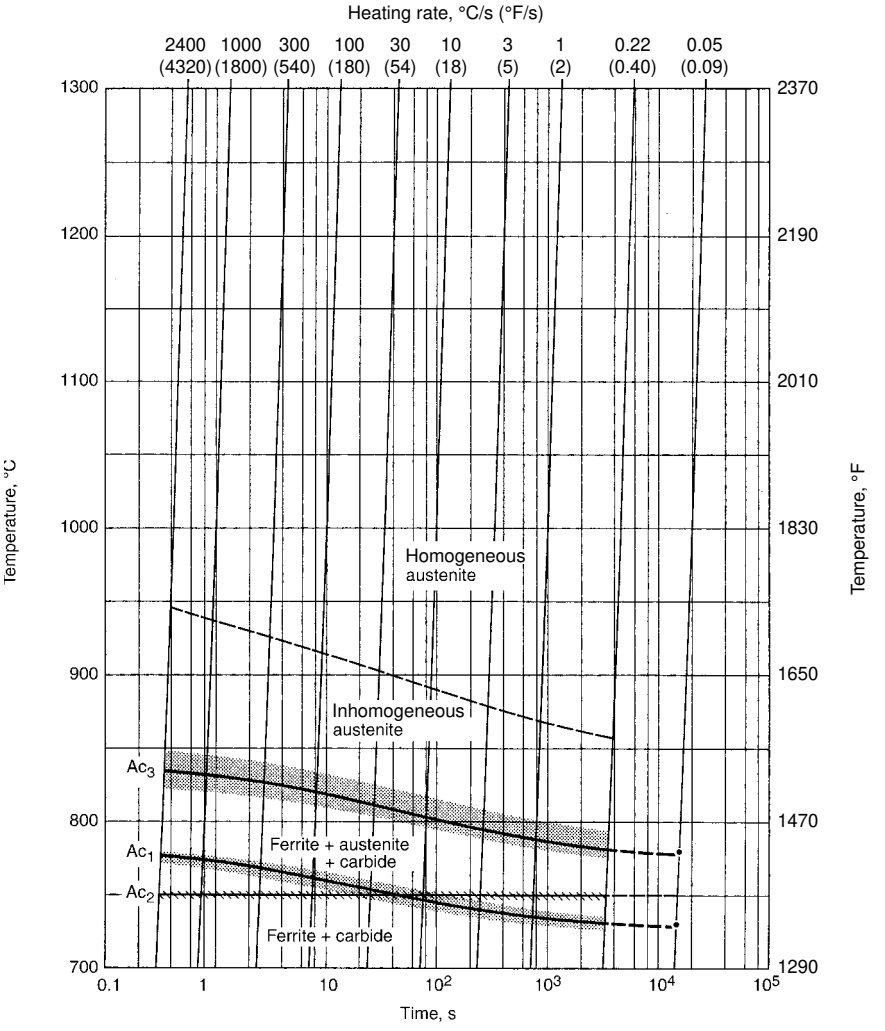

Fig. 8.12 Time-temperature-austenitizing diagram for 42CrMo4 (SAE 4140) steel. Source: Ref 8.20

1.52% Cr. This steel corresponds to SAE 52100. In view of the chromium content of this steel, there is a three-phase field, ferrite-carbide-austenite, marked by two lower critical temperatures, Ac_{1b} and Ac_{1e}, instead of the single Ac_1 temperature characteristic of iron-carbon alloys or steels with low-alloy content. Austenite and carbide coexist between Ac_{1e} and the A_{cm}, as required in a hypereutectoid steel, and therefore, even with very low rates of heating, austenite and carbide coexist at temperatures up to the A_{cm}. The A_{cm} line increases rapidly with increasing heating rate, an effect of the sluggish dissolution of chromium-containing cementite in this steel.

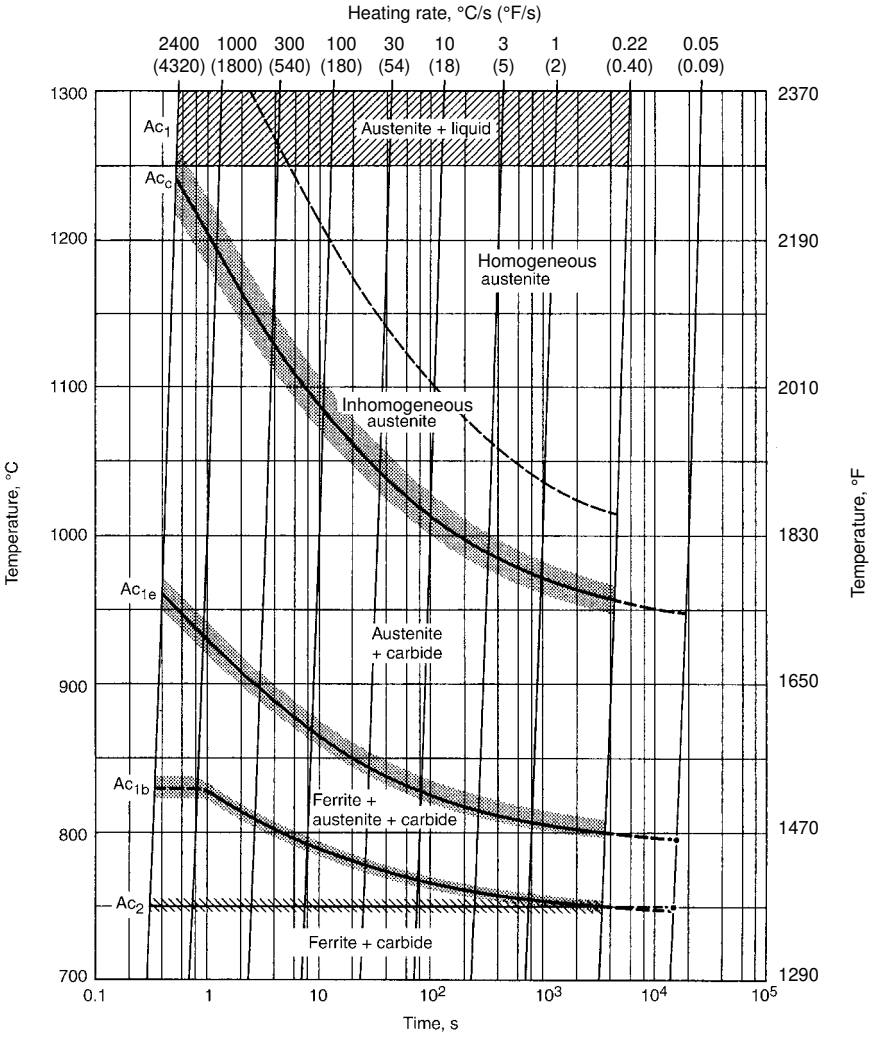

Fig. 8.13 Time-temperature-austenitizing diagram for 100Cr 6 (SAE 52100) steel. Source: Ref 8.20

Austenite Grain Growth in the Absence of Second Phases

Once austenite has formed and completely replaced the low-temperature starting microstructure, grain growth begins immediately. Grain boundaries, with their disordered atomic arrays where grains meet, increase the energy of a microstructure. Therefore, grain-boundary energy provides a thermodynamic driving force that is lowered by the elimination of grain-boundary area and associated grain growth. Austenite grain growth is

most rapid just after a low-temperature ferrite/cementite microstructure has been fully converted to austenite. At this point, the grains are the finest, and the grain-boundary area is a maximum, providing a high driving force for growth. Also as a result of the impingement of grains during the formation of the austenitic microstructure, many grain boundaries are curved. The grain boundaries therefore grow toward their centers of curvature and assume planar shapes to reduce grain-boundary area. Small grains are consumed by larger grains, another process that occurs early in the growth process.

The kinetics of grain growth are represented by an equation of the form (Ref 8.22):

$$D^2 - D_0^2 = Kt \qquad \text{(Eq 8.2)}$$

where D is the grain size at a time t after grain growth has started at a given temperature, D_0 is the grain size at the start of grain growth, and K is a temperature-dependent constant that is related to thermally activated diffusion associated with grain growth. If it is assumed that the grain size at the beginning of grain growth is very fine and can be neglected, by rearranging Eq 8.2, the following equation results:

$$D = Kt^{1/2} \qquad \text{(Eq 8.3)}$$

This equation mathematically represents the rapid first stages of grain growth and the reduced rate of grain growth with increasing time at temperature, provided that no arrays of second-phase particles are present in the austenite.

Figure 8.14 shows grain growth in a plain carbon steel containing 0.22% C and 1.04% Mn, 0.33% Si, and 0.016% Al (Ref 8.23). At high austenitizing temperatures, parabolic growth curves, and the strong effect of temperature and increased atom mobility, are apparent. Very little grain growth occurred at the lower austenitizing temperatures because of the fact that the steel was aluminum killed, and that, as described subsequently, aluminum nitride particles suppressed grain growth. At high temperatures, aluminum nitride particles are dissolved, and there is no restraint to grain-boundary motion.

The Effect of Second-Phase Particles on Austenitic Grain Growth

Particles very effectively restrict austenitic grain growth. When a grain boundary incorporates a second-phase particle, for that boundary to advance beyond the particle, grain-boundary area, equivalent to that occupied by the particle, must be created. Figure 8.15 shows this process

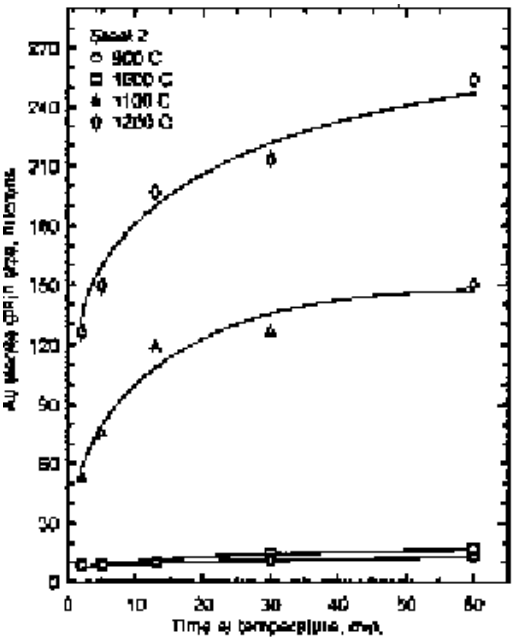

Fig. 8.14 Austenite grain size as a function of time in a plain carbon steel containing 0.22% C and 0.016% Al at several austenitizing temperatures. Source: Ref 8.23

schematically (Ref 8.24). The energy increase associated with increased grain-boundary area creates an effective pinning force on boundary motion by the particle. Zener (8.25) has derived an equation that relates grain size to parameters that characterize particle distributions:

$$R = \frac{4r}{3f} \qquad \text{(Eq 8.4)}$$

where R is the radius of a matrix grain (assumed spherical), r is the radius of the pinning particles, and f is the volume fraction of pinning particles. Assuming a more realistic grain geometry, that of a tetrakaidecahedron (a 14-sided grain shape), Gladman (Ref 8.24, 8.26) has derived the following equation for the effect of particles on effective grain radius, R_0:

$$R_0 = \left[1 - \left(\frac{4}{3}Z\right)\right]\left(\frac{r}{f}\right) \qquad \text{(Eq 8.5)}$$

where $Z = R/R_0$, a factor that represents the size advantage of a growing grain over that of its neighbors. The Gladman equation reduces the proportionality constant between grain radius and the ratio r/f. Nevertheless,

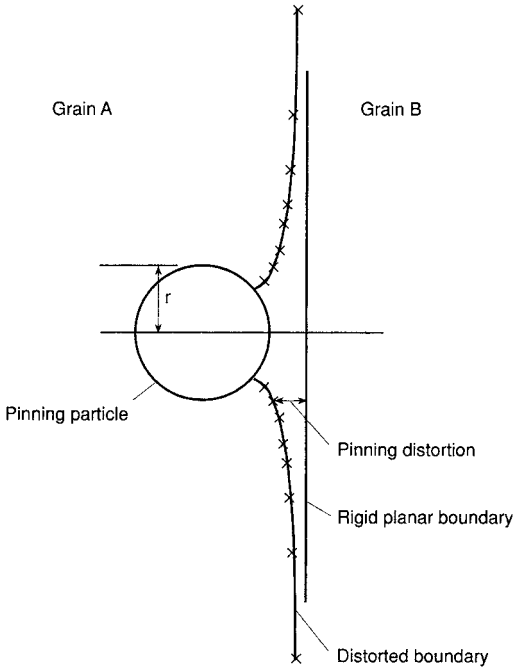

Fig. 8.15 Schematic diagram of grain-boundary pinning by a second-phase particle. Source: Ref 8.24

both the Zener and Gladman equations show the strong effects of particle distributions on grain size. Very fine pinning particles, even when present in low volume fractions, effectively maintain fine grain sizes. This condition is true of aluminum-killed and microalloyed low- and medium- carbon steels, as described subsequently. Coarse pinning particles can also effectively maintain fine grain sizes, provided they are present in high volume fractions. The latter type of grain size control is characteristic of intercritically austenitized high-carbon steels and tool steels.

Second-phase particle distributions in austenite can be so effective that no grain growth occurs within reasonable heating times at relatively low austenitizing temperatures. Therefore, the parabolic growth kinetics associated with early rapid grain growth, as discussed previously, no longer apply. However, with increasing temperature, second-phase particles coarsen and dissolve, and rapid, discontinuous grain growth develops. This type of grain growth is sometimes referred to as secondary recrystallization because the kinetics of discontinuous grain growth are similar to that of recrystallization (Ref 8.27). Recrystallization is characterized by a period of incubation, followed by a rapid increase in the rate of recrystallization following the incubation period. The particle-pinning period that suppresses grain growth is considered to be analogous to the incubation period in recrystallization.

Austenite Grain Size in Aluminum-Killed Steels

Steels deoxidized with aluminum are described as killed steels because the strong affinity of aluminum for oxygen limits gas evolution and creates a quiet or killed bath of liquid steel. Aluminum oxides formed by the deoxidation process mostly float out of liquid steel, but some oxides may be retained as oxide inclusions in solidified steel. Some aluminum also remains in solution in the solid steel, and this characteristic of aluminum-killed steels produces excellent austenite grain-size control. The latter aspect of aluminum additions to steel and many other effects of aluminum, especially its combination with nitrogen, are described in a comprehensive review article by Wilson and Gladman (Ref 8.28)

Aluminum and nitrogen have high solid solubility in austenite at high temperatures but decreased solubility with decreasing temperature, causing aluminum nitride (AlN) crystal formation in austenite according to the following equation (Ref 8.28, 8.29):

$$\underline{\text{Al}} + \underline{\text{N}} = \text{AlN} \qquad \text{(Eq 8.6)}$$

where $\underline{\text{Al}}$ and $\underline{\text{N}}$ represent aluminum and nitrogen dissolved in austenite. The amount of aluminum and nitrogen dissolved is given by the solubility product [%Al][%N], which is temperature dependent according to the equation (Ref 8.30):

$$\log[\%\text{Al}][\%\text{N}] = \frac{-7400}{T} + 1.95 \qquad \text{(Eq 8.7)}$$

Other equations have also been developed and are reviewed by Wilson and Gladman. If the amounts of aluminum and nitrogen cause the value of the solubility product to be exceeded at a given temperature, precipitation of AlN will occur. Equation 8.7 shows that the solubility product decreases with decreasing temperature, reflecting the increased tendency for AlN precipitation at low austenitizing temperatures.

The strong effect of AlN on grain growth has made aluminum-killed steels synonymous with fine-grained heat treated steels. Coarse-grained steels are generally deoxidized with silicon, a practice that does not produce particle dispersions effective in inhibiting austenite grain growth. Figure 8.16 compares austenite grain size, measured by ASTM number, in fine-grained and coarse-grained steels as a function of temperature (Ref 8.31). The aluminum-killed fine-grained steel exhibits almost no grain growth at low austenitizing temperatures, but a discontinuous increase in grain size occurs at a temperature marked the grain-coarsening temperature. This behavior is consistent with secondary recrystallization as discussed previously, in this case caused by the precipitation of fine AlN particles and their eventual dissolution at the grain-coarsening tempera-

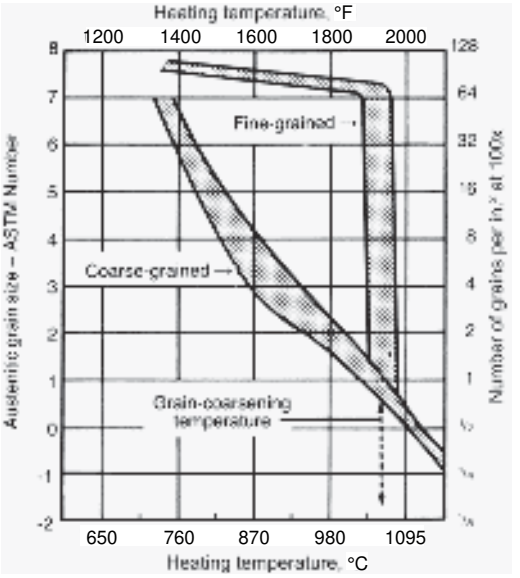

Fig. 8.16 Austenite grain size as a function of austenitizing temperature for coarse-grained and fine-grained steels. Rapid discontinuous grain growth occurs at the grain-coarsening temperature in fine-grained steels. Source: Ref 8.31

ture. In contrast, austenite grain size increases continuously with increasing temperature in the coarse-grained steel, even at low temperatures.

Austenitizing temperatures for hardening steels generally never exceed 980 °C (1800 °F), and therefore, aluminum-killed steels retain a fine austenite grain size. The austenite grain size of coarse-grained steels would grow significantly at low austenitizing temperatures, especially during carburizing treatments that are frequently performed over many hours at 930 to 955 °C (1700 to 1750 °F). Figure 8.17 demonstrates the great difference in austenite grain size that develops when steels of different coarsening behavior are carburized (Ref 8.16).

Figure 8.18 shows the effect of aluminum content on the grain-coarsening temperatures in mild steel (Ref 8.32). Aluminum contents up to 0.08% Al increase the coarsening temperature, but higher additions cause a slight lowering. The latter effect is also shown in Fig. 8.19, where the amount of AlN is plotted as a function of temperature for steels with three different aluminum contents. Despite the higher volume fraction of AlN in the steel containing 0.15% Al, its grain-coarsening temperature is lower than that of the steels with a lower aluminum content. This result is attributed to coarse AlN particles produced during solidification and hot working rather than coarsening and/or solution of aluminum nitride particles during final austenitizing treatments.

A remarkable example of discontinuous grain growth or secondary recrystallization has been documented in aluminum-killed steels cold

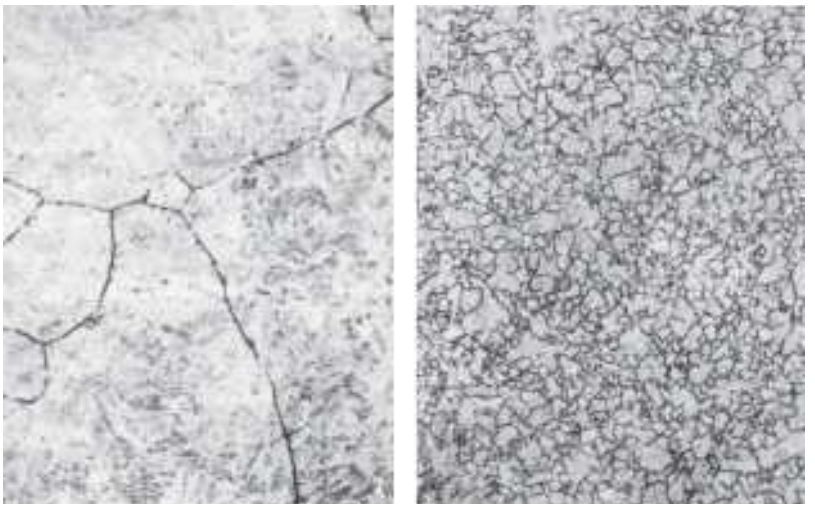

Fig. 8.17 Comparison of austenitic grain size in (a) coarse-grained SAE 1015 steel and (b) fine-grained SAE 4615 steel after carburizing. Light micrographs. Original magnification: 1000×. Source: Ref 8.16

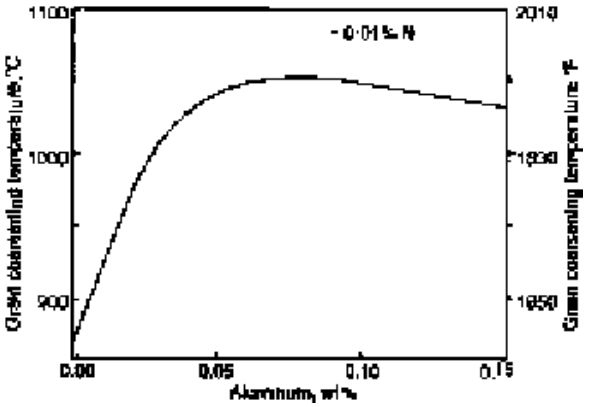

Fig. 8.18 Effect of aluminum content in steel on the grain-coarsening temperature of austenite. Source: Ref 8.32

worked prior to carburizing heat treatment. A relatively recent approach to the manufacture of complex shapes such as gears has been to cold forge rather than hot forge (Ref 8.33). When such parts are carburized, very coarse grains may form within a generally very fine-grain-sized matrix. Figure 8.20 shows an example of discontinuous grain growth in an SAE 8620 steel containing 0.22% C, 0.85% Mn, 0.58% Cr, 0.42% Ni, 0.25% Mo, 0.039% Al, and 0.018% N cold worked 75% prior to austenitizing for 4 h at 930 °C (1700 °F) to simulate a carburizing heat treatment (Ref 8.34).

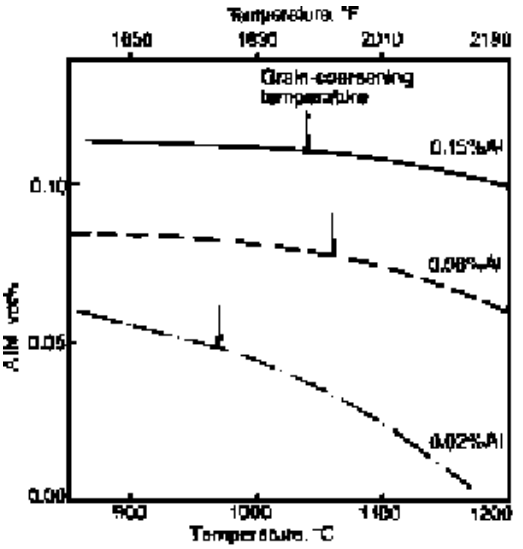

Fig. 8.19 Change in volume percent AlN as a function of temperature in mild steel containing 0.01% N and Al as shown. Grain-coarsening temperatures are marked by arrows. Source: Ref 8.32

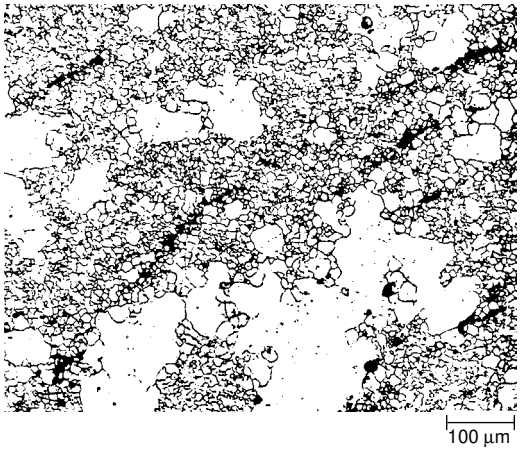

Fig. 8.20 Prior-austenite grain structure showing large difference in grain size in an SAE 8620 steel subjected to a simulated carburizing treatment after specimen has been cold worked 75%. Light micrograph; special picral etch. Source: Ref 8.34

Very coarse grains, greater than 100 μm in size, have grown within a matrix of very fine grains, on the order of 5 μm (ASTM No. 12) in size.

Several factors appear to contribute to the formation of the abnormally coarse austenite grains (Ref 8.34, 8.35). Processing prior to carburizing produces strained ferritic starting structure and extremely fine AlN particles that produce very fine austenite grains on heating to the carburizing

temperature. The very fine as-austenitized grain size with its very high grain-boundary area, together with very fine AlN particles, results in a very unstable austenitic grain structure that, with time at austenitizing temperature, may be very susceptible to discontinuous grain growth. Subcritical annealing treatments prior to cold working were found to greatly reduce sensitivity to abnormal austenite grain growth.

Austenite Grain-Size Control in Microalloyed Steels

The addition of small amounts, on the order of 0.1%, of alloying elements such as niobium, vanadium, and titanium to steel offer an important cost-effective approach to grain-size control and strengthening. The term *microalloying* is applied to such steels to contrast with the more substantial additions of alloying elements, up to several percent or more, in alloy steels such as those specified in the AISI/SAE system described in Chapter 1, "Introduction: Purpose of Text, Microstructure and Analysis, Steel Definitions and Specifications" in this book. Austenitic grain-size control by the microalloying elements niobium, vanadium, and titanium is based on the same principles described relative to aluminum additions for austenitic grain-size control. However, despite the fact that aluminum additions, on the order of 0.02 to 0.04%, for grain-size control qualify aluminum as a microalloying element, aluminum-containing steels are never referred to as microalloyed steel (Ref 8.24). This usage is in part due to the fact that aluminum is usually added to low-alloy steels containing significant amounts of the alloying elements chromium, nickel, and molybdenum, while steels microalloyed with niobium, vanadium, and titanium provide benefits without such additions.

The general approach to evaluate precipitation of and grain-size control by microalloying is based on reactions between substitutional elements, X, including niobium, vanadium, titanium, aluminum, and boron, and interstitial elements, Y, carbon and/or nitrogen, in austenite to form a compound XY_n (Ref 8.36), as:

$$\underline{X} + n\underline{Y} = XY_n \qquad \text{(Eq 8.8)}$$

The underlining indicates that the elements are in solution in austenite. Frequently, the factor n is unity, as is the case for AlN formation (Eq 8.6). The equilibrium constant, K, or the solubility product, for a given reaction is given as:

$$K = [X][Y]^n \qquad \text{(Eq 8.9)}$$

where X and Y are the wt% of elements X and Y dissolved in austenite.

The temperature dependence of the solubility product is given as:

$$\log[X][Y]^n = \frac{-A}{T} + B \qquad \text{(Eq 8.10)}$$

where A and B are constants that may be estimated from free-energy data or determined experimentally, and T is temperature in Kelvin.

Figure 8.21 shows solubility products as a function of temperature for various reactions in austenite (Ref 8.36). The curves are identified by compounds, carbides, nitrides, and carbonitrides, formed from various combinations of elements. The higher the solubility product, the higher is the solubility of the reacting elements. All curves decrease with decreas-

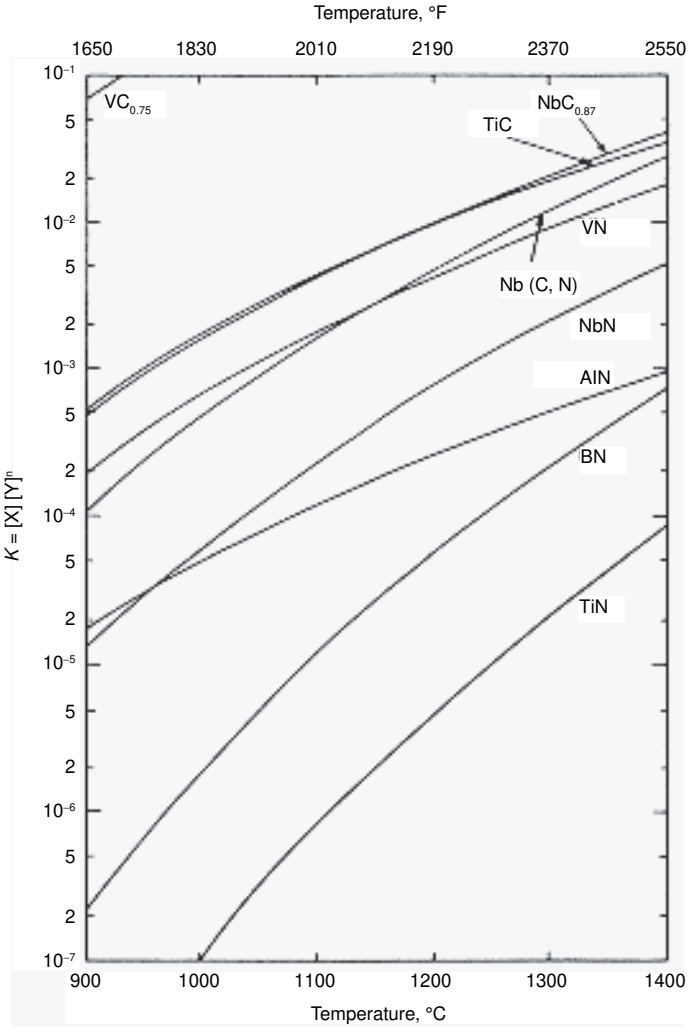

Fig. 8.21 Solubility products vs. temperature for various compounds in austenite. Source: Ref 8.36

ing temperature, indicating that eventually the austenite will become supersaturated with the elements and precipitation will occur. Vanadium and niobium compounds have relatively high solubility, while aluminum, boron, and titanium have relatively low solubility and readily form nitride precipitates at low concentrations in austenite, even at high temperatures. Table 8.3 lists the temperature dependence of a number of solubility products.

Fine particle dispersions of the microalloying elements retard austenitic grain growth, as discussed previously. The more stable the particles, the more effectively grain growth is retarded to higher temperatures. Figure 8.22 shows the relative effects of various elements on the suppression of austenitic grain growth (Ref 8.37). The curve marked C-Mn, representing a plain carbon steel with no particle dispersions, shows continuous increase in grain size with increasing temperature. The other elements, according to their temperature-dependent solubility, all show suppression of grain growth at low austenitizing temperatures. Vanadium has the highest solubility, and therefore, vanadium carbonitride precipitates dissolve at the lowest temperatures, causing discontinuous grain coarsening at lower temperature compared with steels alloyed with the other elements. Titanium nitride is remarkably stable, and therefore, there is minimal or no grain coarsening even at high temperatures typical of hot work and forging (Ref 8.38).

The amounts of the microalloying elements determine when the solubility for a given element is exceeded. Figure 8.23 shows a set of curves for a series of niobium-containing steels (Ref 8.39). The higher the con-

Table 8.3 Temperature dependence of solubility products (K_γ) for various carbides, nitrides, and carbonitrides in austenite

Solubility product	$\log K_\gamma$
[%Al][%N]	$-\frac{6770}{T}+1.03$
[%B][%N]	$-\frac{13,970}{T}+5.24$
[%Nb][%N]	$-\frac{10,150}{T}+3.79$
$[\%Nb][\%C]^{0.87}$	$-\frac{7020}{T}+2.81$
$[\%Nb][\%C]^{0.7}[\%N]^{0.2}$	$-\frac{9450}{T}+4.12$
[%Ti][%N]	$-\frac{15,790}{T}+5.40$
[%Ti][%C]	$-\frac{7000}{T}+2.75$
[%V][%N]	$-\frac{7700}{T}+2.86$
$[\%V][\%C]^{0.75}$	$-\frac{6560}{T}+4.45$

Source: Ref 8.36

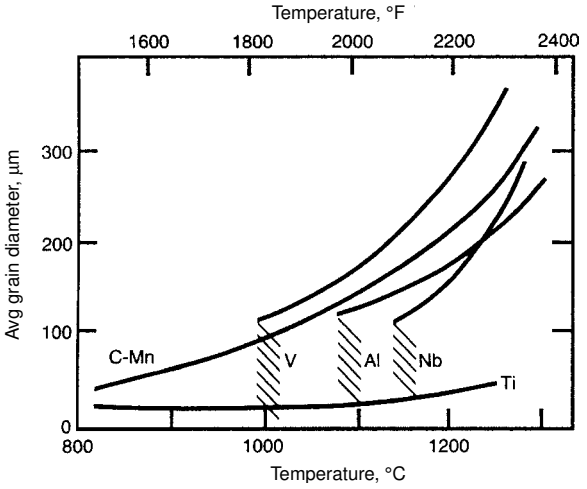

Fig. 8.22 Relative austenite grain-coarsening characteristics of various microalloyed steels. Source: Ref 8.37

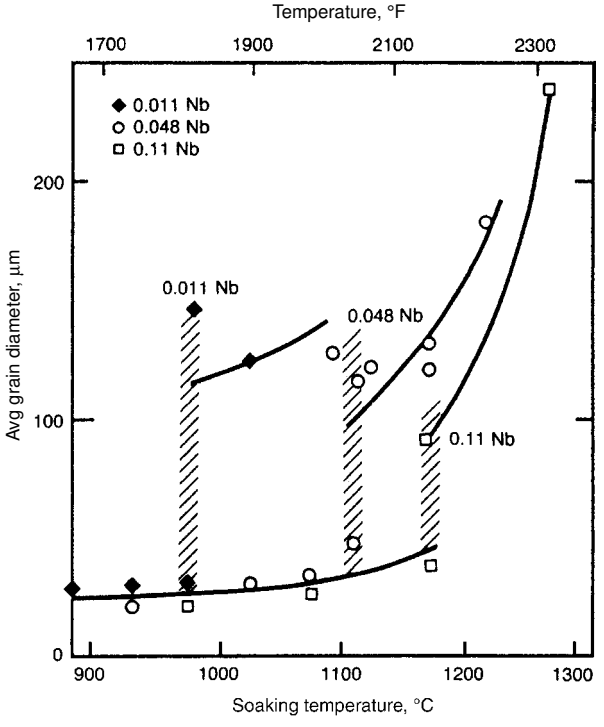

Fig. 8.23 Austenite grain-coarsening characteristics in steels alloyed with various amounts of niobium. Source: Ref 8.39

tent of niobium, the higher are the temperatures at which solubility is exceeded; that is, there is more niobium than can be dissolved in the austenite. As a result, the higher the niobium content, the more effectively grain growth is suppressed at higher temperatures compared with steels with lower concentrations of niobium.

Hot Deformation of Austenite

As noted in the introduction of this chapter, one of the major benefits of austenite is the workability it provides to steels. Primary processing of wrought steels involves casting and subsequent hot rolling to finished shapes that may be further shaped by forging or cold work. Figure 8.24 shows a schematic diagram of the temperature-time steps associated with hot working (Ref 8.40). Cast steel shapes are reheated and subjected to roughing and finishing hot reduction roll passes at successively lower temperatures. The austenitic microstructure responds to the hot deformation by various mechanisms of deformation, recovery, recrystallization, and grain growth, and austenite grain size decreases with decreasing temperature of hot work. At the lowest deformation temperatures, recrystallization may be suppressed, especially in microalloyed steels, and elongated deformed austenite grains may characterize the finished microstructure, as shown schematically in Fig. 8.24.

A schematic diagram of microstructural changes produced by rolling is shown in Fig. 8.25 (Ref 8.40). A steel section, with a microstructure of equiaxed grains, produced either by reheating or after a previous rolling pass, enters a set of rolls. The grains are deformed and elongated by mechanisms of dislocation motion and multiplication, and the resulting strain energy associated with the dislocation defect structure drives recrystallization. The sketch shows that recrystallization may occur after passing

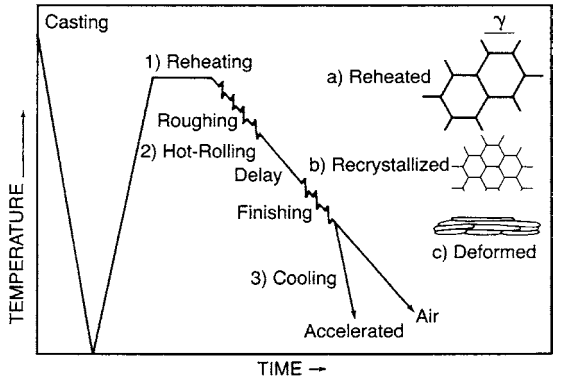

Fig. 8.24 Schematic diagram of stages in hot rolling and associated changes in austenitic grain structure. Source: Ref 8.40

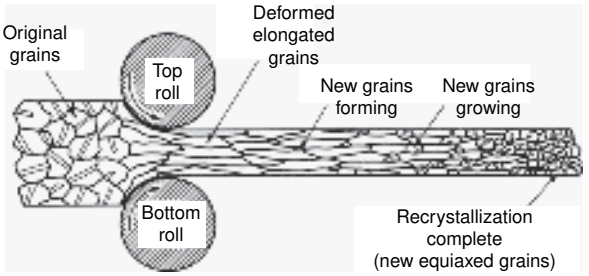

Fig. 8.25 Schematic diagram of changes in austenitic microstructure produced by hot rolling. Source: Ref 8.40

through the rolls, a process referred to as static recrystallization. However, under certain conditions, recrystallization may actually occur as deformation proceeds in the rolls, a process referred to as dynamic recrystallization (Ref 8.41, 8.42). The net effect of recrystallization at successively lower temperatures is to produce equiaxed austenitic microstructures with finer and finer grain sizes.

As noted previously, in microalloyed steels, microalloying element precipitates may completely suppress recrystallization after low-temperature hot rolling. Elongation of the deformed grains brings the original large-angle grain boundaries closer to one another, and when ferrite crystals nucleate on these closely spaced grain boundaries, a very fine ferrite grain structure results. The production of fine-grained ferritic microstructures from unrecrystallized austenite in low-carbon microalloyed steels, an approach referred to as controlled rolling, is well established and has received considerable literature attention (Ref 8.40). A good review from the standpoint of precipitation in austenite and the suppression of static recrystallization has been written by Sellars (Ref 8.43).

The resistance of austenite to the plastic deformation required to produce major changes in section size during hot rolling or to produce complex changes in shape during forging decreases significantly with increasing temperature. Figure 8.26 shows flow curves as a function of temperature for two strain rates for a microalloyed steel containing 0.30% C, 1.46% Mn, 0.13% Cr, and 0.098% V (Ref 8.44). The curves were produced by hot compression testing. The dramatic drop in flow stresses at high deformation temperatures is shown, and at low strains, especially at the lower deformation temperatures, there is a peak in flow stress, followed by a drop in stress. The stress drop is due to dynamic recrystallization, where the deformed substructure of the austenite is replaced by dislocation-free grains during deformation. The recrystallized grains continue to deform, but at lower stresses. The two sets of flow curves also show that deformation at higher strain rates substantially increases flow stresses, a result of reduced time for dynamic recovery of the dislocation substructures introduced in response to deformation.

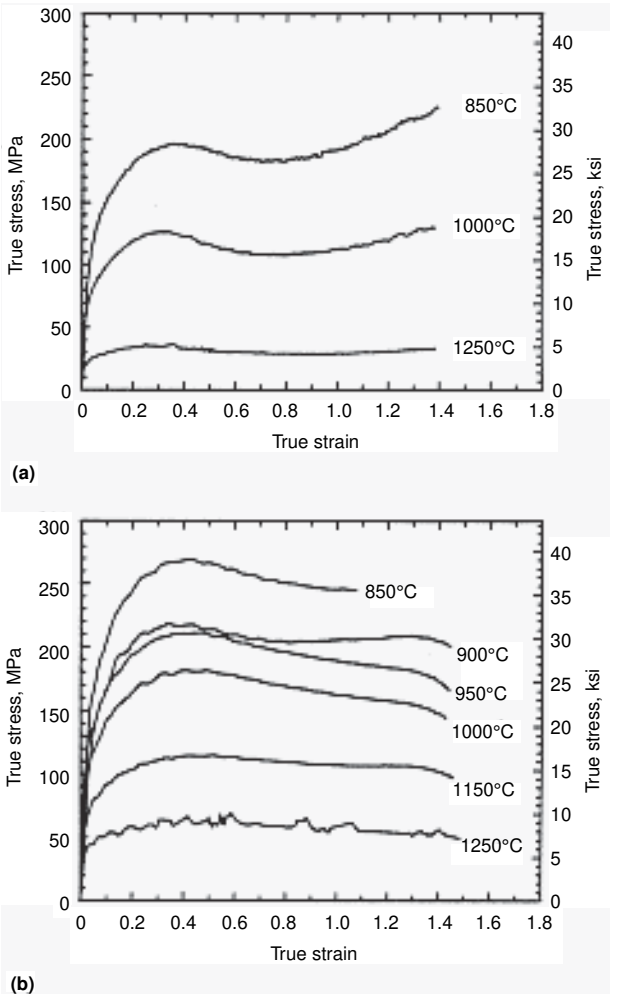

Fig. 8.26 Flow stress curves at various temperatures for a 0.30% C, 0.098% V steel. (a) Deformed at 1.0 s^{-1}. (b) Deformed at 22 s^{-1}. Source: Ref 8.44

REFERENCES

8.1 T.E. Swarr and G. Krauss, Boundaries and the Strength of Low Carbon Ferrous Martensites, *Grain Boundaries in Engineering Materials,* J.L. Walter, J.H. Westbrook, and D.A. Woodford, Ed., Claitors Publishing Division, Baton Rouge, LA, 1975, p 127–138

8.2 R. Millsop, A Survey of Austenite Grain Size Measurements, *Hardenability Concepts with Applications to Steels,* TMS-AIME, Warrendale, PA, 1978, p 316–333

8.3 S.S. Hansen, J.B. Vander Sande, and M. Cohen, Niobium Carbonitride Precipitation and Austenite Recrystallization in Hot-Rolled Microalloyed Steels, *Metall. Trans. A,* Vol 11, 1980, p 387–402

8.4 A. Benscoter, Lehigh University, Bethlehem, PA, private communication, 1975
8.5 A.W. Brewer, K.A. Erven, and G. Krauss, Etching and Image Analysis of Prior Austenite Grain Boundaries in Hardened Steels, *Mater. Charact.,* Vol 27, 1991, p 53–56
8.6 C.A. Apple, Bethlehem Steel Corporation, Bethlehem, PA, private communication, 1980
8.7 "Standard Test Methods for Determining Average Grain Size," E 112, ASTM International
8.8 E.E. Underwood, Quantitative Metallography, *Metallography and Microstructures,* Vol 9, *Metals Handbook,* 9th ed., American Society for Metals, 1985, p 123–134
8.9 T. Gladman, *The Physical Metallurgy of Microalloyed Steels,* Book 615, The Institute of Materials, London, 1997, p 148–153
8.10 G.R. Speich and A. Szirmae, Formation of Austenite from Ferrite and Ferrite-Carbide Aggregates, *Trans. TMS-AIME,* Vol 245, 1969, p 1063–1074
8.11 T.M. Scoonover and G. Krauss, High-Rate Short-Time Austenitizing of 4340 Steel, *Metall. Eng. Q.,* Vol 12, 1972, p 41–48
8.12 S. Matsuda, Microstructural and Kinetic Studies of Reverse Transformation in a Low Carbon Alloy Steel, *New Aspects of Martensitic Transformation,* Japan Institute of Metals, 1976, p 363–367
8.13 S. Watanabe, Y. Ohmori, and T. Kunitake, Formation of Austenite from Lath-Like Martensite, *New Aspects of Martensitic Transformation,* Japan Institute of Metals, 1976, p 368–374
8.14 G. Krauss, Fine Structure of Austenite Produced by the Reverse Martensitic Transformation, *Acta Metall.,* Vol 11, 1963, p 499–509
8.15 C.A. Apple and G. Krauss, The Effect of Heating Rate on the Martensite to Austenite Transformation in Fe-Ni-C Alloys, *Acta Metall.,* Vol 20, 1972, p 849–856
8.16 M.A. Grossmann and E.C. Bain, *Principles of Heat Treatment,* 5th ed., American Society for Metals, 1964
8.17 G.A. Roberts and R.F. Mehl, The Mechanism and Rate of Formation of Austenite from Ferrite-Cementite Aggregates, *Trans. ASM,* Vol 31, 1943, p 613
8.18 R.R. Judd and H.W. Paxton, Kinetic Studies of Austenite Formation from a Spheroidized Ferrite-Carbide Aggregate, *Trans. TMS-AIME,* Vol 242, 1968, p 206–215
8.19 K.R. Hayes, "The Effect of Intercritical Heating and Phosphorus on Austenite Formation and Carbide Distribution of AISI 52100 Steel," M.S. thesis, Colorado School of Mines, Golden, CO, 1984
8.20 Zeit-Temperatur-Austenitisierung-Schaubilder, *Atlas zur Wärmebehandlung der Stähle,* Vol 3, J. Orlich, A. Rose, and P. Wiest, Ed., Verlag Stahleisen M.B.H., Du¨ sseldorf, Germany, 1973

8.21 Zeit-Temperatur-Austenitisierung-Schaubilder, Part 2, *Atlas zur Wärmebehandlung der Stähle,* Vol 4, J. Orlich and H.-J. Pietrzeniuk, Ed., Verlag Stahleisen M.B.H., Du¨ sseldorf, Germany, 1976
8.22 R.E. Reed-Hill, *Physical Metallurgy Principles,* 2nd ed., D. Van Nostrand Company, New York, 1973, p 298–321
8.23 P.T. Mazzare, "Microalloy Precipitate Dissolution and Grain Coarsening Kinetics in 0.2 Weight Percent Carbon Steels," M.S. thesis, Colorado School of Mines, Golden, CO, 1987
8.24 T. Gladman, *The Physical Metallurgy of Microalloyed Steels,* Book 615, The Institute of Materials, London, 1997, p 176–184
8.25 C. Zener, referenced by C.S. Smith, Grains, Phases, Interfaces: An Interpretation of Microstructure, *Trans. AIME,* Vol 175, 1948, p 15–51
8.26 T. Gladman, On the Theory of the Effect of Precipitate Particles on Grain Growth in Metals, *Proc. R. Soc. (London) A,* Vol 294, 1966, p 298–309
8.27 C.G. Dunn and J.L. Walter, Secondary Recrystallization, *Recrystallization, Grain Growth and Textures,* American Society for Metals, 1966, p 461–521
8.28 F.G. Wilson and T. Gladman, Aluminum Nitride in Steel, *Int. Mater. Rev.,* Vol 33 (No. 5), 1988, p 221–286
8.29 W.C. Leslie, *The Physical Metallurgy of Steels,* McGraw-Hill Book Company, New York, 1981
8.30 L.S. Darken, R.P. Smith, and E.W. Filer, Solubility of Gaseous Nitrogen in Gamma Iron and the Effect of Alloying Constituents—Aluminum Nitride Precipitation, *Trans. AIME,* Vol 191, 1951, p 1174–1179
8.31 G.F. Melloy, *Austenite Grain Size—Its Control and Effects,* Metals Engineering Institute, American Society for Metals, 1968
8.32 T. Gladman, The Effect of Aluminum Nitride on the Grain Coarsening Behavior of Austenite, *Metallurgical Developments in Carbon Steels,* Special Report 81, The Iron and Steel Institute, London, 1963, p 68–70
8.33 R. Geiger, Modern Near-Net-Shape Cold Forging, *Metallurgia,* Vol 58 (No. 8), 1991, p 310–314
8.34 K.C. Evanson, "Prevention of Abnormal Austenite Grain Coarsening in Cold-Forge and Carburized SAE 8720 Steel," Ph.D. thesis, Colorado School of Mines, Golden, CO, 1998
8.35 K.C. Evanson, G. Krauss, and D.K. Matlock, Post Cold-Work Ferritic Recrystallization and Its Effect on Abnormal Austenite Grain Growth during Carburizing, *Grain Growth in Polycrystalline Materials III,* H. Weiland, B.L. Adams, and A.D. Rollett, Ed., TMS, Warrendale, PA, 1998, p 599–606
8.36 E.T. Turkdogan, Causes and Effects of Nitride and Carbonitride Precipitation during Continuous Casting, *Iron Steelmaker,* Vol 16, 1989, p 61–75

8.37 P.E. Repas, Metallurgical Fundamentals for HSLA Steels, *Microalloyed HSLA Steels,* ASM International, 1988, p 3–14
8.38 T.N. Baker, Ed., *Titanium Technology in Microalloyed Steels,* Book 662, The Institute of Materials, London, 1997
8.39 L.J. Cuddy and J.C. Raley, Austenite Grain Coarsening in Microalloyed Steels, *Metall. Trans. A,* Vol 14, 1983, p 1989–1995
8.40 G.R. Speich, L.J. Cuddy, C.R. Gordon, and A.J. DeArdo, Formation of Ferrite from Control-Rolled Austenite, *Phase Transformations in Ferrous Alloys,* A.R. Marder and J.I. Goldstein, Ed., TMS-AIME, Warrendale, PA, 1984, p 341–389
8.41 J.J. Jonas and T. Sakai, A New Approach to Dynamic Recrystallization, *Deformation, Processing, and Structure,* G. Krauss, Ed., American Society for Metals, 1984, p 185–228
8.42 H.J. McQueen, The Role of Dynamically Recovered Substructure in Dynamic Recrystallization, *Deformation, Processing, and Structure,* G. Krauss, Ed., American Society of Metals, 1984, p 231–243
8.43 C.M. Sellars, Static Recrystallization and Precipitation during Hot Rolling of Microalloyed Steels, *Deformation, Processing, and Structure,* G. Krauss, Ed., American Society for Metals, 1984, p 245–277
8.44 N.E. Aloi, Jr., "Hot Deformation, Microstructure, and Property Analysis of Ferritic/Pearlitic and Bainitic Microalloyed Forging Steels," M.S. thesis, Colorado School of Mines, Golden, CO, 1994

CHAPTER 9

Primary Processing Effects on Steel Microstructure and Properties

THE PREVIOUS CHAPTERS describing austenite and the solid-state phase transformations that produce microstructures consisting of ferrite, cementite, pearlite, bainite, and martensite have tacitly assumed that the steel sections in which these microstructures form are uniform in composition, containing only the chemical elements incorporated into a steel grade by design. This assumption does not include two very important structural features introduced into all finished steel products by primary processing: inclusions and chemical segregation. *Inclusions* are nonmetallic compounds introduced during steelmaking and casting, and *segregation* is a result of chemistry variations produced during dendritic solidification of steels. Such segregation may cause the microstructural condition referred to as *banding*. The origins of inclusions and banding and their effects on mechanical properties are discussed in this chapter.

Figure 9.1 shows primary temperature-time processing steps used to produce finished steel product shapes or shapes that might be further processed, for example, by forging of bars or cold rolling and annealing of hot-rolled strip. Superimposed on the diagram are the changes in casting that have developed over the last half century. The large size of ingots requires considerable breakdown hot work to produce intermediate products such as slabs, blooms, and billets that in turn require further hot work, as has also been illustrated in Fig. 2.2 in Chapter 2, "History and Primary Steel Processing."

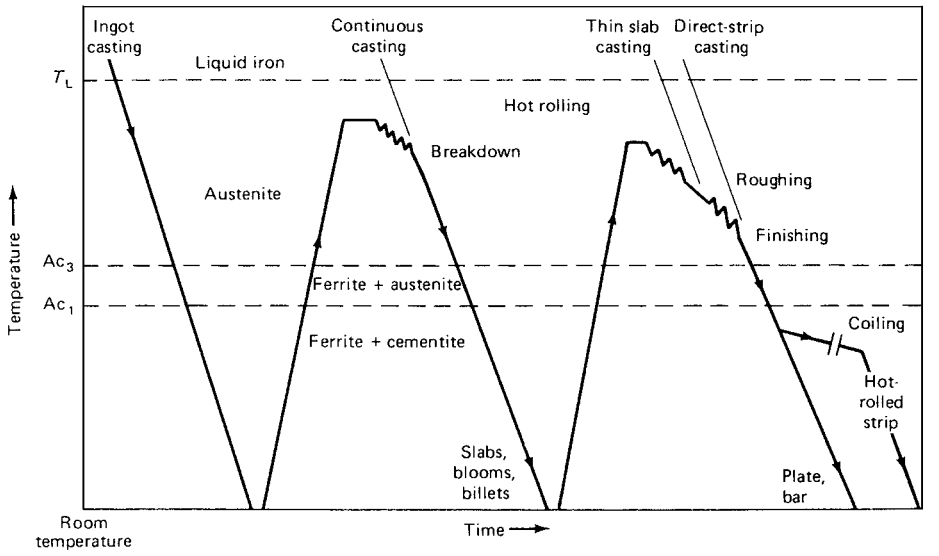

Fig. 9.1 Schematic diagram of temperature-time schedules for primary processing of steel cast by various technologies

The advent of continuous casting eliminated time-consuming ingot reheating or soaking heat treatments and considerable breakdown hot work, resulting in improved surface quality and uniformity of structure with greatly reduced handling and energy costs. Irving has recorded the history of continuous steel casting of steel, from the early development of pilot and production plant facilities in the period 1945 to 1956 through subsequent intensive development, noting that by 1985 over 50% of the world steel production was made by continuous casting (Ref 9.1). Thin slab casting, first successfully applied in 1989 at a Nucor plant in Crawfordsville, IN, produces slabs 50 to 80 mm (2 to 3 in.) thick, instead of the 200 to 300 mm (8 to 12 in.) thick slabs now conventionally continuously cast, and eliminates roughing hot work with corresponding increases in efficiency (Fig. 2.3 in Chapter 2 and Fig. 9.1). Further efficiencies in processing are promised by thin strip casting (Ref 9.2, 9.3). While great improvements in steelmaking have accompanied the changes in casting, inclusions and variations in steel chemistry, although much reduced in scale, are a part of all as-cast and wrought steel products, and therefore merit attention in the processing-structure-property relationships that are part of the physical metallurgy of steels.

Inclusions—Types and Origins

The production of clean steel, i.e., steel with low inclusion content, is a demanding task that, in view of its importance to producing steel of high

mechanical performance, has received considerable attention in the steelmaking literature. This section indicates the complexity of inclusion control based on only a few selected references. These references in turn document in much greater detail accumulated steelmaking knowledge regarding the manufacture of clean steels. The now-classic volume by Roland Kiessling, parts of which were first published between 1964 and 1968, presents an authoritative discussion of inclusions and their origin (Ref 9.4), and the state of the art in inclusion control in 2003 is thoroughly reviewed by Zhang and Thomas (Ref 9.5). Intensive study of the many facets of inclusion formation, control, chemistry, and morphology in many steel types and products continues (Ref 9.6, 9.7).

Inclusions are nonmetallic phases, generally oxides and sulfides, introduced during the making and refining of liquid steel, transfer between vessels containing liquid steel, casting, and precipitation within solid steel. The inclusions produced by reactions taking place in liquid or solidifying steel are termed *indigenous inclusions* and those introduced by incorporation of particles of slag, refractories, or other materials that come into contact with liquid steel are termed *exogenous inclusions* (Ref 9.4). Indigenous inclusions occur, often as very fine particles, in huge numbers in steel, while exogenous inclusions may occur sporadically as coarse, irregularly shaped particles.

Figure 9.2 shows a schematic diagram of a continuous slab casting machine (Ref 9.8). Machines that cast other shapes have similar components. A key feature of modern steelmaking is the use of basic oxygen steelmaking (BOS) furnaces or electric arc furnaces (EAF) to perform the functions of melting (in the case of EAF steelmaking) and primary refinement

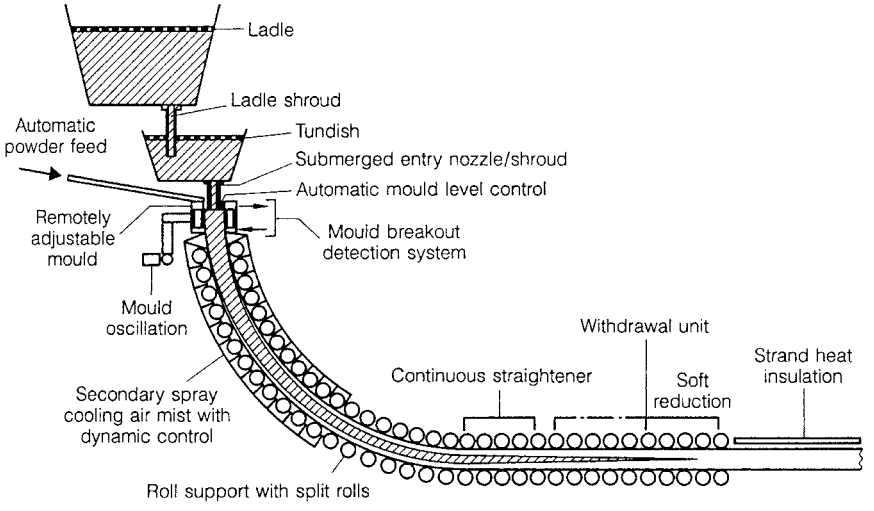

Fig. 9.2 Schematic diagram of the various components of a continuous slab casting machine. Source: Ref 9.8

of liquid steel. Final refining and composition control is performed more efficiently in ladles. Following ladle metallurgical adjustments, liquid steel is transferred to a tundish from which it is poured into the mold of a continuous casting machine (Ref 9.8–9.10). With good control, each vessel for liquid steel offers the opportunity to remove inclusions, but as Fig. 9.3 and 9.4 show, the transfer of liquid steel, flow, and turbulence in the liquid steels, slags, and mold powders that protect liquid steel make up the complex liquid steel-containment-transfer systems for the production of continuously cast steels (Ref 9.5, 9.11). Associated with the transfer of steel between the various vessels may be clogging of tundish nozzles or submerged entry nozzles (SEN) due to buildup of aluminum- or calcium-containing inclusions. Such deposits not only impede the flow of liquid steel but also may break off and become imbedded as detrimental exogenous inclusions in solidifying steel (Ref 9.12). These inclusions are most frequently identified as $MgO\text{-}Al_2O_3$ or $MgO\text{-}Al_2O_3\text{-}CaO$ crystals, and are referred to as *spinels*, a type of crystal that contains ions with different charges, for example Mg and Al, which distribute themselves in ratios between layers of oxygen to balance the charge of the compound.

Many inclusions are complex oxides of manganese, silicon, and aluminum used to deoxidize steel, and Kiessling documents in detail the many

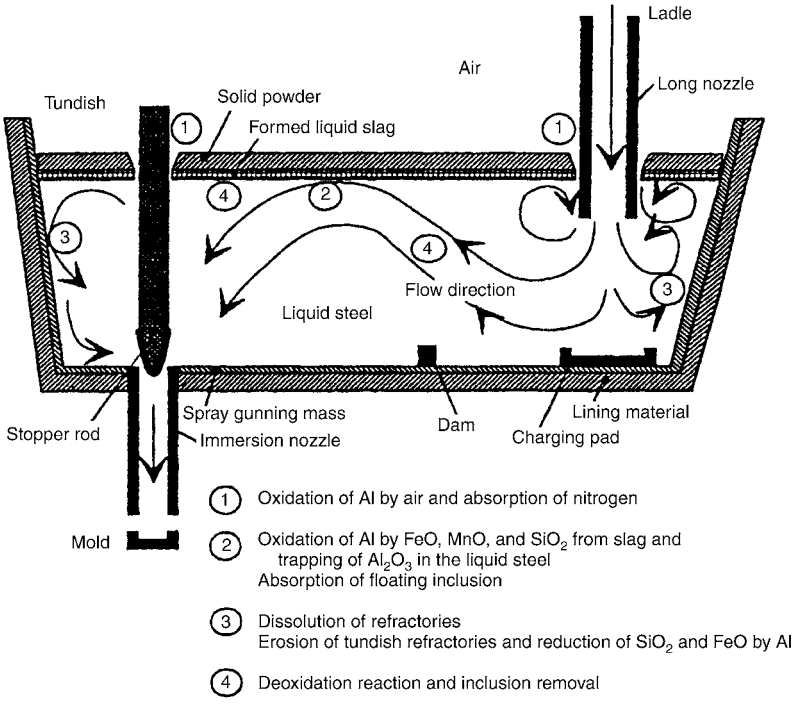

Fig. 9.3 Schematic diagram of a continuous casting tundish and various tundish phenomena that relate to inclusion formation. Source: Ref 9.5

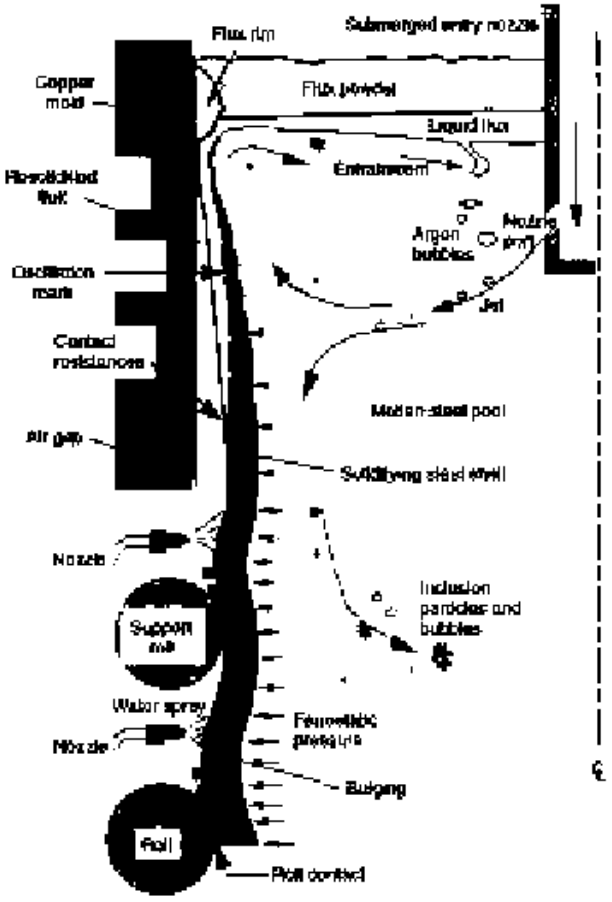

Fig. 9.4 Schematic diagram of a continuous slab casting mold and early-stage mold solidification phenomena. Source: Ref 9.11.

oxides that may form in the MnO-SiO_2-Al_2O_3 ternary oxide system (Ref 9.4). Zhang and Thomas present the following instructive list of sources of inclusions in low-carbon-aluminum-killed (LCAK) steels (Ref 9.5):

1. Deoxidation products, such as alumina, constitute the majority of indigenous inclusions in LCAK steel. They are generated by the reaction between the dissolved oxygen and the added deoxidant, such as aluminum. Aluminum inclusions are dendritic when formed in a high oxygen environment—or may result from the collision of smaller particles.
2. Reoxidation products, such as alumina, are generated i) when the Al remaining in the liquid steel is oxidized by FeO, MnO, SiO_2 and other oxides in the slag and refractory linings, or ii) by exposure to the atmosphere.

3. Slag entrapment, when metallurgical fluxes are entrained in the steel, occurs especially during transfer between steelmaking vessels. This forms liquid inclusions that are usually spherical.
4. Exogenous inclusions from other sources include loose dirt, broken refractory brickwork, and ceramic lining particles. They are generally large and irregularly-shaped. They may act as sites for heterogeneous nucleation of alumina.
5. Chemical reactions, for example, produce oxides from inclusion modification when Ca treatment is improperly performed. Identifying the source is not always easy, as for example inclusions containing CaO may also originate from entrained slag.

The Zhang and Thomas text provides references for these inclusion sources and micrographs to illustrate various inclusion morphologies and distributions.

Oxide inclusions may be liquid at steelmaking temperatures and may therefore be present as spherical particles or, if formed as dendrites, may spheroidize to lower their surface areas and energies (Ref 9.8). The oxides may be quite hard relative to the steel matrix and during hot work may break up into elongated clusters of particles. Also, hard oxide particles might not deform during hot work, and as a result, cracks, in the form of conical gaps at inclusion-matrix interfaces, might form as the austenite flows around the particles (Ref 9.4). Figure 9.5 shows schematically some of the different morphologies and the effects of hot work on the various types of inclusions that may form in aluminum-killed steels (Ref 9.9). Other morphologies may develop depending on alloy composition. For example, dendritic, cuboid, and cruciform nitride precipitates have been

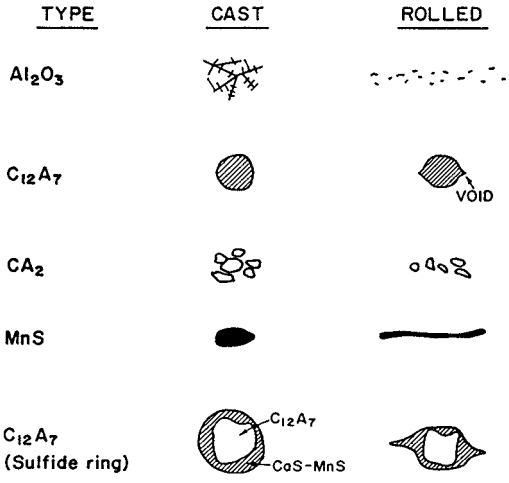

Fig. 9.5 Schematic diagram of the inclusions that form in as-cast aluminum-killed steels and the changes produced in inclusion morphology by hot rolling. "A" represents Al_2O_3 and "C" represents CaO. Source: Ref 9.9

found during processing of low-carbon thin slab steels microalloyed with V and Ti and those microalloyed with V, Nb, and Ti (Ref 9.13).

Manganese sulfide (MnS) particles are a ubiquitous component of steels, and forming them is one of the reasons manganese is added to steels. Without sufficient manganese, sulfur forms FeS, which, because of its low melting point, severely reduces the hot workability of steel. Three morphologies of sulfides have been identified (Ref 9.4, 9.8, 9.14–9.16). Type I is characterized by globular particles randomly distributed in the matrix of steels with high oxygen contents. The spherical shape is attributed to their precipitation as liquid globules rich in sulfur and oxygen in solidifying steel. Type I sulfides formed early in solidification may form as duplex inclusions with MnO. Type II MnS inclusions form as clusters of very fine rods in an interdendritic distribution. Figure 9.6 shows sets of the MnS rods in a deep-etched as-cast steel specimen (Ref 9.16). Metallographic two-dimensional sections through such colonies of rods would show these inclusions as having circular or elliptical shapes. Type II MnS inclusions form in the liquid between solidifying dendrites and are usually found in highly deoxidized aluminum-killed steels. Increased cooling rate may favor the formation of Type II manganese sulfides even when the equilibrium type is I or III (Ref 9.15). Type III MnS inclusions have angular geometric shapes with a range of sizes and random distribution and are found in killed steels with high contents of aluminum, carbon, silicon, and phosphorus contents.

Titanium is sometimes added in small amounts to steel to tie up nitrogen, as for example in boron containing steels, or to restrain austenite grain growth. Kiessling notes that the transition metals Ti, Zr, and Hf, are comparatively strong sulfide formers and that the free energy of formation of titanium sulfide is of the same order as that of MnS (Ref 9.4). Thus ti-

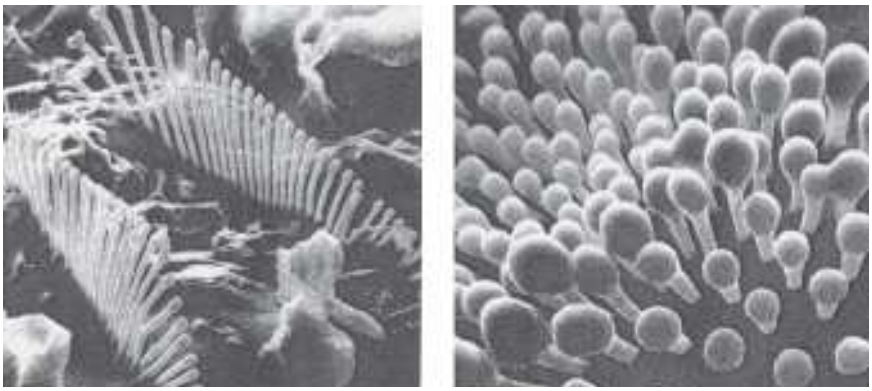

(a) (b)

Fig. 9.6 Three-dimensional view of Type II interdendritic MnS colonies produced by deep etching. (a) Original magnification at 1000×. b) Original magnification at 2000×. SEM micrographs. Source: Ref 9.16

tanium can dissolve in MnS and even replace MnS with TiS if added in large amounts. Titanium decreases the plasticity of MnS, and may result in reduced elongation of MnS during hot work (Ref 9.17).

MnS particles are highly plastic and elongate and flatten during hot work. Figure 9.7 shows a cluster of elongated MnS particles in a longitudinal section of a low-carbon steel. Such elongation produces the anisotropy in mechanical properties described subsequently. In view of the strong effect that elongated manganese sulfides have on the directionality of properties, steelmaking approaches, referred to as *sulfide shape control,* with additions of calcium or rare earth metals have been developed to produce hard sulfides that maintain spherical shapes during hot work (Ref 9.8). An optimal mechanism of inclusion shape control by calcium treatment is shown to result in CaS-MnS formation around $C_{12}A_7$ particles as shown in Fig. 9.5. The processing to achieve this type of inclusion dispersion during steelmaking is described in detail by S. Abraham et al. (Ref 9.18).

Manganese sulfide particles may also dissolve at high temperatures and reprecipitate during cooling to produce the low-toughness condition referred to as overheating, as described in Chapter 19, "Low Toughness and Embrittlement Phenomena in Steels." Spheroidization of elongated MnS particles exposed to high austenitizing temperatures has also been observed (Ref 9.19).

Inclusion Identification and Characterization

The chemical composition of inclusions one micron in size and larger can now be readily determined with the use of electron microprobe ana-

Fig. 9.7 Elongated MnS inclusions in a low-carbon steel. As-polished surface, longitudinal section, light micrograph, original magnification at 500×. Courtesy of Mark Richards, Colorado School of Mines

lyzers with wavelength dispersive spectroscopy (WDS) and scanning electron microscopes capable of energy dispersive spectroscopy (EDS). These instruments excite characteristic X-rays from the various component elements in inclusions to establish chemical composition (Ref 9.20) and are used to identify inclusions on prepared metallographic surfaces and on fracture surfaces. The minimum electron beam size used to excite the X-rays is typically around 1 μm. As a result, the electron beam overlaps or passes through smaller particles, and X-rays are generated from the steel matrix as well as from the inclusion.

Light microscopy is effective in establishing the distributions, shapes, and sizes of inclusions, subject to the resolving power of the light microscope, but cannot determine chemistry. Inclusions are best observed in as-polished sections, as shown in Fig. 9.7. Etching would bring out other features of the microstructures that would make it difficult to view inclusions. A widely used ASTM system based on light microscopy compares at 100× inclusion distributions to standardized charts that rank densities, shapes, and sizes (thin and heavy) of inclusions (Ref 9.21). Four categories of indigenous inclusions typically produced by steelmaking and deoxidation, as modified by hot work, are characterized: Type A, sulfides; Type B, alumina; Type C, silicate; and Type D, globular oxides. The charts for comparison are derived from the early Swedish Jernkontoret (JK) system for inclusion characterization.

There are now many other approaches and instruments to evaluate inclusions, and new techniques are continually under development (Ref 9.22). Kaushik et al. have reviewed a number of direct and indirect methods of inclusion characterization and applied them to a a variety of low-carbon sheet steels (Ref 9.23). Automated scanning electron microcopy (SEM) coupled with energy dispersive spectroscopy (EDS) makes possible rapid measurements of numbers, sizes and chemistries of inclusion distributions. S. Abraham, Raines, and Bodnar have used such instrumentation to develop an approach to determine a parameter referred to as the total inclusion interparticle spacing (TIS) that can be determined for a specific inclusion chemistry or for all types of inclusion in a volume of steel (Ref 9.24). This parameter then can be used to relate to steelmaking sources of inclusions or to mechanical properties such as fracture-related parameters that may be dependent on inclusion densities.

Fatigue fractures are often nucleated at the largest inclusion particle in a part, depending on location and stress distribution. As a result a method, Extreme Value Statistics (EVS), has been developed to estimate the largest inclusion in a given critical area or volume of steel (Ref 9.25–9.27). Sufficient sample areas must be examined to provide statistically valid numbers, and the square roots of inclusion areas are calculated and plotted. EVS analysis was recently applied in a fatigue study of induction hardened 1045 and 4150 steels in which fatigue cracks were initiated at inclusion particles at the case/core interfaces of the induction-hardened

samples (Ref 9.28). All of the inclusions at which cracks initiated were larger than those estimated by the EVS analysis, indicating the wide distribution, outside of the sampling areas, of the actual largest inclusions.

Metallographic methods for inclusion characterization by light and scanning electron microscopy require sectioning or destructive testing of samples. Inclusions and other discontinuities in steel, such as porosity, can also be evaluated in three-dimensional sections by ultrasonic scanning and other analytical techniques (Ref 9.5, 9.29).

Effect of Inclusions on Mechanical Properties

The strong effect of inclusions on fracture and mechanical properties has been comprehensively reviewed by Leslie (Ref 9.30) and has been the subject of many symposia (Ref 9.31, 9.32). Inclusions play a major role in the three-stage ductile fracture process of initiation, growth, and coalescence of microvoids, serving as the hard particles for void initiation, and therefore significantly affect upper shelf energies during CVN testing, as described in Chapter 11, "Deformation, Strengthening, and Fracture of Ferritic Microstructures." Coarse inclusion particles also serve as fatigue initiation sites and may initiate cleavage fracture. The latter effect of inclusions has been documented in microalloyed forging steels containing titanium nitride particles that crack and initiate cleavage cracks in surrounding ferrite grains (Ref 9.33).

A beneficial effect of sulfide inclusions, related to their ability to reduce fracture resistance, is improved machinability produced by the breaking up of chips formed by shear mechanisms of fracture at tool interfaces. Hard oxide and silicate inclusions are detrimental to machinability. Machining and the required cutting tools, including the tool steels discussed in Chapter 24, "Tool Steels," are a major cost of production for some steel parts and have received considerable attention in the literature (Ref 9.34–9.36).

The same section of steel, depending on the orientation of notches, crack planes, and crack propagation directions, may show wide ranges of resistance to fracture. This anisotropy in fracture behavior is primarily related to the orientation of elongated inclusions or inclusion clusters produced by hot work. In order to characterize anisotropy, several systems for notch and crack plane orientation have been developed. Figure 9.8 shows the system established for hot rolled plate (Ref 9.37). The longitudinal or rolling direction, the transverse direction, and the through-thickness or short transverse direction are designated respectively L, T, and S, as shown. For the designation of the crack planes, the first letter indicates the normal to the crack plane, and the second letter indicates the direction of crack propagation. Upper shelf energies of plate specimens decrease in the order LS-LT, TS-TL, and ST-SL (Ref 9.30). The highest energy absorbed occurs in specimens where the crack plane is normal to elongated

or flattened inclusions, and the crack may be deflected along the interfaces of the inclusions. Lower energies are absorbed when the crack travels along the interfaces of the elongated and flattened inclusions.

Figure 9.9 shows the effect of sulfur content, which translates to MnS inclusions, and specimen orientation, on upper shelf energy of as-hot rolled low-carbon steel (Ref 9.38). Lowering sulfur content greatly increases resistance to ductile fracture, and at all sulfur contents, shelf energy is strongly dependent on specimen orientation. The strong effect of elongated manganese sulfide inclusions on ductile fracture has led to the production of very-low-sulfur-content steels used for critical structural applications. Another approach to reducing anisotropy associated with ductile fracture has been the use of sulfide shape control, as described previously, to reduce deformation and elongation of inclusions during hot work.

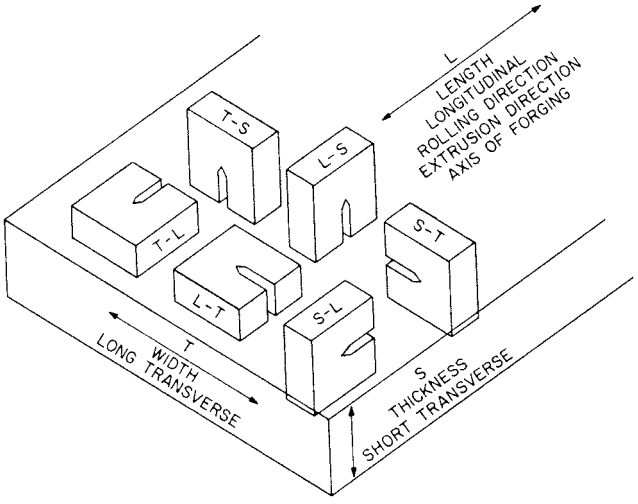

Fig. 9.8 Crack plane orientation code for specimens in rectangular rolled sections. ASTM E 399 Source: Ref 9.37

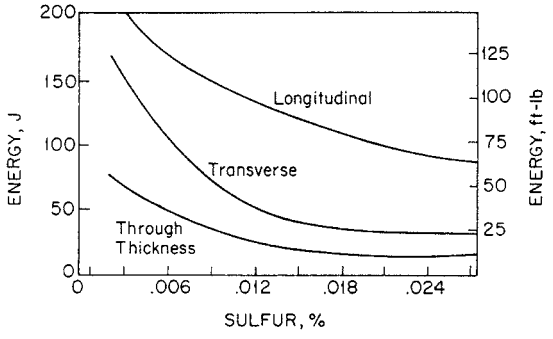

Fig. 9.9 Effect of sulfur content and specimen orientation on the upper shelf impact energy of rolled carbon steel plate. Source: Ref 9.38

Figure 9.10 shows effects of strength, sulfur, and specimen orientation on energy absorbed during CVN impact testing of 4340 plate specimens quenched to martensite and tempered to produce ultimate tensile strengths of 980 MPa (135 ksi) and 1960 MPa (285 ksi) (Ref 9.39). The lower-strength specimens show high sensitivity to sulfide content and orientation, in view of the fact that microvoid initiation at sulfides lowers stresses for otherwise substantial resistance to ductile fracture during post uniform straining. The higher-strength specimens have little capacity for deformation beyond their very high ultimate strengths and, therefore, with or without inclusions, have very low ductile fracture resistance at all test temperatures. The latter characteristics of the deformation and fracture of martensitic microstructures are discussed in more detail in Chapter 18, "Deformation, Mechanical Properties, and Fracture of Quenched and Tempered Carbon Steels."

Solidification: Chemical Changes

As liquid steel, with all of the desired and undesired chemical elements uniformly dissolved in the liquid, solidifies, two interrelated phenomena occur: solid crystal growth and chemical partitioning between the solid

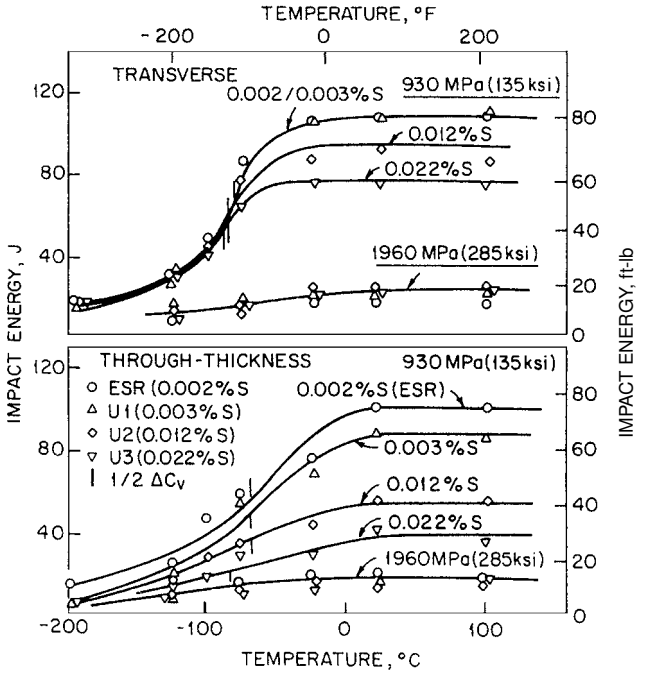

Fig. 9.10 Effect of sulfur content and specimen orientation on impact toughness as a function of test temperature for 4340 plate steels hardened and tempered to two strength levels. Source: Ref 9.39

and the liquid. Figure 9.11 shows schematically a portion of a phase diagram where liquid solidifies to a solid phase α and a diagram through a solid/liquid interface with associated changes in composition (Ref 9.40). The alloy composition is c_0, and the vertical line marked c_0 traces the phase changes that develop with decreasing temperature. The solid sloping lines are the solidus and liquidus lines for this hypothetical alloy system and mark the changes in chemical composition that develop with decreasing temperature in the solid and liquid phases.

Solidification of alloy c_0 starts at T_L, and the intersection of the horizontal dashed line with the solidus line marks the composition of the first solid to form. The first solid has much lower alloy content than does the liquid, and this observation is the basis for the fact that the first solid to form always has the leanest alloy or impurity element content. With decreasing temperature, the compositions of the solid and liquid follow the solidus and liquidus lines and increase in alloy content. At T*, the compositions of the solid and liquid, respectively, are given by c_S* and c_L*, and the discontinuity in compositions at the liquid solid interface is shown in the sketch of Fig. 9.11(b). The differences in composition intensify with decreasing temperature, and, if there is no homogenizing diffusion in the solid phase, the last liquid solidifies into solid with significantly higher concentrations of alloying and residual elements than the solid crystals formed at higher temperatures.

Solute atom redistribution, or chemical partitioning, during solidification is characterized by the solute concentrations in the solid, c_S, and liquid, c_L, phases at a given temperature in the two-phase liquid solid phase field by the equilibrium partition ratio, *k*, as follows (Ref 9.40):

$$k = c_S/c_L \qquad \text{(Eq 9.1)}$$

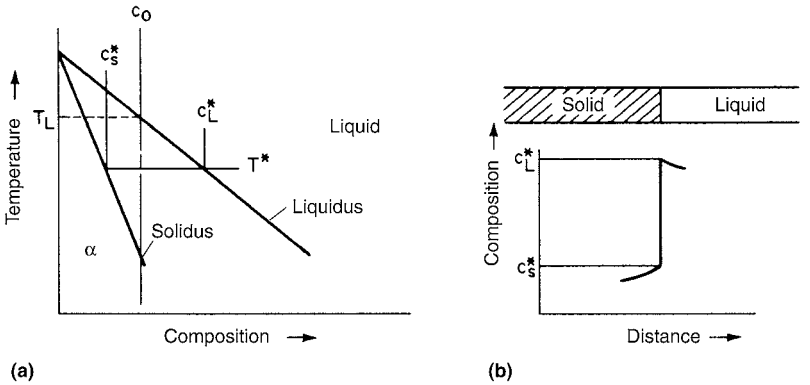

Fig. 9.11 Schematic diagram of binary alloy solidification with equilibrium at the liquid- solid interface. (a) Phase diagram. (b) Composition profile across the solid-liquid interface. Source: Ref 9.40

With the use of *k*, solute redistribution in the solid as a function of the weight fraction of solid, f_S, in a given volume element is given by the Scheil equation as:

$$c_S = kc_0(1 - f_S)^{k-1} \quad \text{(Eq 9.2)}$$

where c_0 is the initial solute concentration within the volume element (Ref 9.40). The Scheil equation is based on a number of simplifying assumptions, including negligible undercooling, complete diffusion in the liquid, negligible diffusion in the solid, and a constant *k* throughout solidification. Other more complicated equations of solute distribution have been developed, including the effects of diffusion in the solid and convection in the liquid (Ref 9.40, 9.41). Nevertheless, Eq 9.2 accurately demonstrates solute enrichment as solidification proceeds.

The schematic portion of a phase diagram shown in Fig. 9.11(a) is typical of many alloy systems, including the Fe-C system, as shown in Fig. 3.1 in Chapter 3, "Phases and Structures." All of the other elements found in steel have similar effects on the liquidus and solidus lines. Table 9.1 lists *k* values, assumed to be independent of temperature, for some elements commonly found in steels (Ref 9.42). Solute elements with the lowest *k* values have the highest tendency to segregate. Therefore, phosphorus has a very high tendency to segregate during solidification. However, the amount of element is also a factor. Therefore, manganese, generally present in much higher concentrations than phosphorus, plays a more important role in segregation and banding in wrought steels than does phosphorus, despite its higher value of *k*.

Solidification—Dendrites and Interdendritic Segregation

Figure 9.12 is a sketch of the three zones of crystal morphology that typically develop in a transverse section of an as-cast steel shape (Ref 9.43). The surface zone is referred to as the chill zone and is produced by a high rate of nucleation of fine randomly oriented, equiaxed crystals in the highly supercooled liquid adjacent to a mold wall. Convection in the

Table 9.1 Equilibrium partition ratios for various elements in steel

Element	*k*
Phosphorus	0.14
Niobium	0.23
Chromium	0.33
Manganese	0.71
Nickel	0.83

Source: Ref 9.42

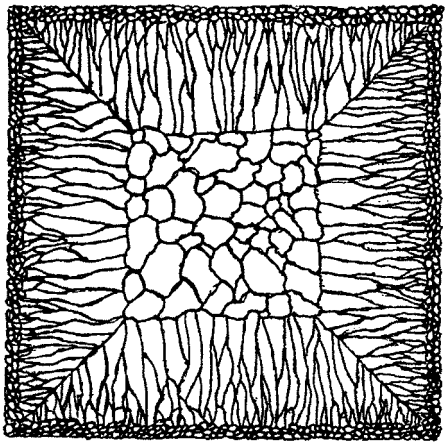

Fig. 9.12 Schematic diagram of zones of crystal morphologies in an as-solidified section of steel. Shown are the outer chill zone, the columnar zone, and the interior equiaxed zone. Source: Ref 9.43

liquid adjacent to the chill zone, produced by pouring and temperature differences, may also contribute to the high density of crystals in the chill zone (Ref 9.43). The second zone develops by the growth of columnar-shaped crystals. The columnar crystals grow in preferred crystallographic directions, <100> in the case of body-centered cubic (bcc) ferrite and face-centered cubic (fcc) austenite, promoted by constitutional supercooling at the tips of growing crystals (Ref 9.40, 9.44). The center zone consists of equiaxed crystals produced by nucleation in the highly supercooled interior liquid and by the breaking off of parts of the crystals in the columnar zone by convection in the liquid (Ref 9.40, 9.43, 9.44).

The equiaxed and columnar crystals in the three solidification zones are in fact *dendrites,* i.e., *branched, tree-shaped crystals,* produced by constitutional supercooling and preferred crystallographic growth. Columnar crystals have a major <100> axis and also secondary and tertiary branches at orthogonal <100> orientations. Figures 9.13 and 9.14 show schematic diagrams that illustrate dendritic crystal solidification and some of the phenomena that accompany solidification. Figures 9.15 and 9.16 show actual rounded tips of dendrite branches that were revealed adjacent to shrinkage porosity in specimens taken from the equiaxed zone of an as-cast stirred billet of 4140 steel (Ref 9.47).

The darker shading between dendrites shown in Fig. 9.13 represents increases in liquid solute atom content or *interdendritic segregation* that develops during solidification as described in the preceding section. Figure 9.14 notes the liquid flow necessary to compensate for shrinkage due to the volume contraction that accompanies solid formation from liquid. Also shown are deformation that might cause hot tearing and small vol-

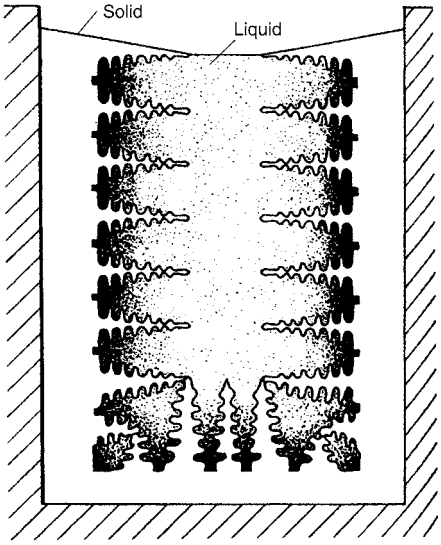

Fig. 9.13 Schematic of dendritic solidification. The dark shading in liquid adjacent to dendrites represents concentrations of solute atoms rejected from the solid dendrites. Source: Ref 9.45

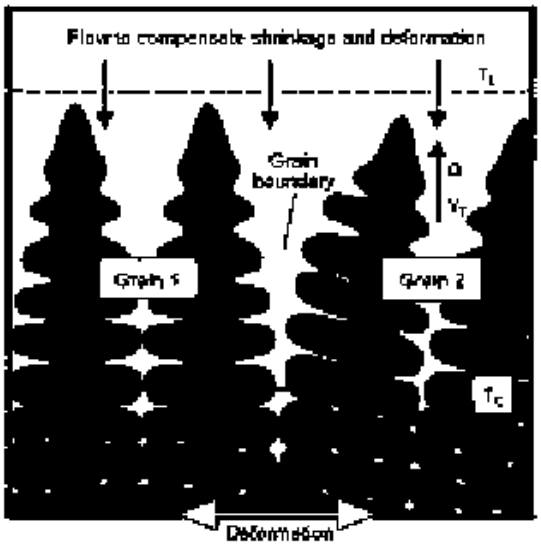

Fig. 9.14 Another schematic view of dendritic solidification. Shown are liquid convection, effects of deformation, and regions (small white circular areas) where dendrite branches have grown together and interdendritic shrinkage will occur. Source: Ref 9.46

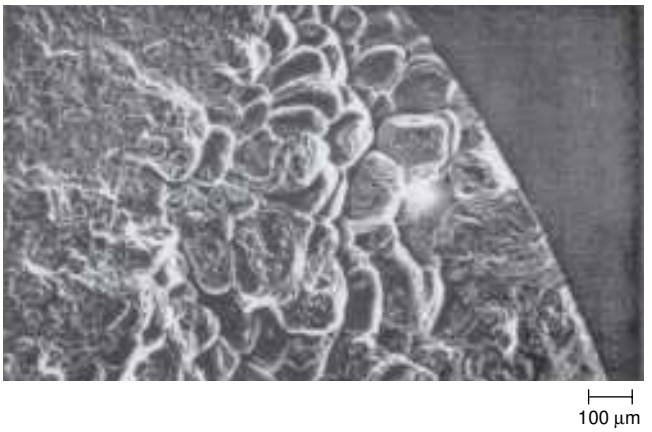

Fig. 9.15 Rounded tips of dendritic crystal branches exposed at shrinkage porosity in the equiaxed solidification zone of an as-cast billet of 4140 steel. SEM micrograph. Courtesy of E.J. Schultz. Source: Ref 9.47

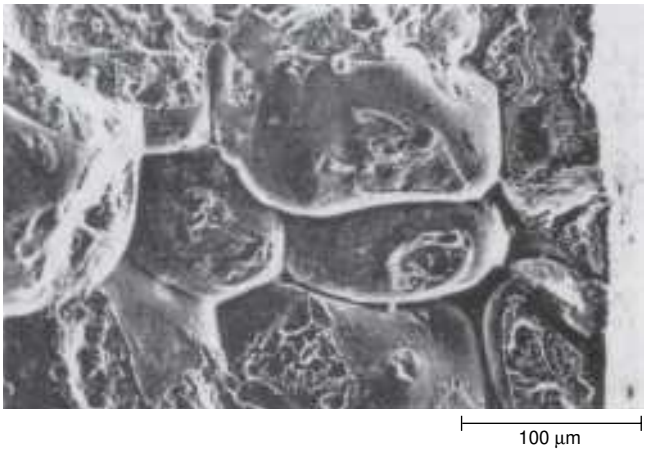

Fig. 9.16 Another view of dendrite branch tips at shrinkage porosity in equiaxed solidification zone of an as-cast 4140 steel billet. SEM micrograph. Source: Ref 9.47

umes of interdendritic shrinkage formed when isolated pockets of liquid solidify after dendrites have grown together. Hot tears that lead to cracking in continuously cast steel billets have been shown to be directly related to dendritic structure, with smooth surfaces conforming to the tips of dendrites (Ref 9.48). The hot tears form at temperatures close to the solidus where the ductility and fracture strength of steel are near zero. In low-carbon steels, with carbon contents between 0.08 and 0.14%, solidification occurs by the formation of delta-ferrite and the peritectic reaction between liquid and delta-ferrite to form austenite. The shrinkage associated with

the change in crystal structure from bcc ferrite to the close-packed fcc structure of austenite may cause distortion and cracking in the shell of continuously cast slabs (Ref 9.48). Other features associated with solidification, not illustrated in the schematics of Fig. 9.13 and 9.14, are the breaking off of dendrite arms, remelting of dendrite tips, dendritic coarsening with increasing distance into the melt, and possible formation of spherical solid particles by separation from dendrite arms at points of reduced radii of curvature (Ref 9.49).

The extent of interdendritic segregation is frequently related to *secondary dendrite arm spacing,* the spacing of dendrite branches normal to the major dendrite axis. Figure 9.17 shows that secondary dendrite arm spacing increases with increasing distance from the chill surface, corresponding to decreasing cooling rates (Ref 9.50), and Fig. 9.18 shows changes in secondary dendrite arm spacing across an as-cast thin slab (Ref 9.51). Smaller section sizes as produced by continuous casting reduce dendrite spacing and thereby reduce the scale of segregation. The size of the columnar solidification zone can be greatly reduced by in-strand or in-mold electromagnetic stirring during continuous casting (Ref 9.47, 9.52). Such stirring of the solidifying liquid increases the size of the equiaxed solidification zone and greatly reduces the amount of centerline shrinkage. Figure 9.19 shows that the relative sizes of the columnar and equiaxed zones are also dependent on superheating of liquid steel (Ref 9.52). High superheat retards the nucleation of equiaxed grains in center-solidifying zones.

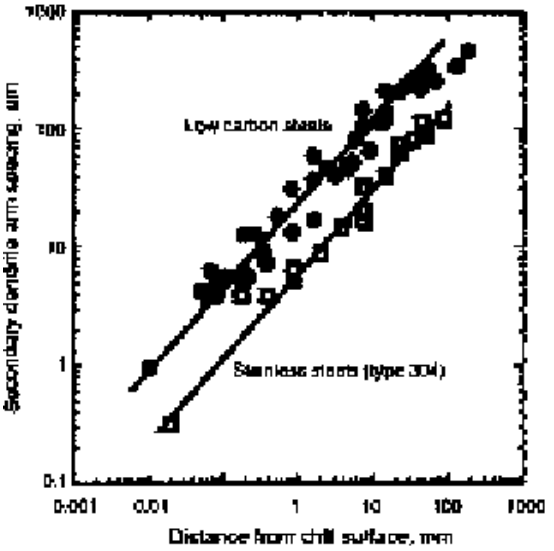

Fig. 9.17 Secondary dendrite arm spacing as a function of distance from the chill surface of steel from various low-carbon and stainless steel casters. Source: Adapted from Ref 9.50

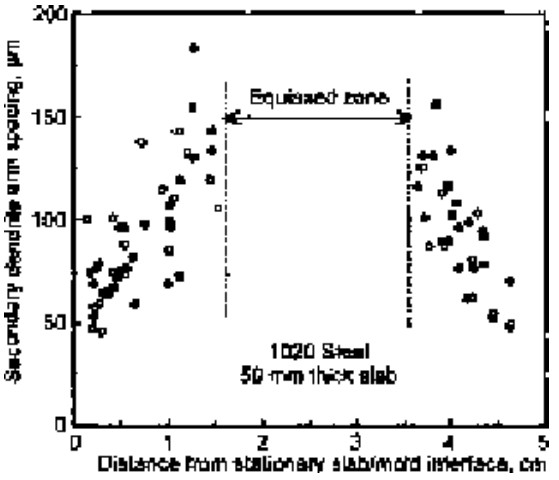

Fig. 9.18 Secondary dendrite arm spacing as a function of distance across an as-cast slab of 1020 steel. Source: Ref 9.51

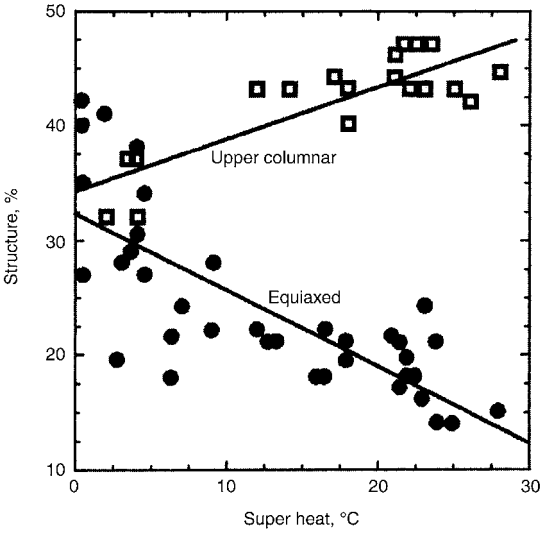

Fig. 9.19 Amount of as-cast columnar and equiaxed zones as a function of liquid steel superheat. Source: Adapted from Ref 9.53

Hot Work and Its Effect on Solidification Structure

The starting microstructure for hot work consists of microstructures derived from dendritic solidification, inclusions residual from steelmaking and casting, chemical variations produced by interdendritic segregation, and porosity caused by the shrinkage associated with the liquid-to-solid volume decrease, as described previously. The soaking or heating of as-

cast structures in preparation for hot work, and the subsequent hot work, significantly ameliorate negative features of as-cast structures. With a reasonable amount of hot work reduction, shrinkage porosity is healed and eliminated, and coarse dendritic microstructures are refined by ferrite-austenite phase transformations on heating and cooling and by deformation and recrystallization during hot work. Inclusions cannot be removed, but as already described, may be changed in size, shape, and distribution by hot work.

The smaller sizes of billets produced by continuous casting has raised questions about the amount of hot work reduction required to produce good uniformity and properties in forgings made from continuously cast and hot-rolled bars. While the smaller sizes of continuously cast billets reduce the scale of dendritic solidification, the reduced amount of hot work of smaller sections reduces the opportunity of homogenization of as-cast microstructures. A review of this subject shows that only relatively small hot work reductions in area, from 3:1 to 7:1, depending on mill practice, are necessary to establish wrought steel performance (Ref 9.54). Hot work produced by forging is also beneficial for some parts (Ref 9.55). Thus, the only area of concern is the conversion of small as-cast billets to large bars and forgings that receive limited hot deformation. Steel cleanliness is important, and inclusions that may affect fatigue and fracture remain throughout hot work. Also, residual variations in chemistry after hot work may contribute to distortion of heat treated parts (Ref 9.56, 9.57).

Interdendritic chemical segregation is modified, but not eliminated, even by extensive hot work processing. Figure 9.20 shows micrographs of transverse sections of bars of 10V45 steel hot rolled from a continuously cast billet 178 by 178 mm (7 × 7 in.) in size. The micrographs show dendritic structures observed in bars with diameters of 76, 64, 38 and 29 mm (3, 2.5, 1.5, and 1 in.), corresponding to reduction ratios of 7:1, 10:1, 27:1, and 49:1 (Ref 9.58). The structures have been revealed by etching with hot picric acid containing sodium tridecylbenzene sulfonate, an etch that responds to chemical variations but not to microstructural features. What is shown in Fig. 9.20 is an etching response to the remnants of interdendritic segregation that, although reduced in size, persists even after extensive hot-rolling reduction. The actual bar microstructures superimposed on these chemical variations consist of ferrite and pearlite, formed on cooling after hot rolling.

Hot rolling aligns the interdendritic variations in chemistry into bands parallel to the rolling direction, producing alternating regions of high and low concentration of various solute elements. Figure 9.21 shows manganese and carbon concentrations as a function of distance across a longitudinal section of a quench-and-tempered 4140 steel bar, containing by heat analysis 1.00% Mn (Ref 9.59). There are large variations in manganese content, from less than 0.6% to more than 1.2%, across the bar, consistent with manganese interdendritic segregation and its sluggish substitutional-

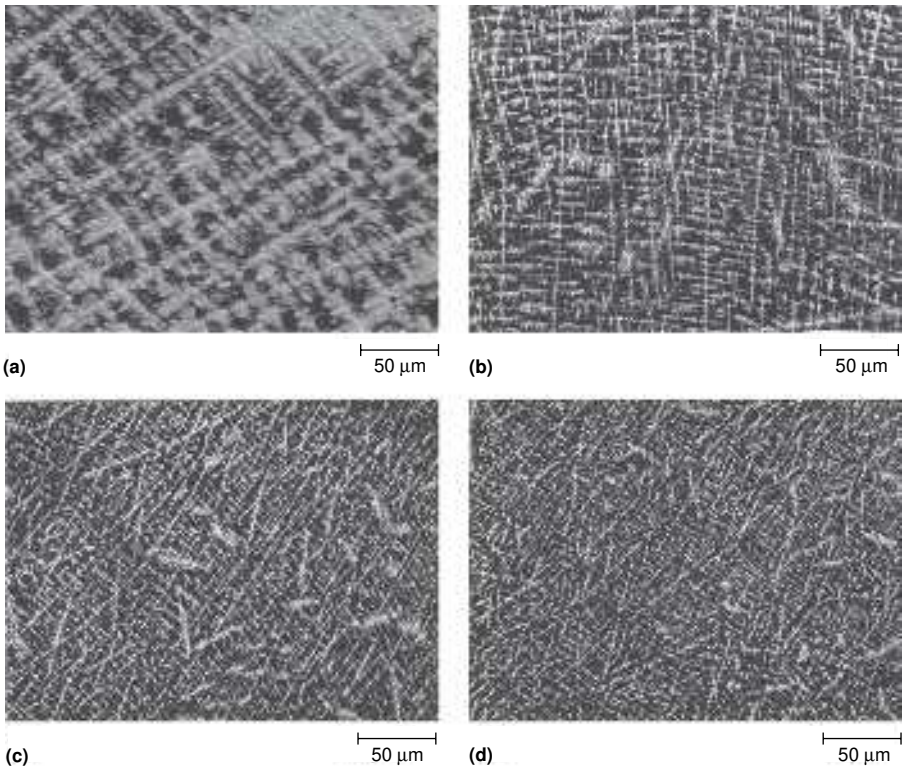

Fig. 9.20 Remnants of interdendritic segregation in 10V45 steel hot rolled to reduction ratios of (a) 7:1, (b) 10:1, (c) 27:1, and (d) 49:1. Transverse sections, picric acid-sodium tridecylbenzene etch, light micrographs. Courtesy of J. Dyck. Source: Ref 9.58

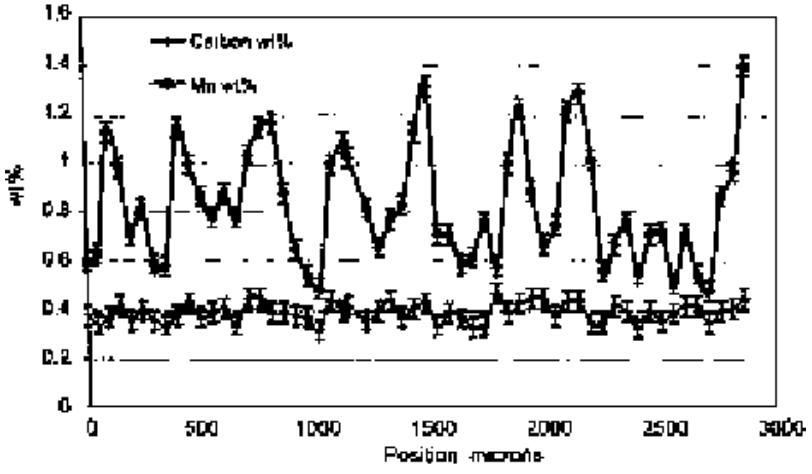

Fig. 9.21 Variations in Mn and C concentrations across a quench-and-tempered 4140 steel bar, 95.25 mm (3.75 in.) in diam, and containing nominally 0.40% C and 1.0% Mn. Electron microprobe analysis. Courtesy of J. Black. Source: Ref 9.59

atom diffusivity. The gradients in carbon content are small, consistent with its rapid interstitial-atom diffusivity, and may be related to the effect of manganese on the activity of carbon, as proposed by Kirkaldy et al. (Ref 9.60). Manganese lowers the activity of carbon, therefore effectively lowering its concentration, and therefore manganese-rich regions would tend to attract carbon. Chromium, similarly, lowers carbon activity, while phosphorus, silicon, and nickel raise carbon activity causing rejection of carbon from regions rich in these elements. Steels are multicomponent alloys, and all elements segregate to some degree. Figure 9.22 shows variations in manganese, chromium, and nickel across an 8617H steel bar, containing by heat analysis 0.18% C, 0.82% Mn, 0.52% Cr, and 0.44% Ni (Ref 9.59).

The residual variations in chemistry due to interdendritic segregation depend on steel composition, the initial as-solidified dendritic structure, and time and temperature of soaking and hot rolling. The latter conditions reduce the intensity of segregation but because of the sluggish diffusivity of substitutional alloying elements, long-time homogenizing treatments at high temperatures are required to eliminate chemical variations. Generally, commercial processing of steels is not sufficient to completely eliminate the chemical gradients that produce banding.

Banded Microstructures

Banded microstructure, or *banding,* is the microstructural condition manifested by alternating bands of quite different microstructures aligned

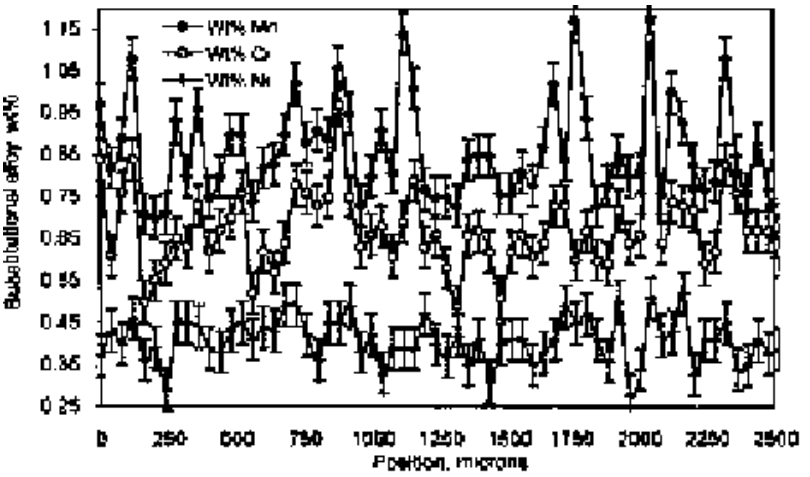

Fig. 9.22 Variations in Mn, Cr, and Ni concentrations across a hot-rolled bar of 8617H steel, 26.2 mm (1 in.) in diameter, and containing by heat analysis 0.82% Mn, 0.52% Cr, and 0.44% Ni. Wavelength dispersive analysis in SEM. Courtesy of J. Black. Source: Ref 9.59

parallel to the rolling direction of steel products. The root cause of banding is remnant interdendritic segregation, as discussed previously, and although that segregation is invariably present, banding may not develop, depending on austenite grain size and cooling conditions that control composition-dependent austenite transformation to other phases. For example, if cooling is rapid enough to form martensite in regions with high and low segregated compositions, the microstructure will be completely martensitic and banding will not result. The only evidence of composition variations might be small etching differences of the martensite formed in the different layers.

Figures 9.23 and 9.24 show, respectively, banding in air-cooled bars of 1020 steel (Ref 9.61) and 10V45 steel (Ref 9.58). The 1020 steel contains 0.22% C, 1.4% Mn and 0.004% S, and the 10V45 steel contains 0.46% C, 0.84% Mn, 0.16% V, and 0.029% S. Alternating bands of ferrite and pearlite are shown in both steels, and the 10V45 steel microstructure has formed in the same specimen in which residual dendritic chemical segregation has been shown in Fig. 9.20(b). The pearlitic areas appear solidly black because the light microscope cannot resolve the fine lamellar ferrite-cementite spacing of the pearlite. Many other good examples of ferrite-pearlite banding are shown in the literature, especially those included in the text by Samuels (Ref 9.62). Banding in hypoeutectoid steels is explained by the effect of alloying elements on the Ar_3 temperature. For example, manganese, because it is often present in high concentrations in steels, is frequently associated with banding. Manganese stabilizes austenite and lowers Ar_3 temperatures. As a result, in steel with high- and low-manganese re-

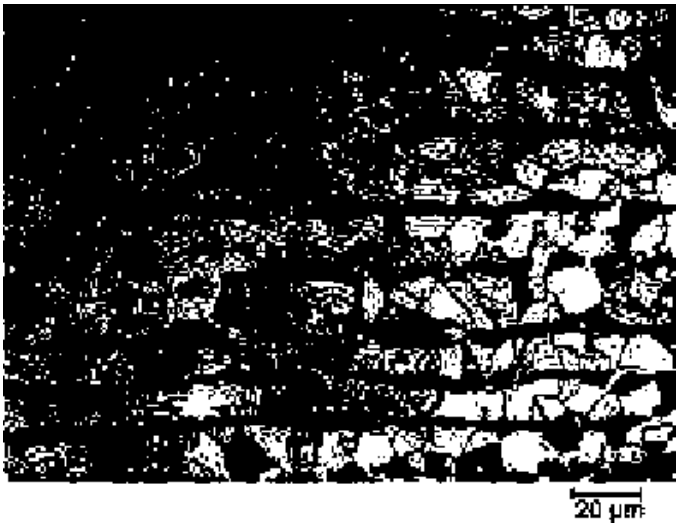

Fig. 9.23 Ferrite (light) and pearlite (dark) bands in 1020 steel hot-rolled plate. Light micrograph, longitudinal section, nital etch. Courtesy of S.W. Thompson. Source: Ref 9.61

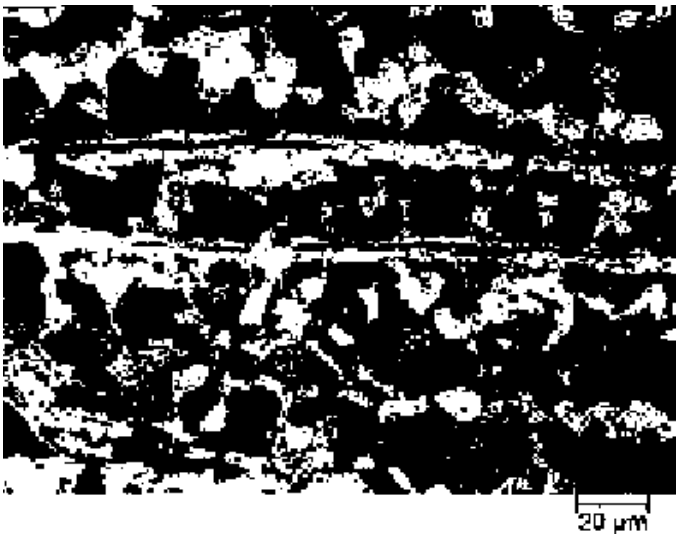

Fig. 9.24 Ferrite bands with MnS inclusions and pearlite bands in 10V45 steel bar hot rolled to a reduction ratio of 27:1. Light micrograph, longitudinal section, nital etch. Courtesy of J. Dyck. Source: Ref 9.58

gions, ferrite forms first in the low-manganese bands. Carbon is rejected from the growing ferrite crystals and concentrates in the austenite with high manganese concentrations where pearlite eventually forms. This process has been described in an article by Thompson and Howell that shows the importance of austenitic grain size to the development of banding (Ref 9.63). When austenite grain size is fine, ferrite nucleates on austenite grain boundaries and triple points in low-manganese regions with high Ar_3 temperatures. These first-formed ferrite grains may impinge as they grow along the rolling direction, creating a "bamboo" ferritic grain structure, but continue to grow normal to the rolling direction, rejecting carbon into high-manganese regions, eventually causing pearlite bands to form. In coarse-grain austenitic microstructures, where the grain size is coarser than the wavelength of segregation, banding may not develop because there are insufficient ferrite nucleation sites in low- manganese regions.

In steels with high concentrations of elongated manganese sulfide inclusions, Kirkaldy et al. have proposed a different mechanism to explain ferrite-pearlite banding (Ref 9.64). The banding shown in Fig. 9.24, where the ferrite has formed around MnS inclusions, is an example of banding produced by this mechanism. Both manganese and sulfur segregate to and are formed in interdendritic regions, and ferrite after hot work would not be expected to nucleate in the high-manganese regions. However, manganese concentrates in MnS with decreasing hot work temperatures, depleting initially high manganese around the inclusions, and stimulating ferrite growth around the inclusions. With the rejection of carbon from the ferrite around the inclusions, pearlite eventually forms in the low-manganese regions.

Most studies of banding have concentrated on hypoeutectoid steels as discussed previously (Ref 9.65), but Verhoeven has examined banding in hypereutectoid steels relative to the beauty of textures produced on the blades of Damascus swords (Ref 9.66). He shows that the textures are due to etching differences of alternate bands of dispersed carbide particles and pearlite, and that small amounts of carbide-forming elements such as vanadium or molybdenum are necessary elements for the banding. The latter elements segregate in interdendritic regions, and after working stabilize banded arrays of spheroidized carbide particles in austenite. These carbide arrays nucleate divorced eutectoid transformation to ferrite and spheroidized cementite particles instead of transformation to the lamellar ferrite-cementite structure of classical pearlite.

The Effect of Banding on Mechanical Properties

Banding may or may not have a significant influence on mechanical properties, and because rolling produces an aligned banded microstructure, is often difficult to separate from the effect of aligned inclusion particles. An early study (Ref 9.67) compared the behavior of a low-carbon steel with banded and homogenized microstructures and found no difference in impact properties below the ductile to brittle transition temperature. However, in impact testing above the transition temperature, both longitudinal and transverse energy absorption were higher in homogenized specimens. Grange (Ref 9.68) studied a split heat of 0.25% C steel, with one part of high purity and the other with sulfur and silicon additions that produced high densities of inclusions. Specimens with and without banding were subjected to tensile and impact testing. Homogenization markedly improved ductile fracture and anisotropy in the clean steel but had little effect on the specimens with high elongated inclusion content. Bands of martensite were sometimes observed in banded specimens and were judged to be deleterious to machining and cold forming operations. Another study (Ref 9.69) of banding and inclusion content in a series of 0.20% C, 1.00% Mn steel with either 0.004 or 0.013% S again showed that inclusions dominated anisotropy and degradation of mechanical properties and that banding had little effect on reduction of area or upper shelf energies. Improvements in properties produced by a high-temperature homogenizing treatment (1315 °C, or 2400 °F, for 10 min) was shown to be a result of coarsening or reduction in aspect ratios of inclusions rather than elimination of banding.

Banding may vary considerably within a given steel section depending on solidification and hot-working conditions, in part because of variations in chemical gradients related to mill-dependent processing. Chemical differences are not sharp and alternate continuously between high and low values because of varying degrees of homogenizing hot work. A recent study has evaluated banding and its effect on tensile properties by produc-

ing laminated specimens that simulate banding with sharp differences in chemistry and systematic variations in band spacings (Ref 9.70–9.72).

Thin sheets of 5140 containing 0.82% Mn and modified 5140 containing 1.83% Mn were alternately stacked and hot- and cold-rolled to produce specimens with spacings between the high- and low-manganese regions of 320, 160, 80, 40, and 20 μm. The difference in manganese was the only difference in composition across the laminated specimens. Tensile specimens were then removed from the various laminated specimens, austenitized at 850 °C (1560 °F) for 20 minutes and cooled at rates of 83 °C/s (149 °F/s), 5.1 °C/s (9.2 °F/s), 2.6 °C/s (4.7 °F/s), 0.6 °C/s (1.1 °F/s), 1 °C/ min (1.8 °F/min), and 0.5 °C/min (0.9 °F/min). The cooling rates were calculated from the rates between 704 and 538 °C (1268 and 970 °F). Specimens were not tempered after cooling. Figure 9.25 shows calculated continuous cooling transformation diagrams for the low- and high-manganese steels (Ref 9.73) and shows dramatic differences in cooling transforma-

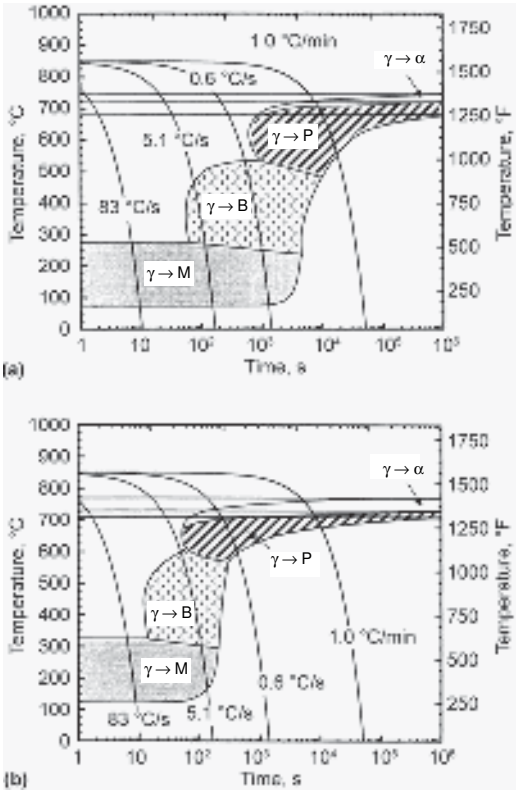

Fig. 9.25 Continuous cooling transformation diagrams for 5140 steel containing (a) 1.83% Mn and (b) 0.82% Mn. Courtesy of T. Majka. Source: Ref 9.70

tions and hardenability related to differences in manganese content. For example, at the relatively low rate of cooling of 0.6 °C/s (1 °F/s) the high-manganese steel would be transformed completely to bainite and the low-manganese steel would be transformed completely to ferrite and pearlite.

Figure 9.26 shows variations in banded microstructures in the laminated high- and low-manganese specimens with various band spacings and all cooled at the same rate of 0.6 °C/s (1 °F/s). Bainitic areas appear grey, ferrite and pearlite regions appear as a mix of white (ferrite) and black (pearlite) features, and fully pearlitic areas appear black. The various microstructures are consistent with changes in transformations shown in Fig. 9.25, but a striking feature of the banded structures is the fully pearlitic zone that appears to separate the high- and low-manganese bands.

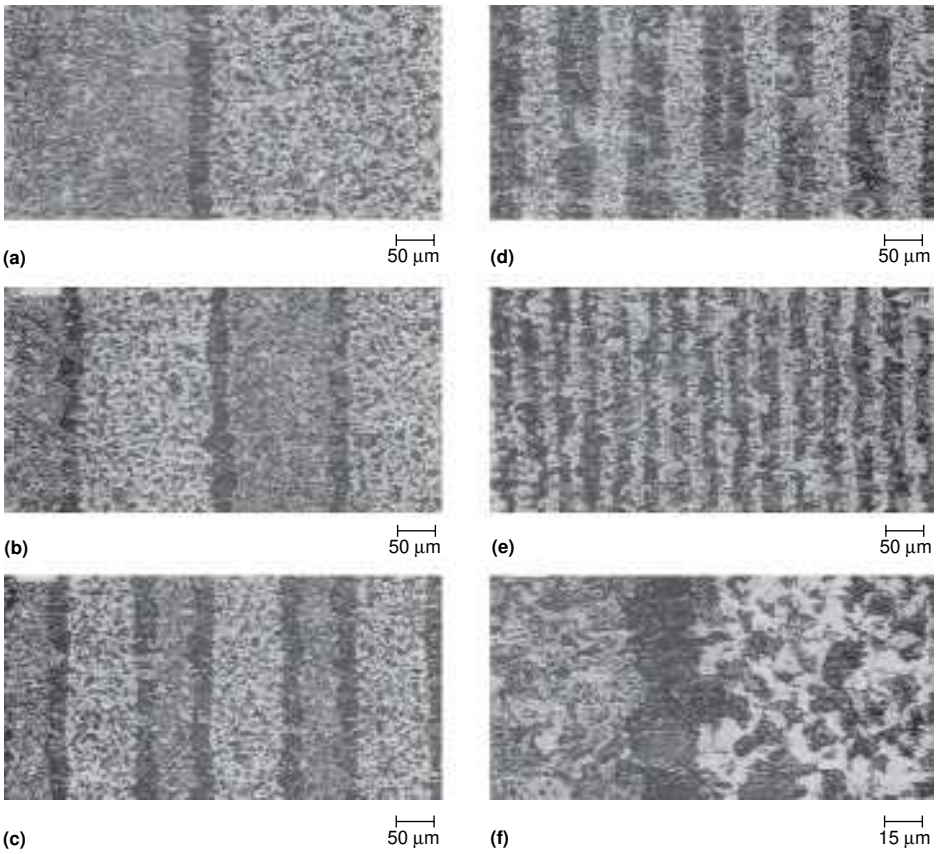

Fig. 9.26 Microstructures of laminated high- and low-Mn 5140 steel bands with band spacings of (a) 320, (b) 160, (c) 89, (d) 40, and (e) 20 μm after cooling at 0.6 °C/s. (1 °F/s) (f) The interface of 320 μm bands at higher magnifications. Light micrographs, nital etch. Courtesy of T. Majka. Source: Ref 9.70

The pearlitic band has been shown to result from carbon rejection into the high-manganese layer from the first ferrite formed in the low-manganese bands (Ref 9.72). A continuous layer of pearlite forms, and grows in the high-manganese layer. In view of the constant cooling conditions, the growth of the pearlite is limited by carbon diffusion to a thickness of 20 to 30 μm in all specimens. Thus, in the specimens with the largest bandwidth, the pearlite band is only a small fraction of the microstructure, while in the specimen with the finest band spacing of 20 μm the pearlite has grown to the full width of the high-manganese band and occupies one-half of the microstructure.

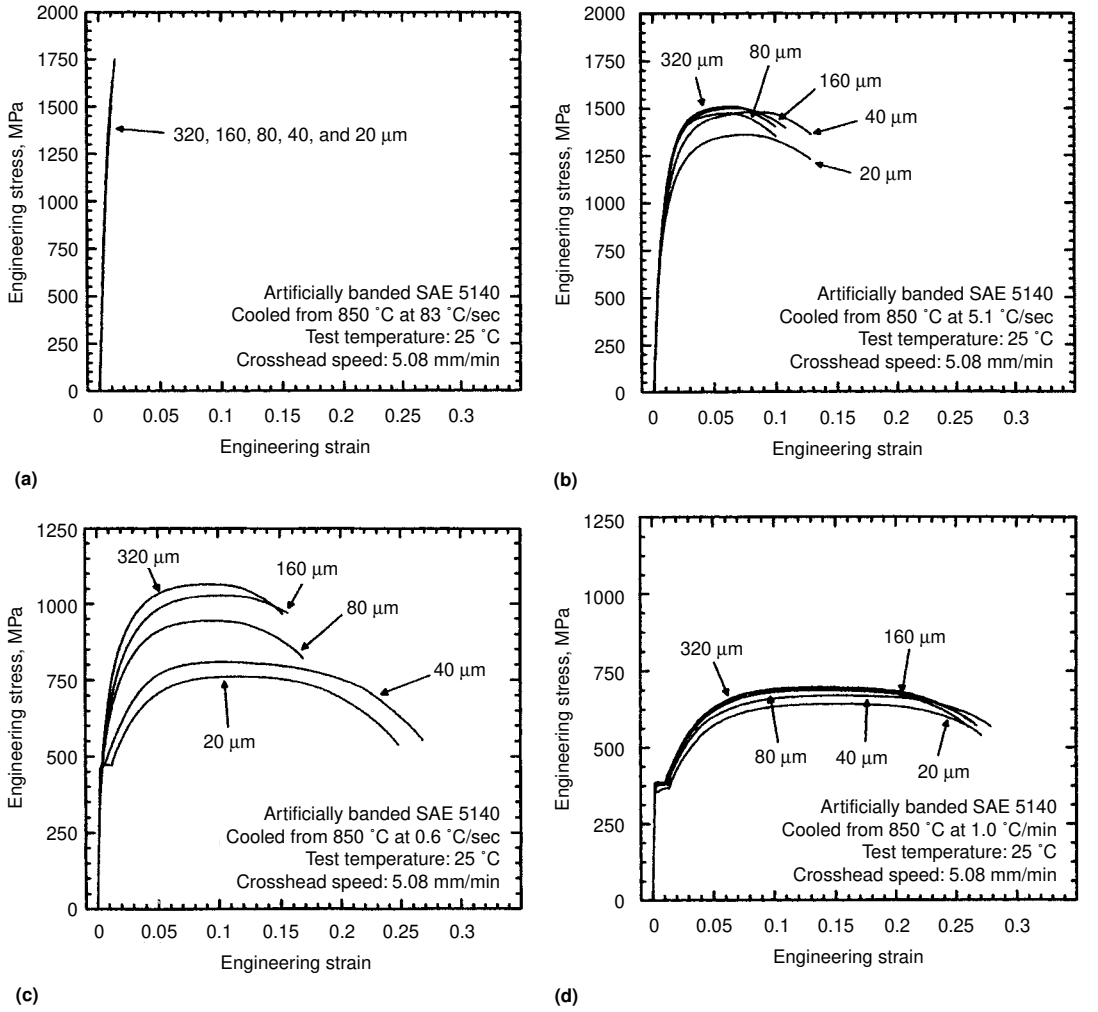

Fig. 9.27 Engineering stress-strain curves for artificially banded 5140 steel with various band spacing after cooling at (a) 83 °C/s (150 °F/s), (b) 5.1 °C/s (9.2 °F/s), (c) 0.6 °C/s (1 °F/s), and (d) 1.0 °C/min (1.8 °F/min). Courtesy of T. Majka. Source: Ref 9.70

Figure 9.27 shows engineering stress-strain curves for the laminated high- and low-manganese specimens with various band widths cooled at various rates. All of the specimens quenched at 83 °C/s (150 °F/s), produced by oil quenching, were completely transformed to martensite, as indicated in Fig. 9.25, and showed no evidence of banding except for slight etching differences. The stress-strain curves for these specimens show brittle behavior (Fig. 9.27a), as a result of quench embrittlement and intergranular fracture of the high-manganese bands, as described in Chapter 19, "Low Toughness and Embrittlement Phenomena in Steels." Tempering alleviates the effects of quench embrittlement. The specimens cooled at intermediate rates showed the greatest variation in deformation behavior (Fig. 9.27b, c) as a result of various layered mixtures of bainite, ferrite, and pearlite formed in response to manganese variations. Specimens cooled at the lowest rates (Fig. 9.27d) show high uniformity in tensile behavior because of complete transformation to ferrite and pearlite in both the high- and low-manganese bands.

In summary, the extent of banding, derived from residual interdendritic segregation present to some degree in all commercial cast and wrought steels, is very much dependent on alloy composition, section size, mill processing, and heat treatment conditions. Banding may or may not have a detrimental effect on intermediate stages of processing or on finished mechanical properties. If questions arise, banding and its effects merit appropriate evaluation on a case-by-case basis.

REFERENCES

9.1 W.R. Irving, *Continuous Casting of Steel,* Book 584, The Institute of Materials, London, 1993

9.2 A.W. Cramb, New Steel Casting Processes for Thin Slabs and Strip, *Iron and Steelmaker,* Vol 15 (No. 7), 1988, p 45–60

9.3 S. Ge, M. Isac, and R. I. L. Guthrie, Progress of Strip Casting Technology for Steel: Historical Developments, *ISIJ Int.,* Vol. 52, 2012, p 2109–2122

9.4 R. Kiessling with the collaboration of N. Lange, *Non-Metallic Inclusions in Steel,* Parts I–IV, Book 194, The Institute of Materials, London, 1978

9.5 L. Zhang and B.G. Thomas, State of the Art in Evaluation and Control of Steel Cleanliness, *ISIJ Int.,* Vol 43, 2003, p 271–291

9.6 P. Kaushik and H. Yin, Thermodynamics, Engineering and Chracterization of Inclusions in Advanced High-Strength Steels, *Iron and Steel Technology,* December 2012, p 165–185

9.7 Special Issue on Fundamentals and Applications of Non-metallic Inclusions in Solid Steel, *ISIJ Int.*, Vol 51, 2011, p 1943–2075

9.8 A. Nicholson and D.S. Thornton, Steelmaking and Non-Metallic Inclusions, *Constitution and Properties of Steels,* F.B. Pickering, Ed.,

Vol 7, *Mater. Sci.Technol.,* VCH Weinheim, Germany, 1992, p 95–146

9.9 R.J. Fruehan, *Ladle Metallurgy Principles and Practices,* ISS, Warrendale, PA, 1985

9.10 *Second Canada-Japan Symposium on Modern Steelmaking and Casting Techniques,* J.J. Jonas, J.D. Boyd, and N. Sano, Ed., TMS of the Canadian Institute of Mining, Metallurgy and Petroleum, Montreal, Quebec, Canada, 1994

9.11 B.G. Thomas, Modeling of the Continuous Casting of Steel—Past, Present, and Future, *Metall. and Mater. Trans. B,* Vol 33B, 2002, p 795–812

9.12 S. Yang, L. Zhang, L. Sun, J. Li, and K. Peaslee, Investigation on MgO-Al_2O_3-Based Inclusions in Steels, *Iron & Steel Technology*, August 2012, p 245–258

9.13 T. N. Baker, Y. Li, J. A. Wilson, A. J. Craven, and D. N. Crowther, Evolution of precipitates, in particular cruciform and cuboid particles, during simulated direct charging of thin slab cast vanadium microalloyed steels, *Mater. Sci.Technol.,*Vol 20, 2004, p 720–730

9.14 *Sulfide Inclusions in Steel,* J.J. DeBarbadillo and E. Snape, Ed., American Society for Metals, 1974

9.15 W.J. McG. Tegart and A. Gittins, The Role of Sulfides in the Hot Workability of Steels, in Ref 9.9, p 198–211

9.16 T.J. Baker, Use of Scanning Electron Microscopy in Studying Sulphide Morphology on Fracture Surfaces, in Ref 9.9, p 135–158

9.17 *Titanium Technology in Microalloyed Steel*, T. N. Baker, Editor, The Institute of Materials, 1997

9.18 S. Abraham, R. Bodnar, and J. Raines, Inclusion Engineering and the Metallurgy of Calcium Treatment, *Iron and Steel Technology,* July 2014, p 57–69

9.19 G.C. Yerby, "The Effects of Direct Quenching after Forging on the Mechanical Properties of Medium Carbon Steel," M.S. thesis, Colorado School of Mines, Golden, CO, 1996

9.20 J.I. Goldstein et al., *Scanning Electron Microscopy and X-Ray Microanalysis,* Plenum Press, 1981

9.21 "Standard Test Methods for Determining the Inclusion Content of Steels," ASTM Designation E45-97 (reviewed 2002), ASTM International, Conshohocken, PA, 2003

9.22 Special Issue on " Diversified Estimation of Nonmetallic Inclusion Particles in Steel", *ISIJ Int.,*Vol 53, 2013, p1905–2012

9.23 P. Kaushik, H. Pielet, and H. Yin, Inclusion Characterization: A Tool for Measurement of Steel Cleanliness and Process Control, *Iron and Steel Technology,* November 2009, p 82–99

9.24 S. S. Abraham, J. Raines, and R. Bodnar, Development of an Inclusion Characterization Methodology for Improving Steel Product Cleanliness, *Iron and Steel Technology*, February 2014, p 219–234

9.25 Y. Murakami, *Metal Fatigue: Effects of Small Defects and Nonmetallic Inclusions*, Elsevier, Amsterdam, 2002
9.26 S. Beretta, C. Anderson, and Y. Murakami, Extreme value models for the assessment of steels contain multiple types of inclusions, *Acta Mater.*, Vol 54, 2006, p 2277–2289
9.27 *Standard Practice for Extreme Value Analysis of Nonmetallic Inclusions in Steel and Other Microstructural Features, E2283-08,* American Society for Testing and Materials, West Conshohocken, PA, 2008
9.28 A. Nissan, *The Effect of Microstructure and Induction Processing on Fatigue Performance and Crack Initiation of Induction Hardened Bar Steel*, PhD Thesis, Colorado School of Mines, Golden, CO, 2012
9.29 *Bearing Steels: The Rating of Nonmetallic Inclusions,* ASTM, Philadelphia, PA, 1975
9.30 W.C. Leslie, Inclusions and Mechanical Properties, *ISS Transactions* Vol 2, p 1–24, 1983
9.31 *Second International Symposium on the Effects and Control of Inclusion and Residuals in Steels,* The Canadian Institute of Mining and Metallurgy, Montreal, Quebec, Canada, 1986
9.32 *Inclusions and Their Influence on Material Behavior,* R. Rungta, Ed., ASM International, 1988
9.33 M.A. Linaza, J.L.Romero, I. San Martin, J.M. Rodriquez-Ibabe, and J.J. Urcola, Improvement of Toughness by Stopping Brittle Processes Nucleated in Ceramic Particles Through Thermomechanically Optimised Microstructures in Engineering Steels, in *Fundamentals and Applications of Microalloying Forging Steels,* C.J. Van Tyne, G. Krauss, and D.K. Matlock, Ed., TMS, Warrendale, PA, 1996, p 311–325
9.34 C.A. Apple, The Relationship between Inclusions and the Machinability of Steel, *Mechanical Working and Steel Processing Proceedings,* Vol XXVII, ISS, 1989, p 415–429
9.35 *Materials Issues in Machining-II and the Physics of Machining Processes-II,* D.A. Stephenson and R. Stevenson, Ed., TMS, Warrendale, PA, 1994
9.36 R. Edwards, *Cutting Tools,* Book 583, The Institute of Materials, London, 1993
9.37 ASTM 399 83, "Standard Test Method for Plane-Strain Fracture Toughness of Metallic Materials," Vol 03.01, 1983, *Annual Book of Standards,* ASTM, p 526
9.38 H.W. Paxton, The Metallurgy of Steels for Large Diameter Linepipe, *Alloys for the Eighties,* Climax Molybdenum Co., Greenwich, CN, 1980, p 185–211
9.39 G.R. Speich and W.A. Spitzig, Effect of Volume Fraction and Shape of Sulfide Inclusions on Through-Thickness Ductility and Impact

Energy of High-Strength 4340 Plate Steels, *Metall. Trans. A,* Vol 13A, 1982, p 2239–2257

9.40 M.C. Flemings, *Solidification Processing,* McGraw-Hill Book Company, 1974

9.41 H.D. Brody and M.C. Flemings, Solute Redistribution in Dendritic Solidification, *Trans. AIME,* Vol 236, 1966, p 615–624

9.42 R.M. Fisher, G.R. Speich, L.J. Cuddy, and H. Hu, *Proceedings of the Darken Conference, Physical Chemistry in Metallurgy,* U.S. Steel, Monroeville, PA, 1976, p 463–488

9.43 T.F. Brower and M.C. Flemings, Formation of the Chill Zone in Ingot Solidification, *Trans. TMS-AIME,* Vol 239, 1967, p 216–219

9.44 R.E. Reed-Hill, *Physical Metallurgy Principles,* 2nd ed., D. Van Nostrand Company, New York, 1973, p 568–608

9.45 M.C. Flemings and G.E. Nereo, Macrosegregation Part I, *Trans. TMS-AIME,* Vol 239, 1967, p 1449–1461

9.46 M. Rappaz, I. Farup, and J.-M. Drezet, Study and Modeling of Hot Tearing Formation, *Proceedings Merton C. Flemings Symposium,* R. Abbaschian, H. Brody, and A. Mortenson, Ed., TMS, Warrendale, PA, 2001, p 213–238

9.47 E.J. Schultz, J.J. Moore, G. Krauss, D.K. Matlock, R. Frost, and J. Thomas, The Effect of the Hot Roll Reduction Ratio on the Axial Fatigue of Continuously Cast and Hardened 4140 Steel, *34th Mechanical Working and Steel Processing Proceedings,* Vol XXX, ISS, 1992, p 309–319

9.48 I.V. Samarasekera, Discovery—The Cornerstone of Research in the Continuous Casting of Steel Billets, *The Brimacombe Memorial Symposium,* Canadian Institute of Mining, Metallurgy and Petroleum, Montreal, Canada, p 399–419

9.49 T.Z. Kattamis and P.W. Voorhees, Coarsening of Solid-Liquid Mixtures: A Review, *Proceedings Merton C. Flemings Symposium,* R. Abbaschian, H. Brody, and A. Mortenson, Ed., TMS, Warrendale, PA, 2001, p 119–128

9.50 A.W. Cramb, *Casting of Near Net Shape Products,* TMS, Warrendale, PA, 1988, p 673–682

9.51 E. Essadiqi, L.E. Collins, M.T. Shehata, and L.K. Chiang, Thin Slab Casting Simulation of 1020 C Steel with Liquid Core Reduction, *2nd Canadian-Japan Symposium on Modern Steelmaking and Casting Techniques,* J.J. Jonas, J.D. Boyd, and N. Sano, Ed., Canadian Institute of Mining, Metallurgy and Petroleum, Montreal, Canada, 1994, p 251–264

9.52 T. Emi, Developments in Continuous Casting at Macro Steel Mills and Future Outlook, *The Brimacombe Memorial Symposium,* Canadian Institute of Mining, Metallurgy and Petroleum, Montreal, Canada, 2000, p 23–38

9.53 W.R. Irving and D.V. Barradell, *Process Control in the Steel Industry,* G. Carlsson and H. Nordberg, Ed., Uddeholm Research, Haggfors, Sweden, 1986, p 7–53
9.54 C.V. White, G. Krauss, and D.K. Matlock, Solidification Structure and the Effects of Hot Reduction in Continuously Cast Steels for Bars and Forgings, *Iron and Steelmaker,* Vol 25 (No. 9), 1998, p 73–79
9.55 R.H. McCreery, Effects of Reduction on the Minimill Steel, *Metal Progress,* 1984, p 29–31
9.56 S. Gunnarson, Effect of Strand Casting on Distortion of Carburized Crown Wheels, *Härt.–Tech. Mitt.,* Vol 46, 1991, p 216
9.57 H. Mallender, Dimension and Shape Changes in Carburizing, *Einsatzharten,* J. Grosch and J. Wunning, Ed., AWT, 1989, p 285–303
9.58 J. Dyck, R.H. Frost, D.K. Matlock, G. Krauss, W.E. Heitmann, and D. Bhattacharya, Effects of Hot Reduction and Bar Diameter on Torsional Fatigue of a Strand-Cast Microalloyed Steel, *Mechanical Working and Steel Processing Proceedings,* ISS, 1988, p 83–94
9.59 J. Black, "Modeling of the Effects of Chemical Segregation on Phase Transformations in Medium-Carbon Bar Steels," M.S. thesis, Colorado School of Mines, Golden, CO, 1998
9.60 J.S. Kirkaldy, J. von Destinon-Forstmann, and R.J. Brigham, Simulation of Banding in Steel, *Can. Metall. Q.,* Vol 1, 1962, p 62–81
9.61 S.W. Thompson and G. Krauss, Precipitation and Fine Structure in Medium-Carbon Vanadium and Vanadium/Niobium Microalloyed Steels, *Metall. Trans. A,* Vol 20A, 1989, p 2279–2288
9.62 L.E. Samuels, *Light Microscopy of Carbon Steels,* ASM International, 1999, p 110–124
9.63 S.W. Thompson and P.R. Howell, Factors Influencing Ferrite/Pearlite Banding and Origin of Large Pearlite Nodules in a Hypoeutectoid Plate Steel, *Mater. Sci. Technol.,* Vol 8, 1992, p 777–784
9.64 J.S. Kirkaldy, R.J. Brigham, H.A. Domain, and R.G. Ward, *Can. Metall. Q.,* Vol 2, 1963, p 233–241
9.65 G. Krauss, Solidification, Segregation, and Banding in Carbon and Alloy Steels, *Metall. Trans. B,* Vol 34B, 2003, p 781–792
9.66 J.D. Verhoeven, *Journal Materials Engineering Performance,* Vol 9, 2000, p 286–295
9.67 W.S. Owen, M. Cohen, and B.L. Averbach, The Influence of Ferrite Banding on the Impact Properties of Mild Steel, *Weld. J., Welding Research Supplement,* 1958, p 368s–374s
9.68 R.A. Grange, Effect of Microstructural Banding in Steel, *Metall. Trans.,* Vol 2, 1971, p 417–426
9.69 W.A. Spitzig, Effect of Sulfide Inclusion Morphology and Pearlite Banding on Anisotropy of Mechanical Properties in Normalized C-Mn Steels, *Metall. Trans. A,* Vol 14A, 1983, p 271–282

9.70 T.F. Majka, "An Analysis of Tensile Deformation Behavior and Microstructural Evolution in Artificially Banded SAE 5140," M.S. thesis, Colorado School of Mines, Golden, CO, 2000

9. 71 T.F. Majka, D.K, Matlock, G. Krauss, and M. Lusk, An Analysis of Tensile Deformation Behavior and Microstructural Evolution in Artificially Banded SAE 5140, *42nd MWSP Conf. Proceedings,* ISS, Warrendale, PA, 2000, p 75–87

9.72 T.F. Majka, D.K. Matlock, and G. Krauss, Development of Microstructural Banding in Low Alloy Steel with Simulated Mn Segregation, *Metall. and Mater. Trans. A,* Vol 33A, 2002, p 1627–1637

9.73 B. Sundman, B. Jansson, and J.O. Anderson, *CALPHAD (Calculation of Phase Diagrams): A Comprehensive Guide,* Elsevier Science, New York, 1985, p 153–190

CHAPTER **10**

Isothermal and Continuous Cooling Transformation Diagrams

THIS CHAPTER DESCRIBES the transformation diagrams that have been developed to define the progress of diffusion-controlled phase transformations of austenite to various mixtures of ferrite and cementite. Both isothermal and continuous cooling transformation diagrams are described, and references to atlases containing collections of these diagrams for a variety of steels are given. The availability of these diagrams makes possible the selection of steels and the design of heat treatments that will either produce desirable microstructures of ferrite and cementite or avoid diffusion-controlled transformations, and thereby produce martensitic microstructures of maximum hardness.

Isothermal Transformation Diagrams

Diagrams that define the transformation of austenite as a function of time at constant temperatures are referred to as isothermal transformation (IT) diagrams or time-temperature-transformation diagrams. An IT diagram for 1080 steel has already been presented in Fig. 4.3 of Chapter 4, "Pearlite, Ferrite, and Cementite," in connection with the description of the nucleation and growth kinetics of pearlite formation. The IT diagram for eutectoid steel with negligible alloy content is quite straightforward. Only pearlite forms above the nose of the IT diagram, and only bainite forms below the nose. The curves defining the beginning and end of pearlite or bainite formation are the major features of the diagram.

Steels with carbon content above or below the eutectoid composition and alloy steels have more complex transformation diagrams. Figure 10.1

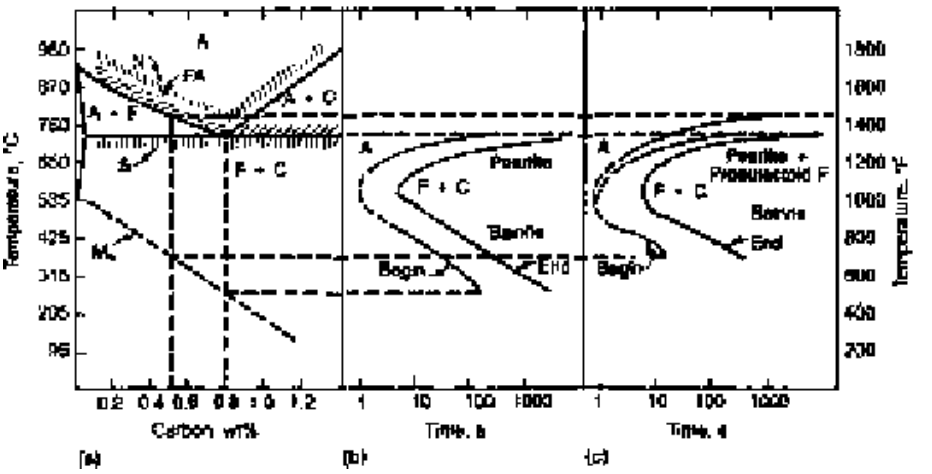

Fig. 10.1 Relationship to (a) iron-carbon diagram of isothermal transformation diagrams of (b) eutectoid steel and (c) steel containing 0.5% C. The regions in (a) identified as N, FA, and S are temperature ranges for normalizing, full annealing, and spheroidizing heat treatments, respectively, as discussed in Chapter 13, "Normalizing, Annealing, and Spheroidizing Treatments; Ferrite/Pearlite and Spherical Carbides," in this book. Source: Ref 10.1

shows schematic IT diagrams for eutectoid steel and a hypoeutectoid plain carbon steel containing nominally 0.5% C. Also shown is their relationship to the iron-carbon diagram. The beginning and ending curves for pearlite formation approach the Ae_1 temperature at very long transformation times and move to shorter times with decreasing transformation temperature for reasons discussed in Chapter 4, "Pearlite, Ferrite, and Cementite," in this book. The IT diagram for the hypoeutectoid steel has an extra curve to mark the beginning of proeutectoid ferrite formation. As indicated in Fig. 10.1, the latter curve approaches the Ae_3 temperature for the 0.5% C steel with increasing transformation time. Hypoeutectoid steels with lower carbon contents would have higher Ac_3 temperatures and therefore expanded regions of proeutectoid ferrite coexistence with austenite. Similarly, hypereutectoid steels would have IT diagrams with curves for the beginning of proeutectoid cementite formation.

Figure 10.1 shows other differences between the IT diagrams for eutectoid and hypoeutectoid steels. One difference is in M_s temperatures: the lower the carbon content, the higher the M_s temperature. Another difference is the acceleration of austenite transformation to proeutectoid ferrite with decreasing carbon content, as shown by the position of the nose of the hypoeutectoid steel at shorter times relative to that of the eutectoid steel. The dotted lines in Fig. 10.1(b) and (c) reflect experimental uncertainty in the exact positions of the beginning of transformation curves.

The IT diagrams have been produced by metallographic examination of series of specimens held for various times at various temperatures between Ae_3 or A_{cm} and M_s. More than a hundred specimens are often re-

quired to determine a complete IT diagram for a given steel (Ref 10.2). The procedure used is to heat the metallographic specimens in the single-phase austenite field for a sufficient time, usually 1 h, to produce a homogeneous austenite. The austenitizing treatment sets the austenite grain size and the extent of carbide solution. Both of the latter microstructural factors may influence the course of isothermal transformation of austenite, and therefore, it is necessary to record the austenitizing temperature used to determine the IT. Once austenitizing is complete, a series of specimens is cooled rapidly, usually by immersion in a molten salt bath, to a given IT temperature. The specimens are held for various times and then quenched to room temperature. The specimens held for the shortest times will transform completely to martensite on cooling because there is insufficient time at the hold temperature for any diffusion-controlled transformation. The austenite in specimens held for longer periods of time would transform to ferrite, cementite, pearlite, and/or bainite, depending on temperature and the composition of the steel. The detection of the first small amounts of these phases in specimens largely transformed to martensite establishes the time for the beginning of transformation at a given temperature. With longer holding times at the transformation temperature, more and more of the austenite transforms to ferrite, cementite, or mixtures of ferrite and cementite, and less of the specimen is martensitic after quenching to room temperature. Finally, after holding for a sufficiently long period of time at temperature, transformation of the austenite is complete prior to quenching, and the time for the end of transformation is established. When the process is repeated for a number of temperatures, the complete IT diagram is established.

Although metallographic examination of specimens isothermally held for various times is the most accurate method of determining IT diagrams (particularly with respect to differentiating regions of proeutectoid ferrite, cementite formation, and pearlite or bainite formation), other experimental techniques are also useful. Hardness measurements, for example, reflect the phases present in transformed specimens. A list of the phases in the order of increasing hardness would include ferrite, pearlite, bainite, and martensite. Hardness would therefore be a maximum for microstructures produced by quenching after short isothermal holding times to a minimum for specimens held long enough for complete isothermal austenite transformation. Beginning and end of transformation could therefore be established by following hardness changes as a function of isothermal holding time. Dilatometry, an experimental technique that measures changes in length of specimens, has also been used to determine IT diagrams. The application of this technique is possible because of the expansion that accompanies the transformation of austenite to ferrite or ferrite-carbide mixtures, as discussed in Chapter 3, "Phases and Structures," in this book. Dilatometry has been used by German investigators (Ref 10.3) for IT diagram determination. By cross checking with metal-

lographic examination, dilatometry has been found to indicate the beginning of transformation after approximately 3% of the austenite has been transformed, as compared with the ability of microstructural examination to reveal the first 1% of austenite transformation. Figure 10.2 compares IT diagrams determined by dilatometry and metallography and shows the greater sensitivity of the latter technique for IT diagram determination.

Continuous Cooling Transformation Diagrams

Many of the heat treatments performed on steel are carried out by continuous cooling rather than by isothermal holding, and as a result, diagrams that represent the transformation of austenite on cooling at various rates have been developed. The latter type of diagram for a given steel is referred to as a continuous cooling (CC) diagram or cooling transformation (CT) diagram (Ref 10.4). Generally, continuous cooling shifts the beginning of austenite transformation to lower temperatures and longer times. Figure 10.3 shows a derived (i.e., not experimentally determined) CT diagram for eutectoid steel and its relationship to the IT diagram (Ref 10.2, 10.5). Also shown in the top part of Fig. 10.3 is a Jominy specimen. The latter specimen is water quenched only at one end, and therefore, the

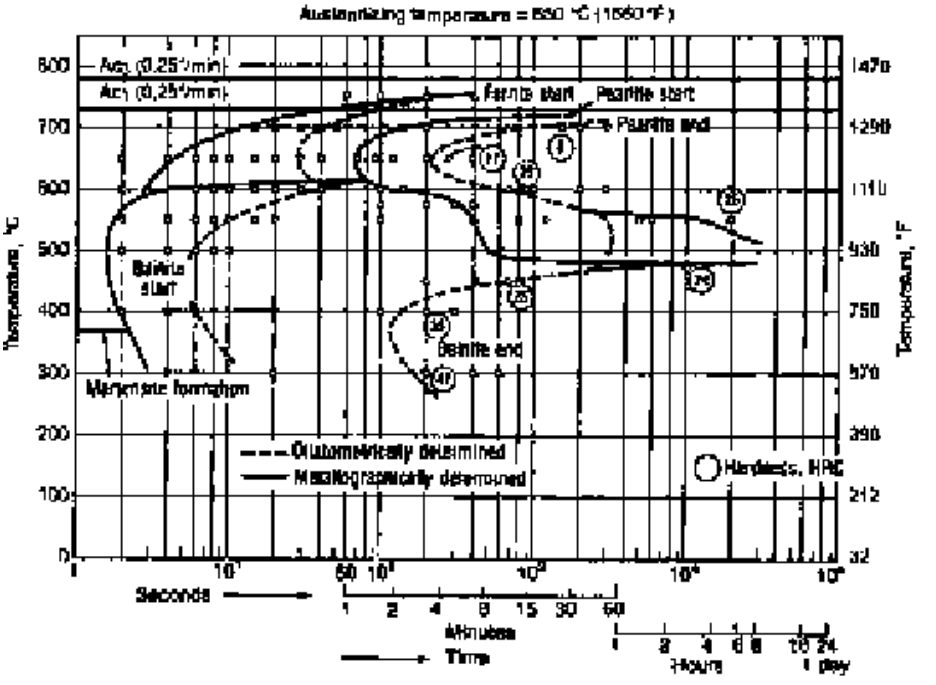

Fig. 10.2 Comparison of isothermal transformation diagram for steel with German designation 42CrMo4 (0.38% C, 0.99% Cr, and 0.16% Mo) determined by dilatometry (dashed lines) and metallography (continuous lines). Source: Ref 10.3

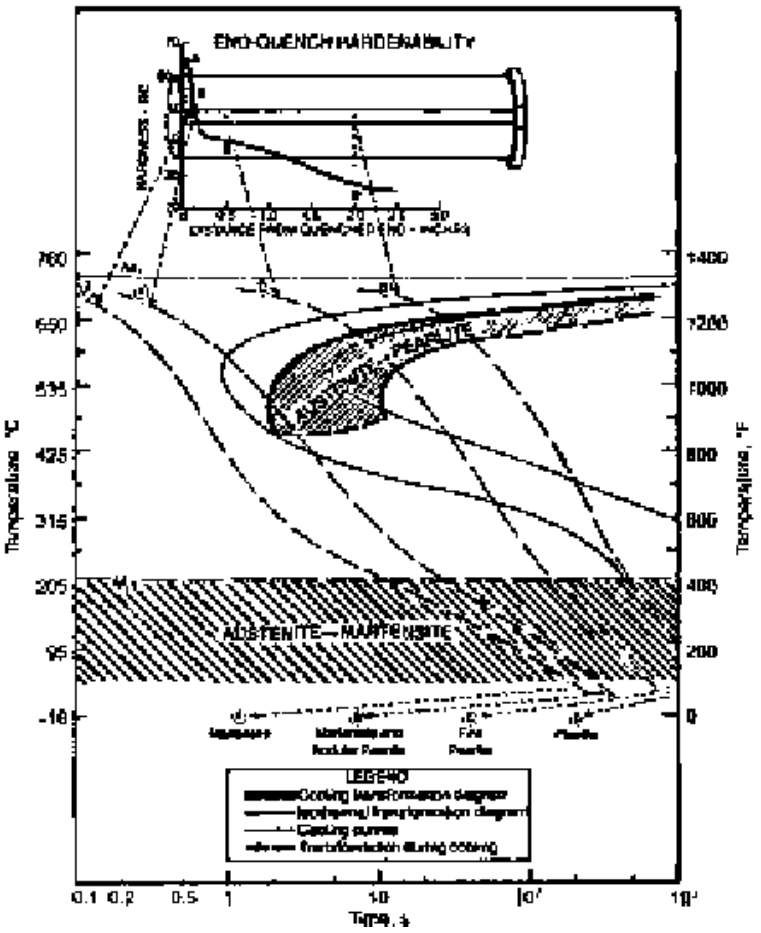

Fig. 10.3 Relationship of cooling transformation (CT) (heavy lines) and isothermal transformation (light lines) diagrams of eutectoid steel. Also shown are Jominy end-quench specimen and four cooling rates from different positions on the specimen superimposed on the CT diagram. Source: Ref 10.5

cooling rate is a maximum at that end and drops with increasing distance into the specimen. The cooling rates at various locations of a Jominy specimen have been measured by attachment of thermocouples, and four of these cooling rates have been superimposed on the lower part of Fig. 10.3. With decreasing cooling rate or increasing distance from the quenched end of the Jominy specimen, the austenite transforms to microstructures containing increasingly greater quantities of pearlite. The decreased hardness associated with the replacement of martensite by pearlite with decreasing cooling rate is also shown in the top part of Fig. 10.3.

In general, especially for hardenable alloy steels, attempts to derive CT diagrams from IT diagrams without experimental verification have proved unsatisfactory (Ref 10.4). For example, the bainite transformation range is

dominated by pearlite formation in eutectoid steel and has not been included in the derived curve of Fig. 10.3. The following list of CT characteristics with no IT counterparts has been published (Ref 10.5):

- The depression of the M_s temperature at slow cooling rates
- The tempering of martensite that takes place on cooling from the M_s temperature to approximately 204 °C (400 °F)
- The prevalence of bainite as a transformation product
- The extraordinary variety of microstructures encountered
- The unexpected occurrence of ferrite in a high-carbon steel such as AISI 52100

The following comments expand on the observations in the preceding list. The depression of the M_s temperature with decreasing cooling rate in a given steel is due to the rejection of carbon into austenite as ferritic or bainitic structures form on cooling. The untransformed austenite therefore has higher carbon concentration and a lower M_s temperature, as discussed in Chapter 5, "Martensite," in this book. The tempering of martensite on cooling is referred to as autotempering and is most common in low-carbon steels with high M_s temperatures. The latter situation results in the presence of martensite over a large temperature range on cooling. During this period of the quench, carbon has sufficient mobility to form the carbides characteristic of tempered martensite. Bainite formation (see third bullet point) is promoted by certain alloying elements, in particular molybdenum, and by the more rapid cooling rates that favor shear transformation over diffusion-controlled transformation. The complexity of microstructures is due to the increasing fineness and intermixing of the austenite transformation products as transformation proceeds at successively lower temperatures on cooling. Finally, proeutectoid ferrite is sometimes observed in high-carbon steels where normally proeutectoid cementite would be expected, because not all of the carbides may be dissolved during austenitizing. As a result, some of the carbon is tied up in carbide particles, and the austenite has a lower-than-expected carbon content approaching that of a hypoeutectoid steel.

In addition to the previously mentioned differences between IT and CT diagrams, frequently there is a gap noted in CT diagrams. This gap represents a temperature range where apparently no transformation occurs on cooling and may be due to carbon enrichment of austenite on cooling as high-temperature ferrite forms and/or changes in incubation times for pearlite and bainite nucleation on cooling (Ref 10.4).

As a result of the differences between isothermal and continuous cooling transformation, CT diagrams are determined primarily by experiment, although there is still some interest in calculating CT diagrams from IT diagrams (Ref 10.4). The use of quenching dilatometers, in which changes in length and temperature with time of a standard specimen are simultane-

ously recorded, is now well established as the major approach to experimental determination of CT diagrams. The changes in specimen length due to the expansion associated with austenite transformation can therefore be related to points on a series of cooling curves. Metallographic examination of the transformed specimens then establishes the microstructure produced by a given cooling sequence. Experimental and instrumental details of the dilatometric approach are given in published atlases of CT diagrams (Ref 10.3, 10.6), and Eldis (Ref 10.7) has critically reviewed the relationship of dilatometry to the construction of CT diagrams.

The CT diagrams for alloy steels are more complicated than that shown in Fig. 10.3 for eutectoid steel. Figures 10.4 and 10.5 show IT and CT diagrams for SAE 4140 steel and 42CrMo4 steel determined by U.S. Steel and Max-Planck Institut für Eisenforschung investigators, respectively. The steels are quite comparable in composition and contain nominally 0.4% C, 1% Cr, and 0.2% Mo as the major alloy additions. The CT diagram in Fig. 10.4 was derived from the IT diagram, and that in Fig. 10.5

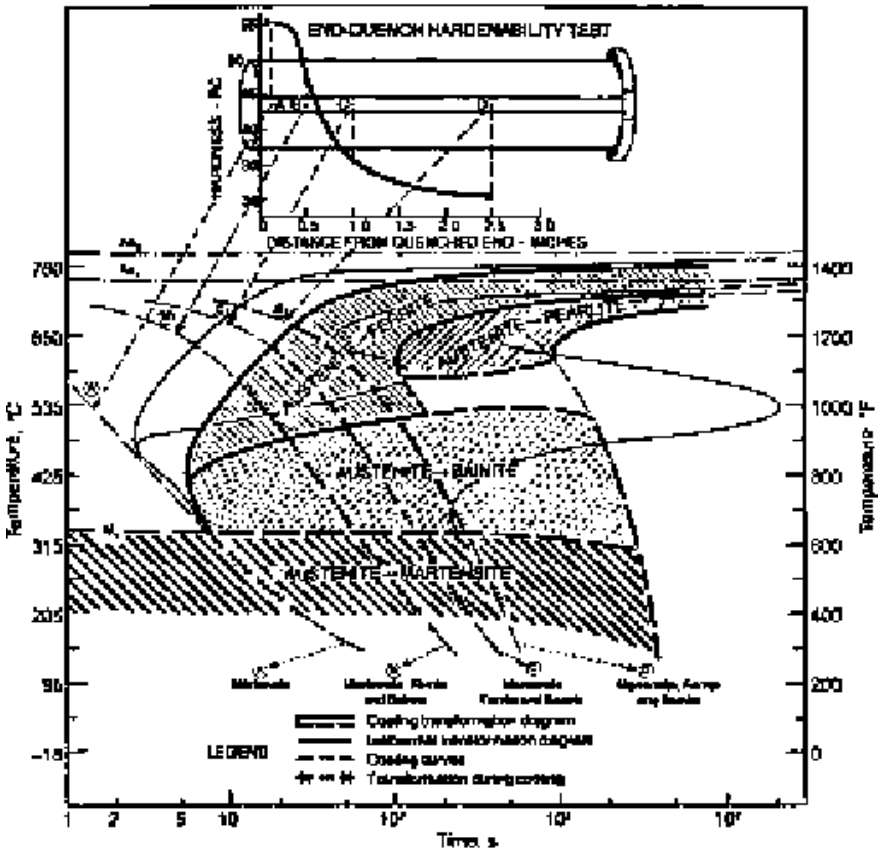

Fig. 10.4 Cooling transformation diagram (heavy lines) for 4140 steel. Also shown are Jominy end-quench data and isothermal transformation diagram (light lines). Source: Ref 10.5

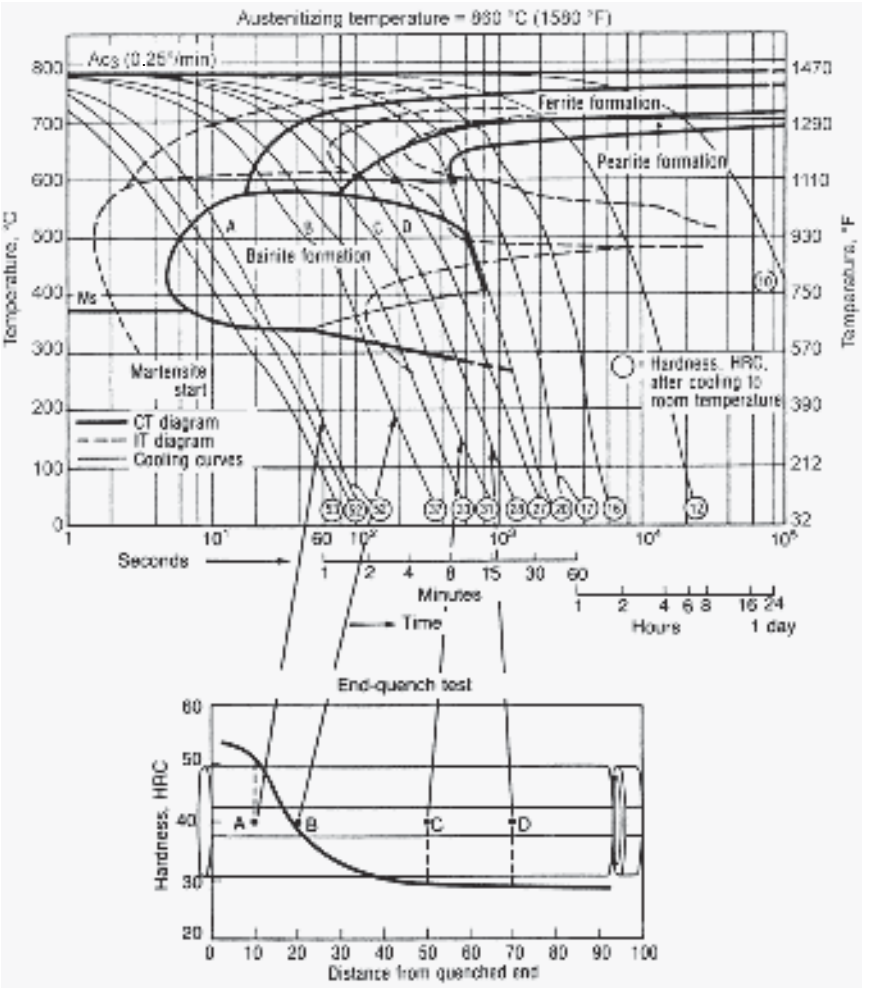

Fig. 10.5 Experimentally determined cooling transformation (CT) diagram (continuous lines) for steel with German designation 42CrMo4 (0.38% C, 0.99% Cr, and 0.16% Mo) for comparison with that derived for a similar steel, 4140, as shown in Fig. 10.4. Isothermal transformation (IT) diagram is also shown (dashed lines). Source: Ref 10.3

was experimentally determined. In the case of the 4140-type steel, there is relatively good agreement between the two methods of CT diagram determination, and the diagrams show the dominance of ferrite and bainite formation at intermediate rates of cooling.

Figures 10.6 and 10.7 are CT diagrams that show a number of effects of alloying on cooling transformation. Two steels, containing 1.4% Ni, 0.36% Si, and 0.85% Mn and differing only in molybdenum content, are compared. The diagrams have been selected from an atlas that systematically characterizes the effects of molybdenum, chromium, nickel, and silicon on CT diagrams of 0.4% C steels (Ref 10.6). The microstructures

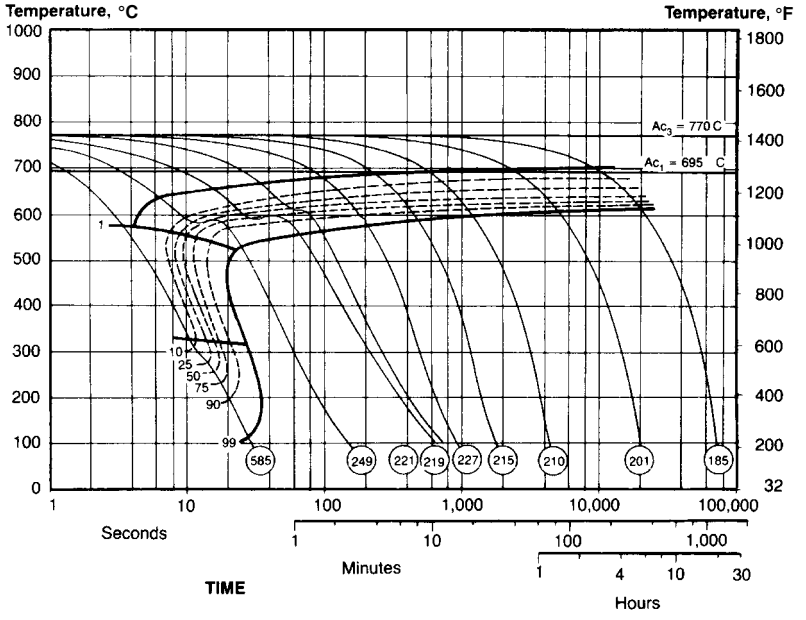

Fig. 10.6 Cooling transformation diagram for a steel containing 0.37% C, 0.36% Si, 0.85% Mn, 1.44% Ni, and 0.02% Mo. The steel was austenitized at 800 °C (1470 °F) for 20 min. The circled numbers correspond to the diamond pyramid hardness of microstructures produced by cooling at the rates shown. Source: Ref 10.6

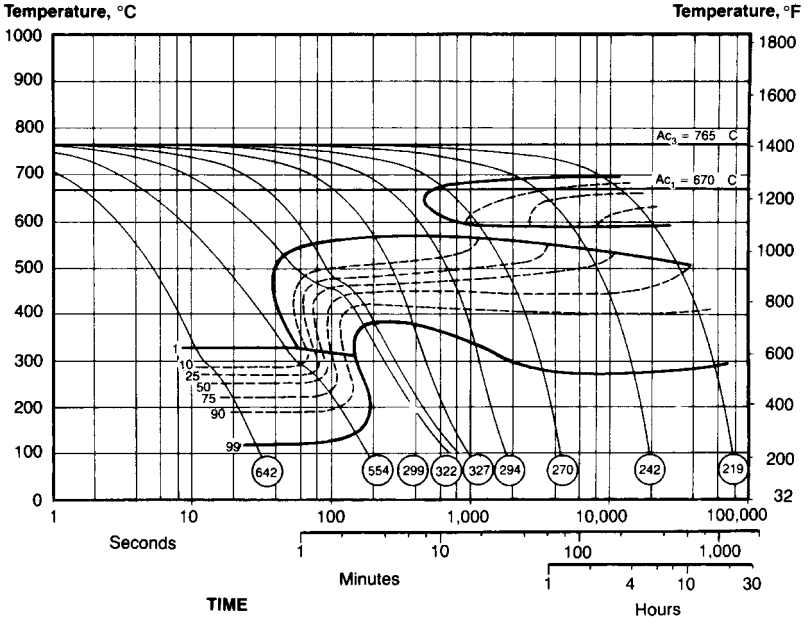

Fig. 10.7 Cooling transformation diagram for a steel containing 0.37% C, 0.36% Si, 0.84% Mn, 1.40% Ni, and 0.47% Mo. The steel was austenitized at 795 °C (1465 °F) for 70 min. The circled numbers correspond to the diamond pyramid hardness of microstructures produced by cooling at the rates shown. Source: Ref 10.6

resulting from selected cooling curves from Fig. 10.6 and 10.7 are shown in Fig. 10.8 and 10.9, respectively. Each cooling curve and microstructure is identified by the diamond pyramid hardness (DPH) of the microstructure produced by that cooling sequence.

Figures 10.6 and 10.7 show that nickel depresses the Ac_3 and Ac_1 temperatures in accord with its role as an austenite stabilizer in steels and increases hardenability (i.e., the ability to form martensite on cooling) primarily by shifting the proeutectoid and pearlite transformation to longer time periods. Although the austenite-ferrite and austenite-pearlite regions are not differentiated in Fig. 10.6, the microstructures in Fig. 10.8 show that equiaxed proeutectoid ferrite and pearlite are the transformation products for continuous cooling that produces DPHs of 219, 210, and 185 (see Fig. 10.8b, c, and d, respectively). Kirkaldy (Ref 10.8) has attributed the improvement in hardenability due to elements such as nickel, copper, and manganese to the lowering of the transformation temperatures and the attendant lower rates of diffusion.

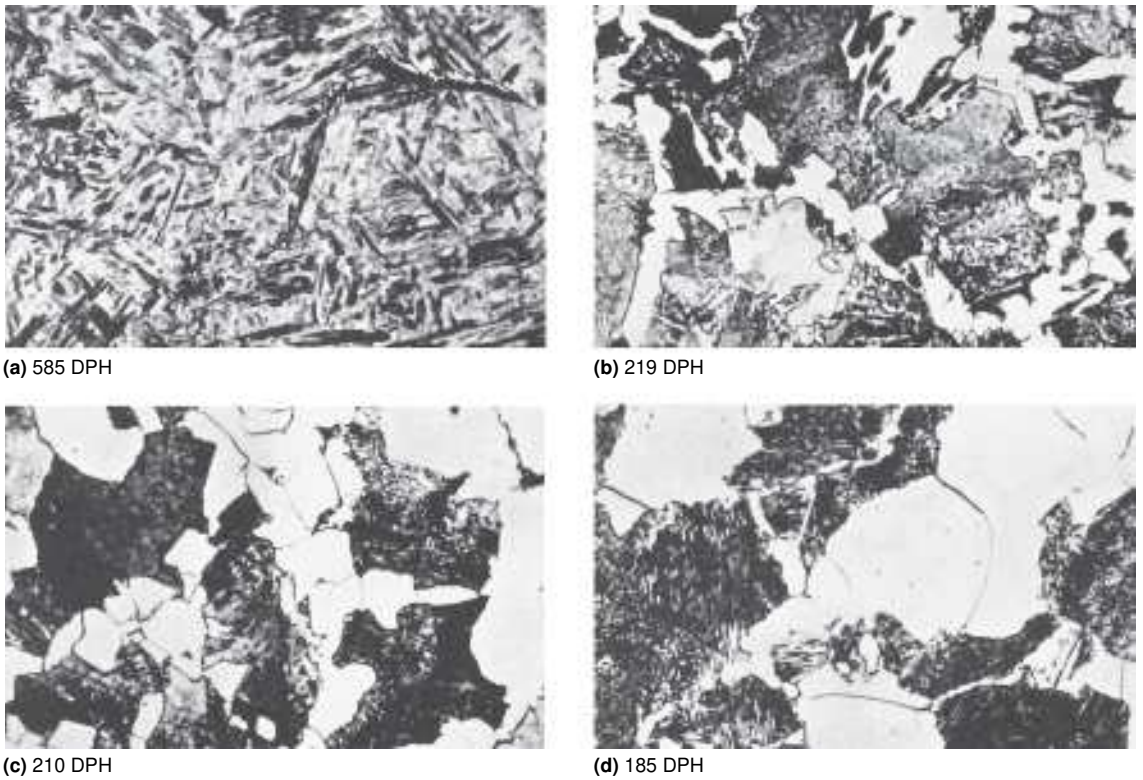

(a) 585 DPH **(b)** 219 DPH **(c)** 210 DPH **(d)** 185 DPH

Fig. 10.8 Microstructures produced by cooling steel shown in Fig. 10.6 at four rates as identified by the diamond pyramid hardnesses (DPH) in Fig. 10.6. Etch: 2% nital. Original magnification: 1000×; shown here at 75%. Source: Ref 10.6

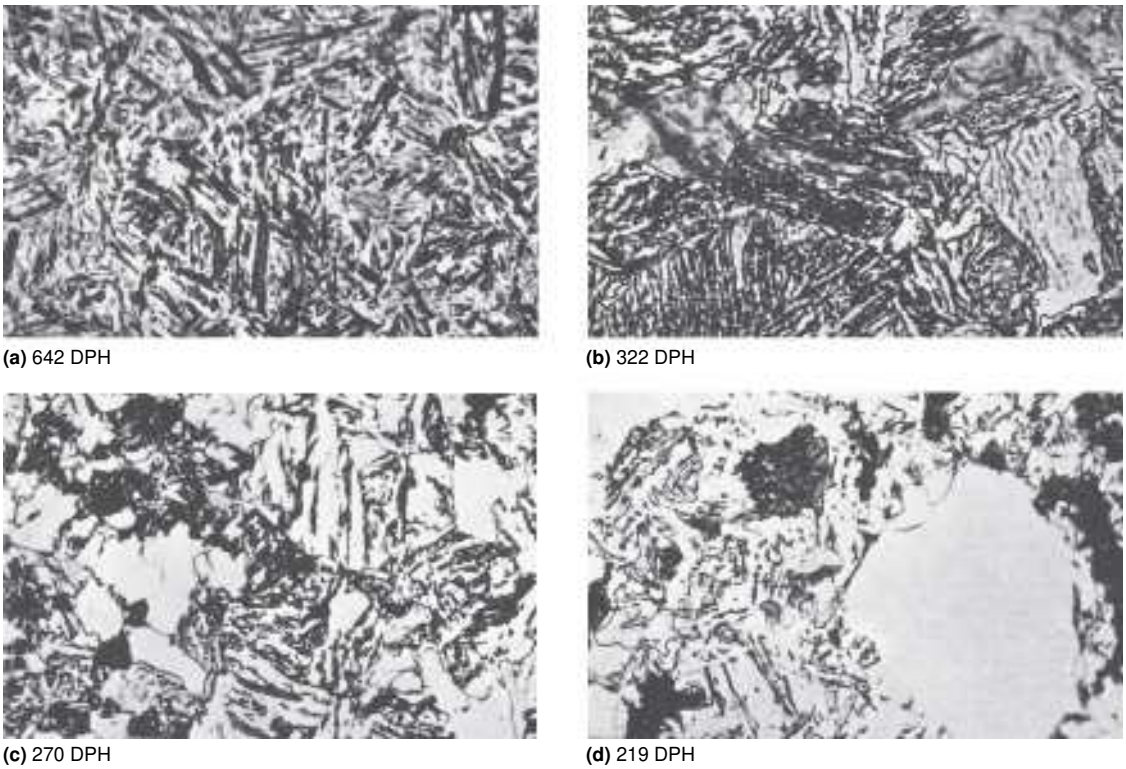

(a) 642 DPH **(b)** 322 DPH **(c)** 270 DPH **(d)** 219 DPH

Fig. 10.9 Microstructures produced by cooling steel shown in Fig. 10.7 at four rates as identified by the diamond pyramid hardnesses (DPH) in Fig. 10.7. Etch: 2% nital. Original magnification: 1000×; shown here at 75%. Source: Ref 10.6

Figures 10.7 and 10.9 show that the addition of approximately 0.5% Mo to the 1.4% Ni steel produces significant changes in cooling transformation characteristics and microstructure. Hardenability is greatly improved, pearlite and equiaxed proeutectoid ferrite formation is severely retarded, and the bainite transformation becomes quite prominent. The gap that sometimes forms between two mechanisms of transformation is also apparent. The strong effect of molybdenum and similar ferrite stabilizers such as chromium and silicon has been attributed (Ref 10.8) to the fact that molybdenum must diffuse or partition during pearlite formation. Since molybdenum diffuses very sluggishly below Ae_1, the pearlite transformation is significantly retarded. Ferrite formation by a shear mechanism, on the other hand, requires no such partitioning of substitutional elements, and as a result, the lower noses for Widmanstätten ferrite and bainite (which is nucleated by ferrite) are prominent features of the CT diagram for the steel containing molybdenum. Of course, the excellent hardenability shown in Fig. 10.7 is due to the combination of both the nickel and molybdenum alloying effects.

Figures 10.6 through 10.9 show other examples of the characteristics of continuous cooling transformation discussed earlier. The M_s temperatures are slightly lowered once some bainite has formed, and the microstructures, especially those produced in the nickel-molybdenum steel (see Fig. 10.9), are quite complex. Figures 10.6 and 10.7 also show the effects of the evolution of the heat of formation of the austenite transformation products on the cooling curves. This phenomenon is referred to as recalescence and causes changes in slopes of the cooling curves and sometimes even temperature increases on transformation. Figures 10.6 and 10.7 show that recalescence is most prominent at high and intermediate cooling rates; at slow cooling rates, the specimen has sufficient time to dissipate to its surroundings the heat generated by transformation. Also, measurable recalescent effects lag the dilatometric detection of transformation and therefore are not suitable for accurate CT diagram determination.

Continuous Cooling Transformation and Bar Diameter

An atlas that presents continuous cooling transformation as a function of bar diameter rather than time has been prepared by the British Steel Corporation (Ref 10.9). This atlas is especially valuable to the heat treater because it permits an estimate of the microstructure that will form in the center of a bar of a given diameter for a large number of engineering steels in air-cooled, oil-quenched, and water-quenched conditions. Accompanying each of the CT diagrams is a plot of hardness as related to the bar diameters in the as-cooled condition and sometimes the hardness after tempering. The bar diameter characterization is essentially a representation of hardenability, a subject that is developed more fully in Chapter 16, "Hardness and Hardenability," in this book but is included here because of its direct relationship to continuous cooling transformations.

Figure 10.10 shows the CT diagram for a plain carbon steel containing 0.38% C, 0.20% Si, and 0.70% Mn. The abscissa is plotted as bar diameter associated with air cooling, oil quenching, and water quenching. Vertical lines associated with a given diameter show the microstructures to be expected in the center of a bar of that diameter. For example, the vertical dashed line identified as "Air cool" shows that a microstructure of ferrite, pearlite, and a small amount of bainite is expected in a 10 mm (0.4 in.) diameter bar that has been air cooled. Likewise, the vertical dashed lines marked "Water quench" and "Oil quench" indicate that martensite and bainite plus martensite, respectively, would be expected for 10 mm (0.4 in.) diameter bars quenched in the two different media. Figure 10.11 shows the CT diagram for a more highly alloyed 0.40% C steel. The diagram

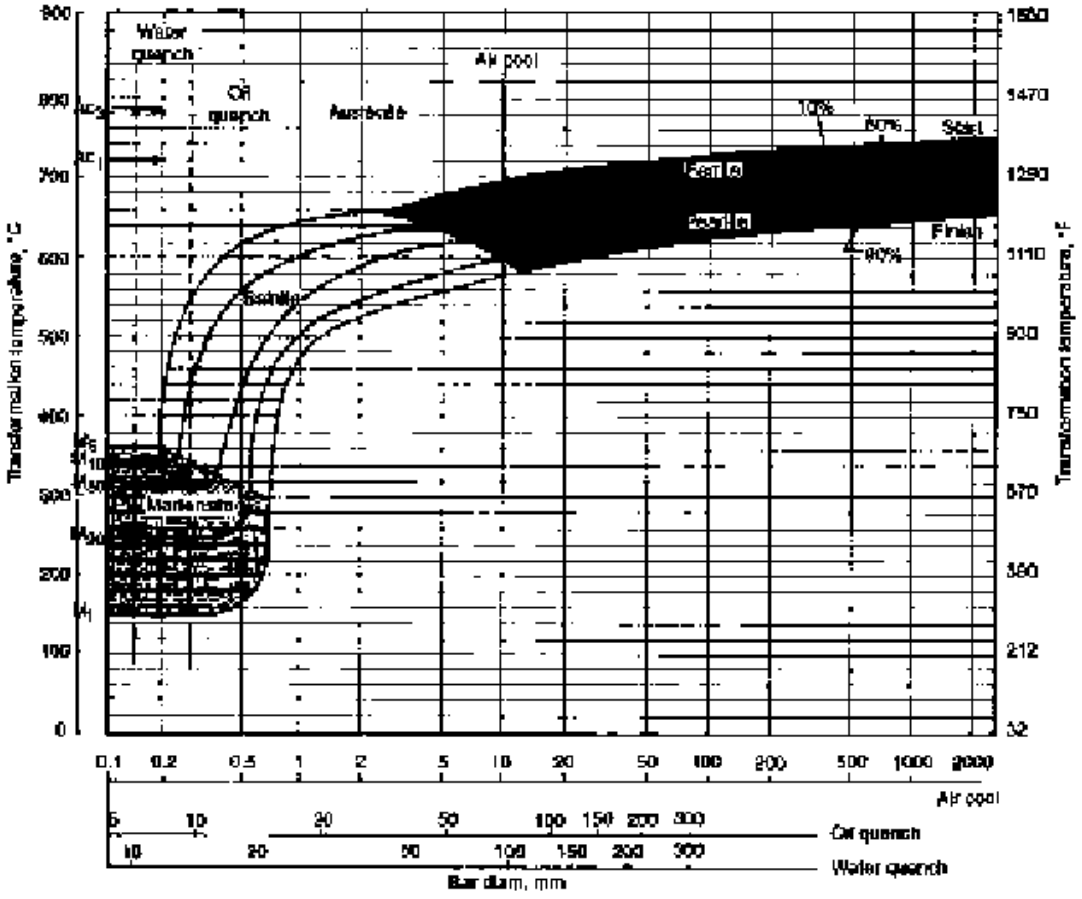

Fig. 10.10 Cooling transformation diagram for plain carbon steel containing 0.38% C and 0.70% Mn. Transformation and microstructures are plotted as a function of bar diameter. Source: Ref 10.9

shows that a 10 mm (0.4 in.) bar of this steel, even if air cooled, would be entirely martensitic and that oil-quenched bars up to 100 mm (4 in.) in diameter would be fully hardened.

The CT diagrams relating microstructure to bar diameter therefore permit a direct assessment not only of the possibility of producing maximum hardness in a bar of given diameter but also of the ability to produce air-cooled or normalized structures with ferrite-pearlite microstructures of low hardness. It should be remembered that the microstructures are those that would be present at the center of the bars, and that microstructure and hardness gradients may exist between the center and surface of the bars because of cooling rate variations between those points. Some variation in microstructures from those represented in the CT diagrams must also be expected because of chemistry variations within specification limits of a

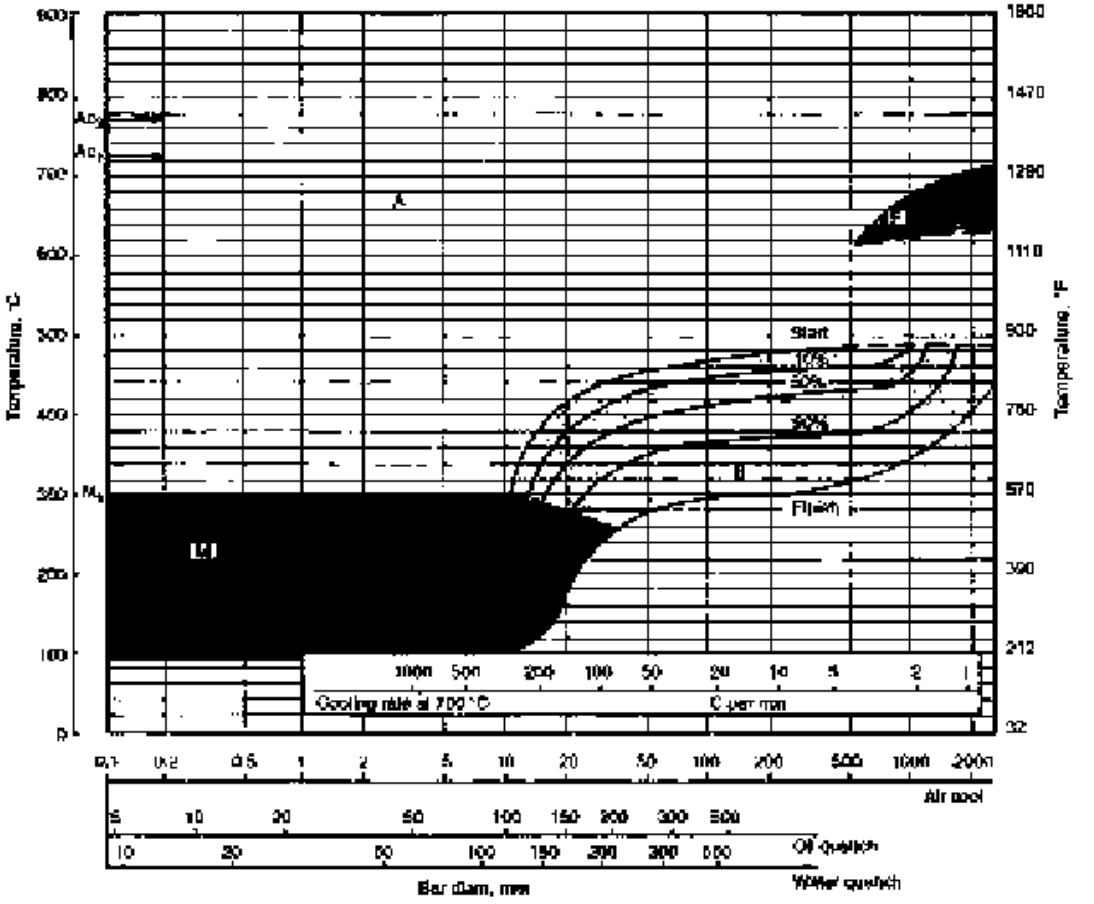

Fig. 10.11 Cooling transformation diagram for an alloy steel with 0.40% C, 1.50% Ni, 1.20% Cr, and 0.30% Mo, plotted as a function of bar diameter. Steel was austenitized at 850 °C (1562 °F); previous treatment: rolling, then softening at 650 °C (1202 °F). Source: Ref 10.9

given grade of steel, variations in austenitizing, and/or different degrees of agitation during water or oil quenching.

Summary

A wealth of information characterizing the isothermal (Ref 10.2, 10.5, 10.10, 10.11) and continuous cooling (Ref 10.3, 10.5, 10.6, 10.9, 10.11–10.14) transformation behavior of a large number of steels is available in the form of atlases, and many transformation diagrams have been collected in a single volume (Ref. 10.15). There is a strong trend to the use of CT diagrams because they better represent the large number of heat treatments that are based directly on continuous cooling. The latter trend is in turn related to the ready availability of CT diagrams, a situation that has

been significantly aided by the development of experimentally convenient and accurate dilatometric techniques for CT diagram determination.

REFERENCES

10.1 G. Krauss and J.F. Libsch, *Phase Diagrams in Ceramic, Glass and Metal Technology,* A.M. Alper, Ed., Academic Press, New York, 1970

10.2 *Atlas of Isothermal Transformation Diagrams,* 2nd ed., United States Steel Corp., Pittsburgh, 1951

10.3 *Atlas zur Wärmebehandlung der Stähle,* Vol 1–4, Max-Planck-Institut für Eisenforschung, in cooperation with the Vereins Deutscher Eisenhüttenleute, Verlag Stahleisen, M.B.H., Düsseldorf, 1954–1976

10.4 A.K. Cavanagh, *Metall. Trans. A,* Vol 10, 1979, p 129–132

10.5 *Atlas of Isothermal Transformation and Cooling Transformation Diagrams,* American Society for Metals, 1977

10.6 W.W. Cias, *Phase Transformation Kinetics and Hardenability of Medium-Carbon Alloy Steels,* Climax Molybdenum Co., Greenwich, CT, 1972

10.7 G.T. Eldis, A Critical Review of Data Sources for Isothermal and Continuous Transformation Diagrams, *Hardenability Concepts with Applications to Steel,* AIME, Warrendale, PA, 1978, p 126–153

10.8 J.S. Kirkaldy, Prediction of Alloy Hardenability from Thermodynamic and Kinetic Data, *Metall. Trans. A,* Vol 4, 1973, p 2327–2333

10.9 M. Atkins, *Atlas of Continuous Cooling Transformation Diagrams for Engineering Steels,* British Steel Corp., Sheffield, 1977; revised U.S. edition published by American Society for Metals, 1980

10.10 *Supplement to Atlas of Isothermal Transformation Diagrams,* United States Steel Corp., Pittsburgh, 1953

10.11 A. Schrader and A. Rose, *Structure of Steels,* Vol 2, *De Ferri Metallographia,* Verlag Stahleisen MBH, Düsseldorf, 1966

10.12 *Transformation Diagrams of Steels Made in France,* Vol 1–4, I.R.S.I.D., St. Germaine-en-Laye, 1953–1960

10.13 M. Economopoulos, N. Lambert, and L. Habraken, *Transformation Diagrams of Steels Made in Benelux Countries,* C.N.R.M., Brussels, 1967

10.14 A.A. Popov and L.E. Popova, *Isothermal and Thermokinetic Diagrams of the Breakdown of Supercooled Austenite,* Metalurgiya, Moscow, 1965

10.15 G.F. Vander Voort, Ed., *Atlas of Time-Temperature Diagrams for Irons and Steels,* ASM International, 1991

CHAPTER 11

Deformation, Strengthening, and Fracture of Ferritic Microstructures

AT SOME STAGE OF PROCESSING, the matrix microstructure of all carbon steels consists of ferrite; therefore, an understanding of the response of ferritic microstructures to stress is essential to understanding the performance of carbon steels. The body-centered cubic (bcc) crystal structure of ferrite has 48 slip systems, as described in Chapter 3, "Phases and Structures." Therefore, at room temperature, microstructures of equiaxed grains of ferrite have high ductility: dislocations can readily move and multiply to produce large permanent changes in the shape of steel structures. However, below room temperature, dislocation movement is restricted and ferritic microstructures become brittle. These aspects of deformation behavior and various micromechanisms that increase strength, especially in low-carbon steels with microstructures consisting primarily of ferrite, are discussed in the following sections.

Tensile Deformation, Strain Hardening, and Ductile Fracture

Figure 11.1 shows a schematic diagram of an engineering stress-strain curve produced by tensile testing of a typical metal specimen (Ref. 11.1). Engineering stress is defined as the applied load divided by the cross-sectional area of the gage length of a tensile specimen. The cross-sectional area is not considered to change during the test. Engineering strain or

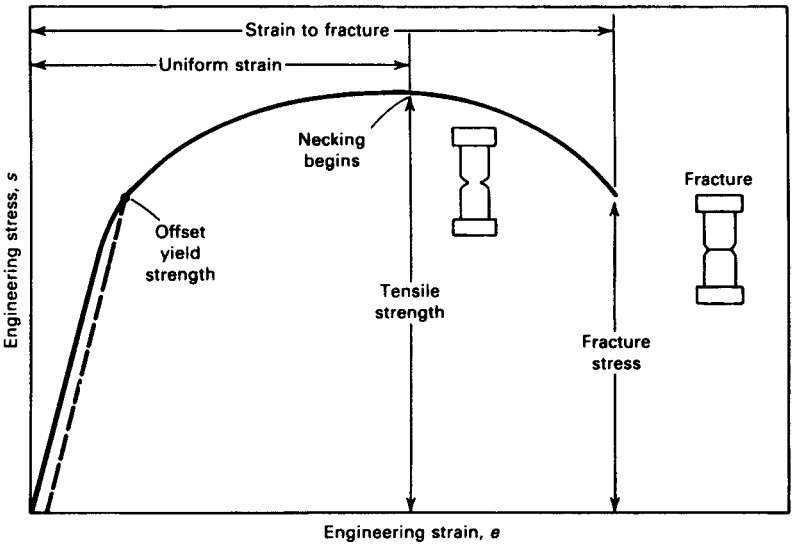

Fig. 11.1 Schematic engineering stress-stain curve typically produced by uniaxial tensile testing (Ref 11.1). The stages of deformation during tensile testing are described in the text.

elongation is obtained by dividing elongation of a specimen gage length by its original length. Deformation under load is at first elastic. This portion of the stress-strain curve is characterized by a straight line, and strain is reversible when load is decreased. A yield strength is established on reaching a stress level sufficient to produce dislocation motion and measurable permanent change in dimension. Often, yield strength is determined at an offset to the linear portion of the curve at a small permanent strain, as shown in Fig. 11.1. A typical value of strain used is 0.002 or 0.2% elongation.

At yielding, plastic or permanent deformation begins. This stage of deformation, referred to as work hardening or strain hardening, develops to produce the uniform strain or elongation measured in a tensile test. Dislocations multiply and higher stresses are necessary to move finer and finer dislocation segments produced by dislocation interactions. The shear stresses required to move dislocation line segments are inversely proportional to the free lengths of dislocation lines, that is, the shorter the free lengths, the higher the stresses required. Kuhlmann-Wilsdorf has theoretically evaluated strain hardening and the formation of associated low-energy-dislocation structures in detail (Ref 11.2) and has presented the following equation to characterize strain hardening (Ref 11.3):

$$\tau = \tau_0 + \text{const}\, G\mathbf{b}/l = \tau_0 + \alpha G\mathbf{b}\rho^{1/2} \qquad \text{(Eq 11.1)}$$

where τ is the momentary flow stress at some point in the strain-hardening process, τ_0 is the friction stress to move a dislocation through a crystal

without obstacles, G is the shear modulus, **b** is the dislocation Burgers vector, l is the average effective dislocation line free length at some moment during strain hardening, and ρ is the dislocation density. Equation 11.1 clearly relates increases in flow stress during strain hardening to dynamic dislocation interactions and increases in dislocation density.

Figure 11.2 shows changes in dislocation substructure that have developed with increasing strain in a 0.05C-0.29Mn-0.03Al steel. High-resolution, high-magnification transmission electron microscopy of thin foils reveals the dislocations as thin linear features. As strain increases, the dislocations arrange themselves into a substructure that consists of cells with dislocation-free areas and cell boundaries that contain high densities of tangled dislocations. As compared with uniform dislocation distributions throughout a crystal, the dislocation cell configuration minimizes free energy associated with plastic deformation (Ref 11.2). Dislocation cell size decreases with increasing strain (Ref 11.4, 11.5), as shown for low-carbon steel and iron in Fig. 11.3, and correlates with increasing flow stress during tensile testing.

Strain hardening continues to increase flow stresses with increasing strain until the ultimate tensile strength is reached. Up to this point in a tensile test, deformation has occurred uniformly throughout the entire gage length of a tensile specimen. However, when the tensile strength is reached, mechanical instability develops and strain concentrates locally to produce the discontinuity in specimen gage length referred to as a neck. The neck develops when applied stress exceeds the strength of the uniformly strain-hardened microstructure. Figure 11.3 shows that substructure size stabilizes at high strains, consistent with reduced strengthening and therefore increased susceptibility to necking.

Necking instability is defined by the intersection of strain-hardening rate and strengthening curves as a function of strain, as shown in Fig. 11.4

Fig. 11.2 Dislocation substructure in a low-carbon steel containing 0.05% C, 0.29% Mn, and 0.03% Al. (a) Specimen strained 5% in tension. (b) Specimen strained 10% in tension. Transmission electron micrographs. Courtesy of J. Pan, Colorado School of Mines. Source: Ref 11.4

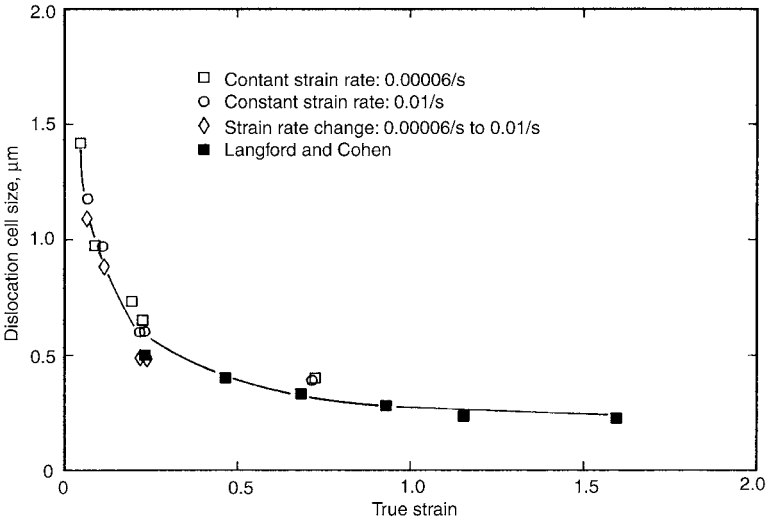

Fig. 11.3 Dislocation cell size as a function of true strain in a low-carbon steel (Ref 11.4) and highly deformed iron (Ref 11.5)

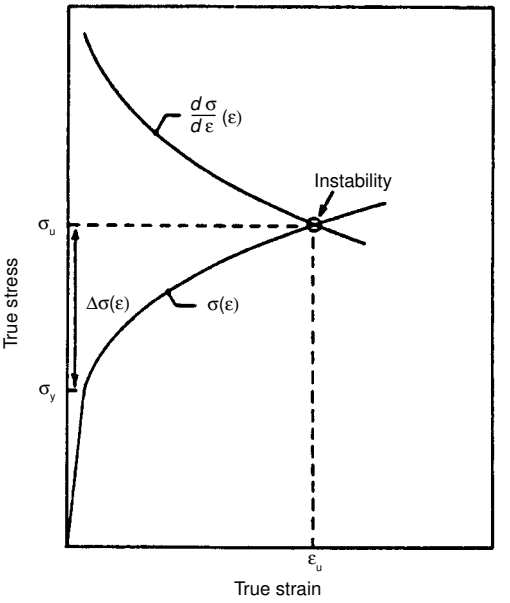

Fig. 11.4 Schematic diagram showing the intersection of the flow curve and strain-hardening curve that defines the mechanical instability or necking condition during tensile testing. Source: Ref 11.7

(Ref 11.6, 11.7). For this definition, stress is defined as the true stress, σ, defined as applied load divided by the reduced cross-sectional area at a point in a tensile test, and strain is defined as the true strain, ε, defined as the natural log of the gage length at a point in a tensile test divided by the

original gage length (Ref 11.1). With these definitions, actual, dynamic changes in stress and strain during testing are taken into account. Figure 11.4 shows that when the strain-hardening rate $d\sigma/d\varepsilon$ equals the flow stress produced by strain hardening, necking instability occurs. The intersection of the curves also defines uniform strain, ε_u. Necking instability is defined by the following equation:

$$d\sigma/d\varepsilon = \sigma \text{ at } \varepsilon = \varepsilon_u \quad \text{(Eq 11.2)}$$

The understanding of the reasons for necking instability is a powerful qualitative way to assess mechanical performance of a steel. Microstructural factors that increase strain-hardening rates, such as finer dislocation substructures or strain-induced transformation of retained austenite, tend to increase uniform elongation and defer necking instability.

Following necking, deformation continues within the neck, and by virtue of the localized reduction in area, true stress continues to increase to fracture. Engineering stress, calculated with a constant cross-sectional area, drops as applied load decreases following attainment of maximum load-carrying capacity at the ultimate tensile strength. Significant post-uniform strain contributes to total elongation or strain to fracture and develops as a result of deformation in the neck. During nonuniform deformation in the neck, ductile fracture is initiated. Ductile fracture is caused by the initiation of microvoids around second-phase particles, plastic growth of the voids, and eventual coalescence of the voids to produce the final ductile fracture surface (Ref 11.8–11.10).

The Ductile-to-Brittle Transition in bcc Ferrite

A phenomenon unique to bcc ferrite microstructures is a severe loss in the ability to plastically deform at low temperatures. The change from ductile deformation and fracture behavior, as discussed previously, to severely reduced ability to plastically deform with decreasing temperature is termed the ductile-to-brittle transition. Stainless steels with face-centered cubic (fcc) austenitic microstructures do not show such severe loss of ductility at low temperatures. In steels, many factors such as strain rate, the presence of notches, grain size, second-phase particles, or pearlite content determine the temperature range in which the transition occurs.

The ductile-to-brittle transition in steels is most commonly established by Charpy V-notch (CVN) testing, in which the energy absorbed during fracture of notched specimens subjected to high-strain-rate loading is measured at various test temperatures. Figure 11.5 shows a schematic set of CVN curves, one representing fracture behavior at typical high-strain-rate impact testing, the other representing testing at a slow strain rate produced by bending (Ref 11.11). Fracture at high test temperatures produces a plateau in energy absorbed, often referred to as the upper shelf, and is

produced by ductile fracture. The energy absorbed in fracture decreases dramatically with decreasing test temperature, until a low-energy, lower shelf is obtained. Reduced rates of straining lower the temperature at which brittle fracture develops but cannot suppress brittle, low-energy fracture.

Figure 11.6 shows examples of ductile and brittle fracture surfaces that developed on CVN impact testing of a steel with ferrite-pearlite microstructure. The ductile fracture surface shows a mix of deep and very fine

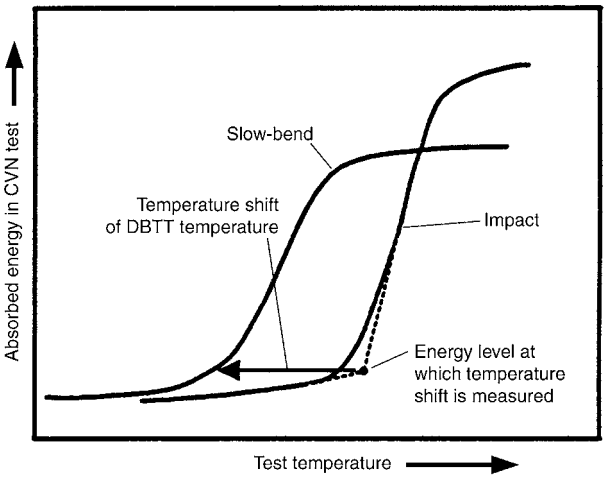

Fig. 11.5 Schematic diagram comparing energy absorbed as a function of temperature during high-rate impact testing and slow bend testing of notched specimens. CVN, Charpy V-notch; DBTT, ductile-brittle transition temperature. Source: Ref 11.11

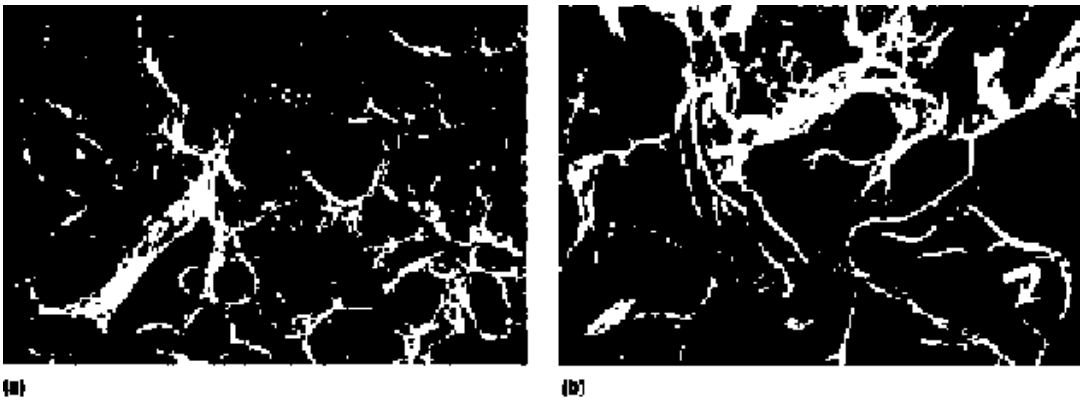

Fig. 11.6 Ductile and brittle fracture surfaces. (a) Mixture of coarse and fine depressions or dimples characteristic of ductile fracture surfaces. Some flat cleavage facets are shown in bottom of micrograph. (b) Flat fracture surface facets characteristic of brittle cleavage fracture. Scanning electron micrographs. Original magnification: 750×. Courtesy of D. Yaney, Colorado School of Mines

microvoids together with some flat cleavage facets. The brittle fracture surface shows large, flat regions where cleavage fracture has occurred. Cleavage in bcc ferrite occurs on {100} planes that have large interplanar spacings relative to the bcc slip planes. The bright lines on the cleavage surfaces are steps between fracture on two parallel but separated cleavage planes. Often, two small steps join, forming a steeper step. The coming together of the small steps creates an arrow pointing in the direction of crack advance, as shown by the arrow in the lower right of the micrograph in Fig. 11.6(b).

Leslie demonstrated the reduced ability of bcc ferrite to plastically deform at low temperatures (Fig. 11.7) by tensile testing of iron specimens with polycrystalline ferritic microstructures (Ref 11.6, 11.12). The iron was gettered with titanium to remove all carbon and nitrogen from interstitial solid solution and thereby eliminate potential interstitial-atom-dislocation interactions, as described in the following section. Thus, the changes in deformation behavior could be directly attributed only to changes in bcc dislocation mobility. At high temperatures, typical ductile stress-strain behavior, with strains up to 0.16, is reflected in Fig. 11.7. The good ductility at relatively low stresses is produced by dislocation motion and multiplication, as described earlier. However, with decreasing temperature there is a sharp increase in yield strength and limited ability to plastically deform. Figure 11.7 also shows low-temperature elastic limits, σ_E, and anelastic limits, σ_A, the stresses, respectively, for reversible edge dislocation motion and for long-range motion of edge dislocations.

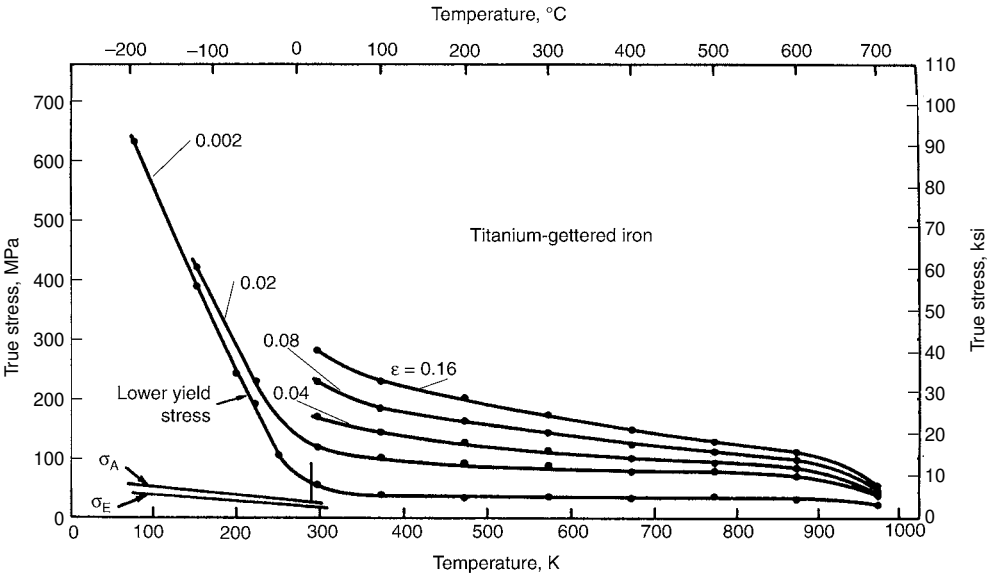

Fig. 11.7 Temperature dependence of yield and flow stresses at various strains in titanium-gettered iron with body-centered cubic ferritic microstructures. Source: Ref 11.6, 11.12

The decreased ability to plastically deform at low temperatures is attributed to the inability of screw dislocations to cross slip. The screw dislocations therefore are restricted to their slip planes, cannot bypass obstacles, and cannot contribute to mechanisms of dislocation multiplication necessary for sustained plastic deformation. The inability of screw dislocations to cross slip has been related to asymmetries in dislocation core structures that develop at low temperatures and to segregation of impurity atoms to dislocation cores (Ref 11.13, 11.14). Transmission electron microscopy shows that only arrays of parallel screw dislocations are present in ferrite deformed at low temperatures and high strain rates (Ref 11.15). This observation implies that edge dislocations migrate from low-temperature-deformed specimens and shows that the tangled dislocation cell structures characteristic of high-temperature deformation are unable to form.

Although the root cause of the transition from ductile to brittle fracture in bcc ferrite is the inability of screw dislocations to cross slip, other microstructural features influence the transition. Fine grain sizes, as discussed subsequently and relative to controlled-rolled low-carbon steels in Chapter 12, "Low-Carbon Steels," in this book, significantly lower ductile-to-brittle transition temperatures. Second-phase particles may fracture and initiate cleavage cracks. McMahon and Cohen (Ref 11.16) have shown that cleavage cracks in low-carbon steels, containing 0.007 and 0.035% C, were initiated by deformation-induced cracking of small cementite particles. When a sharp cementite crack could not be arrested by plastic relaxation in the adjacent ferrite grain, the crack became unstable and propagated on the most suitably oriented {100} ferrite cleavage plane within that grain until arrested at a grain boundary or twin. With sufficient stress, cleavage cracks could be initiated successively in adjacent grains on the most suitably oriented {100} planes, causing cleavage fracture to propagate throughout a specimen cross section. Similar to the role that cementite particles play in cleavage fracture of low-carbon steels, the cracking of coarse TiN particles has been shown to initiate cleavage fracture in medium-carbon steels with ferrite-pearlite microstructures (Ref 11.17). Many other aspects of cleavage fracture are presented in the symposium on cleavage fracture dedicated to George Irwin, recognized as a founder of the engineering discipline of fracture mechanics (11.18).

Continuous and Discontinuous Yielding of Ferritic Microstructures

The initiation of plastic deformation or yielding may take two forms in steels with ferritic microstructures. Continuous yielding results when high densities of unpinned dislocations are present. The high densities of dislocations may be generated by mechanical working or by the introduction of martensite into ferritic microstructures, as is done in the dual-phase steels

described in Chapter 12, "Low-Carbon Steels," in this book. Unpinned dislocations are present when aging time is insufficient to allow interstitial atom diffusion to dislocations or when the interstitial carbon and nitrogen contents are reduced to very low levels, 30 to 50 ppm, as is the case for the ultralow-carbon steels described in Chapter 12, "Low-Carbon Steels." Discontinuous yielding occurs when dislocations are pinned by interstitial atoms.

Figure 11.8 shows schematically the two types of yielding behavior in a low-carbon steel. When a low-carbon steel is heated to and rapidly cooled from a temperature where carbon has a relatively high solubility in ferrite (Fig. 3.4 in Chapter 3, "Phases and Structures," in this book), carbon is supersaturated in the ferritic microstructure at room temperature, and dislocations are relatively free to move with the application of stress. However, with time the microstructure ages, and carbon atoms, which, because of their small size, have high diffusivity in bcc ferrite even at room temperature, diffuse first to dislocations, restricting their motion, and eventually form carbide particles, if time is sufficient or temperatures are elevated. Therefore, higher stresses are required to initiate yielding, as indicated by $\Delta\sigma_y$, and once yielding is initiated, a flat portion of the stress-strain curve results.

Cottrell established the basis of the pinning of dislocations by interstitial atoms in bcc ferrite (Ref 11.19). Carbon and nitrogen atoms produce tetragonal distortions when trapped in a bcc lattice. The associated energy can be relieved by segregation of the interstitial atoms to the elastic strain

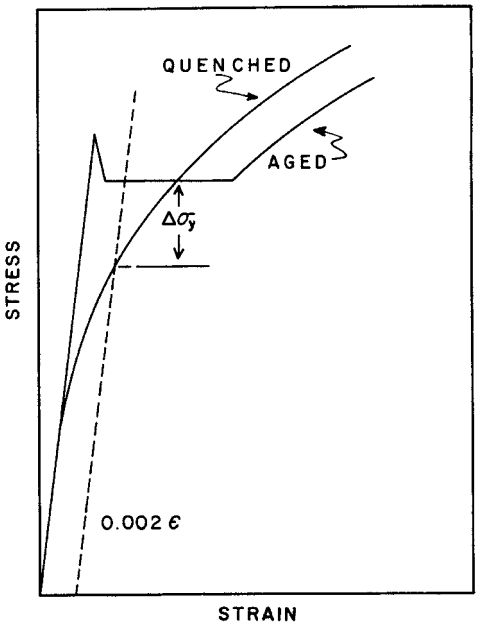

Fig. 11.8 Schematic diagram showing low-strain portions of stress-strain curves with continuous (quenched) and discontinuous (aged) yielding

fields of dislocations. For example, edge dislocations, where the lattice discontinuity is a line extending along the edge of an incomplete plane of atoms, have a tensile strain field below that edge and can accommodate interstitial atoms more readily than octahedral sites in perfect portions of the lattice.

The pinning or Cottrell locking of dislocations by segregated interstitial atoms in ferrite is so strong that effectively all dislocations are immobilized. As a result, for plastic deformation to proceed, new dislocations must be generated, provided a sufficient stress is applied. The burst of new dislocations produces a localized strain, referred to as the Lüders strain, that produces a band of plastic deformation, referred to as a Lüders band. The band propagates across the gage length of a tensile specimen, a process shown schematically in Fig. 11.9 (Ref 11.20). The yielding associated with the passage of a Lüders band is termed discontinuous because the gage length does not deform uniformly; that is, only that part of the gage length within the Lüders band deforms. When the Lüders band has propagated across the entire gage length, uniform or continuous plastic deformation proceeds with increasing stress.

On cold-formed parts subjected to various amounts of deformation, some of which may only be at the level of the Lüders strain, noticeable localized deformation bands, referred to as stretcher strains, develop and distort the surface appearance of lightly deformed sheet steels. To eliminate the formation of Lüders bands, sheet steels are often temper rolled to strains exceeding the Lüders strain. The higher level of plastic deformation ensures that plastic deformation associated with subsequent forming will be continuous and uniform.

Figure 11.8 shows that stress drops after a Lüders band is initiated. The initiation stress is referred to as the upper yield stress, and the stress re-

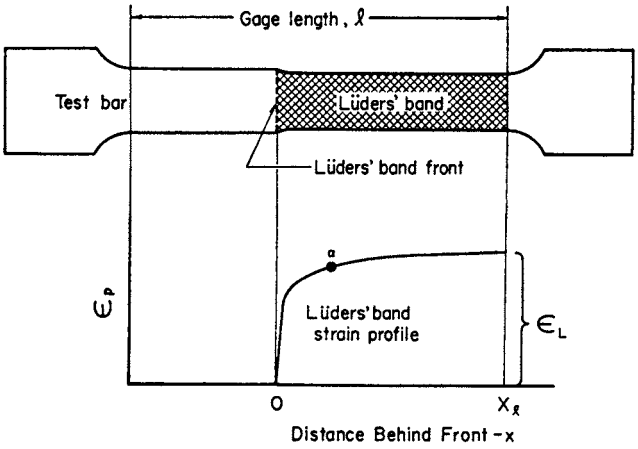

Fig. 11.9 Schematic diagram showing a Lüders band that has partially propagated across the gage length of a sheet tensile specimen. The plastic strain associated with the Lüders band, and the absence of strain where the Lüders band has not propagated, are also illustrated. Source: Ref 11.20

quired to propagate the Lüders band is referred to as the lower yield stress. The drop in stress associated with discontinuous yielding is explained by the stress-dependent velocity of dislocations in a constant strain-rate tensile test (Ref 11.6, 11.20). Stein and Low (Ref 11.21) have shown that dislocations move faster at higher stresses according to the following equation:

$$v = \left(\frac{\tau}{\tau_0} \right)^m \qquad \text{(Eq 11.3)}$$

where v is the dislocation velocity, τ is the applied shear stress, τ_0 is the shear stress for a constant velocity of 1 cm/s, and m is a constant. Figure 11.10 shows the dependence of dislocation velocity on stress and its close

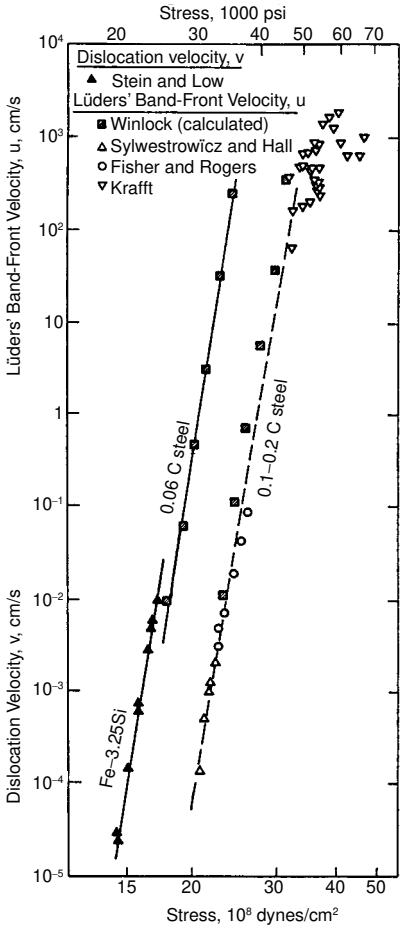

Fig. 11.10 Stress dependence of dislocation velocity as a function of stress in Fe-3.25%Si single crystals, determined by Stein and Low (Ref 11.21) and Lüders band-front velocity in mild steels as a function of stress. The figure is taken from Ref 11.20; the investigations noted are cited in that reference.

relationship to the velocity of Lüders band propagation (Ref 11.20). The stress drop is explained by the requirement to maintain deformation at a constant strain rate, $\dot{\varepsilon}$, during a tensile test according to the following equation:

$$\dot{\varepsilon} = 0.5\mathbf{b}\rho v \qquad \text{(Eq 11.4)}$$

where **b** is the Burgers vector, ρ is the dislocation density, and v, as noted, is the dislocation velocity. Thus, when dislocation density increases to initiate a Lüders band, dislocation velocity must decrease to maintain a constant strain rate, and, according to Eq 11.3, stress must drop.

Aging Phenomena in Ferritic Microstructures

The negligible carbon and nitrogen atom solubility in bcc ferrite at room temperature, and the high diffusional mobility of interstitial atoms in ferrite at and around room temperature, mean that aging effects that produce discontinuous yielding are highly likely in ferritic microstructures of low-carbon steels. Quench aging develops when ferrite is rapidly cooled from temperatures around 730 °C (1350 °F), where the solubility of carbon and nitrogen is high (Fig. 3.4 in Chapter 3, "Phases and Structures," in this book). The resulting supersaturation of ferrite at room temperature, where solubilities of carbon and nitrogen are negligible, leads to Cottrell locking of dislocations, or if the supersaturated ferrite is exposed to temperatures somewhat above room temperature, carbides may precipitate. Figure 11.11 shows examples of precipitate dispersions in quench-aged steels. At low temperatures and short times, metastable carbides precipitate on dislocations after sufficient carbon has segregated. Fine carbides may also precipitate on vacancy clusters in the matrix ferrite. At higher temperatures, cementite forms in platelet and dendritic morphologies (Ref 11.22, 11.23).

The pinning of dislocations produced by deformation, that is, by straining, and the associated return of discontinuous yielding is referred to as strain aging. If the discontinuous yielding returns during aging without additional application of stress, the phenomenon is referred to as static strain aging. Figure 11.12 shows a series of stress-strain curves produced by aging of a deformed low-carbon steel. The lowest curve, with the largest Lüders strain, represents the yielding behavior of the steel prior to deformation. When the steel is deformed to a strain beyond the Lüders strain and retested, as shown by the vertical line at approximately 4% strain, in the absence of aging, the stress-strain curve merely extends the original curve. However, with increased aging times, in this case at 60 °C (140 °F), yield strengths increase and discontinuous yielding returns as more and more carbon atoms segregate to the dislocations produced by the preceding 4% strain.

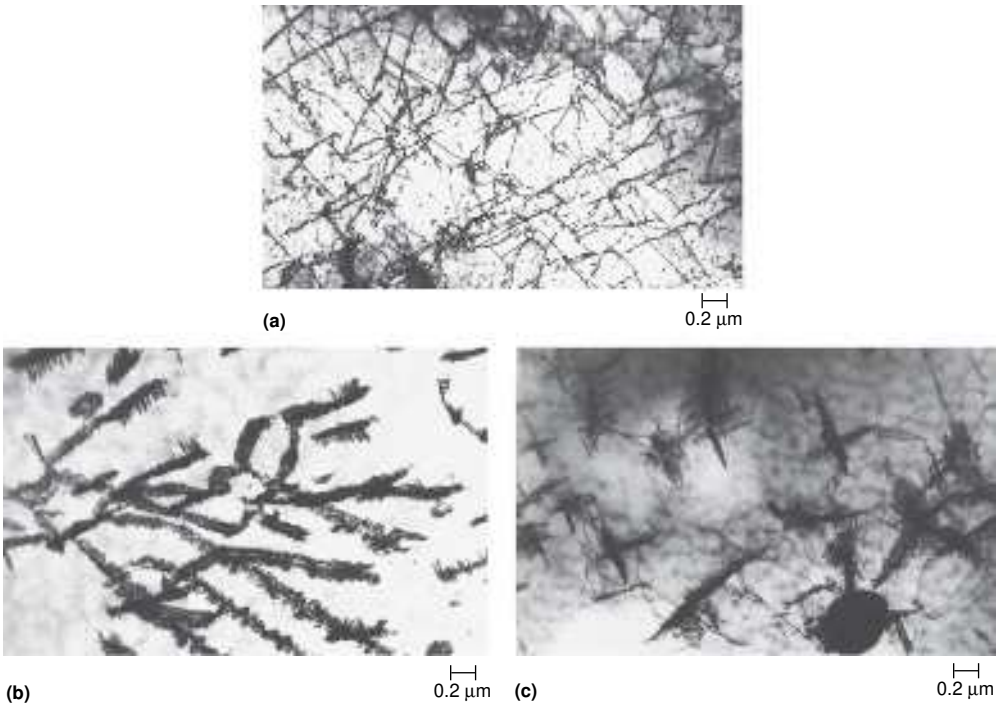

Fig. 11.11 Precipitate dispersions in quench-aged low-carbon steels. (a) Carbides decorating dislocation lines in 0.052% C steel aged for 20 min at 97 °C (207 °F). (b) Plate-shaped carbides formed on dislocations in a 0.077% C steel aged for 115 h at 97 °C (207 °F). (c) Dendritic carbides formed in 0.052% C steel aged for 10 h at 138 °C (280 °F). Transmission electron micrographs courtesy of E. Indacochea, University of Chicago

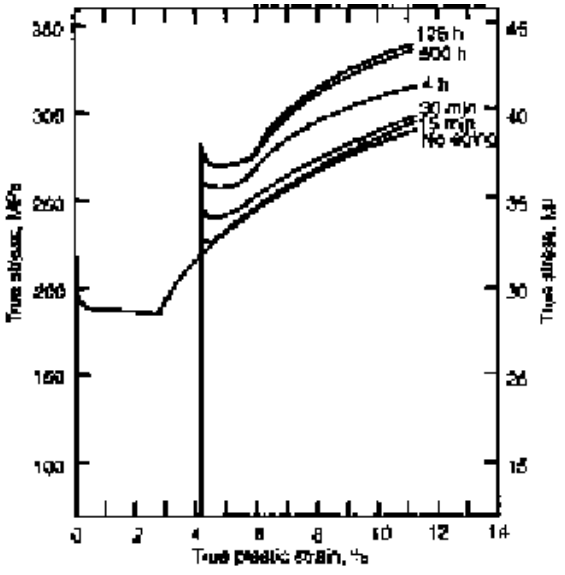

Fig. 11.12 Strain-aging effects on the yielding behavior of a low-carbon steel deformed to 4% true plastic strain and aged for various times at 60 °C (140 °F). Source: Ref 11.6

Carbon atom pinning of dislocations can also occur during deformation or tensile testing in certain ranges of strain rates and temperature. Such aging is referred to as dynamic strain aging. Figure 11.13 shows stress-strain curves produced by testing a low-carbon steel at a series of temperatures (Ref 11.6). Dynamic strain aging is reflected in the serrations most apparent in the specimens tested at 150 and 200 °C (300 and 390 °F). Carbon atoms pin dislocations generated during plastic straining, and stress drops when new bursts of dislocations are formed. Figure 11.13 also shows that at temperatures of 500 °C (930 °F) or higher, discontinuous yielding does not develop, a result attributed to the greater ability of a more relaxed bcc lattice to accommodate the strains associated with interstitial atoms (Ref 11.19).

Grain-Size Effects on Strength and Fracture of Ferritic Microstructures

The effect of grain size on strength and fracture of low-carbon steels is described by the equation first developed by Hall, 1951, and Petch, 1953 (Ref 11.24, 11.25). The Hall-Petch equation for the dependence of stress, σ, on grain size, d, is:

$$\sigma = \sigma_0 + k_y d^{-1/2} \qquad \text{(Eq 11.5)}$$

where σ_0 and k_y are experimental constants. In carbon steels, σ_0 and k_y are often taken as the friction stress to move dislocations in a single crystal of ferrite and an unlocking factor for grain-boundary dislocations, respectively (Ref 11.26).

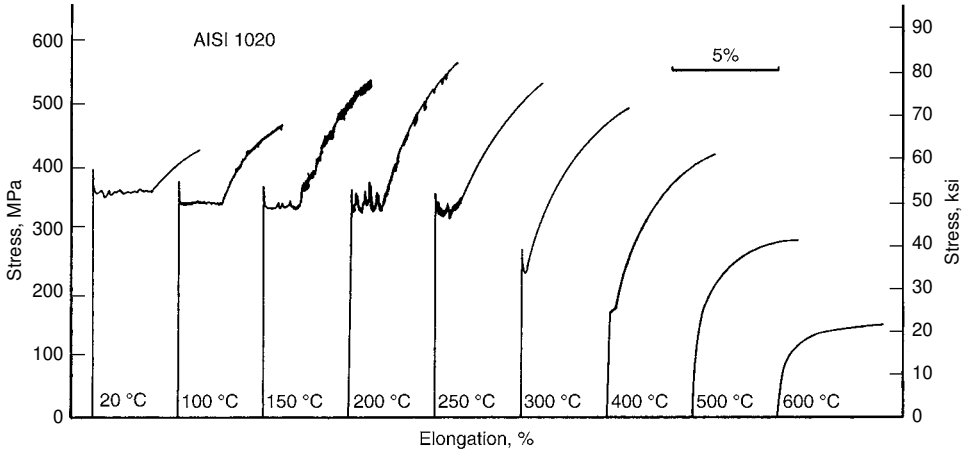

Fig. 11.13 Low-strain portions of stress-strain curves of a low-carbon steel tested at various temperatures as shown. Source: Ref 11.6

Figure 11.14 shows Hall-Petch plots of lower yield strength, flow stresses at various strains, and ductile fracture stress as a function of ferritic grain size in low-carbon steel (Ref 11.26). All of the strength parameters satisfy the reciprocal square-root dependency on grain size. The slope is steepest for the lower yield strength where dislocation pinning, as described previously, requires sufficient stresses to generate new dislocations. At the higher flow stresses, grain boundaries decrease in importance as the dislocation cell structure develops within ferrite grains and controls strengthening. There are several explanations for the strong effect of grain size on strength. Larger grains may permit greater concentrations of dislocations at grain boundaries and may thereby create higher stress for dislocation movement in adjacent grains, or unique grain-boundary dislocation densities or structures in which dislocation sources may be pinned may exist. Matlock et al. (Ref 11.27) have recently reviewed the models for grain-size strengthening. Although several models have been proposed, the finer the grain size, the greater the fraction of the microstructure affected by grain-boundary phenomena, and the higher the stresses to activate dislocation motion. Fine grain sizes also increase ductile fracture stresses, as shown in Fig. 11.14, and lower ductile-to-brittle transition temperatures. In fact, grain-size refinement is the only mechanism that increases both strength and toughness. Figure 11.15 compares the effects of various low-carbon steel strengthening mechanisms on changes in impact transition temperatures (Ref 11.28). Dislocation strengthening, precipitation, and pearlite content of ferritic microstructures, while they all

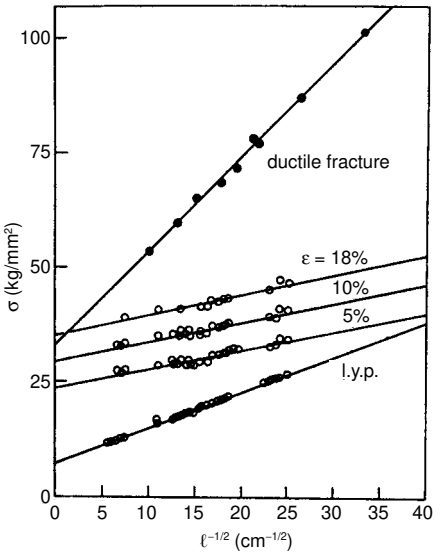

Fig. 11.14 Lower yield strength, flow stresses at various strains, and fracture stress as a function of grain size in low-carbon steels. Source: Ref 11.26

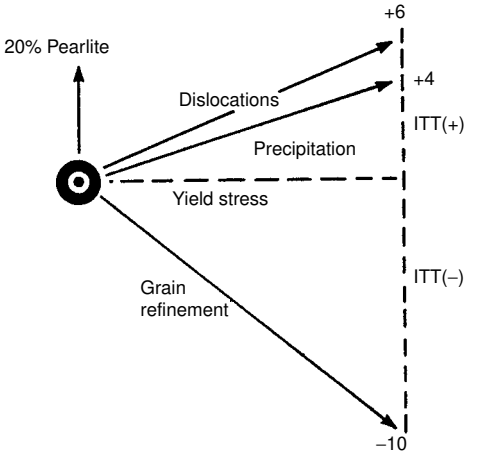

Fig. 11.15 Change in impact-transition temperatures (ITT) produced by 15 MPa (2.2 ksi) increases in strength by various mechanisms and microstructural factors. Only grain-size refinement increases both strength and lowers ITT. Source: Ref 11.28

increase strength, also raise transition temperatures and sensitivity to cleavage fracture; only grain-size refinement lowers transition temperatures. The latter effect is quite strong and has provided a strong driving force for the development of controlled rolling and microalloying capable of producing very fine ferrite grain sizes in steels.

Dispersion Strengthening of Ferritic Microstructures

Many steels contain second-phase particles dispersed in a matrix of ferrite. The particle dispersions may be a result of processing, for example, the dispersions of cementite particles produced by spheroidizing medium- and high-carbon steels or by cold rolling and annealing of low-carbon steels, or by design, as is the case for microalloyed steels. If the particles are closely spaced, on the order of 10 nm more or less, significant strengthening may result from the dispersions.

The strengthening produced by dispersed particles is related to the obstacles that particles present to dislocation motion, as first described by Orowan (Ref 11.29). Figure 11.16 shows this process schematically (Ref 11.30). Dislocations moving under an applied shear stress encounter particles at a spacing L and bow out between the particles. Eventually, the bowed dislocation line segments become unstable and join to produce a new dislocation line on the other side of the particles and dislocation loops around the particles. The increase in shear stress, $\Delta\tau_y$, required for the passage of dislocations between particles is given by the following equation:

$$\Delta\tau_y = G\mathbf{b}/L \qquad \text{(Eq 11.6)}$$

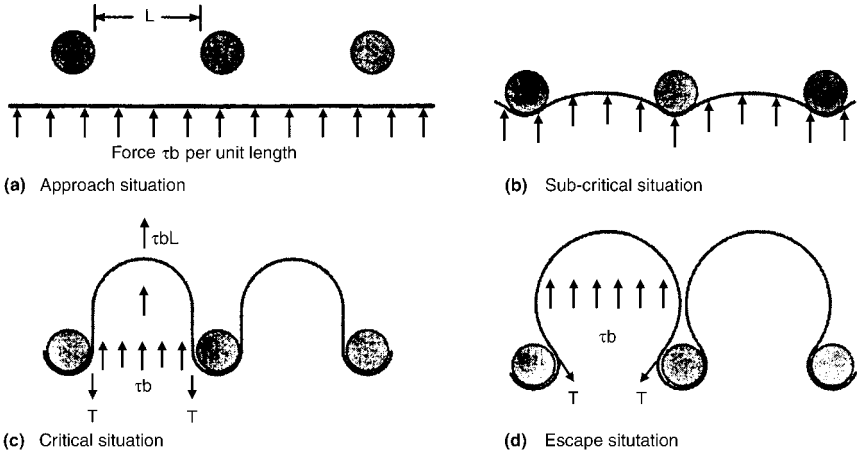

Fig. 11.16 Schematic diagram of stages of Orowan strengthening by dislocation interaction with particles separated by a spacing of *L*. Source: Ref 11.30

where *G* is the shear modulus and **b** is the Burgers vector. Thus, the closer the spacing of particles, the greater is the stress required for plastic deformation. If the particles are too closely spaced, stresses may increase to the level that dislocations will pass through the particles themselves, rather than passing between the particles as described by the Orowan mechanism.

Solid-Solution Strengthening of Ferritic Microstructures

The many chemical elements present in steel either combine to form second-phase precipitate particles or remain in solution within the crystal structures of austenite at high temperatures or ferrite at low temperatures. The atoms of size and electronic structure close to those of iron that do not combine to form carbides, nitrides, or other compounds merely substitute for iron atoms in fcc austenite or bcc ferrite crystals and are said to be in substitutional solid solution. The smaller atoms such as carbon and nitrogen, as noted earlier, go into the interstitial sites between iron atoms and are said to be in interstitial solid solution. The size and electronic differences between substitutional atoms and iron atoms affect lattice parameters of the ferrite crystal unit cell, the modulus of elasticity, and the shear modulus of ferrite (Ref 11.6). Also, the size and electronic structure differences of the substitutional atoms interact with elastic strain fields of dislocations in ferrite and increase the stress necessary to move dislocations.

Figure 11.17 shows the yield strength increases produced in low-carbon steels as a function of alloy content (Ref 11.28). The substitutional ele-

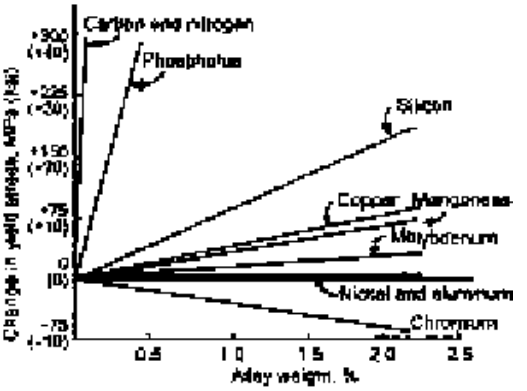

Fig. 11.17 Solid-solution strengthening of ferrite as a function of alloying element content in low-carbon steels. Source: Ref 11.28

ments provide a real but relatively modest solid-solution strengthening. For example, manganese has many functions in steel, including deoxidation, combination with sulfur, and improving hardenability, but is often added at levels of 1.0% or more to low-carbon steels with ferritic microstructures to increase strength. The interstitial elements have very high interstitial solution strengthening capability, but as discussed previously, rapidly leave solid solution to segregate at dislocations or precipitate as carbides and nitrides.

At temperatures below room temperature, substitutional elements, such as silicon, manganese, and nickel, may actually cause softening of ferritic microstructures (Ref 11.6). Although the cause of this phenomenon is not known, the effects of the substitutional atoms may be to enhance screw dislocation cross slip. Nickel, for example, is known to increase resistance to cleavage fracture and to lower ductile-to-brittle transition temperatures.

REFERENCES

11.1 G.E. Dieter, Mechanical Behavior of Materials under Tension, *Mechanical Metallurgy,* 2nd ed., 1976, McGraw-Hill, p 329–348

11.2 D. Kuhlmann-Wilsdorf, Advancing towards Constitutive Equations for the Metal Industry via the LEDS Theory, *Metall. Mater. Trans. A,* Vol 35, 2004, p 369–418

11.3 D. Kuhlmann-Wilsdorf, Theory of Workhardening 1934–1984, *Metall. Trans. A,* Vol 16, 1984, p 2091–2108

11.4 J. Pan, Unpublished research, Colorado School of Mines

11.5 G. Langford and M. Cohen, Strain Hardening of Iron by Severe Plastic Deformation, *Trans. ASM,* Vol 62, 1969, p 623–638

11.6 W.C. Leslie, *The Physical Metallurgy of Steels,* McGraw-Hill Book Company, 1981

11.7 D.K. Matlock, F. Zia-Ebrahimi, and G. Krauss, Structure, Properties, and Strain Hardening of Dual-Phase Steels, *Deformation, Processing, and Structure,* G. Krauss, Ed., American Society for Metals, 1984
11.8 W.R. Garrison, Jr. and N.R. Moody, Ductile Fracture, *J. Phys. Chem. Solids,* Vol 48 (No. 11), 1987, p 1035–1074
11.9 P.F. Thomason, *Ductile Fracture of Metals,* Pergamon Press, New York, 1990
11.10 B. Dodd and Y. Bai, *Ductile Fracture and Ductility with Applications to Metalworking,* Academic Press, London, 1987
11.11 J.M. Barsom and S.T. Rolfe, *Fracture and Fatigue Control in Structures,* 2nd ed., Prentice-Hall, Englewood Cliffs, NJ, 1987, p 128
11.12 W.C. Leslie, Iron and Its Dilute Solid Solutions, *Metall. Trans.,* Vol 3, 1972, p 5–26
11.13 V. Vitek and M.S. Duesbery, The Behavior of Screw Dislocations in BCC Metals under the Effect of Applied Stresses Other than Pure Shear, *Mechanical Properties of BCC Metals,* M. Meshii, Ed., TMS-AIME, Warrendale, PA, p 3–11
11.14 J.P. Hirth, Factors Contributing to Brittle Fracture in Metals, *Mechanical Properties in BCC Metals,* M. Meshii, Ed., TMS-AIME, Warrendale, PA, 1982, p 181–187
11.15 E. Hornbogen, Strengthening Mechanisms in Steel, *Steel-Strengthening Mechanisms,* Climax Molybdenum Company, 1969, p 1–15
11.16 C.J. McMahon, Jr. and M. Cohen, Initiation of Cleavage in Polycrystalline Iron, *Acta Metall.,* Vol 13, 1965, p 591–604
11.17 M.A. Linaza, J.L. Romero, I. San Martin, J.M. Rodriguez-Ibabe, and J. Urcola, Improvement of Toughness by Stopping Brittle Processes Nucleated in Ceramic Particles through Thermomechanically Optimized Microstructures in Engineering Steels, *Fundamentals and Applications of Microalloying Forging Steels,* C.J. Van Tyne, G. Krauss, and D.K. Matlock, Ed., TMS, Warrendale, PA, 1996, p 311–325
11.18 K.S. Chan, Ed., *Cleavage Fracture,* TMS, Warrendale, PA, 1996
11.19 A.H. Cottrell, *Dislocations and Plastic Flow in Crystals,* Oxford University Press, Oxford, England, 1956
11.20 G. Hahn, A Model for Yielding with Special Reference to the Yield-Point Phenomena of Iron and Related BBC Metals, *Acta Metall.,* Vol 10, 1962, p 727–738
11.21 D.F. Stein and J.R. Low, Jr., *J. Appl. Phys.,* Vol 31, 1960, p 362
11.22 W.C. Leslie, R.M. Fisher, and N. Sen, Morphology and Crystal Structure of Carbides Precipitated from Solid Solution in Alpha Iron, *Acta Metall.,* Vol 7, 1969, p 632–644
11.23 W.C. Leslie, The Quench-Aging of Low-Carbon Iron and Iron-Manganese Alloys, *Acta Metall.,* Vol 9, 1961, p 1004–1021

11.24 E.O. Hall, The Deformation and Aging of Mild Steel, *Proc. Phys. Soc. London,* Vol B64, 1951, p 747
11.25 N.J. Petch, The Cleavage Strength of Crystals, *J. Iron Steel Inst.,* Vol 174, 1953, p 25
11.26 R.W. Armstrong, The Yield and Flow Stress Dependence on Polycrystalline Grain Size, *Yield, Flow and Fracture of Polycrystals,* T.N. Baker, Ed, Applied Science Publishers, London, 1983, p 1–31
11.27 D.K. Matlock, D.M. Bruce, and J.G. Speer, Strengthening Mechanisms and Their Applications in Extremely Low C Steels, *IF Steels 2003,* H. Takechi, Ed., The Iron and Steel Institute of Japan, 2003, p 118–127
11.28 F.B. Pickering, High-Strength, Low-Alloy Steels—A Decade of Progress, *Microalloying 75,* Union Carbide Corporation, New York, 1977, p 9–30
11.29 E. Orowan, *Internal Stress in Metals and Alloys,* Institute of Metals, London, 1948
11.30 T. Gladman, *The Physical Metallurgy of Microalloyed Steels,* Institute of Materials, London, 1997

CHAPTER 12

Low-Carbon Steels

General Considerations

LOW-CARBON STEELS, steels that contain less than 0.25% C, make up the highest tonnage of all steels produced in a given year. Structural shapes and beams for buildings and bridges, plate for line pipe, and automotive sheet applications are just a few major applications for low-carbon steels. These applications are driven by manufacturing requirements for good formability and weldability, and performance requirements of good combinations of strengths and fracture resistance for given applications. While early approaches to design of steel structures involved increasing the section size of low-strength, low-carbon steels to increase load-carrying capacity, recent approaches for vehicles have been based on developing low-carbon sheet steel microstructures of higher strength in order to reduce section size and weight in response to powerful economic factors, the need for fuel reduction, and safety concerns. Higher strengths are increasingly produced in steels with lower and lower carbon contents, an approach that improves formability, weldability, and toughness or fracture resistance. As a result, there have been dramatic and continuous changes in the compositions of low-carbon steels, their strength, ductility, and toughness, and the processing approaches for their manufacture.

Figure 12.1 shows the many types of low carbon sheet steels that have been developed at the start of the twenty-first century (Ref 12.1–12.3). Mild steels represent the starting alloys, and developments have proceeded to higher ductilities and reduced strength for increased formability and to higher strengths with reduced ductilities. The steels marked by the box *First generation AHSS* (First Generation Advanced High Strength Steels) in Fig. 12.1 identify the first sets of steels, primarily for automotive applications, with substantially higher strengths than earlier developed steels. Research and applications continue and new generations of advanced high strength steels with improved combinations of ductility

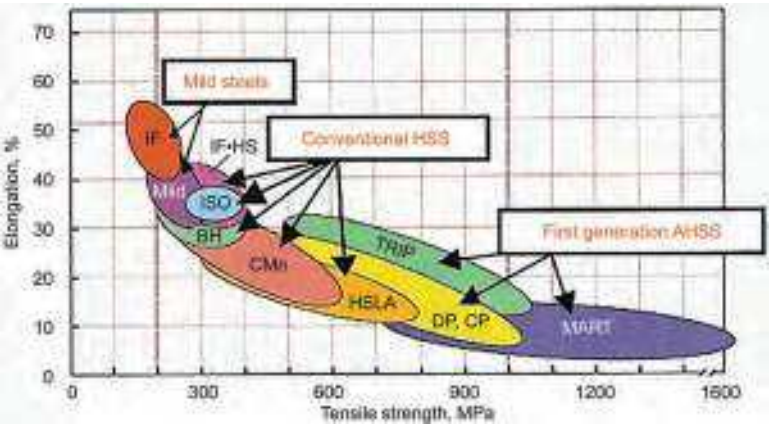

Fig. 12.1 Ranges of elongation and tensile strength combinations for various types of low-carbon steels. BH, bake-hardening; CMn, carbon manganese; CP, complex phase; DP, dual-phase; HSLA, high-strength, low-alloy steel; IF, interstitial-free; IF-HS, interstitial-free high-strengh; ISO, isotropic steels; MART, martensitic; TRIP, transformation-induced plasticity. Source: Ref 12.3

and strength compared to those shown in Fig. 12.1 are being developed (Ref 12.3). Competing with low-carbon sheet steels, high-manganese-containing Twinning-Induced Plasticity (TWIP) steels for higher combinations of strength and ductility, as discussed in a later section of this chapter, are also under intensive development.

The major microstructural component of low-carbon steels has traditionally been equiaxed or polygonal ferrite, but recent developments have added other major microstructural components. Nevertheless, the performance of low-carbon steels depends essentially on the deformation and fracture mechanisms of ferrite described in Chapter 11, "Deformation, Strengthening, and Fracture of Ferritic Microstructures." Microstructures consisting primarily of ferrite have relatively low strength, and therefore, various alloying and processing approaches used to develop high strength in new types of low-carbon steels are discussed in this chapter. The following sections describe hot-rolled low-carbon steels, cold-rolled and annealed low-carbon steels, interstitial-free or ultra-low carbon steels, controlled-rolled-microalloyed steels (also termed high-strength, low-alloy (HSLA) steels), dual-phase steels, and Transformation-Induced Plasticity (TRIP) steels. The latter two groups of steels have been developed to improve combinations of strength and ductility, relative to those of low-carbon steels with primarily as-rolled ferritic microstructures, by alloying and processing that produce unique low-carbon steel microstructures. Martensitic low-carbon steels, long used in automotive applications that require low formability, are now being manufactured in more complicated shapes, and therefore also merit detailed attention in this chapter. Brief descriptions are also given of next-generation AHSS steels: TWIP steels and Quenched and Partitioned (Q&P) steels.

Many of the sheet steel grades for automotive panel applications are now zinc-coated and offer outstanding corrosion protection. The zinc may be applied by hot-dip galvanizing or electrodeposition, and zinc coatings may be heated to produce beneficial layers of Zn-Fe intermetallic phases in a process designated as *galvannealing*. Hot-dip galvanizing adds another heating step, at 450 to 470 °C (840 to 880 °F), as steel sheet passes through liquid zinc baths, and galvannealing is subsequently performed at 500 to 550 °C (930 to 1020 °F). The zinc-coating processing of low-carbon sheet steels, the evaluation of friction and formability of zinc coatings, and the microstructure and performance of zinc coatings constitute a remarkable subset of recent low-carbon steel developments (Ref 12.4–12.6).

Low-Carbon Steel—Hot-Rolled Ferrite-Pearlite Microstructures

Ferrite-pearlite microstructures are produced in air-cooled heavy sections and shapes, and in flat-rolled plate and strip hot rolled from slabs and cooled during coiling. A schematic diagram of primary hot deformation processing applicable to low-carbon steels has been shown in Chapter 9, "Primary Processing Effects on Steel Microstructure and Properties." In low-carbon steels, ferrite is the major microstructural component, and the amount of pearlite is directly proportional to carbon content up to the maximum of 0.25%. The latter microstructures, traditionally formed in plain carbon or mild steels by conventional hot-rolling practices, have provided the base for incentives to modify low-carbon steel processing and microalloying for enhanced properties.

Pickering and his colleagues at the British Steel Corporation have established empirical equations for the properties of low-carbon steels with ferrite pearlite microstructures based on statistical multiple regression analysis (Ref 12.7, 12.8). Chemical and microstructural factors were measured and integrated into the equations, as follows:

$$\text{Yield strength in MPa } (\pm 31 \text{ MPa}) = 88 + 37(\%\text{Mn}) + 83(\%\text{Si}) + 2918(\%\text{N}_f) + 15.1(d^{-1/2}) \quad \text{(Eq 12.1)}$$

$$\text{Maximum uniform strain } (\varepsilon^*) = 0.27 - 0.016(\%\text{pearlite}) - 0.015(\%\text{Mn}) - 0.40(\%\text{Si}) - 0.043\ (\%\text{Sn}) - 1.1(\%\text{N}_f) \quad \text{(Eq 12.2)}$$

$$\text{Total strain at fracture } (\varepsilon_T) = 1.3 - 0.020(\%\text{pearlite}) + 0.30(\%\text{Mn}) + 0.20(\%\text{Si}) - 3.4(\%\text{S}) - 4.4(\%\text{P}) + 0.29(\%\text{Sn}) + 0.015d^{-1/2} \quad \text{(Eq 12.3)}$$

$$\text{Impact transition temperature (°C)} = -19 + 44(\%\text{Si}) + 700(\%N_f) - 11.5(d^{-1/2}) + 2.2(\%\text{pearlite}) \quad \text{(Eq 12.4)}$$

The element compositions are in weight percent, d is the mean linear intercept of ferrite grains in mm, and N_f is free nitrogen dissolved in ferrite and not combined in a stable nitride. The effects of many of the terms in these equations are consistent with the strengthening mechanisms and deformation and fracture considerations discussed in Chapter 11, "Deformation, Strengthening, and Fracture of Ferritic Microstructures." Manganese and silicon contribute to solid-solution strengthening of ferrite, and the positive grain size term correlates with the Hall-Petch equation. The relatively small amount of pearlite in low-carbon steels does not affect yield strength but does affect uniform strain and fracture. The strain-hardening/flow-stress curve analysis in Fig. 12.2(a) shows that the effect of increased pearlite, as related to carbon content, is due to reduced Lüders strain and increased strengthening but is not due to increased strain hardening. Although fine grain size increases yield strength, it does not affect uniform strain. Figure 12.2(b) shows that increases in both flow stresses and strain hardening due to grain size refinement balance their effect on uniform strain and necking instability.

Nitrogen in interstitial solid solution has a potent strengthening effect on ferritic microstructures and significantly raises impact transition temperatures and promotes brittle cleavage fracture. Other elements, because of embrittling effects or tendencies to form inclusions, lower ductile fracture resistance, as shown in Eq 12.3. For example, sulfur forms coarse MnS inclusions that do not affect strength and strain hardening but provide major sites for microvoid initiation in ductile fracture.

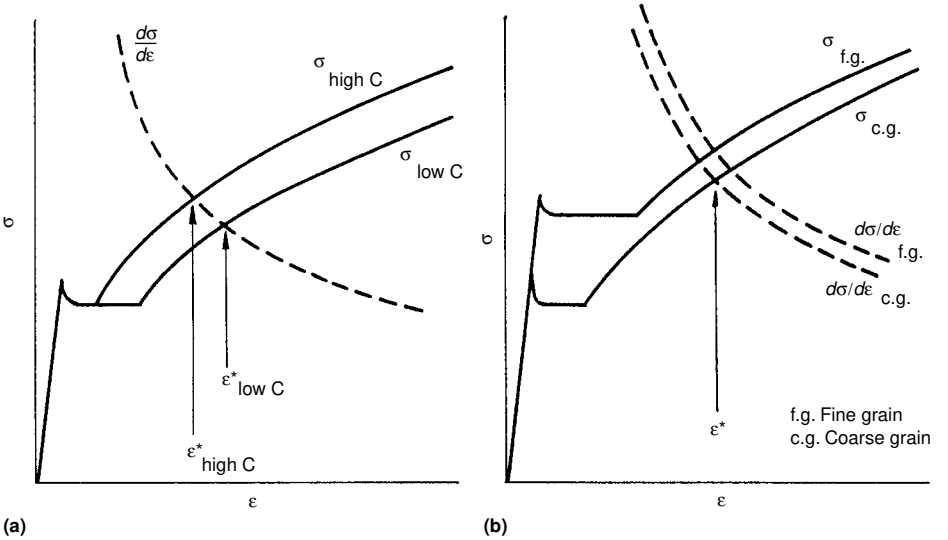

Fig. 12.2 Schematic diagrams of strain-hardening and flow stress curves that show the effect of (a) carbon content and (b) grain size on the uniform elongation ε* of low-carbon steels. Source: Ref 12. 7

The relationships demonstrated in Eq 12.1 to 12.4 have provided guidelines for achieving improvements in mechanical behavior of low-carbon steels. A typical low-carbon steel with ferrite-pearlite microstructure produced by conventional hot rolling, with nominal manganese and silicon contents and nominal grain size, has a yield strength around 210 MPa (30 ksi), as indicated in the mild steel area of Fig. 12.1. That figure also shows that yield strength-ductility combinations of more recently developed steels move in both directions from those of mild steels, consistent with the effects of the parameters documented in the Pickering equations. In particular, alloying and processing approaches that reduce grain sizes for both increased strength and fracture resistance, reduce impurity element and inclusion contents for improved fracture resistance, and reduce carbon content to reduce pearlite content and its effect on fracture, have provided technical driving forces for new steel development.

Low-Carbon Steel—Processing by Cold Rolling and Annealing

Figure 12.3 shows the thermomechanical processing that may be applied to hot-rolled strip to produce cold-rolled and annealed sheet. Annealing to produce formable recrystallized ferritic structures is accomplished by subcritical annealing, i.e., annealing below A_{C1} temperatures without austenite formation. Newer types of sheet steels, such as the dual-phase

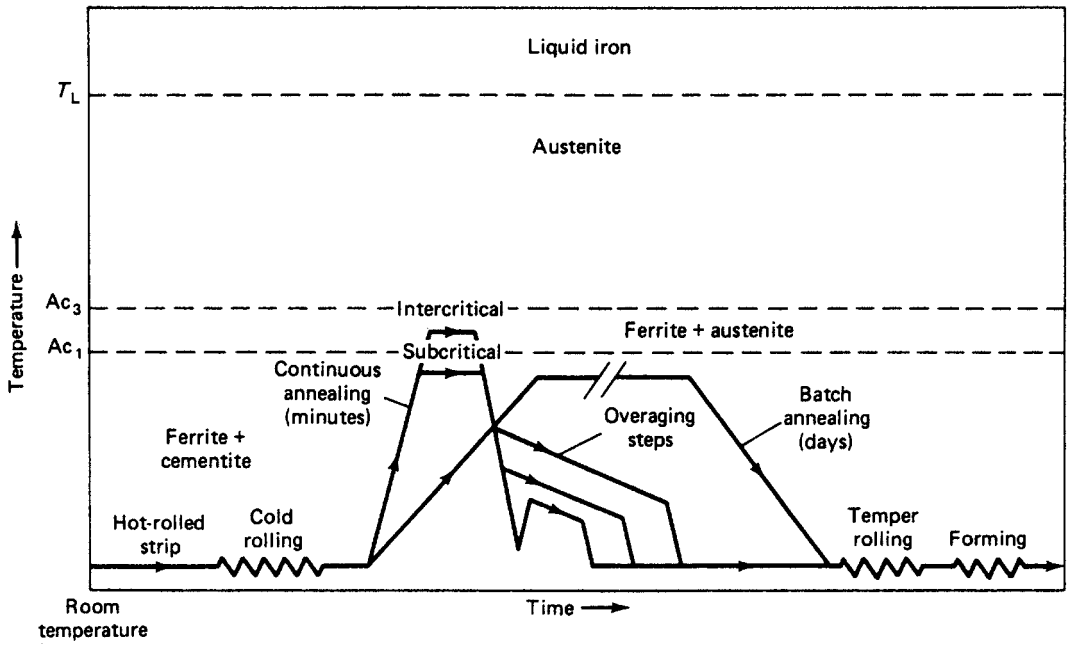

Fig. 12.3 Temperature-time processing schedules for cold-rolled and annealed low-carbon sheet steels. Continuous and batch annealing are schematically compared and intercritical annealing used to produce dual-phase and TRIP steels is indicated.

and TRIP steels described in following sections, are subjected to intercritical annealing, i.e., heating between A_{C1} and A_{C3} temperatures to produce small amounts of austenite within matrix microstructures of equiaxed ferrite grains. On cooling, the austenite transforms to strengthening components of the microstructure.

Cold rolling strain-hardens ferritic microstructures and reduces ductility. Annealing restores ductility of strained ferrite by producing *recrystallization,* a mechanism of microstructural change in which strain-free grains nucleate and grow on heating. Recrystallization is driven by the high strain energy stored in dislocation substructure produced by cold work and is accomplished by short-range iron atom transfer across boundaries between deformed grains and strain-free annealed grains. A study of the recrystallization kinetics of a low-carbon steel showed that the activation energy for recrystallization, determined from the times to achieve 50% recrystallization at various temperatures, is 226 kJ/mol (54 kcal/mol), consistent with the activation energy for the self-diffusion of iron in body-centered cubic (bcc) ferrite (Ref 12.9).

Figure 12.4 shows deformed ferrite grains of an Fe-0.003% C steel (enameling steel) cold rolled 60% and the effect of annealing at 540 °C (1000 °F) for two hours (Ref 12.10). The deformed ferrite grains are elongated, and although the dislocation substructure is not resolvable in the light microscope, slip lines and rough-etching response to the dislocation substructure are apparent. After annealing at 540 °C, the deformed ferrite grains are largely replaced by fine, smooth-etching ferrite grains, as shown in Fig.12.4(b).

Figure 12.5 shows the deformed microstructure of a low-carbon steel (0.08% C-1.45% Mn-0.21% Si) produced by cold rolling 50%, and the effects of annealing at 700 °C (1290 °F) for 20 minutes (Ref 12.9). The

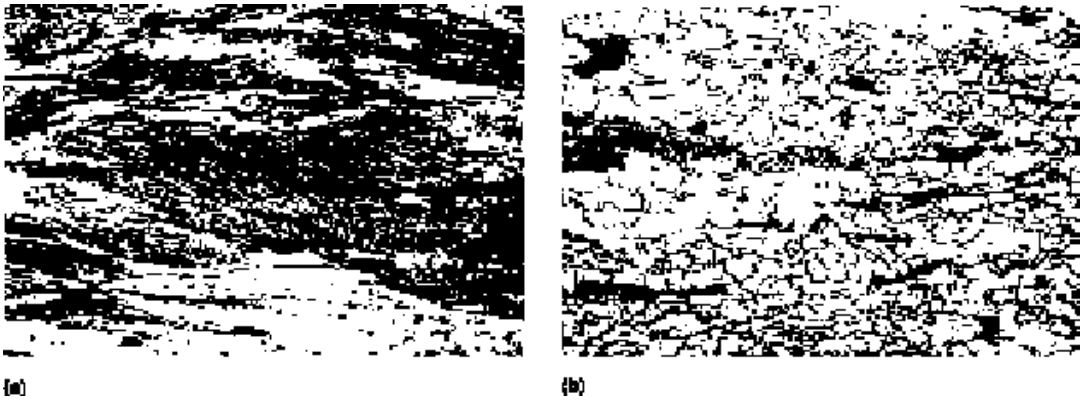

Fig. 12.4 Recrystallization from annealing. (a) Microstructure of a 0.003% C steel cold rolled 60%. (b) Microstructure of the cold-rolled steel after annealing at 540 °C (1000 °F) for 2 h. About 80% of the cold-worked microstructure has recrystallized to fine equiaxed ferrite grains. Light micrographs, nital etch, original magnification 100×; shown here at 75%. Courtesy of D.A. Witmer. Source: Ref 12.10

hot-rolled starting microstructure of this steel, in view of its carbon content, contained a small amount of pearlite. Figure 12.5(a) shows that the pearlite colonies deform and elongate with the ferrite grains. On annealing, in addition to ferrite recrystallization, the cementite lamellae in the pearlite spheroidize to clusters of fine carbide particles, as shown in Fig. 12.5(b).

Figure 12.6 shows recrystallization kinetics for the 0.08% C steel. Generally, recrystallization is characterized by an incubation period, when strain-free grains first nucleate, followed by more rapid recrystallization

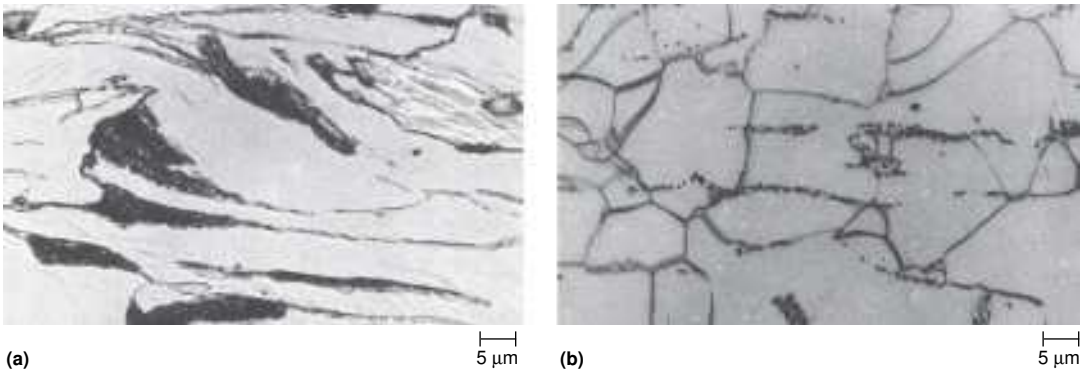

Fig. 12.5 Microstructure of 0.08% C-1.45% Mn-0.21% Si steel. (a) Cold rolled 50%. (b) Annealed at 700 °C (1290 °F) for 20 min. Light micrographs, nital etch. Source: Ref 12.9

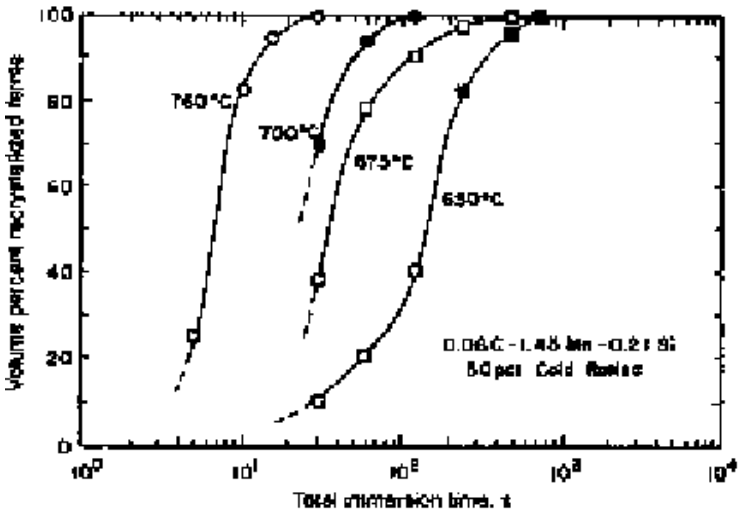

Fig. 12.6 Volume percent ferrite recrystallized in a cold-rolled 0.08% C-1.45% Mn-0.21% Si steel as a function of time in salt bath at temperatures indicated. Source: Ref 12.9

as nucleation continues and nucleated strain-free grains grow. Figure 12.6 shows such classical recrystallization kinetics only in specimens that have been annealed at 650 °C (1200 °F). Recrystallization at higher temperatures was so rapid that the incubation period could not be measured.

Commercially, two approaches are used to anneal cold-rolled sheet steels: batch or box annealing and continuous annealing. In batch annealing, coils of sheet are stacked inside steel covers or shells and heated (Ref 12.11). In view of the fact that many tons of coiled steel must be heated and cooled, batch annealing takes several days. The long heating times produce coarse annealed grains and the slow cooling of the coils ensures that all carbon dissolved during annealing precipitates as coarse carbide particles on cooling, reducing the potential for strain aging.

Continuous annealing is performed by unwinding coils of cold-rolled steel and passing the thin sheet through two-stage furnaces at high rates of speed, processing that requires only minutes for any section of sheet. Although continuous annealing has long been used to produce hot-dipped galvanized sheets, tin plate and stainless steel sheet, it was first applied commercially in the middle 1970s to produce carbon sheet steels with good formability by the Japanese steel companies Nippon Kokan, Nippon Steel, and Kawasaki Steel. Detailed descriptions of the continuous annealing lines applied by these companies are presented in the appendix of Ref 12.12.

Figure 12.7 compares schematically batch and continuous annealing and accentuates the differences in time required for the two processes (Ref 12.13). The first stage of continuous annealing accomplishes recrystallization but also causes carbon to dissolve in accordance with its increased solid solubility at annealing temperatures (Fig. 3.4 in Chapter 3, "Phases and Structures"). The second stage, found to be key to the production of

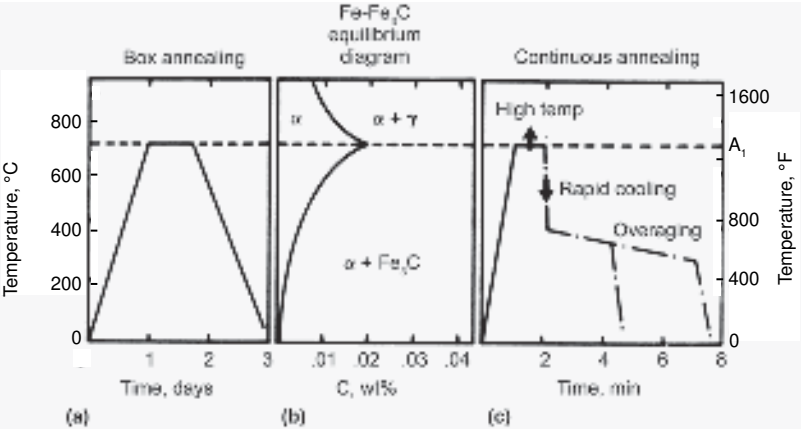

Fig. 12.7 Comparison of (a) box or batch annealing and (c) continuous annealing relative to (b) the low-carbon side of the Fe-Fe_3C equilibrium diagram. Source: Ref 12.13

formable steels, effectively overages the ferritic microstructure, i.e., coarse carbides are precipitated and remove carbon from solid solution. Thus, potential strain- and quench-aging effects that reduce formability are minimized. Various processing approaches used to produce overaging in continuously annealed steels are illustrated in Fig. 12.8 and are also indicated in Fig. 12.3.

Processing of Cold-Rolled and Annealed Sheet Steels for High Formability

Some sheet steels are subjected to severe forming operations. In particular, sheet steel subjected to deep drawing operations may fail because of the onset of necking instability, leading to fracture through the sheet thickness. The production of sheet steels resistant to such failures constitutes a remarkable chapter in the physical metallurgy of steels, i.e., the interrelationships between steel chemistry, processing, microstructure, and properties (Ref 12.14, 12.15). Long-established grades of highly formable low-carbon sheet steels are aluminum-killed, hot-rolled and coiled, cold-rolled and coiled, and batch-annealed to produce excellent performance. Interstitial-free steels and continuous annealing, as discussed subsequently, are more recent developments used to produce steels with high formability.

Aluminum and nitrogen solid solubility in austenite has already been discussed in Chapter 8, "Austenite in Steel." In sheet steels with aluminum contents around 0.03% and nitrogen contents around 20 to 40 ppm, high finishing hot-rolling temperatures, around 890 °C (1630 °F), keep aluminum and nitrogen in solid solution in austentite, and low coiling temperatures, around 580 °C (1080 °F), prevent aluminum nitride precipitation in ferrite (Ref 12.14). Thus, aluminum and nitrogen stay in super-

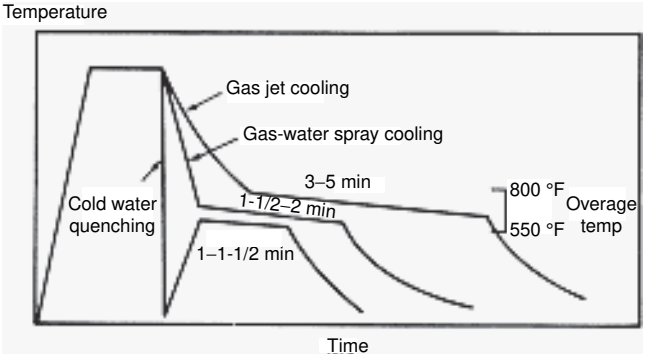

Fig. 12.8 Various processing approaches to produce overaging and the removal of carbon from solid solution in ferrite of low-carbon steels subjected to continuous annealing. Source: Ref 12.13

saturated solid solution during cold rolling. During the slow heating of batch annealing, aluminum and nitrogen atoms cluster and precipitate, retarding recrystallization and the nucleation of ferrite grains with randomly oriented crystal orientations. Nucleation and growth of grains with {111} planes parallel to the rolling plane are favored to produce (111) [110] cube on corner crystallographic textures of the batch annealed sheet.

Steel sheets with (111)[110] texture have ferrite grains oriented to minimize dislocation motion on slip systems that cause thinning and necking instability. Microstructures with these textures have high values of the *plastic strain ratio, r*, defined as:

$$r = \varepsilon_w/\varepsilon_t = \ln(w_i/w_f)/\ln(t_i/t_f) \quad \text{(Eq 12.5)}$$

where ε_w and ε_t are the strains in the width and thickness, respectively; w_i and w_f are initial and final width, respectively; and t_i and t_f are initial thickness and final thickness, respectively, of the gage length of a tensile specimen after testing. Plastic strain ratios are a function of orientation in sheet and are often determined as average values, r_m, as follows:

$$r_m = \frac{1}{4}(r_0 + 2r_{45} + r_{90}) \quad \text{(Eq 12.6)}$$

where r_0 is the r value determined in specimens aligned in the sheet rolling direction, r_{45} is the r value at 45° to the rolling direction, and r_{90} is the r value in the sheet transverse direction. For randomly oriented grains, non-textured sheet would have an r value of 1. Typically, low-carbon aluminum-killed steels resistant to thinning have r values between 1.5 and 1.8 (Ref 12.14).

Interstitial-Free Steels

Interstitial-free (IF) steels, also referred to as ultra-low-carbon (ULC) or extra-low-carbon (ELC) steels, are cold-rolled and annealed sheet steels with very low carbon and nitrogen contents (Ref 12.12, 12.16–12.18). The processing and chemistry of IF steels produce very high ductility and formability, albeit at low strengths, as shown in Fig. 12.1. Large-scale production of IF steels was made possible by dramatic advances in steelmaking, namely, the incorporation of vacuum degassing of oxygen converter steel, and rigorous control of carbon, nitrogen, and oxygen pick-up during casting (Ref 12.19). Products of such steelmaking typically contain only 20 to 50 ppm C, and 10 to 50 ppm N. Despite such low levels of interstitials, further alloying, by additions of titanium and/or niobium, are made to remove carbon and nitrogen from solid solution by the precipitation of carbides, nitrides, and other compounds.

Although IF steels border on being almost pure iron, the method of production, the alloying additions, the microstructural response to thermomechanical treatment, and the resultant properties qualify them as steels. Table 12.1 lists typical ranges of the elements in IF steels. Generally, titanium and niobium are not added together. Titanium is a very strong nitride former and also combines with sulfur to form $Ti_4S_2C_2$.

Therefore, titanium must be added in sufficient quantity to not only form TiN and titanium carbosulfides but also to tie up residual carbon. Niobium is considered only to combine with carbon, and therefore allowances for other niobium compounds are not necessary. In contrast to the aluminum-killed low-carbon steels described in the previous section, where aluminum and nitrogen are kept in solution by a combination of high slab reheat temperatures, high finishing temperatures, and low coiling temperatures, niobium- and titanium-alloyed steels are alloyed and processed to form stable compounds during hot deformation processing prior to cold work. Thus, stabilizing precipitates are retained through cold rolling and are directly available for the control of recrystallization, making IF steels compatible with high heating rates during continuous annealing.

The recrystallization of titanium- and niobium-stabilized IF steel is severely retarded compared with aluminum-killed (AK) low-carbon steels. Figure 12.9 compares the recrystallization behavior of a series of experi-

Table 12.1 Composition ranges (in wt%) of IF steels

C	Si	Mn	P	Al	N	Nb	Ti	S
0.002–0.008	0.01–0.03	0.10–0.34	0.01–0.02	0.03–0.07	0.001–0.005	0.005–0.040	0.01–0.11	0.004–0.01

Source: Ref 12.12, 12.16, 12.17

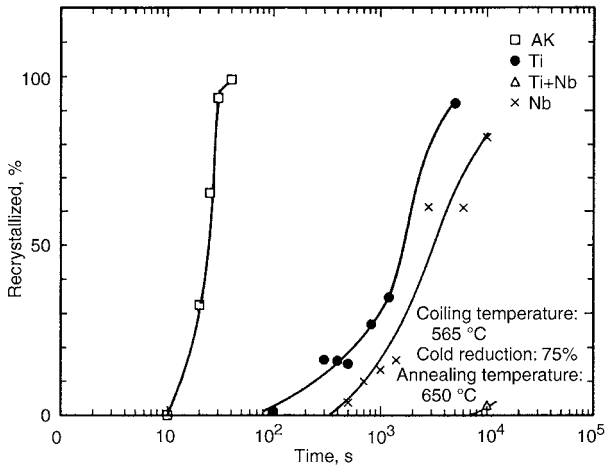

Fig. 12.9 Percent ferrite recrystallization versus time for interstitial-free aluminum-killed (AK), titanium-stabilized (Ti), niobium-stabilized (Nb), and titanium- and niobium-stabilized (Ti + Nb) steels annealed at 650 °C (1200 °F). Courtesy of D.O. Wilshynsky. Source: Ref 12.20

mental IF steels annealed at 650 °C (1200 °F) after 75% deformation and shows the marked retardation of recrystallization in the stabilized IF steels compared with the AK steel (Ref 12.20). The niobium-stabilized steel was found to have the finest distribution of particles, averaging about 8 nm (80 Å), compared with the titanium-stabilized steel, with particles averaging about 14 nm (140 Å). The finer sizes of the niobium particles are consistent with precipitation at lower temperatures compared with the particles in the titanium-stabilized steel. Higher annealing temperatures accelerate recrystallization even with stabilizing precipitate dispersions, and because of the very low carbon content of IF steels, annealing can be performed at high temperatures, 800 to 850 °C (1470 to 1560 °F), in the single-phase ferrite field, compared with higher-carbon steels, for which annealing temperatures are limited to around 700 °C (1290 °F) to avoid austenite formation.

Cold-rolled and annealed IF steels have very strong (111)[110] recrystallization textures (Ref 12.21) and high values of r_m as defined in Eq 12.6. Figure 12.10 shows, in a plot compiled by Hutchinson et al. (Ref 12.22), the strong effect of very low steel carbon content on increasing r_m values. Severe cold work also promotes favorable textures and high r_m values, as shown in Fig. 12.11.

Coupled to the high ductility and excellent formability of IF steels is low strength, as indicated in Fig. 12.1. Yield strengths typically range between 140 and 180 MPa (20 and 26 ksi) and tensile strengths range between 290 and 340 MPa (42 and 49 ksi). In view of the low yield strengths and in-

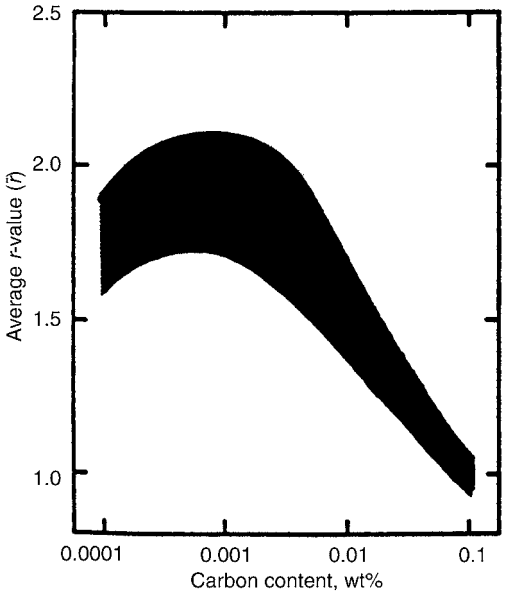

Fig. 12.10 Effect of steel carbon content on r_m values. Source: Ref 12.22

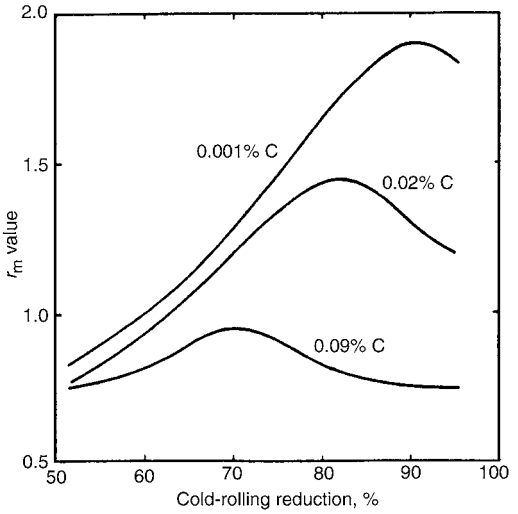

Fig. 12.11 Effect of steel carbon content and cold reduction on r_m values. Source: Ref 12.23

creasingly reduced thickness of automotive sheet steels, denting of outer panels is more common (Ref 12.2). As a result, early in the development of IF steels, attention was paid to increasing strength. Two strengthening approaches are used: solid-solution strengthening and bake hardening.

Figure 11.17, Chapter 11, "Deformation, Strengthening, and Fracture of Ferritic Microstructures," shows that small amounts of phosphorus very effectively solid-solution-strengthen ferrite. Hence, additions of phosphorus to IF steels, up to levels of 0.08% have been used to effectively increase IF strength, as noted by the IF-HS region in Fig. 12.1, and by careful processing to retain high r_m values (Ref 12.24, 12.25). However, the same atomic size and electronic factors associated with the high solid-solution strengthening of phosphorus also cause phosphorus to segregate to grain boundaries in ferritic microstructures. This phenomenon is especially pronounced in IF steels, from which the beneficial segregation of carbon to grain boundaries is absent (Ref 12.26). As a result of phosphorus segregation, *secondary or cold-work embrittlement*, manifested by intergranular fracture along ferrite grain boundaries, may develop in cold-drawn parts (Ref 12.17). Small additions of boron, which also segregates to ferrite grain boundaries and reduces the sites available for phosphorus atoms, and processing to retain some carbon in solution, significantly decrease susceptibility to cold-work embrittlement (Ref 12.17, 12.27).

Bake hardening refers to the increment of strength that develops in cold-formed sheet steel during paint baking of automotive panels. Bake-hardening increments are measured in specimens subjected to small strains and heated at low temperatures and times that simulate paint curing cy-

cles, typically 175 °C (350 °F) for 20 minutes (Ref 12.28). The mechanism for strengthening provided by bake hardening is therefore exactly that of strain aging as described in Chapter 11, "Deformation, Strengthening, and Fracture of Ferritic Microstructures." In IF steels carbon must be made available for aging by control of processing and stabilizing elements to provide both the functions of carbon removal and carbon in solution in bcc ferrite. Niobium-stabilized steels, in which niobium carbide has some solubility at annealing temperatures, especially the higher temperatures that can be used for IF steels, are effectively bake-hardened (Ref 12.17, 12.24).

Interstitial-free steels are now widely used, and the great international interest and state-of-the-art in the application, processing, structure, and properties of this unique type of steel are reviewed in Ref 12.29.

High-Strength, Low-Alloy Low-Carbon Steels

High-strength, low-alloy (HSLA) steels derive their name from their higher strengths relative to plain low-carbon steels with nominal ferrite-pearlite microstructures, as discussed previously. The HSLA steels have been developed over many years, but a great impetus for their use and further development came with their application in the Alyeska Pipeline in Alaska in 1969 and 1970 (Ref 12.30). That project used large tonnages of HSLA steel plate that not only had higher strength than conventionally used plate but also was readily weldable and had high toughness for severe arctic weather conditions. Figure 12.12 shows that fine ferrite grain size is the major strengthening component of HSLA steels relative to low-carbon mild steels with ferrite-pearlite microstructures produced by conventional hot rolling and relatively high finishing temperatures (Ref 12.31).

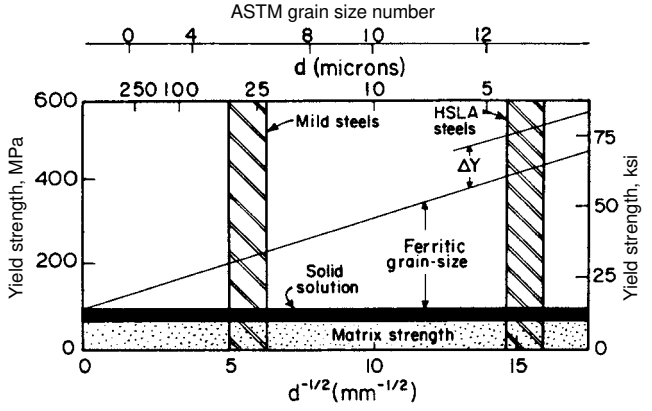

Fig. 12.12 Yield strength as a function of ferrite grain size in low-carbon steels. Contributions of various other strengthening mechanisms, with ΔY a measure of strengthening from precipitation if applicable, are also indicated. Source: Ref 12.31

The alloying of HSLA steels is in fact microalloying, and small amounts of the microalloying elements niobium, vanadium, and titanium, combined with controlled rolling, are responsible for the high strengths of HSLA low-carbon steels (Ref 12. 30–12.38). The solubility products of the microalloying elements and their effect on rolling and austenitic grain size control have already been discussed in Chapter 8, "Austenite in Steel," and the fact that only grain size refinement can increase strength and toughness of ferritic microstructures has been noted in Chapter 11, "Deformation, Strengthening, and Fracture of Ferritic Microstructures." Lower steel carbon contents and the manufacture of clean steels with low inclusion contents and inclusion shape control also have combined with microalloying and controlled rolling to produce good toughness and weldability.

Figure 12.13 shows schematically various hot rolling schedules used for low-carbon steels. The critical temperatures A_{C1} and A_{C3}, and the temperature below which austenite does not recrystallize, T_R, are shown. Microadditions of niobium effectively raise T_R and are extensively used to produce fine-grained HSLA steels. Figure 12.14, from an experimental study, shows the strong effect of small amounts of niobium on austenite recrystallization (Ref 12.39). Specimens of 0.11% C steel were hot rolled at 950 °C (1740 °F), and the deformed austenite was then held at various temperatures for various times. The steel without niobium recrystallizes readily even at low austenitizing temperatures, while the steels with niobium contents between 0.031 and 0.21% barely begin to recrystallize after

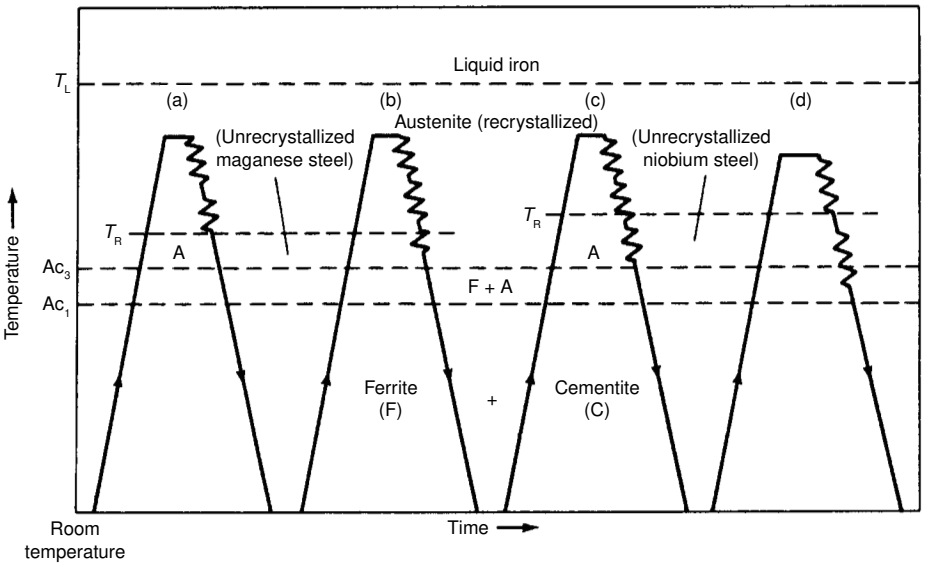

Fig. 12.13 Schematic of temperature-time schedules for thermomechanical and controlled rolling schedules of low-carbon steels. (a) Normal processing. (b) Controlled rolling of C-Mn steels. (c) Controlled rolling of Nb-containing steels. (d) Controlled rolling of Nb-containing steels with finishing temperature below Ac_3. Source: Ref 12.37

hold times as long as 10,000 seconds (167 min). Niobium carbonitride particles were found on austenite grain boundaries, but it was the fine niobium particles that precipitated within the deformed austenite matrix structure that suppressed the nucleation and growth of recrystallized austenite. Niobium carbonitride particles sizes were measured on carbon extraction replicas and found to be on the order of 5 nm (50 Å) in size at austenitizing temperatures of 850 and 900 °C (1560 and 1650 °F).

Figure 12.15 shows schematically the changes in austenitic grain structure and the early stages of ferrite formation that develop with conventional hot rolling and controlled rolling (CR) (Ref 12.30). In recrystallized, equiaxed austenite, ferrite grains nucleate on austenite grain boundaries to

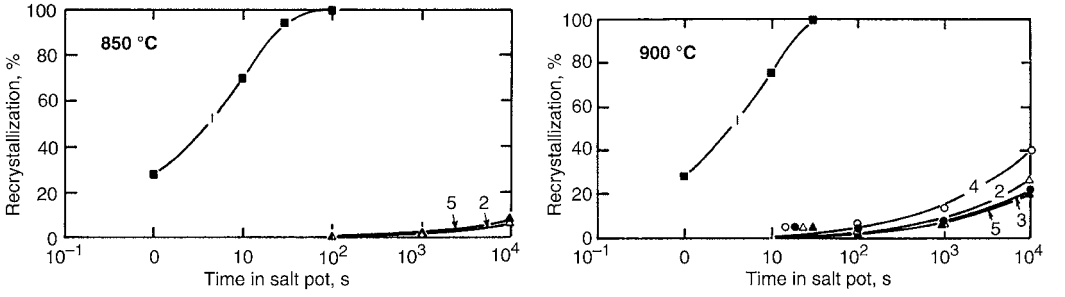

Fig. 12.14 Percent austenite recrystallization in plain carbon 0.11% C-1.30% Mn steel, curve marked 1, and 0.10% C steels with Nb contents between 0.029 and 0.21%, curves marked 2,3,4,5, after hot rolling at 950 °C (1740 °F) and holding at 850 °C (1560 °F) and 900 °C (1650 °F). Source: Ref 12.39

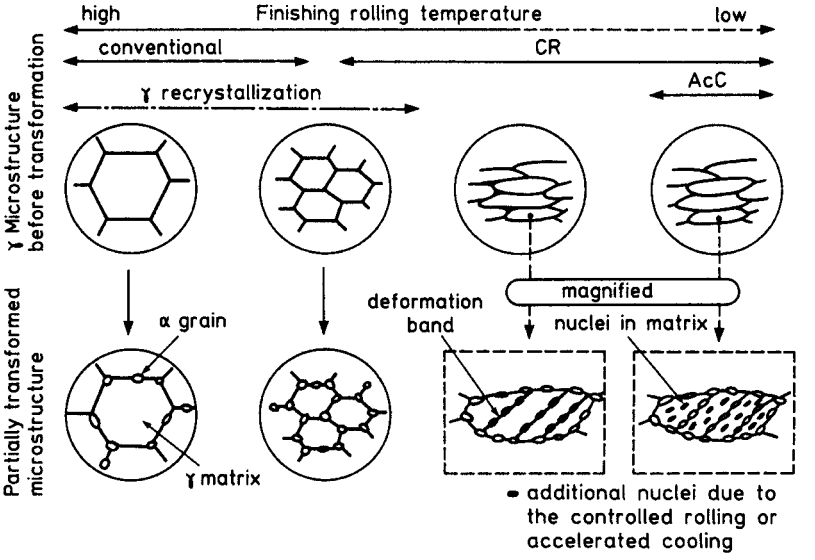

Fig. 12.15 Sketches of microstructural changes in low-carbon steels that develop as a function of finishing temperature in austenite and cooling to initiate ferrite formation. Source: Ref 12.30

produce relatively coarse equiaxed ferrite grains, the size depending on the finishing temperature. In unrecrystallized austenite, ferrite grains not only nucleate on austenite grain boundaries that have been brought together by hot rolling but also on deformation or shear bands in the deformed austenite. Some mills are equipped with water sprays for accelerated cooling, and in such processed steel fine ferrite grains also may nucleate within austenite grains. Another approach to producing fine ferrite grain size is to minimize the size of equiaxed austenite grains by the addition of titanium, which produces nitrides stable at high temperatures. This approach is referred to as *recrystallization-controlled rolling (RCR)*.

Low-Carbon Dual-Phase and TRIP Steels—Background

All of the low-carbon steels discussed to this point have finished microstructures that consist almost entirely of ferrite, sometimes with very fine grain sizes, sometimes with small amounts of pearlite or spheroidized carbides depending on carbon content and heat treatment. The microstructures described in this section are produced by heating hot-rolled or cold-rolled steels to temperatures between the critical temperatures A_{C1} and A_{C3}. Such *intercritical annealing* treatments are designed to produce small islands of austenite in a matrix of ferrite. Depending on cooling conditions, the austenite transforms to martensite, bainite, or other microstructures; sometimes significant amounts of austenite may be retained.

Dual-phase (DP) steels are cooled directly to room temperature from intercritical heating temperatures, while TRIP steels are isothermally transformed at subcritical temperatures after intercritical heating. The austenite retained after subcritical isothermal transformation is capable of strain-induced transformation to martensite, a mechanism that enhances plastic deformation. Such *transformation-induced-plasticity* has led to the term *TRIP* for intercritically annealed and isothermally transformed steels. Figure 12.16 shows schematically the two thermal processing schedules used to produce the microstructures of the two types of steels (Ref 12.40). The direct cooling of dual-phase steels is indicated by the dashed line, and the associated microstructure schematic shows that ideally dual-phase steels consist only of the two phases ferrite (F) and martensite (M); hence the name *dual-phase*. Figure 12.16 indicates that austenite transforms to bainite (B) during a subcritical isothermal hold and that considerable austenite may be retained. On cooling to room temperature, some of the austenite may transform to martensite. The temperatures and times during intercritical heating, T_1 and t_1, and during isothermal interrupted cooling, T_2 and t_2, may be varied to produce a large variety of microstructures and mechanical properties.

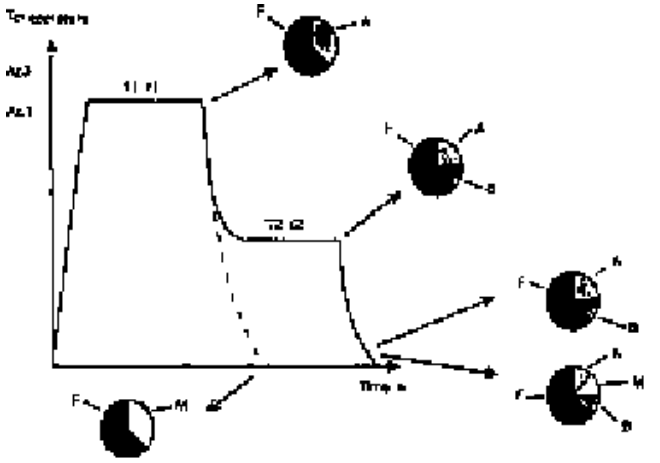

Fig. 12.16 Schematic diagram that illustrates dual-phase steel processing (dashed line) to produce ferrite (F)-martensite (M) microstructures and TRIP steel processing (solid line) to produce ferrite-bainite (B)-austenite (A) and martensite microstructures after intercritical annealing. Source: Ref 12.40

DP and TRIP steels were developed to provide sheet steels with better combinations of strength and ductilities than could be produced by other approaches. Figure 12.1 shows that at yield strengths over 400 MPa (58 ksi), Dual-phase steels have better combinations of strength and ductility than do manganese-strengthened or HSLA steels; TRIP steels have even better ductilities at the higher-strength levels. Dual-phase steels were first developed in the middle 1970s, beginning with landmark papers by Hayami and Furakawa (Ref 12.41) and Rashid (Ref 12.42), and followed by intensive development as recorded in symposia devoted to DP steels (Ref 12.43–12.45). TRIP steels were first developed in the late 1980s based on their improved combinations of strength and ductility relative to DP steels as demonstrated by Matsumura, Sakuma, and Takechi (Ref 12.46).

Dual-Phase Steels—Microstructure and Properties

Figure 12.17 compares engineering stress-strain curves for a plain, low-carbon, mild steel, an HSLA steel (SAE 980 X), and a DP low-carbon steel (GM 980 X) (Ref 12.47). The two high-strength steels had identical compositions (0.1% C, 1.5% Mn, 0.5% Si, and 0.1% V) but were processed differently. The DP steel has a lower yield strength than does the HSLA steel but, because of a higher strain-hardening capacity, reaches the same ultimate tensile strength. Also, the ductility of the DP steel is higher than that of the HSLA steel.

The strain hardening and high strength of DP steels are a result of martensite formation. Hard martensite regions in ferrite provide dispersion strengthening according to the rule of mixtures, i.e., the more martensite,

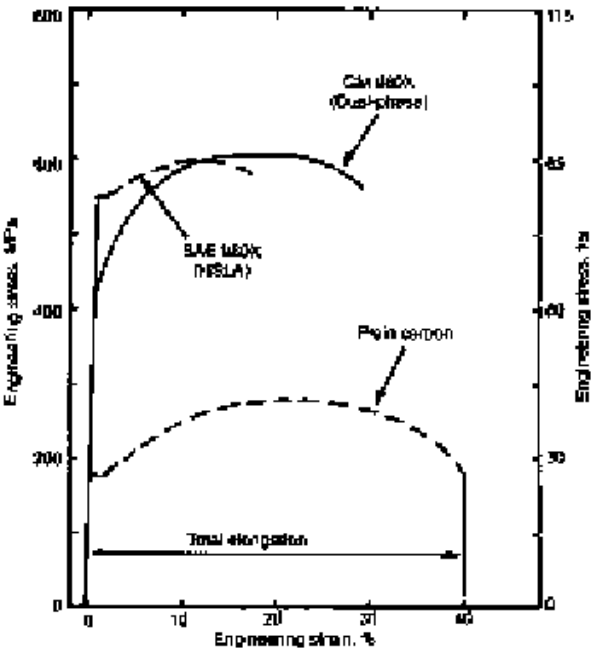

Fig. 12.17 Engineering stress-strain curves that compare deformation behavior of plain carbon, HSLA, and dual-phase steels. Source: Ref 12.47

the greater the strengthening, but also introduce high densities of dislocations into the ferrite around the martensite (Ref 12.48). Figure 12.18 shows transmission electron micrographs of dislocation structures in a 0.06% C-Mn-Si dual-phase microstructure produced by intercritical annealing at 810 °C (1490 °F) and cooling at 60 °C/s (110 °F/s) (Ref 12.49). In the ferrite adjacent to the martensite (the black area in Fig. 12.18a), there is a very high density of dislocations. These dislocations are generated by the shear and volume changes associated with the transformation of austenite to martensite. Dislocation densities are much lower in the ferrite removed from the martensite islands, Fig. 12.18(b). The dislocations around the martensite are not pinned and account for the absence of the discontinuous yielding exhibited in mild steels and HSLA steels, as shown in Fig. 12.17. The martensite-induced dislocations move at low stresses, creating low yield strengths, and interact to produce high rates of strain hardening.

Austenite formation during intercritical annealing is the first step in the production of DP and TRIP steels. Starting microstructure, steel composition, and time and temperature of annealing all determine the distribution of austenite in a retained ferrite matrix. The higher the carbon content of a steel, the greater will be the amount of austenite formed at a given temperature in the ferrite-austenite two-phase field. Also, the higher the intercritical annealing temperature, the greater will be the amount of austenite formed. Austenite forms rapidly at carbide particles or on ferrite grain

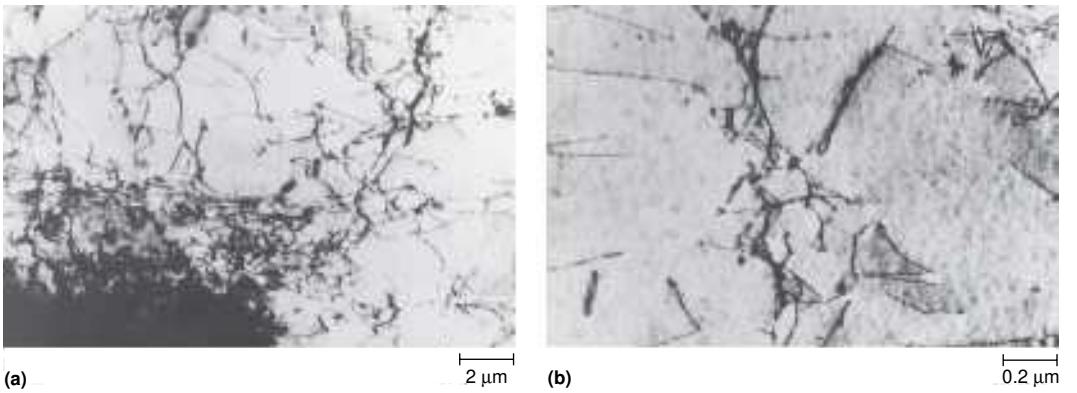

Fig. 12.18 Dislocation substructure in a 0.06% C-Mn-Si dual-phase steel intercritically annealed at 810 °C (1490 °F) and cooled at 60 °C/s (110 °F/s). (a) High dislocation density in ferrite adjacent to a martensitic area (black) and (b) in ferrite removed from martensitic areas. Transmission electron micrographs. Courtesy of D. Korzekwa. Source: Ref 12.49

boundaries as described in Chapter 8, "Austenite in Steel." Initially the growth of high-carbon austenite is dependent only on rapid carbon diffusion, independent of diffusion of substitutional elements such as manganese and silicon, a state of microstructural change termed *paraequilibrium* (Ref 12.50, 12.51). True equilibrium is attained only when manganese, an austenite-stabilizing element, and silicon, a ferrite-stabilizing element, diffuse and partition to austenite and ferrite, respectively. In general, intercritical annealing times are too short to produce true equilibrium microstructures, but scanning transmission electron microscopy (STEM) studies have shown that manganese is enriched in the austenite and depleted in the ferrite immediately adjacent to austenite-ferrite interfaces (Ref 12.51, 12.52). Similarly, silicon has been shown to be rejected from austenite and to concentrate in the ferrite adjacent to intercritically formed austenite (Ref 12.53, 12.54).

In as-hot-rolled ferrite-pearlite starting microstructures, pearlite regions, by virtue of their high carbon content, are converted to austenite during intercritical annealing, and therefore, on cooling, martensite takes the place of the pearlite. A study of a normalized low-carbon steel with a ferrite-pearlite microstructure showed that spheroidization of the cementite of the pearlite is an early intermediate step to austenite formation at carbide particles and ferrite grain boundaries (Ref 12.55). In cold-rolled and annealed low-carbon steels, deformed ferrite recrystallizes, and deformed pearlite colonies spheroidize on heating to intercritical temperatures. Austenite forms on the boundaries between deformed ferrite grains, on boundaries between recrystallized and unrecrystallized grains, and eventually on spheroidized cementite particles (Ref 12.9). Figure 12.19 shows austenite formation within a cold-rolled and partially recrystallized cold-rolled 0.08% C steel heated to 760 °C (1400 °F) for 10 seconds.

The austenite of intercritically annealed low-carbon steels may transform to various microstructures depending on alloy content, which determines hardenability, and cooling rate. Figure 12.20 shows schematically the effect of cooling rate on an austenite grain surrounded by ferrite grains that have been retained during heating, and Fig. 12.21 shows actual microstructures produced at three rates of cooling of a 0.08% C, 1.47% Mn, and 0.053% Nb steel from 810 °C (1490 °F) (Ref 12.56). The micrographs

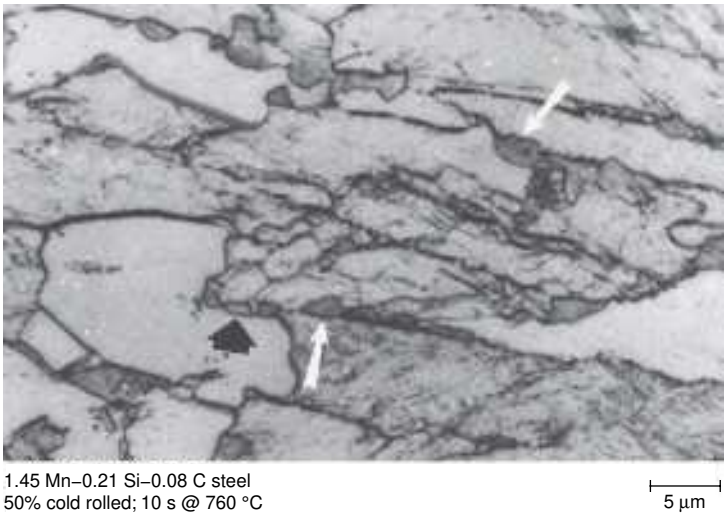

Fig. 12.19 Partially recrystallized microstructure of 0.08% C-1.45% Mn-0.21% Si steel. Black arrow points to austenite adjacent to recrystallized grain, and white arrows point to austenite formed on boundaries between deformed ferrite grains. Light micrograph, nital etch. Source: Ref 12.9

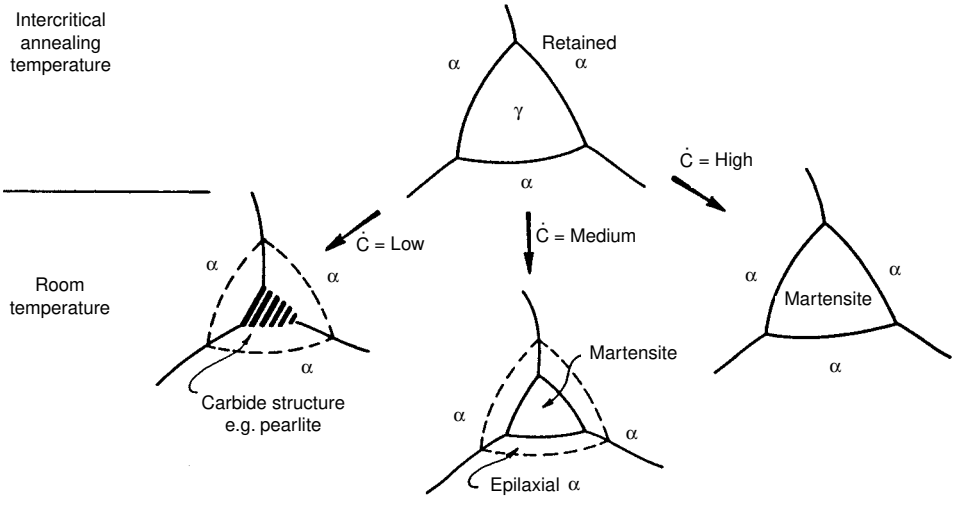

Fig. 12.20 Schematic diagram showing microstructures produced by cooling austenite in intercritically annealed steel at various rates. Source: Ref 12.48

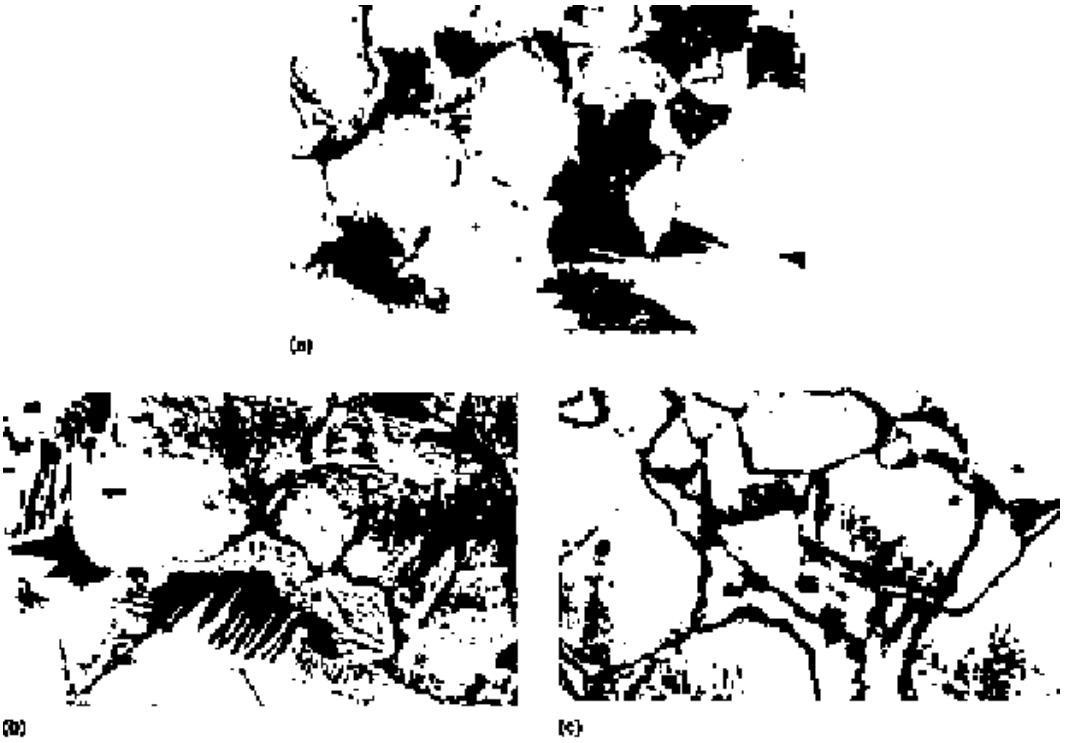

Fig. 12.21 Microstructures of Nb-containing, low-carbon steel intercritically annealed at 810 °C (1490 °F) and cooled at: (a) 1000 °C/s (1800 °F/s), (b) 135 °C/s (243 °F/s), and (c) 12 °C/s (22 °F/s). Light micrographs, boiling alkaline chromate and 2% nital etch, initial magnification 2000×; shown here at 50%. Source: Ref 12.56

were produced by a special etch that differentiates retained ferrite from ferrite produced by the transformation of austenite on cooling (Ref 12.57). The highest cooling rates cause the austenite to transform completely to martensite. At intermediate cooling rates, some of the austenite first transforms to ferrite by *epitaxial growth*. That is, the new ferrite assumes the crystal orientation of the adjacent retained ferrite; a new ferrite grain does not need to be nucleated. The epitaxial ferrite appears white in the micrographs of Fig. 12.21. As noted, the epitaxial ferrite may grow in a manganese-enriched region, adjacent to silicon-enriched retained ferrite. This partitioning of manganese and silicon affects quench aging of the ferrite: carbide precipitation is retarded in the manganese-rich epitaxial ferrite and is stimulated in the silicon-rich retained ferrite, in response to the effect of these elements on the thermodynamic activity of carbon in ferrite (Ref 12.58).

At intermediate and low cooling rates, as epitaxial ferrite grows, carbon is rejected from the growing ferrite, enabling the formation of the ferrite-cementite austenite transformation products bainite and pearlite together with martensite. At the lowest cooling rates, the austenite transforms only to epitaxial ferrite and pearlite. Figure 12.22 is a microstructure map that

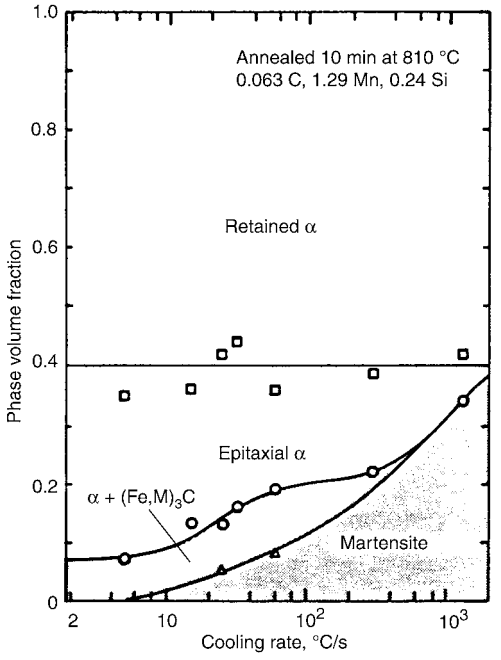

Fig. 12.22 Map of microstructures formed in austenite as a function of cooling rate in a low-carbon steel intercritically annealed to form 40% austenite and 60% retained ferrite. Source: Ref 12.48

shows the changes in microstructure that develop as a function of cooling rate in a 0.063% C, 1.29% Mn, and 0.24% Si steel intercritically annealed at 810 °C for 10 minutes (Ref 12.56). In this example, 40% of the microstructure was converted to austenite that transformed to various microstructures while the amount of retained ferrite remained constant at 60%.

Figure 12.23 shows the changes in mechanical properties that correspond to the microstructures shown in Fig. 12.22. Remarkably high ultimate tensile strengths can be produced in the 40% martensite-60% ferrite dual-phase microstructures in specimens cooled at the highest rates. Ductility, however, is low. The high strength is a result not only of dispersed high-strength martensite patches, but also of the high volume fraction of ferrite with high densities of martensite-induced dislocations. After the slowest cooling, ferrite-pearlite microstructures have low ultimate strength and high ductility as expected. Offset yield strengths, $S_{0.002}$, are relatively high because of discontinuous yielding, as indicated by the curve $2 \times \varepsilon_{YP}$ that marks the magnitude of the Lüders strain.

The best combinations of strength and ductility, depending on application, may be the microstructures produced by cooling rates just fast enough to prevent discontinuous yielding. For these microstructures, there are minima in yield strength, high strain-hardening rates, high ultimate strengths, and good ductilities. The latter deformation characteristics are associated

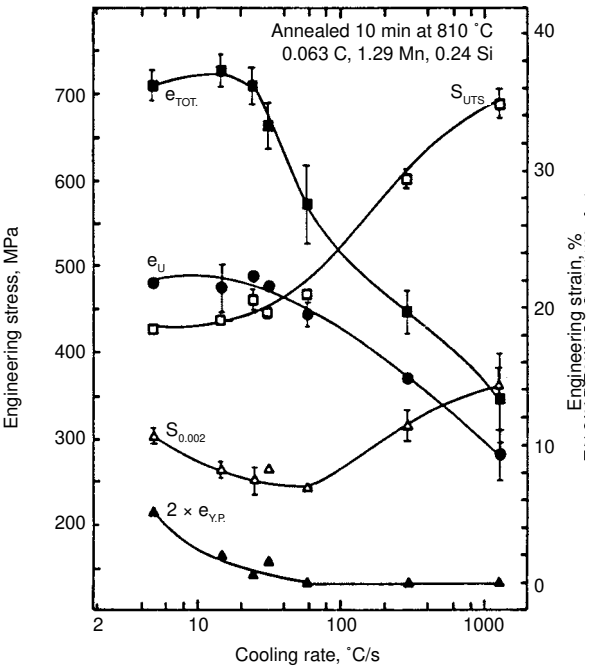

Fig. 12.23 Mechanical properties of the microstructures shown in Fig.12.22. Source: Ref 12.48

with the minimum amount of martensite that produces sufficient unpinned dislocations to prevent discontinuous yielding. Analysis of the stress-strain curves of microstructures cooled at the intermediate rates shows that the curves have an inflection point at low strains, i.e., strain hardening decreases and then increases, an indication that a weak Lüders band may be necessary to supplement the martensite-induced dislocations in order to maintain plastic flow (Ref 12.48, 12.59).

TRIP Steels: Microstructure and Properties

As noted previously relative to Fig. 12.16, TRIP steels are intercritically annealed and isothermally transformed. The isothermal step of the heat treatment is designed to produce large dispersed volume fractions of austenite within the ferrite matrix retained after the intercritical heating step. Retained austenite is also a component of DP steels, and is retained as fine spherical, manganese-rich particles that resist transformation or as an interlath component of martensitic islands (12.53, 12.60).

In TRIP steels, alloying and isothermal times and temperatures are controlled to produce bainite and maximize retained austenite content. Figure 12.24 shows a map of austenite amounts produced as a function of isothermal transformation times and temperatures for a 0.14% C, 1.21% Si,

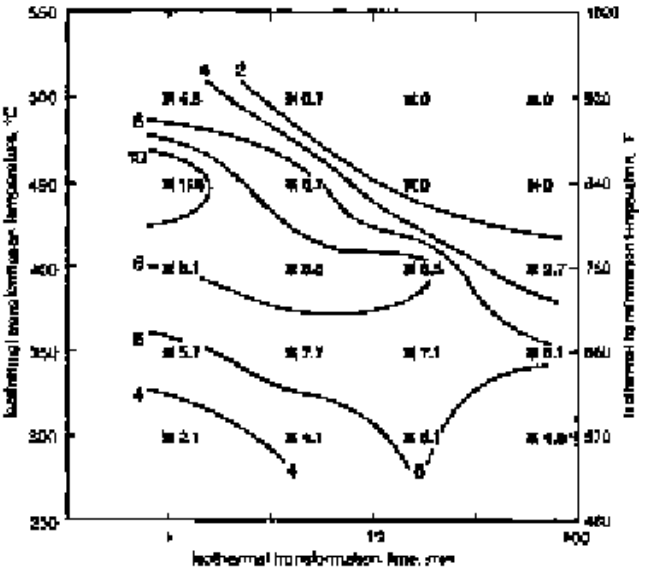

Fig. 12.24 Retained austenite as a function of transformation temperature and time in microstructures produced by isothermal holding of a 0.14% C-1.21% Si-1.57% Mn steel intercritically annealed at 770 °C (1420 °F). Source: Ref 12.61

1.57% Mn steel (Ref 12.61). The maximum amount of austenite is produced at intermediate temperatures around 400 °C (750 °F). At higher temperatures, the bainite transformation proceeds too rapidly, and at lower temperatures, some of the austenite retained transforms to martensite on cooling. Figure 12.25 shows examples of the microstructures produced by isothermal transformation of the 0.14 C-Si-Mn steels at 400 °C for 1 and 4 minutes. Austenite is retained either with acicular ferrite structures or as larger, smooth etching islands. TRIP steels are alloyed with relatively high silicon contents, between 1.2 and 1.5%, in order to minimize cementite formation during austenite transformation to bainite. Silicon does not dissolve in the crystal structure of cementite and therefore prevents cementite formation, an effect well documented in the martensite tempering literature (12.62–12.64). As a result, the bainitic structure consists of acicular ferrite and retained austenite, as discussed in Chapter 7, "Ferritic Microstructures." Also as a result of carbon rejection from ferrite with increasing time at isothermal transformation temperatures, the carbon content of austenite increases. Carbon contents as high as 1.50% have been reported in retained austenite of TRIP steels (Ref 12.65, 12.66). Such high carbon contents lower M_s temperatures and stabilize retained austenite on cooling to room temperature.

Silicon oxidizes readily, and as a result, stable oxides, difficult to remove by pickling, form on high-silicon steels during hot rolling. The sili-

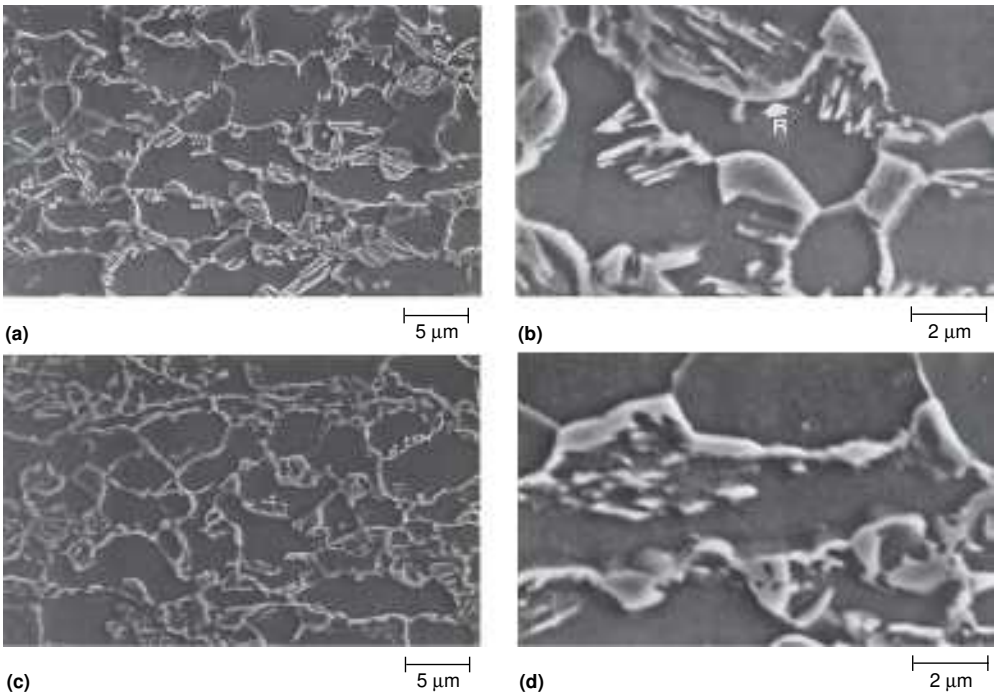

Fig. 12.25 Microstructures of a 0.14% C-Si-Mn steel isothermally held at 400 °C (750 °F) for (a) and (b) 1 min, and for (c) and (d), 4 min. SEM micrographs, nital etch. Source: Ref 12.61

con oxides cause surface finish problems and reduce coatability during galvanizing. As a result, other alloying approaches have been investigated. Aluminum, similar to silicon, is not soluble in cementite (Ref 12.67) and has been evaluated as a replacement for silicon in TRIP steels with good results (Ref 12.65, 12.67–69). However, steels with high aluminum contents, because of its ferrite-stabilizing tendency, cannot be completely austenitized, and therefore, aluminum affects hot workability (Ref 12.70). In view of these processing considerations, alloy development for optimizing microstructures and properties continues.

Figure 12.26 shows stress-strain curves for the 0.14% C-Mn-Si steel with microstructures produced by holding various times at 400 °C. The curve for the microstructure produced by holding 1 minute shows continuous yielding and a high rate of strain hardening to a high ultimate strength. This deformation behavior is a result of martensite formed in the retained austenite on cooling to room temperature. The other curves show discontinuous yielding, a result of the fact that, unlike martensite formation, acicular formation and retained austenite do not generate high densities of dislocations (Ref 12.71). The microstructures produced by isothermal holding at 4 and 15 minutes have high ductilities and good strengths. The stress-strain curves demonstrate the benefit of retained austenite that

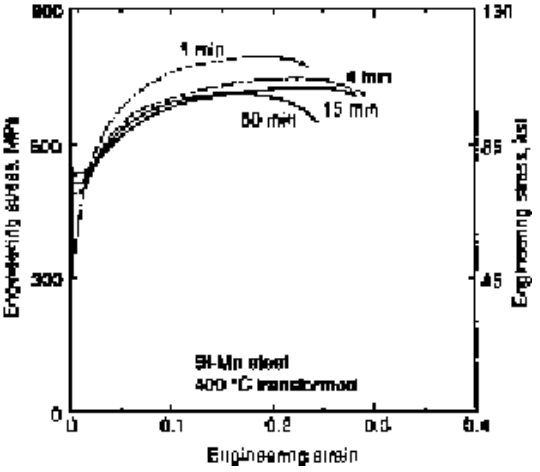

Fig. 12.26 Engineering stress-strain curves for 0.14% C-Si-Mn steel intercritically annealed and held for various times at 400 °C (750 °F). Source: Ref 12.61

transforms mechanically to martensite at high strains (Ref 12.72). The strain-induced martensite, by virtue of its structure and the dislocations it generates, increases strain hardening and defers necking instability, as discussed in Chapter 11, "Deformation, Strengthening, and Fracture of Ferritic Microstructures." The specimen held for 60 minutes has reduced ductility because more of the retained austenite has transformed to bainitic ferrite at temperature.

Figure 12.27 shows changes in austenite content as a function of strain for the 0.14% C-Mn-Si steel isothermally transformed under various conditions. Tensile testing was conducted at three temperatures as shown (Ref 12.73). For all microstructural conditions, retained austenite decreases during straining, indicating that deformation-induced transformation to martensite has occurred. At lower test temperatures, austenite content drops rapidly at low strains. Figure 12.28 shows mechanical properties of the 0.14C-Mn-Si steel isothermally transformed at 400 and 450 °C (750 and 840 °F) for 4 minutes as a function of testing temperature. Ductility is a maximum at test temperatures between 20 and 50 °C (70 and 120 °F). It is in this temperature range where the TRIP effect is the strongest, i.e., strain-induced transformation to martensite occurs at high strains to defer necking instability. At low testing temperatures, the austenite transforms by stress-induced mechanisms at low strains (Ref 12.72) and as a result has little beneficial effect on deferring necking at high strains. At the highest testing temperature, the austenite is too stable and does not mechanically transform. A good state-of-the-art review of TRIP steels in 2012 is given in Ref 12.74.

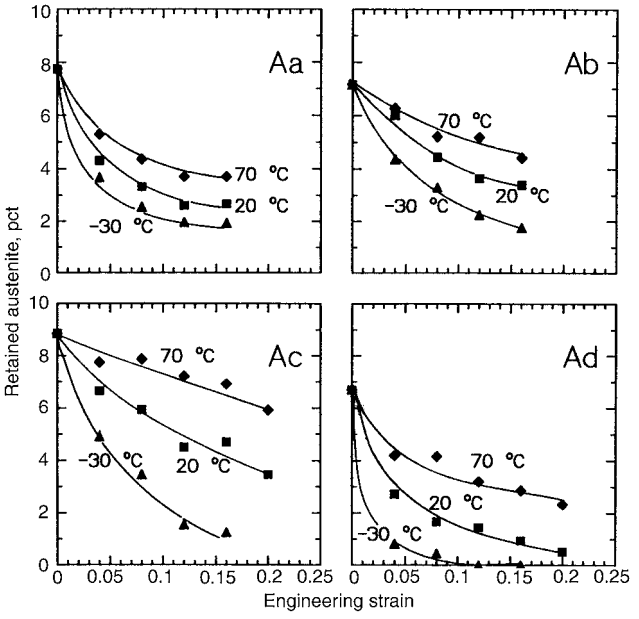

Fig. 12.27 Changes in retained austenite content, measured after tensile testing at room temperature, as a function of strain in intercritically annealed 0.14% C-Si-Mn steel isothermally transformed at 350 °C (660 °F) for 4 min, Aa; 350 °C (660 °F) for 15 min, Ab; 400 °C (750 °F) for 4 min, Ac; and 450 °C (840 °F) for 4 min, Ad. Source: Ref 12.73

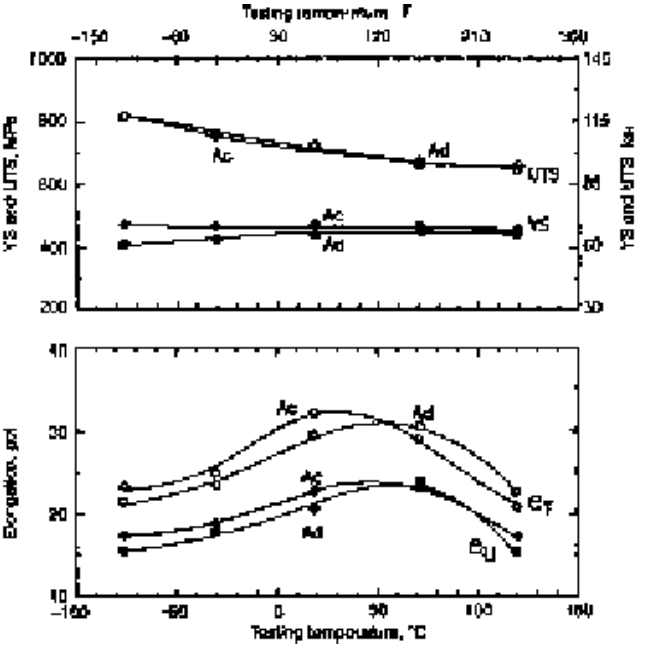

Fig. 12.28 Mechanical properties of 0.14% C-Si-Mn steel intercritically annealed and isothermally transformed, as identified in Fig. 12.27, as a function of testing temperature. Source: Ref 12.73

Low-Carbon Fully Martensitic Sheet Steels

Steels quenched to martensitic microstructures have the highest strength and hardness of any microstructure that can be produced in a given steel, and have long been used in medium- and high-carbon steels for applications that require high strength, wear resistance, and fatigue resistance. Hardenability, tempering, deformation, and fracture of higher carbon quench and tempered steels are topics covered in detail in later chapters. Low-carbon steels have seen more limited use because of low hardenability and low formability, especially in automotive sheet steels.

Figure 12.29 shows engineering stress-strain curves for quench and tempered samples of AISI 10B22 steel (corresponding to European grade 22MnB5) containing 0.224% C, 1.06% Mn, 0.0035% B, 0.0395% Ti, and 0.22% Cr (Ref 12.75). As-quenched martensite in this steel shows continuous yielding, strain hardens to tensile strengths approaching 1,700 MPa (245 ksi), and fractures by ductile microvoid formation after post uniform deformation. In contrast as-quenched high-carbon steels containing more than 0.5 wt% carbon fail by brittle intergranular fracture, as described in Chapter 19, "Low Toughness and Embrittlement Phenomena in Steels." Low temperature tempering reduces strength but increases ductility, and extensive discontinuous yielding with minimal strain hardening develops after tempering at higher temperatures.

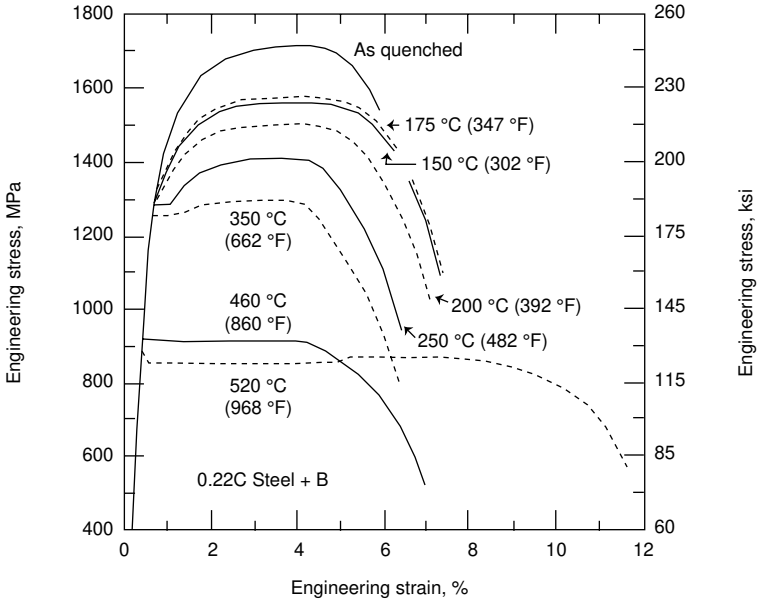

Fig. 12.29 Engineering stress-strain curves for 10B22 steel sheet specimens water quenched to martensite and tempered at the temperatures shown for 1 hour. Source: Ref 12.75

The ductility of the martensitic samples is low, in part because of the sheet specimen geometry. The deformation of sheet specimens and the formability of sheet steels are constrained by sheet width, causing localized deformation and fracture through the thin thickness dimensions of the samples (Ref. 12.76, 12.77). Figure 12.30 compares the reduced ductility of martensitic sheet specimens versus that of martensitic round bar specimens (Ref 12.78).

In view of the low ductilities and therefore the low formability of martensitic low carbon sheet steels, applications have been limited to parts with relatively simple geometries such as bumper reinforcement beams. These parts are produced by forming in multiple rolls designed to produce shapes with a single primary mode of deformation, in contrast to the production of more complicated stamped shapes that involve stretching, bending, drawing, and/or straightening. The thickness of roll formed parts is not changed except for slight thinning at modest bend radii.

However, the need for very high strengths for high crash worthiness and vehicle occupant safety has driven the need to produce martensitic automotive sheet steel parts of more complex shapes, shapes that cannot be cold-stamped. This limitation is solved by hot stamping, where sheet steel is blanked, heated to austenitizing temperatures, formed in dies, and quenched to martensitic microstructures in the dies (Ref. 12.79–12.84). Figure 12.31 shows this process schematically. Austenite has very high ductility and hardened parts with complicated shapes can be readily produced. The die quenching requires good hardenabilty of low carbon steels, a characteristic accomplished by small additions of boron and other alloying elements as noted earlier for a typical 10B22 steels. For the boron, a

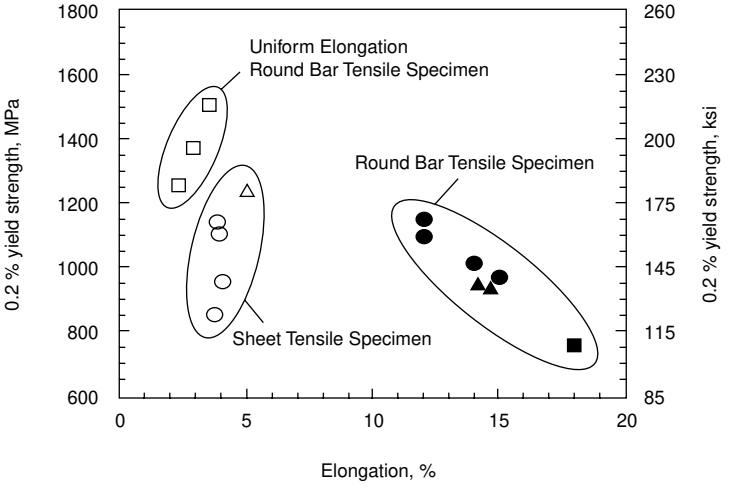

Fig. 12.30 Comparison of elongations of sheet and round bar specimens with as-quenched martensitic microstructures in low-carbon steels. Source: Ref 12.78

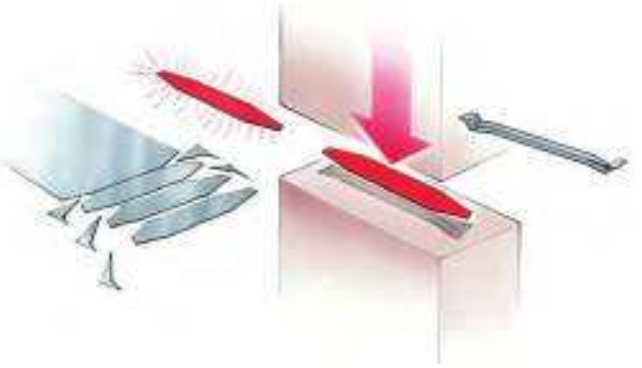

Fig. 12.31 Schematic representation of the steps involved in hot stamping. The part, formed hot in the austenitic condition, is quenched in the die to martensite. Courtesy of Ronald Hughes, SeverStal North America

strong nitride-forming element, to be effective small additions of titanium, a stronger nitride-forming element, have to be made to the steel to protect the boron, i.e. keep it in solution in the austenite to improve hardenability by preventing the formation of ferrite instead of martensite.

High-Manganese TWIP Sheet Steels

Twinning-induced plasticity (TWIP) steels differ in many ways from the types of sheet steels described to this point. These steels, after annealing, are fully austenitic at room temperature, a structure made possible by high additions of manganese, between 12 and 30% (Ref 12.85–12.94). Tensile strengths up to 1,100 MPa (160 ksi) and very high tensile elongations, up to 70%, desirable for formability and fracture resistance, can be produced on deformation. Deformation-induced twinning is a major contributing mechanism to the strain hardening that produces the high uniform strains and tensile strengths, hence the name TWIP. Dislocation deformation mechanisms within the framework of twinning contribute significantly to the strain hardening that produces excellent combinations of strength and ductility. The deformation-induced twins serve as barriers to dislocation glide and subdivide the parent austenite grains, effectively refining the grain size and leading to a dynamic Hall-Petch mechanism of strengthening with increasing strain (Ref 12.85-12.91). Depending on stacking fault energy as influenced by alloy composition and deformation temperature, strain-induced transformation of austenite to α' (bcc) martensite and ε (hcp) martensite may also occur.

Figure 12.32 is a light micrograph that shows the subdivision of austenite grains by deformation twinning in an Fe-0.007C-28Mn-3Al-3Si wt% TWIP steel after 40% strain. The twinned areas in fact consist of bundles of fine twins with separations finer than resolvable in the light micro-

Fig. 12.32 Deformation twins within grains of austenite in an Fe-0.007 wt% C, 28 wt% Mn-3% wt Al-3 wt% Si TWIP steel deformed to 40% strain. 10% Nital etch, light micrograph. Courtesy of José Jiménez, Centro Nacional de Investigaciones Metalúrgicas (CENIM).

scope. A high magnification TEM micrograph taken from a thin foil specimen, Fig. 12.33, shows dislocations interacting with the boundaries of mechanical twins in an Fe-0.007C-28Mn-3Al-3Si wt% alloy after 20% strain. While deformation twinning is a dominant contributing mechanism to the high strain hardening of TWIP steels, the twinning is a function of orientation to the resolved shear stresses during deformation, and some grain orientations may exhibit no twinning and only a substructure consisting of dislocation cells and high-density dislocation walls (Ref 12.91).

As described in Chapter 3, "Phases and Structures," the crystal structure of austenite is face-centered-cubic and is made up of close packed planes of iron and other substitutional atoms stacked in a sequence that repeats regularly every three layers. Discontinuities in this sequence are referred to as stacking faults. Changes in stacking occur at twin/matrix interfaces and stacking faults are produced when perfect dislocations dissociate into two partial dislocations with an intervening stacking fault. The faulting and twinning tendencies of TWIP austenitic structure are characterized by stacking fault energy, in units of mJm^{-2}. Stacking fault energy is a function of alloying and temperature, and is measured by transmission electron microscopy from the geometry of extended dislocation nodes or the equilibrium separation distance of Shockley partial dislocations (Ref 12.92, 12.93). Figure 12.34 is a TEM image showing examples of stacking faults in the austenitic matrix of an Fe-0.005 wt% C-25 wt% Mn-3 wt% Al-3 wt% Si TWIP steel deformed 1.5%. Intense efforts are ongoing to design alloys with stacking fault energies most conducive to twinning by adjusting levels of Mn and additions of C, Al, and Si in TWIP steels. Additions of Al and Si increase and decrease, respectively, stacking fault energy. Carbon contents of the TWIP steels that have been studied are variable but may be quite high, 0.6 or 0.7%, and place TWIP steels well outside of the range of low carbon steels. The higher

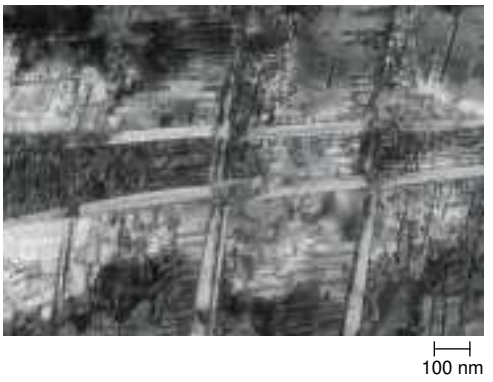

Fig. 12.33 Deformation twins and dislocations in an Fe-0.007 wt% C- 28 wt% Mn-3 wt% Al-3 wt% Si TWIP steel deformed to 20% strain. Thin foil transmission electron micrograph. Courtesy of Dean Pierce, Colorado School of Mines

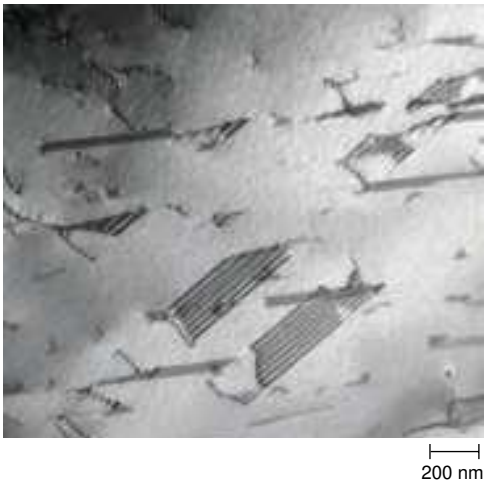

Fig. 12.34 Stacking faults bounded by partial dislocations in austenite of an Fe-0.005 wt% C-25 wt% Mn-3 wt% Al-3 wt% Si TWIP steel deformed to 1.5% strain. Thin foil transmission electron micrograph. Courtesy of James Wittig, Vanderbilt University

carbon contents stabilize austenite and enhance strain hardening (Ref. 12.88). Stacking fault energies that are too low, below approximately 20 mJm^{-2}, promote the formation of ε-martensite, a hcp crystal structure also made up of close-packed planes of atoms. High stacking fault energies, above approximately 50 mJm^{-2}, due to alloying or high deformation temperatures, limit the formation of twins and stacking faults.

As noted in the discussion of TRIP steels, the strain-induced transformation of small amounts of austenite to martensite increases strain hardening and defers necking instability, promoting ductility. The high-

manganese TWIP steels similarly are dependent on high strain hardening to prevent necking instability; in the fully austenitic microstructures the strain hardening is provided by mechanisms of dislocation density increases in an austenitic structure subdivided by twinning. These differences result in much higher ductilities, but similar strengths, in TWIP steels compared to those low-carbon TRIP steels without high manganese contents. The higher ductilities are in part related to the requirement of a critical stress and dislocation activity required to nucleate deformation twins, deferring the strain hardening to higher strains and thereby offsetting necking instability. In steels where epsilon martensite forms, the martensite forms at the onset of plastic deformation, producing high rates of work hardening at low strains, but not at the higher strains that offset necking and promote ductility in TWIP steels.

Quenched and Partitioned Sheet Steels

Quenched and Partitioned (Q&P) steels are produced by a two-step thermal treatment that can produce combinations of ductility and strength above those noted for dual phase and TRIP steels in Fig. 12.1 (Ref 12.95). The steels may be austenitized and quenched from temperatures above the A_{c3} or intercritically austenitized from temperatures between the A_{c1} and A_{c3} temperatures. The first step consists of quenching below M_s temperatures to produce a microstructure of martensite and retained austenite. The amount of martensite formed in the austenite can be estimated from the Koistinen and Marburger equation, Eq 5.2, in Chapter 5, "Martensite." The second step consists of isothermal holding, most often at a temperature above the M_s temperature of the steel. A key component of the Q&P concept is the claim that carbon can diffuse (partition) from the martensite and enrich the retained austenite, ultimately producing high-carbon-partitioned austenite that transforms to strain-induced martensite, as in TRIP steels, producing beneficial strain hardening that increases ductility. While carbon-enriched austenite has been demonstrated, and the carbon partitioning mechanism may occur, there are several other mechanisms of microstructural change that can also operate during the two-step thermal processing of Q&P processed steels.

Similar to TRIP steels, quenched and partitioned steels are alloyed with silicon, and therefore cementite formation in both the martensite and austenite is effectively suppressed. Therefore, in the second step it was assumed possible, because cementite does not form in the martensite, that carbon diffuses from the martensite, as it does in a ferritic structure due to the very low solubility of carbon in a bcc ferrite. However, martensite is much different from ferrite in that the diffusionless, shear transformation of martensite is dependent on a lattice invariant deformation that produces a substructure consisting of a very high density of dislocations in the supersaturated martensite, as described in Chapter 5, "Martensite." It is well

established that carbon diffuses to the strain fields of the dislocations and eventually the dislocation structure provides sites for ε/η transition carbide nucleation and growth within the martensite crystals during the first stage of tempering, as described in Chapter 17, "Tempering of Steel." Unlike cementite formation, transition carbide formation is not retarded by silicon (Ref 12.96). Thus carbon tied up in the transition carbides is not expected to diffuse, as claimed, from the martensite in steels with high silicon contents.

As noted, the second stage of heat treatment in Q&P steels is considered to be the stage where carbon diffuses from martensite. However, other mechanisms of microstructural change can also occur in the martensite/austenite two phase microstructures during interrupted quenching or isothermal holding after quenching. Isothermal heating steps have long been applied in heat treatments such as austempering and martempering to minimize detrimental residual stresses, as described in Chapter 20, "Residual Stresses, Distortion, and Heat Treatment." During austempering, for example, steel parts are quenched to a temperature above the M_s, as are Q&P-processed steels in the second step, and the austenite isothermally transforms to bainite, a mixture of ferrite and cementite in conventional low-alloy steels, as described in Chapter 6, "Bainite." In TRIP steels with high silicon content, austenite transforms isothermally to bainitic or acicular ferrite, cementite formation is suppressed, and carbon diffuses from the ferrite to enrich the austenite around the ferrite with carbon. In Q&P steels, the partitioning temperature is often similar to isothermal temperatures used in TRIP steels, so it should be recognized that acicular ferrite formation, and associated stabilization of carbon-enriched austenite due to ferrite formation, could also be operating in the second step of Q&P processed steels.

Not only changes in austenite during the second step of Q&T processing, but also changes in the martensite formed during the first step must be considered. The changes in the martensite have received less attention thus far in the Q&P literature. The second step is effectively a tempering treatment of martensite, during which carbon supersaturation in martensite is relieved initially by fine transition carbide formation. At higher tempering temperatures transition carbides are replaced by cementite in conventional steels, but with high silicon additions cementite formation and susceptibility to tempered martensite embrittlement, Chapter 19, "Low Toughness and Embrittlement Phenomena in Steels," are suppressed and transition carbides are stable to higher temperatures, providing enhanced combinations of strength and toughness. These mechanisms operate in 300-M steel, a high-silicon modification of 4340 steel that has been extensively used for demanding applications such as aircraft landing gear (Ref 12.97). Benefits to ductility/strength combinations in Q & P steels might thus be expected to be substantially affected by tempering of the martensite apart from any partitioning of carbon from the martensite.

In summary, many mechanisms of microstructural change, depending on specifics of alloying and processing variations within two-step heat treatments of martensite/austenite mixtures in silicon-containing steels, may occur. More research is required to sort out the mechanisms and microstructures that produce beneficial combinations of properties in Q&P processed steels (Ref 12.95).

REFERENCES

12.1 J. Shaw et al., ULSAB-Advanced Vehicle Concepts—Materials, *New Steel Sheet and Steel Bar Products and Processing,* D.W. Anderson et al., Ed., SAE SP-1685, SAE, Warrendale, PA, 2002, p 63–71

12.2 J.G. Speer and D.K. Matlock, Recent Developments in Low-Carbon Sheet Steels, *JOM,* Vol 54, 2002, p 19–24

12.3 M. Y. Demeri**,** Advanced High-Strength Steels: Science, Technology, and Applications, ASM International, Materials Park, OH, 2013

12.4 *Zinc-Based Steel Coating Systems: Metallurgy and Performance,* G. Krauss and D.K. Matlock, Ed., TMS, Warrendale, PA, 1990

12.5 *The Physical Metallurgy of Zinc Coated Steel,* A.R. Marder, Ed., TMS, Warrendale, PA, 1993

12.6 R.P. Foley, D.K. Matlock, and G. Krauss, Metallurgical Review of Process for Obtaining Strength and R-Value in Galvannealed Sheet Steels, in *42nd MWSP Conference Proceedings,* Vol XXXVII, ISS, 2000, p 455–468

12.7 F.B. Pickering, The Effect of Composition and Microstructure on Ductility and Toughness, in *Toward Improved Ductility and Toughness,* Climax Molybdenum Development Co., Japan, 1971, p 9–31

12. 8 F.B. Pickering, Structure-Property Relationships in Steels, *Constitution and Properties of Steels,* F.B. Pickering, Ed., Vol 7, *Mater. Sci. Technol.,* VCH, Weinheim, Germany, 1992, p 41–94

12.9 D.Z. Yang, E.L. Brown, D.K. Matlock, and G. Krauss, Ferrite Recrystallization and Austenite Formation in Cold Rolled Intercritically Annealed Steel, *Metall. Trans. A,* Vol 16A, 1985, p 1385–1392

12.10 D. Witmer and G. Krauss, Effect of Thermal History on the Recrystallization Behavior of Low-Carbon 0.30% Mn Steels Containing Oxygen and Sulfur, *Transactions of the American Society of Metals,* Vol 62, 1969, p 447–456

12.11 Heat Treating Furnaces, *The Making, Shaping and Treating of Steel,* Tenth Edition, United States Steel, Published by the Associa-

tion of Iron and Steel Engineers, Pittsburgh, PA, 1985, p 1267–1276

12.12 *Metallurgy of Continuous-Annealed Sheet Steel,* B.L. Bramfitt and P.L. Mangonon, Jr., Ed., TMS-AIME, Warrendale, PA, 1982

12.13 P.R. Mould, An Overview of Continuous-Annealing Technology for Steel-Sheet Products, in Ref 12.12, p 3–33

12.14 W.C. Leslie, *The Physical Metallurgy of Steels,* McGraw-Hill Book Company, New York, NY, 1981

12.15 D.J. Blickwede, Sheet Steel—Micrometallurgy by the Millions, *Trans. ASM,* Vol 61, 1968, p 653–679

12.16 *Technology of Continuously Annealed Cold-Rolled Sheet Steel,* R. Pradhan, Ed., TMS, Warrendale, PA, 1985

12.17 *Metallurgy of Vacuum-Degassed Steel Products,* R. Pradhan, Ed., TMS, Warrendale, PA, 1990

12.18 *Physical Metallurgy of IF Steels,* The Iron and Steel Institute of Japan, Tokyo, 1994

12.19 A. Cramb and M. Byrne, Steelmaking and Casting Practices for High Quality Interstitial-Free Steels, in Ref 12.16, p 3–27

12.20 D.O. Wilshynsky-Dresler, "Recrystallization Behaviour of Interstitial-Free Steels," Ph.D. thesis, Colorado School of Mines, Golden, Colorado, 1992

12.21 W.B. Hutchinson, Development and Control of Annealing Textures in Low-Carbon Steels, *International Metallurgical Reviews,* Vol 29 (No. 1), 1984, p 25–42

12.22 W.B. Hutchinson, K.I. Nilsson, and J. Hirsch, Annealing Textures in Ultra-Low Carbon Steels, in Ref 12.16, p 109–125

12.23 M. Fukuda, The Effect of Carbon Content against r value—Cold-Reduction Relations in Steel, *Tetsu to Hagane,* Vol 53, 1967, p 559–561

12.24 T. Irie, S. Satoh, A. Yasuda, and O. Hashimoto, Development of Deep Drawable and Bake Hardenable High Strength Steel Sheet by Continuous Annealing of Extra Low-Carbon with Nb or Ti, and P, in Ref 12.11, p 155–171

12.25 A. Okamoto and N. Mizui, Texture Formation in Ultra-Low CarbonTi-Added Cold-Rolled Sheet Steels Containing Mn and P, in Ref 12.16, p 161–180

12.26 C.J. McMahon, Jr., Strength of Grain Boundaries in Iron-Based Alloys, *Grain Boundaries in Iron Based Alloys,* American Society for Metals, 1974, p 525–552

12.27 Y. Maehara, N. Mizui, and M. Arai, Cold Work Embrittlement Accompanied by Intergranular Fracture in Ultra-Low Carbon Ti-Added Sheet Steels, in *Interstitial Free Steel Sheet: Processing, Fabrication and Properties,* L.E. Collins and D.L. Baragar, Ed., Canadian Institute of Mining, Metallurgy and Petroleum, Montreal, Quebec, 1991, p 135–144

12.28 R. Pradhan, Metallurgical Aspects of a Batch-Annealed Bakerdening Steel, in Ref 12.16, p 309–325
12.29 *IF Steels 2003,* H. Takechi, Ed., The Iron and Steel Institute of Japan, Tokyo, 2003
12.30 I. Kozasu, Processing—Thermomechanical Controlled Processing, in *Constitution and Properties of Steels,* F.B. Pickering, Ed., Vol 7 Materials Science and Technology, VCH, Weinheim, Germany, 1992, p 183–217
12.31 M. Cohen and S.S. Hansen, Microstructural Control in Microalloyed Steels, in *MiCon78: Optimization of Processing, Properties, and Service Performance Through Microstructural Control,* ASTM STP 672, H. Abrams, G.N. Maniar, D.A. Nail and H.D. Solomon, Ed., 1979, p 34–52
12.32 *Processing and Properties of Low Carbon Steels,* J.M. Gray, Ed., TMS-AIME, New York, 1973
12.33 *MicroAlloying 75,* Union Carbide Corporation, New York, 1977
12.34 *Welding of HSLA (Microalloyed) Structural Steel,* A.B. Rothwell and J.M. Gray, Ed., American Society for Metals, 1978
12.35 *Thermomechanical Processing of Microalloyed Austenite,* A.J. DeArdo, G.A. Ratz, and P.J. Wray, TMS-AIME, Warrendale, PA, 1982
12.36 *Processing, Microstructure and Properties of HSLA Steels,* A.J. DeArdo, Ed., TMS, Warrendale, PA, 1988
12.37 *Thermomechanical Processing of High Strength Low Alloy Steels,* I. Tamura, C. Ouchi, T. Tanaka, and H. Sekine, Ed., Butterworths, London, 1988
12.38 T. Gladman, *The Physical Metallurgy of Microalloyed Steels,* Book 615, The Institute of Materials, London, 1997
12.39 S.S. Hansen, J.B. Vander Sande, and M. Cohen, Nioboum Carbonitride Precipitation and Austenite Recrystallization in Hot-Rolled Microalloyed Steels, *Metallurgical Transactions A,* Vol 11A, 1980, p 387–402
12.40 L. Laquerbe, J. Neutjens, Ph. Harlet, F. Caroff, and P. Cantinieaux, New Processing Route for the Production of Silicon-Free TRIP-Assisted Cold-Rolled and Galvanized Steels, *41st MWSP Conference Proceeedings,* ISS, Vol XXXVII, 1999, p 89–99
12.41 S. Hayami and T. Furakawa, A Family of High-Strength, Cold-Rolled Steels, *MicroAlloying 75,* Union Carbide Corp., New York, 1977, p 311–320
12.42 M.S. Rashid, GM 980A—A Unique High Strength Sheet Steel with Superior Formability, SAE Paper 760206, 1976
12.43 *Formable HSLA and Dual-Phase Steels,* A.T. Davenport, Ed., TMS-AIME, Warrendale, PA, 1977
12.44 *Structure and Properties of Dual-Phase Steels,* R.A. Kot and J.M. Morris, TMS-AIME, Warrendale, PA, 1979

12.45 *Fundamentals of Dual-Phase Steels,* R.A. Kot and B.L. Bramfitt, Ed., TMS-AIME, Warrendale, PA, 1981
12.46 O. Matsumura, Y. Sakuma, and H. Takechi, Mechanical Properties and Retained Austenite in Intercritically Heat-Treated Bainite-Transformed Steel and Their Variation with Si and Mn Additions, *Metall. Trans. A,* Vol 22A, 1991, p 489–498
12.47 M.S. Rashid and B.V.N. Rao, Tempering Characteristics of a Vanadium-Containing Dual-Phase Steel, in Ref 12.44, p 249–264
12.48 D.K. Matlock, F. Zia-Ebrahimi, and G. Krauss, Structure, Properties and Strain Hardening of Dual-Phase Steels, *Deformation, Processing, and Structure,* G. Krauss, Ed., American Society for Metals, 1984, p 47–87
12.49 D.A. Korzekwa, *Deformation Substructure Development in a C-Mn-Si Dual-Phase Steel,* M.S. thesis, Colorado School of Mines, Golden, CO, 1981
12.50 G.R. Speich, Physical Metallurgy of Dual-Phase Steels, in Ref 12.44, p 3–45
12.51 G.R. Speich, V.A. Demarest, and R.L. Miller, Formation of Austenite during Intercritical Annealing of Dual-Phase Steels, *Metall. Trans. A,* Vol 12A, 1981, p 1419–1428
12.52 P.A. Wycliffe, G.R. Purdy, and J.D. Embury, Austenite Growth in the Intercritical Annealing of Ternary and Quaternary Dual-Phase Steels, in Ref 12.44, p 59–83
12.53 J.M. Rigsbee, Inhibition of Martensite Transformation in Small Austenite Particles in Low Alloy Steels, *Proceedings of International Conference on Martensitic Transformations,* MIT, Cambridge, MA, 1979, p 381–385
12.54 A.D. Romig and R. Salzbrenner, Elemental Partitioning as a Function of Heat Treatment in an Fe-Si-V-C Dual-Phase Steel, *Scr. Metall.,* Vol 16, 1982, p 33–38
12.55 D.Z. Yang, E.L. Brown, D.K. Matlock, and G. Krauss, The Formation of Austenite at Low Intercritical Annealing Temperatures in a Normalized 0.08C-1.45Mn-0.21Si Steel, *Metall. Trans. A,* Vol 16A, 1985, p 1523–1526
12.56 D.K. Matlock, G. Krauss, L.F. Ramos, and G.S. Huppi, A Correlation of Processing Variables with Deformation Behavior of Dual-Phase Steels, in *Structure and Properties of Highly Formable Dual-Phase HSLA Steels,* TMS-AIME, Warrendale, PA, 1980, p 71–87
12.57 R.D. Lawson, D.K. Matlock and G. Krauss, An Etching Technique for Microalloy Dual-Phase Steels, *Metallography,* Vol 13, 1980, p 71–87
12.58 D.A. Korzekwa, D.K. Matlock, and G. Krauss, Aging Susceptibility of Retained and Epitaxial Ferrite in Dual-Phase Steels, *Metall. Trans. A,* Vol 13A, 1982, p 2061–2064

12.59 G.S. Huppi, *Dual-Phase Microalloyed Steels: Temperature and Cooling Rate Effects,* M.S. thesis, Colorado School of Mines, Golden, CO, 1979

12.60 Y. Sakuma, D.K. Matlock, and G. Krauss, Mechanical Behavior of an Intercritically Annealed and Isothermally Transformed Low C Alloy Steel with Ferrite-Bainite-Austenite Microstructures, *J. Heat Treat.,* Vol 8, 1990, p 109–120

12.61 Y. Sakuma, D.K. Matlock, and G. Krauss, Intercritically Annealed and Isothermally Transformed 0.15 pct C steels Containing 1.2 pct Si-1.5 pct Mn and 4 pct Ni: Part I Transformation, Microstructure, and Room-Temperature Mechanical Properties, *Metallurgical Transactions A,* Vol 23A, 1992, p 1221–1232

12.62 W.S. Owen, The Effect of Silicon on the Kinetics of Tempering, *Trans. ASM,* Vol 46, 1954, p 812–829

12.63 S.J. Barnard, G.D.W. Smith, A.J. Garrat-Reed, and J. Vander Sande, Atom Probe Studies: (1) The Role of Silicon in the Tempering of Steel, and (2) Low Temperature Chromium Diffusivity in Bainite, *Solid Phase Transformations,* H.I. Aaronson et al., Ed., TMS-AIME, 1982, p 881–885

12.64 H.K.D.H. Bhadeshia and D.V. Edmonds, The Bainite Transformation in a Silicon Steel, *Metall. Trans. A,* Vol 10A,1 1979, p 895–907

12.65 M. De Meyer, D. Vanderschueren, and B.C. De Cooman, The Influence of Al on the Properties of Cold Rolled C-Mn-Si TRIP Steels, *41st MWSP Conference Proceedings,* ISS, Vol XXXVII, 1999, p 265–276

12.66 M. De Meyer, D. Vanderschueren, K. De Blauwe, and B.C. De Cooman, The Characterization of Retained Austenite in TRIP Steels by X-Ray Diffraction, *41st MWSP Conference Proceedings,* ISS, Vol XXXVII, 1999, p 483–491

12.67 A. Pichler, P. Stiasny, R. Potzinger, R. Tikal, and E. Werner, TRIP Steels with Reduced Si Content, *40th MWSP Conference Proceedings,* ISS, 1998, p 259–274

12.68 S. Traint, A. Pichler, R. Tokal, P. Stiaszny, and E.A. Werner, Influence of Manganese, Silicon, and Aluminum on the Transformation Behavior of Low Alloyed Trip Steels, *42nd MWSP Conference Proceedings,* ISS, Vol XXXVIII, 2000, p 549–561

12.69 P. Jacques, A. Mertens, F. Delannay, F. Girault, J. Humbeck, E.Aernoudt, and Y. Houbaert, Influence of Silicon and Aluminum Contents on the Phase Transformations during Heat Treatment of TRIP-Assisted Multiphase Steels, *Heat Treating, Including Steel Heat Treating in the New Millenium,* ASM International, 2000, p 565–571

12.70 S. Jiao, J. Penning, F. Leysen, and Y. Houbaert, Deformation and Transformation Behavior of Mn-Si and Mn-Al TRIP Steels, *41st*

MWSP Conference Proceedings, ISS , Vol XXXVII, 1999, p 499–508

12.71 B.Y. Choi, D.K. Matlock, and G. Krauss, Bainite Formation and Deformation Behavior in an Intercritically Annealed Fe-1.0 Mn-0.09 C Steel, *Scr. Metall.,* Vol 22, 1988, p 1575–1580

12.72 G.B. Olson, Transformation Plasticity and the Stability of Plastic Flow, *Deformation, Processing and Structure,* G. Krauss, Ed., American Society for Metals, 1984, p 391–424

12.73 Y. Sakuma, D.K. Matlock, and G. Krauss, Intercritically Annealed and Isothermally Transformed 0.15 pct C Steels Containing 1.2 pct Si-1.5 pct Mn and 4 pct Ni: Part II. Effect of Testing Temperature on Stress-Strain Behavior and Deformation-Induced Austenite Transformation, *Metall. Trans. A,* Vol 23A, 1992, p 1233–1241

12.74 P.J. Jacques, Phase Transformations in transformation induced plasticity (TRIP)-assisted multiphase steels, in *Phase Transformations in Steels, Volume 2*, E. Pereloma and D. V. Edmonds, Ed., Woodhead Publishing, Oxford, 2012, p 213–246

12.75 M. Säglitz, D.K. Matlock, and G. Krauss, Tempering and Mechanical Properties of Low-Carbon Boron-Containing Martensitic Sheet Steel, in *International Conference on New Developments in Advanced High-Strength Sheet Steels*, AIST, Warrendale, PA, 2008

12.76 W. F. Hosford and R.M. Caddell, *Metal Forming: Mechanics and Metallurgy*, PTR Prentice Hall, Englewood Cliffs NJ, 1993

12.77 D.L. Steinbrunner, D.K. Matlock, and G. Krauss, Void formation during Tensile Testing of Dual Phase Steels, *Metall. Trans. A*, Vol 19A, 1988, p 579–589

12.78 S. Okamoto, *Strain Rate and Temperature Effects on Deformation Behavior and Mechanical Properties of As-Quenched Low-Carbon Martensite*, M.S. thesis, Colorado School of Mines, Golden, CO, 1990

12.79 J. Faderl and R. Verhof, Press Hardening Steel (PHS): A new Coating and Process Technology, *Proceedings of the International Conference on Steels in Cars and Trucks*, Weisbaden, Germany, Verlag Stahleisen Gmbh, Dusseldorf, 2005

12.80 G. Schiesl, T. Possehn, T. Heller, and S. Skikora, Manufacturing a Roof Frame from Ultrahigh-Strength Steel Materials by Hot Stamping, *Proceedings IDDRG 2004*, Sindelfingen, p 158–166

12.81 M. Naderi, V. Uthaisangsuk, U. Prahl, and W. Bleck, A Numerical and Experimental Investigation into Hot Stamping of Boron Alloyed Heat Treated Steels, *Steel Res. Int.*, Vol. 79, 2008, p 77–84

12.82 P. Hein and J Wilsius, Status and Innovation Trends in Hot Stamping of USIBOR 1500 P, *Steel Res. Int.*. Vol79, 2008, p 85–91

12.83 M. Maikranz-Valentin, U. Weidig, U. Schoof, H.H.Becker, and K. Steinhoff, Components with Optimized Properties due to Ad-

vanced Thermo-mechanical Process Strategies in Hot Sheet Metal Forming, *Steel Res. Int.*, Vol 79, 2008, p 92–97

12.84 J. Lecher, M. Merklein, and M. Geiger, Determination of Thermal and Mechanical Material Properties of Ultra-High Strength Steel for Hot Stamping, *Steel Res. Int.*, Vol 79, 2008, p 98–104

12.85 G. Frommeyer, U. Brux, and P. Neumann, Super-Ductile and High-Strength Manganese TRIP/TWIP Steels for High Energy Absorption Purposes, *ISIJ Int.*, Vol 43, 2003, No. 3, p 438–446

12.86 O. Grassel, L.Kruger, G. Frommeyer,and L. W. Meyer, High strength Fe-Mn-(Al,Si) TRIP?TWIP steels: development-properties-application, *Int. J. Plast.*, Vol 16, 2000, p 1391–1409

12.87 O. Grassel and G. Frommeyer, Effect of martensitic phase transformation and deformation twining on mechanical properties of Fe-Mn--Si-Al steels, *Mater. Sci. Technol.*, Vol 14, 1996, p 1213–1217

12.88 B.C. De Cooman, O. Kwon, and K.-G Chin, State-of-the-knowledge on TWIP steel, *Mater. Sci. Technol.*, Vol 28, 2012, p 513–527

12.89 O. Bouaziz, S. Allain, C.P. Scott, P. Cugy, and D. Barbier, High manganese austenitic twinning induced plasticity steels: A review of the microstructure properties relationships*, Curr. Opin. Solid State Mater. Sci.*, Vol 15, 2011, p141–168

12.90 D.R. Steinmetz, T. Jäpel, B. Wietbrock, P. Eisenlohr, I. Gutierrez-Urrutin, A. Saeed-Akbari, T. Hickel, F. Roters, and D. Raabe, Revealing the strain-hardening behavior of twinning-induced plasticity steels: Theory, simulations, experiments, *Acta Mater.*, Vol 61, 2013, 494–510

12.91 I. Gutierrez-Urrutia and D. Raabe, Dislocation and twin substructure evolution during strain hardening of an Fe-22 wt.% Mn-0.6 wt.% C TWIP steel observed by electron channeling contrast imaging, *Acta Mater.,* Vol 59, 2011, p 6449–6462

12.92 D.T. Pierce, J.A. Jimenez, J. Bentley, D. Raabe, C. Oskay, J.E. Wittig, The influence of manganese content on the stacking fault and austenite/ε-martensite interfacial energies in Fe-Mn-(Al-Si) steels investigated by experiment and theory, *Acta Mater.*, 2014

12.93 D.T. Pierce, J. Bentley, J.A. Jimenez, and J.E. Wittig, Stacking fault energy measurements of Fe-Mn-Al-Si austentic twinning-induced plasticity steels, *Scr. Mater.*,Vol 66, 2012, p 753–756

12.94 Il-Chan Jung and Bruno C. De Cooman, Temperature dependence of the flow stress of Fe-18 Mn-0.6C-xAL twinning-induced plasticity steel, *Acta Mater.*, Vol 61, 2013, p 6724–6735

12.95 J.G. Speer, Phase transformations in quenched and partitioned steels, in *Phase transformations in steels*, Vol 2, E. Pereloma and D.V. Edmonds, Editors, Woodhead Publishing, Oxford, 2012, pp 247–270

12.96 S.J. Barnard, G.D.W. Smith, A.J. Garrat-Reed, J. Vander Sande, Atom Probe Studies: 1) Role of Silicon in Tempering of Steel, and 2) Low Temperature Chromium Diffusivity in Bainite, in *Solid-Solid Phase Transformations*, TMS-AIME, Warrendale, PA, 1982, pp 881–883

12.97 J.L. Youngblood and M. Raghavan, Correlation of Microstructure with Mechanical Properties of 300M Steel, *Metall. Trans. A*, Vol 8A, pp 1439–1448

CHAPTER 13

Normalizing, Annealing, and Spheroidizing Treatments; Ferrite/Pearlite and Spherical Carbides

THIS CHAPTER DESCRIBES heat treatments that are designed to produce uniformity in microstructure, improve ductility, reduce residual stresses, and/or improve the machinability of steels. Several of these heat treatments, in medium-carbon steels, produce microstructures consisting of ferrite and relatively large amounts of pearlite, and therefore, mechanical properties of ferrite/pearlite microstructures in medium-carbon steels are treated in this chapter. The properties of ferrite/pearlite microstructures in low-carbon steels, where mechanical behavior is dominated by the ferrite phase, have been discussed in Chapters 11, "Deformation, Strengthening, and Fracture of Ferritic Microstructures," and 12, "Low-Carbon Steels," and the properties of fully pearlitic microstructures in high-carbon steels are discussed in Chapter 15, "High-Carbon Steels—Fully Pearlitic Microstructures and Wire and Rail Applications." Thermal treatments that produce dispersions of spherical cementite particles, especially spheroidizing treatments that produce such carbides in a matrix of ferrite, are also discussed in this chapter.

Full Annealing

Figure 13.1 shows the temperature ranges, superimposed on the Fe-C diagram, used to produce austenite or austenite/cementite microstructures for various steel heat treatments (Ref 13.1). The temperature band marked

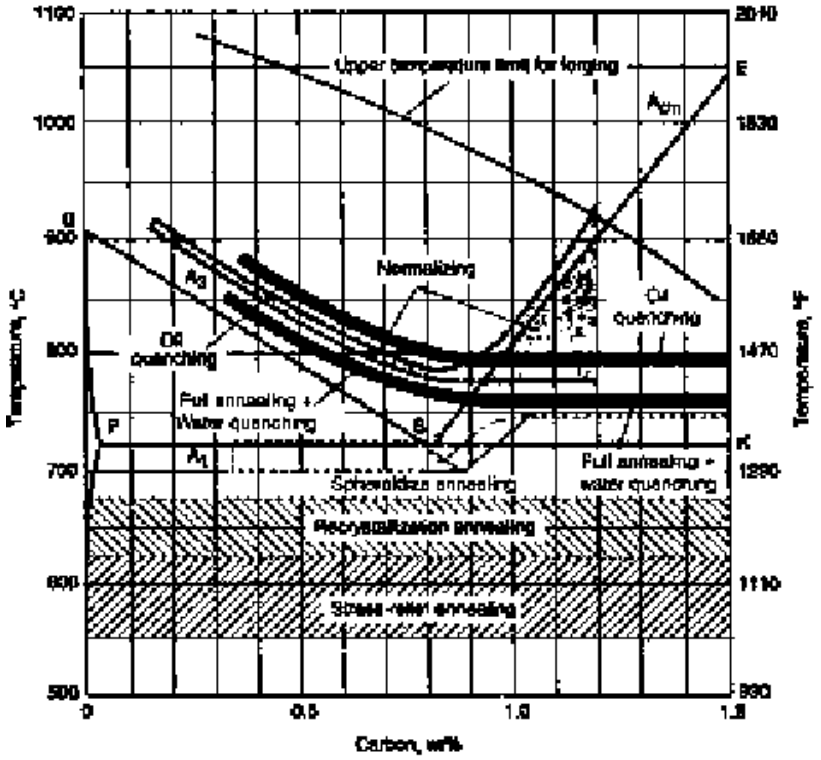

Fig. 13.1 Schematic diagram showing approximate temperature ranges superimposed on the Fe-C diagram for various heat treatments applied to steels. Source: Ref 13.1

"water quenching" also marks the temperatures used for full annealing. *Full annealing,* one of several types of annealing, is the heat treatment in which steels are heated just above the Ac_3 temperature for low- and medium-carbon steels and just above the Ac_1 temperature for hypereutectoid steels, and slowly cooled in furnaces after heating has ceased. When the term "annealing" is used without an adjective in reference to carbon steels, full annealing is the implied heat treatment practice (Ref 13.2). Full annealing involves austenite formation, in contrast to recrystallization annealing treatments applied to cold-rolled steels at subcritical temperatures, as shown in Fig. 13.1, and described in Chapter 12, "Low-Carbon Steels," relative to the processing of low-carbon sheet steels.

Figure 13.2 compares schematically annealing and normalizing (described subsequently) heat treatments. The slow cooling of full annealing causes austenite transformation to ferrite and pearlite close to A_3 and A_1 temperatures, respectively, and ensures that coarse-grained equiaxed ferrite and pearlite with coarse interlamellar spacing will form, producing microstructures of high ductility and moderate strength. Once the austenite has fully transformed to ferrite and pearlite, the cooling rate can be

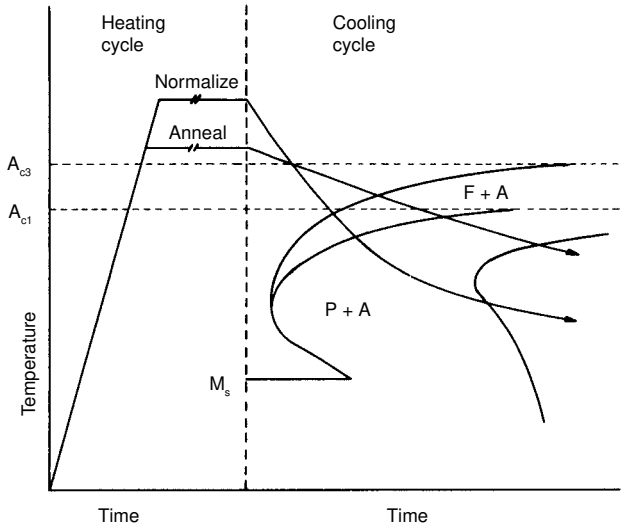

Fig. 13.2 Schematic time-temperature cycles for full annealing and normalizing superimposed on austenite transformation ranges to ferrite and pearlite. Courtesy of M.D. Geib, Colorado School of Mines

increased to reduce processing time and thereby improve productivity. A number of additional rules for developing optimum full annealing practices and properties are given in Ref 13.2.

Although ferrite and pearlite microstructures are most often produced by full annealing at the temperatures shown in Fig. 13.1, microstructures of spheroidized carbide particles in ferrite may sometimes form. Such microstructures are a result of the divorced eutectoid transformation, described in Chapter 4, "Pearlite, Ferrite, and Cementite," in which austenite transforms to spheroidized carbide/ferrite microstructures instead of the lamellar ferrite/cementite structure of classical pearlite (Ref 13.3). Critical to the operation of divorced eutectoid transformation is the presence of spheroidized carbides in austenite, a condition that is built into intercritical austenitizing for annealing of hypereutectoid steels, but which also may occur in hypoeutectoid steels because of undissolved carbides in austenite. Such undissolved carbides may be present because low austenitizing temperatures limit carbide dissolution or because of alloying elements that stabilize carbides and retard carbide dissolution.

Normalizing

Normalizing is the heat treatment that is produced by austenitizing and air cooling to produce uniform, fine ferrite/pearlite microstructures in steel. The higher austenitizing temperatures applied during normalizing compared with those applied during annealing (Fig. 13.1) ensure that most

carbides are dissolved, and the more rapid air cooling (Fig. 13.2) produces finer ferrite grains and pearlite with finer interlamellar spacing than is produced by annealing. In view of the finer microstructures of normalized steels, hardness and strength are somewhat higher, and ductilities somewhat lower, than those of annealed steels. As discussed later, the relative amounts of ferrite and pearlite, as determined primarily by steel carbon content, determine mechanical properties produced in a given normalized steel.

Normalizing is often applied to hot-forged carbon and alloy steels. As shown in Fig. 13.1, forging of bars to complex shapes is accomplished at high temperatures in the austenite phase field, temperatures that may be well above the grain-coarsening temperature of aluminum-killed steels as discussed in Chapter 8, "Austenite in Steel." As a result of high forging temperatures, austenite grain sizes are coarse, and in view of variable deformation in forgings of complex shape, austenite grain size may be quite variable. On cooling, the austenite transforms to coarse, nonuniform ferrite/pearlite microstructures. Reheating during normalizing causes uniform nucleation of new austenite grains, and because normalizing temperatures are kept below grain-coarsening temperatures, austenite grain size remains fine, and the austenite transforms to uniform, fine ferrite/pearlite microstructures during air cooling. The latter microstructures provide excellent starting microstructures for subsequent hardening heat treatments.

As noted in Fig. 13.1, normalizing of high-carbon, hypereutectoid steels may be applied over a range of temperatures. When the austenitizing temperatures are above A_{CM} temperatures, fully austenitized microstructures are produced and all carbides are dissolved. As a result, on cooling cementite allotriomorphs form on austenite grain boundaries, and continuous cementite networks provide brittle fracture paths for quench cracking or brittle fracture where the balance of the microstructure is martensitic. Figure 13.3 shows an example of grain-boundary cementite formation in a hardened 52100 steel and the resulting intergranular fracture along grain-boundary cementite (Ref 13.4). The latter observations were obtained in an experimental study, but for air-hardening tool steels, similar brittle fracture may occur after high-temperature normalizing, and normalizing is not recommended (Ref 13.5).

In high-carbon steels with relatively low hardenability, normalizing above A_{CM} results in grain boundary cementite formation followed by pearlite formation. On austenitizing for hardening the cementite in the grain boundary networks and in the pearlite will spheroidize, but the coarser particles of the grain boundary networks persist and mark the locations of prior austenite grain boundaries. Such arrays of coarse particles have been shown to influence fracture (Ref 13.6). An example of grain-boundary cementite in normalized 52100 steel and residual networks marked by coarse partially spheroidized carbides in hardened 52100 steel

is shown in Fig. 13.4. Austenitizing for hardening has produced an entirely new set of fine austenite grains and the residual network carbides are now intragranular relative to the austenitic structure and the subsequently transformed martensitic structure.

Air cooling associated with normalizing produces a range of cooling rates depending on section size. Heavier sections air-cool at much lower cooling rates than do light sections because of the added time required for thermal conductivity to lower the temperature of central portions of the workpiece. Two important consequences follow from the effect of section size on cooling rate. In heavy sections, the surface may cool at significantly higher rates than the interior. Thus, the transformation of the aus-

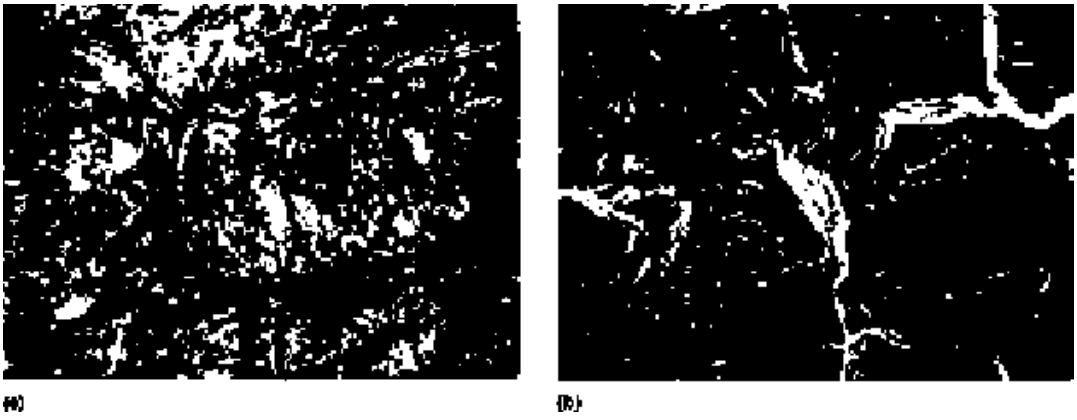

Fig. 13.3 (a) Carbide network at prior austenite grain boundaries in 52100 steel. Light micrograph, nital etch, original magnification 600×; shown here at 75%. (b) Fracture along grain-boundary carbides in 52100 steel. Scanning electron micrograph, original magnification 415×; shown here at 75%. Courtesy of T. Ando, Colorado School of Mines

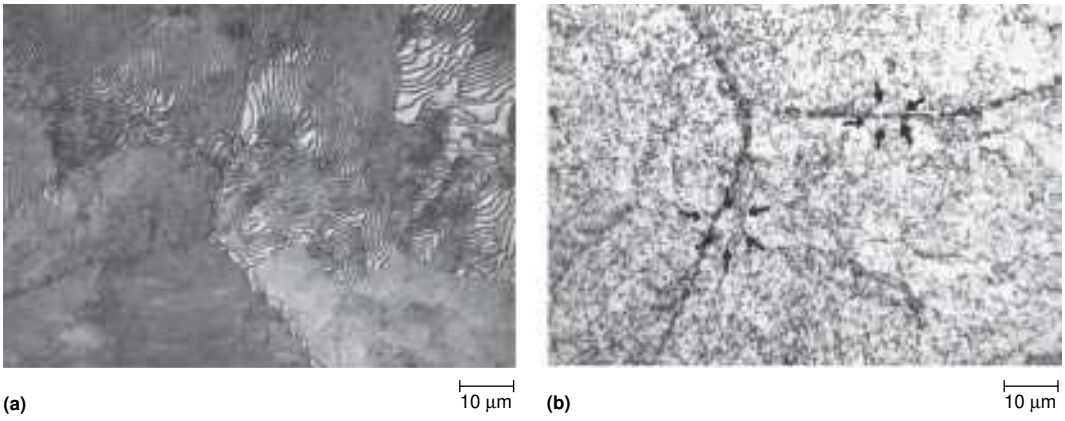

Fig. 13.4 (a) Proeutectoid cementite network in pearlitic microstructure of normalized 52100 steel. (b) Residual cementite network after austenitizing the microstructure in (a) at 850 °C (1650 °F) for hardening. Very fine particles are from spheroidization of cementite in pearlite, and arrows point to fine austenite grains that have formed on austenitizing. Light micrographs, nital etches. Source: Ref 13.6

tenite, with the accompanying volume expansion happens first at the surface. Subsequent interior transformation and volume expansion introduce surface residual tensile stresses. In very light sections, especially in alloy hardenable steels, air cooling may be rapid enough to form bainite or martensite instead of ferrite and pearlite, an effect already noted relative to normalizing of tool steels. The British Steel Corporation atlas of cooling transformation (Ref 13.7) establishes directly for many steels the effect of section size on microstructures produced by air cooling, as described in Chapter 10, "Isothermal and Continuous Cooling Transformation Diagrams." Other aspects of normalizing carbon steels are discussed in Ref 13.2. Although normalizing is most frequently applied to bar and forging steels, plate steels are also normalized, as discussed in a paper by Bodnar et al. (Ref 13.8).

Spheroidizing and Spherical Carbides

The reduction of interfacial energy associated with carbide interfaces provides a powerful thermodynamic driving force for microstructural change in steel. Spherical particles have minimum surface-to-volume ratios relative to other particle shapes, and the coarser, the fewer, and the more spherical shape of carbide particles, the lower the area and interfacial energy component of a microstructure. Thus, spheroidized microstructures are the most stable that can be produced in steels, and the spheroidization process begins in any prior structure heated at temperatures high enough and for long enough to permit the diffusion-dependent formation of spherical particles.

Dispersions of spherical carbide particles are ubiquitous in carbon steels. They result in ferrite from cold rolling and annealing of low-carbon sheet steels that need excellent formability. Long-time annealing treatments produce spheroidized carbide/ferrite microstructures with good formability in medium-carbon steels and good machinability in high-carbon steels and tool steels. In medium-carbon steels dispersions of carbides not dissolved during austenitizing are incorporated into martensitic microstructures, and in high-carbon bearing steels, some carburized steels, and tool steels, spherical carbides are incorporated by design into austenite, and subsequently into the martensite that forms from that austenite. High-temperature tempering of martensite produces dispersions of fine carbide particles in ferrite with excellent combinations of strength and toughness, and if tempering is long enough highly ductile spheroidized microstructures result.

The most ductile, lowest-hardness condition of any steel is associated with microstructures that consist of spherical carbide particles uniformly dispersed in a ferrite matrix. Heat treatments that produce such microstructures are termed *spheroidizing* or *spheroidize annealing* heat treatments. Figure 13.5 shows a dispersion of spherical cementite particles in

Fig. 13.5 Spheroidized microstructure in an Fe-0.66% C-1% Mn steel formed by heating martensite at 700 °C (1300 °F) for 24 h. Light micrograph, picral etch, original magnification 1000×. Courtesy of A.R. Marder and A. Benscoter, Lehigh University

a matrix of ferrite in a 0.66% C- 1.00% Mn steel. The high ductility of such a microstructure is directly related to the continuous ductile ferrite matrix and the coarse, separated carbide particles that offer little resistance to deformation. Nevertheless, the ductility and hardness of spheroidized microstructures vary significantly depending on the density and spacing of the carbide particles as related to steel carbon content and the heat treatment used to produce the spheroidized microstructure.

Figure 13.6 shows the results of systematic studies performed by Gurland et al. on the strengths of spheroidized microstructures in a variety of steels, containing from 0.065 to 1.46% carbon, and spheroidized from martensitic microstructures by tempering for long times at 460° and 700 °C (860 and 129 °F) (Ref 13.9, 13.10). There is a good correlation of hardness with carbide spacing in a Hall-Petch plot. Coarse carbide spacings correlate with low hardness, and accordingly good ductility, and in medium- and high-carbon steels desired coarse spacings are produced only after long-time heat treatments, as discussed later in this section.

There are effectively three stages in the formation of spheroidized microstructures. The first stage involves the formation of spherical particles from the dispersions existing prior to heating. Dispersions produced by heating of martensite form with spherical particles, but very often the starting structure for spheroidizing consists of pearlite where the cementite is plate-shaped and has a very high interfacial area per unit volume (Ref 13.11). Spheroidization starts at areas of curvature in the cementite lamellae and at termination of cementite lamellae (Ref 13.12, 13.13). A representation of this process, obtained by serial sectioning of a 0.74% C

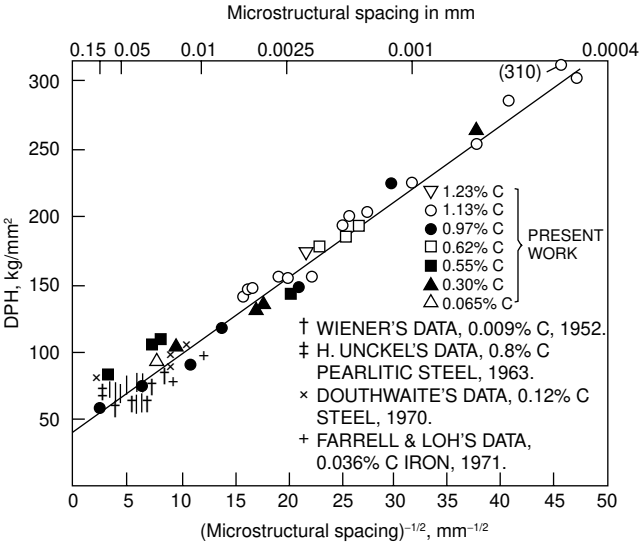

Fig. 13.6 Diamond Pyramid Hardness (DPH) versus the reciprocal square root of carbide spacing in steels with various carbon contents with spheroidized microstructures. Source: Ref 13.10

steel, is shown in Fig. 13.7. Once separated particles have formed, perhaps with carbides particles of higher aspect ratios than that of spherical particles, another stage of the spheroidization process is the formation of uniformly spherical particles.

The first stages of spheroidization, often produced in very short times, result in high densities of fine spherical particles, and mark the beginning of the final stage of spheroidization. The fine particles with small radii of curvature dissolve and coarse particles grow, again a mechanism by which interfacial energy is reduced. This process is referred to as *Ostwald Ripening*, and depends on the diffusion of carbon, iron, and other elements away from small particles, through ferritic or austenitic matrices, to large particles (Ref 13.15). The following equation has been shown to describe the rate of coarsening of particles in spheroidized microstructures (Ref 13.14, 13.16):

$$\frac{dr}{dt} = \frac{2\gamma V_{Fe_3C}^2 X_c D_c^{eff}}{V_{Fe} R T_{r_1}} \left(\frac{1}{\bar{r}} - \frac{1}{r_1} \right) \qquad \text{(Eq 13.1)}$$

where γ is the interfacial energy, V_{Fe_3C} and V_{Fe} are the molar volumes of cementite and ferrite, X_C is the mole fraction of carbon in equilibrium with cementite in ferrite, D_C^{eff} is the effective carbon diffusion coefficient, R is the gas constant, T is the absolute temperature, r_1 is the radius of newly created particles, and $\bar{r}$ is the mean size of the already spheroidized particles.

Equation 13.1 shows that the rate of coarsening is directly related to the effective diffusion of carbon and decreases as the average size of the par-

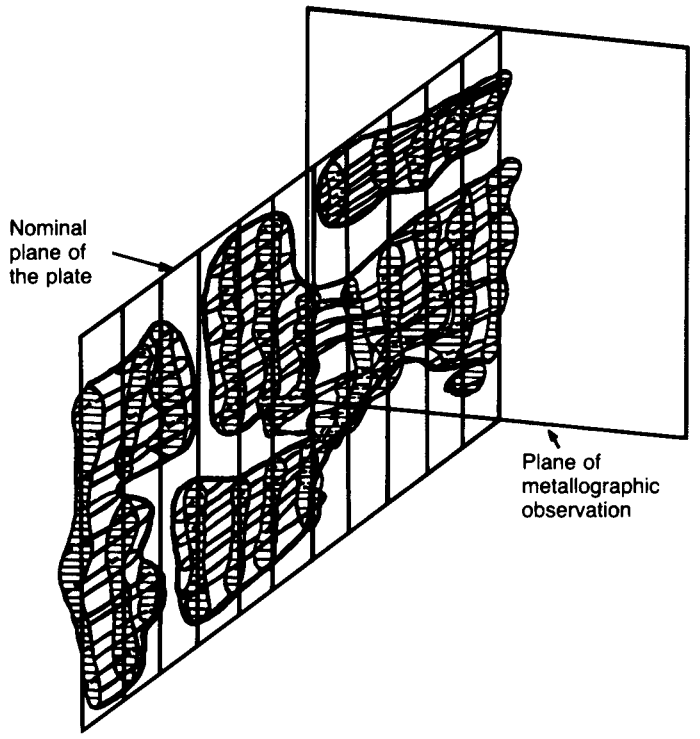

Fig. 13.7 Representation of partial spheroidization of a cementite plate or lamella in coarse pearlite in a high Si steel annealed for 150 h at 700 °C (1290 °F). Source: Ref 13.14

ticles increases. Clearly carbon diffusion is necessary, but Tian and Kraft have shown by determination of the activation energy for spheroidization of an Fe-C alloy (58 kcal/mole) that the rate limiting factor of spheroidization correlates with the volume diffusion of iron atoms (61 kcal/mole), not with the activation energy for the volume diffusion of carbon atoms (20 kcal/mole) (Ref 13.12, 13.13). Spheroidization of pearlite in an AISI 1080 steel containing manganese showed a higher activation energy consistent with the fact that manganese is a carbide-forming element that must also diffuse as carbide particles change shape, dissolve, and grow. Other investigations show the effect of substitutional alloying elements on slowing the rate of carbide dissolution and spheroidization (Ref 13.17, 13.18). Studies of carbide spheroidization in 52100 steels showed that carbides on austenite grain boundaries coarsened more rapidly than particles within grains, consistent with more rapid diffusion rates along grain boundaries than within grains, and that eventually the finer carbides within the grains dissolved, leaving only much coarser grain-boundary carbides. (Ref 13.19, 13.20).

The spheroidization of pearlite in cold-rolled and in normalized low-carbon steels is rapid, producing distributions of fine carbide particles in

minutes on heating to the lower critical temperature (Ref 13.21, 13.22). Commercial spheroidizing heat treatments are much longer, requiring many hours to produce the distributions of widely spaced, coarse carbides that reduce hardness and increase ductility to that needed for intermediate processing operations such as machining and forming. For example, bolt manufacture requires cold work and therefore high ductility for heading and threading of wire rod before final heat treatment. Heat treatment cycles for spheroidizing of AISI 1541 steel, a commonly used medium-carbon steel with high manganese content (1.35-1.65% Mn) for bolts, have consisted of intercritical soaking at 748 °C (1378 °F) for 4 to 6 hours, followed by subcritical soaking at 690 °C (1274 °F) for 10 to 14 hours, and other cycles involving only subcritical heating have been evaluated (Ref 13.23, 13.24).

AISI 1541 steel is difficult to spheroidize because of its relatively high manganese content. A study of a 0.74% C, 0.71% Si showed very long times for spheroidization, up to hundreds of hours, depending on the interlamellar spacing of the starting pearlite, as shown in Fig. 13.8. Silicon cannot be incorporated in the crystal structure of cementite, and therefore must diffuse away from cementite as it changes its shape during spheroidizing (13.25).

Spheroidizing is more rapid than in pearlitic microstructures if carbides are initially in the form of discrete particles, as in bainite, and especially if the particles are formed by tempering of martensite (Ref 13. 26). Many other approaches to spheroidizing are used to accelerate the process. Heating to accomplish either complete or partial austenitizing, and then holding just below A_{C1}, cooling quickly through the A_{C1}, or cycling above and

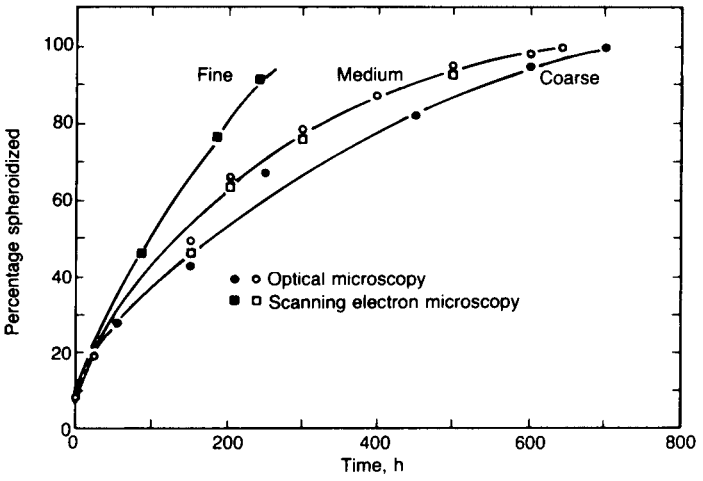

Fig. 13.8 Spheroidization as a function of time at 700 °C (1290 °F) of fine, medium, and coarse pearlites in a steel containing 0.74% C and 0.71% Si. Source: Ref 13.14

below A_{C1} are all techniques used to reduce the time for spheroidization (Ref 13.2, 13.27).

Distributions of spherical carbide particles are important not only in ferritic microstructures, but also in martensitic microstructures. For example, austenitizing treatments for hardening 52100, a steel containing nominally 1.00% C and 1.50% Cr and widely used for bearings, are performed intercritically, between the A_1 and A_{CM} temperatures, in the two-phase cementite/austenite phase field, typically at 850 °C (1560 °F). The retained carbide particles lower the carbon concentration of the austenite (and consequently that of the martensite), lower sensitivity to quench embrittlement, raise M_S temperatures, and reduce the amount of retained austenite in the hardened microstructures. Stickels (Ref 13.28) points out that distributions of fine retained carbides in 52100 steel perform better in rolling contact fatigue than do coarse carbide particles retained after austenitizing spheroidized ferrite/carbide microstructures, and by systematic experiments showed that beneficial ultra-fine dispersions of carbides 0.1 μm in size can be produced by austenitizing starting pearlitic microstructures isothermally formed at 625 to 650 °C (1155 to 1200 °F).

Mechanical Properties of Ferrite-Pearlite Microstructures

Figure 13.9 shows a set of mechanical properties of ferrite-pearlite microstructures as a function of steel carbon content (Ref 13.29). Yield and ultimate tensile strengths increase, and reduction of area, a measure of ductility, decreases, as carbon content increases because of the increase in pearlite content. The microstructures range from essentially 100% ferrite in the low-carbon steels to 100% pearlite in steels of eutectoid carbon content. The divergence of the yield and tensile strengths at high carbon contents indicates that increased amounts of pearlite increase work-hardening rates.

The data in Fig. 13.9 were produced for a given set of conditions. For a given steel, variations in microstructure, such as grain size and pearlite interlamellar spacing, and compositional factors, may influence mechanical properties. The effects of these variations have been quantified by Gladman et al. (Ref 13.30) in the following equation for yield strength of medium-carbon ferrite/pearlite steel microstructures:

$$\begin{aligned}\sigma_{YS}(\text{MPa}) = 15.4\{&f_\alpha^{1/3}[2.3 + 3.8(\%\text{Mn}) + 1.13d^{-1/2}] \\ &+ (1 - f_\alpha^{1/3})[11.6 + 0.25S_P^{-1/2}] \\ &+ 4.1(\%\text{Si}) + 27.6(\%\text{N})\end{aligned} \qquad \text{(Eq 13.2)}$$

where f_α is the volume fraction of ferrite, S_P is the interlamellar spacing of pearlite (the distance in mm from the center on one cementite lamella to

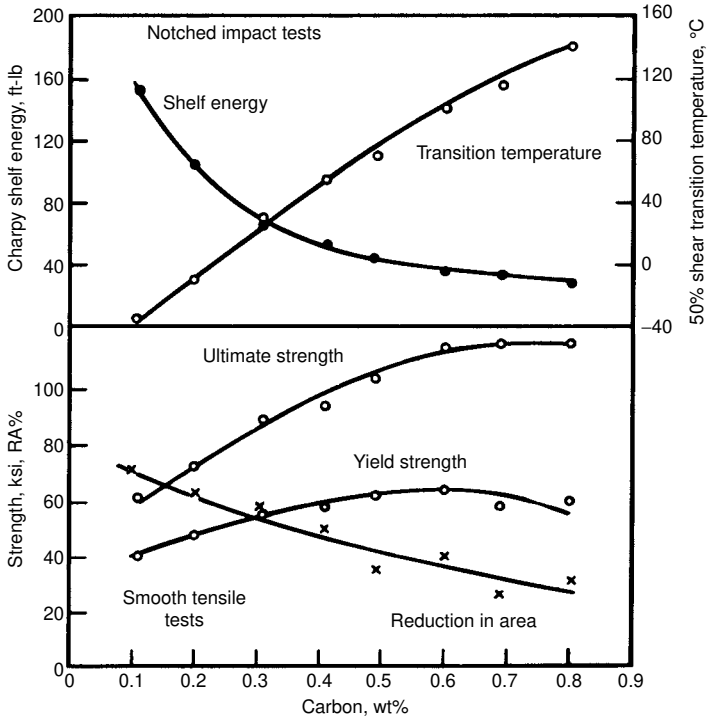

Fig. 13.9 Mechanical properties of ferrite-pearlite microstructures as a function of steel carbon content. Source: Ref 13.29

the center of the next lamella), and d is the mean linear intercept ferrite grain diameter in mm. The first term relates to the strength contributions of ferrite, the second to the contributions of pearlite, and the last two terms the general effects of silicon and nitrogen contents. As the volume fraction of ferrite decreases, the interlamellar spacing of the dominant pearlite most strongly influences yielding.

With increasing steel carbon content, and therefore with increasing pearlite content, Fig. 13.9 shows a significant decrease in impact toughness of ferrite/pearlite microstructures. The ductile-to-brittle transition temperature increases to well above room temperature, and ductile fracture upper shelf energies sharply decrease. Figure 13.10 also shows the negative effects of increasing steel carbon content on impact toughness in CVN energy versus test temperature curves for steels with ferrite/pearlite microstructure (Ref 13.31). Thus, care must be taken in the application of medium-carbon steels with ferrite/pearlite microstructures. Normalized and annealed ferrite/pearlite microstructures in medium-carbon steels, as discussed previously, are often only intermediate processing microstructures prior to hardening heat treatments, and therefore are not used for final applications. If steels with large pearlite contents are used, applica-

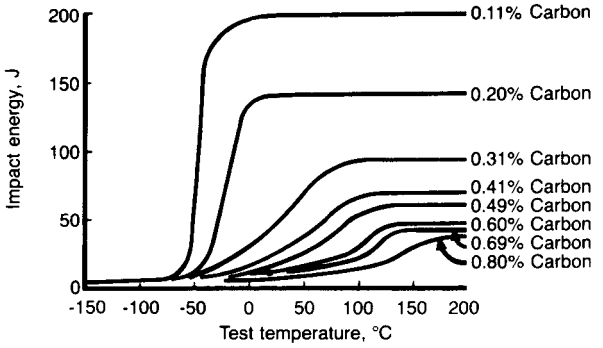

Fig. 13.10 Impact transition curves for steels with various carbon contents and ferrite/pearlite microstructures. Source: Ref 13.31

tions with impact loading should be avoided and the operating stress states for a given operation carefully evaluated. More information on applications and mechanical properties of medium-carbon steels with ferrite/pearlite microstructures is given in Chapter 14, "Non-Martensitic Strengthening of Medium-Carbon Steels—Microalloying and Bainitic Strengthening." Also, even with very low fracture resistance, fully pearlitic steels are widely used, for example, in rail and high-strength wire applications, as discussed in Chapter 15, "High-Carbon Steels—Fully Pearlitic Microstructures and Wire and Rail Applications."

REFERENCES

13.1 K.-E. Thelning, *Steel and Its Heat Treatment,* 2nd ed., Butterworths, London, 1984

13.2 Heat Treating of Carbon and Low-Alloy Steels, Vol 2, 8th ed., *Metals Handbook,* American Society for Metals, 1964, p 1–10

13.3 J.D. Verhoeven and E.D. Gibson, The Divorced Eutectoid Transformation in Steel, *Metall. and Mater. Trans. A,* Vol 29A, 1998, p 1181–1189

13.4 T. Ando and G. Krauss, The Isothermal Thickening of Cementite Allotriomorphs in a 1.5Cr-1C Steel, *Acta Metall..,* Vol 29, 1981, p 351–363

13.5 G. Roberts, G. Krauss, and R. Kennedy, *Tool Steels,* 5th ed., ASM International, 1998

13.6 K. Nakazawa and G. Krauss, Martensite and Fracture in 52100 Steel, *Metall. Trans. A,* Vol 9A, 1978, p 681–689

13.7 M. Atkins, *Atlas of Continuous Cooling Transformation Diagrams for Engineering Steels,* British Steel Corp., Sheffield, 1977

13.8 R.L. Bodnar, F.B. Fletcher, and M. Manohar, The Physical Metallurgy of Normalized Plate Steels, *Materials Science & Technology 2004,* conference proceedings, AIST, Vol 1, 2004, p 89–109

13.9 C.T. Liu and J. Gurland, The Strengthening Mechanism in Spheroidized Carbon Steels, *Trans. Metall. Soc. AIME*, Vol 242, 1968, p 1535–1542
13.10 P. C. Jindal and J. Gurland, On the Relation of Hardness and Microstructure of Tempered and Spheroidized Carbon Steels, *Metall. Trans.*, Vol 5, 1974, p 1649–1653
13.11 L.E. Samuels, Spheroidization and Graphitization, Chapter 7 in *Light Microscopy of Carbon Steels*, ASM International, 1999, p 165–177
13.12 Y.L. Tian and R. W. Kraft, Mechanisms of Pearlite Spheroidization, *Metall. Trans. A*, Vol 18A, 1987, p 1403–1414
13.13 Y.L. Tian and R. W. Kraft, Kinetics of Pearlite Spheroidization, *Metall. Trans. A*, Vol 18A, 1987, p 1359–1369
13.14 S. Chattopadhyay and C.M. Sellars, Quantitative Measurements of Pearlite Spheroidization, *Metallography,* Vol 10, 1977, p 89–105
13.15 R.A. Oriani, Ostwald Ripening of Precipitates in Solid Matrices, *Acta Metall.,* Vol 12, 1964, p 1399–1409
13.16 R.L. Fullman, Measurement of Particle Sizes in Opaque Bodies, *Trans. AIME,* Vol 197, 1953, p 447–452
13.17 J. Agren, Kinetics of Carbide Dissolution, *Scand. J. Metall.,* Vol 19, 1990, p 2–8
13.18 P. Malecki and E.W. Langer, Dissolution of Cementite with Alloying Elements in Austenite, *Scand. J. Metall.,* Vol 19, 1990, p 182–186
13.19 K.R. Hayes, "The Effect of Intercritical Annealing and Phosphorous on Austenite Formation and Carbide Distribution in 52100 Steel," M.S. thesis, Colorado School of Mines, Golden, CO, 1984
13.20 E.L. Brown and G. Krauss, Retained Carbide Distribution in Intercritically Austenitized 52100 Steel, *Metall. Trans. A,* Vol 17A, 1986, p 31–36
13.21 D.Z. Yang, E. L. Brown, D. K. Matlock, and G. Krauss, Ferrite Recrystallization and Austenite Formation in Cold Rolled Intercritically Annealed Steel, *Metall. Trans. A*, Vol 16A, 1985, p 1385–1392
13.22 D.Z. Yang, E. L. Brown, D. K. Matlock, and G. Krauss, The Formation of Austenite at Low Intercritical Annealing Temperatures in a Normalized 0.08C-1.45Mn-0.21Si Steel, *Metall. Trans. A*, Vol 16A, 1985, p 1523–1526
13.23 J.M. O'Brien and W.F. Hosford, Spheroidizing of Medium Carbon Steels, *Steel Heat Treating in the New Millenium,* S.J. Midea and G.D. Pfaffmann, Ed., ASM International, 2000, p 638–645
13.24 J.M. O'Brien and W. F. Hosford, Spheroidization Cycles for Medium Carbon Steels, *Metall. and Mater. Trans. A*, Vol 33A, 2002, p 1255–1261

13.25 S.J. Barnard, G. D. W. Smith, A. J. Garrat-Reed, J. Vander Sande, Atom Probe Studies: 1) Role of Silicon in Tempering of Steel, and 2) Low Temperature Chromium Diffusivity in Bainite, in *Solid-Solid Phase Transformations*, TMS-AIME, Warrendale, PA, 1982, pp 881–883

13.26 E. Karadeniz, Influence of different initial microstructure on the process of spheroidzation in cold forging, *Mater. Des.,* Vol 29, 2008, p 251–256

13.27 W. Hewitt, The Spheroidise Annealing of High-Carbon Steels and Its Effect on Subsequent Heat Treatment, *Heat Treatment of Metals,* Vol 9, 1982, p 56–62

13.28 C.A. Stickels, Carbide Refining Heat Treatments for 52100 Bearing Steel, *Metall. Trans.*, Vol 5, 1974, p 865–874

13.29 A.R. Rosenfield, G.T. Hahn, and J.D. Embury, Fracture of Steels Containing Pearlite, *Metall. Trans.,* Vol 3, 1972, p 2797–2804

13.30 T. Gladman, I.D. McIvor, and F.B. Pickering, Some Aspects of the Structure-Property Relationships in High-Carbon Ferrite-Pearlite Steels, *JISI,* Vol 210, 1972, p 916–930

13.31 F.B. Pickering, The Optimization of Microstructures in Steel and Their Relationship to Mechanical Properties, *Hardenability Concepts with Applications in Steels,* D.V. Doane and J.S. Kirkaldy, Ed., AIME, Warrendale, PA, 1978, p 179–228

CHAPTER 14

Non-Martensitic Strengthening of Medium-Carbon Steels—Microalloying and Bainitic Strengthening

MEDIUM-CARBON STEELS for high-strength, high-fatigue-resistant applications have been traditionally hardened by austenitizing, quenching to martensite, and tempering. When high strength and moderate toughness are required, tempering is performed at low temperatures, around 200 °C (390 °F), and when moderate strengths and high toughness are required, tempering is performed at high temperatures, around 500 °C (930 °F). In order to provide for good hardenability and through-section hardening, steels subjected to hardening heat treatments are alloyed with significant percentages of chromium, nickel, and/or molybdenum. Hardening heat treatments and the mechanical properties of hardened steels are discussed in detail in later chapters.

The intense drive to maintain costs and productivity of steel products over the last several decades has created an entirely new class of steels that compete very favorably with hardened steels at moderate strength levels. This class of steels uses microalloying to develop extra strength in ferrite/pearlite microstructures produced directly on cooling from forging temperatures. Microadditions of vanadium and niobium, below 0.20%, are less expensive than substantial alloying additions of chromium, nickel, and molybdenum used for hardenable steels, and the fact that good strengths

are achieved by direct cooling after forging without subsequent multistep heat treatment adds to reduced costs and increased productivity.

Although microalloyed forging steels have been used since the 1970s in Europe and Japan (Ref 14.1), the first ASTM specification for microalloyed steels was approved only in 1992 (Ref 14.2). By 1996, numerous applications for microalloyed forging steels were reported by American corporations (Ref 14.3). Typical applications for microalloyed forging steels include connecting rods, crankshafts, spindles, wheel hubs, and other vehicle and engine components. The processing and properties of medium-carbon microalloyed steels are quite different from those of low-carbon microalloyed steels, as described in Chapter 12, "Low-Carbon Steels," and several conferences and texts have addressed, sometimes within the larger framework of microalloying, the development and use of the medium-carbon subset of microalloyed steels (Ref 14.1, 14.3–14.5). Depending on alloying, direct cooling after forging may produce bainitic microstructures, as discussed at the end of this chapter.

Processing Considerations

Figures 14.1 and 14.2 compare the processing of hardenable and microalloyed forging steels. Both types of steel are received as hot-rolled bars, which today are largely produced from scrap melted in electric arc furnaces and are subjected to forging at high temperatures. The hardenable steels require multistep heat treating operations in order to produce final

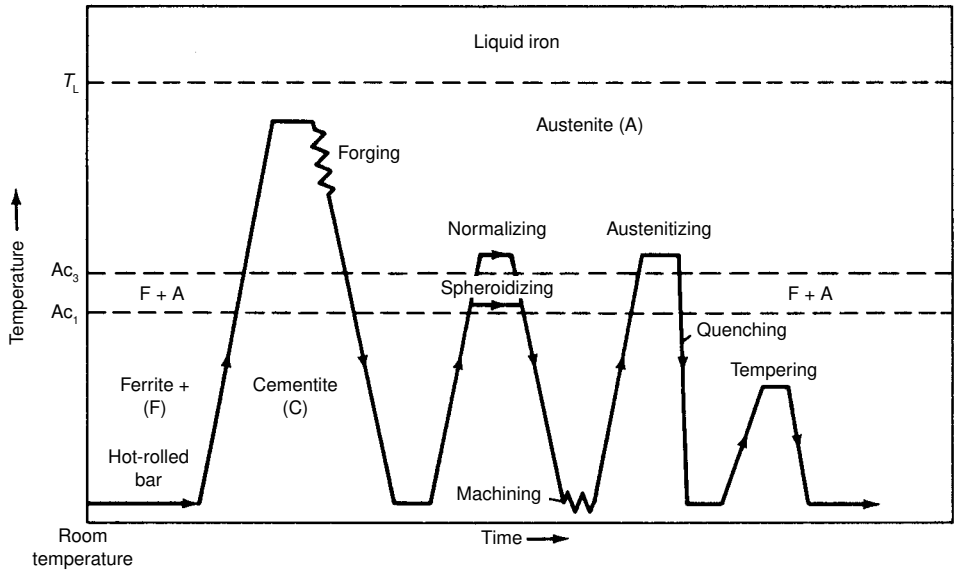

Fig. 14.1 Schematic diagram of the schedule of operations required to harden forged bar steels by quench and tempering heat treatments

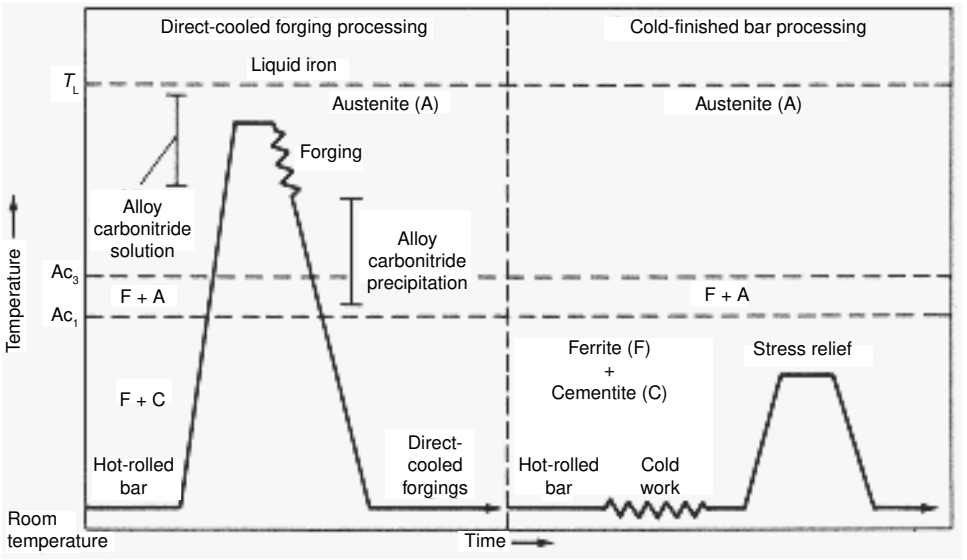

Fig. 14.2 Left diagram: schedule of operations required to strengthen microalloyed forged bar steels by direct cooling after forging. Right diagram: schedule of operations to produce cold-finished bars

microstructures and properties, while the microalloyed steels are merely cooled to room temperature to produce final microstructures and properties. The reduced processing for the microalloyed steels is obvious. Some hot-rolled bar steels are cold worked and stress relieved, and for completeness, this processing is also shown in Fig. 14.2.

As shown in Fig. 14.1 and 14.2, forging of complex shapes requires high-temperature deformation in the austenite phase field. This phase of processing is critical to the successful production of microalloyed forging steels in that microalloying carbonitride precipitates dissolve during heating to forging temperatures. As a result, microalloying elements, most often vanadium, are in solution in austenite and available for precipitation as fine carbonitride particles on cooling, as described in the next section.

Microalloying Considerations

Chapter 8, "Austenite in Steel," presents the temperature-dependent solubility products for the major microalloying elements, vanadium, niobium, and titanium, in austenite. Vanadium precipitates have the lowest stability and dissolve readily on heating to forging temperatures, a characteristic of vanadium that makes it the preferred microalloying element in forging steels. Niobium precipitates have higher stability, and therefore may be harder to dissolve during heating to forging temperatures. Figure 14.3, from early work by Gladman et al., shows the effectiveness of vanadium in increasing the strength of steels with ferrite/pearlite microstruc-

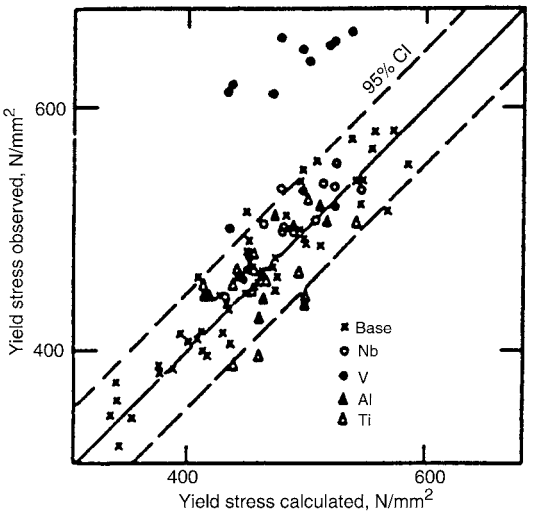

Fig. 14.3 Observed and calculated yield strengths for steels with ferrite/pearlite microstructures and various microalloying elements. Source: Ref 14.6

tures (Ref 14.6). Measured strengths were compared with strengths calculated from Eq 13.2, as discussed in Chapter 13, "Normalizing, Annealing, and Spheroidizing Treatments; Ferrite/Pearlite and Spherical Carbides." Good correlations between measured and calculated yield strengths exist for all microalloying additions except for steels with vanadium. Vanadium additions provided strengths in excess of those expected for typical microstructure and chemistry parameters in ferrite/pearlite microstructures.

Many types of precipitate particles may form in microalloyed forging steels depending on microalloy content and temperature (Ref 14.7–14.10). All of the precipitates are metal, M, carbonitrides, where M may be vanadium, niobium, and/or titanium, and all elements may be present in a given carbonitride particle. According to the solubility relationships, titanium-rich carbonitrides form at the highest temperatures, niobium-rich carbonitrides at intermediate temperatures, and vanadium-rich carbonitrides at the lowest temperatures. When niobium is present, the carbonitrides tend to be rich in carbon, and when vanadium is present, the carbonitrides are rich in nitrogen. The combined characteristics of low-temperature precipitation and strong tendency for nitride formation provide the fine particle strengthening of vanadium-containing medium-carbon forging steels. Thus, in addition to vanadium, sufficient nitrogen content is also necessary for maximum strengthening, and electric arc furnace steelmaking, which typically produces nitrogen contents of 70 to 100 ppm, provides an ideal processing approach for vanadium-microalloyed bar and forging steels.

As noted, titanium-rich nitrides have the highest stability and do not dissolve during forging. Therefore, titanium is not available to provide fine strengthening precipitates during cooling. However, the fine titanium

nitride precipitates stable during forging restrict austenite grain growth, and therefore make a beneficial refining contribution to microstructure. If titanium is added for austenite grain size control, it should be limited to contents of 0.01% or less (Ref 14.11, 14.12). Such low levels of titanium are sufficient to cause the precipitation of fine TiN particles in austenite. Higher concentrations may cause TiN precipitation in liquid steel, and the resulting coarse TiN particles may lower the fracture resistance of finished steel products.

Microstructure of Microalloyed Forging Steels

The extra strength of microalloyed forging steels is due to fine precipitation in the ferrite of direct cooled steels with ferrite/pearlite microstructures. Figure 14.4 shows light microscope and transmission electron microscope (TEM) micrographs of the ferrite/pearlite microstructure in a 0.2% C, 0.15% V steel. Vanadium-rich carbonitride particles are too fine to be resolved in the light microscope, but are resolved in the TEM as rows of very fine particles, less than 10 nm (100 Å) in size. These particles are formed by interphase precipitation at austenite/ferrite interfaces, as described in Chapter 4, "Pearlite, Ferrite, and Cementite," and their small size and high density provide very effective dispersion strengthening. Figure 14.5 shows TEM dark-field micrographs of microalloy precipitate arrays in a 0.38% C steel containing 0.04% Nb and 0.15% V. In these examples, the precipitates appear white because they were imaged with a beam diffracted from the particles. Fig. 14.5(a) shows Nb-rich particles that have formed on boundaries of deformed austenite, and Fig. 14.5(b) shows very high densities of very fine particles that have been produced with ferrite by interphase precipitation (Ref 14.8).

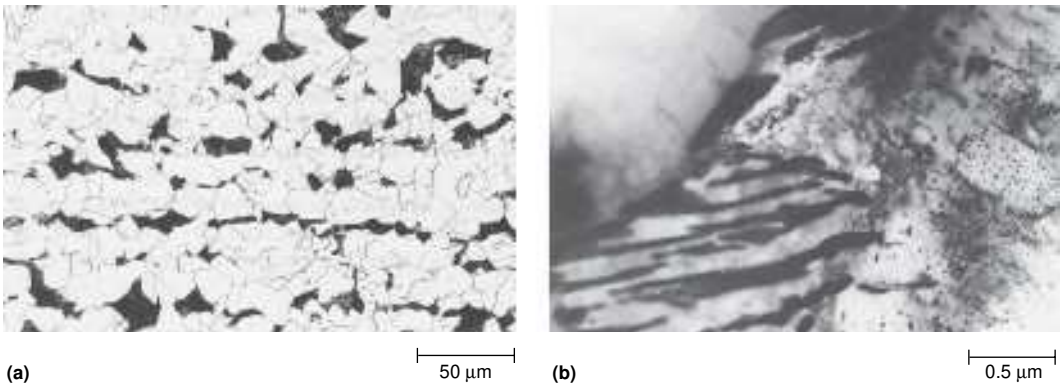

Fig. 14.4 Microstructure of 0.20% C, 0.15% V steel. (a) Ferrite and pearlite, nital etch, light micrograph. (b) Ferrite, pearlite, and fine V(C,N) precipitates. Transmission electron micrograph. Courtesy of S.W. Thompson, Colorado School of Mines

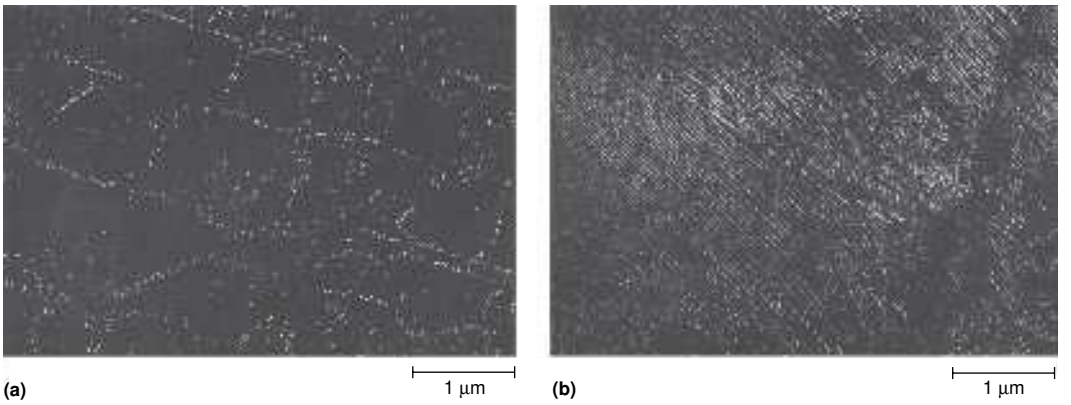

Fig. 14.5 Precipitate distributions in microalloyed steels containing vanadium and niobium. (a) Nb-rich precipitates on deformed austenite substructure. (b) Interphase V-rich precipitates. Dark-field transmission electron micrographs. Courtesy of S.W. Thompson. Source: Ref 14.8

Because the base microstructure consists of ferrite and pearlite, and because the strength of ferrite/pearlite microstructures increases with increasing pearlite content, many microalloyed forging steels have relatively high carbon contents, between 0.4 and 0.5%, and, therefore, base microstructures that consist largely of pearlite. Contributing to low ferrite contents are high forging temperatures that cause significant austenite grain coarsening (Ref 14.13). As a result, on cooling grain-boundary nucleated ferrite can grow only a limited distance into coarse austenite grains before pearlite formation begins, and the base microstructure consists of thin networks of ferrite grains surrounding large areas of pearlite. Examples of the latter type of microstructure are shown in three medium-carbon steels in Fig. 14.6 (Ref 14.14). Extra strengthening in largely pearlitic microstructures is accomplished by interphase V(C,N) precipitation in pearlitic ferrite as well as in proeutectoid ferrite, as has been demonstrated by Dunlop et al. (Ref 14.15) and Edmonds (Ref 14.16).

Figure 14.6 shows not only typical high pearlite content microstructures of microalloyed forging steels but also the effect of microalloying and sulfur content on microstructure. The steels from which the microstructures were derived all had the same carbon content, 0.38%, but differed in vanadium and sulfur contents: the VLS steel was alloyed with 0.053% V and 0.030% S, the NVS steel contained negligible vanadium but a high sulfur content of 0.102%, and the VHS steel contained 0.059% V and high S of 0.094% (Ref 14.14).

The microstructures in Fig. 14.6 have responded to the various chemistries according to a mechanism proposed by Ochi et al. (Ref 14.17): V nitride and V carbide form successively on MnS particles during cooling, and ferrite nucleation is enhanced by the vanadium precipitation, according to the schematic diagram shown in Fig. 14.7. Thus in a vanadium-microalloyed steel, ferrite nucleates and grows not only on austenite grain

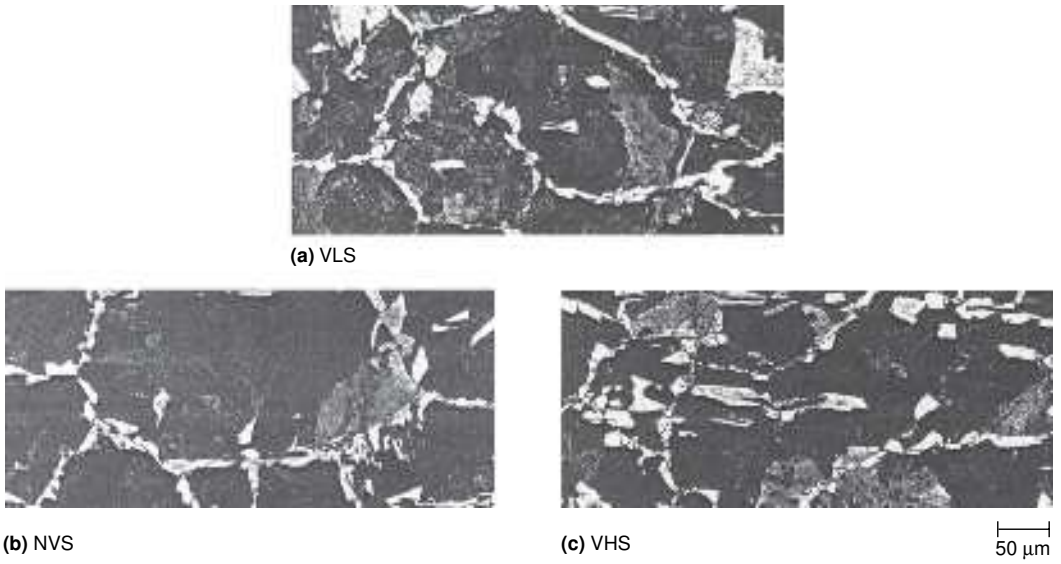

Fig. 14.6 Ferrite/pearlite microstructures formed on cooling from 1200 °C (670 °F). Ferrite appears white; pearlite appears black. Grain boundary ferrite networks and intragranular ferrite are shown. The steels are identified in text. Light micrographs, nital etches. Source: Ref 14.14

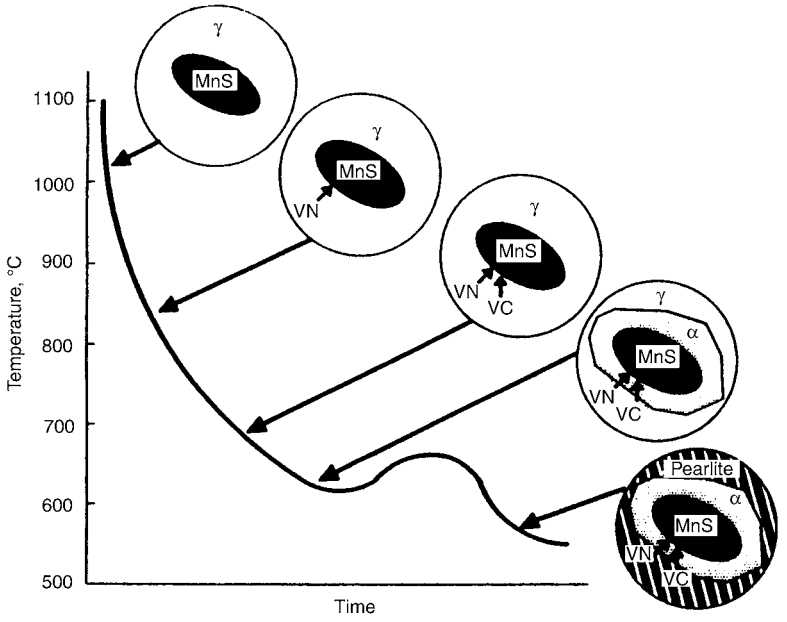

Fig. 14.7 Schematic diagram of the stages of intragranular ferrite formation on a manganese sulfide particle in V-microalloyed steel. Source: Ref 14.17

boundaries but also intragranularly on MnS particles within austenite grains. The resulting *intragranular ferrite* breaks up the massive pearlitic structures formed in a coarse-grained austenite and improves toughness. Figure 14.6 shows that the NVS steel, the steel without vanadium, forms almost no intragranular ferrite, despite its high MnS content, and that intragranular ferrite has formed in the vanadium-containing steels in high densities, especially in the high-sulfur steel. A higher magnification micrograph of intragranular ferrite formation around MnS inclusions in the VHS steel is shown in Fig. 14.8. Fig. 14.9 shows vanadium-rich particles formed on a MnS inclusion in a vanadium-microalloyed medium carbon steel (Ref. 14.18). The particles are thin and plate-shaped, and do not cover large areas of the inclusion particle.

Mechanical Properties of Microalloyed Forging Steels

Direct-cooled microalloyed forging steels serve well where moderate strengths and hardness are required and impact toughness is not a major factor in application. As-quenched martensitic microstructures start with much higher hardness levels, and when tempered back to typical hardness ranges produced in direct cooled microalloyed steels, i.e., HRC 25 to 30, have much higher impact toughness than do the steels with precipitation-strengthened ferrite/pearlite microstructures. Figure 14.10 compares the CVN energy absorbed as a function of test temperature for 4140 steel and two vanadium-strengthened steels, all processed to the same hardness

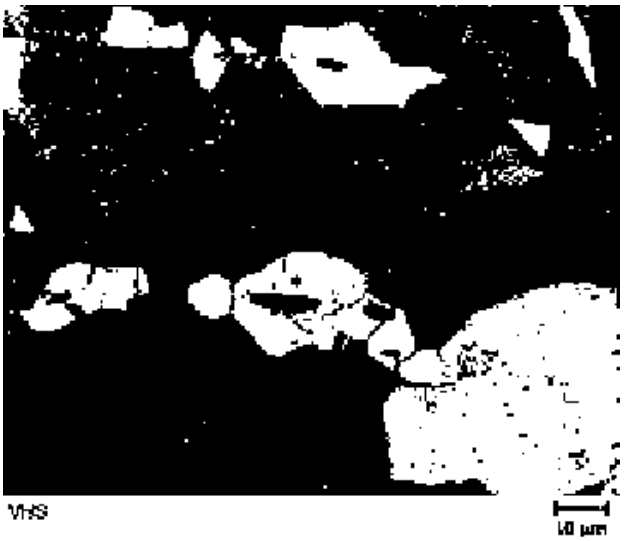

Fig. 14.8 Intragranular ferrite formation at MnS particles in a V-microalloyed steel. Light micrograph, nital etch. Source: Ref 14.14

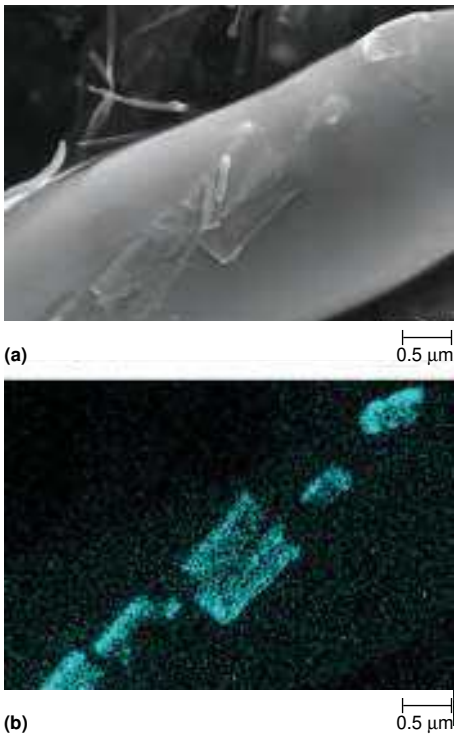

Fig. 14.9 Vanadium-rich particles on a MnS inclusion in a medium-carbon microalloyed steel. (a) Secondary electron SEM micrograph, (b) Vanadium Energy Dispersive Spectroscopic SEM map. Courtesy of Lee Rothleutner, Colorado School of Mines. Source: Ref. 14.18

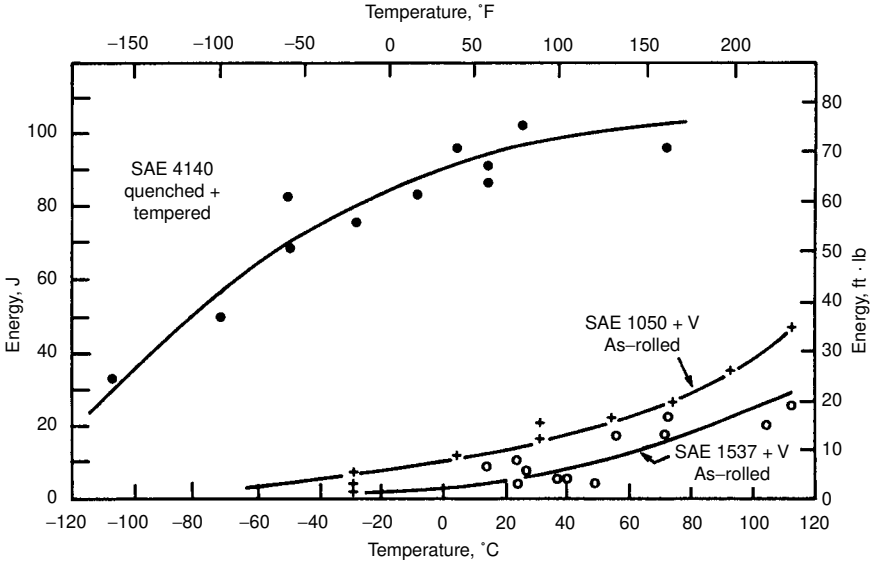

Fig. 14.10 CVN energy absorbed as a function of test temperature for quench and tempered 4140 steel and two medium-carbon steels microalloyed with vanadium at the same hardness. Source: Ref 14.19

(Ref 14.19). The vanadium-strengthened steels have much lower resistance to brittle cleavage fracture than does the quenched and tempered 4140 steel. Nevertheless, under fatigue conditions, where impact is not a concern, the two types of steel perform identically, as shown in Fig. 14.11.

Figures 14.12 through 14.16 show the results of an experimental study that measured tensile and impact properties of a series of direct-cooled, medium-carbon, microalloyed steels (Ref 14.20). Specimens of steels with three levels of C, 0.2%, 0.3%, and 0.4%, without microalloying (0.2C, 0.3C, and 0.4C), with a vanadium microalloying addition of 0.15% (0.2C + V, 0.3C + V, 0.4C + V), and with microalloying additions of 0.15% V plus 0.042% Nb (0.2C + V + Nb, 0.4C + V + Nb) were heated to 1200 °C (2190 °F) for 20 minutes and cooled either in circulating air, still air, or between insulating blankets. For a given steel, the effect of cooling rate is indicated by the sets of data points in the various plots, and in general, the selected cooling rates had little effect on properties. Most of the microstructures consisted of ferrite and pearlite, but some acicular ferrite was noted in low-carbon specimens. Zajac (Ref 14.21) has related VN precipitation on MnS particles to enhanced nucleation of acicular ferrite in microalloyed low-carbon steels.

Figures 14.12 and 14.13 show, respectively, yield and tensile strengths as a function of steel carbon content for the plain carbon and microalloyed steels. Increasing carbon content for all steels increases strengths, and microalloying with vanadium adds a strengthening increment of about

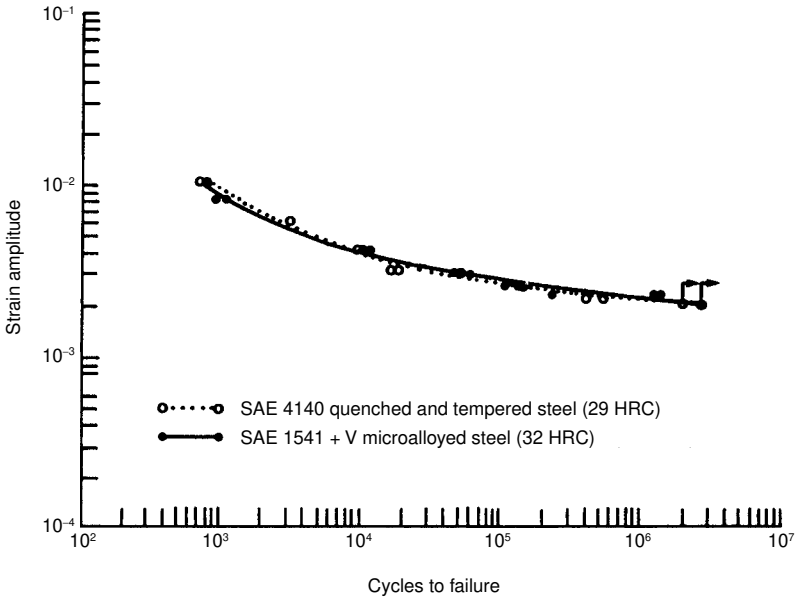

Fig. 14.11 Comparison of fatigue behavior of quench and tempered steel and microalloyed steel at the same hardness. Source: Ref 14.19

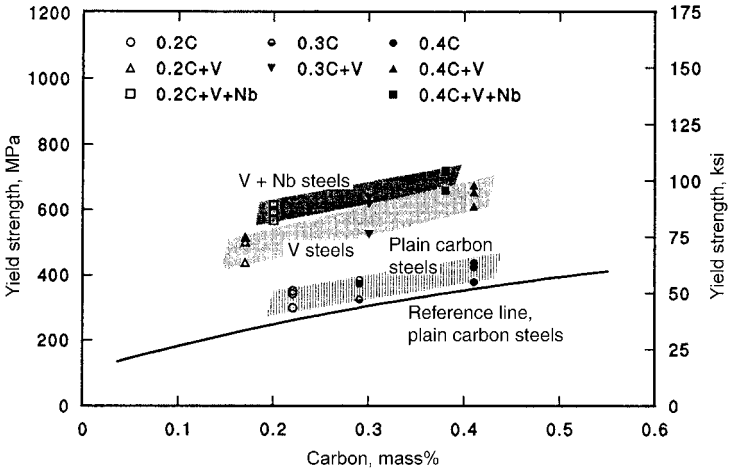

Fig. 14.12 Yield strength of ferrite/pearlite microstructures as a function of steel carbon content for plain carbon steels and steels microalloyed with V and V plus Nb. Source: Ref 14.20

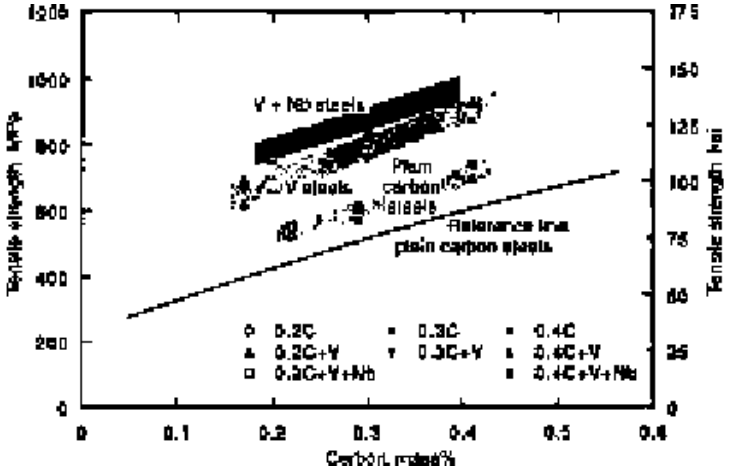

Fig. 14.13 Ultimate tensile strength for ferrite/pearlite microstructures as a function of steel carbon content for plain carbon steels and steels microalloyed with V and V plus Nb. Source: Ref 14.20

200 MPa (30 ksi) at each carbon level. Niobium additions combined with the vanadium additions increase strength even more. Correlations of yield and tensile strengths to hardness for all of the steels are shown in Fig. 14.14.

Figures 14.15 and 14.16, show respectively, impact transition temperatures and CVN energy absorbed at room temperature for all of the steels. Increased steel carbon, by virtue of increasing pearlite content, increases sensitivity to cleavage fracture, even in the plain carbon steels, as noted in Chapter 13, "Normalizing, Annealing, and Spheroidizing Treatments; Fer-

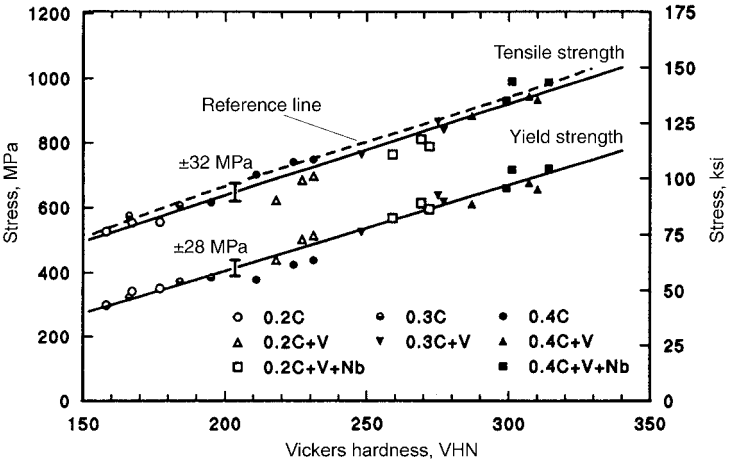

Fig. 14.14 Correlation of yield and ultimate tensile strengths with Vickers hardness for steels with ferrite/pearlite microstructures, with and without microalloying. Source: Ref 14.20

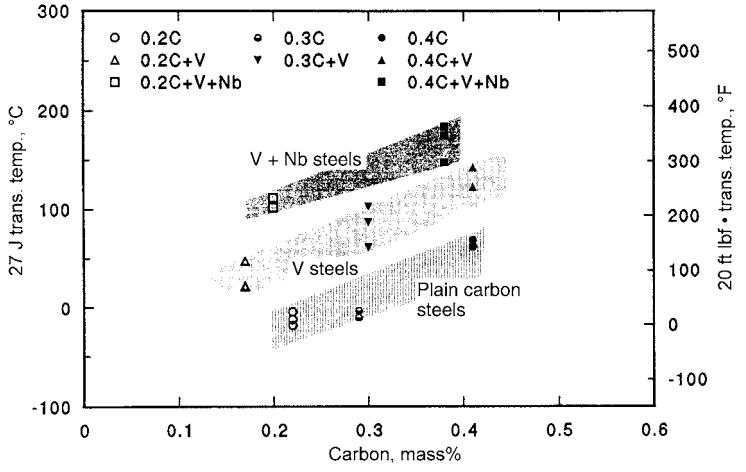

Fig. 14.15 Ductile-to-brittle transition temperature at 27 joules (20 ft-lbs) energy absorbed during CVN testing as a function of steel carbon content for plain carbon steels and steels microalloyed with V and V plus Nb. Source: Ref 14.20

rite/Pearlite and Spherical Carbides." At a given carbon content, the greater the effect of microalloying precipitation, the higher is the impact transition temperature, consistent with the effects of precipitation on toughness. Thus, for a given application, the need for high strength and good impact fracture resistance has to be evaluated. Where toughness is of concern, several approaches can be used to optimize properties. As shown in Fig. 14.15 and 14.16, direct-cooled microstructures with lower carbon contents have better impact fracture characteristics, but strength decreases pro-

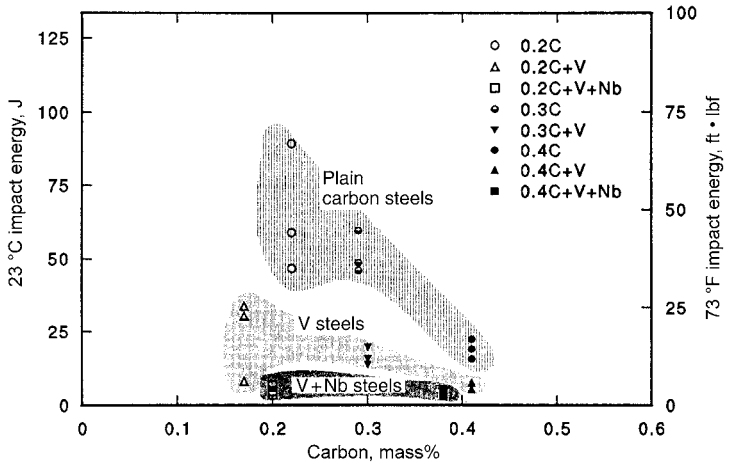

Fig. 14.16 Room temperature energy absorbed during CVN impact testing as a function of steel carbon content for plain carbon steels and steels microalloyed with V and V plus Nb. Source: Ref 14.20

portionately. Also, as noted in the preceding sections, microalloying with titanium and intragranular ferrite formation provide beneficial microstructural refinement to ferrite/pearlite microstructures in microalloyed steels.

As noted earlier, and emphasized by Glodowski (Ref 14.22), not only sufficient vanadium but also sufficient nitrogen is necessary to produce the enhanced strengthening of microalloyed forging steels. Chapter 8, "Austenite in Steel," has shown that aluminum is a stronger nitride former than vanadium, stabilizing aluminum nitrides to higher temperatures than those at which vanadium nitrides are stable, raising the concern that aluminum additions might affect strengthening in vanadium-microalloyed forging steels. This concern has been addressed by examining the microstructure and properties of three V-microalloyed steels identical except for aluminum content (Ref 14.18). Aluminum contents were 0.006, 0.020, and 0.031 wt%, and carbon, nitrogen, and vanadium contents were held constant at 0.37, 0.0153, and 0.088 wt%, respectively. At typically high forging temperatures of 1200 and 1250 °C (2190 and 2280 °F), thermomechanical simulations showed that (vanadium carbonitride) precipitation on cooling was essentially constant, and that even in the steel containing 0.031% Al all aluminum nitride was dissolved and therefore exerted no restraining effect on austenitic grain growth or on the as-cooled microstructure and properties of the vanadium-alloyed forging steels.

However, at lower thermomechanical simulation temperatures of 1050 and 1100 °C (1920 and 2010 °F) there was a strong combination of aluminum with nitrogen, and in the 0.031% aluminum steel residual aluminum nitrides pinned grain boundaries and reduced austenite grain size compared to that in the steels with lower aluminum contents. As a result, ferrite formation increased on the higher grain boundary areas of the high-

aluminum alloy, reducing the amount of pearlite and consequently the hardness produced during cooling. As noted earlier in this Chapter, pearlite is a major strengthening component of as-cooled microalloyed forging steels, and the reduced amount of pearlite, as well as possible reductions in vanadium nitride precipitation due to the aluminum competition for nitrogen, correlate with reduced strengthening in samples cooled from the lower simulated forging temperatures.

An early study of a 1045V steel, a microalloyed forging steel containing 0.45% C, 0.80% Mn, 0.22% V, and small amounts of other elements including 0.025% S, complements some of the considerations discussed above relative to the effect of austenitizing temperature on the microstructure and properties of microalloyed forging steels (Ref 14.13, 14.23). Samples were austenitized at temperatures between 800 and 1300 °C (1470 and 2370 °F) for 30 minutes and cooled to produce ferrite/pearlite microstructures. Dramatic changes in the amounts of ferrite and pearlite produced on cooling resulted as a function of the austenitizing temperature. On cooling, after austenitizing at 800 °C the microstructure consisted of 50 vol% ferrite/50 vol% pearlite, and after austenitizing at 1300 °C, 10 vol% ferrite /90 vol% pearlite. Over that temperature range, austenitic grain size increased from about 20 μm to 500 μm and hardness increased from HRC 20 to HRC 32. These values are the extremes of the ranges in ferrite, pearlite, austenitic grain size, and hardness, and values varied continuously as austenitizing temperatures were increased from 800 to 1300 °C. The results clearly show the effect of fine austenite grain sizes on promoting the nucleation and growth of ferrite, lowering pearlite content, and contributing to lower hardness.

Superimposed on the austenite grain size changes and the amounts of ferrite and pearlite formed as a function of heating temperature, are the effects of the vanadium addition in the 1045V steel. Up to 1050 °C (1920 °F), some vanadium nitrides were undissolved and helped to restrain austenite grain growth, but by heating above that temperature, with vanadium and nitrogen fully dissolved in the austenite, austenite grain size increased, and on cooling precipitation of vanadium nitrides contributed to hardness increases together with increased amounts of pearlite in the coarse-grained austenite.

Impact toughness was also dramatically affected by austenitizing of the 1045V steel (Ref 14.23). Figure 14.17 shows CVN energy absorbed as a function of test temperature for the 1045V steel cooled from three temperatures and in the as-received hot-rolled condition. Clearly large amounts of pearlite, which contribute significantly to the hardness and strength of microalloyed forging steels, produced from coarse austenite grain structures correlate with low impact toughness and high ductile to brittle fracture temperatures. A temperature of 1300 °C is high for forging, and in the case of the 1045V study, produced solution and precipitation of MnS inclusions on austenite grain boundaries. As a result, ductile fracture occurred by microvoid formation at the arrays of MnS particles on the prior

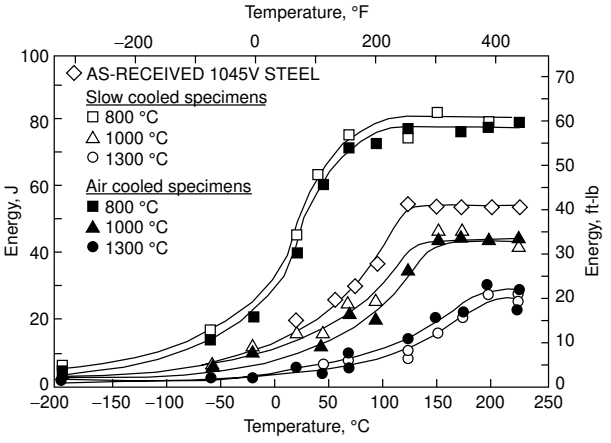

Fig. 14.17 CVN energy absorbed as a function of temperature for specimens of 1045V steel austenitized at various temperatures and cooled at two rates to produce microstructures of ferrite and pearlite. Source: Ref 14.23

austenite grain boundaries, a fracture mechanism described as *overheating* in Chapter 19, "Low Toughness and Embrittlement Phenomena in Steels."

Direct-Cooled Steels with Nontraditional Bainitic Microstructures

Another approach to producing steels with increased strength by direct cooling after forging has been to alloy medium-carbon steels to produce nontraditional bainitic microstructures. The microstructures are termed *nontraditional* in that austenite transforms to acicular ferrite instead of the ferrite and cementite microstructures of traditional bainites, as discussed in Chapters 6, "Bainite" and 7, "Ferritic Microstructures." The key alloying element for the forging steels that transform to nontraditional bainitic microstructures is silicon (Ref 14.24). Silicon cannot be incorporated into the crystal structure of cementite and therefore retards the formation of cementite. As a result, the carbon rejected from growth of bainitic ferrite during cooling of silicon-containing steel increases in the adjacent austenite, stabilizing the austenite and producing large volume fractions of retained austenite in largely ferritic microstructures at room temperature.

Figure 14.18 shows a continuous cooling transformation diagram for a nontraditional bainitic steel containing 0.35% C, 1.40% Mn, 0.76% Si, and 0.19% Mo (Ref 14.25). The diagram shows a prominent intermediate transformation region identified as bainite but which, in fact, because of the high silicon content, was associated with the formation of nontraditional bainitic microstructures. High manganese contents, and small additions of chromium and molybdenum, promote intermediate temperature transformation at cooling rates between ferrite/pearlite and martensitic

transformation ranges. Because forging steels are deformed at high austenitizing temperatures, small additions of titanium are sometimes made to limit austenite grain growth by TiN particles (Ref 14.26, 14.27).

Figures 14.19 through 14.21 compare the microstructure and properties of direct-cooled steels differing only in silicon content (Ref 14.28). The steels contained 0.35% C, 1.50% Mn, 0.11% Ni, 0.14% Cr, 0.25% Mo, 0.10% V, and 0.012% Ti, and the low-and high-silicon contents were 0.32 and 0.76%, respectively. The microstructures of both steels, Fig. 14.19, contained large volume fractions of acicular ferrite. Classical ferrite/cementite bainitic microstructures, as determined by TEM, formed between the acicular ferrite of the low-silicon steel, while retained austenite, about 23% as determined by X-ray analysis, was retained between the acicular ferrite crystals of the high-silicon steel.

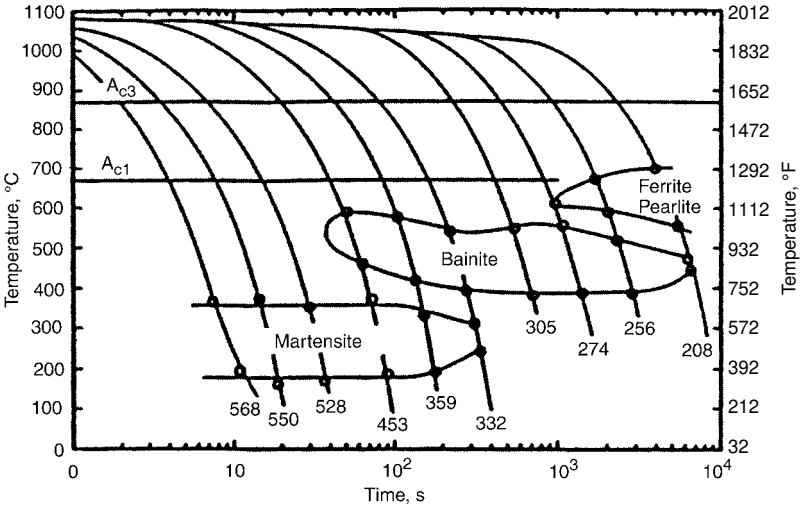

Fig. 14.18 Continuous cooling transformation diagram of a steel containing 0.35% C, 1.40% Mn, 0.76% Si, and 0.19% Mo. Source: Ref 14.25

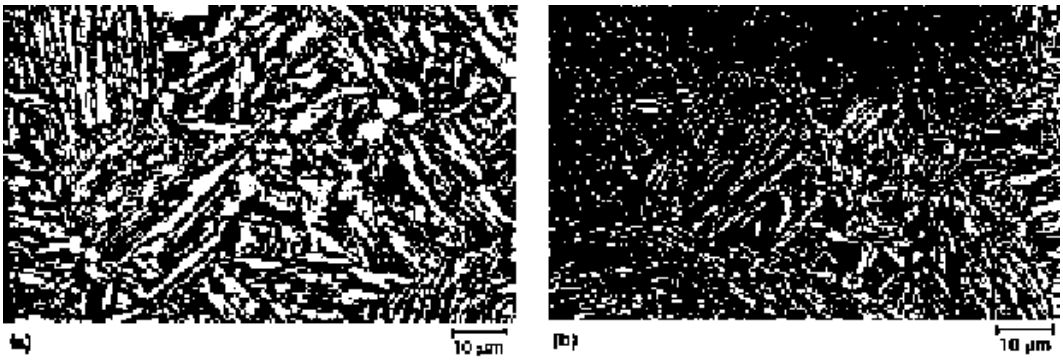

Fig. 14.19 Microstructures of direct-cooled steels containing 0.35% C and (a) 0.32% Si and (b) 0.76% Si. See text for discussion of microstructures. Light micrographs, nital etches. Source: Ref 14.28

Figure 14.20 shows that the ultimate tensile strength and ductility of the direct cooled high-silicon steel are greater than those of the low-silicon steel. These differences are attributed to the strain-induced transformation of retained austenite to martensite at high strains that increases strain hardening and defers necking in the high-silicon steel (Ref 14.29). The same beneficial effects of strain-induced austenite transformation in the high-silicon steel are also shown in the ductile fracture portion of the CVN transition curve in Fig. 14.21. At low-impact-testing temperatures, retained austenite transforms by stress-assisted mechanisms at low strains

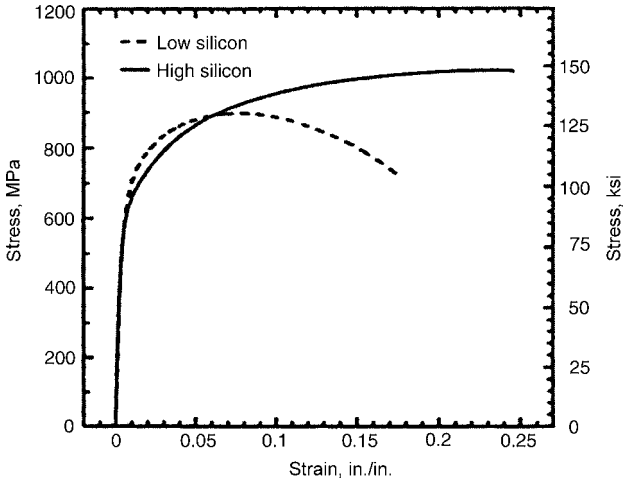

Fig. 14.20 Room temperature stress strain curves for 0.35% C direct-cooled steels with high- and low-silicon contents. Source: Ref 14.28

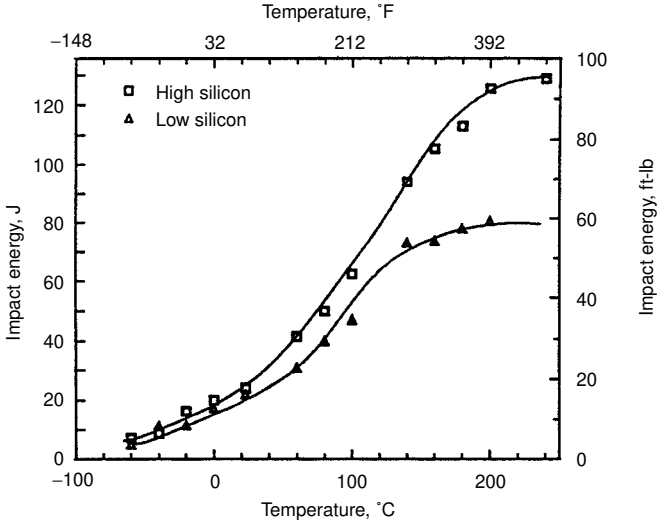

Fig. 14.21 CVN impact transition curves for 0.35% C direct-cooled steels with high- and low-silicon contents. Source: Ref 14.28

and offers little benefit to mechanical properties compared with microstructures with low retained austenite contents (Ref 14.29). Tempering at temperatures high enough to transform retained austenite increases yield strengths and may improve fatigue resistance (Ref 14.30).

The low-strain, stress-assisted transformation of retained austenite at low temperatures, typically below room temperature, causes yield strengths, as defined by the strength at 0.2% strain, of the nontraditional bainitic microstructures to decrease as ultimate tensile strengths increase with decreasing temperatures (Ref 14.31). This result is quite different from that of microstructures that consist largely of ferrite in which yield strengths increase with decreasing temperature, as has been shown in Fig. 11.7 in Chapter 11, "Deformation, Strengthening, and Fracture of Ferritic Microstructures." Fig 14.22 schematically compares early yielding of steels with stable microstructures (such as highly tempered quench and tempered steels such as 4140 and steels with ferrite/pearlite microstructures such as 1045V) to the nontraditional bainitic steels with unstable microstructures because of retained austenite as described above (Ref 14.31). At low deformation temperatures, the stress-assisted transformation of retained austenite causes martensite formation at low strains. The increased volume of the martensite contributes to increased specimen elongation at low stresses compared to the same steel deformed at higher temperatures where the retained austenite is stable to higher strains. However, the greater the early low-temperature formation of stress-induced martensite with its high density of dislocations the greater the strain hardening that leads to ultimate tensile stresses that increase with decreasing temperature.

Summary

This chapter has shown how microalloying and silicon additions affect microstructure and properties of carbon steels. The strengthening mechanisms do not depend upon martensitic strengthening by quench and tempering, and produce moderate increases in strength relative to steels with unalloyed ferrite/pearlite or bainitic microstructures. Lagneborg, Hutchinson, Siwecki, and Zajac in 2014 have written a comprehensive review of the role vanadium plays in microalloyed steels (Ref 14.32). That review is dedicated to the memory of Michael Korchynsky who made early important contributions to the development of vanadium-microalloyed steels.

REFERENCES

14.1 *Fundamentals of Microalloying Forging Steels,* G. Krauss and S.K. Banerji, Ed., TMS-AIME, Warrendale, PA, 1987

14.2 Specification ASTM A 909-92, "Standard Specification for Steel Forgings, Microalloy, for General Industrial Use," in *1994 Annual*

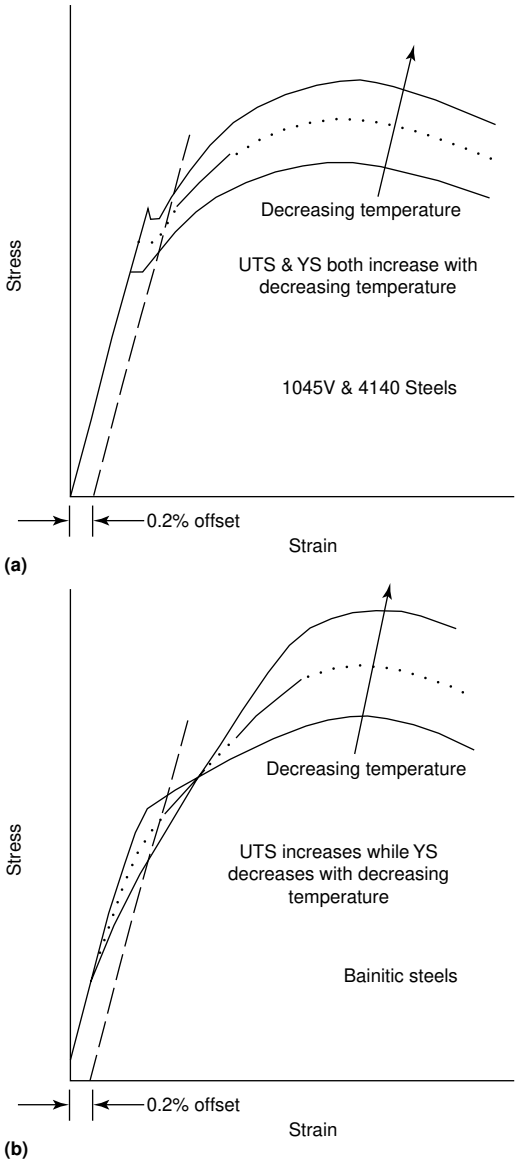

Fig. 14.22 Schematic comparison of early yielding in stress-strain curves in (a) steels with stable microstructures, and (b) steels such as the nontraditional bainitic steels with large amounts of retained austenite. Source: Ref 14.31

Book of ASTM Standards, Vol 1.05, ASTM, Philadelphia, PA, 1994, p 556–559

14.3 *Fundamentals and Applications of Microalloying Forging Steels,* C.J. Van Tyne, G. Krauss, and D.K. Matlock, Ed., TMS, Warrendale, PA, 1996

14.4 T. Gladman, *The Physical Metallurgy of Microalloyed Steels,* Book 615, The Institute of Materials, London, 1997

14.5 *Microalloying in Steels,* J.M. Rodriguez-Ibabe, I. Gutierrez, and B. Lopez, Ed., Trans Tech Publications LTD, Uetikon-Zuerich, Switzerland, 1998

14.6 T. Gladman, I.D. McIvor, and F.B. Pickering, Some Aspects of the Structure-Property Relationships in High-Carbon Ferrite-Pearlite Steels, *JISI,* Vol 210, 1972, p 916–930

14.7 J.G. Speer, J.R. Michael, and S.S. Hansen, Carbonitride Precipitation in Niobium/Vanadium Microalloyed Steels, *Metall. Trans. A,* Vol 18A, 1987, p 211–222

14.8 S.W. Thompson and G. Krauss, Precipitation and Fine Structure in Medium-Carbon Vanadium and Vanadium/Niobium Microalloyed Steels, *Metall. Trans. A,* Vol 20A, 1989, p 2279–2288

14.9 S. Zajac, T. Siwecki, and M. Korchynsky, Importance of Nitrogen for Precipitation Phenomena in V-Microalloyed Steels, in *Low-Carbon Steels for the 90's,* R. Asfahani and G. Tither, TMS, Warrendale, PA, 1993, p 139–149

14.10 R. Lagneborg, T. Siwecki, S. Zajac, and B. Hutchinson, The Role of Vanadium in Microalloyed Steels, *Scand. J. Metall.,* Vol 28 (No. 5), 1999, p 1–241

14.11 M. Korchynsky and J.R. Paules, Microalloyed Forging Steels—A State of the Art Review, *SAE Technical Paper Series,* No. 89081, 1989

14.12 *Titanium Technology in Microalloyed Steels,* T.N. Baker, Ed., Book 662, The Institute of Materials, London, 1997

14.13 M. Leap, E.L. Brown, P. Mazzare, and G. Krauss, The Evolution of Microstructure and Precipitate Dispersions During Reheating in a Vanadium Modified 1045 Steel, in Ref 14.1, p 91–109

14.14 B.G. Kirby, P. LaGreca, C.J. Van Tyne, D.K. Matlock, and G. Krauss, Effect of Sulfur on Microstructure and Properties of Medium-Carbon Bar Steels, *SAE Technical Paper Series,* No. 920532, SAE, Warrendale, PA, 1992

14.15 G.L. Dunlop, C.-J. Carlsson, and G. Frimodig, Precipitation of VC in Ferrite and Pearlite during Direct Transformation on a Medium Carbon Microalloyed Steel, *Metall. Trans. A,* Vol 9A, 1978, p 261–266

14.16 D.V. Edmonds, Precipitation in Microalloyed Higher Carbon Steels, in Ref 14.3, p 111–125

14.17 T. Ochi, T. Takashi, and H. Takada, Improvement of the Toughness of Hot Forged Products through Intragranular Ferrite Formation, *30th MWSP Conference Proceedings,* Vol XXVI, 1989, ISS-AIME, p 65–72

14.18 L.M. Rothleutner, "Influence of Reheat Temperature and Holding Time on the Interaction of V, Al, and N in Air-Cooled Forging Steels," M.S. thesis, Colorado School of Mines, Golden, Colorado, 2012

14.19 P.B. Babu, D.R. Gromer, D.J. Lingenfelser, and G.P. Shandley, Design for Fracture Resistance in Microalloyed Steel Components, in Ref 14.1, p 389–423

14.20 Y. Sawada, R.P. Foley, S.W. Thompson, and G. Krauss, Microstructure-Property Relationships in Plain-Carbon, and V and V + Nb Microalloyed Medium Carbon Steels, *35th MWSP Conference Proceedings,* Vol XXXI, ISS-AIME, 1994, p 263–286

14.21 S. Zajac, Precipitation and Grain Refinement in Vanadium-Containing Steels, *Proceedings International Symposium 2001 on Vanadium Application Technology,* Beijing, China, p 62–82

14.22 R. J. Glodowski, An Empirical Prediction Model of the Incremental Strengthening of Ferrite/Pearlite Steels with Additions of Vanadium and Nitrogen, with Emphasis on the Effective Nitrogen Level, *Int. J. Metall. Eng.,* Vol 2(1), 2013, p 56-61

14.23 M. Leap, D. K. Matlock, and G. Krauss, Correlation of the Charpy Test to Fracture Mechanics in a Vanadium Modified 1045 Steel, in Ref 14.1, p 91–147

14.24 H.K.D.H. Bhadeshia and D.V. Edmonds, The Bainite Transformation in a Silicon Steel, *Metall. Trans. A,* Vol 10A, 1979, p 895–907

14.25 K.J. Grassl, "The Effect of Microstructure Type and Load Rate on the Toughness of Forging Steels," M.S. thesis, Colorado School of Mines, Golden, CO, 1989

14.26 P.A. Oberly, C.J. Van Tyne, and G. Krauss, Grain Size and Forgeability of a Titanium Microalloyed Steel, *SAE Technical Paper Series,* No. 910146, SAE, 1991

14.27 N.E. Aloi, Jr., G. Krauss, C.J. Van Tyne, and Y.-W. Cheng, The Effect of Forging Conditions on the Flow Behavior and Microstructure of a Medium Carbon Microalloyed Forging Steel, *SAE Technical Paper Series,* No. 940787, SAE, 1994

14.28 A.J. Bailey, G. Krauss, S.W. Thompson, and W.A. Szilva, The Effect of Silicon and Retained Austenite on Direct-Cooled Microalloyed Forging Steels with Bainitic Microstructures, *37th MWSP Conf. Proceedings,* Vol XXXIII, 1996, p 455–462

14.29 G.B. Olson, Transformation Plasticity and the Stability of Plastic Flow, in *Deformation, Processing, and Structure,* G. Krauss, Editor, ASM International, 1984, p 391–424

14.30 K. Tsuzaki, C. Nakao, and T. Maki, Formation Temperature of Bainitic Ferrite in Si-Containing Steels, *Mater. Trans.,* JIM, Vol 32 (No. 8), 1991, p 658–666

14.31 G. Krauss and D. K. Matlock, Deformation and fracture of direct-cooled bainitic forging steels, *Proceedings of the International Symposium on Hot Workability of Steels and Light Alloy-Composites,* H. J. McQueen, E. V. Konopleva, and N. D. Ryan,

Editors, Canadian Institute of Mining, Metallurgical and Petroleum, Montreal, Canada, 1996, p 569–582

14.32 R. Lagneborg, B. Hutchinson, et al., The Role of Vanadium in Microalloyed Steels, Swerea KIMAB, Stockholm, Sweden, 2014

CHAPTER 15

High-Carbon Steels—Fully Pearlitic Microstructures and Wire and Rail Applications

THE TRANSFORMATION OF AUSTENITE to pearlite has been described in Chapter 4, "Pearlite, Ferrite, and Cementite," and Chapter 13, "Normalizing, Annealing, and Spheroidizing Treatments; Ferrite/Pearlite and Spherical Carbides," which have shown that as microstructure becomes fully pearlitic as steel carbon content approaches the eutectoid composition, around 0.80% carbon, strength increases, but resistance to cleavage fracture decreases. This chapter describes the mechanical properties and demanding applications for which steels with fully pearlitic microstructures are well suited.

With increasing cooling rates in the pearlite continuous cooling transformation range, or with isothermal transformation temperatures approaching the pearlite nose of isothermal transformation diagrams, Fig. 4.3 in Chapter 4, "Pearlite, Ferrite, and Cementite," the interlamellar spacing of pearlitic ferrite and cementite becomes very fine. As a result, for most ferrite/pearlite microstructures, the interlamellar spacing is too fine to be resolved in the light microscope, and the pearlite appears uniformly dark. Therefore, to resolve the interlamellar spacing of pearlite, high resolution scanning electron microscopy (SEM) and transmission electron microscopy (TEM), are necessary to resolve the two-phase structure of pearlite. Figure 15.1 is a TEM micrograph showing the pearlitic microstructure in a high-carbon steel rail. The interlamellar spacing between the

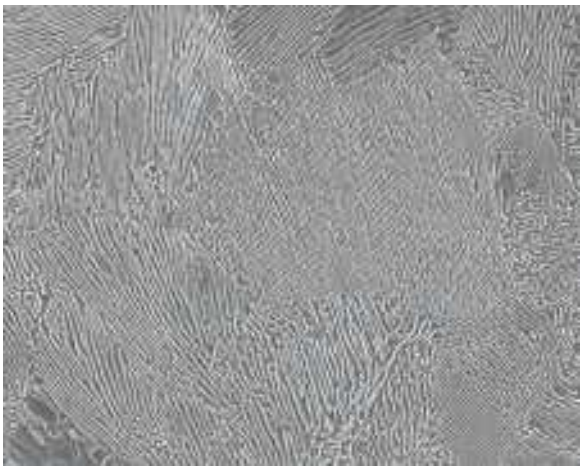

Fig. 15.1 Pearlitic microstructure in rail steel. Nital-etched surface, high resolution SEM micrograph, 8,000×. Courtesy EVRAZ NA

ferrite and cementite phases is quite fine; regions where the lamellae are parallel or almost parallel are referred to as colonies. This remarkable composite structure of ductile ferrite and high-strength cementite is the base microstructure for rail and the starting microstructure for high-strength wire applications.

Mechanical Properties of Fully Pearlitic Microstructures

The Gladman et al. equation, Eq 13.2 in Chapter 13, "Normalizing, Annealing, and Spheroidizing Treatments; Ferrite/Pearlite and Spherical Carbides," for the strength of ferrite/pearlite steels shows that the interlamellar spacing of ferrite and cementite lamellae in pearlite becomes more important as the amount of pearlite increases (Ref 15.1). Hyzak and Bernstein in a study of fully pearlitic microstructures in a steel containing 0.81% C evaluated not only the effect of pearlite interlamellar spacing, S, but also the effect of austenite grain size, d, and pearlite colony size, P, on mechanical properties (Ref 15.2). Figure 15.2 shows the dependence of hardness and yield strength on pearlite spacing, and the following equation incorporates, in addition to interlamellar spacing, the effects of austenitic grain size and pearlite colony size on yield strength:

$$\text{Yield strength (MPa)} = 2.18(S^{-1/2}) - 0.40(P^{-1/2}) - 2.88(d^{-1/2}) + 52.30 \quad \text{(Eq 15.1)}$$

In view of this work, pearlite interlamellar spacing is confirmed to be the major microstructural parameter that controls strength of pearlitic microstructures.

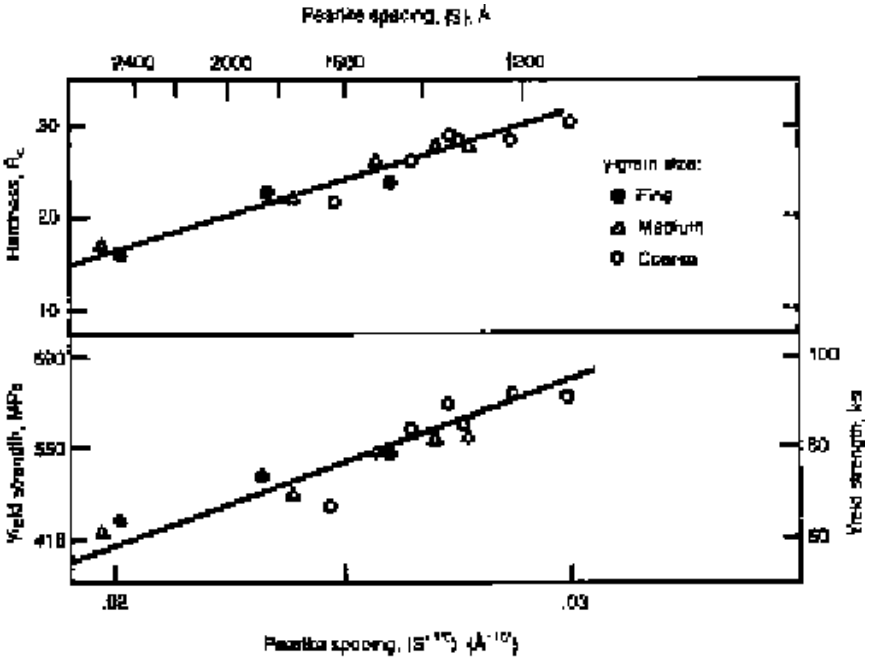

Fig. 15.2 Hardness and yield strength as a function of pearlite interlamellar spacing in fully pearlitic microstructures. Source: Ref 15.2

Resistance to cleavage fracture of fully pearlitic steels is found to be primarily dependent on austenitic grain size according to the following equation (Ref 15.2):

$$\text{Transition temperature (°C)} = -0.83(P^{-1/2}) - 2.98(d^{-1/2}) + 217.84 \qquad \text{(Eq 15.2)}$$

This equation shows that the ductile-to-brittle transition temperature for fully pearlitic steels is invariably above room temperature. Fracture around room temperature is therefore characterized by cleavage on {100} planes of the ferrite in pearlite. In another study, the size of cleavage facets was found to be strongly dependent on, but always smaller than, the austenite grain size and appeared to be related to common ferrite orientations in several adjoining pearlite colonies (Ref 15.3).

Rail Steels: Structure and Performance

The papers of proceedings volumes of several symposia address the ever-increasing demands placed on rail steels and the approaches used to improve rail steel performance (Ref 15.4–15.6). Rails are subject to heavy contact cyclic loading that accompanies increased car size and loading, to 100 and 125 ton capacity, increased train size, and increased train speeds

used to transport bulk products over the last several decades. These increasing demands require manufacturing and metallurgical approaches that offset wear and other types of failure that limit rail life. An early type of rail failure was associated with entrapped hydrogen that produced *shatter crack or flakes* in heavy rail sections, but that difficulty has been effectively controlled by controlled cooling and by vacuum degassing of liquid steel (Ref 15.5–15.7).

Wear of rail has been studied by laboratory testing and also in a unique facility that subjects rail to actual train service. The latter facility, the Facility for Accelerated Service Testing (FAST), Pueblo, Colo., is a 7.7 km (4.8 mile) loop of track on which test trains with 9500 trailing tons have completed up to 120 laps daily in order to evaluate the processing, chemistry, and performance of rails under actual service conditions (Ref 15.8). In a study of rail tested at the FAST facility, wear was found to be a three-stage process (Ref 15.9). The first stage consisted of severe plastic deformation in a thin surface layer of the rail, on the order of 0.1 mm (0.004 in.) in depth, in response to repeated heavy compressive and shear loading produced by the passage of test trains. Two steels were evaluated, and the depth of the deformed zone was shallower in the harder steel. The second stage consisted of the development of subsurface cracks in the severely deformed layer, generally at the interface of the deformed layer and the undeformed microstructure. The propagation of cracks to the surface of the rail and the associated spalling off of small slivers or flakes of the rail constituted the third stage of wear. This sequence of deformation and fracture is repeated many times to produce substantial rail wear. Kapoor has referred to the repeated cycles of compressive deformation as *plastic ratcheting* and notes that cracking serves primarily to create the wear debris (Ref 15.10). Lubrication is sometimes used to minimize the rate of rail wear.

Improved rail wear resistance correlates with fine interlamellar ferrite/cementite spacing of pearlitic microstructures, which, as noted previously, increases hardness and strength. Figure 15.3 shows the hardness correlation with pearlite interlamellar spacing, and Fig. 15.4 and 15.5 show, respectively, that wear decreases with decreasing interlamellar spacing and increasing hardness of pearlitic microstructures in a series of rail steels (Ref 15.11). The latter results were generated by rolling/sliding wear tests in which the maximum Hertzian contact pressure was varied by adjusting the loads applied by test rollers. As shown in Fig. 15.4 and 15.5, increasing contact pressure accelerates wear.

The strong correlation of improved rail wear resistance with fine pearlite interlamellar spacing and high pearlite hardness has led to processing and alloying approaches to produce fine pearlite. An effective processing approach has been to produce pearlite of fine interlamellar spacing and high hardness on the surface of rails by *head hardening*, a heat treatment applied by accelerated cooling with forced air, water sprays, or oil or

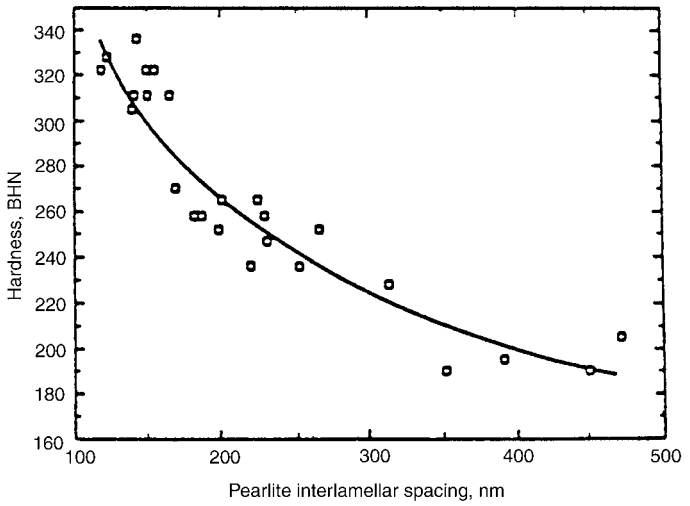

Fig. 15.3 Hardness as a function of pearlite interlamellar spacing for various rail steels. Source: Ref 15.11

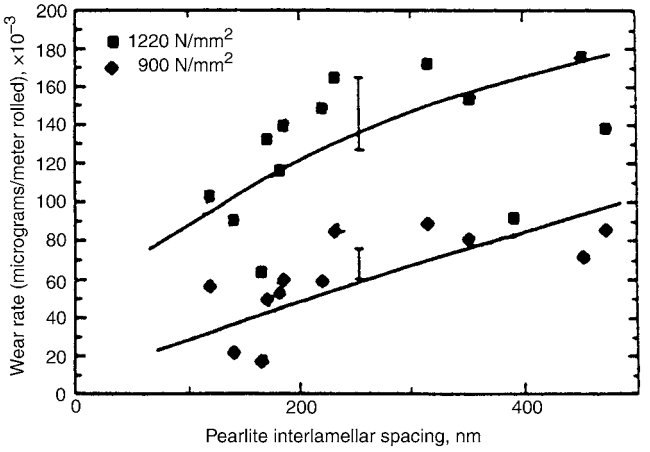

Fig. 15.4 Wear rate as a function of pearlite interlamellar spacing for various rail steels at contact pressures of 1220 N/mm^2 and 900 N/mm^2. Source: Ref 15.11

aqueous polymer quenching either online while the steel is still austenitic immediately after hot rolling or by offline reheating of as-rolled rails (Ref 15.12, 15.13). Figure 15.6 shows the high head hardness of an offline head-hardened rail section (Ref 15.12).

Alloying approaches to refine pearlite interlamellar spacing have included alloying with chromium, molybdenum, vanadium, and silicon (Ref 15.14–15.19). The development of rail steels with hypereutectoid carbon contents also results in fine interlamellar spacings (Ref 15.20). Vanadium

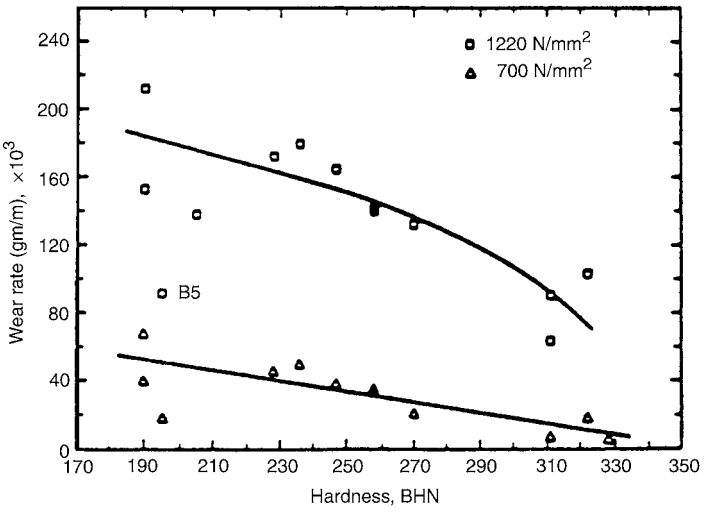

Fig. 15.5 Wear rate as a function of hardness for various rail steels tested at contact pressures of 1220 N/mm² and 700 N/mm². Source: Ref 15.11

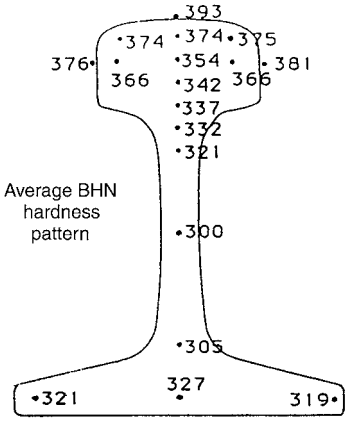

Fig. 15.6 Hardness as a function of location in a transverse section of rail subjected to offline head hardening heat treatment. Source: Ref 15.12

additions in hypereutectoid steels have been found to promote discontinuous cementite formation on austenite grain boundaries (rather than continuous cementite formation in steels without vanadium), interphase precipitation of vanadium carbide close to prior austenite grain boundaries, and precipitation in the pearlitic ferrite (Ref 15.17–15.19).

The rolling contact loading of rails eventually creates complex interactions of strain hardening and residual stress distributions that not only influence wear but may also nucleate and propagate cracks transverse to rail

lengths. Rails in curves are the most severely stressed portions of track, and Fig. 15.7 shows schematically some of the damage phenomena that may originate in rail curves under heavy traffic conditions (Ref 15.21). Subsurface cracks may also develop. *Detail fracture* is defined as "a transverse fatigue crack progressing from the corner of the rail head" (Ref 15.22), and *shelling* is "a condition where the rail steel, stressed beyond its elastic limit, deforms and fails in subsurface shear" (Ref 15.7). Steele and Joerms have analyzed the stress states associated with shelling (Ref 15.23). Compressive residual stresses develop at the surface of rails and are balanced by interior tensile stresses. Shell cracking initiates in lower-hardness regions underneath work-hardened rail surface layers and eventually turns into detail fractures.

In addition to the gradual rail wear that occurs by surface deformation and shallow cracking as discussed earlier, white etching zones, resistant to etching, develop sporadically during heavy rail use (Ref 15.24–15.28). The white etching layers (WEL) have high hardness and are associated with the development of ripples or corrugations in rail and eventually cracking. Intensive evaluation of the structure and substructure of the white etching layers by x-ray diffraction, scanning electron microscopy, transmission electron microscopy, and atom probe tomography shows a complex structure consisting of mixtures of deformed and fragmented pearlite, martensite, and retained austenite. The presence of the martensite and retained austenite establishes that the rail was heated above the lower critical temperature, most likely as the result of wheel/rail friction.

High-Strength Patented and Cold-Drawn Pearlitic Steel Wire

Pearlitic microstructures in steels of eutectoid composition are drawn to wires that have the highest useable tensile strengths of any steel products.

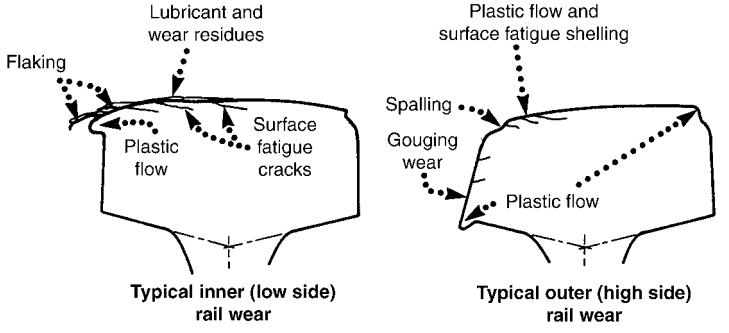

Fig. 15.7 Schematic diagram of wear and damage to curved rails under heavy traffic conditions. Source: Ref 15.21

The strengths depend on steel quality, the microstructure prior to wire drawing, and on the amount of wire drawing to produce a finished wire diameter. Figure 15.8 shows tensile strength as a function of wire diameter for hypereutectoid steel wires capable of resisting delamination (Ref 15.29), and Fig. 15.9 shows the tensile strengths of patented and drawn wires from a number of studies (Ref 15.30). Remarkably high strengths, ranging up to almost 6000 MPa (870 ksi), can be produced. High-strength wires are often further incorporated into bunched arrays for applica-

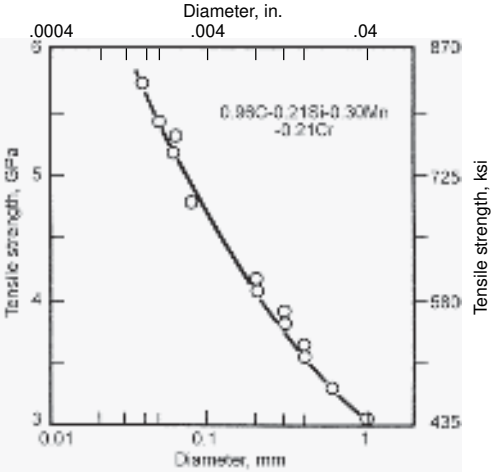

Fig. 15.8 Tensile strength as a function of wire diameter for patented and drawn pearlitic hypereutectoid steel wires. Source: Ref 15.29

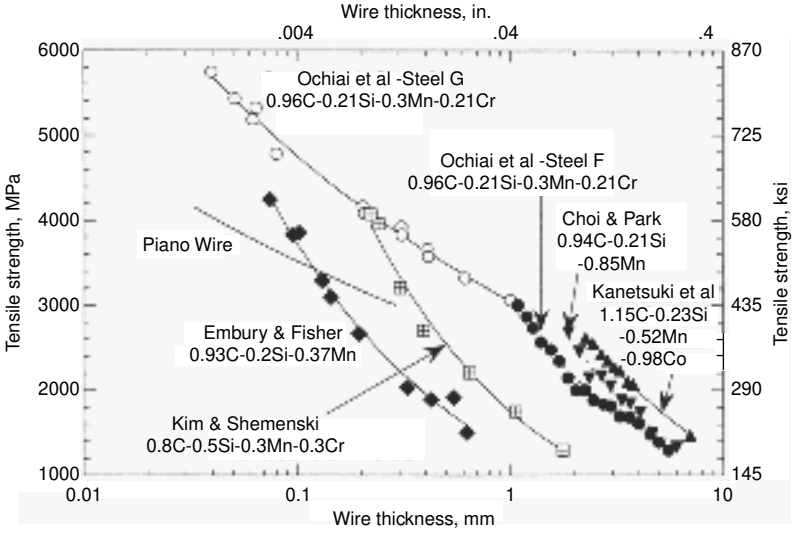

Fig. 15.9 Tensile strength as a function of wire diameter for patented and drawn wires in steels with pearlitic microstructures. Source: Ref 15.30. References to the investigations noted are given in Ref 15.30.

tions such as tire cord, conveyors, hoses, and bridge cables (Ref 15.29, 15.31).

The heat treatment that produces the starting microstructure for wire production is termed *patenting,* after a patented discovery by James Horsfall, Birmingham, England, in 1856 that made steel rod easier to draw (Ref 15.32). Patenting consists of heating to austenite and continuous cooling or isothermal holding to produce a uniform fine pearlite microstructure. Figure 15.10 shows an isothermal transformation diagram for eutectoid steel and the transformation temperature range to produce the desired fine pearlite microstructure for wire drawing (Ref 15.33). The microstructures, strengths, and ductilities of a hypereutectoid steel are shown as a function of transformation temperature in Fig. 15.11. Bainitic microstructures were found to be sensitive to delamination after drawing and, therefore, fine pearlite with a tensile strength of 1500 MPa (220 ksi) was

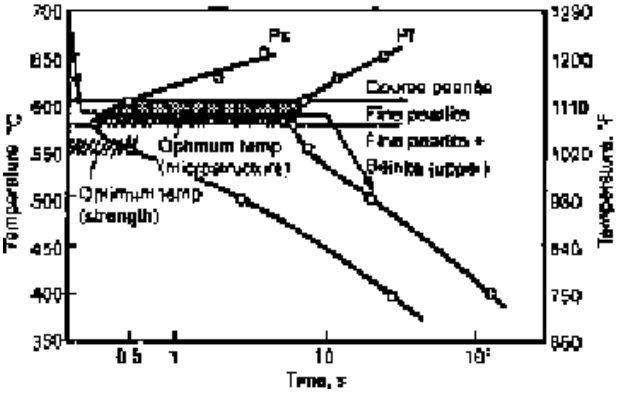

Fig. 15.10 Isothermal time-transformation diagram showing transformation temperature range for production of fine pearlite by patenting heat treatment. Source: Ref 15.33

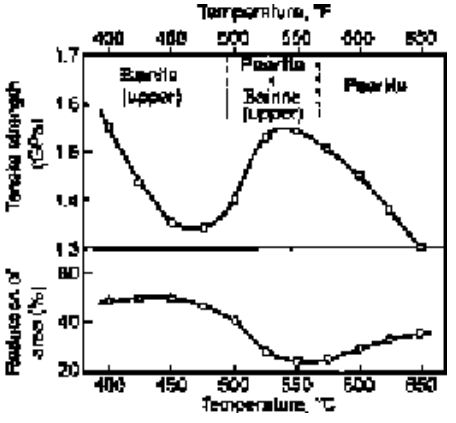

Fig. 15.11 Tensile strength and reduction of area as a function of transformation temperature and microstructure in patented hypereutectoid steels. Source: Ref 15.29

found to be the most suitable starting microstructure for high-strength wire drawing (Ref 15.29).

Patenting may be applied to hot-rolled rod at the start of wire drawing or to cold-drawn wire as an intermediate heat treatment prior to further wire drawing. Fine pearlite has been traditionally produced in rods or wire isothermally transformed in molten lead baths, but alternative processing has been developed to produce good pearlitic microstructures directly after hot rolling to rod in high-speed bar mills (Ref 15.34, 15.35). The latter processing, first commercially applied in 1964, is commonly known as the *Stelmor process*, and by 2003, 240 Stelmor process lines had been installed throughout the world. Stelmor processing consists of water cooling hot-rolled rod to a predetermined temperature, typically between 750 and 959 °C (1380 and 1740 °F), forming the rod into rings on a laying head, and fan air cooling the overlapping rings on a continuously moving conveyor. Cooling rates are adjusted to produce desired microstructures in various grades of steels, and after transformation, the rods are coiled for storage and further processing.

Wire-Drawing Deformation of Pearlite for High-Strength Steel Wire

Fully pearlitic microstructures are highly deformable under wire drawing conditions. As strain increases, in longitudinal sections the lamellar structure of pearlite aligns itself parallel to the longitudinal wire axis (Ref 15.36), and in transverse sections the pearlitic structure becomes wavy and the lamellae within colonies are substantially curved (Ref 15.37). A (110) body-centered-cubic wire texture develops in the ferrite. The combination of closely spaced ductile ferrite and high-strength cementite lamellae makes possible exponential increases of strain hardening as a function of strain, in contrast to the linear increases with strain in ferritic iron wire without cementite (Ref 15.38). Although cementite is potentially brittle, in pearlitic structures the fracture resistance of cementite is a function of lamellae thickness. In coarse pearlite, cementite is brittle, but in microstructures where the interlamellar spacing is 0.10 mm or less, cementite has been shown to be partially or fully plastic (Ref 15.38).

The cementite lamellae of pearlite undergo dramatic changes during high-strain wire drawing (Ref 15.37–15.43). With increasing strain, the cementite lamellae become thinner, and both homogeneous bending and fragmentation of cementite lamellae may occur. In addition to slip deformation of the ferrite and cementite, localized shear band formation through the pearlite lamellae is another observed deformation mechanism. Cementite lamellae have been found to dissolve partially or completely at high strain deformation, and atom probe studies show that the carbon content of cementite decreases, and that of ferrite substantially increases, with the carbon apparently dissolved in the dislocation substructure of the fer-

rite. The carbon in solution in the ferrite then contributes to dynamic strain aging or to strain aging if wire is given subsequent low-temperature heat treatments.

Fracture Mechanisms of Patented and Drawn Steel Wire

As noted, fully pearlitic microstructures are capable of intensive wire drawing deformation. However, the severe deformation may result in unique types of failure. One type of fracture develops internally in response to hydrostatic tensile stresses that develop in the centers of wires during drawing (Ref 15.44). In plane longitudinal sections through damaged lengths of wire the cracks appear v-shaped, leading to the term *chevron cracking* to describe this type of fracture. The cracks are in fact axisymmetric, and when a wire breaks, the fracture surface appears conical, a fracture appearance termed *cuppy fracture* in the wire industry. Fig. 15.12 shows an example of the latter type of fracture. The internal center cracking also leads to the term *centerline bursting* for this phenomenon. Similar stress states to those in wires also create centerline, v-shaped cracks in extruded rods (Ref 15.44). In wires, non-deforming microstructural features in the centers, such as inclusions, grain boundary cementite, or residual centerline segregation that provides sufficient hardenablity for martensite formation, may be associated with initiation of chevron cracking. Therefore, considerable attention must be paid to steel quality and primary steel processing (Ref 15.45, 15.46).

Control of wire-drawing parameters may also minimize chevron cracking (Ref 15.44). A parameter Δ defines the deformation zone geometry for

Fig. 15.12 Example of cuppy fracture in drawn pearlitic wire. SEM micrograph, about 300×.

the generation of hydrostatic tensile stresses as the ratio of the mean diameter of the work to the contact length between the die and the work and is in turn related to reduction ratio and die angle. High values of Δ increase susceptibility to chevron cracking and are produced by lower reductions and high die angles.

Torsional Deformation and Delamination of Patented and Drawn Wires

Some high-strength patented and drawn wires are twisted into cables and bunches. As a result, not only must the wire have high tensile strength, it also must have good torsional strength and good resistance to shear stresses. Figure 15.13 shows the longitudinal and transverse orientation of shear stresses that develop in a torsion-tested wire (Ref 15.47. In wires with fine, uniformly deformed pearlitic microstructures and good surface condition, after a significant number of applied torsional twists, smooth, flat shear fractures develop on transverse wire surfaces. However, under some conditions, surface shear bands develop in response to the longitudinal shear stresses, and these bands eventually nucleate shear cracks characterized by the joining of fine microvoids. With increased twisting, the longitudinal cracks assume a helical or spiral orientation, as shown schematically in Fig. 15.14. The spiral crack is labeled "secondary fracture," and a transverse shear fracture surface, also shown, is labeled "primary fracture."

The longitudinal cracking or splitting along the wire surface during torsion testing is referred to as *delamination* (Ref 15.47, 15.49). Once initiated, compressive stresses close the spiraling delamination crack, and the wire may undergo further twisting despite significant damage. Fig.15.15 compares examples of spiral delamination cracking to deformation and transverse shear fracture in pearlitic wire (Ref 15.39). When delamination

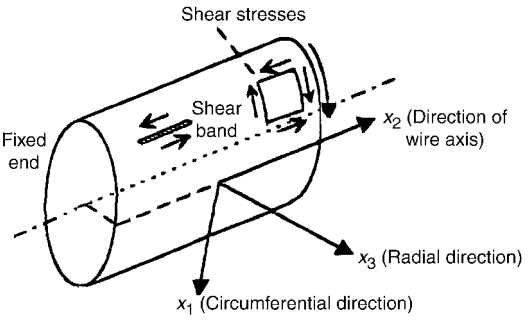

Fig. 15.13 Schematic diagram of a length of wire showing orientations of shear stresses produced during torsion and a longitudinal shear band that may lead to delamination fracture of patented and drawn pearlitic wires. Source: Ref 15.47

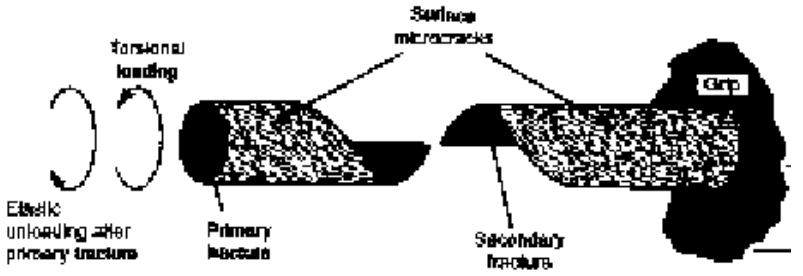

Fig. 15.14 Schematic diagram of torsion-tested wire in which a primary transverse shear fracture and a spiral delamination fracture (labeled "secondary fracture") have developed. Source: Ref 15.48

Fig. 15.15 Examples of wire that failed by delamination (top) and by torsional deformation and transverse shear fracture (bottom). SEM micrographs. Source: Ref 15.39

occurs, there is a sharp drop in load immediately after yielding (Ref 15.49), as shown in Fig. 15.16 for an as-drawn wire and two wires subjected to an aging treatment as described in the following section of this chapter (Ref 15.50).

Good surface conditions are important to prevent delamination, but microstructural factors must also be optimized. Tarui et al. emphasize that fine as-patented pearlite is the key to high-strength wire with good delamination resistance and that upper bainite formed at low transformation temperatures lowers delamination resistance (Ref 15.29, 15.51). Strengthening by chromium and vanadium additions and higher carbon content were found to be more effective than increased drawing reduction in producing strength and while maintaining good delamination resistance. Tarui et al. also show that silicon and chromium additions to patented and drawn microstructures suppress spheroidization of pearlitic cementite and the attendant strength loss during hot dip galvanizing at 450 °C (840 °F). Nam and Bae confirm that coarse pearlite lowers delamination resistance and note that globular cementite particles contribute to the initiation of delamination (Ref 15.51). Low-temperature aging or stress relief treatments

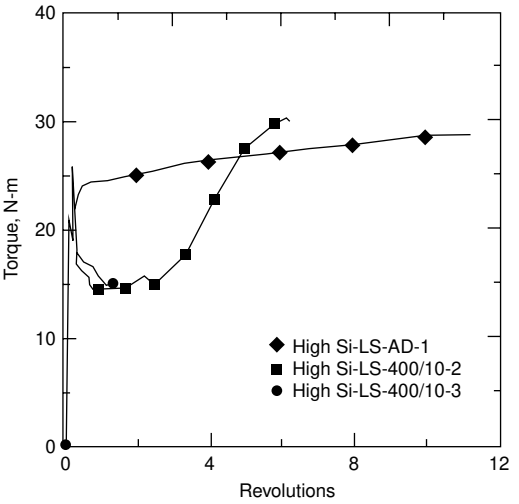

Fig. 15.16 Torque versus number of revolutions for a wire that did not delaminate (High Si-LS-AD-1) and for wires that did delaminate (High Si-LS-400/10 -2 and -3). Source: Ref 15.50

of patented and drawn wires also result in reduced delamination resistance (Ref 15.49).

Effects of Aging and Galvanizing on Properties of Patented and Drawn Wires

The alloying and dramatic changes that occur in the substructure of severely drawn pearlitic wires, namely the high dislocation density and increased carbon in the highly deformed ferrite, set the stage for aging and precipitation hardening during low temperature heating (Ref 15.52). Also hot-dip galvanizing, applied for atmospheric corrosion resistance, performed at 450 to 470 °C (840 to 880 °F) for times on the order of seconds, is a thermal processing step that may affect strengths of patented and drawn high-strength wires for applications such as cables for suspension bridges and other cable applications (Ref 15.29, 15.53-15.58). The hot-dip galvanizing may lower strengths because of recovery of the pearlitic ferrite and spheroidization of the cementite lamellae, and additions of chromium and silicon to high-carbon-wire steel have been shown to reduce softening during galvanizing.

The effects of short-time, low-temperature heating on the changes of mechanical properties of two sets of fully pearlitic wires, one containing 0.23 pct Si (Low Si) and the other containing 1.30 pct Si (High Si), each drawn to strength levels of 1950 MPa (LS) and 2250 MPa (HS), have recently been evaluated (Ref 15.50,15.59). The wires were heated at 350, 400, 450, and 500 °C (660, 750, 840, and 930 °F) for times of 10, 20, 30,

and 60 seconds. Fig. 15.16 has shown the effects of torsional testing on the deformation and fracture of an as-drawn high-Si, low-strength wire (High Si--LS-AD) and on similar wires heated at 400 °C for 10 seconds (400/10). The last digits of the specimen identification designate the number of the sample tested with the same processing history.

Examples of the effects of low-temperature heating on tensile mechanical properties are shown in Fig. 15.17 and 15.18. Except for the longer times at 500 °C, galvanizing and short time heating increase yield and tensile strengths from as-drawn strengths. Longer times at aging temperatures, as shown in Fig. 15.18, decrease strengths, and tensile ductility in almost all heated conditions increases over that in as-drawn wires. The

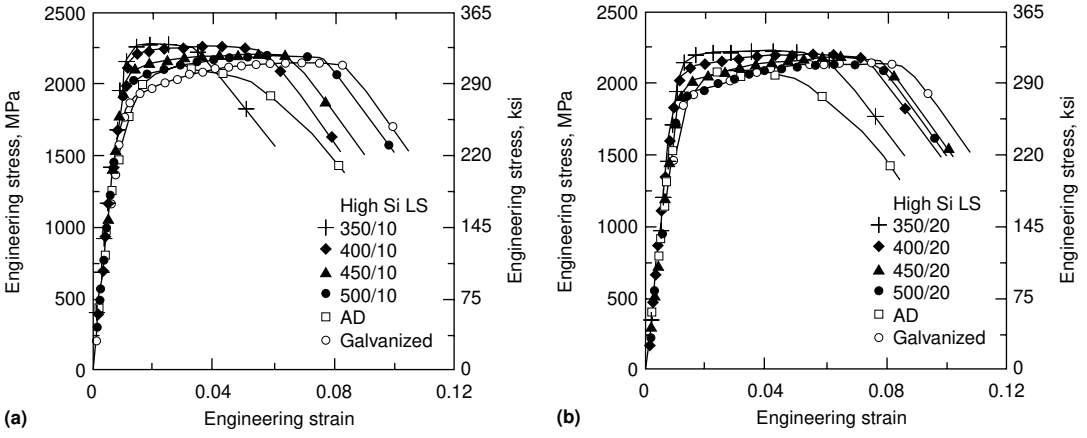

Fig. 15.17 Engineering stress-strain curves for high Si Low Strength (as defined in text) in the as drawn (AD) condition, after galvanizing, and after heating at various temperatures for (a) 10 seconds, and (b) 20 seconds. Source: Ref 15.50

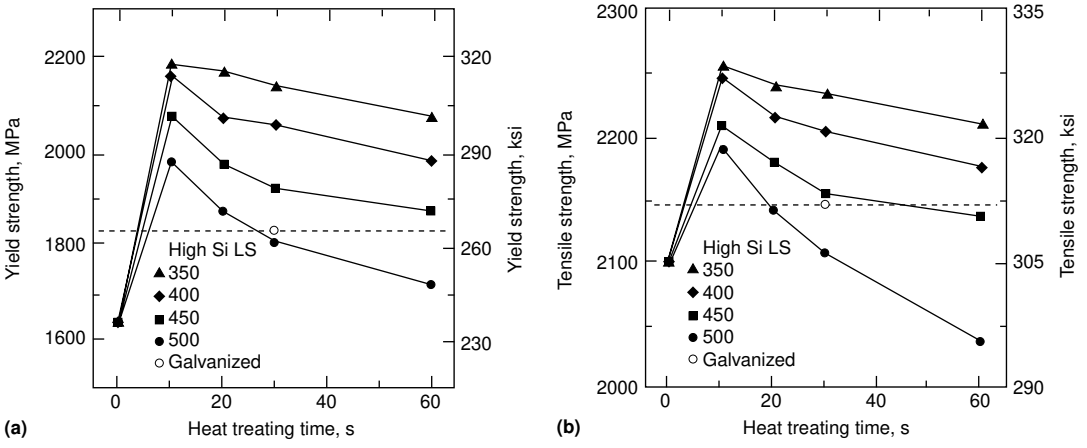

Fig. 15.18 Changes in yield strength (a) and tensile strength (b) as a function of time at temperatures of 350 to 500 °C (660 to 930 °F). The as drawn strengths correspond to the 0 heating time, and the galvanized strengths are given by the horizontal dashed line. Source: Ref 15.50

higher silicon addition increased strength in all conditions and slowed the rate of spheroidization of the pearlitic cementite. In torsion testing, delamination occurred in most heated conditions, and was found to initiate at spherical particles.

REFERENCES

15.1 T. Gladman, I.D. McIvor, and F.B. Pickering, Some Aspects of the Structure-Property Relationships in High-Carbon Ferrite-Pearlite Steels, *JISI,* Vol 210, 1972, p 916–930

15.2 J.M. Hyzak and I.M. Bernstein, The Role of Microstructure on the Strength and Toughness of Fully Pearlitic Steels, *Metall. Trans. A,* Vol 7A, 1976, p 1217–1224

15.3 Y.-J. Park and I.M. Bernstein, Mechanisms of Cleavage Fracture in Fully Pearlitic 1080 Rail Steel, *Rail Steels—Developments, Processing and Use,* STP 644, ASTM, 1978, p 287–302

15.4 *Rail Steels—Developments, Processing, and Use,* D.H. Stone and G.G. Knupp, Ed., STP 644, ASTM, 1978

15.5 *Rail Steels—Developments, Manufacturing and Performance,* B.L. Bramfit, R.K. Steele, and J.H. Martens, Ed., ISS, Warrendale, PA, 1993

15.6 *Rail Steels for the 21st Century,* B.L. Bramfit, R.K. Steele, and J.H. Martens, Ed., ISS, Warrendale, PA, 1995

15.7 G.G. Knupp, W.H. Chidley, J.L. Giove, H.H. Hartman, G.F. Morris, and C.W. Taylor, A Review of the Manufacture, Processing, and Use of Rail Steels in North America—A Report of AISI Technical Subcommitee on Rails and Accessories, *Rail Steels—Developments, Processing, and Use,* D.H. Stone and G.G. Knupp, Ed., STP 644, ASTM, 1978, p 7–20

15.8 R.K. Steele, "A Perspective Review of Rail Behavior at the Facility for Accelerated Service Testing," Report FRA/TTC-81/07, U.S. Department of Transportation, Federal Railroad Administration, Washington, D.C., 1981

15.9 E.L. Brown and G. Krauss, unpublished research, Colorado School of Mines, 1982

15.10 A. Kapoor, Wear by Plastic Ratchetting, *Wear,* Vol 212, 1997, p 119–130

15.11 P. Clayton and D. Danks, Effect of Interlamellar Spacing on the Wear Resistance of Eutectoid Steels under Rolling/Sliding Conditions, *Wear,* Vol 135, 1990, p 369–387

15.12 B.L. George, J.B. McDonald, and F.W. Kokoska, Residual Stresses in Off-Line Head Hardened Steels, in Ref 15.5, p 79–91

15.13 B.L. Bramfit, Advanced In-Line Head Hardening of Rail, *Rail Steels for the 21st Century,* B.L. Bramfit, R.K. Steele, and J.H. Martens, Ed., ISS, Warrendale, PA, 1995, p 23–29

15.14 G.K. Bouse, I.M. Bernstein, and D.H. Stone, Role of Alloying and Microstructure on the Strength and Toughness of Experimental

Rail Steels, *Rail Steels—Developments, Processing, and Use,* D.H. Stone and G.G. Knupp, Ed., STP 644, ASTM, 1978, p 145–166

15.15 S. Marich and P. Curcio, Development of High-Strength Alloyed Rail Steels Suitable for Heavy Duty Applications, *Rail Steels—Developments, Processing, and Use,* D.H. Stone and G.G. Knupp, Ed., STP 644, ASTM, 1978, p 167–211

15.16 Y.E. Smith and F.B. Fletcher, Alloy Steels for High-Strength, As-Rolled Rails, *Rail Steels—Developments, Processing, and Use,* D.H. Stone and G.G. Knupp, Ed., STP 644, ASTM, 1978, p 212–232

15.17 K. Han, T.D. Mottishaw, G.D.W. Smith, D.V. Edmonds, and A.G. Stacey, Effects of Vanadium Additions on Microstructure and Hardness of Hypereutectoid Pearlitic Steels, *Mater. Sci. Eng. A,* Vol 190, 1995, p 207–214

15.18 K. Han, G.D.W. Smith, and D.V. Edmonds, Pearlite Phase Transformation in Si and V Steel, *Metall. and Mater. Trans. A,* Vol 26A, 1995, p 1617–1631

15.19 K. Han, D. V. Edmonds, and G. D. W. Smith, Optimization of Mechanical Properties of High-Carbon Pearlitic Steels with Si and V Additions, *Metall. and Mater. Trans. A*, Vol 32A, 2001, p 1–12

15.20 M. Ueda, K. Uchino, and T. Senuma, Effects of Carbon Content on Wear Property in Pearlitic Steels, *Thermec 2003,* T. Chandra, J.M. Torralba, and T. Sakai, Ed., Part 2, Trans Tech Publications, 2003, p 1175–1180

15.21 J. Kalousek and A.E. Bethune, Rail Wear under Heavy Traffic Conditions, in Ref 15.4, p 63–79

15.22 D.H. Stone and R.K. Steele, The Effect of Mechanical Properties upon the Performance of Railroad Rails, in Ref 15.4, p 21–62

15.23 R.K. Steele and M.W. Joerms, Plastic Deformation and Its Relationship to Rail Performance, in Ref 15.6, p 79–91

15.24 W. Österle, H. Rooch, A. Pyzalla, L. Wang, Investigation of white etching layers on rails by optical microscopy, electron microscopy, X-ray and synchrotron X-ray diffraction, *Materials Science and Engineering*, Vol A303, 2001, p 150–157

15.25 E. Wild, L. Wang, B. Hasse, T. Wroblewski, G. Goerigk, A. Pyzalla, Microstructure alterations at the surface of a heavily corrugated rail with strong ripple formation, *Wear,* Vol 254, 2003, p 876–883

15.26 L. Wang, A. Pyzalla, W. Stadlbauer, E. A. Werner, Microstructure features on rolling surfaces of railway rails subjected to heavy loading, *Mater.Sci. Eng. A*, Vol 359, 2003, p 31–43

15.27 H. W. Zhang, S. Ohsaki, S. Mitao, M. Ohnuma, K. Hono, Microstructural investigation of white etching layer on pearlite steel rail, *Mater.s Sci. Eng. A,* Vol 421, 2006, 191–199

15.28 J. Takahashi, K. Kawakami, M. Ueda, Atom Probe tomography analysis of the white etching layer in a rail track surface, *Acta Mater.*, Vol 58, 2010, p 3602–3612

15.29 T. Tarui, T. Takahashi, H. Tashiro, and S. Nishida, Metallurgical Design of Ultra High Strength Steel Wires for Bridge Cable and

Tire Cord, *Metallurgy, Processing and Applications of Metal Wires,* H.G. Paris and D.K. Kim, TMS, Warrendale, PA, 1996, p 87–96

15.30 D.R. Lesuer, C.K. Syn, O.D. Sherby, and D.K. Kim, Processing and Mechanical Behavior of Hypereutectoid Steel Wires, *Metallurgy, Processing and Applications of Metal Wires,* H.G. Paris and D.K. Kim, TMS, Warrendale, PA, 1996, p 109–121

15.31 O. Arkens, Steel Is Still King in Tyres, *Metallurgy, Processing and Applications of Metal Wires,* H.G. Paris and D.K. Kim, TMS, Warrendale, PA, 1996, p 75–86

15.32 James Horsfal, An Improvement or Improvements in the Manufacture of Wire Rope, British Patent, 1856

15.33 H. Paris, Metallurgy, Processing and Applications of Metal Wires—A Review, *Metallurgy, Processing and Applications of Metal Wires,* H.G. Paris and D.K. Kim, Ed., TMS, Warrendale, PA,1996, p 3–15

15.34 *Ferrous Wire*—Vol 1, Chapter 5A, Controlled Cooling of Wire Rod, *Wire Handbook*

15.35 P.L. Keyser and B.V. Kiefer, STELMOR In-Line Controlled Cooling Process for High Speed Rod Mills, *Materials Solution Conference,* ASM International, 1997

15.36 J.D. Embury and R.M. Fisher, The Structure and Properties of Drawn Pearlite, *Acta Metall.,* Vol 14, 1966, p 147

15.37 G. Langford, A Study of the Deformation of Patented Steel Wire, *Metall. Trans.,* Vol 1, 1970, p 465–477

15.38 G. Langford, Deformation of Pearlite, *Metall. Trans. A,* Vol 8A, 1977, p 861–875

15.39 M. Zelin, Microstructure Evolution in Pearlitic Steels during Wire Drawing, *Acta Mater.,* Vol 50, 2002, p 4431–4447

15.40 M.H. Hong, W.T. Reynolds, Jr., T. Tarui, and K. Hono, Atom Probe and Transmission Electron Microscopy Investigations of Heavily Drawn Pearlitic Steel Wire, *Metall. and Mater.Trans. A,* Vol 30, 1999, p 717–727

15.41 S. Tagashira , K. Sakai, T. Furuhara, and T. Maki, Deformation Microstructure and Tensile Strength of Cold Rolled Pearlitic Steel Sheets, *ISIJ Int.,* Vol 40, 2000, p 1149–1156

15.42 M. Umemoto, Y. Todaka, and K. Tsuchiya, Mechanical Properties of Cementite and Fabrication of Artificial Pearlite, *Mater. Sci. Forum,* Vol 426–432, 2003, p 859–864

15.43 F. Danoix, D. Julien, X. Sauvage, J. Copreaux, Direct Evidence of cementite dissolution in drawn pearlitic wires observed by tomographic atom probe, *Mater. Sci. Eng. A,* Vol 250, 1998, p 8–13

15.44 W.F. Hosford and R.M. Caddell, *Metal Forming: Mechanics and Metallurgy,* PTR Prentice Hall, Englewood Cliffs, NJ, 1993

15.45 I. Chakrabarti, S. Sarkar, M.D. Maheshwari, U.K. Chaturvedi, and T. Mukherjee, Process Enhancements to Improve Drawability of Wire Rods, *Tata Search,* Vol 1, 2004, p 232–240

15.46 S.K. Choudhary, M.N. Poddar, B.K. Jha, and H.J. Billimoria, Inclusion Characteristics of High Carbon Steel for Wire Drawing, *Tata Search,* Vol 1, 2004, p 241–248
15.47 I. Lefever, U.D. D'Haene, W. Van Raemdonck, E. Aernoudt, P. Van Houtte and J. Gil Sevillano, Modeling of the Delamination of High Strength Steel Wire, *Wire J. Int.,* November 1998
15.48 B. Goes, A. Martin-Meizoso, J. Gil-Sevillano, I. Lefever, and E. Aernoudt, Fragmentation of As-Drawn Pearlitic Steel Wires during Torsion Tests, *Eng. Fract. Mech.,* Vol 60 (No. 3), 1998, p 255–272
15.49 W. Van Raemdonck, I. Lefever, and U. D'Haene, Torsions Tests as a Tool for High Strength Wire Evaluation, *Wire J. Int.,* Vol 6, 1994, p 68
15.50 R. Pennington, "Effects of Processing History on the Strength, Ductility, and Fracture Response of 0.9 C-0.2 Cr-1.3 Si Wire," M. S. Thesis, Colorado School of Mines, 2009
15.51 W.J. Nam and C.M. Bae, The Effect of Interlamellar Spacing on the Delamination Behavior of Severely Drawn Pearlitic Steel Wire, in *Metallurgy, Processing and Applications of Metal Wires,* H.G. Paris and D.K. Kim, Ed., TMS, Warrendale, PA, 1996, p 243–250
15.52 C. E. Hinchliffe, G. D. W. Smith, Strain Aging if Pearlitic Steel wire During Post-Drawing Heat Treatments, *Mater. Sci. Tech.*, Vol 17 2001, p 148–151
15.53 T. Tarui, J. Takahashi, H. Tahiro, N. Maruyama, S. Nishida, Microstructure Control and Strengthening of High-carbon Steel Wires, *Nippon Steel Tech. Rep.,* No. 912, Jan 2005, p 56–61
15.54 K. Shimizu, N. Kawabe, Size Dependence of delamination of High-carbon Steel Wire, *ISIJ Int.,* Vol 41, 2001, p 183–191
15.55 A. Bell, S. Hobson, J. Wilkinson, C. O'Connor, S. Sefton, Development of ultra high-strength wire for offshore applications, *Wire J. Int.*, May 2008, p 78–88
15.56 M. Kaiso, N. Ibaraki, Y. Oki, T. Minamida, Development of a new hypereutectoid steel for high-strength wire, *Wire J. Int.*, Feb 2002, p 116–121
15.57 T. Tarui, S. Konno, T. Takahashi, High Strength Galvanized Wire for Bridge Cables, *Mat. Sci. Forum,* Vol 426-432, 2003, p 829–834
15.58 T. Tarui, A. Yoshie, Y. Asano, T. Takahashi, S. Nishida, H. Ohba, I. Ochiai, Wire Rod for 2,000 MPa Galvanized Wire and 2,300 MPa PC Strand, *Nippon Steel Tech. Rep.*, No. 80, July 1999, p 44–49
15.59 R. E. Pennington, W. Van Raemdonck, D. K. Matlock, G. Krauss, The effect of silicon and aging on mechanical properties and fracture response of drawn high-strength pearlitic steel wire, *Wire J. Int.*, June 2011, p 64–7

CHAPTER 16

Hardness and Hardenability

A MARTENSITIC MICROSTRUCTURE is the hardest microstructure that can be produced in any carbon steel; therefore, heat treatments that produce martensite are referred to as *hardening heat treatments*. This chapter first shows that martensitic hardness is a function of steel carbon content and describes some of the mechanisms by which that hardness and associated strength are achieved. Much more information on the mechanical properties and fracture of martensite and its derivative tempered microstructures is presented in Chapter 18, "Deformation, Mechanical Properties, and Fracture of Quenched and Tempered Carbon Steels." Martensite, however, can be produced only when the diffusion-controlled transformations of austenite to ferrite and cementite microstructures such as ferrite, pearlite, and bainite are suppressed. The term *hardenability* relates to the suppression of diffusion-controlled transformations and, therefore, the propensity of a steel to harden under various conditions of cooling. The effects of steel composition, cooling rates, and section size on hardenability, as developed by the now-classical approach of Grossman and Bain and subsequent considerations, are described in this chapter.

Hardness and Carbon Content

The maximum hardness that can be produced in any given carbon steel is that associated with a fully martensitic microstructure. Figure 16.1 shows the much higher hardness of martensite relative to that of ferrite-pearlite or spheroidized microstructures for the entire range of carbon content usually found in steels. The high hardness and associated high strength, fatigue resistance, and wear resistance are the prime reasons for the quenching heat treatments that produce martensite. Almost all mar-

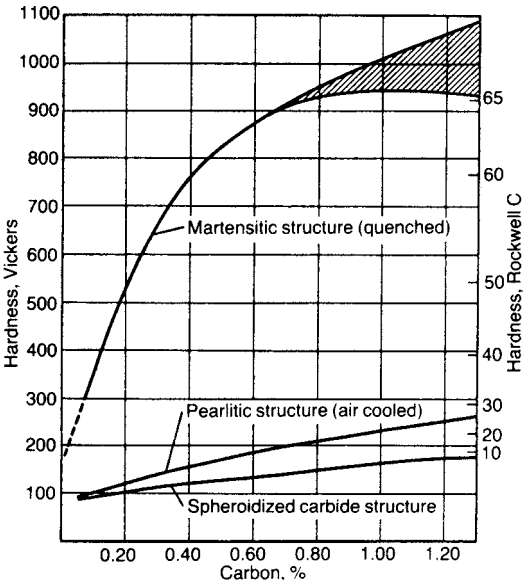

Fig. 16.1 Hardness as a function of carbon content for martensitic, ferrite-pearlite, and spheroidized microstructures in steels. Cross-hatched area shows effect of retained austenite. Source: Ref 16.1

tensite is tempered, and depending on the amount of tempering, hardness in a given quenched and tempered steel may vary from close to the maximum shown for martensite to the minimum associated with the spheroidized carbide structure. Heat treatments to form martensite are extensively applied to steels containing more than 0.3% C. In these steels, the gains in hardness are most substantial. Steels containing less than 0.3% C are difficult to harden in heavy sections but are hardenable in sheet and thin plate to provide excellent combinations of strength and toughness after tempering. Rockwell C readings below 20 are not considered valid and are included in Fig. 16.1 only for comparative purposes. Also the hardness of fully pearlitic microstructures is dependent on pearlite interlamellar spacing and may be much higher than shown in Fig. 16.1.

Figure 16.2 is a summary plot of many investigations of the hardness of martensitic microstructures as a function of the carbon content of steels and Fe-C alloys, and shows the range of hardness that may develop in largely martensitic microstructures in steels of a given carbon content. Special care was taken in all of the investigations to ensure that no proeutectoid phases or mixtures of ferrite and cementite formed. However, the martensitic microstructures may have contained various amounts of retained austenite because M_f drops below room temperature even in low-carbon steels. For example, Fig. 5.8 in Chapter 5, "Martensite," showed that small amounts of retained austenite are present at room temperature in steels with carbon content as low as 0.3%. The most significant effect

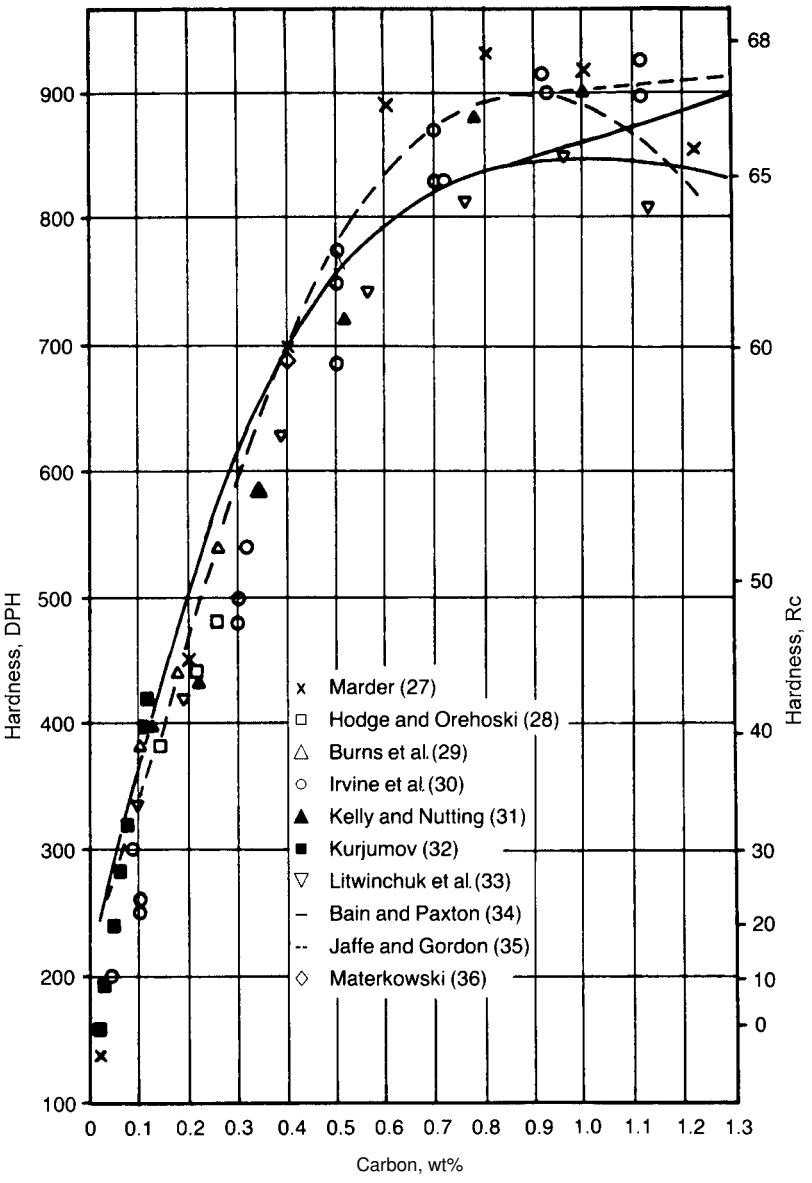

Fig. 16.2 Summary of hardness of martensite as a function of carbon content in Fe-C alloys and steels. From Ref 16.2; investigations listed are given in that reference.

of retained austenite on hardness occurs in steels containing more than 0.7% C; Fig.16.1 and several of the sets of data in Fig. 16.2 show the decrease in hardness that develops with increasing amounts of retained austenite in high-carbon steels.

Some of the investigators whose data is shown in Fig. 16.2 quenched specimens in liquid nitrogen (–196 °C or –320 °F) in order to reduce re-

tained austenite and thereby increase hardness. For example, the continuous curve after Bain and Paxton (Ref 16.1), based on as-quenched hardness at room temperature, is lower than the dashed curve after Jaffee and Gordon (Ref 16.3), who cooled their specimens in liquid nitrogen. The data points marked by *x*'s were taken from specimens cooled in liquid helium (–269 °C or –450 °F) (Ref 16.4) and tend to be higher than the hardness of steels not as deeply cooled. The effectiveness of the subzero treatments is of course greatest in steels containing more than 0.4% C, where significant amounts of retained austenite (see Fig. 5.8) may be present at room temperature.

Apart from differences in retained austenite content, some of the variation in the maximum hardness of various carbon levels might also be due to aging or differences in austenitic grain size. Figure 16.3 shows that room temperature aging significantly increases the hardness of martensitic Fe-Ni-C alloys (Ref 16.5, 16.6). Similar hardness changes with time have been observed in Fe-C martensites (Ref 16.4); thus, if attention is not paid to the time after quenching at which hardness measurements are made, some variation contributing to scatter in reported hardness values may occur.

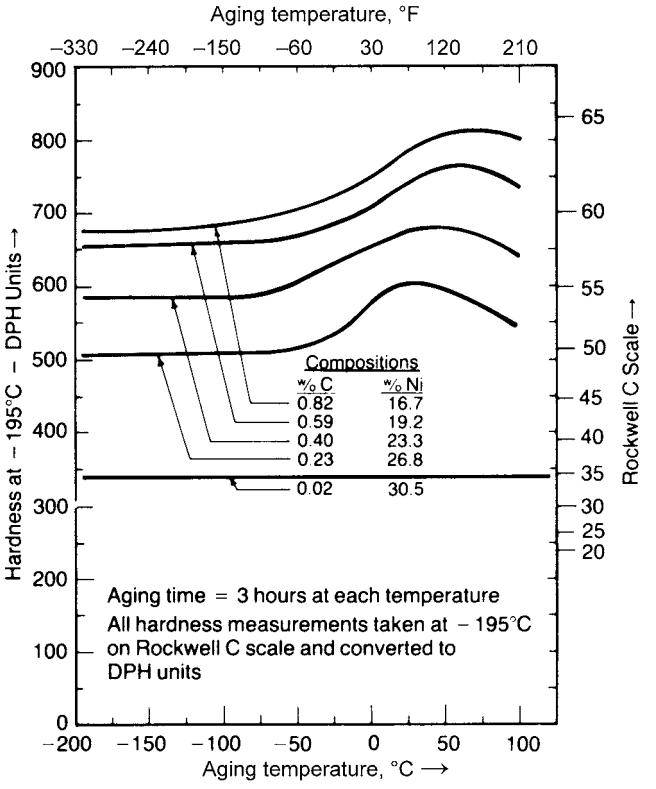

Fig. 16.3 Hardness of Fe-Ni-C alloy martensites at –195 °C (–320 °F) after aging for 3 h at the temperatures shown. Source: Ref 16.5

Austenitic grain size has also been observed to affect the strength of martensite in low-carbon steels (Ref 16.7, 16.8). When the austenite grain size is reduced, significant increases in strength occur. The relationship between austenite grain size and martensite structure is a result of the unique structure of martensite in low- and medium-carbon steels. The martensite laths, as described in Chapter 5, "Martensite," are arranged in packets whose size is directly related to austenite grain size (see Chapter 8, "Austenite in Steel"). Thus, either martensite packet size or austenite grain size may be used to correlate with mechanical properties. Figure 16.4 shows the increase in yield strength with decreasing martensite packet size in an Fe-0.2C alloy. Packet size (D) is plotted as $D^{-1/2}$ in what is referred to as a *Hall-Petch plot*. An interesting observation is that the slope of the Fe-0.2C martensite curve is steeper than that of lath martensite in an Fe-Mn alloy without carbon. This observation was explained by the segregation of carbon atoms to packet boundaries where they make the initial yielding process more difficult; the more so, the finer the packet size (Ref 16.8).

Martensite Strength

The reason for the very high hardness of carbon-containing martensites has long intrigued metallurgists. Cohen in the 1962 Howe Memorial Lecture (Ref 16.5) followed the historical development of the theories of martensite strength in steels and emphasized the important role that carbon atoms trapped in the octahedral interstitial sites play in the strengthening

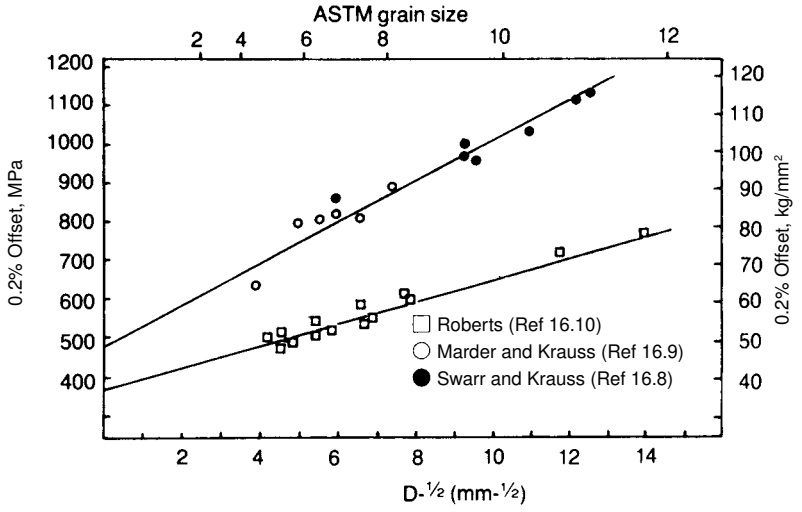

Fig. 16.4 Increase in strength of lath martensites with decreasing packet size, *D*. Upper line is for Fe-0.2C martensite; lower line is for Fe-Mn martensite. Source: Ref 16.8, 16.9, 16.10

of martensite. Figure 16.5 shows a schematic representation of the displacement of the iron atoms by carbon atoms in the body-centered tetragonal lattice of martensite. This distortion of the iron lattice makes the movement of dislocations very difficult and contributes to the high strength of martensite.

In addition to the solid solution strengthening by carbon, the substructure of martensite also contributes to strength. Chapter 5, "Martensite," showed that martensitic transformation was unique in that it introduced a high density of dislocations and/or fine twins into a martensite lath or plate. The contribution to the strength of martensite by the substructure early-on was assumed to be relatively constant as a function of carbon content and, except at low carbon concentrations, does not make nearly as great a contribution as does carbon-dependent strengthening. The following equation (Ref 16.11, 16.12) for the 0.2% offset yield strength of martensite ($\sigma_{0.2}$), determined from a series of Fe-Ni-C alloys with subzero M_s temperatures, permits a quantitative assessment of the carbon and substructure contributions:

$$\sigma_{0.2}(\text{MPa}) = 461 + 1.31 \times 10^3(\%\ \text{C})^{1/2} \qquad \text{(Eq 16.1)}$$

The second term shows the strong effect of carbon and expresses that the strengthening of martensite follows a square-root dependency with respect to carbon content, a functional relationship that correlates well with the initial rapid increase in strength with carbon content and the more gradual strength increases at higher carbon contents. The first term includes the strengthening contribution of 20% Ni (20,000 psi, or 138 MPa), the friction stress or stress to move dislocations in pure bcc iron (10,000 psi, or

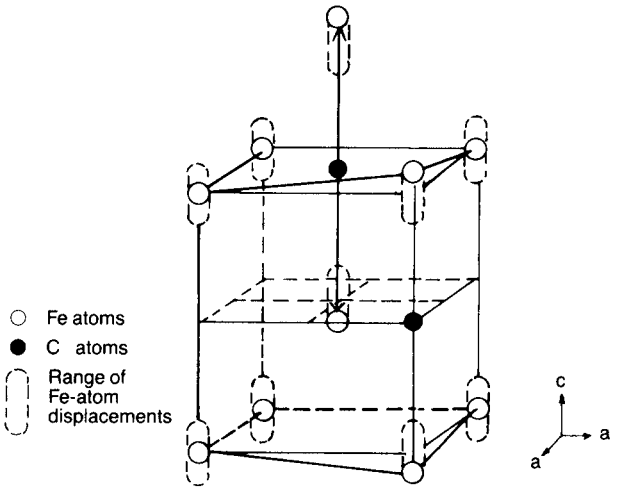

Fig. 16.5 Iron atom displacements due to carbon atoms in martensite. Source: Ref 16.5

69 MPa), and the contribution of the martensitic substructure (37,000 psi, or 255 MPa). Equation 16.1 holds for unaged martensite, a result possible because of the low M_s temperatures of the Fe-Ni-C alloys. The martensite, therefore, was formed and mechanically tested at low temperatures where aging was minimal. Carbon steels, especially those of low carbon content, have high M_s temperatures and undergo considerable carbon atom rearrangement during quenching before reaching room temperature, a process referred to as *autotempering*. The carbon atoms segregate to the dislocation fine structure and/or lath and packet boundaries (Ref 16.13). One result of the segregation, a very high dependency of strength on packet size, has already been mentioned (Ref 16.8). Despite the effects of carbon atom segregation, the yield strength of low-carbon martensite still follows a square-root dependency on carbon content, as shown in the following equation (Ref 16.14):

$$\sigma_{0.2}(\text{MPa}) = 413 + 1.72 \times 10^3(\%\ \text{C})^{1/2} \qquad \text{(Eq 16.2)}$$

This equation was determined from low-carbon Fe-C alloys containing up to 0.2% C and also fits data for martensitic steels containing 0.08 to 0.24% C and 0.4 to 0.5% Mn (Ref 16.15). Again, the first term includes all of the structural contributions to strength, including the austenitic grain size or packet size (in this case, austenite grain size was roughly constant, between ASTM 7 and 9), lath size, and dislocation fine structure. Equations 16.1 and 16.2 are based on yield strength. Ultimate tensile strengths and hardness are strongly dependent on strain hardening as discussed in Chapter 18, "Deformation, Mechanical Properties and Fracture of Quench and Tempered Carbon Steels."

Definitions of Hardenability

The preceding discussion shows that the maximum hardness of any steel is associated with a fully martensitic structure. This microstructure, however, can be produced only if the diffusion-dependent transformation of austenite can be suppressed by sufficiently rapid cooling. There are a number of factors that affect cooling rates throughout a given part and the response of a given steel to those cooling rates. Thus, the formation of martensite and high hardness may vary considerably throughout a given cross section or between identical cross sections fabricated from different steels. The subject of hardenability deals with the latter variations.

Hardenability is defined as the "susceptibility to hardening by rapid cooling" (Ref 16.16), or as "the property, in ferrous alloys, that determines the depth and distribution of hardness produced by quenching" (Ref 16.17). Both of these definitions emphasize hardness. As discussed previously, the source of hardening is the formation and presence of martensite, and therefore a third definition of hardenability, "the capacity of a steel to

transform partially or completely from austenite to some percentage of martensite at a given depth when cooled under some given conditions," more accurately describes the physical process underlying hardening. Siebert, Doane, and Breen in their comprehensive book on hardenability prefer the latter structural definition (Ref 16.18).

Hardness Distribution

An experimental approach that demonstrates the striking effect of various factors on hardenability is the quenching of series of round bars of various diameters. The bars are completely austenitized, quenched, and tempered. Hardness readings are then taken along diameters of the bar cross sections in order to show the distribution of hardness as a function of distance from the surface to the center of the bar.

Figures 16.6 and 16.7 show the results of water quenching bars of SAE 1045 steel, a plain carbon steel, and SAE 6140 steel, an alloy steel, respectively (Ref 16.16). The chemical compositions of the two steels are given in Table 16.1.

Plain carbon and alloy steels are classified by the Society of Automotive Engineers (SAE) and the American Iron and Steel Institute (AISI) and are manufactured to various ranges of compositions (Ref 16.19). For example, the AISI-SAE specifications for steel designated as 1045 permit carbon in the range of 0.42 to 0.50% and manganese in the range of 0.60 to 0.90%. It is therefore important to state the exact composition of a heat of steel (as in Table 16.1) for the most accurate interpretation of the response to hardening.

Figure 16.6 shows that the maximum hardness in the SAE 1045 steel can be achieved only on the surface of bars with small diameters. Even in a 12.7 mm (0.5 in.) diameter bar, the hardness in the interior drops significantly. With increasing bar diameter, the surface hardness of the SAE 1045 steel drops significantly and the center hardness continues to decrease. The alloy steel, SAE 6140, on the other hand, develops higher hardness than the SAE 1045 steel at all bar diameters (see Fig. 16.7) but nevertheless still shows large variations in hardness from the surface to the center of the bars, especially in the larger sizes.

Figures 16.6 and 16.7 show the effects of bar diameter and alloy content on hardness distribution of water-quenched rounds. A third factor that influences hardness distribution is the rate of quenching. Figures 16.8 and 16.9 show the results of oil quenching on the hardness distribution in round bars of various diameters for the SAE 1045 and 6140 steels, respectively. Oil is a much less severe quenching medium than water, and so the cooling rates of oil-quenched bars are appreciably lower than those of water-quenched bars. Figure 16.8 shows that the hardening response of the SAE 1045 steel to oil quenching is very low. Even in the 12.7 mm

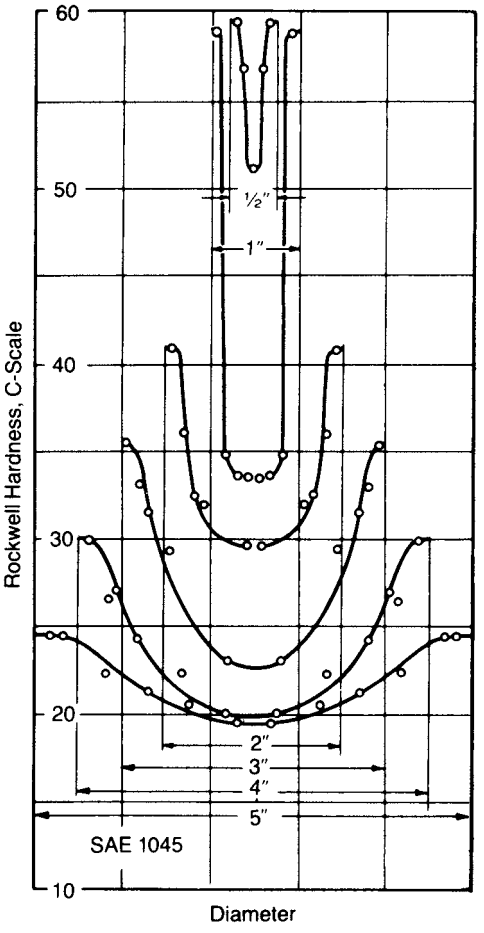

Fig. 16.6 Hardness distributions in water-quenched bars of SAE 1045 steel. The various bar diameters are indicated. Source: Ref 16.16

diameter bar the surface hardness is well below the hardness expected from a fully martensitic structure of a 0.48% C steel (see Fig. 16.1 and 16.2). It is apparent, therefore, that the slower cooling associated with oil quenching has not been able to prevent the diffusion-controlled transformation to ferrite and/or pearlite in the SAE 1045 steel. The SAE 6140 steel, however, hardens well in the same bar sizes (see Fig. 16.9) and only in the larger sizes does the hardness distribution fall off significantly.

Comparison of Fig. 16.6 through 16.9 shows that the alloy steel, SAE 6140, is much more hardenable than the plain carbon SAE 1045 steel. SAE 6140 is therefore said to have a higher hardenability than the SAE 1045 steel. The plain carbon steel can be hardened, but only in small sections and/or with very severe quenches. Fundamentally, the alloying elements in the SAE 6140 steel increase the time required for austenite to

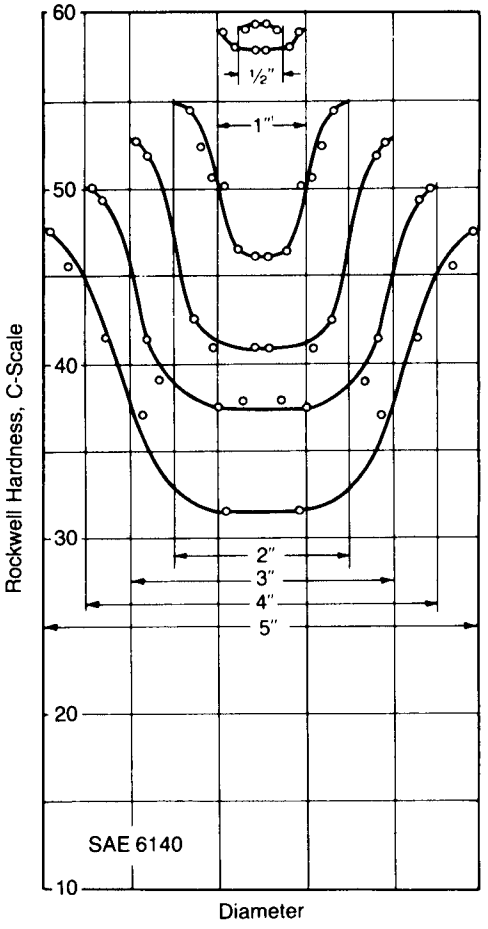

Fig. 16.7 Hardness distribution in water-quenched bars of SAE 6140 steel. The various bar diameters are indicated. Source: Ref 16.16

Table 16.1 Compositions of steels used in bar-quenching experiments

	Composition, %						
Steel	C	Mn	P	S	Si	Cr	V
SAE 1045	0.48	0.60	0.022	0.016	0.17	…	…
SAE 6140	0.42	0.73	0.027	0.023	0.25	0.94	0.17

decompose to ferrite and/or ferrite-cementite mixtures, and thereby make it possible to form martensite at lower cooling rates. The effects of alloying elements on the diffusion-controlled decomposition of austenite in many steels are summarized in the IT and CT diagrams contained in the atlases described in Chapter 10, "Isothermal and Continuous Cooling Transformation Diagrams."

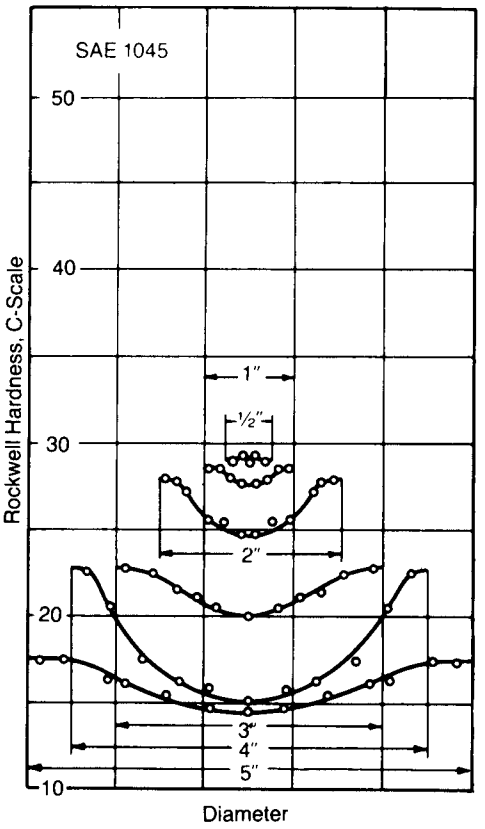

Fig. 16.8 Hardness distribution in oil-quenched bars of SAE 1045 steel. The various bar diameters are indicated. Source: Ref 16.16

Factors Affecting Cooling Rates

Two important factors influence *cooling rates*, or the rates at which heat can be removed from a steel part. One is the ability of the heat to diffuse from the interior to the surface of the steel specimen, and the other is the ability of the quenching medium to remove heat from the surface of the part.

The ability of a steel to transfer heat is characterized by its *thermal diffusivity* (units of area per unit time), or the ratio of its thermal conductivity to the volume specific heat. The thermal diffusivity of austenitic transformation products increases with decreasing temperature, and plots of thermal diffusivity and conductivity for various structures as a function of temperature are reproduced in Ref 16.18. For a given quenching medium, the thermal diffusivity determines the temperature distribution as a function of position at any given time in the quenching process. For example, Fig. 16.10 shows cooling rate as a function of position in a quenched 25

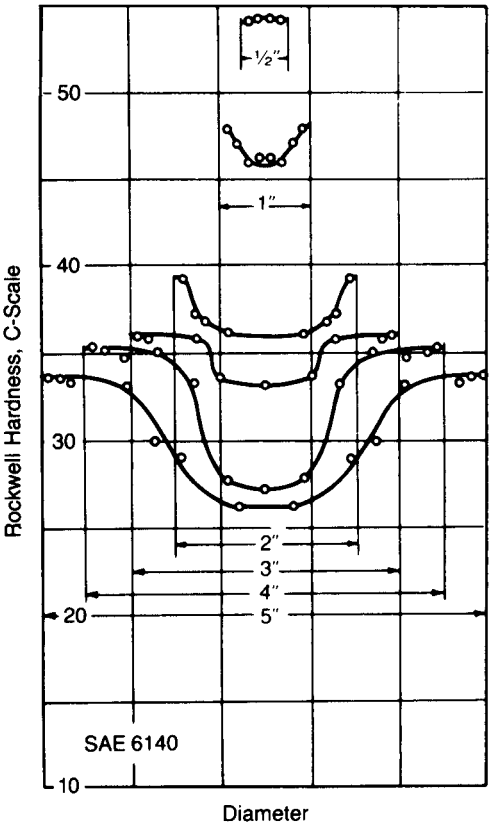

Fig. 16.9 Hardness distributions in oil-quenched bars of SAE 6140 steel. The various bar diameters are indicated. Source: Ref 16.16

mm (1 in.) diameter bar. The slower cooling rates at positions removed from the surface of the bar permit more time for diffusion-controlled transformations, and it is this type of cooling behavior that results in the low center hardness of the bars shown in Fig. 16.6 to 16.9, especially in the larger sizes. Practically, however, little control of thermal properties is possible with steels, and the most important control of cooling rates is performed by proper selection of quenching media.

The transfer of heat at the interface of a steel part and a quenching medium is a complex process that depends primarily on the *emissivity* of the steel (the rate at which the surface of the steel radiates heat) and convection currents within the quenching medium that remove heat from the interface. The complexity of the process is illustrated in Fig. 16.11, a curve obtained by measuring temperature as a function of time in the center of a 12.7 mm (0.5 in.) diameter bar of steel during water quenching (Ref 16.20). Three stages of cooling are shown. The first stage is associated with the development of a layer of water vapor or steam immediately ad-

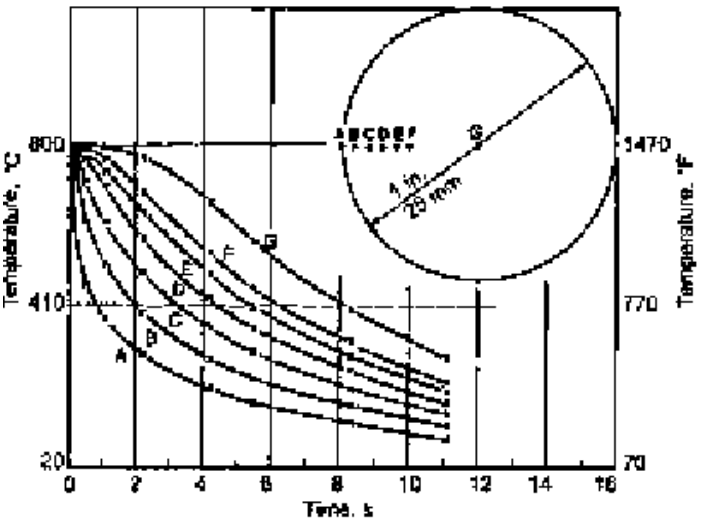

Fig. 16.10 Cooling curves at various positions in a 25.5 mm (1 in.) diameter bar quenched with a severity of quench $H = 4$. Source: Ref 16.16

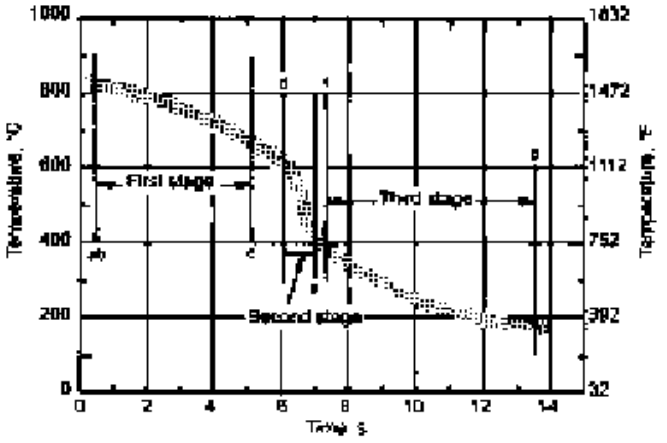

Fig. 16.11 Stages of cooling during water quench. Source: Ref 16.21

jacent to the surface of the steel. The steam insulates the surface and produces a low cooling rate. In the second stage, the vapor blanket breaks down and water comes in contact with the steel. The water vaporizes and bubbles away, thereby continually bringing more water in contact with the surface. Cooling is quite rapid in this stage. When the surface temperature of the steel drops below the boiling point, vaporization stops and cooling is controlled by convection and conduction at the fluid-metal interface. The latter or third stage is characterized by relatively slow rates of cooling.

Understanding the cooling process has important practical consequences. For example, if the low cooling rate of the first stage results in ferrite or pearlite, efforts should be made to increase the cooling rate in this stage. Agitation of the part or the quenchant and the use of brine solutions for quenching are effective in reducing the duration of the first stage of cooling.

Severity of Quench

The effectiveness of a given quenching medium is ranked by a parameter referred to as its *severity of quench* (or *quench severity*). This measure of cooling or quenching power is identified by the letter "H" and is determined experimentally by quenching a series of round bars of a given steel. Figure 16.12 shows schematically the results of oil and water quenching bars of SAE 3140 steel (Ref 16.16). SAE 3140 is a nickel-chromium alloy steel containing nominally 0.40% C. The cross-hatched areas represent the unhardened areas of the various bars, assuming that less than 50% martensite represents an unhardened microstructure. The larger the bar diameter (D), the greater is the unhardened diameter (D_u). Figure 16.13 plots the results of Fig. 16.12 as D_u/D versus D for both the oil- and water-quenched series. The steeper curve is associated with the oil quench, a result of the reduced ability of oil quenching to produce hardening in heavier sections. When the curves of Fig. 16.13 are matched to one of the large number of calculated curves that are characteristic of a wide range

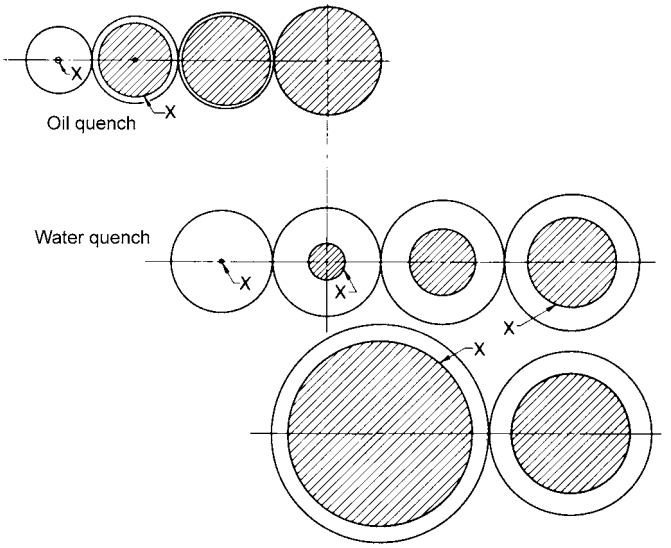

Fig. 16.12 Schematic representation of extent of hardening in oil-quenched and water-quenched bars of SAE 3140 steel of various diameters. The cross-hatched areas represent the unhardened core. Source: Ref 16.16

of quench severities (see Fig. 16.14), H can be determined. The matching can be performed by plotting D_u/D versus D as in Fig. 16.13 on transparent paper and finding the best correspondence to a D_u/D versus HD curve in Fig. 16.14. When the HD values are divided by corresponding D values, the H value is obtained. For example, point A in Fig. 16.13, corre-

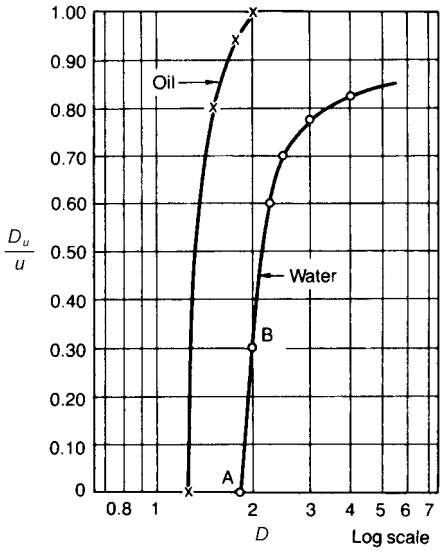

Fig. 16.13 Ratio of unhardened to hardened diameters as a function of bar diameter for oil- and water-quenched bars of 3140 steel. Source: Ref 16.16

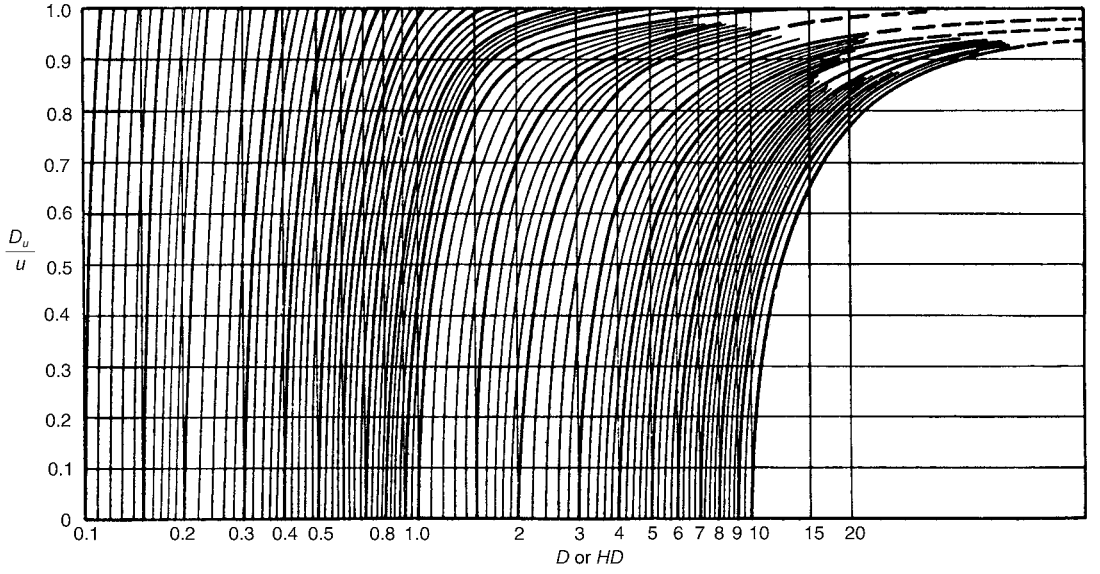

Fig. 16.14 Curves D_u/D vs. D or HD for estimating severity of quench (H) for quenching baths. Source: Ref 16.16

sponding to a bar diameter of 4.65 cm (1.83 in.), would fall on an *HD* value of 2.6 in Fig. 16.14 when the curves are matched. Then $H = 2.6/1.83 = 1.4$ for the water quench of this example.

Table 16.2 lists *H* values for a number of commonly used quenches. The increase in severity of quench from air, $H = 0.02$, through brine quenching, $H = 2$, is shown. Also, the very strong effect of agitation or circulation on increasing the severity of quench in any given quenching medium is apparent. Another useful ranking of quenching media relative to water is shown in Table 16.3. This table not only ranks the cooling media, but also shows the large number of media available for cooling at various rates.

Table 16.3 was compiled in the mid-twentieth century. Since that time, quenching and quenching media have received considerable attention from the heat treating community (Ref 16.24, 16.25). In particular, a notable addition to available quenching media has been made possible by the development of polymer quenchants. The latter quenching media have

Table 16.2 Severity of quench (*H*) for various quenching media

Circulation	Air	Oil	Water	Brine
No circulation of fluid or agitation of piece	0.02	0.25–0.30	0.9–1.0	2
Mild circulation (or agitation)	…	0.30–0.35	1.0–1.1	2–2.2
Moderate circulation	…	0.35–0.40	1.2–1.3	…
Good circulation	…	0.4–0.5	1.4–1.5	…
Strong circulation	0.05	0.5–0.8	1.6–2.0	…
Violent circulation	…	0.8–1.1	4	5

Source: Ref 16.16, 16.22

Table 16.3 Relative cooling rates in different quenching media

Quenching medium	Cooling rate(a) from 717–550 °C (1328–1022 °F) relative to that for water at 18 °C (65 °F)	Quenching medium	Cooling rate(a) from 717–550 °C (1328–1022 °F) relative to that for water at 18 °C (65 °F)
Aqueous solution, 10% LiCl	2.07	Oil 20204	0.20
Aqueous solution, 10% NaOH	2.06	Oil, Lupex light	0.18
Aqueous solution, 10% NaCl	1.96	Water at 50 °C (120 °F)	0.17
Aqueous solution, 10% Na_2CO_3	1.38	Oil 25441	0.16
Aqueous solution, 10% H_2SO_4	1.22	Oil 14530	0.14
Water at 0 °C (32 °F)	1.06	Emulsion of 10% oil in water	0.11
Water at 18 °C (65 °F)	1.00	Copper plates	0.10
Aqueous solution, 10% H_3PO_4	0.99	Soap water	0.077
Mercury	0.78	Iron plates	0.061
$Sn_{30}Cd_{70}$ at 180 °C (355 °F)	0.77	Carbon tetrachloride	0.055
Water at 25 °C (75 °F)	0.72	Hydrogen	0.050
Rapeseed oil	0.30	Water at 75 °C (165 °F)	0.047
Trial oil No. 6	0.27	Water at 100 °C (210 °F)	0.044
Oil P20	0.23	Liquid air	0.039
Oil 12455	0.22	Air	0.028
Glycerin	0.20	Vacuum	0.011

(a) Determined by quenching a 4 mm nichrome ball, which when quenched from 860 °C (1580 °F) into water at 18 °C (65 °F) cooled at the rate of 1810 °C (3260 °F) per second over the range 717 to 550 °C (1328 to 1022 °F). This cooling rate in water at 18 °C (65 °F) is rated as 1.00 in the table, and the rates in the other media are compared with it.
Source: Ref 16.16, 16.23

quenching severities comparable to oil quenches, but are nonflammable and less environmentally damaging with respect to vapors and disposal.

Quantitative Hardenability

Up to this point a number of important aspects of hardenability have been described. High hardness is related to martensite formation, which in turn is dependent on cooling rate. Cooling rate is affected by both specimen size and severity of quench. However, there still remain the questions as to how hardenability is evaluated as a function of steel composition and how the effect of the large number of quenching media on hardness distribution can be evaluated without the time-consuming approach of quenching a series of round bars in the various media. The first and now classical approach to these questions, described next, was developed in the 1930s and 1940s by Grossmann and Bain (Ref 16.16) and their many colleagues and contemporaries.

The Grossmann-Bain approach to hardenability is based on the definition of two parameters: the critical size and the ideal size. The *critical size* is the largest size of a bar quenched in a given medium that contains no unhardened core after quenching. An important aspect of this definition is that the hardness that separates the hardened from the unhardened core of a bar is associated with a microstructure assumed to contain only 50% martensite. This assumption underlies all of the graphical information associated with the Grossmann-Bain approach to hardenability. The reason for selecting the 50% martensite criterion for the critical diameter is shown in Fig. 16.15. Etching differences between the hardened surface of a bar and the unhardened center are most clearly developed close to the 50% martensite-50% pearlite zone in a bar. Likewise, when a quenched bar is broken, the same 50% martensite zone correlates well with a transition from very smooth or faceted intergranular fracture (now known to be related to austenitizing and the presence of impurities such as phosphorus) associated with a predominantly martensitic structure to a rough, transgranular surface associated with ductile fracture of the softer nonmartensitic transformation products of austenite. Therefore, both etching and fracture observations, frequently on a macroscopic scale, could be readily used to evaluate depth of hardening at the 50% martensite level. Detection of martensite at levels above 50% in the microstructure would be much more difficult.

Not only does the etching and fracture response of a quenched bar change abruptly at the 50% martensite level, but hardness also changes rapidly as bar diameter increases through those associated with 50% martensite. Figure 16.16 shows center hardness as function of bar diameter for the chromium-nickel SAE 3140 steel quenched in oil and water. Each quenching medium produces a different critical diameter associated with the rapid changes in hardness with bar diameter close to Rockwell C 50.

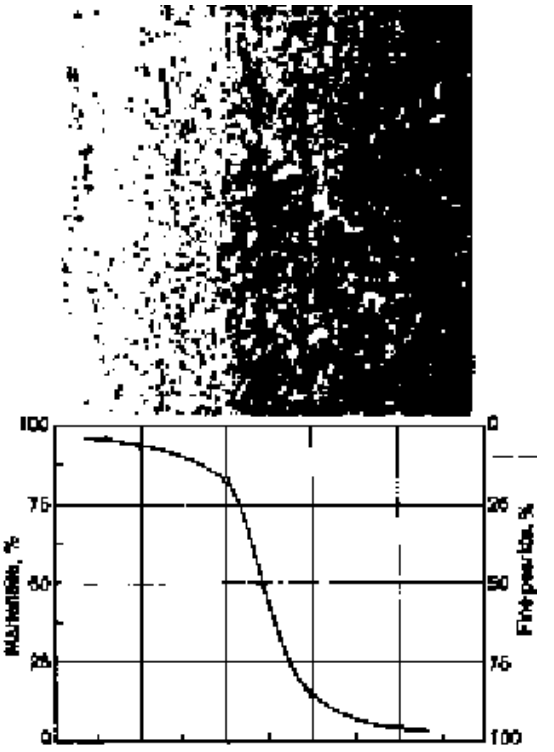

Fig. 16.15 Transition from martensitic to pearlitic microstructure between hardened and unhardened zones of a quenched steel. Source: Ref 16.16

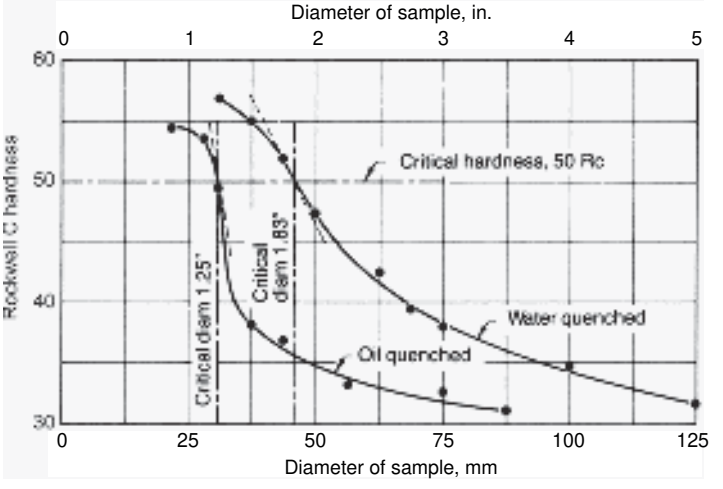

Fig. 16.16 Hardness at the center of water- and oil-quenched bars of SAE 3140 steel of various diameters. Source: Ref 16.16

Judging the position of 50% martensite from hardness changes with bar diameter can be difficult, as for example in the water-quenching data of Fig. 16.16. Therefore, the probable hardness associated with a 50% martensite structure, similar to those given for fully martensitic microstructures in Fig. 16.1 and 16.2, was determined as a function of carbon content. Figure 16.17 shows such a plot based on data from plain carbon steels. Alloy steels are expected to show somewhat higher hardness values, as is the case for the SAE 3140 steel. From Fig. 16.17, the hardness at 50% martensite for a 0.40% C steel would be expected to be Rockwell C 40, but Fig. 16.16 shows that the critical diameter was selected at Rockwell C 50. A possible explanation for this discrepancy may be the presence of large amounts of bainite having relatively high hardness together with 50% martensite in alloy steels, whereas ferrite and pearlite of relatively lower hardness might coexist with 50% martensite in plain carbon steels.

In summary of the preceding discussion, the critical size or diameter of a steel of given composition is directly related to a given quenching medium. The higher the quench severity, the greater is the critical size. The *ideal size*, on the other hand, is defined as the size of bar hardened to 50% martensite by a theoretically perfect quench in which it is assumed that the quench severity is infinite and the surface of the bar cools instantly to the temperature of the quenching medium. The ideal size is a true measure of the hardenability associated with a given steel composition, and it can also be used to determine the critical size of the steels quenched in media of different quench severities.

Figures 16.18 and 16.19 show plots of critical size (D) versus ideal size (D_I) for various quench severities (H). The straight line associated with a theoretically infinite quench severity shows that the critical size equals the

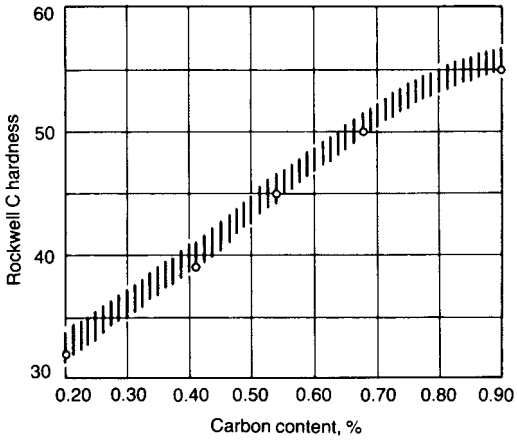

Fig. 16.17 Hardness as a function of carbon content for quenched structures that contain 50% martensite. Source: Ref 16.16

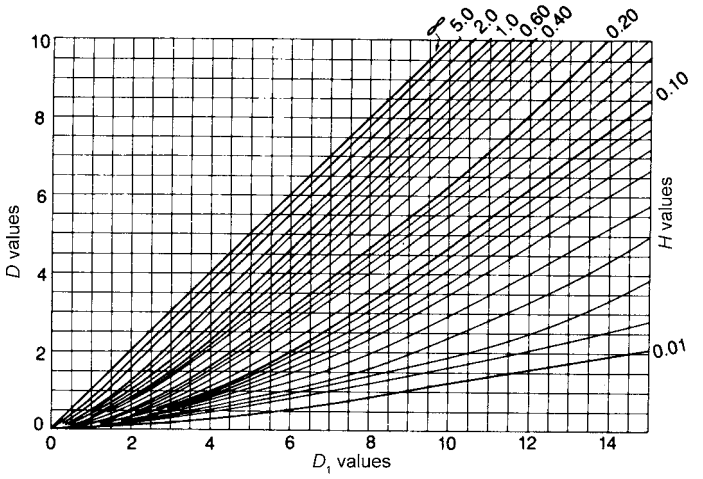

Fig. 16.18 Relationship between actual critical size (D), ideal critical size (D_I), and severity of quench (H). Source: Ref 16.16

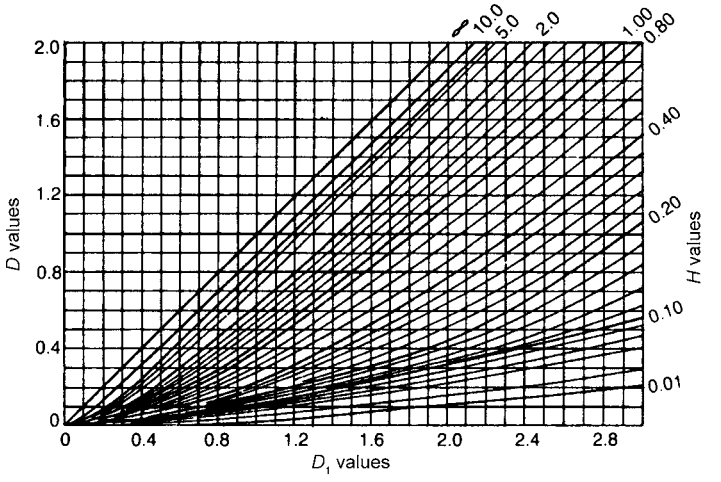

Fig. 16.19 Relationships similar to those shown in Fig. 16.18 but at a larger scale. Source: Ref 16.16

ideal size for a theoretically perfect quench. However, Fig. 16.18 and 16.19 show that as quench severity decreases, the critical size for a given D_I decreases. Thus, the concept of the ideal size permits a rapid estimate of the bar size that will harden to the 50% martensite level in quenches over the entire range of severities. Similar curves between critical plate thickness, ideal plate thickness, and quench severity have also been developed (Ref 16.16).

Determination of Ideal Size—Quantitative Approaches

As noted in the preceding section, the ideal diameter is a true measure of the hardenability of a steel and can be used to compare the hardening response of different steels to the same quenching medium. In the classical Grossmann-Bain approach to hardenability, three factors, austenitic grain size, carbon content, and alloy content, have been considered to affect the ideal diameter. An increase in any of these factors was shown to reduce the rate at which the diffusion-controlled transformations of austenite occur and thereby makes martensite formation more likely at a given cooling rate. The end of this section discusses limitations and modified approaches to this classical determination of ideal diameters.

Figure 16.20 shows the relationship of ideal diameter to carbon content and austenite grain size. This plot is used to establish a base hardenability, D_I, for a steel based on its carbon content and grain size. The base hardenability is then multiplied by factors as given in Fig. 16.21 for the various concentrations of alloying elements. As an example, Table 16.4 shows multiplying factors for concentrations of elements in a nickel-chromium steel containing 0.5% C (Ref 16.16). If the steel has an austenitic grain size of No. 7, then the base ideal diameter from Fig. 16.20 is 6.1 mm (0.24 in.). After multiplying by the factors in Table 16.4, an ideal diameter

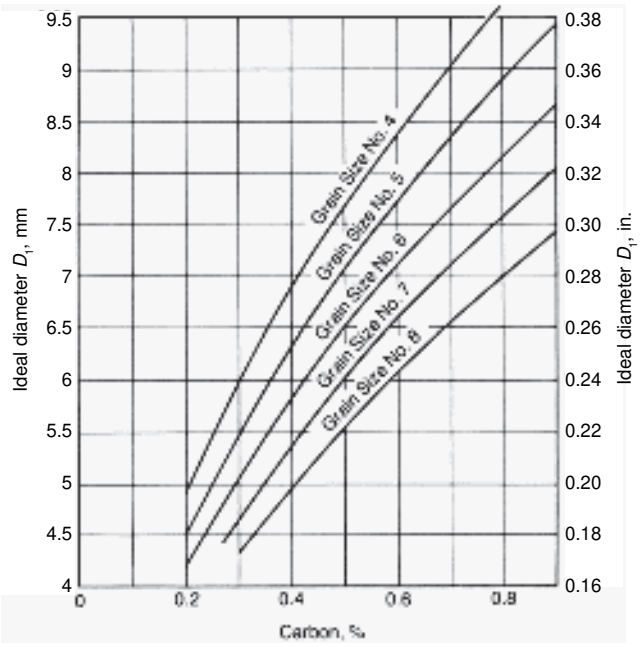

Fig. 16.20 Hardenability, expressed as ideal critical size, as a function of austenite grain size and carbon content of iron-carbon alloys. Source: Ref 16.16

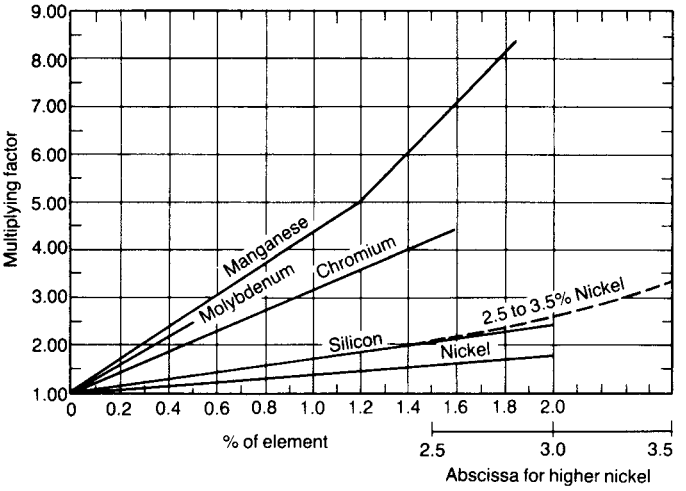

Fig. 16.21 Multiplying factors as a function of the concentration of various common alloying elements in alloy steels. Source: Ref 16.16

Table 16.4 Composition and multipliers for a Ni-Cr steel

Element	Concentration, %	Multiplier
Carbon	0.50	0.24
Manganese	0.80	3.7
Silicon	0.25	1.2
Nickel	1.00	1.4
Chromium	0.28	1.6

of 61 mm (2.4 in.) is obtained for the steel. The multiplying factors have been reviewed and revised over the years, and the reader is referred to Ref 16.18 for an extensive compilation of multiplying factors for the most common alloying elements.

Table 16.5 lists ranges of D_1 for a number of commercial steels. Compositions of these steels are given in Ref 16.19. The letter *H* at the end of the SAE-AISI designation indicates that the steels are produced to specified hardenability limits. The range in D_1 for a given steel is a result of the acceptable ranges of composition for that grade and other factors such as heat treatment conditions and the concentrations of residual elements.

For the application of the classical approach to hardenability, it is often assumed that all the alloying elements, as determined by a heat analysis, are in solution during austenitizing prior to quenching for martensite formation. However, for most hardenable steels the recommended temperatures and times for austenitizing are too low for the complete solution of carbides that are present prior to austenitizing, as for example those in as-rolled ferrite/pearlite microstructures or spheroidized microstructures. Strong carbide-forming elements, such as chromium, molybdenum, and

Table 16.5 Hardenabilities (stated as a range of D_1 values) for various steels

Steel	D_1	Steel	D_1	Steel	D_1
1045	0.9–1.3	4135 H	2.5–3.3	8625 H	1.6–2.4
1090	1.2–1.6	4140 H	3.1–4.7	8627 H	1.7–2.7
1320 H	1.4–2.5	4317 H	1.7–2.4	8630 H	2.1–2.8
1330 H	1.9–2.7	4320 H	1.8–2.6	8632 H	2.2–2.9
1335 H	2.0–2.8	4340 H	4.6–6.0	8635 H	2.4–3.4
1340 H	2.3–3.2	X4620 H	1.4–2.2	8637 H	2.6–3.6
2330 H	2.3–3.2	4620 H	1.5–2.2	8640 H	2.7–3.7
2345	2.5–3.2	4621 H	1.9–2.6	8641 H	2.7–3.7
2512 H	1.5–2.5	4640 H	2.6–3.4	8642 H	2.8–3.9
2515 H	1.8–2.9	4812 H	1.7–2.7	8645 H	3.1–4.1
2517 H	2.0–3.0	4815 H	1.8–2.8	8647 H	3.0–4.1
3120 H	1.5–2.3	4817 H	2.2–2.9	8650 H	3.3–4.5
3130 H	2.0–2.8	4820 H	2.2–3.2	8720 H	1.8–2.4
3135 H	2.2–3.1	5120 H	1.2–1.9	8735 H	2.7–3.6
3140 H	2.6–3.4	5130 H	2.1–2.9	8740 H	2.7–3.7
3340	8.0–10.0	5132 H	2.2–2.9	8742 H	3.0–4.0
4032 H	1.6–2.2	5135 H	2.2–2.9	8745 H	3.2–4.3
4037 H	1.7–2.4	5140 H	2.2–3.1	8747 H	3.5–4.6
4042 H	1.7–2.4	5145 H	2.3–3.5	8750 H	3.8–4.9
4047 H	1.8–2.7	5150 H	2.5–3.7	9260 H	2.0–3.3
4047 H	1.7–2.4	5152 H	3.3–4.7	9261 H	2.6–3.7
4053 H	2.1–2.9	5160 H	2.8–4.0	9262 H	2.8–4.2
4063 H	2.2–3.5	6150 H	2.8–3.9	9437 H	2.4–3.7
4068 H	2.3–3.6	8617 H	1.3–2.3	9440 H	2.4–3.8
4130 H	1.8–2.6	8620 H	1.6–2.3	9442 H	2.8–4.2
4132 H	1.8–2.5	8622 H	1.6–2.3	9445 H	2.8–4.4

Source: Ref 16.16

manganese, are incorporated into the carbides, and slow their diffusion-controlled solution in austenite. Retained carbides therefore lower the amount of both carbon and alloying elements in the austenite that promote hardenability.

Early on, in a 1942 publication, Grossman, aware of undissolved carbides, made the following statement: ”It should be emphasized that in chromium steels (over 0.30% Cr) and Cr-Mo and Cr-V steels, undissolved carbides are likely to be present in the steel as-quenched, and that in such cases the charts can indicate only a maximum possible hardenability, whereas the extent of hardening actually obtained may be much less” (Ref 16.26).

This qualifying statement about the determination of ideal diameters is still valid for the low-alloy low- and medium-carbon steels most frequently hardened. Higher austenitizing temperatures will cause more carbides to dissolve and thereby will increase hardenability, but in higher-carbon steels with carbon contents approaching 0.5 wt% may cause adverse fracture resistance in the form of quench cracking and quench embrittlement.

For high-carbon steels, containing 0.60 to 1.10 wt% carbon, Jatczak extended the Grossmann-Bain approach to hardenability, and developed two sets of alloy multiplying factors depending on austenitizing temperature (Ref 16.27). At temperatures within the two-phase austenite/carbide phase field, multiplying factors are lower than when steels are fully aus-

tenitized at higher temperatures, above the A_{CM} temperature. Again, the reduced hardenability when alloy carbides are retained during austenitizing is a result of both the carbon and the alloying elements tied up in the carbides. Although the hardenability is lower, the mechanical properties of the martensite/carbide microstructures are excellent for applications such as bearings.

Over time the need to establish an austenitic grain size to determine hardenability has been largely eliminated, and grain size has been assumed to be constant at ASTM No. 7 (Ref 16.28). The reason for this change is that most low-alloy, medium-carbon hardenable steels are aluminum-killed and therefore fine-grained to austenitizing temperatures well above those recommended for industrial austenitizing, as shown in Fig. 8.16 in Chapter 8, "Austenite in Steel.". Despite the constant austenitic grain size over a range of temperatures in aluminum-killed steels, the amount of retained carbides, and therefore the hardenability, will vary depending on the austenitizing conditions used below the grain-coarsening temperature.

The Caterpillar Company developed a personal-computer-based program, the Caterpillar Hardenability Calculator (1E0024), that calculates Jominy curves based on steel composition (Ref 16.29). Thousands of heats of low-alloy steels such as AISI 41xx and 86xx steels were used to refine multiplying factors according to the Grossmann approach to hardenability. The calculator assumes an austenite grain size of ASTM Number 7 and provides multiplying factors for boron and nonboron steels. Copies of the Calculator can be obtained by directions given in Ref 16.29.

Jominy Test for Hardenability

Another important approach to the evaluation of hardenability is the use of the end-quench test developed by Walter Jominy and Alfred Boegehold while at the General Motors Laboratories in 1938 (Ref 16.30). The test is now commonly referred to as the *Jominy test* or *Jominy end-quench test*, and has the great advantage of characterizing the hardenability of a given steel from a single specimen rather than from a series of round bars. With identification of starting structures and austenitizing conditions, factors that affect undissolved carbides that influence hardenability as discussed in the previous section, it provides an excellent characterization of hardenability based on chemistry and microstructure.

Figure 16.22 shows the shape and dimensions of a Jominy specimen and the fixture for supporting the specimen in a quenching system. The specimen is cooled at one end by a column of water; thus, the entire specimen experiences a range of cooling rates between those associated with water cooling and those associated with air cooling. After quenching, parallel flats are ground on opposite sides of the specimen, and hardness readings are taken every $\frac{1}{16}$ in. from the quenched end and plotted as shown in Fig. 16.23. Hardenability differences between different grades

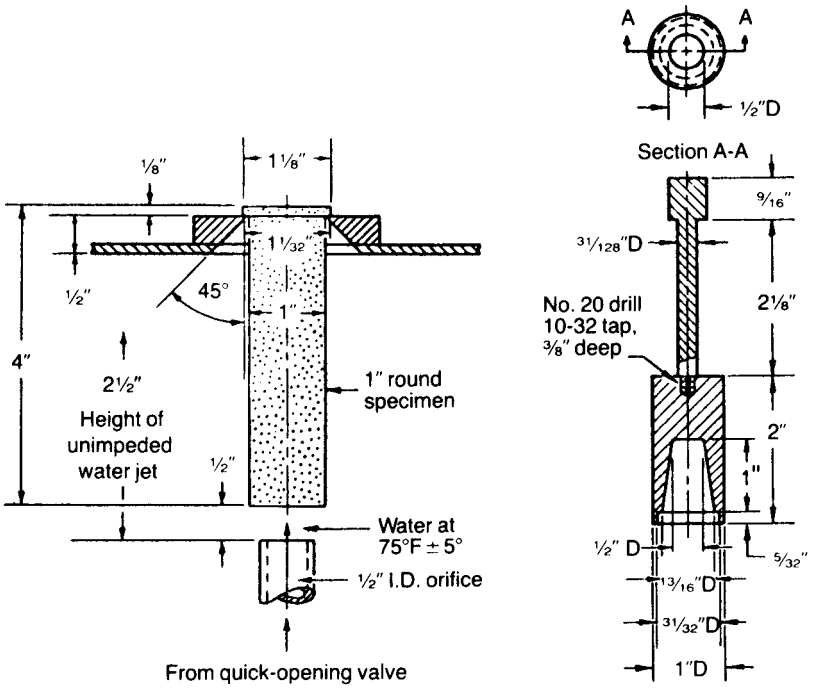

Fig. 16.22 Jominy-Boegehold specimen for end-quench test for hardenability. Source: Ref 16.16

of steels can be readily compared if Jominy curves are available. For example, Fig. 16.24 shows hardenability differences between different grades of alloy steels containing 0.5% C. Higher hardness persists to greater distances from the quenched end in the more hardenable steels.

The Jominy test method is now standardized in specifications of ASTM International (ASTM A255) and the Society of Automotive Engineers (SAE Standard J406). Figure 16.25 shows the method of presentation of the end-quench data for a single heat of AISI 8650 steel (Ref 16.31). For any grade of steel, a hardenability band (see Fig. 16.26) develops because of the small variations in composition allowable in the grade. The SAE/AISI steels designated by the letter *H* (H-steels) are guaranteed to meet established hardenabilities.

A very important feature of the Jominy test is that each position of the specimen corresponds to a well-known cooling rate. The top scale of Fig. 16.25 shows approximate cooling rates corresponding to positions on the Jominy specimen. As discussed previously, it is the cooling rate that determines the amount of martensite, and therefore the degree of hardness, that develops at a given point in a steel specimen. Therefore, if cooling rates as a function of position in parts of various geometries are known, it is possible to use Jominy curves to plot hardness profiles in the parts. Such cor-

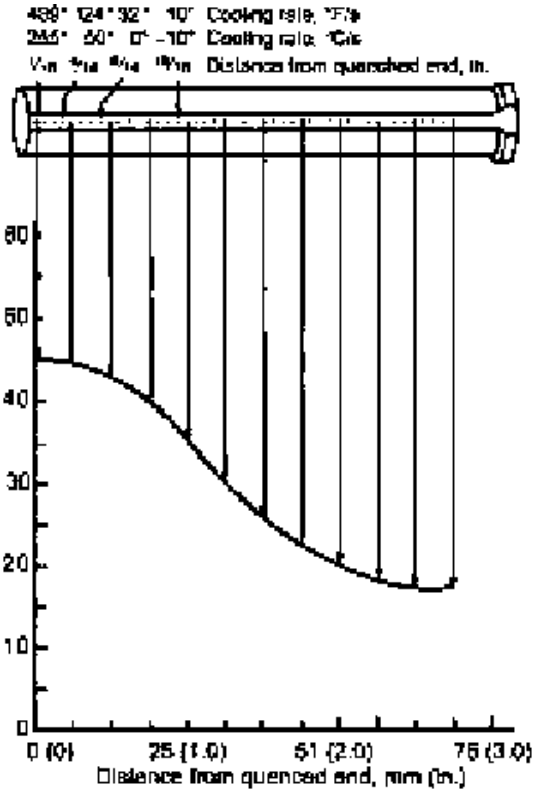

Fig. 16.23 Method of plotting hardness data from an end-quenched Jominy specimen. Source: Ref 16.21

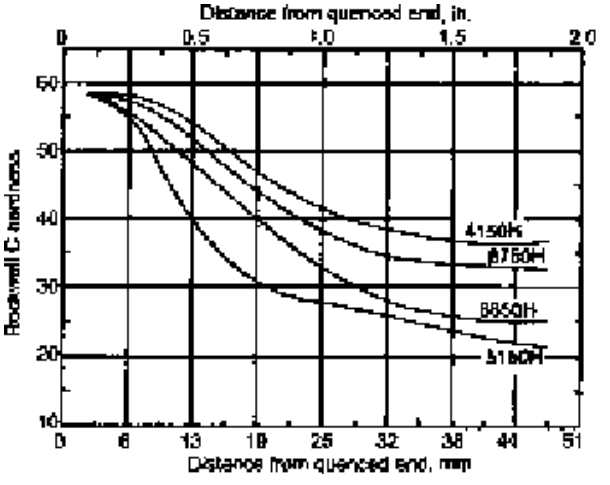

Fig. 16.24 Results of end-quench tests for four different grades of alloy steels, all containing 0.5% C. Source: Ref 16.21

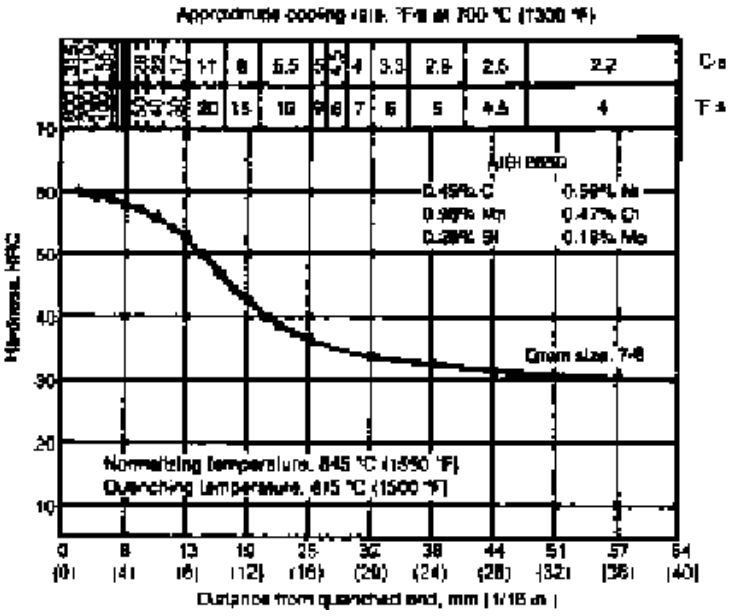

Fig. 16.25 Method for presenting end-quench hardenability data. Data presented here are for AISI 8650 steel. Note relationship of cooling rate (top) to distance from the quenched end. Source: Ref 16.31

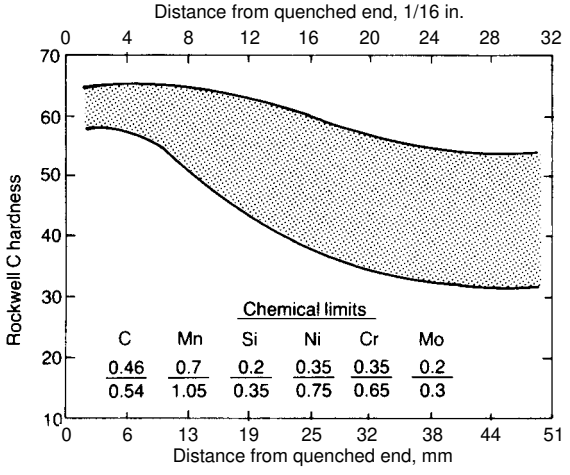

Fig. 16.26 Hardenability band for 8750H steel. Source: Ref 16.21.

relations of cooling rate as a function of position in various sizes of bars and plates quenched in various media are available (Ref 16.31). Figure 16.27 shows equivalent cooling rates for four positions in round bars quenched in water and oil. As bar diameter increases, the cooling rates at the surface and interior points decrease (see top scale of Fig. 16.27). The

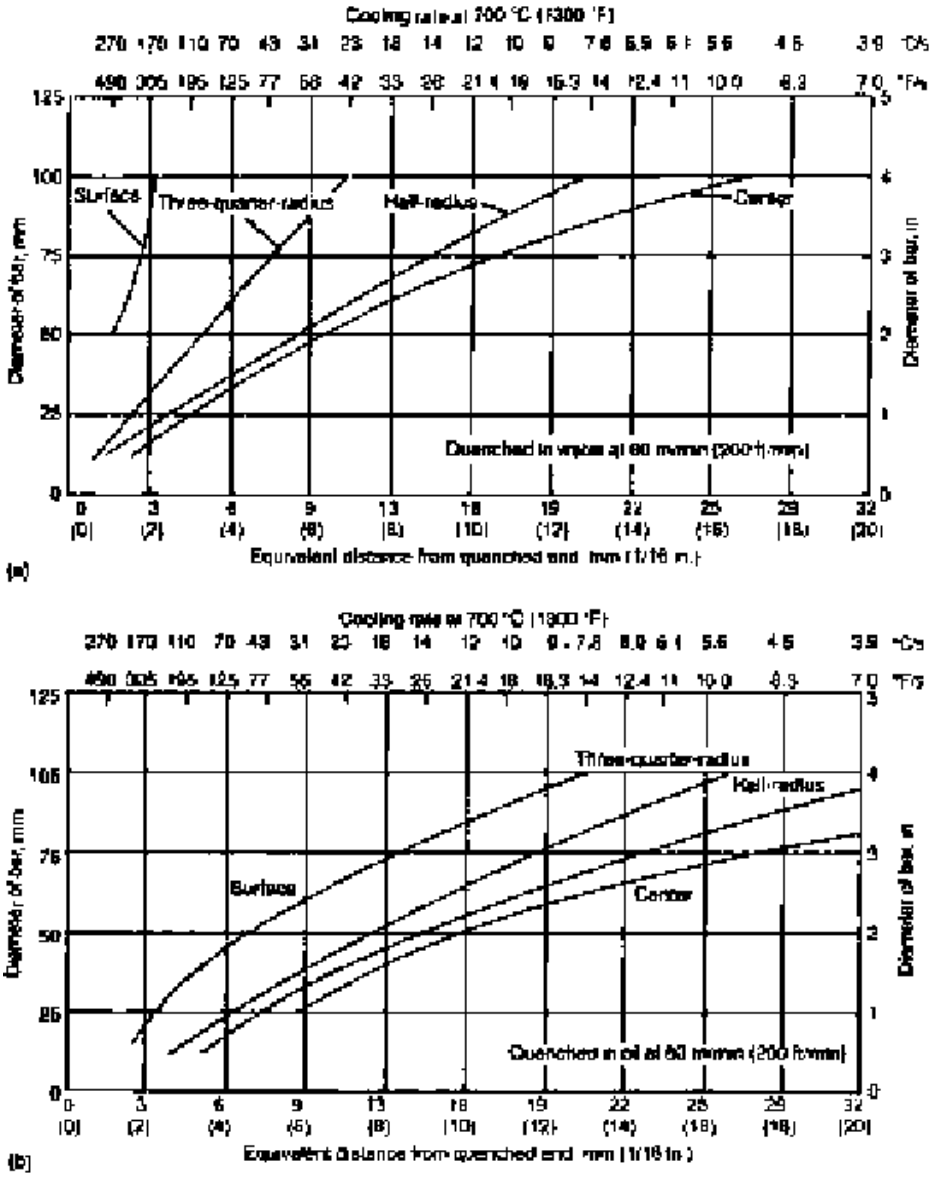

Fig. 16.27 Equivalent cooling rates for round bars quenched in (a) water and (b) oil. Correlation of equivalent cooling rates in the end-quenched hardenability specimen and quenched round bars free from scale. Data for surface hardness are for "mild agitation;" other data are for 60 m/min (200 ft/min). Source: Ref 16.31

cooling rates correspond to equivalent distances from the quenched end (see bottom scale of Fig. 16.27), and those distances can be used to determine the hardness distribution in the rounds from appropriate Jominy curves.

The use of the Jominy data as just described is a highly accurate method of selecting steels of just the right hardenability for a given required hard-

ness distribution. A steel that will not only satisfy the hardness requirements but also has just the right alloy content can be selected, therefore permitting selection at minimum cost from the many steels that might have sufficient or even excess hardenability for the application. On the other hand, alloy steels that can be hardened by moderate quenching may be selected to replace leaner steels in which the severe quenching required to obtain high hardness causes quench cracking.

Boron Effects and Hardenability

Boron in carbon steels is a unique alloying element, and sometimes a residual element from steelmaking, in carbon steels (Ref 16.32–16.35). Boron is a very strong nitride-forming element, ranking second only to titanium, as shown in Chapter 8, "Austenite in Steel," and provides much-enhanced hardenability in low- and medium-carbon steels with only very small additions. The strong nitride-forming ability of boron for some applications of low-carbon steels makes boron additions desirable to remove nitrogen from solution in ferritic microstructures in which, if present, it significantly reduces ductility and raises brittle-to-ductile impact transition temperatures, as discussed in Chapter 12, "Low Carbon Steel." Similarly, boron is added to some German grades of carburizing steels for the purpose of improving toughness by removing nitrogen from solution in high-carbon hardened microstructures.

Enhanced hardenability is the major reason for the addition of boron to steel. However a number of factors must be in place in order for the boron to be effective. First and foremost, the boron must be prevented from combining with nitrogen, which is accomplished by "protecting" the boron by the addition of the stronger nitride-forming element titanium. According to Thelning (Ref 16.36), the amount of titanium required to protect boron is given by the following equation:

$$\% \text{ Ti} = 5(\%\text{N} - 0.003) \qquad \text{(Eq. 16.3)}$$

Another factor regarding the effectiveness of boron for increased hardenability is the need to austenitize at a critical range of temperature prior to quenching for hardening. The mechanism by which boron increases hardenability is the segregation of boron to austenite grain boundaries, reducing the ability of ferrite to nucleate and grow at the austenite grain boundaries. At high austenitizing temperatures, the face-centered cubic matrix structure of the austenite is relaxed and can accommodate the boron atoms, making the boron ineffective. However, at lower temperatures, the boron atoms cannot be accommodated and to relieve matrix strain the boron atoms diffuse to austenite grain boundaries and improve hardenability. This effect of austenitizing temperature on the segregation of boron to austenite grain boundaries has been convincingly shown by

ion microprobe analysis by Ohmori and Yamanaka (Ref 16.37). At an austenitizing temperature of 930 °C (1705 °F) the grain boundary segregation of boron was much higher than after austenitizing at 1130 °C (2065 °F). At lower austenitizing temperatures iron borocarbide particles form, as discussed below, and reduce boron effectiveness in promoting hardenability.

A remarkable aspect regarding the effectiveness of boron on hardenability is that only very small amounts, on the order of 0.001% or 10 parts per million (ppm) by weight, are necessary in contrast to much larger amounts of substitutional alloying elements such as chromium, molybdenum, and nickel that are added to steels to promote hardenability. Fig. 16.28 shows the very strong effect of small amounts of boron on the hardenability of a low-carbon steel. The effect of boron peaks at around 0.001% B and then drops to a stable level as a result of iron borocarbide formation. Repeated heat treatments may reduce the effectiveness of boron on hardenability, an effect termed *boron fade*, also due to iron borocarbide formation. If austenitizing temperatures are high, nitrides formed by elements such as aluminum, vanadium, or niobium may go into solution with the nitrogen and then combine with the boron, reducing its effectiveness in providing hardenability.

Another factor that must be considered in the application of boron for hardenability is steel carbon content. Boron segregated at austenite grain boundaries is very effective in retarding the nucleation of ferrite, the major phase that limits hardenability in low-carbon steels, and ferrite is a major component of bainite in medium-carbon steels, in which, if formed, it lowers hardness relative to martensite. However, with increasing steel carbon content, the effectiveness of boron on hardenability decreases and

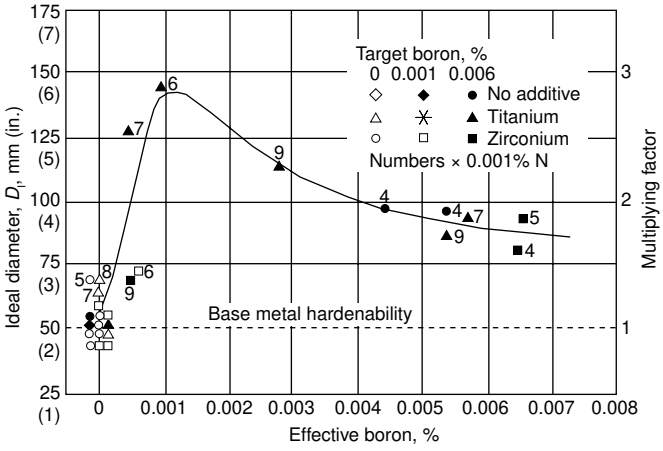

Fig. 16.28 Hardenability of an 8620 type steel, as measured by ideal diameter and multiplying factor, as a function of effective boron content. Source: Ref 16.38

effectively becomes negligible at carbon concentrations between 0.7 and 0.9%, as shown in Fig. 16.29.

As noted previously, a factor that limits the effectiveness of boron is the formation of iron borocarbides. These crystals have the chemistry $M_{23}(B,C)_6$, where M represents the metal fraction, consisting mainly of iron but also Mn and Cr (Ref 16.40). As a result of being tied up in the borocarbide, boron is not able to segregate and hardenability is reduced. There is a temperature above which the borocarbides do not form, and that temperature provides a lower boundary for the austenitizing of boron-containing steels. The formation of iron borocarbides is diffusion dependent and related to carbon and boron content, temperature, and time. Figure 16.30, taken from extensive studies by Taylor and Hansen of 0.2% C boron-containing steels subjected to various processing conditions, shows combinations of boron and carbon content and temperature for which $M_{23}(B,C)_6$ particles form (Ref 16.41, 16.42). Delay times prior to quenching were not influential except in the steels containing more than 50 ppm B. The dashed horizontal line is the temperature above which the borocarbides are not stable and will not form.

A phenomenon termed *superhardenability* has been associated with heats of steel thoroughly deoxidized with additions of aluminum and/or titanium, and superheated prior to teeming. An examination of a 0.30% C steel containing small amounts of the alloying elements nickel, chromium, and molybdenum and the nitride-forming elements aluminum and titanium, in which superhardenability was observed, showed that although boron was not added, the residual amount of boron of typically 3 ppm after steelmaking was raised by severe deoxidation to 8 ppm (Ref 16.43, 16.44). That boron was then protected by a residual titanium content of 0.04 wt%, and the hardenability as measured by Jominy testing was much higher than that compared to an almost identical steel with lower titanium

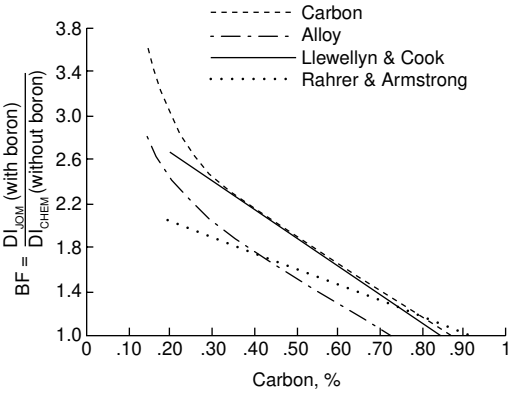

Fig. 16.29 Decrease in the boron factor (BF) with increasing steel carbon content. Source: Ref. 16.39

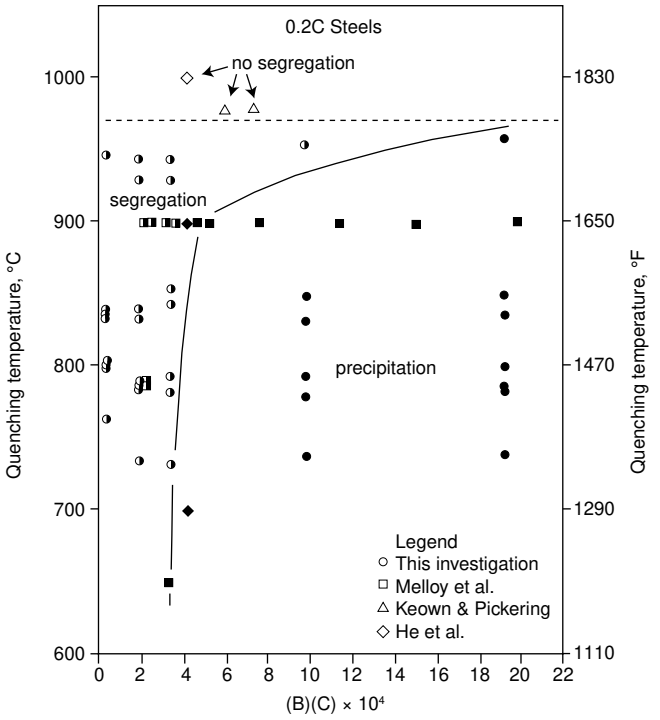

Fig. 16.30 Ranges of boron segregation and $M_{23}(B,C)_6$ precipitation as a function of quenching temperature and the product of B and C concentrations. Source: Ref 16.41

content. Without high titanium content, boron nitrides formed and reduced the effectiveness of residual boron on hardenability.

Phosphorus Effects and Hardenability

Phosphorus in steels is residual from steelmaking and is kept low because of its association with various forms of intergranular embrittlement that increase susceptibility to brittle fracture along prior austenite grain boundaries in hardened steels, as described in Chapter 19, "Low Toughness and Embrittlement Phenomena in Steels." The embrittlements are in part related to the known segregation of phosphorus to austenite grain boundaries during austenitizing prior to quenching, and are enhanced by other factors such as high carbon contents and hydrogen.

Apart from contributions to embrittlement, there are other effects of phosphorus related to microstructural changes in hardened steels. A strong effect is the ability of phosphorus to reduce the rate of hardness decrease during tempering of martensitic microstructures (Ref 16.45). This effect is related to observations that cementite particles resist coarsening and spheroidization, thereby slowing softening, in steels with higher phospho-

rus contents (Ref 16.46, 16.47), an effect attributed to the rejection of phosphorus from the crystal structure of cementite similar to the rejection of silicon from cementite. Direct evidence of the rejection of phosphorus from cementite has been shown by atom probe tomography (Ref 16.48).

Hardenability is also increased by higher phosphorus concentrations, provided steel carbon content is also high. Fig. 16.31 shows Jominy end-quench curves for 4130, 4140, and 4150 steels each with two levels of phosphorus (Ref 16.49,16.50). Phosphorus has almost no effect on hardenability in the 4130 steels, but an increasing effect as steel carbon content increases. Even with low phosphorus, increasing carbon content increases hardenability. The first decreases in hardness in the Jominy curves are associated with the formation of upper bainite, and the reduced rate of the bainite formation was related to retardation of the nucleation of the upper bainite at austenite grain boundaries. Once the bainite colonies had nucleated, their growth was unaffected by elevated phosphorus content.

The combined effect of carbon and phosphorus on hardenability is similar to the combined effect of carbon and phosphorus on quench embrittlement. When carbon content is low, even with higher phosphorus contents, hardenability is unaffected, and fracture in as-quenched or quenched-and-low-temperature-tempered low-alloy steels such as 4130 is ductile and does not occur by intergranular cracking. Thus the combination of phosphorus segregation and cementite formation, as occurs at austenite grain boundaries in higher carbon steels, produces a beneficial effect on hardenability but a negative effect on fracture and toughness.

Summary

A knowledge of hardenability is essential for the selection of steels, the design of their microstructures and properties for demanding applications, and the manufacturing, thermal processing, and heat treatments used to produce those microstructures and properties. There are many interrelated components of hardenability, ranging from the effect of alloying on the diffusion-controlled kinetics of solid-state phase transformations to the characterization of the heat transfer mechanisms of quenching media. In the 1970s two valuable symposia evaluated the state of the art of hardenability: *Hardenability Concepts with Applications to Steel* (Ref 16.51) and *The Hardenability of Steels—Concepts, Metallurgical Influences and Industrial Applications* (Ref 16.18). A detailed review of these two conferences is given in Ref 16.52. Much of the Grossmann-Bain approach remains a framework for establishing the hardenability of steels, but continued research and application have focused on modeling, assessment, and the integration of the many factors that influence hardenability of low-alloy carbon steels (Ref 16.29, 16.53–16.55). The Jominy end-quench test remains an extremely powerful experimental method to assess with respect to hardenability not only the chemistry of a steel but also micro-

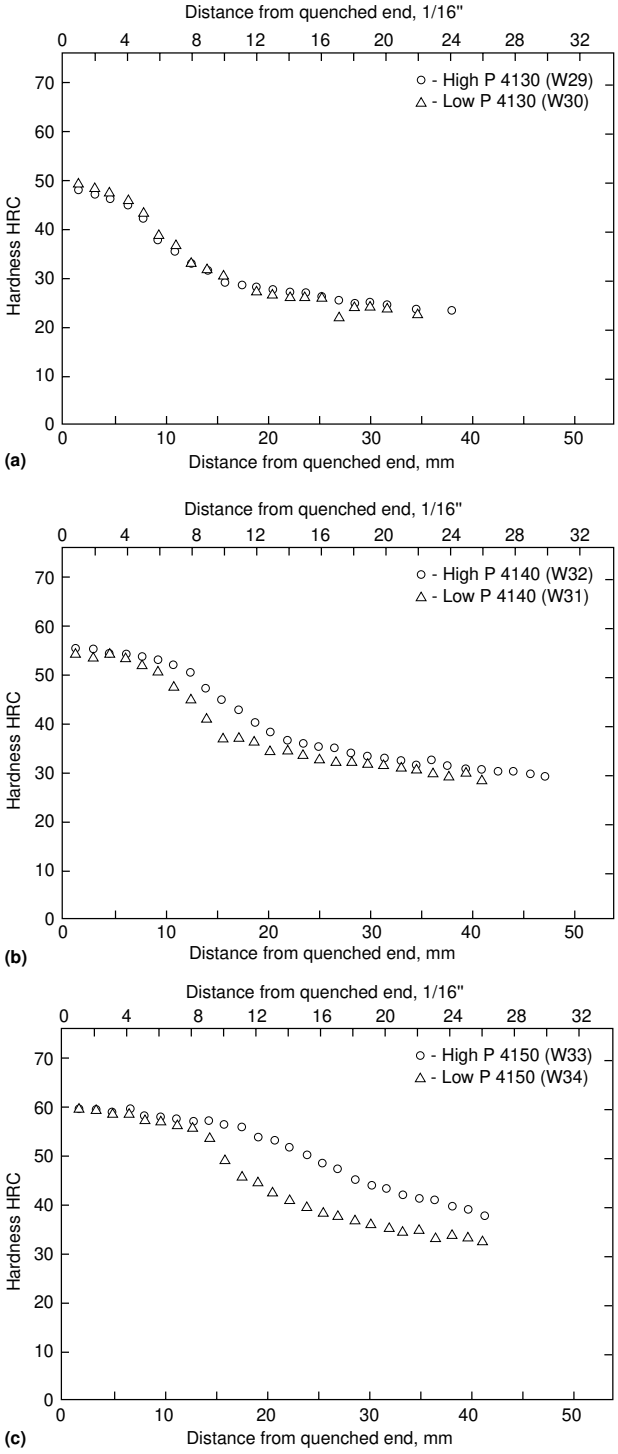

Fig. 16.31 Jominy end-quench curves for 4130 (top), 4140 (middle), and 4150 (bottom) steels each with low (0.002 %) and high (0.018 %) levels of phosphorus. Source: Ref 16.49

structural condition during austenitizing. The emphasis on quenching and quenchants presented in Ref 16.24 and 16.25 has been supplemented by two excellent reviews of the characterization, measurement, and control of cooling and heat transfer during quenching, factors that are essential in the manufacturing achievement of hardness by martensite formation (Ref 16.56, 16.57).

REFERENCES

16.1 E.C. Bain and H.W. Paxton, *Alloying Elements in Steel,* 2nd ed., American Society for Metals, 1961

16.2 G. Krauss, Martensitic Transformation, Structure and Properties in Hardenable Steels, *Hardenability Concepts with Applications to Steel,* D.V. Doane and J.S. Kirkaldy, Ed., AIME, Warrendale, PA, 1978, p 229–248

16.3 L.D. Jaffee and E. Gordon, Temperability of Steels, *Trans. ASM,* Vol 49, 1957, p 359–369

16.4 A.R. Marder, "The Morphology and Strength of Iron-Carbon Martensite," Ph.D. dissertation, Lehigh University, Bethlehem, PA, 1968

16.5 M. Cohen, The Strengthening of Steel, *Trans. TMS-AIME,* Vol 224, 1962, p 638–657

16.6 P.G. Winchell and M. Cohen, The Strength of Martensite, *Trans. ASM,* Vol 55, 1962, p 347–361

16.7 T.E. Swarr and G. Krauss, Boundaries and the Strength of Low Carbon Ferrous Martensites, *Grain Boundaries in Engineering Materials,* Claitor's Publishing Division, Baton Rouge, LA, 1975, p 127–138

16.8 T.E. Swarr and G. Krauss, The Effect of Structure on the Deformation of As-Quenched and Tempered Martensite in an Fe-0.2% C Alloy, *Metall. Trans. A,* Vol 7A, 1976, p 41–48

16.9 A.R. Marder and G. Krauss, The Effect of Morphology on the Strength of Lath Martensite, *Proceedings of Second International Conference on the Strength of Metals and Alloys,* Vol 3, American Society for Metals, 1970, p 822–823

16.10 M.J. Roberts, Effect of Transformation Substructure on the Strength and Toughness of Fe-Mn Alloys, *Metall. Trans.,* Vol 1, 1970, p 3287–3294

16.11 M. Cohen, Strengthening Mechanisms in Steel, *Trans. JIM,* Vol 9, 1968, Supplement

16.12 M.J. Roberts and W.S. Owen, Solid Solution Hardening and Thermally Activated Deformation in Iron-Nickel-Carbon Martensites, *J. Iron Steel Inst.,* Vol 206, 1968, p 375–384

16.13 G.R. Speich, Tempering of Low-Carbon Martensite, *Trans. TMS-AIME,* Vol 245, 1969, p 2553–2564

16.14 G.R. Speich and H. Warlimont, Yield Strength and Transformation Substructure of Low-Carbon Martensite, *J. Iron Steel Inst.,* Vol 206, 1968, p 385–392
16.15 W.H. McFarland, Mechanical Properties of Low-Carbon Alloy-Free Martensite, *Trans. TMS-AIME,* Vol 233, 1965, p 2028–2035
16.16 M.A. Grossmann and E.C. Bain, *Principles of Heat Treatment,* 5th ed., American Society for Metals, 1964
16.17 Definition Relating to Metals and Metalworking, *Properties and Selection*, Vol 1, *Metals Handbook,* 8th ed., American Society for Metals, 1961, p 20
16.18 C.A. Siebert, D.V. Doane, and D.H. Breen, *The Hardenability of Steels—Concepts, Metallurgical Influences, and Industrial Applications,* American Society for Metals, 1977
16.19 Classification and Designation of Carbon and Alloy Steels, *Properties and Selection: Irons and Steels*, Vol 1, *Metals Handbook,* 9th ed., American Society for Metals, 1978, p 117–143
16.20 N.B. Pilling and T.D. Lynch, Cooling Properties of Technical Quenching Liquids, *Trans. AIME,* Vol 62, 1920, p 665
16.21 G.F. Melloy, *Hardness and Hardenability,* P.D. Harvey, Ed., Metals Engineering Institute, Metals Park, OH, 1977
16.22 M.A. Grossmann and M. Asimov, Hardenability and Quenching, *Iron Age,* Vol 145, 1940, p 25–29, 39–45
16.23 F. Wever, *Archiv fü r das Eisenhü ttenwesen,* Vol 5, 1936–37, p 367
16.24 Theory and Technology of Quenching, B. Liscic, H.M. Tensi, and W. Luty, Ed., Springer-Verlag, Berlin, 1992
16.25 G.E. Totten, C.E. Bates, and N.A. Clinton, *Handbook of Quenchants and Quenching Technology,* ASM International, 1993
16.26 M.A. Grossmann, Hardenability Calculated from Chemical Composition, AIME Technical Publication No. 1437, 1942
16.27 C.F. Jatczak, Hardenability in High Carbon Steels, *Metall. Trans.,* Vol. 4, 1973, p 2267–2277
16.28 *Standard Test Methods for Determining Hardenability of Steel,* ASTM Designation A255-10, 2012
16.29 M. Maniruzzaman and M.T. Kiser, Caterillar Hardenability Calculator (1E0024), *Steel Heat Treating Fundamentals and Processes*, Vol 4A, *ASM Handbook*, ASM International, 2013, p 64–71
16.30 W.E. Jominy and A.L. Boegehold, A Hardenability Test for Carburizing Steel, *Trans. ASM,* Vol 26, 1938, p 574–606
16.31 C.F. Jatczak, Hardenability of Carbon and Alloy Steels, *Properties and Selection: Irons and Steels*, Vol 1, *Metals Handbook,* 9th ed., American Society for Metals, 1978, p 471–526
16.32 D.T. Llewellyn and W.T. Cook, Metallurgy of boron-treated low-alloy steels, *Metals Technology,* 1974, p 517–529
16.33 *Boron in Steel*, S.K. Banerji and J.E. Morral, Editors, TMS of AIME, Warrendale, PA, 1980

16.34 P. Maitrepierre, D. Thivellier, J. Rofes-Vernis, D. Rousseau, and R. Tricot, Microstructure and Hardenability of Low-Alloy Boron-Containing Steels, *Hardenability Concepts with Applications to Steel,* AIME, Warrendale, PA, 1978, p 421–447

16.35 B.M. Kapadia, Prediction of the Boron Hardenability Effect in Steel—A Comprehensive Review, *Hardenability Concepts with Applications to Steel,* AIME, Warrendale, PA, 1978, p 448–482

16.36 K.E. Thelning, *Steel and Its Heat Treatment, 2nd ed.,* Butterworths, London, 1984

16.37 Y. Ohmori and K. Yamanaka, Hardenability of Boron-Treated Low Carbon Low Alloy Steels, *Boron in Steel*, S.K. Banerji and J.E. Morral, Editors, TMS of AIME, Warrendale, PA, 1980, p 44–60

16.38 *Properties and Selection: Irons, Steels, and High-Performance Alloys*, Vol 1, *ASM Handbook*, 10th ed., ASM International, 1990, p 470

16.39 C.T. Kunze and G. Keil, A New Look at Boron Effectiveness in Heat Treated Steels, *Boron in Steel*, S.K. Banerji and J.E. Morral, Editors, TMS of AIME, Warrendale, PA, 1980, p 106–126

16.40 P. Rogl, J.C. Schuster, H. Nowotny, Phase Equilibrium and Compound Formation in Fe-M (Metal)-B-X(Nonmetal) Systems, *Boron in Steel*, S.K. Banerji and J.E. Morral, Editors, TMS of AIME, Warrendale, PA, 1980, p 33–43

16.41 K.A. Taylor and S.S. Hansen, The Boron Hardenability Effect in Thermomechanically Processed, Direct-Quenched 0.2 Pct C Steels, *Metall. Trans. A*, Vol 12A, 1990, p 1697–1708

16.42 K.A. Taylor, Grain-Boundary Segregation and Precipitation of Boron in 0.2 Percent Carbon Steels, *Metallurgical Transactions A*, Vol 23A, 1992, p 107–119

16.43 J.B. Breedis and L.J. Cuddy, A Mechanism for Enhanced Hardenability, *Proceedings of the International Conference on Martensitic Transformations, 1993,* Monterey Institute for Advanced Studies, Monterey California, 1993, p 445–450

16.44 M.D. Irwin, *Superhardenability and the Boron Effect,* M.S. thesis, The Pennsylvania State University, 1994

16.45 R.A. Grange, C.R. Hribal, and L.F. Porter, Hardness of Tempered Martensite in Carbon and Low-Alloy Steels, *Metall. Trans. A*, Vol 8A, 1977, p 1775–1785

16.46 E.L. Brown and G. Krauss, Retained Carbide Distrbution in Intercritically Austenitized 52100 Steel, *Metall. Trans A*, Vol 17A, 1986, p 31–36

16.47 B.A. James, D.K. Matlock, and G. Krauss, Interactive Effects of Phosphorus and Tin on Carbide Evolution and Fatigue Properties of 5160 Steel, *38th MWSP Conference Proceedings*, ISS, Vol. 34, 1997, p 579–59

16.48 A.J. Clarke, M.K. Miller, R.D. Field, D.R. Coughlin, P.J. Gibbs, K.D. Clarke, D.J. Alexander, K.A. Powers, P.A. Papin, G. Krauss,

Atomic and Nanoscale Chemical and Structural Changes in Quenched and Tempered 4340 Steel, *Acta Mater.,* Vol 77, September 2014, p 17–24

16.49 F.A. Jacobs and G. Krauss, The Effects of Phosphorus and Carbon on the Hardenability of 41xx Type Steels, *J. Heat Treat.*, Vol. 2, No. 2, 1981, p 139–146

16.50 F.A. Jacobs and G. Krauss, Effects of carbon and phosphorus on bainite formation and hardenability in Cr-Mo medium carbon steels, *Proceedings of Third International conference on Heat Treatment of Materials,* Shanghai, China, Book No. 310, the Metals Society, 1984, p 5.24–5.31

16.51 *Hardenability Concepts with Applications to Steel,* D.V. Doane and J.S. Kirkaldy, Ed., AIME, Warrendale, PA, 1978

16.52 D.V. Doane, Application of Hardenability Concepts in Heat Treatment of Steel, *J. Heat Treat.,* Vol 1, 1979, p 5–30

16.53 Bozidar Liscic, Hardenability, *Steel Heat Treatment Handbook, 2nd ed.,* George Totten, Ed., CRC Press, 2006, p 213–276

16.54 Hardenability Calculation of Carbon and Low-Alloy Steels with Low or Medium Carbon, *Steel Heat Treating Fundamentals and Processes*, Vol 4A, *ASM Handbook*, J. Dossett and G.E. Totten, Ed., ASM International, 2013, p 60–73

16.55 *Thermal Engineering of Steel Alloy Systems*, , Vol 12, *Comprehensive Materials Processing,* George Krauss, Ed., Elsevier, 2014

16.56 E. Troell, H. Kristoffersen, J. Bodin, and S. Segerberg, Controlling the Cooling Process—Measurement, Analysis, and Quality Assurance, *Thermal Engineering of Steel Alloy Systems*, Vol 12, *Comprehensive Materials Processing,* George Krauss, Ed., Elsevier, 2014, p 99–121

16.57 B. Liscic and S. Singer, Calculcation of the Heat Transfer Coefficient Based on Experiments by the Liscic Probes, *Thermal Engineering of Steel Alloy Systems*, Vol 12, *Comprehensive Materials Processing,* George Krauss, Ed., Elsevier, 2014, p 123–176

CHAPTER 17

Tempering of Steel

MOST STEELS that are hardened are subjected to a subcritical heat treatment referred to as *tempering*. Tempering improves the toughness of as-quenched martensitic microstructures but lowers strength and hardness. This chapter describes the mechanical property and microstructural changes that develop during tempering. The most important structural changes involve the formation of various distributions of ferrite and carbides as the supersaturation of as-quenched martensite is relieved and equilibrium mixtures of phases are approached with increased tempering intensity. Embrittlement phenomena that develop on tempering and additional characterization of quenched and tempered steel mechanical behavior are presented in later chapters.

Mechanical Property Changes

Martensite, the object of the quenching treatments described in Chapter 16, "Hardness and Hardenability," is quite hard but may be very brittle. The low toughness of martensitic microstructures is due to a number of factors that may include the lattice distortion caused by carbon atoms trapped in the octahedral sites of the martensite (see Fig. 16.5 in Chapter 16, "Hardness and Hardenability"), impurity atom segregation at austenite grain boundaries, carbide formation during quenching, and residual stresses produced during quenching. Tempering is the heat treatment of hardened steels that has reduction of brittleness or increased toughness as its major objective. Any temperature up to the lower critical may be used for tempering; thus, an extremely wide variation in properties and microstructure ranging from those of as-quenched martensite to spheroidized carbides in ferrite can be produced by tempering. Ultimately it is the balance of hardness (or strength) and toughness required in service that determines the conditions of tempering for a given application. In addition to the tempering-induced changes in properties outlined in this chapter,

Chapter 18, "Deformation, Mechanical Properties, and Fracture of Quench and Tempered Carbon Steels," describes in more detail the effect of tempering on deformation, properties, and fracture of hardened carbon steels.

Figure 17.1 shows impact toughness as a function of tempering temperature for hardened 0.4 and 0.5% C steels (Ref 17.1). There are two tempering temperature ranges that produce significant improvement in toughness from that of the as-quenched state. Tempering in the range of 150 to 200 °C (300 to 400 °F) produces a modest increase in toughness that is adequate for applications that require high strength and fatigue resistance (medium-carbon steels) or where loading is primarily compressive as in bearings and gears (high-carbon steels). The latter applications require the high hardness and associated good wear resistance that high-carbon martensite and light tempers provide. Above 425 °C (800 °F) is the other important tempering temperature range. Figure 17.1 shows that toughness improves significantly after tempering in this range, but as noted subsequently, hardness and strength also decrease significantly. Therefore, tempering above 425 °C is used where high toughness is of major concern, and strength and hardness are important but of secondary concern. Figure 17.1 shows that toughness may actually decrease if steels are tempered in the range of 260 to 370 °C (500 to 700 °F). This decrease in toughness is referred to as tempered martensite embrittlement, 350 °C embrittlement, or 500 °F embrittlement, and is discussed in more detail in Chapter 19, "Low Toughness and Embrittlement Phenomena in Steels." As a result of this embrittlement, the tempering range between 260 and 370 °C is generally avoided in commercial practice. Another type of embrittlement, temper embrittlement, may develop in martensitic steels tem-

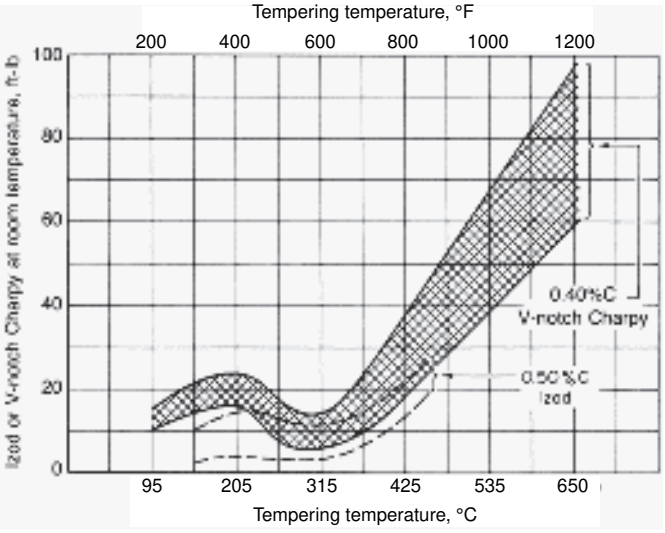

Fig. 17.1 Impact toughness as a function of tempering temperature of hardened, low-alloy, medium-carbon steels. Source: Ref 17.1

pered above 425 °C. Temper embrittlement occurs in certain alloy steels as a result of holding in or slow cooling through certain tempering temperature ranges, and is also discussed in more detail in Chapter 19, "Low Toughness and Embrittlement Phenomena in Steels."

Finally, Fig. 17.1 also shows the substantial effect that increasing carbon content has on impact toughness by comparing the results of tempering 0.5% C steels to those of 0.4% C steels. Steels with carbon contents of 0.5% or greater have very low impact toughness and are used only where high hardness, wear resistance, and/or edge retention are of prime importance. For example, hand tools, such as screwdriver blades and cutting blades of all sorts, are made from quenched and low-temperature tempered medium- and high-carbon steels. Wear resistance and cutting edge retention are excellent in these applications, but the higher the carbon content of the steel, the more susceptible the tool becomes to fracture under bending or tensile stresses. The reasons for decreasing toughness with increasing carbon content of quenched and low-temperature tempered steels are related to quench embrittlement as discussed in Chapter 19, "Low Toughness and Embrittlement Phenomena in Steels."

Figure 17.2, taken from a variety of sources by Grossmann and Bain (Ref 17.1), shows how hardness decreases from the maximum associated with as-quenched martensite with increasing tempering temperature. The effect of carbon content is also shown. The lower hardness of low-carbon steels in the as-quenched condition and throughout tempering is empha-

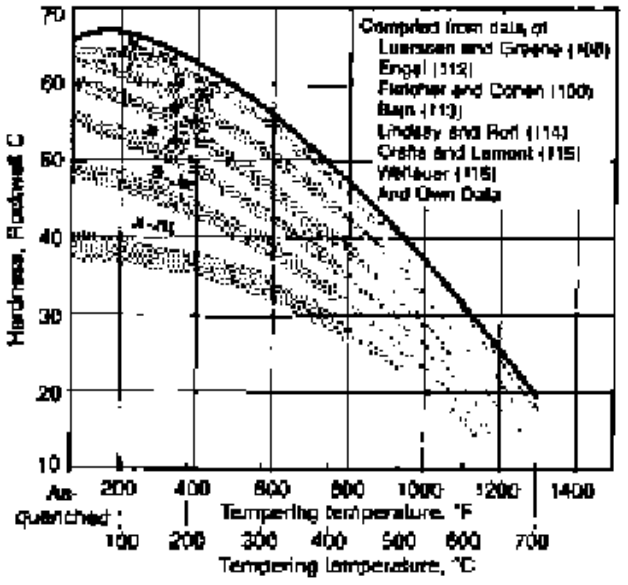

Fig. 17.2 Decrease in hardness with increasing tempering temperature for steels of various carbon contents. Ref numbers after investigators are from list in Grossmann and Bain. Source: Ref 17.1

sized in the curves. Therefore, if maximum hardness is desired, a high-carbon steel should be selected and tempering should be restricted to the 150 to 200 °C (300 to 400 °F) temperature as noted previously. Figure 17.2 indicates a slight hardness increase on low-temperature tempering of the highest carbon steels. Figure 17.3, from an investigation of the early stages of tempering of martensite in an Fe-1.22C alloy (Ref 17.2), shows tempering times and temperatures that produce an increase in hardness above that associated with the as-quenched state. This increase in hardness is a result of the precipitation of a dense distribution of very fine transition carbide particles within the martensite plates.

Generally, the interplay of hardness and toughness is of major concern in the heat treatment and application of quench and tempered steels. However, the changes in other mechanical properties with increasing tempering are also tabulated for common grades of carbon and alloy steel bars (Ref 17.3) and are quite important for the selection of steels and design of heat treatments for some applications. Figure 17.4 shows the changes in mechanical properties that occur when an oil-quenched AISI 4340 steel is tempered at temperatures above 200 °C . Both yield strength and tensile strength decrease continuously and elongation and reduction of area increase with increasing tempering temperature. The as-quenched hardness and the mechanical properties of 4340 steel for selected tempering treatments as a function of bar size are listed in Table 17.1. The strength properties for a given treatment decrease with increasing bar diameter (see Chapter 16, "Hardness and Hardenability").

Figure 17.4 shows two other aspects of the mechanical behavior of tempered carbon steels. One is the fact that there is no decrease in ductility produced by tempering in the temperature range that produces tempered martensite embrittlement. Specimen design and testing account for this observation. The toughness data shown in Fig. 17.1 are based on impact toughness testing accomplished by loading notched specimens at a high strain rate. Figure 17.4, on the other hand, is based on tensile testing of

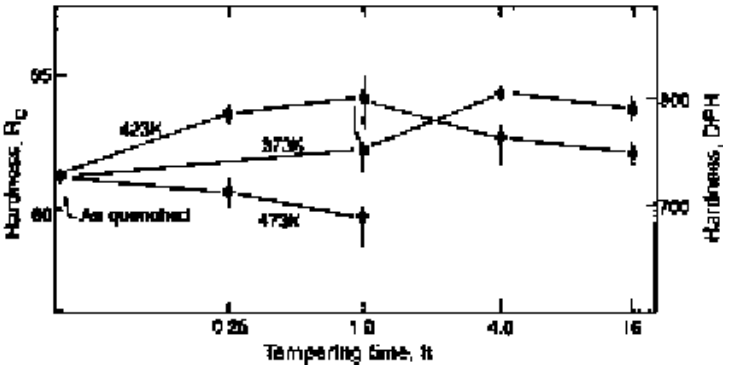

Fig. 17.3 Hardness as a function of time at three tempering temperatures for martensite in an Fe-1.22C alloy. Source: Ref 17.2

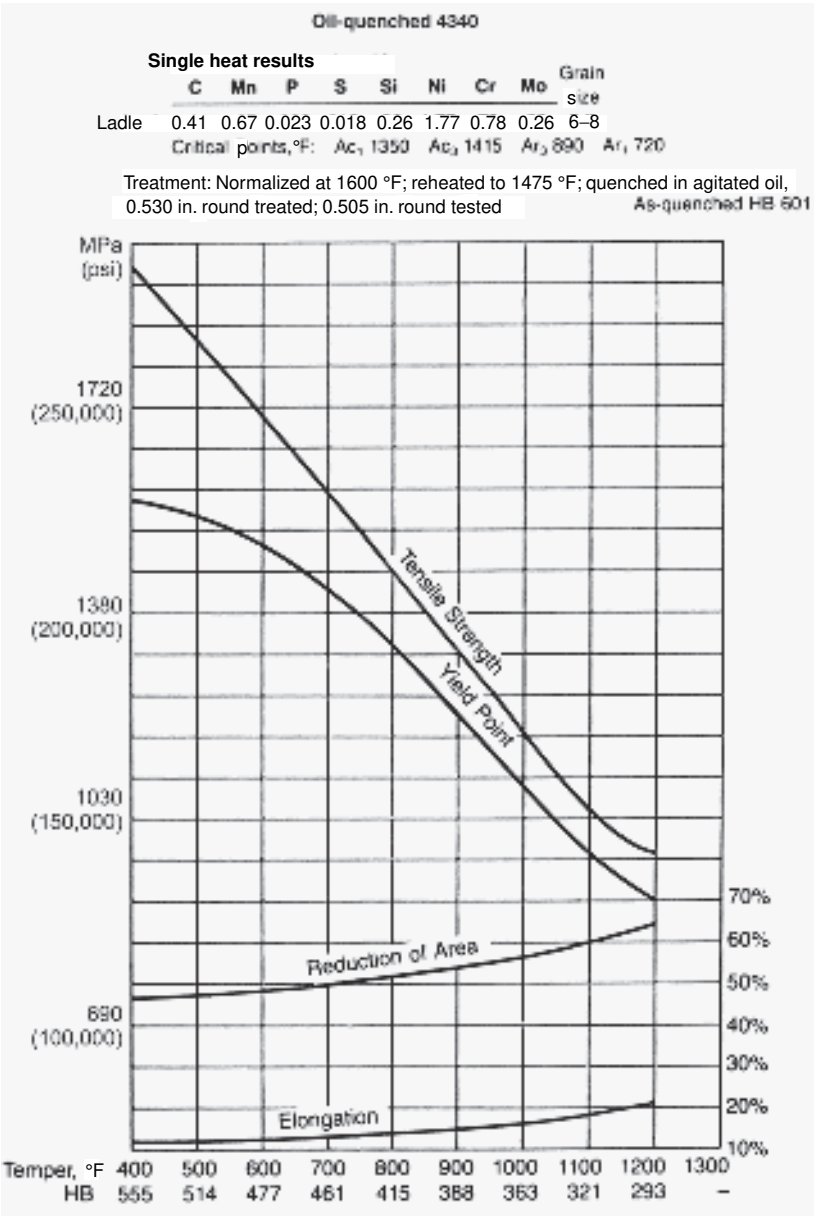

Fig. 17.4 Change in mechanical properties with tempering temperature for oil-quenched 4340 steel. Source: Ref 17.3

smooth round specimens at relatively slow strain rates. Thus, at slow strain rates, without the stress-concentrating effect of a notch, the microstructure of a steel tempered even in the range 260 to 370 °C (500 to 700 °F) can accommodate loading without undue embrittlement. On impact loading, however, the reverse is true and disregard of strain rate and notch effects may lead to unexpected failure in certain applications.

Table 17.1 Mechanical properties of various size rounds of a single heat of 4340 steel after various heat treatments illustrating mass effects

Size round		Tensile strength		Yield strength		Elongation in 50 mm	Reduction	Hardness,
mm	in.	MPa	ksi	MPa	ksi	(2 in.), %	in area, %	HB
Annealed: heated to 810 °C (1490 °F), furnace cooled 12 °C/h (20 °F/h) to 354 °C (670 °F), air cooled								
25.4	1	745	108	472	68.5	22.0	49.9	217
Normalized: heated to 871 °C (1600 °F), air cooled								
12.7	½	1448	210	972	141	12.1	35.3	388
25.4	1	1282	186	862	125	12.2	36.3	363
50.8	2	1220	177	793	115	13.5	37.3	341
101.6	4	1110	161	710	103	13.2	36.0	321
Oil quenched from 800 °C (1475 °F), tempered at 538 °C (1000 °F)								
12.7	½	1255	182	1165	169	13.7	45.0	363
25.4	1	1207	175	1145	166	14.2	45.9	352
50.8	2	1172	170	1103	160	16.0	54.8	341
101.6	4	1138	165	1000	145	15.5	53.4	331
Oil quenched from 800 °C (1475 °F), tempered at 593 °C (1110 °F)								
12.7	½	1145	166	1117	162	17.1	57.0	331
25.4	1	1138	165	1096	159	16.5	54.1	331
50.8	2	1014	147	958	139	19.0	60.4	293
101.6	4	924	134	793	115	19.7	60.7	269
Oil quenched from 800 °C (1475 °F), tempered at 650 °C (1200 °F)								
12.7	½	1000	145	938	136	20.0	59.3	285
25.4	1	958	139	883	128	20.0	59.7	277
50.8	2	931	135	834	121	20.5	62.5	269
101.6	4	855	124	730	106	21.7	63.0	255

As-quenched hardness (oil), HRC

Size round				
mm	in.	Surface	½ radius	Center
12.7	½	58	58	56
25.4	1	57	57	56
50.8	2	56	55	54
101.6	4	53	49	47

Ladle composition: 0.40 C; 0.68 Mn; 0.020 P; 0.013 S; 0.28 Si; 1.87 Ni; 0.74 Cr; 0.25 Mo; grain size 7–8. Source: Ref 17.3

Figure 17.4 also shows that the yield and tensile strengths of the tempered 4340, at first well separated after tempering at low temperatures, tend to approach each other after tempering at high temperatures. This effect is a common characteristic of hardened carbon and low-alloy steels and is related to differences in work-hardening behavior that develop on tempering. Figure 17.5 shows stress-strain curves that illustrate the changes in work hardening that develop with tempering of lath martensite in an Fe-0.2C alloy (Ref 17.4). In this case, the as-quenched martensite was obtained by quenching in a NaOH-NaCl solution and tempering was performed by heating in lead at 400 °C (750 °F) for 1 min. The work-hardening rate in the as-quenched specimen was quite high, as shown by the rapid increase in stress with increasing strain, while the stress-strain curve for the tempered specimen was almost flat, indicating a very low rate of work hardening. This difference in work-hardening behavior is attributed to interaction of dislocations with relatively coarse particles of cementite that form on tempering. In as-quenched specimens, dislocations

tangle and form a tight substructure of fine cells with increasing deformation, but with large cementite particles present, the dislocations remain uniformly distributed and a well-defined dislocation cell structure never develops. Figure 17.6 shows a uniform distribution of dislocations in the tempered Fe-0.2C martensite. This distribution did not change on deformation (Ref 17.4).

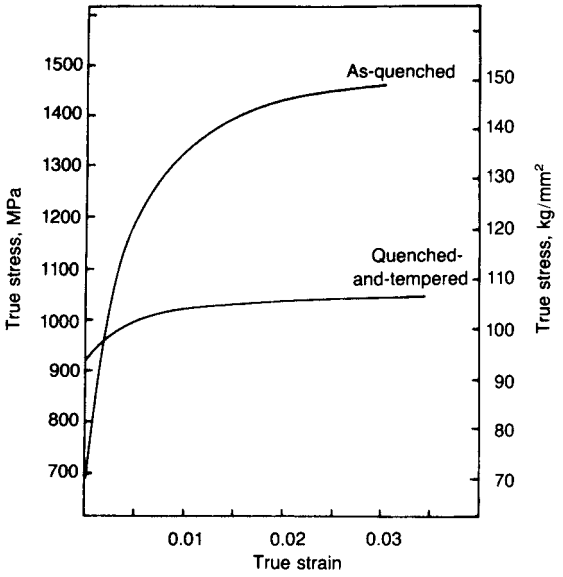

Fig. 17.5 True stress–true strain curves for Fe-0.2C as-quenched and quenched-and-tempered lath martensite with packet size of 8.2 μm. Source: Ref 17.4

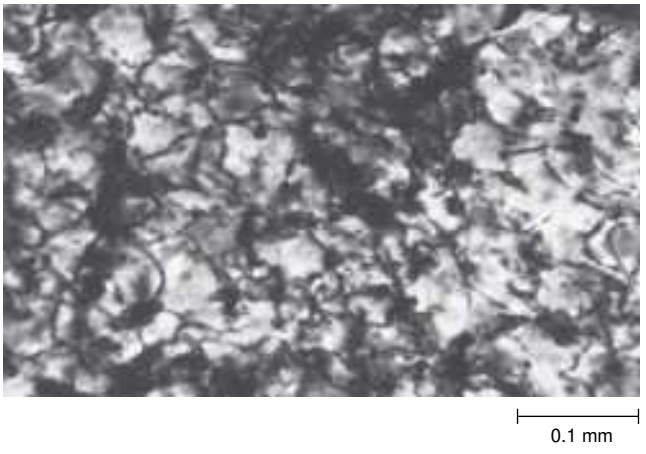

Fig. 17.6 Substructure of lath martensite in 0.2% C steel tempered for 1 minute at 400 °C. Transmission electron micrograph. Courtesy of Thomas Swarr, while at Lehigh University

Alloying Elements and Tempering

In addition to increasing hardenability, certain alloying elements also help to retard the rate of softening during tempering. The most effective elements in this regard are strong carbide formers such as chromium, molybdenum, and vanadium. Without these elements, iron-carbon alloys and low-carbon steels soften rapidly with increasing tempering temperature as shown in Fig. 17.2. Figure 17.7 (Ref 17.5) similarly shows the softening

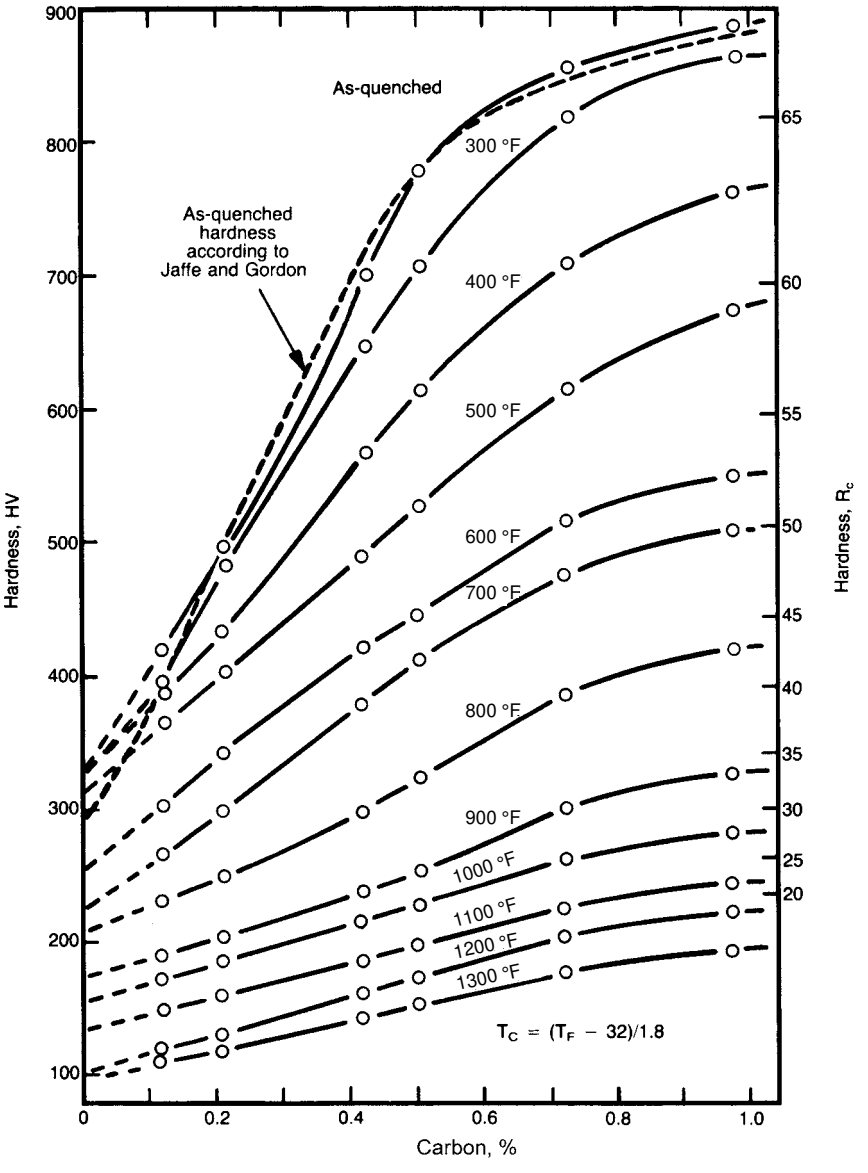

Fig. 17.7 Hardness as a function of carbon content of martensite in Fe-C alloys tempered at various temperatures. Source: Ref 17.5

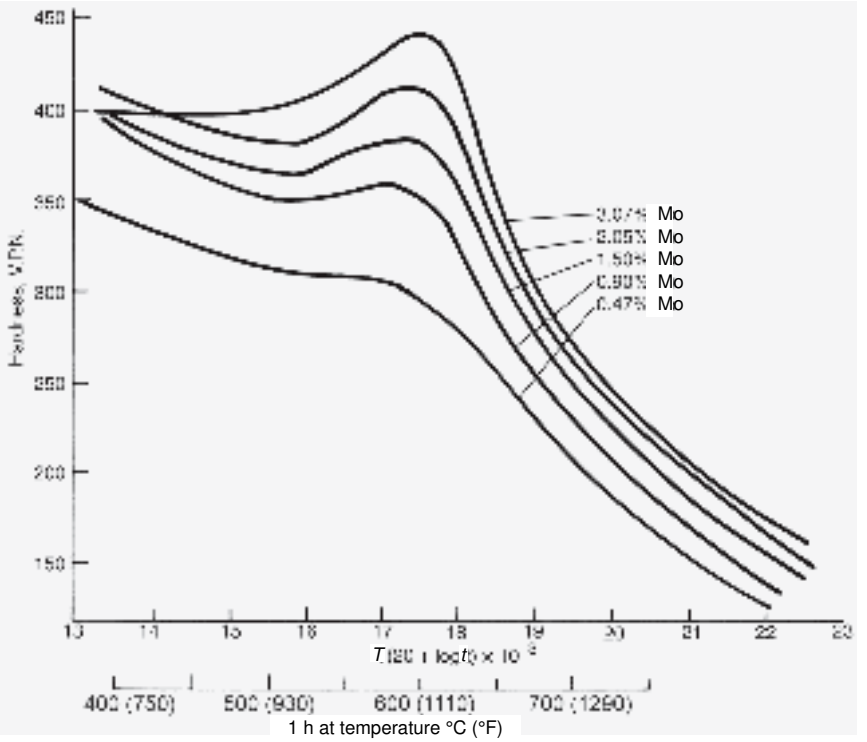

Fig. 17.8 Retardation of softening and secondary hardening during tempering of steels with varying molybdenum content. Source: Ref 17.6

as a function of tempering and carbon content in another form of diagram. This softening is largely due to the rapid coarsening of cementite with increasing tempering temperature, a process dependent on the diffusion of carbon and iron. If present in a steel in sufficient quantity, however, the carbide-forming elements not only retard softening but may also form fine alloy carbides that produce a hardness increase at higher tempering temperatures. This hardness increase is frequently referred to as *secondary hardening*.

Figure 17.8 shows secondary hardening in a series of steels containing molybdenum (Ref 17.6, 17.7). The higher the molybdenum content, the higher is the hardness associated with the secondary hardening peak, and even at 0.47% Mo when no hardness peak is observed, a significant retardation of softening is apparent. The secondary hardening peaks develop only at high tempering temperatures because alloy carbide formation depends on the diffusion of the carbide-forming elements, a more sluggish process than that of carbon and iron diffusion. As a result, not only is a finer dispersion of particles produced, but also once formed, the alloy carbides are quite resistant to coarsening. The latter characteristic of the fine alloy carbides is used to advantage in tool steels that must not soften even though high temperatures are generated by their use in hot working dies or high-speed machining. Also, ferritic low-carbon steels containing chro-

mium and molybdenum are used in pressure vessels and reactors operated at temperatures around 540 °C (1000 °F) because the alloy carbides resist coarsening at those temperatures and therefore provide good creep resistance (Ref 17.8).

Up to this point, tempering has been discussed with temperature as the major variable. The structural changes responsible for the property changes, however, are thermally activated and therefore dependent on both temperature and time. For example, if a single mechanism of structural change is operating during a stage of tempering, say the coarsening of cementite, a given hardness may be obtained by tempering at a high temperature for a short time or by tempering at a lower temperature for a longer time. Generally, if time is not mentioned, as is the case for most of the preceding figures, a constant tempering time of 1 h is assumed.

The interchangeability of time and temperature is accomplished by use of a tempering parameter, $T(20 + \log t) \times 10^{-3}$, where T is temperature in Kelvin, and t is time in hours. Figure 17.8 shows hardness changes plotted as a function of the tempering parameter as well as a function of tempering temperature where the time has been held constant at 1 h. Thus, in a given alloy, tempering treatments with times other than 1 h may be selected to obtain a given hardness. While the tempering parameter is successfully applied to plain carbon steels, caution must be used in applying it to secondary hardening steels. During secondary hardening, the maximum hardness obtained on tempering is frequently a function of temperature (Ref 17.7, 17.8). For example, a higher maximum hardness may be obtained by holding at 600 °C (1110 °F) rather than at 700 °C (1290 °F), and it would be impossible to reproduce the 600 °C hardness maximum even with very short-time tempering at 700 °C. This inability of different combinations of time and temperature to reproduce the same hardness is due to the somewhat coarser distribution of alloy carbides and/or their lower degree of coherency with the matrix at higher secondary hardening temperatures.

The effect of alloying elements on hardness changes produced by tempering martensitic carbon and low-alloy steels has been summarized in an investigation by Grange et al. (Ref 17.5). Steels with silicon, manganese, phosphorus, nickel, chromium, molybdenum, and vanadium additions up to 1.5% were examined. Graphs of hardness differences (ΔH_v) relative to tempered Fe-C alloys, as a function of alloying element content, were obtained for tempering temperatures between 200 and 700 °C (400 and 1300 °F) for constant tempering times of 1 h. Figures 17.9 and 17.10 show plots of ΔH_v versus alloying element content for martensite tempered at 260 °C (500 °F) and 540 °C (1000 °F), respectively. When the ΔH_v for each element at a given tempering temperature from plots similar to those of Fig. 17.9 and 17.10 is added to the base tempered hardness as determined by carbon content and tempering temperature (see Fig. 17.7), the final tempered hardness of a plain-carbon or low-alloy steel may be readily estimated.

Figures 17.9 and 17.10 reflect interesting differences due to the various alloying elements. The strong carbide formers, as discussed relative to

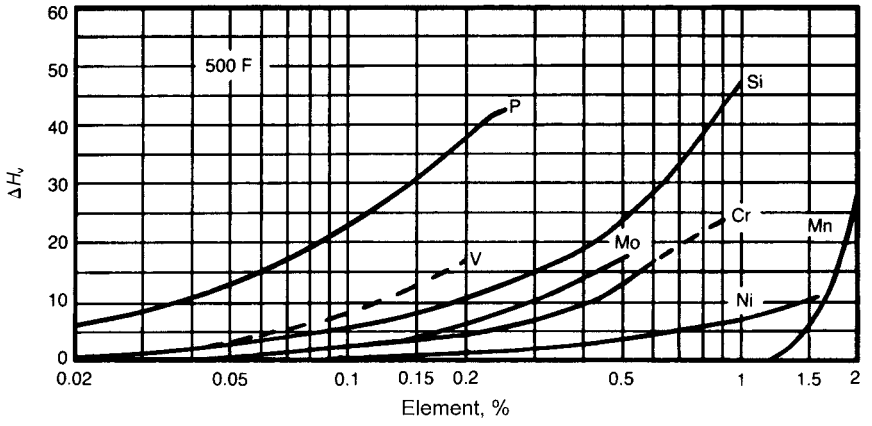

Fig. 17.9 Effect of alloying elements on the retardation of softening during tempering at 260 °C (500 °F) relative to Fe-C alloys. Source: Ref 17.5

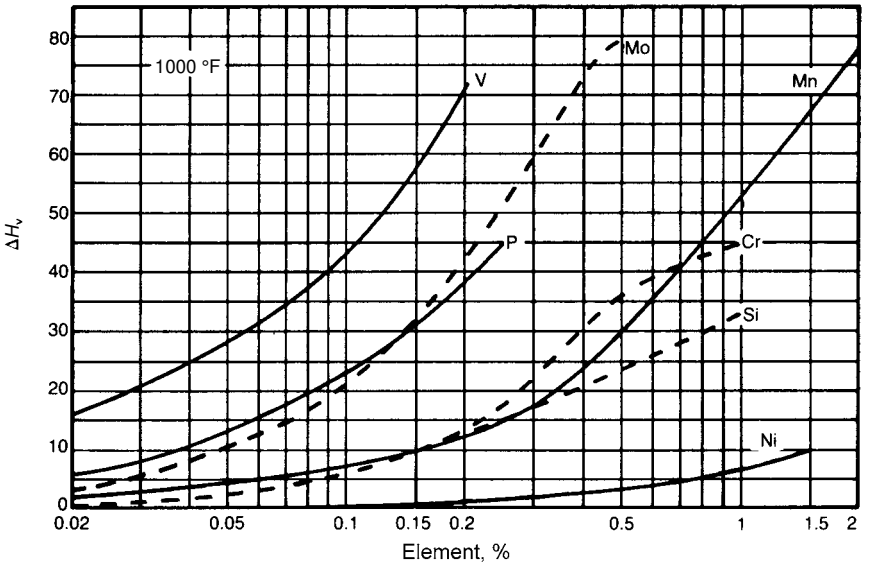

Fig. 17.10 Effect of alloying elements on the retardation of softening during tempering at 540 °C (1000 °F) relative to Fe-C alloys. Source: Ref 17.5

secondary hardening, do not have a large effect until high temperatures are reached. Nickel has a very small and constant effect on tempered hardness at all temperatures, and because it is not a carbide-forming element, its influence is considered to be due to a weak solid-solution-strengthening effect. Silicon has a substantial retarding effect on softening around 315 °C (600 °F), an effect attributed (Ref 17.9) to its inhibition of the transformation of the low-temperature transition carbide to the more stable cementite. Manganese at low tempering temperatures has little effect on softening, but at higher temperatures has a strong effect because of the incorporation

of the manganese into the carbides at higher temperatures (Ref 17.10) and the attendant resistance to cementite coarsening that is associated with manganese diffusion.

Structural Changes on Tempering

The structure of a steel quenched to form martensite is highly unstable. Reasons for the instability include the supersaturation of carbon atoms in the body-centered tetragonal crystal lattice of martensite, the strain energy associated with the fine dislocation or twin structure of the martensite, the interfacial energy associated with the high density of lath or plate boundaries, and the retained austenite that is invariably present even in low-carbon steels. The supersaturation of carbon atoms provides the driving force for carbide formation; the high strain energy the driving force for recovery; the high interfacial energy the driving force for grain growth or coarsening of the ferrite matrix; and the unstable austenite the driving force for transformation to mixtures of ferrite and cementite on tempering. Thus, even without the alloying effects discussed in the preceding section, there are many factors at work to produce the microstructures responsible for the mechanical property changes that develop when martensitic carbon steel is tempered.

An important series of papers on tempering carbon steels was published by Cohen and his colleagues in the 1950s (Ref 17.11–17.14). As a result of systematic X-ray, dilatometric, and microstructural observations, three distinct stages of tempering were identified:

- *Stage I:* The formation of a transition carbide, epsilon carbide (or eta carbide as discussed subsequently), and the lowering of the carbon content of the matrix martensite to about 0.25% C.
- *Stage II:* The transformation of retained austenite to ferrite and cementite.
- *Stage III:* The replacement of the transition carbide and low-carbon martensite by cementite and ferrite.

The temperature ranges for the three stages overlap, depending on the tempering times used, but the temperature ranges of 100 to 250 °C (210 to 480 °F), 200 to 300 °C (390 to 570 °F), and 250 to 350 °C (480 to 660 °F) are generally accepted for the first, second, and beginning third stages, respectively (Ref 17.15). The formation of the alloy carbides responsible for secondary hardening is sometimes referred to as the fourth stage of tempering. Also, it is now recognized that carbon atom segregation to dislocations and various boundaries may occur during quenching and/or holding at room temperature (Ref 17.15–17.17), and carbon atom clustering in as-quenched martensite may precede carbide formation (Ref 17.18, 17.19) that occurs in the first stage of tempering. Even other structural changes due to carbon atom rearrangement have been found to precede

the classical Stage I tempering of iron-carbon martensites (Ref 17.20, 17.21). Nagakura and his colleagues have identified a modulated structure associated with clustering of carbon atoms on (102) planes of martensite and a long-period ordered phase with an orthorhombic structure and composition of Fe_4C (Ref 17.20). The former structure forms on tempering between 0 and 90 °C (30 and 190 °F), while the latter structure forms between 60 and 80 °C (140 and 180 °F). Thus, tempering involves much more than three stages of tempering, but because of their practical importance to understanding the behavior of tempered steels, the three stages just listed are discussed in more detail subsequently.

Transition Carbide Formation. The transition carbide that forms in the first stage of tempering was first identified as having a hexagonal structure and designated epsilon (ε) carbide by Jack (Ref 17.22). More recently, Hirotsu and Nagakura (Ref 17.23, 17.24) have shown that the transition carbide has an orthorhombic structure isomorphous with transition metal carbides of the M_2C type. The transition carbide with the latter structure was designated as *eta (η) carbide*. The structures of the epsilon and eta carbides are very similar and are differentiated primarily by electron diffraction spots that come from a regular array of carbon atoms (or sublattice of carbon atoms) in the eta carbide (Ref 17.23, 17.24). Fig. 17.11 shows the electron diffraction pattern from transition carbides in a crystal of plate martensite in an Fe-1.22C alloy tempered at 150 °C (300 °F) indexed as eta carbide and as epsilon carbide (Ref 17.2). Both indexings are good for their assumed crystal structures, but the indexing as eta is somewhat better based on interplanar spacings.

Both the epsilon carbide, $Fe_{2.4}C$ (Ref 17.11), and the eta carbide, Fe_2C (Ref 17.23), have carbon contents substantially higher than that of the cementite, Fe_3C, that forms at higher temperatures. Mössbauer effect spectroscopy shows that some carbon is retained in the martensite through-

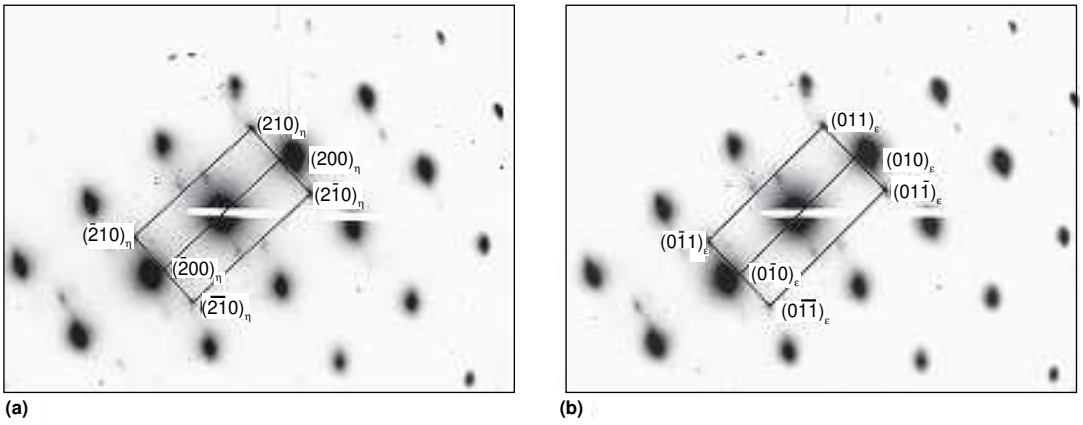

Fig. 17.11 Diffraction pattern from martensite crystal (beam parallel to [100]m, square pattern of spots) containing transition carbides with carbide diffraction pattern indexed as eta carbide (a, beam parallel to [001]η) and as epsilon carbide (b, beam parallel to $[100]_\varepsilon$). Source: Ref 17.2

out the range of transition carbide formation and that carbon is randomly dissolved in the austenite retained with the martensite (Ref 17.2). Two sets of Mössbauer parameters that may come from eta carbide have been identified. Kinetic studies show that the first stage of tempering is dependent on the diffusion of carbon through the martensite with an activation energy of 16,000 cal/mol (Ref 17.11).

Figures 17.12 through 17.14 are transmission electron micrographs that show various aspects of the transition carbide formation in the martensite

Fig. 17.12 Martensitic microstructure in an Fe-1.2C alloy tempered at 150 °C (300 °F). The microstructure consists of plates of various sizes containing uniform arrays of very fine carbides and retained austenite (black patches). Transmission electron micrograph. Source: Ref 17.29

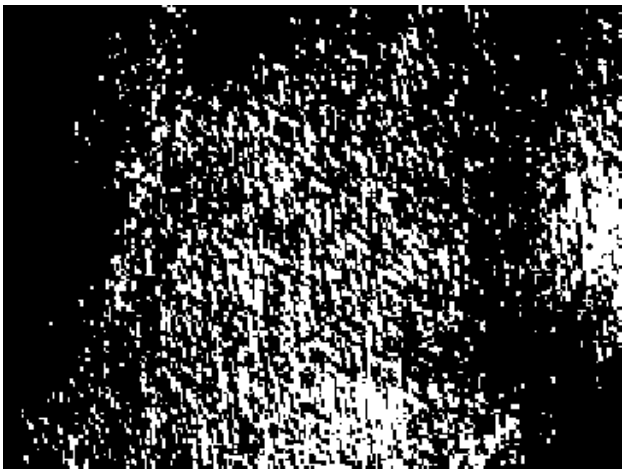

Fig. 17.13 Distribution of eta carbide in martensite plate of an Fe-1.22C alloy tempered at 150 °C (300 °F) for 16 hours. Transmission electron micrograph. Original magnification 80,000×. Source: Ref 17.2

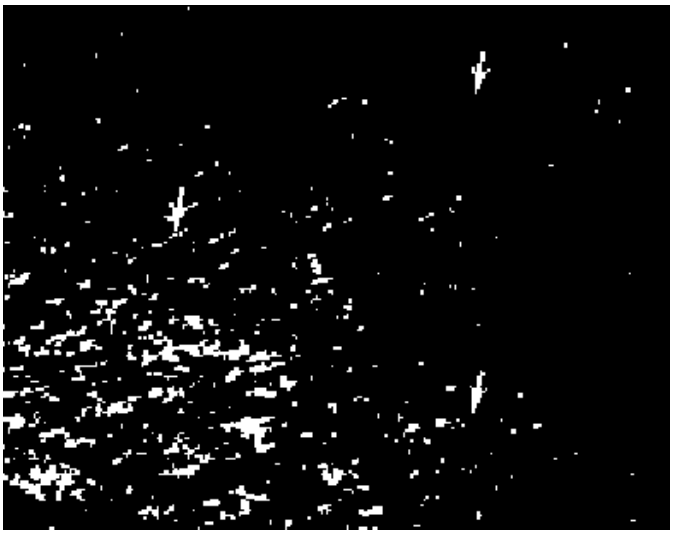

Fig. 17.14 Rows of fine spherical eta carbide particles in a martensite plate of an Fe-1.22C alloy tempered at 150 °C (300 °F) for 16 hours. Dark-field transmission electron micrograph. Original magnification 80,000×. Source: Ref 17.2

of the Fe-1.22C alloy tempered at 150 °C (300 °F) for 16 h. Figure 17.12 shows a typical plate martensitic microstructure with plates of a variety of sizes and patches of retained austenite (black areas) between the plates. Each of the plates contains a highly uniform distribution of fine carbon particles. Figure 17.13 shows a typical array of transition carbides, identified as eta carbides (Ref 17.2), in a single plate of martensite. The carbides appear to be in the form of fine platelets, but Fig. 17.14, a dark-field micrograph taken with illumination from a carbide diffraction spot, shows that the eta carbide is actually present as rows of fine spherical particles about 2 nm (20 Å) in diameter (Ref 17.2, 17.23). The dark contrast in the platelike morphology associated with the carbides in Fig. 17.12 is apparently due to strain effects between the martensitic matrix and the rows of particles.

Early work on the identification of the transition carbide formed in the first stage of tempering as eta carbide was performed on high carbon steels (Ref 17.2, 17.23). Subsequent research shows that eta carbide forms in martensite in steels with a wide range of carbon contents: 0.79% C by Shimizu and Okamoto (Ref 17.25), 0.50% C by Lee and Krauss (Ref 17.26), 0.45% C by Hirotsu and Nagakura (Ref 17.24), 0.30% C by Baoshu, Losz, and Krauss (Ref 17.27), and 0.14% C by Okamoto (Ref 17.28). Fig. 17.15 shows eta transition carbides in a martensite crystal in 4130 steel quench and tempered at 150 °C. Similar to Fig. 17.14, linear arrays of fine transition carbide particles are shown in the low-temperature-tempered martensite of the medium-carbon steel.

Fig. 17.15 Eta transition carbides (rows of very fine bright spherical particles) and cementite particles (bright linear features) in a lath martensite crystal in 4130 steel tempered at 150 °C (300 °F). Dark field transmission electron micrograph taken with a transition carbide diffracted beam. Courtesy of M. Losz while at the Colorado School of Mines

Retained Austenite Transformation on Tempering. The transformation of retained austenite during tempering occurs only by heating at temperatures and times well above those at which transition carbides precipitate. However, as discussed elsewhere, austenite may transform mechanically to martensite under various conditions of stress and strain at temperatures lower than those at which thermal transformation occurs. Figure 17.16 shows the rate of transformation of the retained austenite in an Fe-1.22C alloy at three different tempering temperatures (Ref 17.29). About 19% retained austenite, distributed as shown in Fig. 17.12, was initially present in the as-quenched structure. Even at 180 °C (360 °F), the retained austenite transformed completely to mixtures of ferrite and cementite if held for sufficiently long times. Analysis of the austenite transformation kinetics in Fig 17.16 yielded an activation energy of 1.15×10^5 J/mol (27 kcal/mol) in good agreement with the activation energies for the diffusion of carbon in austenite (Ref 17.30) and the activation energy for the second stage of tempering reported by Roberts et al. (Ref 17.11). Figure 17.17 shows that retained austenite is present in small amounts, about 2 and 4%, in as-quenched specimens of 4130 and 4340 steels, respectively, and that for tempering times of 1 h the transformation of re-

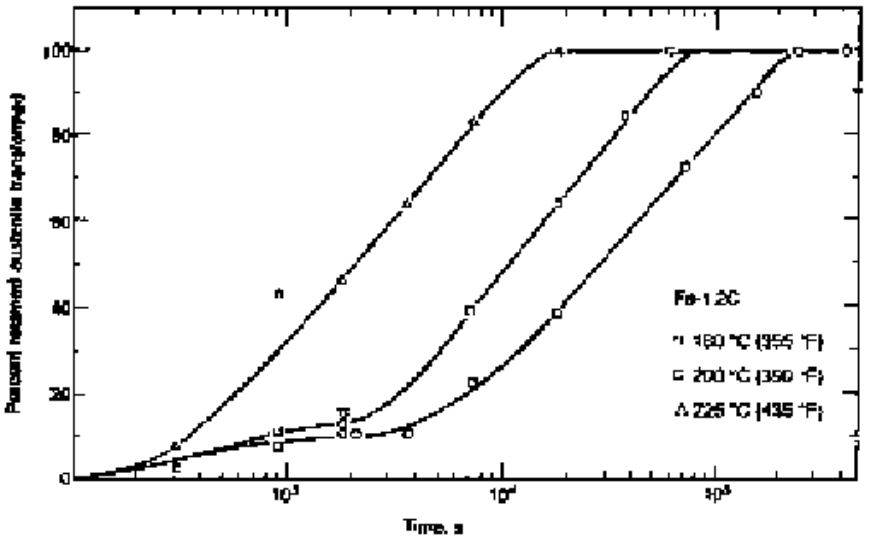

Fig. 17.16 Transformation of retained austenite in an Fe-1.22C alloy as a function of time at three tempering temperatures. Source: Ref 17.29

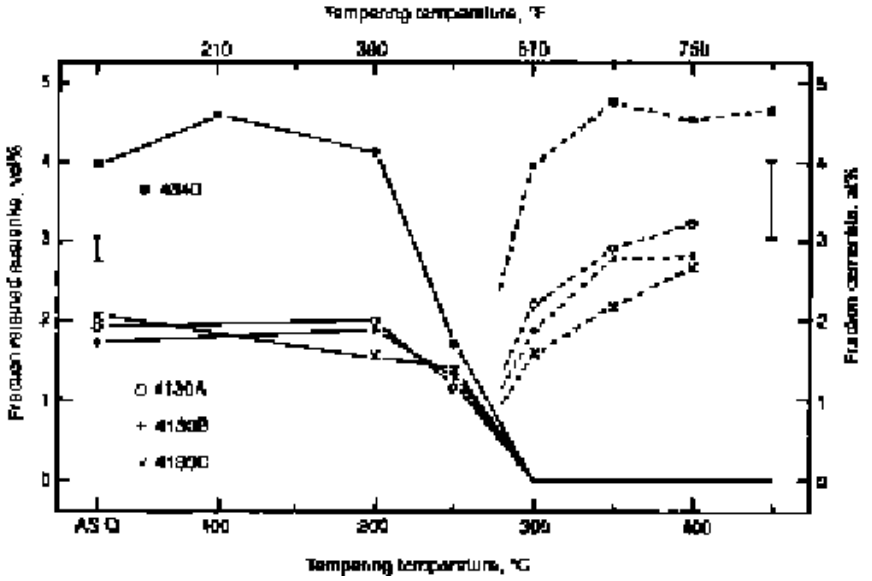

Fig. 17.17 Retained austenite and cementite as a function of tempering temperature in 4340 and 4140 type steels. The amounts of the phases were determined by Mössbauer spectroscopy. Source: Ref 17.30

tained austenite in these low-alloy medium-carbon steels begins only above 200 °C (390 °F). Transformation is complete at about 300 °C (570 °F) (Ref 17.31), and cementite becomes an important part of the microstructure after tempering at 300 °C and higher temperatures. The relatively coarse particles of cementite that form from the retained austenite

contribute to tempered martensite embrittlement as discussed in Chapter 19, "Low Toughness and Embrittlement Phenomena in Steels."

Cementite Formation During Tempering. The third stage of tempering consists of the formation of ferrite and cementite as required by the Fe-C diagram and its modification by other alloying elements. Depending on the tempering temperature between the end of Stage 1 temperature and the A_{C1} temperature there are large variations in the morphology, distribution, and chemistry of the cementite. Figure 17.18 shows a TEM micrograph of the fine structure of a medium-carbon steel containing 0.35% C quenched to martensite and tempered at 470 °C (800 °F). The microstructure is typical of that produced by early but well-established third-stage tempering: the lath martensite morphology is still largely retained and cementite (theta carbide) platelets have precipitated as small platelets within the larger martensite laths. Thin crystals of interlath cementite are also present as a result of the transformation of retained austenite during the second stage of tempering. The intralath cementite crystals have $\{110\}_M$ habit planes and have nucleated at eta-carbide clusters produced during the first stage of tempering (Ref 17.26, 17.32). At higher tempering temperatures the carbides coarsen, spheroidize, and change chemistry.

While light and electron microscopy best show changes in cementite distribution, morphology, and crystallography, atom probe tomography can establish on a nanoscale the chemical composition of carbides in tempered microstructures. Two phases of cementite formation have been established. At the beginning of and into the third stage of tempering, only carbon diffuses to and is incorporated in cementite, a mechanism of nucleation and growth referred to as paraequilibrium, i.e., a microstructural

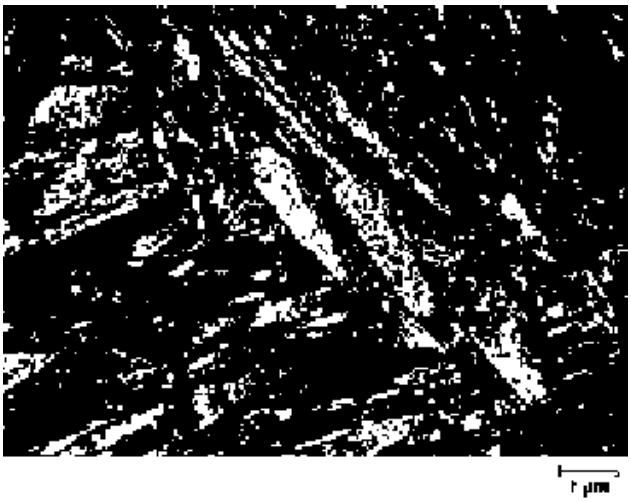

Fig. 17.18 Microstructure of a 0.35% C steel after quenching to martensite and tempering at 470 °C (880 °F). Transmission electron micrograph. Courtesy of Gary Yerby, Colorado School of Mines and Caterpillar Corporation

state based only on carbon diffusion, not involving other elements that might be equilibrium components of cementite.

Deep into the third stage of tempering, when substitutional alloying elements can diffuse, a second phase of cementite formation involves the diffusion of elements into and out of the cementite crystals.

Figures 17.19 and 17.20 show atom probe tomography evidence for atom distribution between the two steps of cementite formation (Ref 17.33). Atom maps and proximity histograms for carbon and substitutional alloying elements are shown. The proximity histograms are based on a constructed interface between the ferrite matrix and a cementite crystal, and the closest distance of each atom to this interface is calculated and the atoms made a part of the concentrations existing at each location relative to the interface (Ref 17.34). Fig. 17.19 shows that only carbon makes up the cementite particle and that no alloying elements have partitioned in martensite tempered into the third stage of tempering at 325° C (615 °F). In contrast at 575 °C (1065 °F) after two hours the atom maps in Fig. 17.20, as indicated by the colored dots for each atom type, show high densities of chromium, manganese, and molybdenum atoms in the cementite compared to the densities in the adjacent ferrite.

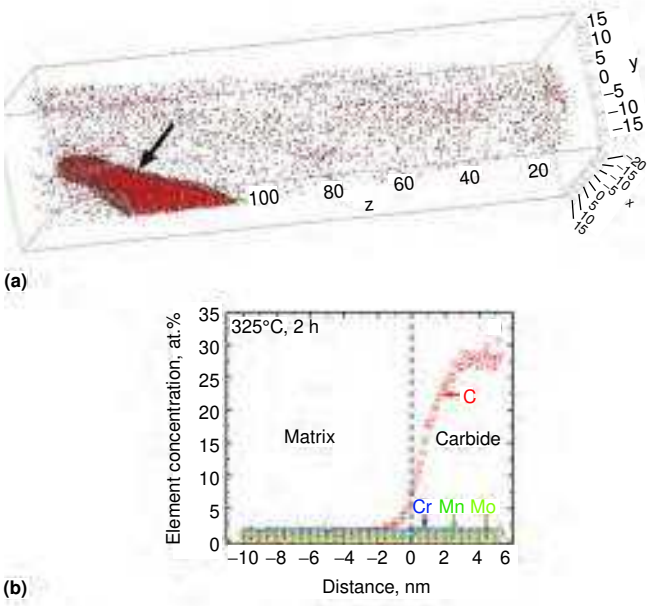

Fig. 17.19 (a) Carbon atom map associated with a cementite crystal (arrow) formed in martensite of 4340 steel during tempering at 325 °C (615 °F) for 2 hours, and (b) the proximity histogram showing concentrations of carbon, chromium, manganese, and molybdenum through the interface of the cementite crystal and the ferritic matrix. Results obtained by atom probe tomography. Source: Ref 17.33

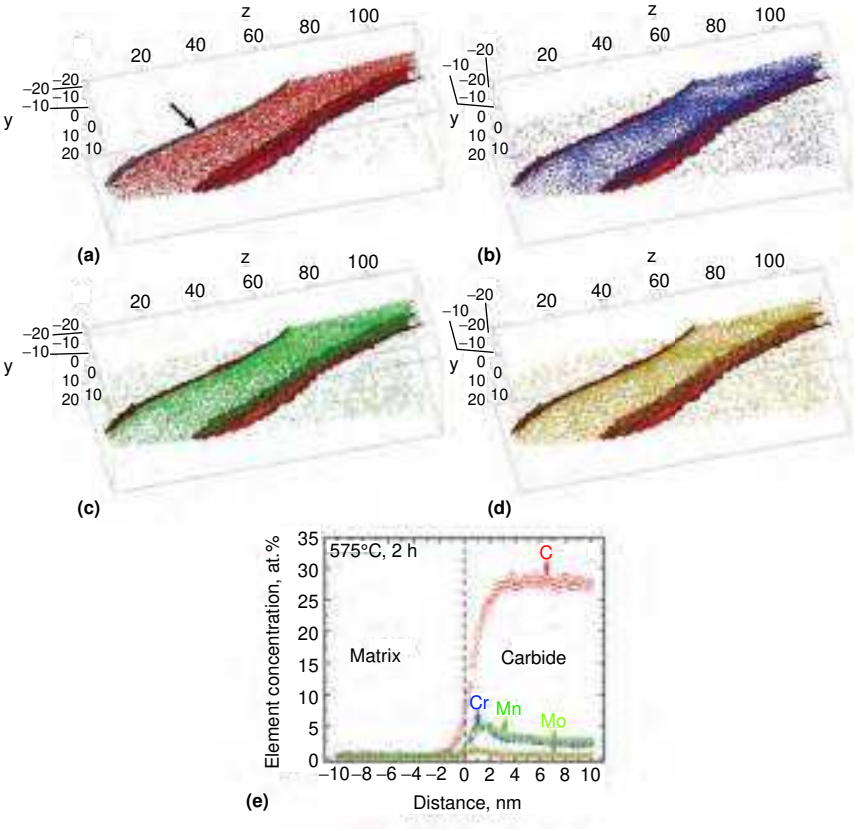

Fig. 17.20 Atom maps for carbon (red) (a), chromium (blue) (b), manganese (green) (c), and molybdenum (yellow) (d) at a cementite crystal (arrow) formed in martensite of 4340 steel after tempering at 575 °C (1065 °F) for 2 hours. The proximity histogram at the bottom (e) shows concentrations of carbon, chromium, manganese and molybdenum through the ferrite matrix and carbide crystal interface. Results obtained by atom probe tomography. Source: Ref 17.33

Chromium, manganese, and molybdenum are carbide-forming elements and, when given enough mobility at higher tempering temperatures, diffuse into cementite as shown. However other elements in steel are not carbide-forming elements and are rejected from cementite as the carbide-forming elements are integrated into the cementite. Atom probe tomography showed that nickel, silicon, aluminum, and phosphorus are rejected from cementite at high tempering temperatures in 4340 steel (Ref 17.33).

There is some evidence, especially in high-carbon steels, that Hagg or chi (χ)-carbide formation precedes cementite or theta (θ)-carbide formation (Ref 17.35, 17.36). The chi carbide has a monoclinic structure and the composition Fe_5C_2. However, despite the differences between cementite and chi carbide, the relatively complex structures of the two carbide phases are similar and difficult to separate by X-ray or electron diffraction techniques. Therefore, in view of the experimental difficulty in separating the presence of chi carbide from that of cementite, the temperature and

compositions of the steels in which chi carbide forms are not yet completely defined.

Figure 17.21 shows the dense carbide distribution that has formed in the martensite of an Fe-1.22C alloy tempered at 350 °C (660 °F). In this case, the carbides were best identified as chi carbide (Ref 17.37). Two carbide morphologies are present: those that have nucleated and grown within the martensite plates, and very long planar carbides that have formed along the plate interfaces, perhaps as a result of the transformation of retained austenite in the second stage of tempering. A third morphology of chi carbide and/or cementite in tempered high-carbon steels consists of parallel arrays of carbides formed on transformation twins sometimes present in high-carbon martensite, especially in the midrib portions of the plates (Ref 17.36). The carbides that have formed within the plates are coarser than the transition carbides and will eventually spheroidize if tempering is performed at higher temperatures. Nagakura et al. (Ref 17.20, 17.38) have shown that the transition from chi carbide, Fe_5C_2, to theta carbide (cementite), Fe_3C, takes place within single particles by development of sets of planes corresponding to higher-order carbides of general composition $Fe_{2n+1}C_n$. The intergrowth of the various carbide structures is referred to as microsyntactic growth and requires only iron atom displacements and carbon diffusion.

In addition to cementite, either effectively pure iron carbide or enriched in alloying elements, other carbides with other crystal structures, chemistries, and distributions may form in alloy steels and retard softening and/or produce secondary hardening during high temperature tempering. Many of the alloy carbides and their formation on tempering have been characterized by Honeycombe and his colleagues. Much of this work,

Fig. 17.21 Cementite and/or chi-carbide formation in martensitic structure of an Fe-1.22C alloy tempered at 350 °C (660 °F) for 1 hour. Transmission electron micrograph. Original magnification 30,000×. Courtesy of Ma, Ando, and Krauss, unpublished research, Colorado School of Mines

including descriptions of the carbide structures produced by tempering vanadium, molybdenum, tungsten, chromium, and titanium steels, is reviewed in Ref 17.39. The alloy carbide distributions formed in the secondary hardening range, 500 to 650 °C (930 to 1200 °F), depend on the nature of the cementite distribution formed at lower tempering temperatures, and the nature of the transformation of cementite to the alloy carbide. Honeycombe (Ref 17.39) presents evidence for two basic modes of alloy carbide formation on tempering. The carbides may form directly from the cementite, a mode referred to as *in situ transformation*, or the carbides may form by separate nucleation, after the cementite particles dissolve in the ferrite matrix. The independently nucleated alloy carbide particles are often nucleated on the dislocations residual from the as-quenched martensite and tend to be much finer than the alloy carbides nucleated on the cementite particles.

Matrix Changes during Tempering

Most of the structural changes discussed previously have involved the formation of various types of carbides during tempering. There are also important changes in the martensitic matrix that accomplish the formation of fully tempered structures consisting of spheroidized carbides in a matrix of equiaxed ferrite grains. Figures 17.22 through 17.24 show changes in the matrix structure that developed during the tempering of lath martensite in an Fe-0.2C alloy (Ref 17.40). Figure 17.22 shows that tempering at 400 °C (750 °F) for 15 minutes produces little change from the appearance of as-quenched lath martensite (see Chapter 5, "Martensite") on the scale resolvable with the light microscope. More pronounced changes are visible in a specimen tempered at 700 °C (1290 °F) (see Fig. 17.23), but even after this rather severe temper, the packet morphology with its paral-

Fig. 17.22 Microstructure of lath martensite in an Fe-0.2C alloy after tempering at 400 °C (750 °F) for 15 min. Light micrograph. Nital etch. Original magnification 500×. Source: Ref 17.40

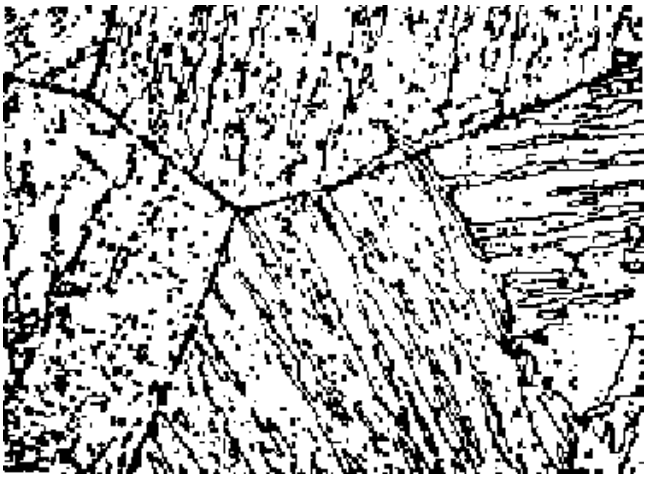

Fig. 17.23 Microstructure of lath martensite in an Fe-0.2C alloy after tempering at 700 °C (1290 °F) for 2 hours. Light micrograph. Nital etch. Original magnification 500×. Source: Ref 17.40

Fig. 17.24 Microstructures of lath martensite in an Fe-0.2C alloy after tempering at 700 °C (1290 °F) for 12 hours. Light micrograph. Nital etch. Original magnification 500×. Source: Ref 17.40

lel subunits is still clearly visible. The major effects of tempering have been to eliminate many of the smaller laths and to produce coarse, spherical cementite particles at the prior austenite grain boundaries and within the packets. More severe tempering, 700 °C for 12 h, begins to break up the remaining parallel blocks of crystals within the packets and more equiaxed ferrite grains begin to form (see Fig. 17.24). The equiaxed grains contain subboundaries made up of regular dislocation arrays, as shown by electron microscopy (Ref 17.40).

Systematic measurement of the change in lath boundary per unit volume as a function of tempering of the Fe-0.2C martensite shows that the

very high lath boundary area per unit volume of the fine laths in as-quenched martensite decreased very rapidly on tempering (Ref 17.40). Fig. 17.25 shows an example of the martensite lath boundary area change, S_V, as a function of tempering at 400 °C. The initial, rapid decrease is primarily due to the elimination of the low-angle boundaries between laths of similar orientation, the boundaries that separate martensite crystals in blocks of lath martensite. There is little change in the large-angle boundaries between the martensite crystals. Simultaneously, cementite particles precipitate and help to stabilize the surviving large-angle lath boundaries to maintain their parallel orientation within the packets.

All of these initial matrix changes occur as a result of recovery mechanisms. The dislocation density is effectively lowered not only by the reduction of dislocations within the laths but also by the elimination of the low-angle lath boundaries. Eventually, with coarsening of the carbide particles, the remaining large-angle boundaries rearrange themselves to produce more equilibrium junctions between grains as typical of the mechanisms associated with grain growth (Ref 17.41). Any residual dislocations within the laths then rearrange themselves into low-angle boundaries within the equiaxed grains. Such subdivisions of large grains by dislocation boundaries is referred to as polygonization. Thus, the formation of the equiaxed ferrite matrix that develops after long-time high-temperature tempering of a low-carbon lath martensite in some steels is accomplished by recovery and grain growth mechanisms (Ref 17.40, 17.42). Apparently, the recovery mechanisms that operate early in tempering lower the strain energy of the as-quenched martensite to the point where there is no longer sufficient driving force for recrystallization.

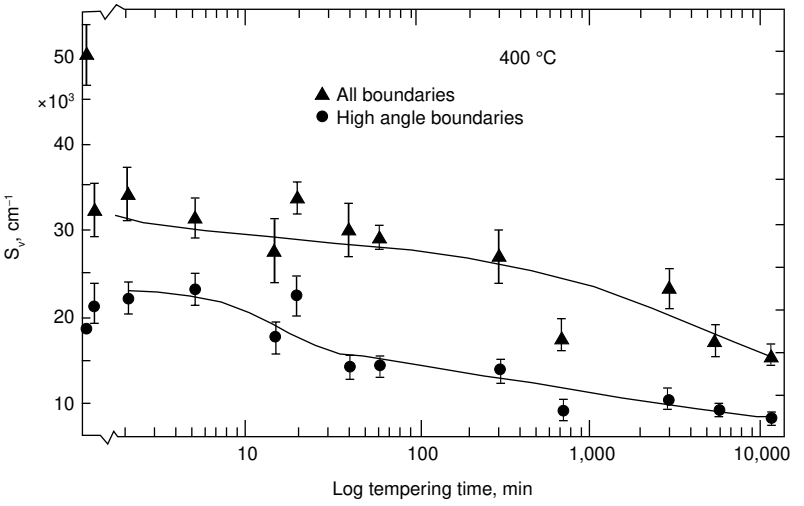

Fig. 17.25 Change in martensite lath boundary area per unit volume in martensite of an Fe-0.20% C alloy tempered at 400 °C (750 °F) for various times. Source: Ref 17.40

The above-described mechanism of equiaxed ferrite grain formation in highly tempered martensitic microstructures apparently proceeds when recovery mechanisms have lowered dislocation densities and strain energy to levels that cannot drive recrystallization. However, several studies have shown that recrystallization may in fact also be the mechanism of equiaxed ferrite grain formation in highly tempered steels (Ref 17.43–17.45). Apparently, recovery of the martensitic dislocation structure is suppressed by alloying and sufficient strain energy is available to cause recrystallization. Figure 17.26 shows the progress of recrystallization of a

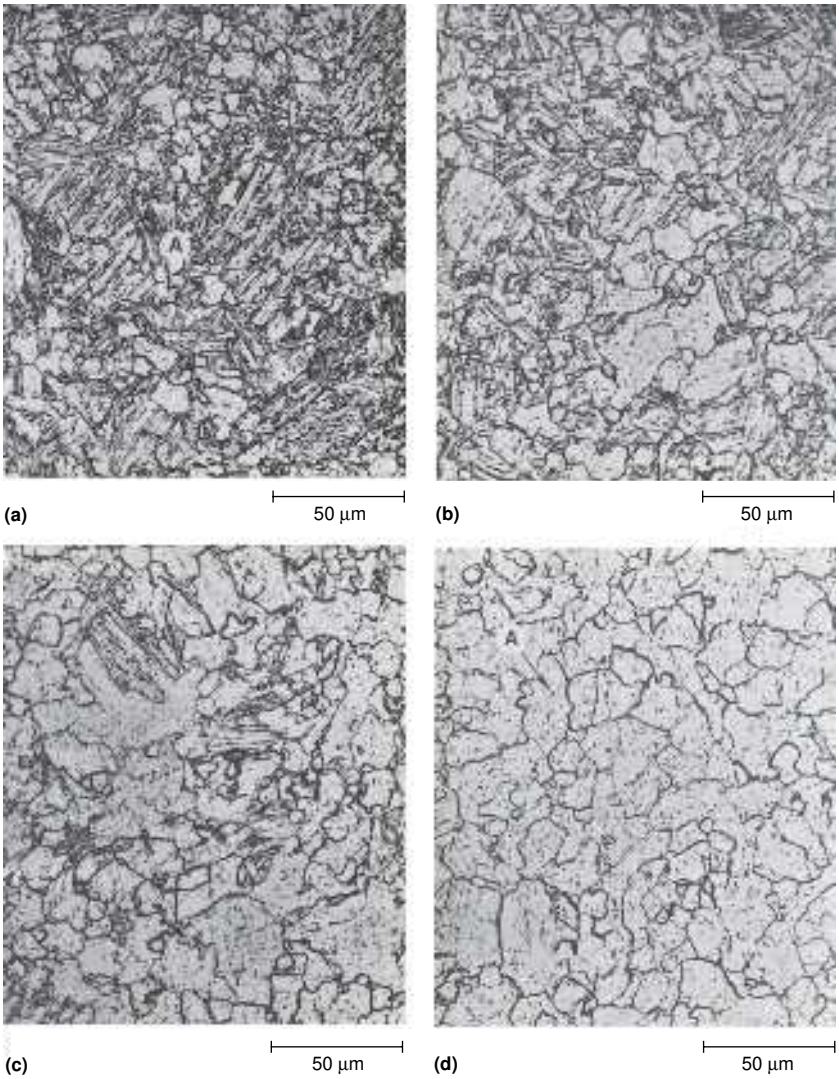

Fig. 17.26 Evolution of recrystallized equiaxed ferrite grains in tempered martensite of a 0.12% C steel tempered at 675 °C (1250 °F) for (a) 1 h, (b) 1.33 h, (c) 1.67 h, and (d) 4 h. Source: Ref 17.45

0.12% C, 1.40% Mn, 0.29% Mo steel as a function of tempering time at 675 °C (1250 °F) (Ref 17.45). Equiaxed, strain-free grains nucleate, as marked A in Fig. 17.26(a), within the tempered lath martensite of the steel. The strain-free grains grow and eventually consume all of the lath-shaped microstructure. The recrystallization proceeds despite the presence of carbide particles, and the final structure consists of relatively coarse spheroidized cementite particles within a matrix of equiaxed ferrite grains. Figure 17.27 shows TEM micrographs of the fine structure of the 0.12% C steel after tempering for one and two hours at 675 °C. The unrecrystallized tempered lath morphology and effectively dislocation-free recrystallized grains are clearly shown. When recrystallization is produced by tempering, hardness drops discontinuously. Figure 17.28 shows the changes in hardness, as determined by microhardness testing, as a function of time for unrecrystallized and recrystallized tempered-martensitic areas in the 0.12% C steel (Ref 17.45). Overall hardness decreases as the amount of strain-free equiaxed ferrite grains increases.

Oxide Colors on Tempered Steels

When as-machined steels are heated or tempered, thin oxide films form, and the color of the oxidation varies with film thickness. Paul Gordon has systematically studied the oxide colors that formed on specimens of an SAE 1035 steel with machined, bright, smooth surfaces as a function of heating time and temperature in circulating air (Ref 17.46). Figure 17.29 shows the results of Gordon's experiments.

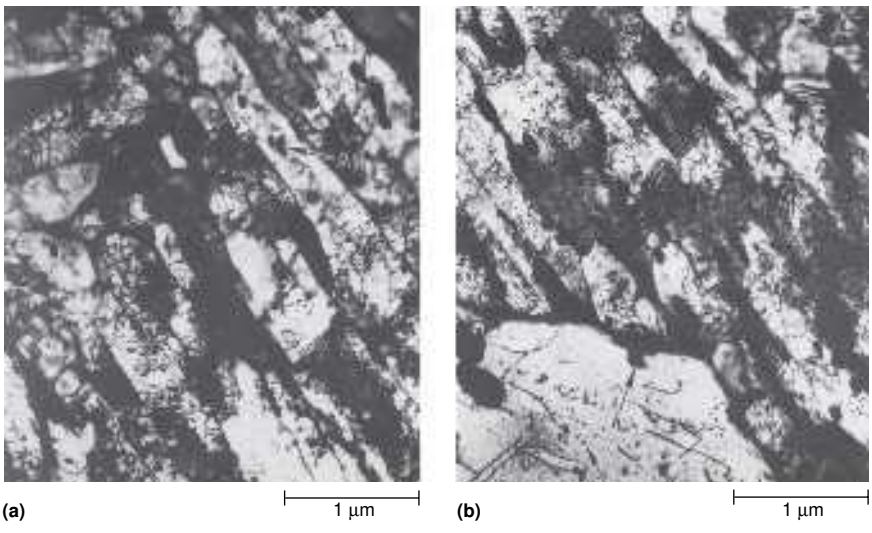

Fig. 17.27 Fine structure of 0.12% C steel quenched to martensite and tempered at 675 °C (1250 °F) for (a) 1 h and (b) 2 h. Source: Ref 17.45

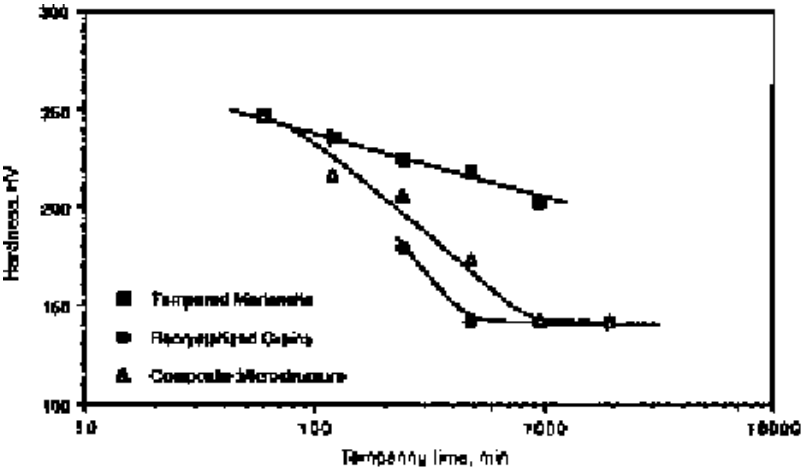

Fig. 17.28 Hardness changes as a function of time in unrecrystallized tempered martensite, recrystallized ferrite, and the overall composite microstructure of a 0.19% C steel quenched to martensite and tempered at 675 °C (1250 °F). Source: Ref 17.45

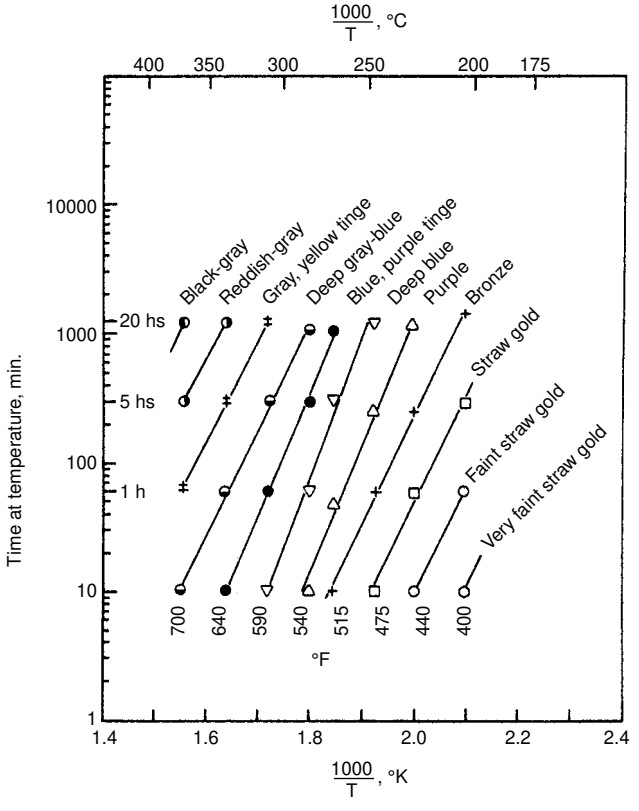

Fig. 17.29 Temper colors on machined, bright surfaces of 1035 steel as a function of heating time and temperature in circulating air. Source: Ref 17.46

REFERENCES

17.1 M.A. Grossmann and E.C. Bain, *Principles of Heat Treatment,* 5th ed., American Society for Metals, 1964

17.2 D.L. Williamson, K. Nakazawa, and G. Krauss, A Study of the Early Stages of Tempering in an Fe-1.2% C Alloy, *Metall. Trans. A,* Vol 10A, 1979, p 1351–1363

17.3 *Modern Steels and Their Properties,* Handbook 2757, 7th ed., Bethlehem Steel Corp., Bethlehem, PA, 1972

17.4 T. Swarr and G. Krauss, The Effect of Structure on the Deformation of As-Quenched and Tempered Martensite in an Fe-0.2% C Alloy, *Metall. Trans. A,* Vol 7A, 1976, p 41–48

17.5 R.A. Grange, C.R. Hribal, and L.F. Porter, Hardness of Tempered Martensite in Carbon and Low-Alloy Steels, *Metall. Trans. A,* Vol 8A, 1977, p 1775–1785

17.6 E.C. Rollason, *Fundamental Aspects of Molybdenum in Transformation of Steel*, Climax Molybdenum Co., London

17.7 K.J. Irvine and F.B. Pickering, The Tempering Characteristics of Low-Carbon Low-Alloy Steels, *JISI,* Vol 194, 1960, p 137–153

17.8 E. Smith and J. Nutting, The Tempering of Low-Alloy Creep-Resistant Steels Containing Chromium, Molybdenum, and Vanadium, *JISI,* Vol 187, 1957, p 314–329

17.9 A.G. Allten and P. Payson, The Effect of Silicon on the Tempering of Martensite, *Trans. ASM,* Vol 45, 1953, p 498–532

17.10 W. Crafts and J.L. Lamont, Effects of Alloys in Steel as Resistance to Tempering, *Trans. AIME,* Vol 172, 1947, p 222–243

17.11 C.S. Roberts, B.L. Averbach, and M. Cohen, The Mechanism and Kinetics of the First Stage of Tempering, *Trans. ASM,* Vol 45, 1953, p 576–604

17.12 B.S Lement, B.L. Averbach, and M. Cohen, Microstructural Changes on Tempering Iron-Carbon Alloys, *Trans. ASM,* Vol 46, 1954, p 851–881

17.13 F.E. Werner, B.L. Averbach, and M. Cohen, The Tempering of Iron-Carbon Martensite Crystals, *Trans. ASM,* Vol 49, 1957, p 823–841

17.14 B.S. Lement, B.L. Averbach, and M. Cohen, Further Study of Microstructural Changes on Tempering Iron-Carbon Alloys, *Trans. ASM,* Vol 47, 1955, p 291–319

17.15 G.R. Speich, Tempered Ferrous Martensitic Structures, *Metallography, Structures and Phase Diagrams,* Vol 8, *Metals Handbook,* 8th ed., American Society for Metals, 1973, p 202–204

17.16 G.R. Speich and W.C. Leslie, Tempering of Steel, *Metall. Trans.,* Vol 3, 1972, p 1043–1054

17.17 G.R. Speich, Tempering of Low-Carbon Martensite, *Trans. TMS-AIME,* Vol 245, 1969, p 2553–2564

17.18 J. Genin and P.A. Flinn, Mössbauer Effect Study of the Clustering of Carbon Atoms during the Room-Temperature Aging of Iron-Carbon Martensite, *Trans. TMS-AIME,* Vol 242, 1968, p 1419–1430

17.19 G.V. Kurdjumov and A.G. Khachaturyan, Phenomena of Carbon Atom Redistribution in Martensite, *Metall. Trans.,* Vol 3, 1972, p 1069–1076

17.20 S. Nagakura, Y. Hirotsu, M. Kusunoki, T. Suzuki, and Y. Nakamura, Crystallographic Study of the Tempering of Martensitic Carbon Steel by Electron Microscopy and Diffraction, *Metall. Trans. A,* Vol 14A, 1983, p 1025–1031

17.21 G. Krauss, Tempering and Structural Change in Ferrous Martensitic Structures, *Phase Transformations in Ferrous Alloys,* A.R. Marder and J.I. Goldstein, Ed., TMS-AIME, Warrendale, PA, 1984, p 101–123

17.22 K.H. Jack, Structural Transformations in the Tempering of High Carbon Martensitic Steel, *JISI,* Vol 169, 1951, p 26–36

17.23 Y. Hirotsu and S. Nagakura, Crystal Structure and Morphology of the Carbide Precipitated from Martensite High Carbon Steel during the First Stage of Tempering, *Acta Metall.,* Vol 20, 1972, p 645–655

17.24 Y. Hirotsu and S. Nagakura, Electron Microscopy and Diffraction Study of the Carbide Precipitated at the First Stage of Tempering of Martensitic Medium Carbon Steel, *Trans. Jpn. Inst. Met.,* Vol 15, 1974, p 129–134

17.25 K. Shimizo and H. Okamoto, High Voltage Electron Microscopy Study of the Metastable Iron Carbide in a Eutectoid Steel, *Trans. Jpn. Inst. Met.,* Vol 15, 1974, p 193–199

17.26 H.-C. Lee and G. Krauss, Intralath Carbide Transitions in Martensitic Medium-Carbon Steels Tempered between 200 and 300 °C, *Fundamentals of Aging and Tempering in Bainitic and Martensitic Steel Products*, ISS, Warrendale, PA, 1992, p 39–43

17.27 G. Baozhu, M.J. Losz, and G. Krauss, Substructure and Flow Strength of Low Temperature Tempered Medium Carbon Martensite, *Proceedings of the International Conference on Martensitic Transformations*, Sendai, The Japan Institute of Metals, 1986, p 367–374

17.28 S. Okamoto, "Strain Rate and Temperature Effects on Deformation Behavior and Mechanical Properties of As-Quenched Low-Carbon Martensite," M.S. thesis, Colorado School of Mines, Golden, CO, 1990

17.29 T.A. Balliett and G. Krauss, The Effect of the First and Second Stages of Tempering on Microcracking in Martensite of an Fe-1.22% C Alloy, *Metall. Trans. A,* Vol 7A, 1976, p 81–86

17.30 C. Wells, W. Batz, and R.F. Mehl, Diffusion Coefficient of Carbon in Austenite, *Trans. AIME,* Vol 188, 1950, p 553–560

17.31 D.L. Williamson, R.G. Shupmann, J.P. Materkowski, and G. Krauss, Determination of Small Amounts of Austenite and Carbide in a Hardened Medium Carbon Steel by Mössbauer Spectroscopy, *Metall. Trans. A,* Vol 10A, 1979, p 379–382

17.32 Y. Nakamura and S. Nagakura, Structure of Iron-Carbide Martensite in the Transition Stage from the First to Third Stage of Tempering Studied by Electron Microscopy and Diffraction, *Trans. Jpn. Inst. Met.,* Vol 27, 1986, p 842–848

17.33 A.J. Clarke, M.K. Miller, R.D. Field, D.R. Coughlin, P.J. Gibbs, K.D. Clarke, D.J. Alexander, K.A. Powers, P.A. Papin, G. Krauss, Atomic and Nanoscale Chemical and Structural Changes in Quenched and Tempered 4340 Steel, *Acta Mater.,* Vol 77, Sept 2014, p 17–24

17.34 M.K. Miller, Atom Probe tomography for studying phase transformations in steels, *Phase transformations in steels,* Vol 2, E. Pereloma and D. V. Edmonds, Ed., Woodhead Publishing, Oxford, 2012, p 532–556

17.35 Y. Imai, Phases in Quenched and Tempered Steels, *Trans. Jpn. Inst. Met.,* Vol 16, 1975, p 721–734

17.36 Y. Ohmori, Hägg Carbide Formation and Its Transformation into Cementite During the Tempering of Martensite, *Trans. Jpn. Inst. Met.,* Vol 13, 1972, p 119–127

17.37 C.-B. Ma, T. Ando, D.L. Williamson, and G. Krauss, Chi-Carbide in Tempered High Carbon Martensite, *Metall. Trans. A,* Vol 14A, 1983, p 1033–1045

17.38 S. Nagakura, T. Suzuki, and M. Kusunoki, Structure of the Precipitated Particles at the Third Stage of Tempering of Martensitic Iron-Carbon Steel Studied by High Resolution Electron Microscopy, *Trans. Jpn. Inst. Met.,* Vol 22, 1981, p 699–709

17.39 R.W.K. Honeycombe, *Steels, Microstructure and Properties,* Edward Arnold Ltd and American Society for Metals, 1981

17.40 R.N. Caron and G. Krauss, The Tempering of Fe-C Lath Martensite, *Metall. Trans.,* Vol 3, 1972, p 2381–2389

17.41 P.G. Shewmon, *Transformations in Metals,* McGraw-Hill, New York, 1969, p 220

17.42 R.M. Hobbs, G.W. Lorimer, and N. Ridley, Effect of Silicon on the Microstructure of Quenched and Tempered Medium-Carbon Steels, *JISI,* Vol 210, 1972, p 757–764

17.43 A. Galibois and A. Dube, Recrystallization Kinetics of Martensitic Extra-Low Carbon Steels, *Can. Metall. Q.* Vol 3 (No. 4), 1964, p 321–343

17.44 A. Galibois and A. Dube, Similarities between the Martensitic and Cold-Worked Structures of Steels, *Can. Metall. Q.,* Vol 6 (No. 2), 1967, p 121–136

17.45 S.J. Tua, R.K. Weiss, G. Krauss, and S.W. Thompson, Structural Changes Induced by High-Temperature Tempering of Martensitic Plate Steels and a Mechanism for the Recrystallization of Martensite, *Fundamentals of Aging and Tempering in Bainitic and Martensitic Steel Products,* G. Krauss and P.E. Repas, Ed., ISS, Warrendale, PA, 1992, p 53–66

17.46 P. Gordon, The Temper Colors on Steel, *J. Heat Treat.,* Vol 1 (No. 1), 1979, p 93

CHAPTER **18**

Deformation, Mechanical Properties, and Fracture of Quenched and Tempered Carbon Steels

CHAPTER 16, "Hardness and Hardenability," and Chapter 17, "Tempering of Steel," describe the mechanical behavior of quenched and tempered steels largely in terms of hardness. Hardness measurements are a powerful, essentially nondestructive, easily applied quality-control technique for heat treated steels and correlate well with the response of steels to heat treatment. Although the hardness of quenched and tempered steels is a continuous function of steel carbon content and tempering conditions, as has been shown, for example, in Fig. 17.7 in Chapter 17, "Tempering of Steel," mechanical properties as measured by tensile testing show discontinuities with these parameters. These discontinuities characterize the various embrittlement phenomena that occur in hardened steels under conditions of tensile and bending loading. Hardness measurements, based on penetration of various types of indenters under various loading conditions, are a result of compressive and shear stresses and rarely produce low-toughness and brittle fractures that limit the application of hardened steels.

Because of embrittlement phenomena, steels with martensitic and tempered martensitic microstructures are sometimes considered to be generally brittle. This characterization is true only for certain steel compositions

and tempering conditions, and some tempered martensites, even at very high strength levels, show plasticity and ductile fracture behavior. This chapter describes the deformation mechanisms and mechanical properties, as determined by uniaxial tensile testing, of hardened low- and medium-carbon steels as a function of carbon content and tempering temperature. Conditions that result in ductile fracture are emphasized, but references are necessarily made to microstructures, sensitive to brittle fracture phenomena, that bracket microstructures that show ductile deformation and fracture behavior under load. Embrittlement phenomena that develop in hardened steels are discussed in detail in Chapter 19, "Low Toughness and Embrittlement Phenomena in Steels."

A map of the fracture mechanisms that may develop in hardened steels as a function of carbon content and tempering temperature is shown in Fig. 18.1. The microstructures, deformation, and fracture mechanisms in untempered martensite, and produced by the conditions identified by the box marked "LTT Martensite/Ductile Fracture," first receive attention in this chapter. Ductile behavior is not exclusively produced by the tempering conditions and carbon contents noted by the box, and even in as-quenched conditions and regions that show tempered martensite embrittlement and temper embrittlement, fracture may be ductile, depending on carbon, alloy, and impurity element content. The effects of high tempering temperatures on the mechanical behavior and properties of medium-carbon steels are discussed in later sections of this chapter.

Finally a section at the end of this chapter briefly summarizes all of the microstructural components that are present in quenched and tempered martensitic carbon steels and their contributions to strength and mechanical behavior as affected by tempering.

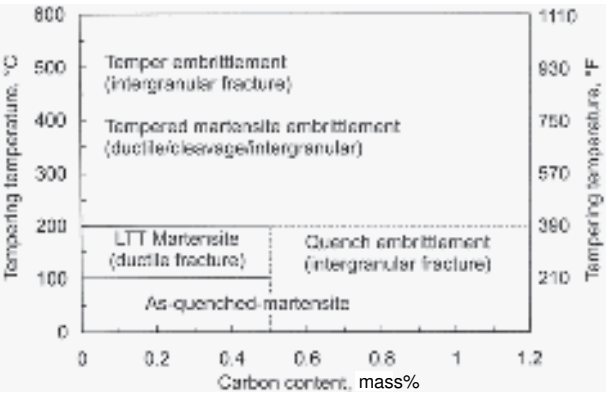

Fig. 18.1 Fracture response, under conditions of tensile loading, as a function of tempering temperature and steel carbon content for carbon and low-alloy carbon steels quenched to martensite. LTT martensite designates low-temperature-tempered martensite

Deformation and Fracture of As-Quenched Martensite

The carbon content of steel has a profound effect on the mechanical behavior of as-quenched martensite. Austenitizing treatments prior to quenching, by virtue of the high solubility of carbon in face-centered cubic austenite, cause carbon to dissolve into the octahedral sites of the crystal structure of austenite. On quenching the carbon atoms are trapped in octahedral sites of the martensitic crystal structure, displacing iron atoms and producing the tetragonal distortion of martensites, as has been shown in Fig. 16.5 in Chapter 16, "Hardness and Hardenability" (Ref 18.1, 18.2). However, because of the low solubility of carbon in body-centered crystal structures, only in Fe-Ni-C alloys, with subzero M_S temperatures where carbon atom diffusion is limited, can most of the carbon atoms remain trapped in octahedral sites and contribute to solid solution strengthening. In Fe-C alloys and plain and low-alloy carbon steels, with M_s temperatures above room temperature, carbon atoms diffuse rapidly from octahedral sites in martensite during quenching, during storage at room temperature, and during deformation.

The effect of carbon atom rearrangement in as-quenched martensitic microstructures in low-alloy carbon steels was studied by Leslie and Sober (Ref 18.3). They evaluated the deformation behavior of AISI 4310, 4320, 4330, and 4340 steels in which nickel, chromium, and molybdenum contents were held constant at 1.8, 0.80, and 0.25%, respectively, and carbon varied between 0.12 and 0.41%. The substitutional alloying elements provide good hardenability; 4320 steel is an important commercial carburizing steel, and hardened 4330 and 4340 are widely used for applications that require high strength. Specimens of the various 43xx steels were quenched from 900 °C (1650 °F) in iced brine, stored in liquid nitrogen, and tensile tested at various strain rates at room temperature and subzero temperatures.

Figure 18.2 shows the data Leslie and Sober obtained for as-quenched 4330 steel. Flow stresses at plastic strains of 0.2, 0.5, and 1.0% are shown, and the increasing flow stresses with strain demonstrate that significant strain hardening occurs under all testing conditions. Flow stresses increase significantly with decreasing test temperatures, and at room temperature, negative strain rate sensitivity, i.e., a decrease in flow stress with increasing strain rate, provides evidence for *dynamic strain aging* or carbon atom segregation to dislocations during testing. Dynamic strain aging is discussed in more detail in the next section of this chapter. Leslie and Sober recognized that rearrangement of carbon atoms during quenching and mechanical testing of steels with M_S temperatures above room temperature provides major contributions to the strength of steels with martensitic microstructures, especially in steels with higher carbon contents. Table 18.1 shows various operating strengthening mechanisms and their contributions

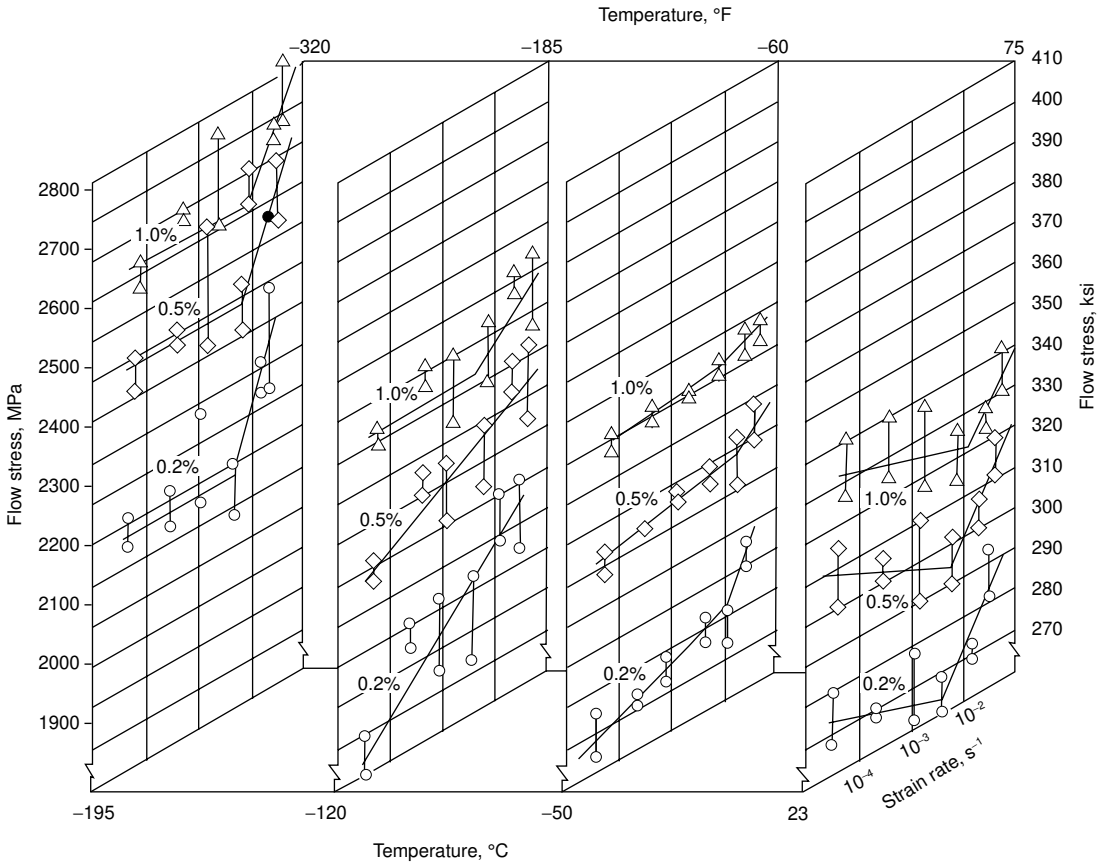

Fig. 18.2 Flow stresses as a function of test temperature and strain rate for as-quenched AISI 4330 steel. Source: Ref 18.3

Table 18.1 Strengthening components in as-quenched 4310 and 4340 steels

	AISI 4310		AISI 4340	
Component	**MPa**	**ksi**	**MPa**	**ksi**
Fine structure	620	90	620	90
Dynamic strengthening during the test	205	30	205	30
Work hardening	345	50	240	35
Rearrangement of carbon atoms during quench	…	…	760	110
Solid-solution strengthening by carbon	…	…	415	60
Total 0.2% offset yield strength	1170	170	2240	325

Source: Ref 18.3

to the 0.2% offset yield strengths of as-quenched 4310 and 4340 steels. Figure 18.3 shows engineering stress-strain curves for as-quenched 4330, 4340, and 4350 steels with martensitic microstructures (Ref 18.4). The 4330 steel, with relatively low carbon content, showed ductile deformation behavior: significant uniform plastic deformation and strain harden-

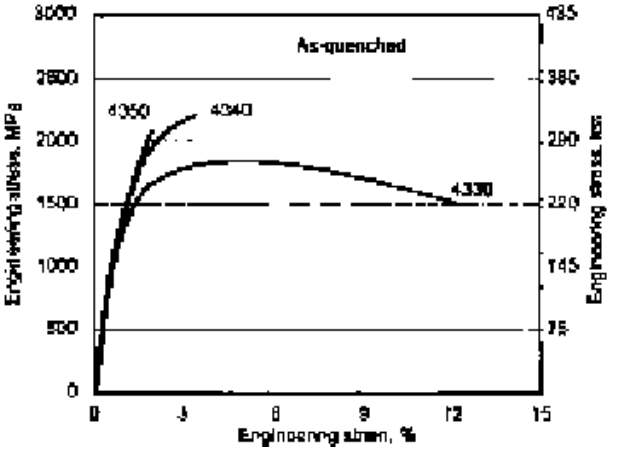

Fig. 18.3 Engineering stress-strain curves for untempered martensitic microstructures in 4330, 4340, and 4350 steels. Source: Ref 18.4

ing, necking, and post uniform elongation. The fracture surface of this specimen consisted of microvoids typical of ductile fracture. The 4350 steel showed brittle behavior and almost no ability to sustain plastic deformation. The fracture surface of the 4350 specimen consisted of intergranular fracture, typical of quench embrittlement, as discussed in Chapter 19, "Low Toughness and Embrittlement Phenomena in Steels." The stress-strain curve of the as-quenched 4340 steel shows limited plastic deformation, short of reaching an ultimate tensile strength associated with necking instability and nonuniform deformation. The fracture surface of the 4340 specimen showed cleavage facets, a possible result of dynamic strain aging that limits ductility.

Dynamic Strain Aging in Martensite

Dynamic interactions between solute atoms and dislocations during deformation are well known in nonferrous and ferrous alloy systems (Ref 18.5). Such interactions may lead to negative strain rate sensitivity, reduced ductility and fracture resistance, and discontinuous plastic flow. The discontinuous plastic flow produces serrations in stress-strain curves, and in view of early work is referred to as the *Portevin-LeChatelier effect* (Ref 18.6). Dynamic strain aging and serrated stress-strain curves are well known in low-carbon steels with microstructures of polycrystalline ferrite (Ref 18.7). Temperatures must be sufficiently high and strain rates sufficiently low in order to permit carbon atom diffusion to dislocations. When dislocation motion is halted by carbon atom pinning, plastic deformation ceases and is resumed only by the generation of new, unpinned dislocations, leading to a stress drop and subsequent strain hardening, until the pinning process is repeated, and another serration is produced.

Dynamic strain aging of martensitic microstructures has received relatively little attention. As noted previously, Leslie and Sober found evidence for negative strain rate sensitivity in 43xx steels (Ref 18.3). Also, Owen and Roberts have studied serrated flow in martensitic Fe-21% NiC alloys with carbon contents between 0.04 and 0.12 wt% (Ref 18.8, 18.9). Specimens were tested as a function of strain rates between 10^{-5} and 10^{-1} and between room temperature and 200 °C (390 °F). Increasing carbon content at a constant strain rate lowered the temperature at which serrated flow initiated, and the temperature dependence of serrated flow initiation was characterized by an activation energy of 81.2 kJ/mol (19.1 kcal/mol).

Dynamic strain aging has been characterized in martensite of a low-carbon steel containing 0.14% C, 1.48% Mn, 0.27% Si, and 0.04% Al (Ref 18.5, 18.10, 18.11). In view of the low hardenability associated with low-carbon steels, the relatively high manganese content of the subject steel provided sufficient hardenability to produce fully martensitic microstructures in sheet tensile specimens when quenched in ice water. Figure 18.4 shows the as-quenched low-carbon steel microstructure, consisting of lath martensite crystals containing a high density of dislocations and interlath retained austenite. Tensile testing at room temperature of specimens with as-quenched martensitic microstructures showed ductile deformation behavior at all strain rates (Fig. 18.5) but with somewhat reduced ductility at the lowest strain rates. Serrated yielding was not observed at room temperature in the 0.14% C steel.

Tensile testing of specimens with martensitic microstructures in the 0.14% C steel at 150 °C (300 °F) showed well-defined serrated yielding at intermediate strain rates. Figure 18.6 shows complete engineering stress-strain curves produced by tensile testing at 150 °C and Fig. 18.7 shows details of the stress-strain curves that exhibited serrated yielding. Serrated

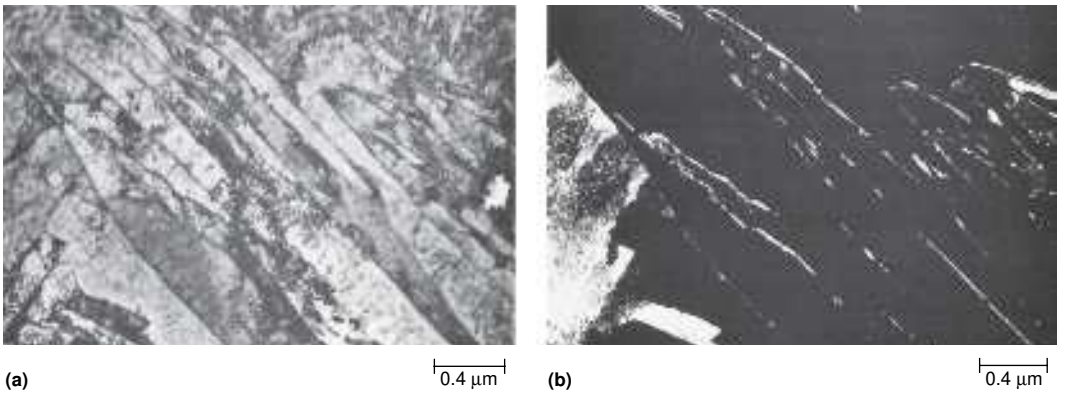

Fig. 18.4 Microstructure of lath martensite in 0.14% C steel. (a) Bright field TEM micrograph. (b) Dark field TEM micrograph taken with diffracted beam from interlath austenite (bright linear features). Source: Ref 18.5

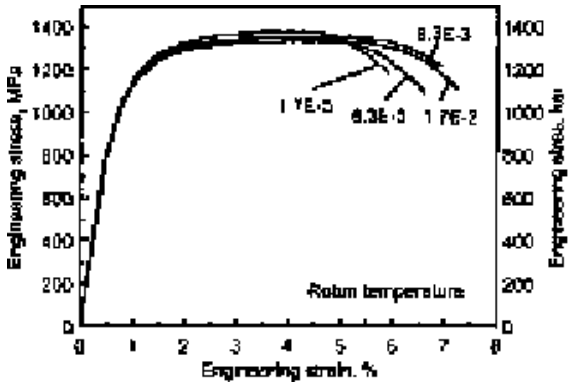

Fig. 18.5 Engineering stress-strain curves for as-quenched martensite in 0.14% C steel tested at various strain rates. Source: Ref 18.5

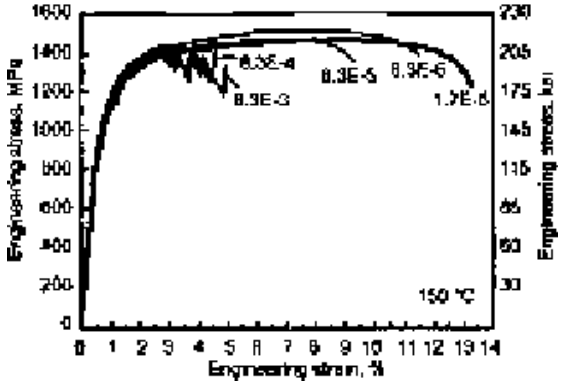

Fig. 18.6 Engineering stress-strain curves for 0.14% C steel with martensitic microstructure measured at 150 °C (300 °F) at various strain rates. Source: Ref 18.10

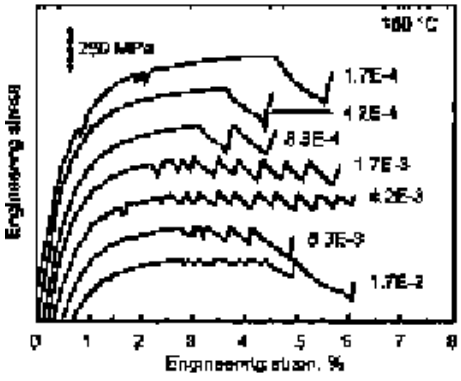

Fig. 18.7 Engineering stress-strain curves with serrated flow from specimens of 0.14% C steel with martensitic microstructure tested at 150 °C (300 °F) at various strain rates. The curves have been vertically displaced to show details of the serrated curves. Source: Ref 18.10

yielding occurred after a critical strain, ε_C, was achieved, and each drop in load corresponded to a shear-band type of surface marking that developed on the sheet tensile specimens. Figure 18.8 shows examples of shear bands that developed during deformation at 150 °C and illustrates that fracture eventually occurred through one of the deformation bands.

The activation energy for the initiation of serrated yielding in the 0.14% C low-carbon steel martensitic specimens was determined to be 77 kJ/mol (18 kcal/mol), in good agreement with the value calculated by Roberts and Owen for serrated flow during deformation of martensite in Fe-Ni-C alloys. These values of activation energy fall within the ranges reported for serrated flow in ferritic microstructures and for the diffusion of carbon in bcc iron (Ref 18.12). Transmission electron microscopy, Fig. 18.9, showed that the dislocation structure of the martensite in specimens in which serrated yielding had developed consisted of residual linear arrays of screw dislocation lines, in contrast to the high density of tangled dislocations characteristic of as-quenched low-carbon martensite. This observation, together with the measured activation energy, indicates that carbon atoms have diffused to screw dislocations during deformation and that the pinned screw dislocations are no longer able to cross-slip and generate the new dislocations required to sustain uniform deformation (Ref 18.7, 18.13). The uniform deformation during the critical strain stage of deformation is attributed to the motion of edge and mixed dislocations of the as-quenched martensite prior to the pinning of the screw dislocations, but eventually this source of mobile dislocations is exhausted.

When the screw dislocations are no longer able to cross-slip, further deformation is possible only by the generation of new unpinned dislocations. When high densities of mobile dislocations are generated in constant-strain-rate tests, stress drops, as described in Chapter 11, “Deformation,

Fig. 18.8 Deformation bands on sheet tensile specimen that showed serrated flow during testing at 150 °C (300 °F). Source: Ref 18.10

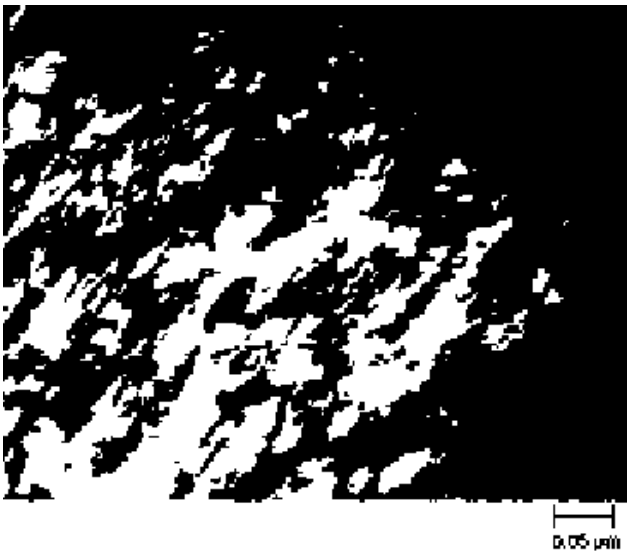

Fig. 18.9 Residual screw dislocation (linear features) substructure in martensite of a 0.14% C steel tensile tested at 150 °C (300 °F) at a strain rate of 8.3×10^{-4} sec^{-1}. Source: Ref 18.5

Strengthening, and Fracture of Ferritic Microstructures," for discontinuous yielding and Lüders band propagation in ferritic microstructures in low-carbon steels. This mechanism explains the stress drops and formation of the localized deformation bands shown in Fig. 18.8, but in deformed martensite the deformation bands do not propagate as do the Lüders bands in ferritic microstructures.

Figure 18.10 summarizes the deformation behavior of low-carbon martensite in the 0.14% C steel tested at 150 °C. As noted relative to Fig. 18.6, only specimens tested at intermediate strain rates develop serrated yielding. Specimens tested at very low strain rates, i.e., those specimens that spend long times at temperature during a test, do not develop serrated yielding, and show high strain hardening and high values of uniform and total elongation. This behavior is explained by the precipitation of carbides during the long time exposures at temperature in the slow strain rate tests. As a result of carbide formation, carbon atoms are not available for segregation and pinning of dislocations; therefore, dislocation multiplication and strain hardening are possible.

The dynamic strain aging and serrated yielding of the hardened low-carbon steel as just described required deformation above room temperature. It is possible that in higher-carbon steels, with higher-martensitic dislocation densities and higher-carbon contents, shorter carbon diffusion distances would make possible significant dynamic strain aging at room temperature, accounting for the as-quenched 4340 stress-strain behavior shown in Fig. 18.5 (Ref 18.14).

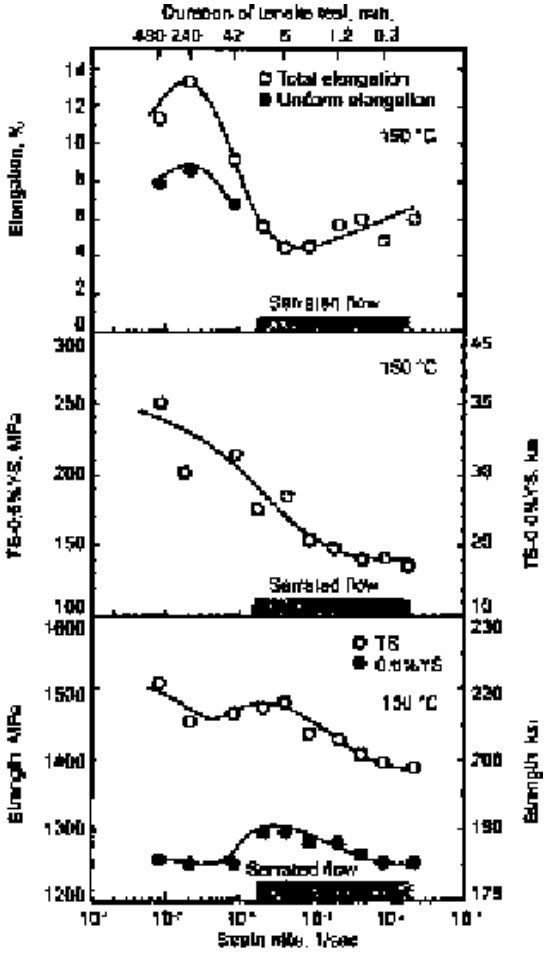

Fig. 18.10 The effect of strain rate on ductility (top), strain hardening (middle), and tensile and yield strengths (bottom) of an 0.14% C steel with martensitic microstructure tested at 150 °C (300 °F). Source: Ref 18.10

Mechanical Behavior of Low-Temperature-Tempered Martensite

As-quenched martensite has the highest hardness of any microstructure that can be produced in a given steel. However, in order to avoid low toughness and brittle fracture, especially in as-quenched higher-carbon steels, as has been shown in Fig. 18.3, quenched steels are tempered over a range of temperatures. To preserve high hardness and strength, martensitic microstructures are tempered at low temperatures, between 150 and 200 °C (300 and 390 °F). Such low-temperature-tempered (LTT) microstructures retain high hardness, achieve high ultimate tensile strengths, and have moderate ductility and fracture resistance, depending on carbon

concentration. Figure 18.11 shows the hardness range associated with LTT steels as a function of carbon content, and Fig. 18.12 shows mechanical properties of 4340 steel as a function of tempering temperature. The differences between yield and ultimate tensile strengths reflect the high strain hardening capacities of LTT 4340 steel microstructures that lead to high tensile strengths. This section describes in detail the effect of carbon content on the fine structure, mechanical properties, deformation mechanisms, and fracture of LTT low-and medium-carbon steels (Ref 18.16, 18.17).

The deformation behavior of LTT hardened microstructures depends primarily on the role that carbon plays in establishing the fine structure that must both resist dislocation motion, in order to provide high yield strength, and sustain dislocation motion, in order to provide high tensile strengths, ductile fracture behavior, and high toughness. Figure 18.4 has shown the lath martensite microstructure in a low-carbon steel, and Fig. 18.13 shows the fine structure of 4130 and 4150 steels quenched to martensite and tempered at 150 °C. Retained austenite does not transform during heating to temperatures below 200 °C, and therefore is a small but

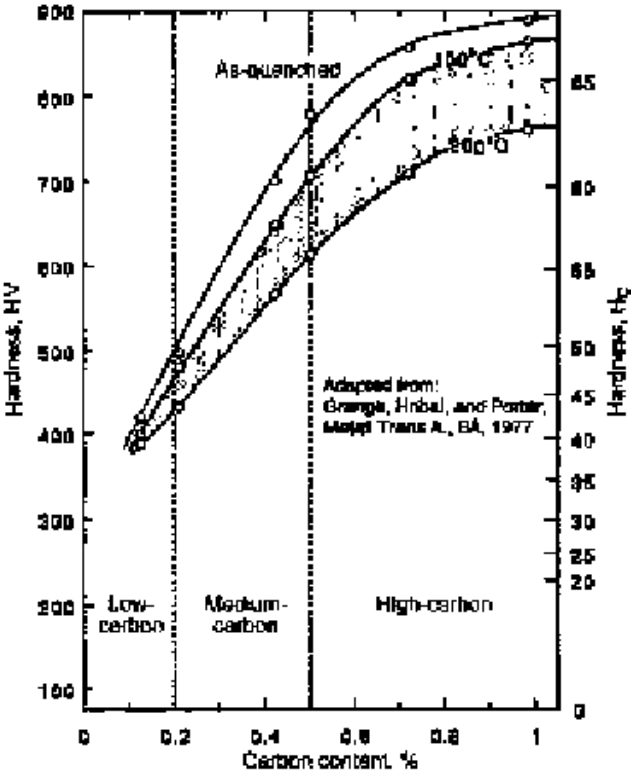

Fig. 18.11 Hardness as a function of steel carbon content for as-quenched and low-temperature-tempered (crosshatched area between 150 and 200 °C, or 300 and 390 °F) martensitic microstructures. Source: Ref 18.15

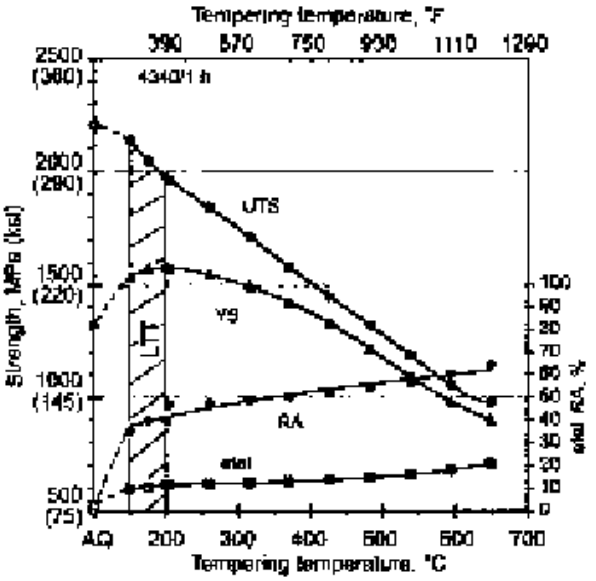

Fig. 18.12 Mechanical properties as a function of tempering temperature for 4340 steel tempered for times of 1 h. Ultimate tensile strength (UTS), yield strength (YS), reduction of area (RA), and total elongation (etel) are plotted, and the properties for low-temperature-tempered (LTT) specimens are noted. Source: Ref 18.4

important LTT microstructural component of hardened low- and medium-carbon steels. The retained austenite is present as thin remnant crystals between martensite laths, and measurements of retained austenite in 4130, 4140, and 4150 steels quenched and tempered at 150 °C showed, respectively, 1.4, 3.8, and 5.9 vol% retained austenite (Ref 18.18).

The dominant component of LTT microstructures is the fine structure or substructure within crystals of tempered martensite. The fine structure consists of high densities of dislocations produced by the lattice invariant deformation and volume changes associated with the martensitic transformation and fine transition carbides that have precipitated to relieve the supersaturation of carbon in the body-centered tetragonal crystal structure of martensite. The dislocations are difficult to resolve, even by transmission electron microscopy, but several studies have shown that the dislocation density in martensite crystals increases with increasing carbon concentration (Ref 18.19–18.21). As carbon content increases, the densities of transition carbides also increase, and spacings between carbides decrease, within the crystals of lath martensite, as shown in Fig. 18.13.

Figure 18.14 shows a family of engineering stress-strain curves for 43xx steels of various carbon contents quenched to martensite and tempered at 150 °C for one hour. All of the curves show continuous yielding, high rates of strain hardening to ultimate tensile strengths, necking instability, and post-uniform necking elongation to ductile fracture. The vari-

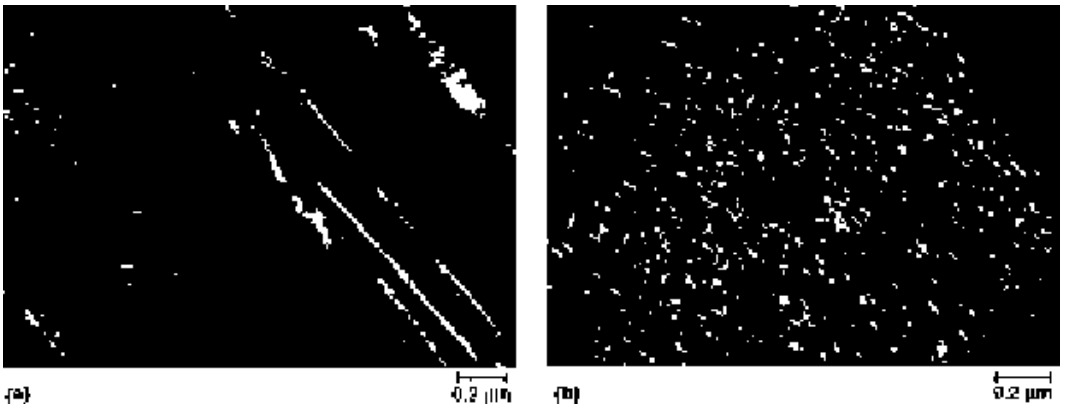

Fig. 18.13 (a) Interlath retained austenite (white diagonal bands) and transition carbides in 4130 steel tempered at 150 °C (300 °F). (b) Dense transition carbide precipitation in a martensite lath in 4150 steel tempered at 150 °C. Dark-field transmission electron micrographs. Courtesy of J.M.B. Losz

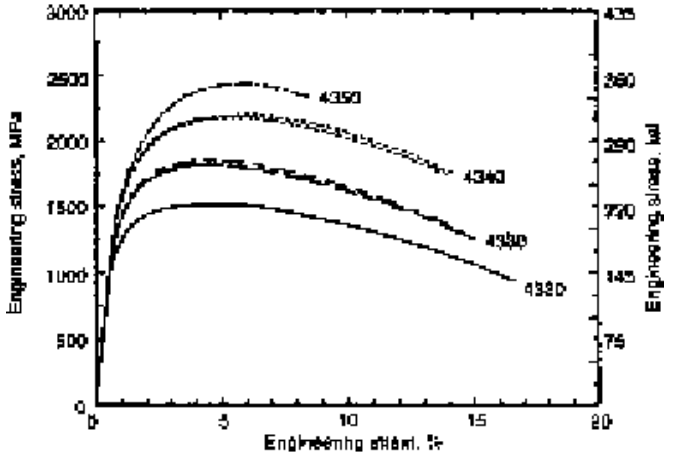

Fig. 18.14 Engineering stress-strain curves for 43xx steels with various carbon contents quenched to martensite and tempered at 150 °C (300 °F) for 1 h. Courtesy of J.A. Sanders

ous stages of deformation are strongly dependent on carbon content. Figures 18.15 and 18.16 show, respectively, strength properties and ductility parameters as a function of steel carbon content for 41xx and 43xx steels with LTT microstructures. With increasing carbon content up to 0.5%, strength parameters increase dramatically, while ductility parameters other than uniform elongation decrease sharply. Only hardness could be measured in LTT steels containing more than 0.5% C because of quench embrittlement. Variations in the amounts of substitutional alloying elements chromium, nickel, and molybdenum in 41xx and 43xx steels have no apparent effect on the mechanical properties of LTT martensites but

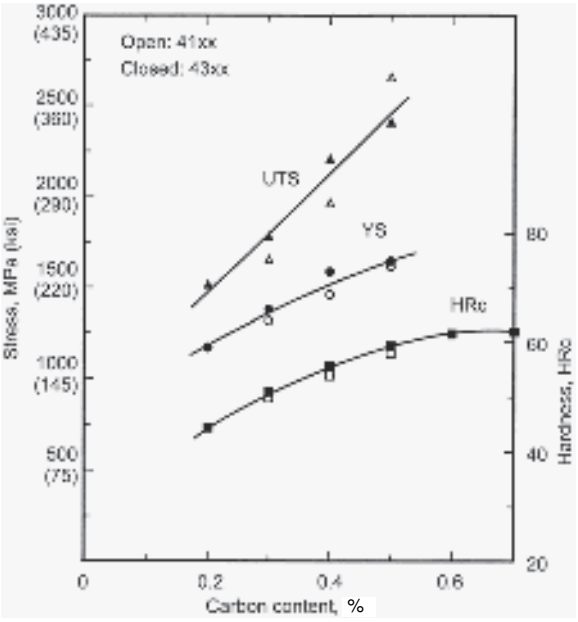

Fig. 18.15 Strength properties as a function of carbon content of 41xx and 43xx steels quenched to martensite and tempered at 150 °C (300 °F) for 1 h

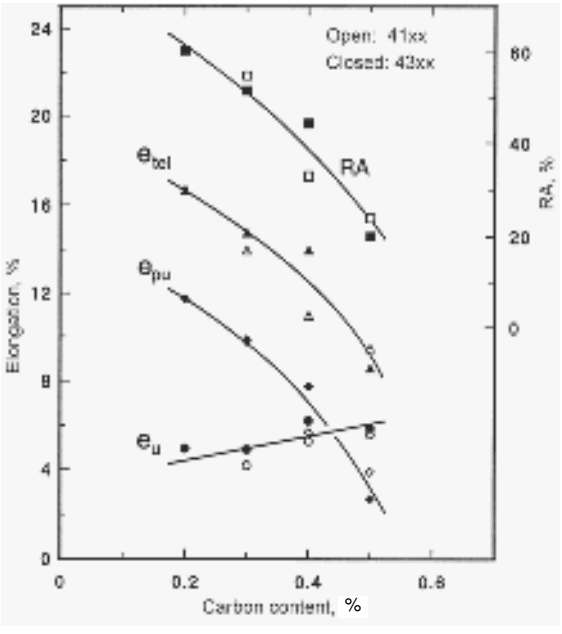

Fig. 18.16 Ductility properties as a function of carbon content of 41xx and 43xx steels quenched to martensite and tempered at 150 °C (300 °F) for 1 h

affect hardenability and at higher tempering temperatures serve to retard softening, as described in earlier chapters.

The mechanical behavior of LTT martensites is very much dependent on their strain-hardening capacities. Elastic limits, i.e., the stresses at which the first plastic flow is measurable, are quite low in as-quenched and LTT martensitic microstructures (Ref 18.22), and Fig. 18.17 shows that elastic limits, measured in the microstrain region, decrease with increasing carbon content (Ref 18.23). The decreases in elastic limits are related to increasing amounts of retained austenite (Ref 18.24, 18.25). With increasing stress, the retained austenite transforms by stress-assisted mechanisms to martensite (Ref 18.26) within the microstrain regime, contributing to very high rates of strain hardening that produce yield strengths measured at 0.002 strain, especially in the medium-carbon steels with higher carbon content, as shown in Fig. 18.17. In high-carbon steels with microstructures consisting of plate martensite and large volume fractions of retained austenite, the austenite transforms to martensite mechanically by strain-induced mechanisms (Ref 18.25, 18.26).

At strains above those that produce macroscopic offset yield strengths, strain hardening continues to increase with increasing carbon content (Ref

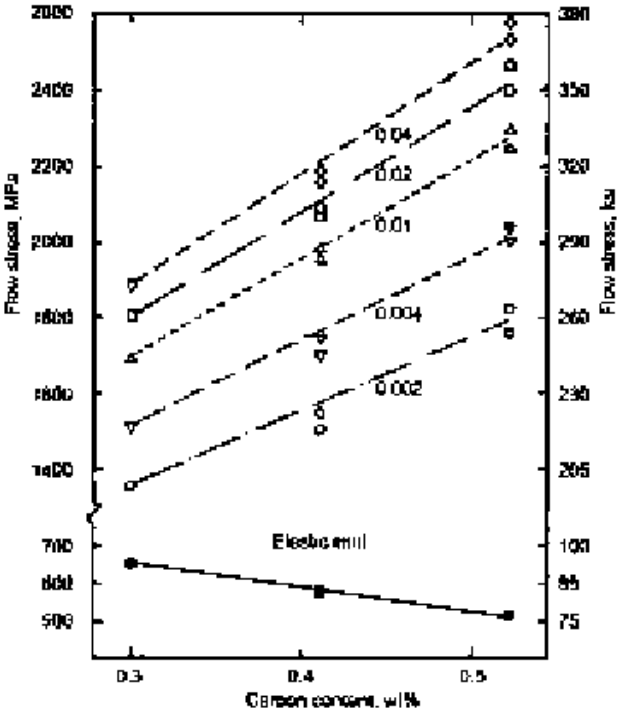

Fig. 18.17 Flow stresses at various plastic strains, determined during compression testing, as a function of carbon content in quenched 41xx steels tempered at 150 °C (300 °F). The elastic limits were determined by strain gage measurements in specimens tempered at 200 °C (390 °F). Source: Ref 18.23

18.16, 18.17). At all strains up to the uniform elongation, the strain-hardening rates of the higher carbon LTT microstructures are higher than those of the low-carbon LTT microstructures. The higher strain-hardening rates lead not only to increased ultimate tensile strengths with increasing carbon content, but also to the increases in uniform elongation shown in Fig. 18.16. The high strain-hardening rates defer necking instability and therefore increase uniform elongation, as described in Chapter 11, "Deformation, Strengthening, and Fracture of Ferritic Microstructures."

Although uniform elongation increases somewhat with increasing carbon content in LTT martensites, all of the other measures of tensile ductility fall sharply with increasing carbon. This carbon dependence is explained by the very high ultimate strengths generated by the strain hardening in the higher-carbon steels. As a result, very little post-uniform strain is required to generate the triaxial stresses required for ductile fracture. The reduced requirement for necking with increasing carbon content is shown on a macroscopic scale in tensile specimens in Fig. 18.18. Figure 18.19 shows the central constrained flat fracture zones and the shear fracture zones that comprise the cup-cone fracture morphologies of the tensile specimens, and Fig. 18.20 and 18.21 show that the central fracture and shear fracture surfaces are characterized by fine microvoids. The central fracture zone has some coarse microvoids, formed around inclusion particles, but most of the microvoids are very fine and have formed around spherical carbide particles, on the order of 50 nm (500 Å) in size, that are typically retained after austenitizing at temperatures commercially used for hardening (Ref 18.27, 18.28). The micromechanism of ductile fracture on the shear lips is also microvoid nucleation, growth, and coalescence, but the microvoids that have formed around undissolved carbide particles are much shallower and more uniform in size than those on the central

Fig. 18.18 Photograph of necking and fracture of tensile specimens of martensitic 41xx steels tempered at 150 °C (300 °F). From left to right: 4130, 4140, 4150

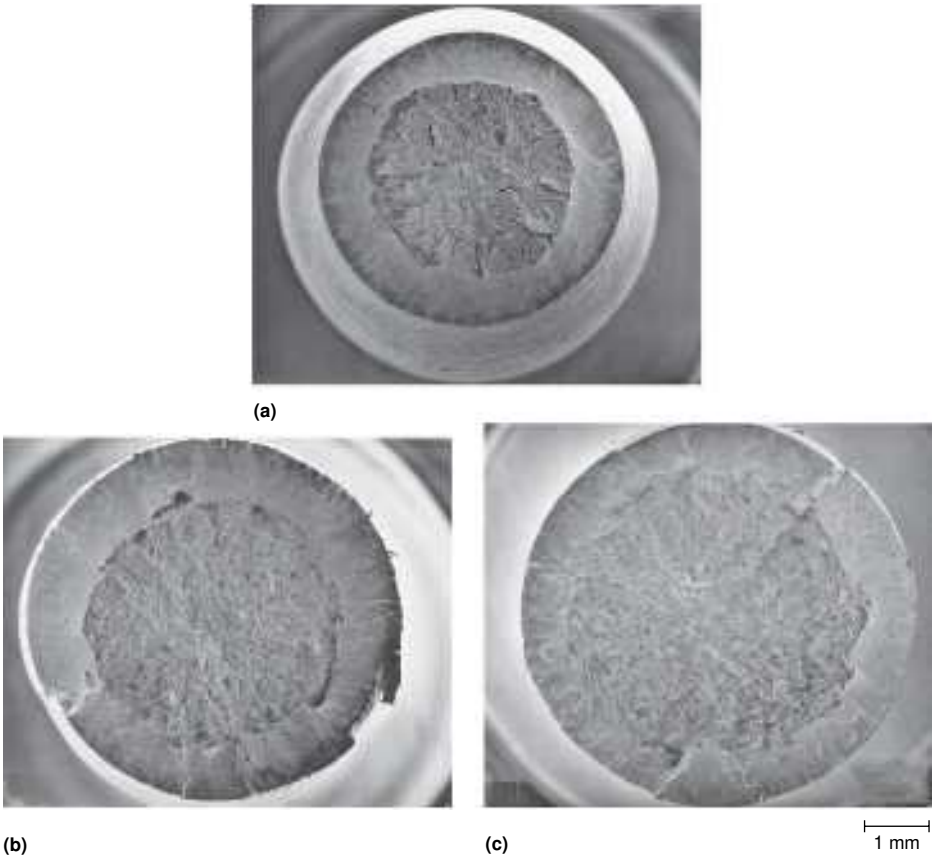

Fig. 18.19 Central and near-surface shear fracture areas of martenstic of 41xx steel tensile specimens tempered at 150 °C (300 °F). (a) 4130. (b) 4140. (c) 4150. SEM micrographs

fracture surfaces of the tensile specimens. Only those particles on the localized shear plane have participated in the ductile fracture process, and few inclusion particles were present on those localized shear planes. The very fine transition carbides, although very important in strain hardening, are too fine to be involved in the ductile fracture process.

Despite the large differences in ultimate tensile strength as a function of carbon content in LTT steels, the critical stresses for microvoid formation at ductile fracture are all about the same, 4000 MPa (580 ksi) (Ref 18.4). This value was calculated from the true plastic stress in the neck of tensile specimens at fracture and the stress concentration due to necking. The specimens were from vacuum-melted steels and therefore had low inclusion contents. Higher coarse inclusion contents would lower fracture stresses. The almost constant fracture stress and the similarity of the fracture surfaces of LTT specimens emphasize the importance of strain hardening in deformation and fracture. Low strain-hardening rates in low-carbon LTT specimens produce low ultimate strengths, and therefore these

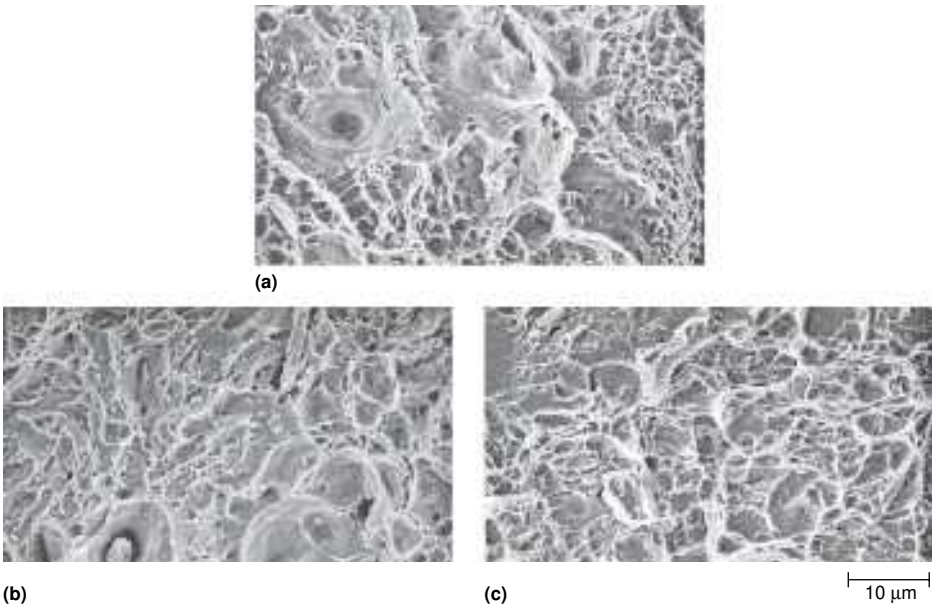

Fig. 18.20 Fracture surface topographies from central fracture regions of martensitic 41xx steel tensile specimens tempered at 150 °C (300 °F). (a) 4130. (b) 4140. (c) 4150. SEM micrographs

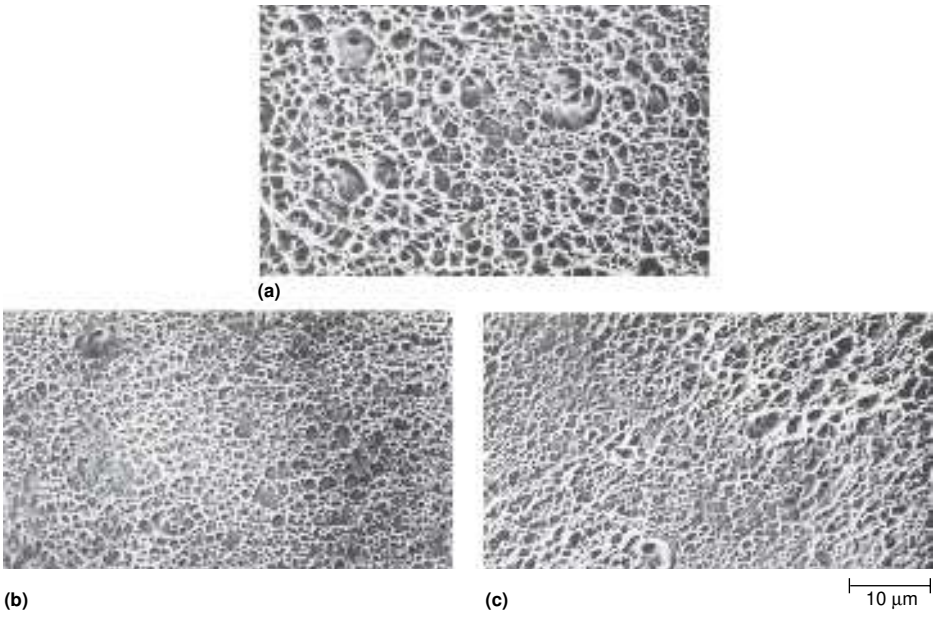

Fig. 18.21 Fracture surface topologies of near-surface shear regions of martensitic 41xx steel tensile specimens tempered at 150 °C (300 °F). (a) 4130. (b) 4140. (c) 4150. SEM micrographs

specimens require considerable necking deformation to reach the critical ductile fracture stress for a given distribution of second-phase particles. In contrast, the high strain-hardening rates of the high-carbon LTT specimens produce much higher ultimate tensile strengths, and therefore little post-uniform deformation is required to produce ductile fracture in specimens with effectively the same distributions of second-phase particles.

The increased strain hardening of LTT martensite with increasing carbon content is related to increasing dislocation densities and increased transition carbide densities with carbon content as described previously. According to the work-hardening theory of Kuhlmann-Wilsdorf (Ref 18.29), the stresses necessary to generate new segments of glide dislocations to sustain plastic deformation are dependent on the longest unrestrained dislocation lengths in a substructure (Ref 18.29). The flow stress, τ, at a given strain is given by:

$$\tau = \tau_0 + \text{constant} \times G\mathbf{b}/l \qquad \text{(Eq 18.1)}$$

where τ_0 is the friction stress for dislocation motion in a crystal structure without other obstacles, G is the shear modulus, $\mathbf{b}$ is the Burgers vector of active dislocations, and l is the average momentary link length or active dislocation length. In LTT martensite free dislocation link lengths are continuously decreased by interactions of dislocations with transition carbides and evolving dislocation substructure and, consequently, flow stresses increase with increasing strain. Finer link lengths are generated in the higher-carbon microstructures with more closely spaced dislocations and more closely spaced transition carbides, and as a result, higher flow stresses and higher rates of strain hardening are generated in the higher-carbon specimens.

The examples of the response of steels with LTT martensitic microstructures to this point have all been presented as a function of temperature for specimens tempered for a constant time, typically one hour. However, the changes in microstructure produced during the first stage of tempering are diffusion dependent and therefore depend on both temperature and time. The effect of both temperature and time on the mechanical properties of LTT martensitic specimens has been characterized in a recent study (Ref 18.4). Samples of 4330, 4340, and 4350 steels quenched to martensite and tempered at 150 °C (300 °F), 175 °C (350 °F), and 200 °C (390 °F) for times of 10 min, 1 h, and 10 h, were subjected to uniaxial tensile testing. The results were plotted as a function of a Hollomon-Jaffe temperature-time parameter of the form $T(C + \log t)$ where temperature T is in Kelvin and time t is in seconds (Ref 18.30). The multiplying effect of temperature and the log term for time in the parameter reflect the greater importance of temperature in producing diffusion-dependent microstructural changes.

Figures 18.22 and 18.23 show, respectively, hardness and ultimate tensile strength as a function of the temperature-time tempering parameter

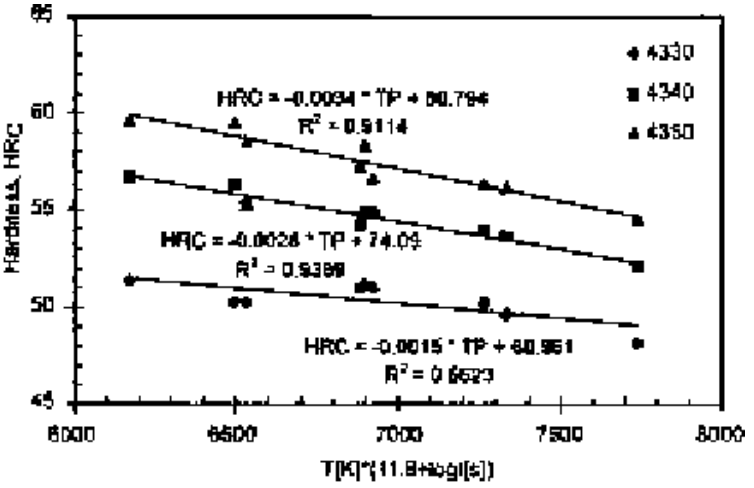

Fig. 18.22 Hardness as a function of temperature-time tempering parameter for 43xx steels tempered for various times at temperatures of 150 °C (300 °F), 175 °C (350 °F), and 200 °C (390 °F). Temperature is in Kelvin and time is in seconds. Source: Ref 18.4

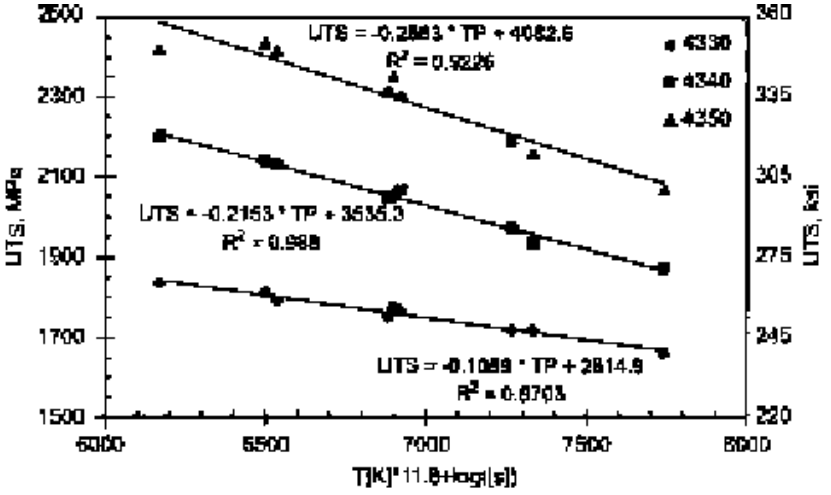

Fig. 18.23 Ultimate tensile strength (UTS) as a function of temperature-time tempering parameter for 43xx steels tempered for various times at 150 °C (300 °F), 175 °C (350 °F), and 200 °C (390 °F). Temperature is in Kelvin and time in seconds. Source: Ref 18.4

for the 43xx steels tempered for various times at temperatures between 150 and 200 °C. For each steel, increasing tempering intensity, either by increasing tempering time or temperature, lowers hardness and tensile strength, and carbon content establishes the baseline for each steel. Figure 18.24 shows an excellent correlation of hardness to ultimate tensile strength for the LTT martensitic microstructures. All of the specimens,

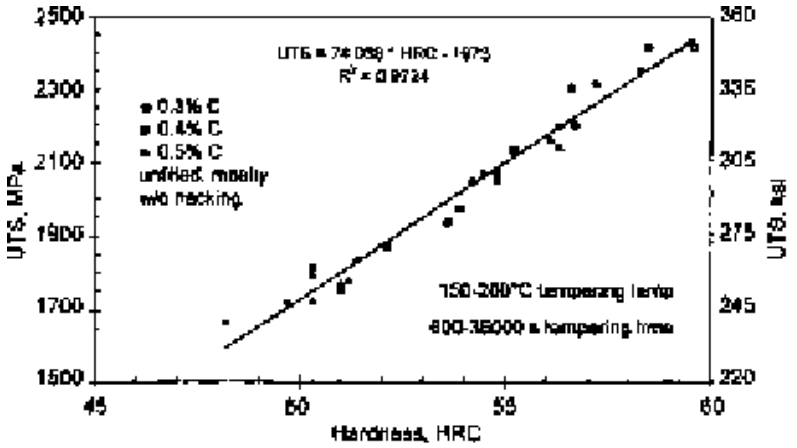

Fig. 18.24 Ultimate tensile strength (UTS) versus hardness for LTT 43xx specimens tempered in the temperature and time ranges noted in the figure. Source: Ref 18.4

except for the 4350 specimens tempered at the lowest temperature for the shortest times, failed by ductile fracture characterized by microvoid formation around second-phase particles close to essentially the same fracture stress of 4000 MPa (580 ksi). The 4350 specimens that did not fail by ductile fracture failed by intergranular brittle fracture typical of quench embrittlement as described in the next chapter.

The continuous decrease in strength with increasing tempering intensity during the first stage of tempering reflects coarsening of the transition carbide arrays and recovery or decreases of high densities of as-quenched dislocations in the matrix martensite. According to the Kuhlmann-Wilsdorf theory, this coarsening of the substructure would increase the free link length of matrix dislocations and reduce flow stresses and strain hardening, leading to reduced ultimate tensile strengths.

Mechanical Behavior of High-Temperature-Tempered Martensite

Figure 18.12 shows that yield and ultimate tensile strengths converge and decrease with increasing tempering temperature for 4340 steel. Although hardness and strength of hardened steels decrease with increasing tempering temperature, high-temperature-tempered (HTT) martensitic microstructures have excellent combinations of strength, ductility, and toughness. The convergence of the yield and ultimate tensile strengths is a result of greatly reduced strain hardening that accompanies the continuous decreases in dislocation densities and the precipitation and coarsening of cementite particles that occur during the second and third stages of tempering as described in Chapter 17, “Tempering of Steel.” These changes in

microstructure effectively increase the free dislocation link lengths in the tempered martensite substructure and reduce the flow stresses necessary for sustained plastic deformation.

This section presents data that extends the work on low-temperature-tempering of 43xx steels to higher tempering temperatures, and is a product of Dr. Young-Kook Lee during a research visit to the Colorado School of Mines in 1998 (Ref 18.31, 18.32). Specimens were quenched to martensite and tempered at 250 °C (480 °F), 300 °C (570 °F), 350 °C (660 °F), 400 °C (750 °F), 500 °C (930 °F), and 600 °C (1110 °F) for times of 10 min, 1 h, and 10 h. Figures 18.25, 18.26, and 18.27 show, respectively, engineering stress-strain curves for 4330, 4340, and 4350 steels tempered at temperatures from 150 to 600 °C (300 to 1110 °F) for1h or 3600 seconds. Dramatic decreases in strength with increasing tempering temperature are shown. Curves of strain hardening as a function of true strain calculated from the tensile data in Fig. 18.25 to 18.27 are shown in Fig. 18.28 to 18.30. The decreases in ultimate tensile strengths for the three steels correlate well with significant decreases in strain hardening. Minima in the strain-hardening curves at low strains identify inflection points on the stress-strain curves that mark the transition to discontinuous yielding after high-temperature tempering, and very little strain hardening occurs in the coarse, recovered microstructures of the specimens tempered at the highest temperatures.

The tensile data of the 43xx steels tempered at temperatures above those that produce first-stage microstructures provide some evidence for

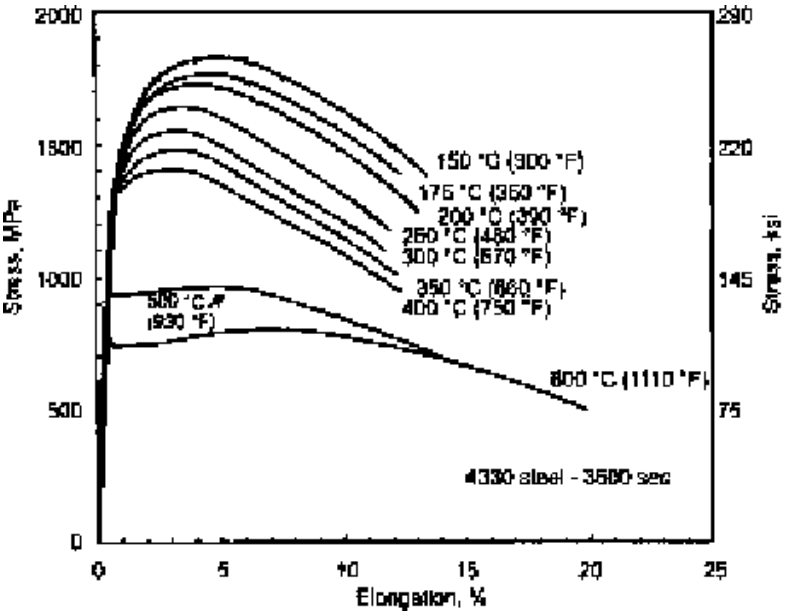

Fig. 18.25 Engineering stress-strain curves for quenched 4330 steel tempered at various temperatures for 1 h. Courtesy of Young-Kook Lee. Source: Ref 18.31

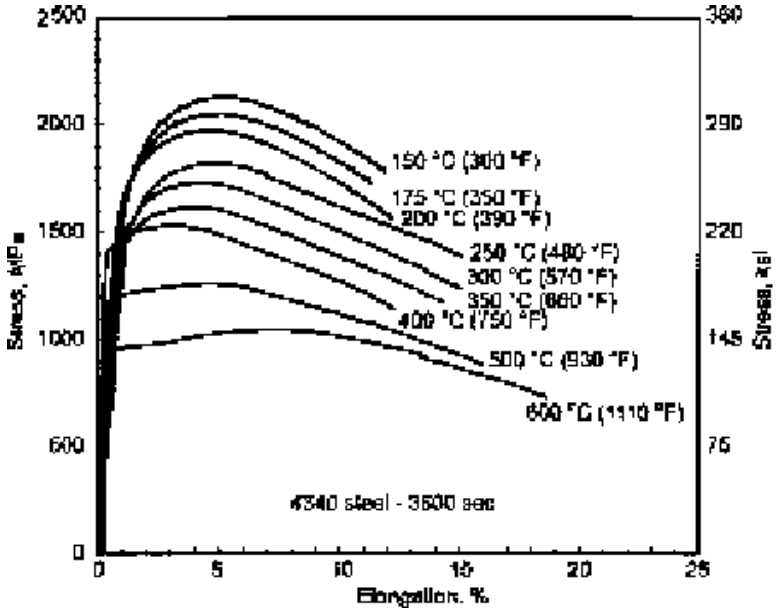

Fig. 18.26 Engineering stress-strain curves for quenched 4340 steel tempered at various temperatures for 1 h. Courtesy of Young-Kook Lee. Source: Ref 18.31

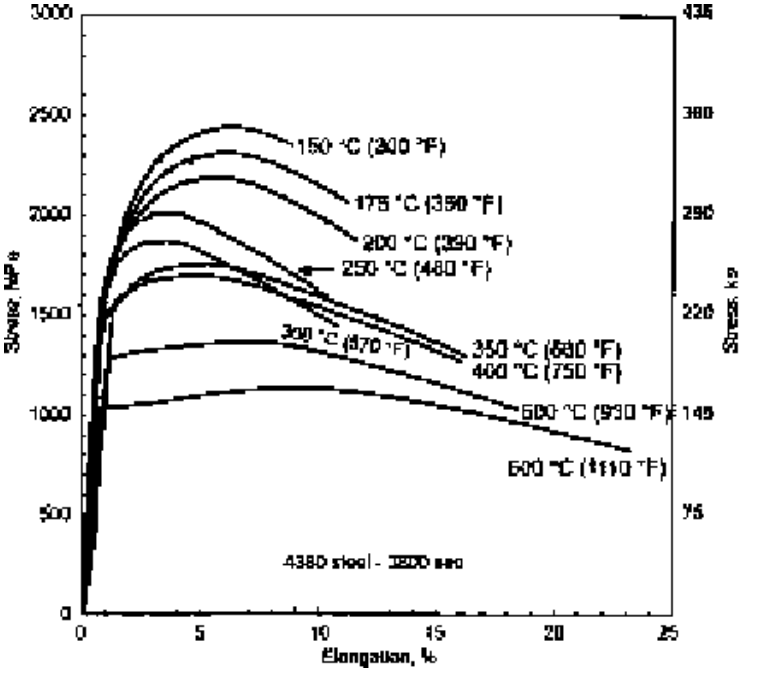

Fig. 18.27 Engineering stress-strain curves for quenched 4350 steel tempered at various temperatures for 1 h. Courtesy of Young-Kook Lee. Source: Ref 18.31

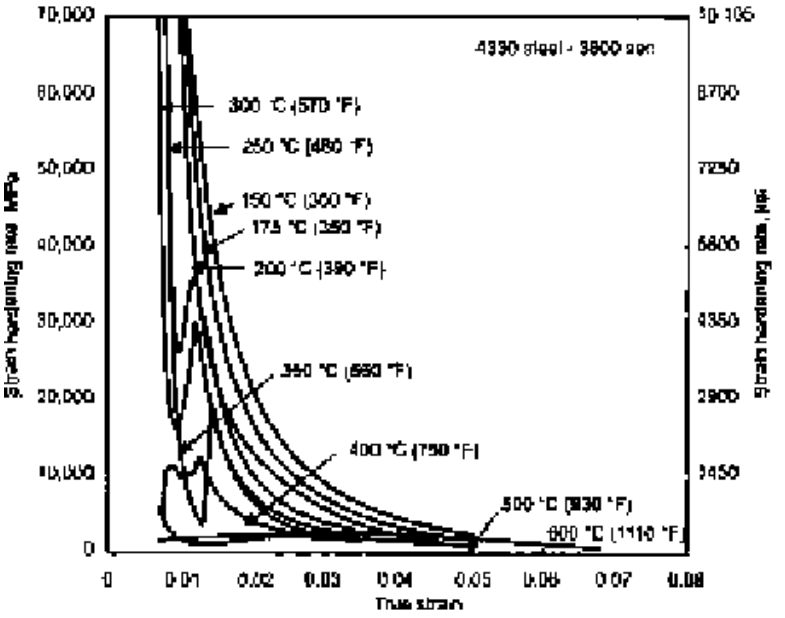

Fig. 18.28 Strain hardening as a function of true strain for quenched 4330 specimens tensile tested after tempering at various temperatures for 1 h. Courtesy of Young-Kook Lee. Source: Ref 18.31

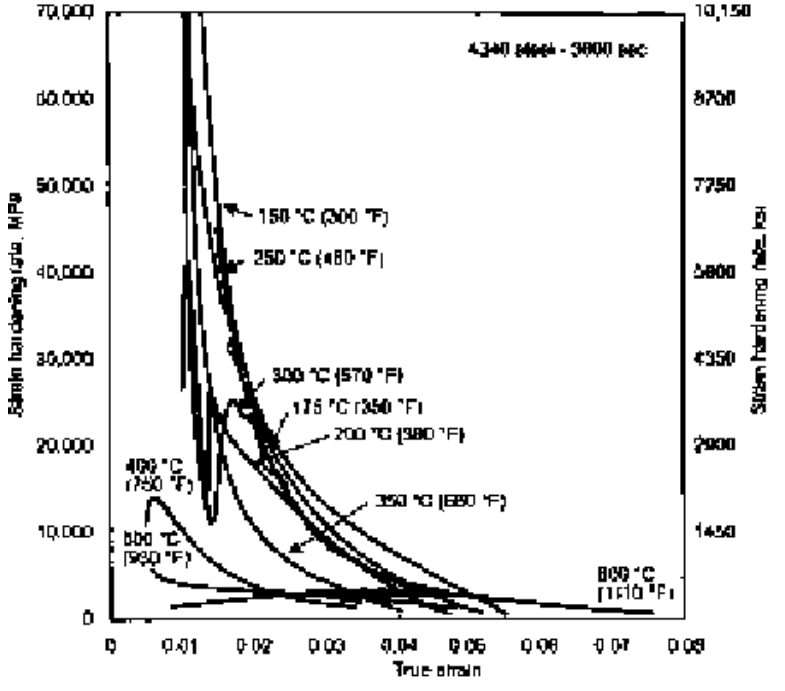

Fig. 18.29 Strain hardening as a function of true strain in quenched 4340 specimens tensile tested after tempering at various temperatures for 1 h. Courtesy of Young-Kook Lee. Source: Ref 18.31

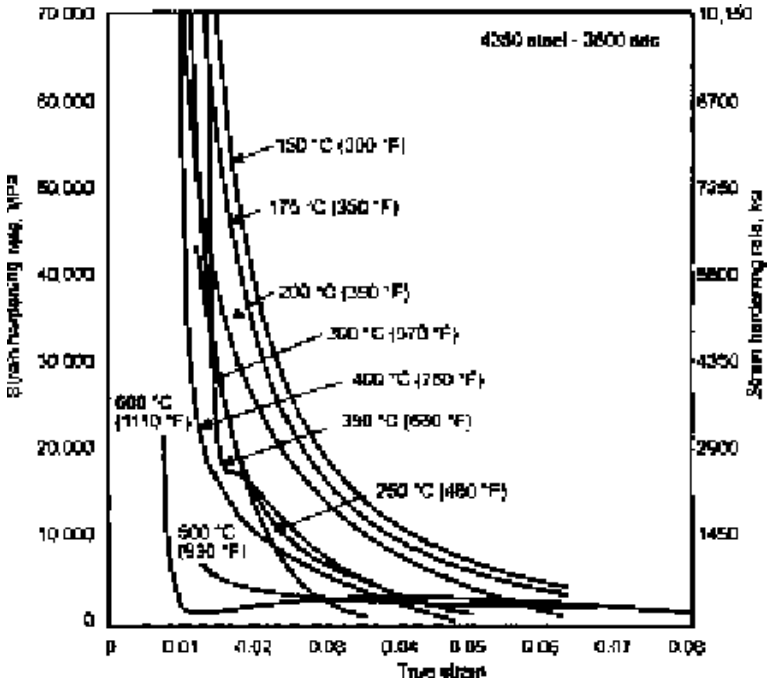

Fig. 18.30 Strain hardening as a function of true strain for quenched 4350 specimens tensile tested after tempering at various temperatures for 1 h. Courtesy of Young-Kook Lee. Source: Ref 18.31

embrittlement phenomena that develop on tempering. In particular, the stress-strain curves for the 4330 steel tempered at temperatures between 250 and 400 °C (480 and 750 °F) show decreased elongation compared with the LTT specimens tempered between 150 and 200 °C (300 and 390 °F). This reduction in ductility, despite reduced strength, is a typical manifestation of tempered martensite embrittlement in slow strain-rate tests and is associated with coarse carbide particles introduced by second- and third-stage tempering. Figures 18.31 and 18.32 show, respectively, reduction of areas measured from tensile specimens of the 43xx steels tempered at one hour and 10 h. Reduction of area of the specimens tempered for one hour show essentially a continuous increase with increasing tempering temperature. However, the specimens tempered for 10 h show a sharp drop in reduction of area at 500 °C (930 °F). This drop in ductility correlates with temper embrittlement, an embrittlement phenomenon that develops at high tempering temperatures, around 500 °C, after long-time temperature exposure. The long times are related to the fact that the embrittlement is associated with cosegregation of substitutional alloying elements, which require long times for diffusion, and impurity elements such as phosphorus, to prior austenite grain boundaries.

Figures 18.33, 18.34, and 18.35 show, respectively, yield strength, ultimate tensile strength, and hardness as a function of the temperature-time

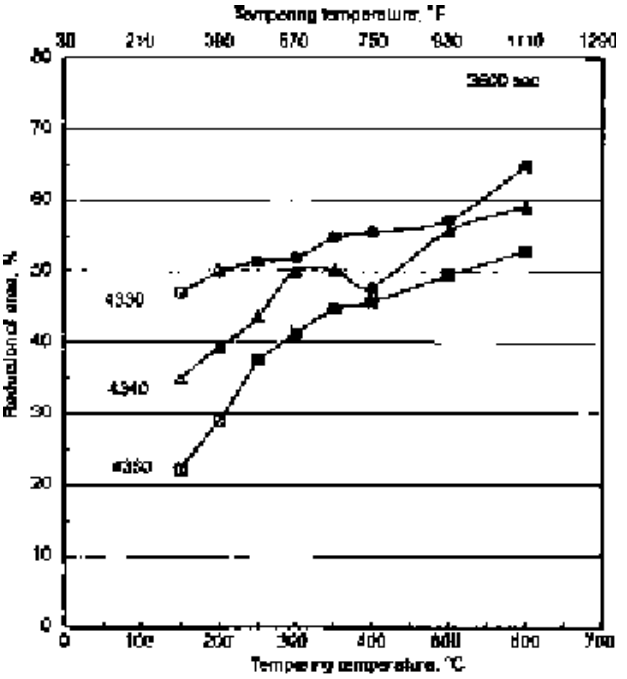

Fig. 18.31 Reduction of area as a function of tempering temperature for quenched 43xx specimens tempered for 1 h (3600 s). Courtesy of Young-Kook Lee. Source: Ref 18.31

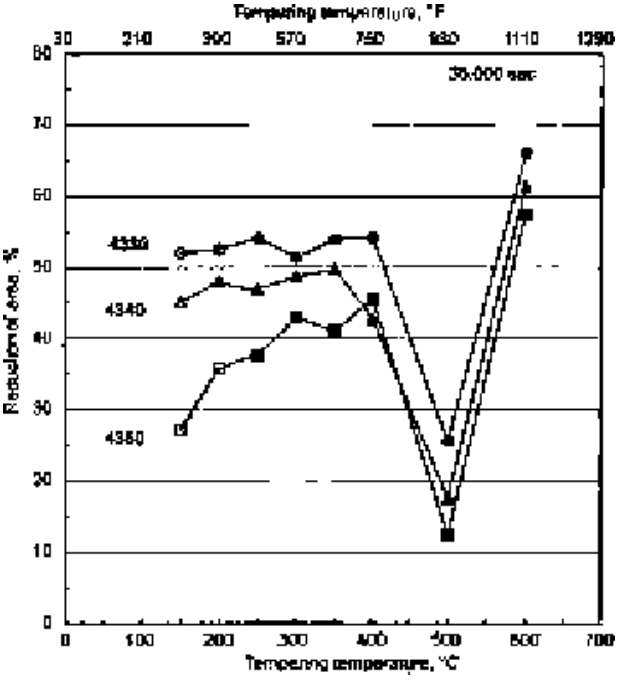

Fig. 18.32 Reduction of area versus tempering temperature for quenched 43xx steels tempered for 10 h (36,000 s). Courtesy of Young-Kook Lee. Source: Ref 18.31

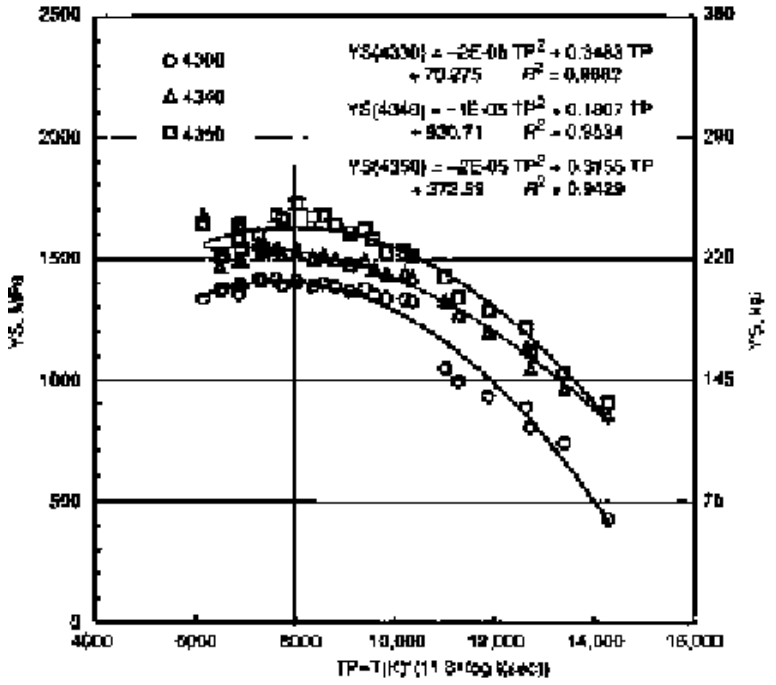

Fig. 18.33 Yield strength as a function of time-temperature tempering parameter for quenched 43xx steels tempered for various times and temperatures. Courtesy of Young-Kook Lee. Source: Ref 18.31

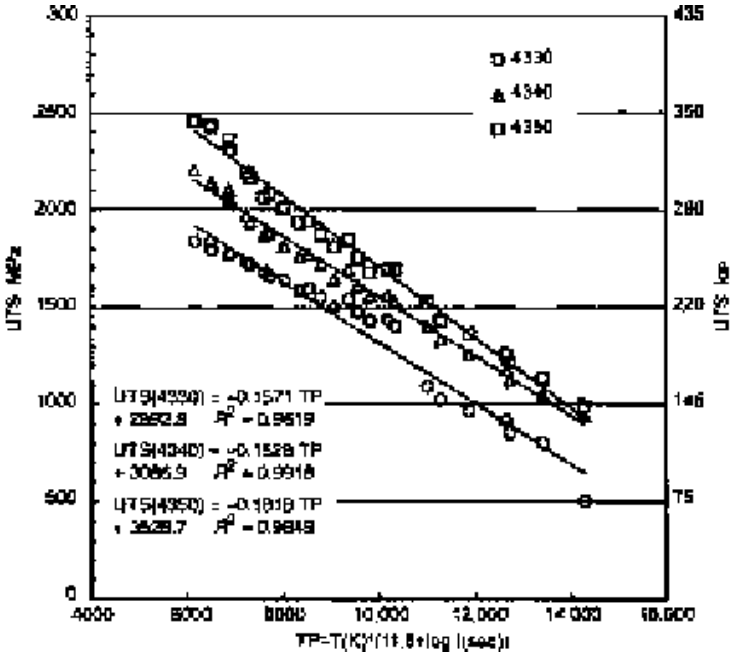

Fig. 18.34 Ultimate tensile strength (UTS) as a function of temperature-time tempering parameter for quenched 43xx steels tempered at various times and temperatures. Courtesy of Young-Kook Lee. Source: Ref 18.31

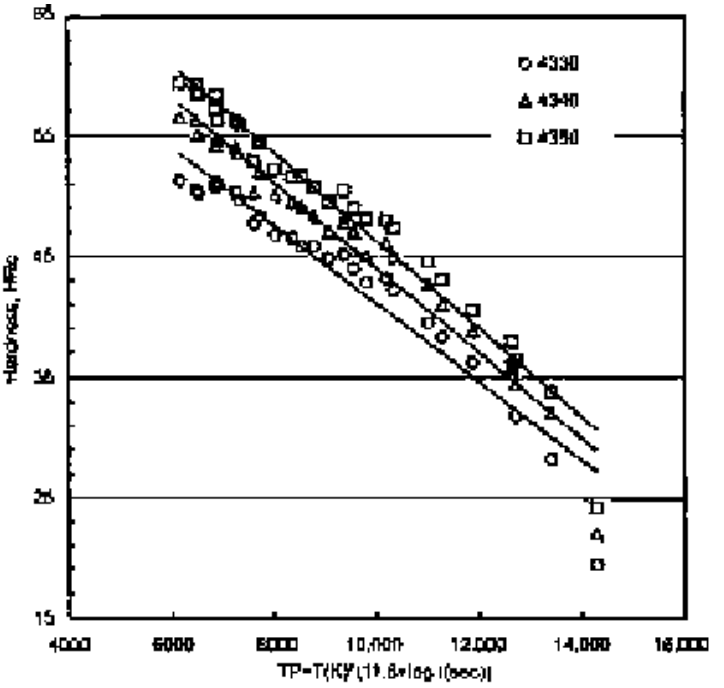

Fig. 18.35 Hardness as a function of temperature-time tempering parameter for quenched 43xx steels tempered at various times and temperatures. Courtesy of Young-Kook Lee. Source: Ref 18.31

tempering parameter for the hardened 43xx steels. The yield strength data (Fig. 18.33) show the transition between LTT and HTT deformation behavior and the strong effect of the lightly tempered structures on producing lower yield strengths. The low yield strengths are related to high densities of unpinned dislocations. When this source of plasticity is reduced by recovery, higher stresses are required to initiate yielding and the stress-strain curves at low strains are less rounded. The ultimate tensile strength and hardness data for all tempering heat treatments provide reasonable straight line fits, but an argument could be made for a change in slope at the transition between LTT and HTT microstructures. The very low hardness values, below valid levels for the Rockwell C scale, for the specimens tempered at the highest temperatures for the longest times, Fig. 18.35, are a result of the recrystallization of the tempered martensite microstructure, as described in Chapter 17, "Tempering of Steel."

Summary of Microstructure, Strengthening, and Fracture Mechanisms of Quenched and Tempered Carbon and Low Alloy Carbon Steels

This chapter has described in detail some of the deformation and fracture mechanisms that operate in the microstructures of quenched and tem-

pered steels. The microstructures have many components, each of which makes some sort of contribution to mechanical behavior. Table 18.2 lists in the left column the many components that may make up the microstructural systems of quenched and tempered carbon steels, depending on alloy composition and tempering. The other columns then briefly state the effect of each component on mechanical behavior after tempering at low and high temperatures. The emphasis is on the mechanisms that drive mechanical behavior: quantitative examples such as stress-strain curves have been given earlier in this chapter.

A version of Table 18.2 was first published in 2011 in an effort to relate tempered martensitic microstructures to hydrogen embrittlement, in view of the possibility that each microstructural component under certain conditions may serve as a trapping site for hydrogen (Ref 18.33). However, apart from consideration of susceptibility to hydrogen embrittlement, Table 18.2 identifies two quite different sets of microstructures and strengthening mechanisms produced by quenching and tempering. One set is pro-

Table 18.2 Components in quenched and tempered low- and medium-carbon steels microstructural systems, their effect on mechanical behavior, and effect of tempering.

LTT refers to low-temperature tempering, 150 to 200 °C, or 300 to 390 °F, and HTT refers to high-temperature tempering, roughly 500 to 650 °C, or 930 to 1200 °F

Microstructural component	Mechanical contribution	Effect of increasing tempering
Inclusions	No strengthening; fracture initiation sites	None
Retained carbides after austenitizing	Microvoid initiation sites during ductile fracture	None during LTT; coarsening during HTT
Dislocations in martensite crystals	Major strengthening component in LTT steels	Major decreases to strengthening due to reductions in densities by recovery mechanisms
Eta transition carbides in martensite crystals	Major strengthening component in LTT steels	Replaced by cementite after tempering above 200 °C (390 °F)
Martensite crystal boundaries	Minor strengthening component in LTT steels	Large angle residual martensite crystal boundaries are a major source of HTT strengthening
Retained austenite	Stress-induced transformation to martensite in LTT steels; above 200 °C (390 °F) transforms to carbides and the carbides cause tempered martensite embrittlement	Transforms to cementite and ferrite above 200 °C (390 °F); silicon retards cementite formation
Martensite packet and/or block boundaries	Minor strengthening component in LTT steels	Intra-packet structure coarsens with increasing tempering
Prior austenite grain boundaries	Minor strengthening component; sites for impurity and carbon atom segregation leading to susceptibility to intergranular fracture in steels with more than 0.5% C in LTT conditions	Strengthening largely unchanged unless tempered martensite recrystallizes at very high HTT. Effects of quench embrittlement are eliminated by HTT, but other types of embrittlement with intergranular fracture may occur
Cementite and/or alloy carbides formed during tempering	Cementite does not form during LTT tempering; during HTT tempering Mn, Cr, Mo are incorporated into cementite, reduce rate of coarsening and softening.	During HTT cementite contributes dispersion strengthening; alloy carbides may precipitate, and may cause secondary hardening
Nitrides, carbides, and/or carbonitrides formed by V, Nb, or Ti	May retard austenite grain growth during austenitizing; retard coarsening during HTT tempering	May precipitate during HTT, may contribute secondary hardening

duced by low-temperature tempering between 150 and 200°C (300 and 390 °F), the other by high-temperature tempering approximately between 500 and 650 °C (930 and 1200 °F). Tempering treatments between these two sets are certainly used industrially, but the two sets identified here are used to relate major differences in substructure to quite different strengthening mechanisms.

The LTT properties are produced by intense strain hardening of the high-density dislocation/transition carbide substructure within martensitic crystals. Only carbon atom diffusion influences the changes in substructure. The stresses required to move and multiply closely spaced dislocations produce the high rates of strain hardening that lead to high ultimate tensile strengths and high hardness.

In contrast, HTT properties in the extreme case are dependent on grain-boundary and dispersion strengthening. Strain hardening is minimal and hydrogen embrittlement resistance is high. In this extreme case, high-temperature tempering may remove all dislocations that are part of as-quenched and LTT substructures, and cementite particles, enriched in alloying elements, and possibly also alloy carbide precipitates, replace very fine transition carbides. As described in Chapter 17, "Tempering of Steel," at least in Fe-C alloys, high-temperature tempering eliminates low-angle boundaries between martensite crystals, but retains the very closely spaced large-angle grain boundaries in packets of the lath martensite that forms in low- and medium-carbon steels, thus providing very fine effective grain size. Fine grain size, Chapter 11, "Deformation, Strengthening, and Fracture of Ferritic Microstructures ," is the one strengthening mechanism that increases both strength and fracture resistance, and in the case of HTT martensite the very fine size of the remnant lath martensite crystals provides exceptional combinations of strength and toughness. Elements such as Mn, Mo, and Cr in low-alloy steels help to keep the tempered martensite (now ferrite) crystal structure fine by maintaining fine carbide sizes that serve to pin boundaries and limit grain growth.

As noted, the HTT microstructures and mechanisms described above, with or without minimal retained dislocation content and retaining the fine lath structure of martensite, represent an extreme combination of strength and structure. More intense tempering eventually produces the equiaxed ferrite/spheroidized cementite microstructure of spheroidized steels.

On the other side of HTT, less intense tempering, or the effects of alloying and austenitizing, may cause dislocations to be retained and contribute to strain hardening and strengthening. These effects are demonstrated when microalloyed steels are either direct-quenched to martensite after hot rolling or reheated and austenitized after hot rolling and quenched to martensite (Ref 18.34, 18.35). High-temperature-tempered martensitic steels direct-quenched from high rolling temperatures may retain microalloying elements in solution in the austenite that is subsequently quenched into the martensite and therefore during high-temperature tempering pre-

vent recovery of dislocation structures and/or cause fine-scale secondary carbide precipitation. This effect is best demonstrated by differences in yielding: direct-quenched HTT stress strain curves show the continuous yielding associated with high retained dislocation contents and associated strain hardening, and reaustenitized samples show the discontinuous yielding associated with low and pinned dislocation densities (Ref 18.36). During reaustenitizing, microalloying elements that would affect high-temperature tempering may be removed from solution in the austenite and therefore not be available to restrain recovery of lath martensitic microstructures during tempering.

The discussion in the previous paragraph shows there is still much to be learned about the mechanisms of strengthening and microstructural change, in particular the interrelationships of alloying, austenitizing, and tempering at higher temperatures, in quenched and tempered steels. Nevertheless the discussion is summarized and framed by the brief statements in Table 18.2 by what is generally known at this point about the complex multi-component microstructural systems of quenched and tempered martensite and the effects of tempering on those microstructures, strengthening, and fracture mechanisms in carbon and low-alloy carbon steels.

REFERENCES

18.1 M. Cohen, The Strengthening of Steel, *Trans. TMS-AIME,* Vol 224, 1962, p 638–657

18.2 G. Krauss, Martensite in Steel: Strength and Structure, *Mater. Sci. Eng.,* Vol A273–275, 1999, p 40–57

18.3 W.C. Leslie and R.J. Sober, The Strength of Ferrite and of Martensite as Functions of Composition, Temperature and Strain Rate, *Trans. ASM,* Vol 60, 1967, p 459–484

18.4 M. Saeglitz and G. Krauss, Deformation, Fracture and Mechanical Properties of Low-Temperature-Tempered Martensite in SAE 43xx Steels, *Metall. and Mater. Trans. A,* Vol 28A, 1997, p 377–387

18.5 Shoji Okamoto, "Strain Rate and Temperature Effects on Deformation Behavior and Mechanical Properties of As-Quenched Low-Carbon Martensite," M.S. thesis, Colorado School of Mines, Golden, CO, 1990

18.6 A. Portevin and F. Le Chatelier, *C.R. Hebd. Seanc Acad. Sci.Paris,* Vol 176, 1923, p 507

18.7 William C. Leslie, *The Physical Metallurgy of Steels,* McGraw-Hill Book Company, New York, 1981, p 90–94

18.8 W.S. Owen and M.J. Roberts, Dynamic Aging Effects in Ferrous Martensite, *Trans. Jpn. Inst. Met.,* Vol 9, 1968, p 911–918

18.9 M.J. Roberts and W.S. Owen, Unstable Flow in Martensite and Ferrite, *Metall. Trans.,* Vol 1, 1970, p 3203–3213

18.10 S. Okamoto, D.K. Matlock, and G. Krauss, The Transition from Serrated to Non-Serrated Flow in Low-Carbon Martensite at 150 C, *Scr. Metall. Mater.,* Vol 25, 1991, p 39–44

18.11 S. Okamoto, D.K. Matlock, and G. Krauss, Strain Rate and Temperature Effects on Deformation Behavior and Mechanical Properties of Low-Carbon Martensite, *Proceedings of ICOMAT-92,* C.M. Wayman and J. Perkins, Ed., Monterey Institute for Advanced Studies, Monterey, CA, 1993, p 451–456

18.12 A.S. Keh, Y. Nakada, and W.C. Leslie, Dynamic Strain Aging in Iron and Steel, *Dislocation Dynamics,* A.R. Rosenfield and G.T. Hahn, Ed., McGraw-Hill, New York, 1968, p 381–408

18.13 J.P. Hirth, Factors Contributing to Brittle Fracture in BCC Metals, *Mechanical Properties of BCC Metals,* M. Meshii, Ed., TMS-AIME, 1982, p 181–187

18.14 G. Krauss, Carbon-Dependent Fracture of As-Quenched Martensite, *Displacive Phase Transformations and Their Applications in Materials Engineering,* K. Inoue et al., Ed., TMS, Warrendale, PA, 1998, p 37–42

18.15 G. Krauss, Heat Treated Martensitic Steels: Microstructural Systems for Advanced Manufacture, *ISIJ Int.,* Vol 35, 1995, p 349–359

18.16 G. Krauss, Verformung und Bruch Martensitischer Stähle, *Härt.-Tech. Mitt.,* Vol 46, 1991, p 7–15

18.17 G. Krauss, Deformation and Fracture in Martensitic Carbon Steels Tempered at Low Temperatures, *Metall. and Mater. Trans. A,* Vol 32A, 2001, p 861–877

18.18 D.L. Willamson, R.G. Schupmann, J.F. Materkowski, and G. Krauss, Determination of Small Amounts of Austenite and Carbide in a Hardened Medium Carbon Steel by Mossbauer Spectroscopy, *Metall. Trans. A,* Vol 10A, 1979, p 379–382

18.19 L.-A. Norstrom, On the Yield Strength of Quenched Low-Carbon Lath Martensite, *Scand. J. Metall.,* Vol 5, 1976, p 159–165

18.20 P.M. Kelly and M. Kehoe, The Role of Dislocations and Interstitial Solute on the Strength of Ferrous Martensite, *New Aspects of Martensitic Transformations, Supplement to Trans. Jpn. Inst. Met.,* Vol 17, 1976, p 399–404

18.21 T. Furuhara, S. Morito, and T. Maki, Morphology, Substructure and Crystallography of Lath Martensite in Fe-C Alloys, *J. Phys. IV France,* Vol 112, 2003, p 255–258

18.22 H. Muir, B. L. Averbach, and M. Cohen, The Elastic Limit and Yield Behavior of Hardened Steels, *Trans. ASM,* Vol 47, 1955, p 380–407

18.23 G. Baozhu, J.M.B. Losz, and G. Krauss, Substructure and Flow Strength of Low-Temperature Tempered Medium Carbon Martensite, *Proceedings of The International Conference on Martens-*

itic Transformations, The Japan Institute of Metals, 1986, p 367–374

18.24 M.A. Zaccone and G. Krauss, Elastic Limits and Microplastic Response in Ultrahigh Strength Carbon Steels, *Metall. Trans. A,* Vol 20A, 1989, p 188–191

18.25 M.A. Zaccone and G. Krauss, Elastic Limit and Microplastic Response of Hardened Steels, *Metall. Trans. A,* Vol 24A, 1993, p 2263–2277

18.26 G.B. Olson, Transformation Plasticity and the Stability of Plastic Flow, *Deformation, Processing, and Structure,* G. Krauss, Ed., ASM International, 1984, p 391–424

18.27 F. Zia-Ebrahimi and G. Krauss, Mechanisms of Tempered Martensite Embrittlement in Medium Carbon Steel, *Acta Metall.,* Vol 32, 1984, p 1767–1778

18.28 A. Reguly, T.R. Strohaeker, G. Krauss, and D.K. Matlock, Quench Embrittlement of Hardened 5160 as a Function of Austenitizing Temperature, *Metall. and Mater. Trans. A,* Vol 35A, 2004, p 153–162

18.29 D. Kuhlmann-Wilsdorf, Theory of Workhardening 1934–1984, *Metall. Trans. A,* Vol 16A, 1985, p 2091–2108

18.30 J.H. Hollomon and L.D. Jaffe, *Trans. AIME,* Vol 162, 1945, p 223–249

18.31 Y.-K. Lee, unpublished research, Colorado School of Mines, Golden, CO, 1998

18.32 Y.-K. Lee and G. Krauss, Effects of Tempering on Tensile Properties of Medium-Carbon Low-Alloy Steels, *J. Korean Soc. Heat Treat.,* Vol 12 (No. 4), 1999, p 327–337

18.33 G. Krauss, Martensitic Microstructural Systems in Carbon Steels and Susceptibility to Hydrogen Embrittlement, *Iron and Steel Technology,* Vol 8 (No. 9), 2011, p 188–195

18.34 R.K. Weiss, "Strength Differences in Direct-Quenched and Reaustenitized-and-Quenched Plate Steels," Ph.D. Thesis, Colorado School of Mines, Golden, CO, 1994

18.35 S. Kennett, "Strengthening and Toughening Mechanisms in Low-C Microalloyed Martensitic Steel as Influenced by Austenite Conditioning," Ph.D. Thesis, Colorado School of Mines, Golden, CO, 2014

18.36 R.P. Foley, R. K. Weiss, S. W. Thompson, and G. Krauss, Tempering Behavior of Martensitic Plate Steels Produced by Direct-Quench and Reaustenitize-and-Quench Processing, *International Symposium on Low-Carbon Steels for the 90's*, R. Asfahani and G. Tither, Ed., TMS, 1993, p 243–256

CHAPTER **19**

Low Toughness and Embrittlement Phenomena in Steels

TOUGHNESS IS THE TERM used to describe the ability of a steel microstructure to resist fracture. Many factors in addition to microstructure affect whether a steel will have high or low toughness, and these factors are incorporated into the many tests used to evaluate fracture behavior. *Charpy V-notch* (CVN) testing evaluates the effect of high strain rate loading and a sharp notch on the energy absorbed for fracture. Tensile tests measure, at low strain rates, reduction of area and total elongation, both parameters sensitive to fracture, and the area under the stress-strain curve offers a measure of the energy absorbed for deformation and fracture. *Fracture toughness* (K_{IC}) testing evaluates stress intensities required to propagate unstable fracture in front of a sharp crack under conditions of maximum constraint of plastic flow. Thus, CVN impact testing and tensile testing evaluate deformation prior to crack initiation as well as fracture propagation mechanisms in relatively large process volumes in test specimens, while fracture toughness evaluates only crack propagation in the presence of an already-created flaw in a relatively small process zone ahead of the flaw. Each type of testing depends on specimen design and dimensions and testing methodology, and the reader is referred to the Handbook literature for details of the various tests (Ref 19.1, 19.2).

There are two quite different stages in the life of steel products when difficulties with fracture resistance and cracking may be a problem. The first stage is during steelmaking, steel solidification, and hot working, i. e., during primary processing. Cracking developed during this stage is identified and corrected in the steel mill, but may occasionally find its way into finished products. The second major stage is in finished steel products,

either associated with final heat treatment or during low-performance and fracture during application. These types of failure and the stress states that cause the failures are described by Wulpi (Ref 19.3).

This chapter describes some of the interrelated processing, chemical, and microstructural causes associated with cracking, low toughness, and embrittlement phenomena in carbon and low-alloy steels and relates these causes to fracture surface characteristics. Embrittlement implies a processed microstructural condition that creates lower toughness than expected for a steel (Ref 19.4). For example, a generally valid rule for coupling properties and toughness states that the lower the hardness and strength, the higher are the ductility and toughness of a microstructure. However, embrittlement phenomena are exceptions to this rule, and tempered martensite embrittlement, for example, lowers ductility and toughness as hardness and strength decrease within a certain range of tempering temperatures. Under some conditions steels have inherently low toughness, as, for example, steels with bcc ferritic microstructures tested at temperatures below their ductile to brittle transition temperatures, as described in Chapter 11, "Deformation, Strengthening, and Fracture of Ferritic Microstructures." Below the transition temperature fracture occurs by transgranular cleavage on <100> planes of the bcc ferrite microstructure.

Cracking During Primary Processing

The formation of inclusions and banding and their possible detrimental effects on toughness have already been discussed in Chapter 9, "Primary Processing Effects on Steel Microstructure and Properties," and are not discussed further here. Instead the various types of cracking that occur early during steel manufacture are discussed. Figure 19.1, taken from the now-classical technical paper by Brimacombe and Sorimachi, shows schematically the many types of cracking that may develop in continuously cast steel (Ref 19.5). Temperature ranges, stresses, microstructures

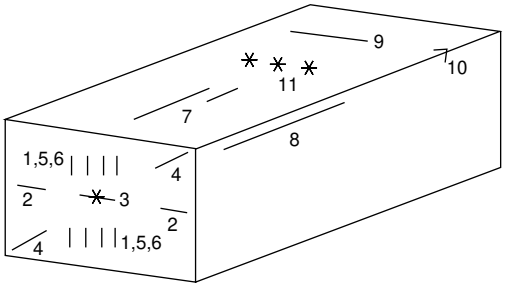

Fig. 19.1 Types of cracks that may develop in the continuous casting of steel. Internal cracks: 1-midway, 2-triple point, 3-centerline, 4-diagonal, 5-straightening/bending, 6-pinch roll. Surface cracks: 7-longitudinal mid-face, 8-longitudinal corner, 9-transverse mid-face, 10-transverse corner, 11-star. Source: Ref. 19.5

and chemical effects are related to each type of cracking. A critical temperature range is between 1340 °C (2440 °F) to the solidus when liquid steel is solidifying in a thin solid shell in the mold. Figure 9.4 from Thomas (Ref 19.6) in Chapter 9, "Primary Processing Effects on Steel Microstructure and Properties," shows the many factors involved during shell formation in the mold, including the protective mold flux and oscillation marks, and the ferrostatic pressure between support rolls below the mold that may cause bulging. At the very high temperatures associated with solidification the strength of the solidifying steel is very low and sulfur and phosphorus significantly increase solidification cracking sensitivity (Ref 19.5).

Brimacombe and his colleagues continued to work on the effects of steelmaking, including for example, comprehensive analysis of mold fluxes and their performance (Ref 19.7), and analysis of oscillation marks and hook formation. The formation is a complex solidification phenomenon that occurs at the beginning of the meniscus interface with the liquid mold flux, especially in very low-carbon steels (Ref 19.8). The steelmaking community lost a very talented metallurgist when Keith Brimacombe died early at the age of 54 in 1997. His memory is honored in a 2000 Symposium (Ref 19.9) and in the annual J. Keith Brimacombe Memorial Lecture of AIST.

Longitudinal mid-face surface cracks (Fig.19.1) tend to form in continuously cast slabs, cast at high speeds, typically in steels with carbon contents in the range of about 0.08 to 0.18 wt% carbon, depending on alloy content. These steels solidify by the formation of bcc ferrite crystals which on cooling must transform to fcc austenite or combine with liquid steel by the peritectic reaction to form austenite as described generally in Chapter 3, "Phases and Structures," and as characterized in detail in Fe-0.14% C and 0.42% C steels by Shibata et al. (Ref 19.10). The decrease in volume when the ferrite transforms to austenite creates uneven shell growth and stresses that lead to cracking of the thin layer of very low strength solid steel at high solidification temperatures.

Samarasekera, in the Brimacombe Symposium (Ref 19.11), states:

> One of the most profound discoveries in the history of continuous casting of steel was the influence of steel carbon content on mould heat transfer and shell growth. The result of a path-breaking study on a pilot caster at U. S. Steel, Singh and Blazek established the role of delta to gamma (austenite) phase transformation on the formation of the solid shell. In the case of peritectic steels, the above transformation takes place close to the meniscus, and is accompanied by a large local shrinkage, which causes the newly formed shell to wrinkle. The accompanying gaps that form on the surface are non-uniform, and give rise to low heat transfer and non-uniform solidification. Steel grades, with carbon contents in the range 0.08–0.14%, are most affected by this phenomenon, and the consequences are profound. In billet casting, these grades transfer less heat to the mould, have lower

overall shrinkage, and require less taper. In slab casting the peritectic grades are susceptible to longitudinal mid-face cracking because of non-uniform shell growth and shrinkage at the meniscus. It is thus extremely difficult to cast peritectic grades at high casting speeds without longitudinal facial cracking in conventional or thin slab casting machines.

Figure 19.2 shows a transverse section through a longitudinal mid-face crack in low-carbon plate steel. The irregular subsurface branched shape of the crack may be related to the crack following interdendritic areas of the steel shell. The crack has been heavily oxidized and by exposure to air is filled with iron oxide. Energy-dispersive spectroscopy (EDS) in the scanning electron microscope showed that the oxide was wüstite or FeO, the oxide of iron that forms only at high temperatures, above 570 °C, (1060 °F) confirming that the crack was present during high temperature processing. Surrounding the oxide-filled crack is a zone of very fine particles, faintly visible in Fig. 19.2. Figure 19.3 shows this zone at higher magnification, and EDS shows that the fine spherical particles are oxides of manganese, silicon, and chromium, all elements with higher oxidizing potentials than iron. These oxides have formed by high-temperature diffusion of oxygen through the solid steel adjacent to the oxygen filled crack. Cracks filled with FeO and adjacent layers of fine alloy oxide particles are markers of all of the various surface cracks that may occur during high temperature primary processing.

Brimacombe and Sorimachi identified not only the high-temperature zone of fracture associated with solidification but also lower-temperature zones of fracture that are associated with cracking during hot working. Others have reviewed mechanisms of reduced hot ductility (Ref 19.12, 19.13). Figure 19.4, taken from Crowther (Ref 19.13), shows schemati-

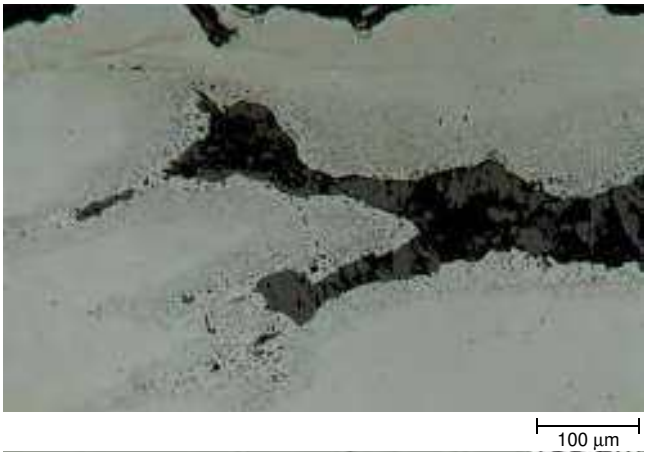

Fig. 19.2 Transverse section through a mid-face longitudinal crack in a low-carbon plate steel. As-polished section, light micrograph

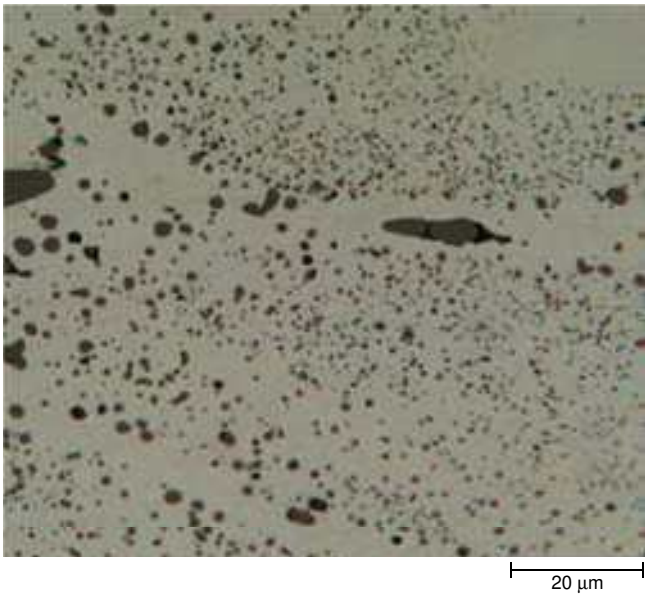

Fig. 19.3 Higher magnification of the zone of spherical oxide particles imbedded in steel adjacent to the crack shown in Fig. 19.2. As polished surface, light micrograph

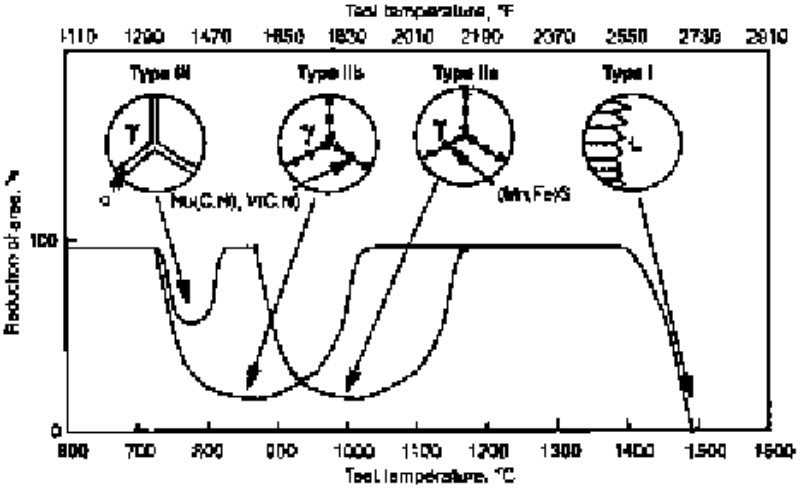

Fig. 19.4 Schematic diagram of ductility troughs that might develop during hot work. Source: Ref 19.13

cally microstructural features and operating temperature ranges for four types of cracking identified during high-temperature tensile testing. The various mechanisms of cracking severely lower hot ductility, as shown by the troughs in reduction of area over various temperature ranges. Type I cracking is associated with incipient melting in interdendritic regions where S and MnS particles may be in high concentration. Although phos-

phorus at lower temperatures has been shown to improve hot ductility, its strong tendency to segregate to interdendritic regions lowers solidus temperatures, and the resulting liquid films at austenite grain boundaries at high temperatures may severely lower hot ductility of as-cast steel (Ref 19.12).

Types IIa and IIb hot shortness are associated with precipitation of particles at austenite grain boundaries: (Mn,Fe)S particles at higher temperatures, and Nb(CN), V(CN), Ti(CN) and Al(N) at lower temperatures, with the extent of precipitation depending on the amounts of the various elements present and their temperature-dependent solubility products. Cracking develops by microvoid formation at the precipitate particles arrayed on austenite grain boundaries. Examples of the reduction in hot ductility associated with low-carbon V/N steels and Nb and Nb/V steels are shown in Fig. 19.5 and 19.6, respectively (Ref 19.14). Type III hot shortness is associated with ferrite formation at austenite grain boundaries, together with grain boundary precipitates. Strain is concentrated in the high-ductility

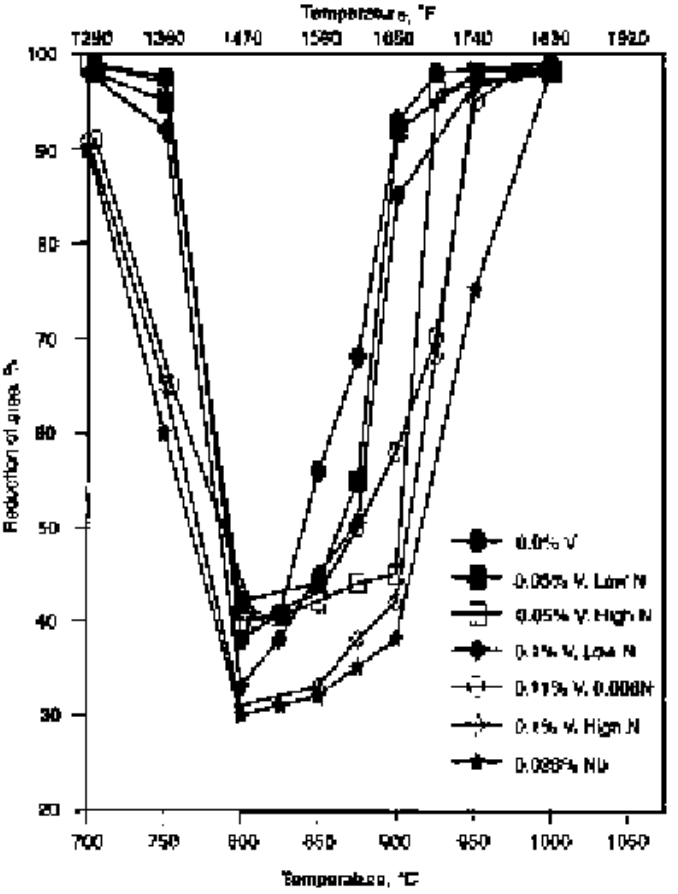

Fig. 19.5 Hot ductility curves showing changes of reduction of area (R of A) as a function of test temperature for steels containing various combinations of V and N. Source: Ref 19.14

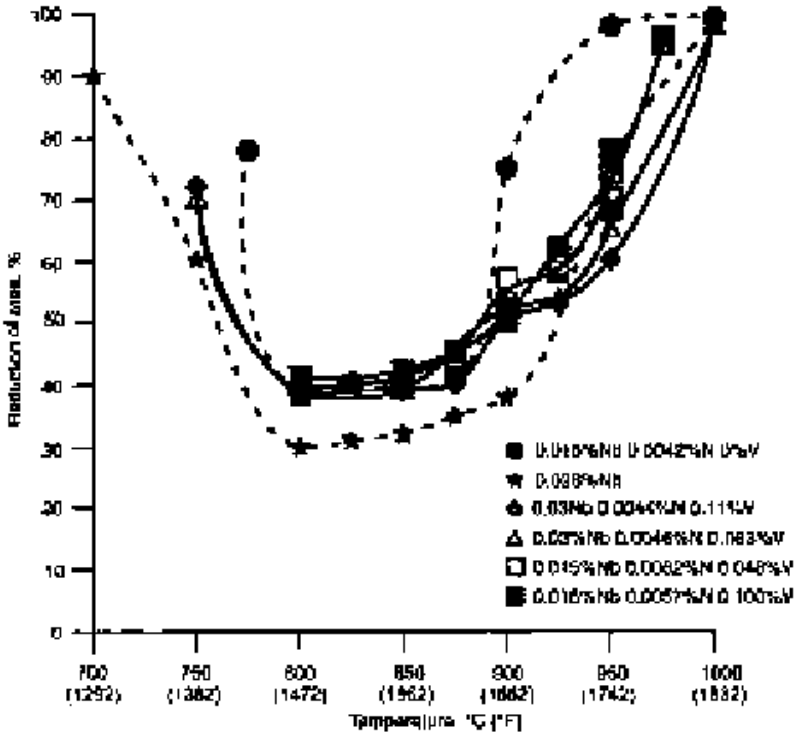

Fig. 19.6 Hot ductility curves showing changes in reduction of area (R of A) as a function of test temperature for steels containing various amounts of Nb and Nb and V. Source: Ref 19.14

ferrite, and microvoid formation develops around particles in the ferrite layers.

Hot Shortness Associated with Copper

The incorporation of copper into steel represents a special case of a chemical factor that leads to reduction of hot ductility and surface cracking of steel products during primary processing. Although copper in high concentrations has long been recognized as an undesirable residual element in steel, the ductility problems associated with copper continue because of the increasing use of scrap that may be rich in copper for electric arc furnace steel production, and the fact that copper is not readily oxidized and removed from liquid steel during steelmaking operations. In recognition of the continuing problems related to copper buildup in steel, a special issue of *ISIJ International* was devoted to this subject in 1997 (Ref 19.15).

Copper does not dissolve in iron-oxide mill scale that develops during reheating and early stages of hot rolling during primary processing. Therefore, as surface iron is oxidized, copper is rejected to and concentrates in

austenite at the steel/scale interface. At temperatures above its melting point, the copper melts and penetrates the steel surface along austenitic grain boundaries, leading to tearing and cracking during hot deformation. Figure 19.7 shows copper penetration from the surface of a medium-carbon steel. The copper is shown in the fine-oxide zone adjacent to an oxide-filled crack assumed to have formed because of copper-induced hot shortness.

Copper-induced cracking is most severe at around 1100 °C (2010 °F). At lower temperatures, copper and copper-rich phases do not melt, and at higher temperatures the copper is incorporated into the mill scale. A recent study shows that the surface scale of steel consists of layers of hematite (Fe_2O_3), magnetite (Fe_3O_4), and wüstite (FeO). Wüstite is the oxide adjacent to the steel, and at 1200 °C (2190 °F), it was found that copper diffuses along grain boundaries in the wüstite and concentrates in the Fe_3O_4 layer (Ref 19.16).

Other elements affect the severity of copper hot shortness. The elements cobalt, nickel, and aluminum increase the solubility of copper in solid steel and the elements vanadium, chromium, manganese, silicon, and tin decrease it (Ref 19.17). With increased solubility of copper, as with nickel, the formation of liquid copper-rich phases and surface cracking is suppressed (Ref 19.18, 19.19). In contrast, tin increases the formation of liquid copper-enriched phases and enhances surface cracking. Additions of 0.4% Si and 0.02% P have been found to reduce the susceptibility to surface hot shortness but increase the rate of surface oxidation (Ref 19.20).

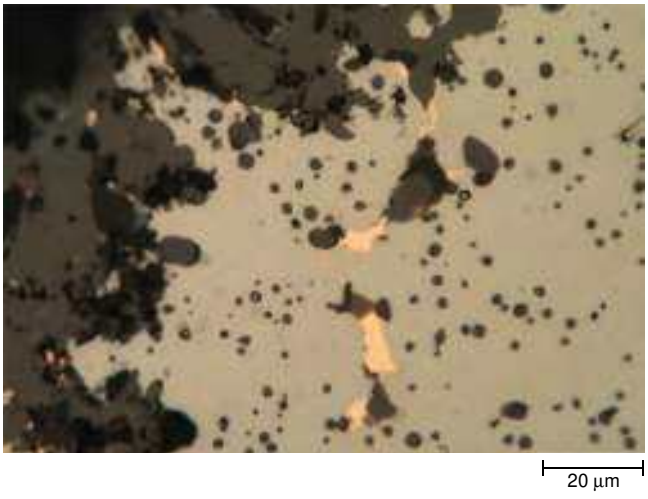

Fig. 19.7 Copper (copper-colored features) penetration adjacent to high temperature oxidized crack in a medium carbon steel. As polished surface, light micrograph

Overheating and Burning during Forging

Forgings are made from as-rolled bar steels and are shaped by deformation at temperatures high in the austenite phase field, typically around 1200 °C (2190 °F) (Ref 19.21). Heating to higher temperatures may create the phenomenon termed *overheating,* and at temperatures in excess of 1400 °C (2550 °F), the phenomenon is referred to as *burning*. These conditions, especially that of overheating, are sensitive to sulfur content, and Fig. 19.8 shows temperature ranges for overheating and burning as a function of sulfur content (Ref 19.22) Burning is caused by melting and oxidation at temperatures high in the austenite phase field, causing severely reduced hot ductility and cracking. While heating at too high a temperature during forging might cause burning, another cause might be interdendritic segregation that has not been sufficiently reduced by soaking and hot mill deformation. The interdendritic regions have higher concentrations of alloying and impurity elements and possibly carbon than dendritic core regions, are the last to freeze on solidification, and accordingly are the first to melt on heating. Thus these regions may have compositions that significantly lower the austenite/liquid two-phase field, causing interdendritic melting and oxidation at temperatures not expected for the same steel grade with more homogeneous composition.

Overheating is caused by the solution of MnS particles at high austenitizing temperatures and the subsequent reprecipitation of MnS particles on austenite grain boundaries during cooling. After quenching and tempering, overheated steel may fracture by microvoid coalescence at the MnS particle arrays on the coarse austenite grain boundaries formed at the high forging temperatures. The resulting intergranular facets, covered with microvoids formed around the MnS particles, are the characteristic

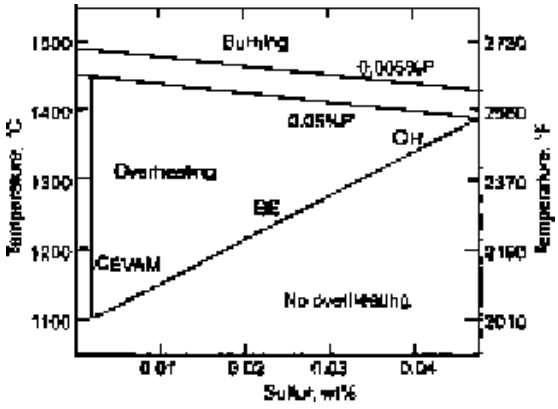

Fig. 19.8 Influence of sulfur content and steelmaking practice on temperature ranges for overheating and burning. Steelmaking practices are: consumable-electrode vacuum arc remelted (CEVAM), basic-electric (BE), and open-hearth (OH). Source: Ref 19.22

fracture morphology of overheated steels (Ref 19. 22–19.25). Although etches have been used to characterize overheating, impact testing followed by scanning electron microscope examination of the fracture surfaces is considered to be the best way to identify overheating (Ref 19.22).

Sulfide particle size and spacing in overheated specimens are a function of manganese and sulfur contents, maximum forging temperature, and cooling rates and determine the severity of reduced toughness due to overheating. High-temperature tempering of hardened forgings increases sensitivity to overheating intergranular fracture (Ref 19.23). This observation is explained by the fact that the plastic zones at notches or crack tips in stressed low-strength, well tempered microstructures encompass large areas of coarse intergranular sulfide networks. In higher-strength microstructures, the plastic zones are smaller and may act only on small fractions of the sulfide networks.

Overheating can be reduced or eliminated in a number of ways. Control of forging temperatures is essential, but sometimes reducing temperature may not be the most efficient approach for complex forgings. Strong sulfide-forming elements such as rare earths, calcium, or zirconium could be added to stabilize sulfides and prevent their resolution, but care must be taken not to use steels with coarse particle dispersions, which by themselves reduce ductile fracture and fatigue resistance. Increased manganese would also stabilize MnS particles but is not recommended for heavy sections because, as discussed later in the section on temper embrittlement, increased manganese promotes temper embrittlement. An attractive solution to overheating, now possible with advanced steelmaking techniques, is the reduction of manganese and sulfur to very low levels, as is being done in steels for very heavy forgings (Ref 19.26.–19.28). Care must be taken to reduce both the manganese and sulfur to sufficiently low levels. Reduction of sulfur alone results in dispersions of very fine MnS particles, which rapidly dissolve and reprecipitate during forging, and may contribute to overheating as indicated in Fig. 19.8.

Aluminum Nitride Embrittlement

Aluminum nitride embrittlement is another low-toughness phenomenon associated with primary processing, most often with carbon steel castings (Ref 19.29–19.31). This type of embrittlement is caused by the precipitation of sheet-shaped aluminum nitride particles on austenite grain boundaries during cooling after solidification of cast steel, or reprecipitation after solution of AlN at high austenitizing temperatures. Toughness is reduced significantly because of intergranular fracture along austenite grain boundaries covered with aluminum nitride. Because of high-temperature austenite formation, the austenite grains are generally quite coarse, and the intergranular fracture facets are readily visible to the unaided eye, leading to the term *rock candy* fracture for this type of embrittlement.

Figure 19.9 shows aluminum nitride and carbide particles extracted from the intergranular fracture surface of a medium-carbon steel casting. The aluminum nitride particles are characteristically very thin, with a plate- or sheet-like morphology, and the hexagonal crystal structure of AlN is readily identified by electron diffraction. The solubility products, morphologies, and many effects of AlN in cast and wrought steel are comprehensively reviewed by Wilson and Gladman (Ref 19.32).

Reheat or Stress Relief Cracking

Welded structures are often given post-weld heat treatments to relieve residual stresses developed during welding, and during those heat treatments cracking may develop in the coarse-grain heat-affected zones or welds of low-carbon steels as a consequence of the relief of the residual stresses. This type of cracking, accordingly, has been termed *stress-relief cracking* or *reheat cracking*, and in view of its importance to welding, has received considerable attention in the welding literature (Ref 19.33, 19.34).

The cracking typically occurs in stress-relief treatments performed at 500 to 650 °C (930 to 1200 °F) and occurs when relaxation strains exceed creep ductility. Fracture develops along very coarse prior austenite grain boundaries in heat-affected zones that have previously reached temperatures up to the melting point of steel during welding. The fracture morphology is therefore intergranular, and depending on temperatures and stress level sometimes the prior austenitic grain boundary surfaces are

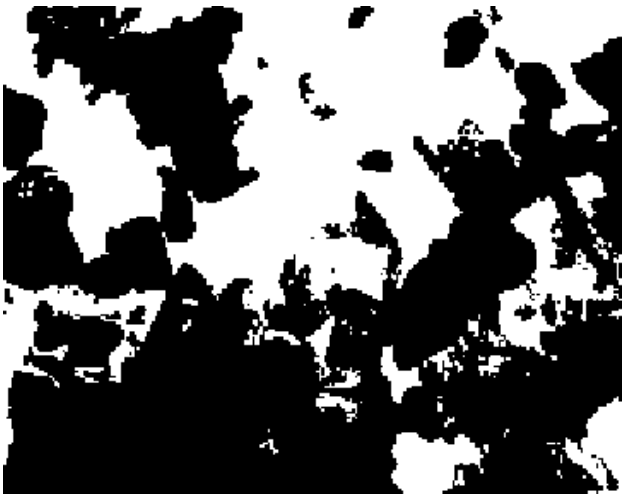

Fig. 19.9 Thin aluminum nitride particles (arrows) extracted from an intergranular fracture surface of an as-cast medium-carbon steel. Dark particles are carbides. Transmission electron micrograph from a carbon extraction replica, original magnification 82,500×; shown here at 75% of original

smooth and featureless and sometimes are covered with very fine microvoids or cavities associated with grain-boundary dispersions of fine particles (Ref 19.35).

Sulfur and boron contents of low-carbon steels have been associated with stress-relief cracking (Ref 19.36). With respect to sulfur, the very high temperatures reached in weld heat-affected zones cause manganese sulfides to dissolve and make the sulfur available to contribute to high-temperature fracture. McMahon et al. propose that sulfur is adsorbed on cavities or crack surfaces and is driven ahead of a crack by high stresses at crack tips where, when it reaches a critical concentration, it causes decohesion and crack advance (Ref 19.37). This mechanism is referred to as *dynamic embrittlement* and has been found to operate not just in steels but also in a number of non-ferrous systems.

Intergranular Embrittlement in Hardened Steels—General Comments

High-strength quenched and tempered steels, as indicated in Chapter 18, "Deformation, Mechanical Properties and Fracture of Quenched and Tempered Carbon Steels," are susceptible to a variety of embrittlement phenomena, including quench embrittlement, tempered-martensite embrittlement, temper embrittlement, hydrogen embrittlement, and liquid-metal-induced embrittlement. All of these mechanisms are associated in some way with intergranular fracture along prior austenite grain boundaries in quenched and tempered microstructures, and although second-phase particles may be present, the grain boundary fractures are smooth with little or no evidence of plastic deformation or microvoid formation, in contrast to the intergranular facets with microvoids typical of low-toughness ductile fracture produced by overheating or some of the hot shortness fracture mechanisms described previously. Generally, the effects of the various embrittlement phenomena are measured at room temperature by the various toughness testing approaches. However, the embrittlements cause increases in ductile-to-brittle transition temperatures, and therefore the apparent severity of an embrittlement may depend on test or loading temperature, as shown in Fig. 19.10.

Quench Embrittlement

The conditions for *quench embrittlement,* an intergranular mechanism of brittle fracture, develop in high-carbon steels during austenitizing or quenching; tempering is not required. Thus, the term has been used to describe a form of brittle fracture in order to differentiate it from embrittlement mechanisms that require tempering (Ref 19.39). Hardened steels that contain more than 0.5% C are most sensitive to quench embrittle-

ment, and the same microstructural features that cause quench embrittlement may also be responsible for the intergranular quench cracking that develops in higher-carbon steels when high surface tensile stresses develop during quenching. Figure 19.11 shows the percent intergranular fracture on CVN fracture surfaces for 52100 and 4340 steels as a function of tempering temperature (Ref 19.39). The 52100 steel was austenitized above its A_{CM} temperature, a condition not commercially applied, as dis-

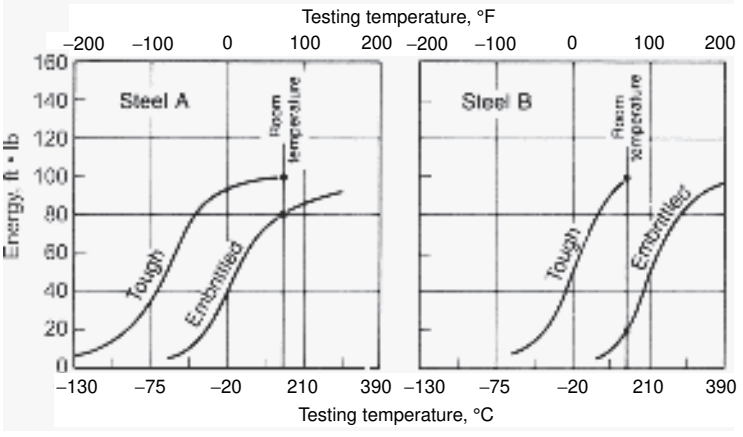

Fig. 19.10 Changes in impact transition curves for two hypothetical steels in tough and embrittled conditions. Large differences in room temperature toughness due to embrittlement are noted for the two steels. Source: Ref 19.38

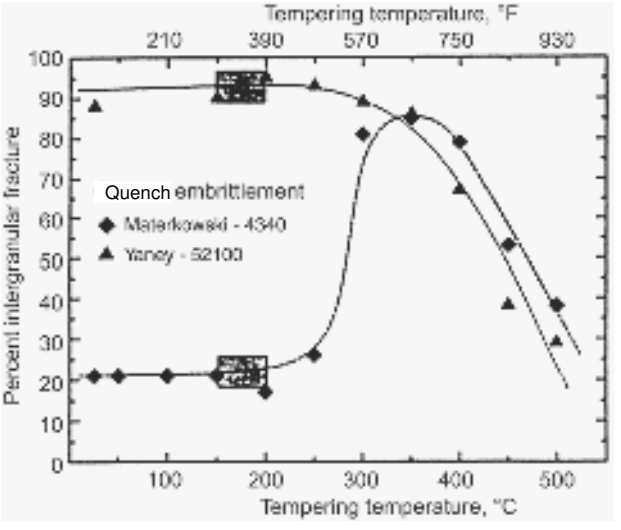

Fig. 19.11 Percent of intergranular fracture on CVN specimen fracture surfaces as a function of tempering temperature for fully austenitized and quenched 52100 steel and 4340 steel. Shaded regions show fracture after tempering at temperatures usually used to produce high strength and reasonable toughness. Source: Ref 19.40, 19.41

cussed subsequently. The 4340 hardened steel develops large amounts of intergranular fracture only after tempering above 300 °C (570 °F), a condition associated with tempered martensite embrittlement, as discussed in the next section. However, the 52100 steel fractures almost completely by intergranular fracture in the as-quenched condition and even after tempering at 200 °C (390 °F) and even higher temperatures. Examples of the intergranular fracture in the as-quenched 52100 steel and the tempered 4340 steel are shown in Fig. 19.12 and 19.13, respectively.

Fig. 19.12 Intergranular fracture surface of CVN-tested as-quenched 52100 steel austenitized above A_{CM} at 965 °C (1770 °F). SEM micrograph. Source: Ref 19.40

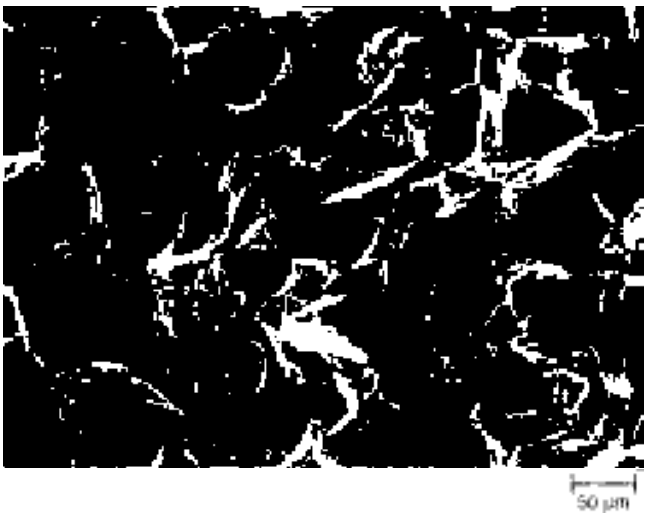

Fig. 19.13 Intergranular fracture surface of CVN-tested 4340 steel oil quenched and tempered at 350 °C (660 °F). SEM micrograph. Courtesy of J. Materkowski. Source: Ref 19.41

As noted, the intergranular fracture surfaces of quench-embrittled specimens are quite smooth, only occasionally showing acicular-shaped carbide particles. Further, light and scanning electron microscopy show no resolvable features on prior austenite grain boundaries. However, auger electron spectroscopy (AES), an analytical technique that has high depth resolution (i.e., it can establish chemistries of very shallow, near-surface regions), has been effective in establishing causes of quench embrittlement. The application of AES to quench-embrittled intergranular surfaces has shown that the prior austenite grain boundaries are associated with strong cementite peaks and phosphorus peaks (Ref 19.42–19.45). Figure 19.14, an isothermal section of the Fe-C-P equilibrium phase diagram, shows that even small amounts of phosphorus reduce the solubility of carbon in austenite and promote cementite formation during austenitizing. Also, experiments have shown that phosphorus enhances cementite allotriomorph formation in 52100 steel held in the two-phase austenite/cementite phase field. Although phosphorus exacerbates quench embrittlement, the key structural factor for embrittlement appears to be the formation of critical amounts of cementite on prior austenite grain boundaries.

The interaction of carbon and phosphorus that produces intergranular crack formation has been evaluated by examination of the depth of intergranular crack formation in low-temperature-tempered carburized steels with various phosphorus contents (Ref 19.39). Higher phosphorus contents were associated with deeper intergranular crack propagation and,

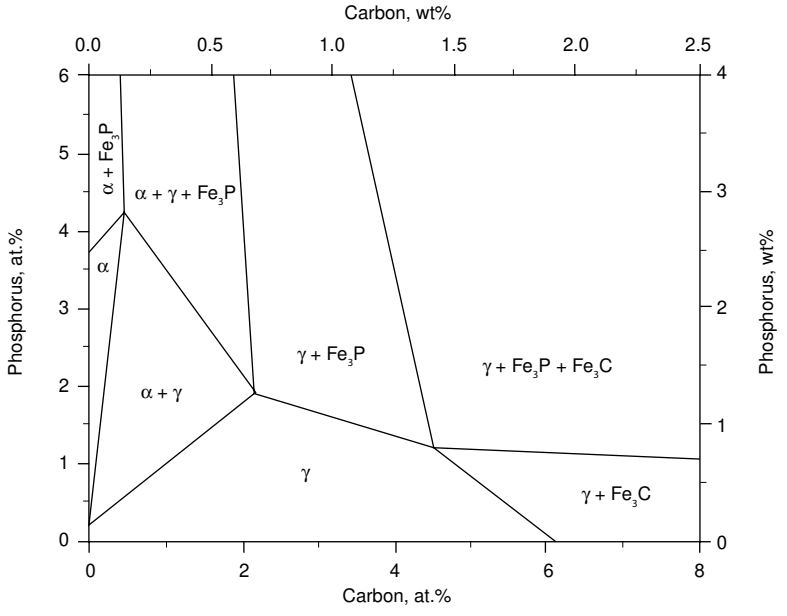

Fig. 19.14 Fe-rich portion of the Fe-C-P system at 950 °C (1740 °F) showing decreases in the solubility of C and Fe_3C formation as P content increases. Source: Ref 19.46

therefore, lower carbon contents. From the latter experiment, Fig. 19.15 was constructed. Shown are carbon-phosphorus combinations that promote intergranular fracture and those that promote ductile fracture. Intergranular fracture develops even with very low levels of phosphorus at around 0.5% C, and the higher the phosphorus content, the lower is the carbon content at which intergranular fracture develops.

Figure 19.16 presents a map showing regions of ductile and intergranular fracture as a function of tempering temperature and steel carbon content. The transition from ductile transgranular to brittle intergranular fracture at 0.5% C in low-temperature-tempered (LTT) steels is noted. Despite the sensitivity of higher carbon hardened steels to quench embrittlement, such steels can be used depending on heat treatment and application. Intergranular fracture is avoided when high-carbon steels such as 52100 are intercritically austenitized in the austenite/cementite phase field prior to quenching. The carbide particles retained during such austenitizing treatments lower carbon content to below that which produces intergranular fracture. Carburized steels, in which carbon is introduced at temperatures in the austenite phase field, are usable because of the surface compressive stresses produced during quenching, as described in Chapter 21, "Surface Hardening." Crack initiation in direct-quenched carburizing steels is still associated with intergranular fracture but at stresses higher than the low stresses that initiate intergranular fracture in through-hardened high-carbon steels with surface tensile residual stresses. High-carbon hard-

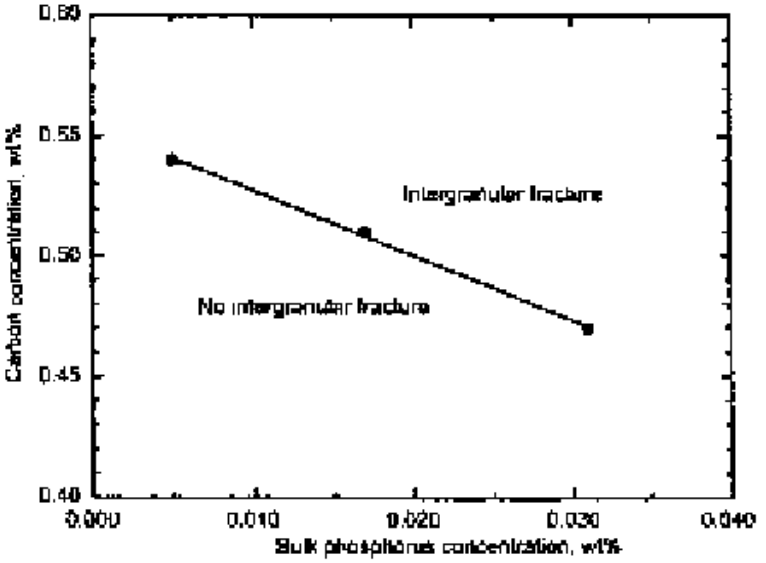

Fig. 19.15 Combinations of C and P that are associated with transgranular and intergranular fracture in low-temperature tempered hardened steels. Source: Ref 19.39

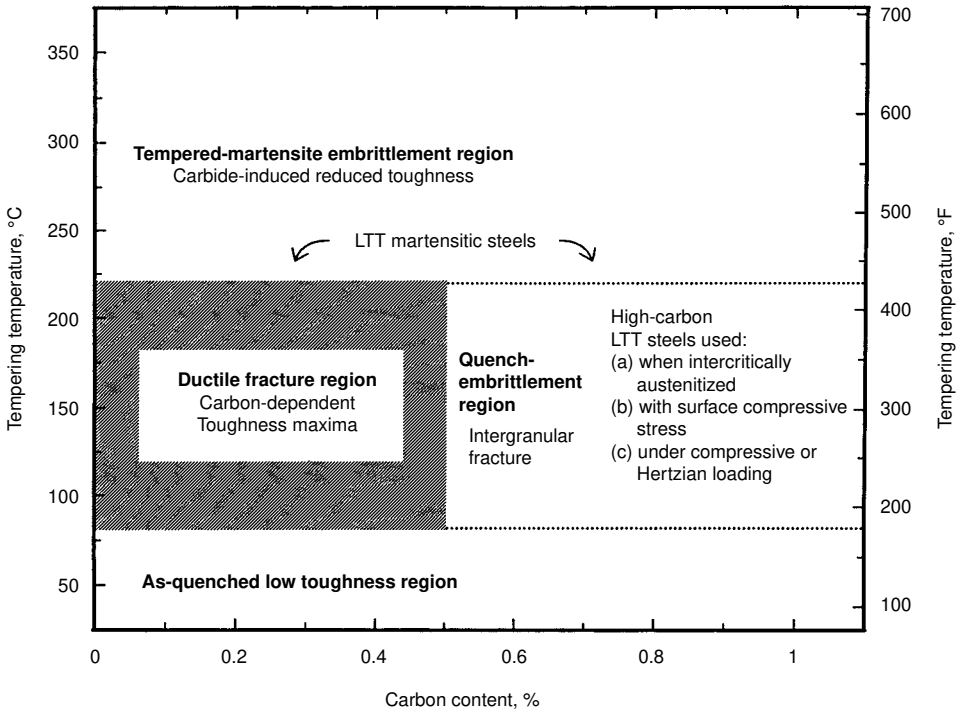

Fig. 19.16 Map of fracture modes in hardened steels produced by tensile and bending loads as a function of tempering temperature and steel carbon content. The transition from ductile to brittle intergranular fracture in low-temperature-tempered (LTT) steels at 0.5% C is shown and approaches that minimize intergranular fracture in high-carbon steels are listed

ened steels subjected to compressive or Hertzian loading, instead of tensile or bending stresses, are also not sensitive to intergranular cracking.

Figure 19.17 plots peak stress measured by tensile testing versus hardness for a number of medium-carbon steels austenitized for 30 min at temperatures between 830 and 890 °C (1530 and 1630 °F), depending on carbon content, and tempered in either oil or salt baths for times of 10 or 60 min at temperatures between 150 and 250 °C (300 and 480 °F) or rapidly induction-tempered (Ref 19.47). These data show the extent to which strength can be reduced by quench embrittlement. For specimens with hardness below 52/53 HRC, peak stress corresponds to ultimate tensile stress, and tensile deformation produces strain hardening, necking, and post-uniform deformation to ductile fracture. Below 53 HRC, increasing hardness correlates with increasing ultimate tensile strength as expected. However, for specimens with higher hardness, peak stress was set by intergranular fracture short of an ultimate tensile strength. The higher the hardness, especially for steels with higher carbon and phosphorus contents, the more brittle is the response to stress, and the lower the peak stress. As specimens were tempered at higher temperatures, hardness de-

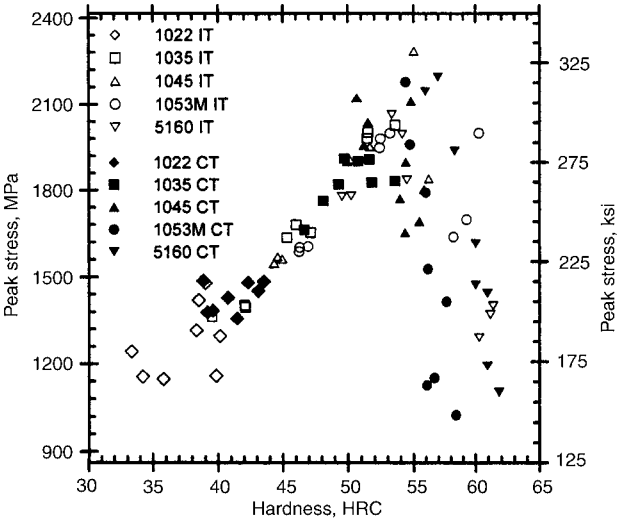

Fig. 19.17 Peak stress versus hardness for quench and tempered 10xx and 5160 steels. For microstructures with hardness below HRC 52/53, the peak stress corresponded to ultimate tensile strengths. For microstructures with hardness above HRC 52/53, peak stress corresponded to a brittle fracture stress. Source: Ref 19.47

creased, and the effects of quench embrittlement gradually decreased, at a rate depending on carbon and phosphorus content, until ductile deformation was established.

Tempered Martensite Embrittlement

Tempered martensite embrittlement (TME) is a microstructural condition that lowers toughness and fracture resistance in hardened steels tempered between 200 and 400 °C (390 and 750 °F). Figure 19.18 shows CVN impact energy absorbed as a function of tempering temperature for three medium-carbon steels, 4130, 4140 and 4150, and a high-carbon steel, 52100, each with high and low levels of phosphorus (Ref 19.40, 19.48). The phosphorus levels in the 41xx steels were 0.02 and 0.002% and for the 52100 steel, 0.09 and 0.23%. The 52100 steel has been intercritically austenitized at 850 °C (1560 °F) to produce a microstructure with spheroidized carbide particles not sensitive to intergranular fracture. Charpy V-notch energy is low in as-quenched specimens as described in Chapter 18, "Deformation, Mechanical Properties, and Fracture of Quenched and Tempered Carbon Steels," increases to a low-temperature maximum after tempering at 200 °C (390 °F), and drops after tempering at 300 °C (570 °F), in the middle of the tempering temperature range that produces TME.

A striking feature of Fig. 19.18 is the strong effect of steel carbon content on impact toughness under all tempering conditions, even in the low-

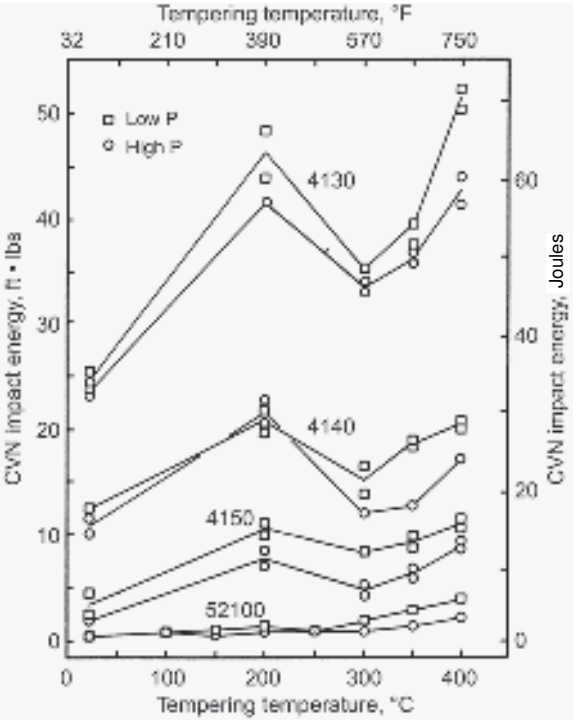

Fig. 19.18 CVN energy absorbed in fracture of 41xx steels and 52100 steels tempered at various temperatures. Each set of steels had heats with low and high P contents. Data are from Ref 19.40 and 19.48

temperature maxima around 200 °C. The hardened 4130 steel, even after tempering in the TME range, has higher toughness than any of the other steels with higher carbon contents even in unembrittled conditions. For the high-carbon 52100 steel, the impact toughness is so low after tempering at 200 °C that any microstructural changes associated with TME are almost not noticeable. This strong effect of carbon is related to the high rates of strain hardening in higher-carbon steels, as discussed in Chapter 18, that reduce the amount of deformation required to reach critical fracture stresses at the roots of notches in Charpy specimens. Lateral contraction of the width of Charpy specimens at the notch root and expansion at the compressive side of CVN specimens correlate well with the amount of plastic deformation required to achieve fracture.

The reduced impact toughness associated with TME is associated with three different modes of fracture that depend on the various carbon and phosphorus contents of the hardened steels. The common feature of all the fracture mechanisms is the formation of cementite in the second and beginning third stage of tempering. Figure 17.17 in Chapter 17, "Tempering of Steel," has shown that the transformation of retained austenite to cementite and ferrite in martensitic 4130 and 4340 steels starts at 200 °C and

is effectively complete after tempering at 300 °C (570 °F). Cementite forms at interlath sites as retained austenite transforms, within martensite crystals as the transition carbide arrays are replaced by cementite particles, and at prior austenite grain boundaries.

In medium-carbon steels containing 0.4% C, the transformation of retained austenite produces two mechanisms of fracture depending on phosphorus content. Figure 19.19 shows several characteristics of the effect of TME on impact toughness in two 4340 steels of the same composition except for phosphorus content (Ref 19.41, 19.49). The impact toughness of the steel with the higher phosphorus content (0.03%) is inferior to that of the steel with the lower phosphorus content (0.003%) after tempering over the entire range of temperatures up to 500 °C (930 °F). Also, both steels show a trough or plateau in energy absorbed after tempering between 200 and 400 °C (390 and 750 °F). The lower toughness of the higher phosphorus-containing steel was related to a sharp increase of intergranular fracture after tempering between 300 and 400 °C (570 and 750 °F), as has been shown in Fig. 19.11. Similar increases in intergranular fracture with tempering of 4340 in the TME range have been shown by Bandyopadhyay and McMahon (Ref 19.50). Figure 19.20 shows the intergranular fracture along prior austenite grain boundaries of the high-phosphorus 4340 steel broken at room temperature after tempering at 400 °C.

The intergranular mode of fracture associated with TME is common and has been related to phosphorus segregation to austenite grain boundaries

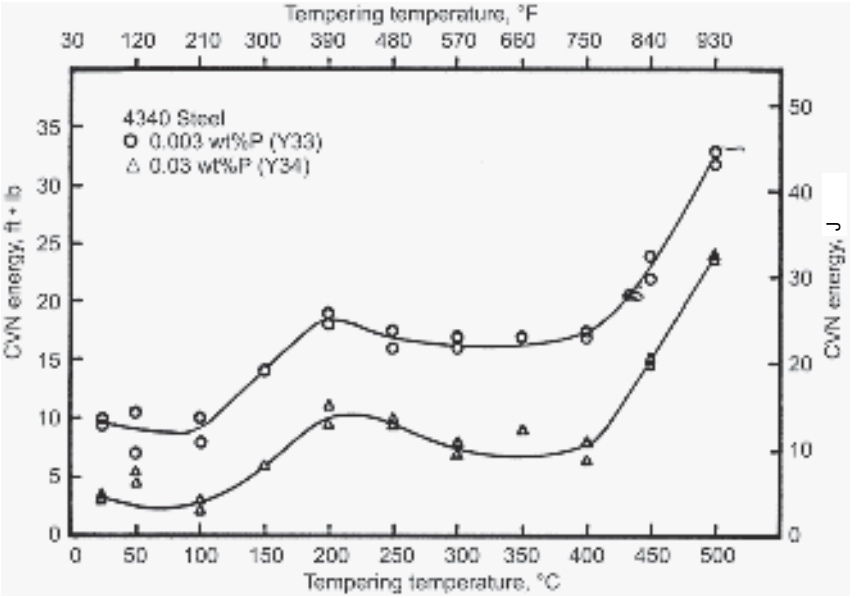

Fig. 19.19 Room temperature CVN energy absorbed for hardened 4340 steel specimens containing either 0.03 or 0.003% P, austenitized at 870 °C (1598 °F), oil quenched, and tempered at temperatures shown for 1 h. Source: Ref 19.49

during austenitizing (Ref 19.51–19.53). Phosphorus, therefore, is present at prior austenite grain boundaries in as-quenched martensitic microstructures, and although in the relatively high-phosphorus 4340 steel there is a degree of quench embrittlement, as demonstrated by low impact toughness and 20% intergranular fracture in LTT specimens, it is only after tempering at temperatures where cementite forms that intergranular TME fully develops.

In contrast to the high-phosphorus-containing 4340 steel, the low-phosphorus-containing 4340 steel shows higher impact toughness and no intergranular fracture in all tempered conditions. Figure 19.21 shows that

Fig. 19.20 Intergranular fracture of 4340 steel containing 0.03% P and tempered at 400 °C (750 °F). Specimen was broken by impact loading at room temperature. Source: Ref 19.49

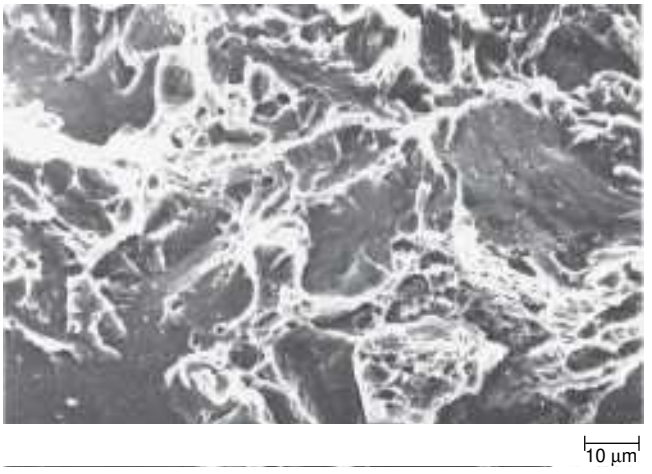

Fig. 19.21 Flat cleavage facets and microvoids on fracture surface of 4340 steel containing 0.003% P and tempered at 350 °C (662 °F). Specimen was broken by impact loading at room temperature. Source: Ref 19.49

flat transgranular cleavage facets interspersed between regions of ductile fracture were associated with the decrease in impact toughness after tempering in the TME range. The cleavage facets are oriented across laths of a packet of martensite (Ref 19.49) and are attributed to cracking initiated at interlath cementite crystals, as proposed by Thomas (Ref 19.54). Figure 19.22 shows interlath carbides in the low-phosphorus-containing 4340 steel tempered at 350 °C (660 °F).

A third mode of TME fracture develops in the lower-carbon-containing 4130 steels. Although there is a significant decrease in impact toughness, Fig. 19.18, the fracture is not brittle and is associated with the ductile fracture in turn associated with coarse carbide particles introduced by tempering (Ref 19. 48, 19.55). Figure 19.23 shows the overload or unsta-

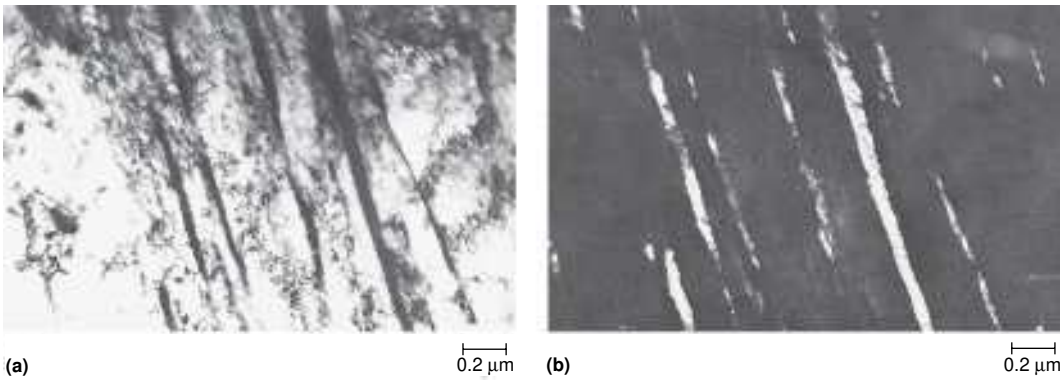

Fig. 19.22 Interlath carbides formed during tempering of 4340 steel containing 0.003% P at 350 °C (660 °F). (a) Bright-field image. (b) Dark-field image taken with a cementite diffracted beam. Transmission electron microscope micrographs. Source: Ref 19.49

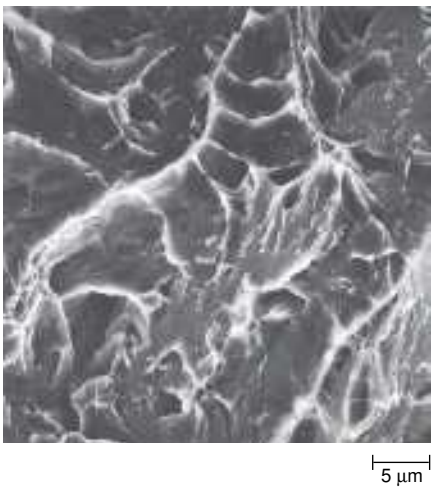

Fig. 19.23 Fracture surface of low-phophorus-containing 4130 steel tempered at 300 °C (570 °F). SEM micrograph. Source: Ref 19.55

ble fracture from a CVN specimen of low-phosphorus 4130 steel tempered at 300 °C (570 °F). The fracture consists largely of microvoids, on the average larger than those observed in specimens tempered at 200 °C (390 °F). The overload fractures of the 4130 steel are preceded by shear initiation and stable crack growth by microvoid coalescence and ductile tearing (Ref 19.48).

Typically, no matter what the appearance of the unstable fracture surface of a CVN specimen, fracture is initiated by shear along the slip line field at the root of CVN specimen notches. For example, Fig. 19.24 shows shear fracture at the root of the notch in a 4340 steel specimen quenched and tempered at 200 °C. Load-time curves obtained by instrumented CVN testing show energy absorption associated with crack initiation, crack propagation, and shear lip formation during fracture (Ref 19.48, 19.55–19.57). The lower the ability of a microstructure to plastically deform, the lower the toughness, and the greater the fraction of absorbed energy associated with crack initiation.

The discussion of TME to this point has concentrated on high strain rate CVN impact fracture. Impact testing applies loads at strain rates of about 10^3 s^{-1} and enhances stress-controlled brittle fracture mechanisms (Ref 19.58). Loading at lower strain rates also reduces fracture resistance in specimens tempered in the TME range. For example, a study (Ref 19.59) of hardened 4140 steel tensile specimens tested at a strain rate of 2.7^{-3} s^{-1} showed evidence of reduced toughness for specimens tempered at 300 and 400 °C (570 and 750 °F). Compared with specimens tempered at 200 °C, the specimens tempered in the TME range showed reduced strain hardening, lower uniform elongations, and lower ultimate tensile strengths, lower fracture stresses, and no improvements in total elongation. The fractures were ductile, in contrast to the brittle TME fractures produced by high-strain-rate testing. The reduced fracture resistance was shown to be asso-

Fig. 19.24 Shear fracture (curved region) along slip line field at notch root of CVN specimen (flat area at top of micrograph) of 4340 steel quenched and tempered at 200 °C (390 °F). Source: Ref 19.56

ciated with higher densities of microvoids that formed not only at carbides retained after austenitizing but also at new carbides produced by tempering in the TME range. Differences in phosphorus content in the 4140 steel specimens subjected to tensile testing had no apparent effect on reduced ductile fracture resistance produced by 300 and 400 °C tempering.

In summary, TME is manifested by ductile, cleavage, and intergranular modes of fracture. Although phosphorus makes worse the reductions in fracture resistance produced by TME, the root cause of TME is the formation of new distributions of cementite produced by second and beginning third-stage tempering. The carbide formation at temperatures above 200 °C is relatively rapid, and the microstructural changes in small sections occur typically in a time of one hour at temperature.

The fact that TME is related to cementite formation has led to the development of 300M steel, a steel with chemistry nominally the same as 4340, but containing high silicon, between 1.45 and 1.8%. Silicon is a non-carbide-forming element and its solubility in cementite is very low. Therefore, nucleation and growth of cementite in the second and third stages of tempering is severely retarded because silicon must diffuse away from nucleating cementite crystals (Ref 19.60, 19.61). The benefits of the fine structure produced by first-stage tempering persist in 300M steels tempered at higher temperatures than steels without silicon and TME occurs only after tempering at higher temperatures (Ref 19.62).

Temper Embrittlement

Temper embrittlement (TE) is an embrittlement condition that develops in hardened carbon and alloy steels after tempering for relatively long times in or cooling slowly through the temperature range 375 to 575 °C (710 to 1070 °F). In view of the relatively long times required for TE to develop, heavy steel sections, such as large shafts and rotors for power-generating equipment, that cool slowly and operate at high temperatures have been sensitive to TE. Catastrophic failures have been attributed to TE and have driven theoretical and analytical efforts to determine the causes of and solutions to TE. Many review articles review the tempering and chemical factors that induce TE (Ref 19.63 to 19.69), and approaches to preventing TE, primarily by control of steel chemistry, are now available.

TE is manifested primarily by an increase of impact transition temperature, as shown in Fig. 19.25 for a 3140 steel, containing nominally 1.15% Ni and 0.65% Cr, embrittled by both isothermal tempering and slow cooling through the critical tempering temperature range (Ref 19.38). Embrittling kinetics follow C-curve behavior with tempering time and temperature, with a nose or minimum time for embrittlement at about 550 °C (1020 °F). Fig. 19.26 shows an early C-curve for TE based on isoembrittlement curves (Ref 19.67,19.70). It takes about an hour at 550 °C for the first increase in transition temperature to be noticeable, and several hundred hours

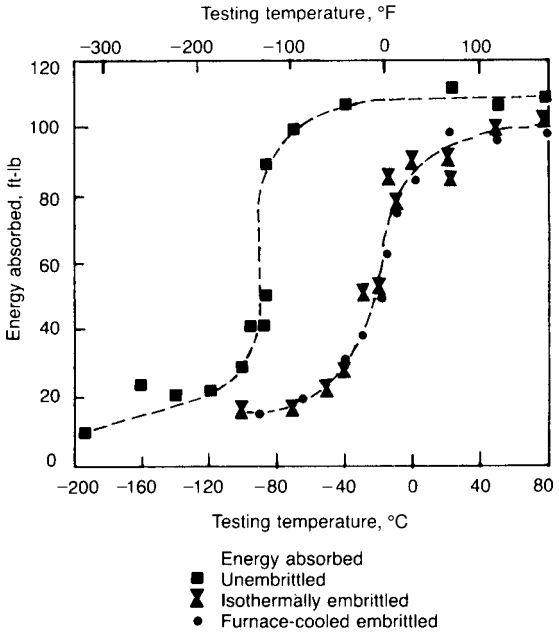

Fig. 19.25 Shift in impact transition curve to higher temperatures as a result of temper embrittlement of SAE 3140 steel subjected to isothermal holding and furnace cooling through the critical temperature range for TE. Source: Ref 19.38

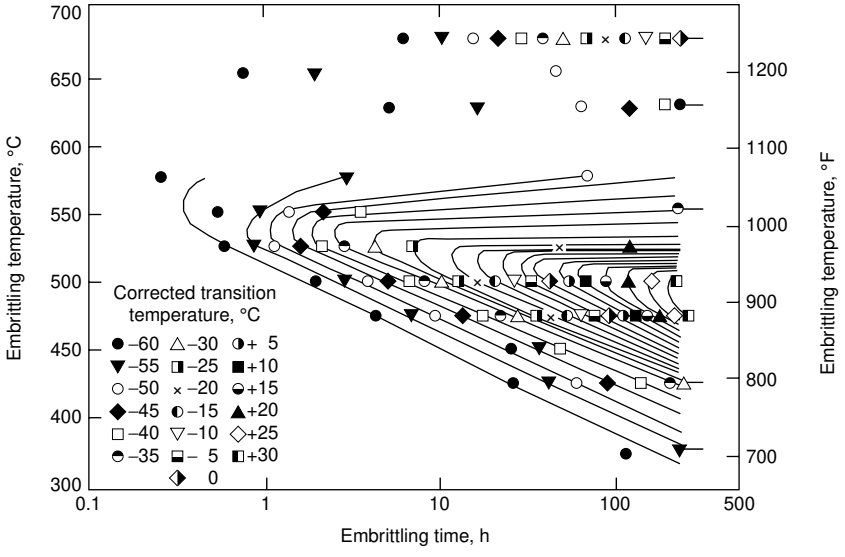

Fig. 19.26 Isoembrittlement curves for a Ni-Cr steel containing 0.39% C, 0.79% Mn, 0.77%Cr, 1.26% Ni, and 0.015% P. Source: Ref 19.67, 19.70

for the first signs of embrittlement at around 375 °C , the lower temperature range for TE. TE is reversible, and de-embrittlement may occur on heating to about 575 °C for only a few minutes.

Chemical factors affecting TE include the requirement that specific impurities most be present for a steel to be susceptible. The impurities most detrimental are antimony, phosphorus, tin, and arsenic. Relatively small amounts of these elements, on the order of 100 ppm (0.01%) or less, have been shown to cause TE. Silicon and manganese in large amounts also appear to be detrimental. Plain carbon steels are not considered to be highly susceptible to TE, provided manganese content is held below 0.5%. Alloy steels are most susceptible, especially the chromium-nickel steels that are frequently used for heavy rotors. Molybdenum, however, reduces susceptibility to TE and, in amounts of 0.5% or less, is an important alloying element added to steels to minimize TE.

The causes of TE have been difficult to identify because, as with TME, there is no readily resolvable microstructural feature identifiable with the characteristic intergranular fracture of embrittled specimens. The only metallographic evidence of embrittlement has been the ability of certain etchants to reveal prior austenite grain boundaries containing segregated phosphorus (Ref 19.63). As for TME, AES has been extremely valuable in determining the chemistry of atomic layers adjacent to intergranular fracture surfaces. Not only are high concentrations of impurity atoms detected at prior austenite grain boundaries, but also gradients of alloying elements such as nickel. Increased concentration of alloying elements may in fact stimulate impurity element segregation. For example, grain boundary carbides may reject nickel as they grow and therefore produce nickel concentration gradients that in turn cause impurity atoms to concentrate (Ref 19.71).

The interactions of impurities and alloying elements associated with segregation have been treated in a thermodynamic model for TE by Guttmann (Ref 19. 72). This research supports the explanation that not just impurity elements but the interaction of those elements with alloying elements is responsible for the segregation that leads to the grain boundary decohesion in temper-embrittled steels. For example, a quantitative assessment of the interactive cosegregation of phosphorus and common alloying elements shows that manganese weakly segregates on its own, but the segregation of nickel, chromium, and molybdenum are driven by strong interactions with phosphorus (Ref 19.73). Grain boundary interaction coefficients increase in the order nickel, manganese, chromium, and molybdenum. The very strong interaction between molybdenum and phosphorus correlates with the known beneficial effect of molybdenum on TE and supports the formation of $(Mo, Fe)_3P$ or Mo-P atom clusters, which prevent the segregation of phosphorus to grain boundaries. The Guttmann et al. study (Ref 19.73) also shows a strong repulsion between carbon and phosphorus, an interaction that is expected to oppose phosphorus segregation.

As noted, the impurity elements phosphorus, antimony, tin, and arsenic have long been associated with TE. Phosphorus can be removed to low levels by modern steelmaking and ladle metallurgy (Ref 19.26), but the elements antimony, tin, and arsenic are not oxidizable during steelmaking and must be controlled by careful selection of scrap that is melted in electric furnaces. A relatively recent approach to eliminating TE is the reduction of manganese and silicon to very low levels, on the order of 0.01 to 0.03% in rotor and nuclear reactor steels (Ref 19.27, 19.28). Manganese and silicon have been traditionally used for alloying and deoxidation, but considerable information now directly ties manganese and silicon, even in moderate amounts, to TE by direct segregation or cosegregation with phosphorus or other alloying elements. For example, Weng and McMahon (Ref 19.74) show that 0.3% Mn greatly increases the susceptibility of a Ni-Cr-Mo-V rotor steel to TE relative to a steel without manganese, and that manganese and phosphorus strongly cosegregate in an Fe-Mn alloy. Other references linking manganese and silicon to TE are reviewed by Bodnar et al. (Ref 19.28).

Liquid-Metal-Induced Embrittlement

The exposure of steels to liquid metals may also cause brittle fracture by intergranular cracking (Ref 19.75). *Liquid-metal-induced embrittlement* (LMIE) is an embrittlement phenomenon that reduces ductility and fracture resistance in a steel exposed to a liquid low-melting point embrittling metal while under tensile stress. Plain carbon and low-alloy steels may be embrittled by exposure to liquid lead, cadmium, brass, aluminum, bronze, copper, zinc, lead-tin solders, and lithium (Ref 19.76). The initiation of fracture by liquid metal is not time dependent but begins immediately on wetting of the microstructure. Often, very low stress is sufficient to cause fracture by LMIE. Several mechanisms for liquid metal embrittlement have been proposed, including an "adsorption-induced decohesion" model, which shows that embrittling atoms at a crack tip lower the cohesive or bonding strength between atoms of the base metal (Ref 19.77).

Breyer and his colleagues have characterized in detail embrittlement of hardened steel by liquid lead (Ref 19.78–19.80). Lead may cause embrittlement if externally applied or if present internally in steel, as is the case with lead added to steels to improve machinability. Figure 19.27 shows an extreme example of the effects of lead embrittlement in a leaded 4145 steel heat treated to strengths close to 1380 MPa (200 ksi). At testing temperatures between 200 and 480 °C (400 and 900 °F), ductility is reduced significantly, with the most severe reduction to zero ductility occurring at and above the melting point of lead, 327 °C (620 °F). Generally, the embrittlement is more severe the higher the strength level of a steel, and therefore, quenched and tempered steels, if leaded, are especially susceptible. The fracture associated with the embrittlement is generally intergranular (Ref 19.80).

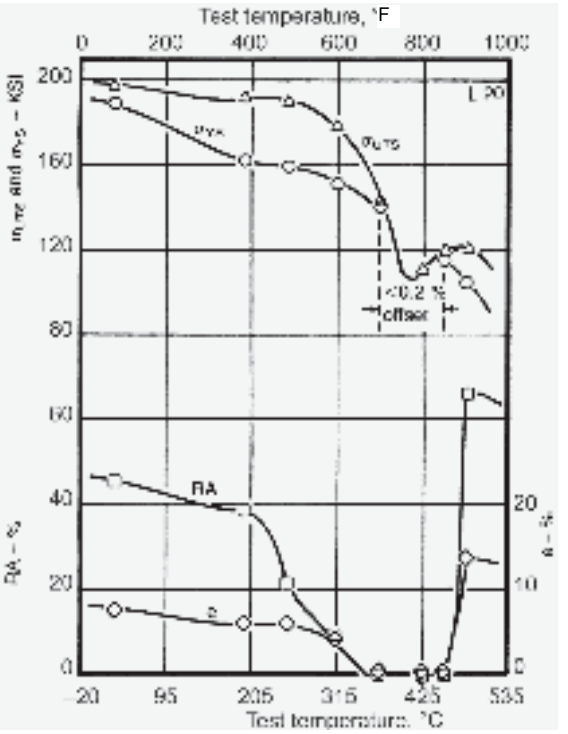

Fig. 19.27 Tensile properties of leaded 4145 steel quenched and tempered to strengths of 200 ksi (1380 MPa) as a function of tensile test temperature. Source: Ref 19.78

In summary, three conditions are necessary for lead embrittlement: the presence of lead either externally or internally in a steel, tensile loading, and temperatures between 200 and 480 °C. The absence of any one of these three conditions will prevent the brittle fracture associated with liquid lead embrittlement.

Hydrogen Embrittlement—General Considerations and Industrial Scenarios

There are many low-toughness and embrittling effects of hydrogen in steels: brittle intergranular and transgranular fracture may occur, peak strengths may be reduced, ultimate tensile strengths may not be attained, ductility as measured by total elongation and reduction of area may be reduced, cracking may develop, crack growth may be greatly accelerated, and in low-strength steels blisters may form. In a review of hydrogen problems, Interrante states that "there are no favorable effects of hydrogen in steel" (Ref 19.81). A very large literature on hydrogen problems has developed, and many reviews, collections of papers, and conferences have been devoted to the effects of hydrogen in steel (Ref 19.82–19.87). More

recently, many other important collections of papers on martensite embrittlement have been published (Ref 19.88–19.91).

This section briefly reviews some of the environmental or product-related effects of hydrogen in steels, including flaking in heavy sections, cold cracking of welds and weld heat-affected zones, hydrogen stress cracking in sour oil and gas environments, and hydrogen embrittlement of quenched and tempered steels. Other industrial scenarios for potential hydrogen embrittlement problems include pressure vessels and piping for hydrogen gas storage and transport, petrochemical refining applications, automotive hydrogen tanks, and nuclear waste disposal systems (Ref 19.89). Atmospheric corrosion may be another source of hydrogen entry into steel (Ref 19.92). Fundamental to these problems are the temperature-related changes in solubility of hydrogen in steel, its very high mobility in steel even at room temperature, and its attraction to regions of localized triaxial tensile stresses and microstructural trapping sites.

The solubility of hydrogen in liquid steel is high and hydrogen may be introduced into liquid steel during steelmaking or welding. Hydrogen solubility drops significantly in delta ferrite, increases in austenite, and decreases again in alpha ferrite. Fig. 19.28 shows hydrogen solubility in iron as a function of crystal structure and temperature (Ref 19.93). As shown, hydrogen solubility drops below one ppm at 600 °C (1110 °F), and extrapolation from that temperature indicates that the solubility of hydrogen at and around room temperature should be almost negligible. Thus the question arises: why should hydrogen be a problem in slowly cooled steel? Answers to this question include facts that hydrogen is attracted to and retained by the many microstructural hydrogen traps in a steel (as discussed in the next section), hydrogen is attracted to regions of triaxial

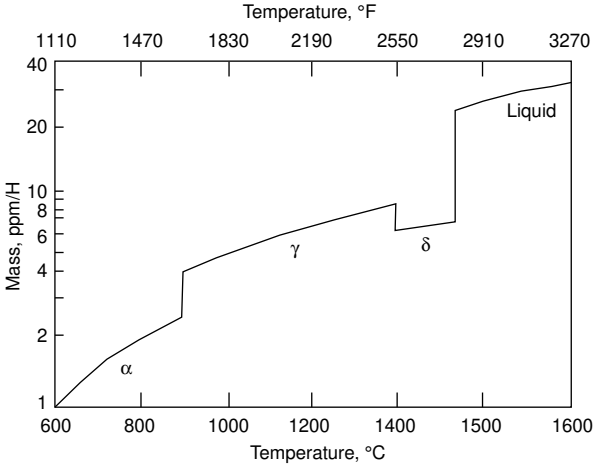

Fig. 19.28 Hydrogen solubility in iron as a function of temperature and crystal structure at one atmosphere pressure of hydrogen. Source: Ref 19.93

tensile stresses present either as residual stresses or produced during loading and deformation, and that perhaps a steel part cross section is too large for hydrogen, even with its high diffusivity, to diffuse from the section during typical high temperature processing steps.

In heavy sections in which hydrogen has not been able to diffuse from the steel, hydrogen concentrates and causes internal cracking or fissures, variously known as flakes, hairline cracks, white spots, or shatter cracks, which develop at temperatures around 200 °C (390 °F) (Ref 19.81). The sensitivity of steels to flaking has traditionally been reduced by holding or cooling very slowly through the temperature range 500 to 650 °C (930 to 1200 °F) in order to give time for hydrogen to diffuse from the steel and reduce its concentration to the lower levels associated with ferrite in this temperature range. Currently, hydrogen flaking problems have been significantly reduced by vacuum degassing of liquid steel to reduce the content of trapped hydrogen to very low levels (Ref 19.26). Hydrogen is gettered by sulfide inclusions, and therefore the control of hydrogen in very clean steels is especially important. In view of the fact that manganese sulfides are strong traps for hydrogen, Fruehan recommends that steel sulfur content be reduced only to levels that will tolerate associated densities of sulfides in a final application (Ref 19.94).

Cold cracking is the term given to hydrogen-induced cracking in welds and weld heat-affected zones (Ref 19.95). Hydrogen may be introduced into welds from moisture in the air, from fluxes, or from cellulosic and other types of electrode coatings, and can readily diffuse into heat-affected zones surrounding weld metal. The microstructural component most sensitive to cold cracking is martensite, and therefore, estimates of the tendency of base metal to form martensite in heat-affected zones, essentially its hardenability, are made in terms of steel chemistry. Carbon most affects hardenability, and its effect and that of other elements have been included in carbon equivalent (C_{equiv}) formulas. An example follows (Ref 19.95):

$$C_{equiv} = C + Mn/6 + (Cr + Mo + V)/5 + (Cu + Ni)/15 \quad \text{(Eq 19.1)}$$

Steels are generally considered to be weldable if C_{equiv} is less than 0.4. The formula shows the great importance of carbon and the need to select low-carbon steels for optimum weldability.

Oil-country steel products such as oil-well casing and tubing when exposed to H_2S-containing sour gas and oil undergo a type of hydrogen embrittlement variously referred to as *hydrogen stress cracking*, *sulfide stress cracking*, or *hydrogen sulfide corrosion cracking*. Various aspects of H_2S corrosion have been addressed in over 100 papers compiled in a volume published by the National Association of Corrosion Engineers (19.96). High-strength tubulars are often made from quenched and tempered steels

such as 4130, containing chromium and molybdenum for hardenability, and for maximum resistance to sulfide stress cracking, tempering at high temperatures, above 620 °C (1150 °F), that produce a maximum hardness of around HRC 22, may be specified. In view of the high-temperature tempering the microstructures consist of highly recovered ferrite, with low dislocation density, and spheroidized carbide particles. However, because of such high tempering temperatures, nickel, which lowers A_{C1} temperatures, is not recommended as an alloying element. A nickel-containing steel may form austenite during high-temperature tempering and introduce during cooling martensite and a high density of dislocations into the tempered microstructure, lowering sulfide cracking resistance.

High-strength quenched and tempered steels are extremely sensitive to hydrogen embrittlement. Often hardened steels for fasteners or other structural applications have been electroplated with chromium or cadmium, and if such parts are not adequately baked, hydrogen introduced by the plating causes brittle fracture. Unique characteristics of such embrittlement have been documented by Troiano et al. (Ref 19.97, 19.98). In particular, their work has shown that there is a delay time required for hydrogen embrittlement failures. In their studies, specimens of 4340 oil quenched and tempered to 1585 MPa (230 ksi) were cathodically charged with hydrogen and immediately plated with cadmium, a procedure that delayed outgassing of hydrogen and ensured a uniform distribution of hydrogen throughout a specimen section after baking. Baking is a low-temperature heat treatment, typically performed at 150 °C (300 °F), which enables hydrogen to diffuse from steel.

Figure 19.29 shows the effect of baking for various times on the applied stress necessary to cause fracture of the hydrogen-charged 4340 specimens. Increasing baking time lowers hydrogen content even in the plated specimens, and sufficient baking eventually restores the strength of charged specimens to that of uncharged specimens. The shorter the baking time is, and the higher the hydrogen content, the lower the stresses and the shorter the time required to cause fracture. The horizontal portions of the curves in Fig. 19.29 are designated *static fatigue limits* or *endurance limits*, i.e., stress levels below which failure would not occur no matter what the duration of stress application. As hydrogen content decreases, the static fatigue limit increases.

The specimens used to obtain Fig. 19.29 were notched, and therefore the static fatigue limits hold for that particular notch geometry. In general, the sharper the notch, the lower is the static fatigue limit, an indication that a critical combination of hydrogen concentration and triaxial tensile stress state in the notch process zone is required for crack initiation. The Troiano studies also showed that an incubation period was necessary for crack initiation. This period is related to the time for hydrogen diffusion to the triaxial stress field at the root of a notch or tip of a crack. The need for an incubation period for hydrogen embrittlement means that high strain

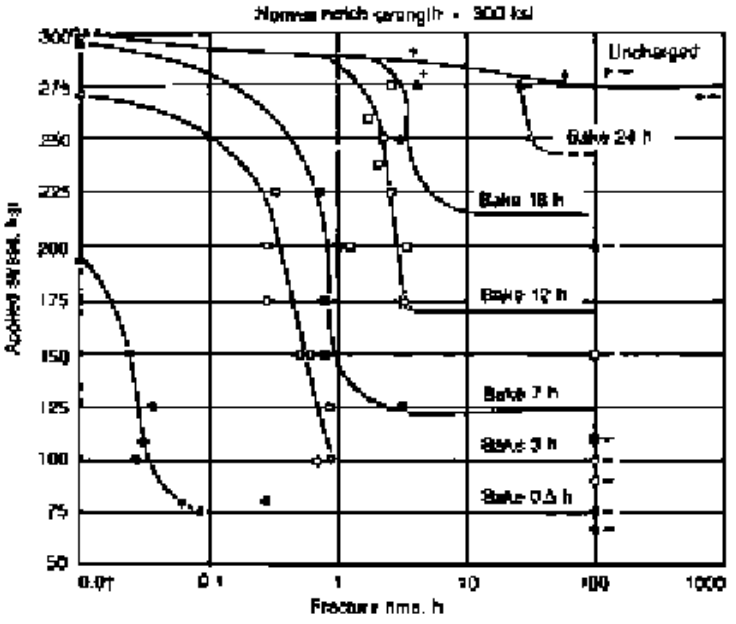

Fig. 19.29 Static fatigue curves for quenched and tempered 4340 notched specimens charged with hydrogen and baked at 150 °C (300 °F) for the times shown. Source: Ref 19.97

rate tests might not effectively detect hydrogen embrittlement, just the reverse of TME and TE. Sustained loading is therefore the most sensitive means of detecting susceptibility to delayed hydrogen failure. The propagation of a crack initiated by internal hydrogen is discontinuous, again because of the requirement for hydrogen diffusion to the stress field at a crack tip. Once a crack advances, it leaves behind the initial hydrogen concentration and is arrested until sufficient hydrogen has again diffused to the crack tip.

The Troiano studies show the importance of time in hydrogen failures. Hydrogen embrittlement failures are the only failures that develop over time with sustained loading, be it external loading or residual tensile stresses as produced, for example, by quenching. The latter situation is the reason for the recommendation of performing tempering as soon as possible after quenching, Thus, time-dependent fracture is an important characteristic that helps to identify hydrogen embrittlement. The studies also show that electroplating can introduce hydrogen and keep hydrogen in a steel, but that with increasing baking time hydrogen can be driven from the steel even with a plated coating. The latter phenomenon is incorporated into a recommended procedure for removing hydrogen from plated high-strength hardened steel (Ref 19.99). Recommended temperatures range from 190 to 220 °C (370 to 430 °F) and times from 4 to 22 hours, depending on the tensile strength of the steel part.

Hydrogen Embrittlement—Mechanisms, Microstructure, and Fracture

The low strength associated with hydrogen brittle fracture of steel is attributed to the weakening and eventual breaking of the cohesive bond between iron atoms by hydrogen. Hydrogen is strongly attracted to dislocation cores and may be transported through the microstructure of a steel by dislocation motion (Ref 19.84, 19.85). Within a microstructure there may be reversible trapping sites for hydrogen, such as alloying element atoms and dislocations, and irreversible traps, such as carbide and inclusion interfaces (Ref 19.100). The irreversible sites will be sinks for hydrogen, but depending on conditions, reversible sites may be sources of hydrogen for embrittlement. Hydrogen also appears to increase the mobility of screw dislocations but reduces their ability to cross-slip, thus causing slip to concentrate on relatively few slip planes (Ref 19.101). When dislocations pile up at obstacles such as carbides or inclusions—which are also, as noted, strong traps for hydrogen—the combination of planar slip and hydrogen concentration lowers cohesive strength on the slip planes, leading to the hydrogen fracture mode that has been referred to as *glide-plane decohesion* (Ref 19.101).

The continuing search for characterizing hydrogen embrittlement has led to a number of terms and acronyms used to describe various aspects and forms of hydrogen embrittlement. These terms and their acronyms are listed here and focus on one or another aspect of hydrogen fracture. The references attached to the terms amplify those aspects and attempt to sort out the sometimes conflicting hypotheses and experimental observations regarding the mechanisms of fracture that develop at the tips of hydrogen-induced cracks. In several of the terms, plasticity as it relates to the effect of hydrogen on dislocation generation and mobility, is regarded as an important feature of hydrogen cracking. Dislocations are associated with the initiation of hydrogen fracture, but when screw dislocations, because of hydrogen, can no longer cross slip and applied loads can no longer be accommodated by plastic deformation and strain hardening to ultimate tensile strengths and ductile fracture, those loads are accommodated by brittle fracture at low stresses, low strains, and low ductilities.

- **HIC,** Hydrogen-Induced Cracking (Ref 19.102)
- **PRHIC,** Plasticity-Related Hydrogen-Induced Cracking (Ref 19.102)
- **IGHIC,** Intergranular Hydrogen-Induced Cracking (Ref 19.102)
- **HEAC,** Hydrogen Environment-Assisted Cracking (Ref 19.103)
- **IHAC,** Internal Hydrogen-Assisted Cracking (Ref 19.103)
- **HELP,** Hydrogen-Enhanced Localized Plasticity (Ref 19.104)
- **HEDE,** Hydrogen-Enhanced Decohesion (Ref 19.104)

Fracture surface morphology due to hydrogen is an important characteristic that helps to confirm that hydrogen embrittlement has in fact oc-

curred. In high-strength quenched and tempered steels, hydrogen fracture is invariably intergranular along prior austenite grain boundaries. Of course other aspects of hydrogen embrittlement such as delayed fracture, sources of hydrogen, and differentiation from other embrittlement mechanisms that produce intergranular fracture, must also be considered in a failure analysis. In steels with grain boundary structures sensitive to quench embrittlement or TME because of impurity atom segregation, hydrogen lowers fracture resistance even more (Ref 19.51). Even in hardened steels, such as 4130, in which microstructures tempered at low temperatures or tempered at temperatures that produce TME where hydrogen-free fracture is associated only with ductile microvoid formation, hydrogen produces intergranular fracture. Figure 19.30 shows the amount of intergranular cracking as a function of tempering temperature for hydrogen-charged 4130 steel specimens broken by bending, and Fig. 19.31 shows intergranular fracture in the 4130 steel tempered at two temperatures (Ref 19.105).

Specimens tempered at low temperatures all failed by intergranular cracking. After high-temperature tempering at 600 and 700 °C (1110 and 1290 °F), the fracture mode of the hydrogen-charged specimens was transgranular through the ferrite/spheroidized microstructure, characterized by flat fracture zones surrounded by ductile fracture and nucleated at inclusion particles (Ref 19.105, 19.106).

In low-carbon steels and highly tempered medium-carbon steels, as noted previously, there are several transverse fracture morphologies. Figure 19.32 shows large cleavage facets through hydrogen-charged as-quenched martensite formed in 10B22 steel (Ref 19.107). The relatively

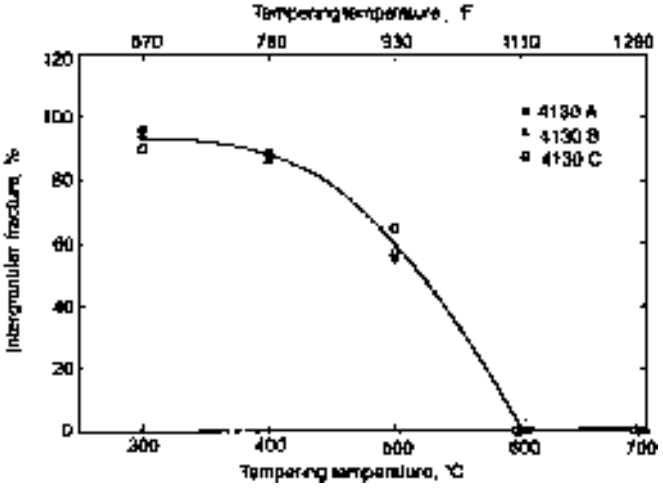

Fig. 19.30 Percent intergranular fracture as a function of tempering temperature of 4130 specimens charged with hydrogen. Source: Ref 19.105

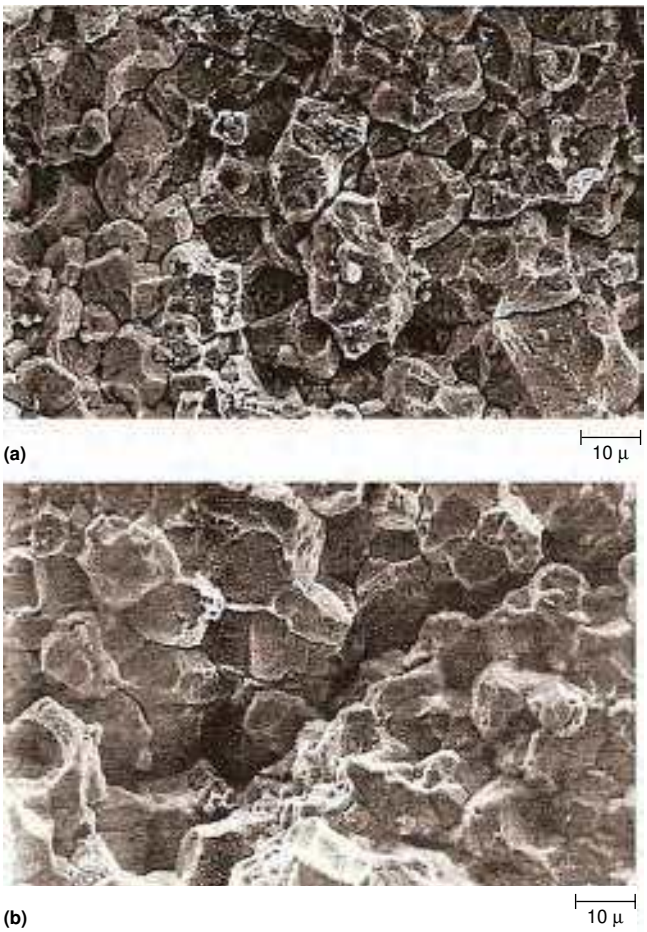

Fig. 19.31 Intergranular fracture in hydrogen-charged quenched 4130 steel tempered at (a) 300 °C (570 °F), and (b) 400 °C (750 °F). Source: Ref 19.105

large facets span many martensite crystals and may correspond to fracture through blocks of martensite crystals with the same orientation. This fracture developed in a tensile specimen by stress-induced fracture well below yield strength of the martensite.

Figure 19.33 shows transgranular fracture through hydrogen-charged 10B22 steel that has been quenched and tempered at 150 °C (300 °F). The fracture surface is brittle and characterized by many fine facets. The arrow points to areas in the fracture surface with parallel steps, perhaps corresponding to fracture along and through parallel martensite crystals in a block or packet of lath martensite. During tensile testing this specimen failed above the yield strength with some plastic deformation, but well short of the ultimate tensile strength and ductility of non-hydrogen-charged

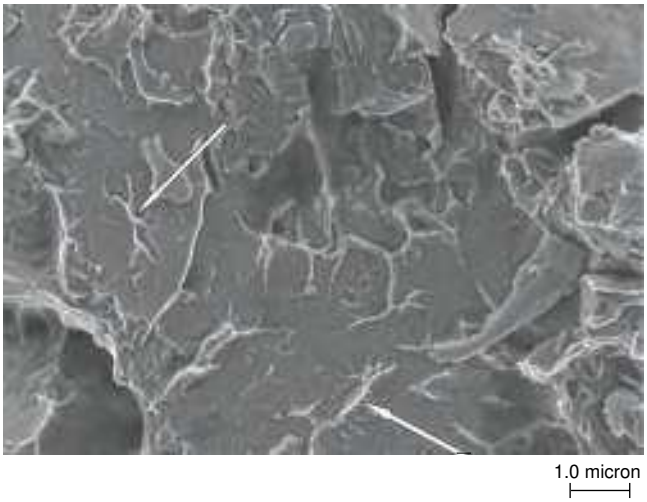

Fig. 19.32 Transgranular cleavage facets in as-quenched martensite of 10B22 steel charged with hydrogen and subjected to tensile testing. The arrows point to secondary fracture in the large cleavage facets. SEM micrograph. Source: Ref 19.107

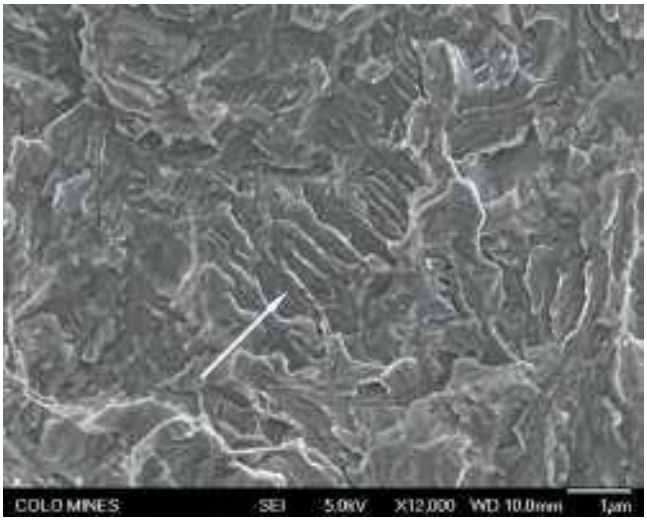

Fig. 19.33 Brittle transgraular fracture surface in a hydrogen-charged sample of 10B22 steel quenched to martensite and tempered at 150 °C (300 °F). The arrow points to a region of parallel steps in the fracture surface. SEM micrograph. Source: Ref 19.107

samples. The small fracture facets are typical of fracture through a low-carbon martensitic microstructure. Cleavage facets in low-carbon steels with ferrite grain microstructures would be much larger, correlating to the size of the ferrite grains.

Figure 19.34 shows a circular zone of brittle fracture that has formed around an inclusion in another area of the fracture surface of the hydrogen-charged 10B22 steel quenched and tempered at 150 °C. The brittle fracture area is surrounded by ductile fracture. As in this low carbon steel sample, this fracture morphology develops in low-carbon weld heat-affected zones and highly tempered medium-carbon steels. The limited zone of brittle fracture around inclusions may be related to the ability of hydrogen to diffuse to stress concentrations around inclusion particles during deformation at a given strain rate.

Fracture surface morphologies point to the microstructural features that are sensitive to decohesion when critical amounts of hydrogen develop. In quenched and tempered martensitic microstructures in low-and medium-carbon steels, as discussed at the end of Chapter 18, "Deformation, Mechanical Properties, and Fracture of Quenched and Tempered Carbon Steels," there are many microstructural components, all of which might be trapping sites for hydrogen. Pressouyre classified the traps into reversible and irreversible groups (Ref 19.100). The reversible traps have low interaction energy with hydrogen and the hydrogen can leave those traps at room temperature or slightly above room temperature. Solute atoms and dislocations are examples of reversible traps. Irreversible traps have high interaction energy with hydrogen and hydrogen cannot leave them unless the steel is heated to high temperatures. Carbide particles and inclusions are examples of irreversible traps. Wei and Tsuzaki give a good recent review of the trapping strength of many of the microstructural compo-

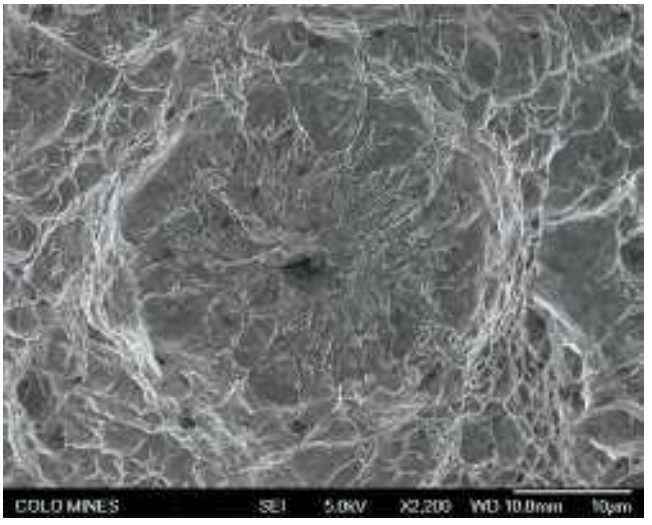

Fig. 19.34 Circular area of brittle fracture around an inclusion particle and surrounded by ductile fracture in a hydrogen-charged quench and tempered 10B22 steel. Source: Ref 19.107

nents in quenched and tempered steels (Ref 19.108). They conclude that dislocations are probably the dominant trap site in martensitic carbon steels. As shown in Chapter 18, "Deformation, Mechanical Properties, and Fracture of Quenched and Tempered Carbon Steels," dislocations are major contributors to the high strength of low-temperature-tempered ultrahigh strength steels, a major factor in limiting usable strength of quenched and tempered steels where hydrogen may be a problem. In order to reduce sensitivity to hydrogen cracking, quenched steels are tempered to temperatures that reduce hardness and strength in microstructures with reduced dislocation densities.

Identification of trapping sites and their participation in hydrogen fracture is an ongoing field of research. Hydrogen thermal desorption spectrometry, an experimental technique that measures hydrogen released during heating, is a powerful way to identify the strength of trapping sites. Figure 19.35 shows the results of desorption measurements in a hydrogen-charged medium-carbon Ti-alloyed steel (Ref 19.109). There are two peaks of hydrogen desorption: a low-temperature peak associated with reversible hydrogen traps, attributed to dislocations, grain boundaries, cementite/martensite interfaces, and fine TiC precipitates, and a high-temperature peak associated with irreversible traps, attributed in the study to coarse TiC particles.

Hydrogen Attack

A quite different type of damage associated with hydrogen, compared with the embrittlement mechanisms described previously, is the phenomenon referred to as hydrogen attack. *Hydrogen attack* is a damage process that occurs at high temperatures in steels exposed to high hydrogen partial pressures and is a major concern in the petrochemical industry regarding

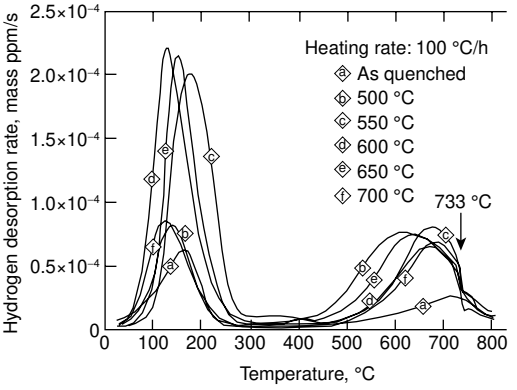

Fig. 19.35 Hydrogen desorption as a function of temperature for hydrogen-charged medium-carbon steel alloyed with titanium and quench and tempered at various temperatures. Source: Ref 19.109

service of pressure vessel steels subjected to hydrogen and hydrocarbons at high pressures. The damage takes the form of grain boundary fissures or cracks that develop from the nucleation, growth, and coalescence of methane bubbles (Ref 19.110). A critical step of the process is the dissolution of cementite. The carbon made available then reacts with hydrogen to form the methane bubbles. The severity of hydrogen attack is determined by hydrogen pressure, temperature, time, and steel alloy content.

Understanding the mechanism of hydrogen attack, especially the step that requires the dissolution of cementite, has led to improved steels with higher carbide-forming alloy additions. More stable carbides resist dissolution and improve hydrogen attack resistance. The American Petroleum Institute provides guidelines for steel selection for hydrocarbon service in the form of Nelson diagrams (Ref 19.111). Figure 19.36 shows a Nelson diagram for a number of steels (Ref 19.112). The curves show maximum temperature/hydrogen partial pressure conditions for hydrogen-attack-free service for each steel. Carbon steels are limited to the lowest temperatures and pressures, and the steels alloyed with the carbide-forming elements chromium and molybdenum, especially at high concentrations, show substantially better performance.

REFERENCES

19.1 Mechanical Testing, *Metals Handbook Desk Edition,* 2nd Ed., J.R. Davis, Ed., ASM International, 1998, p 1308–1342

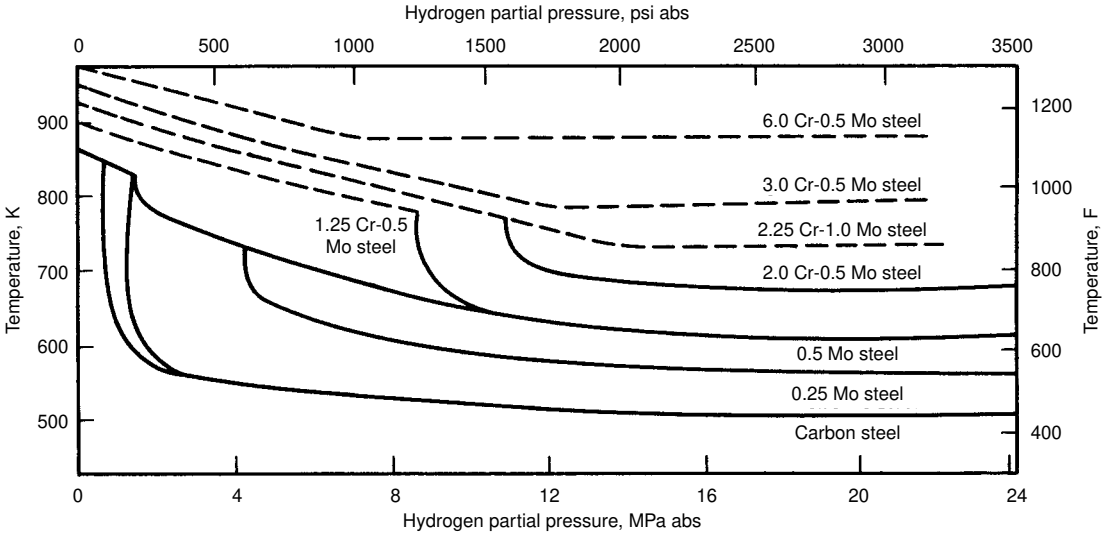

Fig. 19.36 Nelson diagram showing resistance of various steels to hydrogen attack as a function of operating temperature and hydrogen partial pressure. Source: Ref 19.112

19.2 Impact Toughness Testing and Fracture Mechanics, P.K. Liaw, section chair, *Mechanical Testing and Evaluation,* Vol 8, *ASM Handbook,* ASM International, 2000, p 561–678
19.3 D.J. Wulpi, *Understanding How Components Fail,* third ed., B. Miller, Ed., ASM International, 2013
19.4 G. Krauss and C.J. McMahon, Jr., Low-Toughness and Embrittlement Phenomena in Steels, *Martensite,* G.B. Olson and W.S. Owen, Ed., ASM International, 1992, p 295–321
19.5 J.K. Brimacombe and K. Sorimaci, Crack Formation in the Continuous Casting of Steel, *Metal. Trans. B,* Vol 8B, 1977, p 489–505
19.6 B.G. Thomas, Modeling of the Continuous Casting of Steel—Past, Present and Future, *Metallurgical and Materials Transactions B,* Vol 33B 2002, p795–812
19.7 K.C. Mills and A.B. Fox, The Role of Mould Fluxes in Continuous Casting—So Simple Yet So Complex, *ISIJ Int.*, Vol 43 (No. 10), 2003, p 1479–1486
19.8 J. Sengupta, B.G. Thomas, H-J. Shin, G-G Lee, and S-H Kim, A New Mechanism of Hook Formation during Continuous Casting of Ultra-Low-Carbon Steel Slabs, *Metall. and Mater. Trans. A*,Vol 37A, 2006, p 1597–1611
19.9 *The Brimacombe Memorial Symposium,* G. A. Irons and A. W. Cramb, Ed., The Metallurgical Society of CIM (MetSoc), 2000
19.10 H. Shibata, Y. Arai, M. Suzuki, and T. Emi, Kintetics of Peritectic Reaction and Transformation in Fe-C alloys, *Metall. and Mater. Trans. B*, Vol 31B, 2000, p 981–991
19.11 I.V. Samarasekera, Discovery—The Cornerstone of Research in Continuous Casting of Steel Billets, *The Brimacombe Memorial Symposium,* G. A. Irons and A. W. Cramb, Ed., The Metallurgical Society of CIM (MetSoc), 2000, p 399–419
19.12 B. Mintz, The influence of Composition on the Hot Ductility of Steels and to the Problem of Transverse Cracking, *ISIJ Int.,* Vol 39 (No. 9), 1999, p 833–855
19.13 D.N. Crowther, The Effects of Microalloying Elements on Cracking during Continuous Casting, *Proceedings of the International Symposium 2001 on Vanadium Application Technology* (Beijing, China), Vanitec, Westerham, Kent, U.K., p 99–131
19.14 B. Mintz and R. Abushosha, The Hot Ductility of V, Nb/V and Nb Containing Steels, *Microalloying in Steels,* J.M. Rodriguez-Ibabe, I. Gutierrez, and B. Lopez, Ed., Trans Tech Publications Ltd, Uetikon-Zuerich, Switzerland, 1998, p 461–468
19.15 Special Issue: Effects of Cu and Other Tramp Elements on Steel Properties, *ISIJ Int.,* Vol 37 (No. 3), 1997
19.16 Y. Kondo, Behavior of Copper during High Temperature Oxidation of Steel Containing Copper, *ISIJ Int.,* Vol 44 (No. 9), 2004, p 1576–1580

19.17 H. Ohtani, H. Suda, and K. Ishida, Solid/Liquid Equilibria In Fe-Cu Based Ternary Systems, *ISIJ Int.*, Vol 37 (No. 3), 1997, p 207–216
19.18 N. Imai, N. Komatsubara, and K. Kunishige, Effect of Cu, Sn, and Ni on Hot Workability of Hot-Rolled Mild Steel, *ISIJ Int.*, Vol 37 (No. 3), 1997, p 217–223
19.19 N. Imai, N. Komatsubara, and K. Kunishige, Effect of Cu and Ni on Hot Workability of Hot-Rolled Mild Steel, i *ISIJ Int.*, Vol 37 (No. 3), 1997, p 224–231
19.20 S.-J. Seo, K. Asakura, and K. Shibata, Effects of 0.4% Si and 0.02% P Additions on Surface Hot Shortness in 0.1% C-0.5% Mn Steels Containing 0.5% Cu, *ISIJ Int.*, Vol 37 (No. 3), 1997, p 240–249
19.21 *Heat Treater's Guide: Practices and Procedures for Irons and Steels,* 2nd ed., ASM International, 1995
19.22 G.E. Hale and J. Nutting, Overheating of Low-Alloy Steels, *Int. Met. Rev.,* Vol 29, 1984, p 273–298
19.23 T.J. Baker, Use of Scanning Electron Microscopy in Studying Sulfide Morphology on Fracture Surfaces, *Sulfide Inclusions in Steel,* J.J. deBarbadillo and E. Snape, Ed., American Society for Metals, 1975, p 135–158
19.24 N.F. McLeod and J. Nutting, Influence of Manganese on Susceptibility of Low-Alloy Steel to Overheating, *Met. Technol.,* Vol 9, 1982, p 399–404
19.25 R.O. Ritchie and J.F. Knott, On the Influence of High Austenitizing Temperatures and "Overheating" on Fracture and Fatigue Crack Propagation in a Low Alloy Steel, *Metall. Trans.,* Vol 5, 1974, p 782–785
19.26 R.L. Bodnar and R.F. Cappelini, Effect of Residual Elements in Heavy Forgings: Past, Present, and Future, *MiCon 86: Optimization of Processing, Properties and Service Performance through Microstructural Control,* B.L. Bramfitt, R.C. Benn, C.R. Brinkman, and G.F. Vander Voort, Ed., ASTM STP 979, American Society for Testing and Materials, Philadelphia, 1988, p 47–82
19.27 R.L. Bodnar, J.R. Michael, S.S. Hansen, and R.I. Jaffe, Progress in the Design of an Improved High-Temperature 1 pct CrMoV Rotor Steel, *Proceedings 30th Mechanical Working and Steel Processing Conference,* ISS/AIME, Warrendale, PA, 1988
19.28 R.L. Bodnar, T. Ohhashi, and R.I. Jaffee, Effects of Mn, Si, and Purity on the Design of 3.5 NiCrMoV and 2.5 Cr-1 Mo Bainitic Alloy Steels, *Metall. Trans. A,* Vol 20, 1989, p 1445–1460
19.29 B.C. Woodfine and A.G. Quarrell, Effect of Al and N on the Occurrence of Intergranular Fracture in Steel Castings, *JISI,* Vol 195, 1960, p 409–414
19.30 J.A. Wright and A.G. Quarrell, Effect of Chemical Composition on the Occurrence of Intergranular Fracture in Plain Carbon Steels

Containing Aluminum and Nitrogen, *JISI,* Vol 197, 1962, p 299–307

19.31 N.H. Croft, A.R. Entwisle, and G.J. Davies, Intergranular Fracture of Steel Castings, *Advances in Physical Metallurgy and Applications of Steels,* The Metals Society, London, 1982, p 286–295

19.32 F.G. Wilson and T. Gladman, Aluminum Nitride in Steel, *Int. Mater. Rev.,* Vol 33, 1988, p 221–285

19.33 A.G. Vinckier and A.W. Pense, *A review of underclad cracking in pressure vessel components,* WRC Bulletin 197, August 1974

19.34 C.F. Meitzner and A. W. Pense, Stress-relief cracking in low-alloy steel weldments, *Weld. J.*, Vol 48 (10), 1969, p 431s–440s

19.35 C. Huang, J.S. Keske, and D.K. Matlock, Precipitation and Reheat Cracking Susceptibility of A 514 -Type Steels Containing Sulfur and Boron, *42nd MWSP Conference Proceedings*, ISS, Vol 38, 2000, p 341–350

19.36 J.S. Keske, S.W. Thompson, K.K. Khan, and J.D. Defilippi, Reheat-Cracking Susceptibility of ASTM A514-Type Steels Containing Different Levels of Sulfur and Boron, *Proceedings of the International Symposium on Steel for Fabricated Structures,* ASM International, 1999, p 214–223

19.37 D. Bikai, J. A. Pfaendtner, M. Menyhard, and C.J. McMahon, Jr., Sulfur-Induced Dynamic Embrittlement in a Low-Alloy Steel, *Acta Metall.Mater.*, Vol 43, No. 5, 1995, p 1895–1908

19.38 M.A. Grossmann and E.C. Bain, *Principles of Heat Treatment,* 5th ed., American Society for Metals, 1964

19.39 R.S. Hyde, D.K. Matlock, and G. Krauss, Quench Embrittlement: Quenched Carbon and Alloy Steels, *40th MWSP Conference Proceedings,* ISS, Warrendale, PA, 1998, p 921–928

19.40 D.L. Yaney, "The Effects of Phosphorus and Tempering on the Fracture of AISI 52100 Steel," M.S. thesis, Colorado School of Mines, Golden, CO, 1987

19.41 J.P. Materkowski, "Tempered Martensite Embrittlement in 4340 Steel as Related to Phosphorus Content and Carbide Morphology," M.S. thesis, Colorado School of Mines, Golden, CO, 1978

19.42 G. Krauss, The Microstructure and Fatigue of a Carburized Steel, *Metall. Trans. A,* Vol 9A, 1978, p 1527–1535

19.43 H.K. Obermeyer and G. Krauss, Toughness and Interrgranular Fracture of a Simulated Case in EX 24 Type Steel, *J. Heat Treat.,* Vol 1 (No. 3), 1980, p 31–39

19.44 T. Ando and G. Krauss, The Effect of Phosphorus Content on Grain Boundary Cementite Formation in AISI 52100 Steel, *Metall. Trans. A,* Vol 12A , 1981, p 1283–1290

19.45 R.S. Hyde, G. Krauss, and D.K. Matlock, Phosphorus and Carbon Segregation: Effects on Fatigue and Fracture of Gas-Carburized

Modified 4320 Steel, *Metall. and Mater. Trans. A,* Vol 25A, 1994, p 1229–1240

19.46 V. Raghavan, *Phase Diagrams of Ternary Iron alloys: Part 3 Ternary Systems Containing Iron and Phosphorus,* Indian Institute of Metals, Calcutta, India, 1988, p 33–44

19.47 J.D.Wong, D.K. Matlock, and G. Krauss, Effects of Induction Tempering on Microstructure, Properties and Fracture of Hardened Carbon Steels, in *43rd MWSP Conference Proceedings,* Vol 39, 2001, ISS, Warrendale, PA, p 21–36

19.48 F. Zia-Ebrahimi and G. Krauss, Mechanisms of Tempered Martensite Embrittlement in Medium-Carbon Steels, *Acta Metall.,* Vol 32, 1984, p 1767–1777

19.49 J.P. Materkowski and G. Krauss, Tempered Martensite Embrittlement in SAE 4340 Steel, *Metall. Trans. A,* Vol 10A, 1979, p 1643–1651

19.50 N. Bandyopadhyay and C.J. McMahon, Jr., The Micro-Mechanisms of Tempered Martensite Embrittlement in 4340-Type Steels, *Metall. Trans. A,* Vol 14A, 1983, p 1313–1332

19.51 S.K. Banerji, C.J. McMahon, Jr., and H.C. Feng, Intergranular Fracture in 4340-Type Steels: Effects of Impurities and Hydrogen, *Metall. Trans. A,* Vol 9A, 1978, p 237–247

19.52 B.J. Schultz and C.J. McMahon, Jr., *Temper Embrittlement of Alloy Steels,* STP 499, ASTM, 1972, p 104

19.53 H. Ohtani and C.J. McMahon, Jr., Modes of Fracture in Temper Embrittled Steels, *Acta Metall.,* Vol 23, 1975, p 377–386

19.54 G. Thomas, Retained Austenite and Tempered Martensite Embrittlement, *Metall. Trans. A,* Vol 9A, 1987, p 439–450

19.55 F. Zia-Ebrahimi and G. Krauss, The Evaluation of Tempered Martensite Embrittlement in 4130 Steel by Instrumented Charpy V-Notch Testing, *Metall. Trans. A,* Vol 14A, 1983, p 1109–1119

19.56 Gu Baozhu and G. Krauss, The Effect of Low-Temperature Isothermal Heat Treatments on the Fracture of 4340 Steel, *J. Heat Treat.,* Vol 4, 1986, p 365–372

19.57 M. Leap, D.K. Matlock, and G. Krauss, Correlation of the Charpy Test to Fracture Mechanics in a Vanadium Modified 1045 Steel, *Fundamentals of Microalloying Forging Steels,* G. Krauss and S.K. Banerji, Ed., TMS-AIME, Warrendale, PA, 1987, p 113–152

19.58 G.E. Dieter, *Mechanical Metallurgy,* 3rd ed., McGraw-Hill Company, New York, 1986

19.59 J.A. Sanders, P.T. Purtscher, D.K. Matlock, and G. Krauss, Ductile Fracture and Tempered Martensite Embrittlement of 4140 Steel, *Gilbert R. Speich Symposium Proceedings,* G. Krauss and P.E. Repas, Ed., ISS, Warrendale, PA, 1992, p 67–76

19.60 W.S. Owen, The Effect of Silicon on the Kinetics of Tempering, *Trans. ASM,* Vol 46, 1954, p 812–829

19.61 S.J. Barnard G.D.W. Smith, A.J. Garratt-Reed, and J. Vander Sande, Atom Probe Studies: (1) The Role of Silicon in the Tempering of Steel, *Solid-Solid Phase Transformations,* H.I. Aaronson, D.E. Laughlin, R.P. Sekerka, and C.M. Wayman, Ed., TMS-AIME, Warrendale, PA, 1982 p 881–885

19.62 J.L. Youngblood and M. Raghavan, Correlation of Microstructure with Mechanical Properties of 300M Steel, *Metall. Trans. A,* Vol 8A, p 1439–1448

19.63 I. Olefjord, Temper Embrittlement, Review 231, *Int. Met. Rev.,* Vol 23, 1978, p 149–163

19.64 J.H. Hollomon, Temper Brittleness, *Trans. ASM,* Vol 36, 1946, p 473–540

19.65 B.C. Woodfine, Temper Brittleness: A Critical Review of the Literature, *JISI,* Vol 173, 1953, p 229–240

19.66 J.M. Capus, The Mechanism of Temper Brittleness, *Temper Embrittlement in Steel,* STP 407, ASTM, Philadelphia, 1968, p 3–19

19.67 C.J. McMahon, Jr., Temper Brittleness—An Interpretive Review, *Temper Embrittlement in Steel,* STP 407, ASTM, Philadelphia, 1968, p 127–167

19.68 F.L. Carr, M. Goldman, L.D. Jaffee, and D.C. Buffum, Isothermal Temper Embrittlement of SAE 3140 Steel, *Trans. TMS-AIME,* Vol 197, 1953, p 998

19.69 *Impurities in Engineering Materials,* C.L. Briant, Marcel Dekker, Inc, New York, 1999

19.70 L.D. Jaffe and D.C. Buffum, Isothermal Temper Embrittlement, *Trans. ASM,* Vol 42, 1950, p 604–618

19.71 C.J. McMahon, Jr., E. Furubayashi, H. Ohtani, and H.C. Feng, A Study of Grain Boundaries during Temper Embrittlemnt of a Low Carbon Ni-Cr Steel Doped with Antimony, *Acta Metall.,* Vol 24, 1976, p 695–704

19.72 M. Guttmann, The Link Between Equilibrium Segregation and Precipitation in Ternary Solutions Exhibiting Temper Embrittlement, *Met. Sci.,* Vol 10, 1976, p 337–341

19.73 M. Guttmann, Ph. Dumoulin, and M. Wayman, The Thermodynamics of Interactive Co-Segregation of Phosphorus and Alloying Elements in Iron and Temper Brittle Steels, *Metall. Trans. A,* Vol 13A, 1982, p 1693–1711

19.74 Y. Weng and C.J. McMahon, Jr., The Effect of Manganese on Intergranular Embrittlement in Iron and Steel, *Grain Boundary Structure and Related Phenomena,* Proceedings of JIMS-4, 1986, Supplement to *Trans. Jpn. Inst. Met.,* p 579–585

19.75 C.L. Briant and S.K. Banerji, Intergranular Fracture in Steel: The Role of Grain Boundary Composition, Review 232, *Int. Met. Rev.,* Vol 23, 1978, p 164–199

19.76 W.R. Warke, Liquid Metal and Solid Metal Induced Embrittlement, *Failure Analysis and Prevention,* Vol 11, *ASM Handbook,* ASM International, 2002, p 861–867
19.77 R. Venkataraman, M.D. Baldwin, and G.R. Edwards, Embrittlement of Steels by Lead, *Progress in Astronautics and Aeronautics,* Vol 148, 1991, p 310–334
19.78 S. Mostovoy and N.N. Breyer, The Effect of Lead on the Mechanical Properties of 4145 Steel, *Trans. ASM*, Vol 61, 1968, p 219–232
19.79 W.R. Warke and N.N. Breyer, Effect of Steel Composition on Lead Embrittlement, *JISI*, Vol 209, 1971, p 779–784
19.80 R.D. Zipp, W.R. Warke, and N.N. Breyer, A Comparison of Elevated Temperature Tensile Fractures in Nonleaded and Leaded 4145 Steel, STP 453, ASTM, 1969, p 111–133
19.81 C.G. Interrante, Basic Aspects of the Problems of Hydrogen in Steels, *Hydrogen Problems in Steels,* C.G. Interrante and G.M. Presouyre, Ed., American Society for Metals, 1982, p 3–17
19.82 J.P. Hirth, Effects of Hydrogen on the Properties of Iron and Steel, *Metall. Trans. A*, Vol 11A, 1980, p 861–890
19.83 M. Bernstein, R. Garber, and G.M. Pressouyre, Effect of Dissolved Hydrogen on Mechanical Behavior of Metals, *Effect of Hydrogen on Behavior of Materials,* A.W. Thompson and I.M. Bernstein, Ed., TMS-AIME, Warrendale, PA, 1976, p 37–58
19.84 *Effect of Hydrogen on Behavior of Material,* A.W. Thompson and I.M. Bernstein, Ed., TMS-AIME, Warrendale, PA, 1976
19.85 *Hydrogen Effects in Metals,* A.W. Thompson and I.M. Bernstein, Ed., TMS-AIME, Warrendale, PA, 1981
19.86 *Hydrogen Problems in Steels,* C.G. Interrante and G.M. Pressouyre, Ed., American Society for Metals, 1982
19.87 *Hydrogen Effects on Material Behavior,* N.R. Moody and A.W. Thompson, Ed., TMS, Warrendale, Pa, 1990
19.88 *Effects of Hydrogen on Materials: Proceedings of the 2008 International Hydrogen Conference*, Brian Somerday, Petros Sofronis, and Russell Jones, Ed., ASM International, 2009
19.89 *Gaseous hydrogen embrittlement of materials in energy technologies*, Richard P. Gangloff and Brian P. Somerday, Ed., Woodhead Publishing Limited, Cambridge UK, 2012
19.90 Special Issue on Common Bases for Hydrogen Embrittlement Studies, *ISIJ Int.*, Vol 52, Number 2, 2012, p 167–331
19.91 *Hydrogen-Materials Interactions*, Proceedings of the 2012 International Hydrogen Conference, B. P. Somerday and P. Sofronis, Ed., ASME Press, New York, 2014
19.92 E.A. Akiyama, S. Li, Z. Zhang, M. Wang, K. Matsuhiro, K. Tsuzaki, and B. Zhang, Hydrogen Embrittlement of High Strength Steels and Environmental Hydrogen Entry, *Effects of Hydrogen on*

Materials: Proceedings of the 2008 International Hydrogen Conference, Brian Somerday, Petros Sofronis, and Russell Jones, Ed., ASM International, 2009, p 54–61

19.93 E.T. Turkdogan, *Fundamentals of Steelmaking,* The Institute of Materials, Book 656, 1996, p 96

19.94 R.J. Fruehan, A Review of Hydrogen Flaking and Its Prevention, *ISS Trans.,* August 1997, p 6–67

19.95 K. Easterling, *Introduction to the Physical Metallurgy of Welding,* Butterworths, London, 1983

19.96 *H_2S Corrosion in Oil & Gas Production—A Compilation of Classic Papers,* R.N. Tuttle and R.D. Kane, Ed., NACE, Houston, TX, 1981

19.97 H.H. Johnson, J.G. Morlet, and A.R. Troiano, Hydrogen, Crack Initiation, and Delayed Failure in Steel, *Trans. TMS-AIME,* Vol 212, 1958, p 528–536

19.98 A.R. Troiano, The Role of Hydrogen and Other Interstitials in the Mechanical Behavior of Metals, *Trans. ASM,* Vol 52, 1960, p 54–80

19.99 Standard Guide for Post-Coating Treatments of Steel for Reducing Risk of Hydrogen Embrittlement, Specification B 850, ASTM

19.100 G.M. Pressouyre, A Classification of Hydrogen Traps in Steel, *Metall. Trans. A,* Vol 10A, 1979, 1571–1573

19.101 C.J. McMahon, Jr., Effects of Hydrogen on Plastic Flow and Fracture in Iron and Steel, *Hydrogen Effects in Metals,* A.W. Thompson and I.M. Bernstein, Ed., TMS-AIME, Warrendale, PA, 1981, p 219–233

19.102 C.J. McMahon, Jr, X. Liu, J. Kameda, and M.J. Morgan, Recent Observation of Hydrogen-Induced Cracking of High-Strength Steels, *Effects of Hydrogen on Materials: Proceedings of the 2008 International Hydrogen Conference*, Brian Somerday, Petros Sofronis, and Russell Jones, Ed., ASM International, 2009, p 46–53

19.103 R.P. Gangloff, Science-based Prognosis to Manage Structural Alloy Performance in Hydrogen, *Effects of Hydrogen on Materials: Proceedings of the 2008 International Hydrogen Conference*, Brian Somerday, Petros Sofronis, and Russell Jones, Ed., ASM International, 2009, p 1–21

19.104 W.W. Gerberich, D.D. Stauffer, and P. Sofronis, A Coexistent View of Hydrogen Effects on Mechanical Behavior of Crystals: HELP and HEDE, *Effects of Hydrogen on Materials: Proceedings of the 2008 International Hydrogen Conference*, Brian Somerday, Petros Sofronis, and Russell Jones, Ed., ASM International, 2009, p 38–45

19.105 B.D. Craig and G. Krauss, The Structure of Tempered Martensite and Its Susceptibility to Hydrogen Stress Cracking, *Metall. Trans. A,* Vol 11A, 1980, p 1799–1808

19.106 B.D. Craig and G. Krauss, The Resistance of Highly Tempered 4130 Steel to Hydrogen Stress Cracking, i *Hydrogen Effects in Metals,* A.W. Thompson and I.M. Bernstein, Ed., TMS-AIME, Warrendale, PA, 1981, p 795–802

19.107 S-J. Lee, J.A. Ronevich, G. Krauss, and D.K. Matlock, Hydrogen Embrittlement of Hardened Low-Carbon Steel, *ISIJ Int.*, Vol 50, 2010, p 294–301

19.108 F.G. Wei and K. Tsuzaki, Hydrogen trapping phenomena in martensitic, *Gaseous hydrogen embrittlement of materials in energy technologies*, Richard P. Gangloff and Brian P. Somerday, Ed., Woodhead Publishing Limited, Cambridge UK, 2012, Vol 1, p 493–525

19.109 F.G. Wei, T. Hara, T. Tsuchida, and K. Tsuzaki, Hydrogen Trapping in Quenched and Tempered 0.42C-0.30Ti Steel Containing Bimodally Dispersed TiC Particles, *ISIJ Int.,* Vol 43, No. 4, 2003. p 539–547

19.110 P.G. Shewmon, Hydrogen Attack of Carbon Steel, *Metall. Trans. A,* Vol 7A, 1976, p 279–286

19.111 *Steel for Hydrogen Service at Elevated Temperatures and Pressures in Petroleum Refineries and Petrochemical Practice,* API 941, American Petroleum Institute, 1970

19.112 D.A. Canonico, Heavy-Wall Pressure Vessels for Energy Systems, *Alloys for the Eighties,* Climax Molybdenum Company, Greenwich, CT, 1980

CHAPTER **20**

Residual Stresses, Distortion, and Heat Treatment

CHAPTER 19, "Low Toughness and Embrittlement Phenomena in Steels," in this book describes causes of low toughness and embrittlement phenomena that could be directly attributed to chemical and microstructural features of steel. This chapter describes features of thermally or mechanically processed steel parts, namely, residual-stress distributions and distortion, that are not directly related to unique microstructural features but are very much dependent on the response of base microstructures to processing parameters. Residual stress and distortion are related to the response of manufactured parts to temperature and deformation gradients through macroscopic sections. Some residual stresses are beneficial, for example, the compressive surface stresses produced by carburizing or shot peening; others are detrimental, for example, surface tensile stresses introduced by quenching of through-hardening steels. Such tensile stresses reduce fracture and fatigue resistance. This chapter describes the origin of residual stresses and some heat treatments designed to minimize undesirable residual stress, quench cracking, and distortion. Some comments and references to modeling of residual stress and distortion conclude the chapter.

Origins of Distortion

Distortion of a part may be classified as size distortion or shape distortion. Size distortion is caused by thermal expansion or contraction of a microstructure during heating and cooling, and in steels is significantly influenced by changes in crystal structure that accompany phase transfor-

mations during heat treatment. For example, on heating of ferrite/cementite microstructures, there is a volume contraction when the close-packed atom structure of face-centered cubic austenite forms. On cooling, when the austenite transforms to more open body-centered crystal structures of ferrite and martensite, there is a volume expansion. The volume changes are a function of carbon content, and Table 20.1 lists the volume and dimensional changes, including the effects of carbon content, for various microstructural changes produced by heat treatment (Ref 20.1). To offset size changes during heat treatment, allowances for expected dimensional changes can be made in machined part dimensions prior to heat treatment.

Shape distortion is caused by nonuniform thermal and transformation stresses due to temperature variations throughout parts of complicated shape or parts with large differences in section size within the part. Localized regions, which expand or contract due to more rapid heating or cooling relative to adjacent regions, develop stresses that may be high enough, especially at higher temperatures where microstructures have high ductility, to cause nonuniform plastic deformation that results in changes in shape within a part. If such stresses cannot be relieved by plastic flow, residual stresses may be incorporated into a part, as described subsequently. Shape distortion, and residual stresses, are enhanced by non-uniform quenching, high rates of quenching, large section sizes, and variations in section sizes within a part, all factors that contribute to large variations in temperature throughout a part during heating and cooling. Good part design, minimizing abrupt changes in section size and shape, preheating, slower rates of cooling, interrupted cooling, and selection of high-hardenability steels that can be hardened by slower rates of quenching, even by air cooling, as is the case for some tool steels, are all approaches that can be used to minimize distortion, residual stresses, and even quench cracking in susceptible steels.

Origins of Residual Stresses

Two types of physical changes cause the residual stresses produced during cooling of heat treated parts. The one type of change is the thermal

Table 20.1 Size changes associated with microstructural changes in carbon steels

Reaction	Volume change, %	Dimensional change, mm/mm or in./in.
Spheroidite → austenite	–4.64 + 2.21 (% C)	–0.0155 + 0.0074 (% C)
Austenite → martensite	4.64 – 0.53 (% C)	0.0155 – 0.0018 (% C)
Spheroidite → martensite	1.68 (% C)	0.0056 (% C)
Austenite → lower bainite(a)	4.64 – 1.43 (% C)	0.0155 – 0.0048 (% C)
Spheroidite → lower bainite(a)	0.78 (% C)	0.0026 (% C)
Austenite → aggregate of ferrite and cementite(b)	4.64 – 2.21 (% C)	0.0155 – 0.0074 (% C)
Spheroidite → aggregate of ferrite and cementite(b)	0	0

(a) Lower bainite is assumed to be a mixture of ferrite and ε-carbide. (b) Upper bainite and pearlite are assumed to be mixtures of ferrite and cementite Source: Ref 20.1

contraction that occurs during cooling of a single phase or microstructure consisting of a mix of phases in the absence of a phase transformation. The other type of change, as noted previously, is the transformation of austenite to the more open, higher-specific-volume crystal structures of ferrite, cementite, and martensite. The volume expansion due to austenite transformation is the dominant factor in any heat treatment that involves cooling from the austenite phase field, while thermal contraction is the dominant factor in subcritical heat treatment treatments. Residual stresses and distortion arise because cooling rate is a function of section size or position in a part, as noted previously and discussed in Chapter 16, "Hardness and Hardenability," in this book, relative to hardenability; therefore, volume changes occur at different times and locations during cooling.

Figure 20.1, taken from Ebert (Ref 20.2), shows in a schematic series of diagrams all of the changes that take place as a function of time and temperature in a cylindrical specimen cooled in a temperature range where there is no phase transformation. Sketches of the longitudinal stress patterns developed across a slice through a cylinder are shown at four dif-

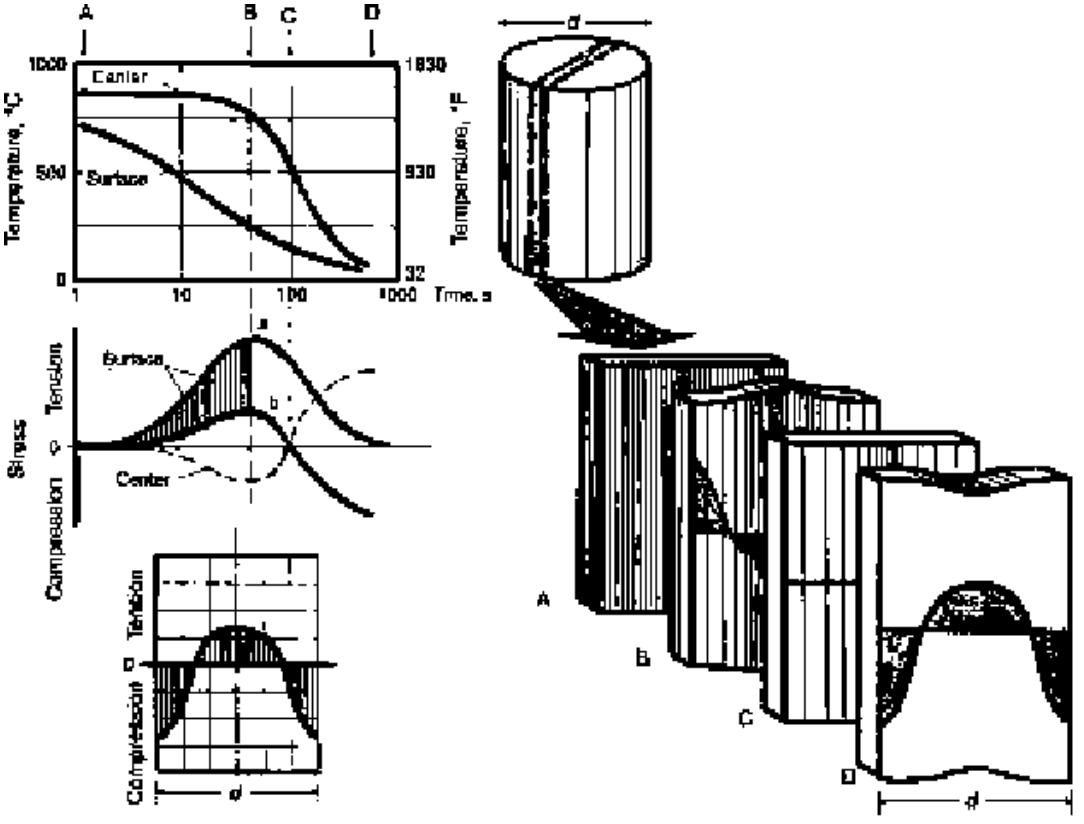

Fig. 20.1 Schematic diagrams showing the evolution of longitudinal residual stresses in steel cooled from subcritical temperatures where no austenite transformations operate. Source: Ref 20.2

ferent stages in the cooling process. The horizontal line in each sketch indicates zero residual stresses; tensile stresses are plotted above the horizontal line, and compressive stresses are plotted below the line. At the start, point A, there are no stresses, but immediately on cooling, temperature differences between the surface and center of the cylinder develop and the surface contracts more rapidly than the center. This contraction is opposed by the center microstructure, and the surface is placed in tension as it attempts to shrink, as shown in the sketch for point B. Eventually, the center significantly cools and contracts, and the residual-stress profile reverses, point C, as the center is placed into tension and its contraction places the surface in compression, point D, on cooling to room temperature.

Figure 20.2 shows schematically the residual-stress evolution of parts that cool at different surface and interior rates from temperatures in the austenite phase field (Ref 20.2). Ebert made this sketch for a carburized steel in which the surface transforms to martensite before the interior transforms, but the diagrams are also valid to illustrate the principles of residual-stress evolution for through-hardened parts where the surface invariably transforms to martensite before the center transforms. In carburized parts, the carbon gradients typically cause the low-carbon core to

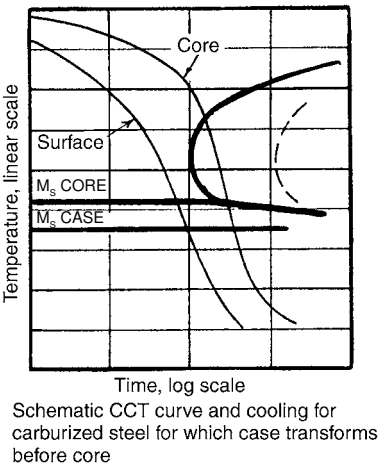

Schematic CCT curve and cooling for carburized steel for which case transforms before core

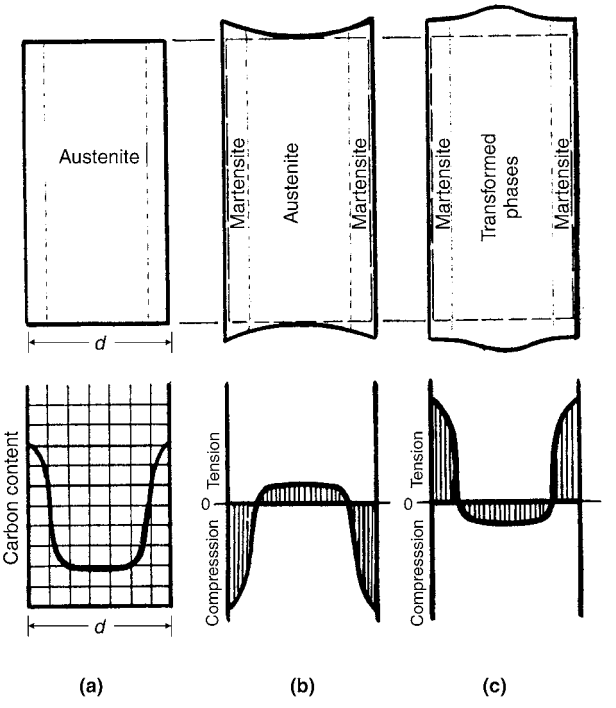

Fig. 20.2 Schematic diagrams showing the evolution of residual stresses in carburized steels where the surface transforms to martensite before the core, or through-hardened steels where the surface transforms to martensite before the center of a part. CCT, continuous cooling transformation. Source: Ref 20.2

transform before transformation of case microstructures, resulting in surface compressive stresses, as described in Chapter 21, "Surface Hardening," in this book. Figure 20.2 shows that when martensite forms first at part surfaces, due to the restraint of the volume expansion by the untransformed center, surface compressive stresses initially develop. However, when the center eventually transforms, either to martensite, bainite, or other ferrite/cementite microstructure, the expansion of the interior puts the surface into residual tension.

High surface residual tensile stresses add to applied tensile stresses and reduce fatigue and fracture resistance of hardened steels. In high-carbon steels subjected to severe quenching, surface tensile stresses may be high enough to cause quench cracking by intergranular fracture mechanisms, as described for quench embrittlement in Chapter 19, "Low Toughness and Embrittlement Phenomena in Steels, in this book. Stress-relief heat treatments and tempering lower surface residual stresses, and several heat treatments, as described in the next section, are designed to minimize the effects of surface tensile stresses.

Heat Treatments to Reduce Surface Residual Tensile Stresses

Practically, the tendencies to distortion, quench cracking, and/or high residual surface tensile stress formation may be reduced by any change in processing that reduces the differences in the rates of cooling between the surface and interior of steel parts. Quite effective in this regard is a change to more moderate quenching for hardening, even to the point of air cooling for tool steels, if problems are encountered with more severe quenching. The effectiveness of a less severe quench in hardening may require the use of a more hardenable, more highly alloyed steel, and the matching of steel composition, section size, and cooling rates is an important application of hardenability. Reducing the temperature difference between austenitizing and a quenchant is also sometimes effective in reducing distortion. For example, steel parts carburized at 950 °C (1750 °F) are often cooled to 840 °C (1550 °F) prior to quenching and may be quenched in oil heated to 70 °C (170 °F) instead of oil at room temperature.

Martempering or interrupted quenching is a hardening treatment that consists of quenching to a temperature just above the M_s temperature of a steel, usually by quenching into a molten salt bath, holding for a time sufficient to equalize temperature through the part, and then air cooling through the M_s to room temperature (Ref 20.3). Figure 20.3 compares schematic diagrams for conventional quenching, martempering, and modified martempering (Ref 20.4, 20.5). The differences in the cooling rates at the surface and center of parts are shown. In conventional quenching, the differences in cooling rates follow through the transformation of austenite to martensite, leading to the development of surface tensile stresses

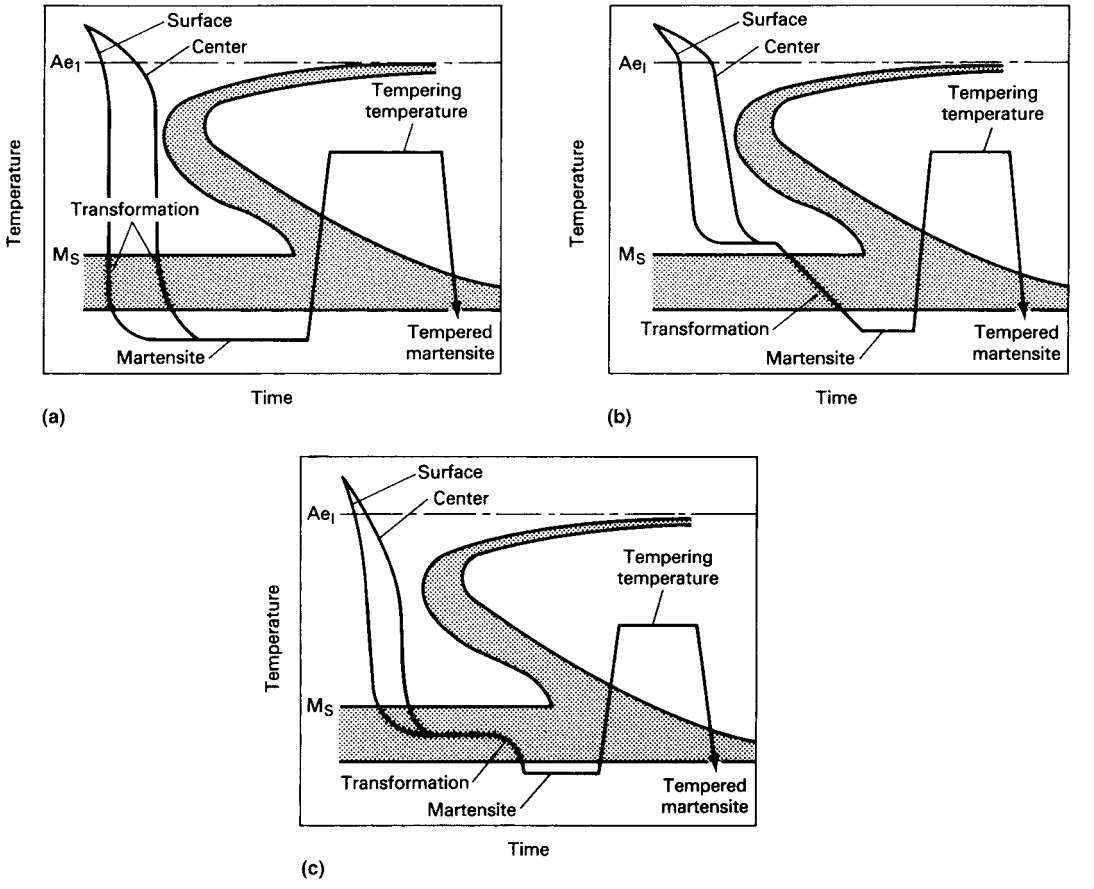

Fig. 20.3 Schematic time-temperature-transformation diagrams showing surface and center cooling rates for (a) conventional quenching, (b) martempering, and (c) modified martempering. Source: Ref 20.4

as described previously. In the martempering treatments, temperatures are allowed to equalize in order to effectively promote simultaneous transformation uniformly throughout a part.

An important requirement for martempering is that no transformation product other than martensite should form. Therefore, steels suitable for martempering must have sufficient hardenability not only with respect to higher-temperature transformation products such as ferrite and pearlite but also with respect to bainite that may form just above the M_s. Also, hot salt has a quenching severity somewhat lower than that of oil, and therefore, a steel for marquenching must have sufficient hardenability to compensate for the reduced rate of cooling in salt. The lower temperatures of modified martempering serve to increase quench severity, making it possible to use steels with lower hardenabilities. Cooling through the martensite transformation range is also important. Water quenching, instead

of air cooling, even when temperature is uniform throughout a part just above M_s, will almost invariably lead to quench cracking (Ref 20.3).

Austempering is another hardening treatment designed to reduce distortion and cracking in higher-carbon steels. The objective of austempering is to isothermally transform austenite to bainite rather than martensite. Figure 20.4 schematically compares conventional quenching with austempering (Ref 20.4, 20.5). Uniform temperatures are again achieved by cooling into molten salt, and the transformation to bainite is accomplished at a constant temperature. No tempering is required, and lower bainites may have comparable or better toughness than quenched and low-temperature-tempered microstructures.

As in martempering, a steel suitable for austempering must have sufficient hardenability to avoid higher-temperature austenite transformation products when quenched into heated molten salt with a relatively low quench severity. Carbon steel parts for austempering are therefore limited in size to obtain sufficiently high cooling rates to avoid ferrite and pearlite formation. If an alloy steel is selected to compensate for the reduced quenching efficiency of hot molten salt, bainite hardenability may also be increased to the point where very long times are required for transformation. Thus, a major processing advantage of austempering, the fact that no tempering is required, may be offset by the increased holding time for bainite formation.

Residual stresses are produced not only during hardening heat treatments but also during processing of parts with largely ferritic or ferrite/pearlite microstructures. For example, machining and cold working may introduce residual stresses due to differences in the amount of deformation between the surface and interior regions of a part. Welding is another process that produces residual tensile stresses. As weld metal solidifies and contracts, it is restrained by the adjacent base metal and placed in tension. In hardened parts, final dimensions may be produced by grinding,

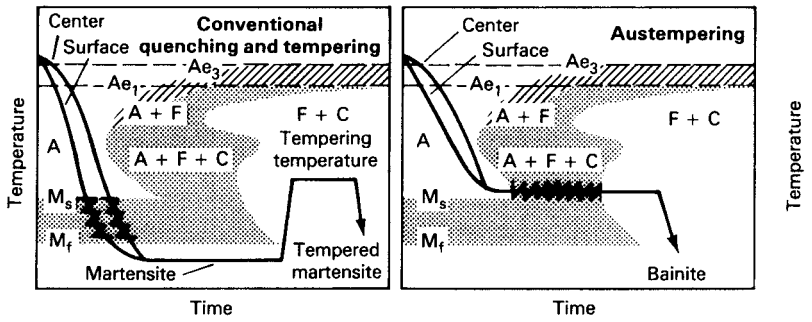

Fig. 20.4 Schematic diagrams of time-temperature-transformation curves with superimposed surface and center cooling rates for conventional quenching and tempering and austempering. Source: Ref 20.4

but excessive grinding may cause heating that causes softening and even the formation of austenite that subsequently transforms to martensite, creating undesirable residual stresses and even grinding cracks. Electrodischarge machining may also introduce unfavorable residual stresses in hardened steels (Ref 20.6).

Residual stresses produced by the processes just described are reduced or eliminated by stress-relief heat treatments applied at subcritical temperature, between 550 and 650 °C (1020 and 1200 °F) for plain carbon and low-alloy steels and between 600 and 750 °C (1110 and 1380 °F) for hot work and high-speed steels (Ref 20.7). Heating to or cooling from stress-relief temperatures must be done slowly, especially in heavy sections or large welded assemblies, to avoid introducing new thermal stresses and possible cracking during stress-relief treatments. The objective of stress relieving is not to produce major changes in mechanical properties. Therefore, the relief of stresses is accomplished by recovery mechanisms that rearrange and reduce densities of dislocations without causing recrystallization, with its major changes in microstructure and mechanical properties. For example, investigation of stress relief in cold extruded mild steel bars showed that residual stresses were almost completely relieved without any hardness decrease after heating at 500 °C (930 °F) for 1 h (Ref 20.8).

Evaluation and Prediction of Residual Stresses and Distortion

Residual-stress profiles are measured by x-ray diffraction analysis (Ref 20.9, 20.10). The residual stresses cause either compression or extension of the interplanar spacings of the crystal lattice planes of the phases in steel specimens, and the changes in interplanar spacings are used to calculate stresses by use of Poisson's ratio and Young's modulus. Because of the limited depth of penetration of x-rays into steel, residual-stress profiles are obtained by serial examination of subsurface layers exposed by electrolytic or chemical polishing.

The need to minimize distortion and detrimental residual stresses has stimulated intensive research into quantitative understanding, control, and modeling of quenching and its effects on the performance of steel parts. Although residual stress and distortion can be measured and the causes and cures are known qualitatively, quantitative predictions of these phenomena in steel parts with complex shapes are extremely difficult. Residual stresses depend on part size and geometry, heat-transfer coefficients between a part and the quenchant, uniformity of the quench, heat flow within the steel, the transformation of austenite to various microstructures as a function of chemistry, position, time and temperature as determined by cooling rates, carbon concentration gradients in carburized steels, and

the temperature-dependent mechanical properties and plastic flow characteristics of mixtures of austenite and its decomposition products.

All of the listed aspects of quenching are being incorporated into computer models that predict residual stresses and distortion, and in ongoing efforts the models make valuable predictions of performance as a function of processing variables (Ref 20.5, 20.11–20.18). A detailed discussion of the modeling is outside the scope of this book, but a recent effort, showing the interdisciplinary and complex components of a predictive modeling program, is noted here. The effort was sponsored under the auspices of the National Center for Manufacturing Sciences and established a consortium team of corporations, national laboratories, and universities that brought extensive computing power and expertise to the problem (Ref 20.18) Figure 20.5 shows the various elements of the model for predicting residual stress and distortion in a small carburized helical gear. To go from what appears to be a straightforward carburizing and quenching heat treatment to calculations of distortion and residual stress requires a remarkable integration of thermal, microstructural, and mechanical interactions, all as a function of time, temperature, and location. Not only was the modeling effort intensive, but also the process required good input data, including heat-transfer boundary conditions in oil and salt, transformation kinetics of the 51*xx* model steel as a function of carbon content, and stress-strain data of austenite and its decomposition products as a function of temperature and strain rate. Some of the data were available in the literature, but some had to be determined experimentally as part of the modeling effort.

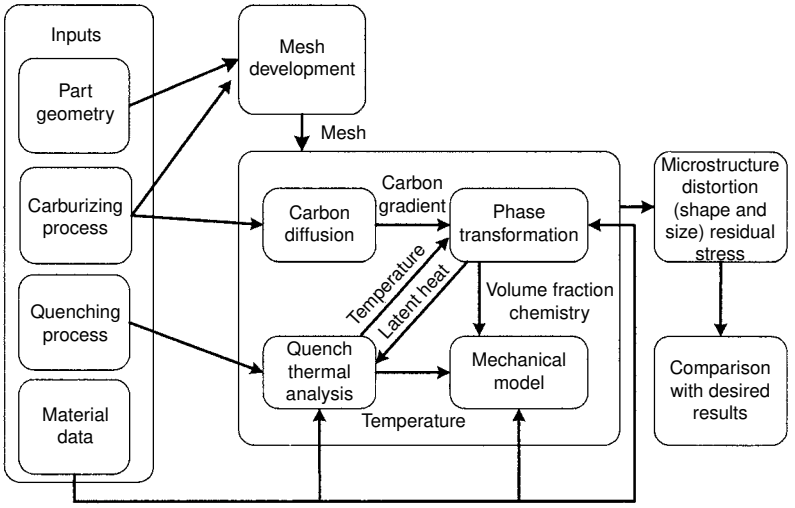

Fig. 20.5 Elements of the National Center for Manufacturing Sciences process model to predict distortion and residual stresses of a carburized helical gear. Source: Ref 20.18

REFERENCES

20.1 B.S. Lement, *Distortion in Tool Steels,* American Society for Metals, 1959

20.2 L.J. Ebert, The Role of Residual Stresses in the Mechanical Performance of Case Carburized Steels, *Metall. Trans. A,* Vol 9, 1978, p 1537–1551

20.3 M.A. Grossmann and E.C. Bain, *Principles of Heat Treatment,* 5th ed., American Society for Metals, 1964, p 189–196

20.4 *Heat Treating,* Vol 4, *ASM Handbook,* ASM International, 1991, p 137, 152

20.5 B. Liscic, H.M. Tensi, and W. Luty, Ed., *Theory and Technology of Quenching,* Springer-Verlag, Berlin, 1992

20.6 G. Roberts, G. Krauss, and R. Kennedy, *Tool Steels,* 5th ed., ASM International, 1998

20.7 K.-E. Thelning, *Steel and Its Heat Treatment,* 2nd ed., Butterworths, London, 1984

20.8 M.B. Adeyeni, R.A. Stark, and G.F. Modlen, Isothermal Stress Relief of Cold Extruded Mild Steel Rods, *Proceedings of the Metals Society, Heat Treatment '79,* Birmingham, England, 1979, p 122–125

20.9 *SAE Handbook Supplement: Residual Stress Measurements by X-Ray Diffraction,* SAE 1784a, SAE, Warrendale, PA, 1971

20.10 G. Scholtes and F. Macherauch, Residual Stress Determination, *Case-Hardened Steels: Microstructure and Residual Stress Effects,* D.E. Diesburg, Ed., TMS-AIME, 1984, p 141–159

20.11 B. Hildenwall and T. Ericsson, Prediction of Residual Stresses in Case-Hardening Steels, *Hardenability Concepts with Applications to Steel,* D.V. Doane and J.S. Kirkaldy, Ed., TMS-AIME, Warrendale, PA, 1978, p 579–605

20.12 T. Ericsson, S. Sjostrom, M. Knuuttila, and B Hildenwall, Predicting Residual Stresses in Cases, *Case-Hardened Steels: Microstructural and Residual Stress Effects,* D.E. Diesburg, Ed., TMS-AIME, Warrendale, PA, 1984, p 113–139

20.13 *Quenching and Carburising,* Book 566, The Institute of Materials, London, 1993

20.14 J. Bodin and S. Segerberg, Measurement and Evaluation of the Quenching Power of Quenching Media for Hardening, *Quenching and Carburising,* Book 566, The Institute of Materials, London, 1993, p 33–54

20.15 G.E. Totten, C.E. Bates, and N.A. Clinton, *Handbook of Quenchants and Quenching Technology,* ASM International, 1993

20.16 G. Totten, Ed., *Quenching and Distortion Control, Proceedings of the First International Conference,* ASM International, 1992

20.17 G.E. Totten, M.A.H. Howes, and S.J. Sjostrom, Ed., *Second International Conference on Quenching and the Control of Distortion,* ASM International, 1996

20.18 W. Dowling, Jr., T. Pattok, B.L. Ferguson, D. Shick, Y.H. Gu, and M. Howes, Development of a Carburizing and Quenching Simulation Tool: Program Overview, *Second International Conference on Quenching and the Control of Distortion,* G.E. Totten, M.A.H. Howes, and S.J. Sjostrom, Ed., ASM International, 1996, p 349–355

CHAPTER **21**

Surface Hardening

SURFACES OF STEEL PARTS are subject to severe static and cyclic stresses, friction, wear, and corrosive environments. Surface modification treatments have evolved to enhance steel performance, as required by many applications. Figure 21.1 shows a number of surface modification

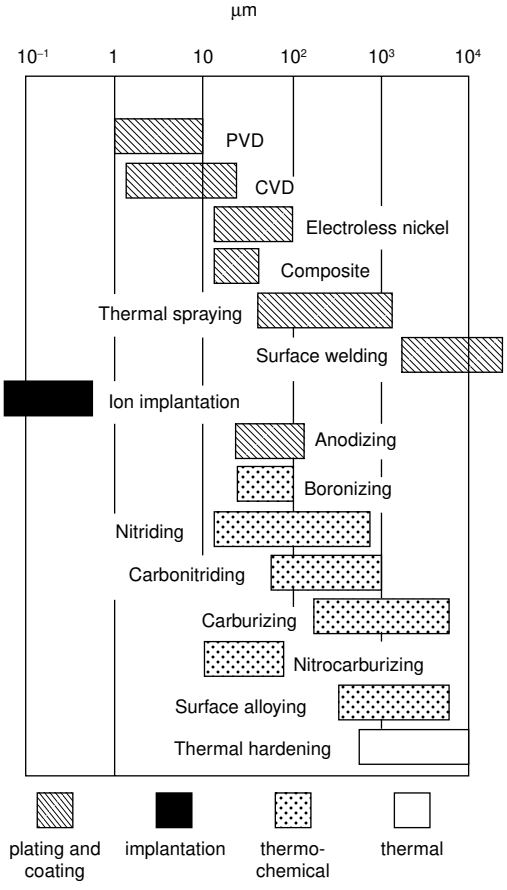

Fig. 21.1 Classification and typical case depths of various surface modification treatments. Source: Ref 21.1

treatments and the range of depths to which each typically hardens steel surfaces (Ref 21.1). There are four classes of treatments. *Plating* or *coating* treatments deposit surface layers of completely different chemistries, structures, and properties on steel substrates. *Ion implantation* drives ions of atoms such as nitrogen into steel substrates, producing shallow but very high surface strengthening. Chapter 22, "Surface Modification," describes a number of these treatments in detail.

The treatments of interest in this chapter are classified as *thermal*, during which surfaces are heated and cooled with no change in composition, for example flame and induction hardening, and thermochemical, where surface chemistry is changed during heating, for example nitriding and carburizing. In this chapter carburizing and nitriding produced in conventional gas atmospheres are discussed; plasma and vacuum carburizing and plasma nitriding are described in Chapter 22, "Surface Modification." Many of these treatments rely in some way on tempered martensitic microstructures, and therefore are referred to as surface hardening treatments. They are widely used for applications such as shafts, gears, and bearings that are used to transmit power and are subject to high bending, contact, and torsional stresses. The relatively deep-hardened cases produced by the thermal and thermochemical hardening treatments help to offset subsurface case/core fracture initiation, and surface crack initiation is reduced by treatment-induced surface compressive stresses.

Flame Hardening

Flame hardening consists of austenitizing the surface of a steel by heating with an oxyacetylene or oxyhydrogen torch and immediately quenching with water. A hard surface layer of martensite over a softer interior core with a ferrite-pearlite structure results. There is no change in composition, and therefore the flame-hardened steel must have adequate carbon content for the desired surface hardness. The rate of heating and the conduction of heat into the interior appear to be more important in establishing case depth than having a steel of high hardenability (Ref 21.2). Figure 21.2 shows hardness gradients produced by various rates of flame travel across a 1050 steel forging. The slower the rate of travel, the greater are the heat penetration and the depth of hardening.

A number of different methods of flame hardening have been developed (Ref 21.3). Localized or spot hardening may be performed by directing a stationary flame head to an area of a stationary workpiece. Progressive methods, in which the torch travels over the workpiece or the workpiece travels under a stationary torch and quenching fixture, are used for long bars. Spinning methods, in which the workpiece is rotated within an array of torches, are often used for small rounds. In this method heating is performed first, then the flames are extinguished, and quenching is finally accomplished by water sprays or dropping the part into a quench tank. In

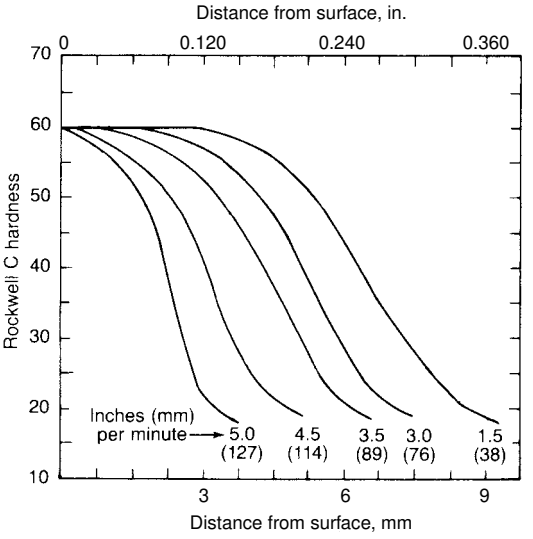

Fig. 21.2 The effect of flame speed on depth of hardening of a 1050 steel forging. Source: Ref 21.3

all cases, the quenched parts are tempered to improve toughness and relieve stresses induced by the surface hardening.

Induction Heating

Induction heating is an extremely versatile method for hardening steel. Uniform surface hardening, localized surface hardening, through-hardening, tempering of hardened pieces, and heating for forging may all be performed by induction heating. Heating is accomplished by placing a steel part in the magnetic field generated by high-frequency alternating current passing through an inductor, usually a water-cooled copper coil. The rapidly alternating magnetic field established within the coil induces current (I) within the steel. The induced currents then generate heat (H) according to the relationship $H = I^2R$, where R is the electrical resistance. Steel, consisting primarily of ferrite or bcc iron, is ferromagnetic up to its Curie temperature (768 °C, or 1400 °F), and the rapid change in direction of the internal magnetization of domains in a steel within the field of the coil also generates considerable heat. When a steel transforms to austenite, which is nonmagnetic, this contribution to induction heating becomes negligible. A wide variety of heating patterns may be established by induction heating depending on the shape of the coil, the number of turns of the coil, the operating frequency, and the alternating current power input (Ref 21.4). Figure 21.3 shows examples of the heating patterns produced by various types of coils.

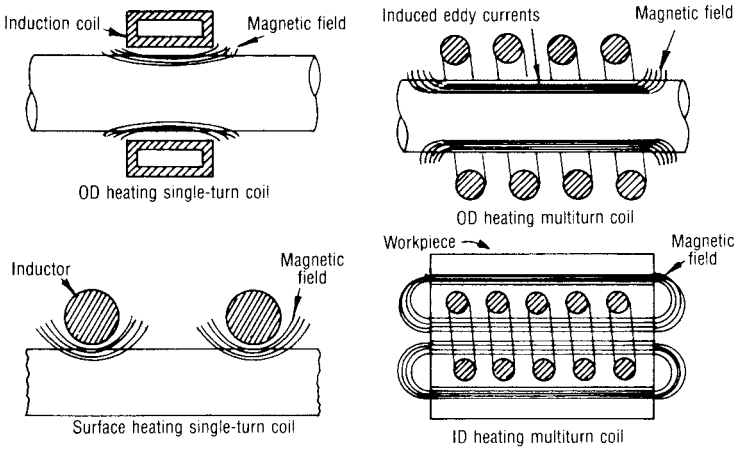

Fig. 21.3 Schematic diagram of the magnetic fields and induced currents produced by several types of induction coils. Source: Ref 21.4

The depth of heating produced by induction is related to the frequency of the alternating current. The higher the frequency, the thinner or more shallow is the heating. Therefore, deeper case depths and even through-hardening are produced by using lower frequencies. The various types of commercial equipment and the selection of operating conditions for a given application are fully described in Ref 21.4 to 21.7.

As in flame hardening, induction heating does not change the composition of a steel, and therefore a steel selected for induction hardening must have sufficient carbon content and alloying for the desired surface hardness distribution. Generally, medium- and high-carbon steels are selected because the high surface strengths and hardness attainable in these steels significantly improve fatigue and wear resistance. Induction hardening introduces residual compressive stresses into the surface of hardened parts. Therefore, the fatigue strengths of induction-surface-hardened parts may be higher than those of through-hardened parts in which quenching develops residual surface tensile stresses that may only be partly relieved during tempering. The greater the depth of hardening by induction heating, however, the more the surface stress state approaches that of through-hardening. Too deep a hardened case may in fact cause surface tensile stresses and even cracking of susceptible steels (Ref 21.4).

The duration of high-frequency induction heating cycles for surface hardening is extremely short, often only a few seconds. As a result, the time for formation of austenite is limited, and compensation is made by increasing the temperature of austenitizing. Figure 21.4 shows how the Ac_3 temperature in a 1042 steel is affected by heating rate and microstructure. The high heating rates of induction heating substantially raise Ac_3. Microstructures with coarse carbides, such as the 1042 steel in the annealed condition as shown, or steels with coarse spheroidized microstruc-

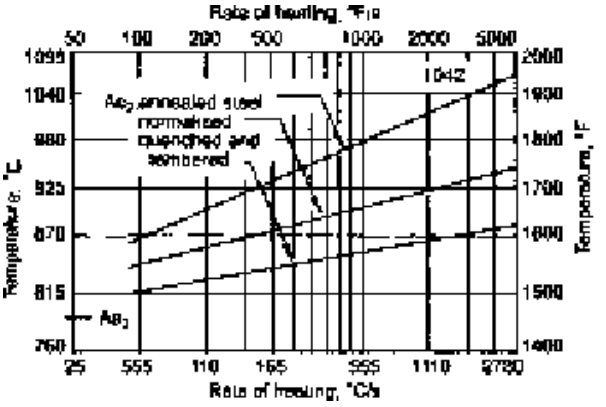

Fig. 21.4 Change in Ac_3 temperature of 1042 steel as a function of microstructure and heating rate. Source: Ref 21.4

tures or alloy carbides, require higher austenitizing temperatures for carbide solution than do steels with finer microstructures. Too high an austenitizing temperature, however, may result in austenite grain coarsening (see Chapter 8, "Austenite in Steel"). An interesting consequence of the very short austenitizing time for induction surface hardening is the development of a hardness above that normally expected for through-hardened martensite. This higher hardness is sometimes referred to as superhardness (see Fig. 21.5) and, as discussed subsequently, may be a result of martensite formed in very fine-grained, imperfect austenite produced by the short-time austenitizing treatments used in induction surface hardening.

As noted, the very short times, on the order of seconds, associated with induction hardening significantly influence austenite formation, case microstructures, and finished hardness profiles. Austenite formation is very much a function of starting microstructure. In view of the fact that starting microstructures consist of low-carbon ferrite and high-carbon cementite, sufficient time must be available for carbon diffusion to produce austenite of the steel carbon concentration. Austenite first forms at ferrite/cementite interfaces, as described in Chapter 8, "Austenite in Steel;" to continue austenite formation, cementite dissolves and supplies carbon, which diffuses through austenite to austenite/ferrite interfaces in order to convert the low-carbon ferrite to austenite. The coarser the starting microstructures, the greater are the diffusion distances and the longer times required for complete austenite formation. Coarse cementite particles will take a longer time to dissolve than fine particles, and sometimes the parallel cementite lamellae of pearlite are retained to produce regions of *ghost pearlite* in an induction-hardened case (Ref 21.8). Similarly, starting microstructures of coarse ferrite and pearlite sometimes result in retained ferrite islands in induction-hardened cases (Ref 21.9).

Figure 21.6 shows schematically a model of austenite formation in pearlite during induction heating. The sketch is based on TEM observa-

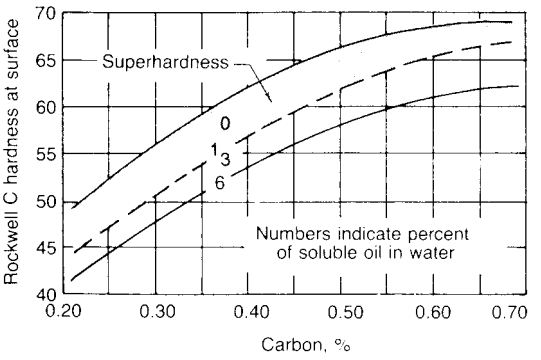

Fig. 21.5 Superhardness produced by induction hardening compared with that produced by conventional furnace hardening (lower solid curve). Source: Ref 21.4

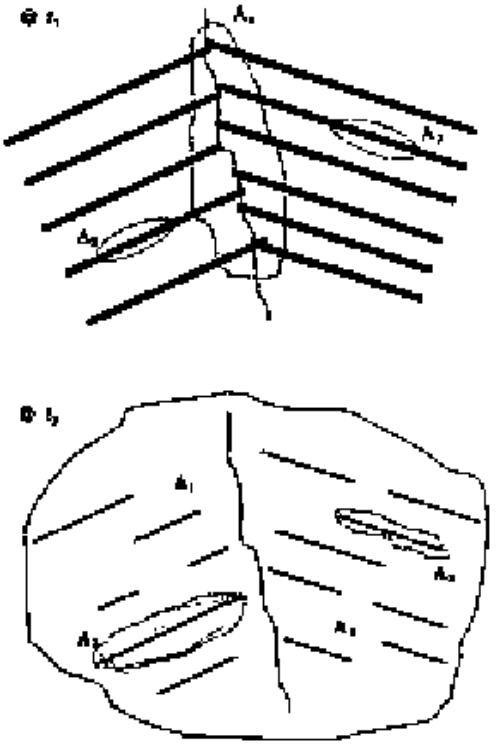

Fig. 21.6 Schematic representation of austenite formation in a microstructure of pearlite at two times. Time t_1 represents nucleation of austenite grains with three orientations, A_1, A_2, and A_3, and time t_2 represents complete austenite formation with some residual cementite lamellae. Source: Ref 21.11

tion of microstructures in an induction-hardened 10V45 steel containing 0.44% C, 0.87% Mn, and 0.12% V (Ref 21.10, 21.11). Austenite nucleates either at pearlite colony interfaces or at individual cementite lamellae, consistent with observations of Speich and Szirmae (Ref 21.12). The coarser austenite nuclei sweep across the ferrite-cementite colonies, dissolving some but not all of the cementite, and incorporating austenite crystals that have formed around individual cementite lamellae. On quenching, the austenite transforms to martensite, some of which forms in very small crystals of austenite, possibly contributing to the enhanced hardness sometimes produced by induction hardening.

Not only is austenitizing affected by the short times and high temperatures of induction heating, but also tempering is affected. A recent study shows that induction tempering produces hardness changes comparable to conventional furnace tempering, but notes that care must be taken not to overcompensate for the significantly shorter times of induction tempering by the use of higher tempering temperatures (Ref 21.13). For example, induction tempering that produced a temperature of 300 °C (570 °F) for effectively 6 seconds produced beginning third-stage tempering and second-stage tempering transformation of interlath austenite in hardened 1053M and 5160 steels.

Figure 21.7 shows hardness profiles for induction-hardened 1550 steel, containing 0.52% C and 1.50% Mn, and 5150 steel, containing 0.50% C, 0.82% Mn, and 0.83% Cr (Ref 21.8). Starting microstructures of both steels were either furnace-cooled ferrite/pearlite of hardness 25 HRC or quenched and tempered martensite of 32/33 HRC. The specimens were

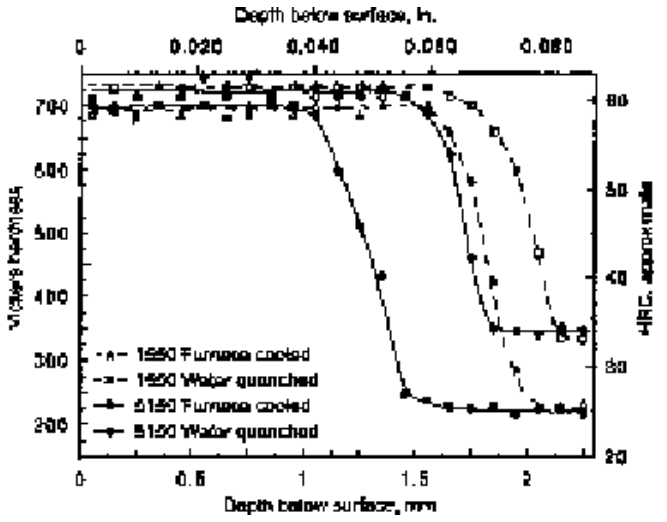

Fig. 21.7 Hardness profiles for 1550 and 5160 after induction hardening time of 1.0 s of two starting microstructures as described in text. Souce: Ref 21.8

induction-hardened at 120 kW and 300 kHz for 1.0 second. Deeper case depths were produced in the specimens with tempered-martensite starting microstructures, which were much finer and more uniform than those of the specimens with furnace-cooled microstructures. However, for a given starting microstructure, deeper case depths were produced in the 1550 steel than in the 5150 steel, a result attributed to the more sluggish dissolution of the chromium-containing carbides during austenitizing of the 5150 steel. Shorter induction-heating times of 0.5 and 0.75 seconds produced shallower case depths and accentuated differences that were due to alloy contents of the steels. An induction-heating time of 1.5 seconds fully austenitized and through-hardened all 1 cm (0.4 in.) diameter specimens regardless of steel chemistry or starting microstructure. Many other scenarios of the effects of time and temperature, as affected by induction processing parameters, and alloying response of course are possible, but the changes illustrated by the study that produced Fig. 21.7 show variations that can occur with subtle changes in alloying, starting microstructures, and processing parameters.

Since induction hardening does not change chemistry, the carbon content of induction-hardened steels must be high enough to produce sufficient high strength and hardness for demanding applications. Thus, steels with carbon concentrations of 0.40 to 0.50% are frequently selected for induction case hardening. Steels with this amount of carbon are sensitive to quench embrittlement, as discussed in Chapter 19, "Low Toughness and Embrittlement Phenomena in Steels," and several cases of intergranular cracking have been reported in induction-hardened steels. One study documented intergranular fracture in induction-hardened axles of a modified 1050 steel under conditions of bending overload and rotating bending fatigue (Ref 21.14). Another fatigue study, of induction-hardened 1045 steels specimens taken from a light-truck axle, showed not only intergranular fracture initiation but also intergranular fatigue crack propagation in specimens subjected to cyclic three-point bending (Ref 21.15).

Although tensile and bending strengths are important in many applications of induction-hardened parts, for shafts and axles the transmission of torque is a major requirement. In a study designed to optimize torsional strength, Ochi and Koyasu evaluated the effect of increasing carbon content on induction-hardened shafts (Ref 21.16). Figure 21.8, from their study, shows torsional strength as a function of steel carbon content and case-hardening depth ratio, t/r, where t is the depth of the case-hardened layer and r is the radius of a shaft. Torsional strength increases with increasing depth of hardening, despite expected decreasing residual surface compressive stresses. Also, increasing carbon content increases torsional strength consistent with increases in the strength of LTT martensite with increasing carbon content, as described in Chapter 18, "Deformation, Mechanical Properties, and Fracture of Quenched and Tempered Carbon Steels." In the Ochi and Koyasu work, all torsion fractures of induction-

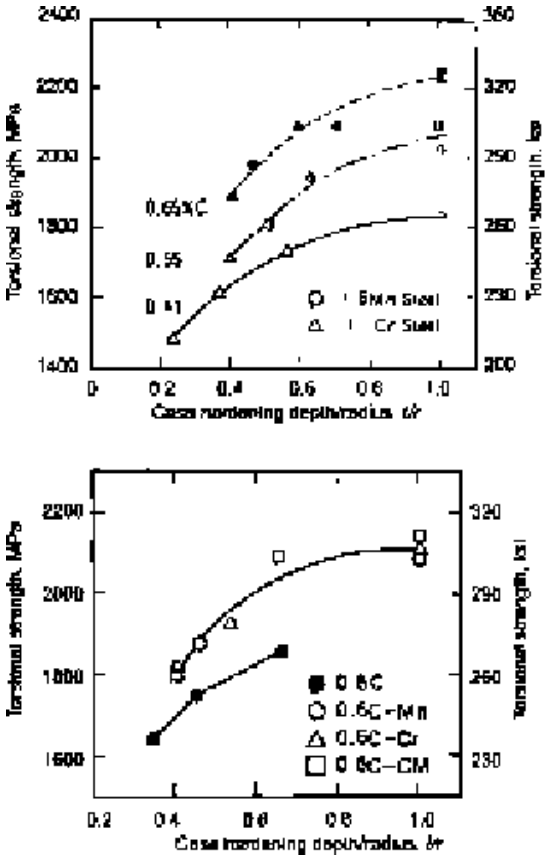

Fig. 21.8 Torsional strength as a function of case depth for various grades of steel. Source: Ref 21.16

hardened steel containing less than 0.6% C were mode III shear fractures that developed on planes of maximum shear. However, when carbon concentrations exceeded 0.6% mode I opening mode brittle fractures developed on planes of high normal stresses. The fractures were intergranular, consistent with quench embrittlement and low brittle fracture strengths of hardened high-carbon steels.

As noted previously, surface-initiated intergranular cracks may develop in induction-hardened steels with higher carbon contents, perhaps overaustenitized and with high phosphorus content. However, in medium-carbon steels not susceptible to quench embrittlement, cracking caused by fatigue may initiate not at the surface of induction hardened parts, but subsurface in the core close to the case/core interface. Figure 21.9, taken from the work of Nissan (Ref 21.17), shows the role that residual stresses play in fatigue performance of an induction-hardened 4145 steel subjected to fully reversed cantilever bending. At the surface the summation of the applied and high residual compressive stresses is slightly compressive,

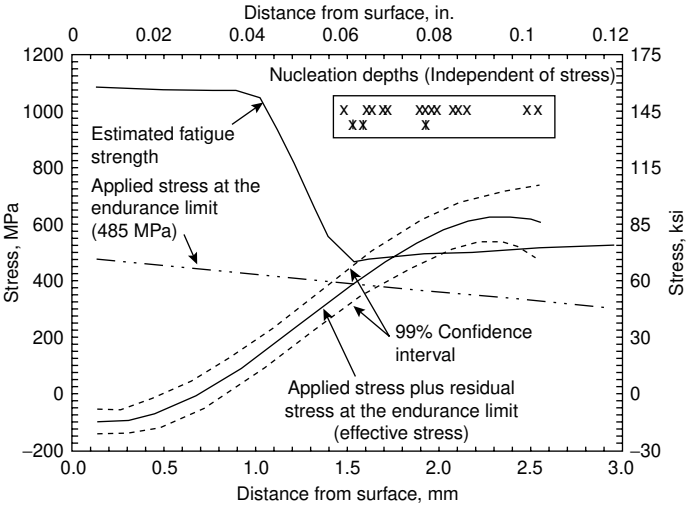

Fig. 21.9 Estimated strength (from hardness), applied experimental stress, and the summation of applied and residual stresses (from x-ray diffraction) as a function of distance from the surface of induction hardened 1045 steel with a ferrite/pearlite as-hot rolled core microstructure. The box in the upper right of the figure shows locations of crack initiation at the case/core and core locations of the induction hardened samples. Source: Ref 21.17

but with increasing distance from sample surfaces, the effective stress gradually increases as residual stresses become less compressive, until at the case/core interface the effective applied stress, now substantially increased by residual tensile stresses, exceeds the strength of the unhardened core microstructure and fracture is initiated there. The subsurface cracks in the 4145 steel were initiated mostly at large inclusion particles, but also in some cases in the ferrite of the unhardened core microstructure.

Carburizing: Processing Principles

Carburizing is a heat treatment in which the carbon content of the surface of a low-carbon steel is increased by exposure to an appropriate atmosphere at a temperature in the austenite phase field. Hardening is accomplished when the high-carbon surface layer is quenched to form martensite. The Fe-C diagram (see Chapter 3, "Phases and Structures") shows that the maximum solubility of carbon in austenite ranges from 0.8% at the eutectoid temperature to about 2% at the eutectic temperature. Although alloying elements reduce carbon solubility, more than enough carbon can be introduced into the austenite of plain carbon or alloy steels by carburizing to produce the maximum martensitic hardness after quenching. Complications of carbide formation, brittle microstructure, and excessive retained austenite develop if carbon content is too high, and for these reasons the maximum carbon content in a carburized steel is generally controlled to between 0.8 and 1%. Carburizing is most fre-

quently performed between 850 and 950 °C (1550 and 1750 °F), but sometimes higher temperatures are used to reduce cycle times and/or produce deeper depths of the high-carbon surface layer.

Two important processes influence the introduction of carbon into austenite during carburizing. One is the environmental reaction that causes carbon to be absorbed at the surface of the steel. Another is the rate at which carbon can diffuse from the surface to the interior of the steel. Carbon is introduced by the use of gaseous atmospheres (gas carburizing), salt baths (liquid carburizing), solid compounds (pack carburizing), and plasma and vacuum carburizing (as discussed in Chapter 22, "Surface Modification") (Ref 21.18). All of these methods have limitations and advantages, but gas carburizing is widely used for large-scale production because it can be accurately controlled and involves a minimum of special handling.

Carbon is introduced into the surface of steel by gas-metal reactions between the various components of an atmosphere gas mixture and the solid solution austenite. Following Harvey (Ref 21.19), one of the most important carburizing reactions is:

$$CO_2(g) + C \rightleftharpoons 2CO(g) \qquad \text{(Eq 21.1)}$$

where C is carbon introduced into the austenite. At equilibrium, a carbon ratio of CO_2 and CO has a certain carbon potential or maintains a certain level of carbon in the austenite. At any temperature, the relationship between the gaseous components and the carbon in solution of the austenite is given by the equilibrium constant K, which for reaction 21.1 is written as:

$$K = \frac{P_{CO}^2}{a_c P_{CO_2}} \qquad \text{(Eq 21.2)}$$

where P_{CO} and P_{CO_2} are the partial pressures of CO and CO_2, respectively, and a_c is activity of carbon. The activity of carbon is related to the weight percent carbon in the austenite by the activity coefficient of carbon (f_c) according to the following equation:

$$a_c = f_c \text{ wt\% C} \qquad \text{(Eq 21.3)}$$

K is a function of temperature, and for the reaction represented in Eq 21.1 can be determined from:

$$\log K = \frac{-8918}{T} + 9.1148 \qquad \text{(Eq 21.4)}$$

where T is the absolute temperature in degrees Kelvin. The partial pressures of CO and CO_2 required to maintain a given surface austenite carbon content are given by combining Eq 21.2 and Eq 21.3 as follows:

$$\text{wt\% } C = \frac{1}{Kf_C} P_{CO}^2 / P_{CO_2} \quad \text{(Eq 21.5)}$$

If the CO content of an atmosphere exceeds the partial pressure required to maintain a given carbon content, the reaction represented in Eq 21.1, as written, will go to the left and carburizing will occur until a new equilibrium is reached. This is the case in commercial carburizing where the carbon content of a low-carbon steel is raised to some desirable higher level. On the other hand, if the CO_2 partial pressure is too high relative to the CO content, the reaction in 21.1 will go to the right and decarburization will occur. The latter condition is sometimes purposely introduced in commercial practice if initial carburizing produces too high a carbon content, say 1.2%, and it is desired to reduce surface carbon to a lower level, say 0.9%. This step in a carburizing cycle is referred to as a *diffusion step*, since much of initially high carbon in the austenite immediately adjacent to the surface diffuses into the interior of the part and produces a deeper case. Equation 21.5 requires a knowledge of the activity coefficient, which varies as a function of temperature and the composition of austenite. Harvey (Ref 21.19) tabulates relationships for the activity coefficients in ternary Fe-X-C systems where *X* may be nickel, silicon, manganese, chromium, molybdenum, or vanadium. Harvey also presents a system for evaluating the activity coefficient and carburizing potentials for steels with more than three components.

The preceding discussion describes the basic concept of gas equilibrium and carburizing. In conventional gas carburizing practice, carburizing atmospheres are produced by combustion of natural gas or other hydrocarbon gas in exothermic or endothermic gas generators and contain CO, CO_2, CH_4, H_2, H_2O, and N_2 (Ref 21.20). Therefore, there are many other reactions that may occur in addition to that represented in 21.1, including the following:

$$CH_4 \rightleftharpoons C + 2H_2 \quad \text{(Eq 21.6)}$$

$$CO + H_2O \rightleftharpoons CO_2 + H_2 \quad \text{(Eq 21.7)}$$

Much of the technology (Ref 21.18) of gas carburizing is based on relationships determined by Harris (Ref 21.21) for Eq 21.1, 21.6, and 21.7 according to the approach just described and with the assumption that the activity of carbon in saturated austenite (austenite with the carbon content given by the A_{cm} at a given temperature) is unity. For carbon concentration in the austenite less than saturation, the activity is assumed to be proportional to the degree of saturation. For example, if the carbon content of austenite at saturation is 1.33%, and one wants to know what partial pressures of CO and CO_2 will maintain 1.0% C in austenite, the activity is equal to 1.00/1.33 = 0.75. These assumptions appear to be valid for plain carbon and low-nickel steels, and within 10% for more highly alloyed

steels (Ref 21.18). A number of curves, based on the Harris approach, relating the CO and CO_2 contents required to maintain various surface carbon contents are given in Ref 21.22 for carburizing temperatures between 825 and 1025 °C (1515 and 1875 °F) in 25 °C (75 °F) increments. Figure 21.10 shows such a curve for 975 °C (1790 °F) increments. As shown, a much higher CO than CO_2 content is required for carburizing, especially for higher surface carbon contents.

Equation 21.7 gives the equilibrium between CO, CO_2, H_2O, and H_2 and is used as the basis of control and determination of the carbon potential of carburizing atmospheres. For the latter purposes, measurements of the contents of H_2O or CO_2 are often used. Carbon dioxide is measured by infrared analyzers. The dew point is defined as the temperature, at a given pressure, at which a gas mixture will precipitate its moisture content and is used to determine the H_2O content of an atmosphere. More recently, carbon potential has been determined by measurement of the partial pressure of oxygen with instruments referred to as oxygen probes. Once the oxygen content is known, the CO and CO_2 contents can be determined by means of the following equilibrium reaction:

$$CO + \tfrac{1}{2}O_2 \rightleftharpoons CO_2 \qquad \text{(Eq 21.8)}$$

The various approaches and instruments for control of carburizing potentials are described in detail in Ref 21.18.

After a given carbon potential is established, the depth of case produced in a given carburizing treatment is determined by the time-dependent diffusion of carbon from the surface to the interior of the steel part. Figure 21.11 shows carbon profiles calculated for an Fe-C alloy carburized at 925 °C (1700 °F) for times between 2 and 16 h, and Fig. 21.12 shows the

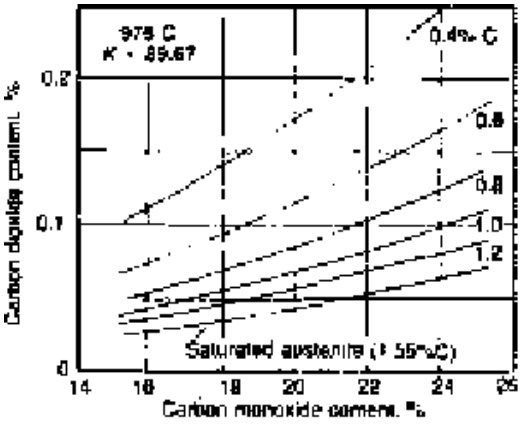

Fig. 21.10 Equilibrium percentages of carbon monoxide and carbon dioxide required to maintain various carbon concentrations at 975 °C (1790 °F) in plain carbon and certain low-alloy steels. Source: Ref 21.22

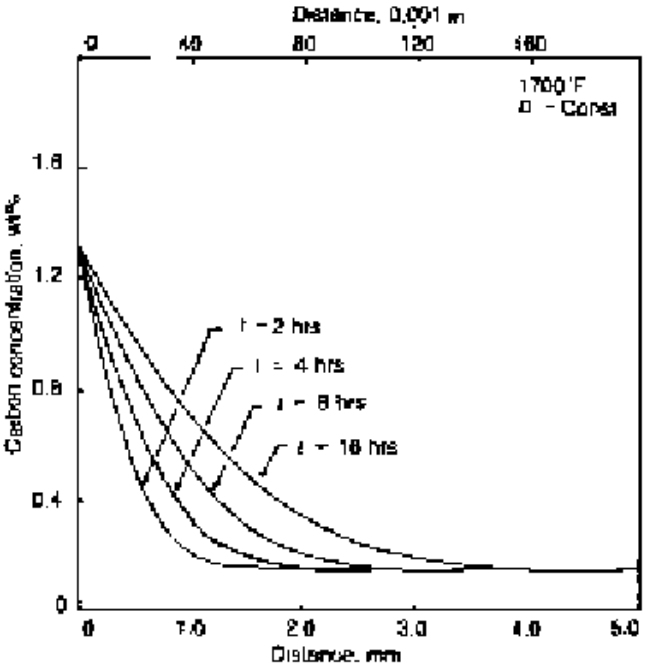

Fig. 21.11 Carbon concentration in an Fe-C alloy as a function of distance calculated for various carburizing times at 925 °C (1700 °F), assuming the diffusion coefficient is independent of composition. Source: Ref 21.23

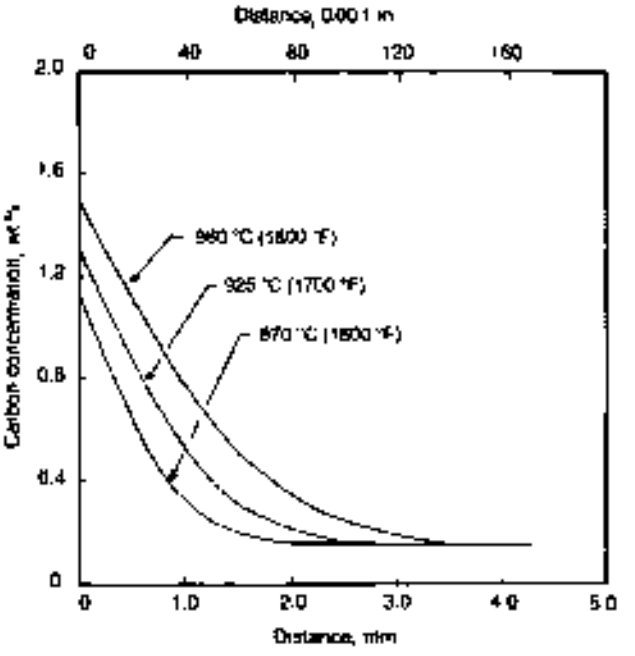

Fig. 21.12 Carbon concentration in an Fe-C alloy as a function of distance calculated for various temperatures for 8 h carburizing, assuming the diffusion coefficient is independent of composition. Source: Ref 21.23

effect of temperature on carburizing an Fe-C alloy when time is held constant at 8 h. These figures demonstrate the important effect of time and temperature on the depth of case produced by carburizing.

Following Goldstein and Moren (Ref 21.23), the curves of Fig. 21.11 and 21.12 were calculated by means of the Van-Ostrand-Dewey solution to the diffusion equation as follows:

$$\frac{C_C - C_S}{C_O - C_S} = \text{erf}\left(\frac{X}{2}\sqrt{Dt}\right) \qquad \text{(Eq 21.9)}$$

where C_s is the surface concentration of carbon as maintained by the carbon potential of the atmosphere; C_o is the initial carbon level in the Fe-C alloy prior to carburizing; D is the diffusion coefficient for carbon in austenite; C_c is the carbon concentration as a function of distance from the surface; and t is the time after the start of carburizing. The diffusion coefficient was assumed to be independent of composition and to have an average value $D_C^{\gamma} = 0.12 \times \exp(-32{,}000/RT)$ cm²/s Ref 21.24). The diffusion coefficient in fact varies with carbon concentration of the austenite.

Equation 21.9, while it demonstrates the basic diffusion principles involved in carburizing, is highly idealized with respect to commercial practice. In particular, the diffusion coefficient of carbon in steels varies not only with carbon but also with alloy content, a situation for which Goldstein and Moren (Ref 21.23) have developed mathematical models that incorporate the effect of other alloying elements on the diffusion process. Apart from this approach, the equations based on empirical analysis of Eq 21.6 by Harris have proven adequate for plain carbon and alloy steels. At any temperature, Eq 21.9 reduces to:

$$X(\text{case depth}) = K\sqrt{t} \qquad \text{(Eq 21.20)}$$

where K is a function of temperature and includes the temperature dependence of the diffusion coefficient. Table 21.1 (Ref 21.3) lists values of case depths at various times for three commonly used carburizing temperatures.

Table 21.1 Case depth calculated by the Harris equation

	Case depth after carburizing at(a):					
	871 °C (1600 °F)		899 °C (1650 °F)		927 °C (1700 °F)	
Time, *t*, h	mm	in.	mm	in.	mm	in.
2	0.64	0.025	0.76	0.030	0.89	0.035
4	0.89	0.035	1.07	0.042	1.27	0.050
8	1.27	0.050	1.52	0.060	1.80	0.071
12	1.55	0.061	1.85	0.073	2.21	0.087
16	1.80	0.071	2.13	0.084	2.54	0.100
20	2.01	0.079	2.39	0.094	2.84	0.112
24	2.18	0.086	2.62	0.103	3.10	0.122
30	2.46	0.097	2.95	0.116	3.48	0.137
36	2.74	0.108	3.20	0.126	3.81	0.150

(a) Case depth = 0.025 $\sqrt{t}$ for 927 °C (1700 °F); 0.021 $\sqrt{t}$ for 899 °C (1650 °F); 0.018 $\sqrt{t}$ for 871 °C (1600 °F). For normal carburizing (saturated austenite at the steel surface while at temperature). Source: Ref 21.3

Carburizing—Alloying, Processing, and Microstructure

The objective of carburizing is to obtain a high-carbon martensitic case with good wear and fatigue resistance superimposed on a tough, low-carbon steel core. Carburizing steels usually have base-carbon contents around 0.2%. Therefore, if hardenability is low, as is the case for plain carbon steels, the core microstructure will consist of ferrite and pearlite of relatively low strength. Many applications, however, require high core strength to support the case in heavy-duty applications. In addition, core strength is required where the stress gradients between the surface and interior of a part in service are high enough to cause subsurface crack initiation in an unhardened core. For these reasons, alloy steels with good core hardenability that form martensite throughout a carburized part are in wide use. Table 21.2, taken from a study of fracture resistance of carburized steels (Ref 21.25), shows the compositions and the hardenabilities in D_I of some commonly used alloy carburizing steels. The EX grades of steels are exchange grade steels not yet assigned standard SAE designations (Ref 21.26). In the case of the carburizing grades, these steels have been developed to match different hardenability ranges of standard grades (as shown in Table 21.2) by means of adjusting alloy content.

Depending on hardenability, i.e., the composition of a carburizing steel, specimen size, and quench severity, quite different hardness gradients may be associated with a given carbon gradient. Maximum hardness at any given carbon level will be associated with a fully martensitic microstructure, but bainite and other low-hardness microstructures might also form if cooling is not sufficient to form martensite at that location. Wyss

Table 21.2 Compositions, grain sizes, and hardenabilities of some carburizing steels

	Group I		Group II		Group III				Group IV
	EX24	SAE 862	EX29	SAE 4320	20NiMoCr6	SAE 4817	SAE 4820	EX32	EX55
Composition, wt%									
Carbon	0.20	0.20	0.20	0.21	0.22	0.17	0.19	0.19	0.17
Manganese	0.88	0.89	0.87	0.58	0.58	0.54	0.60	0.82	0.87
Silicon	0.34	0.34	0.34	0.33	0.54	0.33	0.28	0.27	0.28
Phosphorus	0.015(a)	0.015(a)	0.015(a)	0.015(a)	0.021	0.015(a)	0.016	0.017	0.015(a)
Silicon	0.02(a)	0.02(a)	0.02(a)	0.02(a)	0.027	0.02(a)	0.02	0.02	0.02(a)
Chromium	0.51	0.47	0.48	0.52	0.64	NA(b)	NA(b)	0.53	0.49
Molybdenum	0.26	0.21	0.34	0.26	0.31	0.27	0.27	0.52	0.74
Nickel	NA(b)	0.53	0.54	1.76	1.56	3.56	3.48	0.80	1.84
Aluminum	0.08(a)	0.08(a)	0.08(a)	0.08(a)	0.043	0.08(a)	0.075	0.082	0.08(a)
ASTM grain size	**9½**	**9½**	**9½**	**9½**	**7½**	**9½**	**9½**	**9**	**9½**
D_1 hardenability:									
Inches	1.6	1.7	2.0	1.9	3.0	2.5	2.7	3.3	4.7
Millimeters	41	43	51	48	76	63	69	84	120

(a) Amount added. (b) NA, non added. Source: Ref 21.25

(Ref 21.27) has developed a scheme for calculating hardness gradients from carbon gradients. The first step is to calculate Jominy curves for a given alloy composition at several carbon contents. Then, an equivalent distance from the quenched end of a Jominy specimen is obtained for a given bar diameter and quench severity according to Grossmann's method. That equivalent distance, i.e., an effective cooling rate, is then used to obtain hardness values as a function of carbon content from the various Jominy curves. Then, if carbon content as a function of distance from the carburized surface is known or calculated, hardness as a function of distance can be plotted.

Once the proper surface carbon concentration and depth of case are established by control of the processing parameters, the carburized austenite is quenched to form martensite and tempered. The part may be hardened directly after carburizing or may be cooled and reheated to refine the microstructure. Figure 21.13 shows the microstructure of an EX 24 steel carburized and diffused at 1050 °C (1920 °F) and cooled to 845 °C (1550 °F) prior to quenching in oil (Ref 21.28). This microstructure is typical of that produced in fine-grained steels by direct quenching of carburized cases containing in the range of 0.8 to 1% C at the surface. The martensite has a plate morphology, and as much as 20 or 30% retained austenite might be present, depending on carbon content. Lower carbon contents in a case would produce a finer martensite tending to a lath morphology and would reduce retained austenite content. Figure 21.14 shows the case microstructure produced in an 8620 steel that has been reheated to a temperature below the A_{CM}. The microstructure is highly refined by this treatment, so much so that the matrix martensite and retained austen-

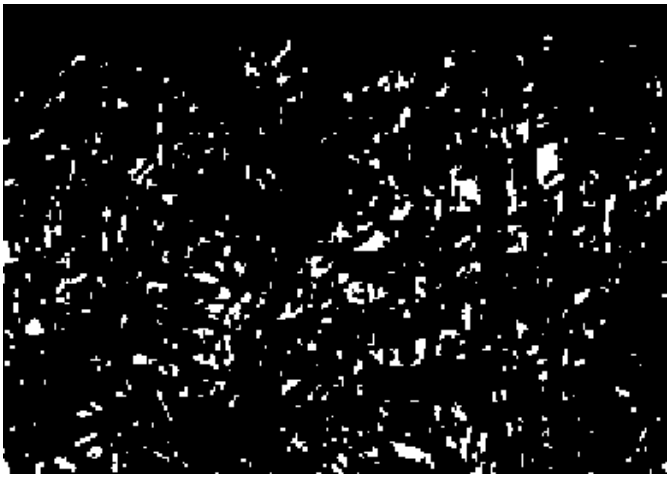

Fig. 21.13 Microstructure adjacent to surface of an EX 24 steel carburized and diffused at 1050 °C (1920 °F), cooled to 845 °C (1550 °F), and oil quenched. Original magnification at 1000×. Source: Ref 21.28

ite are not resolvable in the light microscope. The fine circular white features that are visible are carbides that have been retained because the case was not reheated into the single-phase austenite field.

Figures 21.13 and 21.14 show microstructures that are typical of the results of good commercial practice. Problems due to processing, however, may adversely affect microstructures and properties. One common feature of conventional gas carburizing is the internal surface oxidation that develops to a depth of about 0.025 mm (0.001 in.) from the carburized surface. The microstructures and effects of surface oxidation are discussed in the following sections of this chapter.

Figures 21.15 and 21.16 show the deleterious effects of too high a surface carbon concentration on case microstructure. The high surface car-

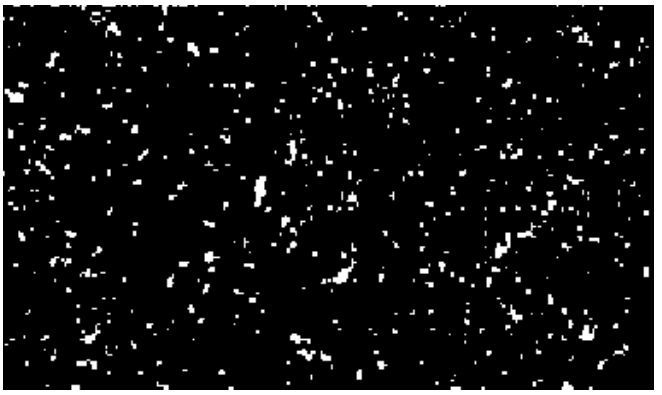

Fig. 21.14 Microstructure adjacent to surface of 8620 steel carburized at 1050 °C (1920 °F), oil quenched from 845 °C (1550 °F), and reheated to 845 °C (1550 °F) and quenched. Original magnification at 1000×. Source: Ref 21.28

Fig. 21.15 High austenite (white phase) content in corner of an 8620 steel sample carburized and diffused at 1050 °C (1920 °F) and cooled to 845 °C (1550 °F) before oil quenching. Source: Ref 21.29

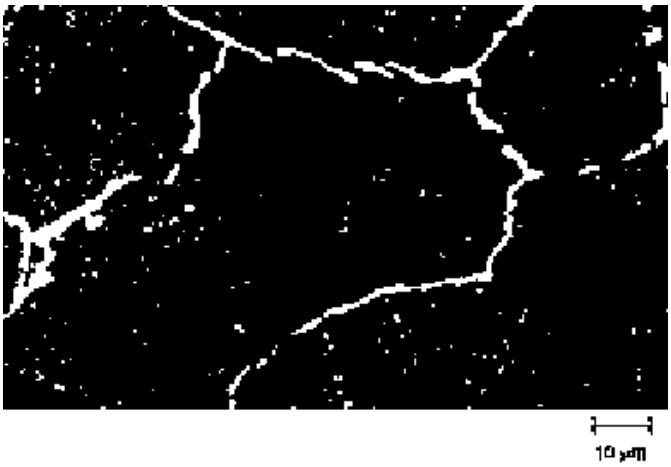

Fig. 21.16 Cementite network in corner of an EX 24 specimen carburized at 1050 °C (1920 °F) oil quenched, and reheated to 845 °C (1550 °F). Source: Ref 21.28

bon concentration may be a result of too short a diffusion cycle after carburizing has first saturated the austenite, or a result of geometry, where carbon has good surface access to a portion of a steel (especially specimen corners) but diffusion to the interior is restricted (Ref 21.29). Figure 21.15 shows a very high retained austenite content in an 8620 steel and Fig. 21.16 shows grain-boundary carbides that have formed in an EX 24 steel that has been reheated for hardening after carburizing. The reheating has caused some agglomeration of the carbides and therefore reduced their detrimental effect on fatigue crack initiation (Ref 21.29).

Another microstructural feature that may adversely affect properties of carburized steels is the microcracking that develops in high-carbon martensitic microstructures because of plate impingement (Ref 21.30). Figure 21.17 shows examples of microcracks that have formed in the case of a coarse-grained 8620 steel (Ref 21.31). The micrograph shows an extreme example of microcracking. Microcracking is much reduced when martensite forms in fine-grain austenite (Ref 21.32); when the martensite morphology approaches that of lath martensite as carbon is reduced below 1% (Ref 21.33); and as a result of tempering (Ref 21.34). Many of the microstructural features described above and their influence on the properties of carburized parts have been extensively reviewed by Parrish (Ref 21.35).

Figure 21.18 shows the results of a study of the effect of martensite morphology, including the effects of microcracking, on fatigue resistance of a carburized coarse-grained 8620 steel (Ref 21.31). All specimens were chemically polished and, therefore, the influence of intergranular oxidation on fatigue cracking was removed from the study. The specimens directly quenched from the carburizing temperature had the coarsest struc-

Fig. 21.17 Microcracks in the martensite of a carburized coarse-grained 8620 steel. Source: Ref 21.31

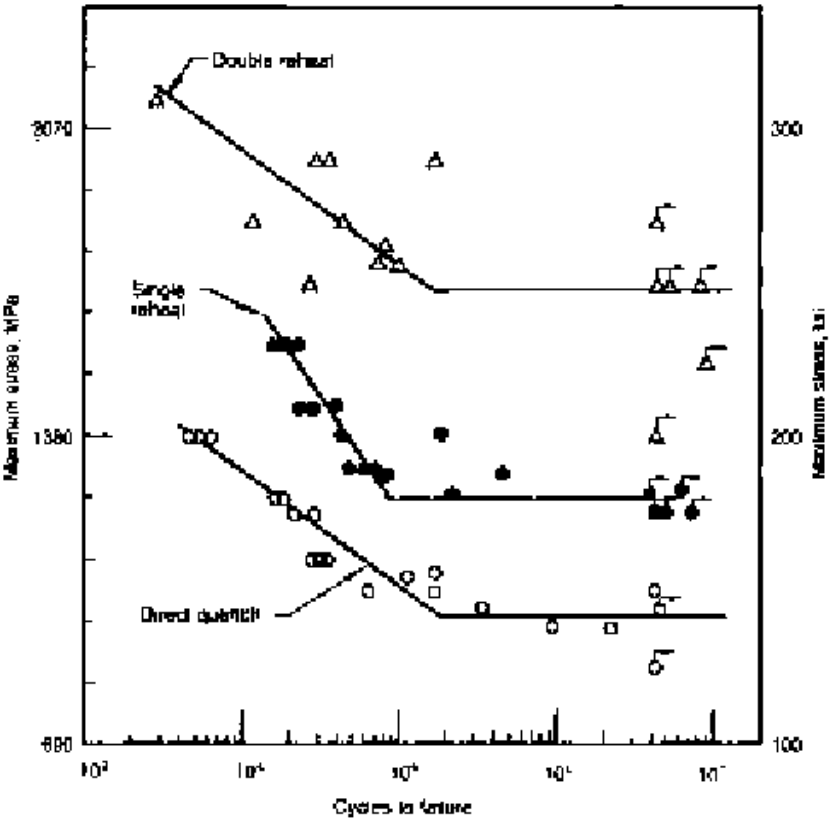

Fig. 21.18 Maximum applied stress versus cycles to failure (*S-N* curve) for four-point bend fatigue specimens of 8620 steel given three different carburizing treatments. Source: Ref 21.31

ture and the highest density of microcracks, some of which were directly exposed on the specimen surfaces by the chemical polishing. The single-reheated specimens had a finer austenite grain structure and therefore finer martensite plates and a lower density of microcracks. Because the retained austenite content and hardness profiles of the direct-quenched and single-reheated specimens were identical, the improved fatigue resistance of the single-reheated specimens is attributed to the smaller size of the microcracks and their lower density in the finer structure. The best fatigue resistance was shown by the double-reheated specimens with case microstructure similar to that shown in Fig. 21.14, i.e., a microstructure produced by reheating below the A_{CM}. The virtual elimination of the surface microcracks, the much finer structure of the martensite, the higher hardness, and reduced retained austenite were probably all factors that contributed to the very high fatigue resistance of the double reheat specimens.

The study (Ref 21.31) of chemically polished carburized specimens showed that microcracks, or most likely as shown an embrittled austenite grain boundary, initiated fatigue fracture in specimens quenched from the austenite field. In specimens reheated to the austenite-cementite field, fatigue cracks were initiated at pits produced by the chemical polishing. A study of fatigue crack origins in a steel carburized to 0.7% C showed that cracks in electropolished specimens initiated mainly at prior austenite grain boundaries and sometimes at inclusion particles (Ref 21.36). In commercially carburized specimens not subjected to any surface polishing or removal treatment, fatigue cracks are most probably initiated at intergranular surface oxides, prior austenite grain boundaries, or surface roughness in one form or another, such as grooves produced by machining. In fine-grained steels or steels carburized to a carbon level that yields lath martensite, microcracking would not be expected to be a major cause of fatigue crack initiation.

The study of the carburized coarse-grained 8620 steel also revealed several characteristics of the fracture of carburized steels. Figure 21.19 shows fatigue fracture origins in direct-quenched and double-reheated carburized specimens. The fatigue crack in the direct-quenched specimen (Fig. 21.19a) was initiated at an embrittled prior austenite grain boundary. The stable fatigue crack was quite smooth (area within dashed semicircle) but on overload and rapid propagation became intergranular. In contrast, both the fatigue and overload portions of the fracture surface of the double-reheated specimen are transgranular and quite smooth. Figure 21.20 shows higher magnification scanning electron micrographs of overload fracture in direct-quenched and double-reheated specimens. The intergranular fracture (see Fig. 21.20a) is frequently observed in direct-quenched carburized steels and is determined by Auger analysis (Ref 21.37–21.39) to be associated with higher phosphorus and carbon concentrations than those found in the bulk of the steel. The shape of the carbon Auger peak indi-

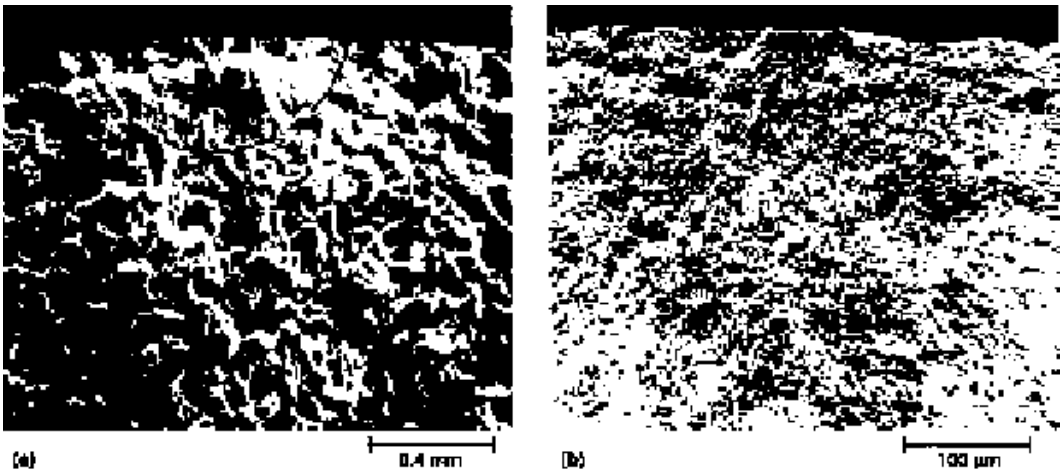

Fig. 21.19 Fatigue crack initiation in carburized coarse-grained 8620 steel (a) quenched directly from carburizing at 927 °C (1700 °F) and (b) reheated after carburizing to 788 °C (1450 °F). Both specimens tempered at 145 °C (300 °F). Scanning electron micrographs. Source: Ref 21.31

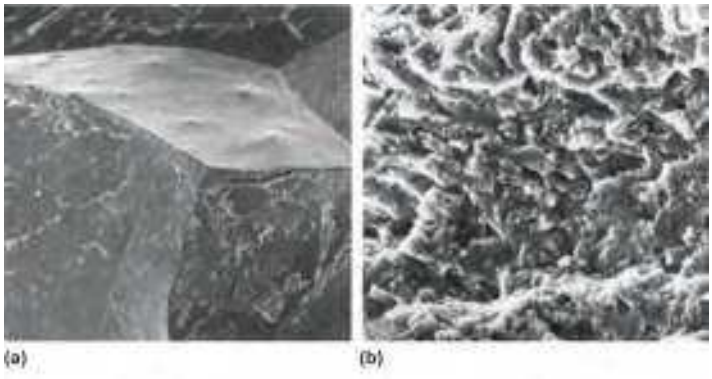

Fig. 21.20 Overload case fracture surfaces in carburized 8620 steel (a) quenched directly after carburizing at 927 °C (1700 °F) and (b) reheated to 788 °C (1450 °F). Both specimens tempered at 145 °C (300 °F). Scanning electron micrographs. Source: Ref 21.37

cates that the carbon at the grain boundary is present in the form of cementite, and thus the intergranular fracture is a manifestation of quench embrittlement as described in Chapter 19, "Low Toughness and Embrittlement Phenomena in Steels." In carburized steels the conditions for intergranular embrittlement are present in as-quenched and tempered conditions that would normally be considered to be immune to intergranular fracture in medium-carbon steels (Ref 21.37).

Carburizing—Surface Oxidation in Gas Atmospheres

The section on carburizing processing shows that oxygen is available in the H_2/H_2O and CO/CO_2 partial pressure equilibria in the gas atmospheres used for carburizing. As a result, some of the alloying elements in carburizing steels are selectively subject to oxidation by H_2O and CO_2, in particular silicon, manganese, and chromium, as shown in Fig. 21.21 (Ref 21.40). Other elements, including molybdenum and nickel, often added to carburizing steels are not oxidized. Chatterjee-Fischer, in an early systematic study, confirmed that indeed surface dispersions of Cr, Mn, Si, and Ti oxides formed during gas carburizing, and that removal of Si from carburizing steels tended to eliminate the surface oxidation (Ref 21.41).

Surface oxide dispersions are best shown on as-polished surfaces, and Figures 21.22 and 21.23, show respectively light and scanning electron micrographs of surface oxide dispersions in gas carburized steels (Ref 21.42). There are two zones of oxidation: a continuous shallow zone about 5 microns deep of fine dispersed particles, and a deeper zone, typically between 10 to 20 microns deep, apparently formed on prior austenite grain boundaries. The latter zone is sometimes referred to as being produced by *intergranular oxidation* (IGO). Energy dispersive spectroscopy in the SEM showed that the outer zone consisted of oxides rich in chromium, and the grain-boundary oxides were rich in silicon and manganese.

The grain boundary oxides are not continuous on the as-polished surfaces. Scanning electron microscopy of fracture surfaces of gas-carburized

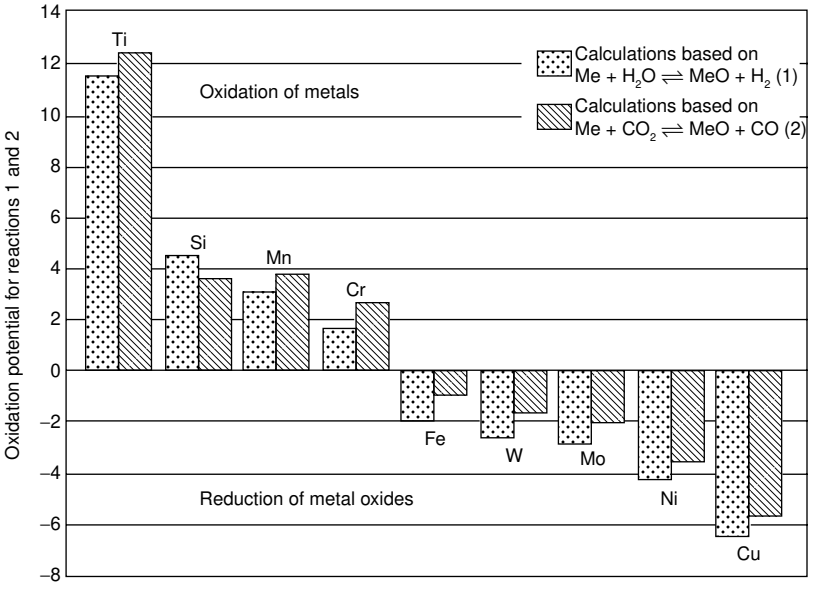

Fig. 21.21 Oxidation potentials of various elements in an endothermic gas atmosphere at 930 °C (1700 °F). Source: Ref 21.40

Fig. 21.22 Surface oxidation in a gas carburized 8627 steel containing 0.92% Mn, 0.27% Si, 0.51%Cr, 0.22% Mo, and 0.52% Ni. As-polished, Ni-plated surface (for edge retention), light micrograph. Source: Ref 21.42

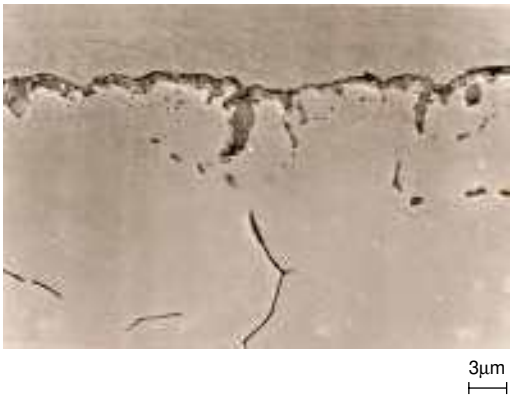

Fig. 21.23 Surface oxidation in a carburized 20MnCr5 steel containing 1.29% Mn, 0.44% Si, 1.24% Cr, 0.25% Ni, and 0.0015% B. As-polished, Ni-plated surface, SEM micrograph. Source: Ref 21.42

zones (Fig. 21.24) shows that the grain boundary oxides do not uniformly cover the prior austenite grain boundaries but instead form in a lamellar morphology with parallel oxide lamellae alternating with the steel matrix (Ref 21.42). This morphology is responsible for the discontinuous grain boundary oxide appearance in Fig. 21.22 and 21.23. In those micrographs the plane of polish has intersected the alternating oxide and matrix lamellar structure that has formed on the austenite grain boundaries.

Surface oxidation is invariably present to some degree in gas carburized steels. In view of the susceptibility of prior austenite grain boundaries to quench embrittlement independent of oxidation, the grain boundary oxidation has a real but relatively low additive impact on fatigue resistance of direct quenched carburized parts if surface residual stresses are compressive (Ref 21.43). As a result many applications can tolerate some surface oxidation. The surface-oxidized zone can be removed by grinding, and of

Fig. 21.24 Fracture at the surface of a carburized 20MnCr5 steel containing 1.29% Mn, 0.44% Si, 1.24% Cr, 0.25% Ni and 0.0015% B after single tooth bending fatigue testing. Lamellar oxide structure on austenite grain boundaries formed during gas carburizing is shown. SEM micrograph. Source: Ref 21.42

course does not form during plasma or vacuum carburizing (Ref 21.44). However, because oxidation removes chromium, silicon, and manganese from solid solution, hardenability may be reduced in steel with low hardenability to the point at which surface compressive stresses are reduced or eliminated, severely lowering fatigue resistance (Ref 21.45-21.47), as discussed in the section on residual stresses.

Carburizing: Residual Stresses and Microstructure

The high-carbon case microstructures of steels directly quenched after carburizing in the austenite phase consist of plate martensite and retained austenite. In Chapter 19, "Low Toughness and Embrittlement Phenomena in Steels ," Figure 19.16 showed that such high carbon contents, typically around 0. 8% carbon, places those microstructures into the quench embrittlement range where low-stress brittle intergranular fracture occurs because of carbon and phosphorus segregation to austenitic grain boundaries. Consistent with this susceptibility to intergranular cracking, as shown in Fig. 21.19, bending and tensile fatigue failures of direct quenched carburized steels are invariably initiated at austenite grain boundaries. However, fracture initiation is offset to high stresses and strengths because of the favorable compressive stresses produced during quenching of austenite with the carbon gradients produced by carburizing.

Koistinen first clearly showed the basis for the formation of the surface compressive stresses (Ref 21.48). Figure 21.25 shows two sets of curves as a function of distance from the carburized surface: cooling curves at increasing times in the quench process, and M_S curves for two carburized steels. The M_S curves follow the carbon gradients. Close to the surface,

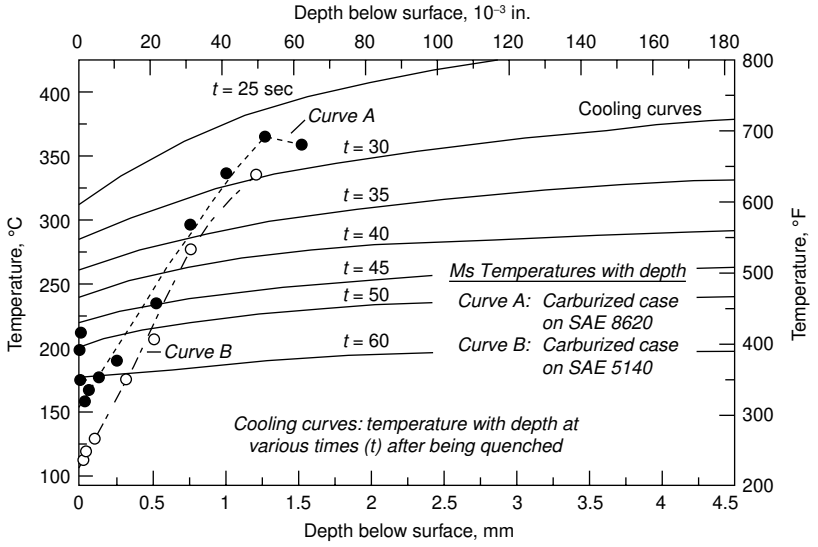

Fig. 21.25 M_S curves for two carburized steels, and cooling curves at increasing times during quenching, as a function of distance from the carburized surface. Adapted by Lee Rothleutner, Colorado School of Mines from Ref 21.48

M_S temperatures, because of the high carbon content of the austenite, are quite low, and as carbon content decreases with increasing distance from a carburized surface, M_S temperatures increase. Because of this gradient in M_S temperatures, in the early stages of quenching, as shown by the intersection of the two sets of curves, the interior of the carburized samples transforms to martensite and hardens while the high carbon case remains austenitic. However, when the surface case microstructure eventually transforms to martensite, the expansion that accompanies the austenite to martensite transformation is restrained by the hard interior microstructure and the surface martensitic microstructure is placed into compression.

The differences in residual stress profiles developed in carburized steels and uncarburized quenched and tempered steels are shown in Fig. 21.26 (Ref 21.49). As shown by the Koistinen explanation, the residual surface stresses in carburied samples are compressive. In contrast the surface residual stresses in uncarburized quenched and tempered steels are tensile because the surface forms martensite first, and when the interior austenite eventually transforms to martensite, the expansion caused by that transformation puts the surface martensite into tension.

Figure 21.27 shows the variation of residual stress profiles that developed from the carburized surfaces of seventy (70) different heats and sets of carburized steels (Ref 21.50). A few of the individual profiles are shown as the dashed lines in the relatively broad band of profiles. A major characteristic of the residual stress profiles is that a maximum in compressive

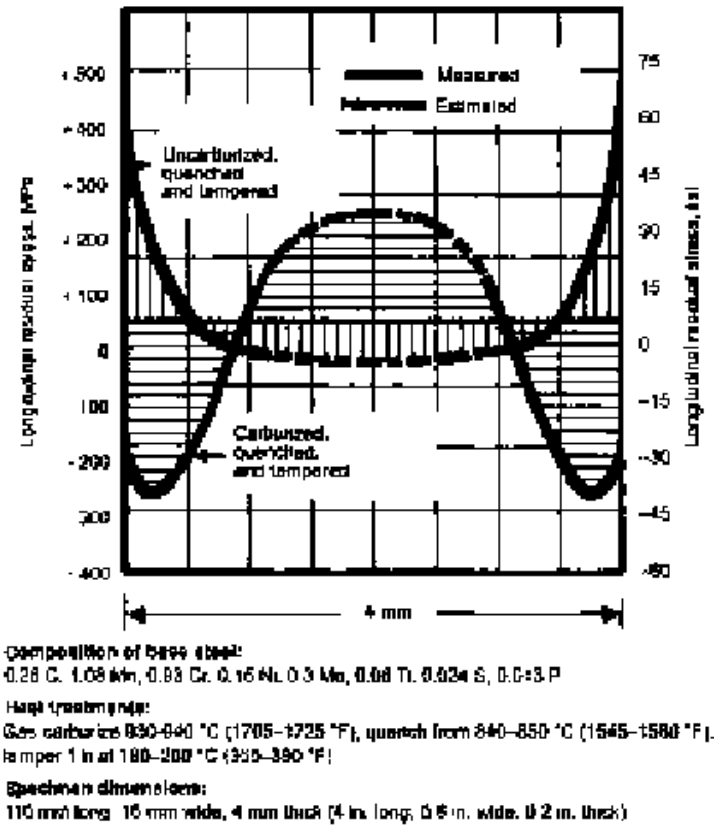

Composition of base steel:
0.26 C, 1.08 Mn, 0.93 Cr, 0.16 Ni, 0.3 Mo, 0.08 Ti, 0.024 S, 0.0+3 P

Heat treatment:
Gas carburize 930–940 °C (1705–1725 °F), quench from 840–850 °C (1545–1560 °F), temper 1 h at 180–200 °C (355–390 °F)

Specimen dimensions:
110 mm long, 16 mm wide, 4 mm thick (4 in. long, 0.6 in. wide, 0.2 in. thick)

Fig. 21.26 Residual stress as a function of distance through the thickness of carburized and uncarburized chromium-carbon steel specimens. Source: Ref 21.49

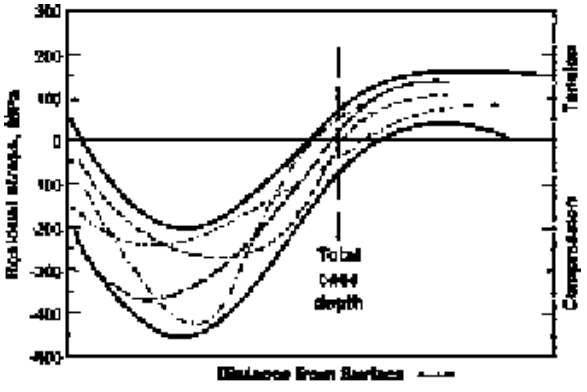

Fig. 21.27 Residual stress as a function of distance from carburized surfaces of 70 different heats of carburized steels. Adapted by Lee Rothleutner, Colorado School of Mines, from Ref 21.50.

stresses is reached at some distance from carburized surfaces. Consistent with the Koistinen explanation of residual stress development, carburized surfaces have the highest carbon content and therefore the most stable austenite, and if this austenite or some fraction of the austenite does not transform to martensite, there is less basis for creating compressive stresses because of restrained martensite expansion (Ref 21.51). Another feature of the residual stress profiles is the transition to residual tensile stresses at the total case depth at which the carbon content falls to that of the uncarburized core. The large variation in the residual stress profiles depends on many factors, including surface carbon content, hardenability, quenching, case depth, and as described below, surface oxidation in gas-carburized steels.

If surface oxidation lowers case hardenability substantially, instead of the surface austenite transforming to martensite at low temperatures, the surface transforms to non-martensitic, diffusion-controlled structures at higher temperatures. As a result, the near surface microstructure is already in place when the interior structure eventually transforms to martensite, and the associated interior expansion puts the surface into tension. The effects of such a transition in surface residual stresses were clearly documented in a study by Dowling et al (Ref 21.52). They showed that bending fatigue resistance was significantly decreased, Fig. 21.28, in a carburized, surface-oxidized low hardenability 8620 steel (0.92% Mn, 0.50% Cr, 0.38% Ni and 0.16% Mo) in comparison to that in a 4615 steel of higher hardenability (0.52% Mn, 0.12% Cr, 1.75% Ni, and 0.54% Mo) and containing nickel and molybdenum not sensitive to oxidation. Figure 21.29 shows the differences in the surface residual stresses in the two steels. Transmission electron microscopy showed that the surface microstructure of the 8620 steel consisted of pearlite.

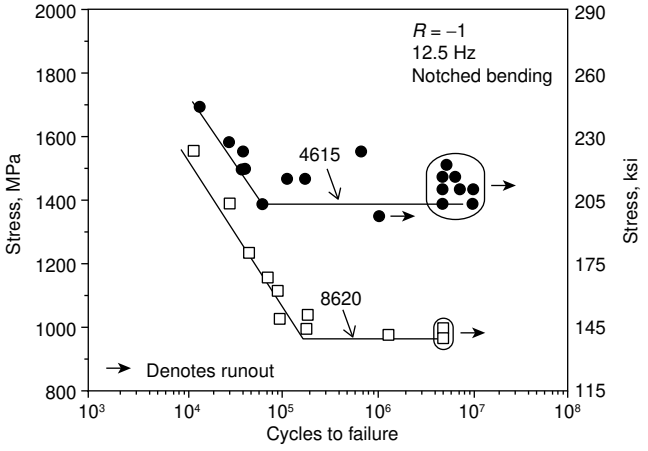

Fig. 21.28 Stress versus cycles to failure for gas-carburized 8620 and 4615 steels. Source: Ref 21.52

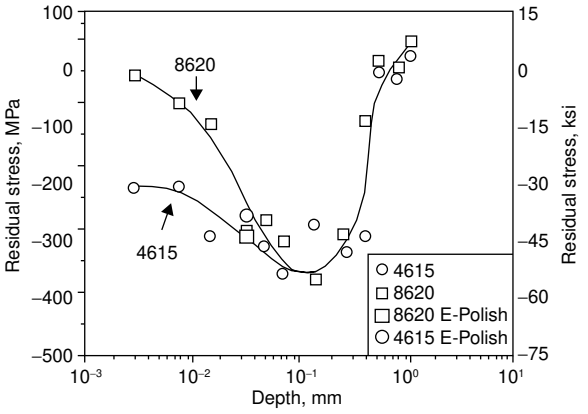

Fig. 21.29 Residual stress profiles for gas-carburized 8620 and 4615 steels. Source: Ref 21.52

Residual stresses in carburized steels are also affected by the deformation-induced transformation of retained austenite to martensite. When large amounts of austenite are present, strain-induced transformation of retained austenite occurs (Ref 21.53, 21.54). Figure 21.30 shows by etching differences how retained austenite transforms to martensite as a function of compressive strain in a high-carbon plate martensite/retained austenite microstructure. Such deformation-induced transformation of retained austenite may be a result of shot peening or cyclic stresses during application. Figure 21.31 shows the dramatic increases in compressive surface stresses that occurred in a carburized 4320 steel as a result of shot peening (Ref 21.55) and Fig. 21.32 shows the reduction in retained austenite that caused the increases in the surface compressive stresses. As the surface retained austenite mechanically transformed to martensite, the volume expansion associated with that transformation was severely restrained by the interior microstructure.

Carburizing: Bending Fatigue and Fracture

This section describes additional observations concerning bending fatigue and fracture of carburized steels, and applies to carburized microstructures of good commercial quality, as shown in Fig. 21.13 and 21.14. The two major types of fatigue fracture described in the previous section appear to be quite reproducible (Ref 21.53, 21.54, 21.56-21.58). One (Fig. 21.19a) is associated with low to moderate fatigue strengths, while the other (Fig. 21.19b) is associated with very high fatigue strengths. The hardened case microstructures of carburized steels are in fact composite microstructures consisting of retained austenite and tempered martensite, and both the amount of retained austenite and the refinement of the mar-

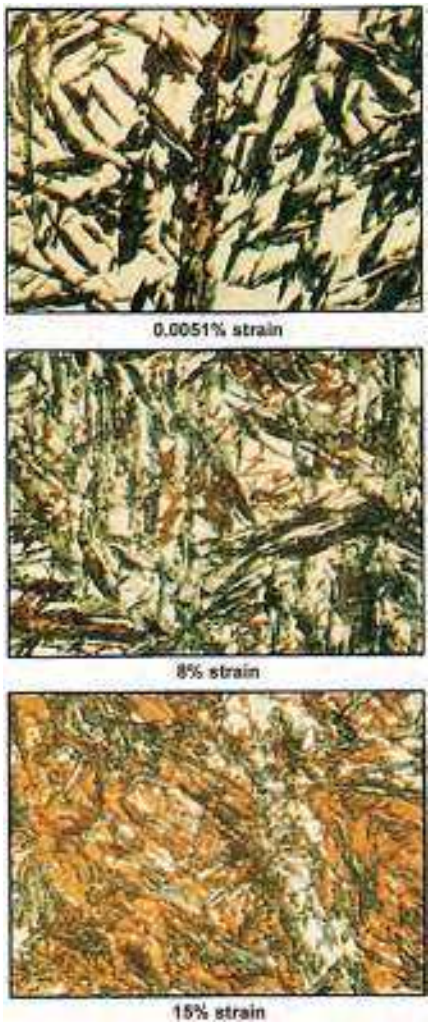

Fig. 21.30 Strain-induced transformation of retained austenite to martensite as a function of strain. As-quenched tempered martensite is dark, retained austenite is white, and strain-induced martensite is orange. Sodium metabisulfite etch, 1000×, light micrographs. Courtesy of Marc Zaccone, Colorado School of Mines. Source: Ref 21.53

tensite significantly influence the nucleation and growth of the two types of fatigue fracture.

The low-stress type of fracture characteristically forms under low-cycle, high-strain fatigue conditions and is related to high retained austenite contents and coarse austenite grain sizes, both microstructural features that favor plastic deformation. The fatigue crack invariably has its initiation at austenite grain boundaries (Ref 21.31, 21.36, 21.57, 21.58). Thus a sharp crack, one or two grain facets in size, initiates the fatigue crack. This grain-boundary crack is related to boundary embrittlement caused by phosphorus segregation during austenitizing and cementite formation dur-

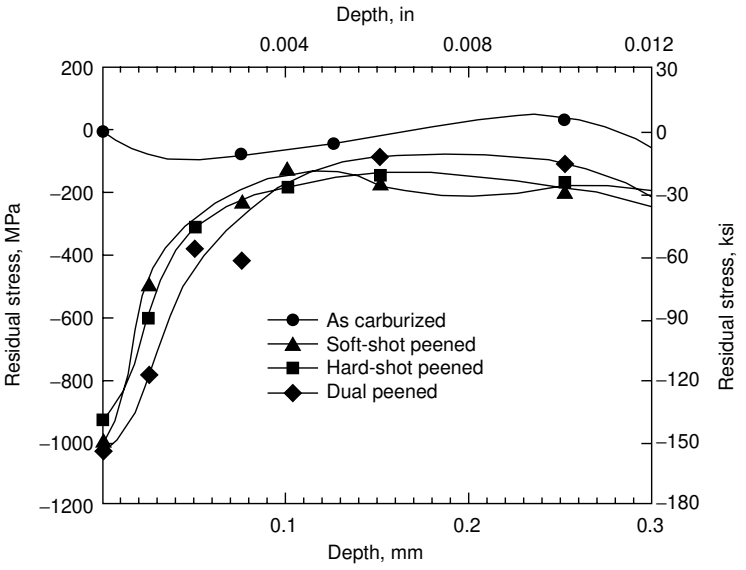

Fig. 21.31 Residual stress profiles in shot peened carburized 4320 steel. Source: Ref 21.55

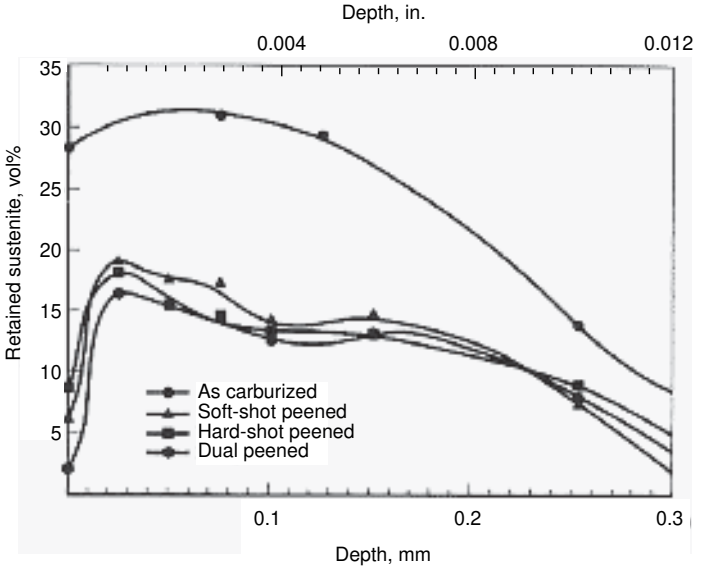

Fig. 21.32 Retained austenite as a function of distance from the surface of carburized 4320 steel in as-carburized sample and after various types of shot peening. Source: Ref 21.55

ing cooling, i. e., as a result of quench embrittlement (Ref 21.37–21.39), and Zaccone (Ref 21.53) has shown that it forms in the first cycle of fatigue but is arrested by the transformation of retained austenite. The strain-induced formation of martensite induces favorable compressive stresses, and not only arrests the grain boundary crack but also slows the propagation of low-cycle fatigue cracks (Ref 21.58, 21.59). Nevertheless, the grain boundary crack initiates a flat, transgranular fatigue crack (Fig. 21.19a), which grows to a size commensurate with the relatively low fracture toughness of high-carbon hardened steel, 20 to 27 MPa$\sqrt{m}$ (18 to 25 ksi$\sqrt{in.}$) (Ref 21.54). When the critical flaw size is reached, overload fracture develops, again typically with a large fraction of intergranular fracture, the fracture mode characteristic of the high-carbon microstructural state conducive to this mode of fatigue crack nucleation and growth.

The high-strength type of fatigue fracture is developed over many stress cycles, typically at surface defects, inclusions, or oxides (Ref 21.31, 21.36, 21.53, 21.54), in contrast to immediate grain-boundary crack initiation in the first few cycles of loading. Thus, microstructural conditions that resist plastic deformation and prevent grain boundary cracking—namely, low retained austenite content and fine austenite grain sizes, which translate into fine mixtures of retained austenite and tempered martensite—prevent the nucleation of fatigue cracks (i.e., contribute to high fatigue limits) or defer fatigue crack initiation to very high stress levels. The roles that austenitic grain size and retained austenite play in high-cycle fatigue were clearly demonstrated in experiments performed by Pacheco (Ref 21.56, 21.57). Figure 21.33 shows results of bending fatigue tests performed on gas- and plasma-carburized specimens of SAE 8719 steel. High fatigue limits correlated with fine austenitic grain sizes (Fig. 21.34) and low retained-austenite contents (Fig. 21.35). The effects of the two microstructural parameters on fatigue limits are shown together in Fig. 21.36.

Carburizing/Through-Hardening—Contact Fatigue, Microstructure, and Fracture

The high-carbon case of carburized steels must be resistant to not only the cyclic tensile stresses generated by bending in rotating shafts and the roots of gear teeth but also to the cyclic contact and sliding shear stresses generated in bearings and in the contact surfaces of gear teeth that transmit power. Heinrich Hertz in 1882 first analyzed stress distributions due to contact loading (Ref 21.60), and since that time in his honor shear stress magnitude and orientation as a function of distance from contact surfaces are referred to as *Hertzian stress distributions*. Wulpi gives a good practical explanation of Hertzian stress distributions, and points out that pure rolling contact is never obtained in view of the sliding that develops due to elastic deflection under contact loading (Ref 21.61). Hertzian analysis

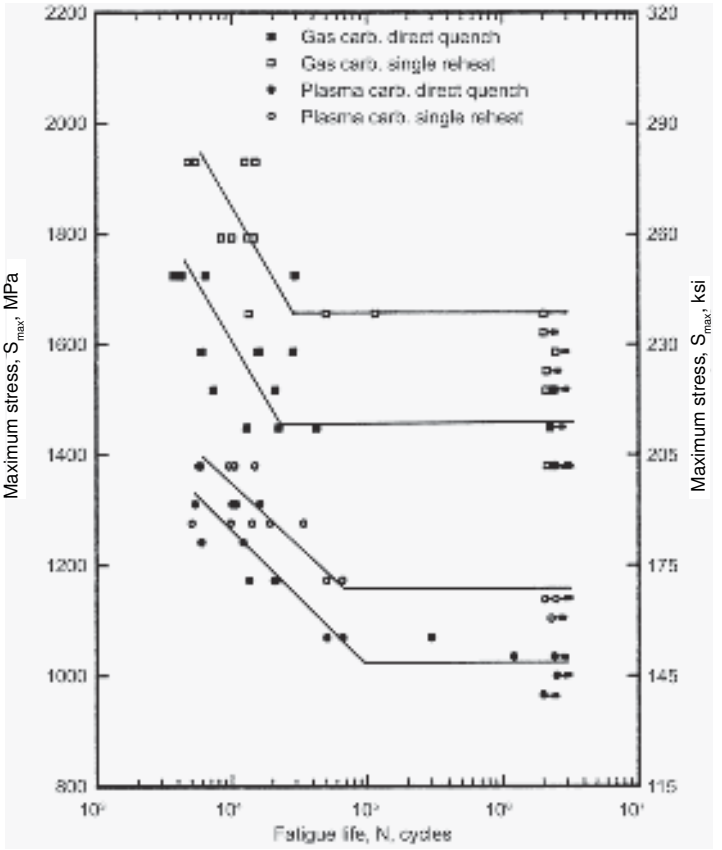

Fig. 21.33 Stress versus cycles for bending fatigue of 8719 steel. Specimens were either gas carburized or plasma carburized and direct quenched after carburizing or reheated as marked. Source: Ref 21.57

shows that maximum shear stresses are developed subsurface, and consistent with that fact, many failures due to high contact loads are initiated subsurface in hardened parts. However, when sliding is present, the associated shear stresses may initiate surface cracking.

The microstructures most resistant to rolling-contact fatigue damage in low-alloy carbon steels are those produced by quenching high-carbon austenite with carbides to martensite and tempering the martensite at low temperatures to hardness around HRC 60, either in the case of carburized steels or through the sections of through-hardening high carbon steels, Both approaches resist subsurface crack initiation, the carburized approach because the case depths are deeper than the Hertzian maximum shear stress depths. A widely used through-hardening steel for bearings is 52100 containing nominally 1.5% chromium and 1.00% carbon. In view of the high carbon content, 52100 steel is intercritically austenitized in the austenite/carbide two-phase field, and therefore dispersed retained carbide

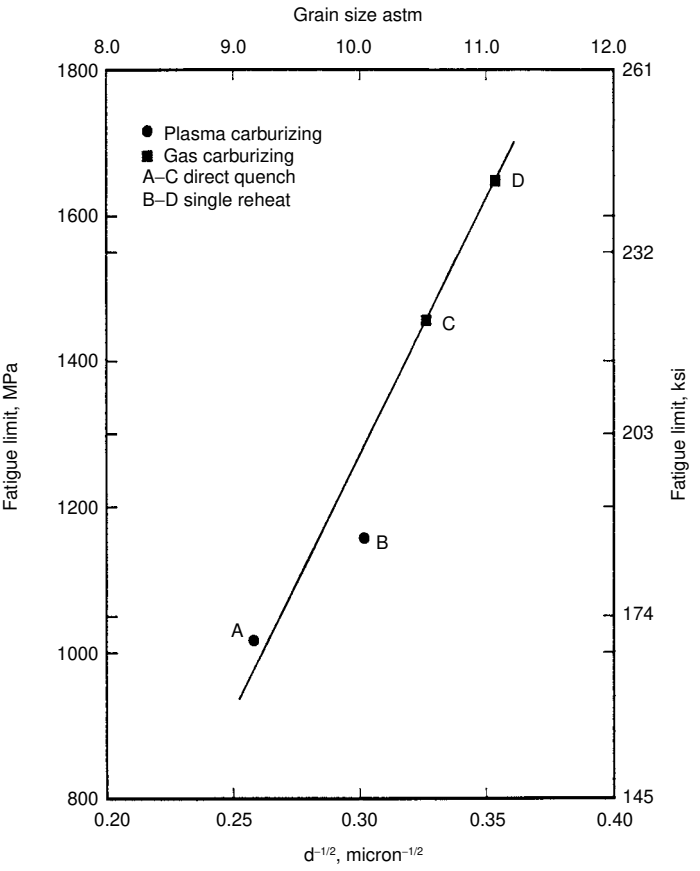

Fig. 21.34 Fatigue limits as a function of austenitic grain size for 8719 steel carburized and hardened as marked. Source: Ref 21.57

particles are a major component of the final heat treated microstructure. Figure 21.37 shows a spheroidized carbide distribution in 52100 steel austenitized at 850 °C (1650 °F). Retained carbides are distributed throughout the matrix of low-temperature-tempered martensite and retained austenite, and their function is to reduce austenite carbon content and move martensite morphology more to lath type than plate type, maintain fine austenitic grain size, and reduce retained austenite. Strengthening is not a major function of retained carbides. That function is provided by the much finer eta-transition carbide and dislocation distributions produced by low-temperature tempering of martensite. Similar microstructures to those in through-hardening steels are produced in the high-carbon case of carburized steels after reheating to and quenching from intercritical austenitizing temperatures.

The damage produced by sliding- and rolling-contact fatigue takes the form of surface pitting, either macropitting or micropitting, as described

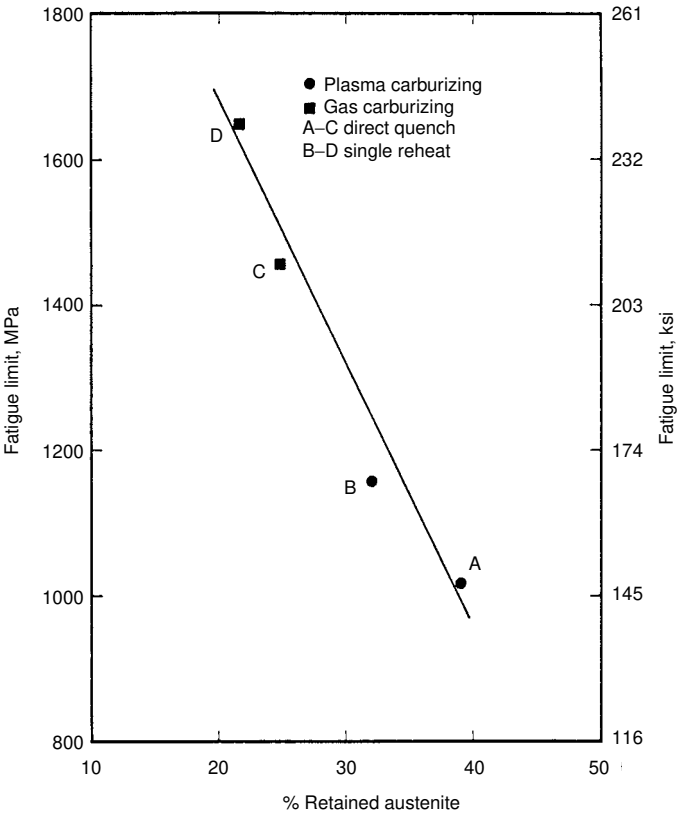

Fig. 21.35 Fatigue limits as a function of retained austenite in 8719 steel carburized and hardened as marked. Source: Ref 21.57

by Hyde (Ref 21.63). Many factors influence resistance to rolling-contact fatigue damage, but key are the strain-induced microstructural changes that develop with increasing cycles of contact stress in the low-temperature-tempered martensitic matrix of hardened parts. These changes are revealed by etching differences of the microstructure. Long associated with rolling-contact fatigue damage are white-etching features surrounding subsurface inclusions. Most frequently the inclusions are hard oxides, not the more plastic manganese sulfides. Figure 21.38 shows an example of such damage in a hardened steel. The two white-etching sides around the initiating inclusion give the impression of wings, and hence these features are commonly referred to as *butterflies*. Cracking develops around the white-etching areas, may even precede the development of the white-etching areas (Ref 21.64-21.66), and eventually propagates to the part surface to produce surface pitting. Recognition that butterfly formation at inclusions is associated with rolling-contact fatigue damage has driven the production of very clean steels by advances in steelmaking.

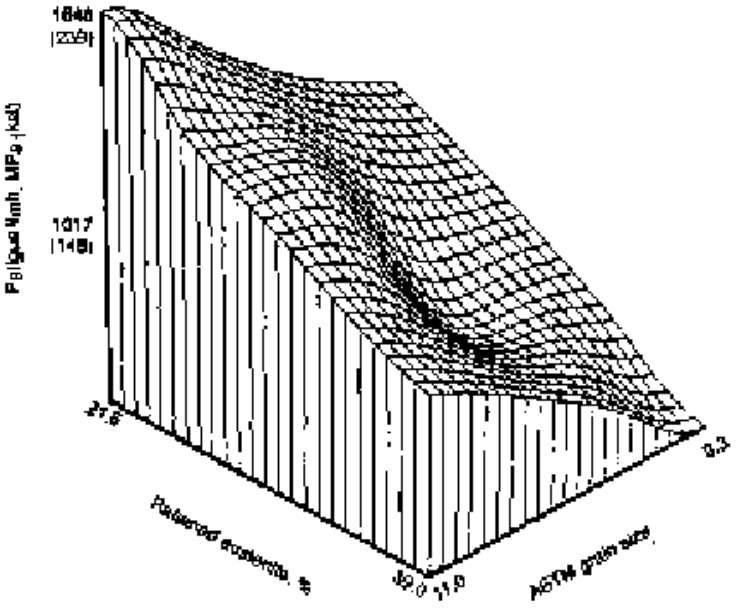

Fig. 21.36 Fatigue limits as a function of austenitic grain size and retained austenite in carburized 8719 steel. Source: Ref 21.57

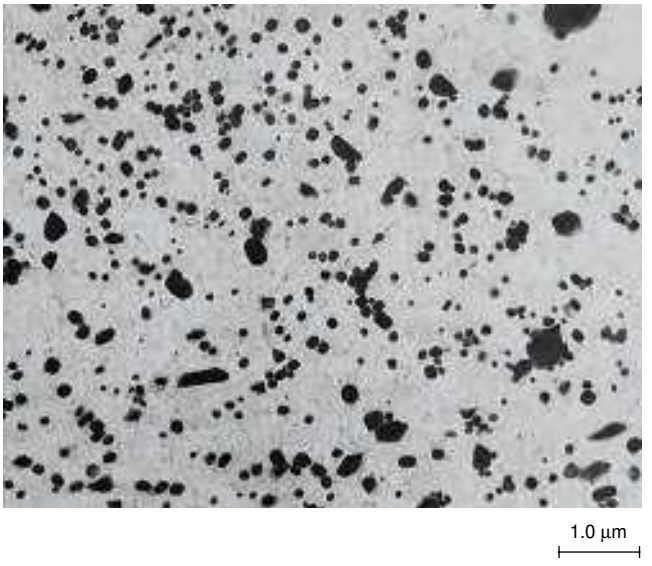

Fig. 21.37 Spheroidized carbides retained after intercritical austenitizing 52100 steel at 850 °C. Carbon extraction replica, transmission electron micrograph. Courtesy of Ken Hayes, Colorado School of Mines. Source: Ref 21.62

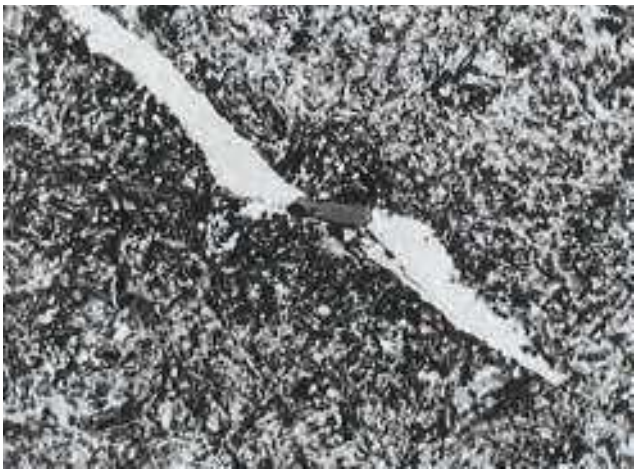

Fig. 21.38 White-etching features in a butterfly morphology around an inclusion particle in a quench and tempered steel subjected to cyclic contact stresses. Light micrograph. Reprinted with permission from ASTM STP987 Effect of Steel Manufacturing Processes on the Quality of Bearing Steels, copyright ASTM International, 100 Barr Harbor Drive, West Conshohocken, PA 19428. Source: Ref 21.64

Even in the absence of inclusions, high contact stresses cause microstructural changes that ultimately lead to surface pitting. These changes are reflected in the development of dark- and white-etching bands at 30- and 80-degree angles to the contact surface and eventual cracking along the bands that leads to surface pitting (Ref 21.67). Figure 21.39 shows an example of this damage in a carburized steel. Much must still be learned about contact fatigue, but the etching differences show that the low-temperature-tempered martensitic substructure is being altered by cyclic shear stresses. The substructure in the martensite crystals consists of dislocations and fine transition carbides and is capable of high rates of strain hardening associated with dislocation generation; it is this substructure that is being altered by the contact shear stresses.

Etching and the reflection of light from etched surfaces reflect underlying microstructures. Dark etching tends to be a result of particle distributions within a matrix, where the particles after etching cause surface roughing and scatter light; white etching tends to be associated with homogeneous structures that etch uniformly, producing flat surfaces that reflect light in the light microscope. Thus an explanation for the formation of white-etching structures might be in part related to an early proposal by Wilson that carbon atoms may have greater binding energy to dislocations than to iron-carbide particles (Ref 21.68). He supported this proposal by showing white-etching regions around hardness indentations of quenched 0.70% carbon steel. Further removed from the hardness indentation where temper carbides had formed and etching created surface roughness, the

Fig. 21.39 Cracking along 30 and 80 degree bands and formation of micropitting in a carburized steel subjected to contact fatigue testing. Light micrograph, nital etch. Courtesy of T. Ochi, Nippon Steel Company.

sample etched dark. He attributed the white etching to the increased dislocation density surrounding the hardness indentation which absorbed the carbon and prevented the formation of carbides normally formed on tempering, resulting in a highly deformed but single-phase martensitic microstructure. Similar substructural changes due to plastic deformation and dislocation multiplication may occur as the result of high shear stresses generated during contact loading.

In view of the fact that the etching differences produced by rolling-contact fatigue occur in the hardened substructure and the structural changes are accordingly very fine, transmission electron microscopy has been applied to identify the substructural changes. Highly deformed martensite, carbon-free ferrite structures, and various carbide distributions have all been observed in the regions with etching differences, and investigations are ongoing to correlate the changes to the progress of rolling-contact fatigue damage and the formation of the etching differences, and to identify the atomic-scale mechanisms of the changes (Ref 21.67, 21.65). The performance of bearing-steel microstructures under conditions of sliding and contact stress has been and remains an important research and development area. Recently Bhadeshia has extensively reviewed all aspects of the bearing steel literature, including contributions regarding damage mechanisms (Ref 21.69).

Nitriding

Nitriding is a surface-hardening heat treatment that introduces nitrogen into the surface of steel while it is in the ferritic condition. Nitriding, therefore, is similar to carburizing in that surface composition is altered, but different in that the nitrogen is added into ferrite instead of austenite. The fact that nitriding does not involve heating into the austenite phase field and subsequent quenching to form martensite means that nitriding can be accomplished with a minimum of distortion and excellent dimensional control.

Steels that are nitrided are generally medium-carbon steels that contain strong nitride-forming elements such as chromium, aluminum, vanadium, and molybdenum. Aluminum, especially, as already discussed with respect to austenite grain size controls (see Chapter 8, "Austenite in Steel"), is a very powerful nitride former and is used in amounts between 0.85 and 1.5% in nitriding steels (Ref 21.70). Prior to nitriding, the steels are austenitized, quenched, and tempered. Tempering is usually performed at temperatures between 540 and 750 °C (1000 and 1300 °F), a range above that at which the nitriding is performed. Tempering above the nitriding temperature provides a core structure that will be stable during nitriding.

Gas nitriding is accomplished with ammonia gas, which dissociates on the surface of the steel according to the following reaction:

$$NH_3 \rightleftharpoons N + 3H \qquad \text{(Eq 21.11)}$$

The resulting atomic nitrogen is absorbed at the surface of the steel.

Depending on temperature and the concentration of nitrogen that diffuses into the ferrite of iron or plain carbon steels, a number of phases may form. Low concentrations of nitrogen cause α", $Fe_{16}N_2$, to precipitate from the ferrite in the form of fine, coherent precipitates. Higher concentrations of nitrogen produce γ', or Fe_4N, the phase that constitutes the brittle white layer of nitrided steels. Even higher concentrations of nitrogen produce e nitride, which when combined with carbon, is considered to be a tribologically desirable phase. Figures 21.40 and 21.41 show respectively the Fe-N diagram (Ref 21.71) and the NH_3 concentrations in NH_3-

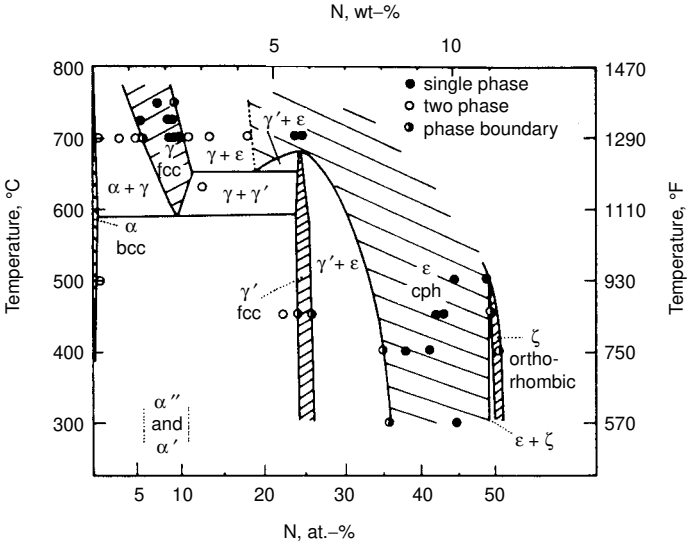

Fig. 21.40 Iron-nitrogen phase diagram. Source: Ref 21.71

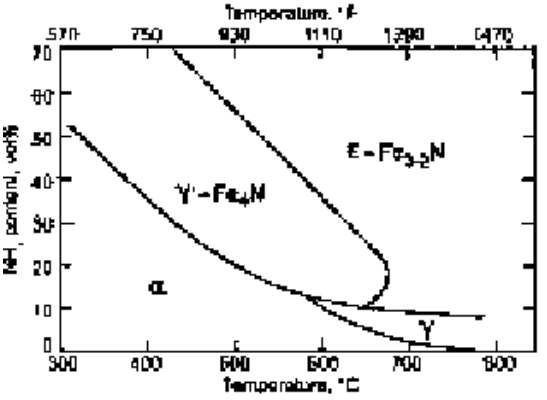

Fig. 21.41 Ammonia concentration in ammonia-hydrogen mixtures and temperature ranges for the formation of various Fe-N phases. Source: Ref 21.72

H_2 gas mixtures that produce the various nitride phases (Ref 21.72). Nitriding of alloy steels produces diffusion zones of fine precipitates, as discussed subsequently.

The nitriding may be accomplished by either a single-stage or a double-stage process. The single-stage process is performed at 500 to 525 °C (930 to 975 °F) with 15 to 30% dissociation of the ammonia, i.e., with an atmosphere that contains 70 to 85% NH_3, the source of the nitrogen. This process produces brittle γ' iron nitride. A patented process developed by Floe (Ref 21.73) uses a two-stage process to minimize the thickness of the white layer. The first stage is similar to that described previously, but in the second stage the dissociation is increased to 65 to 85%, thereby reducing the NH_3 content of the atmosphere that supplies nitrogen to the surface according to the reaction represented in Eq 21.11. As a result, the iron nitride does not grow as rapidly, and in fact dissolves as it supplies nitrogen into the interior of the steel. Nitriding times are quite long, anywhere from 10 to 130 h depending on the application (Ref 21.70), and the case depths are relatively shallow, usually less than 0.5 mm (0.020 in.).

The microstructure of a nitrided steel is shown in Fig. 21.42. The white layer is clearly visible. Below the white layer, fine alloy nitrides have formed but are much smaller than can be resolved in the light microscope. Jack and his colleagues have studied many alloys of iron, nitrogen, and other substitutional alloying elements (Ref 21.74). At the temperatures at which commercial nitriding is performed, very fine clusters or precipitate zones of substitutional alloying elements and the interstitial nitrogen are proposed to form. The substitutional-interstitial zones remain quite fine and do not coarsen readily on heating because of the sluggish diffusion of the substitutional atoms. At lower temperatures only iron nitrides form, and at higher temperatures alloy nitrides form.

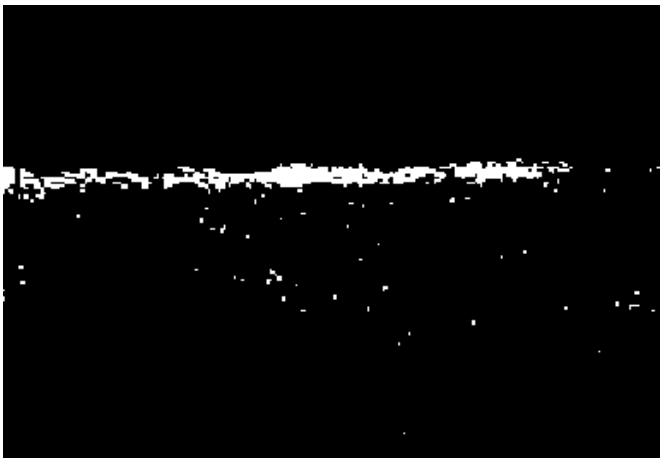

Fig. 21.42 White layer and diffusion zone in nitrided steel. Steel is Nitralloy 135 Modified containing 0.4% C, 1.6% Cr, 0.35% Mo, and 1.13% Al. Base microstructure is tempered martensite of hardness 30 HRC. Etched in 1.5% nital. Original magnification at 500×. Courtesy of D. Stratford, Sundstrand Corp., Denver

Nitrided cases are harder than those produced by carburizing and are quite stable in service up to the temperature of the nitriding process. Nitriding, therefore, produces excellent wear, seizing, and galling resistance under conditions where heat is generated by friction between moving parts in contact. Improved fatigue life is also an important benefit of nitriding. Spies and Dalke have written an excellent comprehensive review of the microstructures and properties produced by nitriding (Ref 21.75).

Carbonitriding

Carbonitriding is a surface-hardening heat treatment that introduces carbon and nitrogen into the austenite of steel. This treatment is therefore similar to carburizing in that the austenite composition is changed and high surface hardness is produced by quenching to form martensite. Carbonitriding surface hardening, however, is dependent to some extent on nitride as well as martensite formation.

The process of carbonitriding utilizes an atmosphere containing ammonia plus a carbon-rich gas or vaporized liquid hydrocarbon that is a source of carbon as in carburizing. The various gas-interchange and gas-metal reactions involved in carbonitriding have been reviewed by Slycke and Ericsson (Ref 21.76). The ammonia dissociates on the surface of the steel and introduces atomic nitrogen. The nitrogen inhibits the diffusion of carbon and this factor, plus the fact that carbonitriding is performed at lower temperatures (705 to 900 °C, or 1300 to 1650 °F) and shorter times than carburizing, results in relatively shallow case depths, from 0.075 to

0.75 mm (0.003 to 0.030 in.). At higher temperatures, the thermal decomposition of ammonia is too rapid, limiting the supply of nitrogen. The lower carbonitriding temperatures are not often used because of the hazard of explosion and the brittle structures formed at the lower temperatures (Ref 21.18). However, a lower-temperature variant of carbonitriding, referred to as austenitic nitrocarburizing, now appears to be well developed (Ref 21.77). The latter process is optimally applied in the temperature range 675 to 775 °C (1247 to 1427 °F) and should be controlled to produce a surface compound layer of epsilon carbonitride. Figure 21.43 shows the carbon and nitrogen contents that produce the tribologically desirable (ε) epsilon phase at 700 °C (1290 °F).

The nitrogen in carbonitrided steels also enhances hardenability and makes it possible to form martensite in plain carbon and low-alloy steels that initially have low hardenability. The nitrides formed due to the presence of nitrogen also contribute to the high hardness of the case. Nitrogen, similar to carbon, lowers M_s temperatures. Therefore, considerable austenite may be retained after quenching a carbonitrided part. If the retained austenite content is so high that it reduces hardness and wear resistance, it may be controlled by reducing the ammonia content of the carbonitriding gas either throughout the cycle or during the latter portion of the cycle (Ref 21.18). Another consequence of excessive nitrogen content in the carbonitrided case is porosity (Ref 21.76).

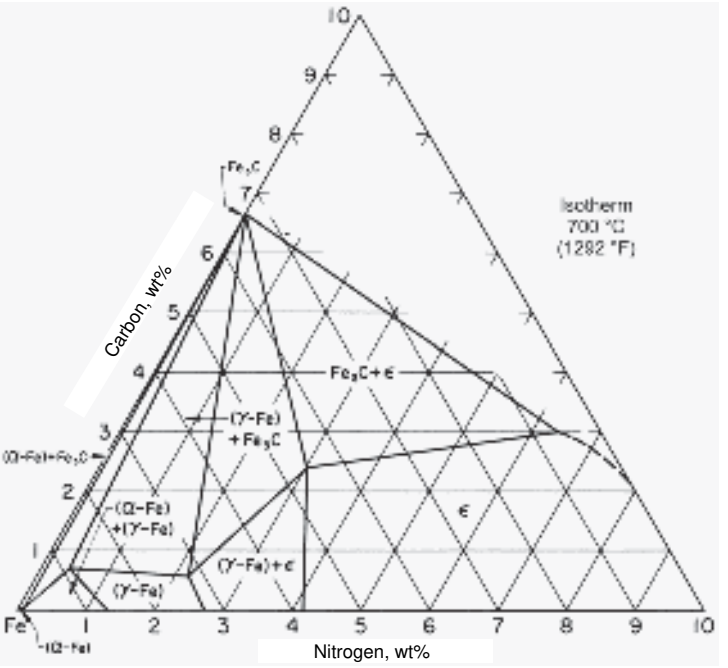

Fig. 21.43 Fe-C-N isothermal section at 700 °C (1290 °F)

Ferritic Nitrocarburizing

Another type of surface hardening that involves the introduction of carbon and nitrogen into a steel is *ferritic nitrocarburizing*. In contrast to carbonitriding but similar to the nitriding process, the carbon and nitrogen are added to ferrite below the Ac_1 temperature. Bell (Ref 21.78) describes a number of ferritic nitrocarburizing processes, both liquid and gaseous. The common beneficial result in all the processes again is a very thin single-phase layer of epsilon carbonitride—a hexagonal ternary compound of iron, nitrogen, and carbon—formed between 450 and 590 °C (840 and 1095 °F) (Ref 21.78).

The epsilon carbonitride compound layer has excellent wear and antiscuffing properties and is produced with minimum distortion. The layer can be formed on inexpensive mild steels with ferrite-pearlite microstructures, thereby greatly improving their wear and fatigue resistance. Figure 21.44 shows the hardness profiles of various steels subjected to a gaseous ferritic nitrocarburizing treatment. The very high hardness and shallow case depths produced by the process in alloy steels are apparent, and even the plain steel benefits significantly. Some of the increased hardness of the case is due to a diffusion zone beneath the compound layer, especially in the more highly alloyed steels with strong nitride formers such as Nitralloy N (1.00 to 1.30% Cr, 0.85 to 1.20% Al, and 0.20 to 0.30% Mo). In this diffusion zone, nitrides or precipitate zones similar to those that form as a result of nitriding are developed as nitrogen diffuses into the interior of the steel from the compound layer. As a general rule, the compound layer gives good tribological properties, but a substantial diffusion zone is required for good fatigue resistance.

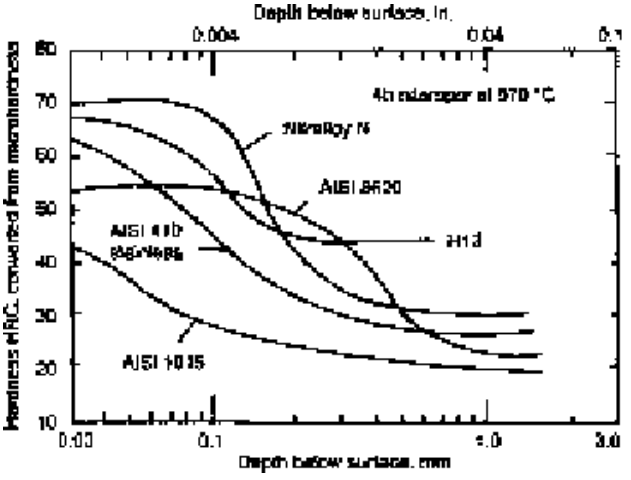

Fig. 21.44 Microhardness profiles in various types of steels after gaseous ferritic nitrocarburizing (Nitemper process). Source: Ref 21.78

Somers and Mittemeijer (Ref 21.79) have documented the following complex sequence of layers formed by nitrocarburizing iron at 570 °C (1058 °F) in an atmosphere of 53.1 vol% NH_3, 43.9 vol% H_2, and 3 vol% CO. Starting at the surface, the following layers form: ε carbonitride ($Fe_2(N,C)_{1-x}$), cementite (θ, or Fe_3C) with a high degree of porosity, ε carbonitride with a lower carbon content, and finally carbon-poor γ' carbonitride ($Fe_4(N,C)_{1-x}$) adjacent to the substrate iron. These layers and the nitrogen and carbon concentration profiles produced by nitrocarburizing 15 h are shown in Fig. 21.45, and a similar layered structure produced by nitrocarburizing 24 h is shown in Fig. 21.46. The work by Somers and Mittemeijer shows that compound formation starts with γ' nucleation and subsequent ε formation on the γ'. The formation of the cementite is caused by pores produced by the recombination of dissolved nitrogen atoms and preferential carbon uptake along pore channels. Further mechanisms and the kinetics of the compound layer formation are also described (Ref 21.79), and Somers has written a thorough review of compound-layer and diffusion-zone structures formed during nitriding and nitrocarburizing (Ref 21.80).

Summary

This chapter has described microstructures and performance of steels subjected to what may be considered to be traditional or conventional surface-hardening heat treatments based on their long histories of application. Newer methods of surface modification that use high-energy beams, plasmas, vacuums, and vapor-deposition processing are discussed in Chapter 22, "Surface Modification." Despite the long history of the conventional techniques, advances in processing, improved properties, and increased understanding of performance continue. Recent references on induction hardening are given in the induction-hardening section of this chapter. Additional reviews of the microstructure and properties of carburized steels are given in Ref 21.81 to21.83. Reference 21.84 reviews bending fatigue and fracture in carburized steel, and Ref 21.63 reviews contact fatigue and fracture of hardened steels, including carburized steels. Advances in the state of the art regarding conventional and new techniques of surface hardening and modification are given in Ref 21.85 to 21.87.

REFERENCES

21.1 T. Bell, Surface Engineering: Past, Present, and Future, *Surf. Eng.*, Vol 6, (1), 1990, p 31–40

21.2 H.W. Grönegress, Einfluss der Härtbarkeit eines Stahles auf das Ergebnis beim Flammenhörten, *Stahl Eisen,* Vol 70, 1950, p 192

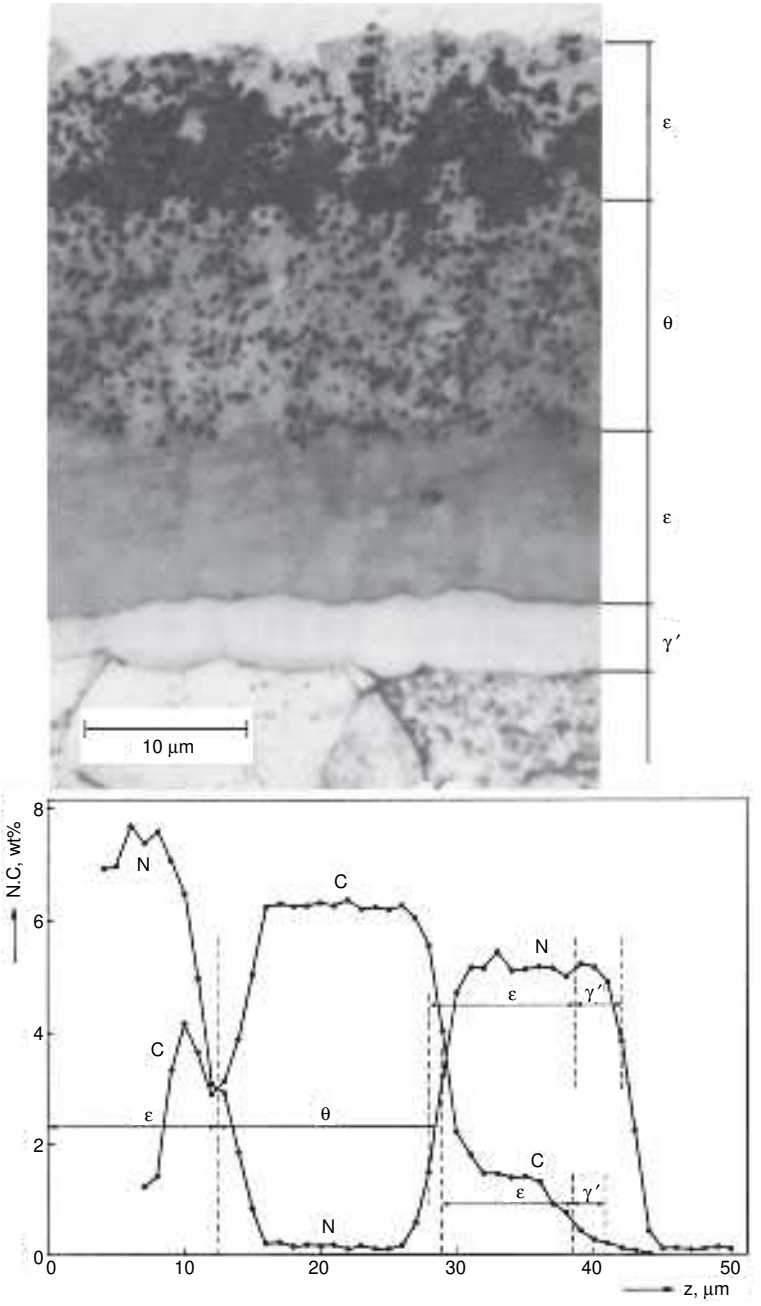

Fig. 21.45 Compound layers (top) and concentration profiles (bottom) of iron gas-nitrocarburized at 570 °C (1058 °F) for 15 h. Courtesy of E. J. Mittemeijer, Delft University of Technology. Source: Ref 21.79

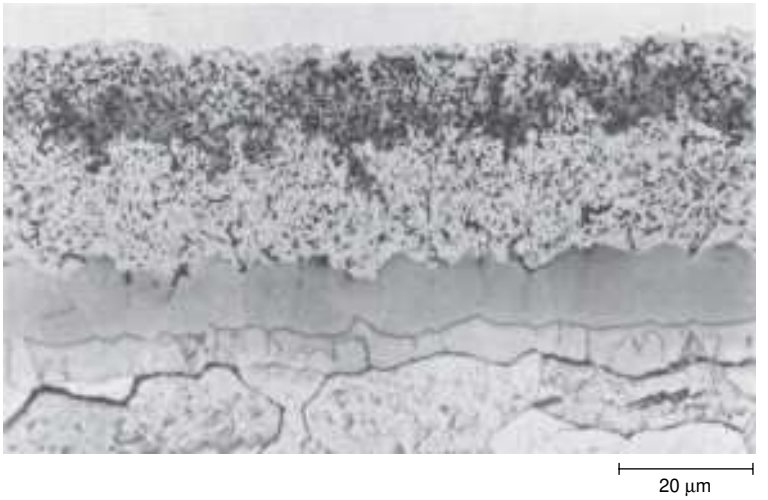

Fig. 21.46 Compound layers in sequence as in Fig. 21.32 in iron gas-nitrocarburized at 570 °C (1058 °F) for 24 h. Courtesy of E.J. Mitteneijer, Delft University of Technology. Source: Ref 21.79

21.3 *Surface Hardening,* P.D. Harvey, Ed., Metals Engineering Institute, American Society for Metals, 1979

21.4 P.A. Hassell and N.V. Ross, Induction Heat Treating of Steel, "*Heat Treating,* Vol 4, *ASM Handbook,* ASM International, 1991, p 164–202

21.5 S.L. Semiatin and D.E. Stutz, *Induction Heat Treatment of Steel,* American Society for Metals, 1986

21.6 S. Zinn and S.L. Semiatin, *Elements of Induction Heating, Design, Control and Applications,* ASM International, 1988

21.7 V. Rudnev and D. Loveless, Induction Hardening: Technology, Process Design, and Computer Modeling, *Thermal Engineering of Steel Alloy Systems*, Vol 12, G. Krauss, Ed., Elsevier, 2014, p 489–580

21.8 D.J. Medlin, G. Krauss, and S.W. Thompson, Induction Hardening Response of 1550 and 5150 Steels with Similar Prior Microstructures, *Induction Hardened Gears and Critical Components,* Gear Research Institute, Evanston, IL, 1995, p 57–65

21.9 T.J. Favenyesi, D.J. Medlin, D.K. Matlock, and G. Krauss, Effects of Prior Microstructure on the Fatigue of Induction Hardened 1050 Steel, *40th MWSP Conference Proceedings,* ISS, 1998, p 733–740

21.10 J.L. Cunningham, "Effects of Induction Hardening and Prior Cold Work on a Microalloyed Medium-Carbon Steel," M.S. thesis, Colorado School of Mines, Golden, CO, 1996

21.11 J.L. Cunningham, D.J. Medlin, and G. Krauss, Effects of Induction Hardening and Prior Cold Work on a Microalloyed Medium Car-

bon Steel, in *Proceedings of the 1997 International Induction Heat Treating Symposium,* ASM International, 1998, p 575–584

21.12 G.R. Speich and A. Szirmae, Formation of Austenite from Ferrite and Ferrite-Carbide Aggregates, *Trans. TMS-AIME,* Vol 245, 1969, p 1063–1074

21.13 J.D. Wong, D.K. Matlock, and G. Krauss, Effects of Induction Tempering on Microstructure, Properties and Fracture of Hardened Carbon Steels, *43rd MWSP Conference Proceedings,* ISS, 2001, p 21–36

21.14 G.A. Fett, Characterization of Semi-Float Axle Shaft Bending Fractures, *SAE Technical paper 940732*, SAE, 1994

21.15 C.G. Santos and C. Laird, Fractography of Induction-Hardened Steel Fractured in Fatigue and Overload, *Mater. Charact.,* Vol 39, 1997, p 25–41

21.16 T. Ochi and Y. Koyasu, Strengthening of Surface Induction Hardened Parts for Automotive Shafts Subject to Torsional Load, *SAE Technical paper 940786,* SAE, 1994

21.17 A.B. Nissan, "The Effect of Microstructure and Induction Processing on Fatigue Crack Initiation of Induction Hardened Bar Steel," Ph. D. Thesis, Colorado School of Mines, Golden, CO, 2012

21.18 *Carburizing and Carbonitriding,* ASM Committee on Gas Carburizing, American Society for Metals, 1977

21.19 F.J. Harvey, Thermodynamic Aspects of Gas-Metal Heat Treating Reactions, *Metall. Trans. A,* Vol 9A, 1978, p 1507–1513

21.20 Furnace Atmospheres, *Heat Treating, Cleaning, and Finishing*, Vol 2, *Metals Handbook,* 8th ed., American Society for Metals, 1964, p 67–84

21.21 F.E. Harris, Reactions between Hot Steel and Furnace Atmospheres, *Met. Prog.,* Vol 47 (No. 1), Jan 1945, p 84–89

21.22 Application of Equilibrium Data, *Carburizing and Carbonitriding,* ASM Committee on Gas Carburizing, American Society for Metals, 1977, p 14–15

21.23 J.J. Goldstein and A.E. Moren, Diffusion Modeling of the Carburization Process, *Metall. Trans. A,* Vol 9A, 1978, p 1515–1525

21.24 C. Wells and R.F. Mehl, Rate of Diffusion of Carbon in Austenite in Plain Carbon, in Nickel, and in Manganese Steels, *Trans. AIME,* Vol 140, 1940, p 279–306

21.25 D.E. Diesburg and G.T. Eldis, Fracture Resistance of Various Carburized Steels, *Metall. Trans. A,* Vol 9A, 1978, p 1561–1570

21.26 W.T. Groves, How to Select the Right EX Steel, *Met. Prog.,* Vol 102, 1972, p 89–99

21.27 U. Wyss, Kohlenstoffund Härteverlauf in der Einsatzhärtungsschicht verschieden legierter Einsatzstähle, *Härt.-Tech. Mitt.,* Vol 43, 1988, p 27–35

21.28 K.D. Jones and G. Krauss, Microstructure and Fatigue of Partial Pressure Carburized SAE 8620 and EX 24 Steels, *J. Heat Treat.,* Vol 1, 1979, p 64–71

21.29 K.D. Jones and G. Krauss, Effects of High-Carbon Specimen Corners on Microstructure and Fatigue of Partial Pressure Carburized Steels, *Proceedings of the Metals Society: Heat Treatment '79*, 22–24 May 1979 (Birmingham, U.K.), The Metals Society, London, 1979, p 188–193

21.30 A.R. Marder and A.O. Benscoter, Microcracking in Fe-C Acicular Martensite, *Trans. ASM,* Vol 61, 1968, p 293–299

21.31 C.A. Apple and G. Krauss, Microcracking and Fatigue in a Carburized Steel, *Metall. Trans.,* Vol 4, 1973, p 1195–1200

21.32 R.P. Brobst and G. Krauss, The Effect of Austenite Grain Size on Microcracking in Martensite of an Fe-1.22 C Alloy, *Metall. Trans.,* Vol 5, 1975, p 457–462

21.33 M.G. Mendiratta, J. Sasser, and G. Krauss, Effect of Dissolved Carbon on Microcracking in Martensite of an Fe-1.39 C Alloy, *Metall. Trans.,* Vol 3, 1972, p 351–353

21.34 T.A. Balliett and G. Krauss, The Effect of the First and Second Stages of Tempering on Microcracking in Martensite of an Fe-1.22 C Alloy, *Metall. Trans. A,* Vol 7A, 1976, p 81–86

21.35 G. Parrish, *The Influence of Microstructure on the Properties of Case-Carburized Components*, American Society for Metals, 1980

21.36 L. Magnusson and T. Ericsson, Initiation and Propagation of Fatigue Cracks in Carburized Steel, *Proceedings of the Metals Society: Heat Treatment '79*, 22–24 May 1979 (Birmingham, U.K.), The Metals Society, London, 1979, p 202–206

21.37 G. Krauss, The Microstructure and Fatigue of a Carburized Steel, *Metall. Trans. A,* Vol 9A, 1978, p 1527–1535

21.38 H.K. Obermeyer, "The Effects of Heat Treatment and Phosphorus Content on Fracture of a 0.85% Carbon Alloy Steel," M.S. thesis, Colorado School of Mines, Golden, CO, 1978

21.39 T. Ando and G. Krauss, The Effect of Phosphorus Content on Grain Boundary Cementite Formation in AISI 52100 Steel, *Metall. Trans. A,* Vol 12A, 1981, p 1283–1290

21.40 I.S. Kozlovskii, A.T. Kalinin, A.J. Novikova, E.A. Lebedeva, and A.I. Festanova, Internal Oxidation during Case Hardening of Steels in Endothermic Atmospheres, *Met. Sci. Heat Treat*., No. 3. 1967, p 157–161

21.41 R. Chatterjee-Fischer, Internal Oxidation during Carburizing and Heat Treating, *Metall. Trans. A,* Vol 9A, 1978, p 1553–1560

21.42 C. Van Thyne and G. Krauss, A Comparison of Single Tooth Bending Fatigue in Boron and Alloy Carburizing Steels, *Carburizing, Processing, and Performance,* G. Krauss, Ed., ASM International, 1989, p 333–340

21.43 B.E. Cornelissen, G. Krauss, and D.K. Matlock, Effects of Alloying and Processing on Surface Oxidation and Bending Fatigue of Carburized Steels, *Progress in Heat Treatment and Surface Engineering,* E.J. Mittemeijer and J. Grosch, Ed., ASM International, 2000, p 117–128
21.44 H.C. Child, Vacuum Carburizing, *Heat Treat. Met.,* Vol 3, 1976, p 60–65
21.45 S. Gunnarson, Structure Anomalies in the Surface Zone of Gas-Carburized, Case-Hardened Steel, *Metal Treatment and Drop Forging,* June 1963, p 219–229
21.46 T. Naito, H. Veda, and M. Kikuchi, Fatigue Behavior of Carburized Steel with Internal Oxides and Nonmartensitic Microstructure Near the Surface, *Metall. Trans. A,* Vol 15A, 1984, p 1431–1436
21.47 B. Hildenwall and T. Ericsson, Residual Stresses in the Soft Pearlite Layer of Carburized Steel, *J. Heat Treat,* Vol 1 (No. 3), 1980, p 3–13
21.48 D.P. Koistinen, The Distribution of Residual Stresses in Carburized Cases and Their Origin, *Trans. ASM,* Vol 50, 1958, p 227–241
21.49 L.J. Ebert, The Role of Residual Stresses in the Mechanical Performance of Case Carburized Steel, *Metall. Trans. A,* Vol 9A, 1978, p 1537–1551
21.50 G. Parrish and G. S. Harper, *Production Gas Carburizing,* Pergamon Press, 1985
21.51 T. Ericsson, Residual Stresses Produced by Quenching of Martensitic Steels, in Vol 12, *Thermal Engineering of Steel Alloy Systems*, G. Krauss, Ed., Elsevier, 2014, p 271–298
21.52 W.E. Dowling Jr., W.T. Donlon, W.B. Copple, and C.V. Darragh, Fatigue Behavior of Two Carburized Low Alloy Steels, *1995 Carburizing and Nitriding with Atmospheres,* J. Grosch, J. Morral, and M. Schneider, Ed., ASM International, 1995, p55–60
21.53 M.A. Zaccone, "Flow Properties of High Carbon Tempered Martensite," M.S. thesis, Colorado School of Mines, Golden, CO, 1987
21.54 B. Kelley, "The Effect of Chromium on the Microstructure and Bending Fatigue Behavior of 0.82% C, 1.75% Ni, and 0.75% Mo Steels," M.S. thesis, Colorado School of Mines, Golden, CO, 1984
21.55 J.A. Sanders, "The Effects of Shot Peening on the Bending Fatigue Behavior of a Carburized SAE 4320 Steel," M.S. thesis, Colorado School of Mines, Golden, CO, 1993
21.56 J.L. Pacheco, "Fatigue Resistance of Plasma and Gas Carburized SAE 8719 Steel," M.S. thesis, Colorado School of Mines, Golden, CO, 1988
21.57 J.L. Pacheco and G. Krauss, Microstructure and High Bending Fatigue Strength in Carburized Steel, *Carburizing: Processing and*

Performance, G. Krauss, Ed., ASM International, 1989, p 227–238

21.58 M.A. Zaccone, B. Kelley, and G. Krauss, Strain Hardening and Fatigue in Simulated Case Microstructures, *Carburizing: Processing and Performance,* G. Krauss, Ed., ASM International, 1989, p 239–248

21.59 M.M. Shea, Impact Properties of Selected Gear Steels, Reprint No. 780772, Society of Automotive Engineers, Warrendale, PA, 1978

21.60 H. Hertz, Űber die berührung fester elastischer Körper (on the contact of solid elastic bodies), *J. Reine und Angewandte Mathematik*, 92, 1882, p 156-171

21.61 D.J. Wulpi, *Understanding How components Fail*, third ed., Brett Miller, Ed., ASM International, 2013

21.62 K.R. Hayes, "The Effect of Intercritical Heating and Phosphorus on Austenite Formation and Carbide Distribution of AISI 52100 Steel," M.S. thesis, Colorado School of Mines, Golden, CO, 1984

21.63 R.S. Hyde, Contact Fatigue of Hardened Steel, *Fatigue and Fracture,* Vol 19, *ASM Handbook*, ASM International, 1996, p 691–703

21.64 H. Schlicht, E. Screiber, and O. Zwirlein, Effects of Material Properties on Bearing Fatigue Strength, *Effect of Steel Manufacturing Processes on the Quality of Bearing Steels,* J. J. Hoo, Ed., STP 987, ASTM, Philadelphia, PA, 1988, p 81–101

21.65 M.-H. Evans, White Structure flaking (WSF) in wind turbine gearbox bearings: effect of 'butterflies' and white etching cracks (WECs), *Mat. Sci. Tech.*, Vol 28, No. 1, 2012, p 3–22

21.66 P. Kramer, "An Investigation of Rolling-Sliding Contact Fatigue Damage of Carburized Gear Steels," M.S. thesis, Colorado School of Mines, Golden, CO, 2013

21.67 H. Swahn, P. C. Becker, and O. Vinsbo, Martensite Decay during Rolling Contact Fatigue in Ball Bearings, Metallurgical Transactions A, Vol 7A, 1976, p1099–1110

21.68 D.V. Wilson, Effect of Plastic Deformation on Carbide Precipitation in Steels, *JISI,* Vol 16, 1954, p 28

21.69 H.K.D.H. Bhadeshia, Steels for Bearing, *Prog. Mater. Sci.*, Vol 57 (No. 2), 2012, p 268–435

21.70 Gas Nitriding, *Heat Treating,* Vol 4, *ASM Handbook,* ASM International, 1991, p 387–409

21.71 K.H. Jack, The Occurrence and the Crystal Structure of α"-Iron Nitride; A New Type of Interstitial Alloy Formed during the Tempering of Nitrogen-Martensite, *Proc. R. Soc.,* Vol A208, 1951, p 216–224

21.72 E. Lehrer, Uber das Eisen-Wasserstoff-Ammoniak-Gleichgewicht, *Zeitsch. Elektrochem,* Vol 36, 1930, p 383–392

21.73 C.F. Floe, A Study of the Nitriding Process: Effect of Ammonia on Case Depth and Structure, *Trans. ASM,* Vol 32, 1943, p 134
21.74 K.H. Jack, Nitriding, *Proceedings of the Metals Society: Heat Treatment '73,* 12–13 Dec 1973 (London, U.K.), The Metals Society, London, 1973, p 39–50
21.75 H-J. Spies and A. Dalke, Case Structure and Properties of Nitrided Steels, *Thermal Engineering of Steel Alloy Systems*, G. Krauss, Editor, Vol 12, *Comprehensive Materials Processing*, M.S.J. Hashmi, Ed., Elsevier, 2014, p 439–488
21.76 J. Slycke and T. Ericsson, A Study of Reactions Occurring during the Carbonitriding Process, *J. Heat Treat.,* Vol 2 (No. 1), 1981, p 3–19
21.77 T. Bell, M. Kinali, and G. Munstermann, Physical Metallurgy Aspects of Austenitic Nitrocarburizing Process, *Heat Treat. Met.*, Vol 14 (No. 2), 1987, p 47–51
21.78 T. Bell, Ferritic Nitrocarburizing, *Heat Treatment of Metals,* Vol 2, 1975, p 39–49
21.79 M.A.J. Somers and E.J. Mittemeijer, Formation and Growth of Compound Layer on Nitrocarburizing Iron: Kinetics and Microstructural Evaluation, *Surf. Eng.,* Vol 3 (No. 2), 1987, p 123–137
21.80 M.A.J. Somers, Development of Compound Layer and Diffusion Zone during Nitriding and Nitrocarburizing of Iron and Steels, *Thermal Engineering of Steel Alloy Systems*, G. Krauss, Ed., Elsevier, 2014, p 413–437
21.81 G. Krauss, Microstructures and Properties of Carburized Steels, *Heat Treating,* Vol 4, *ASM Handbook,* 1991, p 363–375
21.82 G. Parrish, *Carburizing: Microstructures and Properties,* ASM International, 1999
21.83 J. Grosch, Microstructure and Properties of Gas Carburized Steels, in *Thermal Engineering of Steel Alloy Systems,* G. Krauss, Ed., Elsevier, 2014, p 379–411
21.84 G. Krauss, Bending Fatigue of Carburized Steels, in *Fatigue and Fracture,* Vol 19, *ASM Handbook,* ASM International, 1996, p 680–690
21.85 *Surface Engineering & Heat Treatment,* P.H. Morton, Ed., Book 513, The Institute of Metals, London, 1991
21.86 *1995 Carburizing and Nitriding with Atmospheres,* J. Grosch, J. Morral, and M. Schneider, Ed., ASM International, 1995
21.87 *Progress in Heat Treatment and Surface Engineering,* E.J. Mittemeijer and J. Grosch, Ed., ASM International, 2000

CHAPTER 22

Surface Modification

THE NEWER SURFACE-MODIFICATION PROCESSES are a logical extension of heat treatment technology to steels. The objectives remain the same as in the established surface heat treatments: enhanced surface wear, fatigue, corrosion, and oxidation resistance. The use of high-energy beams, plasmas, and vapor-deposition techniques in vacuum environments, however, offers the potential of much more controlled, higher-quality surface modifications than heretofore possible. Also, the possibility of creating new engineered surface structures and surface-core systems is almost limitless because of the ability to deposit almost any material by vapor deposition and the ultrahigh heating and cooling rates of thin surface layers heated by electron and laser beams. This chapter describes some of the newer processes used to apply thermochemical modifications, coatings, and high-energy-density surface modifications to steels. Included are descriptions of plasma nitriding, plasma carburizing, ion implantation and mixing, physical vapor-deposition techniques, chemical vapor deposition, and transformation hardening and melting by laser and electron beams.

Introduction

Surface and near-surface microstructures in load-bearing machine components, tools, and other structural components manufactured from steels and cast irons are directly subjected to much higher static and cyclic stresses, friction, wear, and corrosive environments than interior microstructures. Thus, there are compelling economic and engineering reasons to develop and apply surface modifications that prevent surface-related failures and that extend the range of operating conditions for bulk engineering materials. Long-established but still evolving surface-modification techniques such as induction hardening, gas carburizing, and gas nitriding have already been discussed in Chapter 21, “Surface Hardening,” in this

book. However, in the 1980s a large number of new surface-modification processes were developed. The various techniques in this new generation of processes often use high-energy beams (electron, laser, and ion), electric or magnetic fields, and vacuum environments and thus constitute a significant increase in technology applied to surface modification. Many of the newer techniques were first developed and are still extensively used for thin-film electronic applications (Ref 22.1). However, the new techniques are increasingly being applied to steels and irons, as well as to aluminum, titanium, and high-temperature alloys.

The structural changes and property improvements due to the new surface technologies are process dependent and quite diverse. Types of surface modifications include surface melting and cladding, plating or the formation of hard layers on a substrate, and modification of workpiece subsurface chemistry. The proper selection and application of the various surface processes have led to the development of the interdisciplinary activity of surface engineering, defined as follows (Ref 22.2):

Surface engineering involves the application of traditional and innovative surface technologies to engineering components and materials in order to produce a composite material with properties unattainable in either the base or surface material. Frequently, the various technologies are applied to existing designs of engineering components, but ideally, surface engineering involves the design of the component with a knowledge of the surface treatment to be employed.

At least two journals are currently exclusively devoted to surface engineering (Ref 22.3, 22.4), and a large number of books and conference proceedings describe the many new surface-modification techniques (Ref 22.1–22.12).

The following sections of this chapter briefly describe processing principles, surface characteristics, and examples of applications of some of the newer surface-modification techniques.

Plasma Nitriding

The objectives of plasma nitriding, also referred to as ion nitriding, are the same as that of gas nitriding described in Chapter 21, "Surface Hardening," in this book; that is, the process should produce a hardened surface zone, typically on the order of 0.1 mm (0.004 in.) in depth, in a variety of steels. Nitrogen is adsorbed on the surface of the steel, diffuses inward at temperatures of approximately 500 °C (930 °F), and hardening is accomplished by precipitation of very fine nitride particles in the diffusion zone. Depending on nitrogen concentration, surface layers of face-centered cubic γ' Fe_4N or close-packed hexagonal ε Fe_2N_{1-x} may form, as shown in the iron-nitrogen phase diagram (Fig. 21.40) in Chapter 21, "Surface Hardening" (Ref 22.13). In view of the diffusion-controlled increase in nitrogen content of a steel surface produced by

plasma nitriding, the process is categorized as thermochemical, just as is gas nitriding.

Plasma nitriding, however, uses much different equipment than does gas nitriding. Processing is accomplished in a vacuum-tight, cold-wall chamber with the workload made the cathode (negative) and the chamber walls the anode and grounded. First, hydrogen and then a mixture of nitrogen and hydrogen are added to the chamber. An applied direct current (dc) potential across the cathode workpiece and chamber wall creates a plasma, defined as a gaseous state of matter with good electrical conductivity and consisting of ions, electrons, and charged and neutral atoms and molecules. The initial hydrogen stage creates a glow discharge that heats and cleans the surface of the workpieces, and the addition of the nitrogen initiates and sustains the nitriding action.

Figure 22.1 shows voltage-current relationships for nitrogen-hydrogen mixtures (Ref 22.14, 22.15). Plasma nitriding is performed with current densities in the abnormal glow discharge range. Under these conditions, current increases with voltage, and a uniform purple glow is established around the cathodic workpieces. The visible glow is caused by collisions of electrons with gas molecules in the electric field immediately adjacent to the cathode, that is, in the cathode fall region (Ref 22.16). In this region, ions and neutral atoms acquire high kinetic energy and are accelerated to the cathode, while electrons are accelerated to the anode. Generally, the heating of the workpiece is generated by the plasma-driven impact of the nitrogen ions, and no additional heat source is required. However, in newer system designs, convective heating is used to reduce cycle times (Ref 22.17).

A major advantage of plasma nitriding is the enhanced mass transfer of high-energy nitrogen molecules and ions to the surface of the steel under the action of the electric field (Ref 22.16, 22.17). The kinetics of nitrogen

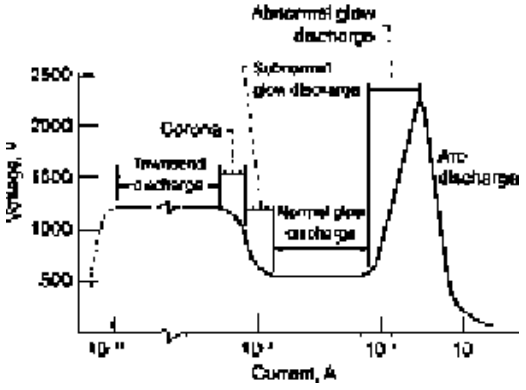

Fig. 22.1 Voltage-current characteristics of various discharges in argon. Plasma nitriding is performed in the abnormal glow discharge range. Source: Ref 22.14, 22.15

penetration into the steel of course remain controlled by solid-state diffusion and nitride precipitation. Safety, reduced gas consumption, reduced energy consumption in cold-wall chambers, clean environmental operation, and good control of γ' white layer structures are other advantages of plasma nitriding (Ref 22.16, 22.17). Temperature variations due to radiation losses in parts stacked closest to cold chamber walls, and the "hollow cathode" effect, a concentration of plasma that causes local over-heating at holes and cavities, may be problems in commercial plasma nitriding operations (Ref 22.18).

Plasma nitriding is widely applied and is the oldest plasma surface technology used commercially. Improvements in friction, scuffing resistance, and fatigue resistance are produced on a wide variety of materials, especially alloy and stainless steels, in a wide variety of machine components that require high surface hardness and good dimensional control (Ref 22.3, 22.5, 22.6). Plasma or ion carbonitriding, in which methane as well as hydrogen and nitrogen are added to the plasma, is also used where ternary Fe-C-N compound surface layers with good scuffing resistance are desired (Ref 22.19).

Plasma Carburizing

Plasma carburizing, similar to plasma nitriding, is another thermochemical glow discharge surface treatment. Carbon is brought to the surface of low-carbon steel in the austenitic state and diffuses to the interior of the workpiece to produce a high-carbon case, as described in Chapter 21, "Surface Hardening," in this book. The workpieces in plasma carburizing are made cathodes in a dc electric circuit. In the presence of a carburizing gas, the resulting glow discharge plasma increases the mass transfer of carbon to the steel surface. Thus, some acceleration of the carburizing process is possible (Ref 22.16, 22.17, 22.20). Case depth is still largely controlled by solid-state diffusion of carbon in the steel, a time-temperature-dependent process that proceeds independently of the plasma. Unlike plasma nitriding, where the impact of ions in the glow discharge is sufficient to heat workpieces to nitriding temperatures (approximately 500 °C, or 930 °F) without an external source of heat, plasma carburizing must be performed in internally heated chambers because of the higher temperatures (approximately 930 °C, or 1700 °F) required to produce austenite with its high solubility for carbon. Relatively little heating of the specimen is generated by energy input of the plasma at normal current densities of approximately 0.2 mA/cm^2 (1.3 mA/in.^{2}) (Ref 22.17).

Plasma carburizing is accomplished by establishing a vacuum, heating the load to carburizing temperatures while sputter cleaning in a hydrogen plasma, and carburizing in a hydrocarbon (propane or methane)-hydrogen-argon plasma (Ref 22.17) at relatively low gas partial pressures (0.1 to 10 torr). The carbon transfer is complex, but it appears that ionized and neu-

tral hydrocarbon molecules strike the steel surface, where they are first weakly attached (physisorbed) by Van der Waal's forces and then chemically bonded by the loss of a hydrogen atom from the gas molecule (chemisorbed) (Ref 22.21). Hydrogen atoms are then released from the molecules, leaving carbon atoms that diffuse into the steel. Following the carburizing, which may include several alternate carburize-diffuse cycles, the specimens are oil quenched in a tank incorporated into the furnace (Ref 22.17).

In addition to reduced carburizing times, plasma carburizing produces very uniform case depths, even in parts with irregular surfaces (Ref 22.17, 22.20). This uniformity is caused by the glow discharge plasma that closely envelops the specimen surface, provided recesses or holes are not too small (Ref 22.20). Also, because plasma carburizing is performed in a vacuum, there is no surface oxidation. Figure 22.2 compares plasma-carburized and gas-carburized 8719 steel (1.0% Mn, 0.5% Cr, 0.5% Ni, and 0.17% Mo) specimens (Ref 22.22). Both specimens are as-polished and have been nickel plated to prevent edge rounding during mechanical polishing. Below the nickel plate, no oxidation is visible in the plasma-carburized specimen, while a well-developed surface oxide layer has formed in the gas-carburized specimen. Surface oxidation may be detrimental to fatigue, especially if surface compressive residual stresses are reduced, but other factors, such as a very fine austenite grain size, can offset the detrimental effect of oxides, provided only martensite forms on quenching, as discussed in Chapter 21, "Surface Hardening," in this book.

Low-Pressure (Vacuum) Carburizing

Carburizing in vacuum furnace systems without the use of plasma technology is being increasingly used. The carburizing is performed at low

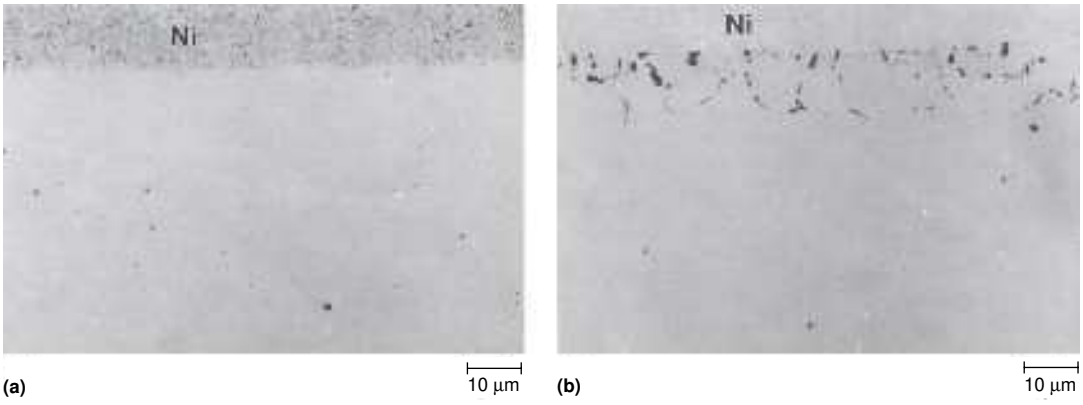

Fig. 22.2 (a) Plasma-carburized 8719 steel. (b) Gas-carburized 8719 steel. Both specimens nickel plated and unetched. Light micrographs. Source: Ref 22.22

pressures, below 20 torr, well below atmospheric pressure, 760 torr, and hence is most accurately described as low-pressure carburizing (LPC) rather than vacuum carburizing. Hydrocarbon gases such as acetylene (C_2H_4) are used to supply carbon to steel surfaces, and initially surface carbon content reaches that of the A_{cm} of the steel. Repeated boost /diffuse steps are used to reach lower surface carbon contents and appropriate case depths. Quenching can be done in oil or by quenching in pressurized inert gas, such as helium. Heat-transfer rates during gas quenching may be low, so hardenability may be a consideration. As noted for plasma carburizing, the use of LPC in vacuum chambers prevents surface oxidation and associated difficulties, as discussed in Chapter 21, "Surface Hardening," in this book. Other microstructural factors, such as grain-size control and residual stresses, remain the same as in gas-carburized steels. Herring describes in detail all aspects of the technology of vacuum heat treatment and carburizing (Ref 22.23).

Ion Implantation and Ion Mixing

Ion implantation is a surface-modification process in which ions with very high energy are driven into a substrate (Ref 22.14, 22.24, 22.25). Ions of almost any atom species can be implanted, but nitrogen is widely used to improve corrosion resistance and tribological properties of steels and other alloys. Although the nitrogen content of alloy surfaces is increased by both nitrogen ion implantation and plasma nitriding, major differences exist between the two processes and the surface modification that they create.

Ion implantation machines accelerate ions, generated by specially designed sources (Ref 22.25), at very high energies, from 10 to 500 keV. In contrast, the energy of ions and atoms in plasma nitriding is much lower, less than 1 keV. Ion implantation is carried out with the substrate close to room temperature, thus minimizing diffusion-controlled formation of precipitates and coarsening of the subsurface microstructure. The low temperature of application and the fact that the process is carried out in accelerators with very good vacuums (10^{-5} torr or better) ensure clean surfaces and reduce undesirable surface chemical reactions such as oxidation. Ion implantation is a line-of-sight process; that is, only relatively small areas directly exposed to the ion beam are implanted. For coverage of areas larger than the beam, either the specimen must be translated or the ion beam must be rastered over the specimen surface.

Figure 22.3 shows ion-implanted nitrogen distributions in iron as a function of ion beam energy (Ref 22.14). The nitrogen concentrations are quite high and have a slightly skewed gaussian distribution. However, the depth of ion penetration is relatively shallow, generally less than 0.25 μm, compared with gas- or plasma-nitrided case depths, which are 100 μm and deeper. This difference in case depth is due to diffusion-controlled case

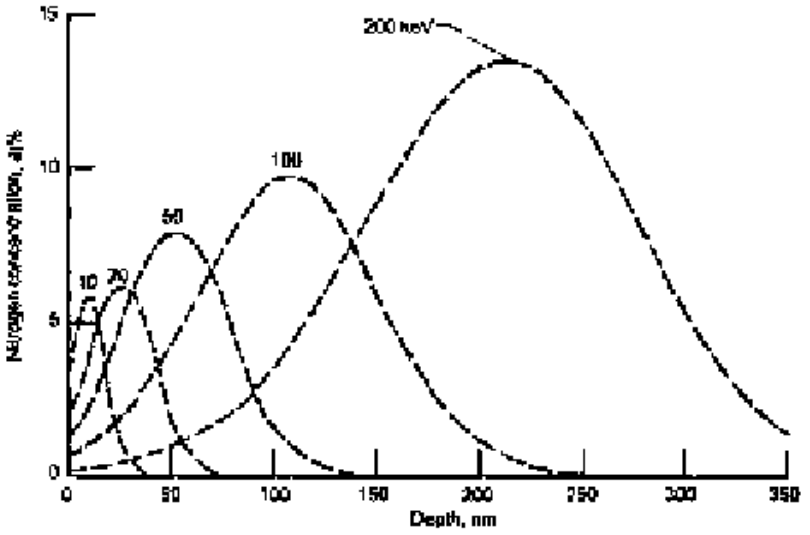

Fig. 22.3 Nitrogen concentration versus depth for implantation of iron performed at various beam energies. Source: Ref 22.14

formation in the nitriding processes and the virtual absence of this mechanism in ion implantation.

Compensating for the shallow case depths of ion implantation are very high strengths or hardness of the nitrogen-implanted surface layers. Ion implantation is a complex, nonequilibrium process that creates significant lattice damage in the form of vacancies and interstitial point defects. Concentrations of implanted species much higher than equilibrium solubility limits may be introduced. In fact, the incorporation of high densities of atoms of significantly different size compared with the substrate lattice may produce amorphous structures or metastable phases (Ref 22.25). Figure 22.4 shows schematically some characteristics of ion implantation by 100 keV nitrogen ions in iron (Ref 22.26). Each ion creates a large number of point defects, and the lower right of Fig. 22.4 illustrates the formation of a cascade of vacancy-interstitial pairs or Frenkel defects by a nitrogen ion. The implanted ions, the lattice defects, and the resulting compressive stresses all act to produce very high strength and hardness of the implanted layer.

The properties of ion-implanted surfaces and shallow case depths make ion implantation suitable for very special applications. Because the surface of the part itself is modified, there are no adhesion problems as are sometimes encountered with coated layers of high hardness. Also, because ion implantation is usually accomplished with very little heating, dimensional stability is excellent. Examples of applications of ion implantation include surface hardening of razor blades (Ref 22.17) and knives (Ref 22.25), a variety of tool steel applications (Ref 22.27), and implantation of 52100 and 440C bearings with titanium and/or nitrogen to improve rolling-contact fatigue resistance (Ref 22.28–22.30). In the latter applica-

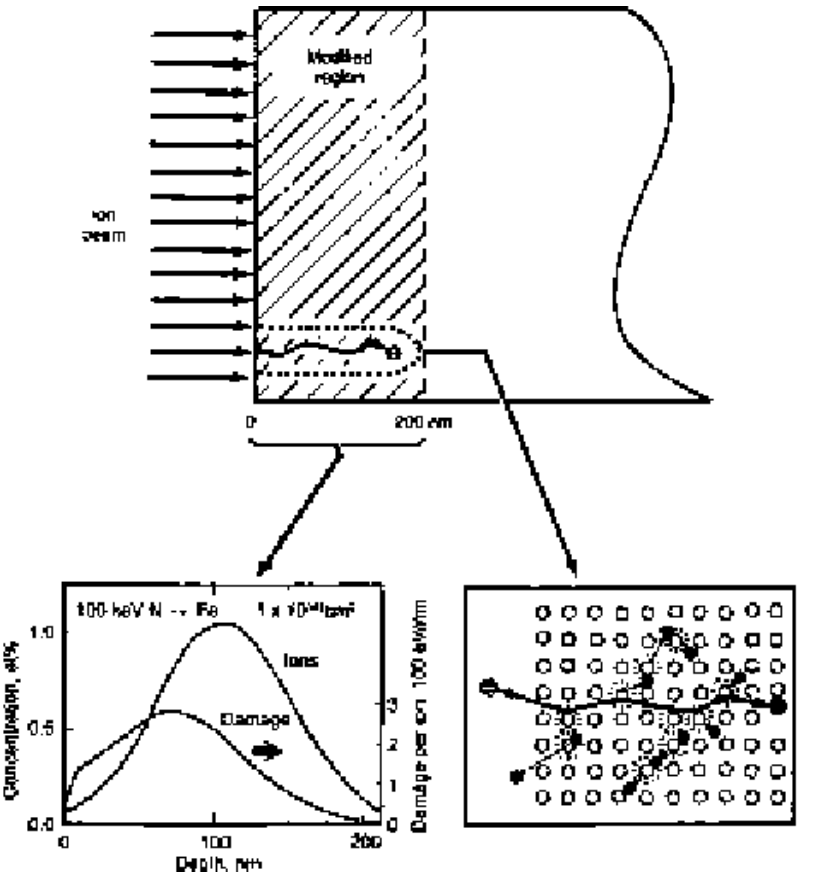

Fig. 22.4 Schematic illustration of implantation of iron with nitrogen ions (top). Nitrogen and damage profiles (lower left). Cascade region of high-defect-density generation (lower right). Source: Ref 22.26

tions, titanium was found to reduce the coefficient of friction, and nitrogen was found to raise hardness by intermetallic compound formation.

Ion-beam mixing is an extension of the use of ion beams to produce coating-ion implanted systems with enhanced properties (Ref 22.14, 22.31). In this process, a surface layer or coating, deposited on a substrate by another technique, is subjected to a high-energy ion beam, as shown schematically in Fig. 22.5 (Ref 22.14). Ions are deposited and transmitted through the coating and into the substrate, producing the same changes produced by direct ion implantation. Moreover, the atoms of the coating are mixed with the substrate, leading to improved adhesion of the coating on the substrate. Ion-beam mixing for improved wear and corrosion performance has been applied to a variety of metal substrates (Ref 22.31). Applications for steels include ion mixing of gold layers on 15.5 PH stainless steel for improved resistance to fretting corrosion and ion mixing of layers on high-carbon steels for improved oxidation resistance.

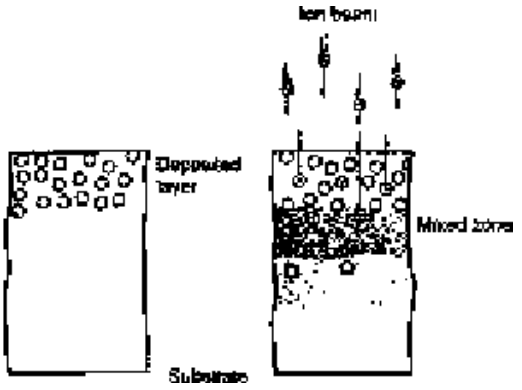

Fig. 22.5 Schematic diagram of ion-beam mixing process. Source: Ref 22.14

Physical Vapor Deposition: Processing

Physical vapor deposition (PVD) surface-modification techniques produce layers or coatings on substrates, in contrast to the previously discussed thermochemical techniques that modify substrate surface composition and structure without layer formation. Physical vapor deposition techniques are used to enhance properties of a great variety of materials, and the technology has again been driven by thin-film electronic applications (Ref 22.1). However, these techniques are being increasingly applied to steels, in particular to extend the life of tools and dies that are used to machine and form steels and other materials.

The term *physical vapor deposition* refers to any process that physically generates and deposits atoms or molecules on a substrate in a high-vacuum environment (Ref 22.32). The atom flux that impinges on a substrate may be generated by evaporation, sputtering, or ion plating. These mechanisms and their modifications lead to a multiplicity of PVD processes (Ref 22.14, 22.16, 22.32). Evaporation is accomplished by heating source materials in high vacuums (7.5×10^{-6} torr or better). At sufficiently high temperatures, atoms or molecules are thermally evaporated from the source, travel through the vacuum, and deposit on a substrate (Ref 22.32). For many applications, deposition processes that are based solely on thermal evaporation are being replaced by sputtering and ion plating, more efficient processes that use glow discharge plasmas.

Sputtering is a coating process in which atoms are ejected mechanically from a target by the impact of ions or energetic neutral atoms. Figure 22.6 shows schematically the mechanism of sputtering in a simple diode system (Ref 22.14). The chamber is initially evacuated, back filled with argon gas, and the target is made cathodic or negative by the application of a dc potential (between –500 and –5000 V). A low-pressure glow discharge

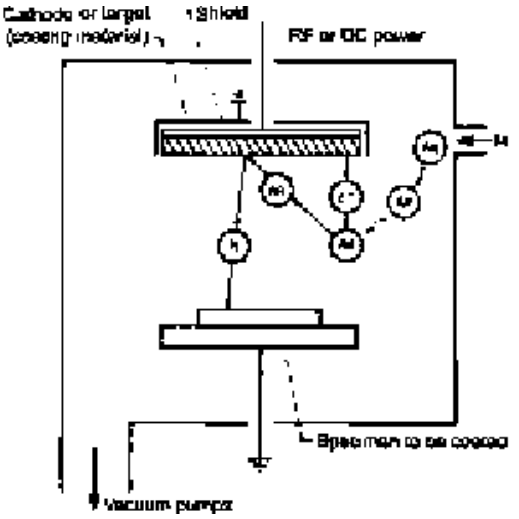

Fig. 22.6 Schematic diagram of mechanisms of sputtering. RF, radio frequency; dc, direct current. Source: Ref 22.14

plasma is created around the target cathode, creating positively charged argon ions that are accelerated to the target. The momentum transfer due to the impact of the argon ions is sufficient to eject target atoms that travel to the substrate and other parts of the chamber. The mechanical transfer of atoms by sputtering is more readily controlled than thermal transfer by evaporation, and sputtered atoms have higher energies than thermally evaporated atoms (Ref 22.32). Even insulators or semiconductors may be sputtered, but to eliminate charge buildup on a nonconducting target, radio frequency (RF) voltages are applied to the system rather than dc voltages.

Simple diode sputtering systems have relatively low rates of deposition. Thus, improved sputtering systems, with magnetic fields applied at the targets, have been developed. The resulting sputtering process is referred to as magnetron sputtering and is schematically illustrated in Fig. 22.7 (Ref 22.14). The magnetic fields, applied by permanent magnets, trap secondary electrons generated by the target and greatly increase ionization in the cathode plasma. Thus, more argon ions strike the target, and sputtering and deposition rates are significantly increased relative to diode sputtering.

Ion plating, also referred to as plasma-assisted PVD or evaporative-source PVD coating, generates coating atoms by thermal evaporation from an appropriate source (Ref 22.14, 22.16, 22.32). The source may be an electrically heated wire, an electron beam, or of hollow cathode design and is made the anode in the system. The substrate is made the cathode by the application of a dc or RF voltage ranging from –500 to –5000 V. In the resulting substrate cathode glow discharge, atoms and ions are accelerated at high energies to the substrate coating. Dense coatings and excellent adhesion because of the bombardment of highly energetic particles, and

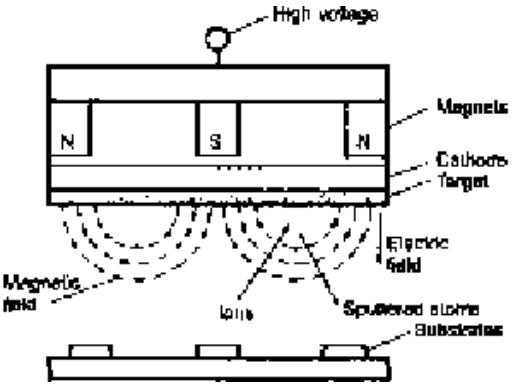

Fig. 22.7 Schematic diagram of magnetron sputtering mechanisms. Source: Ref 22.14

good coverage because of the cathode glow discharge, are important characteristics of coatings produced by ion plating systems.

The diode ion plating systems have been further improved by designs that enhance ionization with ion currents that can be controlled independently of the bias voltage between the evaporative source and the substrate (Ref 22.14). These modified designs are referred to as triode ion plating systems.

In most PVD sputtering and ion plating systems, gases such as nitrogen, methane, or oxygen may be introduced to react with metal atoms generated by sputtering or evaporative source. Such reactive PVD produces metal nitride, carbide, or oxide ceramic coatings.

Physical Vapor Deposition: Microstructures

Coating microstructures produced by PVD processes tend to be quite fine because of extremely rapid effective quench rates. Moreover, coating morphology and adhesion are quite variable, depending on such factors as substrate temperature, pressure of the sputtering gas, and the energy of the incident atoms (Ref 22.32–22.34). The coatings are created by nucleation and growth processes that first involve the adsorption of incident atoms, referred to as adatoms, on a substrate surface. The adatoms then diffuse on the substrate surface to preferred bonding sites such as ledges or vacancies or to growing clusters or nuclei. Three different coating nucleation and growth processes, as reviewed by Rigsbee (Ref 22.32), have been identified: (1) three-dimensional island or Volmer-Weber growth, (2) two-dimensional layer-by-layer or Frank-van der Merwe growth, and (3) initial layer-by-layer growth followed by island growth. This mixed-mode growth is referred to as Stranski-Krastanov growth. The first mode consists of the formation of clusters, the growth of clusters that reach critical size, and

the eventual impingement of the islands to produce a continuous film. Layer growth is typical of systems where adatoms have high surface mobility and bind more strongly to substrate atoms than to each other. The mixed-mode growth may be due to initial epitaxial layer growth terminated by the buildup of residual stresses that eventually produce defect sites for island nucleation and growth.

Two useful diagrams that classify the effects of processing conditions on PVD coating microstructure and morphology have been developed. The first diagram (Fig. 22.8) shows schematically the effect of substrate temperature, T, relative to the melting temperature, T_m, of the coating material. This diagram was developed by Movchan and Demchishin (Ref 22.33) for evaporated metal and oxide coatings. The second diagram (Fig. 22.9) incorporates the effect of sputtering system gas pressure and was

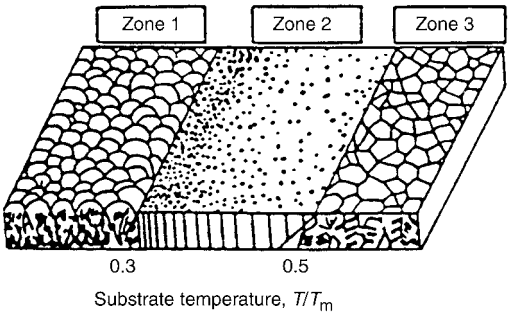

Fig. 22.8 Schematic diagram of structural zone model for coating growth as a function of deposition temperature as proposed by Movchan and Demchishin. Source: Ref 22.33, 22.36

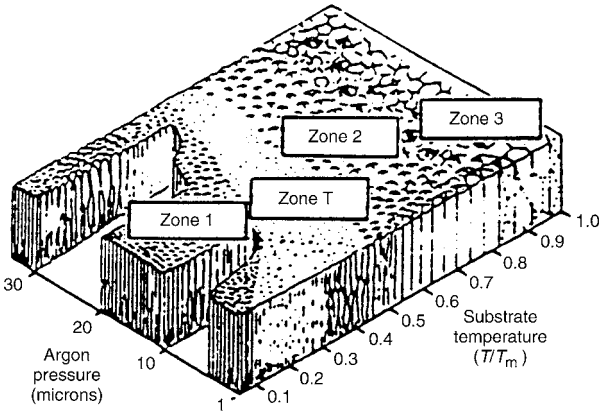

Fig. 22.9 Schematic diagram of structural zone model for coating growth as a function of deposition temperature and argon pressure as proposed by Thornton. Source: Ref 22.34, 22.36

developed for sputtered coatings by Thornton (Ref 22.34, 22.35). The schematic diagrams show that various zones or ranges of operating conditions produce quite different coating morphologies. Recognizing that thermal evaporation and sputtering may produce quite different fine structures within similar microstructures, zone 1 in the Movchan and Demchishin diagram is sometimes referred to as zone 1′ in the Thornton diagram (Ref 22.36).

The coating morphologies that develop in zone 1, at low substrate temperatures, are porous and consist of conical arrays of crystallites that taper from narrow clusters of nucleating crystallites to broader, dome-shaped arrays with increasing film thickness. The rounded tips of these tapered arrays produce relatively rough coating surfaces. The unique tapered morphology is a result of low adatom surface diffusivity at low substrate temperatures (Ref 22.32, 22.36). As a result, relatively few nuclei develop. Those nuclei that do grow effectively shield or shadow intervening areas from incident atoms, and consequently, a high degree of porosity is incorporated between the growing tapered crystallite arrays. Moreover, there is accumulating evidence that the tapered zone microstructures contain a very high density of atomic-scale microvoids and that sputtering produces a more imperfect fine structure than does thermal evaporation (Ref 22.36). Higher argon pressures shift the boundaries of zone 1′ to higher temperatures (Fig. 22.9), because vapor scattering of incident sputtered atoms effectively reduces adatom energy and therefore adatom surface mobility (Ref 22.32, 22.35).

Zone T microstructures, formed at higher substrate temperatures, are denser and the coating surfaces are smoother than zone 1 or zone 1′ microstructures because of increased adatom surface diffusion. These transition microstructures are still very fine and are characterized by columnar growth. Increased substrate surface diffusion and bulk diffusion in the coatings is reflected in zone 2, where coarser, columnar crystals nucleate and grow, and in zone 3, where coarse columnar and even equiaxed grains may grow. Increasing crystal perfection within the growing crystallites and grains accompanies increasing substrate temperatures.

Very high residual stresses develop in zone-1-type PVD coatings and may be either tensile or compressive. Thermal evaporation, a process where the atoms possess thermal energy but relatively low kinetic energy, produces exclusively tensile stresses, while sputtering may produce either tensile or compressive stresses, depending on sputtering conditions (Ref 22.35–22.37). It now appears that the stress state of most sputtered coatings undergoes a transition from tension to compression with decreasing sputtering gas pressure or with increasing sputtering current density at constant pressure. The tensile and compressive stresses are both quite high, on the order of several GPa, and may lead to coating cracking or buckling, respectively (Ref 22.36). The processing and mechanistic reasons for this transition are complex (Ref 22.35–22.37), but the compres-

sive stresses are associated with dense, less columnar coating structures formed by the deposition of highly energetic atoms. Thus, low sputtering gas pressures, which minimize incident atom energy loss by scattering and collisions within the gas phase, favor the formation of dense films and compressive stresses by maintaining high rates of adatom surface diffusion. Likewise, minimizing, by bias sputtering, the content of impurity atoms that limit adatom diffusivity is also beneficial. Thus, processing conditions that produce dense coatings at low substrate temperatures appear to yield the most favorable residual stresses. Deposition at higher substrate temperatures, while producing denser and more perfect coatings as discussed relative to Fig. 22.8 and 22.9, result in coarser microstructures and lower residual stresses.

The most striking application of PVD coatings in ferrous metallurgy is the titanium nitride (TiN) coating of high-speed steels for cutting and machining and tool steels for hot and cold working molds and dies. Many of the commercial PVD processes, dramatic improvements in TiN-coated tool performance, and causes of variability of TiN coatings have been reviewed by Matthews (Ref 22.38). The coatings produced by the various processes range from less than 1 μm to as thick as 6 μm and give the tools a uniform gold color. Deposition temperatures are 500 °C (930 °F) or lower. Hardness of the coatings increases with nitrogen content, with a peak hardness associated with off-stoichiometric compositions of approximately 40 at.% N (Ref 22.39). Typical hardness of commercial TiN coatings is approximately 2500 HV compared with the typical hardness of hardened tool steels of approximately 800 HV (Ref 22.39). Thus, significant improvements in wear resistance are possible with properly applied coatings.

Figures 22.10 to 22.12 show examples of PVD metal nitride coatings that have been deposited on high-speed steel and type 304 stainless steel

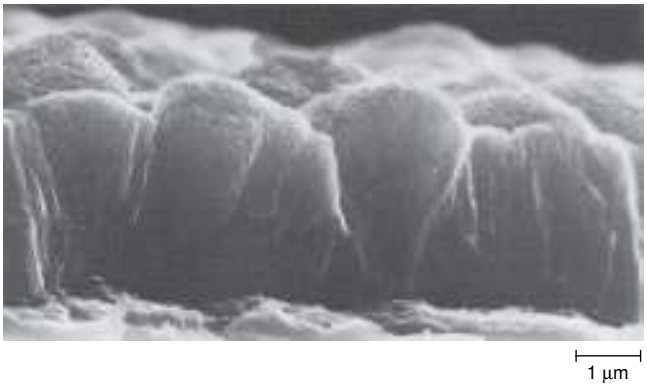

Fig. 22.10 $(Ti_{33}Al_{17})N$ coating deposited by triode ion plating at low substrate current density. Scanning electron micrograph. Courtesy of A.S. Korhonen, Helsinki University of Technology. Source: Ref 22.40, 22.41

Fig. 22.11 $(Ti,Al)N$ coating deposited by triode ion plating at high substrate current density. Courtesy of A.S. Korhonen, Helsinki University of Technology. Source: Ref 22.40, 22.41

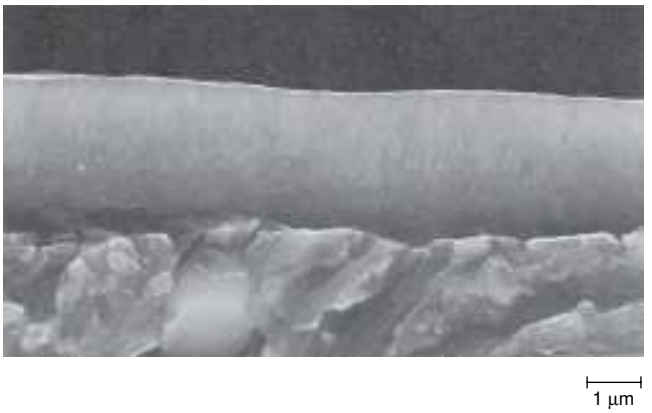

Fig. 22.12 ZrN coating deposited by triode ion plating. Scanning electron micrograph. Courtesy of A.S. Korhonen, Helsinki University of Technology. Source: Ref 22.40, 22.41

substrates by reactive triode ion plating (Ref 22.39–22.41). The metal atoms were evaporated into a chamber with an atmosphere of nitrogen and argon by heating suitable metal targets with an electron beam gun. The substrates were biased negatively, and a glow discharge was created and controlled with heated tungsten filaments. The coatings are between 2 and 3 μm thick, and fracture cross sections of the coatings and adjacent underlying substrates are shown. Figure 22.10 shows a typical zone 1 microstructure of a $(Ti_{33}Al_{17})N$ coating. The crystallite arrays are tapered with rounded tops, and the coating surface is relatively rough. As discussed previously, increasing the substrate current density while holding all other processing parameters constant (Ref 22.41) produces a much denser, smoother (Ti,Al)N coating (Fig. 22.11). The latter coating consists of two

layers. The surface layer structure is columnar, while the layer adjacent to the substrate has a virtually featureless fracture surface. Figure 22.12 shows a zirconium nitride (ZrN) coating that is very smooth and almost featureless within the resolution of the scanning electron microscope. High-resolution transmission electron microscopy shows that the structure of the ZrN coating consists of very fine columnar grains, 30 to 60 nm (300 to 600 Å) in diameter and approximately 200 nm (2000 Å) long (Ref 22.41). Tests of cutting performance ranked ZrN, (Ti,Al)N, and TiN coatings in order of decreasing performance (Ref 22.40).

Chemical Vapor Deposition

Chemical vapor deposition (CVD) is a coating process in which all reactants are gases. A chemical reaction takes place in the vapor phase adjacent to or on a substrate, depositing the reaction products on the substrate. An example of a CVD process is the deposition of tungsten according to the following reaction (Ref 22.42):

$$WF_6(\text{vapor}) + 3H_2(\text{gas}) \xrightarrow{\text{Heated substrate}} W(\text{deposit}) + 6HF(\text{gas})$$

Usually the substrate must be heated to thermally activate the reaction.

Chemical vapor deposition is used to apply metal and ceramic compound coatings for a variety of electronic, corrosion protection, oxidation-resistant, heat-resistant, and machining applications (Ref 22.42, 22.43). The throwing power or ability to cover complex shapes by CVD is good compared with some of the line-of-sight PVD processes, but the chemicals used may be quite toxic.

The CVD technique has been used to coat cemented carbides and tool steels for machining applications. A pertinent study (Ref 22.44) has evaluated wear and failure of ceramic CVD coatings applied to cemented carbide tools used to machine stainless steels. The coatings consisted of various amounts of Al_2O_3, ZrO_2, TiC, and TiN and ranged in hardness from 1540 to 1850 HV. Commonly used TiN CVD coatings are produced by the reaction of titanium tetrachloride and ammonia substrates heated to approximately 1000 °C (1830 °F) (Ref 22.45). As a result of the high substrate temperatures, CVD-coated tools must be hardened after coating, a sequence of operations that produces some distortion. In contrast, PVD coatings, as described in the previous section, are applied to hardened tools at 500 °C (930 °F), and the coated parts need not be heat treated subsequent to deposition.

Salt Bath Coating Process

Hard alloy carbide, nitride, and carbonitride coatings can be applied to steels by means of salt bath processing. One such technique, the Toy-

ota Diffusion (TD) coating process, uses molten borax with additions of carbide-forming elements, such as vanadium, niobium, titanium, or chromium, which combine with carbon from the substrate steel to produce alloy carbide layers (Ref 22.46–22.49). The growth of the layers is therefore dependent on carbon diffusion, and the process requires a relatively high temperature, from 800 to 1250 °C (1472 to 2282 °F), to maintain adequate coating rates. Carbide coating thicknesses of 4 to 7 μm are produced in 10 min to 8 h, depending on bath temperature and type of steel, and coating hardnesses over 3000 HV have been reported for VC and NbC layers (Ref 22.48). The coated steels may be cooled and reheated for hardening, or the bath temperature may be selected to correspond to the steel austenitizing temperature, permitting the steel to be quenched directly after coating. To lower salt bath deposition temperatures, techniques to produce alloy carbonitride coatings have been developed (Ref 22.49). Such coatings are applied to hardened and nitrided steels in vanadium-containing chloride baths at temperatures of 550 to 600 °C (1022 to 1112 °F).

Figure 22.13 shows examples of salt-bath-applied coatings. The NbC coating (Fig. 22.13a) was produced on a martensitic stainless steel (14% Cr, 1.5% C, 0.6% Mo, 0.4% Co) by immersion for 4 h in a borax bath containing 20% ferro-niobium. The NbC-coated steel was air cooled after coating and then reheated to 1060 °C (1940 °F) for hardening. The Cr(C,N) coating (Fig. 22.13b) was produced by immersion of a previously hardened and nitrided (austenitized at 850 °C, or 1562 °F; tempered at 600 °C, or 1112 °F; and nitrided at 570 °C, or 1058 °F) AISI 1045 steel in a chloride bath containing 15% Cr at 570 °C (1058 °F). At the latter temperatures, carbide growth is negligible, and the growth rate of coatings is accelerated by salt treatment of nitrided steels. This approach produces a coating layer and a diffusion layer, as shown in Fig. 22.13(b).

The salt bath coating methods produce hard coatings for applications similar to those for which CVD and PVD coatings are considered. In par-

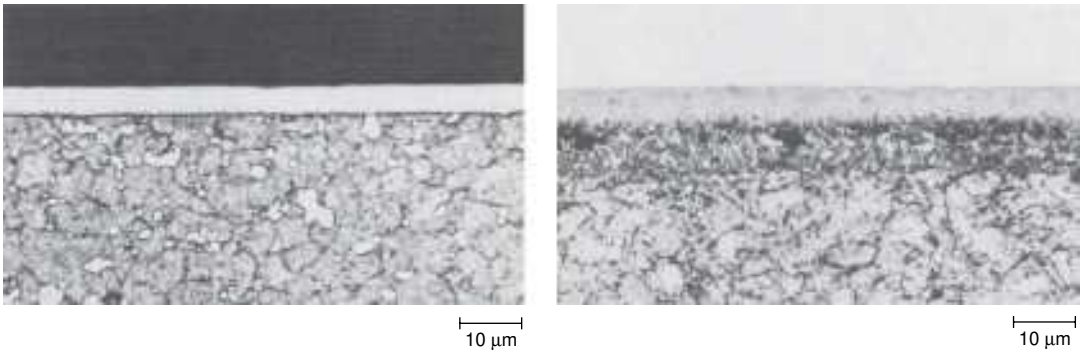

Fig. 22.13 (a) NbC coating deposited on a martensitic stainless steel by a salt bath process. (b) Chromium carbonitride coating deposited on nitrided AISI 1045 steel by a salt bath process. Light micrographs. Courtesy of T. Arai, Toyota Research Laboratories

ticular, the TD coatings have significantly improved the life of mold and die steels for sheet steel stamping, aluminum die casting, and cold forging and extrusion.

Laser and Electron Beam Surface Modification

Laser and electron beams provide very high energy, directed sources of heat, and are used for many surface-modification techniques. Depending on power input, high-energy beams may be used for cutting and welding, surface melting and alloying, and localized surface heat treatment (Ref 22.7, 22.8, 22.10). Welding and cutting require the highest power, and the ability to focus laser and electron beams makes possible very deep, narrow welds of high quality. This technology is highly developed and has followed the continuous development of high-energy density power sources (Ref 22.8, 22.10). Of the laser and electron beam surface-modification techniques, localized surface heat treatment is the most highly developed and commercially applied. Surface melting and alloying, accompanied by very rapid solidification rates, offer unique opportunities for surface modification and now constitute a highly active field of research and development (Ref 22.7).

Heating by laser and electron beams is accomplished by photon interactions of the incident radiation with the electronic structures of the substrate material. The incident energy is very rapidly converted into heat just below the surface, on the order of a few tens of nanometers for laser light and a few micrometers for electron beams, depending on the accelerating voltage, which generally varies between 10 and 100 keV (Ref 22.26, 22.50). Electron beam treatments must be conducted in vacuum, but laser light is not subject to this constraint and therefore offers considerable flexibility in manufacturing operations.

The term *laser* stands for light amplification by stimulated emission of radiation, and three different types of lasers have been developed: Nd:YAG (neodymium dissolved in yttrium aluminum garnet), CO_2, and excimer. An excellent review of the operation and characteristics of the various types of lasers is presented by Bass (Ref 22.50). The Nd:YAG lasers operate at wavelengths of 1.06 μm and are widely used for welding and drilling applications. The CO_2 lasers have the highest power commercially available and operate in the infrared range, frequently at a wavelength of 10.6 μm, while the more recently developed excimer lasers operate at wavelengths in the near-ultraviolet range, between 0.193 and 0.351 μm. Laser light may be reflected, depending on material and wavelength. Therefore, for effective laser heating, wavelengths that are absorbed by the workpiece must be selected, or the irradiated workpiece must be coated with a light-absorbing material.

Laser surface heat treatment is widely used to harden localized areas of steel and cast iron machine components (Ref 22.51). The heat generated

by the absorption of the laser light is controlled to prevent melting and therefore is used to selectively austenitize local surface regions that transform to martensite as a result of rapid cooling by the conduction of heat into the bulk of the workpiece. This process is sometimes referred to as laser transformation hardening to differentiate it from laser surface melting phenomena. There is no chemistry change produced by laser surface heat treatment, and laser heating presents, in addition to induction and flame hardening, an effective processing technique to selectively harden ferrous materials.

Laser heat treatment produces thin surface zones that are heated and cooled very rapidly, resulting in very fine martensitic microstructures, even in steels with relatively low hardenability. High hardness and good wear resistance with less distortion result from this process. The laser can be located at some distance from the workpieces, unlike induction and flame heating, and the laser light is reflected by mirrors to the focusing lens where the width of the heated spot or track is controlled (Ref 22.50, 22.51).

Molian (Ref 22.51) has tabulated the characteristics of 50 applications of laser transformation hardening. The materials hardened include plain carbon steels (1040, 1050, 1070), alloy steels (4340, 52100), tool steels, and cast irons (gray, malleable, ductile). The energy-absorbing coatings are listed, and typical case depths for steels are 250 to 750 μm and for cast irons approximately 1000 μm. The flexibility of laser delivery systems, low distortion, and high surface hardness have made lasers very effective in selective hardening of wear- and fatigue-prone areas on irregularly shaped machine components such as camshafts and crankshafts (Ref 22.50). Electron beams, similar to laser heat treatment, are also used to harden the surfaces of steels. The processing considerations, microstructures, and property changes produced by electron beam hardening of steel have been reviewed by Zenker et al. (Ref 22.52).

A completely different spectrum of surface modifications results when lasers and electron beams are used to melt the surface of a material. Figure 22.14 shows this process schematically (Ref 22.26, 22.53). Differences in energy absorption of electron (e) and laser (V) beams are shown qualitatively in the top illustration, and the melting and resolidification of the surface layers are shown in the bottom illustrations. Heating may be extremely rapid, on the order of nanoseconds, and cooling, accomplished by thermal conduction into the unheated mass of the substrate, is similarly very rapid. Exact rates of heating and cooling are dependent on many factors, such as power input, time of irradiation, laser pulsing, and surface and bulk characteristics of the heated substrate (Ref 22.53, 22.54). The very high heating and cooling rates attainable (10^8 to 10^{10} °C/s) produce extremely rapid solidification and therefore make possible very fine nonequilibrium microstructures. In the extreme, new metastable crystalline phases, glassy or amorphous structures, or highly supersaturated phases

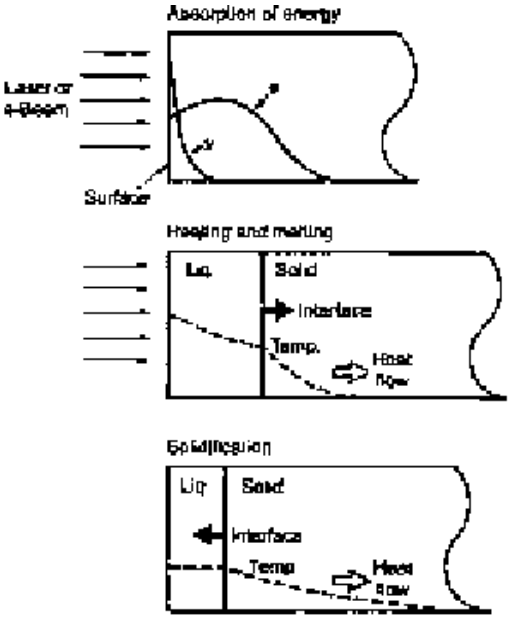

Fig. 22.14 Schematic diagram of the effects of laser- and electron beam heating, melting, and solidification. Source: Ref 22.53

may be developed in rapidly cooled surface layers. The various degrees of equilibrium possible in materials systems have been characterized by Perepezko and Boettinger (Ref 22.55) (Table 22.1). True equilibrium, where coexisting phases have uniform compositions according to the equilibrium phase diagrams, is achieved only by high-temperature, long-time annealing or by very slow cooling. During rapid cooling, equilibrium may be attained only at the interfaces between stable or metastable phases, and in the extreme even such local equilibrium breaks down, greatly modifying or suppressing phase transformations dependent on diffusion. Thus, many new microstructures with unique properties may be produced by rapidly solidified surface-melted alloys.

Laser surface alloying incorporates laser surface melting and cooling, as just described, but in addition changes composition to effect changes in surface structure and properties. The alloying may be accomplished by producing a surface layer of chemistry different from the substrate by another surface-modification technique prior to laser melting or by injecting powders into the laser-melted zone (Ref 22.55).

When the object of laser treatment, either by direct laser melting or by laser surface alloying, is to produce an amorphous or glassy layer, that process is referred to as laser glazing. Glass formation in Si, Pd-Cu-Si, and Fe-Ni-P-B alloys is readily accomplished but is much more difficult in metals and alloys. For example, a study (Ref 22.56) of laser glazing of iron and tool steels, which had been pack boronized prior to laser glazing

to promote amorphization, did not produce evidence of amorphous structures. Apparently, nucleation of crystalline phases occurs too readily at the interface of the molten layer and the unmolten substrate crystal structure. Nevertheless, the laser surface alloying produced layers of very high hardness (2100 HV), containing very fine boride particles, on the tool steels. Cracking and porosity were problems sometimes encountered in the laser glazing study.

The dramatic changes in surface microstructure produced by laser surface melting of M42 high-speed tool steel are shown in Fig. 22.15 and 22.16 (Ref 22.57). The M42 steel contains nominally 1% C, 8% Co, 1.5% W, 1.1% V, 3.75% Cr, and 9.5% Mo and because of the high content of

Table 22.1 Hierarchy of equilibrium

I. Full diffusional (global) equilibrium
A. No chemical potential gradients (compositions of phases are uniform)
B. No temperature gradients
C. Lever rule applicable
II. Local interfacial equilibrium
A. Phase diagram gives compositions and temperature only at liquid-solid interface
B. Includes corrections made for interface curvature (Gibbs-Thomson effect)
III. Metastable local interfacial equilibrium
A. Relevant if stable phase cannot nucleate or grow sufficiently fast
B. Interface conditions given by a metastable phase diagram that is a true thermodynamic phase diagram constrained to be missing the stable phase or phases
C. Also relevant if phases are constrained by elastic stresses
IV. Interfacial nonequilibrium
A. Phase diagram fails to give temperature and compositions at interface
B. Chemical potentials are not equal at interface
C. Free-energy functions of phases useful to yield criteria for the impossible

Source: Ref 22.55

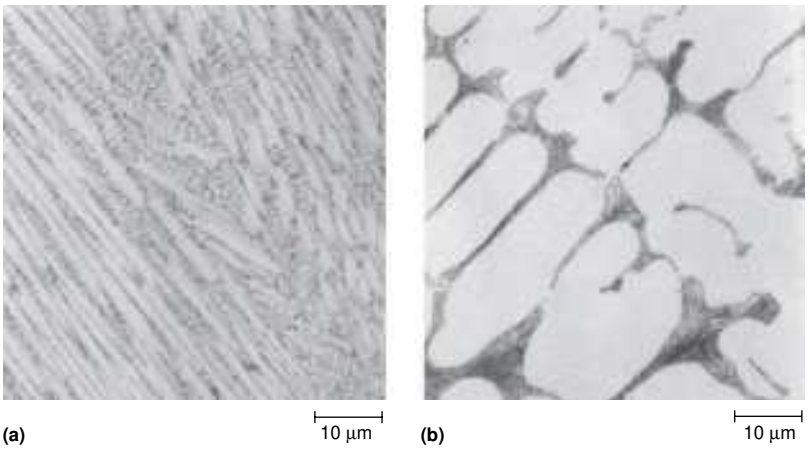

Fig. 22.15 (a) Laser-melted dendritic structure of M42 tool steel. (b) Chill-cast dendritic structure of M42 steel. Light micrographs. Courtesy of T. Bell, University of Birmingham. Source: Ref 22.57

carbide-forming elements, the wrought microstructure contains a high volume fraction of coarse primary carbides. Figure 22.15 shows the considerable refinement of the microstructure of laser-melted M42 relative to chill-cast M42 and shows the absence of primary carbides in the laser melt zone. Dissolution of the carbides was a function of traverse speed, and at higher speeds, carbides were not dissolved. Figure 22.16 shows the laser-melted surface and melting around primary carbides in the matrix below the fine solidification structure of the melt zone. Melting of the carbides is due to a low-melting eutectic reaction. The laser-melted surface layer, produced by slow traverse speeds, apparently because of greater solution of alloying elements for subsequent carbide precipitation, showed much higher peak hardness after triple tempering than conventionally treated steel.

Summary

This chapter has briefly reviewed a number of the newer, high-technology surface-modification treatments that are beginning to be applied to ferrous alloys. Process principles, terminology, coating characteristics, and examples of application have been described in order to provide a comparison of the various techniques. For more information regarding the equipment and processing details, applications, or theoretical aspects of the deposition process, the reader is referred to the references cited throughout the text. That literature is only a sampling and is certain to grow at an increasing rate in view of the very active interdisciplinary research and development now in progress regarding surface-modification techniques of all types.

A number of surface-modification processes, in various stages of maturity and growth, have not been discussed. These processes have evolved somewhat removed from traditional heat treatment and include such pro-

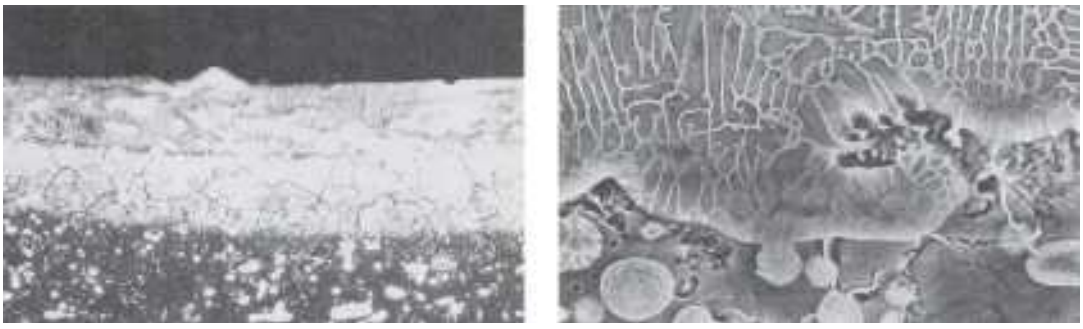

Fig. 22.16 (a) Laser-melted surface layer on M42 tool steel. (b) Higher-magnification view of (a) showing partial melting of carbides at melt interface. Light micrographs. Courtesy of T. Bell, University of Birmingham. Source: Ref 22.57

cesses as electrodeposition, hot dipping, cementation, cladding, thermal spraying, and hardfacing. Each of the processes has a highly developed technology and may be useful in solving a given wear, corrosion, or high-temperature oxidation problem.

Many of the newer surface-modification processes are only now being applied to ferrous alloys. Plasma nitriding, laser hardening of machine components, and PVD coating of cutting tools and dies appear to be the most widely applied at this time. Paralleling the electronics industry, the first applications are to high-value or critical components where the increased costs of higher technology are justified by higher quality and improved performance. Nevertheless, applications of the newer techniques to low-carbon sheet steels are in progress. For example, large-scale, high-deposition-rate electron beam evaporation of aluminum on strip steel has been used to produce aluminum-coated steel with corrosion characteristics comparable to tin plate (Ref 22.58).

The future should see much wider application to a great variety of structural applications. For optimum application and economy of any surface-modification technique, it should be incorporated at the start into the mechanical and materials design and manufacturing sequence of a given component.

REFERENCES

22.1 L.I. Maissel and R. Glang, Ed., *Handbook of Thin Film Technology,* McGraw-Hill, 1970

22.2 T. Bell, A. Bloyce, and J. Lanagan, Surface Engineering of Light Metals, *Heat Treatment and Surface Engineering,* G. Krauss, Ed., ASM International, 1988, p 1–7

22.3 T. Bell, Ed., *Surface Engineering,* Institute of Metals/Wolfson Institute for Surface Engineering, in association with the Surface Engineering Society, London, England

22.4 A. Matthews, Y. Pauleau, and W.D. Sproul, Ed., *Surface and Coatings Technology,* Elsevier Science, New York

22.5 T. Spalvins, Ed., *Ion Nitriding,* ASM International, 1987

22.6 *Plasma Heat Treatment, Science and Technology,* PYC Edition, Paris, 1987

22.7 L.E. Rehn, S.T. Picraux, and H. Wiedersich, Ed., *Surface Alloying by Ion, Electron and Laser Beams,* ASM International, 1987

22.8 Y. Arata, *Plasma, Electron and Laser Beam Technology,* American Society for Metals, 1986

22.9 R.F. Hochman, Ed., *Ion Plating and Implantation,* American Society for Metals, 1986

22.10 E.A. Metzbower and D. Hauser, *Power Beam Processing, Electron, Laser, Plasma-Arc,* ASM International, 1988

22.11 K.N. Strafford, P.K. Datta, and C.G. Googan, Ed., *Coating and Surface Treatment for Corrosion and Wear Resistance,* Ellis Harwood Ltd., Chichester, U.K., 1984
22.12 R.D. Sisson, Jr., Ed., *Surface Modifications and Coatings,* American Society for Metals, 1986
22.13 K.H. Jack, The Occurrence and the Crystal Structure of Iron Nitride; A New Type of Interstitial Alloy Formed during Tempering of Nitrogen-Martensite, *Proc. R. Soc. A,* Vol 208, 1951, p 216–224
22.14 T. Spalvins, Plasma Assisted Surface Coating/Modification Processes: An Emerging Technology, *Ion Nitriding,* T. Spalvins, Ed., ASM International, 1987, p 1–8
22.15 B. Edenhofer, Physical and Metallurgical Aspects of Ionitriding, *Heat Treat. Met.,* Vol 1 (No. 1), 1974, p 23–28
22.16 T. Bell and P.A. Dearnley, Plasma Surface Engineering, *Plasma Heat Treatment, Science and Technology,* PYC Edition, 1987, p 13–53
22.17 B. Edenhofer, M.H. Jacobs, and J.N. George, Industrial Processes, Applications and Benefits of Plasma Heat Treatment, *Plasma Heat Treatment, Science and Technology,* PYC Edition, 1987, p 399–415
22.18 J.P. Lebrun, Technical Developments and Industrial Applications of Ion Nitriding, *Plasma Heat Treatment, Science and Technology,* PYC Edition, 1987, p 425–444
22.19 H. Michael, M. Foos, and M. Gantois, Metallurgical Characterization of Plasma Induced Epsilon-Iron Carbonitride Layers, *Ion Nitriding,* T. Spalvins, Ed., ASM International, 1987, p 117–125
22.20 W.L. Grube and J.G. Gay, High-Rate Carburizing in a Glow-Discharge Methane Plasma, *Metall. Trans. A,* Vol 91, 1978, p 1421–1429
22.21 A.C. Dexter, T. Farrell, M.I. Lees, and B.J. Taylor, The Physical and Chemical Processes of Vacuum and Glow Discharge Carburizing, *Plasma Heat Treatment, Science and Technology,* PYC Edition, 1987, p 58–71
22.22 J. Pacheco, "Fatigue Resistance of Plasma and Gas Carburized SAE 8719 Steel," M.S. thesis T-3750, Colorado School of Mines, Golden, CO, 1988; and J. Pacheco and G. Krauss, in *Carburizing, Processing and Performance,* ASM International, 1989, p 227–238
22.23 D.H. Herring, *Vacuum Heat Treatment: Principles, Practices, and Applications,* BNP Media II, LLC, Troy, MI, 2012
22.24 R.F. Hochman, Surface Modification by Ion Processes—An Engineering Technology, *Ion Plating and Implantation,* R.F. Hochman, Ed., American Society for Metals, 1986, p 1–6
22.25 G. Dearnaley, Ion Implantation and Ion Assisted Coatings for Wear Resistance in Metals, *Surf. Eng.,* Vol 2, 1986, p 213–221

22.26 L.E. Rehn, S.T. Picraux, and H. Wiedersich, Overview of Surface Alloying by Ion, Electron and Laser Beams, *Surface Alloying by Ion, Electron and Laser Beams,* ASM International, 1987, p 1–17
22.27 J.K. Hirvonen, The Industrial Applications of Ion Beam Processes, *Surface Alloying by Ion, Electron and Laser Beams,* L.E. Rehn, S.T. Picraux, and H. Wiedersich, Ed., ASM International, 1987, p 373–388
22.28 D.L. Williamson, F.M. Kustas, and D.F. Fobare, Mossbauer Study of Ti-Implanted 52100 Steel, *J. Appl. Phys.,* Vol 60, 1986, p 1493–1500
22.29 F.M. Kustas, M.S. Misra, and D.L. Williamson, Microstructural Characterization of Nitrogen Implanted 440C Steel, *Nucl. Instrum. Methods Phys. Res. B,* Vol 31, North-Holland, 1988, p 393–401
22.30 F.M. Kustas, M.S. Misra, and P. Sioshansi, Effects of Ion Implantation on the Rolling Contact Fatigue of 440C Stainless Steel, *Ion Implantation and Ion Beam Processing of Materials,* G.K. Hubler, O.W. Holland, and C.R. Clayton, Ed., MRS Symposia Proceedings, Vol 27, 1984, p 675–690
22.31 J.K. Hirvonen, Applications of Ion Beam Mixing, *Ion Plating and Implantation,* R.F. Hochman, Ed., American Society for Metals, 1986, p 49–53
22.32 J.M. Rigsbee, Physical Vapor Deposition, *Surface Modification Engineering,* R.P. Kossowsky, Ed., CRC Press, Boca Raton, FL, 1989, p 231–255
22.33 B.A. Movchan and A.V. Demchishin, Study of the Structure and Properties of Thick Vacuum Condensates of Nickel, Titanium, Tungsten, Aluminum Oxide and Zirconium Oxide, *Fiz. Met. Metalloved.,* Vol 28, 1969, p 653
22.34 J.A. Thornton, High Rate Thick Film Growth, *Ann. Rev. Mater. Sci.,* 1977, p 239–260
22.35 J.A. Thornton, The Microstructure of Sputter-Deposited Coatings, *J. Vac. Sci. Technol. A,* Vol 4, 1986, p 3059–3065
22.36 D.W. Hoffman and R.C. McCune, Microstructural Control of Plasma-Sputtered Refractory Coatings, *Plasma-Based Processing,* J.J. Cuomo, S.M. Rossnagel, and W.D. Westwood, Ed., Noyes, Park Ride, NJ, 1989
22.37 D.W. Hoffman, Fine Tuning the Structures and Properties of Thin Films, *Proceedings of the Joint Symposium of the Chinese and American Vacuum Societies,* Sept 8–10, 1987 (Beijing)
22.38 A. Matthews, Titanium Nitride PVD Coating Technology, *Surf. Eng.,* Vol 1, 1987, p 93–103
22.39 A.S. Korhonen, J.M. Molarius, S. Osenius, and M.S. Sulonen, Ion Plasting of Tools and Dies, *Tool Materials for Molds and Dies,* G. Krauss and H. Nordberg, Ed., Colorado School of Mines Press, Golden, CO, p 217–230

22.40 J.M. Molarius, A.S. Korhonen, E. Harju, and R. Lappalainen, Comparison of Cutting Performance of Ion-Plated NbN, ZrN, TiN, and (Ti,Al)N Coatings, *Surf. Coat. Technol.,* Vol 33, 1987, p 117–131

22.41 I. Penttinen, J.M. Molarius, A.S. Korhonen, and R. Lappalainen, Structure and Composition of ZrN and (Ti,Al)N Coatings, *J. Vac. Sci. Technol. A,* Vol 6, 1988, p 2158–2161

22.42 R.F. Bunshah, Deposition Technologies: An Overview, *Deposition Technologies for Films and Coatings,* R.F. Bunshah et al., Ed., Noyes, Park Ride, NJ, 1982, p 1–16

22.43 A. Kolb-Telieps, Introduction to Surface Engineering for Corrosion Protection, *Surf. Eng.,* Vol 2, 1986, p 203–212

22.44 P.A. Dearnley and V. Thompson, Evaluation of Failure Mechanisms of Ceramics and Coated Carbides Used for Machining Stainless Steels, *Surf. Eng.,* Vol 2, 1986, p 191–202

22.45 M.H. Jacobs, "Process and Engineering Benefits of Sputter Ion Plated Titanium Nitride Coatings," Paper 8512-010, 1985 International Conference on Surface Modifications and Coatings (Toronto), American Society for Metals, 1985

22.46 T. Arai, Carbide Coating Process by Use of Molten Borax Bath in Japan, *J. Heat Treat.,* Vol 1 (No. 2), 1979, p 15–22

22.47 T. Arai, H. Fujita, Y. Sugimoto, and Y. Ohta, Diffusion Carbide Coatings Formed in Molten Borax Systems, *J. Mater. Eng.,* Vol 9, 1987, p 183–189

22.48 T. Arai, Carbide Coating Process by Use of Molten Borax Bath, *Wire,* July 31, 1981, p 102–104, 208–210

22.49 T. Arai, H. Fujita, Y. Sugimoto, Y. Ohta, Vanadium Carbonitride Coating by Immersing into Low Temperature Salt Bath, *Heat Treatment and Surface Engineering,* G. Krauss, Ed., ASM International, 1988, p 49–53

22.50 M. Bass, Lasers and Electron Beams, *Surface Alloying by Ion, Electron and Laser Beams,* L.E. Rehn, S.T. Picraux, and H. Wiedersich, Ed., ASM International, 1987, p 357–372

22.51 P.A. Molian, Engineering Applications and Analysis of Hardening Data for Laser Heat Treated Ferrous Alloys, *Surf. Eng.,* Vol 2, 1986, p 19–28

22.52 R. Zenker and M. Mueller, Electron Beam Hardening, Part I: Principles, Process Technology and Properties, *Heat Treat. Met.,* Vol 15 (No. 4), 1988, p 79–88; and R. Zenker, W. John, D. Rathjen, and G. Fritsche, Electron Beam Hardening, Part 2: Influence on Microstructure and Properties, *Heat Treat. Met.,* Vol 16 (No. 2), 1989, p 43–51

22.53 D.M. Follstaedt and S.T. Picraux, Microstructures of Surface-Melted Alloys, *Surface Alloying by Ion, Electron and Laser Beams,*

L.E. Rehn, S.T. Picraux, and H. Wiedersich, Ed., ASM International, 1987, p 175–221

22.54 C.W. White and M.J. Aziz, Energy Deposition, Heat Flow and Rapid Solidification during Pulsed-Laser and Electron Beam Irradiation of Materials, *Surface Alloying by Ion, Electron and Laser Beams,* L.E. Rehn, S.T. Picraux, and H. Wiedersich, Ed., ASM International, 1987, p 19–50

22.55 J.H. Perepezko and W.J. Boettinger, Kinetics of Resolidification, *Surface Alloying by Ion, Electron, and Laser Beams,* L.E. Rehn, S.T. Picraux, and H. Wiedersich, Ed., ASM International, 1987, p 51–90

22.56 P.A. Molian and H.S. Rajasekhara, Laser Glazing of Boronized Iron and Tool Steels, *Surf. Eng.,* Vol 2, 1986, p 269–276

22.57 T. Bell, I.M. Hancock, and A. Bloyce, Laser Surface Treatment of Tool Steels, *Tool Materials for Molds and Dies,* G. Krauss and H. Nordberg, Ed., Colorado School of Mines Press, Golden, CO, 1987, p 197–216

22.58 S. Schiller, G. Beister, M. Neumann, and G. Jaesch, Vacuum Coating of Large Areas, *Thin Solid Films,* Vol 96, 1982, p 199–216

CHAPTER 23

Stainless Steels

STAINLESS STEELS are a large group of special alloys developed primarily to withstand corrosion. Other desirable features may include excellent formability, high room-temperature and cryogenic toughness, and good resistance to scaling, oxidation, and creep at elevated temperatures. Chromium is the alloying element that imparts corrosion resistance to stainless steels, but many other elements may be added to stabilize other phases, provide added corrosion resistance, or produce enhanced mechanical properties. Austenitic, ferritic, and duplex stainless steels cannot be hardened by heat treatment, and therefore, alloying and thermomechanical processing are designed to minimize the formation of phases detrimental to corrosion resistance or toughness. In austenitic stainless steels, strength is also developed by cold work and strain-induced martensite formation. Martensitic stainless steels can be heat treated by quench and tempering to high hardness and strength. Precipitation-hardening grades of stainless steel have also been developed. This chapter describes alloy design, microstructure, and thermomechanical processing used for optimum performance of the various classes of stainless steels.

Alloy Design and Phase Equilibria

Chromium in excess of 12% by weight is required to impart "stainless" characteristics to iron alloys. Enhanced corrosion resistance relative to other steels is attributed to the ability of chromium to produce tightly adherent oxide layers on stainless steel surfaces. The layer is very thin, on the order of only a few atom layers in thickness, and effectively protects or passivates stainless steels in many corrosive environments (Ref 23.1, 23.2). Thus, all stainless steels contain large amounts of chromium, and an important starting place to understand the phase relationships and microstructures in stainless steels is the iron-chromium (Fe-Cr) equilibrium phase diagram.

Figure 23.1 shows the iron-chromium equilibrium phase diagram. As in the iron-carbon system, the allotropic forms of iron constitute the iron end of the diagram. Chromium is an element that stabilizes the body-centered cubic (bcc) ferrite structure of iron; therefore, with increasing chromium content the high-temperature and low-temperature delta and alpha ferrite fields expand. At approximately 12% Cr, bcc ferrite is completely stable from room temperature up to the melting point. As the ferrite field expands, the austenite field contracts, producing what is often referred to as the gamma (γ) loop. Figure 23.2 shows that other ferrite-stabilizing elements such as vanadium and molybdenum act similarly to chromium when alloyed with iron and also form gamma loops.

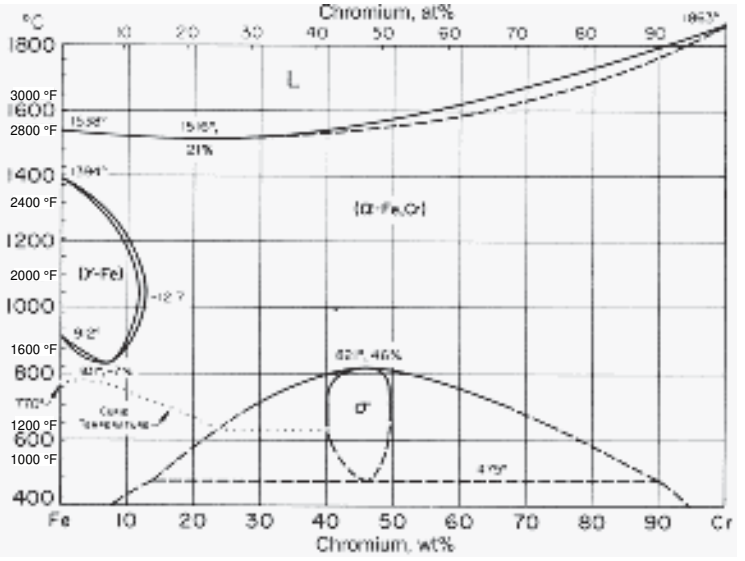

Fig. 23.1 The iron-chromium phase diagram. Source: Ref 23.3

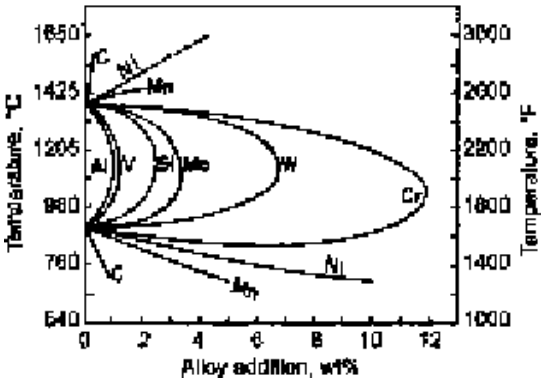

Fig. 23.2 Gamma loops formed in various binary systems of iron. Source: Ref 23.4

The iron-chromium diagram directly produces the basis for martensitic and ferritic stainless steels. The martensitic stainless steels must be able to form austenite, which will transform to martensite on cooling. Therefore, the compositions of martensitic stainless steels must lie within the gamma loop (as expanded by other alloying elements) and contain sufficient chromium to impart stainless corrosion behavior. Ferritic stainless steels are alloyed with much higher amounts of chromium than martensitic stainless steels; therefore, ferrite is stable at all temperatures, as shown in Fig. 23.1. Martensitic and ferritic stainless steels contain alloying elements other than chromium; the effects of these elements are discussed in following sections.

Next to chromium, nickel is the alloying element that most strongly influences alloy design of certain classes of stainless steels. Nickel stabilizes the face-centered cubic (fcc) structure of iron and therefore expands the austenite or gamma phase field when alloyed with iron. The iron-nickel (Fe-Ni) equilibrium phase diagram (Fig. 23.3) shows that with sufficient nickel, austenite is stable at all temperatures above room temperature. In binary iron-nickel alloys, approximately 30 wt% Ni is required to completely stabilize austenite, partly because close to room temperature the diffusion of iron and nickel is too sluggish to form a mixture of ferrite and

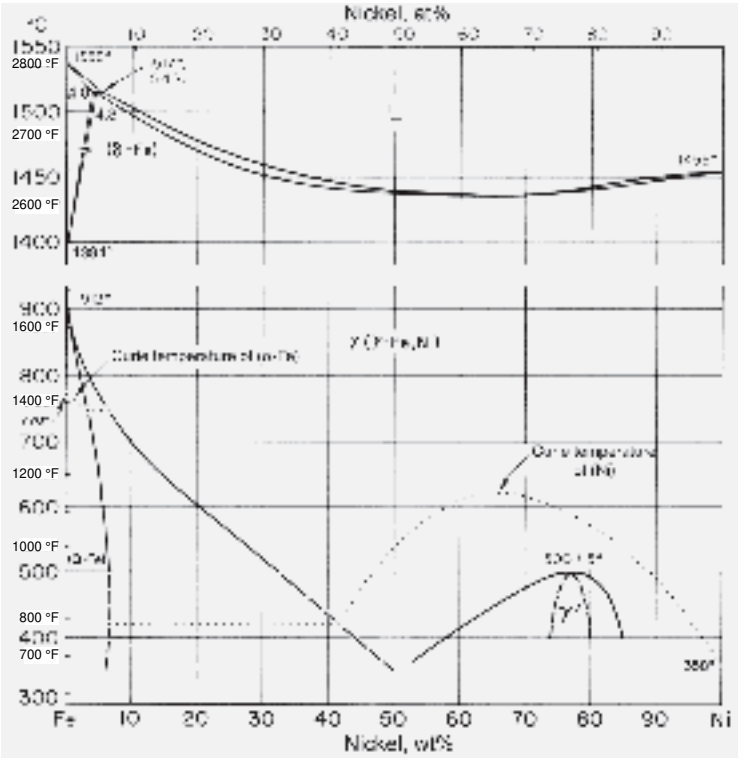

Fig. 23.3 The iron-nickel phase diagram. Source: Ref 23.3

austenite. However, if chromium is also present, in amounts sufficient for stainless corrosion behavior, much less nickel is required to stabilize austenite. Thus, alloys containing typically 18 wt% Cr and 8 wt% Ni are fully austenitic from well below room temperature to melting temperatures. The latter types of steels constitute the very important group of alloys designated as austenitic stainless steels.

Almost all stainless steels have three or more components, and therefore, their phase relationships as a function of temperature and composition are represented by ternary phase diagrams. In the case of systems with more than three components, diagrams that combine the various austenite- and ferrite-stabilizing elements are established, and the phases present at room temperature are related to the two groups of alloying elements. Frequently, vertical sections through ternary systems, in which the amount of a given component is held constant, are used to establish hot working and heat treatment schedules. For example, Fig. 24.4(b) in Chapter 24, "Tool Steels," in this book shows a vertical section through the Fe-C-Cr system at 13% Cr. This vertical section is therefore useful in rationalizing the microstructures of martensitic stainless steels as a function of carbon content and temperature.

Figure 23.4 shows projections of liquidus and solidus surfaces of the Fe-Ni-Cr system for the composition ranges of interest to stainless steels, and Fig. 23.5 shows vertical sections at various constant iron contents through the same systems. Alloys rich in chromium solidify as ferrite, and alloys rich in nickel solidify as austenite. However, many stainless Fe-Ni-Cr alloys solidify as two-phase, austenite-ferrite mixtures, and liquid coexists with austenite and ferrite during solidification. These three-phase fields are shown as the three-sided phase fields that contact the liquid phase field at liquidus surface minima on the vertical sections of Fig. 23.5. These three-phase fields are also defined by the intersections of constant iron planes with the heavy dark lines in Fig. 23.4. Thus, ferrite-austenite microstructures frequently develop in stainless steels. In fact, the duplex stainless steels described later are designed to have microstructures that are approximately 50% ferrite and 50% austenite.

Ferrite-austenite microstructures are also frequently encountered in austenitic stainless steel weld metal and cast austenitic stainless steels. In the latter materials, nonequilibrium solidification and alloying effects combine to produce ferrite-austenite microstructures that may not be present in wrought stainless steels of the same composition (Ref 23.5). Small amounts of ferrite are desirable in austenitic stainless steel weld metal because ferrite has a higher solubility for phosphorus and sulfur, elements that cause fissuring in fully austenitic microstructures (Ref 23.6). Therefore, ferrite reduces susceptibility to hot cracking or hot tearing. On the other hand, too high a ferrite content in austenitic stainless steel welds or castings may lower corrosion resistance and toughness.

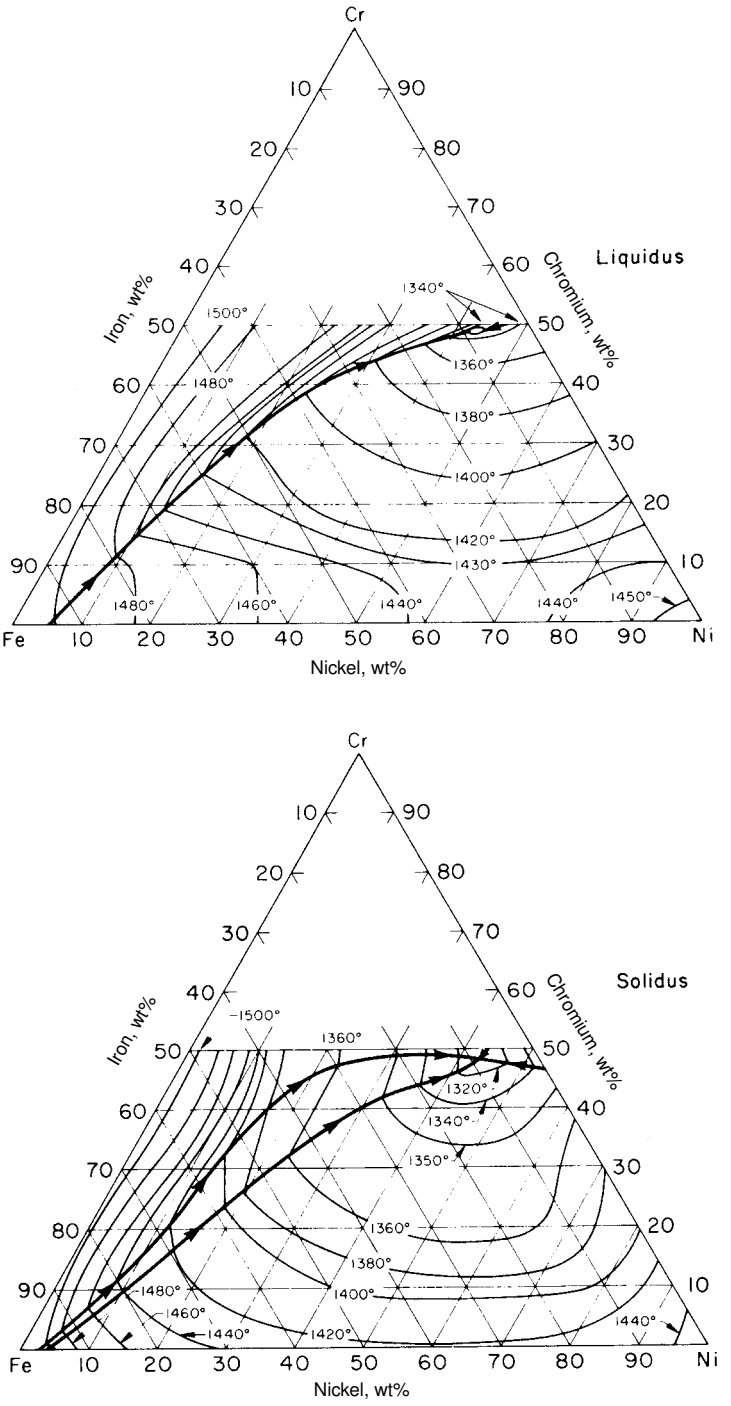

Fig. 23.4 Projections of the liquidus and solidus surfaces of the Fe-Cr-Ni ternary system. Source: Ref 23.3

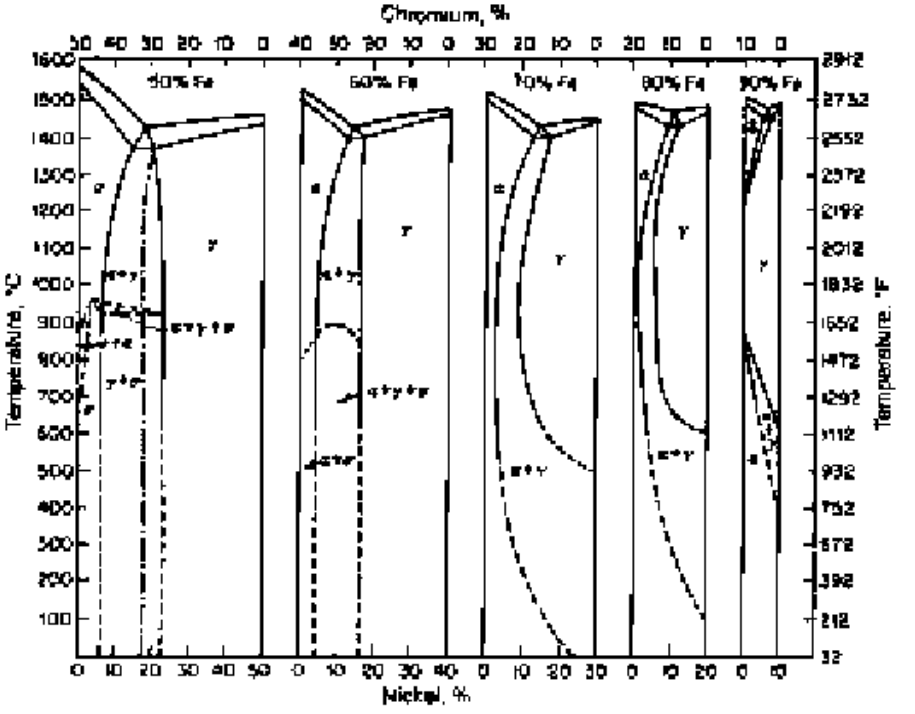

Fig. 23.5 Vertical sections through the Fe-Cr-Ni ternary system at constant iron contents. Source: Ref 23.2

In view of the importance of phase stability and composition, especially with respect to welding of austenitic stainless steels, several diagrams have been developed to show the effects of various combinations of austenite- and ferrite-stabilizing elements on ferrite content in stainless steels. The ferrite-stabilizing elements similar to chromium are molybdenum, silicon, and niobium, while the austenite-stabilizing elements similar to nickel are manganese, carbon, and nitrogen. Thus, nickel and chromium equivalents are calculated according to the various strengths of the elements stabilizing austenite or ferrite. Figure 23.6 shows the Schaeffler diagram (Ref 23.7), Fig. 23.7 shows the DeLong diagram (Ref 23.8), and Fig. 23.8 shows the Siewert, McCowan, and Olson diagram (Ref 23.6). The equations used to calculate the chromium and nickel equivalents are shown on the axes of the various diagrams, and the compositions that produce austenite, martensite, ferrite, or mixtures of various phases are indicated. Ferrite number, which can be calibrated with magnetic attraction because austenite is nonmagnetic and ferrite is magnetic, was selected by the Welding Research Council to correlate with ferrite content and is plotted in Fig. 23.7 and 23.8. The diagrams have evolved with the accumulation of more data regarding compositions and microstructure, and the most recent diagram is based on a large number of alloys covering a wide

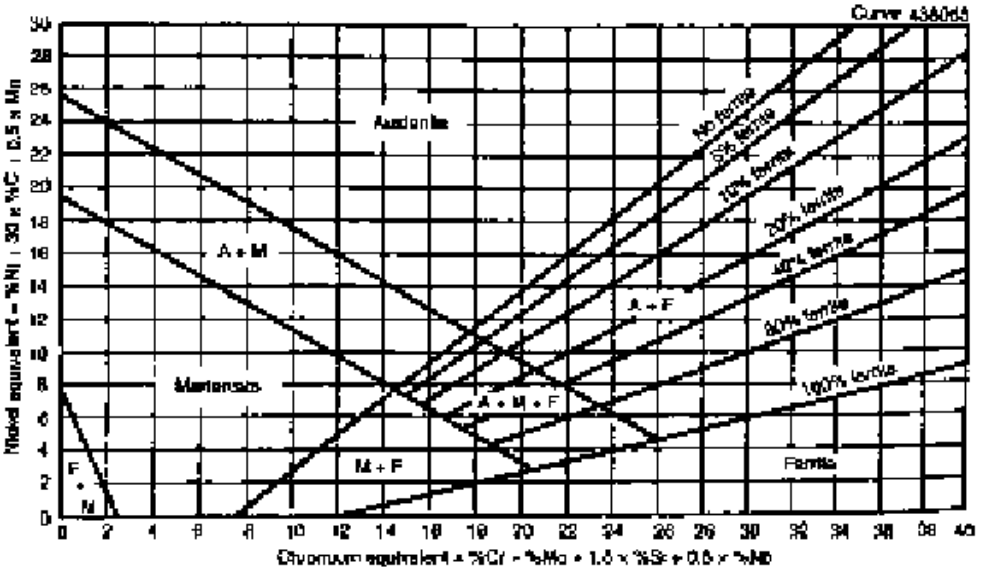

Fig. 23.6 The Schaeffler constitution diagram (1949) for stainless steel weld metal. Source: Ref 23.6, 23.7

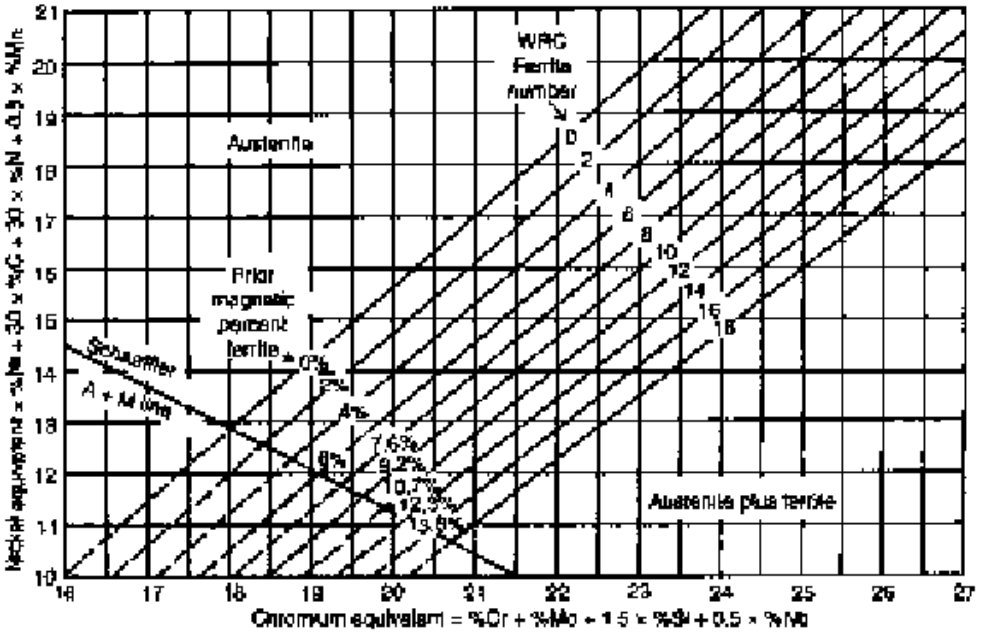

Fig. 23.7 The Delong constitution diagram (1974) with Welding Research Council (WRC) ferrite number system for weld metal. Source: 23.6, 23.8

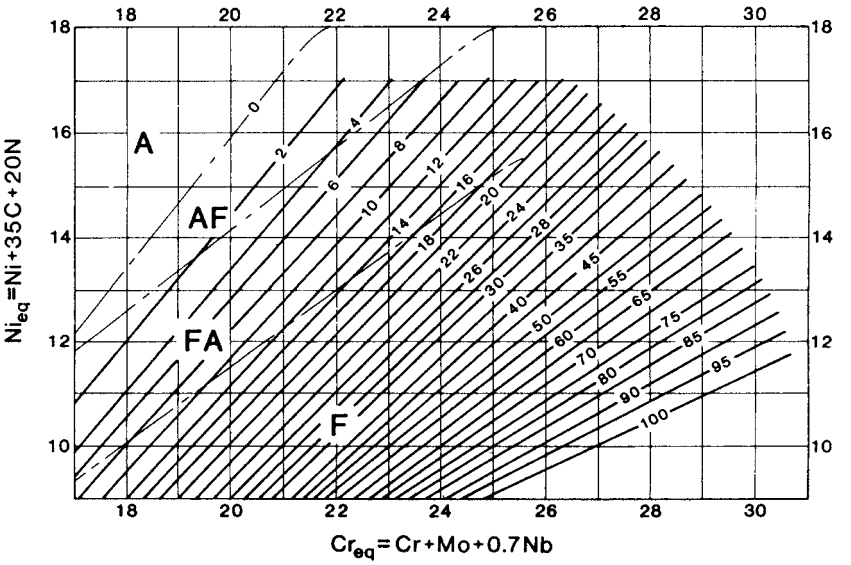

Fig. 23.8 The Siewert, McCowan, Olson constitution diagram (1988) for stainless steels. Ferrite numbers are plotted and A, AF, FA, and F indicate compositions that solidify by austenite, austenite followed by ferrite, ferrite followed by austenite, or ferrite formation, respectively. Source: Ref 23.6

range of compositions, including duplex stainless steels. The Siewert et al. diagram also indicates several solidification ranges that relate to the phase diagrams shown in Fig. 23.4 and 23.5. Complete austenite solidification is indicated by A, primary austenite followed by austenite plus ferrite solidification by AF, primary ferrite followed by austenite plus ferrite solidification by FA, and complete ferrite solidification by F.

Austenitic Stainless Steels

Table 23.1 shows the nominal compositions of AISI type 300 austenitic stainless steels. This table and the others that follow for other groups of stainless steels are taken from an article by Fischer and Maciag (Ref 23.9). The important grades of steels and the nominal amounts of the most important alloying elements are clearly indicated. More extensive tables listing other stainless steels, Unified Numbering System (UNS) alloy numbers, and other information are given elsewhere (Ref 23.10, 23.11).

Stainless steels are selected for corrosion resistance to the atmosphere, seawater, and a vast variety of chemical environments, and the reader is referred to other sources (Ref 23.1, 23.2, 23.10, 23.11) and manufacturers' literature to help select the proper steel for a given environment. Apart from resistance to specific corrosive environments, the austenitic stainless steels have evolved around the following physical metallurgical princi-

ples: varying austenite stability relative to martensite formation during cold work (AISI types 301, 302, and 304), reduction of carbon and alloying to eliminate chromium carbide formation and intergranular corrosion (AISI types 304L, 316L, 321, and 347), alloying with molybdenum to increase pitting resistance (AISI type 316), and heavily alloying with chromium and nickel to produce high-temperature strength and scaling resistance (AISI types 309 and 310).

Figure 23.9 shows the microstructure of annealed type 316L austenitic stainless steel. The microstructure in Fig. 23.9(a) is etched to produce contrast between grains of different orientation, and the microstructure in Fig. 23.9(b) is etched only to show grain boundaries (Ref 23.12, 23.13). The single-phase austenite is present as many equiaxed grains, many of which contain annealing twins. The twins are identified as bands with parallel sides and are formed when changes in the stacking of atoms on close-packed (111) planes occur during recrystallization and grain growth. Austenitic stainless steels are usually annealed at high temperatures to accomplish recrystallization and carbide solution. Water quenching follows annealing to prevent carbide formation during cooling, as discussed in the

Table 23.1 Compositions of selected AISI type 300 austenitic stainless steels

	Nominal composition, %				
AISI type No.	C	Mn	Cr	Ni	Others
301	0.15 max	2.0	16–18	6.0–8.0	…
302	0.15 max	2.0	17–19	8.0–10	…
304	0.08 max	2.0	18–20	8.0–12	…
304L	0.03 max	2.0	18–20	8.0–12	…
309	0.20 max	2.0	22–24	12–15	…
310	0.25 max	2.0	24–26	19–22	…
316	0.08 max	2.0	16–18	10–14	2–3 Mo
316L	0.03 max	2.0	16–18	10–14	2–3 Mo
321	0.08 max	2.0	17–19	9–12	(5 × %C) Ti min
347	0.08 max	2.0	17–19	9–13	(10 × %C) Nb-Ta min

Face-centered cubic, nonmagnetic, not heat treatable. Source: Ref 23.9

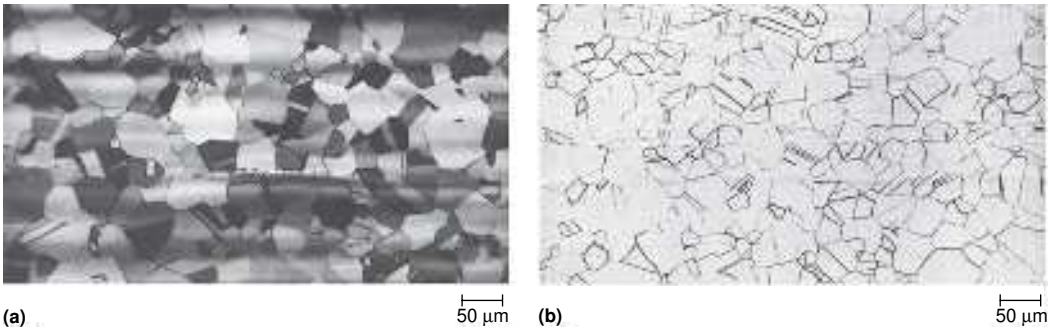

Fig. 23.9 Microstructure of annealed type 316L austenitic stainless steel. (a) Etched in 20% HCl, 2% NH_4FHF, 0.8% PMP (Ref 23.12, 23.13). (b) Etched in waterless Kalling's reagent (Ref 23.12, 23.13). Light micrographs. Courtesy of G. Vander Voort, Carpenter Technology Corp., Reading, PA

next section. Typical minimum mechanical properties of annealed austenitic stainless steels are yield strengths of 205 MPa (30 ksi), ultimate tensile strengths of 515 MPa (75 ksi), and elongations of 40% (Ref 23.10). Properly processed wrought austenitic stainless steels are truly single phase, without carbides, ferrite, or other phases, and with all alloying elements in solid solution. For the latter condition, corrosion resistance for a given grade is at its best.

Intergranular Carbides in Austenitic Stainless Steels

Figure 23.10 shows the microstructure of type 304 austenitic stainless steel in which chromium carbides have precipitated on grain boundaries. In this condition, the steel is said to be sensitized and is highly susceptible to catastrophic intergranular corrosion (Ref 23.1, 23.14). In metallographic sections, the chromium carbide precipitation is revealed by deep grain-boundary attack by certain etching procedures, such as the use of electrolytic oxalic acid etching (Ref 23.12). Generally, the carbides are too fine to be resolved by the light microscope but are indirectly revealed by deep etching of affected grain boundaries. In contrast, as shown in Fig. 23.9, grain boundaries in metallographic specimens of austenitic stainless steel without chromium carbide precipitation are well defined and not deeply etched.

The susceptibility to severe intergranular corrosive attack is caused by the depletion of chromium due to chromium carbide formation on austenite grain boundaries. The carbides have been identified as $M_{23}C_6$, where

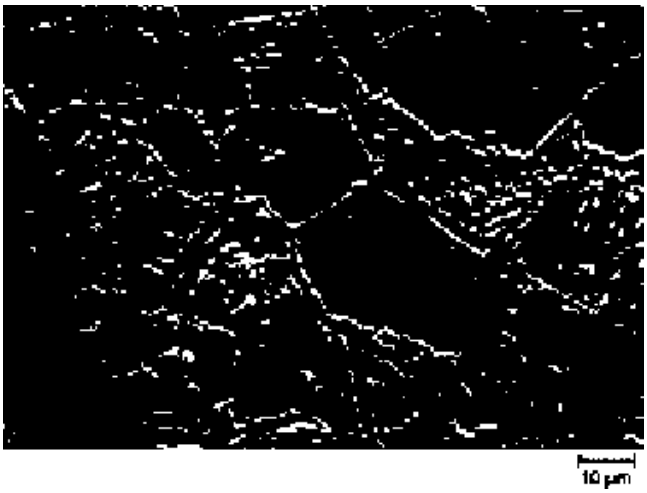

Fig. 23.10 Microstructure of type 304 stainless steel with chromium carbide precipitation on grain boundaries. ASTM A262 Practice A oxalic acid etch. Scanning electron micrograph. Courtesy of G. Vander Voort, Carpenter Technology Corp., Reading, PA

"M" denotes the metal atom content of the carbide, which may include iron and molybdenum as well as chromium. However, the high concentration of chromium in the $M_{23}C_6$ particles locally lowers the chromium content of the austenite to below the 12% required for stainless steel corrosion behavior. Figure 23.11 shows chromium concentration gradients, obtained by analytical transmission electron microscopy, in austenite adjacent to $M_{23}C_6$ particles at twin and high-angle grain boundaries in a 304 stainless steel (Ref 23.15). High-angle grain boundaries are preferred sites for precipitation and diffusion because of the relatively high atomic disorder where grains of different orientations meet. Thus, $M_{23}C_6$ particles readily nucleate and grow, severely depleting the adjacent austenite of chromium, from 19 wt% to approximately 10 wt% in the case of the data shown in Fig. 23.11. Twin boundaries have much better atomic matching than most high-angle boundaries and therefore are not as favorable for nucleation and growth of $M_{23}C_6$ particles.

Figure 23.12 shows a transmission electron micrograph with examples of $M_{23}C_6$ carbides and three types of boundaries in a sensitized 304 stainless steel. In agreement with Fig. 23.11, the carbides are largest on the high-angle grain boundaries (arrows, upper left), quite small on the incoherent twin boundaries (center), and absent on the coherent twin boundaries (normal to the incoherent twin boundaries). In addition to reduced corrosion resistance adjacent to $M_{23}C_6$ precipitation, the lowered chromium content raises the M_s temperatures and may result in martensite formation (Ref 23.15, 23.16).

The catastrophic consequences of intergranular corrosion due to chromium carbide precipitation has led to a number of heat treatment and al-

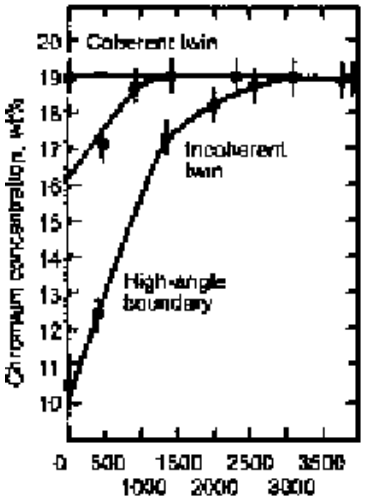

Fig. 23.11 Chromium depletion as a function of distance from various types of grain boundaries in type 304 stainless steel. Courtesy of M.G. Burke, Westinghouse Electric Corp., Pittsburgh. Source: Ref 23.15

loying approaches to minimize or eliminate this problem. One approach is simply to select an extra-low carbon modification of 304 or 316 austenitic stainless steels. These modifications are designated as types 304L and 316L and have an upper limit of 0.03% C. Although chromium carbide formation may not be completely suppressed, it is greatly reduced, and the low-carbon grades are adequate for many applications.

Figure 23.13 shows $M_{23}C_6$ precipitation curves for type 304 stainless steel (Ref 23.14). The kinetics show "C"-curve behavior, with most rapid precipitation occurring between 800 and 900 °C (1472 and 1652 °F). Above 950 °C (1742 °F), chromium and carbon are dissolved as atoms in

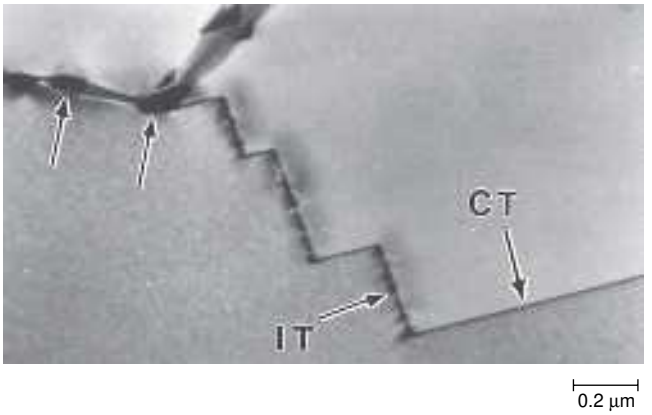

Fig. 23.12 Chromium carbide precipitation on various types of boundaries in type 304 stainless steel. Arrows in upper left point to large carbides on a high-angle grain boundary, and IT and CT refer to incoherent and coherent twin boundaries, respectively. Transmission electron micrograph. Courtesy of M.G. Burke, Westinghouse Electric Corp., Pittsburgh

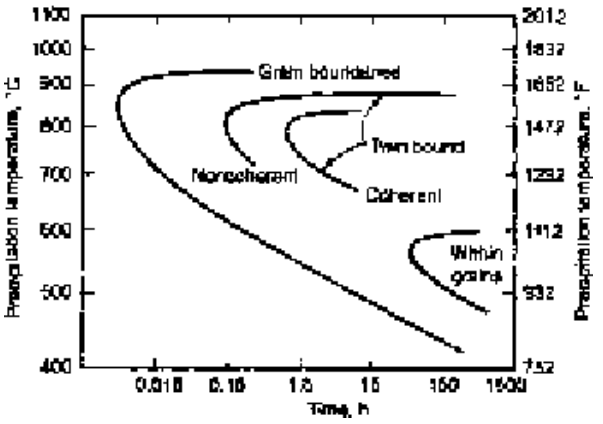

Fig. 23.13 $M_{23}C_6$ carbide precipitation kinetics in type 304 stainless steel containing 0.05% C and originally quenched from 1250 °C (2282 °F). Source: Ref 23.14

the crystal structure of austenite, and there is no thermodynamic driving force for chromium carbide formation. Below 500 °C (932 °F), the diffusion of chromium atoms required for $M_{23}C_6$ formation is too sluggish, and carbide formation essentially stops. Based on the $M_{23}C_6$ precipitation kinetics, wrought austenitic stainless steel products are annealed or solution treated at temperatures between 1040 and 1150 °C (1904 and 2102 °F) and quenched to eliminate sensitization. The solution treatment dissolves the $M_{23}C_6$ carbides, and the rapid cooling prevents the reprecipitation of $M_{23}C_6$ in the critical temperature range around the nose of the C-curve. This approach is also effective in welded austenitic stainless assemblies where $M_{23}C_6$ carbides may have precipitated in heat-affected zones adjacent to weld metal.

Another approach used to eliminate chromium carbide precipitation is to alloy austenitic stainless steels with very strong carbide-forming elements, such as titanium, niobium, or tantalum. Such austenitic stainless steels (types 321 and 347, Table 23.1) are referred to as stabilized grades. The alloying additions form carbides such as TiC and NbC and reduce the carbon available for $M_{23}C_6$ precipitation. Stabilizing heat treatments, performed at temperatures between 840 and 900 °C (1544 and 1652 °F), are designed to produce the most effective intragranular dispersion of the alloy carbides (Ref 23.14). Under most conditions, stabilized austenitic stainless steels are effective in reducing chromium carbide formation and intergranular attack. However, the very high temperatures adjacent to welds may cause even TiC and NbC carbides to redissolve and make possible the precipitation of $M_{23}C_6$ if the weldments are held in or slowly cooled through the $M_{23}C_6$ precipitation temperature range. This may lead to the localized corrosion referred to as "knife-line attack" and may be remedied by subjecting weldments to a final stabilizing heat treatment (Ref 23.1, 23.10, 23.14).

Martensite Formation in Austenitic Stainless Steels

Martensite may form in austenitic stainless steels during cooling below room temperature, that is, thermally, or in response to cold work, that is, mechanically. Eichelman and Hull (Ref 23.17) have developed the following equation for M_s, the temperature at which martensite first forms on cooling, of austenitic stainless steels:

$$M_s(°F) = 75(14.6 - Cr) + 110(8.9 - Ni) + 60(1.33 - Mn) + 50(0.47 - Si) + 3000[0.068 - (C + N)] \quad \text{(Eq 23.1)}$$

This equation shows that the substitutional alloying elements chromium and nickel have a moderate effect on the M_s compared with the very strong effect of carbon and nitrogen. Residual nitrogen contents of austenitic

stainless steel are usually in the range of 300 to 700 ppm (0.03 to 0.07 wt%) (Ref 23.14), and thus when combined with carbon may have a strong effect on stabilizing austenite with respect to martensite formation. When $M_{23}C_6$ carbides form at austenite grain boundaries, both carbon and chromium are removed from the adjacent austenite, M_s is locally raised, and martensite may form at grain boundaries, as mentioned earlier (Ref 23.15, 23.16). This phenomenon is in fact used as one approach to develop martensitic structures in semiaustenitic precipitation-hardening stainless steels, as discussed later.

Two types of martensite form spontaneously on cooling austenitic stainless steels below room temperature: hexagonal close-packed epsilon (ε) martensite and bcc alpha prime (α′) martensite. The epsilon martensite forms on close-packed (111) planes in the austenite and, except for size, is morphologically very similar to deformation twins or stacking fault clusters, which also form on (111) planes (Ref 23.18, 23.19). The α′ martensite forms as plates with (225) habit planes in groups bounded by faulted sheets of austenite on (111) planes (Ref 23.18). The nucleation of α′ martensite and its relationship to ε martensite has been difficult to resolve; evidence for α′ formation directly from austenite and with ε as an intermediate phase is reviewed in Ref 23.14.

Deformation-induced or strain-induced martensite formation is another unique feature of austenitic stainless steels. Strain-induced martensite forms at higher temperatures than does martensite, which forms on cooling, and the parameter M_D, the highest temperature at which a designated amount of martensite forms under defined deformation conditions, is used to characterize austenite stability relative to deformation. Angel (Ref 23.20) has published the following correlation of M_D to the composition of austenitic stainless steels:

$$M_{D30}(°C) = 413 - 462(C + N) - 9.2(Si) - 8.1(Mn) - 13.7(Cr) - 9.5(Ni) - 18.5(Mo) \quad \text{(Eq 23.2)}$$

where M_{D30} is defined as the temperature at which 50% martensite is formed by 30% true strain in tension. Again, carbon and nitrogen have a very strong effect on austenite stability, and the extra-low carbon grades such as 304L are quite sensitive to strain-induced martensite formation, a characteristic that may render them susceptible to reduced performance in high-pressure hydrogen (Ref 23.21). Deformation-induced martensite, however, significantly enhances strength generated by cold work, and types 301 and 302 stainless steels are designed to have lower chromium and nickel contents in order to exploit this strengthening mechanism. The effectiveness of this approach is demonstrated in the comparison of the stress-strain curves of types 301 and 304 stainless steels shown in Fig. 23.14 (Ref 23.22). The much more stable type 304 does not strain harden nearly as much as the type 301 stainless steel.

The extent of strain-induced transformation of austenite to martensite is dependent on temperature, strain rate, and strain, in addition to composition (Ref 23.23). Figure 23.15 shows the effect of temperature and strain on strain-induced martensite formation in type 304 stainless steels. Large amounts of martensite form at low strains during low-temperature deformation, and the amount of strain-induced transformation becomes negligible above room temperature. Figure 23.16 shows stress-strain curves obtained in constant temperature baths for a type 304 stainless steel (Ref 23.24). The strong effect of strain-induced martensite formation at lower temperatures is marked by noticeable inflections in the stress-strain curves. The strain hardening associated with these inflections produces very high

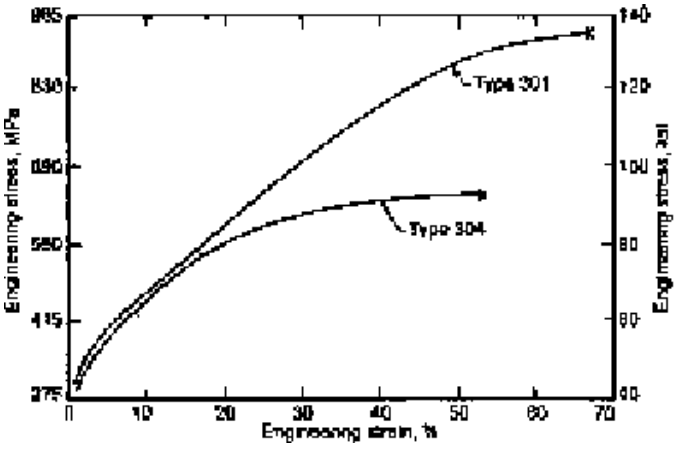

Fig. 23.14 Stress-strain curves for types 304 and 301 austenitic stainless steels. Source: Ref 23.11

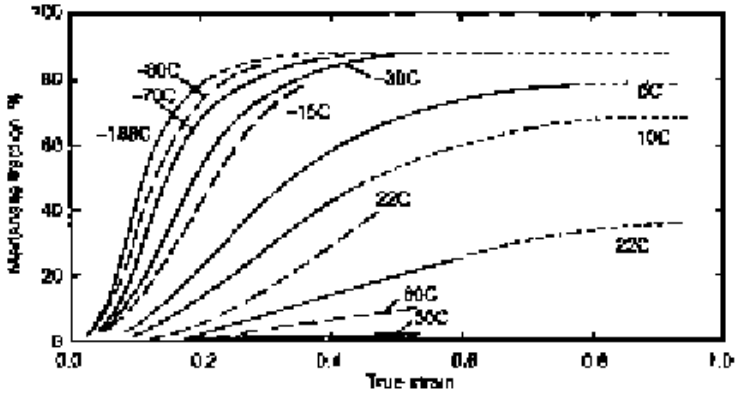

Fig. 23.15 Strain-induced martensite formation as a function of strain at various temperatures. Source: Ref 23.24. Solid lines are original data of Angel (Ref 23.20), dashed lines are data of Hecker et al. (Ref 23.25), and dotted extrapolations are from Olson's analysis (Ref 23.26).

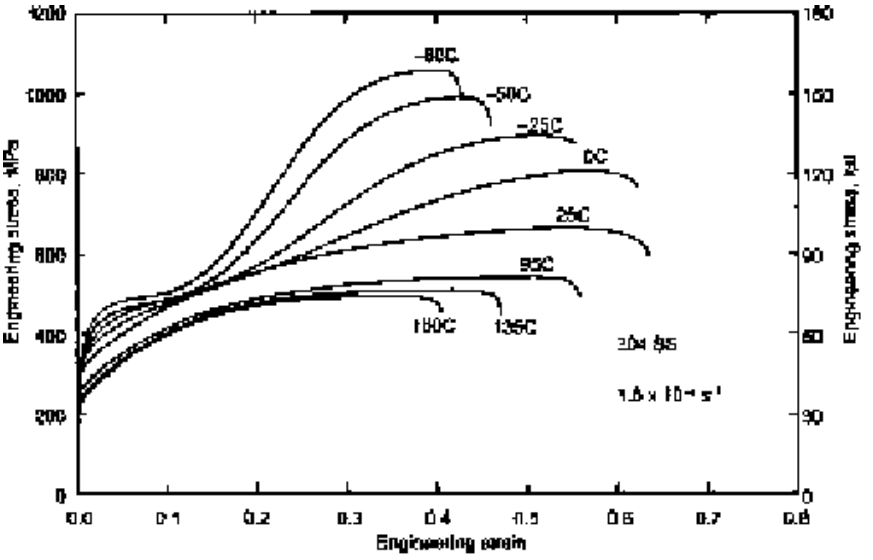

Fig. 23.16 Engineering stress-strain curves for type 304 stainless steels at various temperatures. Source: Ref 23.24

ultimate tensile strengths, and as the strain-induced transformation decreases, the ultimate tensile strength also decreases.

Figure 23.16 shows that the total ductility of the type 304 stainless steels goes through a maximum between 0 and 25 °C (32 and 77 °F). During deformation in this temperature range, the strain-induced martensite transformation is delayed to high strains, where the associated strain hardening is useful in delaying necking and increasing postuniform elongation. Effectively, as soon as necking starts, the additional strain causes that area to locally transform and harden, retarding necking and causing deformation to be displaced to lower-strength regions of the specimen. Above room temperature or as a result of specimen temperature increases associated with deformation heating and necking at room temperature, strain-induced martensite transformation and the associated strain hardening become negligible, even at high strains, and ductility decreases.

Other Phases in Austenitic Stainless Steels

Ideally, austenitic stainless steels have microstructures consisting only of polycrystalline austenite. However, because of segregation during solidification, ferrite tends to form and is commonly found in austenitic stainless steel castings and welds, as discussed earlier. Wrought austenitic stainless steels are homogenized by hot work, and smaller section sizes and sheet usually show uniform austenitic structures. However, heavier

plates and forgings, which receive less hot work, frequently show some ferrite within the austenitic microstructure (Ref 23.27). Figure 23.17 shows delta ferrite in a 304L stainless steel. The ferritic areas have been flattened and elongated as a result of plate rolling.

The presence of ferrite in austenitic stainless steels may lead to the formation of sigma (σ) phase, which may adversely affect ductility, toughness, and corrosion resistance of austenitic stainless steels (Ref 23.14). Sigma phase dominates the central portion of the iron-chromium diagram (Fig. 23.1) and therefore is an important factor in the processing and performance of highly alloyed ferritic stainless steels. As shown by the iron-chromium phase diagram, sigma phase is an intermetallic phase with composition centered about equal amounts of iron and chromium. The crystal structure is complex, body-centered tetragonal, with 30 atoms per unit cell, and may contain other elements such as molybdenum.

In austenitic stainless steels containing ferrite, sigma phase forms in ferritic areas because chromium, which is a major component of sigma, is already concentrated in the ferrite as a result of partitioning during solidification. The transformation of ferrite to sigma is sluggish and depends on alloy composition. Therefore, sigma phase is often found in austenitic stainless steel components that have been subjected to long-time service at temperatures in the range of 500 to 700 °C (932 to 1292 °F) (Ref 23.14).

Sigma phase tends to nucleate and grow preferentially at ferrite-austenite interfaces, but intragranular sigma formation has also been observed in

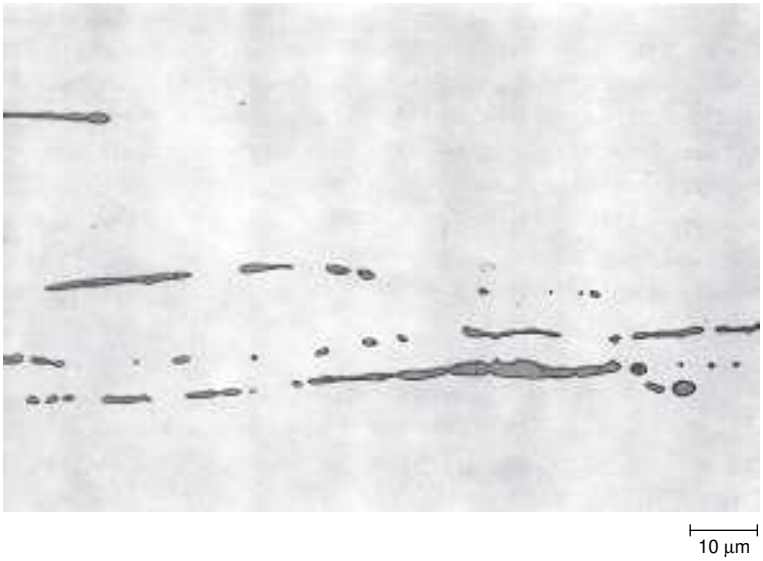

Fig. 23.17 Ferrite in a plate of type 304L stainless steel. Light micrograph. Courtesy of S. Yun, Colorado School of Mines

type 321 stainless steel held 17 years at approximately 600 °C (1112 °F) (Ref 23.28). In austenitic stainless steels subjected to 10,000 h aging at temperatures of approximately 600 °C (1112 °F), Gray et al. (Ref 23.29) have found that austenite formation accompanies the formation of sigma from delta ferrite. Thus, the partitioning of alloying elements for sigma formation appears to be accomplished by the solid-state reaction $\delta \rightarrow \sigma + \gamma$. Sigma phase formation from delta ferrite can be accelerated by strain, as documented by a forging study of austenitic 21-6-9 stainless steel (Ref 23.27). Tseng et al. found that the eutectoid transformation of delta ferrite to sigma and austenite was preceded by the eutectoid transformation of delta to $M_{23}C_6$ and austenite (Ref 23.30).

A number of phases other than ferrite, sigma, and $M_{23}C_6$ may form in austenitic stainless steels. These phases include various alloy carbides and nitrides and intermetallic phases such as Laves and chi. The formation of these phases is alloy specific and dependent on processing and service conditions. The reader is referred to the article by Novak (Ref 23.14) for a comprehensive review of the literature regarding the formation of such phases in austenitic stainless steels.

Other Austenitic Stainless Steels

In addition to the wrought austenitic stainless steel containing roughly 18% Cr and 8% Ni, several other groups of austenitic stainless steels are available for specific applications or processing requirements. Each of the wrought austenitic stainless steels has a counterpart cast alloy with a specific cast alloy designation (Ref 23.31). For example, CF-3, CF-8, CF-3M, and CF-8M correspond to the wrought types 304L, 304, 316L, and 316, respectively. The cast austenitic stainless steels are designed for good castability, and therefore, the composition ranges may vary from those of their counterpart wrought steels. In particular, the chromium and silicon contents are higher and the nickel contents lower in cast alloys compared with wrought alloys. As a result, delta ferrite, which reduces hot cracking as discussed earlier, is usually found in cast austenitic stainless steels.

Many heat-resisting grades of stainless steel have austenitic structures. The heat-resisting grades have much higher chromium and nickel contents for scaling resistance and high-temperature strength compared with the 18Cr-8Ni types of stainless steel. Again, there are counterpart wrought and cast grades of heat-resisting stainless steels (for example, types 309 and 310, and HH and HK, respectively). There are, however, many other cast grades of heat-resistant alloys, and these alloys have much higher carbon contents (0.20 to 0.75%) than do the wrought grades (Ref 23.31). Thus, alloy carbides, which contribute substantially to creep resistance, are an important component of the microstructure of the cast austenitic high-temperature alloys. The heat-resistant austenitic stainless steels are

used at temperatures as high as 1100 °C (2012 °F), sometimes in very aggressive gaseous environments, and are expected to provide many years of service. Thus, temperature-induced microstructural changes, creep-rupture mechanisms, scaling and oxidation, carburization, decarburization, and sulfidation are critical phenomena that affect selection and performance of heat-resistant austenitic stainless steels (Ref 23.32, 23.33).

Other groups of austenitic stainless steels include those in which substitutions for nickel are made. Type 200 austenitic stainless steels (Table 23.2) are alloyed with manganese and nitrogen, both austenite-stabilizing elements, to replace nickel. The 200-series austenitic stainless steels have properties and work-hardening characteristics similar to types 301 and 302 steels. Higher-strength austenitic stainless steels with high manganese and nitrogen and reduced nickel contents (Table 23.3) have also been developed (Ref 23.34). Several of these steels have the trademark Nitronic and are sometimes referred to by their composition in nominal amounts of chromium, nickel, and manganese. The yield strengths of these steels range from 345 to 480 MPa (50 to 70 ksi), significantly above those attainable in annealed type 300 stainless steels. An even newer type of austenitic stainless steel, "supernitrogen" stainless steel, contains up to 1 wt% N (Ref 23.35). This level of nitrogen exceeds the atmospheric solubility of nitrogen in austenite and is made possible by pressurized electroslag remelting. Even higher strengths at good levels of toughness appear to be attainable with these ultrahigh-nitrogen steels.

Table 23.2 Compositions of AISI type 200 austenitic stainless steels

	Nominal composition, %				
AISI type No.	C	Mn	Cr	Ni	Others
201	0.15 max	7.5	16–18	3.5–5.5	0.25N max
202	0.15 max	10.0	17–19	4.0–6.0	0.25N max

Face-centered cubic, nonmagnetic, not heat treatable. Source: Ref 23.9

Table 23.3 Compositions of high-strength manganese austenitic stainless steels

		Minimum mechanical properties				
		Tensile strength		Yield strength(a)		Elongation in 50 mm
Trade designation	Typical composition, %	MPa	ksi	MPa	ksi	(2 in.), %
Nitronic 32(b)	0.10 C, 12.0 Mn, 18.0 Cr, 1.6 Ni, 0.32 N	690	100	380	55	30
Nitronic 40	0.03 C, 9.0 Mn, 21.0 Cr, 7 Ni, 0.03 N	550	80	345	50	45
Nitronic 50	0.04 C, 5.0 Mn, 21.2 Cr, 12.5 Ni, 0.30 N, 2.50 Mo, 0.20 Nb, 0.20 V	690	100	380	55	35
Nitronic 60	0.07 C, 8.0 Mn, 17.0 Cr, 8.5 Ni, 0.14 N, 4.0 Si	655	95	345	50	35
Tenelon	0.08 C, 15.0 Mn, 18.0 Cr, 0.75 Ni, 0.35 N	860	125	480	70	40
Type 216	0.04 C, 8.0 Mn, 21.0 Cr, 6.0 Ni, 0.27 N, 2.3 Mo	690	100	415	60	40

(a) At 0.2% offset. (b) Nitronic is a trademark of Armco, Inc., Middletown, OH. Source: Ref 23.34

Heat Treatment of Austenitic Stainless Steels

The preceding review of the alloying and physical metallurgy of austenitic stainless steels shows that they cannot be strengthened by heat treatment such as quenching to form martensite or by precipitation hardening. Strengthening must be accomplished by alloying, in particular by solid-solution strengthening, and by cold working Strengthening by cold working may involve strain-induced martensite formation.

The heat treatments applied to austenite stainless steels therefore include annealing, treatments to prevent chromium carbide precipitation, and stress relief (Ref 23.10, 23.11, 23.14). Because austenitic stainless steels are very ductile, they are readily wrought to thin sheet or fine-diameter tubing and wire by sequential cold working and annealing cycles. The annealing causes recrystallization of the strain-hardened microstructure and restoration of ductility for subsequent working operations. Heat treatments to prevent sensitization may include solution treatments to dissolve chromium carbides or stabilization treatments to cause the precipitation of alloy carbides and thereby a reduction of the carbon available for chromium carbide precipitation. Finally, stress-relief treatments are applied to weldments, but care must be taken not to stress relieve sensitive alloys in the chromium carbide precipitation temperature range (Ref 23.14).

Ferritic Stainless Steels

Table 23.4 lists the compositions of some common type 400 ferritic stainless steels. Chromium, in amounts sufficient to completely stabilize ferrite (Fig. 23.1), is the major alloying element. Carbon is restricted both to maintain high toughness and ductility and to prevent austenite formation related to the expansion of the gamma loop by carbon. Figure 23.18 shows the polycrystalline, single-phase microstructure of an annealed ferritic stainless steel. Annealing for recrystallization of cold-worked structures is performed in the temperature range 760 to 966 °C (1400 to 1770 °F). Rapid cooling after annealing is required for the more highly alloyed fer-

Table 23.4 Compositions of AISI type 400 ferritic stainless steels

	Nominal composition, %			
AISI type No.	C	Mn	Cr	Others
430	0.08 max	1.0	16.0–18.0	…
430F	0.12 max	1.25	16.0–18.0	0.6Mo max
430F Se	0.12 max	1.25	16.0–18.0	0.15Se min
446	0.20 max	1.5	23.0–27.0	0.25N max

Body-centered cubic, magnetic, not heat treatable. Source: Ref 23.9

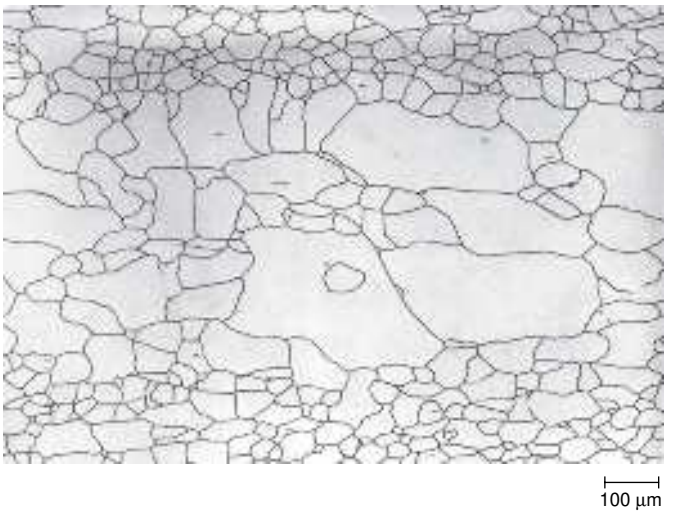

Fig. 23.18 Microstructure of annealed ferritic stainless steel (E-Brite 26-1 containing 26% Cr and 1% Mo). Etched electrolytically in 60% HNO_3-H_2O. Light micrograph. Courtesy of G. Vander Voort, Carpenter Technology Corp., Reading, PA

ritic grades in order to prevent the formation of phases detrimental to ductility and toughness.

The ferritic stainless steels, similar to the austenitic stainless steels, cannot be strengthened by heat treatment. Also, because the strain-hardening rates of ferrite are relatively low and because cold work significantly lowers ductility, the ferritic stainless steels are not often strengthened by cold work (Ref 23.34). Typical annealed yield and tensile strengths for the steels listed in Table 23.4 are 240 to 380 MPa (35 to 55 ksi) and 415 to 585 MPa (60 to 85 ksi), respectively. Ductilities tend to range between 20 and 35%. Higher strengths, up to 515 MPa (75 ksi) yield and 655 MPa (95 ksi) tensile, are obtained in the more highly alloyed ferritic steels, such as 29Cr-4Mo-2Ni and 27Cr-3.5Mo-1.2Ni.

The ductility and toughness of ferritic stainless steels are affected by many factors (Ref 23.36). Fundamentally, the strength and ability of the bcc ferrite structure to sustain plastic deformation are very temperature dependent, especially below room temperature. Strength increases rapidly and ductility drops sharply with decreasing temperature, apparently because screw dislocations lose their ability to cross slip in the bcc structure (Ref 23.37). As a result, ferritic steels undergo a transition from ductile fracture, characterized by microvoid coalescence, to brittle fracture, characterized by cleavage. The temperature at which this fracture transition occurs is referred to as the ductile-to-brittle transition temperature (DBTT),

and the cleavage fracture may be initiated by intergranular cracking or strain-induced cracking of second-phase particles (Ref 23.38, 23.39). In contrast, austenitic stainless steels do not undergo a ductile-to-brittle transition and maintain good ductility and toughness to temperatures well below room temperature. In ferritic stainless steels, the DBTT may be well above room temperature. Figure 23.19 shows the DBTT as a function of section thickness for several ferritic stainless steels (Ref 23.34). The thicker sections offer more constraint to plastic flow, and consequently, brittle fracture occurs without exception above room temperature as section size increases. In contrast, thin sheets in which yielding can take place through the thickness remain ductile and highly formable well below room temperature.

Other factors that influence the DBTT of ferritic stainless steels are grain size, interstitial carbon and nitrogen content, and the presence of various types of second phases. Thus, fine grain size, low interstitial element contents, and the elimination of second phases by proper heat treatment all enhance ductility and toughness (Ref 23.34, 23.36). Improved melting practices, including argon-oxygen decarburization and vacuum melting, and stabilization by additions of titanium or niobium have been extremely important approaches to lowering carbon and nitrogen contents and associated carbide and nitride precipitates detrimental to toughness of ferritic stainless steels (Ref 23.40).

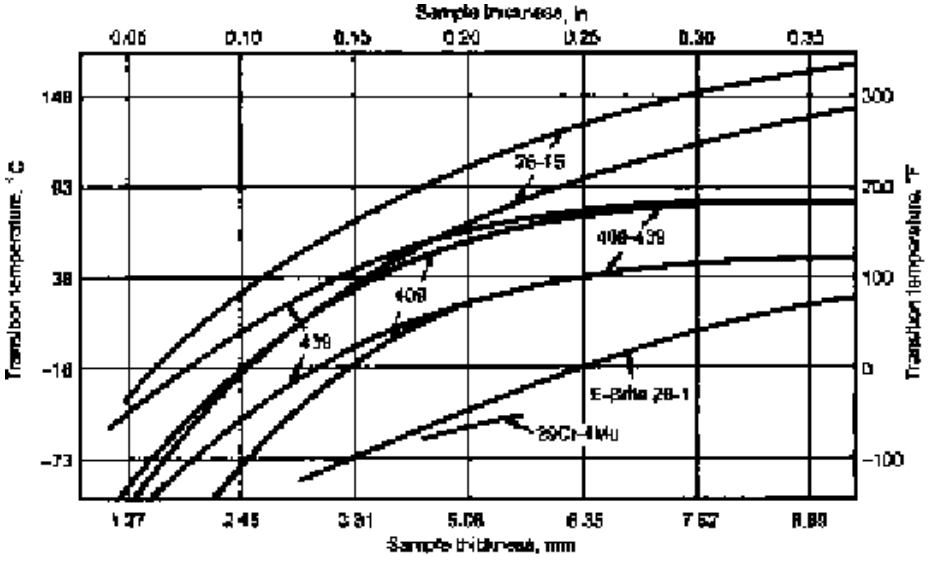

Fig. 23.19 Ductile-to-brittle transition temperatures as a function of section thickness for various ferritic stainless steels. Source: Ref 23.34

Intermetallic Phases in Ferritic Stainless Steels

Ferritic stainless steels are highly alloyed and may form a number of brittle intermetallic phases when exposed to operating temperatures or processing conditions, such as slow cooling of heavy sections, in the temperature range between 500 and 1000 °C (932 and 1832 °F). Prominent among these phases is sigma phase, which dominates the central portion of the iron-chromium phase diagram (Fig. 23.1). The various intermetallic phases form by the arrangement of iron, chromium, molybdenum, and other transition metal atoms into crystal structures that accommodate atomic size and electronic differences that limit the low-temperature solid solubility of alloying elements in the bcc ferritic structure (Ref 23.41). The crystal structures tend to be complex, and the phases are characterized by large unit cells containing many atoms. Table 23.5 lists characteristics of the sigma, chi, and Laves phases that may form in ferritic stainless steels.

Examples of intermetallic phases that have formed at 850 °C (1560 °F) in a 25Cr-3Mo-4Ni ferritic stainless steel are shown in Fig. 23.20. The

Table 23.5 Characteristics of intermetallic phases in ferritic stainless steels

Type of phase	Structure	Lattice parameters	Comments
Sigma (σ)	Body-centered tetragonal $D8_b$, 30 atoms/cell	a = 0.88–0.91 nm c = 0.45–0.46 nm	Parameters of phases collected from superalloys
Chi (χ)	Cubic $A12$, 58 atoms/cell	a = 0.884–0.893 nm	From various steels
Laves	Hexagonal $C14$ or $C36$	a = 0.475–0.495 nm c = 0.770–0.815 nm	Parameters of phases collected from superalloys

Source: Ref 23.42

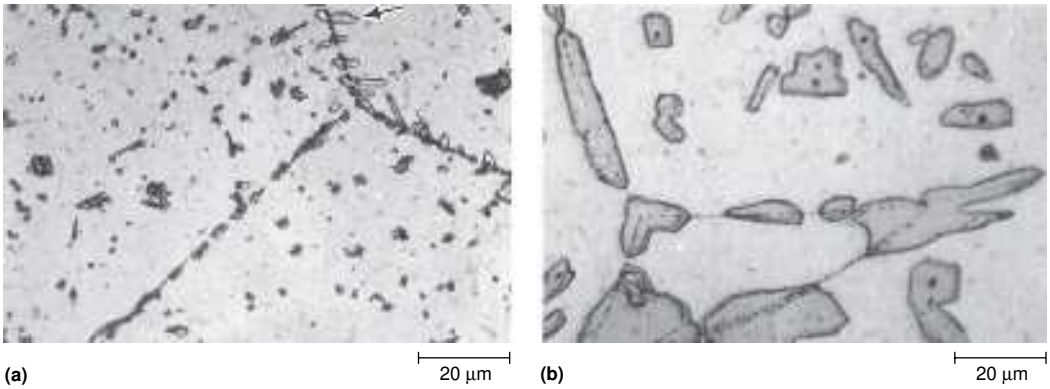

Fig. 23.20 Microstructures of ferritic stainless steel containing 24.5% Cr, 3.54% Mo, 3.90% Ni, 0.17% Nb, and 0.32% Al annealed at 850 °C (1560 °F). (a) Annealed 100 min. Arrow points to chi phase. (b) Annealed 300 min. Dominant second phase (etched gray) is sigma. Light micrographs. Source: Ref 23.42

various phases have formed at grain boundaries and within grains, and sigma phase dominates the microstructure after holding 300 min at 850 °C (1560 °F). A special consequence of the nickel content of this ferritic stainless steel is austenite formation adjacent to sigma phase. Apparently, the depletion of the chromium and molybdenum and concentration of nickel in areas adjacent to the sigma phase decrease the stability of the ferrite phase to where it is replaced by austenite.

The formation of the intermetallic phases follows C-curve kinetics, which are influenced by alloy composition. Figure 23.21 shows such curves for the 25Cr-3Mo-4Ni ferritic stainless steel (Ref 23.42). Leaner alloys would tend to have longer incubation times for the formation of the intermetallic phases. The C-curves are useful in that they define temperature ranges that can be used to dissolve the intermetallic phases and through which specimens must be rapidly cooled to avoid reprecipitation of the phases. The C-curves also identify operating temperatures that should be avoided for application of ferritic stainless steels.

475 °C (885 °F) Embrittlement in Ferritic Stainless Steels

In addition to the high-temperature embrittlement phenomena related to the intermetallic phases described previously, high-chromium ferritic

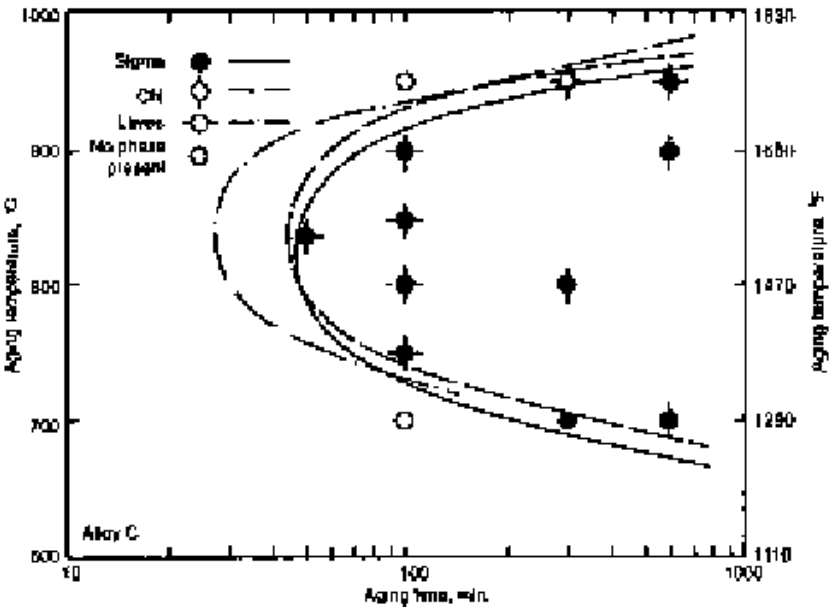

Fig. 23.21 Estimated time-temperature-transformation curves for ferritic stainless steel of composition given in Fig. 23.20. Source: Ref 23.42

stainless steels also may undergo a lower-temperature embrittlement. This phenomenon, termed 475 °C (885 °F) embrittlement, develops in the temperature range 400 to 550 °C (752 to 1022 °F), and its causes were identified only with difficulty because light microscopy and x-ray diffraction showed no evidence of any structural changes. The embrittlement is associated with very fine-scale precipitation, resolvable only by transmission electron microscopy, and the precipitating phase, designated α′, has a bcc structure with almost the same lattice parameter as the parent bcc ferrite (Ref 23.43).

The discovery of the α′ phase necessitated a modification of the central portion of the iron-chromium phase diagram. Williams (Ref 23.44) proposed the modification shown in Fig. 23.22. The dashed lines identify a miscibility gap in the bcc ferritic solid solution. At high temperatures, chromium and iron atoms are randomly distributed on the bcc crystal lattice, but at compositions and temperatures below the dashed lines, the iron and chromium atoms tend to separate and cluster. Therefore, subject to the constraint of diffusion, closely spaced areas become either rich in iron atoms (these areas remain the matrix α phase) or rich in chromium (these areas become the α′ phase). The α′ may form by nucleation and growth of discrete particles, or it may develop by a mechanism referred to as spinodal decomposition, which produces fine clusters of iron and chromium without well-defined interfaces. Regardless of the mechanism of formation, the α′ phase is quite fine, on the order of a few tens of nanometers in size (Ref 23.43–23.46).

The formation of α′ phase at temperatures of approximately 475 °C (885 °F) causes significant changes in mechanical properties of ferritic

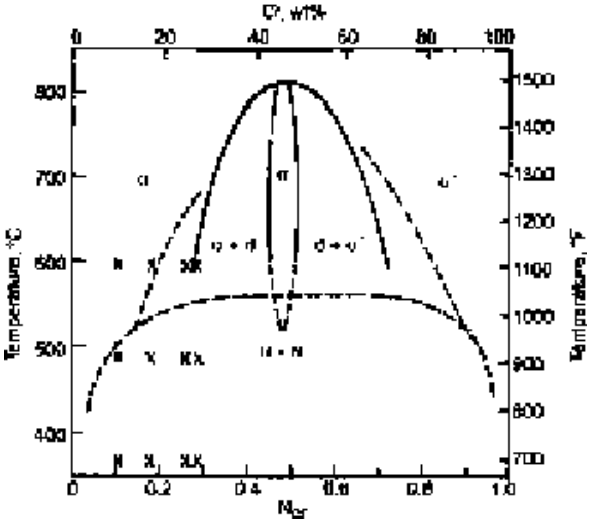

Fig. 23.22 The central portion of the iron-chromium binary diagram as modified by Williams (Ref 23.44) and reproduced in Ref 23.47

stainless steels. Most striking is the dramatic increase in the DBTT as identified by the change in fracture appearance (Ref 23.47). Hardness and yield strength also show significant increases, and tensile elongation shows significant decreases as the α' precipitation develops. These property changes are accompanied by changes in deformation from that characterized by uniform dislocation cell formation and cross slip to that characterized by planar dislocation arrays. The study by Nichol et al. (Ref 23.47) showed that high-purity, high-chromium ferritic stainless steel (29Cr-4Mo-2Ni) was the most sensitive, stabilized grades were less sensitive, and a titanium-stabilized 11% Cr was almost immune to 475 °C (885 °F) embrittlement.

Martensitic Stainless Steels

Martensitic stainless steels can be forged and then heat treated by austenitizing, martensite formation, and tempering for many applications that require not only corrosion resistance but also good edge retention, high strength, high hardness, and wear resistance. This processing approach is made possible by balancing chromium content between that required for stainless steel corrosion properties and that required to ensure full transformation to austenite within the gamma loop on heating. The gamma loop of the iron-chromium system is expanded by carbon and nitrogen, both austenite-stabilizing elements, as shown in Fig. 23.23. Thus, higher carbon and nitrogen contents make possible higher chromium contents in martensitic stainless steels.

Table 23.6 (Ref 23.9) lists the compositions of a number of commonly used AISI 400 grades of martensitic stainless steels. As discussed previously, carbon and chromium are balanced to ensure that full austenitization can be achieved. Several of the grades have low carbon content and

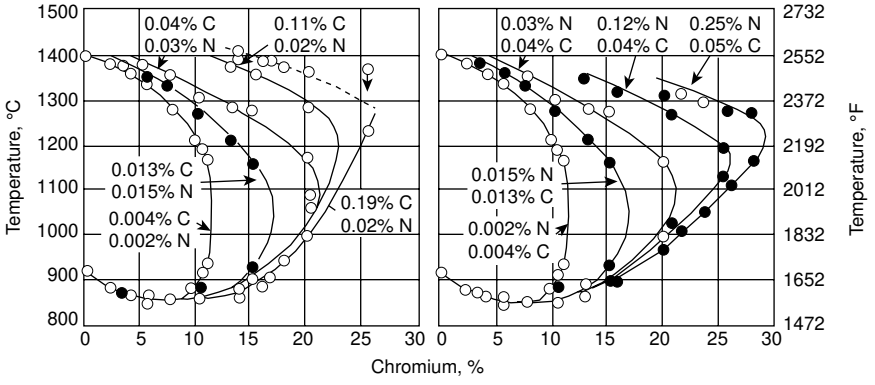

Fig. 23.23 Effect of carbon and nitrogen on gamma loop in iron-chromium alloys. Source: Ref 23.34

therefore are limited to a maximum hardness of approximately 45 HRC. Types 403 and 410 are comparable, except that type 403 is a special-quality grade for applications such as turbine blades. Higher hardness, to 60 HRC, is attainable in the type 440 grades, which have significantly higher specified carbon ranges. More chromium is required in the higher-carbon martensitic stainless steels to offset the chromium tied up in chromium carbide particles. Because of the high chromium content, all of the martensitic stainless steels have good hardenability and may be oil quenched or air cooled for hardening.

The martensitic stainless steels are process annealed to microstructures of ferrite and spheroidized carbides for maximum ductility and machinability. Annealing is accomplished by subcritical heating at temperatures of 650 to 760 °C (1202 to 1400 °F) or by heating to higher temperatures and slow cooling (Ref 23.48). Figure 23.24 shows spherical carbides dispersed in ferrite in annealed types 403 and 416 martensitic stainless steels. The microstructure of the annealed type 416 steel, which contains a delib-

Table 23.6 Compositions of AISI type 400 martensitic stainless steels

	Nominal composition, %				
AISI type No.	C	Mn	Cr	Ni	Others
403	0.15 max	1.0	11.5–13	…	…
410	0.15 max	1.0	11.5–13	…	…
416	0.15 max	1.2	12–14	…	0.15S min
420	0.15 min	1.0	12–14	…	…
431	0.20 max	1.0	15–17	1.2–2.5	…
440A	0.60–0.75	1.0	16–18	…	0.75Mo max
440B	0.75–0.95	1.0	16–18	…	0.75Mo max
440C	0.95–1.20	1.0	16–18	…	0.75Mo max

Body-centered cubic, magnetic, heat treatable. Source: Ref 23.9

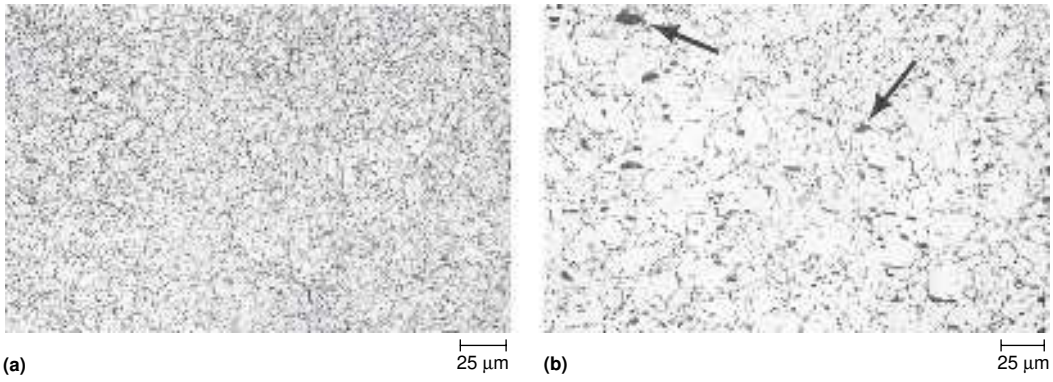

Fig. 23.24 Microstructure of annealed martensitic stainless steels. Fine particles are spheroidized carbides. (a) Type 403 stainless steel etched in 4% picral-HCl. (b) Type 416 stainless steel etched with Vilella's reagant. Arrows point to sulfide particles for machinability. Light micrographs. Courtesy of G. Vander Voort, Carpenter Technology Corp., Reading, PA

erate addition of sulfur, also contains a high density of coarse MnS particles, which are introduced to improve machinability.

Martensitic stainless steels are hardened by austenitizing to between 925 and 1065 °C (1697 and 1949 °F) and oil quenching or air cooling. The austenitizing temperature selected depends on the degree of carbide solution desired and the necessity to avoid delta ferrite formation by over-heating. Higher austenitizing temperatures result in greater carbide dissolution and better corrosion resistance and strength (Ref 23.48). The thermal conductivity of the chromium-containing martensitic stainless steels is considerably lower than that of carbon steels, and therefore, preheating of parts with complex shapes or section changes between 760 and 790 °C (1400 and 1454 °F) may be desirable to equalize temperature and thereby minimize distortion or cracking on heating to the final austenitizing temperature.

Figure 23.25 shows the martensitic structure of hardened type 403 martensitic stainless steel. The microstructure consists entirely of lath martensite. Alloys with higher chromium and carbon contents, such as the type 440 stainless steels, may contain significant volume fractions of alloy carbides and retained austenite after hardening. The mechanical property changes produced by tempering an oil-quenched type 410 martensitic stainless steel are shown in Fig. 23.26 (Ref 23.34). As-quenched hardness and strength are maintained well after tempering up to 450 °C (842 °F) and then drop rapidly. Higher austenitizing temperatures dissolve more chromium, and therefore, the secondary hardening peak is sharpened in the specimens austenitized at 1010 °C (1850 °F). Temper embrittlement

Fig. 23.25 Lath martensite microstructure of hardened type 403 stainless steel. 4% picral-HCl etch. Light micrograph. Courtesy of G. Vander Voort, Carpenter Technology Corp., Reading, PA

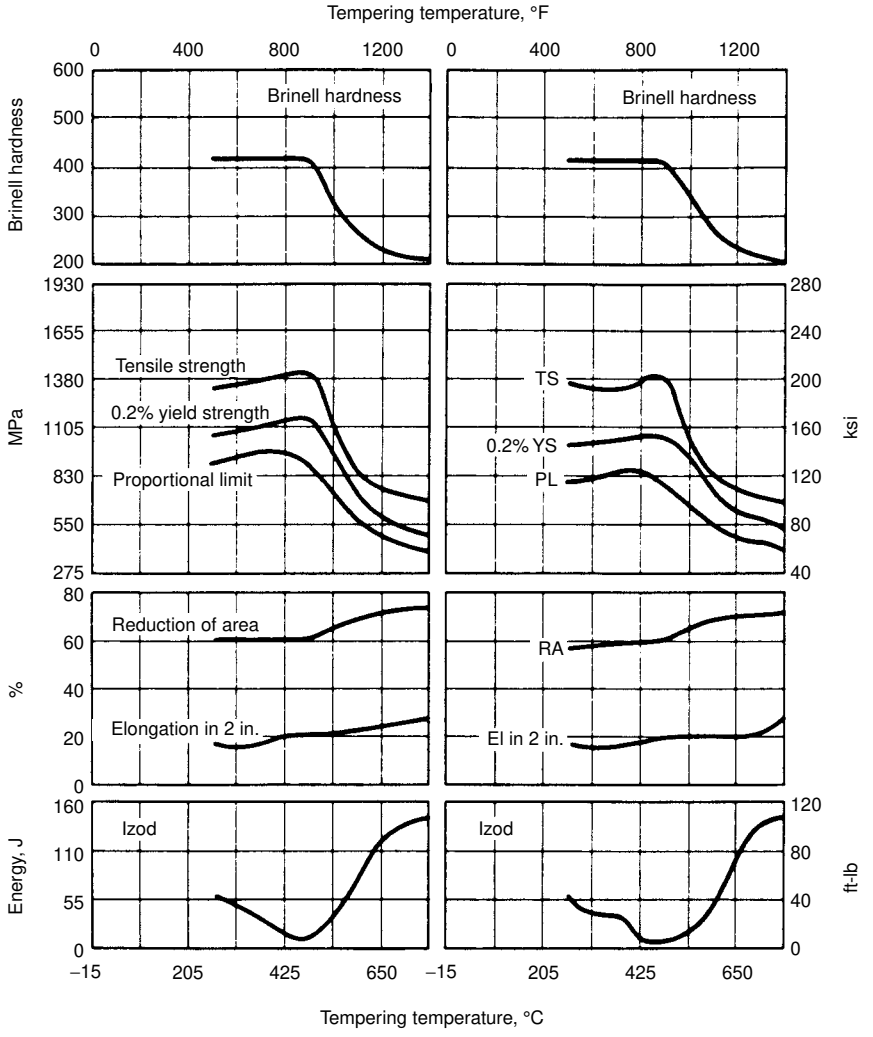

Fig. 23.26 Mechanical properties as a function of tempering temperature of type 410 stainless steel. Data on left are for specimens austenitized at 925 °C (1697 °F), and data on right are for specimens austenitized at 1010 °C (1850 °F). All specimens oil quenched between 65 and 95 °C (149 and 203 °F), stress relieved at 175 °C (347 °F), and tempered for 2 h. Source: Ref 23.34

develops during tempering between 425 and 565 °C (797 and 1049 °F) (Ref 23.34), as shown by the minimum in Izod impact toughness, and tempering in this temperature range should be avoided for impact-sensitive applications.

Precipitation-Hardening Stainless Steels

Precipitation-hardening stainless steels have been developed to provide high strength and toughness while maintaining the corrosion resistance of

stainless steels. This alloy category was necessitated by limits to strengthening austenitic and ferritic stainless steels by solid solution and strain hardening and the limited ductility and toughness of the carbon-strengthened martensite of high-hardness martensitic stainless steels. Strengthening in precipitation-hardening stainless steels is accomplished by the precipitation of intermetallic compounds such as Ni_3Al in austenitic or ductile low-carbon martensitic matrices.

The alloying elements in precipitation-hardening stainless steels may be balanced to produce martensitic structures at room temperature, metastable austenite that can be converted readily to martensite, or completely stable austenite. Thus, alloy design makes possible three classes of precipitation-hardening stainless steels: martensitic, semiaustenitic, and austenitic. The aging or precipitation-hardening treatments applied to all classes are similar and are accomplished at relatively low temperatures, approximately 500 °C (930 °F) for the martensitic and semiaustenitic grades and approximately 700 °C (1290 °F) for the austenitic grades. Table 23.7 lists representative precipitation-hardening stainless steels in each of the three classes. The steels are given the AISI type 600 category but are most commonly referred to by their trade names. Many more grades of precipitation-hardening stainless steels and specific processing information are presented in other references (Ref 23.34, 23.48, 23.49).

Martensitic precipitation-hardening stainless steels were first developed by Smith, Wyche, and Gore (Ref 23.50) and tend to be characterized by low carbon, low nickel, and stabilizing additions that further lower carbon in solution. Thus, the austenite has relatively low stability and transforms to low-carbon martensite at room temperature. This martensite is then strengthened by lower-temperature aging, which forms fine precipitates of nickel-containing intermetallic compounds such as Ni_3Al. Figure 23.27 shows the solution-treated and aged microstructure of PH 13-8 Mo steel. The precipitation cannot be resolved, but the tempering of the lath martensite, which proceeds concurrently with the precipitation reaction, is apparent.

Table 23.7 Compositions of selected precipitation-hardening stainless steels

AISI type No.	Trade name/producer	Nominal composition, %							
		C	Cr	Ni	Mo	Cu	Al	Ti	Other
Martensitic grades									
635	Stainless W (U.S. Steel)	0.06	16.75	6.25	…	…	0.2	0.8	…
630	17.4 PH (Armco Steel)	0.04	16.0	4.2	…	3.4	…	…	0.25Nb
…	PH 13-8 Mo (Armco Steel)	0.04	12.7	8.2	2.2	…	1.1	…	…
Semiaustenitic grades									
631	17.7 PH (Armco Steel)	0.07	17.0	7.1	…	…	1.2	…	…
633	AM 350 (Allegheny Ludlum)	0.05	16.5	4.25	2.75	…	…	…	0.10N
Austenitic grades									
600	A-286 (Allegheny Ludlum)	0.05	14.75	25.25	1.30	…	0.15	2.15	0.30V, 0.005B

Source: Ref 23.34, 23.49

Fig. 23.27 Solution-treated and aged microstructure of martensitic precipitation-hardening stainless steel PH 13-8 Mo. Etched in Fry's reagent. Light micrograph. Courtesy of G. Vander Voort, Carpenter Technology Corp., Reading, PA

The semiaustenitic precipitation-hardening stainless steels are alloyed to have low austenite stabilities that can be further modified by conditioning or solution treatments. Often some delta ferrite is a component of the microstructure. Figure 23.28 shows M_s as a function of austenitizing temperature for several precipitation-hardening steels (Ref 23.51). At high austenitizing temperatures, all elements are in solution, M_s temperatures are well below room temperature, and the microstructure is largely austenitic at room temperature. In this condition, the semiaustenitic precipitation-hardening stainless steels can be readily formed by cold work. At low austenitizing temperatures, alloy carbides precipitate, the austenite stability is lowered, and the M_s increases. As a result, the austenite transforms to martensite on cooling to room temperature. Another approach to producing a martensitic microstructure for aging is to refrigerate parts below room temperature.

Figure 23.29 shows the microstructure of a17-7 PH steel in several heat treated conditions after solution treatment at 980 °C (1796 °F). The tilting surface relief formed by martensite plates formed by refrigeration at –73 °C (–100 °F) is shown in Fig. 23.29(a). The specimen surface was polished flat prior to refrigeration, and at that point the microstructure consisted of austenite and delta ferrite. Figure 23.29(b) shows the microstructure after aging at 480 °C (896 °F) for 5.75 h to 43 HRC. The interfaces of the delta ferrite and the matrix etch heavily because of carbide precipitation. Some of the martensite reverts to austenite during aging, but this phenomenon and the strengthening precipitates are not resolvable in the light microscope.

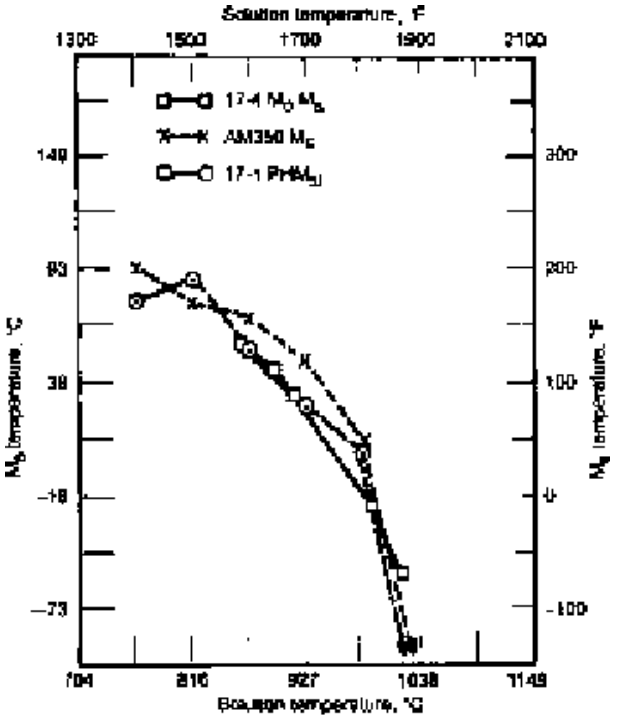

Fig. 23.28 Martensite start (M_s) temperatures as a function of austenitizing temperature for several precipitation-hardening stainless steels. Data from references listed in Ref 23.51. Source: Ref 23.51

Fig. 23.29 Microstructure of 17-7 PH. (a) Surface tilting caused by martensite formation on refrigeration to –73 °C (–100 °F). (b) Refrigerated and aged at 480 °C (896 °F). Electropolished and etched in chromeacetic acid electrolyte. Light micrographs. Source: Ref 23.51

The austenitic grades of precipitation-hardening stainless steels are heavily alloyed to completely stabilize austenite. For example, A-286 contains 15% Cr and 26% Ni in addition to other elements that contribute to precipitation reactions. The strengthening precipitate is the ordered fcc γ' phase $Ni_3(Ti,Al)$, but secondary precipitates that may form during aging include eta (η) or Ni_3Ti, alloy carbides such as (Ti,Mo)C, and a boride, M_3B_2 (Ref 23.52, 23.53). Figure 23.30 shows very fine γ' precipitates in JBK-75, an austenitic precipitation-hardening stainless steel similar to A-286 but developed for better weldability (Ref 23.52).

The martensitic and semiaustenitic precipitation-hardening stainless steels can be readily heat treated to yield and ultimate strengths exceeding 1400 MPa (200 ksi) with good ductility. Solution and conditioning treatments, subzero cooling, and aging treatments are alloy specific, and appropriate handbook and producer recommendations for the various alloys should be followed. The austenitic precipitation-hardening stainless steels do not reach the same high strength levels as the other two classes, but they have excellent elevated-temperature performance and are widely used in the aerospace industry.

Duplex Stainless Steels

Duplex stainless steels are alloyed and processed to develop microstructures consisting of roughly equal amounts of ferrite and austenite. Ferrite in austenitic stainless steels has already been discussed as a weld metal or casting alloy component that minimizes hot cracking, as a pre-

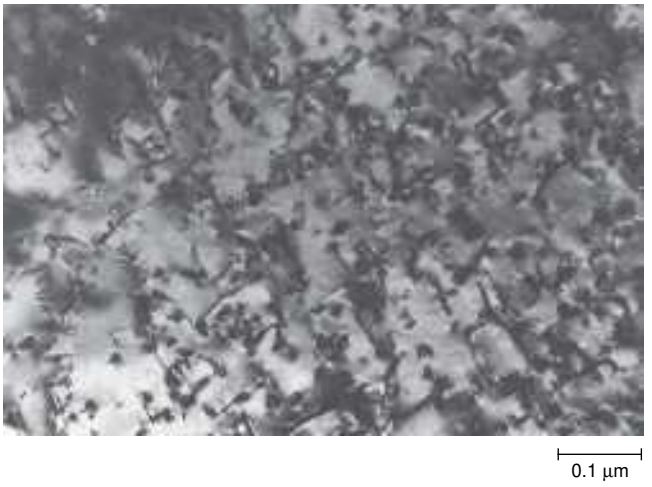

Fig. 23.30 Fine, disc-shaped γ' precipitates in an aged austenitic precipitation-hardening stainless steel, JBK-75. Transmission electron micrograph. Source: Ref 23.53

cursor for sigma phase formation in wrought alloys, and as a consequence of alloying for semiaustenitic precipitation-hardening stainless steels. Duplex stainless steels constitute a new class of materials, because by design they have nearly balanced amounts of ferrite and austenite. This microstructure and a chemistry that is relatively high in chromium and molybdenum produce good corrosion resistance in pitting, crevice, sulfide stress, and chloride stress corrosion environments at strength levels approximately double that of annealed austenitic stainless steels (Ref 23.54). As for ferritic stainless steels, improved steelmaking processes such as argon-oxygen decarburization have made possible the production of low-interstitial-content duplex stainless steels with good ductility and toughness. Both wrought and cast grades of duplex stainless steels have been developed (Ref 23.54).

Table 23.8 lists some selected examples of duplex stainless steels. A much more extensive listing is given by Solomon and Devine (Ref 23.55). Compositions of duplex stainless steels range from 17 to 30% Cr and 3 to 13% Ni, with typically chromium on the high side and nickel on the low side of the ranges to ensure adequate ferrite stability. Molybdenum, a ferrite stabilizer, is also typically present.

Thermomechanical processing of wrought duplex stainless steels is accomplished in the two-phase ferrite-austenite fields shown in the vertical sections of Fig. 23.5. Because the boundaries of the ferrite-austenite fields shift with temperature, the amounts of ferrite and austenite formed during hot working or annealing are a function of temperature. Higher temperatures produce larger amounts of ferrite. Therefore, hot working temperatures must be controlled, usually between 1000 and 1200 °C (1832 and 2192 °F), to maintain the desired balance of ferrite and austenite.

Figure 23.31 shows the microstructure of a 7-Mo PLUS (UNS S32950) duplex stainless steel (Ref 23.56). In this alloy, the white phase is austenite and the continuous gray matrix phase is ferrite (Ref 23.13). In other stainless steels, austenite may be the majority, or matrix, phase. Widmanstätten or acicular grains of austenite have been observed to form on air cooling from temperatures above the austenite solvus (Ref 23.58), and this mechanism of transformation may account for the needlelike morphology of some of the austenite in Fig. 23.31.

Table 23.8 Compositions of selected duplex stainless steels

	Nominal composition, %				
Trade name/producer	**C**	**Cr**	**Ni**	**Mo**	**Other**
AL 2205 (Allegheny Ludlum)	0.02	22.0	5.5	3.0	0.15N
7-Mo PLUS (Carpenter Technology Corp.)	0.02	26.0	4.7	1.4	0.20N
Ferralium 255 (Cabot Corp.)	<0.08	25.5	5.5	3.0	>0.1 N, 1.3–1.4Cu
DPI (Sumitomo)	<0.03	18.5	4.75	2.75	…
U45 (Creusot-Loire Steels)	<0.03	22.0	5.75	3.0	<0.2N

Source: Ref 23.55 to 23.57

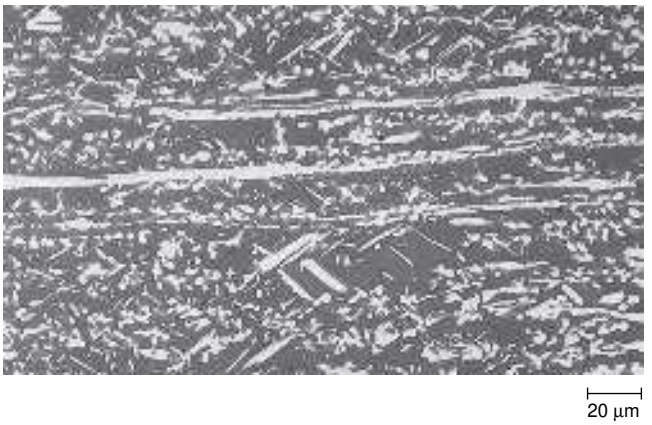

Fig. 23.31 Microstructure of duplex stainless steel 7-Mo PLUS (UNS S32950). Gray phase is ferrite and white phase is austenite. Etched electrolytically in 20% NaOH. Light micrograph. Courtesy of G. Vander Voort, Carpenter Technology Corp., Reading, PA

As a result of hot working or annealing of cold-worked shapes, both the ferrite and austenite areas of duplex stainless steels are polycrystalline. Etching to show the grain structure of the highly alloyed ferrite and austenite is extremely difficult, and most published light micrographs show only the two phases without delineating grain structure. Figure 23.32 shows the grain structure in cold-rolled and annealed Al 2205 (UNS S31803) duplex stainless steel. This micrograph was made by transmission electron microscopy, and each grain was identified as bcc ferrite (F) or fcc austenite (A) by electron diffraction. Some of the austenite grains contain annealing twins, and the grain size of both phases is quite fine. Both phases have recrystallized with a very low density of dislocations, and many of the grain boundaries have established equilibrium triple points characterized by 120° dihedral angles. However, some boundaries remain highly curved, especially those between ferrite and austenite grains, reflecting the more sluggish kinetics of establishing phase equilibrium by partitioning of chromium, nickel, and molybdenum between the two phases before interfacial energies can be minimized.

The mechanical properties of duplex stainless steels are a function of the deformation behavior of ferrite and austenite. Figure 23.33 shows stress-strain curves obtained by testing sheet tensile specimens of an Al 2205 duplex stainless steel (Ref 23.57). As test temperature decreases, yield and ultimate strengths increase significantly, but ductility remains almost the same. This behavior reflects the strength and strong temperature dependence of the flow strength of bcc ferrite, that is, very sharp increases in flow stress with decreasing temperature below room temperature (Ref 23.37), which would normally be accompanied by sharp decreases in

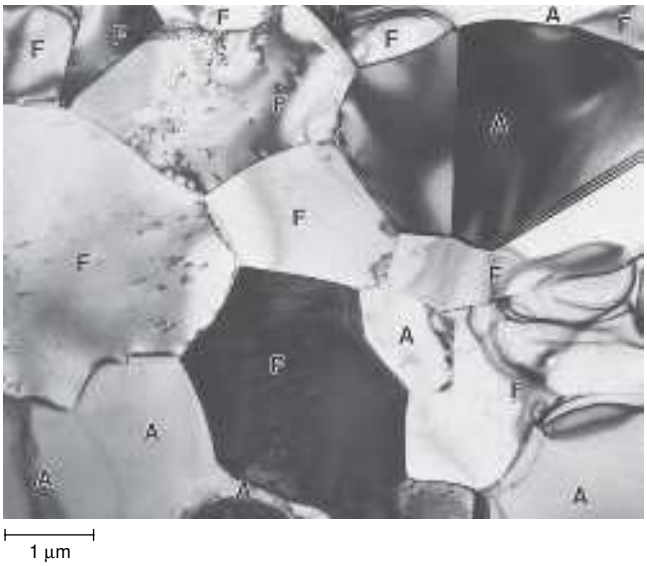

Fig. 23.32 Ferrite (F) and austenite (A) grains in duplex stainless steel Al 2205 (UNS S31803). Transmission electron micrograph. Courtesy of S.W. Thompson, Colorado School of Mines, Golden, CO

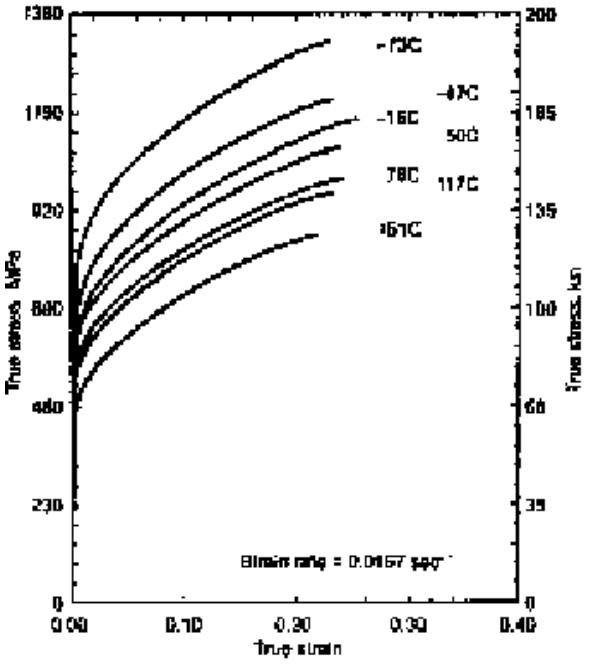

Fig. 23.33 Stress-strain curves for duplex stainless steel Al 2205 (UNS S31803) as a function of temperature. Source: Ref 23.57

ductility. However, the fcc austenite compensates for the lower ductility of the ferrite, in part by providing increased rates of strain hardening by strain-induced transformation of austenite to martensite (Ref 23.57).

The highly alloyed duplex stainless steels, similar to austenitic and ferritic stainless steels, are subject to the deleterious effects of phases other than ferrite and austenite on corrosion resistance, ductility, and toughness (Ref 23.54–23.56). The ferrite phase is susceptible to 475 °C (885 °F) embrittlement and sigma phase formation at temperatures between 600 and 950 °C (1112 and 1742 °F), and chromium carbides may form between 560 and 1050 °C (1040 and 1922 °F) (Ref 23.56). As a result, rapid cooling through critical temperature ranges may be required during processing and fabrication, and upper temperature limits for service must be recognized.

Superduplex stainless steels, containing 0.2 to 0.3% N for increased pitting resistance, have been developed. The latter steels are described, and an excellent review of duplex stainless steel technology is given in Ref 23.59.

Summary

This chapter has described the alloying, microstructure, and thermomechanical processing of the major types of stainless steels. These alloys meet many critical needs for materials that require excellent corrosion resistance and structural integrity. An extensive stainless steel literature exists, and good handbooks are available (Ref 23.2, 23.10, 23.11, 23.60). A dynamic search continues for improved processing and grades with better corrosion resistance, strength, high-temperature performance, formability, and toughness. The success of stainless steel application and development depends in large part on understanding the complex phase relationships in these highly alloyed materials. This understanding should result in the application of process controls and the selection of steels for service conditions that exploit beneficial microstructures and limit the formation of damaging phases.

REFERENCES

23.1 M.G. Fontana and N.D. Greene, *Corrosion Engineering,* McGraw-Hill, 1967

23.2 D. Peckner and I.M. Bernstein, *Handbook of Stainless Steels,* McGraw-Hill, 1977

23.3 *Metallography, Structures and Phase Diagrams,* Vol 8, *Metals Handbook,* 8th ed., American Society for Metals, 1973

23.4 P.G. Nelson, *Constitution and Heat Treatment of Stainless Steels,* Metals Engineering Institute, American Society for Metals, 1969

23.5 J.C. Lippold and W.F. Savage, Solidification of Austenitic Stainless Steel Weldments, Part I: A Proposed Mechanism, *Weld. Res. Suppl.,* 1979, p 362s–374s
23.6 T.A. Siewert, C.N. McCowan, and D.L. Olson, Ferrite Number Prediction to 100FN in Stainless Steel Weld Metal, *Weld. Res. Suppl.,* 1988, p 289s–298s
23.7 A. Schaeffler, Constitution Diagram for Stainless Steel Weld Metal, *Metal Prog.,* Vol 56 (No. 11), 1949, p 680–680B
23.8 W.T. DeLong, Ferrite in Austenitic Stainless Steel Weld Metal, *Weld. J.,* Vol 53 (No. 7), 1974, p 273s–286s
23.9 G.J. Fischer and R.J. Maciag, The Wrought Stainless Steels, *Handbook of Stainless Steels,* McGraw-Hill, p 1–1 to 1–10
23.10 Stainless Steels, in *Metals Handbook Desk Edition,* J.D. Redmond, Ed., American Society for Metals, 1985, p 15–1 to 15–21
23.11 *Properties and Selection: Stainless Steels, Tool Materials, and Special-Purpose Metals,* Vol 3, *Metals Handbook,* 9th ed., American Society for Metals, 1980, p 1–185
23.12 G.F. Vander Voort, *Metallography: Principles and Practice,* ASM International, 1984
23.13 G.F. Vander Voort, The Metallography of Stainless Steels, *J. Met.,* Vol 41 (No. 3), 1989, p 6–11
23.14 C.J. Novak, Structure and Constitution of Wrought Austenitic Stainless Steels, *Handbook of Stainless Steels,* McGraw-Hill, 1977, p 4–1 to 4–78
23.15 E.P. Butler and M.G. Burke, Preferential Formation of Martensite in Type 304 Stainless Steel: A Microstructural and Compositional Investigation, *Solid-Solid Phase Transformations,* H.J. Aaronson et al., Ed., TMS-AIME, Warrendale, PA, 1982, p 1403–1407
23.16 S.R. Thomas and G. Krauss, Cyclic Martensitic Transformation and the Structure of a Commercial 18Cr-8Ni Stainless Steel, *Trans. TMS-AIME,* Vol 239, 1967, p 1136–1142
23.17 A.H. Eichelman, Jr. and F.C. Hull, The Effect of Composition on the Temperature of Spontaneous Transformation of Austenite to Martensite in 18-8 Type Stainless Steel, *Trans. ASM,* Vol 45, 1953, p 77–104
23.18 R.P. Reed, The Spontaneous Martensitic Transformations in 18 pct Cr, 8 pct Ni Steels, *Acta Metall.,* Vol 10, 1962, p 865–877
23.19 M.C. Mataya, M.J. Carr, and G. Krauss, The Bauschinger Effect in a Nitrogen-Strengthened Austenitic Stainless Steel, *Mater. Sci. Eng.,* Vol 57 (No. 2), 1983, p 205–222
23.20 T. Angel, Formation of Martensite in Austenitic Stainless Steels, *J. Iron Steel Inst.,* Vol 177, 1954, p 165–174
23.21 R.M. Vennett and G.S. Ansell, The Effect of High-Pressure Hydrogen upon the Tensile Properties and Fracture Behavior of 304L Stainless Steel, *Trans. ASM,* Vol 60, 1967, p 242–251

23.22 K.G. Brickner, Stainless Steels for Room and Cryogenic Temperatures, *Selection of Stainless Steels,* American Society for Metals, 1968, p 1–29
23.23 J.P. Bressanelli and A. Moskowitz, Effects of Strain Rate, Temperature and Composition on Tensile Properties of Metastable Austenitic Stainless Steels, *Trans. ASM,* Vol 59, 1966, p 223–239
23.24 G.L. Huang, D.K. Matlock, and G. Krauss, Martensite Formation, Strain Rate Sensitivity, and Deformation Behavior of Type 304 Stainless Steels Sheet, *Metall. Trans. A,* Vol 20, 1989, p 1239–1246
23.25 S.S. Hecker, M.G. Stout, K.P. Staudhammer, and J.L. Smith, Effects of Strain State and Strain Rate on Deformation-Induced Transformation in 304 Stainless Steel: Part I and Part II, *Metall. Trans. A,* Vol 13, 1982, p 619–626, 627–635
23.26 G.B. Olson, Transformation Plasticity and the Stability of Plastic Flow, *Deformation, Processing and Structure,* G. Krauss, Ed., American Society for Metals, 1984, p 391–424
23.27 M.C. Mataya and M.J. Carr, Characterization of Inhomogeneities in Complex Austenitic Stainless Steel Forgings, *Deformation, Processing and Structure,* G. Krauss, Ed., American Society for Metals, 1984, p 445–501
23.28 J. Bentley and J.M. Leitnaker, Stable Phases in Aged Type 321 Stainless Steel, *The Metal Science of Stainless Steels,* E.W. Collings and H.W. King, Ed., TMS-AIME, Warrendale, PA, 1979, p 70–71
23.29 R.J. Gray, V.K. Sikka, and R.T. King, Detecting Transformation of Delta-Ferrite to Sigma-Phase in Stainless Steels by Advanced Metallographic Techniques, *J. Met.,* 1978, p 18–26
23.30 C.C. Tseng, Y. Shen, S.W. Thompson, M.C. Mataya, and G. Krauss, Fracture and the Formation of Sigma Phase, $M_{23}C_6$ and Austenite from Delta-Ferrite in an AISI 304L Stainless Steel, *Metall. Mater. Trans. A,* Vol 25, 1994, p 1147–1158
23.31 E.A. Schoeffer, The Cast Stainless Steels, *Handbook of Stainless Steels,* McGraw-Hill, 1977, p 2–1 to 2–18
23.32 C. Edeleanau, Ed., *Materials Technology in Steam Reforming Processes,* Pergamon Press, London, 1966
23.33 L. Dillinger, R.D. Buchheit, J.A. VanEcho, D.B. Roach, and A.M. Hall, *Microstructures of Heat-Resistant Alloys,* Alloy Casting Institute Division, Steel Founders' Society of America, Cleveland, 1970
23.34 R.A. Lula, *Stainless Steel,* American Society for Metals, 1986
23.35 R.P. Reed, Nitrogen in Austenitic Stainless Steels, *J. Met.,* Vol 41 (No. 3), 1989, p 16–21
23.36 R.A. Lula, Ed., *Toughness of Ferritic Stainless Steels,* STP 706, American Society for Testing and Materials, Philadelphia, 1980
23.37 W.C. Leslie, *The Physical Metallurgy of Steels,* McGraw-Hill, 1981

23.38 J.F. Grubb, R.N. Wright, and P. Farrar, Jr., Micromechanisms of Brittle Fracture in Titanium-Stabilized and α′-Embrittled Ferritic Stainless Steels, *Toughness of Ferritic Stainless Steels,* R.A. Lula, Ed., STP 706, American Society for Testing and Materials, Philadelphia, 1980, p 56–76

23.39 M.K. Veistinen and V.K. Lindroos, Cleavage Fracture Strength of a 26Cr-1Mo Ferritic Stainless Steel, *New Developments in Stainless Steel Technology,* R.A. Lula, Ed., American Society for Metals, 1985, p 29–43

23.40 R.Q. Barr, Ed., *Stainless Steel '77,* Climax Molybdenum Company, Greenwich, CT, 1977

23.41 C.S. Barrett and T.B. Massalski, *Structure of Metals,* 3rd ed., McGraw-Hill, 1966

23.42 E.L. Brown, M.E. Burnett, P.T. Purtscher, and G. Krauss, Intermetallic Phase Formation in 25Cr-3Mo-4Ni Ferritic Stainless Steel, *Metall. Trans. A,* Vol 14, 1983, p 791–800

23.43 R.M. Fisher, E.J. Dulis, and K.G. Carroll, Identification of the Precipitate Accompanying 885 °F Embrittlement in Chromium Steels, *Trans. AIME,* Vol 197, 1953, p 690–695

23.44 R.O. Williams, Further Studies of the Iron-Chromium System, *Trans. AIME,* Vol 212, 1958, p 497–502

23.45 R. Lagneborg, Metallography of the 475 C Embrittlement in an Iron-30 pct Chromium Alloy, *Trans. ASM,* Vol 60, 1967, p 67–68

23.46 P.J. Grobner, The 885 °F (475 °C) Embrittlement of Ferritic Stainless Steels, *Metall. Trans.,* Vol 4, 1973, p 251–260

23.47 T.J. Nichol, A. Datta, and G. Aggen, Embrittlement of Ferritic Stainless Steels, *Metall. Trans. A,* Vol 11, 1980, p 573–585

23.48 P.M. Unterweiser, H.E. Boyer, and J.J. Kubbs, Ed., *The Heat Treater's Guide,* American Society for Metals, 1982

23.49 D.C. Perry and J.C. Jasper, Structure and Constitution of Wrought Precipitation-Hardenable Stainless Steels, *Handbook of Stainless Steels,* McGraw-Hill, 1977, p 7–1 to 7–18

23.50 R. Smith, F.H. Wyche, and W. Gore, A Precipitation Hardening Stainless Steel of the 18 percent Chromium, 8 percent Nickel Type, *Trans. AIME,* Vol 167, 1946, p 313

23.51 G. Krauss, Jr. and B.L. Averbach, Retained Austenite in Precipitation Hardening Stainless Steels, *Trans. ASM,* Vol 52, 1960, p 434–450

23.52 T.J. Headley, M.M. Karnowsky, and W.R. Sorenson, Effect of Composition and High Energy Rate Forging on the Onset of Precipitation in an Iron-Base Superalloy, *Metall. Trans. A,* Vol 13, 1982, p 345–353

23.53 M.C. Mataya, M.J. Carr, and G. Krauss, Flow Localization and Shear Band Formation in a Precipitation Strengthened Austenitic Stainless Steel, *Metall. Trans. A,* Vol 13, 1982, p 1263–1274

23.54 R.A. Lula, Ed., *Duplex Stainless Steels,* American Society for Metals, 1983
23.55 H.D. Solomon and T.M. Devine, Jr., Duplex Stainless Steels—A Tale of Two Phases, *Duplex Stainless Steels,* R.A. Lula, Ed., American Society for Metals, 1983, p 693–756
23.56 T.A. DeBold, Duplex Stainless Steel—Microstructure and Properties, *J. Met.,* Vol 41 (No. 3), 1989, p 12–15
23.57 C.L. Beech, "Effect of Temperature and Strain Rate on the Mechanical Properties and Deformation Behavior of a Duplex Stainless Steel," M.S. thesis, Colorado School of Mines, Golden, CO, 1989
23.58 H.D. Solomon, Age Hardening in a Duplex Stainless Steel, *Duplex Stainless Steels,* R.A. Lula, Ed., American Society for Metals, 1983, p 41–69
23.59 R.N. Gunn, Ed., *Duplex Stainless Steels,* Abington Publishing, Cambridge, England, 1997
23.60 R. Lacombe, B. Baroux, and G. Beranger, Ed., *Stainless Steels,* Les Editions de Physique, Les Ulis, France, 1993 (English translation by J.H. Davidson and J.B. Lindquist)

CHAPTER 24

Tool Steels

TOOL STEELS are the steels used to form and machine other materials and therefore are designed to have high hardness and durability under severe service conditions. Tool steel heat treatment is similar to that of the hardenable low-alloy steels discussed earlier; that is, final properties are produced by austenitizing, martensite formation, and tempering. However, most tool steels are highly alloyed, and special precautions must be taken throughout processing to achieve the proper balance of alloy carbides in a matrix of tempered martensite for a given tool application. This chapter describes the alloy and process design of the various classes of tool steel and the microstructures produced during tool steel heat treatment.

Introduction

Tool steels are a very large group of complex alloys that have evolved for many diverse hot and cold forming applications. Their industrial importance and complexity have led to considerable text and handbook literature about their development, processing, and application (Ref 24.1–24.10). Details of processing, such as recommended cooling rates and heat treatment times and temperatures for specific steels, are found not only in the literature but also in detailed information distributed by major manufacturers of tool steels. The purpose of this chapter is to develop the principles of tool steel alloy design and to describe the role that heat treatment plays in the evolution of tool steel microstructure and properties.

Classification of Tool Steels

The various types of tool steels are categorized into a number of classes, each of which, according to essentially identical classification systems adopted by the American Iron and Steel Institute (AISI) and the Society of Automotive Engineers (SAE), is identified by a letter representing a

unique characteristic, chemistry, or use of that class of steels. Table 24.1 lists nominal chemistries and the various classes of tool steels (Ref 24.11). The listed tool steel designations are used throughout the balance of this chapter, and a brief summary of the major features of each class follows.

The water-hardening tool steels, AISI type W, have the lowest alloy content and therefore the lowest hardenability of any of the tool steels. As a result, the W tool steels frequently require water quenching, and heavy sections harden only to shallow depths. Thin sections can be hardened by oil quenching to minimize quench cracking and distortion.

The shock-resistant tool steels, AISI type S, have lower carbon content and somewhat higher alloy content than the W steels. The medium carbon content improves toughness and makes the type S steels good for applications with shock and impact loading.

Tool steels for cold work include three classes of steels: AISI types O, A, and D. All classes have high carbon content for high hardness and high wear resistance in cold work applications, but differ in alloy content, which affects hardenability and the carbide distributions incorporated into the hardened microstructures. The relatively low-alloyed oil-hardening grades, O, are oil quenched, but the high-alloyed A and D grades are hardenable by air cooling and therefore are less susceptible to distortion and cracking during hardening. The high chromium and molybdenum contents of the A and D tool steels also contribute to high carbide particle contents and excellent wear resistance. The low-alloy special-purpose tool steels, type L, by virtue of their somewhat lower carbon content, have higher toughness than do the O grades.

Tool steels used for dies to mold plastics, AISI type P, are exposed to less severe wear than metal-working steel and therefore have low carbon content. A key requirement is good polishability and excellent surface finish. Type 420 martensitic stainless steel is also used for plastic molds when corrosion may be a factor limiting performance of lower-alloyed P steels.

Hot work tool steels, AISI type H, fall into groups that have either chromium, tungsten, or molybdenum as the major alloying element. The H steels are used for hot forging, extrusion, and metal die-casting dies. The medium carbon content and relatively high alloy content make the H steels air hardenable and resistant to impact and softening during repeated exposure to hot working operations.

The high-speed tool steels are very highly alloyed, with tungsten and molybdenum as the major alloying elements in the T and M grades, respectively. The tungsten, molybdenum, chromium, and vanadium in these steels produce very high densities of stable carbides. As a result, the high-speed tool steels are capable of retaining hardness at temperatures as high as 600 °C (1112 °F) and are widely used for high-speed cutting and machining applications.

Maraging steels are also listed in Table 24.1 and are sometimes selected for tool and die applications. The maraging steels develop high strength

Table 24.1 Classification and approximate compositions of principal types of tool steels

		Identifying elements, %								
AISI	UNS	C	Mn	Si	Cr	V	W	Mo	Co	Ni
Water-hardening tool steels										
W1	T72301	0.60–1.40(a)	…	…	…	…	…	…	…	…
W2	T72302	0.60–1.40(a)	…	…	…	0.25	…	…	…	…
W5	T72305	1.10	…	…	0.50	…	…	…	…	…
Shock-resisting tool steels										
S1	T41901	0.50	…	…	1.50	…	2.50	…	…	…
S2	T41902	0.50	…	1.00	…	…	…	0.50	…	…
S5	T41905	0.55	0.80	2.00	…	…	…	0.40	…	…
S6	T41906	0.45	1.40	2.25	1.50	…	…	0.40	…	…
S7	T41907	0.50	…	…	3.25	…	…	1.40	…	…
Oil-hardening cold work tool steels										
O1	T31501	0.90	1.00	…	0.50	…	0.50	…	…	…
O2	T31502	0.90	1.60	…	…	…	…	…	…	…
O6(b)	T31506	1.45	0.80	1.00	…	…	…	0.25	…	…
O7	T31507	1.20	…	…	0.75	…	1.75	…	…	…
Air-hardening medium-alloy cold work tool steels										
A2	T30102	1.00	…	…	5.00	…	…	1.00	…	…
A3	T30103	1.25	…	…	5.00	1.00	…	1.00	…	…
A4	T30104	1.00	2.00	…	1.00	…	…	1.00	…	…
A6	T30106	0.70	2.00	…	1.00	…	…	1.25	…	…
A7	T30107	2.25	…	…	5.25	4.75	1.00(c)	1.00	…	…
A8	T30108	0.55	…	…	5.00	…	1.25	1.25	…	…
A9	T30109	0.50	…	…	5.00	1.00	…	1.40	…	1.50
A10(b)	T30110	1.35	1.80	1.25	…	…	…	1.50	…	1.80
High-carbon high-chromium cold work steels										
D2	T30402	1.50	…	…	12.00	1.00	…	1.00	…	…
D3	T30403	2.25	…	…	12.00	…	…	…	…	…
D4	T30404	2.25	…	…	12.00	…	…	1.00	…	…
D5	T30405	1.50	…	…	12.00	…	…	1.00	3.00	…
D7	T30407	2.35	…	…	12.00	4.00	…	1.00	…	…
Low-alloy special-purpose tool steels										
L2	T61202	0.50–1.10(a)	…	…	1.00	0.20	…	…	…	…
L6	T61206	0.70	…	…	0.75	…	…	0.25(c)	…	1.50
Mold steels										
P2	T51602	0.07	…	…	2.00	…	…	0.20	…	0.50
P3	T51603	0.10	…	…	0.60	…	…	…	…	1.25
P4	T51604	0.07	…	…	5.00	…	…	0.75	…	. . .
P5	T51605	0.10	…	…	2.25	…	…	…	…	. . .
P6	T51606	0.10	…	…	1.50	…	…	…	…	3.50
P20	T51620	0.35	…	…	1.70	…	…	0.40	…	. . .
P21	T51621	0.20	1.20(Al)	…	…	…	…	…	…	4.00
Chromium hot work tool steels										
H10	T20810	0.40	…	…	3.25	0.40	…	2.50	…	…
H11	T20811	0.35	…	…	5.00	0.40	…	1.50	…	…
H12	T20812	0.35	…	…	5.00	0.40	1.50	1.50	…	…
H13	T20813	0.35	…	…	5.00	1.00	…	1.50	…	…
H14	T20814	0.40	…	…	5.00	…	5.00	…	…	…
H19	T20819	0.40	…	…	4.25	2.00	4.25	…	4.25	…
Tungsten hot work tool steels										
H21	T20821	0.35	…	…	3.50	…	9.00	…	…	…
H22	T20822	0.35	…	…	2.00	…	11.00	…	…	…
H23	T20823	0.30	…	…	12.00	…	12.00	…	…	…
H24	T20824	0.45	…	…	3.00	…	15.00	…	…	…
H25	T20825	0.25	…	…	4.00	…	15.00	…	…	…
H26	T20826	0.50	…	…	4.00	1.00	18.00	…	…	…

(continued)

(a) Other carbon contents may be available. (b) Contains free graphite in the microstructure to improve machinability. (c) Optional. Source: Ref 24.11

Table 24.1 (continued)

AISI	UNS	Identifying elements, % C	Mn	Si	Cr	V	W	Mo	Co	Ni
Molybdenum hot work tool steels										
H42	T20842	0.60	…	…	4.00	2.00	6.00	5.00	…	…
Proprietary hot work tool steels										
6G	…	0.55	0.80	0.25	1.00	0.10	…	0.45	…	…
6F2	…	0.55	0.75	0.25	1.00	…	…	0.30	…	1.00
6F3	…	0.55	0.60	0.85	1.00	0.10	…	0.75	…	1.80
Tungsten high-speed tool steels										
T1	T12001	0.75(a)	…	…	4.00	1.00	18.00	…	…	…
T2	T12002	0.80	…	…	4.00	2.00	18.00	…	…	…
T2	T12004	0.75	…	…	4.00	1.00	18.00	…	5.00	…
T5	T12005	0.80	…	…	4.00	2.00	18.00	…	8.00	…
T6	T12006	0.80	…	…	4.50	1.50	20.00	…	12.00	…
T8	T12008	0.75	…	…	4.00	2.00	14.00	…	5.00	…
T15	T12015	1.50	…	…	4.00	5.00	12.00	…	5.00	…
Molybdenum high-speed tool steels										
M1	T11301	0.80(a)	…	…	4.00	1.00	1.50	8.00	…	…
M2	T11302	0.85–1.00(a)	…	…	4.00	2.00	6.00	5.00	…	…
M3 Class 1	T11313	1.05	…	…	4.00	2.40	6.00	5.00	…	…
M3 Class 2	T11323	1.20	…	…	4.00	3.00	6.00	5.00	…	…
M4	T11304	1.30	…	…	4.00	4.00	5.50	4.50	…	…
M6	T11306	0.80	…	…	4.00	2.00	4.00	5.00	12.00	…
M7	T11307	1.00	…	…	4.00	2.00	1.75	8.75	…	…
M10	T11310	0.85–1.00(a)	…	…	4.00	2.00	…	8.00	…	…
M30	T11330	0.80	…	…	4.00	1.25	2.00	8.00	5.00	…
M33	T11333	0.90	…	…	4.00	1.15	1.50	9.50	8.00	…
M34	T11334	0.90	…	…	4.00	2.00	2.00	8.00	8.00	…
M36	T11336	0.80	…	…	4.00	2.00	6.00	5.00	8.00	…
Ultrahard high-speed tool steels										
M41	T11341	1.10	…	…	4.25	2.00	6.75	3.75	5.00	…
M42	T11342	1.10	…	…	3.75	1.15	1.50	9.50	8.00	…
M43	T11343	1.20	…	…	3.75	1.60	2.75	8.00	8.25	…
M44	T11344	1.15	…	…	4.25	2.00	5.25	6.25	12.00	…
M46	T11346	1.25	…	…	4.00	3.20	2.00	8.25	8.25	…
M47	T11347	1.10	…	…	3.75	1.25	1.50	9.50	5.00	…

Maraging steels

Type	Identifying elements, % C	Mn	Si	Al	Ti	Mo	Co	Ni
Grade 90	0.03 max	0.10 max	0.12 max	0.10	0.30	3.25	8.50	18.00
Grade 110	0.03 max	0.10 max	0.12 max	0.10	0.50	4.85	7.75	18.00
Grade 125	0.03 max	0.10 max	0.12 max	0.10	0.70	5.00	9.00	18.00

(a) Other carbon contents may be available. (b) Contains free graphite in the microstructure to improve machinability. (c) Optional. Source: Ref 24.11

and hardness by quite different mechanisms (Ref 24.12, 24.13) than steels dependent on carbon content for strength. Despite low carbon content, the high cobalt and nickel content of the maraging steels ensures that martensite forms on air cooling. The low-carbon, low-strength martensite is then hardened by fine-scale precipitation of intermetallic compounds, such as Ni_3Mo, by aging at approximately 480 °C (896 °F). Excellent combinations of high strength and toughness are associated with the aged low-carbon martensitic microstructures, and the maraging steels are used for

many structural applications, including tools and dies, which require ultrahigh strength and toughness. Brandis and Haberling (Ref 24.9) describe maraging steels for hot work and plastic mold applications, and new grades of maraging steels, free of cobalt, are currently under active development (Ref 24.13).

Tool Steel Alloy Design

Tool steel alloy design is in large part based on alloying steel with strong carbide-forming transition elements such as chromium, molybdenum, tungsten, and vanadium. These elements partition between carbides and the austenitic matrix during solidification, hot work, annealing, and austenitizing for hardening. During hardening, the alloy carbides formed in austenite are retained, and the austenite matrix transforms to martensite. Further alloy-element partitioning occurs during tempering as retained austenite transforms and fine alloy carbides precipitate in tempered martensite. Strengthening and wear resistance are provided by all elements of the microstructure: the retained carbides, the tempered martensite, and the carbides formed on tempering.

Table 24.2 shows the carbides formed by the transition elements in the various groups of the periodic table (Ref 24.14). The transition metal carbides have very high hardness, high melting points, and unique electrical properties and are often used in pure form (Ref 24.14). Tungsten carbide (WC) is the major component of cemented carbide cutting tools, and transition metal carbide and nitride coatings (as discussed in Chapter 22, "Surface Modification," in this book) are increasingly being used to improve wear resistance of tool steels.

Table 24.2 Transition metal carbides

Carbide formation is fairly common among the transition elements, except for the second and third rows of group VIII(a)

III	IV	V	VI	VII	VIII		
$Sc_{2-3}C$ ScC_2 Sc_2C_3	TiC	V_2C VC	$Cr_{23}C_6$ Cr_7C_3 Cr_3C_2	$Mn_{23}C_6$ Mn_3C Mn_3C_2 Mn_7C_3	Fe_3C	Co_3C Co_2C	Ni_3C
Y_2C Y_2C_3 YC_2	ZrC	Nb_2C NbC	Mo_2C Mo_3C_2 MoC_{1-X}	TcC	Ru	Rh	Pd
LaC_2	HfC	Ta_2C TaC	W_2C W_3C_2 WC	ReC	OsC	Ir	Pt

(a) ☒ indicates no carbide formation for this element. Source: Ref 24.14

In steels, the transition metal carbide crystal structures incorporate iron atoms as well as several major carbide-forming elements, and therefore, the letter "M" is used to designate the total metal atom component of a carbide. Table 24.3 lists the types of carbides, crystal lattice, and some characteristics of each of the various carbides found in tool steels (Ref 24.3). The crystal structures of the carbides are described in detail by Jack and Jack (Ref 24.15).

The wear resistance of tool steels increases with increasing carbide volume fraction and carbide hardness. Figures 24.1 and 24.2 are two graphical comparisons of the hardness of various alloy carbides relative to the hardness of martensite and cementite, Fe_3C, the carbide typically found in plain carbon and low-alloy carbon steels. As shown, the transition metal carbides attain very high hardness and thus contribute significant wear resistance to tool steels, which are alloyed to contain large volume fractions of carbides. For example, high-speed tool steels may contain as much as 30 vol% of carbides consisting of a mixture of MC, $M_{23}C_6$, and M_6C (Ref 24.1).

The amount and type of carbides in a tool steel depend on carbon content, alloy content, and temperature. Isothermal and vertical sections through ternary Fe-*X*-C systems (where "*X*" represents a transition metal such as chromium) are available to predict the carbide phases that will form in a given ternary alloy (Ref 24.2). However, tool steels are more complex than ternary alloys, often containing three or four major alloying elements, as shown in Table 24.1. In the more complex steels, the carbides are identified and their amounts quantified by a variety of experimental techniques, including metallography, selective etching, x-ray diffraction and chemical analysis of extracted carbide residues, electron microprobe analysis, and scanning transmission electron microscopy. Another approach to characterizing the phases in tool steels is based on computing techniques that use thermodynamic functions to predict both carbide and matrix chemistry in complex systems (Ref 24.17–24.23). A discussion of

Table 24.3 Characteristics of alloy carbides found in tool steels

Type of carbide	Lattice type	Remarks
M_3C	Orthorhombic	This is a carbide of the cementite (Fe_3C) type. "M" may be Fe, Mn, Cr with a little W, Mo, V.
M_7C_3	Hexagonal	Mostly found in Cr alloy steels. Resistant to dissolution at higher temperatures. Hard and abrasion resistant. Found as a product of tempering high-speed steels
$M_{23}C_6$	Face-centered cubic	Present in high-Cr steels and all high-speed steels. The Cr can be replaced with Fe to yield carbides with W and Mo.
M_6C	Face-centered cubic	Is a W- or Mo-rich carbide. May contain moderate amounts of Cr, V, Co. Present in all high-speed steels. Extremely abrasion resistant
M_2C	Hexagonal	W- or Mo-rich carbide of the W_2C type. Appears after temper. Can dissolve a considerable amount of Cr
MC	Face-centered cubic	V-rich carbide. Resists dissolution. Small amount that does dissolve reprecipitates on secondary hardening

Source: Ref 24.3

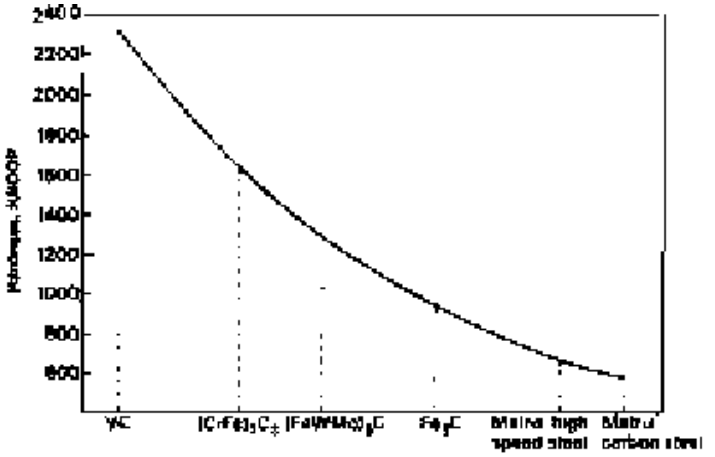

Fig. 24.1 Hardness comparisons of alloy carbides, cementite, and a carbon steel matrix. Source: Ref 24.3

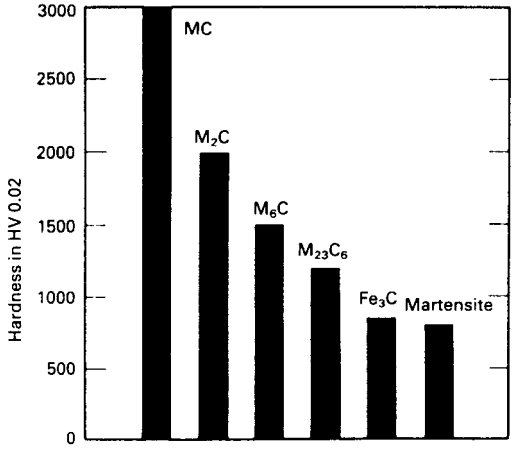

Fig. 24.2 Relative hardness of alloy carbides, cementite, and martensite in high-speed steels. Source: Ref 24.16

the thermodynamic calculations is outside the scope of this chapter, but the selected references show the growing use of these methods. The calculations are coupled to experimental determination of thermodynamic parameters and experimental verification of the phases and their compositions.

Examples of isothermal and vertical sections of portions of the Fe-Cr-C system are shown in Fig. 24.3 and 24.4 (Ref 24.24, 24.25). Compositions of some typical tool steels are plotted on the diagrams, and although the compositions are understated with respect to vanadium and molybdenum contents, it is instructive to relate the alloy compositions to the phase relationships demonstrated in the diagrams. The isothermal section shows

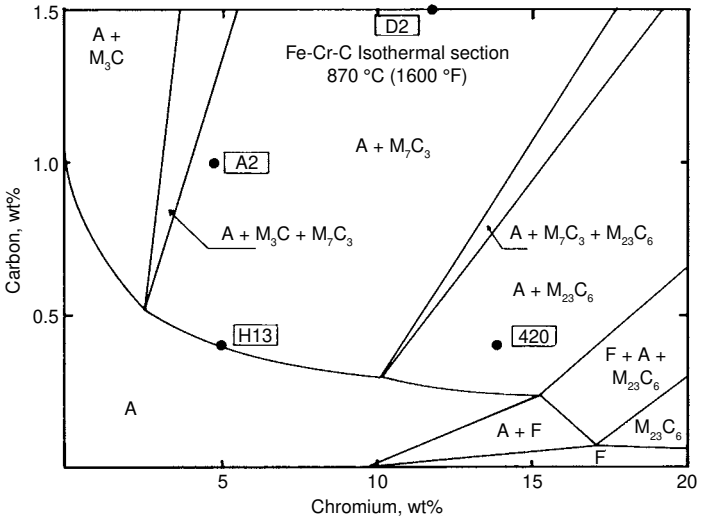

Fig. 24.3 Isothermal section of iron-rich corner of the Fe-Cr-C system at 870 °C (1598 °F). Compositions of alloys indicated are based only on chromium and carbon contents, but the alloys contain other elements that may introduce other phases. Source: Ref 24.24, 24.26

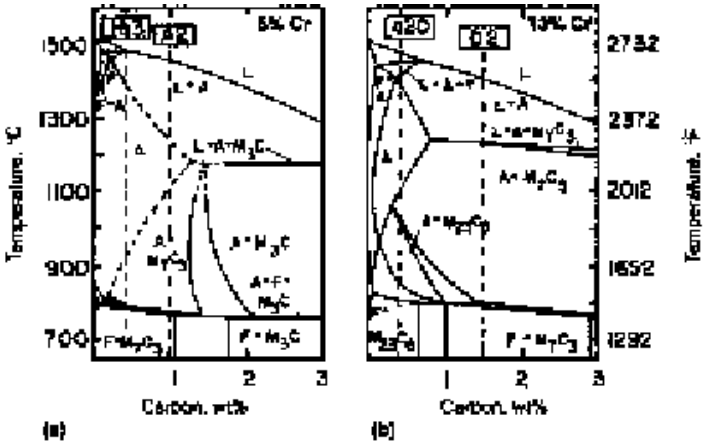

Fig. 24.4 Vertical sections for (a) 5% Cr and (b) 13% Cr. Vertical dashed lines represent alloys based only on chromium and carbon contents. A, F, and L designate austenite, ferrite, and liquid, respectively. Source: Ref 24.25, 24.26

the various carbides that coexist with austenite at 870 °C (1598 °F). As chromium content increases, the carbide chemistry and crystal structure changes from M_3C to M_7C_3 to $M_{23}C_6$ to accommodate increasing amounts of chromium atoms. The H-13, A-2, and D-2 tool steels all contain M_7C_3 carbides in equilibrium with austenite at 870 °C (1598 °F), and as the

carbon content of the steels increases from that of H-13 (0.4% C) to D-2 (1.50% C), the amount of M_7C_3 carbide increases.

The vertical sections (Fig. 24.4) are for Fe-Cr-C alloys containing 5 and 13 wt% Cr. Compositions of the coexisting phases usually lie outside the vertical section, but the sections show temperature ranges over which the various carbides coexist with austenite and ferrite. The latter information is useful in designing hot work schedules and heat treatments for annealing and hardening.

Primary Processing of Tool Steels

Figures 24.5 and 24.6 show schematically the thermomechanical processing and final heat treatment schedules applied to tool steels (Ref 24.26). Processing starts with melting and solidification. Tool steels are melted in electric arc or induction furnaces from carefully selected scrap and alloying additions, and for special high-quality grades, previously cast ingots may be subjected to consumable electrode vacuum or electroslag remelting and solidification (Ref 24.1–24.3, 24.6). Ingot size is generally kept small to reduce dendrite arm spacing and segregation during cooling. New processing techniques such as atomization of tool speed melts into fine powders and subsequent compaction are also being applied to provide highly homogeneous microstructures (Ref 24.3, 24.6).

The high alloy content of multicomponent tool steels results in significant segregation and primary alloy carbide formation during solidification. The high-speed tool steels, by virtue of their very high alloy content, have the most complex solidification sequence (Ref 24.6, 24.16, 24.27).

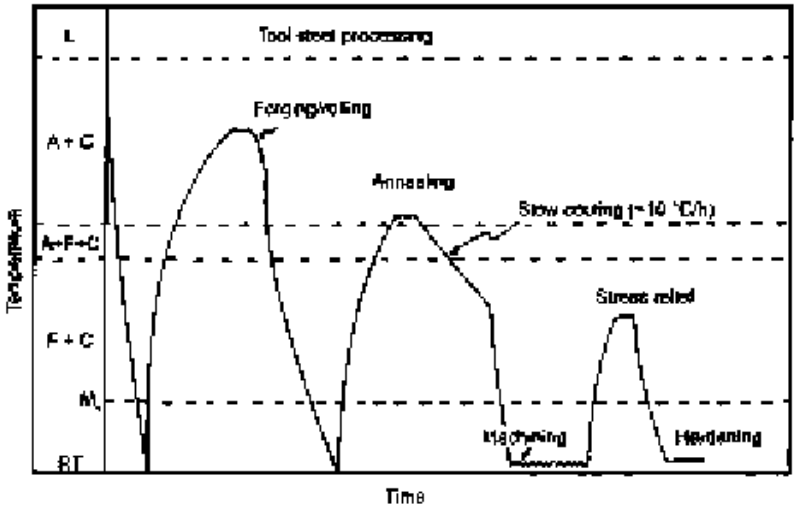

Fig. 24.5 Schematic diagram of tool steel processing up to the final hardening heat treatment. Source: Ref 24.26

Figures 24.7 and 24.8 show some of the microstructural features developed during solidification of an M2 high-speed steel. Solidification begins with the formation of primary dendrites of delta ferrite. Such a dendrite is shown in the center of Fig. 24.7, an x-ray microradiograph taken from a

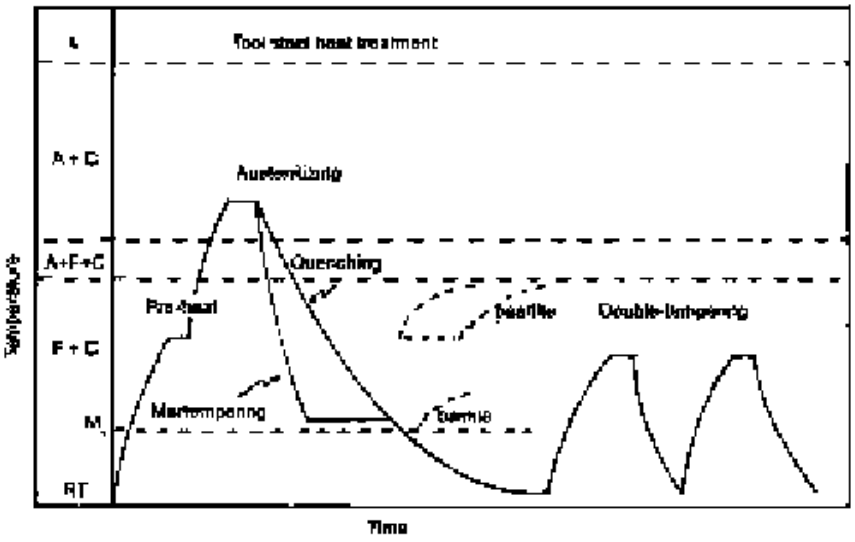

Fig. 24.6 Schematic diagram of tool steel hardening heat treatment steps. Source: Ref 24.26

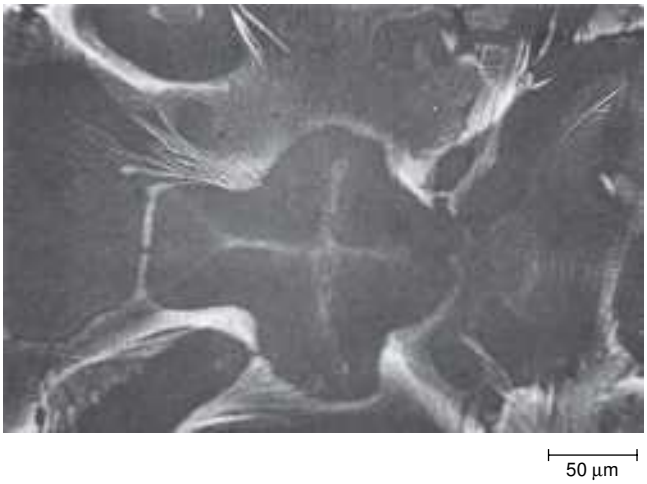

Fig. 24.7 Primary dendrite with axis normal to the plane of polish in an M2 high-speed steel. Microradiograph. Dark areas are due to exposure of x-ray film by transmitted radiation, and white areas are structures of higher absorption. Courtesy of R.H. Barkalow and R.W. Kraft, Lehigh University, Bethlehem, PA. Source: Ref 24.27

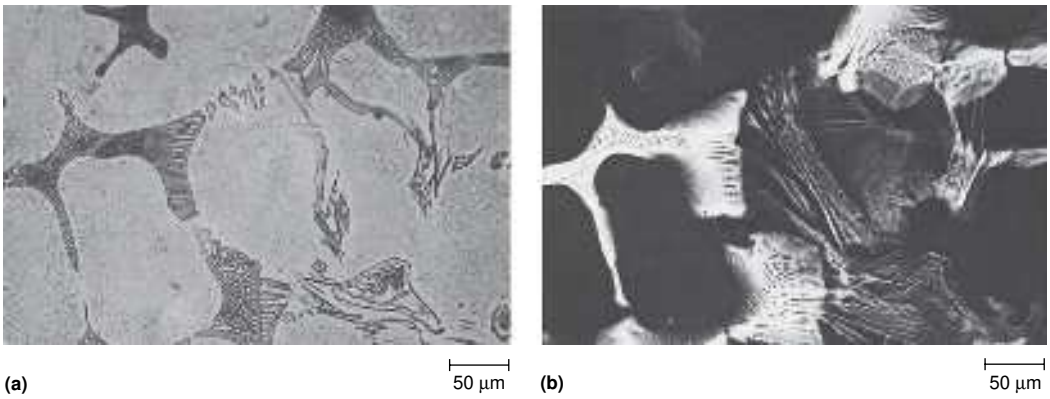

Fig. 24.8 Feathery, herringbone, and MC eutectics in M2 high-speed steel. (a) Light micrograph. $KMnO_4$ etch. (b) Microradiograph of same area. Chromium radiation. Courtesy of R.H. Barkalow and R.W. Kraft, Lehigh University, Bethlehem, PA. Source: Ref 24.27

thin specimen of the M2 steel. The micrograph is produced by exposure of an x-ray film to the transmitted x-ray radiation, and the light areas represent structure where alloying elements with high absorption coefficients are concentrated. The delta ferrite later transforms by a eutectoid reaction to an austenite-carbide aggregate. Following the formation of the primary ferrite crystals, a peritectic-type reaction causes some liquid to combine with the ferrite to form a rim of austenite around the dendrite arms. The remaining liquid is enriched in carbide-forming elements, and final solidification occurs by complex eutectic solidification, which produces several morphologies of carbides and austenite. Figure 24.8 shows examples of feathery (austenite plus M_6C and MC), herringbone (austenite plus M_6), and blocky (austenite plus MC) eutectic morphologies in M2 high-speed steel (Ref 24.27). Boccalini and Goldenstein (Ref 24.28) have written a comprehensive review of solidification in high-speed steels.

Following ingot solidification, tool steels are soaked at high temperatures and hot worked by forging, extrusion, or rolling in the temperature range of austenite or austenite-carbide stability. Roberts (Ref 24.29) has reviewed the dynamic recovery and recrystallization phenomena that affect the flow behavior of austenite during hot work of stainless and tool steels. Hot working not only reduces section size but also reduces segregation produced during solidification. Also, in high-speed steels, hot work breaks up the interconnected carbide structures formed by eutectic solidification. However, until sufficient homogenization has occurred, the carbides spheroidize and align in bands, causing anisotropy in hot ductility. The aligned alloy carbides may be sites of void formation and cracking, and consequently, highly alloyed tool steels require careful hot work to prevent cracking.

Annealing of Tool Steels

Following hot work to bar or plate, tool steels are machined into tools and dies of required shape. Annealing (Fig. 24.5) is required to put the hot work microstructures into a condition suitable for machining and subsequent hardening.

The objective of tool steel annealing treatments is to produce a microstructure consisting of uniformly dispersed spheroidized carbides in a matrix of ferrite. Such a microstructure has low hardness, which renders it machinable and reduces wear on cutting tools. Annealing also refines coarse-grained structures that may have formed during high-temperature hot work, eliminates hard martensite or pearlite microstructure that may have formed during cooling after hot work, and homogenizes the effects of nonuniform deformation that may have developed during hot work of complex or heavy sections.

Figure 24.9 shows the annealed microstructure of type D2 tool steel. The high alloy content of D2 causes two distributions of carbide particles to develop. The coarse particles are primary M_7C_3 carbides, which form during melting and are dispersed during hot work. The finer spheroidized particles are a result of secondary low-temperature precipitation or phase transformations. Tool steels with lower alloy content than D2 would have only the finer spheroidized carbides and lower carbide densities.

Annealing is accomplished by heating just to the temperature where all ferrite transforms to austenite. Carbide particles are retained and spheroidized, and the austenite transforms to ferrite and additional spheroidized carbides on cooling. If tool steels are annealed at too high a temperature, the

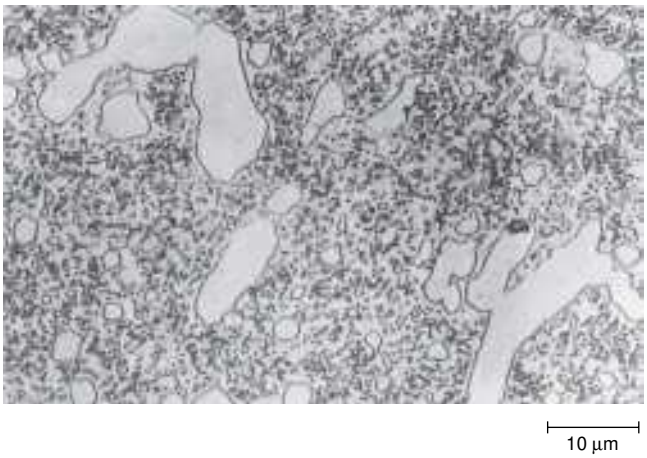

Fig. 24.9 Annealed microstructure of D2 tool steel. Light micrograph. Courtesy of J.R.T. Branco, Colorado School of Mines

alloy carbides dissolve and the enriched austenite may form carbides on austenitic grain boundaries or transform to pearlite or martensite on cooling, producing too hard a microstructure for good machinability. Similarly, the high hardenability of tool steels makes slow cooling from annealing temperatures essential to ensure that the austenite transforms to ductile ferrite-spheroidized carbide microstructures instead of pearlite or martensite.

Stress Relief of Tool Steels

Residual stresses may be introduced into tool steels by plastic deformation, which accompanies metal removal during machining operations. The residual stresses may cause distortion during heating and hardening and therefore must be removed by a low-temperature, subcritical heat treatment (Fig. 24.5). Stress relief is typically performed at 650 °C (1202 °F), where ferrite and carbides are stable. The carbides are largely unaffected by stress relief, but high dislocation densities in ferrite strained by machining are reduced by recovery or eliminated by recrystallization of the ferrite. Heavy sections should be very slowly cooled from 650 °C (1202 °F) to at least 300 °C (572 °F) after stress relief, according to Thelning (Ref 24.7). This precaution reduces temperature gradients between the surface and centers of heavy sections and thereby avoids the development of new residual stresses.

Hardening of Tool Steels

The final processing of tool steels consists of heat treating to produce the required hardness and other properties for a given steel and applications. Figure 24.6 shows that final hardening consists of a number of steps, including preheating, austenitizing, cooling or quenching, and tempering. The goal of this processing sequence most often is to produce a microstructure of tempered martensite. Sometimes, martempering to equalize temperature prior to martensite formation, or austempering to a microstructure of lower bainite, is performed by holding at temperatures above M_s (see Chapter 20, "Residual Stresses, Distortion, and Heat Treatment" in this book).

Preheating and Austenitizing

Highly alloyed tool steels, because of their high hardness and complex microstructures even in the annealed and stress-relieved state, are susceptible to distortion and cracking on heating if temperature gradients develop through a cross section. Such gradients cause expansion because of heating and contraction and because of austenite formation occurring in

different locations of a part. The resulting gradients in volume create stresses that sometimes are high enough to cause cracking, especially in tool steels with low ductility and low resistance to fracture. For these reasons, preheating is applied to alloy tool steels to establish thermal equilibrium prior to heating to the final austenitizing temperature (Ref 24.3, 24.7).

Austenitizing is a very critical step in the hardening of a tool steel. It is in this step where the final alloy element partitioning between the austenitic matrix (which will transform to martensite) and the retained carbides occurs. This partitioning fixes the chemistry, volume fraction, and dispersion of the retained carbides. The retained alloy carbides not only contribute to wear resistance but also control austenitic grain size. The finer the carbides and the larger the volume fraction of carbides, the more effectively austenitic grain growth is controlled. Thus, if austenitizing is performed at too high a temperature, undesirable grain growth may occur as the alloy carbides increasingly coarsen or dissolve into the austenite. A special case of grain coarsening is associated with rehardening high-speed tool steel. Kula and Cohen (Ref 24.30) showed that the discontinuous growth that leads to coarse-grained intergranular fracture or "fish-scale" fracture was due to this dissolution of fine carbides formed from martensitic or bainitic microstructures during a second austenitizing. The discontinuous coarsening did not occur in high-speed tool steels with spheroidized carbide-ferrite microstructures.

The alloying elements not tied up in retained carbides are in solution in the austenite, and thus the carbides provide an important mechanism by which austenite composition is fixed. The austenite composition then sets the hardenability, M_s temperature, retained austenite content, and secondary hardening potential of a tool steel.

Figure 24.10 shows the effect of increasing austenitizing temperature on the as-quenched, as-quenched and subzero cooled, and tempered hardness of an A2 tool steel (Ref 24.7). The highest as-quenched hardness is produced by austenitizing at 950 °C (1742 °F), the recommended austenitizing temperature for A2. In this condition after quenching, the retained austenite content is finely dispersed and at a minimum, and therefore, subzero cooling has little effect on hardness. With increasing austenitizing temperature, more alloying elements go into solution, the M_s temperature drops, and more austenite is retained at room temperature. As a result, the as-quenched room-temperature hardness decreases, and subzero cooling has a greater effect as more of the large volume fraction of retained austenite transforms to martensite on subzero cooling. Figure 24.10 shows that eventually tempering, by a combination of retained austenite transformation and secondary hardening, will also raise the hardness of asquenched structures with large amounts of retained austenite. Not shown is the deleterious increase in austenite grain size that develops as more and more carbides dissolve at the higher austenitizing temperatures (Ref 24.7).

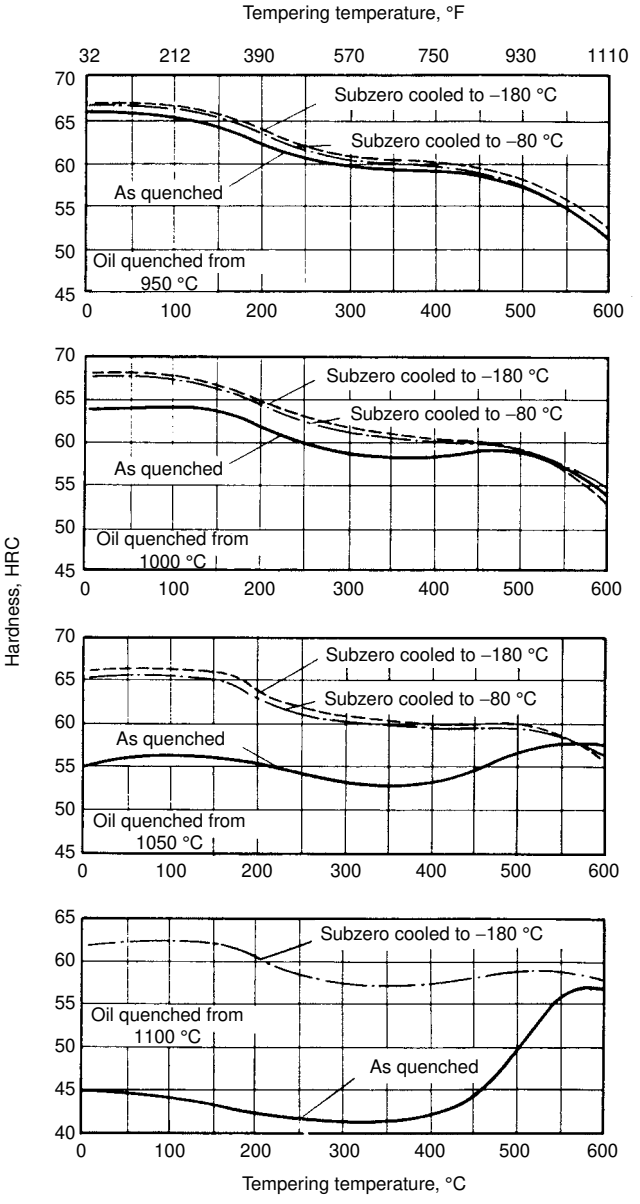

Fig. 24.10 Influence of austenitizing and tempering temperatures on hardness of A2 tool steel. Source: Ref 24.7

Hardenability and Martensite Formation

The hardenability of most tool steels is high; therefore, oil quenching or air cooling, depending on alloy composition, austenitizing conditions, and section size, is sufficient to produce required microstructures and proper-

ties with a minimum of distortion and quench cracking. Medium- carbon, low-alloy steels have been extensively evaluated for hardenability, as discussed in Chapter 16, "Hardness and Hardenability," in this book, and Jatczak (Ref 24.31) has evaluated the effects of various alloying elements on the hardenability of high-carbon steels. An important difference between medium-carbon hardenable steels and high-carbon tool steels is the strong effect of austenitizing and retained carbide content on hardenability. For example, high austenitizing temperatures decrease alloy carbide content, increase the alloy element content of the matrix austenite, and consequently increase hardenability relative to low austenitizing temperatures applied to the same steel. Therefore, the effects of alloying elements on hardenability in high-carbon steels may be quite different depending on austenitizing conditions (Ref 24.31).

Martensite forms in tool steels when cooling conditions and hardenability are sufficient to prevent diffusion-controlled transformation to proeutectoid carbides, pearlite, and bainite. The matrix austenite composition determines the morphology of the martensite microstructure (see Chapter 5, "Martensite," in this book). Figure 24.11 shows lath martensite formed in H-13 steels, and Fig. 24.12 shows plate martensite formed in A-2 steel. In both microstructures, retained austenite and retained carbides are present, but to a much lesser extent in the H-13 steel than in the A-2 steel. The retained austenite is present in thin sheets between the parallel martensite laths of the H-13 steel, and as triangular regions between the nonparallel plates of the A-2 steel. Although there are many crystallographic variants of the martensite laths or plates formed in a given austenite grain, all of the austenite retained in a given austenite grain has the same orientation despite its quite dispersed appearance within the martensite. The austenite retained after quenching may be transformed to martensite by subzero

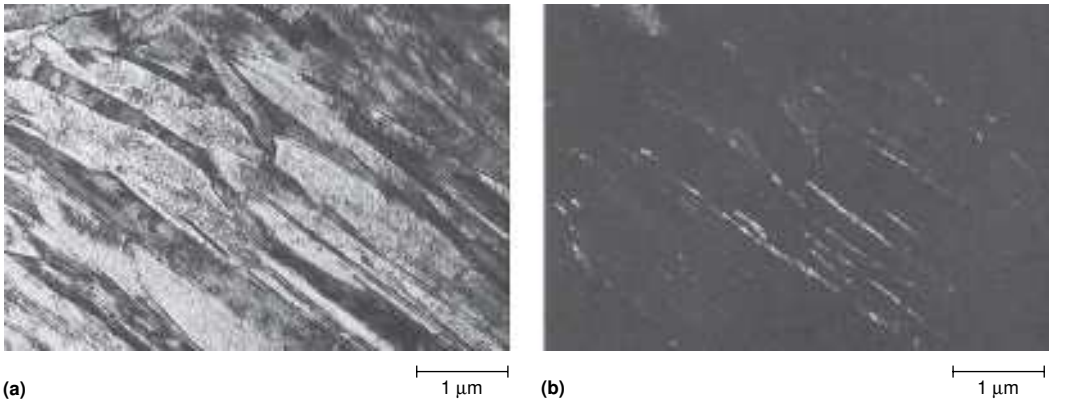

Fig. 24.11 Lath martensite formed in H-13 tool steel. (a) Bright-field image. (b) Dark-field image of same area illuminating interlath retained austenite. Transmission electron micrographs. Courtesy of J.R.T. Branco, Colorado School of Mines

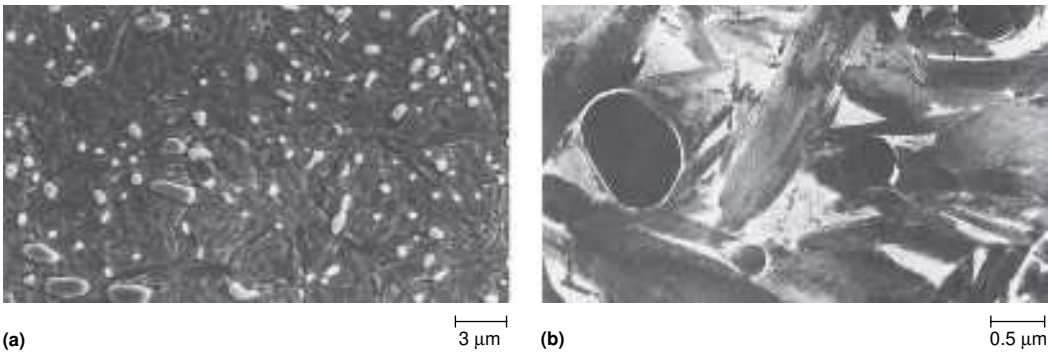

Fig. 24.12 Retained carbides and plate martensite formed in A2 tool steel. (a) Scanning electron micrograph. Courtesy of A. Wahid, Colorado School of Mines, Golden, CO. (b) Transmission electron micrograph showing martensite, retained carbides, and retained austenite. Courtesy of J.R.T. Branco, Colorado School of Mines

cooling, as discussed relative to Fig. 24.10, or more commonly is transformed to carbides and ferrite during high-temperature tempering.

Grain-Boundary Carbide Formation

Tool steels are susceptible to grain-boundary carbide formation during relatively slow oil quenching or air cooling for hardening. Figure 24.13 shows schematically the effects of three cooling rates on the transformation of a typical tool steel. The high hardenability of tool steels effectively suppresses pearlite formation at all cooling rates. Bainite formation is also readily suppressed except in heavy sections, which cool slowly. However, the formation of small amounts of carbides on austenite grain boundaries is difficult to suppress, as shown by the intersection of the two slower cooling rates with the carbide initiation curve, C_i. The small amounts of carbides do not significantly affect hardness but may lower tool steel fracture resistance, leading to quench cracking, intergranular fracture of overheated tool steels, or reduced performance of hot work die steels such as H-13 (Ref 24.32–24.34).

Phosphorus segregates to austenite grain boundaries during austenitizing for hardening and contributes to fracture problems in high-carbon steel. The combination of segregated phosphorus and high carbon content leads to cementite grain-boundary allotriomorph formation even during oil quenching (Ref 24.35, 24.36), and the phosphorus and carbides lower the fracture strength of the prior-austenite grain boundaries (Ref 24.37, 24.38). As a result, if quenching or service stresses are high enough, failure by intergranular cracking occurs, especially in steels with coarse austenitic grain sizes. The susceptibility to grain-boundary cracking is reduced by maintaining recommended austenitizing temperatures, which in most tool steels of high carbon content are designed to produce fine austenitic

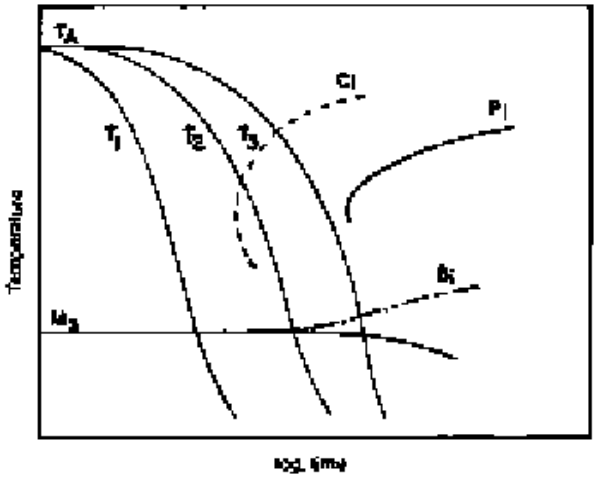

Fig. 24.13 Schematic continuous cooling diagram for a typical tool steel. Cooling rates in decreasing order are represented by T_1, T_2, T_3, and C_i, P_i, and B_i represent the initiation of carbide, pearlite, and bainite formation, respectively. Source: Ref 24.26

grain sizes. The latter microstructures, when hardened and tempered at low temperatures, fracture by transgranular shear or ductile fracture associated with microvoid formation around the retained carbide particles (Ref 24.38).

Tempering of Tool Steels

Tempering is the final heat treatment step applied to tool steels (Fig. 24.6). As in the lower-alloy steels discussed in Chapter 17, "Tempering of Steel," in this book, tempering has the important function of improving toughness in both low-alloy and tool steels. However, secondary hardening or the precipitation of alloy carbides at high tempering temperatures is much more important in tool steels than in low-alloy steels. Also, double or even triple tempering steps are applied to tool steels to ensure that toughness is improved after microstructural changes are induced by the first tempering steps.

Figures 24.14 to 24.16 show examples of hardness as a function of tempering temperature for A-2, H-13 (Ref 24.39), and several high-speed tool steels (Ref 24.40), respectively. The curves for the A-2 and H-13 are based on double tempering and that of the high-speed steels on triple tempering. Each tempering treatment was at least 2 h in duration. The peak hardness associated with secondary hardening at approximately 500 °C (932 °F) increases with increasing alloy content and depends, as discussed earlier, on the balance of retained carbides, retained austenite, and the composition of the martensite in the as-quenched condition. In the A-2

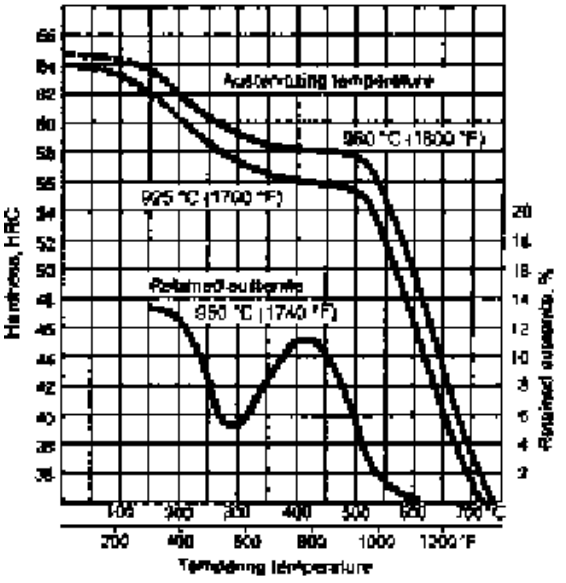

Fig. 24.14 Hardness and retained austenite as a function of tempering temperature for A-2 tool steel. Source: Ref 24.39

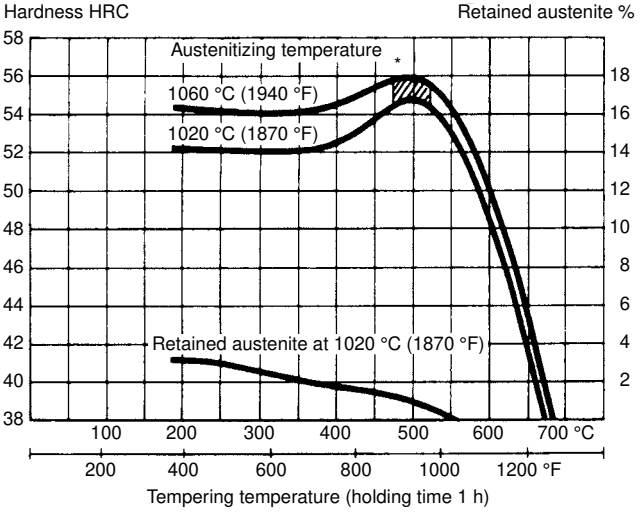

Fig. 24.15 Hardness and retained austenite as a function of tempering temperature for H-13 tool steel. Source: Ref 24.39

and H-13 steels, higher martensite carbon content offsets the effects of increased retained austenite on hardness in the specimens austenitized at the higher temperatures.

The formation of alloy carbides during tempering requires the diffusion of carbide-forming elements. The atoms of the latter mostly diffuse sub-

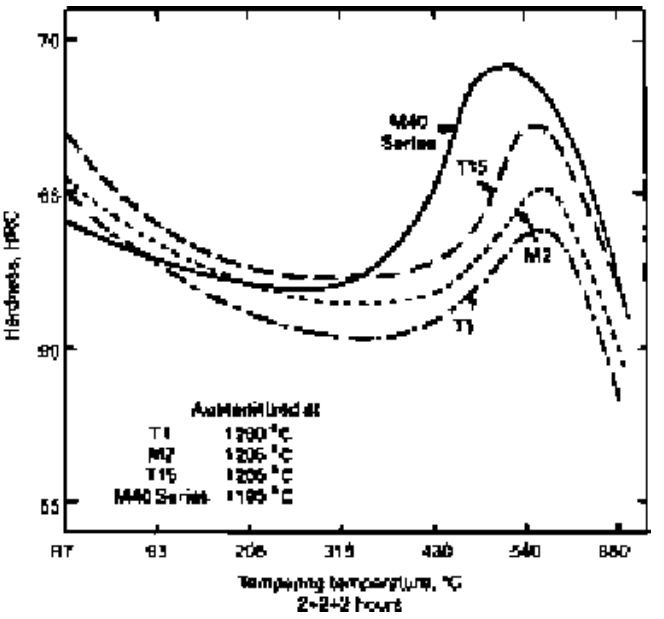

Fig. 24.16 Hardness as a function of tempering temperature for various high-speed tool steels. Source: Ref 24.40

stitutionally through the body-centered cubic iron lattice of the tempered martensite, a process characterized by low diffusion coefficients. The sluggish diffusion makes effective diffusion distances very short, leading to very fine, closely spaced alloy-carbide precipitates. The same sluggish diffusion retards carbide coarsening during high-temperature service and makes tool steels resistant to softening during hot forging, die casting, and high-speed cutting operations.

At low tempering temperatures, transition iron carbides and cementite (M_3C) form, as discussed in Chapter 17, "Tempering of Steel," in this book. At higher tempering temperatures, because of increased diffusivity of the alloying elements, alloy carbides precipitate. Honeycombe (Ref 24.41) has reviewed alloy carbide formation on tempering and shown that many of the alloy carbides form as fine discs or needles on preferred crystallographic habit planes within the plates or laths of tempered martensite. Figure 24.17 shows fine precipitates formed in a lath of tempered martensite in H-13 steel tempered at 550 °C (1022 °F).

The crystallography and composition of the alloy carbides that form during tempering are very sensitive to the specific alloying elements present. In tool steels containing chromium, the sequence of precipitation with increasing tempering may be M_3C, then M_7C_3, followed by $M_{23}C_6$ (Ref 24.42), while in tool steels rich in molybdenum, the sequence may be M_3C, followed by M_2C, followed by M_6C (Ref 24.43). Binary carbides,

Fig. 24.17 Alloy carbides in a lath of martensite in H-13 tool steel tempered 100 h at 550 °C (1022 °F). Transmission electron micrograph. Courtesy of J.R.T. Branco, Colorado School of Mines

that is, those formed between a single element and carbon, coarsen readily during tempering or in high-temperature service. Carbides composed of multiple alloying elements coarsen at lower rates. Multiple alloying may also change the sequence of carbide precipitation just noted. For example, $M_{23}C_6$ may form after M_2C and prior to M_6C in steels with high ratios of chromium and molybdenum to carbon (Ref 24.26).

Retained Austenite Transformation and Double Tempering in Tool Steels

Retained austenite transforms to ferrite and cementite during tempering. In low-alloy steels, retained austenite transforms to cementite and ferrite between 200 and 300 °C (392 and 572 °F) (see Chapter 17, "Tempering of Steel," in this book). The austenite in highly alloyed tool steels, however, is much more stable and does not fully transform until temperatures in excess of 500 °C (932 °F) are attained, as shown in Fig. 24.14 and 24.15. Figure 24.18 shows interlath carbides that have formed in H-13 steel tempered at 600 °C (1112 °F). The carbides are rather coarse and planar, and similar carbide distributions may be responsible for the drop in impact toughness noted in H-13 steels tempered between 475 and 535 °C (887 and 995 °F). Double tempering would tend to spheroidize and render less harmful interlath carbides formed by the transformation of retained austenite. Double tempering is also believed to temper any martensite that may have formed by transformation of retained austenite to martensite during cooling after the first tempering treatment.

Fig. 24.18 Interlath carbides (arrow) formed in H-13 tool steel tempered at 600 °C (1112 °F) for 2 h. Transmission electron micrograph. Courtesy of J.R.T. Branco, Colorado School of Mines. Source: Ref 24.26

Summary

This chapter has reviewed the principles of alloying and processing on the properties and microstructures of tool steels. Tool steels have evolved to perform machining and the most difficult hot and cold forming operations on steels and other materials, and considerable practical information about selection, processing, heat treatment, and performance has been generated over the years (Ref 24.1–24.20). Research continues to improve processing, alloying, and performance. Factors that control strength and toughness are of special concern in tool steels that inherently have low toughness (Ref 24.44–24.46). A model for evaluating cutting performance of high-speed tool steels based on matrix strengthening and undissolved carbides has been proposed in a paper that also provides a good review of applicable literature (Ref 24.47). Other tool steel developments have been presented in international conferences held every two or three years since 1987. The proceedings volumes from these conferences provide excellent reviews of the developing state-of-the-art in tool steel science and technology (Ref 24.9, 24.48–24.51).

REFERENCES

24.1 G.A. Roberts and R.A. Cary, *Tool Steels,* 4th ed., American Society for Metals, 1980

24.2 G. Roberts, G. Krauss, and R. Kennedy, *Tool Steels,* 5th ed., ASM International, 1998

24.3 R. Wilson, *Metallurgy and Heat Treatment of Tool Steels,* McGraw-Hill, London, 1975

24.4 P. Payson, *The Metallurgy of Tool Steels,* Wiley, New York, 1962
24.5 M.G.H. Wells and L.W. Lherbier, Ed., *Processing and Properties of High Speed Tool Steels,* TMS-AIME, Warrendale, PA, 1980
24.6 G. Hoyle, *High Speed Steels,* Butterworths, London, 1988
24.7 K.-E. Thelning, *Steel and Its Heat Treatment,* 2nd ed., Butterworths, London, 1984
24.8 J.R. Davis, Ed., Tool Steels, *Metals Handbook Desk Edition,* 2nd ed., ASM International, 1998, p 346–361
24.9 G. Krauss and H. Nordberg, Ed., *Tool Materials for Molds and Dies,* Colorado School of Mines Press, Golden, CO, 1987
24.10 *Properties and Selection: Irons, Steels, and High-Performance Alloys,* Vol 1, *ASM Handbook,* ASM International, 1990
24.11 P.D. Harvey, Ed., *Heat Treatment of Tool Steels,* Metals Engineering Institute, American Society for Metals, 1981
24.12 S. Floreen, The Physical Metallurgy of Maraging Steels, *Met. Rev.,* Vol 12, 1968, p 115–128
24.13 R.K. Wilson, Ed., *Maraging Steels—Recent Developments and Applications,* TMS-AIME, Warrendale, PA, 1988
24.14 L.E. Toth, *Transition Metal Carbides and Nitrides,* Academic Press, New York, 1971
24.15 D.H. Jack and K.N. Jack, Carbides and Nitrides in Steels, *Mater. Sci. Eng.,* Vol 11, 1973, p 1–27
24.16 H. Brandis, E. Haberling, and H.H. Weigard, Metallurgical Aspects of Carbides in High Speed Steels, *Processing and Properties of High Speed Tool Steels,* M.G.H. Wells and L.W. Lherbier, Ed., TMS-AIME, Warrendale, PA, 1980, p 1–18
24.17 B. Uhrenius and H. Harvig, A Thermodynamic Evaluation of Carbide Solubilities in the Fe-Mo-C, Fe-W-C, and Fe-Mo-W-C Systems at 1000 °C, *Met. Sci.,* Vol 9, 1975, p 67–81
24.18 T. Wada and E.K. Ohriner, Phase Equilibrium in the Fe-Mo-W-C Systems Containing $(Mo_{0.7}W_{0.3})C$ Carbide, *CALPHAD,* Vol 8, 1984, p 69–74
24.19 H. Wada, Thermodynamics of the Fe-Cr-C System at 985 K, *Metall. Trans. A,* Vol 16, 1985, p 1479–1490
24.20 S. Hertzman, A Study of Equilibria in the Fe-Cr-Ni-Mo-C-N System at 1273 K, *Metall. Trans. A,* Vol 18, 1987, p 1767–1778
24.21 J.-O. Andersson, A Thermodynamic Evaluation of the Fe-Cr-C System, *Metall. Trans. A,* Vol 19, p 627–636
24.22 P. Gustafson, An Experimental Study and a Thermodynamic Evaluation of the Cr-Fe-W System, *Metall. Trans. A,* Vol 19, 1988, p 2531–2546
24.23 P. Gustafson, A Thermodynamic Evaluation of the C-Cr-Fe-W System, *Metall. Trans. A,* Vol 19, 1988, p 2547–2554
24.24 L.R. Woodyatt and G. Krauss, Iron-Chromium-Carbon System at 870 °C, *Metall. Trans. A,* Vol 7, 1976, p 983–989

24.25 K. Bungardt, E. Kunze, and E. Horn, Investigation of the Structure of the Iron-Chromium-Carbon System, *Arch. Eisenhüttenwes.,* Vol 29, 1958, p 193

24.26 J.R.T. Branco and G. Krauss, Heat Treatment and Microstructure of Tool Steels for Molds and Dies, *Tool Materials for Molds and Dies,* G. Krauss and H. Nordberg, Ed., Colorado School of Mines Press, Golden, CO, 1987, p 94–117

24.27 R.K. Barkalow, R.W. Kraft, and J.I. Goldstein, Solidification of M2 High Speed Steel, *Metall. Trans. A,* Vol 3, 1972, p 919–926

24.28 M. Boccalini and H. Goldenstein, Solidification of High Speed Steels, *Int. Mater. Rev.,* Vol 46, 2001, p 92–115

24.29 W. Roberts, Dynamic Changes That Occur during Hot Working and Their Significance Regarding Microstructural Development and Hot Workability, *Deformation, Processing, and Structure,* G. Krauss, Ed., American Society for Metals, 1984, p 109–184

24.30 E. Kula and M. Cohen, Grain Growth in High Speed Steel, *ASM Trans.,* Vol 46, 1954, p 727–798

24.31 C.F. Jatczak, Hardenability in High Carbon Steels, *Metall. Trans.,* Vol 4, 1973, p 2267–2277

24.32 H. Nilsson, O. Sandberg, and W. Roberts, Influence of Austenitization Temperature and the Cooling Rate after Austenitization on the Mechanical Properties of the Hot Work Tool Steel H-11 and H-13, *Tools for Die Casting,* Uddeholm and Swedish Institute for Metals Research, 1983, p 51–70

24.33 M.L. Schmidt, Effect of Austenitizing Temperature on Laboratory Treated and Large Section Sizes of H-13 Tool Steel, *Tool Materials for Molds and Dies,* G. Krauss and H. Nordberg, Ed., Colorado School of Mines Press, Golden, CO, 1987, p 118–164

24.34 D.L. Cocks, Longer Die Life from H-13 Die Casting Dies by the Practical Applications of Recent Research Results, *Tool Materials for Molds and Dies,* G. Krauss and H. Nordberg, Ed., Colorado School of Mines Press, Golden, CO, 1987, p 340–350

24.35 H.M. Obermeyer and G. Krauss, Toughness and Intergranular Fracture of a Simulated Carburized Case in Ex-24 Type Steel, *J. Heat Treat.,* Vol 1 (No. 3), 1980, p 31–39

24.36 T. Ando and G. Krauss, The Effect of Phosphorus Content on Grain Boundary Cementite Formation in AISI 52100 Steel, *Metall. Trans. A,* Vol 12, 1981, p 1283–1290

24.37 D.L. Yaney, "The Effects of Phosphorus and Tempering on the Fracture of AISI 52100 Steel," M.S. thesis, Colorado School of Mines, Golden, CO, 1981

24.38 G. Krauss, The Relationship of Microstructure to Fracture Morphology and Toughness of Hardened Hypereutectoid Steels, *Case-Hardened Steels: Microstructural and Residual Stress Effects,* D.E. Diesburg, Ed., TMS-AIME, Warrendale, PA, 1983, p 33–58

24.39 "Cold Work Tool Steel (AISI A2)" and "Hot Work Tool Steel (AISI H13)," Data sheets, Uddeholm Steel Division, Hagfors, Sweden
24.40 S.G. Fletcher and C.R. Wendell, *ASM Met. Eng. Q.,* Feb 1, 1966, in G. Hoyle, *High Speed Steels,* Butterworths, London, 1988, p 146
24.41 R.W.K. Honeycombe, *Steels: Microstructure and Properties,* Edward Arnold Ltd. and American Society for Metals, 1982
24.42 R.G. Baker and J. Nutting, The Tempering of 2.25%Cr-1%Mo Steel for Quenching and Normalizing, *J. Iron Steel Inst.,* Vol 192, 1959, p 257–268
24.43 K.H. Kuo and C.L. Jia, Crystallography of $M_{23}C_6$ and M_6C Precipitate in a Low Alloy Steel, *Acta Metall.,* Vol 33, 1985, p 991–996
24.44 F.B. Pickering, The Properties of Tool Steels for Mold and Die Applications, *Tool Materials for Molds and Dies,* G. Krauss and H. Nordberg, Ed., Colorado School of Mines Press, Golden, CO, 1987, p 3–32
24.45 H. Berns, Strength and Toughness of Hot Working Tool Steels, *Tool Materials for Molds and Dies,* G. Krauss and H. Nordberg, Ed., Colorado School of Mines Press, Golden, CO, 1987, p 45–65
24.46 R.M. Hemphill and D.E. Wert, Impact and Fracture Toughness Testing of Common Grades of Tool Steels, *Tool Materials for Molds and Dies,* G. Krauss and H. Nordberg, Ed., Colorado School of Mines Press, Golden, CO, 1987, p 66–91
24.47 S. Karagöz and H.F. Fischmeister, Cutting Performance and Microstructure of High Speed Steels: Contributions of Matrix Strengthening and Undissolved Carbides, *Metall. Mater. Trans. A,* Vol 29, 1998, p 205–216
24.48 H. Berns, H. Nordberg, and H.-J. Fleischer, Ed., *New Materials and Processes for Tooling,* Verlag Schürmann & Klaffes KG, Bochum, Germany, 1989
24.49 H. Berns, M. Hofmann, L.-A. Norstrom, K. Rasche, and A.-M. Schindler, Ed., *New Materials Processes Experiences for Tooling,* MAT SEARCH, Andelfingen, Switzerland, 1992
24.50 H. Berns, H.-F. Hinz, and I.-M. Hucklenbroich, Ed., *Progress in Tool Steels,* Verlag Schürmann & Klagges, Bochum, Germany, 1996
24.51 F. Jeglitsch, R. Ebner, and H. Leitner, Ed., *Tool Steels in the Next Century,* Montanuniversita¨t Leoben, Leoben, Austria, 1999

APPENDIX

Hardness Conversions

Approximate equivalent hardness numbers and tensile strengths for steels(a)

Vickers hardness No.	Brinell hardness No. 3000 kg load 10 mm ball		Rockwell hardness No.				Rockwell superficial hardness No., superficial Brale indenter			Knoop hardness No., 500 g load and greater	Shore Scleroscope hardness No.	Tensile strength (approx.) 1000 psi	Vickers hardness No.
	Standard ball	Tungsten carbide ball	A scale, 60 kg load, Brale indenter	B scale, 100 kg load, ⅛ in. diam ball	C scale, 150 kg load, Brale indenter	D scale, 100 kg load, Brale indenter	15N scale, 15 kg load	30N scale, 30 kg load	45N scale, 45 kg load				
940	. . .	. . .	**85.6**	. . .	**68.0**	**76.9**	**93.2**	**84.4**	**75.4**	920	97	. . .	940
920	. . .	. . .	**85.3**	. . .	**67.5**	**76.5**	**93.0**	**84.0**	**74.8**	908	96	. . .	920
900	. . .	. . .	**85.0**	. . .	**67.0**	**76.1**	**92.9**	**83.6**	**74.2**	895	95	. . .	900
880	. . .	(767)	**84.7**	. . .	**66.4**	**75.7**	**92.7**	**83.1**	**73.6**	882	93	. . .	880
860	. . .	(757)	**84.4**	. . .	**65.9**	**75.3**	**92.5**	**82.7**	**73.1**	867	92	. . .	860
840	. . .	**(745)**	**84.1**	. . .	**65.3**	**74.8**	**92.3**	**82.2**	**72.2**	852	91	. . .	840
820	. . .	**(733)**	**83.8**	. . .	**64.7**	**74.3**	**92.1**	**81.7**	**71.8**	837	90	. . .	820
800	. . .	**(722)**	**83.4**	. . .	**64.0**	**73.8**	**91.8**	**81.1**	**71.0**	822	88	. . .	800
780	. . .	**(710)**	**83.0**	. . .	**63.3**	**73.3**	**91.5**	**80.4**	**70.2**	806	87	. . .	780
760	. . .	**(698)**	**82.6**	. . .	**62.5**	**72.6**	**91.2**	**79.7**	**69.4**	788	86	. . .	760
740	. . .	**(684)**	**82.2**	. . .	**61.8**	**72.1**	**91.0**	**79.1**	**68.6**	772	84	. . .	740
720	. . .	**(670)**	**81.8**	. . .	**61.0**	**71.5**	**90.7**	**78.4**	**67.7**	754	83	. . .	720
700	. . .	**(656)**	**81.3**	. . .	**60.1**	**70.8**	**90.3**	**77.6**	**66.7**	735	81	. . .	700
690	. . .	**(647)**	**81.1**	. . .	**59.7**	**70.5**	**90.1**	**77.2**	**66.2**	725	. . .	. . .	690
680	. . .	**(638)**	**80.8**	. . .	**59.2**	**70.1**	**89.8**	**76.8**	**65.7**	716	80	355	680
670	. . .	**(630)**	**80.6**	. . .	**58.8**	**69.8**	**89.7**	**76.4**	**65.3**	706	. . .	348	670
660	. . .	**620**	**80.3**	. . .	**58.3**	**69.4**	**89.5**	**75.9**	**64.7**	697	79	342	660
650	. . .	**611**	**80.0**	. . .	**57.8**	**69.0**	**89.2**	**75.5**	**64.1**	687	78	336	650
640	. . .	**601**	**79.8**	. . .	**57.3**	**68.7**	**89.0**	**75.1**	**63.5**	677	77	328	640
630	. . .	**591**	**79.5**	. . .	**56.8**	**68.3**	**88.8**	**74.6**	**63.0**	667	76	323	630
620	. . .	**582**	**79.2**	. . .	**56.3**	**67.9**	**88.5**	**74.2**	**62.4**	657	75	317	620
610	. . .	**573**	**78.9**	. . .	**55.7**	**67.5**	**88.2**	**73.6**	**61.7**	646	. . .	310	610
600	. . .	**564**	**78.6**	. . .	**55.2**	**67.0**	**88.0**	**73.2**	**61.2**	636	74	303	600
590	. . .	**554**	**78.4**	. . .	**54.7**	**66.7**	**87.8**	**72.7**	**60.5**	625	73	298	590
580	. . .	**545**	**78.0**	. . .	**54.1**	**66.2**	**87.5**	**72.1**	**59.9**	615	72	293	580
570	. . .	**535**	**77.8**	. . .	**53.6**	**65.8**	**87.2**	**71.7**	**59.3**	604	. . .	288	570
560	. . .	**525**	**77.4**	. . .	**53.0**	**65.4**	**86.9**	**71.2**	**58.6**	594	71	283	560
550	**(505)**	**517**	**77.0**	. . .	**52.3**	**64.8**	**86.6**	**70.5**	**57.8**	583	70	276	550
540	**(496)**	**507**	**76.7**	. . .	**51.7**	**64.4**	**86.3**	**70.0**	**57.0**	572	69	270	540
530	**(488)**	**497**	**76.4**	. . .	**51.1**	**63.9**	**86.0**	**69.5**	**56.2**	561	68	265	530
520	**(480)**	**488**	**76.1**	. . .	**50.5**	**63.5**	**85.7**	**69.0**	**55.6**	550	67	260	520
510	**(473)**	**479**	**75.7**	. . .	**49.8**	**62.9**	**85.4**	**68.3**	**54.7**	539	. . .	254	510

(continued)

(a) For carbon and alloy steels in the annealed, normalized, and quenched-and-tempered conditions; less accurate for cold-worked condition and for austenitic steels. The values in boldface type correspond to the values in the joint SAE-ASM-ASTM hardness conversions as printed in ASTM E 140, Table 1. The values in parentheses are beyond normal range and are given for information only.

Approximate equivalent hardness numbers and tensile strengths for steels(a) (continued)

Vickers hardness No.	Brinell hardness No. 3000 kg load 10 mm ball		Rockwell hardness No.				Rockwell superficial hardness No., superficial Brale indenter			Knoop hardness No., 500 g load and greater	Shore Scleroscope hardness No.	Tensile strength (approx.) 1000 psi	Vickers hardness No.
	Standard ball	Tungsten carbide ball	A scale, 60 kg load, Brale indenter	B scale, 100 kg load, ⅛ in. diam ball	C scale, 150 kg load, Brale indenter	D scale, 100 kg load, Brale indenter	15N scale, 15 kg load	30N scale, 30 kg load	45N scale, 45 kg load				
500	**(465)**	**471**	**75.3**	. . .	**49.1**	**62.2**	**85.0**	**67.7**	**53.9**	528	66	247	500
490	**(456)**	**460**	**74.9**	. . .	**48.4**	**61.6**	**84.7**	**67.1**	**53.1**	517	65	241	490
480	**(448)**	**452**	**74.5**	. . .	**47.7**	**61.3**	**84.3**	**66.4**	**52.2**	505	64	235	480
470	**441**	**442**	**74.1**	. . .	**46.9**	**60.7**	**83.9**	**65.7**	**51.3**	494	. . .	228	470
460	**433**	**433**	**73.6**	. . .	**46.1**	**60.1**	**83.6**	**64.9**	**50.4**	482	62	223	460
450	**425**	**425**	**73.3**	. . .	**45.3**	**59.4**	**83.2**	**64.3**	**49.4**	471	. . .	217	450
440	**415**	**415**	**72.8**	. . .	**44.5**	**58.8**	**82.8**	**63.5**	**48.4**	459	59	212	440
430	**405**	**405**	**72.3**	. . .	**43.6**	**58.2**	**82.3**	**62.7**	**47.4**	447	58	205	430
420	**397**	**397**	**71.8**	. . .	**42.7**	**57.5**	**81.8**	**61.9**	**46.4**	435	57	199	420
410	**388**	**388**	**71.4**	. . .	**41.8**	**56.8**	**81.4**	**61.1**	**45.3**	423	56	193	410
400	**379**	**379**	**70.8**	. . .	**40.8**	**56.0**	**80.8**	**60.2**	**44.1**	412	55	187	400
390	**369**	**369**	**70.3**	. . .	**39.8**	**55.2**	**80.3**	**59.3**	**42.9**	400	. . .	181	390
380	**360**	**360**	**69.8**	(110.0)	**38.8**	**54.4**	**79.8**	**58.4**	**41.7**	389	52	175	380
370	**350**	**350**	**69.2**	. . .	**37.7**	**53.6**	**79.2**	**57.4**	**40.4**	378	51	170	370
360	**341**	**341**	**68.7**	(109.0)	**36.6**	**52.8**	**78.6**	**56.4**	**39.1**	367	50	164	360
350	**331**	**331**	**68.1**	. . .	**35.5**	**51.9**	**78.0**	**55.4**	**37.8**	356	48	159	350
340	**322**	**322**	**67.6**	(108.0)	**34.4**	**51.1**	**77.4**	**54.4**	**36.5**	346	47	155	340
330	**313**	**313**	**67.0**	. . .	**33.3**	**50.2**	**76.8**	**53.6**	**35.2**	337	46	150	330
320	**303**	**303**	**66.4**	(107.0)	**32.2**	**49.4**	**76.2**	**52.3**	**33.9**	328	45	146	320
310	**294**	**294**	**65.8**	. . .	**31.0**	**48.4**	**75.6**	**51.3**	**32.5**	318	. . .	142	310
300	**284**	**284**	**65.2**	(105.5)	**29.8**	**47.5**	**74.9**	**50.2**	**31.1**	309	42	138	300
295	**280**	**280**	**64.8**	. . .	**29.2**	**47.1**	**74.6**	**49.7**	**30.4**	305	. . .	136	295
290	**275**	**275**	**64.5**	(104.5)	**28.5**	**46.5**	**74.2**	**49.0**	**29.5**	300	41	133	290
285	**270**	**270**	**64.2**	. . .	**27.8**	**46.0**	**73.8**	**48.4**	**28.7**	296	. . .	131	285
280	**265**	**265**	**63.8**	(103.5)	**27.1**	**45.3**	**73.4**	**47.8**	**27.9**	291	40	129	280
275	**261**	**261**	**63.5**	. . .	**26.4**	**44.9**	**73.0**	**47.2**	**27.1**	286	39	127	275
270	**256**	**256**	**63.1**	(102.0)	**25.6**	**44.3**	**72.6**	**46.4**	**26.2**	282	38	124	270
265	**252**	**252**	**62.7**	. . .	**24.8**	**43.7**	**72.1**	**45.7**	**25.2**	277	. . .	122	265
260	**247**	**247**	**62.4**	(101.0)	**24.0**	**43.1**	**71.6**	**45.0**	**24.3**	272	37	120	260
255	**243**	**243**	**62.0**	. . .	**23.1**	**42.2**	**71.1**	**44.2**	**23.2**	267	. . .	117	255
250	**238**	**238**	**61.6**	99.5	**22.2**	**41.7**	**70.6**	**43.4**	**22.2**	262	36	115	250
245	**233**	**233**	**61.2**	. . .	**21.3**	**41.1**	**70.1**	**42.5**	**21.1**	258	35	113	245
240	**228**	**228**	**60.7**	98.1	**20.3**	**40.3**	**69.6**	**41.7**	**19.9**	253	34	111	240
230	219	219	. . .	96.7	(18.0)	. . .	. . .	. . .	. . .	243	33	106	230
220	209	209	. . .	95.0	(15.7)	. . .	. . .	. . .	. . .	234	32	101	220

(continued)

(a) For carbon and alloy steels in the annealed, normalized, and quenched-and-tempered conditions; less accurate for cold-worked condition and for austenitic steels. The values in boldface type correspond to the values in the joint SAE-ASM-ASTM hardness conversions as printed in ASTM E 140, Table 1. The values in parentheses are beyond normal range and are given for information only.

Approximate equivalent hardness numbers and tensile strengths for steels(a) (continued)

Vickers hardness No.	Brinell hardness No. 3000 kg load 10 mm ball		Rockwell hardness No.				Rockwell superficial hardness No., superficial Brale indenter			Knoop hardness No., 500 g load and greater	Shore Scleroscope hardness No.	Tensile strength (approx.) 1000 psi	Vickers hardness No.
	Standard ball	Tungsten carbide ball	A scale, 60 kg load, Brale indenter	B scale, 100 kg load, ⅛ in. diam ball	C scale, 150 kg load, Brale indenter	D scale, 100 kg load, Brale indenter	15N scale, 15 kg load	30N scale, 30 kg load	45N scale, 45 kg load				
210	200	200	. . .	93.4	(13.4)	. . .	. . .	. . .	. . .	226	30	97	210
200	190	190	. . .	91.5	(11.0)	. . .	. . .	. . .	. . .	216	29	92	200
190	181	181	. . .	89.5	(8.5)	. . .	. . .	. . .	. . .	206	28	88	190
180	171	171	. . .	87.1	(6.0)	. . .	. . .	. . .	. . .	196	26	84	180
170	162	162	. . .	85.0	(3.0)	. . .	. . .	. . .	. . .	185	25	79	170
160	152	152	. . .	81.7	(0.0)	. . .	. . .	. . .	. . .	175	23	75	160
150	143	143	. . .	78.7	. . .	. . .	. . .	. . .	. . .	164	22	71	150
140	133	133	. . .	75.0	. . .	. . .	. . .	. . .	. . .	154	21	66	140
130	124	124	. . .	71.2	. . .	. . .	. . .	. . .	. . .	143	20	62	130
120	114	114	. . .	66.7	. . .	. . .	. . .	. . .	. . .	133	18	57	120
110	105	105	. . .	62.3	. . .	. . .	. . .	. . .	. . .	123	. . .	. . .	110
100	95	95	. . .	56.2	. . .	. . .	. . .	. . .	. . .	112	. . .	. . .	100
95	90	90	. . .	52.0	. . .	. . .	. . .	. . .	. . .	107	. . .	. . .	95
90	86	86	. . .	48.0	. . .	. . .	. . .	. . .	. . .	102	. . .	. . .	90
85	81	81	. . .	41.0	. . .	. . .	. . .	. . .	. . .	97	. . .	. . .	85

(a) For carbon and alloy steels in the annealed, normalized, and quenched-and-tempered conditions; less accurate for cold-worked condition and for austenitic steels. The values in boldface type correspond to the values in the joint SAE-ASM-ASTM hardness conversions as printed in ASTM E 140, Table 1. The values in parentheses are beyond normal range and are given for information only.

Index

B

C

D

E

F

G

H

I

J

K

L

M

N

O

P

Q

R

S

T

U

V

W

X

Y

Z